AD-A242 752

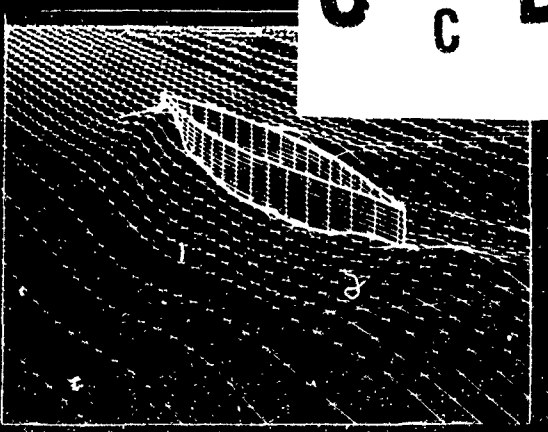
The Proceedings

Third International Conference on Numerical Ship Hydrodynamics

June 16-19, 1981

Palais des Congrès, Paris, France

DTIC
ELECTE
NOV 12 1991
S C D



DISTRIBUTION STATEMENT
Approved for public release;
Distribution Unlimited

AD-A242 752

The Proceedings

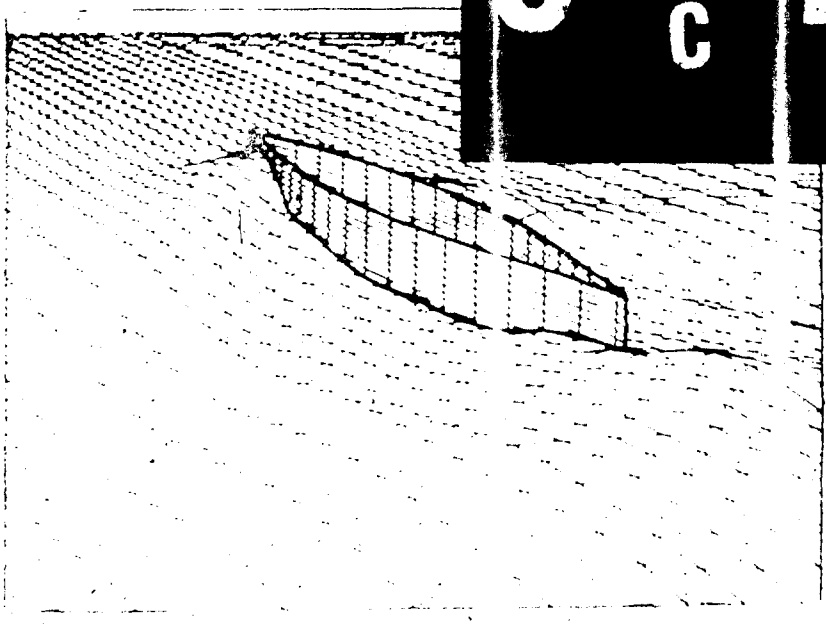
Third International Conference on

Numerical Ship Hydrodynamics

June 16-19, 1981

Palais des Congrès, Paris, France

DTIC
ELECTE
NOV 12 1991
S C D



DISTRIBUTION STATEMENT A
Approved for public release;
Distribution Unlimited

DTNSRDC TECH INF CTR

Carderock Collection

OCT 08 1985

842365

91-15348

91 1108 082

The
Proceedings

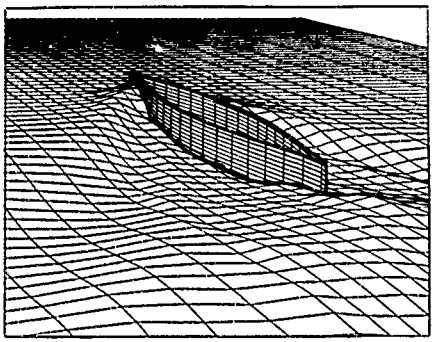
Third International Conference on

Numerical Ship Hydrodynamics

Edited by
Jean-Claude Dern
and
Henry J. Haussling

Sponsored by
Office of Naval Research
David W. Taylor
Naval Ship Research and Development Center
&
Délégation Générale pour l'Armement
Direction des Recherches, Études et Techniques
Direction Technique des Constructions Navales
Bassin d'Essais des Carènes

June 16-19, 1981
Palais des Congrès
Paris, France



Bassin d'Essais des Carènes
8 boulevard Victor
75732 Paris Cedex 15

QUALITY INSPECTED 4

Accession For
NTIS GRA&I
DTIC TAB
Unannounced
Justification
By
Distribution/
Availability Codes
Dist | Avail and/or Special
A-1

Dedicated
to the late
Dr. Richard B. Chapman
and
Dr. Jean-François Demanche

ORDERING INFORMATION

Third International Conference on Numerical Ship Hydrodynamics
may be ordered by mailing a request to the following address :

Mrs. Christiane Chamaud
Bassin d'Essais des Carènes
8, boulevard Victor
75732 Paris Cedex 15
France

Please include name, address, zip code and country in all requests

---

Bassin d'Essais des Carènes, 1982

All rights reserved
No part of this publication may be reproduced,
stored in a retrieval system
or transmitted in any form or by any means,
electronic, mechanical photocopying, recording or otherwise,
without the prior permission of the copyright owner

PREFACE

The Third International Conference on Numerical Ship Hydrodynamics was held in Paris, France, on 16-19 June 1981 at the Palais des Congrès. The Conference was sponsored jointly by the Délégation Générale pour l'Armement, the David W. Taylor Naval Ship Research and Development Center and the Office of Naval Research

For a third time researchers from throughout the world came together to present and discuss their latest work in this rapidly evolving and increasingly more important specialty. While the first two Conferences were quite international in character, this meeting was the first of the series held outside of the United States and hence the multinational nature of the research was even further highlighted. Perhaps partly because of both the location in Europe and the large time span of four years since the previous meeting, such a large number of high quality papers were submitted that the Conference duration was extended to four days from the originally planned three. Even so, many good papers had to be rejected

It was gratifying to see that so many researchers are tackling the important and difficult vortex flow problems. On the other hand, it was disappointing to receive very little response to the call for papers in the areas of boundary layer flows, flow induced structural vibrations, and hydrodynamic noise. Perhaps this lack of response will serve to stimulate researchers to consider the opportunities in these challenging areas

As usual, the success of this Conference was due to the collective efforts of a large number of individuals This opportunity is taken to mention the contributions of those whose efforts would otherwise be unrecorded. The personal help of Professor Daniel Euvrard is gratefully acknowledged Special thanks go to Mr Arestier and his staff in the Reprography Service who worked efficiently in preparing all the preprints associated with the Conference. Finally, we wish to thank Mrs Christiane Chamaud, Secretary to the Conference for her invaluable assistance in the many aspects of the organization of the Conference Thanks are also due to Mrs Evelyne Lescureux of the Documentation Service who contributed to the success of the Conference

ORGANIZATION AND PAPERS COMMITTEE

Co-chairmen

Jean Claude Dern
Henry J. Haussling

Members

Ralph D Cooper
Robert E. Whitehead
Hans J. Lugt
Justin H McCarthy
Joanna W Schot
Bohyun Yim
Max Aucher
Jean François Demanche
Colmar Rehbach

CONTENTS

Preface V

OPENING SESSION

Introductory Address, Max Aucher, Director of Bassin d'Essais des Carènes 1

Opening Address, Jean Touffait, Directeur Technique des Constructions Navales 3

SESSION I NONLINEAR WAVES AND WAVE RESISTANCE

Chairman J V. Wehausen, University of California, U S A.

Invited Paper **Some Free-Surface Phenomena Around Ships to be Challenged by Numerical Analysis,** E Baba 9

Free-Surface Potential Flow Computation Using a Finite Element Method, A. Oomen 27

Numerical Explanation of Nonlinear Nondispersive Waves Around Bow, H Miyata, A Suzuki and H. Kajitani 37

A Ray Theory for Nonlinear Ship-Waves and Wave Resistance, B-Yim 55

A Numerical Approach of the Nonlinear Wave Resistance Problem, O Daube and A Dulieu 73

SESSION II NONLINEAR WAVES AND WAVE RESISTANCE

Chairman J H McCarthy, David W Taylor Naval Ship Research and Development Center, U S A

Numerical Studies of the Neumann-Kelvin Problem for a Two-Dimensional Semi-Submerged Body, K Suzuki 83

Parabolic Approximations for Ship Waves and Wave Resistance, J M Vanden Broeck and J B Keller 97

Nonlinear Waves Behind an Accelerated Transom Stern, R M Coleman and H J Haussling 111

Flow About Transom Sterns, R T Van Eseltine and H J. Haussling 121

Analysis of a Breaking Free Surface Wave Using Boundary Fitted Coordinates for Regions Including Reentrant Boundaries, U Ghia, C T Shin and K N Ghia 133

SESSION III TRANSIENT AND NONLINEAR SOLUTIONS TO BODY-WAVE AND WATER WAVE PROBLEM

Chairman J W. Schot, David W Taylor Naval Ship Research and Development Center, U S A

Invited Paper **A Short Review of Mathematics and Numerical Methods in Transient Ship Hydrodynamics,** D Euvrard 151

Implementation of Open Boundary Conditions for Nonlinear Free Surface Wave Problems, S M Yen and D R Hall 163

Applications of a Generalized Vortex Method to Nonlinear Free Surface Flows, G R Baker, D I Meiron and S A. Orszag 179

Recent Progress Towards an Optimal Coupling of Finite Elements and Singularity Distribution Procedures, D Euvrard, A. Jami, M Lenoir, D Martin 193

Numerical Solving of Transient Linear Hydrodynamic Problems by Coupling Finite Element and Integral Representation, A Jami 211

Time-Dependent Behaviour of Floating Bodies, C Licht 221

SESSION IV TRANSIENT AND NONLINEAR SOLUTIONS TO BODY WAVE AND WATER WAVE PROBLEM

Chairman R Whitehead, Office of Naval Research, U S A

Time-Domain Method for Computing Forces and Moments Acting on Three Dimensional Surface-Piercing Ship Hulls with Forward Speed, R B Chapman 237

Three-Dimensional Time Dependent Nonlinear Ship Motion Simulation Using the Inertial Marker Particle Technique, G I Bounianoff 249

Nonlinear Ship Motions, Tor Vinje and Per Brevig 257

A Numerical Simulation of Large Amplitude Sloshing, T J Bridges 269

Three-Dimensional Instabilities of Finite Amplitude Gravity Waves, J W McLean, Y C Ma, D U Martin, P G Saffman and H C Yuen 285

SESSION V VORTEX FLOWS AND LIFTING BODIES

Chairman S Bindel, Direction des Recherches, Études et Techniques, France

Invited Paper **Numerical Modelling of Vortex Flows in Ship Hydrodynamics A Review,** H J Lugt 297

A Discrete Vortex Analysis of Flow About Non-Circular Cylinders, R L Shoaff and C B Franks 319

Calculation of Vortex-Shedding Flow Around Oscillating Circular and Lewis-Form Cylinders, Y Ikeda and Y. Himeno 335

Hydrodynamic Forces of the Oscillating Flat Plate, K Kudo 347

Multigrid Methods Applied to a Water Wave Problem, S McCormick and J W Thomas 359

Advanced Numerical Methods Hydrofoil System Design and Experimental Verification, W M Feifel 365

SESSION VI VORTEX FLOWS AND LIFTING BODIES

Chairman M Aucher, Bassin d'Essais des Carènes, France

Unsteady 3-D Lifting-Surface Theory with the Free-Surface Effect, J Leclerc and P Saisün 379

Base-Ventilated Foils, R Baubeau 387

Supercavitating Hydrofoils in Nonlinear Theory, C Pellone and A. Rowe 399

Forces on Rudders Behind a Maneuvering Ship, H Söding 415

Propeller-Induced Hull Pressures and Forces, J P Breslin 427

SESSION VII FLOATING BODIES IN WAVES

Chairman P Guével, École Nationale Supérieure de Mécanique, Nantes, France

A Localized Finite Element Method for Three-Dimensional Ship Motion Problems, K J Bai 449

Computation of Relative Motion of Ships to Waves, C M Lee 465

The Interaction of an Incident Wave Field with a Floating Slender Body at Zero Speed, P D Sclavounos 481

Radiation Forces on Ships with Forward Speed, R W Yeung and S H Kim 499

Forces and Moments in the Rigid Connections Between a Barge and its Tug with Forward Speed in Wave, J Bougis and P Vellier 517

Potential of a Moving Pulsating Source, J F Demanche 533

SESSION VIII : WATER WAVES AND FLOATING BODIES

Chairman : R D. Cooper, Flow Research, U S.A.

On the Null-Field Equations for Water-Wave Radiation Problems, P.A. Martin and F. Ursell 543

Some Results on Approximation by Exponential Series Applied to Hydrodynamic Problems, J C Daubisse 551

Solution of Two-Dimensionel Stamming by Meane of Finite Pressure Elements L.J Doctors . 559

Initial Asymptotics in Problem of Blunt Body Entrance into Liquid, V V. Pukhnachov and A.A. Korobkin 579

List of Participants 593

Index to Authors and Discussers 599

SÉANCE D'OUVERTURE
DE LA TROISIÈME CONFÉRENCE INTERNATIONALE
D'HYDRODYNAMIQUE NAVALE NUMÉRIQUE

Max Aucher
Directeur du Bassin d'Essais des Carènes

Mesdames et Messieurs,

Je vous souhaite à tous la bienvenue à cette 3ème Conférence Internationale d'Hydrodynamique Navale Numérique et j'espère que vous y trouverez un très grand intérêt.

Des participants sont venus de tous les coins du monde pour y assister. Il serait trop fastidieux d'énumérer ici tous les pays représentés. Le résultat d'une telle représentation sera, j'en suis sûr, que les communications présentées et discussions qui suivront, assureront une large diffusion internationale des travaux de cette conférence.

La première chose que j'ai à faire maintenant et la plus importante peut-être est de vous présenter l'Ingénieur Général Touffait, Directeur Technique des Constructions Navales, qui représente Monsieur Martre, Délégué Général de l'Armement. Monsieur Martre avait bien voulu accepter la Présidence d'Honneur de cette Conférence. Malheureusement, d'autres obligations dues à l'importance de sa charge ne lui permettent pas de participer personnellement à cette séance d'ouverture de la conférence, ce qu'il regrette très vivement.

Bien qu'il ne soit pas hydrodynamicien, l'Ingénieur Général Touffait a un long passé d'architecte naval essentiellement pour les sous-marins. Les problèmes qui lui ont été posés l'ont amené à fréquenter les hydrodynamiciens chargés d'étudier le comportement de ces navires en immersion profonde, mais aussi en surface et en plongée à faible immersion. Il a pu ainsi saisir l'importance croissante que prenait dans la conduite de ces études, le calcul numérique aidé par l'existence de calculateurs de plus en plus rapides et puissants.

Monsieur l'Ingénieur Général Touffait, c'est avec plaisir que je vous passe la parole.

Jean Touffait
Directeur Technique des Constructions Navales

Mesdames et Messieurs,

Confirmant les propos de Monsieur Aucher je me dois tout d'abord d'exprimer de la part de Monsieur Martre Délégué Général pour l'Armement ses très vifs regrets de ne pouvoir présider l'ouvertur de ce Congrès.

En tant que Directeur Technique des Constructions Navales de la Marine Nationale Française, c'est un honneur et un plaisir pour moi que de souhaiter la bienvenue à tous les participants de cette 3ème Conférence sur le Calcul Numérique en Hydrodynamique Navale , c'est aussi une tâche difficile pour un non spécialiste d'essayer de vous dire en quelques mots comment il ressent vos préoccupations.

C'est un grand honneur pour le Bassin d'Essais des Carènes de Paris qui fait partie de ma Direction d'avoir été choisi par l'Office of Naval Research et le David Taylor Naval Ship Research and Development Center comme première institution étangère chargée d'organiser hors des Etats-Unis cette Conférence sur les applications des méthodes de calcul avancées à l'Hydrodynamique Navale

Je suis heureux de constater que vous êtes nombreux, que beaucoup de participants sont venus parfois de très loin pour assister à cette Conférence , j'espère que tous trouveront à la fois un vif intérêt professionnel en écoutant les nombreux exposés techniques prévus, et un vif intérêt touristique en visitant Paris en dehors des séances de travail.

Neuf ans se sont déjà écoulés depuis le 9ème Symposium d'Hydrodynamique Navale tenu à Paris en 1972 et il n'est que de consulter les articles publiés à cette époque, et les conférences qui vont être faites ici aujourd'hui et les prochains jours pour apprécier le développement qu'a pris le calcul numérique dans le domaine de l'hydrodynamique navale.

Le calcul numérique est devenu à la fois une science et un art qui fait que les théories mathématiques les plus complexes peuvent être exploitées par les Ingénieurs

Dans un passé encore récent, les Ingénieurs cherchant à approfondir la connaissance des phénomènes,soucieux, comme moi, d'obtenir ces résultats concrets et chiffrés susceptibles d'étayer des décisions en matière d'architecture navale, avaient le choix entre deux possibilités extrêmes : linéariser les problèmes ou espérer que des savants mathématiciens arriveraient à trouver des solutions mathématiques à des systèmes d'équations fort complexes.

Mais, la linéarisation des problèmes pour faciliter la résolution des équations a fait que pendant longtemps les travaux théoriques des hydrodynamiciens ont porté sur des formes géométriques simples ayant des applications assez limitées pour l'ingénieur. A l'opposé, les théories mathématiques proclamées rigoureuses faisaient appel à une formulation si complexe et sans solution à l'horizon que l'ingénieur aux prises avec la réalité quotidienne perdait rapidement tout espoir de résultat et pensait qu'il ne s'agissait là que d'une pure spéculation de l'esprit.

Il n'en est plus de même actuellement, grâce au développement continuel de la capacité des ordinateurs scientifiques et aux progrès dans les techniques et méthodes de programmation et de résolution des équations.

Il n'est que de consulter le programme de cette Conférence pour voir que la résolution des problèmes non linéaires et instationnaires -c'est-à-dire des problèmes difficiles serrant de plus près la réalité des choses- feront l'objet de nombreuses communications la résolution de ces problèmes est en passe de devenir monnaie courante.

Cependant et quelle que soit la complexité des équations auxquelles des solutions numériques sont apportées, quelles que soient la qualité et la précision des calculs aboutissant à ces valeurs numériques, l'esprit contestataire d'un ingénieur architecte naval ne se sentira pas pleinement rassuré Il aimera voir sur le réel de préférence, à l'échelle de 12 pouces par pied, à défaut sur un modèle à échelle réduite, les résultats des calculs confrontés à des mesures expérimentales et si possible confortés par eux.

Là aussi, je suis sûr que de nombreux auteurs seront heureux de vous montrer l'accord entre leurs calculs et les résultats expérimentaux Certains auteurs dit-on ont même plus confiance dans leurs calculs que dans les résultats expérimentaux quand ceux-ci sont obtenus par des moyens de mesures sophistiqués et délicats.

Aussi et grâce au calcul numérique, grâce aux travaux que vous avez effectués, à ceux que vous allez présenter à partir d'aujourd'hui, à ceux que vous poursuivez, l'architecte naval se sent rassuré car il peut rapprocher les résultats des calculs théoriques, de ceux des essais sur modèles, les résultats des essais sur modèles de ceux des essais sur réels, les résultats des calculs théoriques de ceux des essais sur réels Voir évoluer un sous-marin sur une trajectoire perturbée prévue par le calcul et déjà vérifiée par un essai sur modèle libre est une très grande satisfaction et justifie un grand merci à ceux qui le permettent, et dont il faut aussi saluer le pragmatisme ou la modestie quand ils savent et osent, au vu des essais sur modèle ou réel, retoucher leurs théories of certains coefficients hydrodynamiques !

Nous sommes donc reconnaissants à tous les auteurs qui ont bien voulu apporter leur contribution à cette Conférence et je remercie à l'avance tous les participants qui par leur intervention depuis la salle vont animer et enrichir les débats.

Le Comité de Sélection a eu une tâche très difficile pour faire un choix dans les sujets de communication reçus. Bien que la durée de la Conférence ait été portée de 3 à 4 jours, il n'a été possible de retenir que la moitié des sujets soumis au Comité. Que les auteurs qui n'ont pas pu être retenus se rassurent, il ne faut pas voir dans cette décision qui a été pénible à prendre par le Comité de Sélection un manque d'intérêt pour leurs travaux.

Pour terminer, je voudrais remercier tous ceux qui ont contribué au succès de cette Conférence.

Tout d'abord les organismes qui par leur soutien financier en ont assuré les moyens matériels ; je veux citer sans ordre de préférence :

l'Office of Naval Research et le NSRDC côté Etats-Unis,

la Direction des Recherches, Etudes et Techniques,

ainsi que la Direction Technique des Constructions Navales, toutes deux de la Délégation Générale pour l'Armement.

Ensuite ceux qui personnellement ont passé un temps appréciable de leur activité dans la préparation matérielle de cette Conférence, et qui ont eu à résoudre un certain nombre de difficultés imprévues ; je voudrais citer en particulier :

le Docteur Robert Whitehead de l'Office of Naval Research,

l'Ingénieur en Chef Jean-Claude Dern du Bassin d'Essais des Carènes, Président de la Conférence,

le Docteur Henry Haussling du David Taylor Naval Ship Research and Development Center, Vice-Président de la Conférence.

Je voudrais, maintenant, Mesdames et Messieurs, rassurer les premiers auteurs qui doivent parler ; je ne vous importunerai pas plus longtemps.

Je déclare ouverte la 3ème Conférence Internationale d'Hydrodynamique Navale Numérique, et je souhaite que vous conserviez tous de cette Conférence un agréable souvenir.

Session I

NONLINEAR WAVES AND WAVE RESISTANCE

J V. Wehausen
Session Chairman
University of California
U.S.A

SOME FREE-SURFACE PHENOMENA AROUND SHIPS TO BE CHALLENGED BY NUMERICAL ANALYSIS

Eiichi Baba
Nagasaki Technical Institute,
Mitsubishi Heavy Industries, Ltd
1-1 Akunoura-machi
Nagasaki, Japan

Abstract

Numerical methods are important for prediction of wave resistance of full ship forms which can not be tackled by linear thin-ship theory. To make these numerical methods more reliable, detail investigations into the characteristics of nonlinear free-surface phenomena such as breaking waves around ships are necessary. In this paper some recent studies are reviewed to get better understanding of free-surface phenomena relating to breaking waves around bow, shoulder and stern of ships. First, a numerical study on the air bubble entrainment in breaking waves around protruding bulb is presented together with flow visualization test results. Then studies on the free-surface shear flow related to bow wave breaking are reviewed. Finally, interaction of viscous boundary layer at the free-surface along the hull and the formation of breaking waves is explained. One of the important findings in these studies is that free-surface shear flow is closely related with the formation of breaking waves around ships.

1. Introduction

Prediction of wave resistance of ship and improvement of hull form are major objectives in the research of ship wave and wave resistance. Improvement of the prediction method widens the ability of hull form improvement. Ceaseless efforts have been devoted hitherto for improvement of prediction method and hull form design of low wave resistance.

In 1979 various calculation methods were presented at Workshop on Wave Resistance Computations held in David W. Taylor Naval Ship Research and Development Center [1]. One of the major conclusions of the workshop was: The wave resistance predictions by first order thin-ship theory are rather consistent in comparison with experimental data and not worse than the envelope of predictions of seemingly more sophisticated methods presented at the Workshop for the Wigley, Inui S-201, Series 60 of block coefficient 0.60, and ATHENA hulls. However, the prediction by linear thin-ship theory is unacceptable for the full form HSVA tanker.

This conclusion encourages us to use first order thin-ship theory for the design purposes for ships of block coefficient less than 0.60. The first order thin-ship theory is very convenient, since wave resistance can be calculated rather easily by integrating wave resistance formula which is expressed as a functional of ship geometry. If a direction of improvement of hull form is shown even qualitatively, the theory becomes an effective tool for design of low wave resistance hull form.

Fruitful applications of first order wave resistance theories made so far to design problem are based on the following pioneering works:

(1) Series of studies on ship forms of minimum wave resistance by Weinblum [2], Wehausen et al [3] Karp et al [4], Maruo and Bessho [5].

(2) Studies of bulbous bow by Wigley [6] and Inui [7].

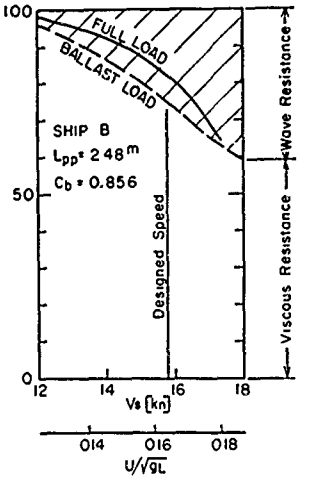
(3) Application of wave pattern analysis to ship form improvement by Inui [7], Sharma [8], Baba [9] and Tsutsumi [10].

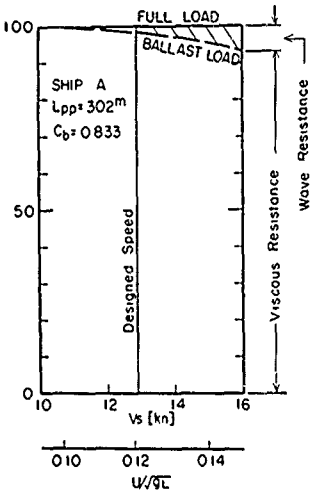
On the other hand, for high block coefficient ships, it was concluded at Washington Workshop that the prediction by linear thin-ship theory was unacceptable. Among the methods presented at workshop, numerical methods which solve nonlinear free-surface conditions showed good prediction of wave resistance of a full form. For instance the methods of Dawson, Chan and Chan gave good agreement with experimental data.

Thus we may say that the numerical method plays its important role on the prediction of wave resistance of full forms which are beyond applicability of conventional linear thin-ship theory. Therefore its application to hull form design is anxiously awaited as the next step.

In order to make clear the objective of our research effort in dealing with full ship forms it is worthy to know first what portion of total resistance of full forms is attributed to wave resistance. Some examples of the division of total resistance of full ship forms are shown in Fig. 1.1. The resistance predictions were made based on the towing tests in Nagasaki Experimental Tank.

The viscous resistance consists of frictional resistance, viscous pressure resistance and resistance due to roughness. The wave resistance consists of wave pattern resistance and wave breaking resistance. From these figures it is recognized first that the wave resistance is much less than the viscous resistance. For instance, wave





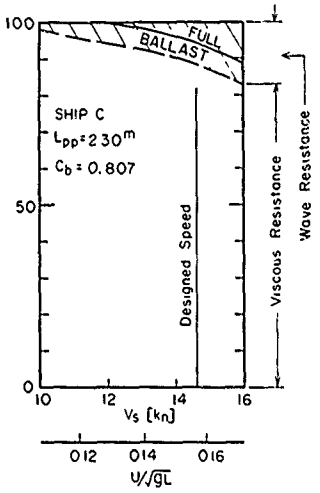


Fig. 1.1 Examples of decomposition of total resistance of full ships

resistance of a ship operating at low speeds (Ship A) is almost null in full load condition. However, in the case of a ship operating in higher speeds, for instance Ship B, wave resistance accounts for about 20% of total resistance at the designed speed. There is an enough room of research effort in reducing wave resistance of a certain class of full ships.

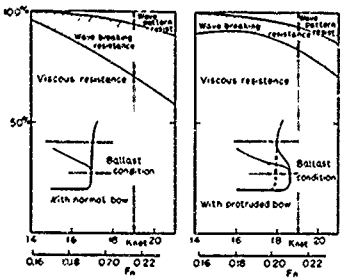


Fig. 1.2 Decomposition of total resistance of a tanker of $C_b = 0.80$ in ballast condition

Fig. 1.2 shows an example of further decomposition of wave resistance components of a ship with and without protruding bow. From this figure it is recognized that the protruding bow is effective in reducing wave breaking component. At present, however, the reason for reduction of wave breaking resistance by protruding bow has not been clarified yet. This is one of the important problems to be challenged by numerical analysis.

In 13th Symposium on Naval Hydrodynamics held in Tokyo in 1980 Chan and Chan presented an interesting numerical work on the effect of protruding bulb [11]. Numerical instability in calculating bow waves appeared in higher Froude number for a ship with protruding bulb than for the ship without protruding bulb.

The numerical instability experienced by Chan and Chan at the bow suggests the non-existence of the potential flow leading to breaking or the instability of potential flow leading to breaking. It is considered then that the protruding bulb suppresses the formation of bow wave breaking.

Chan and Chan's work is an indication of practical use of numerical analysis for bow wave problem. In their method, exact boundary value problems were solved within the framework of potential theory by numerically integrating a set of time-dependent, three-dimensional equations in a body fitted computational mesh system.

On the free-surface around full ship forms highly turbulent phenomenon such as wave breaking is often observed. The treatment of such a flow is essentially beyond the ability of potential theory. At present even the mechanism of inception of breaking ship waves has not been explained yet. Detailed investigations into the mechanism of ship wave breaking are indispensable for the development of sound theories and numerical analyses. To this end precise experimental observations of the free-surface phenomena around a ship are considered to be an effective way. A knowledge and understanding of the phenomena may thrust the improvement of both theory and numerical analysis.

When the flow phenomenon is complex, analytical or numerical approach is very difficult unless the problem is simplified. In the process of simplification, efforts are necessary to grasp the essential feature of the phenomenon.

The topic of the next section does not relate directly with breaking ship waves which are dealt with in the succeeding sections. Before going into the major topics, an example of studies is inserted in which experimental observation played an important role on the simplification of a problem and made it possible to carry out numerical analysis efficiently.

By showing this example firstly, the author wishes to emphasize the necessity of tight linkage of experimental observation and numerical analysis in dealing with complex free-surface phenomena around ships.

In Sections 3 and 4 some recent studies relating to breaking ship waves are reviewed and attempts are made to look for directions of further studies.

2. Air bubble entrainment around protruding bulb

It is often observed in the light load condition of a ship with protruding bulb that water film climbs up and covers the upper part of the protruding bulb. The water film usually breaks there as shown in Fig. 2.1. A large amount of air is entrained through the process of breaking of water film. It has been reported that these air bubbles flowed into the propeller as shown in Fig. 2.2 and closely associated with the occurrence of the excessive vibration of a ship [12].

In order to find a reason for the entrainment of air bubbles from the protruding bulb and also to find a way to prevent the entrainment, numerical analyses and flow visualization tests were carried out in Nagasaki Experimental Tank.

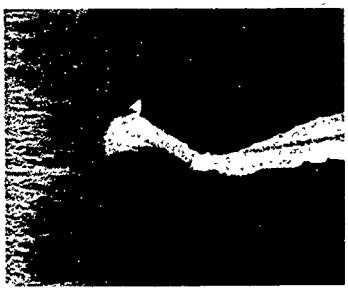


Fig. 2.1 Air bubble entrainment at protruding bulb

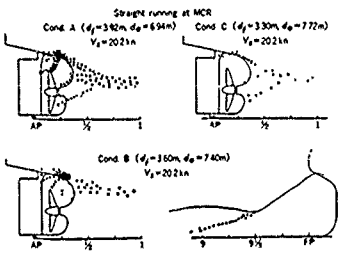


Fig. 2.2 Behaviour of air bubbles observed in flow visualization tests

The water flow which climbs up the upper part of the protruding bulb falls down again in a form of water film along the side surfaces of the bulb. This water flow can be regarded as a kind of water jet which adheres to the curved surface of the obstacle. According to this observation a simple two-dimensional flow model which represents the flow phenomena around the bulb was considered. That is, a sort of two-dimensional near field problem was considered by taking the transverse cross section of the protruding bulb. Then the flow characteristics of the water jet along the side wall of the bulb were analysed by means of a finite difference method based on a time-marching technique. The procedure of calculation is explained in Appendix. In the numerical analysis the circular cylinder is surrounded by water and a water jet is ejected from a slit attached to the side wall of the cylinder. Numerical calculations of transportation of air bubbles were also carried out by use of the velocity field calculated by the finite difference method. Analysed results were compared with the results of flow visualization tests by use of simple models, i.e. a water jet from the tap and a circular cylinder partially submerged in the water.

Fig. 2.3 shows a comparison of experimental and numerical results. From this figure it is observed that the water jet ejected from one side of the circular cylinder immediately adheres to the surface of the circular cylinder and a large number of air bubbles are transported to the other side of the cylinder. The numerical analyses explained well the experiment.

It is evident that this strong adhesion of water jet to the curved surface is attributed to the so-called Coanda effect. As a next step, the water jets were attached from both sides of the cylinder as shown in Fig. 2.4. The air bubbles are transported into the bottom region of the cylinder. On the other hand, when the water jets were attached to the side surfaces of a rectangular cross section shape, the air bubbles were not sent into the bottom, but scattered away from the corners of the section as shown in Fig. 2.5.

From these observations it is considered that the reason for the air entrainment at the protruding bulb is due to the adhesion phenomenon of water jet to the curved surface of the bulb.

Based on this finding, a means to avoid the air entrainment was considered. A pair of small strips were attached to the cylinder surface so as to separate the water jet at the strips. Fig. 2.6 shows the result of attachment of the strips. It is evident that the air bubbles are scattered away from the surface of the cylinder.

The present study is a successful example in which experimental observation played an important role on the simplification of the problem and made it possible to carry out numerical analysis efficiently.

In the following sections some recent experimental studies related to the breaking waves observed around bow, shoulder and stern of a ship are reviewed with some possible interpretations.



Fig. 2.3 Water jet ejected from one side of a circular cylinder

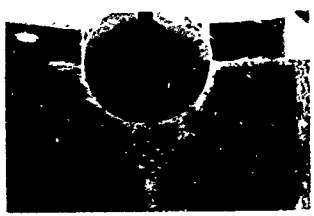
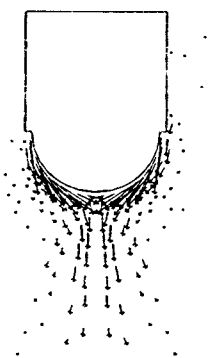
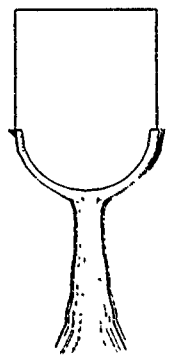


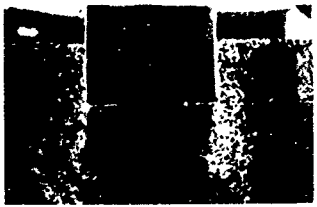
Fig. 2.4 Water jets ejected from both sides of a circular cylinder,
(a) Calculated flow pattern
(b) Movement of air bubbles

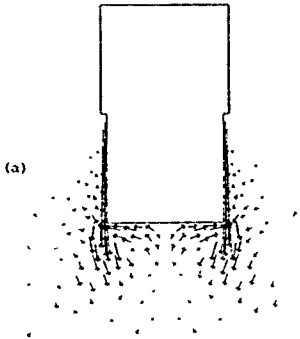


(a)



(b)





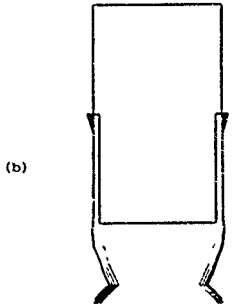
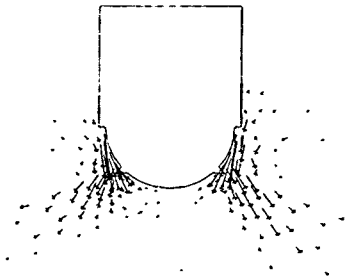


Fig. 2.5 Water jets ejected from both sides of a rectangular section
(a) Calculated flow pattern
(b) Movement of air bubbles





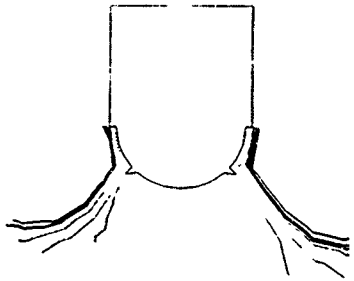


Fig. 2.6 Water jets ejected from both sides of a circular cylinder with strips
(a) Calculated flow pattern
(b) Movement of air bubbles

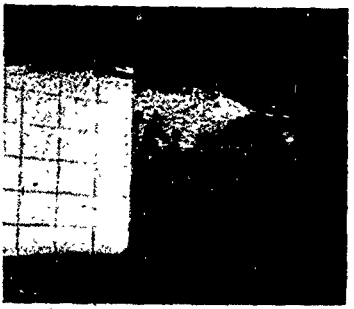


Fig. 3.1 Cross section of breaking bow waves

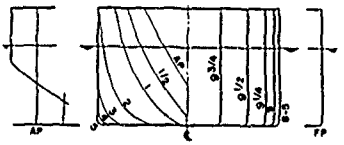


Fig. 3.2 Lines of a ship model used for experiments

3. Free-surface shear flow and bow wave breaking

3.1 Experimental study

A vertical cross section of the breaking bow wave is shown in Fig. 3.1. The photograph was taken by Kayo and Takekuma using broken pieces of metal leaf as flow tracer [13]. Body plan of the model is shown in Fig. 3.2. The principal dimensions are as:

$L_{pp} = 6.0^{m}$, $B = 1.0^{m}$, $d = 0.2^{m}$, $C_b = 0.80$

Fig. 3.3 shows velocity distributions in the longitudinal center plane ahead of the bow measured by means of a 5-hole pitot tube of 3mm diameter. In the wave breaking region near the free-surface it is observed that the upper layer of water advances with a small relative speed to the bow. Below this surface layer complex vortical motions are observed. Kayo and Takekuma noticed a resemblance of this vortical fluid motion to the phenomena of decelerated stagnation flow with separation, e.g. the flow normal to a plate with a thin splitter plate attached to it as shown in Fig. 3.4.

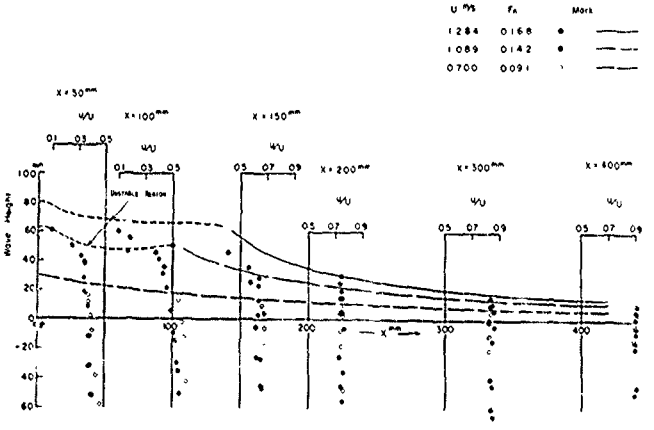


Fig. 3.3 Measured velocities and free-surface heights in front of bow



Fig. 3.4 Retarded stagnation flow with separation in front of a flat plate with a splitter plate (from Ref. 14)

In order to examine whether the bow wave breaking phenomenon has the same property as the flow separation, Kayo and Takekuma decelerated the free-surface ahead of the region of bow wave breaking. For this purpose a thin vinyl sheet was made afloat in front of a ship model and towed smoothly with the same speed as the model.

As shown in Fig. 3.5 the front of breaking waves advanced forward considerably with the vinyl sheet and the region of the breaking waves expanded. It is worthy to notice that the artificial retardation of surface flow stimulated breaking waves even in the case of low Froude number (F_n = 0.091) where no wave breaking had been observed.



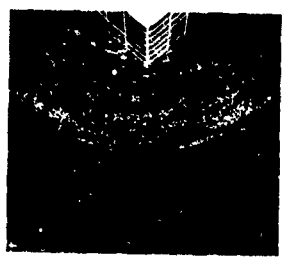
without vinyl sheet
U = 0.700 m/s
F_n = 0.091



without vinyl sheet
U = 1.089 m/s
F_n = 0.142



with vinyl sheet
U = 0.700 m/s
F_n = 0.091



with vinyl sheet
U = 1.089 m/s
F_n = 0.142

Fig. 3.5 Breaking bow waves around the bow of a full ship model with and without artificial rotardation of free-surface

Further, an additional experiment was conducted by Kayo and Takekuma. That is, air jet was blowed near the free-surface so as to accelerate the free-surface in front of the bow in contrary to the previous experiments. Fig. 3.6 shows the result of air jet blowing. It is observed that the breaking phenomenon is reduced slightly by the accerelation of free-surface.

Towing tests were also conducted by changing the size and location of the vinyl sheet in order to find the effect of breaking waves on ship resistance. Fig. 3.7 shows comparative curves of residual resistance coefficients. A result for the case of air blowing is also shown in this figure. A remarkable resistance increase by use of vinyl sheet was shown. On the other hand, a small reduction is observed for the case of air blowing in accordance with a small amount of reduction of bow wave breaking.



without air blowing

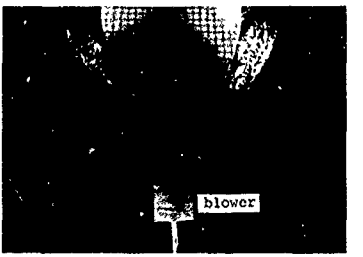


Fig. 3.6 Acceleration of free-surface by air blowing

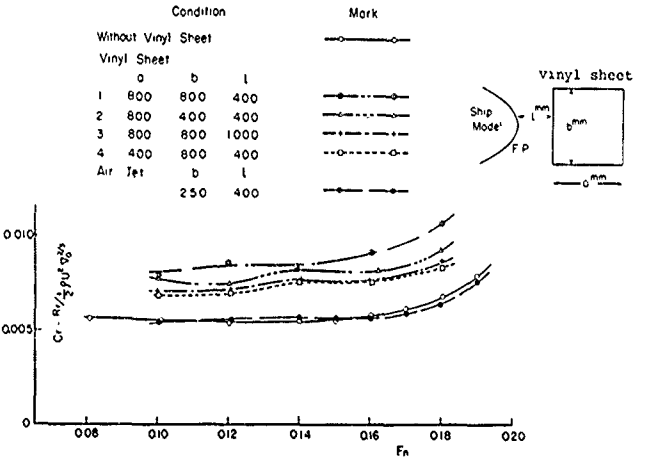


Fig. 3.7 Comparison of residual resistance coefficient curves when free-surface shear layer in front of bow was controlled artificially

In the above experiments the free-surface was controlled artificially so as to magnify the phenomenon. At present, however, it is not known well to what extent of free-surface shear is induced in front of the bow of a ship. In the case of a horizontally semi-submerged circular cylinder the free-surface shear was measured by Honji [15]. For the case of ordinary bow forms further experimental and theoretical studies are anxiously awaited.

3.2 Characteristics of free-surface flow when shear is applied on it

3.2.1 Laminar separation model

In the previous section it is noticed that near the free-surface in front of the bow there are complex vortical motions surrounding the blunt bow. It was also found that artificial retardation of free-surface makes these vortical motions much stronger.

The generation of such vortex motions is interpreted as a stability problem of a surface of tangential discontinuity on which the velocity tangential to the free-surface is discontinuous. This tangential discontinuity is not so sharp because of the viscosity. In this case the problem of stability of such a flow is mathematically similar to that of the stability of flow in a laminar boundary layer with a point of inflexion in the velocity profile [16].

Kayo and Takekuma conjectured then that the front of bow wave breaking can be regarded as a sort of separation point of boundary layer in positive pressure gradient (equivalent to positive free-surface slope toward bow). Then attempts were made to estimate the separation point of a simple shaped body such as a circular cylinder by use of two-dimensional laminar boundary layer theory. In their estimation upstream splitter plate was supposed in front of the semi-submerged circular cylinder, and the length of the splitter plate was varied.

The condition of the separation point was calculated by use of the approximation method due to Kármán and Pohlhausen [14]:

$$\frac{1}{U^6}\frac{dU}{dx}\int_0^x U^5 dx = -0.33$$

where U is the potential flow velocity at the outer edge of the boundary layer developed on the free-surface. x is the point of separation measured from the leading edge of the assumed splitter plate. In the laminar separation the separation point is independent of the Reynolds number as shown in the above equation.

The estimated separation points are compared with the forward edge of upstream vortex measured by Honji for a semi-submerged circular cylinder of radius r = 5cm at Reynolds number Ur/ν = $10^3 \sim 10^4$. Comparison was also made with Suzuki's experiments for much larger semi-submerged circular cylinders [17]. The radii of the cylinders are 0.135m and 0.107m respectively and

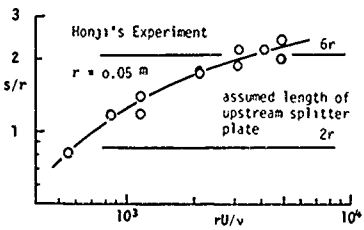


Fig. 3.8 Comparison of estimated separation points with measured distance s/r of forward edge of the upstream vortex in Honji's experiment. s is measured from the front of cylinder

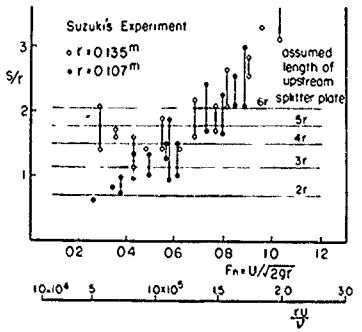


Fig. 3.9 Comparison of estimated separation points with measured distance s/r of forward edge of breaking waves in Suzuki's experiment

they were towed at Reynolds numbers Ur/ν around 10^5 (Froude number $U/\sqrt{2gr} = 0.2 \sim 1.2$). Figs. 3.8 and 3.9 show estimated separation points for various assumed lengths of upstream splitter plate attached to the semi-submerged cylinders.

The measured distance of forward edge of the upstream vortex in Honji's experiment or the breaking waves in Suzuki's experiment seems to be dependent on Reynolds number. Their orders of magnitude, however, agree with the estimated ones. This comparison encourages us to consider the inception of bow wave breaking as a sort of flow separation at the free-surface in positive pressure gradient. Suzuki already noted this physical property in his experimental and theoretical studies [17].

3.2.2 Secondary flow model

After establishment of a non-uniform initial flow under the influence of viscosity, the shear flow field is treated approximately as an inviscid flow around bow when the approaching velocity varies in the depthwise direction. This fluid dynamic problem is essentially same as the secondary flow problem observed around obstruction in river bed or at junction of wings with an aircraft fuselage.

Hawthorne studied such flow as an inviscid rotational flow problem. He approximated the velocity field as the sum of two components of velocity [18]:

$$UV + v$$

where U is the velocity in the x-direction varying only in the z direction as shown in Fig. 3.10. V is the vector of two-dimensional flow around the body in an xy plane when the far upstream velocity is unity. V is invariant with z and the vector UV then describes the basic quasi two-dimensional flow around the body in an xy plane. Vector v is an additional small velocity which represents three-dimensional effect.

In inviscid steady flow the equation of motion is written as:

$$\text{curl}\,[(UV + v) \times \text{curl}(UV + v)] = 0$$

with continuity condition

$$\text{div}(UV + v) = 0$$

The perturbation vorticity $(\xi, \eta, \zeta) = \text{curl } v$ in the directions of the streamline, normal, and z-axis, respectively, was obtained in terms of U and V under the assumption that $|v|$ is small compared

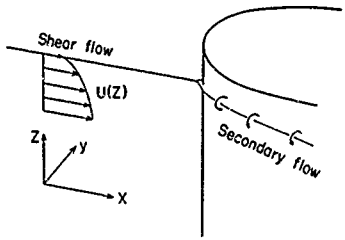


Fig. 3.10 Strut in shear flow and evolution of secondary flow

with Uq, where q is the scalar of V:

$$\xi = 2q \cdot \frac{dU}{dz} \cdot \int_{-\infty} \left(\frac{d\theta}{q^2}\right)$$

$$\eta = \frac{1 - q^2}{q} \cdot \frac{dU}{dz}$$

$$\zeta = 0$$

where θ is the angle between the direction V and the x-axis.

It is noted that the perturbation vorticity (ξ, η) is proportional to the initial shear dU/dz and tends to large values near the stagnation point ($Uq \to 0$). This theoretical result explains well the experimental finding that the shear flow intensified by vinyl sheet induces large vortical motions around bow.

Hawthorne calculated $\xi/(dU/dz)$ values for various leading edge forms. The results are shown in Fig. 3.11. It is found from the figure that the streamwise vorticity ξ is magnified more strongly for blunter leading edges than for sharper leading edges.

If we look bow wave breaking as a sort of secondary flow, this theoretical calculations help us to explain the effect of protruding bulb in reducing breaking bow waves. That is, the protruding bulb is effective in sharpening the entrance and as a result reducing the secondary flows.

The present simple inviscid theoretical model indicates applicability of this sort of approach to the study of flow around bow.

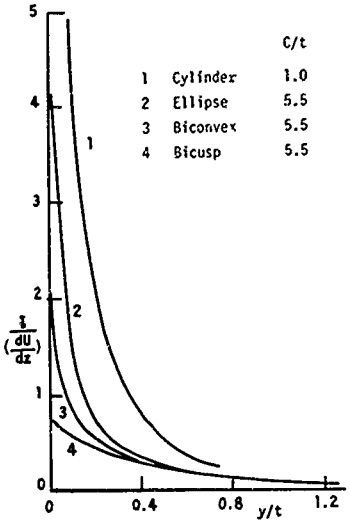


Fig. 3.11 Streamwise vorticity ξ, for various leading edge forms
y = coordinate normal to original flow
t = thickness of profile

4. Effects of viscous boundary layer along the hull surface on the formation of breaking waves

4.1 Free-surface flow around shoulder part of full forms

In addition to the bow wave breaking, breaking waves around the shoulder part of full entrance forms are sometimes observed. In the previous section it was found that shear flow on the free-surface is closely related with the formation of wave breaking. Based on this experimental finding one may consider that viscous boundary layer developed along the hull surface affects the formation of breaking waves developed along the hull as the case with shoulder wave breaking.

In order to examine this conjecture one side of the entrance part of full ship model shown in Fig. 3.2 was roughened artificially so as to magnify the phenomenon.

Water proof abrasive papers were put on the portside of the hull surface. The grain size of the abrasive paper was around 200μm (No.80 Japanese Industrial Standards). Then shoulder wave breaking phenomena at port and starboard parts are compared in Fig. 4.1. On the roughened surface side the breaking waves started about 2% Lpp forward and the intensity of breaking phenomenon was increased. Comparison of measured head loss behind shoulder breaking waves is shown in Fig. 4.2. It was confirmed that the head loss due to wave breaking was larger for the roughened side.

This experiment indicates that there is an interaction between viscous shear flow in the boundary layer near the free-surface and the formation of breaking wave at shoulder part of full ship forms.



$U = 1.4^{m/sec}$ $U/\sqrt{gL} = 0.18$



$U = 1.6^{m/sec}$ $U/\sqrt{gL} = 0.21$

Fig. 4.1 Comparison of shoulder wave breaking. Portside of entrance was roughened by abrasive paper.

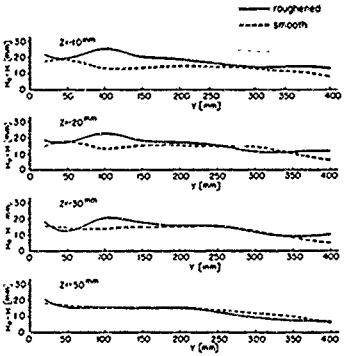


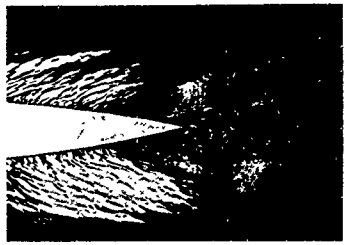
Fig. 4.2 Comparison of headloss distributions behind shoulder wave breaking $U/\sqrt{gL} = 0.18$, $Y = 0$ at hull side

4.2 Free-surface flow around stern of a ship

In the previous section characteristics of breaking waves around the entrance part of full forms are discussed mostly emphasizing the interaction of viscous shear flow and wave breaking.

Around stern of a ship, wave breaking phenomenon is also observed [19]. Fig. 4.3 shows stern flow patterns observed by Doi for an Inuid S-103 [20]. He noticed that the starting point of stern wave breaking varies with Froude number. Fig. 4.4 shows wave profiles on the hull surface of S-103 and arrows show the positions of starting point of stern wave breaking. It is interesting to notice that starting points appear on steep slope of wave profiles as observed at fore shoulder of full forms. Doi calculated viscous boundary layer taking account of free-surface deformation. Shape factor H is used for estimation of boundary layer separation and it is assumed that separation will occur when the shape factor becomes 1.8. In Fig. 4.5 a good correlation is shown between calculated separation points and observed starting points of stern wave breaking.

This study may lead us to consider that the formation of breaking waves at steep wave slope is closely related with the viscous shear flow developed along the hull surface as observed in shoulder wave breaking. At present, however, conditions of inception for breaking waves such as wave slope, free-surface shear stress and local velocity are not clarified yet and are left for the future investigations.



$F_n = 0.28$



$F_n = 0.30$



$F_n = 0.34$

Fig. 4.3 Stern flow patterns of S-103 observed by Doi

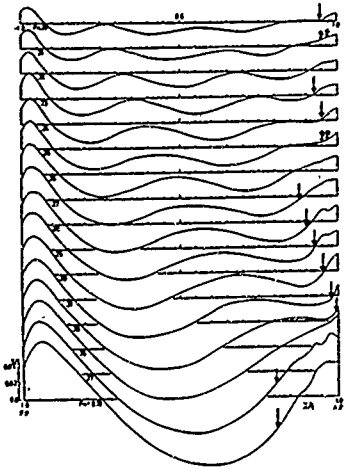


Fig. 4.4 Wave profiles on hull surface S-103 measured by Doi

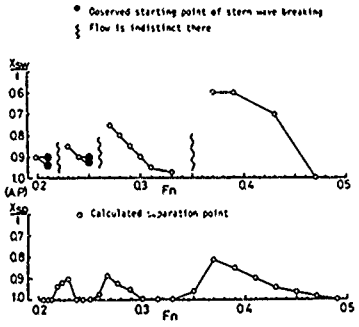


Fig. 4.5 Comparison of observed starting points of stern wave breaking with calculated separation points (Doi reference 20)

5. Concluding remarks

In the present paper some recent studies were reviewed to get better understanding of free-surface phenomena relating to breaking waves around bow, shoulder and stern of ships.

One of the important findings in the studies is that free-surface shear flow is closely related with the formation of breaking waves around ships. Based on this finding further investigations have to be pursued to understand a general nature of breaking wave phenomenon. The followings are considered to be major subjects of study:

(1) Theoretical and experimental studies of free-surface shear layer in front of the bow of a ship

(2) Theoretical and numerical studies on the formation of vortical motions around blunt bow

(3) Study on the characteristics of viscous boundary layer at the free-surface along the hull and its interaction with breaking ship waves

In these areas of research a tight linkage is necessary between theory and experiment, and at the same time between numerical methods dealing with viscous boundary layer problems and free-surface problems. Among these studies experimental observation of the free-surface phenomena is important to grasp the essential feature of the phenomenon. This makes it possible to solve the problems efficiently.

6. Acknowledgments

The author expresses his sincere gratitude to the Organization Committee who gave him a privileged opportunity to participate in this conference. The author thanks Dr.Itiro Tani, Professor Emeritus of Tokyo University for his stimulating discussions. Through the discussions the present author was motivated to look bow wave breaking as a kind of secondary flow phenomenon under the influence of free-surface shear. Thanks are due also Mr.Yasuaki Doi of Hirosima University, Dr.Yoshio Kayo, Mr.Katsuyoshi Takekuma and Dr. Takeshi Adachi of Nagasaki Technical Institute of Mitsubishi Heavy Industries for their contributions in preparing the present paper.

7. References

1. Proceedings of the Workshop on Ship Wave-Resistance Computations, David Taylor NSRDC, November 1979.
2. Weinblum,G., Schiffe geringsten Widerstandes, Proc. 3rd International Congr. Appl. Mech. Stockholm, 1930.
3. Wehausen,J.V., Reichert,G. and Gauthey,J.R., Ships of Minimum Wave Resistance, University of California, Inst. of Engg. Res. 82-21, 1961.
4. Karp,S. Kotik,J. and Lurye,J., On the Problem of Minimin Wave Resistance for Struts and Strut-like Dipole Distributions, 3rd. Symp. on Naval Hydrodynamics, Wageningen, 1960.
5. Maruo,H. and Bessho,M., Ships of Minimum Wave Resistance, Journal of The Society of Naval Architects of Japan, Vol.114, 1963.
6. Wigley,W.C.S., The Theory of the Bulbous Bow and its Practical Application, Northeast Coast Institution of Shipbuilders, 1935-36.
7. Inui,T., Wave-Making Resistance of Ships, Trans. of The Society of Naval Architects and Marine Engineers, Vol.70, 1962.
8. Sharma,S.D., An Attempted Application of Wave Analysis Techniques to achieve Bow Wave Reduction, 6th. Symp. on Naval Hydrodynamics, Washington D.C., 1966.
9. Baba,E., An Application of Wave Pattern Analysis to Ship Form Improvement, Journal of The Society of Naval Architects of Japan, Vol. 132, 1972.
10. Tsutsumi,T., Ogiwara,S., On the Principal Particulars of Ship Hull Form and Wave Pattern Resistance (II), Journal of The Society of Naval Architects of Japan, Vol.137, 1975.
11. Chan,R.K.-C. and Chan,F.W.-K., Numerical Solution of Transient and Steady Free-Surface Flows about a Ship of General Hull Shape, Proc. of 13th. Symp. on Naval Hydrodynamics, Tokyo, 1980.
12. Takekuma,K., Vibration Problems with a Class of Cargo Liners and the Solution from Fitting a Fin, RINA International Symposium on Propeller Induced Ship Vibration, London, 1979.
13. Kayo,Y. and Takekuma,K., On the Free-Surface Shear Flow Related to Bow Wave Breaking of Full Ship Models, Journal of The Society of Naval Architects of Japan, Vol.149, 1981.
14. Schlichting,H., Boundary Layer Theory, 6th Edition, McGraw-Hill Book Company, P.192, 1968.
15. Honji,H., Observation of a Vortex in Front of a Half-Submerged Circular Cylinder, Journal of the Physical Society of Japan, Vol.40, No.5, 1976.
16. Landau,L.D. and Lifshitz,E.M., Fluid Dynamics, Pergamon Press, Addison-Wesley Publishing Co. INC. P.114, 1959.
17. Suzuki,K., On the Drag of Two-Dimensional Bluff Bodies Semi-Submerged in a Surface Flow, Journal of The Society of Naval Architects of Japan, Vol.137, 1975.
18. Hawthorne,W.R., The Secondary Flow about Struts and Aerofoils, Journal of The Aeronautical Sciences, Vol. 21, 1954.
19. Baba,E., Wave Breaking Resistance of Ships, Proc. International Seminar on Wave Resistance, Tokyo, 1976.
20. Doi,Y., Observation of Stern Wave Generation, Proc. of the Continued Workshop on Ship Wave Resistance Computations, Izu Shuzenji, Japan, 1980.
21. Adachi,T., Tsujimura and Imaizumi, M., A Numerical Method of Unsteady Flow Analysis in a Duct with Junction, Bulletin of Japan Society of Mech. Engng. 20 (148), 1284-1290, 1977.
22. Gentry,R.A., Martin,R.E., and Daly, B.J., An Eulerian Differencing Method for Unsteady Compressible Flow Problems, J. Comp. Phys.1, 87-118, 1966.

Appendix

Numerical method employed in calculating flow pattern around two-dimensional body on which the water jet is attached

In the present calculation a computer program which was developed primarily for the analysis of two-dimensional compressible perfect gas flow was used [21].

In low Mach numbers, say less than 0.5, effect of compressibility of the fluid does not appear and the similarity of flow pattern is established between compressible fluid and incompressible fluid.

In this computation use was made of Modified FLIC Method developed by Adachi of Mitsubishi Nagasaki Technical Institute. The method is based on the well known FLIC (fluid in cell) method [22], one of time-marching techniques.

Modified FLIC Method uses triangular elements conventionally used in finite element method for convenience of application to arbitrary boundary shape. Fig. A.1 shows an arrangement of elements around a cylinder.

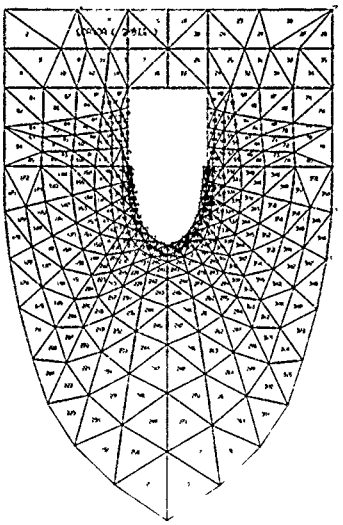


Fig. A.1 Arrangement of triangular elements around a cylinder

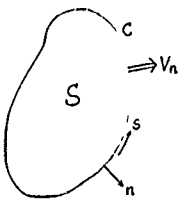


Fig. A.2 Notation in Eq. A-1

The air jet was ejected with speed 0.25 Mach and with atmospheric pressure. Then gas flow patterns around a body were converted into water flow based on the above mentioned similarity law.

Then the behavior of air bubbles entrained in the water jet was analysed.

Mathematical equations used in the present calculations are outlined as follows.

1. Basic equations of flow analysis

The integral form of conservation laws of mass, momentum and energy are expressed for inviscid flow S as:

$$\frac{d}{dt}\int_S F\,dS \left(=\frac{\partial}{\partial t}\int_S F\,dS + \int_C F\,Vn\,ds\right) = -\int_C Q\,ds \qquad (A\text{-}1)$$

The equation of state: $p = \rho RT$ (A-2)

where

$$F = \begin{Bmatrix} \rho \\ \rho u \\ \rho v \\ \rho E \end{Bmatrix} \qquad (A\text{-}3)$$

$$Q = \begin{Bmatrix} 0 \\ p\ell \\ pm \\ pVn \end{Bmatrix} \qquad (A\text{-}4)$$

ρ : density
p : pressure
T : temperature
u,v : velocities for x, y directions
E : total energy = $Cv\,T + \frac{1}{2}(u^2 + v^2)$
Cv : specific heat at constant volume
R : gas constant
(ℓ,m) : direction cosines of the outward normal vector n on contour C of the flow region S (See Fig. A.2)
Vn : velocity for n direction on C

2. Finite difference approximation

Calculation region is divided into triangular elements, and an arbitrary element taken out of them is given with symbols as shown in Fig. A.3, where i, i = 1,2,3 mean vertex or its opposite side. Calculation is made of

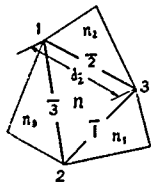


Fig. A.3. Triangular element and its notation

the element shown in Fig. A.3 by Eq. (A-1). In FLIC method, finite difference with respect to time is made in two steps. In Step 1, ignoring the convective term within a small time interval δt, an intermediate value is obtained from Eq. (A-1) and Eq. (A-4) on the basis of the value $\bar{F}$ at $t = n\delta t$. In Step 2, a value $F^{(n+1)}$ at a new time $t = (n+1)\delta t$ is obtained from the conservation laws (the formula in parentheses in Eq. (A-1)) on the assumption that $\bar{F}$ flows in and out through the side $\bar{I}$, $\bar{I} = 1,2,3$ of the element n. The equations are given below:

Step 1

$$\bar{F}_n = F_n^{(n)} - \frac{\delta t}{S_n} \sum_{\bar{I}=1}^{3} Q_{\bar{I}}\, d_{\bar{I}} \qquad \text{(A-5)}$$

where

$$Q_{\bar{I}}^{(n)} = \begin{Bmatrix} 0 \\ p_{\bar{I}}^{(n)} t_{\bar{I}} \\ p_{\bar{I}}^{(n)} n_{\bar{I}} \\ p_{\bar{I}}^{(n)} V_{n\bar{I}}^{(n)} \end{Bmatrix} \qquad \text{(A-6)}$$

$$p_{\bar{I}} = (S_n p_{n\bar{I}} + S_{n\bar{I}} p_n)/(S_n + S_{n\bar{I}})$$

$$V_{n\bar{I}} = (t_{\bar{I}} (S_n u_{n\bar{I}} + S_{n\bar{I}} u_n) + n_{\bar{I}} (S_n v_{n\bar{I}} + S_{n\bar{I}} v_n))/(S_n + S_{n\bar{I}})$$

S_n : area of the element n
$d_{\bar{I}}$: length of the side $\bar{I}$
Superfix (n): time step number $t = n\delta t$
Suffix n : element number
Suffix $\bar{I}$: side number

Step 2

$$F_n^{(n+1)} = \bar{F}_n - \frac{\delta t}{S_n} \sum_{\bar{I}=1}^{3} \left\{ \delta_{\bar{I}}\, \bar{F}_{n\bar{I}} + (1 - \delta_{\bar{I}}) \bar{F}_n \right\} \bar{V}_{n\bar{I}}\, d_{\bar{I}}$$

where

$$\delta_{\bar{I}} = \begin{cases} 1, & V_{n\bar{I}} < 0 \text{ inflow through side } \bar{I} \\ 0, & V_{n\bar{I}} > 0 \text{ outflow through side } \bar{I} \end{cases}$$

3. Equations of motion of entrained air bubbles

$$\frac{dV_P}{dt} = (1 - \frac{\rho_w}{\rho_P}) g + \frac{3}{4} \frac{\rho_w}{\rho_P D_P} C_D |V_w - V_P| \cdot (V_w - V_P)$$

Suffix P : particle (air bubble)
w : water
D_P : diameter of particle
C_D : viscous drag coefficient
g : acceleration of gravity

The finite difference approximation of the above equation is written as:

$$V_P^{(n+1)} = V_P^{(n)} + \alpha \cdot \delta t \left\{ (1 - \frac{\rho_w}{\rho_P}) g + \frac{3}{4} \frac{\rho_w}{\rho_P D_P} C_D |V_{w_N} - V_P^{(n)}| (V_{w_N} - V_P^{(n)}) \right\}$$

$$\alpha = \frac{1 - \exp[-\frac{3}{4} \frac{\rho_w}{\rho_P D_P} \cdot C_D |V_{w_N} - V_P| \delta t]}{\frac{3}{4} \frac{\rho_w}{\rho_P D_P} \cdot C_D |V_{w_N} - V_P| \delta t}$$

$$X_P^{n+1} = X_P^n + \frac{1}{2} \delta t \left\{ V_P^{(n+1)} + V_P^{(n)} \right\}$$

V_{w_N}: velocity of the Nth element which is determined by the flow analysis explained previously

FREE-SURFACE POTENTIAL FLOW COMPUTATION USING A FINITE ELEMENT METHOD

A. Gomen
Maritime Research Institute Netherlands
Wageningen, The Netherlands

Abstract

The exact nonlinear problem of the steady three-dimensional free surface flow past a surface-piercing body is split into a Neumann problem defined by the Laplace equation with kinematic boundary conditions and a free-surface correction problem. These problems are solved alternately until the converged solution is obtained. The three-dimensional Neumann problem is reduced to a system of two-dimensional problems which are solved by means of a finite element method. For the derivation of the free surface correction, perturbations of the potential and free surface elevation are introduced, which have to satisfy the Laplace equation and both free surface conditions. The radiation condition is implicitly taken into account by the free surface correction procedure. The results are shown to agree reasonably well with experimental data for a Series 60 model.

1. Introduction

The problem dealt with in this paper is that of a steady irrotational flow of an inviscid incompressible fluid past a body in the presence of a free surface. This nonlinear boundary-value problem is described by the Laplace equation together with certain kinematic and dynamic boundary conditions. The main difficulty in solving these equations is the fact that boundary conditions have to be prescribed at a free surface which is initially unknown and has to be determined as a part of the solution. One can avoid this difficulty by applying linearization of these boundary conditions and prescribing them at the position of the undisturbed free surface. But this may be inaccurate in certain cases; the importance of nonlinear effects has always been a subject of interest.

With the increase of computor speed it has become feasible to solve the exact nonlinear problem by purely or partly numerical methods. The difficulty of the unknown free surface position is in these methods usually handled by first solving the Laplace equation in a fixed domain, with only one of the free surface boundary conditions applied at an assumed free surface position. The solution generally does not satisfy the boundary condition that has been dropped, and a correction of the free surface is necessary. Then again the Laplace equation is solved in the new domain. This iteration process is repeated until the solution satisfies both free surface conditions.

Within this framework various approaches have been attempted more or less successfully. The Laplace equation can be solved by a finite element, finite difference /1/ or surface singularity method /2/, and can be combined with either the kinematic or the dynamic boundary condition. Moreover, the derivation of the free surface correction can be done in various ways, and largely determines the success or failure of the method. The wrong choice may cause divergence /2/, or a solution with waves upstream of the body or without any waves at all.

In the present method, the Laplace equation with the kinematic boundary conditions is solved by means of a finite element method. Perturbations of the potential and free surface elevation are then introduced which satisfy the Laplace equation, the bottom boundary condition and both free surface conditions which have been linearized in terms of these perturbations. The variation of the perturbation potential in depth direction is rather roughly approximated so as to reduce the correction problem to a two-dimensional one. But since in the course of the iteration process the perturbations vanish, neither this approximation nor the linearization have any influence on the final solution.

After the formulation of the problem we shall first deal with the solution of the Neumann problem obtained from the Laplace equation and the kinematic boundary conditions. Section 4 describes

the free surface correction procedure. Finally the results of some numerical tests are shown, and the method is applied to a Series 60 C_B=0.60 model for which expe .mental data are available.

2. Formulation of the problem

The system of coordinates is fixed to the ship and the fluid far upstream is moving with constant velocity U_o, see Fig. 1.

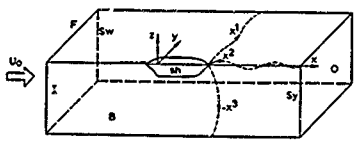


Fig. 1. Coordinate system.

The curvilinear coordinates are chosen such that the boundaries of the computational domain coincide with coordinate planes. The inflow and outflow boundaries are planes x^2=constant. The symmetry plane Sy and the sidewall Sw are planes x^1=constant. The bottom B and the free surface F plus the ship hull Sh are planes x^3=constant.

The generation of the x^1, x^2 and x^3-coordinate lines is performed as follows. We start with the specification of the grid points along the intersection line ℓ of the free surface and the ship hull or symmetry plane. The x^1 coordinate lines on the free surface are then computed such that:

1. at the hull $dx/dy=\sin\alpha$, where $\tan\alpha$ is the direction of the intersection line ℓ;

2. $dx/dy=0$ at the side wall;

3. the chord lines between successive points on an x^1-line are of equal length;

4. in each interval, the angle between the x^1-line and the chord line is equal at both nodes, and is half the corresponding angle in the previous interval.

5. on the ship hull itself, the x^1-coordinate lines follow the frame-lines.

Upstream and downstream of the ship the x^1-coordinate lines are computed in the same way, but with a value of α which is zero at the inflow and outflow boundary and approaches the correct value at the bow or stern quadratically.

The same method is used for the x^3-coordinate lines, only then there are two directions to be determined, dx/dz and dy/dz.

The flow is assumed to be irrotational, incompressible and frictionless. Under these conditions the problem is formulated in terms of a velocity potential $\phi(x^1, x^2, x^3)$.

The mathematical equations for the fluid motion are then, in curvilinear coordinates:

1. In the computational domain the velocity potential ϕ must satisfy the Laplace equation:

$$\frac{1}{\sqrt{g}}\frac{\partial}{\partial x^i}\left(\sqrt{g}\, g^{ij}\frac{\partial\phi}{\partial x^j}\right)=0 \quad \text{or} \quad \Delta\phi=0$$

2. At the boundaries of the region the kinematic boundary condition must be satisfied:

$$\frac{1}{\sqrt{g^{jj}}}\, g^{ji}\frac{\partial\phi}{\partial x^i} = f^j \quad \text{or} \quad \frac{\partial\phi}{\partial n_j} = g^j$$

3. At the free surface the dynamic boundary condition must be satisfied:

$$\tilde{g}\eta(x^1, x^2)+\tfrac{1}{2}\left(g^{ij}\frac{\partial\phi}{\partial x^i}\frac{\partial\phi}{\partial x^j}\right)+\frac{P}{\rho} = C$$

4. Far upstream the influence of the ship must tend to zero:

$$\lim_{x\to-\infty} \quad \phi=U_o x+C$$

5. Far downstream the velocity must be bounded.

$$\lim_{x\to+\infty} \quad \phi=U_o x<\infty$$

6. Because the solution of the equations is unique to within an arbitrary constant we may simply require that somewhere in the computational domain $\phi(x^1, x^2, x^3)=0$.
In these equations:

- i, j = 1, 2, 3
- g^{ij} = metric tensor quantity
- g = determinant g^{ij} matrix
- $\tilde{g}$ = gravitational acceleration
- $\eta(x^1,x^2)$ = free surface elevation
- $P(x^1,x^2)$ = pressure distribution
- ρ = mass density
- x^1,x^2,x^3 = curvilinear coordinates
- ϕ = $\phi(x^1,x^2,x^3)$=velocity potential
- f^j = 0 at fixed walls and exact free surface
  = U_o (uniform) velocity at inflow/outflow boundaries.

The unknown quantities are the velocity potential ϕ and the position of the free surface $\eta(x^1, x^2)$. The radiation

condition 4. is approximated by the prescription of a uniform inflow U_0 at the upstream boundary I. The downstream radiation condition 5. is reduced to the specification of a uniform outflow at the outflow boundary O. This necessitates the introduction of a fictitious wave damping over at least one wave length near the boundary in order to avoid oscillations.

3. The Neumann problem

As stated before, the iterative procedure for solving this nonlinear problem consists of the solution of the linear Neumann problem and a surface correction. For the Neumann problem the position of the free surface is given by an initial guess or, in later iterations, a calculated improved position. At this surface the kinematic boundary condition is applied (velocity tangential to the surface) while the dynamic free surface condition is ignored.

The use of a finite element technique to solve the three-dimensional Neumann problem would lead to an extremely large number of equations. For this reason the three-dimensional problem is replaced by a set of coupled two-dimensional problems following the method of Korving /3/. This is based on the assumption that the variation of the velocity potential is depth direction is smooth enough to be approximated by an interpolation polynomial of third degree. Therefore the computational region is divided into a set of N-1 subregions separated from each other by planes x^3=constant. In each subregion the potential is approximated by a third degree polynomial in x^3 that agrees with the actual values of the potential and its derivative in x^3-direction at the boundaries of the subregion. As the interpolation polynomial a cubic spline function is chosen with continuous first and second derivatives at the planes between the subregions:

$$\phi^{(j)}(x^1,x^2,x^3) = \sum_{k=0}^{1} \{ \ell_k^{(j)}(x^3)\phi^{j+k}(x^1,x^2) + m_k^{(j)}(x^3)\phi_u^{j+k}(x^1,x^2) \} \qquad (3.1)$$

with

$$j = 1(1)\ N-1$$

$$\phi^j(x^1,x^2) = \phi^{(j)}(x^1,x^2,x_j^3)$$

$$\phi_u^j(x^1,x^2) = \left.\frac{\partial\phi^{(j)}(x^1,x^2,x^3)}{\partial x^3}\right|_{x^3=x_j^3}$$

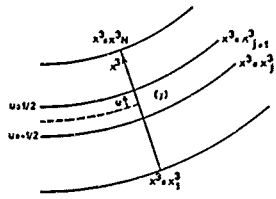


Fig. 2. Subregion division.

$$\ell_0^{(j)}(x^3) = 2(u-\tfrac{1}{2})^2(u+1)$$

$$\ell_1^{(j)}(x^3) = -2(u+\tfrac{1}{2})^2(u-1)$$

$$m_0^{(j)}(x^3) = \delta(u+\tfrac{1}{2})(u-\tfrac{1}{2})^2$$

$$m_1^{(j)}(x^3) = \delta(u-\tfrac{1}{2})(u+\tfrac{1}{2})^2$$

$$\delta = x_{j+1}^3 - x_j^3$$

$$u = \frac{1}{\delta}\left(x^3 - \frac{x_j^3+x_{j+1}^3}{2}\right)$$

We now apply the collocation method, which implies that the Laplace equation is solved only at the boundary planes of the subregions. This means that the threedimensional problem is reduced to a set of twodimensional problems which are coupled through the $\partial^2\phi/\partial(x3)2$-terms. Substitution of the above approximations into the Laplace equation at each x^3=constant plane yields N partial differential equations; the continuity requirement of the second derivative at the planes j=2(1)N-1 provides N-2 equations, and the kinematic boundary conditions at the bottom and the free surface give another two equations. Thus we have obtained 2N equations for the 2N unknowns ϕ^j and ϕ_u^j, j=1(1)N.

To solve this system by a finite element method the solution is approximated by:

$$\phi^j(x^1,x^2) = \sum_{s=1}^{M} a_s^j\, p^s(x^1,x^2) \text{ and}$$

$$\phi_u^j(x^1,x^2) = \sum_{s=1}^{M} b_s^j\, p^s(x^1,x^2) \qquad (3.2)$$

where $p^s(x^1,x^2)$ is a set of linearly independent functions. The Galerkin method now implies that when this approximation is substituted into the equations the inner product of the equations with a function p^s must be zero.

This gives the integral equation:

$$\iint_{S_i} \Delta^* \phi^i \, p^s \, dx^1 \, dx^2 + \int_{\Gamma_i} \alpha_{ij} ((n^k \phi_{,k})^j - f^j) p^s \, d\xi = 0$$

$$s=1(1)M$$

$$i,j=1(1)N \qquad (3.3)$$

with

Δ^*	= operator connected with the Laplace equation
S_i	= surface of $x^3 = x_i^3$ plane
Γ_i	= contour of surface S_i
$(n^k \phi_{,k})^j - f^j =$	0: kinematic boundary condition
$\alpha_{ij} d\xi$	= $\sqrt{a_{(i)}} \delta_j^{(i)} d\xi$ with $\sqrt{a}\, d\xi$ connected with the formula defining an element of area $do = \sqrt{a}\, d\xi\, dx^3$ with ξ measured along Γ_i
δ_j^i	= 0 $i \neq j$
	= 1 $i=j$

An equation without second derivatives obtained by partial integration (Greens theorem):

$$\iint_S \Delta\phi \, p^s dxdy = - \iint_S \nabla\phi \nabla p^s \, dxdy + \int_\Gamma p^s \nabla\phi . n \, ds \qquad (3.4)$$

This leads here to the following integral equation:

$$\iint_{S_i} \left[\frac{\partial G_{ij}^{\alpha 3}}{\partial x^3} \frac{\partial \phi^j}{\partial x^\alpha} + \frac{\partial G_{ij}^{33}}{\partial x^3} \phi_u^j + G_{ij}^{\alpha 3} \frac{\partial \phi_u^j}{\partial x^\alpha} + \frac{G_{ij}^{33}}{\delta} \left(\frac{3}{\delta} A_{\ell j} \phi^j + B_{\ell j} \phi_u^j \right) \right] p^s dx^1 dx^2 =$$

$$\iint_{S_i} \left[\left(G_{ij}^{\alpha\beta} \frac{\partial \phi^j}{\partial x^\alpha} + G_{ij}^{3\beta} \phi_u^j \right) \frac{\partial p^s}{\partial x^\beta} \right] dx^1 dx^2 - \int_{\Gamma_i} \alpha_{ij} f^j p^s d\xi \qquad (3.5)$$

$i, j, \ell = 1(1)N$

$\alpha, \beta = 1,2$

$s = 1(1)M$

with

$$G_{ij}^{\gamma c} = \sqrt{g}\, g_{ij}^{\gamma c} \mu_j^i \qquad \gamma, c = 1(1)3$$

$$\mu_j^i = 0 \quad i \neq j$$

$$= \tfrac{1}{2} \quad i=j=1,N$$

$$= 1 \quad i=j=2(1)N-1$$

δ = distance between planes x_i^3 and x_{i+1}^3

$$A_{ij} = \begin{pmatrix} -1 & 1 & & & 0 \\ 1 & -2 & 1 & & \\ & \ddots & \ddots & \ddots & \\ & & 1 & -2 & 1 \\ 0 & & & 1 & -1 \end{pmatrix} \quad B_{ij} = \begin{pmatrix} -2 & -1 & & & 0 \\ 1 & 0 & -1 & & \\ & \ddots & \ddots & \ddots & \\ & & 1 & 0 & -1 \\ 0 & & & 1 & 2 \end{pmatrix}$$

In order to transform the system into a diagonally dominant set of subsystems, first a ϕ_u^{*j} is introduced with:

$$\phi_u^{*1} = \phi_u^{*N} = 0 \qquad (3.6)$$

$$\phi_u^{*j+1} + 4\phi_u^{*j} + \phi_u^{*j-1} = \phi_u^{j+1} + 4\phi_u^j + \phi_u^{j-1}$$

$$j=2(1)N-1$$

Substitution of this transformation makes it possible to calculate the eigenvalues and eigenfunctions of the dominant terms of the equation:

$$A_{ij}\phi^j + \frac{6}{\delta} B_{ij}\phi_u^{*j} - \lambda u_{ij}\phi^j = 0 \quad i,j=1(1)N \qquad (3.7)$$

together with

$$C_{ij}\phi_u^{*j} = -\frac{3}{\delta} B_{ij}\phi^j \qquad j=1(1)N$$

$$i=2(1)N-1$$

following from the continuity of the second derivative of the spline function, and $\phi_u^{*j=0} \quad J=1,N$

$$C_{ij} = \begin{pmatrix} 1 & 4 & 1 & & 0 \\ & \ddots & \ddots & \ddots & \\ & & 1 & 4 & 1 \\ 0 & & & & \end{pmatrix}$$

The eigenfunctions of ϕ^j and ϕ_u^{*j} are found to be

$$E_\ell^j = C_\ell^1 \cos(j-1)\beta_\ell \quad \text{and}$$

$$E_{u\ell}^j = -\frac{3}{\delta} C_\ell^1 \frac{\sin \beta_\ell \sin(j-1)\beta_\ell}{2+\cos \beta_\ell},$$

respectively, and the eigenvalues are

$$\lambda_\ell = -2 \frac{1-\cos \beta_\ell}{2+\cos \beta_\ell} \text{ with } \beta_\ell = \pi \frac{(\ell-1)}{N-1}$$

$$\ell=1(1)N.$$

By transforming ϕ^j and ϕ_u^{*j} to ψ^ℓ according to:

$$\phi^j = E_\ell^j \psi^\ell \qquad (3.8)$$

$$\phi_u^{*j} = E_{u\ell}^j \psi^\ell \qquad j,\ell=1(1)N$$

and multiplying the system of equations with the transpose of the matrix of

eigenfunctions $(E^i_j)^T$, we obtain the required diagonally dominant set of subsystems. Then each subsystem may be solved independently provided that this is part of a process of successive iteration. The reduction to this diagonally dominant form is, however, only possible if the angles between the coordinate lines are at least 45 degrees.

The solution is obtained by the use of triangular finite elements in each plane S_i, with shape functions p^s such that at nodal point r $p^s(x^1_r,x^2_r)=\delta^s_r$. Within an element that contains nodal point s, p^s is a linear function of x^1 and x^2, and $p^s(x^1,x^2)=0$ in all other elements. The calculation of the metric tensor quantities in the elements is based on the assumption that the base vectors along the x^1 and x^2 coordinate lines are constant in each element, but the components of the base vector in x^3-direction are linear functions of x^1 and x^2. This leads to the result that in each element G^{33} is constant, G^{13} and G^{23} are linear and G^{11}, G^{12} and G^{22} are quadratic in x^1 and x^2. Substitution of these functions into the integral equation (3.5), together with the linear expression for p^s (and ϕ and ϕ_u), shows that all terms of the first two integrands are of second order in x^1 and x^2.

After the calculation of ψ^l the values of ϕ^j and $\phi_u{}^j$ are computed by backsubstitution. From the values of the velocity potential at the nodal points the velocity can be calculated by a central difference method.

4. The free surface correction.

Since in the solution of the Neumann problem the dynamic free surface condition has not been taken into account, the pressure at the free surface generally will not have its desired (usually constant) value. One might try to correct the free surface shape by simply substituting the calculated velocities into the dynamic free surface condition, i.e. by putting $\Delta\eta=\Delta p/\rho g$ where Δp is the deviation from the specified pressure; but this does not lead to a wavelike solution /4/. Presumably it is essential to apply a correction derived from both free surface conditions.

In contrast to the solution of the Neumann problem, the free surface correction is calculated in the Cartesian (x,y,z) system. The equations to be satisfied by the corrected potential ϕ' are:

1. Laplace equation: $\Delta\phi'=0$ (4.1)
2. Kinematic boundary conditions
$$\frac{\partial\phi'}{\partial n}=g^j \text{ at all boundaries} \quad (4.2)$$
3. Dynamic boundary condition:
$$\tilde{g}\eta+\tfrac{1}{2}(\phi_x'^2+\phi_y'^2+\phi_z'^2)+\frac{p}{\rho}=\tfrac{1}{2}U_o^2+\frac{p_o}{\rho} \text{ at } z=\eta$$

Again the problem is a nonlinear one. It is simplified by introducing a disturbance potential ϕ and a surface correction ξ according to:

$\phi'=\phi+\psi$
$\eta=\eta_o+\xi$,

where ϕ is the solution of the Neumann problem and η_o is the free surface elevation on which this solution was based. For instance, when $\eta_o=0$ everywhere, ϕ is the double body potential; in fact this is normally used as a first approximation to start the iteration process.
In the spirit of the low speed theory we suppose these corrections ψ an ξ and their derivatives to be sufficiently small to allow linearization of the free surface boundary conditions.
Thus we obtain:

1. $\Delta\psi=0$ (4.4)
2a. $\frac{\partial\psi}{\partial n}=0$ at fixed boundaries and inflow/outflow boundaries (4.5)
2b. $-\frac{\partial\psi}{\partial z}+G\xi_x+H\xi_y+E\psi_x+F\psi_y=0$ at $z=\eta_o$ (4.6)
3. $\tilde{g}\xi+C\xi_x+D\xi_y+A\psi_x+B\psi_y-Q=0$ at $z=\eta_o$ (4.7)

with

$A = G+E\phi_z \qquad G = \phi_x$
$B = H+F\phi_z \qquad H = \phi_y$
$C = G\phi_z \qquad E = \eta_{ox}$
$D = H\phi_z \qquad F = \eta_{oy}$
$\phi_z = GE+HF$
$Q = \tfrac{1}{2}(U_o^2-\phi_x^2-\phi_y^2-\phi_z^2)-\frac{p-p_o}{\rho}-\tilde{g}\eta_o$

Obviously, the solution of (4.4)-(4.7) with $\eta_o=0$ everywhere gives the "double body linearized" flow which is the final result of e.g. the method of Dawson /5/. But since we want to calculate the exact solution of the nonlinear problem, we have to continue the iterative procedure until eventually the corrections ψ and ξ vanish. The final solution is then that of the last Neumann problem. So neither the linearization nor any other approximations made in the derivation of the surface correction have any influence on this final solution; only the convergence properties might be affected. The free surface correction problem is now simplified as follows. Firstly we ignore the ship hull boundary condition. Furthermore, we approximate the depthwise variation of the disturbance potential by

$$\phi(x,y,z)=\phi(x,y,o)\frac{\cosh\alpha(z+H)}{\cosh\alpha H}$$

where α is a coefficient to be determined.

In this way the bottom boundary condition $\phi_z=0$ at $z=-H$ is satisfied.

The free surface is divided into small elements $(\Delta x,\Delta y)$; in each element the disturbance potential is locally approximated by

$$\phi(x,y,z)=(A_o+A_1x + B_1y + A_2x^2 + C_1xy + B_2y^2 + A_3x^3 + C_2x^2y + C_3xy^2 + B_3y^3+\ldots)\frac{\cosh\alpha(z+H)}{\cosh\alpha H} \tag{4.8}$$

and the surface correction by

$$\xi(x,y)= a_o+a_1x+b_1y+a_2x^2+c_1xy+b_2y^2+ a_3x^3+c_2x^2y+c_3xy^2+b_3y^3+\ldots \tag{4.9}$$

Where x and y are local coordinates with the origin at the centre of the element $(\Delta x,\Delta y)$.
The expressions (4.8) and (4.9) are substituted into the equations (4.4), (4.6) and (4.7), which have to be satisfied for all x and y within the element. Therefore the sum of the terms of equal powers in x and y must be zero. With the approximations (4.8) and (4.9) this means that in the free surface conditions an error of $0(\Delta x^3,\Delta y^3)$ is made.

In this way a system of fifteen equations is found in twenty unknowns plus an unknown value of α.
Elimination of the coefficients of ϕ and the coefficients a_3, c_2, c_3 and b_3 of ξ (which are dependent) results in the relations:

$$a_2 + b_2 = \frac{\alpha^2}{2}\left(\frac{Q}{\tilde{g}} - a_o\right) \tag{4.10}$$

$$E^*a_1+F^*b_1+a_2+H^*c_1+H^{*2}b_2=\beta g^*\left(\frac{Q}{\tilde{g}} - a_o\right)+ -g^*\frac{Q_y}{\tilde{g}}F-g^*\frac{Q_x}{\tilde{g}}E \tag{4.11}$$

with

$$E^*=-Eg^*+\tfrac{1}{2}(E+FH^*)$$
$$F^*=-Fg^*+\tfrac{1}{2}H^*(E+FH^*)$$
$$g^*=\tilde{g}/_{2G^2}$$
$$H^*=H/G$$
$$\beta =\alpha\tanh\alpha(H+\eta_o)$$

For a two dimensional case this means if $\beta\approx\alpha$:

$$a_2=\frac{\alpha^2}{2}\left(\frac{Q}{\tilde{g}}-a_o\right) \text{ and}$$

$$E^*a_1+a_2=\alpha g^*\left(\frac{Q}{\tilde{g}} - a_o\right)-g^*\frac{Qx}{\tilde{g}}E$$

When we start with an undisturbed free surface ($\eta_o=0$), $E=E^*=0$ in the first cycle, so $\alpha=2g^*$ and $a_2=\frac{\alpha^2}{2}\left(Q/\tilde{g}-a_o\right)$.

For the threedimensional case, equation (4.10) is multiplied by $2(Q/\tilde{g}-a_o)$,

$$2a_2\left(\frac{Q}{\tilde{g}}-a_o\right)+2b_2\left(\frac{Q}{\tilde{g}}-a_o\right)=\alpha^2\left(\frac{Q}{\tilde{g}}-a_o\right)^2 , \tag{4.13}$$

and equation (4.11) is written as:

$$\frac{T}{g^*}+\frac{a_2}{g^*}=\alpha\left(\frac{Q}{\tilde{g}} - a_o\right) \tag{4.14}$$

with $T=E^*a_1+F^*b_1+H^{*2}b_2+g^*\frac{Q_y}{\tilde{g}}F +$

$$+g^*\frac{Q_x}{\tilde{g}}E;$$

again $\beta\approx\alpha$ has been used. Eliminating α from (4.13) and (4.14) we find

$$a_2=-T+g^{*2}\left(\frac{Q}{\tilde{g}}-a_o\right)+ \pm\tfrac{1}{2}\sqrt{4g^{*4}\left(\frac{Q}{\tilde{g}}-a_o\right)^2-8g^{*2}\left(\frac{Q}{\tilde{g}}-a_o\right)(T-b_2)} \tag{4.15}$$

in which we have to use the positive sign for correspondence with the result for the twodimensional case.
Obviously more equations in the same unknowns are needed. These are found by requiring continuity of ξ and its first and second derivative between neighbouring elements. For simplicity, the coefficients c_1,c_2,c_3 in (4.9) are put zero, which implies continuity of ξ_{xy}.

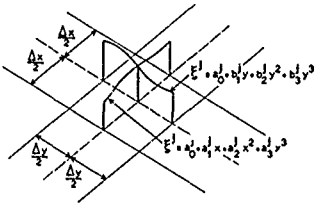


Fig. 3. ξ approximation in one element.

Using a spline approximation in y-direction with continuity up to the second derivative at the boundaries of the elements (at the points $(o,\pm\Delta y/2)$ in each element) one obtains the relations

$$a_o^{j-1}-2a_o^{j}+a_o^{j+1}=\frac{\Delta y^2}{12}(b_2^{j-1}+22b_2^{j}+ +b_2^{j+1}),\quad j=1(1)n. \tag{4.18}$$

The boundary conditions $\partial\xi/\partial y=0$ at $y=y_1$ and $y=y_n=y_w$ are implemented by defining

$$a_o^{\,o}=a_o^{\,1}, \quad a_o^{\,n+1}=a_o^{\,n}$$
$$b_2^{\,o}=b_2^{\,1}, \quad b_2^{\,n+1}=b_2^{\,n}$$

Equation (4.18) relates the coefficients in neighbouring elements; the solution is obtained simultaneously for a whole row of elements at one x-position. Similarly the continuity of x-derivatives at $(0,\pm\Delta x/2)$ would lead to an implicit relation requiring a simultaneous solution for the whole free surface. Presumably this could lead to a solution with waves upstream of the disturbance. It is here that we take into account the radiation condition: we require continuity of ξ, ξ_x and ξ_{xx} only at the upstream point $(0, \Delta x/2)$ in each element:

$$3a_o^{\,j}-a_2^{\,j}\frac{\Delta x^2}{4}=3\xi^j+3\xi_x^j\frac{\Delta x}{2}+\xi_{xx}^j\frac{\Delta x^2}{4} \qquad (4.19)$$

where the right hand side is evaluated at $(0,-\Delta x/2)$. From (4.15) and the spline relations, the coefficients can be computed, and ξ is found for the x-position considered. Then the equations for the next row of elements are solved. Therefore, a disturbance at a certain x-position can only cause waves downstream; upstream its influence is only transmitted by the solution of the Neumann problem. A similar "numerical radiation condition" has been used by Dawson /5/, who approximated the free surface condition by one-sided, upstream finite differences.

As has been mentioned in Section 3, in the solution of the Neumann problem a uniform outflow is prescribed. This might cause errors due to wave reflections or instability unless the free surface shape is made to conform with this uniform flow by the imposition of an artificial wave damping. To this end a pressure distribution on the free surface is introduced such that the waves generated by the ship are cancelled at the outflow boundary. The pressure distribution is connected with the free surface elevation according to:

$$p=+\rho g\eta\frac{(x-x_\ell)^2}{(x_o-x_\ell)^2} \quad ,$$

with

x_o = x-coordinate of outflow boundary

$x_\ell = x_o-\lambda$, where λ = wave length at the symmetry plane.

In this way, $\eta=\eta_x=o$ at the outflow boundary.

As has been shown by Bai /6/ this pressure distribution has a negligible influence on the flow in the vicinity of the ship provided that the downstream boundary is not too close to the stern.

5. Discussion of results

It is known that in numerical methods defined in curvilinear coordinate systems one has to be particularly careful in the calculation of the metric coefficients; different approximations may give totally different results though they may converge to the same solution for vanishing grid spacings. In Chapter 3 it has been mentioned that a linear variation of G^{13} and G^{23} and a quadratic variation of G^{11}, G^{12} and G^{22} within one element is allowed. The importance of this assumption is illustrated in Fig. 4, which shows the solution of the trivial problem of a uniform flow without free surface, calculated in a nonorthogonal coordinate system. With the above assumption the exact result is found, but when within each element all G^{ij} are kept constant, significant errors occur in the whole computational domain.

Another test of the solution of the Neumann problem concerned the flow past a sphere at the centre of a square channel for which the analytic solution is known. The channel width amounted to 5 sphere diameters, the computational domain extended from 3 diameters upstream to 7 diameters downstream of the centre of the sphere. The following discretisations were used:

1. 3 planes in depth, with 228 elements on each plane;
2. 5 planes in depth, with 228 elements each;
3. 3 planes, 864 elements each;
4. 3 planes, 1892 elements each.

In Figs 5 and 6, the differences between the numerical and the analytic solution are shown. It appears that only with the largest number of elements a reasonable accuracy near the stagnation point is obtained; a comparison of the results with discretisations 3. and 4. suggests a second-order accuracy. The influence of the number of x^3-planes is more noticeable at the bottom of the channel, which is as expected; the number of elements makes less difference here, because at some distance the details of the body geometry have less influence. Obviously small elements are required to resolve the large gradients near the stagnation points; for bodies with a fine bow and stern a larger element size will be permissible.

The complete solution method has been applied to the Series 60 $C_B=0.60$ model which has been a test case of the Workshop on Ship Wave Resistance Computations /7/. In Fig. 7 the results

of the present method for three Froude numbers are compared with experimental results. The experiments were done with a model free to sink and trim, while in our calculations this has not been taken into account; therefore complete agreement cannot be expected. Even so the results are rather disappointing. Particularly there is a phase shift in all wave profiles. This may partly be attributed to the fact that the wave elevation had to be extrapolated from the points where the surface correction is applied (a rectangular grid) towards the hull. Therefore another calculation was made in which one row of grid points coincided with the hull surface though the nonorthogonality was not taken into account. In the three iterations performed this resulted in a different wave profile that showed a better agreement with the experimental phase. Anyhow the results are much less accurate than those of Dawson /7/, although the present method uses the exact free surface conditions. This cannot be due to the neglection of sinkage and trim only, because for Fn=0.22 Dawson's calculations concerned a fixed model, too.

The change of the wave profile in the course of the iteration process is displayed in Fig. 9. After 6 iterations the wave profile has converged reasonably well along the first ½L, but further aft the wave height still increases. The phase difference between the numerical and the experimental profile is gradually decreasing, but we do not expect it would ultimately disappear. Most important of all is the very slow convergence near the stern. The downstream marching surface correction method implies that in this region the free surface deviation will converge most slowly.

The wave resistance has been calculated from the calculated, wave pattern behind the model by applying a formula used in experimental "transverse cut" methods. It agrees reasonably well with the experimental data, apart from an Fn-independent contribution from the viscous drag.

The calculations for the Series 60 model were performed with three x^3-planes with 3062 elements on each; each iteration required 86 seconds execution time on a CDC Cyber 175 computer. Including I/O time, the costs amounted to $ 210 per iteration.

6. Conclusions

The method presented should in principle converge to the solution of the exact problem without any linearization. This advantage over most other methods has, however, not been borne out by the results obtained up to now. The application to the flow past a sphere showed the necessity of a large number of elements near blunt bodies. For free surface flows, the iterative procedure used for correcting the free surface shape converges slowly in the downstream part of the computational domain. This means that the computation time becomes excessively large unless a coarse grid is used and the resulting large discretisation errors are accepted. It might be that the solution of the free surface correction problem has been simplified too much, e.g. by the prescription of the depthwise variation; in that case a more accurate calculation of the correction might accelerate the convergence and reduce the total computation time.
Other recommendable refinements are the incorporation of the effects of sinkage and trim by a repositioning of the ship in each iteration, and the specification of boundary conditions at the sidewalls which give a better representation of the flow in an infinite domain.
Though the calculations have shown the possibility to arrive at a converged solution, much remains to be done before the present method is useful for practical applications.

7. Acknowledgment

The author wishes to express his deep appreciation to Dr. C. Korving of the Delft University of Technology whose method was the basis for this program and to H.C. Raven for his stimulating and critical help.

8. References

1. R.K.-C. Chan, "Finite Difference Simulation of the Planar Motion of a Ship", Second International Conference on Numerical Ship Hydrodynamics, September 1977.

2. J.L. Hess, "Progress in the Calculation of Nonlinear Free-Surface Problems by Surface-Singularity Techniques", Second International Conference on Numerical Ship Hydrodynamics, September 1977.

3. C. Korving, "A Three-Dimensional Method for the Calculation of Flow in Turbomachines Using Finite Elements on a Blade-to-Blade Surface of Revolution", Delftse Universitaire Pers, 1974.

4. C. Korving and A.J. Hermans, "The Wave Resistance for Flow Problems with a Free Surface", Second International Conference on Numerical Ship Hydrodynamics, September 1977.

5. C.W. Dawson, "A Practical Computer Method for Solving Ship Wave Problems", Second International Conference on Numerical Ship Hydrodynamics, September 1977.

6. K.J. Bai, "A Note on Numerical Radiation Condition", Proceedings of the Continued Workshop on Ship Wave-Resistance Computations", October 1980.

7. Proceedings of the Workshop on Ship Wave-Resistance Computations, November 1979.

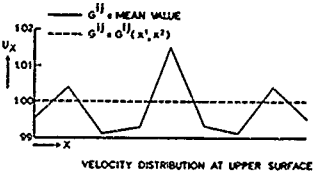




FIG 4 INFLUENCE G^{ij} DEFINITION

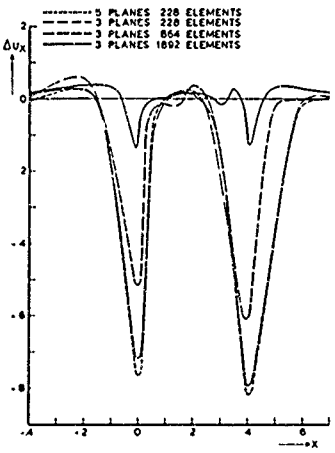


FIG 6 ERROR IN AXIAL VELOCITY AT UPPER SURFACE IN SYMMETRY PLANE

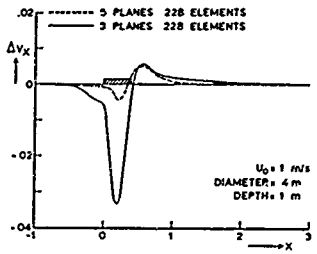


FIG 5 ERROR IN AXIAL VELOCITY AT CHANNEL BOTTOM,

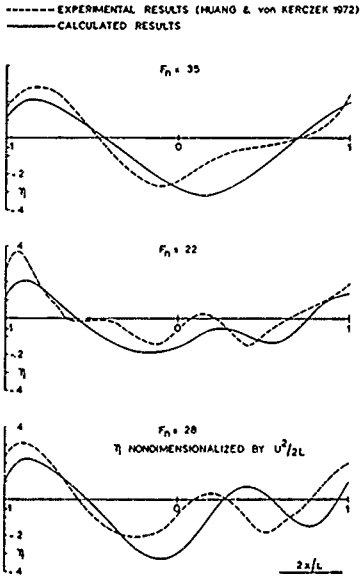


FIG 7 SERIE 60, C_B = .6 WAVE PROFILES

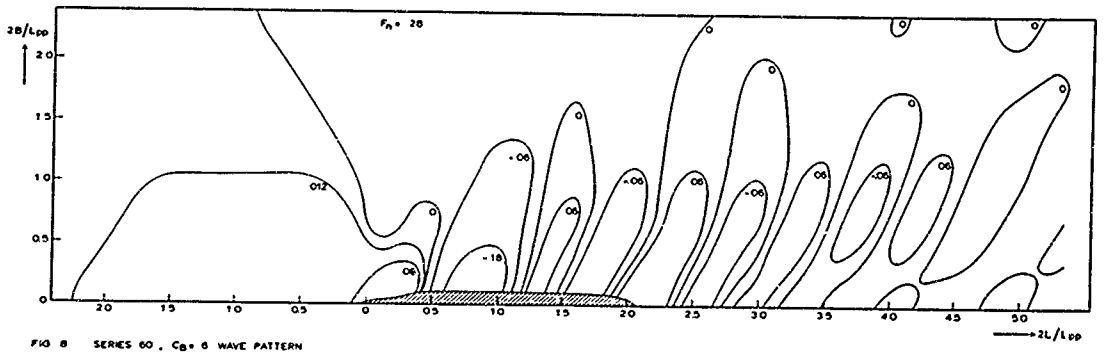


FIG 8 SERIES 60 , C_B = .6 WAVE PATTERN

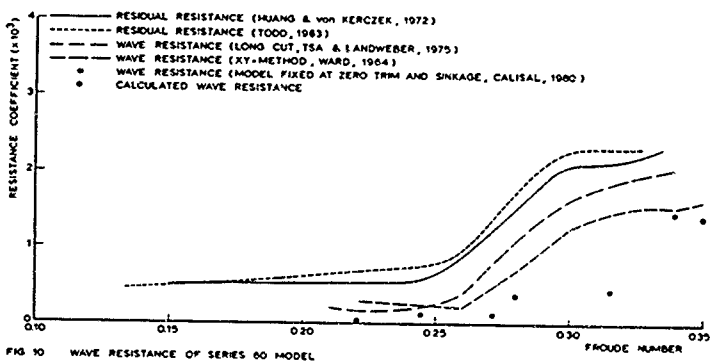


FIG 10 WAVE RESISTANCE OF SERIES 60 MODEL

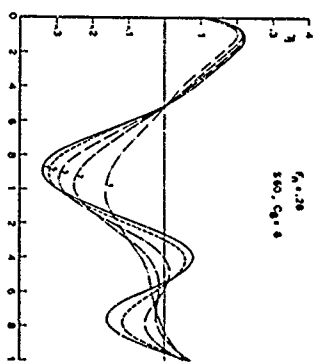


FIG 9 ITERATION PROCESS WAVE ELEVATION

NUMERICAL EXPLANATION OF NONLINEAR NONDISPERSIVE WAVES AROUND BOW

Hideaki Miyata,
University of Tokyo, Tokyo
Akira Suzuki,
Ishikawajima Harima Heavy Industries, Tokyo
Hisashi Kajitani,
University of Tokyo, Tokyo

Abstract

It was found by Miyata that ships in steady straight course in deep water generate nonlinear waves named Free Surface Shock Wave. Almost all ships generate free surface shock waves in the neighborhood of ships in the thin layer adjacent to the free surface and they contribute to resistance. Their typical characteristics that have been experimentally clarified indicate that they are nonlinear nondispersive waves governed by nonlinear equations. The theoretical explanation of the new wave making phenomenon is attempted by a newly developed modified MAC-method. The computed results for a 2-D rectangular body and 3-D wedge models are compared with experimental ones in the form of wave profile and distribution of velocity components. The typical characteristics of the nonlinear waves around bows which are experimentally verified are also demonstrated by the numerical computations.

1. Introduction

In 1977 one of the authors intuitively found the existence of a kind of nonlinear waves in the vicinity of a ship in steady straight course in deep water. Since then, our attention has been focused on the wave motions in the vicinity of ships. The experimental investigations at the experimental tank of the University of Tokyo have demonstrated that these waves have proper characteristics that deserve the term of nonlinear wave[1)-6)]. They are so analogous, in many respects, to shock waves in supersonic flow and shallow water shock waves[6)] that they are named free surface shock wave (sometimes abbreviated as "FSSW in this paper).

The experimental investigations have shown that FSSWs occur around ships of any hull form and that they contribute to ship resistance in a quite different manner from linear waves. The role of FSSWs played in ship resistance is especially important for ships of wide beam-length or of shallow draft[2)3)]. On the other hand it has come to be clearly understood that the bulbous bow is very effective not only for the cancellation of linear dispersive waves but also for the attenuation of resistance due to FSSWs[4]. Anyway, the phenomenon of FSSW is most important for the clarification of the wave-making of ships and for the design of hull forms of minimum resistance. Without further advanced investigations into this new phenomenon no significant progress will be expected.

Suppose that waves are classified into linear and nonlinear ones, FSSWs evidently belong to the latter, i.e., they are finite amplitude waves governed by nonlinear equations. Therefore, neither a potential theory nor a Fourier analysis can be applied to this problem.

At the present time nonlinear wave phenomena are the subject of extensive study in many branches of physics and engineering. In the field of fluid dynamics solitary waves in shallow water and shock waves in supersonic flow have been familiar nonlinear waves for a long time, and FSSWs will share the term of nonlinear wave in fluid dynamics.

Some nonlinear waves have the dispersive property and the others the dissipative one. In concern with "classical" gravitational waves on water surface, the dispersion is very important if the depth of the water is deep enough. Waves having different wave number have different velocities and nonlinear steepening of the wave can be compensated by the dispersive spread. However, if the depth of water is small, the phase velocity is equal to $\sqrt{gh}$, i.e., the dispersion is not important. In this case, nonlinear effects become conspicuous. The most important nonlinear effect is the steepening of wave front. FSSWs are obviously very analogous to the latter case, though the depth of water is deep, as can be understood by the experimental results[1)-5)]. Therefore, we will be able to claim that FSSWs are nonlinear nondispersive waves.

It seems very difficult to theoretically explain FSSWs because they are governed by nonlinear equations. The most popular method of solution is a numerical procedure which is, in many cases very powerful for the problem of nonlinear waves. In this paper a modified Marker-and-Cell method is adopted for the analysis of bow waves in front of a 2-D rectangular floating body and those around a wedge-shaped 3-D body. The Stanford University Modified Marker-And-Cell (SUMMAC) method developed by Chan and Street[7)8)] is further modified so as to make the detailed analysis of FSSWs around the bow possible. The governing equations are the Navier-Stokes equations and these nonlinear partial differential equations are resolved into finite-difference equations in two or three space dimensions

The free-surface and body-surface conditions are carefully treated. The improved version of SUMMAC scheme is called the Tokyo University Modified Marker-And-Cell (TUMMAC) method in this paper.

In Chapter 3 the characteristics of FSSWs are briefly summarized with experimental results, most of which are concerned with FSSWs around wedge models. For the readers who are interested in the other vast experimental results, the previous works in the references[1)~7)] will provide fruitful information. Some discussions on the nonlinear equations are also added in this chapter. The modifications of the MAC method and the computational procedures are described in Chapter 4. In Chapter 5 bow waves in front of a 2-D rectangular body are experimentally examined and they are compared with the calculated results by the TUMMAC scheme. In Chapter 6 the TUMMAC scheme is extended into a three-dimensional one, which offers numerical solutions of nonlinear bow waves in the vicinity of wedges of finite draft.

Normal and oblique FSSWs both have opportunity to occur depending on Froude number and entrance angle[1)~3)], but, experiments and calculations in this paper are mostly undertaken under the condition which generates oblique FSSWs.

2. Nomenclature

DT	time increment
DX	longitudinal width of a cell
DY	lateral width of a cell
DZ	vertical height of a cell
d	draft of model
Fd	Froude number based on d
Fh	Dº based on h
$F\tilde{h}$	Dº based on $\tilde{h}$
Fn	Dº based on model length
g	gravitational acceleration
H	$U^2/2g$
h	shallow water depth
$\tilde{h}$	equivalent shallow water depth
P	pressure
P_0	pressure at free surface
Rn	Reynolds number based on d
T	time
U	speed of uniform stream
u,v,w	disturbance velocity components in x, y and z directions, respectively
ΔV	velocity change across wave front
x	axis parallel to model centerline, positive aftward, origin at FP
y	axis parallel to model beam
z	axis vertical, positive upward
α	entrance angle
β	shock angle (angle of wave front line)
ζ	wave height
ν	kinematic viscosity
ρ	density of water
ψ	P/ρ

(subscript)

i,j,k	denoting x,y and z directions, respectively
n	normal to shock front
t	tangential to shock front

(superscript)

n	denoting time step

3. Characteristics of Free Surface Shock Waves and Their Governing Equations

3.1 Characteristics of Free Surface Shock Waves

The characteristics of FSSWs are entirely different from those of linear dispersive waves. The typical characteristics are 1) formation of lines of discontinuity, 2) unsteadiness and steepness of wave crests, 3) satisfaction of the shock relation, 4) systematical change of the angle of wave front (shock angle), 5) nondispersive propagation and 6) dissipation of wave energy into momentum loss far behind.

In Fig.1 (a) some wave pattern pictures are present, which are photographed with aluminum powder film on the water surface. With the increase of the entrance angle of the ship model the angle of the foremost wave crest increases and a black region appears where the aluminum powder cannot pass across the wave front. The discontinuity of the water flow is intensified by the increase of shock angle. Fig.1 (b) illustrates the change of FSSW formation due to change of advance speed. Both normal and oblique FSSWs occur depending on entrance angle and Froude number based on draft. A normal FSSW is transformed into an oblique one with the increase of advance speed when the entrance angle is not very large, whereas it cannot be transformed and remains to be normal when the entrance angle is very large[1)~3)]. In Fig.2 a result of visualizing the free surface flow is seen, in which the paths of small paper tips are distorted by the lines of discontinuity. FSSWs are nonlinear waves that form lines of discontinuity across which water particles undergo sudden abrupt change in velocity.

The appearance of a wave crest around a round-nosed model in Fig.3 is very similar to turbulent bore. The wave profile is not smooth but it is steep and accompanies unsteady motions.

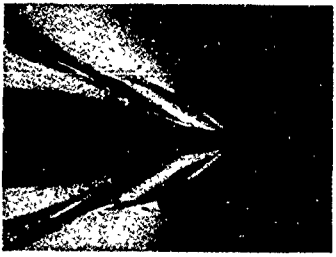
The vectors of disturbance velocity are shown in Fig.4, which are obtained from the measurement of flow field in the vicinity of the front of the foremost nonlinear wave generated by a wedge model. A small 5-hole pitot tube whose outer diameter is 2.1mm is made use of. At the points circled in Fig.4 measurement was impossible because of too great disturbance velocity. In the flow region adjacent to the free surface both x and y components of the disturbance velocities show abrupt change, i.e., the disturbance velocity is remarkably great behind the wave front and it is discontinuously reduced at the wave front. The values of u and v are so great behind the wave front that they can never be interpreted as a disturbance velocity due to the orbital motion of linear dispersive waves. Instead, the distribution of the horizontal velocity components u and v is similar to that of nonlinear shallow water waves such as turbulent bore, showing abrupt velocity change at the wave front and constantly large disturbance velocity behind the wave front.

The physical shock relation is that the tan-

α = 5°



α = 10°



α = 15°

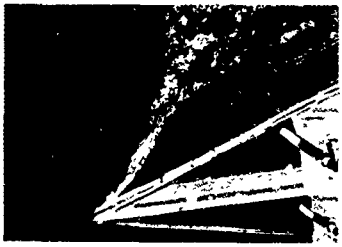


Fig. 1 (a) Wave pattern pictures of entrance angle series at Fn = 0.267

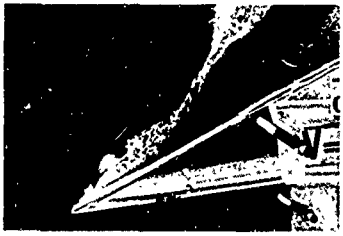
Fd = 1.01 normal FSSW



Fd = 1.51 oblique FSSW



Fd = 2.02 oblique FSSW



l (b) Wave pictures of wedge model (α = 25°, d = 0.1m)

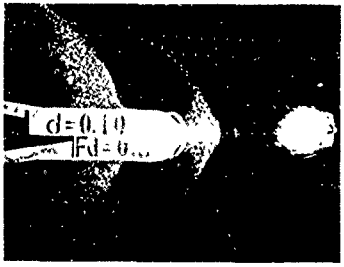


Fig. 2 Visualized streamlines on the free surface (WM1-A, d = 0.1m, Fd = 0.8)

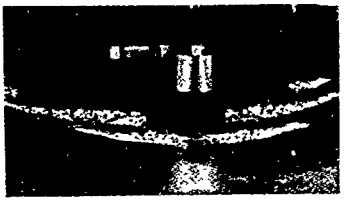


Fig.3 Appearance of nonlinear bow waves (WM1-B, d = 0.08m, Fn = 0.20)

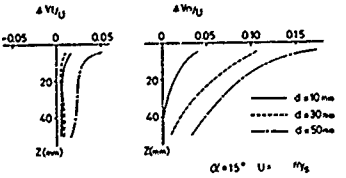


Fig.5 Normal and tangential components of velocity change across wave front (wedge model)

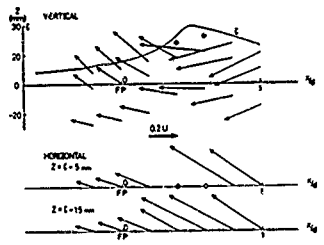


Fig.4 (a) Vertical and horizontal disturbance velocity vectors near the foremost wave front on the line y/d = 0.6 (wedge model, α = 20°, d = 0.1m, Fd = 1.01)

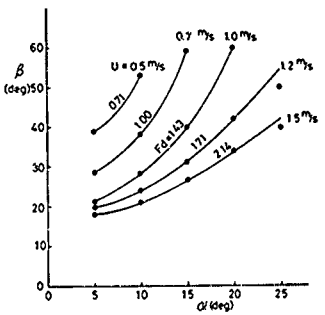


Fig.6 Relation between entrance angle and foremost wave-front angle (wedge model)

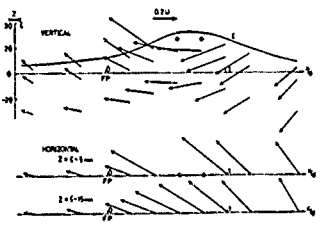


Fig.4 (b) Vertical and horizontal disturbance velocity vectors near the foremost wave front on the line y/d = 0.8 (wedge model, α = 20°, d = 0.1m, Fd = 1.01)

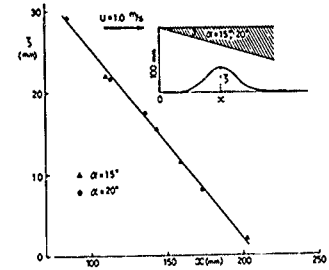


Fig.7 Relation between wave height and position of wave crest (wedge model, draft from 0.01m to 0.1m)

gential component of the velocity change across wave front is null while the component of the velocity change normal to the wave front is great. In other words velocity vectors are suddenly distorted outward at the wave front by the violent disturbance velocities normal to the wave front. The measured components of the velocity change are shown in Fig.5. The tangential component ΔVt is approximately negligible for the three cases, while the normal component ΔVn is very large especially in the flow near the free surface. The FSSWs are phenomena that occur in the thin flow-layer near the free surface and they approximately satisfy the shock relation there. The FSSW can be a kind of shock wave.

The angles of front lines of the foremost waves around bows of wedge models are measured and figured in Fig.6. It is clearly observed that the angle of the wave front to the centerline of the models (shock angle) is systematically varied. The angle increases with the increase of entrance angle and with the decrease of advance speed. This systematical change is very analogous to that of shock waves in shallow water[6], which satisfies the following relation.

$$\tan\alpha = \frac{\tan\beta(\sqrt{1 + 8Fh^2\sin^2\beta} - 3)}{2\tan^2\beta - 1 + \sqrt{1 + 8Fh^2\sin^2\beta}} \qquad (1)$$

$$\text{where} \quad Fh = U/\sqrt{g\tilde{h}} \qquad (2)$$

This property is also most interesting and important, since the wave-crest angle of linear dispersive waves (Kelvin waves) does not depend on the entrance angle nor the draft. There are two kinds of FSSW, namely, oblique and normal ones, as stated before, and the experimental results in Fig.6 are confined to oblique ones. It is noted that normal FSSWs whose β is $\pi/2$ occur when α is great and advance speed is low.

If the foremost waves around wedge models are certain shock waves, it will be imagined that the discontinuity will be intensified with the increase of shock angle. The wave height and the longitudinal position of the maximum height are measured on a line parallel to the centerline. The result is shown in Fig.7. With the forward shift of wave crest, i.e., with the increase of shock angle the wave height which is the measure of the strength of discontinuity is linearly increased.

The concept of equivalent shallow water depth was introduced for the practical purpose of improving the method of hull form design[4][6]. The equivalent shallow water depth is calculated from the measured shock angle β of wedge models according to Eqs.(1) and (2), i.e., Fh is determined by Eq.(1) and then $\tilde{h}_1$ is derived by Eq.(2). The calculated equivalent shallow water depth is illustrated in Fig.8. The equivalent shallow water depth is approximately independent of the advance speed. This implies that FSSWs do not have dispersive property, since the velocity of wave is $\sqrt{g\tilde{h}_1}$ that is independent of advance speed when the above analogical simplification is admittable.

Fig.9 shows measured velocity vectors in the

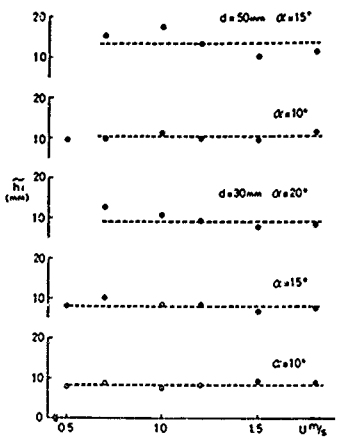


Fig.8 Dependence of equivalent shallow water depth on advance speed (wedge model)

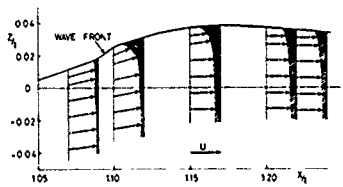


Fig.9 Measured velocity vectors illustrating discontinuity and diffusion process of free surface shock wave from stern

neighborhood of the front of a FSSW from the stern of a 2-D model ship of simple hull form. In this case FSSWs are superposed on the linear transverse wave. At the front of FSSW the water flow undergoes abrupt drop in velocity in the thin layer adjacent to the free surface and consequently the vertical distribution of velocity vectors becomes very steep immediately behind the wave front, whereas it is nearly uniform before the front. The steep slope is due to the remarkable disturbance velocity in the forward direction normal to wave front. It is noted that the steep slope is gradually attenuated and the velocity distribution tends to be uniform far behind the wave front. This shows a kind of dif-

fusion process and indicates the role of viscosity. The appearance of the wave front in Fig.3 also suggests that the dispersion is not important for FSSWs but that the diffusion and the dissipation will have the possibility to play a significant role. At far behind ships the effect of FSSWs is revealed in momentum loss, and the resistance due to FSSWs is approximately measured by integrating the momentum loss[2)5)] This means that the energy of FSSWs is dissipated into something different from wave energy.

3.2 Governing Equations

The governing equations for fluid flows are the equation of continuity and the equation of motion as follows for incompressible flow.

$$\frac{\partial u}{\partial x} + \frac{\partial v}{\partial y} + \frac{\partial w}{\partial z} = 0 \tag{3}$$

$$\frac{\partial u}{\partial t} + u\frac{\partial u}{\partial x} + v\frac{\partial u}{\partial y} + w\frac{\partial u}{\partial z}$$

$$= X - \frac{1}{\rho}\frac{\partial p}{\partial x} + \nu\left(\frac{\partial^2 u}{\partial x^2} + \frac{\partial^2 u}{\partial y^2} + \frac{\partial^2 u}{\partial z^2}\right)$$

$$\frac{\partial v}{\partial t} + u\frac{\partial v}{\partial x} + v\frac{\partial v}{\partial y} + w\frac{\partial v}{\partial z}$$

$$= Y - \frac{1}{\rho}\frac{\partial p}{\partial y} + \nu\left(\frac{\partial^2 v}{\partial x^2} + \frac{\partial^2 v}{\partial y^2} + \frac{\partial^2 v}{\partial z^2}\right) \tag{4}$$

$$\frac{\partial w}{\partial t} + u\frac{\partial w}{\partial x} + v\frac{\partial w}{\partial y} + w\frac{\partial w}{\partial z}$$

$$= Z - \frac{1}{\rho}\frac{\partial p}{\partial z} + \nu\left(\frac{\partial^2 w}{\partial x^2} + \frac{\partial^2 w}{\partial y^2} + \frac{\partial^2 w}{\partial z^2}\right)$$

Although Eq.(4) is really the governing equation, it is, in the classical boundary value problems, only dealt with as a boundary condition in an integrated form, i.e., the so-called dynamic boundary condition For most of the theories of wave resistance the governing equation is Eq.(3) which is a linear equation that analytically gives linear solutions. The Navier-Stokes equations are, however, the nonlinear equations which may have possibility of generating nonlinear waves including FSSWs. To handle with the problem of FSSWs the linearization of the equations cannot be admitted, and the nonlinear equations are to be solved.

The governing equations for shallow water waves are as follows.

$$\frac{\partial \bar{p}}{\partial t} + \frac{\partial(\bar{p}u)}{\partial x} + \frac{\partial(\bar{p}v)}{\partial y} = 0 \tag{5}$$

$$\frac{\partial u}{\partial t} + u\frac{\partial u}{\partial x} + v\frac{\partial u}{\partial y} + \frac{1}{\bar{p}}\frac{\partial \bar{p}}{\partial x} = 0$$

$$\frac{\partial v}{\partial t} + u\frac{\partial v}{\partial x} + v\frac{\partial v}{\partial y} + \frac{1}{\bar{p}}\frac{\partial \bar{p}}{\partial y} = 0 \tag{6}$$

where $\bar{p} = \rho(\zeta + h)$, $\bar{p} = \frac{\rho g}{2}(\zeta + h)^2$ (7)

Neglecting the diffusion terms, this equation is a nonlinear hyperbolic equation which is the same with the equation of compressible flow. If the equivalent shallow water depth[4)6)] is introduced, i.e., h is replaced by $\bar{h}$, the problem of FSSWs can be solved in the same manner with shallow water waves. However, the equivalent shallow water depth was introduced only for the purpose of developing a practical method of hull form improvement, and this way is not suitable for the theoretical interpretation of the new phenomenon.

The simple one-dimensional nonlinear equations familiar to nonlinear wave problems are the Burgers equation and the K-dV equation, which are described as follows, respectively.

$$\frac{\partial u}{\partial t} + u\frac{\partial u}{\partial x} = \nu\frac{\partial^2 u}{\partial x^2} \tag{8}$$

$$\frac{\partial u}{\partial t} + u\frac{\partial u}{\partial x} = \delta\nu\frac{\partial^3 u}{\partial x^3} \tag{9}$$

The difference between the above two equations is only on the right-hand-side term, i.e., the difference of the second and the third derivatives. However, the characteristics of waves expressed by the two equations are quite different. The term of second derivative in the Burgers equation works with dissipative property, whereas that of third derivative in the K-dV equation works with dispersive property. Thus, the two equations are the typical governing equations for nonlinear dissipative waves and nonlinear dispersive waves, respectively. The governing equation for supersonic shock waves is the Burgers equation[3)12)] The steepening of waves caused by the nonlinear convection term is balanced with the dissipative effect of the diffusion term.

It will be noted that the Navier-Stokes equations are very similar to the Burgers equation. The nonlinear convective terms in the Navier-Stokes equations may steepen the wave slope and this steepening may be eased by the diffusive terms. In general, shock waves are formed as a balance of the convective terms of the equations and the wave-form easing tendency of diffusion terms. Therefore, the Navier-Stokes equations should be the governing equation for the analysis of nonlinear nondispersive waves in the vicinity of ships. The viscous terms are retained, because they will play an important role through either a physical process or a numerical process.

The numerical procedure will not be very proper for the analysis of linear dispersive waves,

since the solution is very sensitively influenced by the boundary condition on the outer boundaries of the limited computational domain. This may partly because of the property of dispersive propagation. However, FSSWs are local nonlinear waves whose solution can be derived as a result of the balance of convective and diffusive effects at the wave front. Therefore, the numerical solution will be less sensitively influenced by the outer boundary conditions.

4. Modified Marker-And-Cell Method

4.1 Finite-Difference Representations

The Navier-Stokes equations in conservation form are transformed into finite-difference representations in the same manner with the SUMMAC scheme but in three space dimensions. Terms that involve only space derivatives are approximated by central differences. The x-directional finite difference representation is, for example, as follows.

$$\frac{u^{n+1}_{i+1/2\,jk} - u_{i+1/2\,jk}}{\partial t}$$

$$= -\frac{(u_{i+1jk})^2 - (u_{ijk})^2}{\partial x}$$

$$-\frac{(uv)_{i+1/2\,j+1/2\,k} - (uv)_{i+1/2\,j-1/2\,k}}{\partial y}$$

$$-\frac{(uw)_{i+1/2\,jk+1/2} - (uw)_{i+1/2\,jk-1/2}}{\partial z}$$

$$+\frac{\phi_{ijk} - \phi_{i+1jk}}{\partial x}$$

$$+\nu\left(\frac{u_{i+1/2\,j+1\,k} - 2u_{i+1/2\,jk} + u_{i+1/2\,j-1\,k}}{\partial y^2}\right.$$

$$\left.+\frac{u_{i+1/2\,jk+1} - 2u_{i+1/2\,jk} + u_{i+1/2\,jk-1}}{\partial z^2}\right) \qquad (10)$$

where, for example

$$u_{ijk} = \frac{1}{2}(u_{i+1/2\,jk} + u_{i-1/2\,jk})$$

$$(uv)_{i+1/2\,j+1/2\,k}$$

$$= \frac{1}{4}(u_{i+1/2\,jk} + u_{i+1/2\,j+1\,k})(v_{ij+1/2\,k} + v_{i+1\,j+1/2\,k}) \qquad (11)$$

In the above equations, variables with superscript n+1 are related to the (n+1)-th time step. Variables lacking a superscript are evaluated at the n-th step.

From Eq (10) and the similar representations for the followings,

$$\frac{v^{n+1}_{ij+1/2\,k} - v_{ij+1/2\,k}}{\partial t}$$

$$\frac{w^{n+1}_{ijk+1/2} - w_{ijk+1/2}}{\partial t}$$

$$\frac{u^{n+1}_{i-1/2\,jk} - u_{i-1/2\,jk}}{\partial t}$$

$$\frac{v^{n+1}_{ij-1/2\,k} - v_{ij-1/2\,k}}{\partial t}$$

$$\frac{w^{n+1}_{ijk-1/2} - w_{ijk-1/2}}{\partial t}$$

the following equation is obtained.

$$\frac{D^{n+1}_{ijk} - D_{ijk}}{\partial t}$$

$$= - Q_{ijk} + R_{ijk} + \nu \left(\frac{D_{i+1jk} - 2D_{ijk} + D_{i-1jk}}{\partial x^2} \right.$$

$$+ \frac{D_{ij+1k} - 2D_{ijk} + D_{ij-1k}}{\partial y^2}$$

$$\left. + \frac{D_{ijk+1} - 2D_{ijk} + D_{ijk-1}}{\partial z^2} \right) \qquad (12)$$

Here

$$D_{ijk} = \frac{u_{i+1/2jk} - u_{i-1/2jk}}{\partial x}$$

$$+ \frac{v_{ij+1/2k} - v_{ij-1/2k}}{\partial y}$$

$$+ \frac{w_{ijk+1/2} - w_{ijk-1/2}}{\partial z} \qquad (13)$$

$$Q_{ijk} = \frac{1}{\partial x^2} \left[(u_{i+1jk})^2 - 2(u_{ijk})^2 + (u_{i-1jk})^2 \right]$$

$$+ \frac{1}{\partial y^2} \left[(v_{ij+1k})^2 - 2(v_{ijk})^2 + (v_{ij-1k})^2 \right]$$

$$+ \frac{1}{\partial z^2} \left[(w_{ijk+1})^2 - 2(w_{ijk})^2 + (w_{ijk-1})^2 \right]$$

$$+ \frac{2}{\partial x \partial y} \left[(uv)_{i+1/2j+1/2k} - (uv)_{i-1/2j+1/2k} \right.$$

$$\left. - (uv)_{i+1/2j-1/2k} + (uv)_{i-1/2j-1/2k} \right]$$

$$+ \frac{2}{\partial y \partial z} \left[(vw)_{ij+1/2k+1/2} - (vw)_{ij-1/2k+1/2} \right.$$

$$\left. - (vw)_{ij+1/2k-1/2} + (vw)_{ij-1/2k-1/2} \right]$$

$$+ \frac{2}{\partial x \partial z} \left[(uw)_{i+1/2jk+1/2} - (uw)_{i-1/2jk+1/2} \right.$$

$$\left. - (uw)_{i+1/2jk-1/2} + (uw)_{i-1/2jk-1/2} \right] \qquad (14)$$

$$R_{ijk} = - \left[\frac{1}{\partial x^2} (\psi_{i+1jk} - 2\psi_{ijk} + \psi_{i-1jk}) \right.$$

$$+ \frac{1}{\partial y^2} (\psi_{ij+1k} - 2\psi_{ijk} + \psi_{ij-1k})$$

$$\left. + \frac{1}{\partial z^2} (\psi_{ijk+1} - 2\psi_{ijk} + \psi_{ijk-1}) \right] \qquad (15)$$

The D terms do not vanish in general, because of the errors in the numerical procedure, whereas $D \equiv 0$ is required to rigorously conserve mass. Thus, $D \neq 0$ is aimed at at the (n+1)-th step and D^{n+1}_{ijk} in Eq. (12) is set zero.

The equation for the pressure is derived as,

$$R_{ijk} = - \frac{D_{ijk}}{\partial t} + Q_{ijk}$$

$$- \nu \left(\frac{D_{i+1jk} - 2D_{ijk} + D_{i-1jk}}{\partial x^2} \right.$$

$$\left. + \frac{D_{ij+1k} - 2D_{ijk} + D_{ij-1k}}{\partial y^2} \right.$$

$$+ \frac{D_{ijk+1} - 2D_{ijk} + D_{ijk-1}}{\partial z^2} \Bigg) \qquad (16)$$

R_{ijk} is defined when u, v, w are given and then the pressure ($\psi = P/\rho$) is derived by the following equation.

$$\psi_{ijk} = \frac{1}{2\left(\frac{1}{\partial x^2} + \frac{1}{\partial y^2} + \frac{1}{\partial z^2}\right)} \left(\frac{\psi_{i+1jk} + \psi_{i-1jk}}{\partial x^2} \right.$$

$$+ \frac{\psi_{ij+1k} + \psi_{ij-1k}}{\partial y^2}$$

$$\left. + \frac{\psi_{ijk+1} + \psi_{ijk-1}}{\partial z^2} + R_{ijk} \right) \qquad (17)$$

Eq. (17) is iteratively solved and the obtained pressure is substituted in Eq. (10) so that the velocity components at the (n+1)-th step are obtained.

For 2-D cases the terms including v or y are dropped in the above equations.

4.2 Boundary Conditions

The kinematic free surface condition is satisfied by the movement of marker particles. In the 2-D case the particle velocities are obtained from the u and w fields. The wave profile is defined by the new positions of the markers in the same manner with the original MAC method[12]. When this method is applied to 3-D cases the new wave height is obtained at irregular positions of the disturbed water surface, which makes the two-dimensional interpolation difficult. Therefore, the old positions of marker particles are iteratively obtained so that the new positions are located straightly above the center of the cells.

For the dynamic free surface condition "irregular stars" of the SUMMAC method are made use of so that $P=P_0$ is satisfied at the exact location of the free surface.

On the surface of the floating body the free-slip condition is applied. The waterlines of 3-D bodies do not coincide with the diagonals of the cells, instead, they bisect the horizontal sides of the cells so that the positions where u and v are evaluated are located on the body-surface.

The computational domain is limited within the depth two or three times as deep as draft, and velocities are smoothly connected with the double model flow in the deeper region.

The simple and convenient outer boundary condition is made use of, i.e., the velocity components on the cells at the outer boundaries are extrapolated from the neighboring inner cells along the local flow direction, and they are assumed same with the velocity components on the neighboring inner cells.

5. Nonlinear Waves in Front of a Rectangular 2-D Model

The 2-D nonlinear waves generated in front of a rectangular floating body are supposed to essentially have the same characteristics with those of an usual 3-D bow, though they will have much more violent appearance. Therefore, the simple cases of 2-D flows are studied in this chapter.

5.1 Experimental Results

A box-shaped model RM1 in Fig.10 was manu-

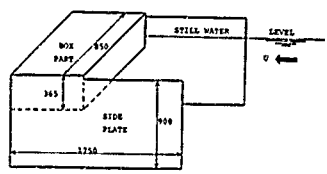


Fig.10 Rectangular model (RM1) for 2-D experiments

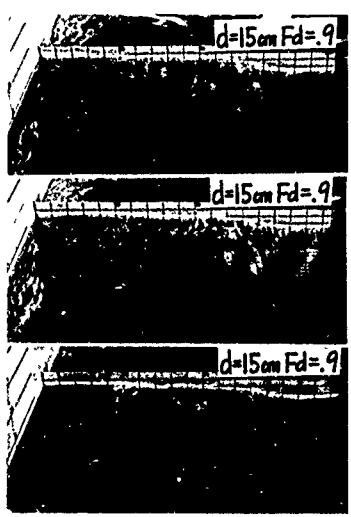


Fig.11 Observed bow waves in front of RM1 (d = 0.15m, Fd = 0.9)

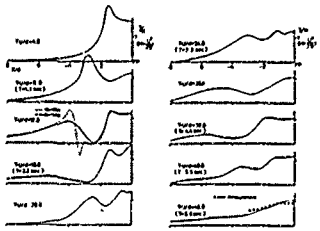


Fig.12 Time sequence of calculated 2-D wave profile (d = 0.15m, Fd = 0.9)

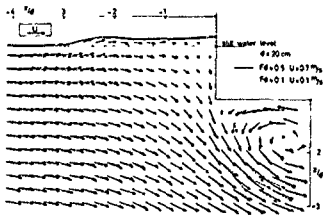


Fig.13 Calculated velocity vectors at different Froude numbers (d = 0.2m)

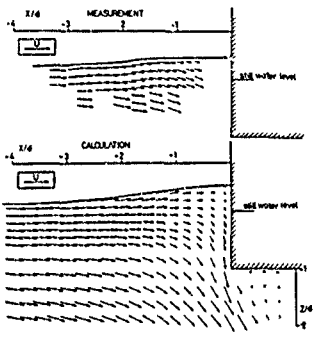


Fig.14 Comparison of measured and calculated velocity vectors (d = 0.15m, Fd = 0.9)

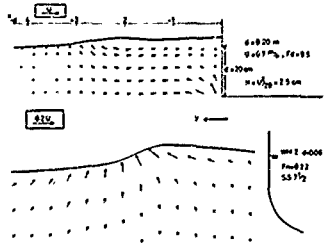


Fig.15 Comparison of disturbance velocity vector distribution between a 2-D model (RM1, d = 0.2m, Fd = 0.5) and a simple 3-D model (WM2, d = 0.06m, Fd = 1.39)

factured for a 2-D flow to be realized in the towing tank. The side-walls are necessary to realize a 2-D flow though they simultaneously have an unfavorable effect, i.e., they generate waves and interact with the flow caused by the box-part. Thus, it is very difficult to realize a complete 2-D flow ; therefore, it is assumed that a 2-D flow is locally realized on the vertical plane on the centerline of the model. Wave profiles and velocity components are measured on this plane with a wave recorder of point lowering type and a five-hole pitot tube.

Some examples of wave pictures are shown in Fig.11. The appearance of the wave front looks turbulent, which is similar to the appearance in Fig.3 of a 3-D case. The wave slope is steepened here and it seems to be eased by some dissipative effect, which results in the turbulent appearance. At the condition in Fig.11 the waves in front of the bow are not steady but they periodically change their shape and position of wave front. The unsteadiness of the waves will have certain connection with the nonlinearity of the phenomenon.

5.2 Calculations by TUMMAC

The 2-D version of the TUMMAC method is applied to the case in Fig.11. The domain of computation is as shown in Fig.13. The number of cell is about 2500. The floating body is impulsively started and the calculation is continued until $T \cdot U/d = 48$ ($T = 6.6$ sec) with the interval of $DT \cdot U/d = 0.01$, i.e., the calculation is repeated 4800 times.

The time sequential development of the wave profile is present in Fig.12. A steep wave is generated in front of the body and it is attenuated and finally reaches to the wave profile that agrees well with the measured mean wave profile at $T \cdot U/d = 48$. However, the calculated wave profile at $T \cdot U/d = 48$ is not the steady solution, but it is changed through the further computa-

tional steps into the wave profile same with that at T·U/d = 32, and then into that at T·U/d = 40. The waves periodically change their shapes with the period of about 2 second. The unsteadiness of the wave is also revealed in the calculation. Throughout the above computation artificial viscosity is introduced, i.e., the Reynolds number based on draft is assumed 100. When it is assumed 200 the slope of the wave becomes extremely steep and the computation cannot be continued. The artificial viscosity is necessary in order to obtain steady solutions by the present scheme.

The calculations are carried out at other different conditions and the influence of Froude number is illustrated in Fig.13 in which wave profiles and distributions of velocity vectors are compared between two advance speed, i.e., Fd = 0.5 and 0.1. At Fd = 0.1 the elevation of the free surface is comparatively negligible and the velocity vectors near the free surface are oriented horizontally or somewhat downward, while at Fd = 0.5 the conspicuous wave with steep slope at the front is generated and it is naturally accompanied with upward oriented velocity vectors at the wave front. The most outstanding difference between the two conditions consists in the difference of the orientation of the flow in the vicinity of the free surface. Fig.13 indicates that the conspicuous wave is generated when the advance speed exceeds a certain value. At the bottom corner of the body the flow is separated and consequently a tremendous vortical motion appears. This will have some influence on the flow near the free surface, though the details are not studied

Extensive experimental results of 2-D waves by floating bodies can be found in the paper by K. Suzuki[12], and our experimental results, most of which are abbreviated here, will be reported in the near future.

The distribution of velocity vectors is compared between experiment and calculation in Fig.14. The region where measurement was possible is limited. The agreement is not complete but satisfactory. The distribution of disturbance velocity vectors calculated by the TUMMAC method in a 2-D case is compared with that measured in the y-Z plane of the flow around a ship model of simple hull form in Fig.15 The figure of the 3-D case shows the disturbance velocity vectors of the flow near the front of an intense FSSW In both cases the disturbance velocity vectors are great and oriented upward and outward near and behind the wave front, while they are considerably weakened in the outer region. It is supposed that the essential characteristics of the nonlinear waves around the bow are not quite different between each other.

6. Nonlinear Bow Waves of a Wedge Model

The 3-D version of the TUMMAC method is made use of for the theoretical explanation of the bow waves of a wedge model whose characteristics are experimentally investigated[13] and summarized in Chapter 3. The wedge model whose entrance angle is 20 degree (wedge angle is 40 degree) is served for the computation In case d = 0.1m the dimensions of a cell are DX = 0.05m, DY = 0.0182m, DZ = 0.025m. The arrangement of the cells at the undisturbed condition is illustrated in Fig 16. The number of the cells is about 5500. The time increment DT·U/d is 0.01 or 0.05 , the calculated result in case DT·U/d = 0.05 agrees well with the case of smaller time increment.

6.1 Bow Wave Formation

For the 3-D cases the wedge model is constantly accelerated from rest until it reaches to the assumed advance speed when T·U/d = 5. The time sequence of the calculated wave pattern is shown in Fig.17. At T·U/d = 20 the wave pattern reaches to the steady state. During the

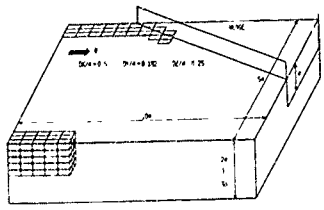


Fig.16 Cell arrangement for 3-D case at initial condition

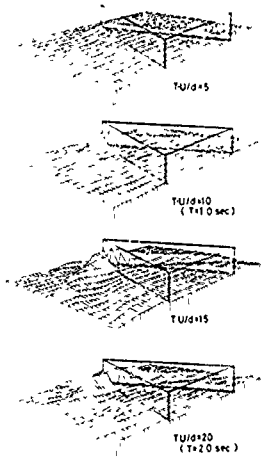


Fig.17 Time sequence of wave pattern around wedge model (α = 20°, d = 0.1m, Fd = 1.01)

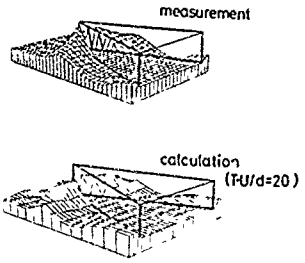


Fig.18 Comparison of wave patterns (α = 20°, d = 0.1m, Fd = 1.01)

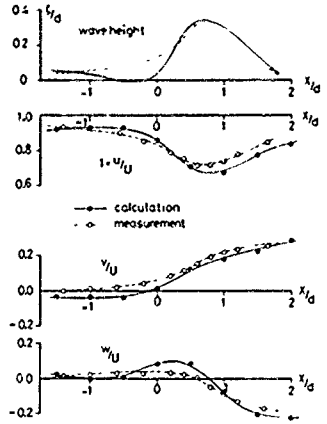


Fig 20 Longitudinal distribution of velocity components (α = 20°, d = 0.1m, Fd = 1.01, y/d = 0.8, 40mm below free surface)

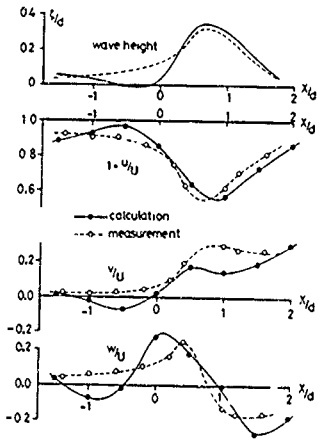


Fig.19 Longitudinal distribution of velocity components (α = 20°, d = 0.1m, Fd = 1.01, y/d = 0.8, 5mm below free surface)

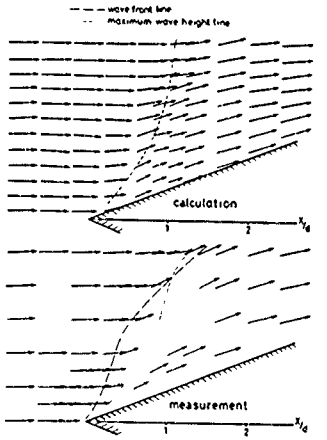


Fig 21 Distribution of velocity vectors (α = 20°, d = 0.1m, Fd = 1.01, 5mm below free surface)

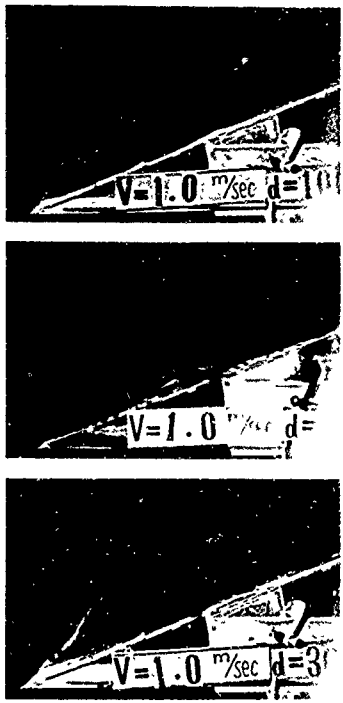


Fig 22 Wave pattern pictures of a wedge model (α = 20°, U = 1.0m/s, d = 0.1, 0.05 and 0.03m from above)

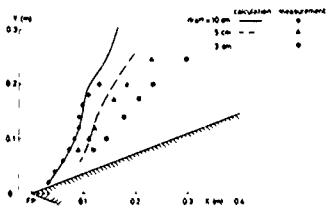


Fig. 23 Lines of maximum wave height (α = 20, U = 1.0m/s)

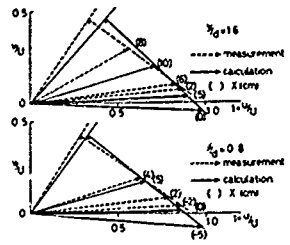


Fig. 24 (a) Velocity change across wave front (α = 20°, d = 0.1m, Fd = 1.01, U = 1.0 m/s)

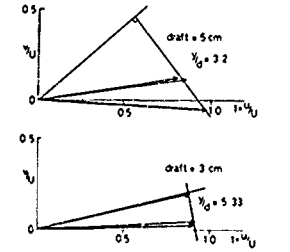


Fig. 24 (b) Velocity change across wave front (α = 20°, d = 0.05 and 0.03m, Fd = 1.43 and 1.84 U = 1.0m/s)

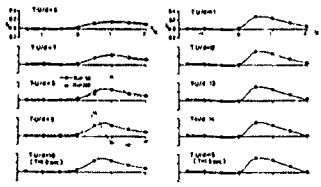


Fig 25 Time sequence of wave profile illustrating the effect of diffusion terms (α = 20°, d = 0.1m, Fd = 1.01, y/d = 0.82)

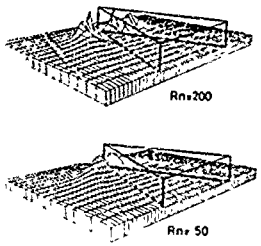


Fig.26 Effect of diffusion terms on wave formation (α = 20°, d = 0.1m, Fd = 1.01, T·U/d = 9.0)

sequence the foremost waves from the bow first become conspicuous and magnify their height and slope, and then, the second waves which have comparatively smaller height and slope appear behind them. The calculated wave elevation in the vicinity of the bow of the wedge is compared with experiment in Fig.18. The calculated result is a little rough in comparison because of the finite horizontal width of the cell. However, the steep bow wave is numerically obtained and it approximately agrees with experiment, showing great angle of wave crest to the centerline. It should be noted that the height of the waves shown in Figs.17 and 18 is multiplied by 2 This is a case of oblique FSSWs that are analogous to oblique shock waves in supersonic flow. When the entrance angle is increased, normal FSSWs occur being detached from the bow, which one can observe at the bows of large tankers or bulk carriers. The TUMMAC method can explain both kinds of FSSWs, because there exists no essential difference between the two.

In the above calculation the kinematic viscosity of water is artificially increased up to 2.5×10^{-5} and the Reynolds number based on draft is assumed to be 50. The cell Reynolds number is about 25. This treatment is necessary to obtain stabilized solution. The effect of the diffusive terms will be discussed later on.

6.2 Velocity Components

The calculated velocity components are compared with measurement on the two curved lines parallel to and below the free surface by 0.005m and 0.040m respectively in Figs.19 and 20. The agreement is good and the characteristics of the nonlinear bow waves that have been experimentally clarified are also evidently observed in the calculated results. For example, the v-component becomes to be a remarkable value behind the wave front.

In Fig 21 velocity vector distributions are compared on the curved horizontal plane which is parallel to and very close to the disturbed free surface. Near the wave crest measurement was impossible because of the abrupt upward and outward change of flow direction. In both experimental and computational results the velocity vectors are suddenly distorted outward at the wave front, though it is attenuated near the side-walls of the computational domain in the upper figure. This property of the horizontal velocity change is one of the most significant feature of the free surface shock waves around the bow. The theoretical approach can also explain the occurrence of the nonlinear nondispersive wave system when the Navier-Stokes equations are numerically solved.

In Fig.21 the lines of maximum wave height are drawn and they agree fairly well between each other. Experimental investigations show that the location of this line is dependent on Froude number based on draft and entrance angle. Therefore, the theoretical explanation of the location of the line is very important practically as well as theoretically, because the angle of this line to the centerline of the ships has intimate relation with wave resistance. The decrement of the angle usually leads to the reduction of wave resistance due to FSSWs[3].

6.3 Effect of Draft on Wave Formation

The formation of the FSSWs around the bow is dependent on the draft of the body. With the decrease of the draft the angle of the wave front (shock angle) decreases and the wave height is simultaneously lowered as can be observed in the pictures in Fig.22 which were photographed at the constant speed of advance. This physical property is analogous to the occurrence of shock waves in supersonic flow and it is imagined that a critical speed exists and it is a function of draft.

The computations by the TUMMAC method have been carried out on the three draft conditions of Fig.22. The results are illustrated in Figs.23, in which the lines of maximum wave height are shown. It must be noted that these lines, in general, do not accord with lines of wave front observed in Fig.22. The calculated lines qualitatively agree with measurements. The dependence of the wave form on draft is evidently realized by the present calculations. The phase of the bow wave is shifted aftward and the wave height is decreased with the decrease of draft, which is another significant property of FSSWs.

6 4 Shock Relation

The velocity change across the front of FSSWs, as stated in Chapter 3, satisfies the shock relation. The velocity component normal to the wave front solely undergoes sudden abrupt change across the wave front, while the tangential component is retained constant. The calculated results are shown in Fig.24 together with some experimental results in dotted lines. The numbers in parentheses indicate the x-directional coordinate of the calculated positions from the bow in centimeter. The above-mentioned shock relation is almost satisfied by the calculated velocity vectors, and it is clear that the shock angle is rapidly reduced with the decrease of draft. The occurrence of the nonlinear nondispersive waves (FSSWs) has been demonstrated by not only ex-

perimental analyses but also theoretical calculations.

6.5 Effect of Diffusive Terms

The kinematic viscosity is artificially increased so that stable realistic solutions can be obtained. The diffusive terms in the Navier-Stokes equations play a significant role in the course of the computation of nonlinear nondispersive waves. The effect of the diffusive terms is illustrated in Fig 25, in which it is shown that the wave slope becomes extremely steep and the wave profiles show unrealistic feature by the too strong contribution of the nonlinear convective terms when Rn = 200 while realistic wave profiles are obtained when Rn = 50. The wave profiles in case Rn = 50 have a steep slope at the wave front and the slope is moderate behind the crest which is the common feature of measured profiles of FSSWs[9] in the neighborhood of ships. The calculated wave elevation in case Rn = 200 is compared with the realistic calculation at Rn = 50 in Fig.26. The steep unrealistic wave elevation is observed and the computation cannot be continued further.

The introduction of the artificial viscosity is unavoidable when the TUMMAC method is made use of for the computation of nonlinear free surface waves. The nonlinear convective terms in the finite-difference equations must be balanced by a considerable easing effect of the viscous diffusion terms in the course of numerical computation, while it must be also noted that the calculated first and second derivatives of velocity are eased by the discrete representation of the velocity distribution.

From the physical point of view the diffusive effect have a considerable possibility to play a significant role in the formation of FSSWs, which is supported by the extensive experimental results. The appearance of the FSSWs cannot be naturally understood without the dissipative effect by a kind of viscosity. In the field of supersonic flow Lighthill[9] clarified the effect of diffusive terms in the formation of shock waves and he showed that the conservation equations for supersonic flow can be transformed into the Burgers equation. The FSSWs are very analogous to shock waves in supersonic flow and, therefore, the role of dissipation can be analogically recognized, i.e., the FSSWs may be formed as a result of the balance of the nonlinear convective effect with the diffusive effect. For futher verification the governing equations of the present problem must be converted into the Burgers equation, because the similarity of the Navier-Stokes equations to the Burgers equation only indicates the possibility from the theoretical point of view.

7. Conclusion

The nonlinear nondispersive waves around ships, called "free surface shock waves" have been explained by the solutions of the newly improved modified MAC method. It has been verified that the typical characteristics of free surface shock waves are also realized in the numerical solutions. Ships in forward motion generate nonlinear nondispersive waves (free surface shock waves) as well as linear dispersive waves (Kelvin waves) The estimation of wave resistance must inevitably includes sound evaluation of resistance due to free surface shock waves as well as Kelvin waves.

The TUMMAC scheme is powerful for the analysis of free surface shock waves which are finite amplitude waves governed by nonlinear equations. The present TUMMAC scheme will be further improved so that the stable state is attained more easily and it can be applied to ships of general hull form. The design method for optimum hull forms will be greatly improved by making use of the improved version of the TUMMAC method.

The computations have been carried out by the computer system of the Computer Center, the University of Tokyo.

The authors wish to express special gratitude to Dr. R. K.-C. Chan, JAYCOR, California, for his invaluable suggestions with respect to computational techniques. They also wish to thank Mr. Kanai who supported the experiments and Miss K. Kobuke who has carefully typewritten this paper.

Reference

1. Inui T., Kajitani, H., Miyata, H. Experimental Investigations on the Wave Making in the Near-Field of Ships, J. of the Kansai Soc. of Naval Arch., Japan, Vol 173, (1979)

2. Inui, T., Kajitani, H., Miyata, H., Tsuruoka, M., Suzuki, A., Ushio, T. Nonlinear Properties of Wave Making Resistance of Wide-beam Ships, J. of the Soc. of Naval Arch. of Japan, Vol.146, (1979)

3. Miyata, H., Inui, T., Kajitani, H. Free Surface Shock Waves around Ships and Their Effects on Ship Resistance, J. of the Soc. of Naval Arch. of Japan, Vol.147, (1980)

4. Takahashi, M., Kajitani, H , Miyata, H., Kanai, M. . Characteristics of Free Surface Shock Waves around Wedge Models, J of the Soc. of Naval Arch of Japan, Vol.148, (1980)

5. Kawamura, N., Kajitani, H., Miyata, H., Tsuchiya, Y. Experimental Investigation on the Resistance Component Due to Free Surface Shock Waves on Series Ships, J. of the Kansai Soc. of Naval Arch., Japan, Vol.179, (1980)

6. Miyata, H. . Characteristics of Nonlinear Waves in the Near-Field of Ships and Their Effects on Resistance, Proc. of the 13th Symposium on Naval Hydrodynamics, (1980)

7. Inui, T. From Bulbous Bow to Free Surface Shock Wave, 3rd G. Weinblum Memorial Lecture, Ifs Bericht Nr. 402 (1980)

8. Preiswerk, E Anwendung Gasdynamischer Methoden auf Wasserstromung mit Freier Oberfläche, Mitt. Inst. Aerodynamik, Eidgen. Techn. Hochsch., Zürich, No.7, (1938)

9. Lighthill, M.J. Viscosity Effects in Sound Waves of Finite Amplitude, Surveys in Mechanics, Cambridge Univ. Press, (1956)

10. Taniuchi, T., Nishihara, K. : Nonlinear Wave Motion, Iwanami-Shoten, Japan, (1977)

11. Chan, R.K.-C., Street, R.L. : SUMMAC— A Numerical Model for Water Waves, Technical Report No.135, Dept. of Civil Eng., Stanford Univ., (1970)

12. Chan, R.K.-C., Street, R.L. : A Computer Study of Finite Amplitude Water Waves, J. of Computational Physics 6, (1970)

13. Welch, J.E., Harlow, F.H., Shannon, J.P. Daly, B.J. : The MAC Method, Los Alamos Scientific Laboratory, Univ. of California, (1966)

14. Suzuki, K : On the Drag of Two-Dimensional Bluff Bodies Semi-Submerged in a Surface Flow, J. of the Soc. of Naval Arch. of Japan, Vol.137, (1975)

10 and 14 are written in Japanese.

DISCUSSIONS
of the paper
by H Miyata, A. Suzuki and H Kajitani

NUMERICAL EXPLANATION OF NONLINEAR NONDISPERSIVE WAVES AROUND BOW

Discussion
by H.C. Raven

As pointed out in your paper, in the calculations with the TUMMAC program an artificial viscosity of $2.5 \cdot 10^{-2}$ had to be used in order to get reasonable results. In Section 6.5 you discuss the physical relevance of viscosity for the FSSW ; though this may be an argument in favour of your use of the Navier-Stokes equations, it has, of course, nothing to do with the instability encountered in the calculations at Re = 200. If the effect of viscosity would be so large, your results would be of no relevance for wave breaking at full scale.

The artificial viscosity has just been used for gluing the free surface together, as shown in Fig 26. What the results would look like for even higher viscosity values can only be guessed. Did you investigate this ?

What is precisely the cause of the breakdown at higher Re is hard to say ; the deviations do not represent the usual point-to-point oscillation resulting from a too large grid Reynolds number. Fig. 25 suggests that a wave is reflected by the downstream boundary ; therefore it may be advisable to reconsider the simple extrapolation applied there.

Authors' reply

It is very hard to discuss the effect of Reynolds number or the diffusion terms, because finite difference treatments require either implicit or explicit diffusion in most cases. The FTCS scheme of the TUMMAC program requires an articial viscosity, while an upstream differencing, which does not require the introduction of an artificial viscosity, includes implicit diffusion terms. One can compute the same wave formation by the upstream differencing at Re∞ These are problems concerned with numerical stability and, as you pointed out, the physical role of viscosity cannot be discussed with these computational results.

Our argument on the effect of viscosity on wave formation is based on experimental results (Ref. 4 and the successive experiments which is to appear) The waves around wedge models are ruled by Froude number based on draft and simultaneously the wave elevation suffer from scale effect, i.e., waves of a smaller model are more attenuated.

The most substantial aspects of FSSW are generation of very steep waves and singular formation of the wave system. The TUMMAC program can explain these nonlinear wave making phenomena. The phenomena following the steep wave generation are wave breaking, turbulence on the free surface and energy deficit, to which the present computations are not available.

The wave profiles in Fig. 25 are supposed not to be reflected by the downstream boundary. However, we consider it is important to improve the open boundary conditions for better agreement.

Discussion
by Choung M. Lee

It is an impressive correlation between the calculated wave pattern around the wedge model with the measured results. However, I notice in Fig. 18 and 19 that the calculated free-surface elevation ahead of the wedge has a substantial suppression just ahead of the wedge whereas the observed free surface appears to behave like a monotonically decreasing function as x decreases from zero. I wonder if there should be an additional constraint in your calculation that $\tau_{xx} \neq 0$ for $x < 0$ to model the measured phenomenon.

Authors' reply

The suppression of wave just ahead of the wedge is presumably due to the abrupt increase of wave height at the bow and to the way of finite differencing. This unfavorable results cannot be observed in computations by upstream differencing. The treatment of the conditions for the cell at the fore-end of a wedge is very important and difficult. The additional constraint may not be necessary for the future improved version of the TUMMAC program.

Discussion
by K. Mori

It is very interesting that the free surface disturbance velocities show abrupt changes in the flow region adjacent to the free surface. The discusser wonders why such a flow can be reproduced by use of extrapolation technique in matching the free surface condition. The discusser supposes, if the observation is true, the flows in the "adjacent region" should be treated

similarly to boundary layer flows where much smaller meshes are used than those for potential flows. So it seems also strange that such "abrupt flows" can be reproduced by use of rather coarse meshes which are the same for all the domain. Though it is not clear how many points within the "adjacent region" are used in the extrapolation (perhaps no more than one !), the final results may be suspected to fall in different results when mesh sizes are changed. Have you examined ? If you may, please show us how much such "abrupt changes" are realized in your computations, like in Fig. 9

Authors' reply

Fundamental understanding of the phenomenon is most important for this problem. The nonlinear free surface phenomena are not boundary layer separation but essentially nonlinear wave making phenomena, which I have verified by experiments. The qualitative success of our TUMMAC solutions also indicates that they are nonlinear wave making phenomena.

It is well known that the MAC-method can cope with nonlinear wave problems especially in 2-D shallow water problems. The steep velocity slope is a consequence of nonlinear waves which generate discontinuity. The computed velocities near the free surface are present in Figs. 19 to 20, which show good agreement The change of the dimensions of cells does not give serious difference to the solutions.

A RAY THEORY FOR NONLINEAR SHIP WAVES AND WAVE RESISTANCE

Bohyun Yim
David W Taylor Naval Ship Research and Development Center
Bethesda, Maryland 20084, U S A.

Abstract

Analytical and numerical methods for application of ray theory in computing ship waves are investigated. The potentially important role of ray theory in analyses of nonlinear waves and wave resistance is demonstrated. The reflection of ship waves from the hull boundary is analyzed here for the first time.

When a wave crest touches the ship surface, the ray exactly follows the ship surface. When the wave crest is nearly perpendicular to the ship surface the ray is reflected many times as it propagates along the ship surface. Many rays of reflected elementary waves intersect each other. The envelope to the first reflected rays forms a line like a shock front which borders the area of large waves or breaking waves near the ship.

For the Wigley hull, ray paths, wave phases, and directions of elementary waves are computed by the ray theory and a method of computing wave resistance is developed. The wave phase is compared with that of linear theory as a function of ship-beam length ratio to identify the advancement of the bow wave phase which influences the design of bow bulbs. The wave resistance of the Wigley hull is computed using the amplitude function from Michell's thin ship theory and compared with values of Michell's wave resistance The total wave resistance has the phase of hump and hollow shifted considerably.

Introduction

Significant developments in the ship wave theory have been made in recent years. These include the application of ray theory[1,2*] and the experimental discovery of a phenomenon called a free surface shock wave.[3]

Because a ship is not thin enough to apply both the thin ship theory and the complicated free-surface effect, theoretical development of an accurate ship wave theory has been slow. The problem should be evaluated differently from the conventional means. Ray theory has been used in geometrical optics or for waves having small wave lengths. Ursell[4] used the theory to consider wave propagation in non-uniform flow, and Shen, Meyer, and Keller[5] used it to investigate water waves in channels and around islands. Recently Keller[2] developed a ray theory for ship waves and pointed out that the theory could supply useful information about the waves of thick ships at relatively slow speeds. However, he had difficulty obtaining the excitation function for wave amplitude and solved only a thin-ship problem. Inui and Kajitani[1] applied the Ursell ray theory[4] to ship waves, using the amplitude function from linear theory.

Because the ray is the path of wave energy, it is not supposed to penetrate the ship surface; and this was emphasized by Keller.[2] However, neither Keller nor Inui and Kajitani consider nonpenetration of the ray seriously. Recently Yim[6] found the existence of rays which emanated from the ship bow and reflected from the ship surface.

In the present paper, further study has revealed many bow rays reflecting from the ship surface, creating an area in which these rays intersect each other. The envelope to the first reflected rays forms a line like a shock front which borders the area of large waves or breaking waves near the ship. This will be referred to as the second caustic. This phenomenon was observed by Inui et al.[7] in the towing tank and called a free surface shock wave (FSSW). Much has been done concerning the theoretical investigation of FSSW by introducing a fictitious depth for a shallow water non-dispersive wave.[3]

The ray equation and the ship boundary condition are analyzed further to show the existence of reflecting rays, except in the case of a flat wedgelike ship surface. The ray path is very sensitive to the initial boundary condition near the bow or the stern, and should be identified at downstream infinity not by the initial condition. The conservation law of wave energy in the nonuniform flow is different from that of the uniform flow due to the exchange of energy with the local flow.[8] Therefore, the linear wave amplitude as a function of initial wave angle near the bow or stern is meaningless and cannot be used in the ray theory. It is shown that the amplitude function for the ray theory matched with the

*A complete listing of references is given on pages

linear theory far downstream is reasonable and likely to produce a reasonable result as in the two dimensional theory.[9]

The wave phase in the ray theory is obtained, together with the ray path, independent from the amplitude function. Both the phase and the ray path are quite different from the prediction of linear theory near the ship. The rays far downstream are straight as in the linear theory yet have phases different from the linear theory; they are parallel to the linear ray with the same wave angle but do not coincide. The difference in wave phases is the main factor that makes the wave resistance different from the linear theory. Ray paths and phase difference are computed for various parameters of the Wigley ship, with and without a bulbous bow. The ray paths for different drafts and different beam-length ratio of the Wigley hull are slightly different, widening the wave area near the hull for the wider beam and/or larger draft. However, the phase difference is more sensitive to the beam-length ratio and/or draft-length ratio, by always advancing the linear wave phase.

The wave resistance of the Wigley hull is computed and shown to have a considerable shift of phase of hump and hollow.

The most interesting phenomenon of a ship with a bulbous bow is the reduction of slopes of rays and the second caustic, i.e., the larger the bulb, the greater the reduction. This fact was observed in the towing tank.[3] There exists a bulb size which totally eliminates the reflecting rays.[10] However, the phase difference due to the bulb[11] is very small showing that the phase difference, which has been observed in the towing tank, is the effect of nonuniform flow caused by the main hull.

Ray Equations

The concept of ray theory in ship waves is analogous to the concepts used in geometrical optics and in geometric acoustics. A ship is considered advancing with a constant velocity -U which is the direction of the negative x axis of a right handed rectangular coordinate system O-xyz with the origin O at the ship bow on the mean free surface, z=0, z is positive upwards.

First the phase function s(x,y,z) is defined so that the equation (s = constant) represents the wave front where the value of s is the optical distance from the wave source, e.g., the ship bow. When Keller[2] developed his ray theory of ships by expanding boundary conditions and a solution, which should satisfy both the Laplace equation and the boundary conditions, in a series of Froude number squares F^2, he obtained:

$$(\nabla s)^2 = 0 \tag{1}$$

$$s_z = -1\,(S_t + \nabla\phi \cdot \nabla s)^2 \text{ at } z = 0$$

By eliminating S_z from these two equations he obtained a dispersion relation

$$(s_x^2 + s_y^2)^{1/2} = (S_t + \phi_x s_x + \phi_y s_y)^2 \text{ at } z = 0 \tag{2}$$

where ϕ is the double model potential. When steady state motion is assumed with respect to the moving coordinate system, 0 - xyz,

$$s_t = 0$$

When the angle between the normal $\bar{n}$ to the phase curve s and the axis is denoted by θ,

$$\bar{n} = \bar{I}\cos\theta + \bar{J}\sin\theta \tag{3}$$

Then the wave number vector is defined by

$$\bar{k} = k_1\bar{I} + k_2\bar{J} = s_x\bar{I} + s_y\bar{J}$$
$$= \bar{n}k = \bar{I}k\cos\theta + \bar{J}k\sin\theta \text{ at } z = 0 \tag{4}$$

From equations (2) and (4)

$$k = \left[\frac{1}{u\cos\theta + v\sin\theta}\right]^2 \tag{5}$$

where

$$-\phi_x = u \text{ and } -\phi_y = v$$

These results are an approximation within the order of F^4, and the phase function and its related equations are all limited to their values at z = 0. Thus, from now on, unless otherwise mentioned, all the physical values are at z = 0. The ray equation of ship waves is obtained from the irrotationality of the wave number vector

$$\frac{\partial k_2}{\partial x} - \frac{\partial k_1}{\partial y} = 0 \tag{6}$$

From Equations (4) through (6),

$$\{2\sin\theta\,(u\sin\theta - v\cos\theta) + \cos\theta\,(u\cos\theta + v\sin\theta)\}\frac{\partial\theta}{\partial x}$$
$$+ \{2\cos\theta\,(-u\sin\theta + v\cos\theta) + \sin\theta\,(u\cos\theta + v\sin\theta)\}\frac{\partial\theta}{\partial y} \tag{7}$$
$$= 2\sin\theta\,(\cos\theta\frac{\partial u}{\partial x} + \sin\theta\frac{\partial v}{\partial x})$$
$$- 2\cos\theta\,(\cos\theta\frac{\partial u}{\partial y} + \sin\theta\frac{\partial v}{\partial y})$$

This is the ray equation which can be solved by the method of characteristics, and is equivalent to simultaneous ordinary differential equations.

$$\frac{dy}{dx} = \frac{\{v - \frac{1}{2}\sin\theta\ (u\cos\theta + v\sin\theta)\}}{\{u - \frac{1}{2}\cos\theta\ (u\cos\theta + v\sin\theta)\}} \qquad (8)$$

$$\{2\sin\theta\ (\cos\theta\frac{\partial u}{\partial x} + \sin\theta\frac{\partial v}{\partial x})$$

$$- 2\cos\theta\ (\cos\theta\frac{\partial u}{\partial y} + \sin\theta\frac{\partial v}{\partial y})\}\frac{d\theta}{dx} = \{2\sin\theta(u\sin\theta \qquad (9)$$

$$- v\cos\theta) + \cos\theta\ (u\cos\theta + v\sin\theta)\}$$

Here $u\cos\theta + v\sin\theta$ is the velocity component normal to the phase curve of the flow relative to the ship. Because the wave is stationary relative to the ship, the phase velocity through the water surface should be

$$-u\cos\theta - v\sin\theta$$

The group velocity is one-half of the phase velocity. Thus the ray direction in Equation (8) is along the resultant of the group velocity taken normal to the phase curve and of the velocity of the basic flow as Ursell has shown.[4] Because the wave energy is propagated at the group velocity, the ray path is interpreted as the path of energy relative to the ship. This can be obtained by solving Equations (8) and (9) with the proper initial condition. The phase s can be obtained from equations (4) by

$$s = \int \vec{k}\ d\vec{r}$$

as in potential theory; s(x,y) is a function of (x,y) but is unrelated to the integration path. However,

$$ds = k\cos\theta\ dx + k\sin\theta\ dy \qquad (10)$$

can be solved together with the ray equations along the ray path.

Rays of Ship Waves and Linear Theory

To investigate the path of a ray of a ship wave, a ship, represented by a double model source distribution m (x,y) on $y = o$, $h \geq z \geq -h$, is considered. Although the linear relation between the source strength m and the ship surface

$$y = \varepsilon f(x,z) \qquad (11)$$

is

$$m = \frac{1}{2\pi}\frac{dy}{dx} \qquad (12)$$

the actual double model ship body streamline should be obtained by solving

$$\frac{dy}{dx} = \frac{v}{u} \qquad (13)$$

through the stagnation point where u and v are the velocity components of the total velocity caused by the double model source distribution m and the uniform flow relative to the ship.

In the linear ship wave theory a smooth source distribution produces two systems of regular ship waves: the bow and the stern waves starting from the bow and stern, respectively, represented[11] as

$$\zeta(x,y) = \int_{-\pi/2}^{\pi/2} A(\theta)\exp\{i\, s_1(x,y,\theta)\}\, d\theta \qquad (14)$$

where

$$s_1 = k_o \sec^2\theta\ \{(x - x_1)\cos\theta + y\sin\theta\} \qquad (15)$$

x_1 = the x coordinate of the bow or stern

$k_o = \frac{g}{U^2}$

g = acceleration due to gravity

A(θ) = amplitude function which is a function of source distribution m

The regular wave ζ is the solution of linear ship wave theory far from the ship.[11] Actually, it is easy to see that the exponential function satisfies both the Laplace equation and the linear free-surface boundary condition for any value of x_1. Havelock interpreted Equation (14) by discussing the integrand as elementary waves,[12,13] i.e., the regular waves are aggregates of elementary waves starting from the bow and stern of a ship. The normal direction of each elementary wave crest is $\vec{n} = \vec{i}\cos\theta + \vec{j}\sin\theta$.

Because the local disturbance of the double model decays rapidly away from the ship, even in nonlinear theory in the far field, the regular wave should be of the form of Equation (14) with possibly different values of x_1 and A(θ). When the integral of ζ is evaluated by the method of the stationary phase[14] by taking roots of

$$\frac{\partial s}{\partial\theta}(x,y,\theta) = 0 \qquad (16)$$

or

$$2\tan^2\theta + \frac{x}{y}\tan\theta + 1 = 0 \qquad (17)$$

in general two values of θ are obtained for a given value of each x and y, satisfying,

$$\frac{x}{|y|} \geq 8^{\frac{1}{2}} \qquad (18)$$

Furthermore, when

$$\frac{x}{|y|} = 8^{\frac{1}{2}}$$

$$|\tan\theta| = 8^{-\frac{1}{2}}$$

or

$$\theta = 35 \text{ deg}$$

and the value of the integral of Equation (14) for any x,y in $x/|y| \geq 8^{\frac{1}{2}}$ can be evaluated by the stationary phase method as the sum of two waves: transverse waves (0 deg < |θ| < 35 deg) and divergent waves (35 deg < |θ| < 90 deg).

Except for the amplitude function exactly the same result for the relation of x,y and θ as in the linear theory can be obtained from Equation (8) by substituting u = 1 and v = 0. Thus, this means that the energy of each elementary wave propagates on the uniform flow along a straight line ray. The rays are confined in $x/|y| \geq 8^{\frac{1}{2}}$, both of the elementary waves at θ = 0 and θ = 90 deg correspond to the ray y /x = 0, and θ = 35 deg corresponds with the ray $x/|y| = 8^{\frac{1}{2}}$. One ray between these two rays corresponds to two elementary waves where one is transversel and the other is divergent.

When the velocity is not uniform due to the flow perturbation caused by a ship, the ray is not straight but curved near the ship as shown in Figure 1. It is known that wave energy flux divided by the relative frequency with respect to the coordinates for which the fluid velocity is zero, is conserved along the curved ray tube.[8] If the coordinates are fixed in space, then the ship waves are unsteady relative to the fixed coordinates and the frequency is

$$\omega_t = U k \cos\theta \qquad (19)$$

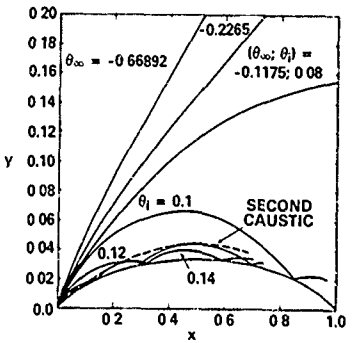


Figure 1 - Ray Paths for a Wigley Hull
(b = 0.1, h = 0.0625)

because only the transformation of coordinates (x,y) to (x - Ut, y) is needed to get the unsteady flow. Strictly speaking the relative frequency is

$$\omega_t = k u \cos\theta + k v \sin\theta$$

but for our discussion, the approximate value serves the purpose. This means that for a uniform flow the wave energy is constant along the ray because for a uniform flow u = U, v = 0, k = g/(U² cos²θ), and θ is constant along the straight ray. However, the wave energy is not constant along the curved ray in nonuniform flow, but is dependent upon the local velocity components and θ because the relative frequency is a function of the local velocity and θ as in Equations (5) and (19) and θ changes along the curved ray. The wave energy will change considerably along the curved ray near the bow or stern because u and v change to zero at the wave source, the stagnation point, while in the far field it will be constant along the ray as in linear theory. Near the stagnation point, the wave number increases according to Equation (5) and the wave energy also increases due to the energy conservation law.[8] Thus, the wave may break near the stagnation point.

Because wave amplitude is so difficult to obtain from the ray theory[2], the linear theory has been considered as an approximation.[1] A good result was obtained for a two dimensional flow problem.[9] However, extreme care is needed in the three dimensional theory because θ changes by a large amount along the ray, near the stagnation point, and the wave energy depends upon θ. The matching amplitude function of ray theory with the values from linear theory should be done at the far field where θ and the direction of the ray are, respecitvely, identical for both cases for each elementary wave. In addition, the initial condition has to be taken in the neighborhood, but not exactly at, the stagnational point because, although the stagnation point is the wave source, at the stagnation point the ray equations are indeterminant, u and v being zero. However, because of the large change of u and v near the stagnation point, the ray path is very sensitive to the initial values of x, y and θ, the nearer to the stagnation point, the more sensitive. Therefore, the identification of ray paths should be correlated with the values of θ at infinity. Then all the ray paths can be properly and uniquely identified by θ_∞.

Since perturbations of the ship decay rapidly away from the ship, θ also rapidly approaches θ_∞. The relation between the initial value and the value at infinity of θ has little meaning, although it was misunderstood before[1,6] because θ changes very rapidly near the stagnation point.

Rays of Ship Waves and Ship Boundaries

Ship waves created by a smooth ship hull propagate as regular bow and stern waves from the bow and stern stagnation points to infinity along rays. Because a ray carries the wave energy it cannot penetrate the ship surface. If the linear free-surface condition is considered with the exact hull boundary condition, as has been popular in recent ship wave analysis[13], the straight rays which pass through the hull boundary have to be considered. For a ray theory with the exact hull boundary condition, the ray is not allowed to penetrate the ship. In fact, when the initial wave crest touches the ship boundary it can be proved that the ray of such a wave grazes along the ship boundary without penetrating the ship boundary.

In Equation (8) when the wave crest touches the hull

$$u\cos\theta + v\sin\theta = 0 \tag{20}$$

because θ is the angle between the normal to the crest and to the axis, and the velocity normal to the ship hull is zero on the hull. Equation (8) then becomes

$$\frac{dy}{dx} = \frac{v}{u}$$

showing that the ray touches the ship hull streamline from Equation (13).

When the wave crest touches the hull, from Equations (11) and (13)

$$\frac{v}{u} = f_x \tag{21}$$

and from Equations (20) and (21)

$$\tan\theta = \frac{-1}{f_x} \tag{22}$$

Differentiating Equation (22) with respect to x along the ship hull

$$\frac{d\theta}{dx} = \frac{f_{xx}}{f_x^2 + 1} \tag{23}$$

However, inserting Equation (20) into Equation (9) yields

$$\frac{d\theta}{dx} = \frac{\cot\theta\,\frac{\partial u}{\partial x} + \frac{\partial v}{\partial x} - \cot^2\theta\,\frac{\partial u}{\partial y} - \cot\theta\,\frac{\partial v}{\partial y}}{u(1 - \frac{v}{u}\cot\theta)} \tag{24}$$

Differentiating Equation (21) with respect to x along the hull yields

$$\frac{\partial}{\partial x}\frac{v}{u} = \frac{-\frac{v}{u}\frac{\partial u}{\partial x} + \frac{\partial v}{\partial x} - \frac{v}{u}\frac{\partial u}{\partial y}\frac{\partial y}{\partial x} + \frac{\partial v}{\partial y}\frac{\partial y}{\partial x}}{u} \tag{25}$$

From Equations (20), (21), (22), and (25) it can be shown that Equations (23) and (24) are equivalent. That is, when the wave crest touches the ship boundary, the ray equations and the ship hull streamline equations are equivalent.

When the wave crest is perpendicular to the ship hull

$$\frac{v}{u} = \tan\theta \tag{26}$$

If Equation (26) is inserted into Equation (8)

$$\frac{dy}{dx} = \tan\theta = \frac{v}{u} \tag{27}$$

The ray also touches the ship initially. However, Equation (9) is not compatible with Equation (26) on the hull. This can be proved in a similar way as follows:

Differentiating Equation (26) with respect to x along the ship hull

$$\frac{d\theta}{dx} = \frac{f_{xx}}{f_x^2 + 1} \tag{28}$$

Inserting Equation (26) into Equation (9) gives

$$\frac{d\theta}{dx} = \frac{2\tan\theta\left(\frac{\partial u}{\partial x} + \tan\theta\,\frac{\partial v}{\partial y}\right) - 2\left(\frac{\partial u}{\partial y} + \tan\theta\,\frac{\partial v}{\partial y}\right)}{u\,(1 + \frac{v}{u}\tan\theta)}$$

From Equations (25), (27), and (29), noting

$$\frac{\partial u}{\partial y} = \frac{\partial v}{\partial x}$$

$$\frac{d\theta}{dx} = \frac{-2\,f_{xx}}{f_x^2 + 1} \tag{30}$$

Equations (28) and (30) are compatible only when $f_{xx} = 0$, or f_x = constant.

That is, only when the ship is a flat plate does the ray of the wave, whose crest is perpendicular to the ship, follow the ship boundary. This means that when the ship bow is like a wedge, the ray of the bow wave, whose crest is perpendicular to the wedge surface, initially follows the wedge surface.

When the ray equations are solved numerically by the Runge-Kutta method, with initial values near the bow stagnation point, the ray touches and follows the ship boundary at

$$\theta_i = -\frac{\pi}{2} + \alpha \tag{31}$$

where α is the half entrance angle of the ship bow and θ_i denotes the initial value of θ.

When θ_i increases from this value the ray moves gradually away from the ship as shows in Figures 1 through 4. The rays are curved near the ship but at far downstream they are straight and the ray direction becomes exactly the same function of θ as the linear theory. Thus at infinity the rays are inside $|dx/dy| = 8^{\frac{1}{2}}$. However, when θ_i approaches zero, the curved ray near the ship gradually approaches the ship, and eventually crosses the ship boundary, as in Figures 1 through 4. Here the wave reflection should be considered to prevent the ray penetration of the ship hull.

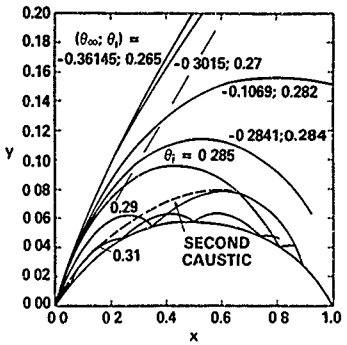


Figure 2 - Ray Paths for a Wigley Hull
(b = 0.2, h = 0.0625)

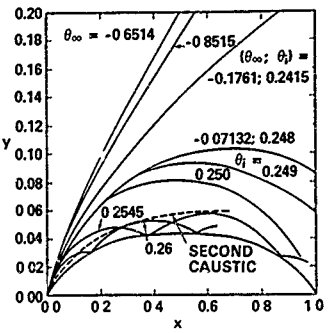


Figure 3 - Ray Paths for a Wigley Hull
(b = 0.2, h = 0.03)

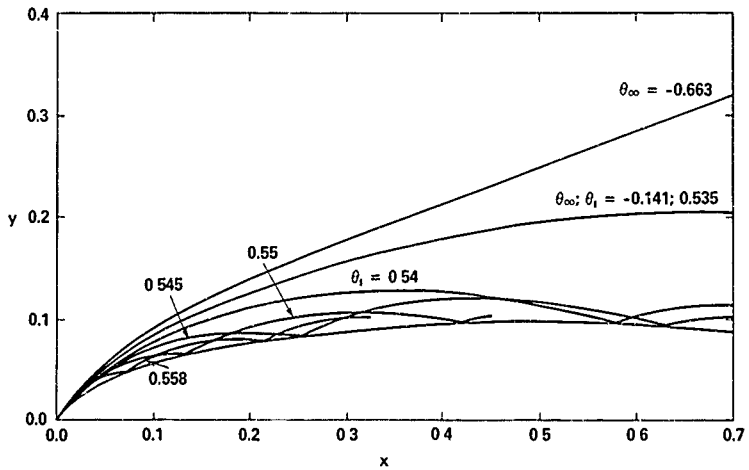


Figure 4 - Ray Paths for a Wigley Hull (b = 0.5, h = 0.0625)

Ray Reflection

There are no waves coming from places other than the ship bow or the ship stern. In the ray theory, the flow field perturbed by the ship deflects the ray path starting from the ship bow toward the ship. Thus, some rays of bow waves impinge on the ship hull. Because the ray theory is for small Froude numbers and the wave phenomenon is considered only on the free surface, it is reasonable to consider only reflected waves, as in geometrical optics, neglecting transmitted waves when the oncoming waves impinge on the ship hull.

Let the ray at the wave angle θ on the ship boundary (x,y) be reflected to θ_r and $f_x = \tan\theta_o$ as in Figure 5.

Then,

$$\theta_r - \theta_o = \theta_o - \theta$$

or

$$\theta_r = 2\theta_o - \theta \qquad (32)$$

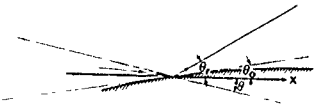


Figure 5 - Angles of Waves Reflecting on the Ship Hull

Whenever the ray intersects the ship boundary at (x,y) with angle θ, then the value of θ at (x,y) will be changed to $\theta_r = 2\theta_o - \theta$, and x,y,θ are continuously calculated by the Runge-Kutta's method. Then the ray will reflect as in Figures 1 through 4. Here if θ_o is zero, it is easily seen in Equation (31) that the impinging ray angle Ⓗ changes to -Ⓗ for the reflected ray angle. This fact can be easily shown to be true even for $\theta_o \neq 0$ by just the rotation of the coordinate system.

Numerical Experiments of Ray Paths and Free Surface Shock Waves

Because the ray equations can be solved only numerically, careful numerical experiments with the ray equations may give valuable information. For simplicity, the Wigley hull source distribution with

$$m = \frac{1}{2\pi}\frac{df_1}{dx}$$

where

$$f_1 = 2b\,(\lambda - x^2)\left\{1 - \left(\frac{z}{h}\right)^2\right\} \qquad (33)$$
$$b = \pm b_1$$

is considered for various numbers of b and h which are related to the hull beam and draft, respectively. The actual hull shape corresponding to the source Equation (33), is obtained by plotting the body streamline passing through stagnation points as the solution of

$$\frac{dy}{dx} = \frac{v}{u}$$

where u and v corresponding to Equation (32), are shown in Appendix A together with u_x, u_y, and v_y for the ray equation. Equations (8)[x], (9), and (10)[y], together with the streamline equation, are solved by the Runge-Kutta method with initial conditions (x,y,θ) near the stagnation points with various values of θ.

Many ray paths both reflecting and non-reflecting from the surfaces of various Wigley hulls are shown in Figures 1 through 4. These paths were computed by a high speed Burroughs computer at David Taylor Naval Ship Research and Development Center. The reflection condition is incorporated in the high-speed computation with a routine to find the intersection of the ray and the ship boundary which is pre-calculated and saved in the memory. The step sizes of integrations and interpolation were determined after many numerical tests, and the shown results are considered to be reasonably accurate. For a given initial condition, the solution is stable and converges well.

In Figures 1 through 4, some common features of rays can be drawn as follows. The rays in $-\pi/2 < \theta_\infty < 0$ far behind the ship behave like rays of linear theory except wave phases are advanced in the ray theory and those near $\theta_\infty = 0$ are rays propagating from the ship bow and reflecting from those of ship hull. The rays near the ship are very different from the linear theory as Inui and Kajitani[1] pointed out. The curved rays from the bow have a far larger slope than those of linear theory and the phase of each ray is considerably advanced. The magnitude of the phase difference is more sensitive to the beam-length ratio and the draft-length ratio than the magnitude of the ray slope.

When $\theta_\infty = 35$ deg, the ray will be the outermost ray and the ray angle at ∞ will be approximately $\tan^{-1} 8^{-\frac{1}{2}}$ as in the linear theory and there is the corresponding initial value of θ or θ_i near the bow, or the origin. However, the θ_i which is corresponding to a single value of θ_∞ is very sensitive to small changes of x and y near the origin. At a fixed point near the origin there exists a unique correspondence between θ_i and θ_∞.

When from the θ_i which is corresponding to $\theta_\infty = 35$ deg, the initial value of θ_i increases, θ_∞ also increases and the ray angle decreases. In general, when $\theta_i = 0$, θ_∞ is still a negative value. When θ_i increases further, θ_∞ approaches zero and the ray pass is very close to the stern. At this point, there exists a certain increment of θ_i which makes the ray barely touch the ship stern, at $\theta_i = \theta_{i0}$. When θ_i slightly increases from θ_{i0}, the ray reflects from the ship hull near the stern. With the increment of θ_i the reflection point moves toward the bow. When $\theta = \theta_{i1}$ the ray once reflected touches the stern again. When θ_i increases further from θ_{i1}, the ray reflects

twice from the ship hull. In this way, further increment of θ_i makes the ray reflect from the ship hull three, four ... times. However, at θ_i near the value of α, the ray tries to penetrate the ship hull at the starting point of the bow. This cannot be allowed because this kind of ray should come from outside of the ship. Let the border point of θ_i be θ_{iu}. This means that rays of initial value of θ between $\theta_{io} < \theta_i < \theta_{iu}$ reflect from the ship hull. As is clear in Figures 1 through 4, in general, all the rays before reflection do not intersect each other. However, reflected rays intersect other rays. The once reflected rays intersect not only with each ray once reflected from ship boundary points close to each other, but also with at least one ray before reflection.

In the stationary phase, each ray has an amplitude. Likewise in the ray theory, each ray carries it's energy. The reflected ray may have approximately the same energy as the ray at $\theta_i = \theta_{io}$ or $\theta_\infty \neq 0$ where the amplitude function of the linear theory is in general more significant than amplitudes of the other values of θ_∞. Because the phase must be approximately close to each other for the waves near $\theta_\infty = 0$, the wave height of the once reflected ray may be close to three times that of the transversal wave for $\theta_\infty = 0$. When the envelope of the once reflected waves is drawn, the domain bounded by the ship surface and the envelope, denoted by Dm, must be distinctly different from other domains because in Dm there are not only once reflected rays but also twice or multi-reflected rays on which more than three reflected rays intersect by an argument similar to that used for the once reflected rays. The envelope of the once reflected rays behaves like the shock front which was observed in Japan.[3]

In general, a line is called a caustic when on one side of the line one can find a continuous distribution of rays but not on the other side, and along the caustic the wave slope is found to be large. The wave near the ray angle $\theta_\infty = 35$ deg is the caustic, and the wave height near the caustic far downstream can be obtained by an application of the Airy function in the linear theory. The envelope of the once reflected rays may be a kind of caustic formed by the refracted bow wave rays due to the non-uniform flow perturbed by the ship. Shen, Meyer, and Keller[5] studied such caustics caused by the sloping beach of channels and around islands. Thus, the additional caustic of ship waves may be called the second caustic of ship waves, and should not be confused with the first caustic which is the known caustic at $\theta_\infty = 35$ deg.

Second Caustic of Ship Waves of Various Ships

For the Wigley hull, several different values of parameters b and h were taken to find their effect on the second caustic. In addition, the effect of a bulbous bow on the second caustic was considered. The most distinguishable physical characteristic of the second caustic is its distance from the ship hull. This is related to the distance of reflected rays from the ship hull. If the number of reflection rays increases, or if θ_i increases from θ_{io}, the maximum distance between the ray and the ship hull decreases. The distance, before or after the ray reflection, approximately behaves like a sine curve. The maximum distance between the ray before the first reflection and the ship hull divided by the x coordinate of the point of the first reflection a/x_1 is plotted in Figure 6 for various ships. The value of a/x_1 for different values of θ_i are approximately the same for a given hull and are related to the area between the second caustic and the ship hull where there may be breaking waves or turbulent waves. Thus, if the area is large, viscous dissipation of energy becomes large. Accordingly, the measured momentum loss behind the ship for the breaking waves becomes large.

The values of a/x_1, increase with increasing beam-length ratio. However, the most interesting part is the effect of the bulbous bow.[10] When the bulb size is increased or the doublet strength is increased the curvature of the ray near the bow becomes less, although the streamline near the bow is such that the entrance angle is slightly large. The values of a/x_1 decrease with increasing bulb size, and eventually the ray for $\theta_\infty \neq 0$ cannot propagate without peretrating the ship hull at the beginning. That is, there is no reflecting ray coming out of the bow with a bulb of the proper size, as shown in Figure 7.

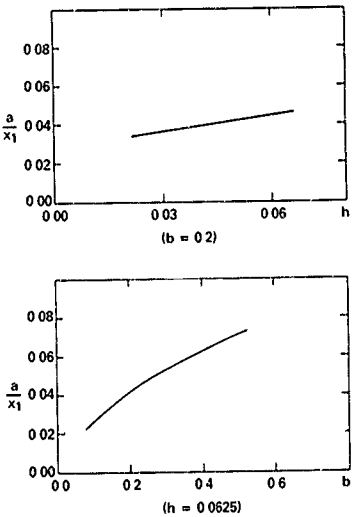


Figure 6 - Width of the Second Caustic a/x_1 for Wigley Hulls

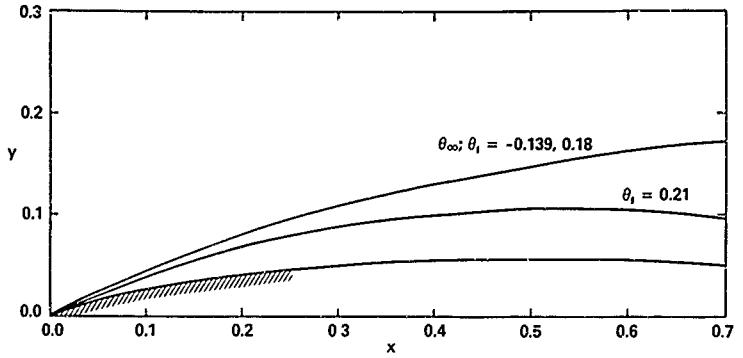


Figure 7 - Rays of the Wigley Ship (b = 0.2, h = 0.0625) with Bulb (radius, r_b = 0.0214L, depth, z_1 = 0.5h)

These phenomena associated with the second caustic are exactly the same as those of the "free surface shock wave" which was observed in the towing tank.

Finally it should be pointed out that the ray of the wave whose crest is perpendicular to the hull surface follows exactly along the flat surface as was proven by Equations (28) and (30) and the following paragraphs. This means that rays originating from the vertex of a wedge very likely never reflect on the wedge surface. This is because rays near the ray which follows the ship surface did not intersect each other near $\theta_1 = -\pi/2 + \alpha$, or $\theta_\infty = -\pi/2$. Rays near $\theta_\infty = 0$ impinge on the ship surface due to the effect of the waterline curvature of the ship. Therefore, if a ship has a wedge bow, the second caustic must be found near or behind the shoulder. Because the first caustic near the bow may be very prominent and both waves near the first caustic and waves near the stagnation point break, careful experimental analysis and more theoretical study of the bow near field may be needed.

Wave Amplitude and Phase

Because the perturbation due to a ship, or both regular waves and local disturbances, decays at far field, the linear theory must hold in the far field. In particular, the wave resistance can be calculated from the energy passing through a vertical plane x= constant far downstream; the linear theory which is properly matched to the near field of the ship will be used for calculating the wave resistance. As explained in Equation (14) and the following paragraphs, the expression for regular waves far downstream is known to be of the form of Equation (14) where the amplitude function

$$A(\theta) = P(\theta) + i\,Q(\theta) \tag{34}$$

may be taken as an approximation from the linear theory but the phase difference x_i must be obtained from matching with the near field. If the near field is also expressed by the linear theory

$$P + i\,Q = \frac{2}{\pi} k_o \int_{-h}^{0} \int_{0}^{1} k_o z \sec^2\theta \; ik_o x \sec\theta \; dx\,dz \; f_x e \qquad \sec^3\theta \; e \tag{35}$$

where f_x is the derivative of Equation (11) with respect to x. When the inner integrand of Equation (35) is integrated with respect to x, the value with the limit x = 1 will form stern waves and the value with the limit x = 0 will form bow waves.[11] Then the bow waves can be represented by

$$\zeta_b = \int_{-\pi/2}^{\pi/2} A_b(\theta) \exp\{i\, s_1(\theta)\}\, d\theta \tag{36}$$

where

$$A_b(\theta) = P_b + i\,Q_b \tag{37}$$

When the phase s is computed from Equation (10) along with the ray path from Equations (8) and (9) considering that s = 0 at the bow near the origin, there are two results different from those of linear theory. (1) the ray path is deflected as if the elementary wave of the linear theory started from $(x_1,0)$ not from the origin, and (2) the phase change denoted by s_1 should be considered. That is, the

equivalent linear elementary wave may be written as

$$A_b(\theta) \exp\left[i k_o \sec^2\theta \left\{(x-x_1)\cos\theta + y\sin\theta\right\} + i k_o \Delta s\right] \tag{38}$$

where x_1 is obtained as an intersection of the tangent to the ray at ∞ and the x axis and

$$k_o \Delta s = k_o s - k_o \sec^2\theta \left\{(x-x_1)\cos\theta + y\sin\theta\right\} \tag{39}$$

The value of

$$s_2(\theta) = \Delta s - x_1 \sec\theta \tag{40}$$

can be obtained at any point along the ray. In general, x_1 is negative and $s_2(\theta)$ is positive meaning that the bow wave phase in the ray theory is larger or more advanced than the phase of the linear theory. This fact has long been observed in experiments in towing tanks.

The advancement of wave phase is computed for various ships and the values of s_2 and x_1 at $x = 2$ are shown in Figures 8 through 10. When the beam-length ratio increases and/or the draft-length ratio increases, the values of s_2 increase and the values of x_1 decrease for all values of θ_w. As compared with the increment of the slopes of rays near the ship, the increment of the phase angle is more sensitive to the beam- and/or draft-to-length ratios.

The most interesting phenomenon about the phase difference is in regard to the bulbous bow.[10] That is, the phase differences for hulls with and without bulbs are almost the same even with a considerably larger bulb. In the past, because of the observed phase difference of ship waves, the bulb was located far forward to obtain good bow wave cancellation.[11] According to the present analysis, if there is no other reason, the bulb position need not be far forward. Because the nonuniform flow created by the ship is much more significant than that of the bulb, as far as phase change is concerned, both the ship bow waves (in general, positive sine waves) and the bulb waves (negative sine waves) propagate through the same region and cancel each other.

As for the amplitude function, although it was shown by Doctors and Dagan[9] that ray theory produced the best result for a two-dimensional submerged body even though they used a linear amplitude function, the surface piercing three-dimensional case may be quite different. The amplitude function is mainly related to the singularity strength which satisfies the ship hull boundary condition and some improvement might result by considering the sheltering effect. However, in the present study, the linear amplitude function is used to simplify the problem, showing the effect of curved rays.

Wave Resistance

If all the elementary waves are assumed to be propagated without reflection, the amplitude function and the phase difference studied in the previous sections will supply enough information for the calculation of wave resistance. Because at far downstream, the wave height may be considered linear, the Havelock wave resistance formula[15] may be used for the waves represented by Equations (36) through (40), considering that the wave with the changed phase $s_{2b}(\theta)$ has the amplitude

$$(P_b + iQ_b)\, e^{ik_o s_{2b}(\theta)}$$

$$\frac{R}{\frac{1}{2}\rho U^2 L^2} \equiv C_w = \frac{1}{\pi}\int_{-\pi/2}^{\pi/2} \left|(P_b + iQ_b)\, e^{ik_o s_{2b}(\theta)}\right|^2 \cos^3\theta\, d\theta \tag{41}$$

or in Srettensky's formula[16]

$$C_w = \frac{16\pi^2 k_o}{w} \sum_{j=0}^{\infty}{}' \epsilon_j \frac{1 + \left\{1 + \left(\frac{4\pi j}{k_o w}\right)^2\right\}^{\frac{1}{2}}}{\left\{1 + \left(\frac{4\pi j}{k_o w}\right)^2\right\}^{\frac{1}{2}}} \left|A_b(dj)\, e^{ik_o s_{2b}(dj)}\right|^2 \tag{42}$$

where

$$A_b(dj)\, e^{ik_o s_{2b}(mj)} =$$

$$\int_{-h}^{0}\int_{0}^{1} dx\,dz\; m \exp\left\{k_o d_j (z d_j + ix) + ik_o s_2\right\}$$

$$m = \frac{1}{2\pi} f_x \tag{43}$$

$$d_j = \left[\tfrac{1}{2} + \tfrac{1}{2}\left\{1 + \left(\frac{4\pi j}{k_o w}\right)^2\right\}^{\frac{1}{2}}\right]^{\frac{1}{2}} = \sec\theta_j$$

w = width of the towing tank nondimensionalized by ship length L

$$\epsilon_o = 1$$

$$\epsilon_j = 2 \text{ for } j > 1$$

Because

$$\left|(P_b + iQ_b)\, e^{ik_o s_2(\theta)}\right|^2 = \left|P_b + iQ_b\right|^2$$

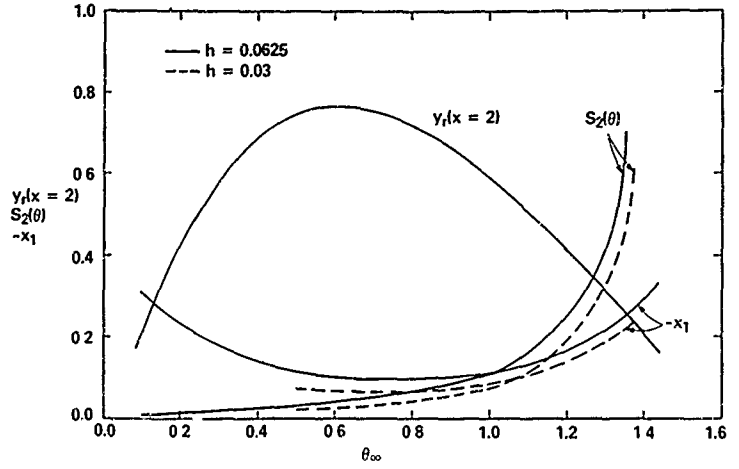


Figure 8 - The y Coordinate of Ray at x = 2, Phase Function $S_2(\theta)$ and the Starting Point of Elementary Wave, x_1, of a Wigley Hull (b = 0.2)

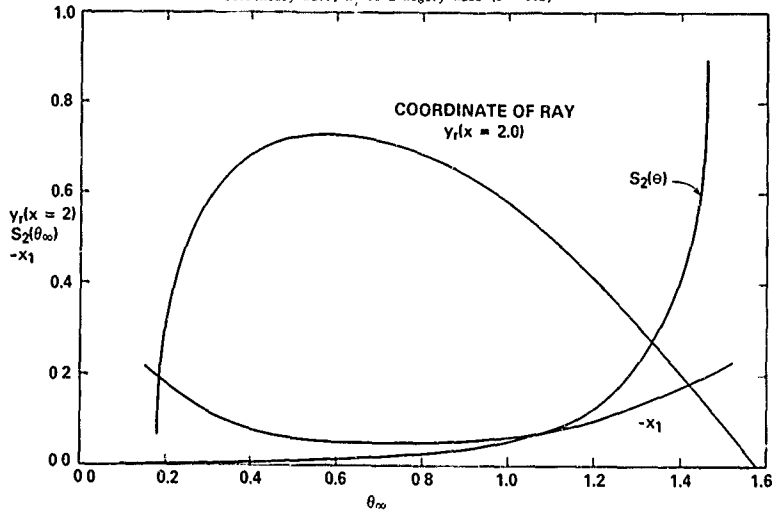


Figure 9 - y (x = 2), $S_2(\theta_\infty)$, and $-x_1$ of a Wigley Hull (b = 0.1, h = 0.0625)

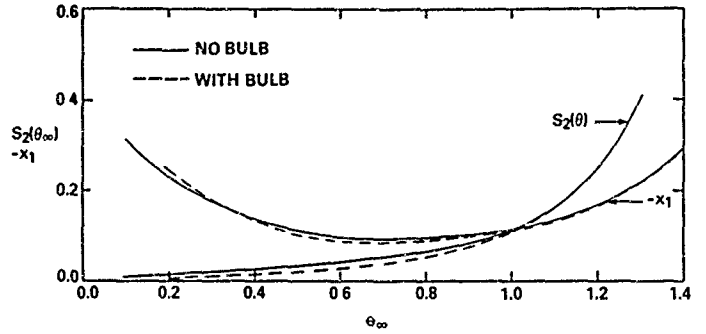


Figure 10 - $S_2(\theta_\infty)$, and $-x_1$ of a Wigley Hull (b = 0.2, h = 0.0625) with and without Bulb (r_b = 0.0285L, z_1 = 0.7h)

the phase difference of each elementary wave does not change bow wave resistance from the linear theory.

The stern wave amplitude is exactly the same as the linear value

$$A_s(\theta) = P_s + iQ_s$$

but the phase difference $\theta_{2s}(\theta)$ should be computed by the ray theory together with the ray path which is shown in Figure 11. Then it is also obvious that the stern wave resistance is the same as the linear stern wave resistance. The total wave resistance may be obtained similarly by considering that the total wave amplitude is

$$(P_b + iQ_b)\, e^{ik s_{2b}(\theta)} + (P_s + iQ_s)\, e^{ik_0 (s_{2s}(\theta) - \sec\theta)} \qquad (44)$$

Here, the bow and stern wave interaction appears in the wave resistance. That is, only the interaction term changes due to the phase change caused by the nonuniform flow. This fact is exactly the same as in two-dimensional theory [9].

The actual computation of wave resistance is performed by the Sruttensky formula using the relation

$$\theta_j = \cos^{-1}\left(\frac{1}{d_j}\right) = \tan^{-1}\left(d_j^2 - 1\right)^{\frac{1}{2}} \qquad (45)$$

and the corresponding values of s_2 are obtained by interpolation. When a portion of elementary waves near $\theta_\infty = 0$ is reflected from the ship hull, the larger part of the energy in this portion of elementary waves will be dissipated by breaking waves, and the wave resistance will decrease, but the momentum loss due to breaking waves will increase. If such energy was considered to be totally missing in the wave resistance, j in the Srettensky formula for bow waves would start not from zero but from a certain number minimum $J = J_1$ such that

$$\theta_{J_1} > \theta_{\infty_1}$$

where θ_{∞_1} is the value of θ_∞ from which bow waves start to reflect. If $\theta_{\infty_1} = \theta_{J_1}$, $\varepsilon_{J_1} = 1$, and $\varepsilon_j = 2$ for $J > J_1$, and if $\theta_{J_1} > \theta_{\infty_1}$, $\varepsilon_{J_1} = 2$ for $J \geq J_1$.

The result is shown in Figure 12 where a considerable shift of the phase of hump and hollow of the wave resistance due to bow stern wave interaction is noticeable.

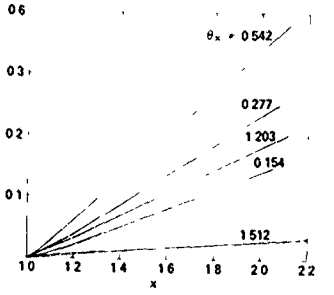


Figure 11 - Ray Paths of Stern Waves of a Wigley Hull (b = 0.2, h = 0.0625)

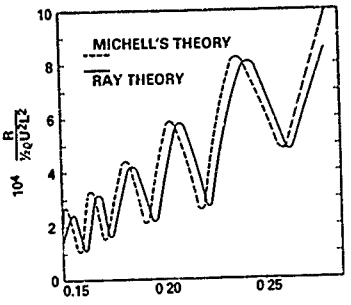


Figure 12 - Wave Resistance of the Wigley Ship (b = 0.2, h = 0.0625)

Discussion

Recently Eggers[17] obtained a dispersion relation from a low speed free-surface boundary condition which was a slightly modified version of the one Babal[18] used. Eggers showed that there was a small region near the stagnation point where the wave number became negative; since this was not permissible for a wave and it could be interpreted to mean that there was no wave in the region. He suggested that his form might help alleviate the sensitivity of the initial condition to the ray paths. According to the energy conservation law[8] or the wave propagating through nonuniform flow the wave energy flux is proportional to the wave number along the ray tube. When the wave number along a ray is considered, although the Keller dispersion relation has an infinite wave number only at the stagnation point, the Eggers dispersion relation has an infinite wave number in the flow near the bow. Thus, near such a singular point or a singular line, waves may break and the present theory cannot be applied. When Eggers[1] equation was incorporated into the ray equation in the present ray computer program it was found that the ray path was still very sensitive to a small change of initial value (x,y,θ) and the curved ray still reflected from the ship hull.

In the experiments[7] conducted at Tokyo University, the second caustic can be noticed, and near the second caustic the flow field is violently different from the linear theory. However, it seems that extreme caution is needed to distinguish the second caustic from the first caustic. The case of experiments[3] with wedges is interesting because, according to the present theory, there cannot be a second caustic on the wedge although the first caustic should be there. However, the wave phases of the wedge should be advanced and quite sensitive to the draft- and beam-length ratios due to the nonuniform flow caused by the wedge. On the other hand, the present theory is still not exact although it takes into account the effect on the propagation of water waves of nonuniform flow due to the double model. Thus, the nonlinear effect of water waves is not totally analyzed here. Nevertheless, the present theory supplies a great deal of hope to an entirely different approach to the ship wave theory - the ray theory.

Although the strictly linear amplitude function is used for simplicity in the present study, a slightly improved amplitude function may be easily incorporated by adding the sheltering effect or other effects. However, it should be noted here that, in any case, the bow wave resistance and the stern wave resistance are the same as the results without the ray theory and the effect of the ray theory would appear as a shift of the phase of hump and hollow in the total wave resistance. Therefore, the computational results would not match the results of towing tank experiments unless the viscous boundary layer effect on the stern wave or some other effect is considered.[19]

Acknowledgements

This work was supported by the Numerical Naval Hydrodynamics Program at the David W. Taylor Naval Ship Research and Development Center. This Program is jointly sponsored by DTNSRDC and the Office of Naval Research.

Appendix A

For the computation of ray paths of a ship, the flow velocity and its derivatives on (x,y,o), u,v,u_x, v_x, u_y are needed. A Wigley hull has the double model source distribution

$$m = b_1(-2x_1 + 1)\left\{1 - \left(\frac{z_1}{h}\right)^2\right\}$$

in

$$0 < x_1 < 1, \quad y_1 = 0, \quad h > z_1 > -h$$

Thus,

$$-u(x,y,o) = 2\int_o^b\int_o^1 m\frac{\partial}{\partial x}\left(\frac{1}{r}\right)dx_1\,dz_1 - 1$$

$$= -2\int_o^h\int_o^1 m\frac{\partial}{\partial x}\left(\frac{1}{r}\right)dx_1\,dz_1 - 1$$

$$= 2b_1\left\{\int_o^h \frac{1 - \frac{z_1^2}{h^2}}{r\,(x_1 = 1)}\,dz_1 + \int_o^h \frac{1 - \frac{z_1^2}{h^2}}{r\,(x_1 = o)}\,dz_1\right\} - 1$$

$$- 4b_1\left\{\frac{2}{3}h\log\{x_1 - x + r(z_1 = h)\}\right. -$$

$$\int_0^h \frac{(x_1 - x)\, y^2}{(z_1^2 + y^2)\, r}\, dz_1$$

$$+ \int_0^h \frac{(r_1 - x)}{r}\, dz_1$$

$$- \frac{1}{3h^2} \int_0^h \left\{ y^4 \frac{(x_1 - x)}{(z_1^2 + y^2)\, r} \right.$$

$$\left. - \frac{(x_1 - x)\,(z_1^2 - y^2)}{r} \right\} dz_1 \Bigg]_{x_1 = 0}^{x_1 = 1}$$

$$-v\,(x,y,0) = 2 \int_0^h \int_0^1 m \frac{\partial}{\partial y} \left(\frac{1}{r}\right) dx_1\, dz_1$$

$$= -2\, b_1 \int_0^h \left[\frac{2x^2 - 3x + 1}{(z_1^2 + y^2)\, r(x_1 = 1)} \left(1 + \frac{y^2}{h^2}\right) - \frac{2x^2 - 3x + 1}{r\,(x_1 = 1)\, h^2} \right.$$

$$- \frac{2z_1^2}{r(x_1=1)\, h^2} + \frac{2}{r(x_1=1)}$$

$$- \frac{2x^2 - x}{(z_1^2 + y^2) r(x_1=0)} \left(1 + \frac{y^2}{h^2}\right)$$

$$\left. + \frac{2x^2 - x + 2z_1^2}{r(x_1=0)\, h^2} - \frac{2}{r(x_1=0)} \right] dz_1$$

$$-u_x = -4b_1 \log \left| \frac{r(x_1=1,\ z_1=0)}{r(x_1=0,\ z_1=0)} \right|$$

$$+ \frac{4}{h^2} \left[- \left(\tfrac{1}{2} z_1\, r(x_1=1) \right.\right.$$

$$- \frac{a_1^2}{2} \log \left| z_1 + r(x_1=1) \right| \frac{(x-1)}{a_1^2}$$

$$+ 2 \left\{ \left(\frac{z_1}{2} + \frac{a_1^2}{4} \right) \log \left| z_1 + r(r_1=1) \right| \right.$$

$$\left.\left. - \frac{z_1}{4}\, r(r_1=1) \right\} \right.$$

$$- \frac{x}{a_0^2} \left(\tfrac{1}{2} z_1\, r(x_1=0) \right.$$

$$\left. - \frac{a_0^2}{2} \log \left| z_1 + r(x_1=0) \right| \right)$$

$$- 2 \left\{ \left(\frac{z_1^2}{2} + \frac{a_0^2}{4} \right) \log \left| z_1 + \right. \right.$$

$$\left.\left. r(x_1=0) \right| - \frac{z_1}{4}\, r(x_1=0) \right\} \Bigg]_{z_1=0}^{h}$$

where $a_1^2 = (x-1)^2 + y^2$

$$a_0^2 = x^2 + y^2$$

$$-u_y\,(x,y,0) = 2 \int_0^h \int_0^1 m \frac{\partial^2}{\partial y \partial x} \left(\frac{1}{r}\right) dx_1\, dz_1$$

$$= -2by \left[\frac{h}{\{(1-x)^2 + y^2\}\, r(1,h)} \right.$$

$$+ \frac{1}{r(1,h)\, h} + \frac{1}{r(0,h)\, h}$$

$$- \frac{1}{h^2} \log \frac{(h + r(1,h)\{h + r(o,h)\}}{r(1,0) \cdot r(0,0)}$$

$$\left. + \frac{h}{(x^2+y^2)\, r(o,h)} \right]$$

$$+4by \left\{ \int_0^h \frac{(1-x) \left(1 + \frac{y^2}{h^2}\right) dz_1}{\left(z_1^2 + y^2\right) r(x_1=1)} \right.$$

$$+ \int_0^h \frac{x \left(1 + \frac{y^2}{h^2}\right)}{\left(z_1^2 + y^2\right) r\ (x_1=0)} dz_1$$

$$- \frac{1}{h^2} \int_0^h \frac{1-x}{r(x_1=1)}\, dz_1$$

$$\left. - \frac{1}{h^2} \int_0^h \frac{x}{r(x_1=0)}\, dz_1 \right\}$$

$$- V_y = b_1 \left(6y^2 + \frac{6y^4}{h^2}\right) \times$$

$$\times \left[\frac{1}{3}(1-2x)\left(\frac{1}{x_1-x} + \frac{(x_1-x)^2 - y^2}{(x_1-x)\, y^2} \right) \right.$$

$$\times \int_0^h \frac{ds_1}{(z_1^2+y^2)r}$$

$$+ \frac{2}{3} \frac{h}{\left\{(x_1-x)^2 + y^2\right\} r(z_1=h)}$$

$$+ \frac{1}{3}(1-2x)\left(\frac{-h}{(x_1-x)\left\{(x-x_1)^2+y^2\right\} r(z_1=h)} \right.$$

$$\left. \left. + \frac{hr \quad (z_1=h)}{(h^2 + y^2)\ (x_1-x)\ y^2} \right) \right]_{x_1=0}^{1}$$

$$- 6\, by^2 \left[\frac{1}{3h^2} \left(\frac{2y^2 + (1-2x)\ (x_1-x)\ h}{(x_1-x)^2 + y^2 \quad r(z_1=h)} \right. \right.$$

$$\left. + 2 \log \frac{h + r(z_1=h)}{r(z_1=0)} - \frac{2h}{r(z_1=h)} \right)$$

$$\left. + \frac{2(x_1-x)\ (1-2x)}{3h^2} \int_0^h \frac{dz_1}{(z_1^2 + y^2)r} \right]_{x_1=0}^{1}$$

$$- \frac{v\ (x,y,0)}{y}$$

where $r(a,b)_1 = r(x_1=a,\ a_1=b)$

In these expressions the integrals

$$\int \frac{z_1^n}{r}\, dz_1$$

and

$$\int \frac{dz_1}{(z_1^2 + y^2)r}$$

are available in closed forms.[20]

References

1. Inui, T. and H. Kajitani, "Study on Local Non-Linear Free Surface Effects in Ship Waves and Wave Resistance," Schiffstechnik, Band 24, Heft 118 (Nov 1977).

2. Keller, J., "The Ray Theory of Ship Waves and the Class of Streamlined Ships," J. of Fluid Mechanics, Vol. 91, Part 3, pp. 465-488 (1978).

3. Miyata, H., "Characteristics of Nonlinear Waves in the Near-Field of Ships and Their Effects on Resistance," Proc. of 13th ONR Symposium on Naval Hydrodynamics (1980).

4. Ursell, F., "Steady Wave Patterns on a Non-Uniform Steady Fluid Flow," J. of Fluid Mechanics, Vol 9, pp. 333-346 (1960).

5. Shen, M.C., R.E. Meyer and J.B. Keller, "Spectra of Water Waves in Channels and Around Islands," The Physics of Fluids, Vol 11, No. 11, pp. 2289-2304 (1968).

6. Yim, B., "Notes Concerning the Ray Theory of Ship Waves," Proc. of the Continued Workshop on Ship Wave-Resistance Computations, pp. 139-153 (1980).

7 Inui, T., H. Kajitani, H. Miyata, M. Tsuruoka, and A. Suzuki, "Nonlinear Properties of Wave Making Resistance of Wide-Beam Ships," J. of the Society of Naval Arch. of Japan, Vol. 146, pp. 18-26 (Dec 1979).

8. Lighthill, J., "Waves in Fluids," Cambridge University Press, Cambridge, London pp. 332-337 (1978).

9. Doctors, L. and G. Dagan, "Comparison of Nonlinear Wave-Resistance Theories for a Two-Dimensional Pressure Distribution," J. of Fluid Mechanics, Vol. 98, Part. 3, pp. 647-672 (1980).

10. Yim, B., "Design of Bulbous Bow by the Ray Theory of Ship Waves," to be published.

11. Yim, B., "A Simple Design Theory and Method for Bulbous Bows of Ships," J. of Ship Research, Vol. 18, No. 3, pp. 141-152 (Sep 1974).

12. Havelock, T.H., "Wave Patterns and Wave Resistance," Tran. of the Inst. of Naval Architects, Vol. 76, pp. 430-443 (1934).

13. Inui, T., "Wave-Making Resistance of Ships," Trans. of SNAME, Vol. 70, pp. 283-313 (1962).

14. Lamb, H., "Hydrodynamics," Dover Pub., New York, N.Y., p. 395, (1945).

15. Havelock, T.H., "The Calculation of Wave Resistance," Proc. of the Royal Society (London), Vol. A144, pp. 514-521 (1934).

16. Srettensky, L.N., "On The Wave Making Resistance of a Ship Moving Along in a Canal," Philosophical Magazine, Vol. 22, 7th Series (1936).

17. Eggers, K., "On the Dispersion Relation and Exponential Variation of Wave Components

Satisfying the Slow Ship Differential Equation on the Undisturbed Free Surface," International Joint Research on Study on Local Nonlinear Effect in Ship Waves, Research Report 1979, Edited by T. Inui, pp. 43-62 (Apr 1980).

18. Baba, E. and M. Hara, "Numerical Evaluation of Wave Resistance Theory for Slow Ships," Proc. 2nd International Conference on Numerical Ship Hydrodynamics, University of California, Berkeley, pp. 17-29 (1977).

19. Moreno, M., L. Perez-Rojas and L. Landweber, "Effect of Wake on Wave Resistance of a Ship Model," Iowa Institute of Hydraulic Research, Report 180 (Aug 1975).

20. Yim, B., "Theory of Ventilating on Cavitating Flows about Symmetric Surface Piercing Struts," David W. Taylor Naval Ship Research and Development Center, Report 4616 (Sep 1976).

DISCUSSION
of the paper
by B Yim

A RAY THEORY FOR NONLINEAR SHIP WAVES AND WAVE RESISTANCE

Discussion
by H Miyata

I think it is a difficult problem to connect nonlinear waves in the near-field and nonlinear propagation of linear waves For the author s second caustic to be understood it will be necessary to demonstrate the variation of wave front lines with the change of advance speed

In my opinion the ray theory should be applied to dispersive propagation of linear waves after they are influenced by free surface shock waves at the time of generation

Author s reply

Professor Miyata's comment is deeply appreciated because all of his experimental results are closely related to the present study

Certainly all the waves depend upon the advance speed as in the ordinary ship wave theory However, in the ray theory, ray path, reflection, phase difference, etc can be represented without specific information of advance speed The approximate wave form can be sketched by representing the phase as $k_0(x \cos \cdot + y \sin) + k_0$'s where inverse Froude number square appears as a factor using an appropriate amplitude function, as in the representation of linear waves by the method of stationary phase However, the second caustic line itself in the present approach is not a function of Froude number, although the wave form in the vicinity of the caustic may change according to the Froude number

The large difference between the second caustic and the nondispersive shock wave could be that for the second caustic no unusual assumption was needed to justify the shock-wave-like phenomenon while the nondispersive shock wave can never exist without the small depth which had to be just assumed for ship waves in the deep water

A NUMERICAL APPROACH OF THE NONLINEAR WAVE RESISTANCE PROBLEM

O Daube and A. Dulieu
Laboratoire d'Informatique
pour la Mécanique et les Sciences de l'Ingénieur
B P 30, 91406 Orsay Cedex (France)

ABSTRACT

In this paper a numerical method for solving the non linear wave resistance problem for a ship with constant forward speed is presented. An iterative procedure is used, at each step of which, a linear problem with known boundaries is solved by distributing Rankine sources over the wetted hull and a finite part around the ship of the free surface. a convenient form for the free surface conditions is derived from the real ones.

Results for the Serie 60 and for the Wigley hull are presented and compared with experimental and other numerical results. These results seem to be quite satisfactory.

I INTRODUCTION

In the last decade, a lot of numerical work has been devoted to the very old wave resistance problem for a ship moving with a constant forward speed. This fact was evidenced by the first two International Conferences on Numerical Ship Hydrodynamics and by the Workshops on ship-wave resistance which took place in Washington (Nov 1979) and in Tokyo (Oct 1980).

The development of high-speed computers and of numerical methods enable the numerician hydrodynamicists to try to deal with the complete non linear problem, in order to get-it is at least expected so- a better evaluation of the wave resistance of a ship and if possible a practical program to compute it.

The classical way to deal with non linear problems is to solve a sequence of linear problems, the solutions of which are expected to converge to the solution of the original non linear problem. When there exists, as a part of the unknowns, a free surface, the classical way is to start the computations with an initial guess of the location of this free surface and then, step by step, to compute successive locations of it. We use in this paper this approach.

We shall first recall the non dimensionnal physical equations and then derive an unique free surface condition to be applied on the successive locations of the free surface. Then, at each step of the iterative procedure, we solve a linear harmonic problem with known boundaries which are the wetted hull and the free surface location computed at previous step. Once this problem is solved, we compute the hydrodynamic characteristics and especially the wave resistance coefficient and the new free surface elevation. Then, if necessary, the iterative procedure is continued.

The numerical basis of the work is the Hess and Smith's singularity method [1]. Rankine sources are distributed on the wetted hull and on a finite part of the free surface. Numerical tests concernig the extension of the paneled free surface have been performed and are presented.

The results presented concern the wave resistance coefficient and the wave profile along the hull. Wave field around the ship is also vizualised.

These results are seen to be quite satisfactory and it is emphasized that, after some particular points will be cleared, the method will provide an efficient way to get a good evaluation of the wave resistance for a sufficiently large class of ships and Froude number.

More details concerning this paper can be found in the Doctoral Thesis of the first author [2].

II PHYSICAL EQUATIONS

All equations are written in non-dimensionnal form with respect to.

- U_∞ the constant forward speed of the ship
- L the half length of the ship
- g the acceleration of gravity

The Froude number F is defined by:

$$F = \frac{U_\infty}{\sqrt{2gL}}$$

We also define a parameter υ by :

$$\upsilon = \frac{1}{F^2}$$

The basic hypothesis are those of an irrotationnal flow of incompressible inviscid fluid with influence of gravity.

In a frame fixed to the ship, (see fig. 1), the steady state problem can be stated as follows:

Let be D the fluid domain
H the wetted hull
FS the free surface

We must find a velocity potential Φ in D, satisfying :

$$\nabla^2 \Phi = 0 \quad \text{in } D \qquad (1)$$

II.1 Boundaries conditions

a) On the hull H

The normal derivative $\frac{\partial \phi}{\partial n} = 0$ (2)

b) On the free surface-FS

A slip cinematic condition :

$$\frac{\partial \phi}{\partial n} = 0 \qquad (3)$$

A constant pressure dynamic condition :

$$vz + (\vec{\nabla}\phi)^2 - 1 = 0 \qquad (4)$$

c) At infinity :

The flow becomes uniform and the free surface elevation vanishes. A radiation condition is also required to impose downstream propagation of the waves. Its numerical implementation will be discussed later.

III. TRANSFORMATION OF THE FS CONDITIONS

As it was said in the introduction, we want, at each step of the iterative procedure, to solve a problem with known boundaries. For this purpose we need only one condition on the assumed location of the free surface. This unique is derived from the two real one (3) and (4) in the following manner

Let be :

L a free surface streamline

M a point on L

$\vec{s} = \frac{\partial \vec{OM}}{\partial \sigma}$ unit tangent vector to L in M

σ curvilinear abscissa of M on L

(see figure 2)

If $\vec{V}$ is the velocity at M, the cinematic condition (3) may be written as below :

$$\vec{V} = \vec{\nabla}\phi = V\vec{s} = V\frac{\partial \vec{OM}}{\partial \sigma}$$
$$V = \|\vec{V}\| = \frac{\partial \phi}{\partial \sigma} \qquad (5)$$

This form to derivate the dynamic condition (4) with respect to σ and then taking into account the relations (5), we obtain

$$\frac{\partial^2 \phi}{\partial \sigma^2} + \frac{v}{2V^2}\frac{\partial \phi}{\partial z} = 0 \quad \text{on FS} \qquad (6)$$

It may be noticed that the form of relation (6) is very similar to the classical linearized condition if we assume $\sigma \sim x$ and $V \neq 1$. But in relation (6), the condition is written on the exact location of the free surface.

The radiation condition has not yet been taken into account. This is achieved in a similar manner to Dawson's one [3]. The second derivative which appears in relation (6) is transformed by upstream finite difference along the streamline L using the values of the potential ϕ at M and at former points on L. (see figure 2)

$$\left(\frac{\partial^2 \phi}{\partial \sigma^2}\right)_1 = \sum_{k=0}^{k=p} \alpha_{ik}\phi_{i-k} \qquad (7)$$

At this stage the question which arises is to make a convenient choice of the number of points M_i and for the coefficients α_{ik} .

In [2] an analysis of difference equation

$$\sum \alpha_{ik} f_{i-k} + \frac{v}{2} f_i = 0 \qquad (8)$$

analog of the ordinary differential equation :

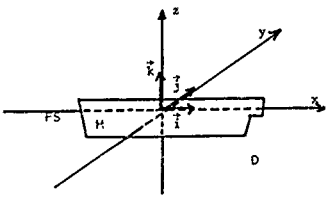


figure 1

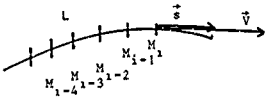


figure 2

$$\frac{d^2 f}{dx^2} + \frac{v}{2} f = 0 \qquad (8)$$

shows that a reasonable choice for p seems to be p=4 (e.g. 5 points of discretization) in order to avoid a too important wave damping which is inherent to such transformations. Furthermore, the coefficients α_{ik} are chosen so that the terms in

$$\phi \quad \phi' \quad \phi''' \phi^{(5)}$$

vanish in the Taylor expansion of the right hand term of (7).

This analysis shows also that the transformation (7) introduces in fact a slight Froude number shift and that the maximum grid size must vary as the fundamental wave-length, e.g. as the square of the Froude number. This fact probably prevents most of the numerical methods to handle low Froude numbers, say $F < 0.2$, at least on a classical sequential computer.

IV. ITERATIVE PROCEDURE

We shall now define more precisely the problem Pn to be solved at each step.

IV.1 Formulation of the problem Pn

At each step (n) of the iterative procedure, we solve .

find a potential $\phi^{(n+1)}$ which satisfies .

$$\nabla^2 \phi = 0 \quad \text{in } D^n \qquad (10)$$

$$L_n(\phi^{(n+1)}) = 0 \quad \text{on } \mathcal{D}^n = H^n \cup FS^n \qquad (11)$$

$$\vec{\nabla}\phi^{(n+1)} \to \vec{I} \text{ as } x^2 + y^2 + z^2 \to \infty \qquad (12)$$

where H^n, FS^n, D^n are respectively the wetted hull, the free surface location, the fluid domain computed at the previous step (n-1)

L_n is a linear boundary operator deduced from the relations (2),(6),(7) :

$$L_n = \frac{\partial}{\partial n} \quad \text{on} \quad H^n \qquad (13)$$

$$L_n = \sum \alpha_{ik} \delta_k + \frac{v}{2(v^2)^n} \frac{\partial}{\partial z} \quad \text{on } FS^n \quad (14)$$

where δ_k is defined by $(\delta_k f)_i = f_{i-k}$

IV.2 Numerical method

The basic numerical method must be able to deal with the successive locations of the free surface. Moreover the problem Pn is an exterior harmonic one. So, the Hess and Smith's singularity method [1] seems to be well adapted to the resolution of Pn, despite the quite unusual form of the boundary condition (14). Another advantage is that only a 2D surface has to be paneled and not a 3D domain as in finite difference or finite elements methods.

As done by Dawson [3], the wetted hull H^n and a finite part around the ship of the free surface FS^n are divided in small quadrangular panels. On each of the panel n°i a constant density Q_i of Rankine source is distributed. Let be

- $\overline{Q}$ the column vector of the source density Q_i
- $\overline{\phi}$ the column vector of the values of the potential at the center of panel n° i .
- $\overline{\partial L}$ the column vector of the values of the derivatives $(d\phi/dl)_i$ of the potential in the direction l.

There exist square matrix $A\phi$ and $A\partial L$ such :

$$\overline{\phi} = A\phi . \overline{Q}$$
$$\overline{\partial L} = A\partial L . \overline{Q} \qquad (15)$$

The boundary conditions (13) and (14) are then written at the center of each panel, which involve a linear system with unknown Q_i. This system is solved by a Gauss-Seidel like method.

Once the the new values of the source densities Q are known, one can compute the velocity at the center of each panel and then the hydrodynamic characteristics as the wave resistance coefficient and the free surface elevation.

IV.3 Computation of the free surface elevation

In this section, we make an assumption which will have to be removed in further developments of the proposed method.

We assume that the free surface streamlines have always the same projection in the plane (z=0). This is kept true during the whole iterative procedure and for any Froude number. This hypothesis is in fact a slow ship one. These projections are the double model streamlines in the plane (z=0).

The free surface elevation is calculated by integrating the third component of the cinematic condition (5).

$$\frac{\partial z}{\partial v} = \frac{1}{V} \frac{\partial \phi}{\partial z} \qquad (16)$$

As for $\partial^2\phi/\partial v^2$ there are coefficients β_{ik} to compute the first derivative :

$$\frac{\partial z}{\partial v} = \sum_{k=0}^{k=3} \beta_{ik} z_{i-k} \qquad (16)$$

where z_{i-k} means the elevation of the free surface at points on the free surface streamline L (see figure 2)

Then the knowledge of the free surface elevation at upstream point, enables to compute the elevation at point M_i by :

$$z_i^{(n+1)} = \left(\frac{1}{V_i^{n+1}} \frac{\partial \phi}{\partial z_i} - \sum_{k=1}^{k=3} \beta_{ik} z_{i-k}^{(n+1)} \right) / \beta_{i0} \quad (17)$$

Finally, with the assumption made, the new point M_i^{n+1} is defined by

$$x_i^{n+1} = x_i^n$$
$$y_i^{n+1} = y_i^n$$
$$z_i^{n+1} \quad \text{by relation (17).}$$

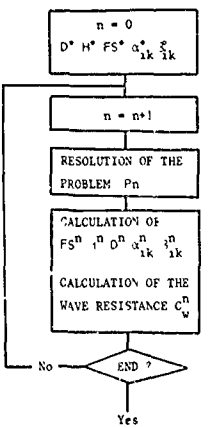
It is implicit that the free surface elevation is assumed to vanish upstream of the paneled part of the free surface, in order to start the computations with relation (17).

The value of the velocity modulus which appears in relation (17) is calculated with the help of the coefficients β_{ik} and the values of the potential :

$$V_i^{(n+1)} = \sum_{k=0}^{k=3} \beta_{ik} \phi_{i-k}^{(n+1)}$$

IV 4 Summary of the iterative procedure

The iterative procedure may be described as.



The calculations are stopped when the difference between two successive locations of the free surface becomes sufficiently small

V. COMPUTATION OF THE WAVE RESISTANCE

We compute the wave resistance coefficient C_x defined by :

$$C_x = \frac{R_W}{\rho V_\infty^2 L^2}$$

where ρ is the volumic density of the water, and R_W the dimensional wave resistance.

This is achieved by integrating the pressure forces on the wetted hull. At a point $P(x,y,z)$ of the hull H, the pressure coefficient C_p is defined by :

$$C_p(x,y,z) = u_z + v^2 - 1 \qquad (18)$$

so that

$$C_x = \iint_H (u_z + v^2 - 1)\vec{n}.\vec{i}\,dS \qquad (19)$$

Because of round-off errors it seems preferable to compute the term in z by using Stokes theorem:

$$\iint_H z\vec{n}.\vec{i}\,dS = -\frac{1}{2}\int_{WL} z^2 dy$$

where WL is the wave profile along the hull. The second part of the integral (19) is calculated in a classical numerical way.

VI. EXTENSION OF THE PANELED FREE SURFACE

In order to estimate the minimum downstream extension of the paneled free surface, several numerical tests were made on the Serie 60 hull. Only the first step of the iterative procedure described in sec. IV has been considered and the calculations were made for different extensions of the paneled free surface and for several Froude number F.

If DARR is the distance between the bow and the downstream boundary of the paneled free surface, normalized with respect to L, it is shown on fig. 3 and 4 the variation of the wave resistance coefficient C_x as a function of DARR for two Froude numbers, F=0.25 and F=0.28.

It can be seen that for short distances DARR, the wave resistance coefficient strongly oscillates and that for greater values of DARR, the coefficient C_x seems to tend to a mean value $\bar{C}_x$. A strip which represents a variation of 4% around $\bar{C}_x$ is drawn on the figures and it can be seen that a reasonable value of DARR is about one half length of the ship. This fact confirms the appreciation given by Dawson [3].

Finally, it is shown on figure 5 a typical paneling of the free surface.

In the whole calculations, the lateral extension of the paneled free surface was taken equal to 0.5 and the upstream extension equal to 1.5.

As a matter of fact, the determination of DARR is rather empirical, and it would be desirable to treat in a better way the downstream boundary, may be by writing an absorption condition as Orlanski's one [4].

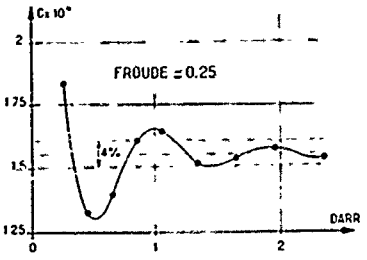


figure 3

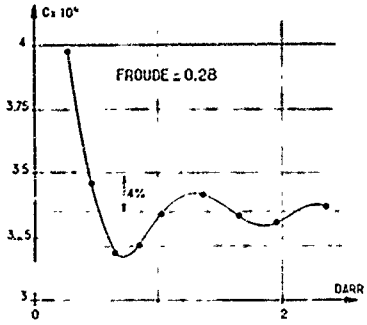


figure 4

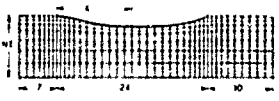


figure 5

VII. RESULTS

In this section, we present the results which were obtained with the help of the presented method for two ships :

- The Serie 60 Cb 0.6 hull
- The Wigley hull defined by

$y = 0.1(1-x^2)(1-(8z)^2)$ if $z < 0$

$y = 0.1(1-x^2)$ if $z \geq 0$

$-1 \leq x \leq +1$

Our results will be compared,when possible, with experimental datas and with other numerical results,mainly with the results which were presented at the Workshop on Ship Wave-Resistance Calculations (Washington Nov 1979).

VII.1 Description of the results

* We give the variation of the Wave-resistance coefficient C_w :

$$C_w = \frac{R_w}{\frac{1}{2}\rho V_s^2 S}$$

where S is the wetted hull at rest.
The relation between the coefficient C_w and the coefficient C_x defined in sec. VI is:

$$C_w = \frac{2L^2}{S} C_x$$

* We give the wave profile η along the hull, normalized with respect to $2V_s^2/g$

Let be h the free surface elevation with respect to L,then there is the relation :

$$\eta = \frac{h}{F^2} = 4h$$

* We give at lastviews of the wave-field around the hull,some iso-height lines and the crest - lines of the free surface

VII.2 Serie 60

VII.2.1 Wave-resistance coefficient

On the figure 6 we have reported the experimental values given by Todd [4] and those given by Huang and Von Kerczek [5] (in fact,the values in [5] are values of the residual resistance). The results we obtained are also reported on this figure 6.

Roughly,it can be said that the aspect of the experimental curves is found.However,significant differences can be observed at both ends of our curve.For low values of F,this fact can be explained by the too great size of the free surface panels (see sec. III).For $F > 0.35$,the difference can be explained by the fact that in our calculations,the ship is assumed to fixed. The importance of sanking and trim is well known and will be evidenced in VII.3 for the Wigley hull.

On figure 7,in addition of experimental datas, we have reported numerical results for the fixed ship given by other authors: Dawson [3] ,Guevel & Delhommeau [6] ,Gadd [7].

- The Dawson's results are everywhere smaller than our's,which seems to confirm that it is important to take into account the non-linearities.
- The main difference with the Guilloton's method used by Guevel and al. is that our curve does not show so distinct hollow and dump as those they obtained.
- There is a good agreement between our results and Gadd'ones up to F=0.3.The Gadd's curve does not seem to exhibit a flat part about F=0.3,and anyway he did not give results for $F > 0.32$

VII.2.2 Wave profile along the hull

On figures 8 and 9,are shown the calculated wave profiles along the hull for F=0.30 and F=0.32.We have also reported the Huang and Von Kerczkek's experimental profiles [5] and those which were calculated by Dawson [3] and Guevel et al. [6]

Two points may be noticed.

a) The hollows and the crest of the second wave along the hull are found slightly downstream of the experimental one.This difference is an illustration of the Froude number shift introduced by the transformation of the free surface conditions(see sec. III).The calculated profile for F=0.30 seems to be closer to the experimental one for F=0.32 than to the profile for F=0.30 .

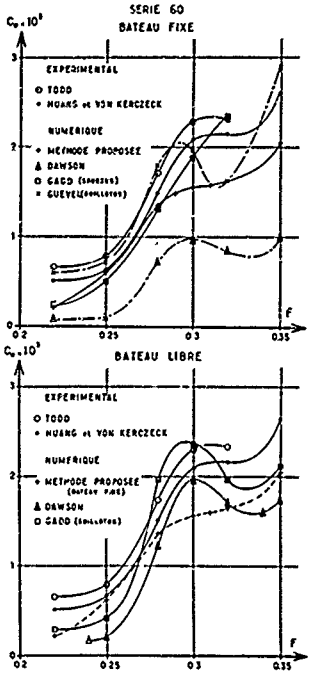


Figure 6 a. 7

b) Concerning the bow wave,it can be observed that its calculated crest lies upstream of the experimental one for $F < 0.32$,and downstream for $F > 0.32$.

The amplitude of the bow wave is found smaller than the real one by each author.This is probably due to the fact that the panels are not enough refined.

On figure 10,are gathered the calculated profiles for all Froude numbers.The following well-known phenomenon can be observed:

- -downstream displacement of the bow wave when F increases.
- -disappearance of the second hull wave when F increases.

In figure 11, a perspective view of the wave field around the ship for F = 0.3 is shown. It must be noticed that the z-coordinates have been multiplied five times.

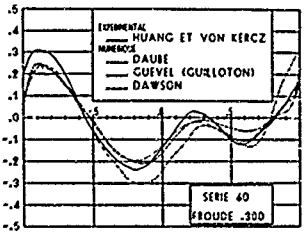


figure 8

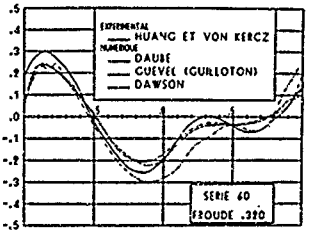


figure 9

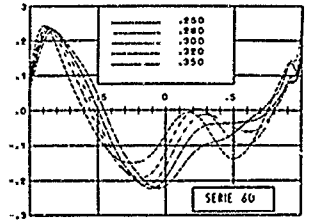


figure 10

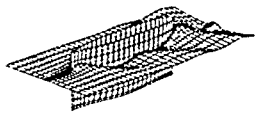


figure 11

VII.3 Wigley hull

This hull is defined analytically by

$-1 \leq x \leq +1$

$y = 0.1(1 - x^2)$ for $z \geq 0$

$y = -0.1(1 - x^2)(1 - 6\ Hz^2)$ for $-0.125 \leq z \leq 0.$

VII.3.1 Wave resistance coefficient

In figure 12, we have reported the experimental data from Lackenby [8], the numerical results from Delhommeau [6], Dawson [3] and our own results. The observations we have made concerning the Serie 60 hull may also be made in the case of the Wigley hull. In particular, the necessity of taking into account the sink and trim in order to improve the quality of the results is one more time evidenced.

Let P be the non-dimensional weight of the ship and V the non-dimensional volume of the wetted hull at rest. Then we have

$$P = \nabla V$$

where ∇ is the parameter defined in section II. The trim angle, α, is then defined by

$$\tan(\alpha) = (C_Z - P)/C_X \qquad (20)$$

Unfortunately, at this point, numerical troubles are to be expected. In fact, C_Z and P are of the same order of magnitude (~ 0.1). Thus, a relative error of 1 % on these values (which actually would be a rather good accuracy, with regards to discretization and round-off errors) would involve an absolute error on $C_Z - P$ of magnitude 10^{-3}. Meanwhile, C_X is of magnitude 10^{-4}. One can immediately see that using relation (20) to compute the trim angle α, requires a much higher accuracy on C_Z and P than it can reasonably expected.

This is the reason why we have neglected the trim angle and we have computed the sink Δh by the approximate relation

$$\nabla h\, S_{WL} \simeq C_Z - P$$

where S_{WL} is the surface of the waterline section of the hull.

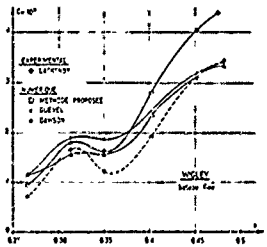


Figure 12

Even with this rather rough approximation, regarding to the restrictions on $C_Z - P$ stated before, the wave resistance curve is greatly improved as can be seen in figure 13. The range of Froude numbers for which our results are close to experimental datas have been wided.

The discrepancy increases with the Froude number and shows that the trim angle can no longer be neglected for higher Froude numbers. The results from Dawson [5] , plotted on both figures 12 and 13, show the same influence of sink and trim.

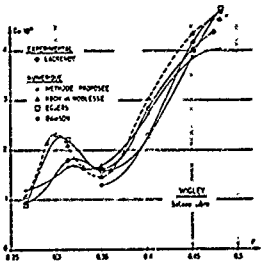


Figure 13

VII.3.2 Wave profile along the hull

Figures 14 and 15 show the computed wave profiles along the hull for F = 0.313 and F = 0.452. We have also reported Shen and Cross experimental data and results which have been computed by Delhommeau et al [6] and Dawson [3] . Similar remarks as for the Serie 60 can be made here.

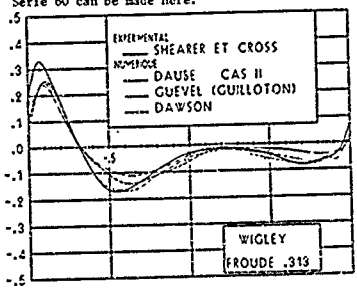


Figure 14

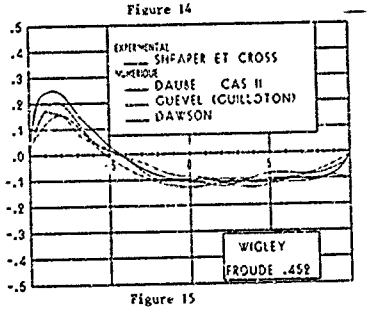


Figure 15

VII.3.3 Crest lines

The crest lines are defined (see section IV.3) as the lines along which the vertical derivative $\frac{\partial \phi}{\partial z}$ of the potential vanishes. These lines for $\frac{g}{F^2}$ = 0.266 and F = 0.35 are shown in figures 16 and 17.



Figure 16

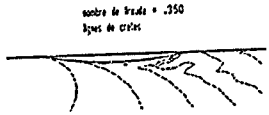


Figure 17

CONCLUSION

The method that we have presented here was found to be efficient for the computation of the non linear flow around a ship, and especially for the evaluation of the wave resistance, at least for the class of hull which were used. The results we have obtained show the importance of taking into account the non linearities. This fact is well evidenced by comparing our results with hose of Dawson.

However, some points have to be improved and two can be pointed out

- We have to remove the assumption made in section IV.3 concerning the projections of the free-surface streamlines on the plane (z = 0)
- The sink and trim must be more correctly computed.

REFERENCES

[1] Hess, J.L., Smith, A.M.O.: "Calculation of Potential Flow About Arbitrary Body", Progress in Aeronautical Science, vol. 8, Pergamen Press, 1967.

[2] Daube, O. : "Contribution au Calcul Non Linéaire de la Résistance de Vagues d'un Navire", Doctoral Thesis, Université de Paris VI, 1980.

[3] Dawson, C.W. : "Calculation With the XYZ Free Surface Program for Five Ship Models" Workshop on Ship Wave Resistance Calculation, DTNSRDC, Nov. 1979.

[4] Orlanski, I. : "A Simple Boundary Condition for Unbounded Hyperbolic Flows", Journal of Computational Physics, vol. 21, 1976.

[5] Huang, T.T., Von Kerczek, C. : "Shear Stress and Pressure Distribution on a Surface Ship Model ; Theory and Experiments", 9th Symposium on Naval Hydrodynamics, ONR, Paris, 1972.

[6] Delhommeau, G., Guevel, P., Cordonnier, J.P.: "The Guilloton's Method", Workshop on Ship Wave Resistance Calculation, DTNSRDC, Nov. 1979.

[7] Gadd, G.E. : "Contribution to Workshop on Ship Wave Resistance Calculation", DTNSRDC, Nov. 1979.

[8] Leckenby, H. : "An Investigation into the Nature and Interdependance of the Components of Ship Resistance", Transactions of the Royal Institute of Naval Architects, Vol. 107, 1965.

Session II

NONLINEAR WAVES AND WAVE RESISTANCE

J H. McCarthy
Session Chairman
David W. Taylor Naval Ship
Research and Development Center
U S.A.

NUMERICAL STUDIES OF THE NEUMANN-KELVIN PROBLEM FOR A TWO-DIMENSIONAL SEMI-SUBMERGED BODY

Katsuo Suzuki
National Defense Academy
Yokosuka, Japan

Abstract

Neumann-Kelvin problem of the two-dimensional flow past a semi-submerged circular cylinder is solved numerically by three kinds of methods, the integral equation methods in which a wave source is used as the kernal function, the multi-pole expansion method, and the so-called boundary element method in which Rankine type of singularities are used. The problem has an eigen solution which satifies the homogeneous boundary condition (zero normal velocities) on the body surface, that is, it has infinitely many solutions. An additional condition required to fix the solution uniquely is to give the value of stream function on the body surface. The solution of which stream function vanishes on the body surface is proposed from the discussion on the mass conservation under the linear free surface. The flow for the slightly different value of the stream function from zero is shown to be an approximate flow around the body with a slight sinkage. By using this fact the method to estimate the wave resistance of the body free to sink is proposed.

1. Introduction

Consider the two-dimensional problem of the steady free-surface flow past a body which pierces the water surface. It is well known that the free surface condition is nonlinear, particular near the front and rear stagnation points. The nonlinear problem might be solved by iteration procedure. As the first step of the procedure the linear solution or the double-model solution is taken usually. In the present paper the Neumann-Kelvin solution is treated as it is considered to be a first approximation of the exact nonlinear exact problem.

The Neumann-Kelvin problem for a semi-submerged circular cylinder was first solved numerically by [illegible] Mizuno [2]. They found that the problem has infinitely many solutions and that the wave resistance can have zero value. These astonishing facts have been recognized widely. For the three-dimensional problem, Bessho [3] discussed that the Neumann-Kelvin solution is not determined uniquely without the additional condition in relation to the so-called line integral terms. In his discussion to Bessho, on the basis of the singularity of the line integral term, Eggers [4] indicated the possibility of existence of the eigen solution. Bessho [5], also, showed that the eigen solution exists for a two-dimensional plate vertically piercing the water surface. Recently Ursell [6] proved for a semi-submerged circular cylinder that there is a unique least-singular solution which has finite velocities at the corners between the body surface and the linearized free surface. It is also indicated from his discussion that there are infinitely many solutions depending on the singularity in the corners.

The further step to be studied on this problem is which solution is to be selected as an appropriate approximation for the exact nonlinear solution and/or what phenomena the eigen solution means. The validity of determining the appropriate approximation should be justified after the full nonlinear problem is solved. However, Suzuki [7,8] proposed an additional condition to fix the solution uniquely from the discussion on the conservation of mass under the linearized free surface.

The proposed condition is that the wave heights along the ship sides are zero (equal to the statical wave surface). Although this condition looks curious at a glance, his argument is oased on the reasoning that the forces acting on the body, say, wave resistance, are to be deduced from the macroscopic physical quantities, say, mass, momentum. In the two-dimensional problem the alternative condition is that the value of the stream function vanishes on the body surface(equal to upstream free surface).

It was shown by Bessho [5], Suzuki [7,8] that the flow for the slightly different value of the stream function from zero is an approximate flow around [illegible] by with a slight sinkage. By [illegible] fact the wave resistance of a [illegible] sink can be estimated app- [illegible] This seems to be an advan-

tage of the present method, for the usual wave resistance theories give the wave resistance only for the fixed ships. It was reported by some authers at Wasington Workshop on Ship Wave Resistance Computations (1979) that the wave resistance for the ships free to sink is considerably larger than the fixed ships. The present method seems to be expected for estimating the wave resistance of the ships free to sink and trim.

In the present paper the Neumann-Kelvin problem for a semi-submerged circular cylinder is solved numerically by using three methods. One of them is the integral equation method in which the wave source potential is used as the kernel function. The second one is the multi-pole expansion method used by Ursell [6]. The third one is the so-called boundary element method (BEM) in which Rankine type of singularities are use Such methods are recently used successfully in the surface flow problem, e.g., Dawson [9], for the nonlinear problem, e.g., Hess [11]. They used the sources, vortices as the singularities and the derivatives were calculated by finite difference technique. In the present paper a boundary element method is presented, in which the numerical differenciation is avoided by using a partial integration. This method improves the accuracy of the solution.

The fundamental difficulty of applying the BEM to the free-surface flow consists in treati.. the so-called radiation cond.,there are no waves upstream. Some methods have been proposed, e.g., upstream-finite-difference- and-open-boundary technique by Salvesen-Kerczek [10], Dawson [9], BEM-and-eigen asymptotic-hybrid method by Yeung-Bouger [11], rigid-boundary method by Hess [10], initial-value-problem method by Haussling-Coleman [12] damping-device method by Chan [13].

In the pr ent paper a doulets-least-square method is presented, in which two artificial doublets are located downstream to cancel the downstream waves generated by the body or to cause no waves infinitely downstream and the radiation condition, the wave heights both in front of the body and after the doublets vanish, is satisfied on some points of the radiation region in a sense of least square. This technique has less dependecy on the truncation point of the down stream region and it will be easy to apply the technique to the nonlinear problem or the three dimensional problem. The another advantage is that the forces acting on the body can be obtained by calculating the Lagally forces acting on the point doublets not by integrating the pressure on the body surface.

2. Neumann-Kelvin Solutions

[2-1] Representations of the Neumann-Solution

The Neumann-Kelvin problem is a boundary value problem of a free-surface flow past a semi-submerged body, the free-surface condition is linearized and the body-surface condition is exactly given. Let the complex potential of the two-dimensional Neumann-Kelvin solution be;

$$F(z) = \phi(z) + i\Psi(z) = -Uz + f(z),$$

where U(=1) means the uniform flow in the negative x-direction, $f(z)=\phi(z)+i\psi(z)$ the disturbed complex potential and $z=x+iy$ (see Figure 1, disregard the downstream point doublets at the moment). Let the elevation of water surface be $\eta(x)$. The kinematic condition of the free-surface is written as the following after linearized:

$$\psi(x,0) = \eta(x).$$

Here, we assume that the value of the stream function, Ψ, is zero on the free surface befor linearized. The linearized dynamical condition of the free-surface is

$$\phi_x(x,0) - \kappa\eta(x) = 0,$$

where $\kappa=g/U^2$. Elimination of η between the above two conditions gives the linearized free surface condition as [Wehausen-Laiton,15]:

$$\phi_x(x,0) - \kappa\phi(x,0) = 0, \quad \text{on } F_A, F_F. \qquad \cdots(1)$$

The boundary condition on the body surface is written as:

$$\phi_n = \phi_n - \frac{\partial x}{\partial n} = 0, \quad \text{on } H, \qquad \cdots(2\text{-}1)$$

where the subscript, n, denotes the derivative in normal direction, alternatively,

$$\Psi = \psi - y = \Psi_H(\text{const.}), \quad \text{on } H. \qquad \cdots(2\text{-}2)$$

The complex potential of the Neumann-Kelvin solution can be represented as follows:

$$f(z)=\int_{H+F_A+F_F+\Sigma} (\phi_n(\zeta)G(z;\zeta)-\phi(\zeta)G_n(z;\zeta))ds, \qquad \cdots(3\text{-}1)$$

or, in the alternative form,

$$f(z)=i\int_{H+F_A+F_F+\Sigma} (\phi_n(\zeta)G(z;\zeta)-\phi(\zeta)G_n(z;\zeta))ds, \qquad \cdots(3\text{-}2)$$

where

$$G(z;\zeta)=\frac{1}{2\pi}\ln(z-\zeta).$$

The contribution from the external surface, Σ, will vanish as it become infinitely far from the body. The kernel function, $G(z;\zeta)$, in the representation (3-1) can be replaced by the complex potential of wave source, $W_Q(z;\zeta)$, as defined in Appendix A. Furthermore, partial integrations of the integral on F, using the relations in Appendix A, gives the other representation of f(z) [6]:

$$f(z)=\int_H\{\phi_n(\zeta)W_Q(z;\zeta)-\phi W_{Qn}\}ds - \frac{1}{\kappa i}\phi_\zeta W_Q-\phi W_{Q\zeta}\Big]_{P_A}^{P_F}, \qquad \cdots(4\text{-}1)$$

where P_F, P_A are the end points of the body. The second term corresponds to the so-called line integral term in the three-dimension Neumann-Kelvin solution. The expression (3-2) can be rewritten similarly oy the wave vortex potential, $W_\Gamma(z;\zeta)$, as defined in Appendix A:

$$f(z)=\int_H\{\psi(\zeta)W_{\Gamma n}(\zeta;z)-\psi_n W_\Gamma\}ds. \qquad \cdots(4\text{-}2)$$

The integral on the free surface F_A, F_P vanishes by itself and the line integral term disappear.

If we assume the Neumann-Kelvin solution defined inside the body then we obtain from eq.(4-1,2) the following representations expressed by surface sources, normar doublets, vortices and tangential doublets:

$$f(z)=\int_H\sigma(\zeta)W_Q(z;\zeta)ds-\frac{1}{\kappa}(\sigma_F W_{QF}+\sigma_A W_{QA}), \qquad \cdots(5\text{-}1)$$

$$f(z)=-\int_H\mu W_{Qn}ds+\frac{1}{\kappa i}[\mu W_{Q\zeta}]_{P_A}^{P_F}, \qquad \cdots(5\text{-}2)$$

$$f(z)=-\int_H\gamma W_\Gamma ds, \qquad \cdots(5\text{-}3)$$

$$f(z)=\int_H\gamma W_{\Gamma n}ds, \qquad \cdots(5\text{-}4)$$

where subscripts F, A mean the values at the points P_F, P_A respectively.

[2-2] Eigen Solution and Zero-Vertical Flux Flow

In the last section we assume implicitly that the velocity potential and the stream function are continuous even at the corners, P_F, P_A. However the continuity of the velocity at the corners has not been postulated nor used. Ursell [6] proved that when the velocity is, too, assumed to be continuous at the corners, there is a unique solution which is called the eigen singular solution by him. Hence any form of expression for the Neumann-Kelvin solution is to give the same solution subject to the above assumption.

When we consider the present central intersection, that is, no continuity requirement of the velocity at the corners, [illegible] the body contour intersects the free surface (y=0) at right angle. If not so, we must deal with the more complicated flow model. When the velocities are assumed not to be continuous at the corners, the Green's type of expression (4-1) can be written as follows:

$$f(z)=\int_H\{\phi_n(\zeta)W_Q(z;\zeta)-\phi W_{Qn}\}ds - \frac{1}{\kappa}[\phi_{\zeta H}W_Q-\phi W_{Q\zeta}]_P^{P_A}-\frac{1}{\kappa}[\Delta\phi_\zeta W_Q]_{P_F}^{P_A}, \qquad \cdots(6)$$

where $\Delta\phi_\zeta=\phi_{\zeta F}-\phi_{\zeta H}$, and $\phi_{\zeta P}$, $\phi_{\zeta H}$ means the x-velocities at the corners on the free surface and on the body surface, respectively. By using the free surface condition (1) at the corners, the body surface conditions (2-1,2) and the right angle intersection, we can obtain the following relations [Suzuki,14]:

$$\Delta\phi_\zeta(P_A)=\Delta\phi_\zeta(P_F), \qquad \cdots(7)$$

$$\Psi_H=\frac{1}{\kappa}(1+\Delta\phi_\zeta). \qquad \cdots(8)$$

That is, the x-velocity difference at the each corner must coincide with each other and the value of the stream function on the body surface is prescribed in terms of the difference.

There is a least singular solution, $f_0(z)$ when $\Delta\phi_\zeta=0$ as proved by Ursell. Let the difference, $f(z)-f_0(z)$, be $C_P f_h(z)$. Then we get:

$$f(z)=f_0(z)+C_P f_h(z), \qquad \cdots(9)$$

where

$$C_P=-2\Delta\phi_\zeta. \qquad \cdots(10)$$

Both f(z) and $f_0(z)$ satisfy the body surface condition, i.e.,

$$\frac{\partial\phi}{\partial n}=\frac{\partial\phi_0}{\partial n}=\frac{\partial x}{\partial n}, \quad \text{on H}, \qquad \cdots(11)$$

or, from eq.(8),

$$\left.\begin{aligned}\psi-y&=\frac{1}{\kappa}(1+\Delta\phi_\zeta) \quad (=\Psi_H),\\ \psi_0-y&=\frac{1}{\kappa} \quad (=\Psi_{H0}),\end{aligned}\right\} \text{on H} \qquad \cdots(12)$$

where $f(z)=\phi(z)+i\psi(z)$, $f_0(z)=\phi_0(z)+i\psi_0(z)$. Hence $f_h(z)$ must satisfy the homogeneous condition on the body surface:

$$\frac{\partial\phi_h}{\partial n}=0, \quad \text{on H}, \qquad \cdots(13)$$

and it also must satisfy:

$$\psi_h=-\frac{1}{2\kappa}, \qquad \cdots(14)$$

where $f_h(z)=\phi_h(z)+i\psi_h(z)$. It is clear that $f_h(z)$ has unit x-velocity difference

at the each corner, as shown by Eggers [4,15], Ursell [16], the y-velocity diverges logarithmically at the corners. So, we call $f_h(z)$ singular eigen solution since it has no effect on the normal velocities on the body surface. Thus, when the velocities of the Neumann-Kelvin solution is not assumed to be continuous at the corners, the solution can be written in the sum of the least singular solution $f_0(z)$ and the singular eigen solution $C_P f_h(z)$. The coefficient of the singular eigen solution, C_P, can be given arbitrarily. Therefore, the Neumann-Kelvin problem can be said to have infinitely many solution. The additional condition to determine the solution (9) uniquely is to give the value of C_P, or $\Delta\phi_F$, alternatvely, the value of the stream function on the body surface, Ψ_H.

Although the additional condition is to be given so that the solution becomes a good or appropriate approximation of the full exact solution, it is difficult at the present stage. In the free surface flow problem we are concerned mainly with the forces acting on the body, say, wave resistance, sinkage force, which are considered as related to the macroscopic quantities, say, mass, mometum. So, here we take notice of the flow flux out of the free surface. We have assumed that the value of the stream function including a uniform flow vanishes on the free surface infinitely upstream. Thence, the value of the stream function on the body surface, Ψ_H, means the flow flux out of the free surface ($y=0$) in front of the body. As for the least singular solution, the flow flux is $1/\kappa$ and the wave elevations at the corners $\kappa\eta$ is 1. When $C_P=2$ or $\Delta\phi_F=-1$, the flow flux vanishes. So we call the solution zero-vertical flux flow and the solution is considered to show the approximate flow appropriate in the above mentioned sense.

It is only pointed out here that the Neumann-Kelvin solution (9) can be deduced by the other procedure, the perturbation process [Suzuki,16]. In the process the coefficient C_P turns out the value at the each corner of the nonhomogeneous pressure term in the free surface condition of the second order. Thence the solution (9) can be also considered as the linear approximation including a part of the higher order solutions.

[2-3] Some Numerical Results

By using the numerical method to be mentioned in the next chapter, some calculations are performed for the flow past a half-immersed circular cylinder (the radius=a). The streamlines of the least singular solution are shown in Figuer 2. It shows that a quantity of water flux through the upstream free surface and that it flows into through the downstream free surface. The strong vortex-like flow around the circle is also shown. We could not accept such a flow pattern. The streamlines of the singular eigen solution are shown in Figure 3, the wave heights in Figue 4 and the value of the velocity potential on the circle in Figure 5. The last two ones are obtained by a boundary element method to be mentioned in section 3-3. The zero-vertical flux flow is shown in Figure 6. It appears to be rational rather than the least singular solution.

3. Numerical Method

[3-1] Integral Equation Method

We applied three numerical methods. The first one is the integral equation method of which unknowns are the wave sources. The sources are linearly distributed on the line segments which compose the contour, H_1, in Figure 1, submerged inside the body, the submergence (ratio of the radii) being SM. The calculation technique is similar to Webster 's [17], though the present case is two-dimensional and the wave sources are used instead of the Rankine sources. It has same advantages for the free surface flow as pointed by himself compared to Hess-Smith method. The complex potential is written in the following form from eq.(5-1, 6) and the analytic continuation for the regular part:

$$f(z)=\int_{H_1}\sigma(\zeta)W_Q(z;\zeta)ds-\frac{1}{\kappa}(\sigma_{F_1}W_{QF_1}+\sigma_{A_1}W_{QA_1})$$

$$+C_P\frac{1}{\kappa}(W_{QF}-W_{QA}), \qquad \cdots(15)$$

where the subscripts F_1, A_1 means the values at the corner points P_{F_1}, P_{A_1} on H_1. In eq.(14). C_P must be given previously by the relation (10). The boundary integral equation of zero-normal velocity is:

$$\mathrm{Re}\{\frac{\partial}{\partial n}[-z+f(z)]\}=0, \quad \text{on } H. \qquad \cdots(16)$$

The alternative Dirichlet condition for the stream function is:

$$I_m\{-z+f(z)\}=\Psi_H, \quad \text{on } H, \qquad \cdots(17)$$

where Ψ_H is given by the additional condition:

$$\Psi_H=\frac{1}{\kappa}(1-\frac{1}{2}C_P). \qquad \cdots(18)$$

The discretized formulae are omitted (refer to [16] in Japanese version). An example of the source distribution for the various cases is shown in Figure 9.

[3-2] Multi-Pole Expansion Method

This method was first presented by

Ursell [18] in the wave-body problem and it was developed by him [6] to the Neumann-Kelvin problem for the two-dimensional semi-submerged circle. The same methodwas presented by the auther [14,16] in a little different form:

$$f(z)=\sigma_1 W_m(z;0)+\sigma_2 W_\mu(z;0)+\sum_{n=1}^{N}\sigma_{n+2}h_n(z)$$

$$+\frac{1}{\kappa}C_P(W_{QF}-W_{QA}), \qquad \cdots(19)$$

where $W_m(z;0)$, $W_\mu(z;0)$ are the wave-doublets in direction of x, y, respectively, located at the origin, and $h_n(z)$ is the so-called wave-free potential:

$$h_n(z)=\frac{1}{z^n}(1-i\frac{n}{\kappa z}), \quad (n\geq 1).$$

The strength, σ_i, of the i-th term is determined by the boundary condition (2-1) or (2-2). The streamlines and the forces were mainly calculated by these two methods. The results coincides with each other, but multi-pole expansion method has an advantage in saving computing time ,though only for the circular cylinder. The strengths, σ_1, σ_2 of the wavy terms are shown in Figure 10.

[3-3] Boundary Element Method

In this method the representation (3-2) is directly used. To avoid a truncation trouble at downstream, or to cancel the downstream propagating waves, artificial doublets in two directions are located at appropriate downstream point (see Figure 1). The stream function is written as follows:

$$\phi(z)=\phi_F(z)+\phi_H(z)+A\phi_A(z)+B\phi_B(z). \quad \cdots(20)$$

Here,

$$\phi_F(z)=\int_{F_A+F_F}(\phi_n(\zeta)L(z-\zeta)-\phi(\zeta)L_n(z-\zeta))ds, \qquad \cdots(21)$$

$$\phi_H(z)=\int_H(\phi_n(\zeta)L(z-\zeta)-\phi(\zeta)L_n(z-\zeta))ds, \qquad \cdots(22)$$

$$\phi_S(z)+i\psi_A(z)=-\frac{1}{2\pi}\frac{1}{z-z_D}, \qquad \cdots(23)$$

where ϕ_A, ψ_B are the stream function for doublets in direction of x, y, and L is the real part of the complex Rankine source potential:

$$G(z-\zeta)=L(z-\zeta)+iT(z-\zeta)$$

$$=\frac{1}{2\pi}\log(z-\zeta).$$

The RHS of eq.(21) is transformed into the following form by using the free-surface condition, $\psi_n=\kappa\phi$:

$$\phi_F(z)=-\int_{F_A+F_F}\phi(\zeta)(\kappa L(\xi-z)-Ln(\xi-z))d\xi, \qquad \cdots(21\text{-}1)$$

Here, it is to be noted that the second term in the above integrand degenerates into the residue, $1/2\,\phi(z)$, when z is on F_A or F_F. Divide F_A, F_F into small segments and assume that ϕ is constant, $S_j=\kappa\phi_j$, in each segment, ΔF_j. By using $L_\eta=-T_\xi$ and integrating by part we obtain:

$$\phi_F(z_1)=-\sum_j S_j[\frac{1}{\kappa}T(\xi-z_1)+L^*(\xi-z_1)]_{\Delta F_j},$$

$$\text{for } z_1 \text{ on } H, \cdots(21\text{-}2)$$

where z_1 is the middle points of the i-th segment of H and

$$G^*(\zeta-z)=L^*(\zeta-z)+iT^*(\zeta-z)$$

$$=\frac{1}{2\pi}(\zeta-z)\{\log(\zeta-z)-1\}.$$

When $Z_1$is on F_A or F_F, eq.(21-2) becomes:

$$\phi_F(x_1)=\frac{1}{2\kappa}Si-\sum_j S_j[L^*(\xi-x_1)]_{\Delta F_j}. \quad \cdots(21\text{-}3)$$

Next, consider the uniform flow inside the body and we get for z outside the body:

$$0=\int_{H+F_0}(y_nL(z;\zeta)-yL_n)ds,$$

where F_0 means the free surface inside the body. Subtraction of the above equation from eq.(22) gives:

$$\phi_H(z)=\int_H(\Psi_nL-\Psi L_n)ds-\int_{F_\phi}Lds,$$

where $\Psi(z)=-y+\psi(z)$. By using $\Psi_n=\phi_s$, $L_n=T_s$, partial integration gives:

$$\phi_H(z)=-[\phi L]_{F_A}^{F_F}-\int_H\phi L_s ds-\Psi_H[T]_{F_A}^{F_F}$$

$$-\int_{F_\zeta}Lds. \qquad \cdots(22\text{-}1)$$

Here, the third term vanishes when z is on F_A or F_F and the residue, $1/2\,\Psi_H$, is to be added to the RHS when z is on H. The velocity potential ϕ is indefinite by a constant, the artificial condition is required, e.g.:

$$\int_H\phi ds=0. \qquad \cdots(24)$$

After discretizing eq.(22-1), we have:

$$\phi_H(z)=\sum_j S_j[L(\zeta-z)]_{\Delta HJ}^{*}-\Psi_H[T(\xi-z)]_{F_A}^{F_F}$$

$$-[L^*(\xi-z)]_{F_A}^{F_F}, \qquad \cdots(22\text{-}2)$$

where S_j means $\phi(z_j)$ and the subscript, *, of the first term denotes that it

does not include the values at the corners. The condition(24) becomes:

$$\sum_j S_j \Delta H_j = 0. \qquad \cdots(24\text{-}1)$$

Substitution of eq.(21-3),(22-2) into eq.(20) gives the simultaneous equations for the unknowns S_j, A, B and the given Ψ_H. When z_1 is on H:

$$\sum_j S_j \{\frac{1}{\kappa}[T(z_1-\zeta)]^*_{\Delta F_j} + [L^*(z_1-\zeta)]_{\Delta F_j}\}$$

$$-\sum_j S_j [L(z_1-\zeta)]^*_{\Delta H_j} - A\phi_A(z_1) - B\phi_B(z_1)$$

$$= -\Psi_H \{\frac{1}{2} + [T(z_1-\zeta)]^{F_F}_{F_A}\} - [L^*(z_1-\zeta)]^{F_F}_{F_A} - y_1. \qquad \cdots(25\text{-}1)$$

When z_1 is on F_A or F_F.

$$\frac{1}{2\kappa} S_1 + \sum_j S_j [L^*(z_1-\zeta)]_{\Delta F_j} - \sum_j S_j [L(z_1-\zeta)]^*_{\Delta H_j}$$

$$-A\phi_A(\xi_1) - B\phi_B(\xi_1) = -[L^*(z_1-\zeta)]^{F_F}_{F_A}. \qquad \cdots(25\text{-}2)$$

As for the singular eigen solution, the second and third term in the RHS of eq.(25-1) must be omitted.

The simultaneous equations (25) have two eigen vectors corresponding to the two doublets. The two indefinite vectors are to be determined by the so-called radiation condition:

$$S_j = \kappa n_j = 0, \qquad \cdots(26)$$

for two segments, ΔF_j, in far field. However, to get astable solution it is needed to impose the condition over a quater wave-length by means of least squares (see Figure 4). The well-known method SVD (singular values decomposition) [19] was very powerful subroutine for obtaining the eigen vectors and also the least squares solutions.

The present BEM is easy to be formulated and to be numerically solved and it turns out to have the high accuracy compared with the similar method proposed earlier (see Appendix B for the free-surface flow past a point vortex).

There is another advantage in the present method, i.e., the forces acting on the body can be calculated by the extented Lagally forces acting on the doublets instead of the pressure integration over the body surface. Only the formulae shall be shown. The complex force $C_P = C_X - iC_Y$ acting on the body can be written by the sum of the doublets Lagally force, C_D, and the dynamical Archemidean force, [Bessho,3,5]:

$$\left.\begin{aligned} C_P &= C_D + C_F, \\ C_D &= 2C\frac{dW_{RD}}{dz}(z_D), \\ C_F &= 2i\kappa \int_{F_A+F_F} \eta(\xi)\,d\xi, \end{aligned}\right\} \qquad \cdots(27)$$

where $W_{RD}(z)$ is the complex potential excluding the doublets potential [Milne-Thomson,20] and $C = A + iB$. As for only the wave resistance we can more easily calculate it by the strength of the doublets:

$$C_W = 2\kappa^3 (A^2+B^2) e^{2\kappa Y_D}, \qquad \cdots(28)$$

where $z_D = x_D + iy_D$.

4. Wave Resistance for a Body Free to Sink

Consider the flow for the value of Cp in eq.(9) which deviates slightly from 2:

$$C_p = 2 + 2\kappa s, \qquad \cdots(29)$$

or from eq.(8),(10)

$$\Psi_H = -s. \qquad \cdots(30)$$

When s is assumed to be small, the value of the stream function on the imaginary surface below the body surface by s is given as the following:

$$\Psi(x, y-s) = \Psi(x,y) - s\frac{\partial \Psi}{\partial y}(x,y)$$

$$\doteqdot \Psi_H + s$$

$$= 0 \qquad \cdots(31)$$

where $z = x + iy$ is on the body surface and the perturbed velocity ϕ_y is assumed to be of higher order than uniform flow. It turns out that the flow for eq.(29) represents approximately the zero-vertical flux flow past the surface sunken by s from the original body surface. To confirm it the streamlines of the above approximate flow and the zero-vertical flux flow past a really submerged circular cylinder by s are compared in Figure 11.

The wave resistance, C_W, and the sinkage force, $-C_Y$, are drawn via sinkage by the above approximation inFig.12. The curves can be drawn only by the three values of them since the forces are the quadratics of Cp or s:

$$\left.\begin{aligned} C_W &= Y_2 s^2 + Y_1 s + Y_0, \\ C_Y &= Y_2 s^2 + Y_1 s + Y_0. \end{aligned}\right\} \qquad \cdots(31)$$

In the figure the forces calculated for the really sunken circular cylinder are plotted too (exact linear). They show good agreement, in particular, for the sinkage force.

The equilibrium condition for the body free to sink is:

$$C_Y + C_S(\Delta) = 0, \qquad \cdots(32)$$

where $C_s(\Delta)$ is the change of the buoyancy force for the dipping s of the body of which displacement is Δ and $C_s(\Delta_0) = \frac{1}{2}\kappa s$, Δ_0 is $\rho g S_0$, S_0 is the sectional area below the still water surface. Figure 12 telles that, if $\Delta = \Delta_0$, the equilibrium state does not occur at $\kappa a = 0.4$, and the sinkage force is larger that the hydrostatic force however deeply the circle sinks. When the displacement is assumed to be negative ($-2\Delta_0$), eq. (22) has two roots as shown in Figure 12. The smaller one (black square) shows the stable equilibrium state.

Thus we can know the dipping and the wave resistance for the circle free to sink though the negative displacement is not realistic and the circle is pressed up over the atatical water surface.

The sinkage curves for the circular cylinder of various displacement are in Figur 13 and the wave resistance curves for the cylinder free to sink in Figure 14.

5. Wave-Free Solution and Double-Model Approximations

As shown in Figure 12 the Neumann-Kelvin problem has a wave free solution of which wave resistance is zero for an approximate sinkage or coeficient, Cp, of the singular solution. It can be proved generally for longituginally symmetric body [16]. As an example the streamlines of the wave-free soltion is shown in Figure 15. The surface sources obtained by the method mentioned in section3-1 are compared with the double model solution in Figure 16.

The sources of the wave-free solution are a-symmetric longitudinally and they are close to the double-model solution. In other words the double-model solutions may be good approximation of the wave-free Neumann-Kelvin solutions and they become wave-free for some Froude numbers as shown in Figure 17. Furthermore, as pointed out by Kotic Morgan [21], the double-model approximations have infinitely many values of wave resistance related to the line-integral terms. From the above two reasons a double-model approximation might be selected by the consideration on the mass conservation, say, shelering effect [22], or on the condition of being free to sink.

6. Conclusions and Acknowledgement

The main results are the followings:

1) The singular eigen solution exsists in the two-dimensional Neumann-Kelvin problem.

2) The zero-vertical flux flow is rational rather than the least-singilar solution from the view point of the mass conservation.

3) The present boundary element method is suprior to the finite-difference method in the computing time and the accuracy.

4) The singular eigen solution represents approximately the flow past a slightly sunken body and its strength is proportional to the sinkage.

5) The wave resistance for a body free to sink and at any displacement can be approximately calculated by using the above relation.

6) Semi-submerged circular cylinders are unstable to sink unless it has a negative displacement.

7) The double-model approximations are close to the wave-free solution.

The auther wishes to express his deep appreciation to Prof. M. Bessho for his guidance and patient encouragement. He would like to thank Prof. H. Kagitani and prof. K. Eggers for the discussion on an earier version of this paper.

References

1) R. Brard, JSR 16,1972.
2) M. Bessho, T. Mizino, Sci. Eng. Rep. Defense Academy 1-1, 1963.
3) M. Bessho, International Seminar on Wave Resistance, Tokyo, '76.
4) K. Eggers, Disc. to Bessho, ISWR, Tokyo, 1976.
5) M. Bessho, T. West SNA 51, 1976.
6) F.Ursell, 13th ONR Symp.,1980.
7) K. Suzuki, Korkshop on Wave Resistance Computations, Washington, 1979.
8) K. Suzuki, Informal Continued Workshop on Wave Resistance Computations & Depth Study Meeting, Izu, 1980.
9) C. W. Dawson, 2nd International Conference on Numerical Ship Hydrodynamics, 1977.
10) J. H. Hess, 2nd ICNSH., 1977
11) R. W. Yeung, Y. C. Bouger, 2nd ICNSH, 1977
12) H. J. Haussling, R. M. Coleman, 2nd ICNSH, 1977.
13) R. K. Cnan, 1st ICNSH, 1975.
14) K. Suzuki, Disc. to Ursell, 13tn ONR Symp., 1980.
15) K. Eggers, Inf. Cont. Workshop W.R.C. & Depth Study Meeting, Izu, 1980.
16) K. Suzuki, "On the Two-Dimensional Neumann-Kelvin Problem", unpublished, 1978.
17) W. C. Webster, JSR 19, 1975.
18) F. Ursell, Q.J.Mech.App.Math. 2, 1949
19) G. E. Forsythe, "Computer Methods for Mathematical Computations", Prentice-Hall, 1977.

20) L. M. Milne-Thomson, "Theoretical Hydrodynamics", MacMillan, 1962.
21) J. Kotic, R. Morgan, JSR 13,1969.
22) T. Inui et al, JSNA Japan 124, 1969.

Appendix A. Wave Kernel Functions and Their Relations.

The complex potential of a wave source located at ζ is written as the followings:

$$W_Q(z;\zeta)=\log(z-\zeta)+\log(z-\bar{\zeta})+2S_\kappa(z-\bar{\zeta}),$$

where

$$S_\kappa(z)=e^{-i\kappa z}E_1(-i\kappa z)+\begin{cases}0 & \text{for } \mathrm{Re}(z)\geq 0,\\ 2\pi i e^{-i\kappa z} & \text{for } \mathrm{Re}(z)<0,\end{cases}$$

$$E_1(z)=\int_z^\infty \frac{e^{-u}}{u}\,du \qquad \text{for } |\arg(z)|<\pi.$$

For a wave vortex we have:

$$W_\Gamma(z;\zeta)=-i[\log(z-\zeta)-\log(z-\bar{\zeta})-2S_\kappa(z-\zeta)].$$

For a wave doublet in x-direction,

$$W_m(z;\zeta)=-\frac{1}{z-\zeta}+\frac{1}{z-\bar{\zeta}}+2i\kappa S(z-\bar{\zeta}),$$

in y-direction,

$$W_\mu(z;\zeta)=\frac{i}{z-\zeta}+\frac{i}{z-\bar{\zeta}}-2\kappa S_\kappa(z-\bar{\zeta}).$$

They have the following relations:

$$W_m=\frac{d}{dz}W_Q \qquad ; \qquad W_\mu=-\frac{d}{dz}W_\Gamma,$$

and

$$\frac{dW_Q}{d\zeta}=-\frac{dW_Q}{dz}=i\frac{dW_\Gamma}{dz}=-i\frac{dW_\Gamma}{d\zeta}.$$

As for the free- surface condition they satisfy the following relations:

$$\left.\begin{aligned} W_{Q\xi\xi}+\kappa W_{Q\eta}&=0,\\ W_{m\xi\xi}+\kappa W_{m\eta}&=0,\\ W_{\Gamma\eta}-\kappa W_\Gamma&=0,\\ W_{\mu\eta}-\kappa W_\mu&=0,\end{aligned}\right\} \quad \text{for } Z=0.$$

Appendix B. Free-Surface Flow past a Vortex.

The linearized free-surface flow past a vortex of the vorticity, Γ, submerged by h is solved by the BEM mentioned in section 3-3. The boundary integral equation is written in the following form:

$$\frac{1}{2}\phi(x)+\kappa\int_\mu \psi(\xi)L(x-\xi)d\xi-A\phi_A(x)-B\phi_B(x)$$
$$=\mathrm{Im}\frac{\Gamma}{2\pi i}\log(x+ih), \qquad \ldots(B\text{-}1)$$

where the stream function, $\psi(x)$ on the free surface, F, and the strength, A, B, of the artificial doublets are the unknowns. The wave heights are shown in Figure B-1. In spite of the rough spacing the agreement with the exact solutions are very satisfactory. The obtained forces acting on the vortex are compared in Table B-1 with the exact values and the values obtained by the other BEM in which the derivative is calculated by the five-point central finite-difference method. It is clear that the present method is suprior to the finite-difference method in saving computer time and memories.

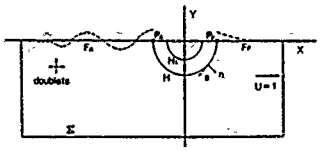


Fig.1 Two-dimensional Neumann-Kelvin problem.

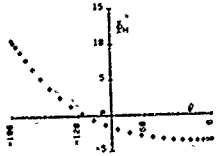


Fig.5 Velocity potential of singular eigen solution on a circular cylinder ($\kappa a=0.4, C_p=1.0$).

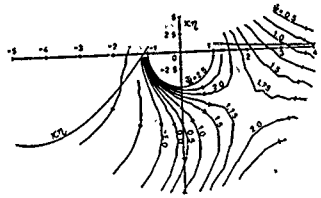


Fig.2 Streamlines of least singular solution ($\kappa a=0.4, C_p=0.0$).

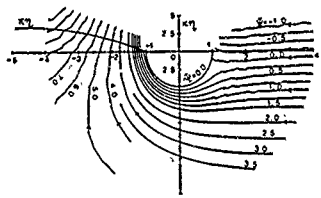


Fig.6 Streamlines of zero-vertical flux flow ($\kappa a=0.4, C_p=2.0$).

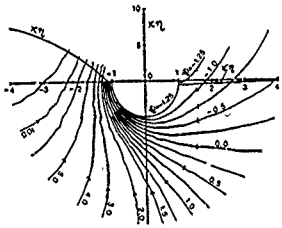


Fig.3 Streamlines of singular eigen solution ($\kappa a=0.4, C_p=1.0$).

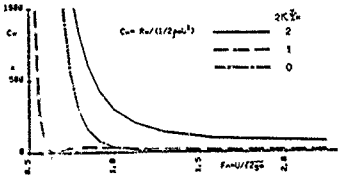


Fig.7 Wave resistance for various values of ∇_H.

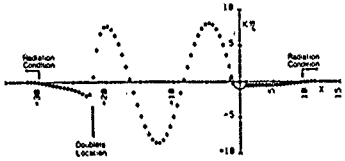


Fig. Wave heights of singular eigen solution ($\kappa a=0.4, C_p=1.0$).

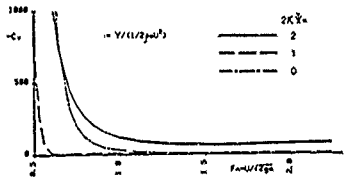


Fig.8 Sinkage force for various values of ∇_H.

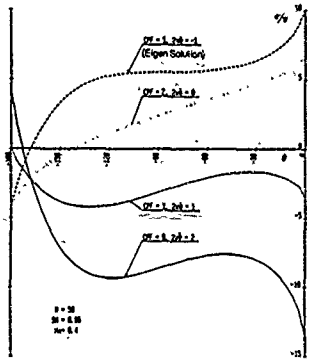


Fig.9 Surface source distributions (κa=0.4).

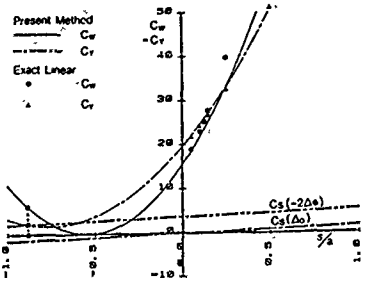


Fig.12 Wave resistance and sinkage force via sinkage and equilibrium condition.

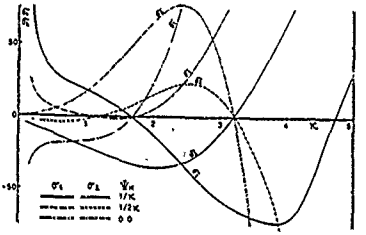


Fig.10 Strength of wave terms.

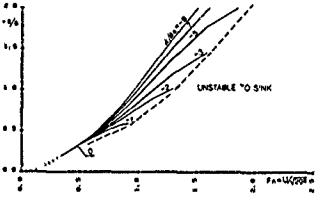


Fig.13 Sinkage curves for various displacement conditions.

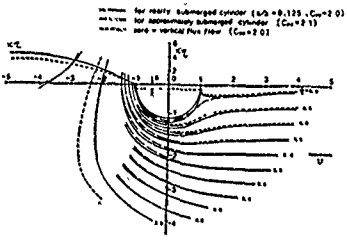


Fig.11 Comparison of streamlines.

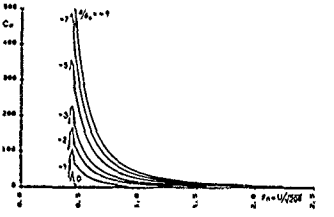


Fig.14 Wave resistance for a circular cylinder free to sink.

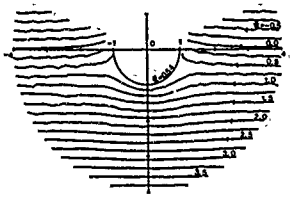


Fig.15 Streamlines of wave free solution ($\kappa a=0.4, c_p=1.568$).

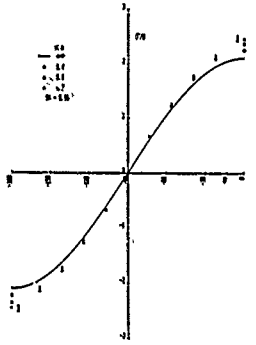


Fig.16 Comparison of surface sources between wave free solutions and double-model solution.

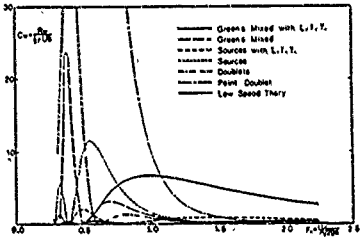


Fig.17 Comparison of wave resistance among various double-model approximations.

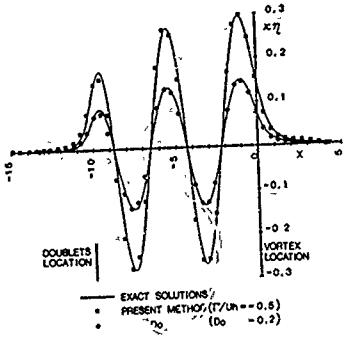


Fig.B-1 Wave heights for a submerged vortex ($\kappa h=1.45$)

		Linear Theory		Present Method		Finite Difference Method
Item \ F/√h		20.5	20.2	20.5	20.2	20.2
Spacing per a wave length				10.1	10.1	40.6
Wave Resistance × 10³	doublets wave resistance	3.99	0.61	4.21	0.67	0.74
	doublets Legally force			4.05	0.65	0.67
	vortex Legally force			4.05	0.65	0.71
Lift	vortex Legally force			1.08 +0.92	0.11 +0.39	0.11 +0.39
	dynamical Archimedian force + doublets Legally force			1.01 +1.01	0.10 +0.40	0.15 +0.45
	infinite region	21.6	20.10			
	right wall surface	1.04 +0.96	0.11 +0.39			

Table B-1. Forces acting on a submerged vortex ($\kappa h=1.45$).

DISCUSSIONS
of the paper
by K. Suzuki

NUMERICAL STUDIES OF THE NEUMANN-KELVIN PROBLEM FOR A TWO-DIMENSIONAL SEMI-SUBMERGED BODY

Discussion
by G. L. Hearn

I can immerdiately appreciate the advantage of calculating directly the forces acting on the body employing Lagally forces rather than numerically integrating the pressure over the wetted surface. Furthermore given that the additional downstream doublets permits fulfillment of the appropriate radiation condition then numerically your modified BEM approach provides a welcomed panacea. Certainly, considerable effort is saved through deployment of Rankine sources. However, it is not clear how the selected position of the doublets affects the solution in general and in terms of the ψ_A and ψ_B contributions. Could you please elaborate on how the doublets are positioned and explain why the upstream downstream constants associated the linearised dynamic free surface condition are zeroised in the text. The author is thanked for an interesting comparison of the different numerical techniques.

Discussion
by M. Lenoir

Professor Suzuki's approach appears to be extremely interesting, I should like to make certain remarks concerning the linearized free surface condition.

- The condition $\phi_x = K\bar{y}$ used by the author is not the one that can be most generally constructed eliminating the height of the free surface between the kinematic and dynamic equations. In fact, we obtain :

$$\phi_x = K\bar{y} + C_1 \quad \text{upstream} \qquad \phi_x = K\bar{y} + C_2 \quad \text{downstream}$$

- If we allow for the fact that the solution is defined except for an arbitrary additive constant, then it may be decided that $C_1 = 0$.

- But then, the problem for the stream function depends on two arbitrary constants, one on the body, the other on the free surface downstream.

Moreover, if two such arbitrary constants are applied, together with an associated stream function, the corresponding potential can be reconstructed, and it meets all the conditions that can be expected, in particular it has the same farfield behaviour as the well known Green function.

Can you specify the reasons why you have imposed $C_2 = 0$, i.e. a homogeneous free surface condition both upstream and downstream ?

Discussion
by G. Fernandez

Mr. Le Noir has indicated that his analysis of the problem showed that the complete determination of the stream function of the problem required knowledge of two constants. I should like to say this opinion appears to be logical. The equations of the Neumann-Kelvin problem are obtained by linearization so that some informations are lost. Now I have conducted a study based on the method of matched asymptotic expansions, in the case of a semi-submerged body, with a Froude number (based on the draft) of order 1. In this case, it can be shown that the indetermination of the solution of the Neumann-Kelvin problem can be removed by examining the local non-linear behaviour of the flow in the vicinity of the ship.

In the two-dimensional case, the local study concerns two points : the bow and stern ; we therefore really require two constants. One of them is linked to the flow of fluid lost in the jet developing in front of the body when the Froude number is high enough. The second is linked to the behaviour of the fluid aft. It can be used to impose the regularity of the solution at this point.

It therefore appears to be difficult to obtain a global condition involving a relation between the forward and afterward flows as your paper suggests.

Thus my question complements Mr. Lenoir's : can you explain why in your specific case a degree of freedom can be suppressed, leaving only an arbitrary constant ?

Author's reply to G. Fernandez, M. Lenoir and G.L. Hearn

The difference between our solutions is due to the difference of the flow models dealt with us. At first it must be noted that in the present paper any momentum (mass) flux flow (ex. splash-like phenomenon as pointed out by G. Fernandez) is not assumed. So, we started from the exact kinematic condition on the free surface which can be written in terms of stream

function as:

$$\Psi = \phi - y = \text{const.} \quad \text{on } y = \eta(x), \quad \ldots. \quad (S\text{-}1)$$

where η denotes the elevation of the free surface. The constant value of RHS on the upperstream free surface coincides with the value on the downstream free surface. That is because the upperstream and downstream free surfaces are the same streamline. When linearizing eq. (S-1) we obtain the following expression without loosing generality :

$$\phi = \eta \qquad \text{on } y = 0. \quad \ldots. \quad (S\text{-}2)$$

This condition corresponds to the condition, $C_1 = C_2$, of the discussers. On the above assumption there are still infinitely many solutions as mentioned in the paper. When we deal with the momentum flux flow ($C_1 \neq C_2$) the problem have solutions of more degree of freedom. The N-K solutions might be said to diverge in wide range, the simplest one is the least singular solution (Ursell), the wider one is for the case of momentum flux flow. The present paper deals with the middle case of problem. The author have tried to obtain numerically the solution for $C_1 \neq C_2$ by using the present methods but unfortunately the stable and significant solution could not be obtained. This fact might not tell the question against the existence of the moment flux solution. The author would like to hope that the discussers present numerical results for the momentum flux flow which must give us new and important suggestions for the complicated problem laid between the physical phenomena and the simplified theory.

As for the location of the artificially introduced doublets in BEM, we may select any position in principle only in order to delete the oscillatory waves far downstream in the linear theory. However, in order to make the doublets not affect the flow near the object, the doublets must be located two or three wave length downstream far from the object at the moderate Froude number. The effect can be easily estimated by the Rankine doublet properties. The depth of the doublets is also arbitrary. But it is desirable that the doublets are located at the depth of several times length of the free surface segments but not so deep, as the draft of the obstacle. This is only the technique related to the accuracy in the numerical calculations.

PARABOLIC APPROXIMATIONS FOR SHIP WAVES AND WAVE RESISTANCE

Jean-Marc Vanden-Broeck
Department of Mathematics
and
Joseph B. Keller
Department of Mathematics and Mechanical Engineering
Stanford University
Stanford, California 94305

Abstract

A new method, the parabolic approximation, is presented for calculating ship waves and ship wave resistance. In it Laplace's equation is replaced by a Schrödinger equation in which distance along the ship is the time-like coordinate. This equation can be solved numerically by marching from the bow to the stern.

We show analytically, for some typical cases, that the parabolic approximation yields results in good agreement with the solution of the exact linear problem, for small values of the Froude number. We find that the interaction term in the wave resistance R, which is the part of R that oscillates as the Froude number varies, is predicted exactly by the parabolic approximation, but the non-oscillatory part is not. In most cases the exact and parabolic results for this part differ by less than 13%.

1. Introduction

In the theory of ship waves, the flow about the ship and the wave motion must be determined simultaneously everywhere because the flow is governed by an elliptic partial differential equation. Consequently it is difficult to calculate them. But the waves travel only from bow to stern, and at low Froude number they are confined within 19.47° of this direction. Therefore it ought to be possible to calculate the waves by starting at the bow and marching toward the stern, in the direction in which the waves propagate, just as if this were the time-like direction and the governing equation were parabolic. In fact this is the case in the parabolic approximation (Keller 1979).

We shall present the parabolic approximation and use it to solve the flow problem both for a thin ship and for a pressure distribution on the free surface. Then we shall compare the results with the exact solutions of these problems. Both the exact and the parabolic solutions are expanded for low Froude number F, at which the parabolic approximation should be most accurate. The purpose of this analysis is to find out how accurate the parabolic approximation is in simple cases where the exact solution is known. This will help us estimate how accurate it is in cases where the exact solution is not known.

The problem is formulated in Section 2, the parabolic approximation is introduced in Section 3 and the solution for a thin ship is obtained in Section 5 and compared there with the exact result of Michell for a ship with sharp bow and stern. At low F, both wave resistance results consist of a bow term, a stern term and an interaction term. Remarkably, the interaction term, which oscillates as F varies, is precisely the same in the two cases. The other terms are similar in form, and numerically they are in good agreement, as is shown in Table 1. In Section 6 we compare the two results for ships with rounded bow and stern. This is a severe test, because the parabolic approximation should not be expected to be good in this case. Nevertheless it still yields results in fair agreement with those of the Michell theory, as is shown in Table 2. In Sections 7-9 we make similar comparisons for the flow past a steady pressure distribution on the free surface, which is analogous to the flow past a flat ship. Here also the agreement between the parabolic solution and the exact solution is quite good. Finally in Sections 10-13 various modifications of the parabolic approximation are discussed.

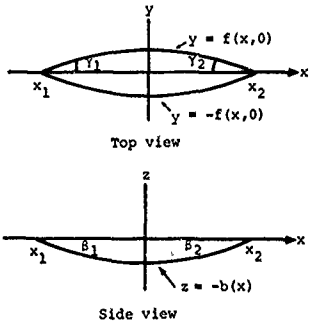


Figure 1. Top and side views of the ship. The top view is also used in Sections 7-9 to represent the domain in which $p^5(x,y)$ is different from zero.

2. Formulation

We seek the velocity potential $Ux + \phi(x,y,z)$ and the free surface $z = \eta(x,z)$ of an inviscid incompressible fluid flowing past a ship with surface B, and/or past a pressure distribution $p^S(x,y)$ on the free surface. (See Figure 1.) The fluid has density ρ and velocity U along the x-axis at infinity, the z-axis points upward, g is the acceleration of gravity, $k = gU^{-2}$ and p^S vanishes at infinity. With these definitions, the potential equation and the boundary conditions, linearized for ϕ and η small, are

$$\phi_{xx} + \phi_{yy} + \phi_{zz} = 0 , \quad z < 0 , \tag{2.1}$$

$$\frac{\partial\phi}{\partial n} = - U \frac{\partial x}{\partial n} \text{ on } B , \tag{2.2}$$

$$\phi_{xx} + k\phi_z = -p^S_x(x,y)/\rho U \text{ on } S , \tag{2.3}$$

$$\phi_z \to 0 , \quad \text{as } z \to -\infty , \tag{2.4}$$

$$\phi = o(x^{-1/2}) \text{ as } x \to -\infty . \tag{2.5}$$

Here S is the projection of the free surface on $z = 0$. When $p^S = 0$ these are the linearized equations for flow past a ship, while when the ship is absent, they describe the flow past the pressure distribution p^S.

The wave resistance R is

$$R = -\rho \int_{B+S} (U\phi_x + gz) n_x \, dS . \tag{2.6}$$

Here n_x is the x-component of the unit normal n pointing out of the fluid.

3. The Parabolic Approximation

Following Keller (1979) we write

$$\phi(x,y,z) = u(x,y,z)e^{ikx} . \tag{3.1}$$

Here, as usual, ϕ is the real part of the right side of (3.1) and we shall use the same convention in the rest of this paper. By substituting (3.1) into (2.1)-(2.5), we obtain an equivalent set of equations for u.

The parabolic approximation is obtained by dropping u_{xx} from these equations. We shall call the solution of the resulting problem u^p. This approximation is valid when u_{xx} is negligible compared to ku_x, i.e. when u is a slowly varying function of x. It is convenient to rewrite this problem in terms of $\phi^p = u^p e^{ikx}$. The resulting equations can be obtained from (2.1)-(2.5) by replacing ϕ_{xx} by $2ik\phi^p_x + k^2\phi^p$ in (2.1) and (2.3). In this way we obtain the following equations, from which we omit the superscript p:

$$2ik\phi_x + k^2\phi + \phi_{yy} + \phi_{zz} = 0 , \quad z < 0 , \tag{3.2}$$

$$\frac{\partial\phi}{\partial n} = - U \frac{\partial x}{\partial n} \text{ on } B , \tag{3.3}$$

$$2ik\phi_x + k^2\phi + k\phi_z = - \frac{p^S_x(x,y)}{\rho U} , \text{ on } S , \tag{3.4}$$

$$\phi_z \to 0 \text{ as } z \to -\infty , \tag{3.5}$$

$$\phi = 0 \text{ for } x \le x_1 . \tag{3.6}$$

Relation (3.6) is the equivalent for the parabolic approximation of the upstream condition (2.5). In it x_1 denotes the abscissa of the bow, or the upstream end of the pressure distribution. (See Figure 1.) Equation (3.2) is a Schrödinger equation, in which x plays the role of time. Thus the system (3.2)-(3.6) can be solved numerically by starting at $x = x_1$ with $\phi = 0$ and marching toward the stern.

4. Green's Function and Green's Theorem

To solve (3.2)-(3.6) we define the adjoint Green's function $G(x,y,z,x',y',z')$ by

$$-2ikG_x + k^2G + G_{yy} + G_{zz} = 8\pi\delta(x-x')\delta(y-y')\delta(z-z') , \quad z < 0 , \tag{4.1}$$

$$-2ikG_x + kG + G_z = 0 , \quad z = 0 , \tag{4.2}$$

$$G_z \to 0 \text{ as } z \to -\infty , \tag{4.3}$$

$$G = 0 \text{ for } x > x' . \tag{4.4}$$

In Appendix A, G is calculated and its asymptotic form for k large is found to be

$$G \sim -8k \int_0^{\pi/2} d\theta \, t(\theta) \sin[km(\theta)(x-x')] \cdot \cos[k\sec^2\theta \sin\theta (y-y')] e^{k(z+z')\sec^2\theta} d\theta , \quad \text{for } x < x' , \tag{4.5}$$

$$G = 0 , \quad \text{for } x > x' .$$

Here $t(\theta)$ and $m(\theta)$ are defined by

$$t(\theta) = \sec^3\theta , \tag{4.6}$$

$$m(\theta) = 1 + \frac{\tan^2\theta}{2} . \tag{4.7}$$

By using Green's theorem we can reformulate the problem (3.2)-(3.6) as the integro-differential equation (see Appendix B)

$$\phi(x,y,z) = \frac{1}{4\pi} \int_B (\phi G_{n^*} - G\phi_{n^*}) dS + \frac{i}{2\pi} \int_W G\phi \, dy' + \frac{1}{4\pi k\rho U} \int_S p^S_{x'} G|_{z'=0} \, dx'dy' . \tag{4.8}$$

Here W is the water line and n^* is the outward unit normal to the curve of intersection of B with a plane $x = \text{constant}$. When (x,y,z) is on B

or on S, the right side of (4.8) has to be multiplied by 2.

The equivalent of (4.8) for the exact problem (2.1)-(2.5) is [Wehausen (1973)]:

$$\phi(x,y,z) = \frac{1}{4\pi}\int_B (\phi\tilde{G}_n - \tilde{G}\phi_n)dS$$
$$- \frac{1}{4\pi k}\int_W (\tilde{G}\frac{\partial\phi}{\partial x'} - \phi\frac{\partial\tilde{G}}{\partial x'})dy'$$
$$+ \frac{1}{4\pi k\rho U}\int_S p^S_{x'}G|_{z'=0}\,dx'dy' \quad . \quad (4.9)$$

The Green's function $\tilde{G}$ has the asymptotic form (4.5) for k large with the functions t(θ) and m(θ) defined by

$$t(\theta) = \sec^2\theta \quad , \quad (4.10)$$

$$m(\theta) = \sec\theta \quad . \quad (4.11)$$

The asymptotic expressions for G and $\tilde{G}$ are amost identical, differing only in the definitions of m(θ) and t(θ). In both cases we have

$$t(\theta) = 1 + 0(\theta^2) \quad , \quad (4.12)$$

$$m(\theta) = 1 + \frac{\theta^2}{2} + 0(\theta^4) \quad . \quad (4.13)$$

The integral in (4.5) can be evaluated asymptotically for k large by replacing sin and cos by exponentials and using the method of stationary phase. The phases of the four exponentials which occur are stationary at the roots θ of the equation

$$\frac{y}{x}(1 + 2\tan^2\theta) = \pm m'(\theta)\cos\theta \quad . \quad (4.14)$$

When m is given by (4.11), for each sign this equation has two roots which lead to the transverse and longitudinal waves, and (4.5) becomes the well-known Kelvin ship wave pattern. There are no real roots of (4.14) outside the angle $|\tan^{-1}y/x| = 19.47°$. When m is given by (4.7), (4.14) can be written as a quadratic equation for $\tan^2\theta$. It has one positive root which yields

$$\tan\theta = \pm[\frac{1}{2}(1 - 4y^2/x^2)^{-1/2} - \frac{1}{2}]^{1/2} \quad . \quad (4.15)$$

In order that (4.15) satisfy (4.14), the sign in (4.15) must be the same as that in (4.14). Thus in the parabolic approximation there is only one stationary point for each choice of sign. It corresponds to the longitudinal wave. There are no real roots outside the angle

$$|\tan^{-1}y/x| = \tan^{-1}1/2 = 26.56° \quad . \quad (4.16)$$

5. Thin Ships

We shall now consider the flow past a thin ship with its surface given by $y = \pm f(x,z)$, and with $p^S = 0$. For such a ship (3.3) becomes

$$\frac{\partial\phi}{\partial y} = \pm Uf_x \quad , \quad y = 0\pm \quad . \quad (5.1)$$

For the parabolic approximation we use (4.8) while for the original problem we use (4.9), and in both cases we neglect second order terms in the thickness. Then if H denotes either G or $\tilde{G}$ we can write both results in the form

$$\phi(x,0,z) = \frac{U}{2\pi}\int_{B_1} H(x,0,z,x',0,z') \cdot f_{x'}(x',z')dx'dz' \quad . \quad (5.2)$$

Here B_1 is the projection of B on the plane y = 0.

Similarly we neglect second order terms in the thickness in (2.6), use (5.2), and obtain

$$R = -2\rho U\int_{B_1}\phi_x f_x dS$$
$$= -\frac{\rho U^2}{\pi}\int_{x_1}^{x_2}\int_{-b(x)}^{0} dxdz\, f_x(x,z)\int_{x}^{x_2}\int_{-b(x')}^{0} dx'dz'$$
$$\cdot f_{x'}(x',z')H_x(x,0,z,x',0,z')dx'dz' \quad . \quad (5.3)$$

Here $z = -b(x)$ is the equation of the ship's profile (see Figure 1).

Upon substituting (4.5) into (5.3) we obtain the asymptotic form of R for k large. We can write it as

$$R \sim \frac{4}{\pi}\rho gk\int_0^{\pi/2} d\theta\, m(\theta)t(\theta)[P(\theta)^2 + Q(\theta)^2] \quad , \quad (5.4)$$

where

$$P + iQ = \int_{x_1}^{x_2} dx \int_{-b(x)}^{0} dz$$
$$\cdot f_x(x,z)e^{k\sec^2\theta z + ikm(\theta)x} \quad . \quad (5.5)$$

For the exact problem (5.4) is correct for any value of k, but for the parabolic approximation, it is just asymptotic for k large.

To expand (5.4) for k large, we integrate by parts with respect to z in (5.5) and get

$$P + iQ \sim \int_{x_1}^{x_2} e^{ikm(\theta)x}\left[\frac{f_x(x,0)}{k\sec^2\theta} - \frac{f_x[x,-b(x)]}{k\sec^2\theta}\right.$$
$$\left. \cdot e^{-k\sec^2\theta b(x)}\right]dx \quad . \quad (5.6)$$

Now integrating each term in (5.6) by parts with respect to x leads to

$$P + iQ \sim \frac{1}{ik^2\sec^2\theta m(\theta)}\left[f_x(x_2,0)e^{ikm(\theta)x_2}\right.$$
$$\left. - f_x(x_1,0)e^{ikm(\theta)x_1}\right.$$

$$- \frac{f_x(x_2,0)e^{ikm(\theta)x_2}}{1 + i\sec^2\theta b'(x_2)[m(\theta)]^{-1}} + \frac{f_x(x_1,0)e^{ikm(\theta)x_1}}{1 + i\sec^2\theta b'(x_2)[m(\theta)]^{-1}} \Bigg| . \quad (5.7)$$

We next use (5.7) in (5.4) and obtain, after some algebra,

$$R \sim \frac{4\rho g}{\pi k^3} \Bigg\{ J(\beta_1)\tan^2\gamma_1 + J(\beta_2)\tan^2\gamma_2 - 2\tan\gamma_1\tan\gamma_2 |b'(x_2)||b'(x_1)| \cdot \int_0^{\pi/2} [m(\theta)]^{-3} t(\theta)\{1 + \sec^4\theta[m(\theta)]^{-2}\} \cdot \{b'(x_2)]^2\}^{-1/2}\{1 + \sec^4\theta[m(\theta)]^{-2} \cdot \{b'(x_1)]^2\}^{-1/2} \cos(k(x_2 - x_1)m(\theta) + \tan^{-1}[\frac{b'(x_1)\sec^2\theta}{m(\theta)}] - \tan^{-1}[\frac{b'(x_2)\sec^2\theta}{m(\theta)}]) \Bigg| . \quad (5.8)$$

Here

$$J(\beta) = \tan^2\beta \int_0^{\pi/2} \frac{t(\theta)d\theta}{m(\theta)[m^2(\theta) + \tan^2\beta\sec^4\theta]} . \quad (5.9)$$

The angles γ_1, γ_2, β_1 and β_2 appearing in (5.8) are defined in Figure 1.

The integral in (5.8) can be evaluated asymptotically for k large by the method of stationary phase. By using (4.12) and (4.13), we obtain after some algebra

$$R \sim \frac{4\rho g L^3 F^6}{\pi} \{J(\beta_1)\tan^2\gamma_1 + J(\beta_2)\tan^2\gamma_2 - (2\pi)^{1/2} F \tan\gamma_1\tan\gamma_2 \sin\beta_1 \sin\beta_2 \cdot \cos(F^{-2} + \beta_1 + \beta_2 + \tfrac{\pi}{4})\} . \quad (5.10)$$

In (5.10) we have introduced the Froude number F defined by

$$F = U(gL)^{-1/2} , \quad (5.11)$$

where $L = x_2 - x_1$ is the length of the ship.

Relations (5.9) and (5.10) hold for both the exact problem and for the parabolic approximation. They show that $m(\theta)$ and $t(\theta)$ appear only in $J(\beta)$. This leads to the remarkable result that the interaction term in the wave resistance, which is the part of R that oscillates as F varies, is predicted exactly by the parabolic approximation. The only difference between the exact and parabolic results is in the expression for $J(\beta)$.

We now substitute (4.10) and (4.11) into (5.9) and integrate to obtain for the exact problem

$$J_e(\beta) = \tan^2\beta[1 + \sin\beta\tan\beta \log \frac{\sin\beta}{1 + \cos\beta}] . \quad (5.12)$$

Formula (5.10) with $J(\beta)$ given by (5.12) is exactly the expression derived by Keller and Ahluwalia (1976) from the Michell thin ship theory.

By substituting (4.6) and (4.7) into (5.9) we obtain for the parabolic approximation

$$J_p(\beta) = \tan^2\beta \cdot \int_0^{\pi/2} \frac{\sec^3\theta\, d\theta}{[1 + \frac{\tan^2\theta}{2}][(1 + \frac{\tan^2\theta}{2}]^2 + \tan^2\beta\sec^4\theta)} . \quad (5.13)$$

To test the validity of the parabolic approximation for a thin ship we present in Table 1 values of $J_e(\beta)$ and $J_p(\beta)$ based upon (5.12) and (5.13) respectively, for various values of β. The agreement is remarkably good for small values of β, i.e. for a slender ship. The parabolic approximation becomes less good as β approaches $\pi/2$. However the error never exceeds 13%.

β	$J_e(\beta)$	$J_p(\beta)$
0.05	0.248×10^{-2}	0.257×10^{-2}
0.1	0.098×10^{-1}	0.102×10^{-1}
0.15	0.215×10^{-1}	0.227×10^{-1}
0.25	0.057	0.061
0.5	0.192	0.213
1.0	0.504	0.569
1.57	0.667	0.753

Table 1. $J_e(\beta)$ and $J_p(\beta)$.

The right side of (5.10) vanishes when $\gamma_1 = \gamma_2 = 0$, i.e. when the ship is cusped at bow and stern, so then $R = o(F^6)$. To get a non-zero asymptotic result in this case, we proceed as follows, and set $\beta_1 = \beta_2 = \pi/2$ for simplicity. We integrate (5.6) by parts twice with respect to x to obtain

$$P + iQ \sim -\frac{e^{ikm(\theta)x_2}}{k^3 m^2(\theta)\sec^2\theta} f_{xx}(x_2) - \frac{e^{ikm(\theta)x_1}}{k^3 m^2(\theta)\sec^2\theta} f_{xx}(x_1) . \quad (5.14)$$

We now substitute (5.14) into (5.4) and evaluate the interaction term for k large by the method of stationary phase. This yields for a ship with cusped bow and stern and $\beta_1 = \beta_2 = \pi/2$, the result

$$R \sim \frac{4\rho g L^3 F^4}{\pi} \{E c_1 + E c_2 - (2\pi)^{1/2} F\, c_1 c_2 \cdot \cos(F^{-2} + \tfrac{\pi}{4})\} . \quad (5.15)$$

Here

$$c_i = L f_{xx}(x_i) , \quad i = 1,2 . \quad (5.16)$$

The constant E in (5.15) is defined by

$$E = \int_0^{\pi/2} d\theta\, \frac{t(\theta)}{m^3(\theta)\sec^4\theta} . \quad (5.17)$$

As before we see that the interaction term is the same for both the exact solution and the parabolic approximation. The two results for R differ only in the values of E. By substituting (4.10) and (4.11) into (5.17) and evaluating the integral numerically we obtain

$$E_e \sim 0.53 . \quad (5.18)$$

Similarly after using (4.6) and (4.7) in (5.17) we obtain

$$E_p \sim 0.56 . \quad (5.19)$$

The agreement between (5.18) and (5.19) is again remarkably good.

6 Thin Ships with Rounded Bow and Stern

The thin ship approximation is based on the assumption that both $f(x)$ and $|f_x(x)|$ are small. Therefore it is not valid for ships with rounded bow and stern. Nevertheless this case provides a severe test of the parabolic approximation. Near the bow and stern, f_x varies rapidly with x and therefore so does u, whereas it was assumed that u varies slowly with x. Hence the parabolic approximation should be poor in this case. We shall see that it is still surprisingly good.

Let us split the integral in (5.6) in two at $x = 0$, set $x = x_1 + t^2$ in the first integral and $x = x_2 - t^2$ in the second, and obtain

$$P + iQ \sim \int_0^{(-x_1)^{1/2}} \frac{e^{ikm(\theta)(t^2 + x_1)}}{k\sec^2\theta} \cdot \left\{ 2t f_x(x_1 + t^2) - 2t f_x[x_1+t^2, -b(x_1+t^2)] \cdot e^{-k\sec^2\theta b(x_1+t^2)} \right\} dt + \int_0^{(x_2)^{1/2}} \frac{e^{ikm(\theta)(x_2-t^2)}}{k\sec^2\theta} \left\{ 2t f_x(x_2 - t^2) - 2t\, f_x[x_2-t^2, -b(x_2-t^2)] e^{-k\sec^2\theta b(x_2-t^2)} \right\} dt . \quad (6.1)$$

We now evaluate these integrals asymptotically by the saddle point method and after some algebra we obtain

$$P + iQ \sim \frac{e^{ikm(\theta)x_2}\, g_2(\pi L)^{1/2}}{2k^{3/2}\sec^2\theta[m(\theta)]^{1/2}} \cdot \left\{ \frac{e^{-ir(\theta,\beta_2)}}{a(\theta,\beta_2)} - e^{-i\pi/4} \right\} - \frac{e^{ikm(\theta)x_1}\, g_1(\pi L)^{1/2}}{2k^{3/2}\sec^2\theta[m(\theta)]^{1/2}} \cdot \left\{ \frac{e^{ir(\theta,\beta_1)}}{a(\theta,\beta_1)} - e^{i\pi/4} \right\} . \quad (6.2)$$

Here

$$r(\theta,\beta_i) = \tfrac{1}{2}\tan^{-1}\{m(\theta)[\sec^2\theta \tan\beta_i]^{-1}\} , \quad i = 1,2 , \quad (6.3)$$

$$a(\theta,\beta_i) = \left(\frac{\sec^4\theta}{m^2(\theta)}\tan^2\beta_i + 1\right)^{1/4} , \quad i = 1,2 , \quad (6.4)$$

$$g_i = 2L^{-1/2} \lim_{t\to 0}\{t\, f_x[x_i - (-1)^i t^2]\} , \quad i = 1,2 . \quad (6.5)$$

As before we substitute (6.2) into (5.4) and evaluate the interaction term asymptotically by the method of stationary phase to get

$$R \sim \rho g L^3 F^4 \{g_1^2 M(\beta_1) + g_2^2 M(\beta_2) - g_1 g_2 (2\pi)^{1/2} F\, N(\beta_1\beta_2)\} . \quad (6.6)$$

Here

$$M(\beta) = \int_0^{\pi/2} d\theta\, \frac{t(\theta)}{\sec^4\theta} \left| \frac{1}{a^2(\theta,\beta)} + 1 - \frac{2\cos[\frac{\pi}{4} - r(\theta,\beta)]}{a(\theta,\beta)} \right| , \quad (6.7)$$

$$N(\beta_1,\beta_2) = \frac{\cos[F^{-2} - r(0,\beta_1) - r(0,\beta_2) + \frac{\pi}{4}]}{a(0,\beta_1)a(0,\beta_2)} - \frac{\cos[F^{-2} - r(0,\beta_1)]}{a(0,\beta_1)} - \frac{\cos[F^{-2} - r(0,\beta_2)]}{a(0,\beta_2)} + \sin(F^{-2} + \tfrac{\pi}{4}) . \quad (6.8)$$

Relations (4.12) and (4.13) imply that $N(\beta_1,\beta_2)$ is the same for both the parabolic approximation and the exact problem. This leads

to the same result as in the previous section, that the interaction term in R is predicted exactly by the parabolic approximation. The only difference between the exact and parabolic results is in $M(\beta)$. We now use (4.10) and (4.11) in (6.7) to get $M_e(\beta)$, and (4.6), (4.7) in (6.7) to get $M_p(\beta)$. Numerical integration yields the values of $M_e(\beta)$ and $M_p(\beta)$ shown in Table 2 for various values of β. The agreement is again quite remarkable for small values of β. However the error reaches 28% as β approaches $\pi/2$.

β	$M_e(\beta)$	$M_p(\beta)$
0.05	0.94×10^{-3}	1.01×10^{-3}
0.1	0.36×10^{-2}	0.40×10^{-2}
0.15	0.79×10^{-2}	0.90×10^{-2}
0.25	0.20×10^{-1}	0.24×10^{-1}
0.5	0.71×10^{-1}	0.89×10^{-1}
1.0	0.23	0.30
1.57	0.79	1.0

Table 2. $M_e(\beta)$ and $M_p(\beta)$.

7. Pressure Distribution

We now consider the flow past a prescribed pressure distribution $p^S(x,y)$ on the free surface, in the absence of a ship. We assume that $p^S(x,y) = p^S(x,-y)$ and that

$$p^S(x,y) = 0 \text{ for } |y| \geq f(x) . \tag{7.1}$$

For the parabolic approximation we use (4.8) for ϕ while for the original problem we use (4.9). Then if H denotes either G or $\bar{G}$ we can write both results in the form

$$\phi(x,y,z) = \frac{1}{4\pi k\rho U} \int_S p^S_{x'} H \, dx'dy' . \tag{7.2}$$

Integrating (7.2) by parts with respect to x' and using (7.1) we obtain

$$\phi(x,y,z) = -\frac{1}{4\pi k\rho U} \int_S p^S H_{x'} \, dx'dy' . \tag{7.3}$$

We next calculate R given by (2.6), noting that $\eta_x = \phi_z/U$ at $z = 0$, and using (7.3) for ϕ, to get

$$R \sim \frac{1}{U} \int_S p^S \phi_z \, dxdy$$

$$= -\frac{1}{4\pi k\rho U^2} \int_S \int_S p^S(x',y') p^S(x,y) \cdot H_{x'z} \, dx'dy'dxdy . \tag{7.4}$$

Upon substituting (4.5) into (7.4) we obtain the asymptotic form of R for k large. We can write it as

$$R \sim \frac{k^2}{\pi\rho U^2} \int_0^{\pi/2} d\theta m(\theta) t(\theta) \sec^2\theta [P(\theta)^2 + Q(\theta)^2] , \tag{7.5}$$

where

$$P + iQ = \int_{x_1}^{x_2} dx \int_{-f(x)}^{f(x)} dy \, p^S(x,y) e^{ikm(\theta)x} \cdot e^{iksin\theta\sec^2\theta y} . \tag{7.6}$$

Again (7.5) is correct for any value of k for the exact problem. With the appropriate values of m and t it is exactly the expression derived by Havelock (1932).

8. Narrow Pressure Distribution

When the pressure distribution is narrow, i.e. $f(x) \ll k^{-1} \ll 1$, we can evaluate (7.5) asymptotically for k large as follows. We first integrate (7.6) by parts with respect to x and use (7.1) to obtain

$$P + iQ = -\int_{x_1}^{x_2} dx \int_{-f(x)}^{f(x)} dy \, \frac{p^S_x(x,y) e^{ikm(\theta)x}}{ikm(\theta)} \cdot e^{iksin\theta\sec^2\theta y} . \tag{8.1}$$

Then we integrate (8.1) by parts with respect to y and get

$$P + iQ \sim -2 \int_{x_1}^{x_2} dx \, p^S_x[x,f(x)] \cdot \frac{\sin[kf(x)\sin\theta\sec^2\theta]}{ik^2\sin\theta\sec^2\theta m(\theta)} e^{ikm(\theta)x} . \tag{8.2}$$

For a thin distribution of pressure $kf(x) \ll 1$, and the integral (8.2) can be approximated by

$$P + iQ \sim 2i \int_{x_1}^{x_2} ox \, p^S_x[x,0] \frac{f(x) e^{ikm(\theta)x}}{km(\theta)} . \tag{8.3}$$

Integrating by parts twice with respect to x in (8.3) and using the fact that $f(x_1) = f(x_2) = 0$, we obtain

$$P + iQ \sim \frac{2ip^S_x(x_2,0) f'(x_2) e^{ikm(\theta)x_2}}{k^3 m^3(\theta)} - \frac{2ip^S_x(x_1,0) f'(x_1) e^{ikm(\theta)x_1}}{k^3 m^3(\theta)} . \tag{8.4}$$

As in Section 5, we substitute (8.4) into (7.5) and evaluate the interaction term asymptotically for k large by the method of stationary phase to obtain

$$R \sim \frac{4F^6 L^3}{\pi\rho g}\{Q\tan^2\gamma_1[p_x^s(x_1,0)]^2 + Q\tan^2\gamma_2 \cdot [p_x^s(x_2,0)]^2 - (2\pi)^{1/2}F\tan\gamma_1\tan\gamma_2 \cdot [p_x^s x_1,0)p_x^s(x_2,0)]\cos(F^{-2}+\tfrac{\pi}{4})\}\ , \qquad (8.5)$$

where

$$Q = \int_0^{\pi/2} d\vartheta\ \sec^2\theta\ \frac{t(\theta)}{m^5(\theta)}\,d\theta\ . \qquad (8.6)$$

As before we see that the interaction term is the same for both the exact solution and the parabolic approximation. The only difference between the two results for R is in the definition of Q. Substituting (4.10) and (4.11) into (8.6) we obtain

$$Q_e = \int_0^{\pi/2} \cos\theta d\theta = 1\ . \qquad (8.7)$$

Substituting (4.6) and (4.7) into (8.6) we obtain

$$Q_p = \int_0^{\pi/2} \frac{\sec^5\theta}{[1+\frac{\tan^2\theta}{2}]^5}\,d\theta \sim 0.93\ . \qquad (8.8)$$

The agreement between (8.7) and (8.8) is again remarkably good.

We note that for the exact problem, (8.5) for a pressure distribution is identical to the leading order term for β small of the result (5.9) for a ship, provided that $p^s(x,0) = \rho g b(x)$.

9. Broad Pressure Distribution

Finally we evaluate (7.5) for k large when the pressure distribution is broad, i.e. when $f(x) \gg k^{-1}$.

We first rewrite (8.2) in the form

$$P + iQ \sim \int_{x_1}^{x_2} dx\ \frac{p_x^s[x,f(x)]}{k^2\sin\theta\sec^2\theta m(\theta)} \cdot \{e^{ik[f(x)\sin\theta\sec^2\theta + m(\theta)x]} - e^{ik[-f(x)\sin\theta\sec^2\theta + m(\theta)x]}\}\ . \qquad (9.1)$$

It is convenient to assume that $f'(0) = 0$ and that $f(x)$ is monotonic increasing for x negative and monotonic decreasing for x positive. Then the integral (9.1) possesses stationary points at $x = \alpha_1(\theta)$ and $x = \alpha_2(\theta)$ defined by

$$f'(\alpha_1) = \frac{m(\theta)}{\sin\theta\sec^2\theta}\ , \qquad (9.2)$$

$$f'(\alpha_2) = -\frac{m(\theta)}{\sin\theta\sec^2\theta}\ . \qquad (9.3)$$

Evaluating (9.1) for k large by the method of stationary phase, we obtain

$$P + iQ \sim p_x[\alpha_2,f(\alpha_2)] \cdot e^{ikf(\alpha_2)\sin\theta\sec^2\theta + ik\alpha_2 m(\theta)} \cdot \left(\frac{2\pi}{k|f''(\alpha_2)\sin\theta|}\right)^{1/2} \frac{e^{-i\pi/4\,\mathrm{sign}\theta}}{k^2\sin\theta\sec^3\theta m(\theta)} - p_x[\alpha_1,f(\alpha_1)]e^{-ikf(\alpha_1)\sin\theta\sec^2\theta + ik\alpha_1 m(\theta)} \cdot \left(\frac{2\pi}{k|f''(\alpha_1)\sin\theta|}\right)^{1/2} \frac{e^{i\pi/4\,\mathrm{sign}\theta}}{k^2\sin\theta\sec^3\theta m(\theta)}\ . \qquad (9.4)$$

On substituting (9.4) into (7.5), we get

$$R \sim \frac{F^2L^2}{\rho g}(D_1 + D_2 + I_{1,2})\ , \qquad (9.5)$$

where

$$D_i = 2\int_{\delta_i}^{\pi/2} \frac{p_x^2[\alpha_i,f(\alpha_i)]t(\theta)d\theta}{|f''(\alpha_2)\sin\theta|\sin^2\theta\sec^4\theta m(\theta)}\ , \qquad i = 1,2\ , \qquad (9.6)$$

$$I_{1,2} = 4\int_{\max(\delta_1,\delta_2)}^{\pi/2} \frac{p_x[\alpha_1,f(\alpha_1)]p_x[\alpha_2,f(\alpha_2)]}{[f''(\alpha_1)f''(\alpha_2)]^{1/2}|\sin\theta|} \cdot t(\theta)\cos\{k[f(\alpha_2)-f(\alpha_1)]\sin\theta\sec^2\theta + k(\alpha_2-\alpha_1)m(\theta) - \tfrac{\pi}{2}\,\mathrm{sgn}\theta\}/\sin^2\theta\sec^4\theta m(\theta)\,d\theta. \qquad (9.7)$$

In (9.6) and (9.7), δ_i is defined by

$$f'(x_i) = (-1)^{i+1}\frac{m(\delta_i)}{\sin\delta_i\sec^2\delta_i}\ , \qquad i = 1,2\ . \qquad (9.8)$$

It is interesting to consider the particular case of a pressure distribution with round ends. Then $|f'(x_1)| = |f'(x_2)| = \infty$ and $I_{1,2}$ has a stationary point at $\theta = 0$. This leads to the same result as in the previous sections that the interaction term $I_{1,2}$ is predicted exactly by the parabolic approximation.

In the case of a pointed distribution of pressure, there is no stationary point. Then the integral $I_{1,2}$ can be evaluated by integration by parts and it is then of higher order in F.

Finally let us mention that (9.5) is of order F^2 whereas (8.5) is of order F^6. Therefore there is a non-uniformity associated with the thickness of the pressure distribution. Taking the limit as the thickness tends to zero and

then the limit as k tends to infinity yields $R = O(F^6)$. Taking the limits in the opposite order yields $R = O(F^2)$. It is important to note that the parabolic approximation describes the non-uniformity accurately.

10. Parabolic Approximation Using the Double Body Solution

The parabolic approximation can be altered in various ways. One way is to seek the velocity potential as a perturbation of the double body potential $Ux + \phi^0(x,y,z)$ as in Keller (1979). Thus we write the velocity potential as $Ux + \phi^0(x,y,z) + \varphi(x,y,z)$ and then the problem (2.1)-(2.5) takes the form

$$\varphi_{xx} + \varphi_{yy} + \varphi_{zz} = 0 , \quad z < 0 , \tag{10.1}$$

$$\frac{\partial \varphi}{\partial n} = 0 \text{ on } B , \tag{10.2}$$

$$\varphi_{xx} + k\varphi_z = -\frac{p_x^s(x,y)}{\rho U} - \phi_{xx}^0 \text{ on } S , \tag{10.3}$$

$$\varphi_z \to 0 \text{ as } z \to -\infty , \tag{10.4}$$

$$\varphi = o(x^{-1/2}) \text{ as } x \to -\infty . \tag{10.5}$$

Equations (10.1)-(10.5) are equivalent to the exact problem (2.1)-(2.5) since no further approximation has been introduced.

We now introduce the parabolic approximation as in Section 3, by writing φ in the form (3.1). Then we proceed as in Section 3 to obtain from (10.1)-(10.5) the "parabolic" system

$$2ik\varphi_x + k^2\varphi + \varphi_{yy} + \varphi_{zz} = 0 , \quad z < 0 , \tag{10.6}$$

$$\frac{\partial \varphi}{\partial n} = 0 \text{ on } B , \tag{10.7}$$

$$2ik\varphi_x + k^2\varphi + k\varphi_z = -\frac{p_x^s(x,y)}{\rho U} - \phi_{xx}^0 \text{ on } S , \tag{10.8}$$

$$\varphi_z \to 0 \text{ as } z \to -\infty , \tag{10.9}$$

$$\varphi \to 0 \text{ as } x \to -\infty . \tag{10.10}$$

This system can be solved numerically by marching from bow to stern.

On comparing (10.6)-(10.10) with (3.2)-(3.6) we see that the inhomogeneity has been moved from the boundary condition on the ship, which is now homogeneous, to the free surface condition. This inhomogeneity acts like a distribution of pressure on the free surface, of strength $\rho U\phi_x^0$.

If the boundary condition (10.7) is omitted and the definition of ϕ^0 is extended to the complete plane $z = 0$, the problem reduces to that of a pressure distribution on the free surface. The accuracy of the parabolic approximation in that case treated in Sections 7-9 indicates how accurate it will be for the complete problem (10.6)-(10.10).

The method of this section may complement other work in which the solution is sought as a perturbation of the double body flow (Ogilvie (1968), Keller (1974), Baba (1976), Maruo (1977), etc.).

11. Two-Dimensional Parabolic Approximation

The parabolic approximation described in Section 3 can be further simplified by using the fact that for k large the wave motion decays exponentially in z. Therefore we write

$$\phi(x,y,z) = w(x,y,z)e^{kz} . \tag{11.1}$$

By substituting (11.1) into (3.2)-(3.6) we obtain an equivalent set of equations for w.

The two-dimensional parabolic approximation is obtained by dropping w_{zz} from these equations. We shall call the solution of the resulting problem w^p. It is convenient to rewrite this problem in terms of $\phi^p = w^p e^{kz}$. The resulting problem can be obtained from (3.2)-(3.6) by replacing ϕ_{zz}^p by $2k\phi_z^p - k^2\phi^p$ in (3.2). In this way we obtain the following equations from which we omit the superscript p:

$$2ik\phi_x + \phi_{yy} + 2k\phi_z = 0 , \quad z < 0 , \tag{11.2}$$

$$\frac{\partial \phi}{\partial n} = -U\frac{\partial x}{\partial n} \text{ on } B , \tag{11.3}$$

$$2ik\phi_x + k^2\phi + k\phi_z = -\frac{p_x^s(x,y)}{\rho U} \text{ on } S , \tag{11.4}$$

$$\phi_z \to 0 \text{ as } z \to -\infty , \tag{11.5}$$

$$\phi = 0 \text{ for } x \le x_1 . \tag{11.6}$$

The system (11.2)-(11.6) can be reduced to a system of equations on S by eliminating ϕ_z between (11.2)-(11.4). Thus we obtain

$$2ik\phi_x + 2k^2\phi - \phi_{yy} = -2\frac{p_x^s(x,y)}{\rho U} \text{ on } S , \tag{11.7}$$

$$\phi_x n_x + \phi_y n_y - \left(i\phi_x + \frac{\phi_{yy}}{2k}\right)n_z = -U\frac{\partial x}{\partial n} \text{ on } W , \tag{11.8}$$

$$\phi = 0 \text{ for } x \le x_1 . \tag{11.9}$$

Equation (11.7) is a one-dimensional Schrödinger equation in which x plays the role of time. The system (11.7)-(11.9) can be solved numerically by marching from bow to stern, as in the original parabolic approximation. However now the calculation is confined to the free surface S on the plane $z = 0$.

12. Application to Thin Ship

For a thin ship, the boundary condition (11.8) is replaced by

$$\phi_y = \pm U f_x(x,0) \text{ on } y = 0\pm , \quad z = 0 . \tag{12.1}$$

The solution of (11.7) and (11.9) with the boundary condition (12.1) is

$$\phi(x,y,z) = -\frac{U}{(2ik\pi)^{1/2}} \int_{x_1}^{x} \exp\left[-\frac{iky^2}{2(x-\zeta)} + ik(x-\zeta) + kz\right] \cdot \frac{f_x(\zeta,0)d\zeta}{(x-\zeta)^{1/2}} . \tag{12.2}$$

In the remaining part of this section we will consider only cylindrical ships so that $f(x,z) = f(x)$. Then the wave resistance R, which is given by the first line of (5.3), yields after integration with respect to z

$$R = -2\rho U \int \phi_x f_x dzdx = -\frac{2\rho U}{k} \int_{x_1}^{x_2} \phi_x(x,0,0) f_x(x) dx . \tag{12.3}$$

Integrating by parts and using (11.9), we can write (12.3) in the form

$$R = -\frac{2\rho U}{k} \left[\phi(x_2,0,0) f_x(x_2) - \int_{x_1}^{x_2} \phi(x,0,0) f_{xx}(x) dx\right] . \tag{12.4}$$

To evaluate $\phi_x(x,0,0)$ asymptotically for k large we find it convenient to introduce the change variable $z = x - v^2$ in (12.2). Thus we obtain

$$\phi(x,0,0) = -\left(\frac{2}{ik\pi}\right)^{1/2} U \int_0^{(x-x_1)^{1/2}} f_\zeta(x-v^2) e^{ikv^2} dv . \tag{12.5}$$

The main contributions to the integral in (12.5) for k large come from $v = 0$ and $v = x^{1/2}$. They are respectively of order k^{-1} and $k^{-3/2}$. After some algebra we obtain

$$\phi(x,0,0) \sim -\frac{Uf_x(x)}{k2^{1/2}} + \frac{Uf_x(x_1)\exp[ik(x-x_1) - i\,3\frac{\pi}{4}]}{(x-x_1)^{1/2}(2\pi)^{1/2}k^{3/2}} . \tag{12.6}$$

Substituting (12.6) into (12.4) we have

$$R \sim \frac{4\rho g L^3 F^6}{\pi}\left[\frac{\pi 2^{1/2}}{8}\tan^2\gamma_1 + \frac{\pi 2^{1/2}}{8}\tan^2\gamma_2 - \left(\frac{\pi}{8}\right)^{1/2} F\tan\gamma_1 \tan\gamma_2 \cos\left(F^{-2} - \frac{\pi}{4}\right)\right] . \tag{12.7}$$

Let us now compare (12.7) with the exact expression (5.10) with J(β) given by (5.12) and $\beta_1 = \beta_2 = \pi/2$. We see that that the results are of the same form. The leading order terms (i.e. the bow and stern terms) agree within sixteen percent since $J(\pi/2) = 2/3 = .67$ and $\pi 2^{1/2}/8 = .55$. The interaction terms are also of the same form but they differ in amplitude by a factor of about 4, and they differ in phase by $\pi/2$. Thus the two-dimensional parabolic approximation is not as good as the three-dimensional one.

It is interesting to note that Michell's integral predicts exagerated "humps and hollows" in the curve of R versus F at low Froude numbers. Therefore fortuitiously formula (12.7) is in better agreement with experimental results than the exact result (5.10).

13. Numerical Scheme

In this section we show how to solve the system (11.7)-(11.9) numerically. For simplicity we consider only the case of a thin ship.

First we introduce the mesh points

$$x_I = x_1 + (I-1)\frac{x_2 - x_1}{N-1} , \quad I = 1,\ldots,N , \tag{13.1}$$

$$y_J = (J-1) \times E , \quad J = 1,\ldots,M . \tag{13.2}$$

Here E is the interval of discretization along the y axis.

Using the notation

$$\phi(I,J) = \phi(x_I,y_J) ,$$

we can rewrite (11.7) in the form

$$\phi_x(I,J) = i\phi(I,J) - i\frac{\phi_{yy}(I,J)}{2k} . \tag{13.3}$$

The second derivative with respect to y in (13.3) is approximated by second order difference formulas

$$\phi_{yy}(I,J) = \frac{\phi(I,J+1) - 2\phi(I,J) + \phi(I,J-1)}{E^2} , \quad J \geq 2 , \tag{13.4}$$

$$\phi_{yy}(I,1) = \frac{\phi(I,2) - \phi(I,1) + f_x(x_I)E}{E^2} . \tag{13.5}$$

In (13.5) we have used the condition (12.1).

We now define the marching procedure by the implicit scheme

$$\phi(I+1,J) = \phi(I,J) + \left[\frac{\phi_x(I,J) + \phi_x(I+1,J)}{2}\right]\frac{x_2 - x_1}{N-1} . \tag{13.6}$$

We close the system by the condition

$$\phi(I,J) = 0 , \quad \forall I \text{ for } J \geq M+1 . \tag{13.7}$$

Substituting (13.4)-(13.6) into (13.3) we obtain a linear system of equations which enable us to compute $\phi(I+1,J)$, $J = 1,\ldots,M$ when $\phi(I,J)$ are known. This system involves a tridiagonal matrix so that no matrix inversion is needed. Relation (11.9) yields $\phi(1,J) = 0$. Therefore we can compute successively $\phi(2,J)$, $\phi(3,J)$,...,etc.

Preliminary computations indicated that some care had to be taken to handle the singularity at the bow. It was found that this could be achieved by replacing (13.6) at the first step by

$$\phi(2,J) = \phi_x(2,J)\frac{x_2 - x_1}{N-1} . \tag{13.8}$$

To illustrate the numerical scheme we consider a local solution near a bow characterized by $f_x = 0.2$. Without loss of generality we choose $x_1 = 0$. Since there is no stern for this local solution, we rewrite (13.1) in the more appropriate form

$$kx_I = (I-1)h , \quad I = 1,\ldots,N .$$

Here h is the interval of discretization along the x-axis.

For comparison we consider the analytic solution (12.2), which yields in the present case

$$\frac{k\phi(x,0,0)}{U} = 0.2\,(2)^{-1/2}(1-i)\cdot\left|c\left[\left(\frac{2kx}{\pi}\right)^{1/2}\right] + iS\left[\left(\frac{2kx}{\pi}\right)^{1/2}\right]\right| . \tag{13.9}$$

Here

$$C(x) = \int_0^x \cos\left(\frac{\pi}{2}t^2\right)dt , \tag{13.10}$$

$$S(x) = \int_0^x \sin\left(\frac{\pi}{2}t^2\right)dt , \tag{13.11}$$

are the Fresnel integrals. The values of $k\phi/U$ are obtained by taking the real part of (13.9).

In Table 3 we compare the exact answer (13.9) with the numerical values at different values of kx for serval values of h. For each value of h we have decreased E until convergence to the listed number of decimal places was obtained. The value of M in (13.2) was chosen large enough for the converged answers to be independent of M. Table 3 shows that the scheme converges as h is decreased.

kx \ h	.55	.28	.14	Exact
0.555	7.44	9.44	9.6	9.7
2.778	18.96	18.94	18.56	18.56
5.555	10.24	10.64	10.8	10.8
11.11	12.	12.24	12.32	12.32

Table 3. Values of $\phi \times 10^2$.

14. Concluding Remarks

The results of Sections 5 and 6 show that the parabolic approximation yields good results for k large for a thin ship with β small. This suggests that it should also yield good results for a flat ship, i.e. a thick ship with β small. However the waterline should not be broad since the normal n in (4.9) has been replaced by the normal n^* in (4.8).

A different marching procedure for slender bodies at high Froude number was introduced by Ogilvie (1967) and applied to flat ships by Tuck (1975). The parabolic approximation has also been used by Tuck and Mei (1980) and Haren and Mei (1981) to study the diffraction of waves by slender bodies.

Appendix A

We seek the Green's function G in the form

$$G = -\frac{1}{\pi^2}\int_{-\infty}^{+\infty}\int_{-\infty}^{+\infty}\int_{-\infty}^{+\infty} e^{ip(x-x')}\cdot\frac{e^{iq(y-y')}e^{ir(z-z')}}{2kp + q^2 - k^2 + r^2 + i\mu}\,dpdqdr + \int_{-\infty}^{+\infty}\int_{-\infty}^{+\infty} g(p,q)\cdot e^{ipx}e^{iqy}e^{(q^2+2kp-k^2)^{1/2}z}\,dpdq . \tag{A.1}$$

Here μ is a Rayleigh friction coefficient and g(p,q) is a function to be determined. It can be verified easily that (A.1) satisfies (4.1), (4.3) and (4.4).

Performing the integral over r in (A.1), we obtain

$$G = -\frac{1}{\pi}\int_{-\infty}^{+\infty}\int_{-\infty}^{+\infty} e^{ip(x-x')}\cdot\frac{e^{iq(y-y')}e^{-|z-z'|(q^2+2kp-k^2)^{1/2}}}{(2kp + q^2 - k^2)^{1/2}}\,dpdq$$

$$+ \int_{-\infty}^{+\infty}\int_{-\infty}^{+\infty} g(p,q)e^{ipx}e^{iqy}e^{(q^2+2kp-k^2)^{1/2}z}\,dpdq\,. \tag{A.2}$$

Here the square root is defined in a complex plane cut along the positive imaginary axis.

Substituting (A.2) into (4.2) yields

$$g(p,q) = \frac{1}{\pi}\frac{e^{-ipx'}e^{-iqy'}e^{z'(2kp+q^2-k^2)^{1/2}}}{(2kp+q^2-k^2)^{1/2}} - \frac{2k}{\pi}\frac{e^{-ipx'}e^{-iqy'}e^{z'(2kp+q^2-k^2)^{1/2}}}{k^2-2kp+k(2kp+q^2-k^2)^{1/2}}\,. \tag{A.3}$$

Introducing the notation

$$a(x,y,z,x',y',z') = -\frac{1}{\pi}\int_{-\infty}^{+\infty}\int_{-\infty}^{+\infty} e^{ip(x-x')} \cdot e^{iq(y-y')}e^{-|z-z'|(2kp+q^2-k^2)^{1/2}}\,dpdq\,, \tag{A.4}$$

we can now write G in the form

$$G = a(x,y,z,x',y',z') - a(x,y,z,x',y',-z') - \frac{2k}{\pi}\int_{-\infty}^{+\infty}\int_{-\infty}^{+\infty} e^{ip(x-x')} \cdot \frac{e^{iq(y-y')}e^{(z+z')(2kp+q^2-k^2)^{1/2}}}{k^2-2kp+k(2kp+q^2-k^2)^{1/2}}\,dpdz\,. \tag{A.5}$$

The main contribution to G for k large is given by the residue of the pole of the integral in (A.5). After some algebra we can write in in the form (4.5).

Appendix B

The Green's function G can be used to reformulate the problem (3.2)-(3.6) as an integrodifferential equation. Using the divergence theorem we derive the following identities:

$$\begin{aligned}
&\int_{x_1}^{x} dx' \int_{-\infty}^{+\infty} dy' \int_{-\infty}^{0} dz' \\
&\quad \cdot [\phi(G_{y'y'} + G_{z'z'}) - G(\phi_{y'y'} + \phi_{z'z'})] \\
&= \int_{x_1}^{x} dx' \int_{-\infty}^{+\infty} dy' \int_{-\infty}^{0} dz'[\nabla\cdot(\phi\nabla G - G\nabla\phi)] \\
&= \int_{B+S} (\phi G_{n^*} - G\phi_{n^*})ds\,.
\end{aligned} \tag{B.1}$$

Here $\nabla = (\frac{\partial}{\partial x'}, \frac{\partial}{\partial z'})$ and n^* is the unit outward normal to the curve in which B + S intersects a plane x = constant. In the last integral in (B.1) we have used the fact that $G = G_n = 0$ for $x > x'$ to rewrite the integral as an integral over the complete surface B + S.

Upon substituting (3.2) and (4.1) into (B.1) and using the fact that $\phi(x_1,y,z) = G(x,y,z,x,y',z') = 0$, we obtain

$$\begin{aligned}
\int_{B+S} (\phi G_{n^*} - G\phi_{n^*})ds &= 8\pi \int_{x_1}^{x} dx' \int_{-\infty}^{+\infty} dy' \int_{-\infty}^{0} dz' \\
&\quad \cdot \phi(x',y',z')\delta(x-x')\delta(y-y')\delta(z-z') \\
&\quad + 2ik \int_{-\infty}^{+\infty} dy' \int_{-\infty}^{0} dz'[\phi G]_{x_1}^{x} = 4\pi\phi(x,y,z)\,.
\end{aligned} \tag{B.2}$$

By using (3.4) and (4.2) we obtain after integration by parts,

$$\begin{aligned}
\int_{S} (\phi G_{n^*} - G\phi_{n^*})ds &= \int_{S} (\phi G_{z'} - G\phi_{z'})dx'dy' \\
&= \int_{S}\left(\phi G_{z'} + G\frac{p^S_{x'}(x',y')}{\rho kU} + k\phi G + 2iG\phi_{x'}\right)dx'dy' \\
&= \int_{S} \phi(G_{z'} + kG - 2iG_{x'}) + C\frac{p^S_{x'}(x',y')}{\rho kU}dx'dy' \\
&\quad + 2i\int_{W} G\phi dy' \\
&= \int_{S} G\frac{p^S_{x'}}{\rho kU}dx'dy' + 2i\int_{W} G\phi dy'\,.
\end{aligned} \tag{B.3}$$

Here W is the water line.
After substituting (B.2) and (B.3) into (B.1) we finally obtain (4.8).

This research was supported by the Office of Naval Research, the Air Force Office of Scientific Research, the Army Research Office, and the National Science Foundation.

References

1. Baba, E. 1976 Mitsubishi Tech. Bull. No. 109, pp. 1-20.

2. Haren P. and Mei, C. C. 1981 J. Fluid Mech. 104, pp. 505-526.

3. Havelock, T. H. 1932 Proc. Roy. Soc. A 138, pp. 339-348.

4. Keller, J. B. 1974 Proc. 10th Symp. Naval Hydro., Office of Naval Research, Dept. of Navy, Arlington, Va., pp. 543-545.

5. Keller, J. B. 1979 J. Fluid Mech. 91, pp. 465-488.

6. Keller, J. B. and Ahluwalia, D. S. 1976 J. Ship Res. 20, pp. 1-6.

7. Maruo, H. 1977 Bull. Faculty Eng. Yokohama Nat. Univ. 26, pp. 59-75.

8. Mei, C. C. and Tuck, E. O. 1980 SIAM J. Appl. Math. 39, pp. 178-191.

9. Ogilvie, T. F. 1967 Journal of Engineering Mathematics, Vol. 1, pp. 215-235.

10. Ogilvie, T. F. 1968 Dept. Naval Arch., Univ. of Michigan, Ann Arbor, Report No. 002.

11. Tuck, E. O. 1975 J. Hydronautics 1, pp. 3-12.

12. Wehausen, J. 1973 "Wave Resistance of Ships," Advances in Applied Mechanics, Vol. 13, Academic Press, New York, pp. 93-245.

DISCUSSIONS
of the paper
by J M. Vanden-Broeck and J B. Keller

PARABOLIC APPROXIMATIONS FOR SHIP WAVES AND WAVE RESISTANCE

Discussion
by P.D. Sclavounos

The present paper is an interesting application of the parabolic approximation to the wave-resistance of slender ships and/or pressure distributions.

I would like to concentrate on Section 10, where the method is applied after the total velocity potential is decomposed in the double-body solution $\phi^{\circ}(X, Y, Z)$ and a wave component $\varphi(X, Y, Z)$, which is written in the form

$$\varphi(X, Y, Z) = u(X, Y, Z)\, e^{ikx}.$$

Due to slenderness, $u(X, Y, Z)$ is assumed to be a slowly varying function of x. In the free-surface condition (10.8), the term $u_{xx}\, e^{ikx}$ is neglected in the left-handside, while the double x-derivative of the double-body solution, ϕ°_{xx} is kept in the right hand-side. The slenderness assumptions suggest that the orders of magnitude of $u_{xx}\, e^{ikx}$ and ϕ°_{xx} are the same, assuming that $e^{ikx} = O(1)$. It is interesting to point out that a term analogous to ϕ°_{xx} is not present in the application of the parabolic approximation to the diffraction problem [Mei and Tuck (1980) and Haren and Mei (1981)], where the body-boundary condition is oscillatory and not slowly varying as in the wave-resistance case. Could the authors comment on the assumptions involved in the free-surface condition (10.8).

Authors' reply

Dr. Sclavounos is quite correct that we have neglected the term $u_{xx}e^{ikx}$ in (10.8) but retained ϕ°_{xx}. We cannot neglect ϕ°_{xx} because it is the only inhomogeneous term in the problem. We do neglect $u_{xx}e^{ikx}$ because, when k is large, it will be small compared to $2iku_x e^{ikx}$, which we retain. Thus we expect $2iku_x e^{ikx}$ to be comparable to ϕ°_{xx}, and $u_{xx}e^{ikx}$ to be small compared to either of them.

Discussion
by K. Eggers

I must apologize that my discussion does not exactly meet the subject of Dr. Vanden-Broeck's paper, which I could not read earlier. My remarks are mainly related to previous work of the second author, referred to in the morning session by Dr. Kim. I consider them relevant as well to Prof. Miyata's presentation this morning.

As far as I can understand, the flow model advocated by Prof. Keller heavily rests on the assumption that the energy transport due to free surface waves is not affected through the non-uniform (double body) flow the waves are superposed to. But Longuet-Higgins showed some 20 years ago that the assumption that energy is transported with the vector sum of flow- and wave-group velocity is incorrect, thus rays as defined by Ursell cannot be considered as lines of energy transport ! We have to modify the dispersion relation between wave angle and wave length in dependence of the absolute local value of the double body flow.

I found that such modification leads to an enlargement of the Kelvin angle near the ships' ends (measured against the double body flow direction) well in accord with experimental observation which may even explain a substential part of the phenomena reported by Prof. Miyata through a dispersive flow model.

I feel that this effect may even be of relevance to the bow-stern interference effect of Dr. Vanden-Broeck's resistance expression (say his equation 12.7), as a change in wave length along a ray connecting bow and stern (i.e. along the waterline) should imply a change in phase at least, if not even in amplitude.

Professor Keller's reply

In my papers on ship waves [4] , [5] , I used the dispersion equation for waves on the surface of a moving fluid. This dispersion equation follows from the statement that the magnitude of the wave vector k is equal to the square of the Doppler-shifted frequency $\omega - k\cdot\nabla\phi$, where ϕ is the velocity potential of the underlying fluid motion. Ursell has derived this result from the basic equations by asymptotic analysis. The dispersion equation yieds equations for the rays and wave-fronts, and for the group velocity vector c_g it gives $c_g = 1/2\ k^{-3/2}k - \nabla\phi$. Thus c_g is obtained by vector addition of the group velocity of waves on a stationary fluid and the velocity of the fluid.

Professor Eggers has pointed out that the energy flux vector associated with waves in a moving fluid is not in the direction of c_g. The distinction between wave and group velocities is well known in the theory of linear waves in

nonisotropic media, but here the nonlinearity of the boundary conditions makes it even more complicated. To obtain the correct equation governing the transport of energy, I found it necessary to perform a rather lengthy calculation involving asymptotic expansions. The previous results of Longuct-Higgins were not adequate for this purpose because corrections to the basic flow had to be included.

I would be interested in seeing the modification of the dispersion equation which Professor Eggers has found.

NONLINEAR WAVES BEHIND AN ACCELERATED TRANSOM STERN

R.M. Coleman and H.J. Haussling
David W. Taylor
Naval Ship Research and Development Center
Bethesda, Maryland 20084

ABSTRACT

Finite difference techniques are used with boundary-fitted coordinate systems to compute the unsteady potential flow past the stern of a semi-infinite, flat-bottomed body at the free surface of an incompressible fluid. The flow is assumed to separate smoothly from the hull at a sharp trailing edge. Fully nonlinear free-surface boundary conditions are employed. The complicated time-dependent flow regions arising in this nonlinear water wave problem are transformed using numerically-generated coordinate systems into a rectangular time-independent computational region with a uniform mesh. A range of six draft-based Froude numbers Fr is considered from Fr = 1.75 to Fr = 2.35. At Fr = 2.35 an almost steady-state solution is obtained that compares well with previous numerical results. At all other values of Fr studied, the calculations are continued until breaking conditions are encountered. As the Froude number increases, the time needed for the stern waves to achieve maximum height and the distance from the stern to the maximum peak both increase. The maximum height attained increases with Froude number up to approximately Fr = 2.25 or Fr = 2.3. Beyond this region the maximum height decreases with Froude number and, instead of breaking, the solution approaches the known steady-state result in an oscillatory fashion.

I. INTRODUCTION

The overall performance of a ship is greatly influenced by the flow of water near the bow and stern. Accordingly, researchers have given much attention to the details of this flow including the free-surface waves produced. Many of these investigations, both experimental and theoretical, have dealt with hull shapes having a transom stern. However, the difficulty of the complete three-dimensional problem has restricted most studies of the nonlinear aspects of this flow to two dimensions.

Vanden-Broeck [1] used an integro-differential formulation for steady two-dimensional potential flow past a flat-bottomed body with a transom stern. Assuming that the flow detaches at the corner of the body, he found that a steady-state nonlinear solution exists only for draft-based Froude numbers greater than 2.23. Simultaneously, Haussling [2] obtained numerical solutions for the unsteady problem using both flat and curved hulls. His work was consistent with Vanden-Broeck's calculations at Froude numbers for which a steady-state solution exists. Accurate results were not obtained at Froude numbers less than 3.0 because of limitations of the mathematical/numerical treatment. The present study extends Haussling's earlier work to a wider range of Froude numbers through an improved approach. In particular, the assumption of a single-valued free surface has been dropped. Finite difference techniques using boundary-fitted coordinates are employed to compute numerical solutions in the fully nonlinear case. Haussling & Coleman [3] used a similar boundary-fitted coordinate scheme to compute very steep free surface waves generated by a submerged body.

The current work concentrates on Froude numbers near the critical value of 2.23. At higher Froude numbers, a steady-state solution is obtained and the free-surface profile is compared to previous numerical results. At Froude numbers for which no steady solution exists, the calculations are continued until a breaking wave develops behind the stern. These results are used to investigate how the time of breaking and the maximum height and position of the breaking wave depend on the Froude number.

II. MATHEMATICAL FORMULATION

We consider the flow resulting from the abrupt acceleration from rest to final speed U of a semi-infinite ship hull moving in the free surface of a tank of water. The fluid, which is initially at rest, is of uniform depth h and occupies the region Ω as defined in Figure 1. The hull is of draft d and has a span equal to that of the tank. The hull moves with respect to a fixed (x,y)-coordinate system which has its origin at the original intersection of the stern with the undisturbed free surface. We assume that the flow is irrotational and that the fluid is incompressible and lacks surface tension. We also assume that the free surface, $\partial\Omega_1$, can be described in parametric form at any time t by specifying x and y as functions of s, distance along the free surface: $x = x(s,t)$; $y = y(s,t)$. The free surface runs

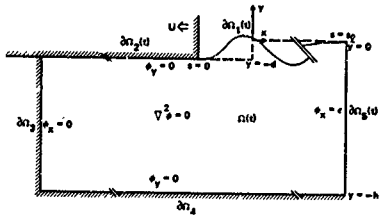


Figure 1. Geometry of Initial/Boundary-Value Problem

from $s = 0$ at the stern to $s = s_\ell$ at the downstream boundary. We further assume that immediately after acceleration the flow detaches tangentially from the hull at the corner: $x = x(0,t)$; $y = y(0,t) = -d$. The upper fluid boundary coincides with the hull upstream from the detachment point and is a free boundary downstream from this point. Wall conditions are enforced on $\partial\Omega_2$, $\partial\Omega_3$, and $\partial\Omega_4$. As the hull moves out of the tank, the loss of mass causes a drop in the mean level of the free surface. To prevent a lowering of the mean level, fluid is introduced at the downstream boundary at a slow rate c. Since the major part of the disturbance moves upstream with the hull, this addition of fluid to Ω has no deleterious effect on the free-surface profile if the downstream boundary is chosen to be a suitable distance from the hull at $t = 0$.

The dimensionless form of the two-dimensional initial/boundary value problem in the fixed frame is as follows:

$$\phi_{xx} + \phi_{yy} = 0 \qquad \text{in } \Omega(t) \qquad (1)$$

$$\left.\begin{aligned} \frac{Dy}{Dt} &= \phi_y \\ \frac{Dx}{Dt} &= \phi_x \\ \frac{D\phi}{Dt} &= -y/Fr^2 + (\phi_x^2 + \phi_y^2)/2 \end{aligned}\right\} \text{ on } \partial\Omega_1(t) \qquad \begin{matrix}(2)\\(3)\\(4)\end{matrix}$$

$$\phi_y = 0 \qquad \text{on } \partial\Omega_2(t) \qquad (5)$$

$$\phi_x = 0 \qquad \text{on } \partial\Omega_3 \qquad (6)$$

$$\phi_y = 0 \qquad \text{on } \partial\Omega_4 \qquad (7)$$

$$\phi_x = -1/(y(s_\ell,t)-h)=c \qquad \text{on } \partial\Omega_5(t) \qquad (8)$$

$$\phi(t=0) = 0 \qquad \text{in } \Omega(t) \qquad (9)$$

$$\left.\begin{aligned} y(t=0) &= 0 \\ x(t=0) &= s \end{aligned}\right\} \text{ on } \partial\Omega_1(t) \qquad \begin{matrix}(10)\\(11)\end{matrix}$$

The subscripts x and y denote partial differentiation with respect to these variables and $D/Dt = \partial/\partial t + \nabla\phi\cdot\nabla$ indicates differentiation following a fluid particle. The characteristic length and velocity scales in the dimensionless quantities are d, the draft, and U, the speed of the hull. The draft-based Froude number is $Fr = U/\sqrt{gd}$, where g is the gravitational acceleration. The pressure p on the hull can be computed from the Bernoulli equation

$$p = -D\phi/Dt + (\phi_x^2 + \phi_y^2)/2 - y/Fr^2 \qquad (12)$$

III. THE TRANSFORMATION

The time-dependent physical region $\Omega(t)$ in (x,y)-space is transformed to a rectangular computational region Ω' in (ξ,η)-space as seen in Figure 2.

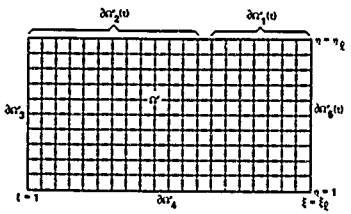


Figure 2. The Computational Region and Coordinate System

The boundaries of Ω are mapped onto the boundaries of Ω' as indicated. For instance, the free surface $\partial\Omega_1$ (Figure 1) is mapped onto $\partial\Omega'_1$ (Figure 2). The shape of the computational region is independent of time and thus remains constant as the movement of the hull causes the free surface to deform. The transformed coordinates

$$\xi = \xi(x,y,t) \qquad \eta = \eta(x,y,t) \qquad (13)$$

are computed as solutions to the equations

$$\begin{aligned} \xi_{xx} + \xi_{yy} &= P(\xi,\eta,t) \\ \eta_{xx} + \eta_{yy} &= Q(\xi,\eta,t) \end{aligned} \qquad (14)$$

with appropriate boundary conditions. The source functions P and Q are specified such that the resulting (ξ,η)-coordinate system is suitable for the calculations. These non-

homogeneous terms provide an effective means of controlling the distribution of coordinate lines in the physical region as shown in the Appendix.

For computational purposes, Equations (14) are transformed to (ξ,η)-space by interchanging dependent and independent variables to yield

$$\begin{aligned} \alpha x_{\xi\xi} - 2\beta x_{\xi\eta} + \gamma x_{\eta\eta} + J^2(Px_\xi + Qx_\eta) &= 0 \\ \alpha y_{\xi\xi} - 2\beta x_{\xi\eta} + \gamma y_{\eta\eta} + J^2(Py_\xi + Qy_\eta) &= 0 \end{aligned} \tag{15}$$

where

$$\begin{aligned} \alpha &= x_\eta^2 + y_\eta^2 & \beta &= x_\xi x_\eta + y_\xi y_\eta \\ \gamma &= x_\xi^2 + y_\xi^2 & J &= x_\xi y_\eta - x_\eta y_\xi \end{aligned} \tag{16}$$

The transformation can then be determined by solving Equations (15) subject to the appropriate boundary conditions. Figure 3 shows a sequence of coordinate configurations in the physical plane generated during the calculation of the potential flow problem.

Since the governing equations and boundary conditions are to be solved in the computational plane, they must be transformed to the (ξ,η)-coordinate system. Equation (1) is rewritten as

$$\alpha\phi_{\xi\xi} - 2\beta\phi_{\xi\eta} + \gamma\phi_{\eta\eta} + J^2(P\phi_\xi + Q\phi_\eta) = 0 \tag{17}$$

Equations (2), (3), and (4) become

$$\left.\begin{aligned} \frac{Dy}{Dt} &= (x_\xi\phi_\eta - x_\eta\phi_\xi)/J && (18) \\ \frac{Dx}{Dt} &= (y_\eta\phi_\xi - y_\xi\phi_\eta)/J && (19) \\ \frac{D\phi}{Dt} &= -y/Fr^2 + ((y_\eta\phi_\xi - y_\xi\phi_\eta)^2 \\ &\quad + (x_\xi\phi_\eta - x_\eta\phi_\xi)^2)/(2J^2) && (20) \end{aligned}\right\} \text{ on } \partial\Omega_1'$$

Equations (5) and (6) are replaced by

$$x_\xi\phi_\eta - x_\eta\phi_\xi = 0 \qquad \text{on } \partial\Omega_2' \tag{21}$$

$$y_\eta\phi_\xi - y_\xi\phi_\eta = 0 \qquad \text{on } \partial\Omega_3' \tag{22}$$

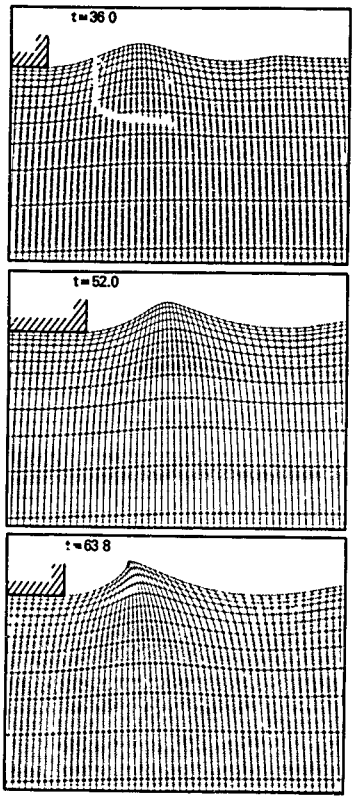


Figure 3. Time-Dependent Coordinate System for Stern Waves at Fr = 2.0

At the bottom and downstream boundaries Equations (7) and (8) become

$$x_\xi\phi_\eta - x_\eta\phi_\xi = 0 \qquad \text{on } \partial\Omega_4' \tag{23}$$

$$y_\eta\phi_\xi - y_\xi\phi_\eta = -J/(y(s_{\xi},t)-h) \qquad \text{on } \partial\Omega_5' \tag{24}$$

Since the shape of the fluid region is not known in advance but is part of the solution, the transformation cannot be carried out in advance. Equations (15), which generate the transformation, must be solved at each time step in conjunction with the solution of the fluid flow problem (17)-(24).

IV. THE NUMERICAL SCHEME

This section presents the numerical aspects of both the transformation and flow problem solution. The domain of integration in the (ξ,η)-plane is replaced by a uniform network of points specified by $(\xi = i, \eta = j)$, with $i = 1,\ldots,\xi_\ell$ and $j = 1,\ldots,\eta_\ell$ (Figure 2). The differential equations used to compute the transformation and the potential are replaced by difference equations involving the values of the variables at these grid points.

To compute the transformation, Equations (15) are replaced by central difference formulae yielding

$$\begin{aligned}\begin{Bmatrix} x_{ij} \\ y_{ij} \end{Bmatrix} = &\left[(\alpha_{ij} + J_{ij}^2 P_{ij}/2) \begin{Bmatrix} x_{i+1,j} \\ y_{i+1,j} \end{Bmatrix} \right. \\ &+(\alpha_{ij} - J_{ij}^2 P_{ij}/2) \begin{Bmatrix} x_{i-1,j} \\ y_{i-1,j} \end{Bmatrix} \\ &+(\gamma_{ij} + J_{ij}^2 Q_{ij}/2) \begin{Bmatrix} x_{i,j+1} \\ y_{i,j+1} \end{Bmatrix} \\ &+(\gamma_{ij} - J_{ij}^2 Q_{ij}/2) \begin{Bmatrix} x_{i,j-1} \\ y_{i,j-1} \end{Bmatrix} \\ &-(\beta_{ij}/2) \begin{Bmatrix} x_{i+1,j+1}+x_{i-j,j-1}-x_{i-1,j+1} \\ y_{i+1,j+1}+y_{i-1,j-1}-y_{i-1,j+1} \end{Bmatrix} \\ &\left. \begin{matrix} -x_{i+1,j-1} \\ -y_{i+1,j-1} \end{matrix} \right\} \Big] /2(\alpha_{i,j} + \gamma_{i,j}) \end{aligned} \tag{25}$$

where α_{ij}, β_{ij}, γ_{ij}, and J_{ij} are central difference approximations to Equations (16).

The source terms P and Q are specified to produce an expanding grid in the vertical direction with fine spacing near the free-surface (Figure 3). A complete discussion of how these source terms are defined can be found in the Appendix.

Equation (17) is replaced by the difference equation

$$\begin{aligned}\phi_{ij} = &\left[(\alpha_{ij}+J_{ij}^2 P_{ij}/2)\phi_{i+1,j} \right. \\ &+(\alpha_{ij}-J_{ij}^2 P_{ij}/2)\phi_{i-1,j}+(\gamma_{ij}+J_{ij}^2 Q_{ij}/2)\phi_{i,j+1} \\ &+(\gamma_{ij}-J_{ij}^2 Q_{ij}/2)\phi_{i,j-1}-(\beta_{ij}/2)(\phi_{i+1,j+1} \\ &\left. +\phi_{i-1,j-1}-\phi_{i+1,j-1}-\phi_{i-1,j+1}) \right] /2(\alpha_{ij}+\gamma_{ij}) \end{aligned} \tag{26}$$

Euler's modified method of time differencing is used to replace the free-surface boundary conditions (18), (19), and (20) by

$$y_{i,\eta_\ell}^{n+1} = y_{i,\eta_\ell}^{n} + \Delta t(F_i^{n+1} + F_i^n)/2 \tag{27}$$

$$x_{i,\eta_\ell}^{n+1} = x_{i,\eta_\ell}^{n} + \Delta t(G_i^{n+1} + G_i^n)/2 \tag{28}$$

$$\phi_{i,\eta_\ell}^{n+1} = \phi_{i,\eta_\ell}^{n} + \Delta t(H_i^{n+1} + H_i^n)/2 \tag{29}$$

where the superscripts refer to time levels, Δt is the time increment, and F_i, G_i, and H_i are the finite-difference approximations to the right-hand sides of (18), (19), and (20). The discretized versions of the boundary conditions (21)-(24) are found by replacing each derivative with the appropriate finite-difference formula.

The finite-difference forms of the potential, transformation, and boundary condition equations are solved in a combined iterative procedure using successive over-relaxation (SOR). Grid points on the hull and free surface are allowed to move with the fluid while the position of the grid points in the interior of the fluid is determined by the transformation. Thus a new grid point distribution and the flow field are computed simultaneously. The iterations are halted when the percentage change of x, y, and ϕ from iteration to iteration is less than some specified small number, usually on the order of 0.1%.

A numerical filtering scheme was introduced to eliminate the instability which is usually present in such marching methods for nonlinear water wave problems. After each advancement of the free-surface variables, x_{i,η_ℓ}^{n+1}, y_{i,η_ℓ}^{n+1}, and ϕ_{i,η_ℓ}^{n+1}, new quantites are computed according to the smoothing formula

$$f_i' = \left[-f_{i+2} - f_{i-2} + 4(f_{i+1}+f_{i-1}) + 10 f_i \right] /16 \tag{30}$$

This same filtering technique was used successfully by Haussling & Coleman [3] to eliminate such a numerical instability previously encountered in free-surface calculations with very steep wave slopes.

V. RESULTS

The six different Froude numbers considered are listed in Table 1.

Froude Number (Fr)	Length of channel	Initial Δx	Maximum peak-to-trough height (A)	Time to maximum height	Minimum distance to first peak (D)	Comp. time required
2.35	238	0.85	3 91	160 0	11.43	9600 sec.
2.30	238	0 85	4.12	148.0	9.82	7000 sec.
2.25	196	0.70	4.13	121.6	9.73	5800 sec.
2.20	196	0.70	3.95	104.1	8.16	4000 sec.
2 00	196	0 70	3.21	63 8	6 51	2600 sec.
1.75	196	0.70	2.31	35 0	5 00	1500 sec

Table 1. Miscellaneous Data

This table contains numerical and computational data for each case including some quantities which will be defined later. The length of the tank was approximately equal to its depth for each Froude number. The initial position of the transom stern was about one linear wave length, $2\pi Fr^2$, away from the downstream boundary for all the runs. In all cases, 5901 points were used to resolve the fluid region Ω. The computer program required about 200K words of memory on the CDC Cyber 74 located at DTNSRDC.

The case with highest Froude number, Fr = 2.35, is the only case which did not produce breaking conditions. This was chosen as the first test case to verify that the mathematical/numerical scheme would produce a solution consistent with those obtained earlier by different methods. As the free-surface evolves for this froude number, the height of the first peak behind the stern reaches a maximum at dimensionless time t = 160. The height then decreases and approaches the steady-state value which is about 90% of the maximum achieved. As this peak develops, it moves toward the stern until it reaches its maximum height. It then moves away from the stern slightly as the solution approaches the known steady-state result in an oscillatory manner. Figure 4 compares the free-surface profile for this Froude number at t = 210 to that for the steady-state solution obtained by Vanden-Broeck. (In Figure 4, and in some subsequent figures, results are presented from a frame of reference moving with the hull so that the stern is in the same location at all times.) Also included in Figure 4 is the linear solution showing that nonlinear effects are quite significant at this Froude number. It is evident that the two nonlinear solutions agree well near the first peak and trough even though the free surface for the transient problem has

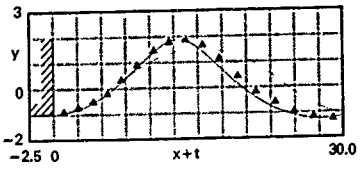


Figure 4. Free Surface Elevation for Fr=2.35. ——, Almost Steady Nonlinear at t=210; ▲, Steady-State Nonlinear (Vanden-Broeck); ------, Steady-State Linear

not yet developed fully farther downstream. Figure 5 shows the distribution of pressure on the hull at t = 210.

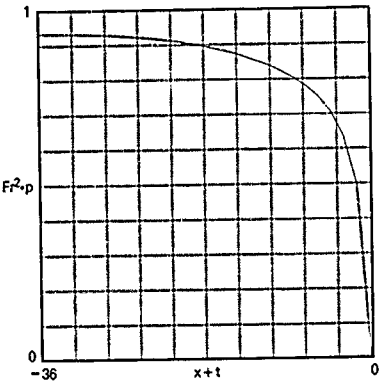


Figure 5. Almost Steady-State Pressure on the Hull for Fr=2.35 at t=210.

The pressure at the upstream boundary undergoes small oscillations about the expected hydrostatic value as the free-surface profile approaches its ultimate form.

For the lower Froude numbers, the initial free-surface evolution is similar to that at Fr = 2.35. However, as the first peak grows and moves toward the stern, the upstream face becomes vertical near the crest. Beyond this state accurate resolution is no longer possible with this method and the calculations cease to converge. The free-surface development for three different Froude numbers is shown in Figure 6. In reality, these waves become breaking stern waves in which water spills down the

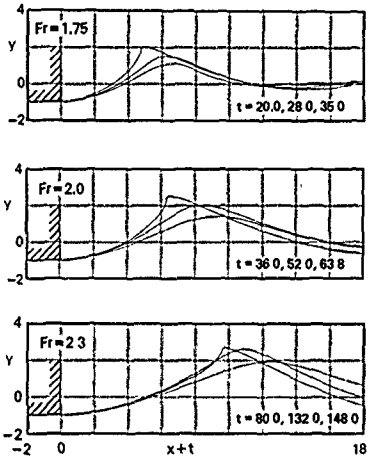


Figure 6. Free Surface Development for Three Froude Numbers

upstream face. (Although this method cannot predict the exact moment of breaking, for convenience we will refer to the time at which a vertical face is reached as the time of breaking.) For all the breaking cases, the first peak achieves its maximum height and is nearest the stern at the time of breaking. The free-surface profiles at the latest computed time are superimposed in Figure 7.

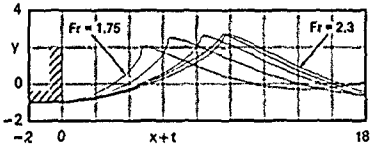


Figure 7. Surface Elevations at Time of Breaking for Various Fr

It is difficult to relate earlier steady-state results based on waves far downstream to the unsteady results of the current study in which these downstream waves never develop. Two quantities which are meaningful for both steady and unsteady results are D and A as defined in Figure 8. D denotes the distance

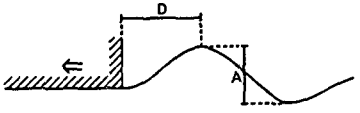


Figure 8. Definition of D and A

from the stern to the first wave peak downstream and A denotes the peak-to-trough height of this wave. In a steady-state solution, the value of A does not differ greatly from similar measurements taken farther downstream. Hence, values of A in unsteady solutions can be compared to downstream wave heights in steady-state solutions.

The maximum values of A for all cases are plotted against the square of the Froude number in Figure 9.

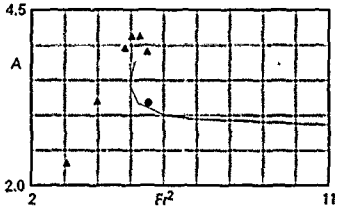


Figure 9. Peak-to-Trough Wave Heights. ▲, Maximum; ●, Almost Steady-State; ———, Steady-State (Vanden-Broeck)

In addition Figure 9 shows the steady-state value of A for Fr = 2.35 and steady-state wave heights given by Vanden-Broeck for elevations far downstream from the hull. At Fr = 2.35, the almost steady-state value of A agrees well with the results of Vanden-Broeck. As mentioned earlier, A at steady-state is about 90% of the maximum achieved. For Fr = 2.25 and Fr = 2.3 the current transient approach does not produce steady-state solutions, despite the fact that one or more such solutions are known to exist for Froude numbers in this range. It seems likely that these Froude numbers are ones for which stable solutions can be achieved after an abrupt acceleration only by passing through intermediate conditions where breaking is present. Figure 9 shows that A is greatest for Froude numbers in the critical region around Fr = 2.25 and Fr = 2.3. As the Froude number decreases, breaking conditions occur at decreasing values of A.

The minimum value of D (distance from stern to first peak) for each of the six cases is plotted against the square of the Froude number in Figure 10.

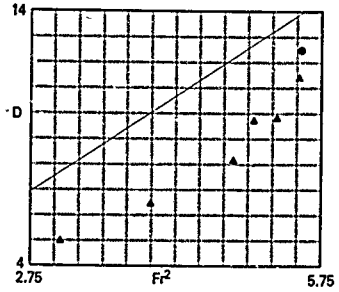


Figure 10. Distance to First Peak.
▲, Minimum Nonlinear; ●, Steady-State Nonlinear
————, Steady-State Linear

For all Froude numbers considered, minimum D occurs simultaneously with maximum A. These extrema are achieved at the time of breaking for the breaking cases. In the only non-breaking case, Fr = 2.35, the minimum value of D is about 90% of its steady-state value also shown in Figure 10. In addition, Figure 10 displays the linear steady-state value of D which is proportional to Froude number squared. It can be seen that minimum and steady-state values of D for the nonlinear calculations are less than the corresponding linear steady-state values.

The time from the abrupt acceleration until A reaches its maximum (time of breaking for all cases except Fr = 2.35) increases with Froude number. These times are plotted versus the square of the Froude number in Figure 11.

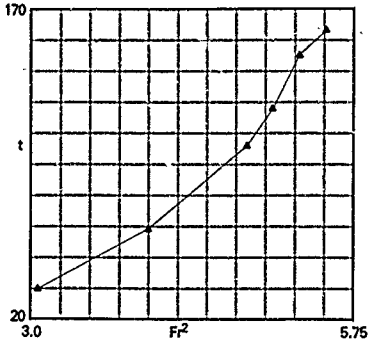


Figure 11. Time Required to Reach Maximum Wave Height A

VI. CONCLUSIONS

Finite-difference techniques are used with boundary-fitted coordinates to analyze the unsteady nonlinear waves generated by the stern of a semi-infinite two-dimensional flat-bottomed ship at the free surface of a fluid. The flow is assumed to separate smoothly from the hull at a sharp trailing edge. A range of six draft-based Froude numbers is considered from Fr = 1.75 to Fr = 2.35. At Fr = 2.35 an almost steady-state solution is obtained that compares well with previous numerical results. At all other values of Fr studied, the calculations are continued until breaking wave conditions are encountered. Higher resolution or an improved mathematical model or both are needed in order to continue the computations beyond the time of breaking. As the Froude number increases, the time needed for the stern waves to achieve maximum height and the distance from the stern to the maximum peak both increase. The maximum height attained increases with Froude number up to approximately Fr = 2.25 or Fr = 2.3. Beyond this region the maximum height decreases with Froude number and, instead of breaking, the solution approaches the known steady-state result in an oscillatory fashion.

The current study gives an important picture of the way in which unsteady solutions fit in with the steady solutions of previous work. Three Froude number ranges can be defined. For Fr < 2.23, no steady-state solution exists and the unsteady approach yields a solution which evolves until a breaking condition occurs. For 2.23 < Fr < Fr*, one or more steady-state solutions exist and the unsteady method also leads to breaking stern waves. The present results indicate that Fr* lies between 2.3 and 2.35. For Fr > Fr*, a steady-state solution exists and the unsteady flow approaches this solution asymptotically.

VII. ACKNOWLEDGMENT

This work was supported by the Numerical Naval Hydrodynamics Program at the David W. Taylor Naval Ship Research and Development Center. This program is jointly sponsored by the DTNSRDC and Office of Naval Research.

VIII. APPENDIX

To obtain uniform horizontal spacing for the original mesh at t = 0, the mesh points were evenly spaced on both horizontal boundaries and P was choosen as zero throughout the field (P = 0). Since approximately uniform

horizontal spacing is desired during all the calculations, the time-independent P function is given by

$$P_{ij}=0 \quad \text{for } i=1,\ldots,\xi_\ell \text{ and } j=1,\ldots,\eta_\ell$$

To provide an expanding grid in the vertical direction with highest resolution near the free surface, the points on each vertical boundary were given the desired distribution and a Q source term for both boundaries was calculated as follows :

$$Q_{1,j} = (-y_{\eta\eta}/y_\eta^3)_{1,j} \quad \text{for the upstream boundary}$$

$$Q_{\xi_\ell,j} = (-y_{\eta\eta}/y_\eta^3)_{\xi_\ell,j} \quad \text{for the downstream boundary}$$

where $j = 1,\ldots,\eta_\ell$. The Q function for points in the field is then given by the linear distribution

$$Q_{ij} = Q_{1,j} + (Q_{\xi_\ell,j} - Q_{1,j})(i-1)/(\xi_\ell-1)$$

for $i = 2,\ldots,\xi_\ell-1$ and $j = 2,\ldots,\eta_\ell-1$. Plant [4] used this form of Q function which is similar to those derived by Thompson [5] and Ghia [6]. Its use ensures that the spacing throughout the flow field is similar to the coordinate spacing on the boundary.

The upstream boundary does not change with time and therefore the $Q_{1,j}$ remain constant throughout the calculations. The downstream boundary, however, intersects the free surface and may change in height as the free surface evolves. This change requires a redistribution of grid points on the downstream boundary. If a redistribution of points occurs at any time step, then the $Q_{\xi_\ell,j}$, and hence the Q_{ij} in the field, must be recalculated to maintain the proper grid spacing.

REFERENCES

[1] Vanden-Broeck, J.-M., "Nonlinear Stern Waves," J. Fluid Mech (1980), Vol. 96, part 3, pp. 603-611.

[2] Haussling, H.J., "Two-dimensional Linear and Nonlinear Stern Waves," J. Fluid Mech. (1980), Vol. 97, part 4, pp. 759-769.

[3] Haussling, H.J. and R.M. Coleman, "Nonlinear Water Waves Generated by an Accelerated Circular Cylinder," J. Fluid Mech. (1979), Vol. 92, part 4, pp. 767-781.

[4] Plant, T.J., "An Exact Velocity Potential Solution of Steady, Compressible Flow over Arbitrary Two-Dimensional and Axisymmetric Bodies in Simply Connected Fields," AFFDL-TR-77-116 (1977), Air Force Flight Dynamics Laboratory, Wright-Patterson Air Force Base.

[5] Thompson, J.F. and S.P. Shanks, "Numerical Solution of the Navier-Stokes Equations for 2-D Surface Hydrofoils," MSSU-EIRS-ASE-77-4 (1977), Engr. and Industrial Research Station, Mississippi State Univ.

[6] Ghia, U., et al, "An Optimization Study for Generating Surface-Oriented Coordinates for Arbitrary Bodies in High-Re Flow," AFFDL-TR-77-117 (1977), Air Force Flight Dynamics Laboratory, Wright-Patterson Air Force Base.

DISCUSSION
of the paper
by R.M. Coleman and H.J. Haussling

NONLINEAR WAVES BEHIND AN ACCELERATED TRANSOM STERN

Discussion
by Shee-Mang Yen

I have questions concerning the mesh generation and filtering

(1) Mesh generation

(a) What is a typical time step Δt ?

(b) What is the number of time steps you used for solutions using this time step.

(c) Do you update the mesh system after each time step ?

(d) Is it necessary to rezone the mesh when it changes very rapidly (e.g. near wave breaking) ? How is it done ?

(e) What is the percentage of computation time used for the mesh generation for a typical run ?

(2) Filtering

(a) Do you filter after each time step ?

(b) Do you filter the entire flow field or locally ?

(c) Does the filtering start from the beginning ($t = 0$) ?

Authors' reply

The authors would like to thank Professor Yen for his discussion. The time step used for each case varied with Froude number ranging from $\Delta t = 0.2$ for $Fr = 1.75$ to $\Delta t = 0.5$ for $Fr = 2.35$. Only for $Fr = 2.35$ was an almost steady-state condition reached. For this Froude number, the computation was continued for 420 time steps and the solution was stable at this point. All other cases were run until breaking conditions were encountered beyond which accurate resolution was not possible and the calculations ceased to converge. The number of time steps varied from approximately 175 for $Fr = 1.75$ to 300 for $Fr = 2.3$

The mesh and the velocity potential are calculated simultaneously at each time step so that the coordinate system adapts to the time-dependent physical region as the free-surface evolves. Since the equations which generate the transformation are solved at each time step in conjunction with the solution of the fluid flow problem, it is difficult to separate the time used to compute the mesh from that used for the velocity potential. We estimate that between 25 % and 30 % of the total computation time is spent on the mesh with more time needed when the free-surface is changing rapidly.

The filtering technique is imposed, beginning at $t = 0$, along the entire free-surface at each time step.

FLOW ABOUT TRANSOM STERNS

R.T. Van Eseltine and H.J. Haussling
David W. Taylor
Naval Ship Research and Development Center
Bethesda, Maryland 20084

ABSTRACT

A finite difference method is used to analyze the linearized unsteady waves generated by the stern of a 3-D semi-infinite ship hull in the water surface. The flow is assumed to detach from the base of the transom stern or farther upstream if the hull pressure falls to zero. The wetted area is computed as part of the solution. To optimize the distribution of grid points, an exact mapping is applied which maps the physical region onto a box computational region. The transformations are chosen such that the grid lines are concentrated in the areas in which accuracy is needed. The solution is advanced in time by a marching scheme which couples the solution of the Laplace equation and hull boundary condition with the dynamic and kinematic free-surface conditions.

Two hull shapes are studied for various draft-based Froude numbers. Pressures, wave patterns, and flow fields are presented and compared with experimental data. Reasonable agreement with experimental data is shown. To obtain quantitative results for realistic hull shapes, the importance of retaining a nonlinear term in the linearized governing equations is shown. This paper demonstrates that a numerical scheme based on linearized free-surface potential flow can yield useful results, at least for the types of hulls and Froude number range considered.

I. INTRODUCTION

The details of the flow at the bow and stern determine the main hydrodynamic characteristics of a ship hull. Experimental and theoretical studies of bow and stern flows were discussed by Baba [1]. Because it is difficult to study the details of these flows simultaneously, researchers have studied semi-infinite hulls with only a bow or only a stern. Dagan & Tulin [2] studied steady flows generated by bows of two-dimensional (2-D), semi-infinite hulls. Steady nonlinear flows generated by sterns of 2-D, semi-infinite hulls were investigated by Vanden-Broeck & Keck [3], Vanden-Broeck, et al [4], and Vanden-Broeck [5]. Haussling [6] and Coleman & Haussling [7] studied unsteady nonlinear flows caused by sterns of 2-D, semi-infinite hulls.

To study features of bow and stern flows, researchers have also extensively investigated planing hulls. Doctors [8,9] has published extensive surveys of the literature in this area. The steady, linear, 2-D planing problem was often treated with the assumption that the hull had a monotonically increasing draft from bow to stern. This problem was often attacked using an inverse approach in which the flow due to a moving pressure disturbance is computed first. Then the strength of the pressure is determined by an integral equation such that the free surface will coincide with the hull. The wetted length is usually fixed and the location of the hull is determined. Haussling & Van Eseltine [10] used a direct method for the unsteady case of the linear, 2-D planing hull problem. The location of the hull was fixed and the wetted length was determined. The draft of the hull was not assumed to increase monotonically from bow to stern.

In the three-dimensional (3-D), linear planing problem, the wetted area must be determined. To do this, researchers often simplify the problem by making assumptions on the shape and speed of the hull. For example, Casling [11] and Casling & King [12] assumed infinite Froude number and a hull with a low aspect ratio. They also restricted the shape of the hull to ensure that the flow detached only at the transom stern.

The present paper describes a numerical scheme for studying the stern flow generated by a 3-D transom stern hull moving at a constant speed. The hull is semi-infinite (no bow), and the problem is linearized. The location and shape of the hull are fixed, and the wetted area is determined as part of the solution. Pressure and wave elevations are computed and compared with experimental data. Although this work considers only the stern, it represents a step forward in that there are no fundamental restrictions on hull shape or speed.

II. MATHEMATICAL FORMULATION

The problem considered is the flow development due to an impulsively accelerated semi-infinite hull (no bow) moving at constant speed U in a water surface. The hull is of finite beam b and draft d. The flow is assumed to be irrotational, and the fluid is considered

to be incompressible and inviscid and to lack surface tension. A right-handed (x',y',z') coordinate system moving with the hull has its origin at the intersection of the stern, the hull centerline, and the undisturbed free surface. The z'-axis points upward and the x'-axis points in the direction opposite to the movement of the hull (Figure 1).

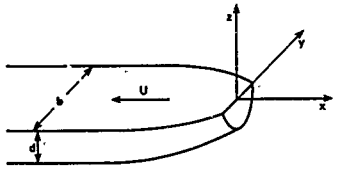


Figure 1 - Transom Stern and Coordinate System

The water is bounded by the hull and a free surface but otherwise is infinite in extent. Therefore, the water surface consists of the wetted area of the hull, $\partial\Omega_H$, and the free surface, $\partial\Omega_F$ (Figure 2).



Figure 2 - Aerial View of Stern and Coordinate System

The water surface is described at any time t' by specifing z' as a single-valued function of x' and y', i.e., $z' = \eta'(x',y',t')$. The hull is described by $z' = f(x',y')$ and thus $\eta' = f$ in $\partial\Omega_H$. The velocities, pressures, and the water surface are assumed to be continuous after the acceleration of the hull.

The flow is assumed to detach at the base of the transom stern immediately after the impulsive acceleration. The wetted area is then allowed to change and is computed as part of the solution. The wetted area is uniquely determined by two conditions: the pressure on the part of the water surface that coincides with the hull must be greater than zero (atmospheric), $p' > 0$ in $\partial\Omega_H$; and the free water surface must be below the hull, $\eta'(x',y',t') < f(x',y')$ in $\partial\Omega_F$.

The variables are nondimensionalized according to the scheme

$$(x',y',z') = d(x,y,z) \qquad t' = (d/U)t$$
$$\phi' = dU\phi \qquad p' = \rho U^2 p \qquad \eta' = d\eta$$

where the primes denote dimensional variables, $\phi(x,y,z,t)$ is the potential for the velocities relative to a reference frame at rest, p is the pressure, and ρ is the density of the fluid.

If the velocities and the upper boundary slope in the x-direction are assumed to be small and the problem is linearized, the nondimensional linearized initial/boundary-value problem in the moving frame of reference may be stated as follows:

1. in the region occupied by the fluid

$$\phi_{xx} + \phi_{yy} + \phi_{zz} = 0 \qquad \left\{ \begin{array}{l} -\infty \le x \le \infty \\ -\infty \le y \le \infty \\ -\infty \le z \le 0 \end{array} \right. \qquad (1)$$

2. at the hull

$$\left. \begin{array}{ll} \phi_z = \eta_x + \eta_y\phi_y, & \text{at } z=0 \\ \eta = f(x,y) & \\ p > 0 & \end{array} \right\} \quad x,y \in \partial\Omega_H \qquad \begin{array}{l} (2) \\ (3) \\ (4) \end{array}$$

3. at the free surface

$$\left. \begin{array}{l} \eta_t = -\eta_x - \eta_y\phi_y + \phi_z \\ \phi_t = -\phi_x - \eta/Fr^2 \end{array} \right| \text{ at } z=0 \left\{ \begin{array}{l} \\ x,y \in \partial\Omega_F \\ \\ \end{array} \right. \qquad \begin{array}{l} (5) \\ (6) \\ (7) \end{array}$$
$$\eta < f(x,y)$$

4. in the far field

$$\phi_x = 0 \qquad \text{at } x = \pm\infty \qquad (8)$$
$$\phi_y = 0 \qquad \text{at } y = \pm\infty \qquad (9)$$
$$\phi_z = 0 \qquad \text{at } z = -\infty \qquad (10)$$

5. and initially

$$\left. \begin{array}{l} \phi = 0 \\ \eta = \left\{ \begin{array}{ll} f(x,y), & x,y \in \partial\Omega_H \\ 0 & \text{otherwise} \end{array} \right. \end{array} \right\} \text{ at } t=0 \qquad (11)$$

where subscripts x, y, z, and t denote differentiation with respect to these variables, $Fr = U/\sqrt{gd}$ is the Froude number based on draft, and g is the gravitational acceleration.

Although it is assumed that the derivative of the upper boundary in the x-direction is small, the derivative in the y-direction is not assumed to be small to allow for realistic sidewalls. Thus, the nonlinear term $\eta_y\phi_y$ is retained in equations (2) and (5). In addition, the retention of this term allows the discontinuity that exists in η_x in the y-direction to be reflected in $\eta_y\phi_y$. Numerical experiments show that, if $\eta_y\phi_y$ is not included in the equations, the surface discontinuity is balanced by a highly unrealistic discontinuity

in the velocity. Except for the inclusion of this term, equations (1) through (11) constitute an unsteady version of the usual flat-ship theory for planing surfaces.

The pressure on the hull can be computed by the linearized Bernoulli equation

$$p = -\phi_t - \phi_x - \eta/Fr^2. \tag{12}$$

Therefore, the pressure can be considered as composed of a hydrostatic pressure p_h and a dynamic pressure p_d, where

$$p_h = -\eta/Fr^2 \tag{13}$$

and

$$p_d = -\phi_t - \phi_x. \tag{14}$$

III. NUMERICAL SCHEME

Since the problem is symmetric about the centerline, equation (9) is replaced by

$$\phi_y = 0 \qquad \text{at } y = -\infty \text{ and } y = 0 \tag{15}$$

In addition, equation (8) is approximated by

$$\phi_x = 0 \qquad \text{at } x = -L_1 \text{ and } x = +L_2 \tag{16}$$

The error introduced by replacing the boundary condition at $x = \pm\infty$ with equation (12) is small if L_1 and L_2 are sufficiently large. To optimize the distribution of grid points, an exact mapping is applied in the y- and z-directions before the problem is discretized. The transformations used are

$$y = a_1/(r+1) + a_2 r + (a_3/2)r^2 + (a_4/3)r^3 + (a_5/4)r^4 + a_6 \tag{17}$$

and

$$z = (\ln(s))/c. \tag{18}$$

These transformations are applied to map the infinite physical region in (x,y,z) space onto a box computational region in (x,r,s) space. The box computational region is bounded by $x = -L_1$, $x = +L_2$, $r = -1$, $r = 0$, $s = 0$, and $s = +1$ (Figure 3). The parameters c and a_1 through a_6 are used to control the spacing of the grid lines (discussed later in this section).

The governing equations are transformed according to the relations

$$(\phi_x)_{\text{at } y,z=\text{constant}} = (\phi_x)_{\text{at } r,s=\text{constant}}$$
$$\phi_y = \phi_r/y_r \tag{19}$$
$$\phi_z = \phi_s/z_s$$

where the subscripts r and s denote differentiation with respect to these variables. For

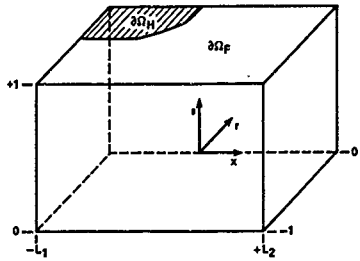


Figure 3 – Computational Region and Coordinate System

instance, the Laplace equation transforms into

$$\phi_{xx} + A\phi_{rr} + B\phi_{ss} + C\phi_r + D\phi_s = 0 \tag{20}$$

where

$$A = 1/y_r^2$$
$$B = 1/z_s^2$$
$$C = -y_{rr}/y_r^3 \tag{21}$$
$$D = -z_{ss}/z_s^3$$

and where x derivatives now imply that (r,s) rather than (y,z) are being held constant.

The domain of the computational region is replaced by a uniformly spaced 101 x 41 x 21 grid system. The grid spacing is defined by Δx in the x-direction, Δr in the r-direction, and Δs in the s-direction. The parameter c is chosen to obtain the desired rate of expansion of the z grid lines. The parameters a_1 through a_6 are used to control

1. the number of r grid lines representing the hull,
2. the y spacing at the maximum beam,
3. the y spacing at the centerline,
4. the y location of the next-to-last r grid line (the last r grid line is at $y = -\infty$)

subject to the conditions that the $r = 0$ grid line corresponds to $y = 0$ and the y spacing at the maximum beam is a minimum.

The time advancement of the solution of the boundary-value problem has three basic parts. The first part consists of determining

the wetted area of the hull. Grid points representing the water surface are either wetted hull points or free-surface points. If at the beginning of a time step the pressure is negative at one or more hull grid points, the wetted area is decreased and those points are treated as free-surface points throughout the time step. Alternatively, if any free-surface grid points have moved upward to meet the hull, those points become hull points. Thus, during the flow development, a grid point on the water surface can change its character between that of a hull point and that of a free-surface point.

The second part of the time advancement process consists of advancing in time the free-surface elevation, η, and the free-surface potential, ϕ_f ($\equiv\phi(x,y,0)$ in $\delta\Omega_F$), according to the transformed versions of equations (5) and (6). Euler's modified method is used to replace these equations by difference equations of the form

$$\eta_{i,j}^{m+1} = \eta_{i,j}^{m} + \Delta t(F_{i,j}^{m+1} + F_{i,j}^{m})/2 \qquad (22)$$

and

$$\phi_{f\,i,j}^{m+1} = \phi_{f\,i,j}^{m} + \Delta t(G_{i,j}^{m+1} + G_{i,j}^{m})/2 \qquad (23)$$

where the superscripts refer to time levels, the subscripts i,j refer to the x and r location of the grid point, Δt is the time increment, and $F_{i,j}$ and $G_{i,j}$ are approximations to the right hand sides of the transformed free-surface boundary equations (5) and (6). The derivatives involved in $F_{i,j}$ and $G_{i,j}$ are approximated by standard second-order central spatial differencing for derivatives with repect to x and r, and second-order one-sided spatial differencing for derivatives with respect to s. Because of the complications added to the equations by the transformations, the finite-difference equations cannot be solved directly but are solved using a Gauss-Seidel iterative procedure.

The third part of the time advancement process consists of the solution of the Laplace equation (20), given the transformed boundary conditions of equations (2), (10), (15), (16), and a known ϕ_f from part two. Standard second-order central differencing is used. Again, iterative techniques must be used and the difference equations are solved with successive overrelaxation.

The three parts of the time advancement process are linked in the following way: At the beginning of a time step, the wetted area of the hull is determined by the method described in part one. Then, initial estimates of η and ϕ are obtained by extrapolation from previous time steps. The iterative procedures of parts two and three are combined into one iterative procedure where new estimates of η and ϕ_f are found from equations (22) and (23). These new estimates are then used in the finite difference version of equation (20) to obtain new estimates of ϕ. This ϕ is then used to further update η and ϕ_f. This combined procedure is repeated until there is less then 0.1% change in ϕ everywhere from iteration to iteration. This time advancement process is used repeatedly to advance the quantities in time to simulate the flow development, with the transformed initial conditions of equation (11) as a starting point.

Three numerical instabilities were encountered in the solution to this problem. The first instability occured at the upstream boundary where the free surface continued to grow in time. A pressure damping technique was applied to a small region on the free surface near the upstream boundary. Since this pressure is proportional to ϕ_z at the surface, it will tend to exert a force on the free surface in the direction opposite to the movement of the surface. Thus, the pressure applied does negative work and can only remove energy from the system. The proportionality constant varied linearly from zero at the tenth grid line to a value of one at the upstream boundary. The pressure stabilized the free surface at the upstream boundary but had little effect on the important part of the solution.

The second numerical instability encountered was on the hull, where the steepness of the sidewall slopes in the y-direction caused the scheme to diverge within the iterative procedure. To stabilize this procedure, under-relaxation was applied to the finite difference version of equation (2). The under-relaxation factor was chosen proportional to $1/\eta_y^2$ with an upper limit of one.

The third numerical instability occured on the free surface near the hull. Filtering was applied at the free surface at the beginning of each time step to eliminate this problem. Such filtering schemes, originally discussed by Shapiro [13], have been successfully used many times (e.g., Longuet-Higgins & Cokelet [14] and Haussling [6]). New values for η and ϕ_f were computed according to the smoothing formula

$$h_n' = (-h_{n-2}-h_{n+2}+4(h_{n-1}+h_{n+1})+10h_n)/16 \qquad (24)$$

where the prime denotes the new estimate and the subscript n denotes the grid point in the x- or r-direction.

A computer program was written for a Texas Instruments Advanced Scientific Computer (TI-ASC) to implement the numerical scheme. To vectorize the calculations, a "red-black" method [15] was used in sweeping the grid in the iterative procedure. Each time step averaged 4 to 5 iterations and required about 1.7 seconds of TI-ASC central processor time. Each solution presented in this paper was computed for 1000 time steps and took approximately 30 minutes of TI-ASC central processor time. By the last time step, the transient effects near the stern were no longer significant, and the flow near the stern could be considered almost at steady-state. The results presented are for these late times and thus represent almost steady-state situations.

IV. RESULTS

The numerical scheme was first applied to a semi-infinite hull, Hull A, whose cross-sectional shape was independent of x. The cross section of Hull A has the same shape as the transom stern on the research ship Athena. Figure 4 shows the shape of this hull and Table 1 gives the values of the pertinent parameters used in the numerical scheme.

TABLE 1.- LIST OF PARAMETERS

Parameter	Hull A	Hull B
b	10.0	3.15
L_1	72	66
L_2	48	24
Δx	1.2	0.8
Δr	0.025	0.025
Δs	0.05	0.05
Δt	0.8	0.25
c	0.6	0.4
a_1	−2.1106	−0.1651
a_2	17.8894	19.8348
a_3	12.5692	−414.4292
a_4	−225.3210	−2217.4637
a_5	−336.8649	−2710.3631
a_6	2.1106	0.1651

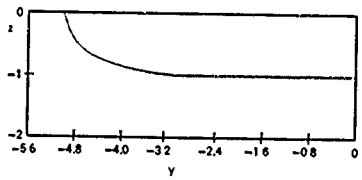


Figure 4 - Body Plan of Hull A

Figure 5 shows the almost steady-state wave elevations for Fr = 2 and Fr = 6. At Fr = 2, the water surface rises rapidly to a peak very close behind the transom. The distance from the stern to the first peak downstream is shorter than that in the 2-D linear problem at this Fr. As expected, at higher Fr the peak shifts farther downstream, and the free surface near the transom stern tends to retain the shape of the hull.

The numerical scheme was also applied to another semi-infinite hull, Hull B, whose cross-sectional shape varied with x to simulate the stern of a typical Navy combatant ship (Figure 6). The shape of Hull B is the same as

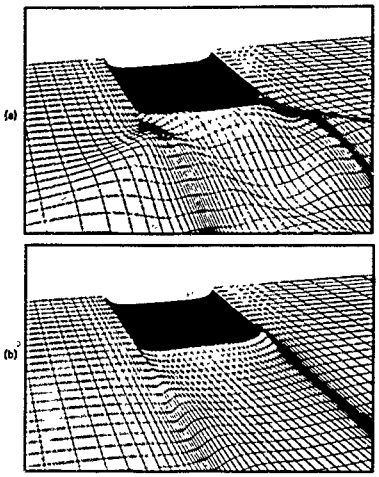


Figure 5 - Wave Elevations for Hull A at (a) Fr=2 and (b) Fr=6

that of the model tested by Jenkins et al [16], except that the cross-sectional shape at the maximum beam of the model was extended infinitly far upstream for Hull B. Table 1 gives the values of interest used in the numerical scheme. Wave elevations are displayed for Fr = 1.66 in Figure 7, Fr = 2.14 in Figure 8, and Fr = 2.67 in Figure 9. The shaded region represents the wetted area of the hull. As Fr increases, the first peak behind the transom moves farther downstream, and its amplitude tends to increase until Fr = 2.14 is reached. Beyond this value of Fr, the amplitude decreases.

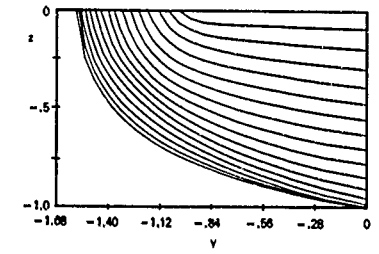


Figure 6 - Body Plan of Hull B

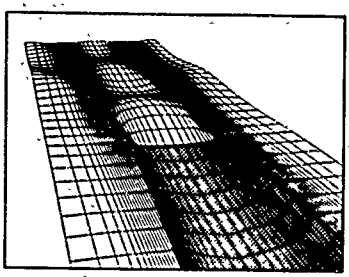


Figure 7 - Wave Elevations and Wetted Hull Surface (Shaded) for Hull B at Fr=1.66

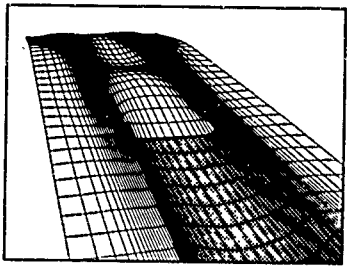


Figure 8 - Wave Elevations and Wetted Hull Surface for Hull B at Fr=2.14

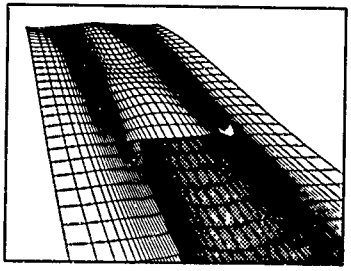


Figure 9 - Wave Elevations and Wetted Hull Surface for Hull B at Fr=2.67

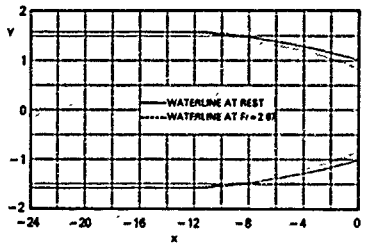


Figure 10 - Aerial View of Waterlines for Hull B at Rest and at Fr=2.67

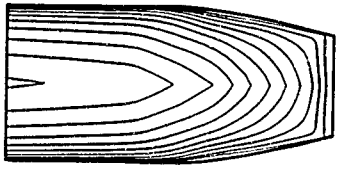


Figure 11 - Aerial View of Total Pressure on Hull B at Fr=2.14. Contours Plotted are p=0.02, 0.04, 0.06, ...

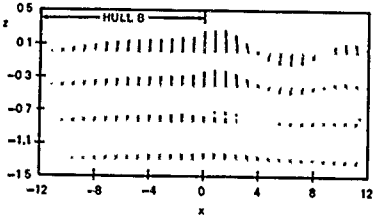


Figure 12 - Velocity Vectors in the Centerplane for Hull B at Fr=2.14

Figures 7, 8, and 9 show that the wetted area diminishes with increasing Froude number. This is emphasized in Figure 10, which shows an aerial view of the waterlines for Hull B at rest and while moving with a Fr = 2.67. Figure 11, displaying contours of pressure at Fr = 2.14, shows the transition of the pressure from hydrostatic far upstream to atmospheric where the flow detaches from the hull. Figure 12 displays velocity vectors in the centerplane for Fr = 2.14 and indicates a sharp rise in ϕ_z as the fluid leaves the transom.

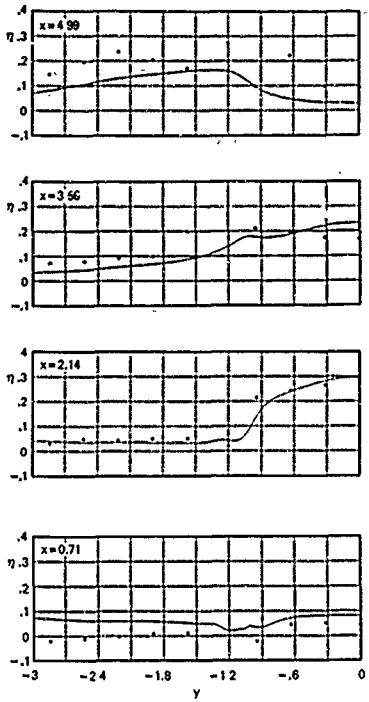


Figure 13 - Computed (——) and Measured (•) Wave Elevations in the y-z Plane for Various Distances Behind Hull B at Fr=1.66

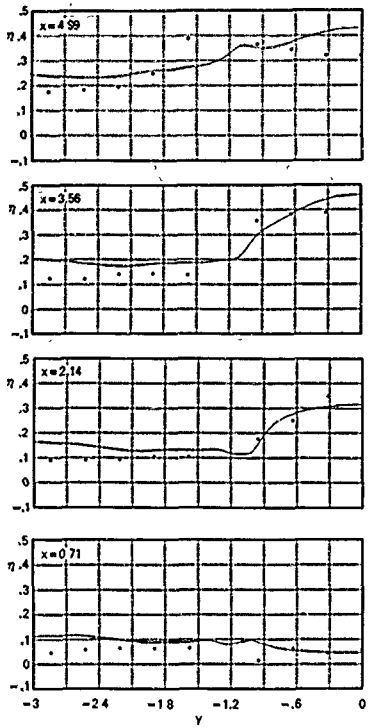


Figure 14 - Computed (——) and Measured (•) Wave Elevations in the y-z Plane for Various Distances Behind Hull B at Fr=2.14

Jenkins et al measured steady wave elevations and pressures near the transom on a model whose afterbody had the same shape as Hull B. Computed and measured wave elevations in the y-z plane are compared for various values of x in Figures 13 through 15. The computed wave elevations show reasonable agreement with the experimental elevations; in particular the location and magnitude of the first peak behind the transom compare very well. Differences in the results can be attributed to experimental inaccuracy and to inaccuracies in the mathematical/numerical scheme.

Comparisons of computed and measured dynamic pressure near the transom for Fr of 1.66, 2.14, and 2.67 are shown in Figure 16. Agreement is reasonable except at the lowest Fr. This may be caused by the lack of resolution needed to compute dynamic pressures at this Fr or by the thickness of the boundary layer at the transom in the experiments. At Fr of 2.67, some of the disagreement is probably due to the effects of the bow wave which are not included in the numerical scheme.

The results discussed so far were obtained with the nonlinear term $\eta_y \phi_y$ included in the governing equations. Results for Hull B were also obtained without this term. For Fr of 2.14, wave elevations along the centerplane for both numerical schemes are compared with the measured data of Jenkins et al in Figure 17. The effect of the nonlinear term is to shift the first peak toward the transom and to decrease its magnitude, leading to results

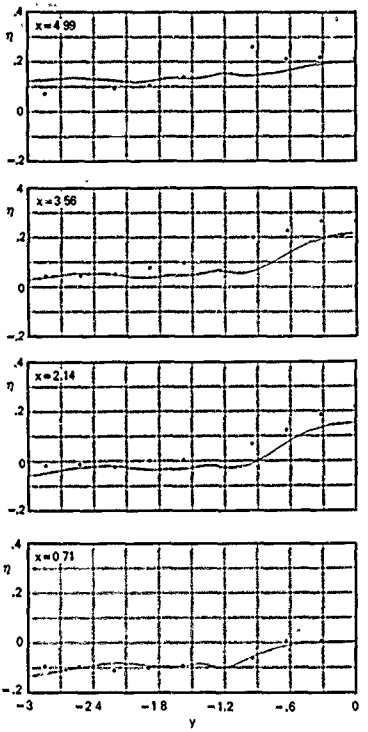


Figure 15 - Computed (——) and Measured (·) Wave Elevations in the y-z Plane for Various Distances Behind Hull B at Fr=2.67

which are in better agreement with the experimental data measured by Jenkins.

The effect of the nonlinear term on total pressure is to decrease the pressure near the transom but to increase it slightly farther upstream. For Fr = 2.14, Figure 18 compares the measured dynamic pressure in the centerplane near the transom with the computed dynamic pressure of both numerical schemes. Again, the inclusion of the nonlinear term leads to results that are in better agreement with measured data.

The significance of the term $\eta_y \phi_y$ can be further highlighted by a study of the balance

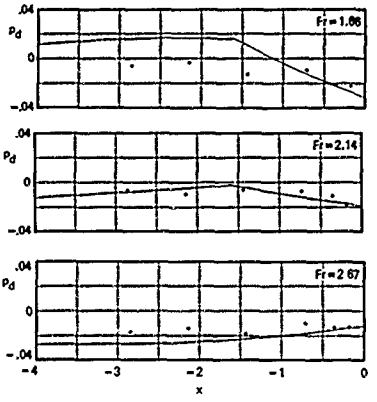


Figure 16 - Computed (——) and Measured (·) Dynamic Pressure Near the Transom of Hull B at Various Froude Numbers

among the various terms in the boundary conditions. At steady-state, the hull and free-surface conditions, equations (2) and (5), are equivalent and represent a balance in either two or three terms involving velocities and surface slopes, depending on whether the nonlinear term is included. The almost steady-state results in Figure 19 indicate that, when $\eta_y \phi_y$ is included, a discontinuity in η_x at the ship sidewall is balanced by a discontinuity in η_y.

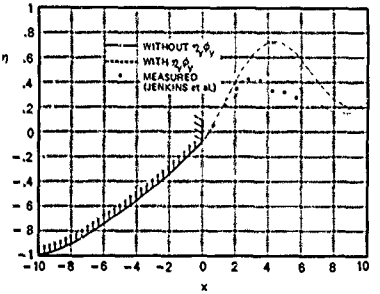


Figure 17 - Measured Wave Elevations and Wave Elevations Computed With and Without the Term $\eta_y \phi_y$ in the Hull and Free-Surface Boundary Conditions

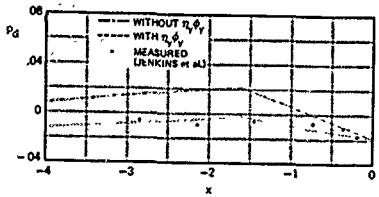


Figure 18 - Measured Dynamic Pressure and Dynamic Pressure Computed With and Without the Term $\eta_y\phi_y$ in the Hull and Free-Surface Boundary Conditions

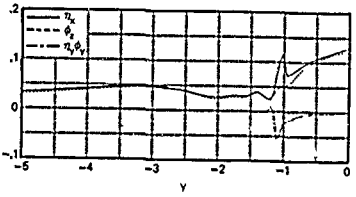


Figure 19 - Values of the Terms in the Surface Boundary Conditions at x=-0.8 When $\eta_y\phi_y$ is Included

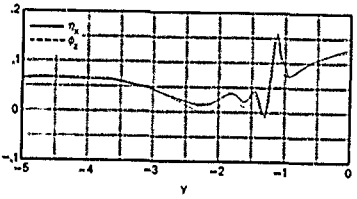


Figure 20 - Values of the Terms in the Surface Boundary Conditions at x=-0.8 When $\eta_y\phi_y$ is Excluded

Figure 20 reveals that, when the nonlinear term is omitted, the discontinuity is forced to appear in the velocity ϕ_z and hence in the other velocity components as well. Since discontinuities in the surface slopes at the hull-free-surface intersection are realistic, but discontinuities in the velocity are unrealistic, the inclusion of the nonlinear term is necessary for reasonable results.

V. CONCLUSION

A numerical method has been used to analyze the linearized unsteady waves generated by the stern of a 3-D semi-infinite hull in the water surface. The unsteady flows approached steady-stat solutions asymptotically. The flow was assumed to detach from the base of the transom stern or farther upstream if the hull pressure fell to zero. The wetted area was computed as part of the solution.

It was shown that, if realistic hull shapes are to be treated accurately, the nonlinear term $\eta_y\phi_y$ must be included in the boundary conditions. The inclusion of this term leads to continuous fluid velocities and improved agreement with experimental results.

As the Fr increased for realistically shaped hulls, the wetted area tended to decrease and the location of the first peak behind the transom tended to move downstream. In addition, the amplitude of this peak increased with Fr until the Fr reached 2.14. Beyond this value of Fr, the amplitude decreased. Wave elevations compared reasonably well with experimental data for the Froude numbers considered in this paper. Similarly, the dynamic pressure compared reasonably with the experimental data except at the lowest Fr.

This work demonstrates that a numerical scheme based on linearized free-surface potential flow can yield useful results, at least for the types of hulls and Froude number range considered. Such a scheme should aid researchers and designers in understanding transom stern flows. However, for treating more general flow situations, additional work is still needed to develop the capability of handling more phenomena such as those due to nonlinear and viscous effects.

VI. ACKNOWLEDGEMENTS

This work was supported by the Numerical Naval Hydrodynamics Program at the David W. Taylor Naval Ship Research and Development Center. This program is jointly sponsored by DTNSRDC and the Office of Naval Research.

REFERENCES

[1] Baba, E., "Wave Breaking Resistance of Ships," International Seminar on Wave Resistance, Tokyo, 1976, The Society of Naval Architects of Japan.

[2] Dagan, G. and M.P. Tulin, "Two-dimensional Free-Surface Gravity Flow Past Blunt Bodies," J. Fluid Mech., vol. 51, 1972, p. 529.

[3] Vanden-Broeck, J.M. and E.O. Tuck, "Computation of Near-Bow or Stern Flows, Using Series Expansion in the Froude Number," Proc. of the Second International Conference on Numerical Ship Hydrodynamics, University of California, Berkeley, Ca., 1977, p. 371.

[4] Vanden-Broeck, J.M. et al, "Divergent Low Froude Number Series Expansion of Nonlinear Free-Surface Flow Problems," Proc. Roy. Soc. Lond. A 361, 1978, p. 207.

[5] Vanden-Broeck, J.M., "Nonlinear Stern Waves," J. Fluid Mech., vol. 96, 1980, p. 603.

[6] Haussling, H.J., "Two-Dimensional Linear and Nonlinear Stern Waves," J. Fluid Mech., vol. 97, 1980, p. 759.

[7] Coleman, R.M. and H.J. Haussling, "Nonlinear Waves Behind an Accelerated Transom Stern," Third International Conference on Numerical Ship Hydrodynamics, Paris, France, 1981.

[8] Doctors, L.J., "Representation of Three-Dimensional Planing Surfaces by Finite Elements," Proc. of the First International Conference on Numerical Ship Hydrodynamics, David W. Taylor Naval Ship Research and Development Center, Bethesda, Md., 1975, p. 517.

[9] Doctors, L.J., "Theory of Compliant Planing Surfaces," Proc. of the Second International Conference on Numerical Ship Hydrodynamics, University of California, Berkeley, Ca., 1977, p. 185.

[10] Haussling, H.J. and R.T. Van Eseltine, "Numerical Solution of Planing-Body Problems," David W. Taylor Naval Ship Research and Development Center Report 76-0118, August, 1976.

[11] Casling, E.M., "Planing of a Low-Aspect-Ratio Flat Ship at Infinite Froude Number," J. of Engineering Math., vol. 12, No, 1, January 1978, p. 43.

[12] Casling, E.M. and G.W. King, "Calculation of the Wetted Area of a Planing Hull With a Chine," J. of Engineering Math., vol. 14, No. 3, July 1980, p. 191.

[13] Shapiro, R., "Linear Filtering," Mathematics of Computation, vol. 2, 1975, p. 1394.

[14] Longuet-Higgins, M.S. and E.D. Cokelet, "The Deformation of Steep Surface Waves. I. A Numerical Method of Computation," Proc. Roy. Soc. Lond. A 350, 1976, p. 1.

[15] Young, D.M., Iterative Solutions of Large Linear Systems, Academic Press, N.Y., 1971.

[16] Jenkins, D. et al, "Flow Characteristics of a Transom Stern Ship," David W. Taylor Naval Ship Research and Development Center Report, (to be published)

DISCUSSIONS
of the paper
by R T. Van Eseltine and H.J. Haussling

FLOW ABOUT TRANSOM STERNS

Discussion
by Shee-Mang Yen

Results look very impressive. I am not sure about your treatment of the outflow boundary. Is it fixed ? If so, how is it chosen ? How is the boundary condition implemented here ?

Discussion
by H. Miyata

The authors' understanding that means that discontinuities in the velocity are unrealistic seems to me unrealistic. Waves in the near-field of ships are nonlinear being accompanied with discontinuity, as the experimental investigations at the University of Tokyo indicate. As for stern waves discontinuities in the velocity is clearly measured, as can be seen in our papers [1], [2]. In this connection, the linearization of the dynamic free surface condition will not be accepted for realistic solutions.

It is also noted that bow waves and boundary layer interact with stern waves, especially in case Froude number is moderate.

[1] Miyata, H. et al : Resistance Reduction by Stern-End-Bulb (First Report), (Second Report), J. Soc. Naval Arch. of Japan, vol. 148 (1980), 149 (1981).

[2] Doi , Y., et al : Characteristics of Stern Waves Generated by Ships of Simple Hull Form (First Report), J. Soc. Naval Arch. of Japan, vol. 150 (1981) (to appear)

Authors' Reply
to Shee-Mang Yen and H. Miyata

The authors would like to thank Profs. Yen and Miyata for their discussions. To answer the questions raised by Prof. Yen, the downstream boundary was fixed at an appropriate distance from the transom stern. This distance was chosen such that this boundary does not influence the solution near the stern. For the specific hulls investigated this distance was 24 draft lengths from the transom. As stated in the paper, $\phi_{xx} = 0$ was applied at the downstream boundary through the use of a second-order one-sided finite difference equation.

We agree with Prof. Miyata that bow waves and the boundary layer interact with stern waves. However, the isolation of stern waves from the effects of bow waves and the boundary layer is useful in understanding stern flows. Moreover, we feel that this method in conjunction with experiments contributes to the knowledge of when such interactions are important. Although velocity discontinuities may exist, we believe that the nature of velocity discontinuity in our problem is solely due to the inadequacies of the full linearization in handling the steep sidewalls of the hull. Finally, we feel this work aids in determining when linearization is sufficient for obtaining realistic results.

ANALYSIS OF A BREAKING FREE-SURFACE WAVE USING BOUNDARY-FITTED COORDINATES FOR REGIONS INCLUDING REENTRANT BOUNDARIES

U. Ghia, C.T. Shin and K.N. Ghia
Department of Aerospace Engineering and Applied Mechanics
University of Cincinnati
Cincinnati, Ohio 45221, U.S.A.

Abstract

A procedure has been developed, using the elliptic differential-equation approach, for generating boundary-fitted coordinates for regions with highly curved boundaries as well as reentrant boundaries, such as those encountered in breaking surface waves. An excellent initial distribution of the coordinates is obtained as the non-iterative solution of the locally self-similar approximate form of the transformation equations. An alternating-direction implicit method is employed for determining the numerical solution of the coordinate equations. The conditions of periodicity on the left and right boundaries are enforced in an implicit manner. The resulting coordinates are nearly orthogonal and provide reasonable resolution everywhere, including the reentrant region. The procedure is applied to the solution for a free-surface wave starting from an initial sinusoidal form and encountering the breaking phenomenon. For this purpose, an adaptive coordinate system is formulated.

1. Introduction

Motions involving free surfaces can be analyzed by a variety of methods depending upon the nature of the approximations made in the analyses. One of the difficulties encountered, in general, arises due to the fact that one of the boundaries, namely, the free surface, is unknown. In unsteady motions, the free surface continuously deforms with time.

Advances in computer technology have enabled significant accomplishments in a number of fields and fluid dynamics is one of these. Some of the very complex flow problems, which defied theoretical analysis until recently, have become tractable numerically. A variety of free-surface flow problems were studied by Harlow and coworkers (see Harlow and Amsden [1970]) using the Marker-and-Cell (MAC) method of Fromm [1963] and the LINC calculation procedure of Hirt, Cook and Butler [1970]. The MAC method employs an Eulerian representation in which the fluid particles, denoted by mass-less marker particles move about in a fixed Eulerian mesh. The main difficulty with the Eulerian representation is that the free-surface cannot be easily resolved accurately. The LINC (or Lagrangian Incompressible) method uses a Lagrangian representation in which the computational mesh points move with the fluid, so that the fluid boundaries move with the boundaries of the computational domain. This feature of the LINC method makes it particularly attractive for use with problems involving free surfaces. However, large distortions of the free surface cause large deformations of the computational mesh. When these mesh deformations become sufficiently large, the mesh may become unacceptable from the viewpoint of numerical accuracy and stability. Hence, an arbitrary Lagrangian-Eulerian (ALE) procedure was developed by Hirt [1970]. The ALE technique combines the desirable features of the Lagrangian representation with the desirable characteristics of the Eulerian representation, while eliminating or minimizing the restrictions of both of these representations. In this technique, the computational mesh points remain fixed during the Eulerian-computation phase and move with the local fluid velocity during the Lagrangian-calculation phase or they can be moved about in the fluid according to an arbitrarily prescribed manner, so as to provide an acceptable computational mesh at all time.

The governing differential equations used in all three methods mentioned in the preceding paragraph were the Navier-Stokes equations for incompressible viscous flow, represented with velocities and pressure as the dependent variables. The MAC method was used to study such interesting flow problems as a drop of water splashing on a shallow pool, the formation of a backward-breaking wave when a sluice

gate is suddenly opened, and a wave crashing on a sloping beach, i.e., a plunging breaker. The LINC method was used to study the sloshing motion of a fluid in a tank after the fluid was impulsively set in oscillation by application of a sinusoidal pressure pulse at the free surface during the first cycle of the calculation. These computations had to be terminated after one period of oscillation because of large mesh distortions. This restriction was removed by the ALE procedure which allows rezoning of the mesh to avoid large-mesh distortions.

Another approach successful in the analysis of plunging breakers is that developed by Longuet-Higgins and Cokelet [1976]. It, too, is a combined Lagrangian-Eulerian approach in which the kinematical and the dynamical conditions at the free surface are expressed very simply in terms of Lagrangian time rates of change of the velocity potential and the coordinates following fixed particles on the free surface. Instead of solving the problem in a two-dimensional region, the flow region consisting of one wavelength of a travelling oscillatory wave was transformed to the region inside a simple closed contour. This contour or boundary then corresponds to the free surface. By proceeding in small time steps, the method can trace the time history of unsteady irrotational surface waves that are spatially periodic. Advancing the solution in time requires the knowledge of velocity components along and normal to the free surface. The tangential velocity component can be determined in a straightforward manner from the velocity potential along the free surface. The determination of the normal velocity component is reduced, by the use of Green's theorem, to the solution of an integral equation which is best accomplished in an Eulerian framework. The method is accurate and efficient. It was used to numerically follow the temporal development of the free surface of an initially symmetric progressive wave to which an asymmetric pressure distribution was applied initially. The wave surface was observed to steepen and overturn forward. The method was also applied by Cokelet [1977] to an unsteady free surface wave initially of exactly sinusoidal form but having moderate or large amplitude. This wave was also observed to steepen and curl over forward. This latter problem has been employed in the present study as well, for the purpose of determining the capability of the present approach as regards numerical treatment of breaking waves.

Free-surface flows have also been studied using boundary-fitted general curvilinear coordinates generated by numerically determined coordinate transformations, e.g., Shanks and Thompson [1977] and Haussling and Coleman [1977]. In both of these studies, the free surface flows considered were those generated by the translation, oscillation or swaying of a body that was fully or partially submerged in the fluid. The coordinate system was allowed to deform with time so as to always align a coordinate curve of one family with the deforming free surface. However, the boundary-point distribution of the second family of coordinates, x in both references, was maintained fixed, although their distribution in the interior of the solution domain varied according to the numerical transformation. This implied that the mesh points slide along the free surface to maintain their initial x-coordinate distribution while their y-coordinate is determined from the local surface slope and Eulerian velocity components. The approach is quite general and has been used successfully for a number of flows involving free surfaces. Nevertheless, it requires that the free-surface slope be finite everywhere and precludes the consideration of breaking waves. Recently, Haussling and Coleman [1980] modified this approach to allow both coordinates of the mesh points on the free surface to move with their corresponding local velocity components, in a Lagrangian sense, as was done by Longuet-Higgins and Cokelet [1976]. With this modification, Haussling and Coleman [1980] were able to follow the development of a free surface wave until it very nearly approached breaking.

The present study represents an effort towards generalizing the numerical coordinate-transformation procedure to include in it certain features that can enable consideration of breaking waves. One of the primary goals, therefore, is to circumvent the requirement that the free-surface elevation y be a single-valued function of x, as this condition is not satisfied by waves during breaking and thereafter. Another objective is to develop a coordinate system that does not become highly skewed or non-orthogonal as the mesh points on the free surface move with the free surface in a Lagrangian manner. Both of these objectives are achieved by suitable redefinition of the shape of the computational domain and the orientation of the coordinates. Other aspects of the present study are aimed towards achieving accuracy and efficiency in the numerical solution of the transformed equations.

2. Consideration for Coordinate System for Breaking Waves

The breaking phenomenon is encountered at sea under wind action, on beaches and in tidal estuaries. It is a shock wave phenomenon similar to that encountered in gas dynamics. It is characterized by a high rate of energy dissipation. A number of equivalent definitions can be given for the breaking criterion. Breaking is said to occur when (a) the particle velocity at the wave crest becomes larger than the wave speed; (b) the particle acceleration at the crest tends to separate the particles from the bulk of the fluid; (c) the free-surface pressure given by Bernoulli's equation is incompatible with the ambient-pressure; or (d) the free surface becomes vertical. The last form of the criterion is the most convenient one to consider from the viewpoint of formulating a coordinate system suitable for breaking waves. Following breaking, the free surface rolls over itself, i.e., it constitutes a reentrant boundary.

2.1 Boundary-Oriented Coordinates for Regions with Reentrant Boundaries

Figure 1 shows a schematic representation of a surface wave for which a portion of the free surface is a reentrant boundary. The region shown in the sketch may represent, for example, the instantaneous shape of an unsteady physical solution domain, cut off suitably upstream and downstream, and bounded by the free surface at the top and a bottom boundary below. Such configurations pose a unique difficulty in the generation of boundary-oriented coordinates, when adequate resolution and near orthogonality are to be maintained in the region of the breaking wave. The usual procedure is to align a single coordinate curve of one and the same family of coordinates with the entire free surface. The corresponding computational domain is a single rectangle and the associated computer program for solution of the problem is relatively simple. However, in the physical domain, the coordinate system becomes highly non-orthogonal in the reentrant region. Moreover, even for moderate resolution of this region, the coordinates may exhibit a strong tendency for overlap or cross-over, leading to non-uniqueness and, hence, a singularity, in the transformation in the interior of the computational domain. It should be noted that a singularity at a boundary of the computational domain can be tolerated if it is appropriately handled. Therefore, a suitable computational domain corresponding to the physical region represented in Fig. 1 was chosen to be as shown in Fig. 2. This computational domain consists of two rectangles, such that the top rectangle E'F'G'H', which forms a 'cap' for the lower rectangle A'B'C'D', represents the reentrant region EFGH of Fig. 1.

The theory underlying the coordinate transformation is the same as that used earlier by Thompson and co-workers for external flow (e.g., Thompson, Thames and Mastin [1974] and by Ghia and co-workers for internal flow (e.g., Ghia U. and Ghia, K. [1975]). Primarily, this consists of determining the new coordinates (ξ,η) as solutions of Poisson equations of the form

$$\nabla^2\xi \triangleq \xi_{xx} + \xi_{yy} = P \qquad (1)$$

and

$$\nabla^2\eta \triangleq \eta_{xx} + \eta_{yy} = Q \quad . \qquad (2)$$

The boundary conditions needed for a unique solution of Eqs. (1) and (2) consist of specified Dirichlet or Neumann conditions such that the transformed coordinates are boundary-oriented. The forcing functions P and Q in Eqs. (1) and (2) are specified so as to provide desired control for the resulting coordinate distribution in the interior of the problem domain. Further discussion on these, as well as on the boundary conditions, is deferred until later in this section. For the purpose of numerical solution of Eqs. (1) and (2), the roles of the independent and the dependent variables in these equations need to be interchanged. The corresponding inverted equations may be expressed as follows:

$$a\, x_{\xi\xi} + 2b\, x_{\xi\eta} + c\, x_{\eta\eta} + J^2(P\, x_\xi + Q\, x_\eta) = 0 \qquad (3)$$

$$a\, y_{\xi\xi} + 2b\, y_{\xi\eta} + c\, y_{\eta\eta} + J^2(P\, y_\xi + Q\, y_\eta) = 0 \qquad (4)$$

where

$$a = x_\eta^2 + y_\eta^2 \quad ,$$

$$b = -(x_\xi x_\eta + y_\xi y_\eta) \quad ,$$

$$c = x_\xi^2 + y_\xi^2 \quad , \qquad (5)$$

and J, the Jacobian of the coordinate transformation, is defined as

$$J = x_\xi y_\eta - x_\eta y_\xi \quad . \qquad (6)$$

For the purpose of first illustrating the advantage of a 'cap' to represent the reentrant region of Fig. 1, Dirichlet boundary conditions, i.e., functional values of x and y, are prescribed on the entire boundary of the computational domain shown in Fig. 2. An alternating-direction implicit (ADI) method is employed to determine the numerical solution of the transformation equations. During each directional sweep of the method, the tridiagonal systems of discretized equations for both coordinates are solved simultaneously using a generalization of the Thomas algorithm. The values of the finite-difference indices at the boundaries are themselves subscripted in order to program the Thomas algorithm in a compact manner for the multi-rectangular computational domain including the 'cap'. The procedure has been used to efficiently determine the boundary-oriented coordinates shown in Fig. 3. These coordinates are nearly orthogonal and provide reasonable resolution everywhere, including the reentrant region. The form of the initial conditions is found to have a significant effect on the convergence rate of the solution. A procedure of obtaining an initial distribution is developed in the next sub-section.

2.2 Initialization by Locally Self-Similar Solution

Numerical solutions of complex boundary-value problems with severe non-linearities, as in Eqs. (3) and (4), exhibit true non-linear instability. Accordingly, small initial errors decay whereas large initial errors amplify and cause the solution to rapidly become unbounded. In such situations, the starting solution employed plays an important role in the convergence of the solution. For the coordinate equations, Ghia, Hodge and Hankey [1977] suggested an initialization procedure based on simple geometrical considerations, employing weighted linear interpolation between adjacent points on one side and the boundary points on the other side of a given point. This geometrical initialization procedure yielded starting solutions that had a striking resemblance to the final solution and led to rapid convergence. However, this feature is lost when the procedure is used in regions with reentrant boundaries. Applied to the configuration of Fig. 1, it yields the initial coordinate distribution shown in Fig. 4. Clearly, this is not the best possible initialization in the reentrant region, although it does lead to a convergent final solution.

In general, the solution of a simplified limiting form of the governing differential equations can provide a good starting solution (e.g., Davis [1972]). Therefore, assuming 'local self-similarity', the coordinate equations (3) and (4) are simplified as follows. For the configuration of Fig. 1, the coordinate solution is assumed to be locally self-similar with respect to the η direction. Accordingly, the second-derivative terms $x_{\eta\eta}$ and $y_{\eta\eta}$ are neglected, while the first-derivative terms x_η and y_η are approximated by two-point backward differences. Thus, for similarity in the η-direction, the coordinate equations reduce to the following:

$$a\, x_{\xi\xi} + 2b\, x_{\xi\eta} + J^2(P\, x_\xi + Q\, x_\eta) = 0, \quad (7)$$

$$a\, y_{\xi\xi} + 2b\, y_{\xi\eta} + J^2(P\, y_\xi + Q\, y_\eta) = 0, \quad (8)$$

where a, b, c and J are as defined by equations (5) and (6). The terms x_η, y_η appearing in the nonlinear coefficients, as well as the mixed derivative terms $x_{\xi\eta}$, $y_{\xi\eta}$, are approximated by two-point backward differences at the preceding η=constant line in order to maintain the initialization procedure completely non-iterative. Equations (7) and (8) are then rearranged as follows:

$$a\, x_{\xi\xi} - 2(x_\eta x_{\xi\eta})x_\xi + J^2 P\, x_\xi + J^2 Q\, x_\eta - 2(x_{\xi\eta} y_\eta) y_\xi = 0\,, \quad (9)$$

$$a\, y_{\xi\xi} - 2(y_{\xi\eta} y_\eta) y_\xi + J^2 P\, y_\xi + J^2 Q\, y_\eta - 2(x_\eta y_{\xi\eta}) x_\xi = 0\,. \quad (10)$$

These equations can be solved by the same coupled Thomas algorithm as employed during the ξ-implicit sweep of the ADI method for equations (3) and (4). The initial solution along the first interior line ($\eta = \Delta\eta$) may not be determined by the procedure outlined. This line is initialized by a simple geometric interpolation procedure. Equations (9) and (10) are then used to determine the initial solution elsewhere. The resulting initial solution for the configuration of Fig. 1 is shown in Fig. 5. It represents an excellent initial guess for the final solution shown in Fig. 3. The total CPU time, including initialization, was 3.15 seconds for a grid of (11 x 21) points using the AMDAHL 470/V6 computer. The corresponding CPU time with the geometric initialization of Fig. 4 was 14.82 seconds. Therefore, the initialization procedure suggested in the present work leads to a gain of a factor of five in the efficiency of

the solution. It should be noted that, for some problem configurations, the coordinates may be more nearly self-similar with respect to ξ than with respect to η. Similar approximations as discussed above with respect to η would then need to be made with respect to ξ and the resulting equations would then be implicit along lines of η=constant. This has also been tested by the present authors for other problem configurations.

Other considerations that become necessary for the coordinates used to represent breaking waves are better discussed with the actual transient development of the free surface. Hence, the free surface-wave problem is formulated next.

3. Model Problem of Free Surface Encountering Breaking

In order to be able to concentrate effort on the development of coordinate systems suitable for breaking waves, a simple model problem is selected as the free-surface flow problem. Accordingly, the model problem considered is that of an oscillatory progressive wave train on the free surface of a body of deep water. Initially, the wave is of exact sinusoidal form, with a steepness ratio exceeding the Michell limit of 0.142, so that the wave does encounter the breaking phenomenon as the free surface develops with time. The motion is assumed to be periodic in space. Hence, it is sufficient to consider a region of the physical domain whose lateral extent equals one wavelength of the sinusoidal wave. The bottom boundary is placed at a depth sufficiently below the free surface so that no fluid flows across this boundary. The physical coordinate system and the initial configuration of the physical solution domain are shown in Fig. 6, with the free surface given by

$$y = 2\pi + \frac{1}{2}\sin(x+\pi) \quad \text{at } t = 0. \tag{11}$$

For this wave, the steepness ratio, defined as the total amplitude (= 1) divided by the wavelength (= 2π), is $1/2\pi$, i.e., ≈ 0.159.

The differential equation describing the motion for $t > 0$ is derived under the assumptions that the fluid is inviscid and incompressible, and that surface tension and diffusion of vorticity into the interior are negligible. These are reasonable approximations until breaking occurs and lead to a velocity potential ϕ satisfying the simple Laplace equation for describing the flow. Hence, the governing equation to be solved in the interior is

$$\nabla^2\phi = 0 \quad \text{for} \quad t > 0 \ . \tag{12}$$

The boundary conditions for equation (12) are obtained from the periodicity of the motion at $x = 0$ and $x = 2\pi$, from the vanishing of the normal velocity at $y = 0$ and from Bernoulli's equation at the free surface. These are expressed mathematically as follows:

At the periodic boundaries x_{min} and x_{max},

$$\phi(x_{min},y,t) = \phi(x_{max},y,t) \ , \tag{13a}$$

$$\phi_x(x_{min},y,t) = \phi_x(x_{max},y,t) \ , \tag{13b}$$

The left and right boundaries are denoted as x_{min} and x_{max} (and not merely by their initial positions 0 and 2π) since they move with the travelling wave and deform with time.

At the bottom boundary, $y = 0$,

$$\phi_y(x,0,t) = 0 \ . \tag{14}$$

At the free surface,

$$\frac{D\phi}{Dt} = -(y - 2\pi) + \frac{1}{2}(\phi_x^2 + \phi_y^2) \tag{15}$$

where D/Dt denotes material or Lagrangian derivative.

The initial distribution of the potential function is taken to be:

$$\phi(x,y,0) = -\frac{\cos(x+\pi)\cosh y}{2\cosh(2\pi)} \ . \tag{16}$$

The initial-boundary value problem described by equations (12)-(16) needs to be solved in the region which, at $t = 0$, appears in the physical domain as shown in Fig. 6, and which deforms with time for $t > 0$. Hence, the problem is transformed to the boundary-oriented coordinates (ξ,η) discussed in Section 2. Accordingly, ϕ is governed by the following equation in the (ξ,η) plane:

$$a\,\phi_{\xi\xi} + 2b\,\phi_{\xi\eta} + c\,\phi_{\eta\eta} + J^2(\bar{P}\,\phi_\xi + \bar{Q}\,\phi_\eta) = 0 \tag{17}$$

where $\bar{P}$ and $\bar{Q}$ are determined by evaluating the left-hand sides of equations (1) and (2), respectively. These vary

with time and will, in general, not equal the prescribed values of P and Ω exactly.

The transformed forms of the boundary conditions (13)-(15) are as follows:

At the periodic boundaries $\xi = 0$ and $\xi = \xi_{max}$,

$$\phi(0,\eta,t) = \phi(\xi_{max},\eta,t) \quad , \tag{18a}$$

$$\phi_\xi(0, ,t) = \phi_\xi(\xi_{max},\eta,t) \quad . \tag{18b}$$

At the bottom boundary, $\eta = 0$,

$$\phi_\eta(\xi,0,t) = 0 \quad . \tag{19}$$

At the free surface,

$$\frac{D\phi}{Dt} = -(y - 2\pi) + \frac{1}{2}\left[(\phi_\xi y_\eta - \phi_\eta y_\xi)^2 + (\phi_\eta x_\xi - \phi_\xi x_\eta)^2\right]\frac{1}{J^2} \quad . \tag{20}$$

The free surface is represented by the line $\eta = \eta_{max}$ in the uncapped transformed-plane configuration but by a combination of ξ and η boundaries in the capped configuration described in Section 2.

The initial distribution of ϕ as given by equation (16) involves no derivatives and, hence, transforms simply as a scalar point function in the (ξ,η) plane.

The deformation of the physical solution domain and the development of the free surface with time can be traced numerically by recomputing the coordinate transformation given by equations (3) and (4) subject to the following boundary conditions:

At the periodic boundaries $\xi = 0$ and $\xi = \xi_{max}$,

$$x(0,\eta) = x(\xi_{max},\eta) + 2\pi \quad , \tag{21a}$$

$$x_\xi(0,\eta) = x_\xi(\xi_{max},\eta) \quad ; \tag{21b}$$

$$y(0,\eta) = y(\xi_{max},\eta) \quad , \tag{22a}$$

$$y_\xi(0,\eta) = y_\xi(\xi_{max},\eta) \quad . \tag{22b}$$

At the bottom boundary, $\eta = 0$,

$$x_\eta(\xi,0) = 0 \tag{23a}$$

$$y(\xi,0) = 0 \quad . \tag{23b}$$

At the free surface, the mesh points move with the local fluid velocity, so that, for $t > 0$,

$$\frac{Dx}{Dt} = \phi_x = (\phi_\xi y_\eta - \phi_\eta y_\xi)/J, \tag{24a}$$

and

$$\frac{Dy}{Dt} = \phi_y = (\phi_\eta x_\xi - \phi_\xi x_\eta)/J \quad . \tag{24b}$$

At $t = 0$, the initial distribution of the coordinates is determined by solving equations (3) and (4) subject to conditions (21a,b) and (22a,b) at the periodic boundaries and a uniform distribution of x at the bottom boundary where $y = 0$ as well as at the top boundary where y is given by equation (11) for the free surface at $t = 0$.

The procedure for advancing the solution by a finite time increment Δt from the known solution for x, y and ϕ at time t consists of the following main steps:

1. The new-time value of ϕ at the free surface is determined from the free-surface condition (20).

2. The new-time value of ϕ in the interior is determined by solution of Eq. (17) subject to boundary conditions (18a,b), (19) and the free-surface values determined in step 1 above.

3. The configuration of the free surface is advanced according to equations (24a,b).

4. The coordinate distribution in the interior is determined by solution of equations (3) and (4) subject to boundary conditions (21a,b), (22a,b) and the free-surface values of x, y determined in step 3 above.

The procedure is repeated until such time as the solution is desired. A filtering technique similar to that used by Longuet-Higgins and Cokelet [1976] has been used in the present work also, in order to remove an instability that otherwise appeared in the solution, particulary at the free surface, at a fixed time t, regardless of the size of the time step Δt employed. Also, at later times, it is found necessary to reduce the size of Δt so as to avoid any point on the free surface from overtaking its neighboring

point. Thus, $\Delta t = 0.02$ is used for the first 150 time steps, after which $\Delta t = 0.01$ has been used.

3.1 Determination of Forcing Function Q(η)

For the model problem just described, changes in the flow variables are largest near the free surface which, in the uncapped configuration, is placed at $\eta = \eta_{max}$. To achieve increased accuracy using a given number of mesh points, grid points are concentrated near this boundary by employing an appropriate distribution for Q(η) in equations (3) and (4). In the present study, constant steps $\Delta\eta$ are made to correspond to physical y steps that decrease linearly with increasing η, i.e.,

$$\frac{\partial y}{\partial \eta} = B - C\,\eta \quad . \tag{25}$$

The parameters B and C are determined from the condition that $y = y_{max}$ at $\eta = \eta_{max}$ and from the prescribed ratio of the y steps near the two boundaries. Thus, with

$$\frac{\Delta y_m}{\Delta y_0} = A \quad , \tag{26}$$

where $A < 1$ for grid-point concentration near y_{max}, B and C have the following values:

$$B = \left(\frac{2}{1+A}\right) \frac{y_{max}}{\eta_{max}}$$

and

$$C = 2\,\frac{(1-A)}{(1+A)}\,\frac{y_{max}}{\eta_{max}^2} \quad . \tag{27}$$

Along a vertical line, the transformation equation (4) can be approximated as

$$y_{\eta\eta} + Q\,y_\eta^3 = 0 \tag{28}$$

so that Q can be evaluated as

$$Q = \frac{C}{(B-C\eta)^3} \quad . \tag{29}$$

For the free surface-wave problem, y_{max} changes with ξ. Hence, B and C must vary with ξ. Also, y_{max} changes with time, so that Q must also change in time. However, for the present, Q has been retained simply as Q(η); use of a capped configuration as well as another feature discussed in Section 4 can relieve any additional difficulties associated with resolution.

3.2 Implicit Enforcement of Periodicity Boundary Conditions

In the framework of an ADI method of numerical solution, the periodicity conditions (13a,b) for the velocity potential φ as well as (21a,b) and (22a,b) for the coordinates x, y can be conveniently enforced in an implicit manner. During the ξ-implicit sweep of the ADI procedure, the φ-equation, for example, can be expressed symbolically in the form

$$\phi'' + p\,\phi' + q\,\phi = r \quad , \tag{30}$$

where primes denote differentiation with respect to ξ. The periodicity conditions are expressed as

$$\phi_0 = \phi_m \quad \text{and} \quad \phi_0' = \phi_m' \tag{31a,b}$$

where the subscripts '0' and 'm' denote that φ (or φ') is evaluated at $\eta = 0$ and $\eta = \eta_{max}$, respectively. Then, the solution φ is of the form

$$\phi = \phi_0\,f + \phi_0'\,g + h \tag{32}$$

where f, g and h are solutions of the boundary-value problems shown in Table I below.

Table I. Boundary-Value Problems for f, g and h in Equation (32)

Variable	Differential Equation	Boundary Conditions
f	$f'' + p\,f' + q\,f = 0$	$f_0 = 1,\ f_m' = 0$
g	$g'' + p\,g' + q\,g = 0$	$g_0 = 0,\ g_m = 1$
h	$h'' + p\,h' + q\,h = r$	$h_0 = 0,\ h_m' = 0$

All three of these boundary-value problems can be solved using central differences and the Thomas algorithm, by a relatively compact computer program. Thereafter, the boundary values are determined as

$$\phi_0 = \frac{[h_m(1-g_0') + h_0' g_m]}{[(1-f_m)(1-g_0') - f_0' g_r]} = \phi_m \quad (33a)$$

and

$$\phi_0' = \frac{[h_0'(1-f_m) + f_0' h_m]}{[(1-f_m)(1-g_0') - f_0' g_m]} = \phi_m' \quad (33b)$$

A similar procedure is followed for the coordinates x and y, with proper care to note the specific form of condition (21a) for x. This treatment of the periodicity conditions provides for implicitly updating the boundary values, as opposed to lagging them by one time step as would occur in an explicit treatment. Implicit consideration of boundary conditions enhances the convergence rate of the numerical solution, in general.

4. Transient Development of Free Surface for Model Problem

Results are presented mainly in terms of coordinates in the physical solution domain as it deforms with time as the wave progresses. The temporal development of the free surface can be clearly observed in this manner. Also, the modifications needed in the coordinates in order to consider breaking waves also become more evident.

Figures 7a-c show the transient deformation of the physical region and the coordinates which appeared initially as shown in Fig. 6. The forcing function P has been set to zero in these calculations. The forcing function Q is determined as described in Section 3.1, with A = 0.15 up to t = 2.10 beyond which A is decreased by two percent at each successive physical time step Δt. The value used for Δt is 0.02 up to t = 3.0 and Δt = 0.01 thereafter. The computational domain consists of a single rectangle. Use of a 'capped' configuration in the initial stages of the development is unnecessary and, in fact, leads to a coordinate system that is less appropriate than the uncapped configuration. A 'cap' is to be introduced at later times when a reentrant shape for the free surface becomes imminent.

As seen in Fig. 7, the mesh points at the free surface are diverted away from the position of minimum surface-elevation and tend to concentrate near the position of maximum elevation. As pointed out by Longuet-Higgins and Cokelet (1976), this is an advantageous occurrence since the flow changes more rapidly near the position of maximum elevation of the free surface. At t = 1.1, (Fig. 7a), the maximum surface steepness occurs near the top right corner, whereas at t = 2.0, (Fig. 7b), it occurs near the top left corner. The adaptive coordinate system formulated is adequate for treating this changing form of the solution domain. In Fig. 7b, the angle at the top right corner has reduced considerably below its initial value of $\pi/2$. This feature becomes much more prominent with increasing time, as seen in Fig. 7c which corresponds to t = 2.6. The calculations were repeated with twice the number of mesh points along the vertical coordinate in order to ascertain if a deficiency in the resolution was contributing to such behavior of the solution. A comparison of Fig. 7d with Fig. 7c shows that the flow features remain virtually unaltered at t = 2.6 for the two mesh sizes employed. Hence, it is evident that, if large deviations from orthogonality are to be avoided for the coordinates, some means must be developed for first eliminating the non-orthogonal intersection of the boundaries at the top right corner.

4.1 Adaptive Rearrangement of Coordinates to Main Near-Orthogonality

For the present flow problem, the motion is periodic in x. Hence, a strip of the solution region can be removed from the right and placed on the left. This would correspond to starting with a region that was initially bounded by $x = x_0$ and $x = x_0 + 2\pi$, with $x_0 \neq 0$, instead of the initial region shown in Fig. 6 which is bounded by x = 0 and $x = 2\pi$. The ensuing analysis and results would remain altered. Such a rearrangement of the solution domain is illustrated in Fig. 8 which corresponds to t = 2.4. The configuration in Fig. 8a shows the coordinate system, prior to any modification, so that the top right corner has a sharp acute angle. Eleven $\Delta\xi$ strips are then removed from the right and placed on the left to obtain the rearranged configuration shown in Fig. 8b. The criterion actually adopted for determining the number of strips to be shifted was that the points at the corners correspond to the minimum elevation of the free surface. The resulting configuration of the solution region is such that the coordinates are more nearly orthogonal at the corners than for the original configuration.

It is important to observe that, without any further modification, this rearranged grid by itself does not provide any additional advantages over the original configuration. This is because the rearrangement described does not alter the relative positions of the mesh points on the boundaries, so that

the coordinate transformation remains unaltered. This is illustrated in Fig. 9a which corresponds to t = 3.00. The solution domain was rearranged continuously during the computational procedure by shifting $\Delta\xi$ strips from one boundary to the other so as to maintain the top corners at the location of minimum elevation of the free surface. Thus, the skewness of the coordinates near the corners is reduced considerably. But the high degree of non-orthogonality, that previously existed near the corners, now persists in the vicinity of the position of maximum curvature or maximum elevation of the free surface. This is seen more clearly in the enlarged view of the vicinity of this point in Fig. 9b which corresponds to t = 3.10. It is clear from these results that some additional modification of the coordinate system is necessary in order to continue the solution further in time. The primary advantage gained by shifting $\Delta\xi$ strips from one boundary to the other is that, by minimizing skewness at the corners, it makes further meaningful modifications of the coordinate system possible. Two such modifications are discussed next.

The effect of the first modification considered is shown in Fig. 10. This modification consists of sliding the mesh points along the free surface so that the coordinate system is considerably less distorted all along the free surface. Following this rearrangement of the free-surface points, the coordinate transformation as well as the velocity potential ϕ must be recalculated at the same physical time level at which the boundary-point modification is made. Thereafter, the solution procedure is as described in Section 3, i.e., the modified mesh-point distribution deforms with time in a Lagrangian manner until such time as further sliding of these mesh points is necessitated due to breaking. It should be noted that the potential function as well as the velocities at the rearranged mesh points on the free surface have to be determined by a two-dimensional interpolating procedure since $\phi = \phi(x,y)$ or $\phi = \phi(\xi,\eta)$. A suitable procedure would be similar to that used earlier by Ghia and Sathyanarayana [1979] in another flow problem.

The second modification, which may be preferable for free-surface flows, consists of introducing a 'cap' in the vicinity of the position of maximum curvature of the free surface. This position is determined as part of the computational procedure. With this modification, the corresponding computational domain consists of two adjoining rectangles as shown earlier in Fig. 2. Figure 11 shows an enlarged view of the vicinity of the maximum elevation of the free surfaces, including a cap at t = 2.24. Again, the coordinate transformation as well as the velocity potential must be re-computed at the same physical time when the cap is first introduced, in order to obtain their proper solution in the modified coordinate system. In Figs. 10 and 11, the lower portion of the solution domain has not been included because the modifications illustrated in these figures have minimal influence in this lower region.

As mentioned earlier, the 'capped' configuration introduces singularities at the boundaries. These and their possible treatment is described next.

4.2 Treatment of Singularities in Capped Configuration

With reference to the sketch in Fig. 12a, the region AB_1B_2C is to be represented by a 'cap'. The corresponding computational region is indicated by $A'B_1'B_2'C'$ in Fig. 12b. With this arrangement of the coordinates, singularities are introduced at the points A and C as well as at B_1 (or B_2), i.e., at A', C' and along $B_1'B_2'$ in the computational domain. The point B_1 (or B_2) is at the position of maximum curvature of the free surface and corresponds to the center of the cap in the physical domain. The curvature at this point is not necessarily infinite even during and well after breaking, as shown by Longuet-Higgins and Cokelet [1976]. Hence, none of the singularities are of the geometric type. They arise because ϕ_x and ϕ_y become of the indeterminate form $\frac{0}{0}$ at these points. It should be recalled that, although no differential equations are solved at the free-surface boundary, the values of ϕ_x and ϕ_y at the free surface are needed for advancing ϕ, x and y at the free surface according to equations (15) and (24). In reality, ϕ_x and ϕ_y remain bounded at these points so that their indeterminate form must possess a finite limiting value at each of these points.

For the present problem, it is noted that the points A and C are on a smooth portion of the free surface with mild curvature. Hence, ϕ_x and ϕ_y at these points are determined by interpolation from their values at the neighboring points.

To treat the singularity along $B_1'B_2'$ corresponding to the single point B_1 or B_2, a locally uncapped coordinate

system is introduced at the point B_1 (or B_2). The values of ϕ_ξ and ϕ_η required for calculating ϕ_x and ϕ_y [equations (15) and (20)] are then obtained as follows. An uncapped coordinate system introduced locally at B_1 is shown in the physical domain in Fig. 12c. Determination of ϕ_ξ at the point B_1, denoted as (i,j), would then involve the values of ϕ and ξ at the points denoted as (i,j-1) and (i,j+1) in this sketch. Similarly, determination of ϕ_η at B_1, using a three-point backward difference, would involve the values of ϕ and η at the points indicated as (i,j), (i-1,j) and (i-2,j) in Fig. 12c. The corresponding points in the present capped configuration in the transformed plane are indicated by the heavy dots shown in Fig. 12d. Hence, the expressions for ϕ_ξ and ϕ_η at B_1 are obtained as

$$\phi_\xi\Big|_{B_1,B_2} = \frac{(\phi_{IMAX0-1,JMAX2} - \phi_{IMAX0-1,JMAX1})}{(\xi_{JMAX2} - \xi_{JMAX1})} \quad (34)$$

and

$$\phi_\eta\Big|_{B_1,B_2} = \frac{1}{2\Delta\eta}\,[3\phi_{IMAX0,JC} - 4\phi_{IMAX0-1,JC} + \phi_{IMAX0-2,JC}]. \quad (35)$$

Use of these forms for ϕ_ξ and ϕ_η leads to non-singular forms for ϕ_x and ϕ_y at B_1 or B_2.

Calculations are presently underway for continuing the solution of the free-surface wave problem further in time. Being a true transient solution, it is somewhat time-consuming in terms of computer time. About 12 seconds of CPU time of an AMDAHL 470/V6 computer are required for advancing the solution for the flow as well as the coordinates through each physical time step Δt.

5. Summary and Concluding Remarks

A combined Eulerian-Lagrangian approach has been used to develop a procedure for studying free-surface flows. The mesh points on the free surface move in a Lagrangian manner with the local fluid velocity, while the coordinate distribution in the interior is determined by a numerical coordinate transformation procedure for generating boundary-oriented coordinates for arbitrary domains. In general terms, the method may be likened to the ALE procedure of Hirt [1970], with considerably greater formalism built into the adaptive modifications made in the boundary-oriented deforming coordinate system. While it may lack the high degree of accuracy achievable by the method of Longuet-Higgins and Cokelet [1976], it possesses the increased capability of using general Navier-Stokes equations instead of the simple velocity-potential equation to represent the flow. In the present paper, the flow was assumed to be represented by the velocity potential in order to simplify the problem and increase computer turn-around time so as to enable formulation of the important new features of the method. However, the method is in no way limited to the use of the velocity-potential equation.

Application to a free-surface wave of initially sinusoidal form, with steepness ratio $1/(2\pi)$, is studied. As the wave progresses, the free surface steepens and will eventually roll over itself. Near-orthogonality and reasonable resolution can be maintained for the steepening wave surface by rearrangement of the periodic solution domain followed by sliding the computational points along the free surface or by use of a multi-rectangular computational domain at later times. In the latter approach, the singularities introduced at three points of the free-surface are carefully treated. Several aspects of the study are general and should be useful in other flow problems as well. These include the procedures developed for (1) generating boundary-oriented coordinates for regions with reentrant boundaries, (2) generating a non-iterative initial solution by use of a locally self-similar approximate form of the equations and (3) implicit enforcement of the periodicity boundary conditions. Efforts are presently under progress to include adaptive alteration of the size and the position of the secondary rectangle or 'cap' at the free surface. Consideration of viscosity and surface tension are subjects for future work; this would include the replacement of the velocity-potential equation by the Navier-Stokes equations to represent the flow.

Acknowledgement

This research is supported, in part, by Contract No. N00167-80-M-5266 of the Naval Ship Research and Development Center, U.S.A. The authors are grateful to Drs. H.J. Haussling and R.M. Coleman, of NSRDC, for useful discussions during the course of this study.

References

Cokelet, E.D., (1977), "Numerical Experiments on the Deformation of Steep Water Waves," Proc. I.M.A. Conf. on Mathematics in Oceanography, Univ. of Bristol; referred in Longuet-Higgins, M.S., (1977), "Advances in the Calculation of Steep Surface Waves and Plunging Breakers," Proc. 2nd Int. Conf. Numerical Ship Hydrodynamics, Univ. of California, Berkeley.

Davis, R.T., (1972), "Numerical Solution of the Navier-Stokes Equations for Symmetric Laminar Incompressible Flow Past a Parabola," Journal of Fluid Mechanics, Vol. 51, Pt. 3, pp. 417-433.

Fromm, J.E., (1963), "A Method for Computing Nonsteady, Incompressible Viscous Fluid Flows," Los Alamos Scientific Laboratory report LA-2910.

Ghia, U. and Ghia, K.N., (1975), "Numerical Generation of a System of Curvilinear Coordinates for Turbine Cascade Flow Analysis," Aerospace Engineering Report AFL 75-4-17, University of Cincinnati.

Ghia, U, Hodge, J.K. and Hankey, W.L, (1977), "An Optimization Study for Generating Surface-Oriented Coordinates for Arbitrary Bodies in High-Re Flow," AFFDL-TR 77-117, presented at AIAA 3rd Computational Fluid Dynamics Conference, Albuquerque, New Mexico.

Ghia, U. and Sathyanarayana, K., (1979), "Three-Dimensional Viscous Flow in Joukowski Ducts," Flow in Primary, Non-Rotating Passages in Turbomachines, ASME Publication, Editor: H.J. Herring.

Harlow, F.H. and Amsden, A.A., (1971), Fluid Dynamics, LA-4700, Los Alamos Scientific Laboratory, University of California, Los Alamos, New Mexico.

Haussling, H.J.and Coleman, R.M., (1979), "Nonlinear Water Waves Generated by an Accelerated Circular Cylinder," Journal of Fluid Mechanics, Vol. 92, Part 4, pp. 767-781.

Haussling, H.J. and Coleman, R.M., (1980), Private Communication.

Hirt, C.W., (1970), "An Arbitrary Lagrangian-Eulerian Computing Technique," Proc. 2nd International Conf. on Numerical Methods in Fluid Dynamics, University of California, Berkeley.

Hirt, C.W., Cook, J.L. and Butler, T.D., (1970), "A Lagrangian Method for Calculating the Dynamics of an Incompressible Fluid with Free Surface," J. Computational Phys., Vol. 5, p. 103.

Longuet-Higgins, M.S. and Cokelet, E.D., (1976), "The Deformation of Steep Surface Waves on Water. I. A Numerical Method of Computation," Proc. R. Soc. Lond., Series A, Vol. 350, pp. 1-26.

Shanks, S.P. and Thompson, J.F., (1977), "Numerical Solution of the Navier-Stokes Equations for 2D Hydrofoils In or Below a Free Surface," Proc. 2nd International Conf. on Numerical Ship Hydrodynamics, University of California, Berkeley.

Thompson, J.F., Thames, F.C. and Mastin, C.W., (1974), "Automatic Numerical Generation of Body-fitted Curvilinear Coordinate System for Field Containing any Number of Arbitrary Two-Dimensional Bodies," Journal of Computational Physics, Vol. 15, p. 299.

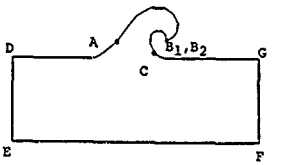


Fig. 1. Schematic Representation of Solution Domain with Reentrant Free Surface; Physical Plane (x,y).

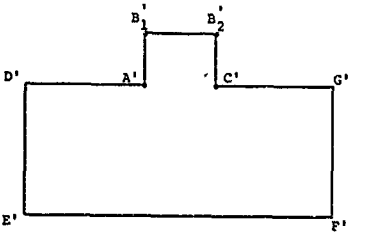


Fig. 2. Multi-Rectangular Computation Domain (ξ,η) for Reentrant Physical Region.

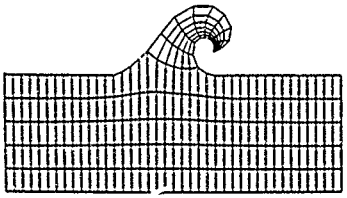


Fig. 3. Boundary-Fitted Coordinates for Breaking Free-Surface Wave.

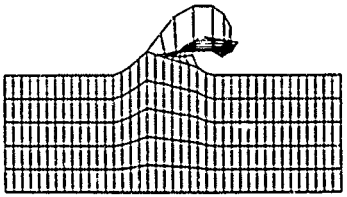


Fig. 4. Starting Solution for Coordinates for Breaking Free Surface - Geometric Initialization Procedure.

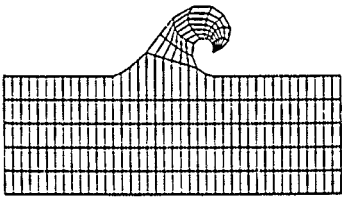


Fig. 5. Starting Solution for Coordinates for Breaking Free Surface - Locally Self-Similar Initialization.

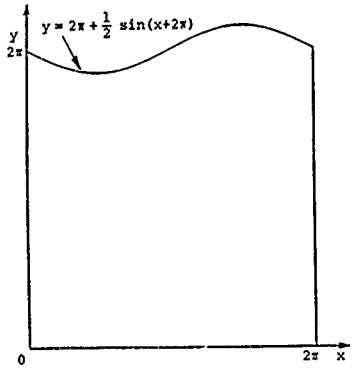


Fig. 6. Initial Region for Model Problem of Free-Surface Wave.

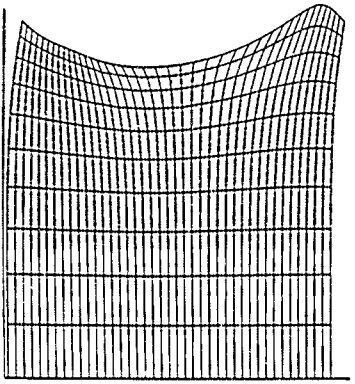
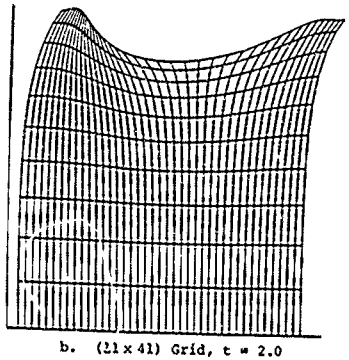
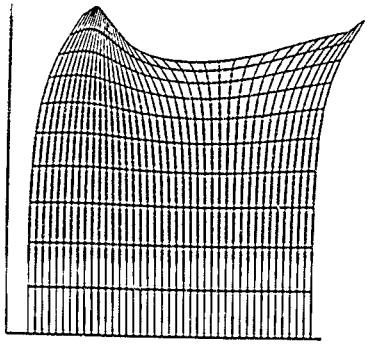


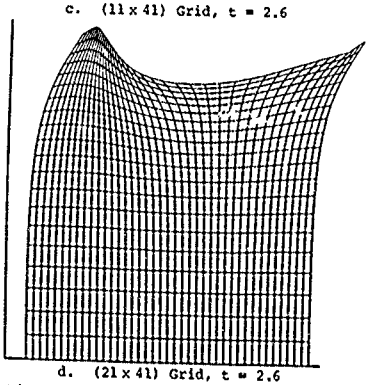
Fig. 7a. Temporal Development of Free-Surface Wave; (11 x 41) Grid, t = 1.1.



b. (21 x 41) Grid, t = 2.0

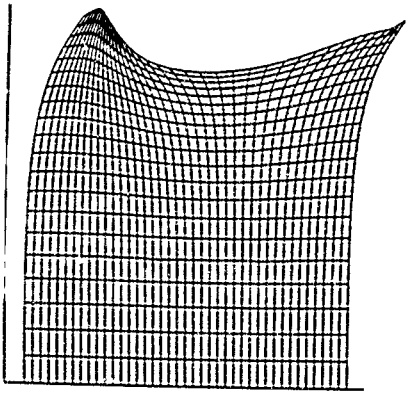


c. (11 x 41) Grid, t = 2.6

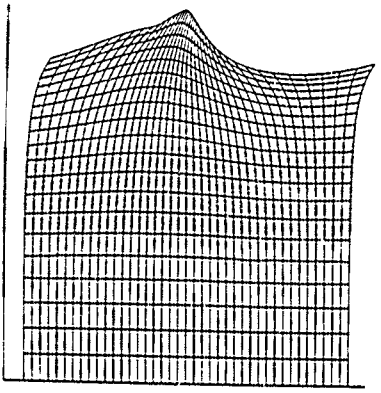


d. (21 x 41) Grid, t = 2.6

Fig. 7. Temporal Development of Free-Surface Wave.

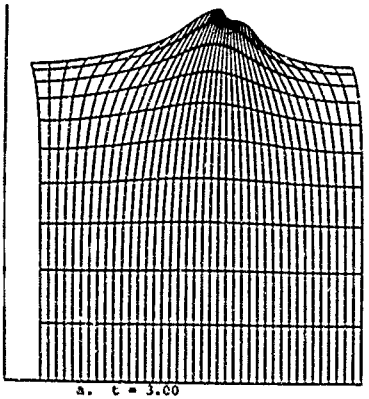


a. Original Configuration

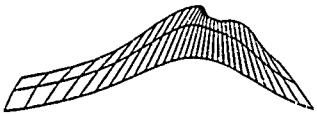


b. Rearranged Configuration.

Fig. 8. Rearrangement of Periodic Solution Domain.



a. t = 3.00



b. Vicinity of Maximum Elevation; t = 3.10.

Fig. 9. Temporal Development of Free-Surface Wave Using Rearranged Solution Domain.

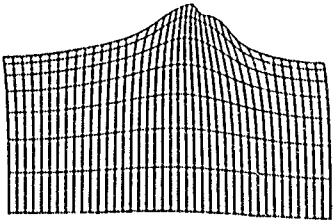


Fig. 10. Rearrangement of Coordinates by Sliding Mesh Points Along Free Surface; t = 3.02

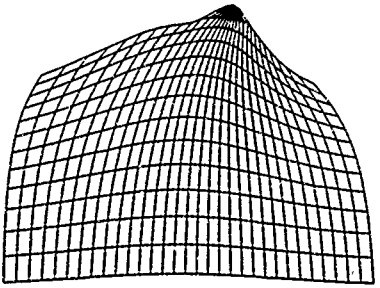
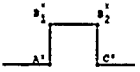


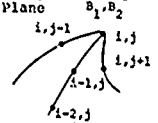
Fig. 11. Rearrangement of Coordinates to Correspond to Multi-Rectangular Computational Domain; t = 2.24.



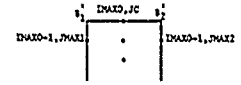
a. Reentrant Region in Physical Plane



b. Secondary Rectangle in Computational Plane



c. Free Surface Near Point of Maximum Curvature



d. Mesh Points for ϕ_ξ and ϕ_η at B_1, B_2

Fig. 12. Treatment of Singularities in 'Capped' Coordinate Configuration.

DISCUSSION
of the paper
by U. Ghia, C.T. Shin and K.N. Ghia

ANALYSIS OF A BREAKING FREE-SURFACE WAVE USING BOUNDARY-FITTED COORDINATES FOR REGIONS INCLUDING REENTRANT BOUNDARIES

Discussion
by J.V. Wehausen

Figures 7 and 8 seem to deserve further comment. According to the classical existence theorems of Levi-Civita and Struik for waves of permanent type, such waves are symmetric about both crest and trough, the result being valid presumably only for the interval of amplitude/wavelength for which their series converge. On the other hand, it has been known for about fifteen years that this solution is unstable if the water is deep enough (e.g. Benjamin and Feir). Given that the initial configuration here (Figure 6) is symmetric, how should one interpret the evident asymmetry developing in Figures 7 and 8 ? Is it perhaps associated with the large amplitude/wavelength of Figure 6, putting this configuration beyond the region of validity of the classical existence theorems, or is something else involved ? I would appreciate any insights that the authors wish to offer.

Authors' reply

The observation made by Dr. Wehausen is very pertinent as it makes one pause to examine the fundamental phenomena occurring in this flow problem. First of all, I should point out that this flow has been studied earlier by Longuet-Higgins and Cokelet and also by Haussling and Coleman. The present paper uses this problem primarily to examine and extend the applicability of a new coordinate configuration to flow domains with reentrant boundaries.

Irrotational Stokesian wave theories, such as those of Levi-Civita and Struik, assume the motion to be perdiodic in space and the wave profile to be that of a steady state. For waves of finite amplitude, the nonlinearity is partly taken into account by the use of a power series in terms of the wave steepness (for deep water) and carrying out the analysis to include higher order approximations. Accordingly, an initially symmetric progressive wave of finite amplitude in deep water, continues to remain symmetric about the crest and trough, although the trough may flatten and the crests become sharper. However, for sufficiently deep water, this steady symmetric solution is unstable and, if true unsteadiness is admitted in the solution procedure, gives way to an unsteady unsymmetric solution exhibiting the breaking phenomenon.

It is perhaps worth recalling what occurs in viscous flow past a circular cylinder. Under the assumption of steady-state flow symmetric about the cylinder axis, the solution exhibits a single recirculating vortex occurring downstream of the cylinder and positioned symmetrically on either side of the cylinder axis. As the flow Reynolds number increases, this symmetric steady-state solution becomes unstable and an unsteady computation made without the assumption of symmetry exhibits shedding of vortices alternately above and below the axis, leading to the well-known von Karman vortex street, with no possibility for existence of a true steady state. This problem has been widely studied for a long time.

It is possible that a more definitive answer to Dr. Wehausen's comment is not presently available. But I believe that admitting unsteadiness and not assuming symmetry yields a solution that is a step closer to that encountered in reality.

Session III

TRANSIENT AND NONLINEAR SOLUTIONS TO BODY-WAVE AND WATER-WAVE PROBLEM

J.W. Schot
Session Chairman
David W. Taylor Naval Ship
Research and Development Center
U.S.A.

A SHORT REVIEW OF MATHEMATICS AND NUMERICAL METHODS IN TRANSIENT SHIP HYDRODYNAMICS

D. Euvrard
Groupe Hydrodynamique Navale (E.R.A. 070664 du C.N.R.S.)
École Nationale Supérieure de Techniques Avancées
Centre de l'Yvette, 91120 Palaiseau (France)

Abstract

• The transient problems in ship hydrodynamic research are among the most attractive for different reasons. Firstly, some linearized problems such as wave resistance or diffraction of waves by a ship with forward speed, are difficult to handle with in their stationary or time-harmonic formulation ; they could be more easily solved as limiting cases of time-depending problems. Secondly a transient approach defines a natural iterative procedure which usually permits to deal with nonlinear problems.

• This point of view is comforted by the success of this kind of methods in aerodynamics, mechanics of continua and thermodynamics. However the mathematical and numerical treatment of transient ship hydrodynamics turns out to be rather difficult.

• Indeed many eulerian or lagrangian schemes have proved to be very efficient for nonlinear problems involving free surfaces. Let us quoteG.I.BOURIANOFF,B.R.PENUMALLI [1] for eulerian methods, M.J. FRITTS and J.P. BORIES [2] for lagrangian methods, and also the review papers by B.D. NICHOLS and C.W. HIRT [3] and by C. VON KERCZED [4]. But those methods are devised for bounded domains and do not appear to be well suited to take radiation of waves up to infinity into account. For the latter reason in the following we shall rather take an interest in linearized theories describing precisely the radiation of energy towards infinity.

• A first possible track has been investigated by J.T. BEALE. He considered the motion of a body freely floating on the surface of a fluid of infinite extend and finite depth. Making use of the semigroup theory, he proved a theorem of existence and uniqueness of the solution. Later on, C. LICHT introduced an implicite time-discretization, combined with a finite-element (or a localized finite-element) method in space. He gave error estimates and got numerical results, but for a given size of the computation domain the solution remains no longer valid after the main wave-front has reached the outer boundary.

We shall give some details about BEALE's approach, together with an intuitive presentation of his mathematical background. Next we shall briefly present and comment on LICHT's work, which will be detailed here anyway by the author himself [12].

• A second possible trend has been investigated by A. FINKELSTEIN, who determined the Green function of the transient problem in two and three dimensions, assuming finite (and constant) or infinite depth. H. ADACHI and S. OHMATSU, using this Green function, worked out a singularity distribution method. They showed that the irregular frequencies of the associated time-harmonic problem are related to some indesirable oscillations they encountered : however they gave practical rules to avoid theoccurrence of such oscillations. We shall summarize here the main results from KINKELSTEIN, ADACHI and OHMATSU.

• R.M. GARIPOV gave a theorem of existence and uniqueness based on a transformation of the problem into a wave equation at the free surface. Following a rather general numerical method due to A. JAMI and M. LENOIR (involving a coupling of integral representation and finite elements), A. JAMI solved the problem of a forced motion of a submerged body. We shall only sketch GARIPOV's mathematical formulation, the coupling method from JAMI and LENOIR (which is discussed in a separate paper [25]), and the application of the method to transient flows (which will be developped by JAMI in [23]).

• Finally we regret we have no time and no place to review other interesting methods as

- the finite-difference method from H.J. HAUSSLING and R.T. VAN ESELTINE [5] (which could probably enter BEALE's mathematical framework), or

- A. HARTEN's method [6] which makes use of ordinary sources on the boundary of the fluid domain (and which has some connection with YEUNG's techniques), or

- a number of other methods...

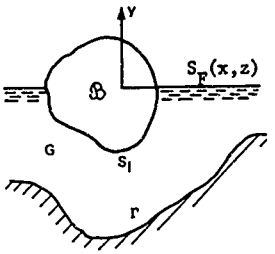
Moreover we shall be interested in P.B. CHAPMAN's method, which has been announced for the present meeting [27].

Note that in our short review, we shall keep in mind the old but still basic paper from F. JOHN [7].

I. The works of J.T. BEALE and J. LICHT

I.1. BEALE's basic paper [8].

a) The problem and the associated functional spaces.



Sketch 1 (BEALE, LICHT)

Let $\mathcal{B}$ be *a rigid body floating freely* in an ocean of infinite extent but of *bounded depth* (see sketch 1). Let Γ be the bottom of this ocean and S_F its mean free-surface (located in the plane y=0) ; as we shall only consider a linearized approximation of the water-waves, the free-surface conditions will be imposed on S_F. In a similar way, we shall assume the amplitude of the body-motions remains small, therefore the slip condition is imposed on a fixed surface, namely the mean position S_I of the hull. G will denote the fluid domain with boundary $\Gamma+S_F+S_I$. At any time t we want to know the state

$$u(t) = (\phi,\eta,s,v) \qquad (1)$$

of the coupled liquid-solid system, where

- ϕ is the velocity potential,
- η the free-surface elevation,
- s a vector having as components the 6 position parameters of the body and
- v a vector having as components the 6 velocity parameters of the body.

• The total energy $\mathcal{E}(t)$ of the mechanical system is the sum of the liquid kinetic energy, the liquid potential energy, the body kinetic energy and the body potential energy, namely

$$\frac{2\mathcal{E}(t)}{\rho} = \int_G |\vec{\nabla}\phi|^2 dv + g\int_{S_F} \eta^2 dS + |\mathbb{E}v\cdot v + |\mathbb{K}s\cdot s, \qquad (2)$$

where ρ is the liquid density, g the gravity acceleration, $\rho|\mathbb{E}$ the 6 × 6 inertial matrix of the body and $\rho|\mathbb{K}$ a 6 × 6 hydrostatic restoring matrix. Both matrices $|\mathbb{E}$ and $|\mathbb{K}$ are symmetrical.

• J.T. BEALE looks for ϕ in the space

$$H_D(G) = \text{closure of } \mathcal{D}(G), \qquad (3)$$
$$\text{which is } \{\text{functions of } C^\infty(G) \text{ with compact supports}\},$$

for the norm

$$||\phi||_{H_D(G)} = ||\vec{\nabla}\phi||_{(L^2(G))^3} . \qquad (4)$$

Let us point out that a potential $\phi \in H_D(G)$ may not be square-integrable while, on the contrary, the velocity $\vec{\nabla}\phi$ must be square-integrable.

• η will be sought of course in $L^2(S_F)$. Finally we shall look for u(t) in

$$\mathcal{H} = H_D(G) \times L^2(S_F) \times |R^6 \times |R^6 . \qquad (5)$$

Let us point out that $\mathcal{H}$ is nothing but the space of possible states of finite energy of the system.

---

* In fact, in most applications, the velocity potential ϕ will belong to a strictly smaller space, namely

$$W^1_o(G) = \{\phi \in H^1_{loc}, \frac{\phi}{(1+r^2)^{1/2}} \in L^2(G), \vec{\nabla}\phi \in (L^2(G))^3\},$$
$$r = (x^2+y^2+z^2)^{1/2} ,$$

equipped with the same norm (4). Note that when ϕ is regular at finite distance and behaves like $1/r^\alpha$ at infinity, ϕ belongs to W^1_o if, and only if, $\alpha > 1/2$.

In most problems involving unbounded domains, W^1_o is considered today as the standard functional space. By using $W^1_o(G)$ [which is more tractable] instead of $H_D(G)$, we could somewhat simplify BEALE's arguments...

b) The equations of the motion.

Let us list the set of well-known equations of the fluid motion.

• The fluid is assumed incompressible, thus ϕ satisfies Laplace's equation

$$\nabla^2\phi = 0 \text{ in } G. \tag{6}$$

• ϕ and η satisfy the classical linearized free-surface conditions

$$\phi_t\Big|_{y=0} = -g\eta \ , \ \eta_t = \frac{\partial\phi}{\partial y}\Big|_{y=0}. \tag{7}$$

• We must impose the slip-condition on the bottom Γ and the hull S_I

$$\frac{\partial\phi}{\partial n}\Big|_\Gamma = 0, \quad \frac{\partial\phi}{\partial n}\Big|_{S_I} = v*p, \tag{8}$$

where p means the generalized normal to the hull.*

• Finally we must apply the fundamental principle of dynamics to the body

$$|E\, v_t = -|K\, s - \int_{S_I} \phi_t\, p\, dS, \tag{9}$$

indicial notation meaning the first t-derivative.

c) Transformation of the equations of the motion into a differential system of first order.

• J.T. BEALE introduces 6 auxiliary functions h_i satisfying problems P_i $(1\le i\le 6)$

$$(P_i)\begin{cases} \nabla^2 h_i = 0 & \text{in } G, \\ h_i = 0 & \text{on } S_F, \\ \dfrac{\partial h_i}{\partial n} = 0 & \text{on } \Gamma, \\ \dfrac{\partial h_i}{\partial n} = p_i & \text{on } S_I. \end{cases}$$

It is well-known that each of these 6 problems has one and only one solution in the space $H^1(G)$ of square-integrable functions having square-integrable first derivatives.

Then J.T. BEALE builds the 6×6 matrix $|H$ of coefficients

$$H_{ij} = \int_{S_I} h_i\, p_j\, dS. \tag{10}$$

Using Green's second and first formulae, we see that $|H$ is symmetrical and positive definite. The vector field of components h_i on G is denoted h.

• J.T. BEALE also introduces the function Ψ, harmonic in G, equal to η on S_F and the normal derivative of which vanishes on S_I and Γ. Such a function does not always exist, thus the operator $B : \eta\in L^2(S_F) \to B\eta = \nabla\Psi\in H^1(G)$ is defined on a strict subset of $L^2(S_F)$ called the domain of B.

By making use of $|H$ and B, we can write equations (6) to (9) under the form

$$\frac{du}{dt} = Au, \tag{11}$$

with

$$\left.\begin{aligned} (Au)_1 &= -g\, B\eta + (Au)_4 * h \\ (Au)_2 &= \frac{\partial\phi}{\partial y}\Big|_{S_F} \\ (Au)_3 &= v \\ (Au)_4 &= (|E*|H)^{-1}\{-|K*\textstyle\int_{S_I} gB\eta p dS) \end{aligned}\right\} \tag{12}$$

In particular, $\phi_t=(Au)_1$ is harmonic, since $\nabla^2(B\eta)=0$ and $\nabla^2 h_i=0 (1\le i\le 6)$. D(A) will denote the domain of the operator A.

d) The total energy $\mathcal{E}(t)$ [as defined by (2)] is a constant.

As this result is often only considered as intuitive, and may be unfounded, we decide to give hereafter a detailed proof.

Let u and $\tilde{u}=(\tilde{\phi},\tilde{\eta},\tilde{s},\tilde{v})$ be arbitrary elements of $D(A) \subset \mathcal{H}$ and $\mathcal{H}$ respectively. Their scalar product in $\mathcal{H}$ is taken as

$$(u|\tilde{u})_{\mathcal{H}} = \int_G \vec{\nabla}\phi*\vec{\nabla}\tilde{\phi}\, dv + g\int_{S_F} \eta\tilde{\eta} dS + |E v*\tilde{v} + |K s*\tilde{s}\ . \tag{13}$$

Hence $2\mathcal{E}/\rho = (u|u)_{\mathcal{H}}$ and, according to (12), $\frac{1}{\rho}\frac{d\mathcal{E}}{dt} = (u_t|u)_{\mathcal{H}} = (P*Q)+R*S+T$, with

$$P = -g\int_G \vec{\nabla}\phi*\vec{\nabla}\Psi dv = -g\int_{S_F} \frac{\partial\phi}{\partial y}\underbrace{\Psi}_{=\eta} dS - g\int_{S_I} \Big(\sum_{i=1}^{6} v_i p_i\Big)\Psi dS$$

(thanks to Green's first formula),

---

* $\vec{n}$ being the usual normal to the hull, directed outward the fluid, and M_o being some reference point, then $p_i=n_i$ for $1\le i\le 3$ and

$p_i = (\vec{M_oM}\wedge\vec{n}(M))_{i-3}$ for $4\le i\le 6$.

$$Q = \int_G \sum_{i=1}^{6} [(|E^*|H)^{-1}A]_i \vec{\nabla} h_i \cdot \vec{\nabla} \dot{e} \, dv,$$

$$A = -|K^* + \int_{S_I} g \vec{\nabla} p \, dS, \quad Y = Bn,$$

$$R = g \int_{S_F} \frac{\partial \dot{e}}{\partial y} n \, dS, \quad S = |K \, s \cdot v$$

$$T = \sum_{i=1}^{6} [|E(|E^*|H)^{-1}A]_i v_i = \sum_{i,j=1}^{6} E_{ij} [(|E^*|H)^{-1}A]_j v_i.$$

By Green's first formula,

$$Q = \sum_{i=1}^{6} [(|E^*|H)^{-1}A]_i \{ \int_{S_I} h_i \frac{\partial \dot{e}}{\partial n} \, dS + \int_{S_F} h_i \frac{\partial \dot{e}}{\partial y} \, dS \}$$

$$= \sum_{j=1}^{6} v_j P_j \qquad = 0$$

$$= \sum_{i,j=1}^{6} [(|E^*|H)^{-1}A]_i H_{ij} v_j.$$

Using $H_{ij} = H_{ji}$, interchanging i and j in Q, and adding the result to T, we find

$$Q + T = \sum_{i,j=1}^{6} (E_{ij} + H_{ij}) [(|E^*|H)^{-1}A]_j v_i = \sum_{i=1}^{6} A_i v_i,$$

$$A_i = -(|K \dot{s})_I + \int_{S_I} g \nabla p_I \, dS,$$

and finally

$$(Au|u)_{\mathcal{H}} = (u_t|u)_{\mathcal{H}} = \frac{1}{\rho} \frac{d\mathcal{E}}{dt} = 0, \qquad (14)$$

and consequently $\mathcal{E}$ remains constant. □

e) A theorem of existence and uniqueness.

•The operator A and the scalar product (13) being linear,

$$(A(u+v)|u+v)_{\mathcal{H}} = (Au|u)_{\mathcal{H}} + (Av|v)_{\mathcal{H}} + (Au|v)_{\mathcal{H}} + (Av|u)_{\mathcal{H}},$$

and from (14), we infer

$$\forall u, \forall v, \quad (Av|u)_{\mathcal{H}} = -(Au|v)_{\mathcal{H}}. \qquad (15)$$

i.e. *A is skew self-adjoint.* Moreover some complementary topological properties can be established : namely *A is closed, and its domain D(A) is dense in the subspace of $\mathcal{H}$ of the u satisfying (6) and (8).*

In that case, Stone's theorem asserts that *"A generates a one-parameter strongly continuous group of unitary operators".*

The mathematical background of this theorem is *the theory of semigroups* : see for instance P.D. LAX and R.S. PHILLIPS ([9],pp245-254) or M. SCHECHTER ([10], pp 224-242). Here we shall briefly summarize the latter presentation, which is a more inductive reasoning.

• *If A were a constant and u a scalar function,* we could integrate the ordinary differential equation (11) with a given initial condition u(0), and obtain the solution

$$u(t) = \exp(tA)u(0) = \left(\sum_{n=0}^{+\infty} \frac{t^n}{n!} A^n \right) u(0), \qquad (16)$$

the series (16) being uniformly convergent on [0,T], for any fixed positive T and A.

• *In fact, A is an operator* defined in the vector-space $\mathcal{H}$, and u is a vector of $\mathcal{H}$. *If this operator were bounded,* i.e. if we had $||Au|| \leq ||A|| \, ||u||$ for any u, with $||A|| < +\infty$, we could still solve (11) with u(0) given. In that case, considering $A^n = A(A(A....))$ and exp(tA) as operators, we could still easily give a meaning to its series representation (16).

• *In fact, the operator A is not bounded,* and the domain D(A) is strictly smaller than $\mathcal{H}$. But under the assumptions of Stone's theorem (and even weaker assumptions) it is still possible to define the operator $E_t = \exp(tA)$ for any t>0 (as a limit of bounded auxiliary operators).

The set of operators $E_t = \exp(tA)$ for t≥0 is called a *semigroup of operators* with infinitesimal generator A. It has the following properties

$$\left.\begin{array}{ll} \text{(i)} & E_0 = I, \\ \text{(ii)} & E_s E_t = E_{s+t}, \ s \geq 0, \ t \geq 0, \\ \text{(iii)} & E_t x \text{ is continuous in } t \geq 0 \text{ for any } x \in \mathcal{H}, \\ \text{(iv)} & E_t x \text{ is differentiable in } t>0 \text{ for each } x \in D(A) \subset \mathcal{H}, \text{ and } \frac{d}{dt}(E_t x) = A(E_t x). \end{array}\right\} \qquad (17)$$

Properties (i) and (ii) correspond to the general concept of "semigroup", while (i), (iii) and (iv) mean that $E_t u(0)$ is the unique solution of our initial-value problem, provided that $u(0) \in D(A)$.
Moreover there exists a real constant α such that $(\lambda I - A)^{-1}$ exists and is bounded on $\mathcal{H}$ for any $\lambda > \max(0, -\alpha)$:

$$||(\lambda I - A)^{-1}|| \leq \frac{1}{\lambda + \alpha}. \qquad (18)$$

In the present case, and since A is skew self-adjoint, E_t can be defined even for t<0, i.e. *the evolution is time-reversible* : the semigroup is in fact *a group,* and α=0.

Let us conclude :

the equation (11), together with an initial data u(0)∈D(A), has one and only one solution

in D(A), for any t, and this solution has a constant energy.

I.2. LICHT's numerical approximation [11],[12].

• It is well-known that, if A generates a semigroup, the implicit finite-difference scheme

$$\frac{u^{k+1}-u^k}{\Delta t} = Au^{k+1}, \quad \Delta t = \frac{T}{n}, \quad 0 \le k \le n-1, \qquad (19)$$

is uniformly convergent on [0,T], for any positive T.

Let us only sketch the proof of stability. Equ. (19) takes the form

$$(I-\Delta t A)u^{k+1} = u^k, \qquad (20)$$

whence

$$\|u^{k+1}\| \le \|(I-\Delta t A)^{-1}\| \, \|u^k\|$$

$$= \|(\frac{1}{\Delta t} I - A)^{-1}\| \, \frac{1}{\Delta t} \|u^k\| \qquad (21)$$

$$\le \|u^k\|$$

by applying (18), with $\lambda = 1/\Delta t$ and $\alpha = 0$. □

• Of course it is not possible to work numerically in an unbounded domain G. For this reason C. LICHT truncates G at a finite distance R_n from the origin ; let G_n be the corresponding bounded domain and S_n its outer boundary. He writes the approximate problem P_n that replaces the previous problem P = {(11), (12) + initial condition}. P_n involves a boundary condition

$$\phi_c + \nu \frac{\partial \phi}{\partial n} = 0, \quad \nu \ge 0 \quad \text{on} \quad S_n, \qquad (22)$$

$\nu = 0$ corresponding to a Dirichlet condition, $\nu = +\infty$ to a Neumann condition and $\nu > 0$ to an "absorbing" condition. (Note that if $\phi_c = -i\omega\phi$, (22) reduces to the usual radiation condition for time-harmonic flows).

For a given time-interval [0,T], C. LICHT proves that P_n is well-posed and that the corresponding solution converges towards the solution of P when n tends to infinity with $\lim_{n\to\infty} R_n = +\infty$.

• In a second step, C. LICHT approximates the space-operator in G_n using standard finite elements which convergence he also proves, even in the case of a curved hull S_I.

• C. LICHT Has written a computing program devoted to that method in the 2D-case. He gives more technical details about it in [12]. Let us notice that if the time-step Δt is constant, the linear system to be solved at each time-step always involves in its left hand-side the same symmetrical matrix, thus this matrix can be factorized once for all using choleski's algorithm.

Moreover C. LICHT generalized the method to take tsunamis into account.
A number of LICHT's results are shown is [12]. Let us take out and comment on two of his figures, Figure 4 and Figure 6.

• Strictly speaking, the information propagates with an infinite velocity, and at any positive time t all fluid particles are aware of the starting of the fluid motion. But in practice there appears something like an energy wave-front that propagates with a finite velocity. This is quite obvious on LICHT's figure 4, where the energy decay

- is negligible for t<2s.
- but becomes significant for t>2s, and strongly depends on the absorption constant ν[see (22)].

• LICHT's computations can actually be trusted only for $t < t_n$, where t_n (equal to 2s in the case of figure 4) increases with n. But fortunately the transient phase between t=0 and the asymptotic equilibrium position turns out to be very short, so that the preceeding remark is not a fix, as we can infer from the good agreement in figure 6 between LICHT's results, ADACHI-OHMATSU's singularity distribution results and KOTIK-LURYE's analytical results.

II. The works of A.B. FINKELSTEIN and H. ADACHI-S.OHMATSU

II.1. FINKELSTEIN's Green functions for transient flows [13].

Here combining equations (7) together we eliminate the free-surface elevation η, thus we obtain the following free-surface condition for φ :

$$(\phi_{tt} + g \frac{\partial \phi}{\partial y})\Big|_{y=0} = 0. \qquad (23)$$

More than 20 years ago, A.B. FINKELSTEIN gave the Green function of the transient problem, in 2 or 3 dimensions, in both cases of finite and infinite depth. Let $H_M(P;t)$ be any of those four Green's functions, then :
$\nabla_P^2 H_M(P;t) = \delta_M(P)\delta(t)$. $H_M(P;t)$ must also satisfy the free-surface condition (23), together with conditions at infinity and on the bottom. Moreover the condition $H_M\big|_{\substack{y=0 \\ t<0}} = 0$ is imposed.

For instance, in the 3D case and for an infinite depth, $H_M(P;t)$ reads

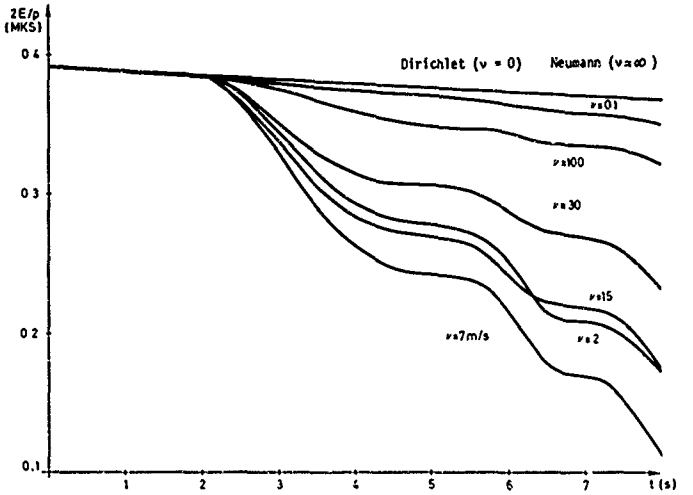


Figure 4 - ENERGY OF THE SYSTEM ($\phi_t + \nu \partial_n \phi$ = 0-20m away) (TAKEN OUT FROM C. LICHT [12])

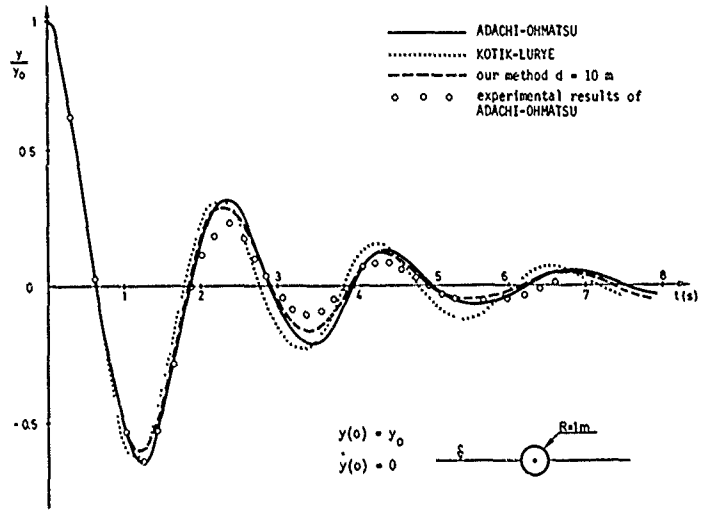


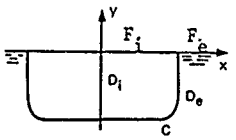
Figure 6 - HEAVE MOTION (TAKEN OUT FROM C. LICHT [12])

$$
\left.
\begin{aligned}
&H_M(P;t) = \delta(t)G_M(P) + Y(t)F_M(P;t),\\
&\qquad M=(x,y,z),\ P=(\xi,\eta,\zeta),\\
&G_M(P) = E_M(P) - E_{M'}(P),\\
&\qquad E_M(P) = -\frac{1}{4\pi|\overrightarrow{MP}|}\\
&\text{(M' being symmetrical from M with respect to the linearized free-surface y=0),}\\
&F_M(P;t) = -\frac{16}{\pi^2 g t^2}\int_0^{\pi/2} \mathrm{Re}\{p^2\frac{d}{dt}[pL(p)]\}d\beta\\
&p=\frac{gt^2}{4q},\quad q=r+i(y+\eta)\cos\beta,\\
&\qquad r=[(x-\xi)^2+(z-\zeta)^2]^{1/2},\\
&\qquad L(p)=\int_0^1 \exp[p(1-s^2)]ds.
\end{aligned}
\right\} \quad (24)
$$

From now on, we shall assume that the depth is infinite.

II.2. ADACHI-OHMATSU's study of the integral equation of a time-depending flow problem [14], [15].

Let us now consider a problem of *time-depending forced oscillations* of a hull : the (small) motion of the hull being given, we want to compute the flow potential Φ and then to find the resulting forces on the hull.



Sketch 2 (ADACHI-OHMATSU)

Using Green's third identity, the knowledge of the Green function (24) allows to give an integral representation for the potential Φ_e of the transient problem in the outer region D_e (see sketch 2) :

$$
\left.
\begin{aligned}
\forall M\in D_e,\ \Phi_e(M;t) &= \int_C [\Phi_e(P;t)\frac{\partial G_M}{\partial n_P}(P)\\
&\quad - v(P;t)G_M(P)]ds_P\\
&+ \int_0^t\int_C [\Phi_e(P;t-\tau)\frac{\partial F_M}{\partial n_P}(P;\tau)\\
&\quad - v(P;t-\tau)F_M(P;\tau)]ds_P d\tau.
\end{aligned}
\right\} \quad (25)
$$

where $v(P;\tau)$ is the given normal velocity on the hull.

The main advantage of *such a representation* is of course the fact that it *reduces the problem to finding Φ_e on the hull, the Laplace equation, free-surface condition and conditions at infinity being thus automatically and exactly satisfied.*

a) The singularity distribution method using sources and doublets.

In (25) we have already taken the slip condition on the hull into account. Thus all what we still have to impose is the continuity of Φ_e in $\overline{D}_e$: $\Phi_e(P)$ for $P\in D_e$ converges to $\Phi_e(P_o)$ when P tends to $P_o\in C$. Thus we find the following integral equation for $\Phi_e|_C$:

$$
\left.
\begin{aligned}
\forall M\in C,\ -\frac{1}{2}\Phi_e(M;t) &+ \int_C \Phi_e(P;t)\frac{\partial G_M}{\partial n_P}(P)ds_P\\
&+ \int_0^t\int_C \Phi_e(P;t-\tau)\frac{\partial F_M}{\partial n_P}(P;\tau)ds_P d\tau\\
&= \int_C v(P;t)G_M(P)ds_P\\
&+ \int_0^t\int_C v(P;t-\tau)F_M(P,\tau)ds_P d\tau.
\end{aligned}
\right\} \quad (26)
$$

b) The singularity distribution method using only sources.

Assuming temporarily that the outer solution Φ_e is known, we consider the adjoint problem P_i for Φ_i in D_i. Φ_i satisfies the Laplace equation in D_i, together with the free-surface condition (23) on F_i (see sketch2) and the homogeneous initial conditions $\Phi_i=\Phi_{it}=0$ for t=0, and we impose the Dirichlet condition $\Phi_i|_C=\Phi_e|_C$.

When P_i is well-posed (see [22]), then setting

$$
\sigma(P;t) = \frac{\partial\Phi_i}{\partial n}(P;t) - \frac{\partial\Phi_e}{\partial n}(P;t), \forall P\in C, \quad (27)
$$

we can transform the integral representation (25) into

$$
\begin{aligned}
\forall M\in D_e,\ \Phi_e(M;t) &= \int_C \sigma(P;t)G_M(P)ds_P\\
&+ \int_0^t\int_C \sigma(P,t-\tau)F_M(P;\tau)ds_P d\tau.
\end{aligned} \quad (28)
$$

The corresponding integral equation for σ reads

$$\forall M \in C, \quad -\frac{1}{2}\sigma(M;t) + \int_C \sigma(P;t)\,\frac{\partial G_M}{\partial n_P}(P)\,ds_P + \int_0^t \int_C \sigma(P;t-\tau)\,\frac{\partial F_M}{\partial n_M}(P;\tau)\,ds_P\,d\tau = v(P;t). \tag{29}$$

N.B. In the frequency domain (i.e. in the time-harmonic case) the method a) involving the integral equation (26) turns out to be POTASH's method [16], while the method b) involving the integral equation (29) corresponds to FRANK's [17]. The corresponding problem of the irregular frequencies for ϕ_e (i.e. the problem of eigenvalues for ϕ_i) had already been studied by S.OHMATSU in [18].

c) The numerical experiments of DAOUD and OHMATSU.

M. DAOUD [19] and S. OHMATSU [14] made computations using respectively equ.(26) and equ.(29) ; they obtained quite contradictory results.

• M. DAOUD, using both sources and doublets and solving equ.(26), did not find any problem of irregular frequency and got quite realistic results.

• On the contrary, S.OHMATSU, using only sources and solving equ.(29), got non-realistic results. For instance, as we can see in figure 2, taken out from [14], an excitation imposed during a finite time (upper curve, showing the forced velocity of a semi-submerged circular hull, versus time) gives rise to a non-damped response (lower curves, giving $\sigma(\theta,t)$ for two different locations θ on the hull) ! Moreover it turns out that the frequency of the ever lasting oscillatory part of σ coincides approximately with the first irregular frequency of the same hull in the time-harmonic oscillation problem ...

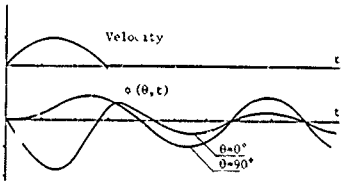


Figure 2, taken out from H. ADACHI and S. OHMATSU [14].

d) The basic study of ADACHI and OHMATSU.

In [14], H. ADACHI and S. OHMATSU give a satisfactory explanation of such opposite behaviours of both solutions of equ. (26) and (29).

• First, they show that the time-harmonic problem corresponding to a free-surface constant $\nu = \omega^2/g$ is the Fourier transform in time of the time-depending problem. As a matter of fact, both Green's functions are related by the same Fourier transform.

• Then they show that the time-harmonic problem corresponding to (26) (i.e. POTASH's problem) is well-posed, even when $\omega/2\pi$ is an irregular frequency (i.e. a resonance frequency of the inner problem P_i), because the classical FREDHOLM "compatibility condition" appears to be always satisfied by the right-hand side of equ.(26). Of course, this condition will not be exactly satisfied after discretization, thus some "numerical instabilities" may appear ; but after application of the inverse Fourier transform, no problem occurs in solving equ.(26) in the time-domain.

• On the contrary, H. ADACHI and S.OHMATSU show that the time-harmonic problem corresponding to equ. (29) (i.e. FRANK's problem) is ill-posed when ω equals any of the irregular pulsations ω_i. More precisely, any interesting result of the time-harmonic problem, for instance the source-density as defined by (27), will grow up to infinity like $(\omega-\omega_i)^{-1}$ in the limiting process $\omega \to \omega_i$. And because of the classical result

$$\overline{\mathcal{F}}\left[\mathrm{pv}\left(\frac{1}{\omega-\omega_i}\right)\right] = \frac{i}{2}\,\mathrm{sgn}\,t\; e^{i\omega_i t}, \tag{30}$$

S OHMATSU can explain his paradoxal results !

• Finally H. ADACHI and S. OHMATSU claim that they can transform equ. (29) into a well-posed problem by modifying the Green function (24).

And their resulting computations (see figure 6 already quoted) fully confirm their theoretical speculations.

III. The works of R.M. GARIPOV and A. JAMI

III.1. GARIPOV's theoretical work.

A few authors, among whom R. FRIEDMAN and M. SHINBROT [20], R.M. GARIPOV [21], J. BOUJOT [22], ... gave to time-depending problems a theoretical basis somewhat different from that presented later by BEALE. Like FINKELSTEIN, ADACHI and OHMATSU (but unlike BEALE) they consider forced oscillations of a floating body.

Let us follow for instance R.M. GARIPOV.*

Let v(t) be the given normal velocity of the hull C (see sketch 2 or sketch 3).

Let us recall the problem P for the (outer) potential $\overset{v}{\phi}$:

$$(P)\begin{cases} \Delta\overset{v}{\phi} = 0 \text{ in } D_e \text{ (sketch 2)} \\ \qquad \text{or } \overset{v}{\Omega} \text{ (sketch 3)}, \\ \dfrac{\partial\overset{v}{\phi}}{\partial n} = v(t) \text{ on C}, \\ \overset{v}{\phi}_{tt} + g\dfrac{\partial\overset{v}{\phi}}{\partial y} = 0 \text{ on } F_e \text{ (sketch 2)} \\ \qquad \text{or } S_F \text{ (sketch 3)}, \\ \overset{v}{\phi} = \overset{v}{\phi}_t = 0 \quad \text{for } t=0. \end{cases}$$

Let ϕ be the trace of $\overset{v}{\phi}$ on S_F at time t. We can split P into two (quasi-)steady problems

$$(P_o)\begin{cases} \Delta\phi_o = 0 \text{ in } \Omega, \\ \dfrac{\partial\phi_o}{\partial n} = v(t) \text{ on C}, \\ \phi_o = 0 \text{ on } S_F, \end{cases}$$

and

$$(P_1)\begin{cases} \Delta\phi_1 = 0 \text{ in } \Omega, \\ \dfrac{\partial\phi_1}{\partial n} = 0 \text{ on C}, \\ \phi_1 = \phi \text{ on } S_F. \end{cases}$$

(We assume ϕ is a given function for the moment).

* v being given in $L^2(C)$, P_o has one and only one solution ϕ_o in W^1_o (see footnote of § I.1.a)). Indeed, it is easy to see that the derivative $f = -g\dfrac{\partial\phi_o}{\partial y}\Big|_{S_F}$ belongs to $L^2(S_F)$.

* We assume the body is submerged. Let k_1 be the operator

ϕ_1 defined on $S_F \longrightarrow K_1\phi = g\dfrac{\partial\phi_1}{\partial y}\Big|_{S_F}$ the normal derivative (on S_F) of the unique solution of P_1.

K_1 is a *self-adjoint, positive, unbounded operator* in $L^2(S_F)$ *with dense domain*.

* Then the solution $\overset{v}{\phi}$ of P will be the sum $\phi_o + \phi_1$, provided that ϕ satisfies the "wave-equation"

$$\phi_{tt} + K_1\phi = f \qquad (31)$$

in $L^2(S_F)$, with initial conditions $\phi(0)=\phi_t(0)=0$.

It can be shown that the latter problem has (at least) one solution.

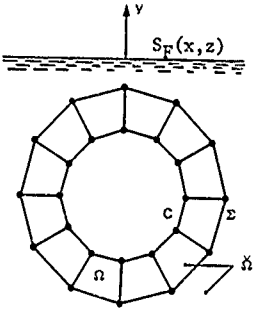
Then $\phi = \phi_o + \phi_1$ thus constructed can be shown to be the unique solution of P, using a classical energy argument.

III.2. JAMI's numerical method.

In the present conference, A. JAMI exhibits a contribution to the numerical solving of the time-depending problem of a floating body subject to forced oscillations [23].

The mathematical background to which he refers is the one we have just described in § III.1, and which asserts the existence (and uniqueness) of the solution of the problem.

Then A. JAMI uses the integral representation (25) involving the Green function (24). He introduces a time discretization with step $\Delta t = t^n - t^{n-1}$ and he chooses a second order finite difference scheme in time to approximate the convolution appearing in the last integral of equ. (25) : though the convergence of such a scheme has not yet been proved, it has been numerically tested and can actually be trusted.



Sketch 3 (JAMI)

Next A. JAMI reduces, for each time step, the problem P set in the unbounded domain $\overset{v}{\Omega}$ to an equivalent problem P in a bounded domain Ω (see sketch 3) by writing (25) on the outer (or "coupling") boundary of Ω ; this equivalence must be put down to the account of the Green function, which contains the whole information concerning the flow (especially at infinity).

* GARIPOV considered the case of a finite depth and this proof was extended by JAMI to the case of an infinite depth.

More precisely, the potential ϕ^n at time t_n must satisfy Laplace's equation in the computational domain Ω, together with the usual slip-condition on the hull C. If the body is surface-piercing, so is the computing domain Ω too, and a finite difference scheme must be introduced to approximate the free surface condition (23) on $S_F \cap \bar{\Omega}$. If the body is submerged, the computing domain can be chosen submerged too, and the free-surface condition can be disregarded.

Now, on the outer boundary Σ of Ω (sketch 3) the discretized form of the integral representation (25) is imposed : this means a coupling between $\phi_{|\Sigma}$ and $\phi_{|C}$. Using an extension operator from C into Ω*, the problem P at each time step in the bounded domain Ω is given a variational formulation which is amenable to classical finite element techniques. *The integral representation is not singular and can be computed via Gauss quadratures, thus allowing finite element discretizations of high order of accuracy.*

This method of coupling between integral representation and finite elements has been designed by A. JAMI and M. LEMOIR (see [24]) in two main versions ; each of them has been *intensively worked out and tested on a number of 2D or 3D problems* belonging to aerodynamics, sea-keeping, wave-resistance, coastal engineering or acoustics. A survey concerning this method is presented in [25].

Though the coupling method was initially designed ... for time-depending problems in ship hydrodynamics, it has been applied only recently to this very problem. The method is very stable and exhibits *a specially favorable precision/cost ratio,* since in practice one layer of finite elements appears to be sufficient. Sketch 3 shows a 12 element-discretization for a submerged circular cylinder of radius 1/2 and which center is located at the depth a ; the elements shown here are quadrangles of first order, but second order isoparametric elements are currently operated.

The last figure in this paper is due to JAMI [23]. For the forced oscillations $Y(t)\cos(\mu t)$ the time harmonic flows is established within the first cycle, what several authors already observed [26]. In figure 3, time-depending and time-harmonic solutions are compared (Let us notice that both computations have been performed using the same coupling method, which proves to be rather general...)

Though the time-discretization has not yet been mathematically justified, JAMI's method appears to be numerically effective, specially when the phenomenon under consideration is to last some time, since the condition at infinity is taken exactly into account thus avoiding the use of any approximate absorbing outer boundary condition.

* Such an extension operator makes the formal presentation of the method somewhat difficult, but it must be pointed out that the discretized version of this operator is very easy to handle.

IV. Conclusion

We can now try to give some brief conclusions and suggestions about the methods devoted to *transient linearized free-surface problems in unbounded domains.*

IV.1. Comments on theoretical results

a) R. FRIEDMAN and M. SHINBROT, R.M. GARIPOV, J. BOUJOT ... consider the problem of the *forced oscillations* of a floating body, the only unknown of which is the velocity potential ϕ. They reduce the problem to finding the trace ϕ of ϕ on the linearized free surface y=0 : ϕ must satisfy a wave equation in that plane. *Assuming that the whole fluid is at rest à t=0,* they establish a theorem of existence.

b) On the contrary, J.T. BEALE considers *a body free to oscillate* . the unkowns are the velocity potential, the wave height and the body position and velocity. The initial data may be arbitrary. J.T. BEALE establishes a theorem of existence and uniqueness using the powerful technique of semigroups.

c) J.T. BEALE initially assumed the water-depth finite and $\mathbb{K}$ positive-definite. As a matter of fact, it is possible to get rid of the first assumption by changing the functional space, and C. LICHT proved that the second assumption is not necessary. The case of a forced motion also enters the scope of the method. Moreover C. LICHT recently showed that tsunamis and hydroelasticity could also be taken into account.

The only fundamental hypothesis is that *the total energy of the system is finite.* Therefore our conclusion is that, on the theoretical point of view, *BEALE's approach* (which the most recent) *is probably the most general.*

It is quite remarquable that such a theoretical basis exists for transient flows, since no theorem of existence or uniqueness is known at the present time for steady flows or for the diffraction of waves by a ship with forward speed. Of course the problem of finding such flows as limiting cases of time-depending problems remains quite open (even time-depending problems with non-linearized moving bodies do not seem to enter directly the scope of BEALE's theory).

IV.2. Comments on numerical methods.

a) C. LICHT's method of approximation involving *finite elements in space* and *finite differences in time* has the great advantage to rely upon BEALE's theoretical background and to have been *fully justified using mathematical arguments.* Moreover it has the same character of generality as BEALE's theoretical study, to which it is closely connected.

b) But in the case where we want to follow a phenomenon for a long time, LICHT's method

(just like lagrangian or eulerian schemes) cannot be applied, because *the longer the computation lasts, the wider the computational domain must be*. The situation could be bettered by using for the space discretization a localized finite element technique (like K.J. BAI's or C.C. MEI's, see [25]) as C. LICHT suggests himself. But it seems that LICHT's method should be restricted to rather short transitory phenomenous.

c) To compute long time-depending phenomenons it seems that we should use a method involving a Green's function and an integral representation. In that case the domain of computation remains bounded at any time : namely the hull itself in H. ADACHI's and S.OHMATSU's method, or a small and fixed computational domain around the body in A. JAMI's method.

Thanks to H. ADACHI and S. OHMATSU the problem of irregular frequencies now seems to be solved, and the first significant computations using a singularity distribution procedure have been performed. Thanks to A. JAMI it is possible to avoid any singular behaviour of the integral representation, thus using numerical quadratures and working out finite elements of high order of accuracy so as to save computing-time.

It remains to justify the discretization of the time-convolution involved in the integral representation, and to take (probably using time-implicit finite-differences) the dynamics of freely floating bodies into account. But *one basic assumption* seems difficult to remove if we want to handle with care the conditions at infinity using any of the available methods : the assumption that *the body and the fluid are at rest at some initial time ...*

Indeed, J.T. BEALE and C. LICHT do not need *explicity* such an assumption, but the problem set by C. LICHT in a bounded domain Ω is only an *approximation* of the problem in the unbounded domain Ω, and the information located outside Ω *is lost*. On the contrary, under the assumption that the fluid be at rest à t=0, the problem set by A. JAMI in the bounded domain $\overset{\vee}{\Omega}$ is *strictly equivalent* to the problem $\overset{\vee}{P}$ in the unbounded domain $\overset{\vee}{\Omega}$.

Bibliography

[1] G.I. BOURIANOFF, B.R. PENUMALLI, *"Theoretical Simulation of Ship Motion by Eulerian Hydrodynamic Technique"*, 2d International Conference on Numerical Ship Hydrodynamics, Berkeley, September 1977.

[2] M.J. FRITTS, J.P. BORIES, *"Transient Free-Surface Hydrodynamics"*, 2d International Conference on Numerical Ship Hydrodynamics, Berkeley, September 1977.

[3] B.D. NICHOLS, C.W. HIRT, *"Nonlinear Hydrodynamic Forces on Floating Bodies"*, 2d International Conference on Numerical Ship Hydrodynamics, Berkeley, September 1977.

[4] C. VON KERCZEK, *"Numerical Solution of Naval Free-Surface Hydrodynamics Problems"*, 1st International Conference on Numerical Ship Hydrodynamics, Bethesda, October 1975.

[5] H.J. HAUSSLING, R.T. VAN ESELTINE, *"Finite-Difference Methods for Transient Potential Flows with Free Surfaces"*, 1st International Conference on Numerical Ship Hydrodynamics, Bethesda, October 1975.

[6] A. HARTEN, *"An Efficient Differentio-Integral Equation Technique for time-Dependant Potential Flows with a Free-Surface"*, 1st International Conference on Numerical Ship Hydrodynamics, Bethesda, October 1975.

[7] F. JOHN, *"On the Motions of Floating Bodies"* I and II, Communications on Pure and Applied Mathematics, Vol.2 (1949), pp 13-57 and vol. 3 (1950), pp 45-100.

[8] J.T. BEALE, *"Eigenfunction Expansions for Objects Floating in an Open Sea"*, Communications on Pure and Applied Mathematics, Vol. 30, pp 283-313 (1977).

[9] P.D. LAX, R.S. PHILLIPS, *"Scattering Theory"*, Academic Press, New York, 1967.

[10] M. SCHECHTER, *"Principles of functional Analysis"*, Student Edition, Academic Press, New York, 1971.

[11] C. LICHT, *"Etude théorique et numérique de l'évolution d'un système fluide-flotteur"*, thèse de Docteur Ingénieur, E.N.S.M., Nantes, Octobre 1980.

[12] C. LICHT, *"Time-Dependant Behaviour of Floating Bodies"*, 3d International Conference on Numerical Ship Hydrodynamics", Paris, June 1981.

[13] A.B. FINKELSTEIN, *"The Initial Value Problem for Transient Water Waves"*, Communications on Pure and Applied Mathematics, vol. 10 (1957), pp. 511-522.

[14] H. ADACHI, S. OHMATSU, *"On the Influence of Irregular Frequencies in the Integral Equation Solutions of the Time-Dependant Free Surface Problems"*, Journal of the Society of Naval Architects of Japan, vol. 146 (1979), pp 119-128.

[15] H. ADACHI, S. OHMATSU, *"On the Time-Dependant Potential and its Application to Wave Problem"*, 13th O.N.R. Symposium on Naval Hydrodynamics, Tokyo, 1980.

[16] R.L. POTASH, *"Second-Order Theory of Oscillating Cylinders"*, Journal of Ship Research, vol. 15, n° 4 (December 1971), pp 295-324.

[17] W. FRANK, *"Oscillations of Cylinders In or Below the Free Surface of Deep Fluids"*, D.T.-N.S.R.D.C. Report 2375, Bethesda, Maryland, October 1967.

[18] S. OHMATSU, *"On the Irregular Frequencies in the Theory of Oscillating Bodies in a Free Surface"*, Papers of Ship Research Institute, Tokyo, 1975.

[19] N. DAOUD, *"Potential Flow Near to a Fine Ship's Bow"*, Rep. N° 177, Department of Naval Architecture and Marine Engineering, University of Michigan, Ann Arbor, 1975.

[20 R. FRIEDMAN, M. SHINBROT, *"The Initial Value Problem for the Linearized Equation of Water Waves"*, Journal of Mathematics and Mechanics, vol. 17, n° 2 (1967) and vol. 18, n° 12 (1969).

[21] R.M. GARIPOV, *"On the Linear Theory of Gravity Waves : the Theorem of Existence and Uniqueness"*, Archives of Rational Mechanics and Analysis , vol. 24 (1967), pp 352-362.

[22] J. BOUJOT, *"Sur l'analyse des caractéristiques vibratoires d'un liquide contenu dans un réservoir"*, Journal de Mécanique, vol. 11, n° 4 (1972), pp 649-671.

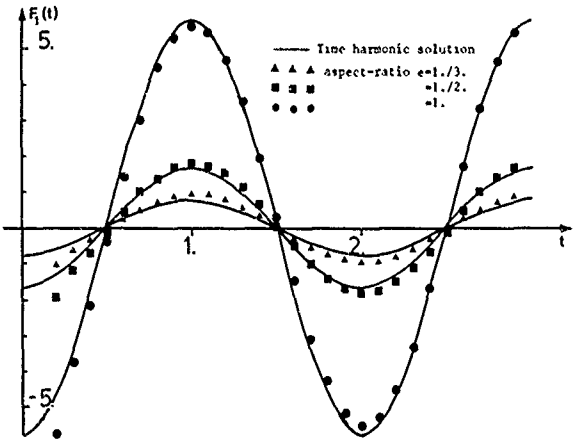
[23] A. JAMI, *"Numerical Soving of Transient Linear Hydrodynamics Problems by coupling Finite Elements and Integral Representation"*, 3d International Conference on Numerical Ship Hydrodynamics, Paris, June 1981.

[24] M. LENOIR, A. JAMI, *"A Variational Formulation for Exterior Problems in Linear Hydrodynamics"*, Computer Methods in Applied Mechanics and Engineering, vol.16 (1978), pp 341-359.

[25] D. EUVRARD, A. JAMI, M. LENOIR, D. MARTIN, *"Recent Progress Towards an Optimal Coupling of Finite Elements and Singularity Distribution Proceedures in Numerical Ship Hydrodynamics"*, 3d International Conference on Numerical Ship Hydrodynamics, Paris, June 1981.

[26] O.M. FALTINSEN, *"Numerical Solutions of Transient Nonlinear Free Surface Motions Outside or Inside Moving Bodies"*, 2d International Conference on Numerical Ship Hydrodynamics, Berkeley, September 1977.

[27] R.B. CHAPMAN, *"Time-Domain Method for Computing Forces and Moments acting on three dimensional Surface-Piercing Ship Hulls with Forward Speed"*, 3d International Conference on Numerical Ship Hydrodynamics, Paris, June 1981.



JAMI [23] *Sway motions of elliptic submerged cylinders* of center $(0,y_c)$.

$v(t) = Y(t)\, n_1 \cos \omega t$, $\omega = \pi$, $a = 0.75$

IMPLEMENTATION OF OPEN BOUNDARY CONDITIONS FOR NONLINEAR FREE-SURFACE WAVE PROBLEMS*

S M. Yen and D R. Hall
Coordinated Science Laboratory, University of Illinois
Urbana, Illinois 61801, U.S.A.

Summary

We have studied two approaches for solving potential flows for nonlinear free surface wave problems using a fixed, small computational domain. In each approach, we have used Orlanski's method to implement the open boundary condition at the outflow boundary. The two approaches differ in the treatment of high frequency errors that appear in the solution and that inhibit accurate treatment of the open boundary condition. In the first approach, we used filtering to minimize high frequency errors. However, it was found to be effective only at an early time; therefore, it is suitable only for obtaining transient solutions. In the second approach, we modified our time marching schemes so that the schemes are characterized by damping. This damping is more effective in controlling high frequency errors. Transient and steady state solutions have been obtained for the pressure distribution and the accelerating strut problems.

I. Introduction

The numerical solution of the nonlinear free surface problems requires the treatment of complexities in flow geometry, flow features and boundary conditions that are characterized by these problems. In our earlier study [1], we have developed two computational schemes to deal with some of these complexities and applied these methods to several nonlinear free surface problems. In one scheme, we use the finite element method to make the field calculation of the velocity potential and the finite difference method is used for the time evolution. The feasibility of this scheme was demonstrated by numerical solutions obtained for the two-dimensional problems of the pressure distribution and the submerged body. In the other scheme, a finite difference method that couples an explicit, single stage, second order time integration scheme with the solution of the Laplace equation for the velocity potential is used. The feasibility of this scheme has been demonstrated by numerical solutions obtained for a two-dimensional pressure distribution problem and a three-dimensional accelerating strut problem.

In both schemes, the computational domain is expanded downstream periodically during the computation as the disturbance on the free surface is propagated close to the downstream boundary. Therefore, the undisturbed condition is applied on the cut-off downstream boundary.

In order to obtain the longer time and steady state solutions, we have to use a fixed downstream boundary set close to the disturbance so that we can increase the computation efficiency by dealing with a small computational domain. The present phase of our study has been focused on the application of our numerical schemes to the nonlinear free surface problems with a fixed, small computational domain. There are three major tasks involved in this study: (1) investigate the implementation of the open boundary condition at the outflow boundary to allow the waves to pass through it and (2) improve our numerical schemes so that accurate numerical solutions can be obtained using the open boundary condition at the outflow boundary, and (3) apply the methods developed to selected nonlinear free surface problems.

We have studied in detail the method to implement the open boundary condition used by Chan [2]. It is based on Orlanski's scheme [3] in which the Summerfeld radiation condition is applied at the outflow boundary and the phase velocity is calculated numerically. We have conducted numerical experiments to study systematically the errors of Chan's numerical scheme to implement the advection equation and to study ways to minimize these errors.

Transient solutions have been obtained for the pressure distribution problem and have been compared with those obtained for expanding domain in order to establish their accuracy. These accuracy studies have led to the determination of the position of fixed outflow boundary. Using the methods we have developed, we have obtained accurate transient and steady state solutions for the pressure distribution problem. In addition, transient solutions have been obtained for the accelerating strut problem.

We have been studying an alternative method to implement the open boundary condition. In this method, we use directly the

*This research was supported by the National Science Foundation under Grant NSF ENG 77-20436 and the Office of Naval Research under Contract N00014-80-C-0740.

governing free surface equation instead of the advection equation at the outflow boundary. This method does have a problem of slow instability which can be dealt with.

In this paper, we shall first review briefly the nonlinear free surface problems under study and our numerical schemes to solve these problems using an expanding domain. Then, we will present the results of our study of the numerical scheme to implement Orlanski's method, our numerical schemes to solve nonlinear free surface wave problems using a fixed, small computational domain, and numerical solutions obtained.

II. Free Surface Wave Problems

We consider the potential flow produced by a disturbance moving forward on or near a free surface. The flow is governed by the potential equation, free surface boundary conditions and conditions at other boundaries. The free surface is characterized by two distinct conditions, kinematic and dynamic conditions.

We shall summarize below the basic equations and the boundary conditions for the domain bounded by the free surface and three cut-off boundaries approximating boundaries at infinity. We show, as an example, the pressure distribution problem in Fig. 1. The coordinate system (x,y,z) is attached to the disturbance with negative y oriented toward the acceleration of the gravity. The flow variables are the potential function ϕ, the velocity $V(V_x,V_y,V_z)$, and the pressure p. All the variables in the basic equations and boundary conditions are nondimensionalized with respect to U, L, and P_0 which are the reference values of velocity, length and pressure respectively. We introduce two flow parameters.

$$Fr = \frac{U}{\sqrt{gL}} \tag{1}$$

and

$$\sigma = \frac{P_0}{\rho g L} . \tag{2}$$

The free surface height is defined as

$$y = \eta(x,z;t) . \tag{3}$$

A two-dimensional problem of a moving disturbance can be defined as follows:

$$\begin{aligned}
&\phi_{xx} + \phi_{yy} = 0 && \text{in } \mathcal{D}.\\
&\eta_t = \phi_y - \phi_x \eta_x && \text{on } y = \eta.\\
&\phi_t = -\tfrac{1}{2}(\phi_x^2 + \phi_y^2) - \frac{1}{Fr^2}\eta - \frac{\sigma}{Fr^2} p && \text{on } y = \eta.\\
&\phi = x && \text{on cut-off boundaries.}\\
&\frac{\partial \phi}{\partial n} = 0 && \text{on solid boundary.}\\
&\phi = 0,\ \eta = -\sigma p && \text{at } t = 0 \text{ in } \mathcal{D}.
\end{aligned} \tag{4}$$

Here p is the applied pressure on the free surface.

In addition to the pressure distribution problem, we have also considered the strut problem. For this problem, we use the elliptic cylindrical coordinate system (δ,θ,y) to discretize the computational field. The constant δ and constant θ level curves are respectively confocal ellipses and hyperbolas with foci $(-c,0)$ and $(c,0)$. Here, c is the semifocal distance

$$c = (a^2 - b^2)^{\frac{1}{2}} \tag{5}$$

where a and b are the semi-major and semi-minor axes of the base ellipse respectively. The base ellipse is represented by $\delta_b = \ln[(a+b)/c]$. The metric or scale factor h associated with the transformation from the Cartesian to the elliptic cylindrical system may be expressed by

$$h^2 = c^2(\sinh^2\delta + \sin^2\theta). \tag{6}$$

The problem considered is defined as follows:

$$\begin{aligned}
&\phi_{\delta\delta} + \phi_{\theta\theta} + h^2\phi_{yy} = 0 && \text{in } \mathcal{D}.\\
&\eta_t = \phi_y - (\phi_\delta \eta_\delta + \phi_\theta \eta_\theta)/h^2 && \text{on } y = \eta\\
&\phi_t = cU_c \cosh\delta\cos\theta - \frac{\eta}{Fr^2} \\
&\quad + [U^2 - (\nabla\phi)^2]/2 && \text{on } y = \eta\\
&\text{where } (\nabla\phi)^2 = \phi_y^2 + (\phi_\delta^2 + \phi_\theta^2)/h^2\\
&\phi = cU\cosh\delta\cos\theta && \text{on } \delta = \delta_\infty.
\end{aligned} \tag{7}$$

The cut-off boundary is δ_∞. At the bottom boundary $y = y_\ell$, it is assumed that ϕ is equivalent to the potential function for a two-dimensional flow past an elliptic cylinder. After a slight modification to obtain compatibility with the boundary condition at δ_∞, we get

$$\phi = cU(\cosh\delta_\infty)(\cos\theta)\left\{\frac{a\cosh\delta - b\sinh\delta}{a\cosh\delta_\infty - b\sinh\delta_\infty}\right\} \quad \text{on } y = y_\ell \tag{8}$$

III. Numerical Methods for Expanding Computational Domain

We shall describe here the numerical methods developed previously for expanding computation domain.

Finite Element Method

In this method, the finite element method is used for the field calculation of the velocity potential while the time evolution is updated by using the finite difference method. The finite element method for field calculation is given in detail in ref. 1.

The time advancement of the free surface boundary conditions is carried out using a predictor-corrector method. Let the free surface boundary conditions be expressed by

$$\eta_t = F(x,y;t)$$

and

$$\phi_t = G(x,y;t) \quad . \tag{9}$$

The Euler method predicts the values at a particular x position at the new time step by

$$\underline{\eta}_{n+1} = \eta_n + \Delta t\, F_n$$

and

$$\underline{\phi^*}_{n+1} = \phi^*_n + \Delta t\, G_n \tag{10}$$

where ϕ^* denotes ϕ on the free surface, the subscript n refers to the time level, and Δt is the time increment. The values at the new time-step are obtained from the corrector step by

$$\eta_{n+1} = \eta_n + \frac{\Delta t}{2}\,(F_n + \underline{F}_{n+1})$$

and

$$\phi^*_{n+1} = \phi^*_n + \frac{\Delta t}{2}\,(G_n + \underline{G}_{n+1}) \quad . \tag{11}$$

In computing F and G, the spatial derivatives can be computed from the finite element algorithms. However, when the triangular mesh is used, the derivatives have comparably larger errors. In this case, the spatial derivatives are obtained from polynomial approximations after the iterative solutions converge at each time step.

The successive overrelaxation method is used to solve the Laplace equation iteratively with the specified values of ϕ^* on the given boundary η. The updating of η and ϕ^* is carried out by the predictor-corrector method after the iterative solutions converge within a required limit. The predictor-corrector method has less stringent conditions for stability and converges even in nonlinear problems; however, it does require two solutions for each time-step.

Finite element solutions were obtained for the pressure distribution problem and the problem of submerged bodies. The pressure distribution problem is shown schematically in Fig. 1. In this problem, we consider the distribution

$$p = f(x) = \begin{cases} \frac{P_0}{2}\,(1-\cos\frac{2\pi x}{L}) & 0 \le x \le 1 \\ 0 & \text{elsewhere} \end{cases} \tag{12}$$

where P_0 is the maximum pressure in the surface distribution. The pressure distribution is initially at rest and starts to move with the uniform speed U in the negative direction on the x-axis. The span of the applied pressure is chosen as the length unit. The computational domain is bordered by the free surface and three cut-off boundaries. The downstream boundary is expanded periodica to contain the entire region of disturbance within the computational domain. The domain is initially divided into regular triangular elements with $\Delta x = \Delta y = 0.05$.

Finite Difference Method

Our finite difference method is to couple an explicit, single stage, second order time integration scheme with the solution of the Laplace equation for the potential function. In this method, the free surface conditions are integrated to provide a Dirichlet condition at the surface for the Laplace equation, the Laplace equation is solved, and the solution is used together with the free surface conditions to determine the derivatives needed for another time integration.

The time integration scheme is expressed by

$$\eta_{n+1} = \eta_n + \Delta t(\eta_t)_n + (\Delta t^2/2)(\eta_{tt})_n \tag{13}$$

and

$$\phi^*_{n+1} = \phi^*_n + \Delta t(\phi^*_t)_n + (\Delta t^2/2)(\phi^*_{tt})_n + \Delta\eta[(\phi^*_y)_n + (\Delta\eta/2)(\phi^*_{yy})_n + \Delta t(\phi^*_{yt})_n] \quad . \tag{14}$$

The subscript n denotes values at time $t = t_n$, ϕ^* denotes ϕ at $y = \eta$,

$$\Delta t = t_{n+1} - t_n$$

and

$$\Delta\eta = \eta_{n+1} - \eta_n$$

The Dirichlet condition at the new surface provided by the application of Eqs. (13) and (14) and the other boundary conditions for the problem are used to solve the Laplace equation.

The final step of the method is to compute the derivatives appearing on the right hand side of Eqs. (13) and (14).

Finite difference solutions were obtained for the pressure distribution problem. A uniformly spaced grid with $\Delta x = \Delta y = \Delta = 0.0625$ was used except for the spacing between nodes at the surface and those at $y = -\Delta$. The spacing between such nodes was $\Delta y = (\Delta + \eta)$.

The strut problem was solved on an elliptic cylindrical coordinate system by using the finite difference method. The parameters of this problem are: $a = 0.5$, $b = 0.05$, and $Fr^2 = 0.025$. The outer boundary of the domain used is an ellipse with axes

$$a_\infty = c \cosh \delta_\infty$$

and $$b_\infty = c \sinh \delta_\infty$$

where $$c^2 = a^2 - b^2$$

and $$\delta_\infty = \pi + \ln[(a+b)/c] \quad .$$

The other boundaries were the free surface, the symmetry axis, the surface of the strut, and $y = -4\pi/25$. At the boundary $y = -4\pi/25$, the flow is assumed to be completely horizontal as it would be at infinite depth. The two-dimensional flow past an elliptic cylinder is therefore used as a condition at this boundary. The

grid used to solve this problem was uniform with spacing $\Delta = \pi/50$ in all three directions of the elliptic cylindrical coordinate system. As in the previous problem, the spacing between nodes at the surface and those at $y = -\Delta$ was $\Delta y = (\Delta + \eta)$.

IV. Implementation of Orlanski's Scheme

The fixed outflow boundary, as shown schematically for the pressure distribution problem in Fig. 2, requires special and careful treatment in order to prevent wave reflections that may impair the accuracy of solutions or, even, destroy the calculations. Chan [2] used Orlanski's method [3] to implement boundary conditions at the open boundary. This method consists of imposing the Sommerfeld radiation condition at the outflow boundary and numerically evaluating the phase velocity of the boundary. We shall first briefly review Chan's scheme.

The Sommerfeld radiation condition is

$$Q_t + CQ_x = 0 \tag{15}$$

where Q is any perturbed variable (η and ϕ in the free surface wave problems) and C is the phase velocity of the wave. The open boundary condition is implemented using the following expression:

$$Q_{IB}^{n+1} = Q_{IB-1}^{n-1} + [1-2C(\Delta t/\Delta x)](Q_{IB}^{n} - Q_{IB-1}^{n}) \ . \tag{16}$$

The subscript IB denotes the outflow boundary. n is the time level. The phase velocity C is calculated from Q_t and Q_x obtained from free surface computations as follows:

$$C = (\Delta x/2\Delta t)(Q_{IB-1}^{n}+Q_{IB-2}^{n-1}-Q_{IB-1}^{n-1}-Q_{IB-2}^{n-2})/(Q_{IB-2}^{n-1}-Q_{IB-1}^{n-1}). \tag{17}$$

The crest or trough condition is treated by:

$$\text{if} \quad |Q_{IB-1}^{n} - Q_{IB}^{n}| < 10^{-10}|Q_{max} - Q_{min}|,$$

$$\text{then he sets} \quad Q_{IB}^{n+1} = Q_{IB}^{n} \ . \tag{18}$$

Finally, the limits on the phase velocity are set as follows:

$$C = \begin{cases} \Delta x/\Delta t, & \text{if} \quad C^* > (\Delta x/\Delta t). \\ C^*, & \text{if} \quad 0 \le C^* \le \Delta x/\Delta t. \\ 0, & \text{if} \quad C^* < 0 \ . \end{cases} \tag{19}$$

in which C^* is the right hand side of Eq. (17).

Basically, Chan's method has two explicit steps: (1) calculate the phase velocity at the outflow boundary IB by using the values of the variable of the present and previous time levels in the vicinity of IB, and (2) calculate the value of the variable at the next time level n+1 at the outflow boundary IB.

Since we use the total instead of perturbed potential and variable instead of constant time steps, we have to modify Eqs. (16) and (17). The modified expressions are as follows. For the potential function,

$$\phi_{IB}^{n+1} = \phi_{IB-1}^{n-1} + [1-2\frac{C_\phi(\Delta t^n)'}{\Delta x}](\phi_{IB}^{n} - \phi_{IB-1}^{n}) + 2\,C_\phi(\Delta t^n)' \ , \tag{20}$$

in which $(\Delta t^n)' = (\Delta t^n + \Delta t^{n-1})/2$,

$(\Delta t^{n-1})' = (\Delta t^{n-1} + \Delta t^{n-2})/2$,

Δt^n = nth time step,

$t^{n+1} = t^n + \Delta t^n$,

C_ϕ = phase velocity for potential function ϕ.

For the wave height,

$$\eta_{IB}^{n+1} = \eta_{IB-1}^{n-1} + [1-2\frac{C_\eta(\Delta t^n)'}{\Delta x}](\eta_{IB}^{n} - \eta_{IB-1}^{n}), \tag{21}$$

in which C_η = phase velocity for wave height η.

The phase velocities C_ϕ and C_η are evaluated using the following expressions:

$$C_\phi = \frac{\Delta x}{2(\Delta t^{n-1})'} \cdot \frac{\phi_{IB-1}^{n} + \phi_{IB-2}^{n-1} - \phi_{IB-1}^{n-1} - \phi_{IB-2}^{n-2}}{(\phi_{IB-2}^{n-1} - \phi_{IB-1}^{n-1} + \Delta x)}, \tag{22}$$

$$C_\eta = \frac{\Delta x}{2(\Delta t^{n-1})'} \cdot \frac{\eta_{IB-1}^{n} + \eta_{IB-2}^{n-1} - \eta_{IB-1}^{n-1} - \eta_{IB-2}^{n-2}}{(\eta_{IB-2}^{n-1} - \eta_{IB-1}^{n-1})}. \tag{23}$$

We also take into account the wave crest or trough passing out of the downstream boundary. When this phenomenon happens, the denominators of Eqs. (22) and (23) get very small. Thus, when

$$|\phi_{IB-2}^{n-1} - \phi_{IB-1}^{n-1} + \Delta x| \le 10^{-7} \ , \tag{24}$$

we set

$$\phi_{IB}^{n+1} = \phi_{IB}^{n} \ ,$$

when $|\eta_{IB-2}^{n-1} - \eta_{IB-1}^{n-1}| \le 10^{-9}$, (25)

we set

$$\eta_{IB}^{n+1} = \eta_{IB}^{n} \ .$$

We constrained the range of the values of C_ϕ and C_η could take. Letting C_ϕ^* be the right hand side of Eq. (22),

$$C_\phi = \begin{cases} 0 \quad , & \text{if } C_\phi^* < 0. \\ C_\phi^* \quad , & \text{if } 0 \le C_\phi^* \le \Delta x/\Delta t. \\ \Delta x/\Delta t, & \text{if } C_\phi^* > \Delta x/\Delta t. \end{cases} \tag{26}$$

Similarly, letting C^*_η be the right hand side of Eq. (23),

$$C_\eta = \begin{cases} 0 & , \text{ if } C^* < 0. \\ C^*_\eta & , \text{ if } 0 \le C^*_\eta \le \Delta x/\Delta t \, . \\ \Delta x/\Delta t, & \text{if } C^*_\eta > \Delta x/\Delta t \, . \end{cases} \tag{27}$$

As to be discussed later, we have found an alternative method to evaluate C_ϕ and C_η that leads to more accurate implementation of the open boundary condition. In this method, we use the derivatives of ϕ and η that have already been calculated on the free surface at nodes upstream of the outflow boundary. The expression for C_ϕ and C_η using this method are

$$C_\phi = -\frac{\phi_t}{\phi_x} = -\frac{\left[(\phi_t)^{n-1}_{IB-2} + (\phi_t)^{n-1}_{IB-1}\right]}{\left[(\phi_x)^{n-1}_{IB-2} + (\phi_x)^{n-1}_{IB-1} - 2\right]} \, , \tag{28}$$

and

$$C_\eta = -\frac{\eta_t}{\eta_x} = -\frac{\left[(\eta_t)^{n-1}_{IB-2} + (\eta_t)^{n-1}_{IB-1}\right]}{\left[(\eta_x)^{n-1}_{IB-2} + (\eta_x)^{n-1}_{IB-1}\right]} \, . \tag{29}$$

In numerically implementing Eq. (15) for the potential ϕ, the spatial derivative Q_x is better represented by

$$(Q_x)_{I+\frac{1}{2}} = \frac{Q_{I+1} - Q_I}{\Delta x} - \frac{\eta_{I+1} - \eta_I}{\Delta x}(Q_y)_{I+\frac{1}{2}} \, . \tag{30}$$

The second term in this expression is to correct for error due to any significant change in wave height η at the outflow boundary.

As to be discussed later, we have found that, for long time solutions, the wave height at the outflow boundary becomes unstable. We are able to insure stability by setting the lower limit of C_η to be the free stream velocity. The new limits of C_η becomes

$$C_\eta = \begin{cases} 1 & , \text{ if } C^*_\eta < 1. \\ C^*_\eta & , \text{ if } 1 \le C^*_\eta \le \Delta x/\Delta t. \\ \Delta x/\Delta t & , \text{ if } C^*_\eta > \Delta x/\Delta t. \end{cases} \tag{31}$$

V. Advection Experiments

Our first effort in using a fixed, small computational domain is to solve the pressure distribution problem and to compare the solutions to those obtained with the expanding computational domain. We set the outflow boundary $x_{IB} = 1.5$. Transient solutions have been obtained for $Fr = 1/\sqrt{2\pi}$ and $\sigma = 0.01$. It was found that two-grid interval ($2\Delta x$) waves of appreciable magnitude start to appear at $t = 0.8$ near the outflow boundary, spread quickly upstream and eventually cause the calculation to stop at $t = 5$. The appearance of $2\Delta x$ waves over the solution of the wave height at $t = 1$ is shown in Fig. 3.

The contamination of the solution by $2\Delta x$ waves discussed above led to our effort to conduct "advection" experiments to evaluate the performance of schemes that could be used to implement accurately the Summerfeld advection equation at the open boundary.

There are two experiments. In one experiment, a sine wave of several combinations of parameters (amplitude, wave length and advection velocity) is advected through a boundary. In the other, a $2\Delta x$ wave is superposed on the advecting sine wave. In each experiment, we find the solution of the Summerfeld advection equation using the chosen numerical schemes at the boundary. Each solution will yield boundary values of amplitude, phase, and phase velocity from which we may evaluate the performance of the schemes. The performance characteristics evaluated include amplitude and phase errors and stability.

The following schemes have been tested:

1. Chan

$$Q^{n+1}_{IB} = Q^{n-1}_{IB-1} + [1-2C(\Delta t/\Delta x)][Q^n_{IB} - Q^n_{IB-1}] \tag{32}$$

2. Chan - BET

$$Q^{n+1}_{IB} = Q^{n-1}_{IB-1} + a_1[Q^{n+1}_{IB-1} - Q^{n-1}_{IB}] + a_2[Q^n_{IB} - Q^n_{IB-1}] \tag{33}$$

in which

$$a_1 = (1-\alpha)(1-2\alpha)/[(1+\alpha)(1+2\alpha)]$$

$$a_2 = 2(1-2\alpha)/(1+\alpha)$$

$$\alpha = C(\Delta t/\Delta x) \, .$$

3. Upwind

$$Q^{n+1}_{IB} = Q^n_{IB} - C(\Delta t/\Delta x)[Q^n_{IB} - Q^n_{IB-1}] \, . \tag{34}$$

4. Atmospheric

$$Q^{n+1}_{IB} = Q^{n-1}_{IB}[1 - C(\Delta t/\Delta x)]/[1 + C(\Delta t/\Delta x)] + Q^{n+1}_{IB-1}[2C(\Delta t/\Delta x)]/[1 + C(\Delta t/\Delta x)]. \tag{35}$$

The results of the first experiment may briefly be summarized as follows: (1) both Chan and Chan-BET schemes yield accurate solutions, and (2) the solutions of the other two schemes contain significant amplitude, phase, and phase velocity errors.

In the second experiment, we tested the performances of numerical schemes not only with $2\Delta x$ wave error but also with (and without) phase velocity error. It was found that (1) all the schemes tested perform poorly with $2\Delta x$ waves present, (2) the effect of the phase velocity error without $2\Delta x$ waves present is not as significant; however, it becomes large in

the presence of $2\Delta x$ waves. These findings are significant in that the $2\Delta x$ waves are present in the solution of free surface wave calculations (as shown in Fig. 3); therefore, some means has to be used to eliminate them.

In general, these numerical experiments have helped us to identify two problems in numerically implementing the open boundary condition: high frequency errors in the free surface wave solution and phase velocity error in the calculation of the boundary condition. We shall discuss in the following section our method to deal with these problems.

VI. Numerical Schemes for a Finite, Small Computation Domain

On the basis of the results of the numerical experiments, we have formulated the following requirements for numerical schemes that could be used for free surface wave problems for a finite, small computational domain (1) some means should be used to minimize the $2\Delta x$ waves in the solution, (2) the open boundary condition should be implemented so that the phase velocity should be calculated independent of the open boundary condition to insure the accuracy of its calculation and (3) a correction is necessary in implementing the open boundary condition for the potential function at the free surface. We have developed two numerical methods to meet these requirements.

The first method has two features: (1) filtering is used to eliminate the $2\Delta x$ waves as they grow in the solution and (2) the phase speed calculation at the outflow boundary is decoupled from the open boundary condition by using derivatives from the free surface calculation according to Eqs. (28) and (29). We shall describe the development of our filtering scheme.

We wanted to eliminate the $2\Delta x$ waves by using filtering. Two methods of filtering were tried (1) point filtering, filtering only at the boundary, and (2) full filtering: filtering over the entire free surface as well as at the boundary. Results indicated the point filtering scheme does not work; therefore, we used only the full filtering scheme. The filtering scheme is given in Appendix A.

The results of the first method, applied to the pressure distribution problem, are presented in the next section.

In the second method, we modified our time marching integration schemes so that the high frequency wave errors are damped by the dissipation and dispersion. We shall describe these modifications.

First we modified our schemes so that they would be dissipative. For the second order Taylor's series, we changed it to third order with the third term as the damping term as fo follows:

$$Q^{n+1} = Q^n + \Delta t\, Q_t^n + [(\Delta t)^2/2]Q_{tt}^n + [(\Delta t)^3/6]Q_{ttt}^n \tag{36}$$

with a damping factor

$$|\lambda| = 1 - P^6/12 + P^6/36$$

in which $P = \omega\Delta t$ and ω = frequency. In our other time integration scheme, we use the following predictor-corrector scheme:

$$\bar{Q}^{n+1} = Q^n + \Delta t\, Q_t^n$$

$$Q^{n+1} = Q^n + (\Delta t/2)(Q_t^n + \bar{Q}_t^n) \quad . \tag{37}$$

We propose three modifications as follows:

MPC-I

$$\bar{Q}^{n+1} = Q^n + \Delta t(Q_t^n) + [(\Delta t)^2/2]Q_{tt}^n \tag{38}$$

$$Q^{n+1} = Q^n + (\Delta t/2)(Q_t^n + \bar{Q}_t^n)$$

$$|\lambda| = 1 - P^6/4 + P^6/16$$

MPC-II

$$\bar{Q}^{n+1} = Q^n + \Delta t(Q_t^n)$$

$$\bar{\bar{Q}}^{n+1} = Q^n + (\Delta t/2)(Q_t^n + \bar{Q}_t^n) \tag{39}$$

$$Q^{n+1} = Q^n + (\Delta t/2)(Q_t^n + \bar{\bar{Q}}_t^n)$$

$$|\lambda| = 1 - P^6/16$$

MPC-III

$$\bar{Q}^{n+1} = Q^n + \Delta t(Q_t^n)$$

$$Q^{n+1} = Q^n + \Delta t(\bar{Q}_t^n) \quad . \tag{40}$$

Secondly we changed from center differencing of the spatial derivatives to upwind differencing. We have found that the schemes become effective in damping the $2\Delta x$ waves when we use upwind differencing. Figure 4 shows the effectiveness of the second method in minimizing the high frequency errors in the wave height solution for the pressure distribution problem at $t = 7$.

VII. Numerical Solutions

We shall describe here the numerical solutions obtained using the two methods given in Section VI, as well as a few additional revisions that were found to be necessary to insure accuracy of calculations.

We have applied the first method in which filtering is used to treat the high frequency errors to the pressure distribution problem for $Fr = 1/\sqrt{2\pi}$ and $\sigma = P_0/\rho gL = 0.01$. The field calculation is made by using a finite difference method. The outflow boundary is set at $x = 2$. The filtering was found to be effective in eliminating high frequency errors without impairing the accuracy of calculations for integration at early times. Some of the results are shown in Figs. 5, 6, and 7. We observe that the filtering eliminates $2\Delta x$ waves that appear downstream as well as upstream and waves reflected from the outflow boundary.

We are able to obtain accurate early transient solutions. We show one of the solutions for $t=5$ in Fig. 8. However, we have found that the error due to filtering accumulates such that it will eventually impair the accuracy of calculations. It seems, therefore, that the use of filtering is not suitable to obtain long time and steady state solutions.

The second method in which damping is used to treat the high frequency errors was also applied to the pressure distribution problem using the finite element method for field calculations. Specifically, the MPC-II was used with upwind differencing and the correction term for the potential function calculation at the free surface outflow boundary. The parameters used were $Fr = 1/\sqrt{4\pi}$ and $\sigma = 0.01$. The outflow boundary is also set at $x=2$. The wave height of the steady state solution obtained is shown in Fig. 9. The corresponding linear calculation by Haussling [4] is also shown for comparison.

We are currently trying to obtain a solution to the accelerating strut problem by using the second method. However, we are considering the use of our original time marching scheme with upwind differencing of the spatial derivatives. Figure 10 shows the result on wave height at $t=0.16$ with the following parameters: $a=0.5$, $b=0.125$ and $(Fr)^2=0.025$.

VIII. Alternative Method of Implementation of Open Boundary Condition

An alternative method of implementing the open boundary condition at the free surface is being studied. In this method, we used the wave height free surface boundary condition at the outflow boundary. We feel that the use of the free surface boundary should be physically more comparable to the condition near the outflow boundary. The problem with using this technique is that it is unstable under some conditions. Since the instability develops slowly, we use our experience with filtering to the following second order smoother to smooth the wave height at IB and IB-1:

$$\eta^+_{IB} = (9\eta_{IB-4} - 20\eta_{IB-3} + 6\eta_{IB-2} + 12\eta_{IB-1} + 6\eta_{IB})/13 \tag{41}$$

$$\eta^+_{IB-1} = (-2\eta_{IB-4} + 3\eta_{IB-3} + 3\eta_{IB-2} + 6\eta_{IB-1} + 3\eta_{IB})/13 \tag{42}$$

in which η^+ is the smoothed wave height. These expressions have been developed on the basis of a second order interpolation formula with a $2\Delta x$ wave smoother. In practice, our smoother is used to detect the onset of the instability and is then applied to the wave height solution at the boundary. Comparing the wave height solution using both open boundary techniques, we found that the free surface boundary condition gives slightly better results near the outflow boundary. Figure 11 shows two solutions for the pressure distribution problem at $t=4$ using the two techniques.

IX. Concluding Remarks

1. To implement accurately the open boundary condition at the outflow boundary using Orlanski's method, we have found that (a) an accurate numerical scheme should be used to solve the advection equation at the boundary, (b) the numerical calculation of the phase velocity should be decoupled from the open boundary condition, (c) the evaluation of spatial derivative of the potential at the free surface (needed in the calculation of phase velocity) should take into consideration the change in wave height and (d) limiting values of the phase velocity should be set properly to insure stability of calculations at the boundary.

2. The most important task in developing methods to solve free surface wave problems using a fixed, small computational domain is to find ways to eliminate the two-grid interval ($2\Delta x$) waves that appear in the solution and that inhibit the accurate implementation of the open boundary condition. We have studied two approaches to minimize these waves. One approach is to use filtering. It was found to be effective in eliminating the $2\Delta x$ waves only at an early time. The second approach is to incorporate damping in our time marching schemes. The damping is more effective in controlling the high frequency errors. However, careful studies should be made to ascertain its influence on the accuracy of solutions.

References

1. Yen, S. M., Lee, K. D. and Akai, T. J., "Finite Element and Finite Differences Solutions of Nonlinear Free Surface Wave Problems," Proceedings of the Second International Conference on Numerical Ship Hydrodynamics, Berkeley, CA, pp. 305-318, 1977.

2. Chan, Robert K. C., "Finite Difference Simulation of the Planar Motion of a Ship," Proceedings of the Second International Conference on Numerical Ship Hydrodynamics, Berkeley, CA, pp. 39-52, 1977.

3. Orlanski, L., "A Simple Boundary Condition for Unbounded Hyperbolic Flows," Journal of Computational Physics, 21, 1976.

4. Haussling, H. J. and Van Eseltine, R. T., "Finite Difference Methods for Transient Potential Flows with Free Surfaces," Proceedings of the First International Conference on Numerical Ship Hydrodynamics, p. 295, 1975.

Appendix A

Filtering Scheme

We wish to filter out the $2\Delta x$ waves which contaminate the solution of the pressure distribution problem. Since the filtering also affects the waves of longer wave length of the solution, we have to choose a scheme that minimizes the effect on the solution.

We chose the linear filtering formulae developed by Shapiro [1]. These formulae are designed to eliminate the $2\Delta x$ waves without affecting the phase of the wave. The amount of damping of the lower frequency waves depends on the frequency and order of the formula used. We shall discuss here Shapiro's formulae and their implementation.

Shapiro's filtering formulae are based on the symmetrical operation

$$f_i^{(1)} = (\tfrac{1}{4})(f_{i-1} + 2f_i + f_{i+1}) \quad . \tag{A.1}$$

Here $f(x_i) = f_i$ for discrete values of x such that $x_i = i\Delta x$ where i is an integer. And, f(x) is an integrable function of time or space in one dimension.

We express $f(x_i)$ in terms of a sum of Fourier components of general form $A_n \cos n(x_i - \phi_n)$ where A_n = the amplitude of the wave component with wave number n, $n = 2\pi/\lambda$, λ = the wave length of the component, and ϕ_n = the phase of the component. If A_n is the nth component of f_i, and $A_n^{(1)}$ is the nth component of $f_i^{(1)}$, then

$$A_n^{(1)} = [1 - \sin^2(n\Delta x/2)]A_n \quad . \tag{A.2}$$

Thus, the operation defined in (A.1) damps the amplitude of each of the Fourier components of f_i by the factor $[1 - \sin^2(n\Delta x/2)]$. This factor is called the amplitude response function of the operation (A.1).

Shapiro derived a filtering formula of order p. For example, (A.1) is the formula of order zero and

$$f_i^{(4)} = (1/256)[186\, f_i + 56(f_{i+1} + f_{i-1}) - 28(f_{i+2} + f_{i-2}) + 8(f_{i+3} + f_{i-3}) - f_{i+4} - f_{i-4}] \tag{A.3}$$

is the formula of order three.

The amplitude response function, R_{p+1}, for the pth order formula is defined as

$$R_{p+1} = 1 - \sin^{2p+2}(n\Delta x/\lambda) \quad . \tag{A.4}$$

The characteristics of the filtering formulae can be summarized as follows. The phase of any component remains unchanged after filtering. As the wavelength increases, R_{p+1} approaches unity. And, as the order of the filtering scheme increases, R_{p+1} smoothly approaches unity. Thus, the larger wavelengths are damped less.

We wish to choose the order of the formula such that repeated applications of the formula do not seriously damp the significant wave component [1] and to apply the filtering as close to the boundary as possible. Since all high frequency waves are undesirable, the damping should be high for these wave components. Thus we should select the lowest order formula such that the shortest wavelength of interest would not be seriously damped.

For the solution shown in Fig. 12 the smallest wavelength of interest is > the $12\Delta x$ wave. To choose the order of the formula for this solution, we constructed a table of the order p vs $(R_{p+1})^n$ for $\lambda = 12\Delta x$ and various values of filtering steps, n. The results are shown in Table A.1. For a chosen value of damping and an estimated number of steps .., we could find the order of scheme p from this table. We used the third order scheme foi the results shown in Figs. 5, 6, and 7. The allowable accumulative damping was chosen to be 0.99 and the number of filtering steps was 250.

Table A.1 - Values of the Amplitude Response Function, R_{p+1}, for Various Orders p, $\lambda = 12\Delta x$.

p	R_{p+1}	$(R_{p+1})^{25}$	$(R_{p+1})^{100}$	$(R_{p+1})^{250}$
0	.933013	.176681	.000974	.000000
1	.995513	.893656	.637794	.324864
2	.999699	.992512	.970384	.927596
3	.999980	.999497	.997988	.994979
4	.999999	.999966	.999865	.999663
5	1.000000	.999998	.999991	.999977
6	1.000000	1.000000	.999999	.999998
7	1.000000	1.000000	1.000000	1.000000

We shall also describe in further detail the application of the filtering scheme to the pressure distribution problem, as shown schematically in Fig. 8. Our intention was to filter the wave heights using Eq. (A.3) over as much of the free surface as possible. Near the upstream and downstream boundary, where we could not use Eq. (A.3), we used Eq. (A.1). Also, by numerical experimentation, we found the best way to implement our scheme was to filter every 20 time steps using the zero order scheme near the downstream boundary and filter over the entire free surface every 80 time steps.

Reference

[1] Shapiro, Ralph, "Linear Filtering," Mathematics of Computation, Vol. 29, No. 132, pp. 1094-1097, 1975.

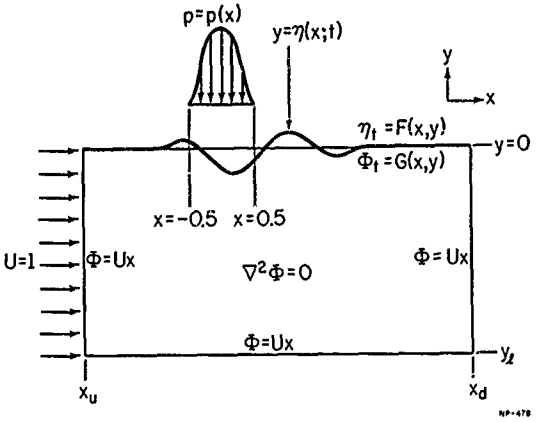


Fig. 1. Schematic of the Two-dimensional Pressure Distribution Problem.

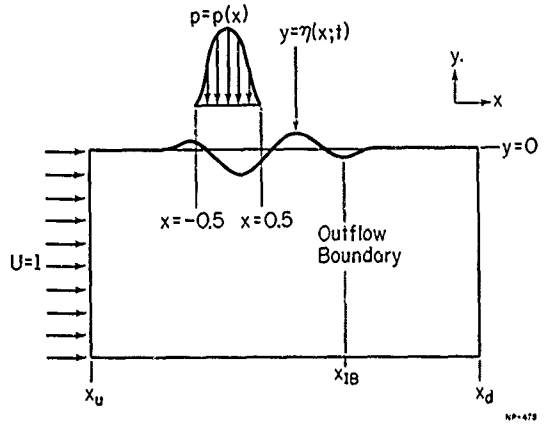


Fig. 2. Computational Domain with Fixed Outflow Boundary (x_{Ib}).

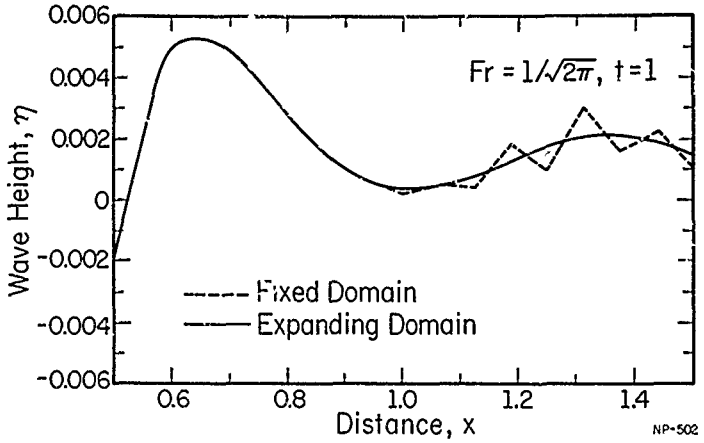


Fig. 3. Appearance of Two-grid Interval ($2\Delta x$) Wave in the Solution of the Pressure Distribution Problem for $Fr = 1/\sqrt{2\pi}$.

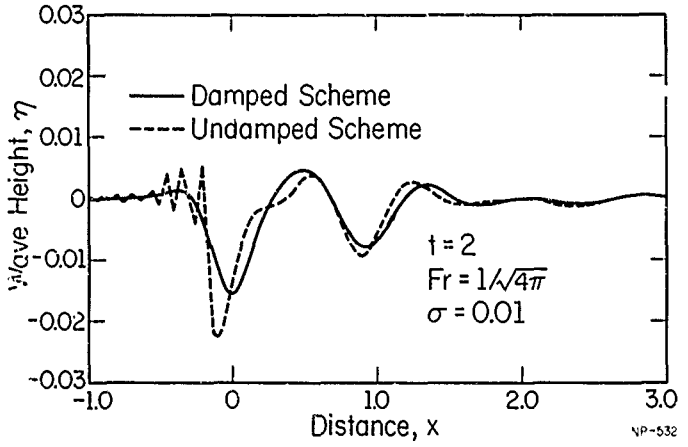


Fig. 4. Solution of the Pressure Distribution Problem by Using Damping in the Time-Integration Scheme.

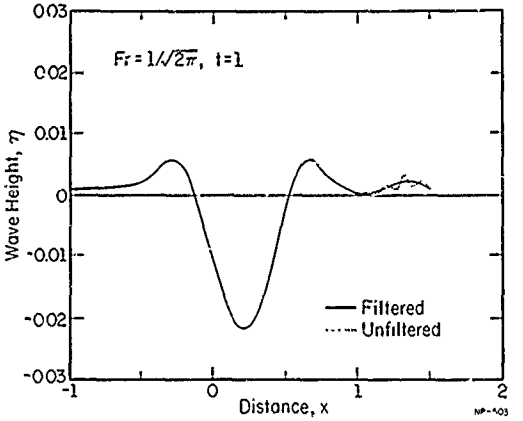


Fig. 5. Elimination of $2\Delta x$ Waves in the Solution of the Pressure Distribution Problem ($Fr = 1/\sqrt{2\pi}$) at $t = 1$ by Using Filtering.

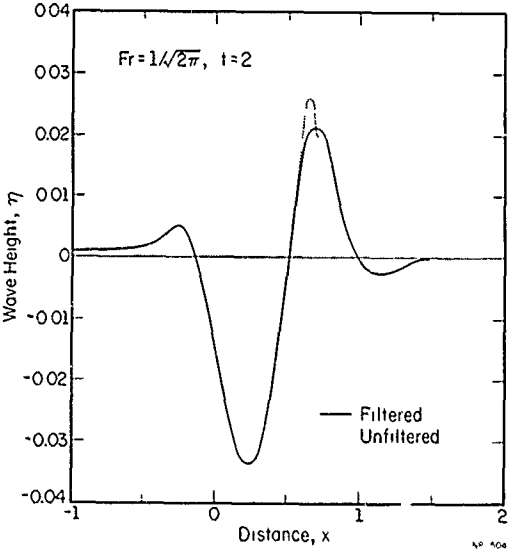


Fig. 6 Treatment of Reflected Wave in the Solution of the Pressure Distribution Problem ($Fr = 1/\sqrt{2\pi}$) at $t = 2$ by Using Filtering.

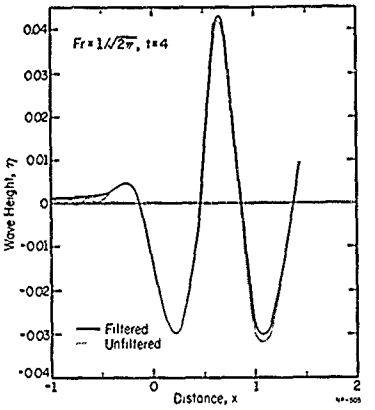


Fig. 7. Elimination of $2\Delta x$ Waves Appearing Near the Inflow Boundary in the Solution of the Pressure Distribution Problem ($Fr = 1/\sqrt{2\pi}$) at $t = 4$ by Using Filtering.

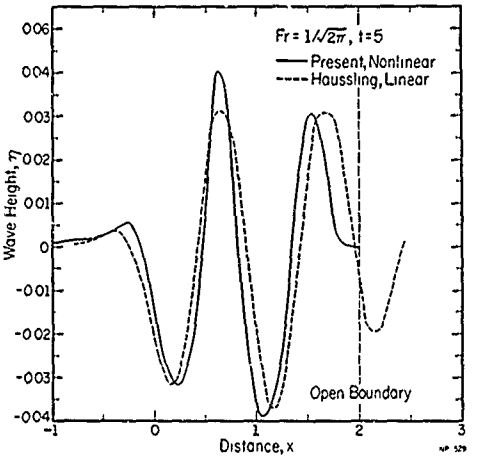


Fig. 8. Wave Height Solution of the Pressure Distribution Problem ($Fr = 1/\sqrt{2\pi}$) at $t = 5$ Obtained by Using a Fixed, Small Computational Domain. Comparison with a Linear Solution.

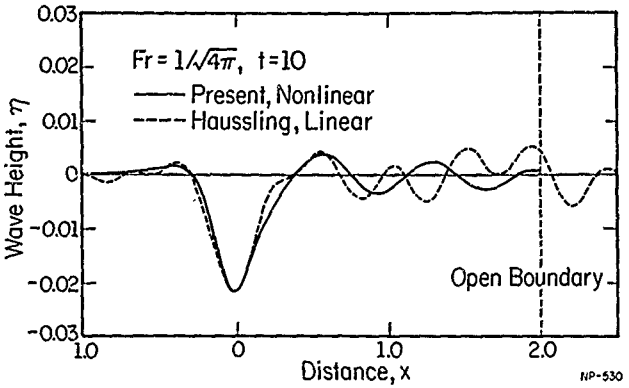


Fig. 9. Steady State Wave Height Solution of the Pressure Distribution Problem ($Fr = 1/\sqrt{2\pi}$) Obtained by Using a Fixed, Small Computational Domain. Comparison with a Linear Solution.

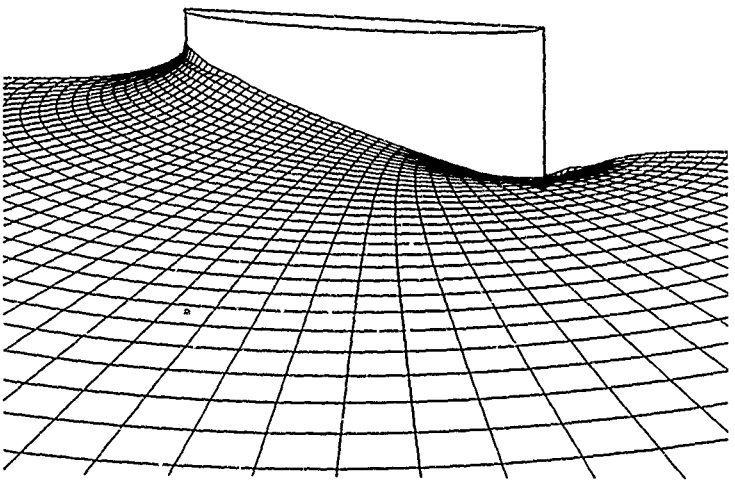


Fig. 10. Free Surface Elevation Around an Accelerating Strut at $t = 0.16$. $(Fr)^2 = 0.025$.

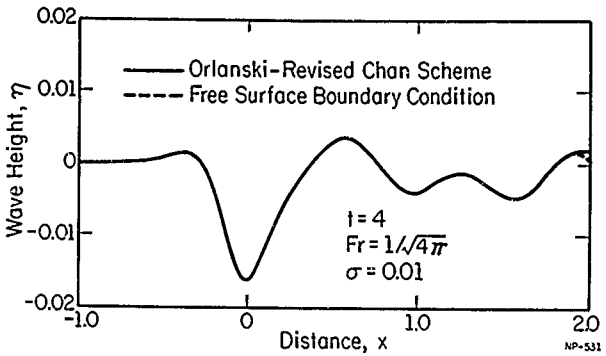


Fig. 11. Nonlinear Free Surface Wave Solutions Obtained by Using Two Different Treatments of the Open Boundary Condition at the Outflow Boundary.

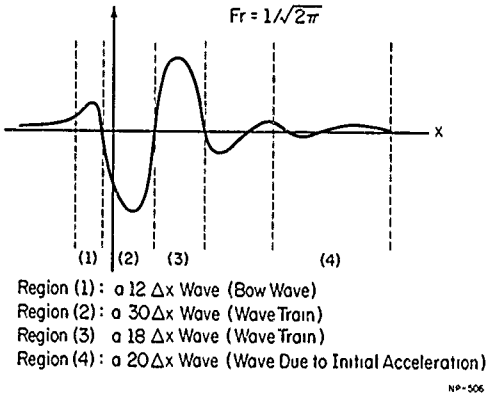


Fig. 12. Typical Wave Profile for the Pressure Distribution Problem. Fr = $1/\sqrt{2\pi}$, σ = 0.01.

DISCUSSION
of the paper
by S M. Yen and D R. Hall

IMPLEMENTATION OF OPEN BOUNDARY CONDITIONS FOR NONLINEAR FREE-SURFACE WAVE PROBLEMS

Discussion
by R.I. Van Eseltine

The strong statement that "the use of filtering is not suitable to obtain long time and steady state solutions" questions the use of filtering by other researchers (e.g.; Longuet-Higgins, Cokelet, Orszag, Haussling, Coleman, and myself) to obtain such solutions. Longuet-Higgins and Cokelet [1] have shown that energy is conserved with filtering. In addition, Haussling [2] and Coleman and Haussling [3] have obtained solutions to two-dimensional nonlinear flows with the use of filtering that compare very well to the steady-state solutions of Vanden-Broeck who did not use filtering. In a paper presented at this conference Baker, Meiron and Orszag [4] compared a numerical solution, which was obtained with the use of filtering, to an exact solution. Very good agreement was obtained and once again it was shown that the filtering does not affect the conservation of energy.

Such success with filtering cannot be ignored and thus the strong statement that the authors of this paper have made is subject to question. Because of the success of other researchers with filtering, I suggest that the authors' surprising results should be reexamined closely. The breakdown they observe must be for reasons other than the use of filtering.

[1] Longuet-Higgins, M.S. and Cokelet, E.D., "The Deformation of Steep Surface Waves. I.A. A Numerical Method of Computation", Proc. Roy. Soc. Lond. A 350, 1976, p. 1.

[2] Haussling, H.J., "Two-Dimensional Linear and Nonlinear Stern Waves", J. Fluid Mech , vol. 97, 1980, p. 759.

[3] Coleman , R.M. and Haussling, H.J., "Nonlinear Waves Behind an Accelerated Transom Stern", Third International Conference on Numerical Ship Hydrodynamics, Paris, France, 1981.

[4] Baker, G.R., Meiron, D.I. and Orszag, S A., "Applications of a Generalized Vortex Method to Nonlinear Free Surface Flows", Third International Conference on Numerical Ship Hydrodynamics, Paris, France, 1981.

Authors' reply

A filtering scheme is used to remove the spurious component of a numerical solution. The order of filtering scheme and the frequency of its application should be chosen so that its effect on the numerical solution is minimized. We followed this guideline in our attempt to control the high frequency errors that appear in our numerical solution of the pressure distribution problem using the open boundary. Our attempt was successful in the solution up to $t = 5$ (2500 time steps). The solution becomes unstable after that time. This instability is due to the numerical scheme to solve the free surface condition as well as the open boundary condition that exacerbates the high frequency problem.

We have conducted numerical experiments to study the effect of filtering on the numerical solution of the pressure distribution problem. In one experiment, we applied a first order filtering scheme every time step as well as every five time steps. We have found that the numerical solution is significantly damped when the filtering is applied every time step. The damping is reduced when the filtering is applied every five time steps ; however, the solution is distorted. Since we are trying to control the high frequency error due to the instability of the one step numerical scheme, using damping in the numerical scheme is more suitable for our purpose. However, it would be of interest to explore the possibility of finding a filtering scheme that could be used to control the high frequency error without influencing significantly the accuracy of the solution.

APPLICATIONS OF A GENERALIZED VORTEX METHOD TO NONLINEAR FREE-SURFACE FLOWS*

Gregory R. Baker †, Daniel I. Meiron and Steven A. Orszag
Department of Mathematics
Massachusetts Institute of Technology
Cambridge, Massachusetts 02139

Abstract

The motion of free surfaces in incompressible, irrotational, inviscid layered flows is studied by evolution equations for the position of the free surfaces and appropriate dipole (vortex) and source strengths. The resulting Fredholm integral equations of the second kind may be solved efficiently in both storage and work by iteration in both two- and three-dimensions. Applications are presented for such problems as breaking water waves over finite bottom topography, and wave generation by body motion and surface pressure distributions, the latter problems requiring radiation boundary conditions.

1. Introduction

It is well known that the solution to the Dirichlet and Neumann problems for Laplace's equation may be expressed in terms of boundary integrals of source or dipole distributions. The equations determing the source and dipole strengths are Fredholm integral equations of the first and second kind, as enumerated in Table 1.

Table 1: Classification of Fredholm Integral Equation by Problem Type and Choice of Representation

Problem Type	Representation: Source	Dipole
Dirichlet	First Kind	Second Kind
Neumann	Second Kind	First Kind

These equations are normally solved by direct matrix inversion techniques such as Gaussian elimination. However, when the problems are formulated in terms of integral equations of the second kind, it is not necessary to resort to such costly inversion methods; the required Fredholm equations have globally convergent Neumann series so they may be solved by simple iterative procedures.[1-3] These iterative methods lead to new and efficient techniques for the solution of time-dependent, irrotational, incompressible flows in layered media in the presence of both free surfaces and solid bodies.

With N points used to resolve the fluid interfaces (in either two or three space dimensions), our iterative boundary integral methods require only $O(N)$ computer storage and $O(N^2)$ arithmetic operations per time step. These storage and operation counts should be contrasted with more conventional methods based on direct matrix inversion that require $O(N^2)$ storage and $O(N^3)$ work per time step. As problem complexity increases, our new methods offer increasing advantages over more classical approaches.[4]

In this paper, we survey applications of our methods to free-surface water wave problems. In Sec. 2, we outline the kinematical and dynamical equations used to evolve these flows. In Sec. 3, applications to large-amplitude breaking water waves over bottom topography are given. Here periodic boundary conditions are applied on the free surface. Then, in Sec. 4, problems that require the application of a radiation boundary condition are studied. Finally, in Sec 5, we outline extensions of our methods to three-dimensional flow problems.

* Work supported by the General Hydromechanics Research Program of the Naval Sea Systems Command under Contract N0[illegible]14-80-C-0127.

† Present address: Department of Mathematics, University of Arizona, Tucson, Arizona 85721.

2. Equations of Motion in Two Dimensions

Here we present the equations governing the evolution of free surfaces which separate regions of inviscid, irrotational fluid with constant, but possibly different, densities. A detailed derivation of these equations is given elsewhere.[2] In order to obtain a Fredholm equation of the second kind (that is solvable by iteration), we represent the free surfaces located at $z^{(Fk)} = x^{(Fk)} + iy^{(Fk)}$, where $x^{(Fk)}$, $y^{(Fk)}$ are the coordinates of the kth free surface, by distributions of dipoles of strength $\mu^{(Fk)}$ $(k=1,\ldots,K_F)$. Similarly, impermeable (solid) interfaces located at $z^{(Bk)} = x^{(Bk)}+iy^{(Bk)}$ are represented by distributions of sources of strength $\sigma^{(Bk)}$ $(k=1,\ldots,K_B)$.

The complex velocity potential $\phi = \phi+i\psi$ where ϕ,ψ are the potential and stream function, respectively, may be expressed as

$$\phi(z) = \frac{1}{2\pi i}\sum_k \int \frac{\mu^{(Fk)}(e) z_e^{(Fk)}(e)\,de}{z-z^{(Fk)}(e)} + \frac{1}{2\pi}\sum_k \int \frac{\mu^{(Bk)}(e) z_e^{(Bk)}(e)\,de}{z-z^{(Bk)}(e)} + \phi_E, \tag{1}$$

$$\sigma(Bk) = \frac{\partial \mu^{(Bk)}(e)}{\partial e} \tag{2}$$

where the subscript e refers to differentiation with respect to a Lagrangian variable, defined below, which parametrizes the free surfaces or with respect to a variable which parametrizes the solid boundaries.

It may be shown that the potential generated from the dipole sheet is discontinuous across a free surface while the stream function is continuous. The jump in potential is given by the dipole sheet strength $\mu^{(Fk)}$. Also, $\mu^{(Bk)}$ may be interpreted as the jump in stream function across the kth solid boundary. The potential ϕ_E may be used to represent an external or circulatory flow around the closed solid boundaries.

The Lagrangian variable e which parametrizes the kth free surface is specified by requiring that the evolution equation for the position of the kth free surface be

$$\frac{\partial z^{(Fk)*}(e)}{\partial t} = \frac{\phi_e}{z_e^{(Fk)}} + \frac{\beta}{2}\frac{\mu_e^{(Fk)}}{z_e^{(Fk)}}, \tag{3}$$

where the superscript $*$ implies complex conjugation. When the potential is evaluated at a free surface, the integrals in (1) should be taken in the principal value sense, which corresponds physically to choosing the average velocity at the free surface. Since $\mu_e^{(Fk)}$ is proportional the jump in tangential velocity, (3) gives the decomposition of the velocity in terms of its average and difference across the kth free surface. The parameter β allows one the choice of a weighted average of the velocities on either side of the free surface. For example, if $\beta = 1(-1)$ then the Lagrangian markers follow the motion of the upper (lower) fluid.

The dipole distribution at a free surface automatically satisfies the kinematic condition that $\partial\phi/\partial n$ be continuous. On the other hand, the requirement that the normal fluid velocity at the kth solid boundary be that of the boundary gives an equation for $\mu^{(Bk)}$. Thus,

$$\mu^{(Bk)}(e) = 2\,\mathrm{Im}\,\phi(e) \tag{4}$$

where $\mathrm{Im}\,\phi(e)$ is the imaginary part of the potential evaluated at this solid boundary. Equation (4) is a Fredholm equation of the second kind for $\mu^{(Bk)}$. However, it is more useful to have an equation for $\frac{\partial \mu^{(Bk)}}{\partial t}$ since this quantity appears directly in the dynamical evolution equation [see (6) below]. Differentiating (4) gives a Fredholm integral of the second kind for $\partial\mu^{(Bk)}/\partial t$

$$\frac{\partial \mu^{(Bk)}}{\partial t} = 2\,\mathrm{Im}\,\frac{\partial \phi}{\partial t} \tag{5}$$

The kinematic conditions for the flow are now satisfied by (1), (3), and (5). Finally, the dynamic conditions lead to evolution equations for $\mu^{(Fk)}$. The Lagrangian time derivative of $\mu^{(Fk)}$ is given by

$$\frac{\partial \mu^{(Fk)}}{\partial t} = \frac{1}{2}(\beta + \frac{A}{2}) \frac{(\mu_e^{(Fk)})^2}{\left|z_e^{(Fk)}\right|^2}$$

$$+ 2A \left\{ Re(\frac{\partial \phi}{\partial t}) - \frac{1}{2} qq^* - \frac{\beta}{2} Re(\frac{q}{z_e^{(Fk)}}) \mu_e^{(Fk)} \right.$$

$$\left. + g \; Im \; z^{(Fk)} \right\} \qquad (6)$$

where $q^* = \phi_e / z_e^{(Fk)}$, $Re(\frac{\partial \phi}{\partial t})$ is the real part of the Lagrangian time derivative of the complex potential evaluated at the free surface, g is the gravitational constant and A is the Atwood number (the ratio of the density difference to the density sum at the free surface). Since the equation for $\frac{\partial \phi}{\partial t}$ involves the expression $\int \frac{\frac{\partial \mu}{\partial t}^{(Fk)} z_e^{(Fk)}(\sigma) d\sigma}{z - z^{(Fk)}(\sigma)}$, (5) is also a Fredholm integral equation of the second kind for $\frac{\partial \mu^{(Fk)}}{\partial t}$.

Equations (1), (3), (5), and (6) form a basic set of evolution equations which are consistent with the dynamic and kinematic constraints on the flow. They may be used to advance the free surface forward in time. These equations are not the most general equations for irrotational free surface flow. For example, we can include in a straightforward way effects due to the presence of surface forces such as surface tension or modified dynamical constaints that replace Bernoulli's equation (6).

A formal identification with a vortex sheet representation for free surfaces can be made by defining $\gamma^{(Fk)} = \mu_n^{(Fk)}$; then $\gamma^{(Fk)} / (z_\sigma^{(Fk)} z_\sigma^{(Fk)*})^{1/2}$ is the vortex sheet strength. The complex velocity $q = u + iv$ may be obtained by differentiating (1) and integrating by parts.

$$q^* = \frac{1}{2\pi i} \sum_k \int \frac{\gamma^{(Fk)}(\sigma) d\sigma}{z - z^{(Fk)}(\sigma)}$$

$$+ \frac{1}{2\pi} \sum_k \int \frac{\sigma^{(Bk)}(\sigma) d\sigma}{z - z^{(Bk)}(\sigma)} + Q_E^* \qquad (7)$$

The first term represents the Biot-Savart formula, the second term represents the source distribution at solid boundaries and Q_E^* is the external flow if present. The evolution equation for $\gamma_{(Fk)}$ is obtained by differentiating (6)

$$\frac{\partial \gamma^{(Fk)}}{\partial t} = (\frac{A}{4} + \frac{\beta}{2}) \frac{\partial}{\partial \sigma} \frac{(\gamma^{(Fk)})^2}{z_\sigma^{(Fk)} z_\sigma^{(Fk)*}}$$

$$+ 2A \left\{ Re(z_\sigma^{(Fk)} \frac{\partial q^*}{\partial t} + \frac{\beta}{2} \frac{\gamma^{(Fk)} q_\sigma}{z_\sigma^{(Fk)}}) \right.$$

$$\left. + g \; Im(z_\sigma^{(Fk)}) \right\} \qquad (8)$$

This equation describes the baroclinic generated of vorticity due to the presence of density gradients. The above formulation is entirely equivalent to (1) and (5) and may also be used to study the evolution of free surfaces.[3] In general, we have found the dipole representation to be superior for the study of breaking waves and the vortex sheet representation superior for problems in which radiation conditions are required.

The dipole formulation is easily implemented for the case of infinite periodic domains as it is possible to sum the kernels in closed form so that numerical integrations need be carried out over only one period. Results for periodic domains are presented in Sec. 3. However, many free surface flow problems are concerned with the generation of waves due to the motion of bodies or other external influences. In such problems, a periodic computational domain is of limited value since waves may interact across neighboring periodicity intervals. In fact, we minimize wave reflections by introducing damping layers which border the computational domain in which both the wave elevation and vortex sheet strength are damped[5]. Specifically,

$$\frac{\partial \gamma^{(Fk)*}}{\partial t} = R - \nu(x)(\gamma^{(Fk)} - h^{(k)}) \qquad (9)$$

$$\frac{\partial \gamma^{(Fk)}}{\partial t} = R - \nu(x) \gamma^{(Fk)} \qquad (10)$$

where $\nu(x)$ is the damping coefficient and R represents the right-hand side of (3) and (8). The damping coefficient is chosen to be a quadratic in x so that it and its derivative vanish at the point where the damping layer meets the computational domain. Applications of this technique are given in Sec. 4.

3. APPLICATIONS: PERIODIC BOUNDARY CONDITIONS

Steady and Unsteady Traveling Waves on an Infinite Depth Fluid

A simple but non-trivial test of the time dependent numerical scheme is obtained by calculating the propagation of steady interfacial waves. The initial wave profile and vortex sheet strength are obtained by solving nonlinear integral equations for Atwood ratios $A = -1.0$ (a surface wave) and $A = -0.8181$. These steady state integral equations are derived in detail elsewhere[2]. In our test the wave heights for the surface and interfacial waves are chosen to be $h = 0.4$ and 0.36, respectively, where h is the average of the crest and trough amplitudes and the wavenumber $k = 1$. Therefore, both test cases correspond to nonlinear waves (90% of the maximum Stokes wave amplitude for the surface wave).

In order to maintain the smoothness of the wave profile it proved necessary to employ smoothing. We use the five point smoothing operator described by Longuet-Higgins & Cokelet.[6] Without occasional smoothing the interface takes on a jagged appearance and the calculation cannot be continued.

An Adams-Moulton predictor-corrector scheme is used to advance the interface and vortex sheet strength forward in time. The time dependent solution is checked for accuracy by comparing the locations of the markers with the known solution at time $t = 0$ translated in the x-direction by an amount ct where c is the nonlinear phase speed of the wave. For the surface wave $c = 1.082$ and for the interfacial wave $c = 0.952$. The results are plotted in Figs. 1 and 2 at times when the waves have propagated through one period. At these times the numerical and theoretical profiles agree to one part in 10^4 (using 400 time steps per period).

A useful diagnostic on the calculation is conservation of energy. The kinetic energy is given by

$$E_K = \frac{\rho_2}{2}\iint (u_2^2+v_2^2)d\Lambda_2 + \frac{\rho_1}{2}\iint (u_1^2+v_1^2)d\Lambda_1 \qquad (11)$$

Using Green's theorem E_K may be rewritten as a boundary integral:

$$E_K' = \frac{4E_K}{\rho_1+\rho_2} = \int_0^s \psi\tilde{\gamma}\,ds + 2\left(\frac{\rho_2-\rho_1}{\rho_1+\rho_2}\right)\int_0^s \psi\frac{\partial\phi}{\partial s}\,ds \qquad (12)$$

where ψ and ϕ are the average stream function and potential respectively. The potential energy E_P' is given by

$$E_P' = \frac{4E_P}{\rho_1+\rho_2} = 2\left(\frac{\rho_2-\rho_1}{\rho_1+\rho_2}\right)\int_0^s y^2\frac{dx}{ds}\,ds \qquad (13)$$

In Lagrangian form $\tilde{\gamma} = \gamma/(ds/d\alpha) = \frac{du}{ds}$ so that the total energy is given by

$$E_T' = E_P' + E_K' =$$

$$\int_0^{2\pi} \psi\gamma\,d\alpha + 2A\left[\int_0^{2\pi}\psi\frac{\partial\phi}{\partial\alpha}\,d\alpha + \int_0^{2\pi} y^2\frac{dx}{d\alpha}\,d\alpha\right] \qquad (14)$$

It can be easily shown using the equations of motion that

$$\frac{dE'}{dt} = 0.$$

For the simulations of steady waves energy is conserved to better than one part in 10^4. The five point smoothing operator used does not affect conservation to this level of accuracy.

The application of a fifth-order Lagrange polynomial extrapolation in time reduces the number of iterations to just two per predictor-corrector step in the evaluation of du/dt. Thus, our operation count is truly $O(N^2)$. For 400 time steps using 128 interface markers the computation time is less than 30 seconds on a CRAY-1 computer.

Having demonstrated the reliability of the iterative vortex method for finite amplitude steady flows we show that the method is capable of following unsteady waves well into the breaking regime. As an initial condition, we choose a Stokes wave which is 80% of maximum height. A pressure distribution of the form

$$p_s(x,t) = p_0 \sin(t)\sin(x-ct)$$

is applied at times $0 \leq t \leq \pi$ and is switched off at $t = \pi$. Thus the energy is increased smoothly until $t = \pi$. This run is similar to the case considered by Longuet-Higgins & Cokelet[6]. As is seen in Figure 3 the wave overturns and a jet of fluid is ejected from the forward face of the wave. For this run the time step was $\Delta t = 2\pi/400$ with smoothing applied every 10 time steps; 64 Lagrangian markers were used. The iterative method continues to converge until the curvature at the tip becomes too great to resolve with the number of points used.

Large-Amplitude Surface Waves on a Finite Depth Fluid

Here we report results obtained by applying the vortex-source technique to the calculation of periodic surface waves over periodic bottom topography. The rate of convergence for the coupled integral equations (5,6) is somewhat slower than for the case of infinite depth discussed above. For infinite depth (corresponding to a simply-connected domain) the largest eigenvalue in the integral equation (6) is essentially a function of the aspect ratio of the geometry. For finite depth which corresponds to a doubly connected domain the largest eigenvalue can be related to the depth to wavelength ratio. Therefore as the geometry becomes sufficiently shallow the dominant eigenvalue tends toward one. Indeed, for linear shallow water waves the dominant eigenvalue is $0(e^{-kd})$ where d is the depth and k is the wavenumber. Thus, a larger number of iterations are needed in the initial stages of the time integration. However, once a sufficient number of previous time levels are known extrapolation schemes significantly reduce the number of iterations to two to three per time step.

In all runs made with this method we used 128 points on the free surface and 128 on the bottom. An equivalent simulation using Green's third formula would entail the inversion of a 256×256 matrix at each time step.[7] The use of fewer points results in inadequate resolution of regions of large curvature at the interface.

As an accuracy test, we first calculated linear waves over a flat bottom. For depth d the phase velocity of the waves is

$c = \sqrt{k \tanh kd}$. For waves of amplitude $a(a<<1)$ this relation was found to be satisfied to within errors of order $0(a^2)$. A second check on the code is obtained by noting that the expression for the wave energy is still valid since the normal velocity $\frac{\partial \phi}{\partial n}$ vanishes along the bottom. In all runs reported here energy is conserved to better than one part in 10^4.

The initial conditions for all the nonlinear runs reported below are

$$x(e, t = 0) = e$$

$$y(e, t = 0) = a \cos(e)$$

$$x_B(e) = e$$

$$y_B(e) = -d + b \sin(e)$$

$$Y(e, t = 0) = a/\sqrt{\tanh(d)} \quad (1+\tanh d)\cos(e)$$

$$\sigma(e, t = 0) = -a/\sqrt{\tanh(d)} \sin(e)$$

For small values of the amplitude a and with $b = 0$, these conditions correspond to a linear wave propagating to the right at the speed $\sqrt{\tanh d}$. The period of the linear wave is $t_0 = 2\pi/\sqrt{\tanh d}$. In order to simulate a plunging breaker we choose $a = 0.5, d=1.$ and $b = 0$. The results are plotted in Fig. 4. At time $t = 0.26t_0$ $(= 1.85)$ the profile has become vertical and at $t = 0.42\ t_0 (= 3.0)$ a jet has been ejected from the forward face of the crest. The profile is similar to that of a plunging breaker.

A spilling breaker is generated by the initial conditions $a = 0.2$ $d = 0.5$ and $b = 0.1$. This is a slightly unsteady wave propagating over a sinusoidal bottom. A sequence of wave profiles is plotted in Fig.5. At $t = 0.43\ t_0 (= 4.0)$ the wave crest is spilling.

In order to provide a more detailed picture of the dynamics of the plunging breaker we have examined the velocities and accelerations of the fluid surface. Following Peregrine et al[8], we plot a phase (hodograph) plane of the surface x-velocity versus the y-velocity. By drawing the radius vector to any point on this hodograph plane the magnitude and direction of the velocity may be deduced. We plot the results for the plunging breaker (see Fig. 4) *in Fig. 6.* The curves are plotted at time intervals $t_0/20$ where $t_0 = 2\pi/\sqrt{\tanh(1)} = 7.2$.

The crest of the wave is located at the rightmost point of the hodograph while the trough corresponds to the leftmost point. The front (back) of the wave corresponds to the upper (lower) half of the elliptical curves. As the wave steepens the velocities at the crest increase. At the point of plunging the crest velocities point downwards toward the interface. The magnitudes of the velocities in the forward jet are greater than the nonlinear phase speed of the highest wave at this depth. In addition the rate of increase of the velocities (i.e. the acceleration) is also apparently increasing.

The accelerations for this plunging breaker are plotted in Fig. 7. At early times the acceleration is essentially orthogonal to the velocity vector. The front and back of the travelling wave now correspond to the rightmost and leftmost points, respectively, of the elliptical profiles while the crest and trough are located at the bottom and top.

As the wave approaches breaking the surface profiles of acceleration depart markedly from the steady state shown in Fig. 7. The largest accelerations are located in the region just below the crest. These accelerations are four to five times larger than the acceleration due to gravity and are pointed in the forward direction. Peregrine et al have also observed large accelerations in the crest region in qualitative agreement with our results.

Despite the large forward accelerations observed just under the crest of the breaker the tip of the wave appears to be in free fall. At time $t = 0.28\ t_0 (=2.0)$, the acceleration at the tip exceeds g (1.0 in our units) by approximately 30%. The forward face of the wave is essentially vertical at this time. At later times the acceleration at the tip decreases to 1.0. Indeed, at $t = 0.41\ t_0 (=2.97)$, there is a region about the tip in which the fluid accelerations vary by less than five percent from free fall. In this region the acceleration vectors are closely aligned with the -y axis.

The qualitative similarity of our results with those of Peregrine et al indicate that the flow in the plunging region of breakers is a local phenomenon. The remainder of the wave is subject to relatively low accelerations and does not appear to influence the dynamics of the plunging jet.

Longuet-Higgins has recently proposed several analytic forms for the complex potential in the breaking region[9]. A detailed comparision between this theoretical approach and the numerical approach of this section is currently under way.

4. Wave Generation and Radiation Conditions

In Sec. 2, radiation boundary conditions were incorporated in the boundary integral equations used to study problems involving wave generation. The effectiveness of these radiation conditions is demonstrated by the following test case. The free surface is given the initial elevation, $y = 0.2 \exp(-x^2)$, and then allowed to collapse under the influence of gravity. Waves are generated which move away from the source of the disturbance. By symmetry only the motion of surface for $x > 0$ need by studied. Damping is applied in the region $6 \leq x \leq 10$. In Fig. 8 we plot the elevation at $x = 0$ as a function of time for the case of no damping, the case where $\nu(x) = \alpha(x-6)^2$, $6 \leq x \leq 10$, with $\alpha = 0.5$, and the "exact" behaviour. Notice from Fig. 8 that without damping, reflected waves cause serious inaccuracies in the description of the free surface for $t \geq 7$ (g, the gravitational constant, is chosen to be 1) as described below. Values of the damping coefficient α greater than 0.5 give no significant improvement in results and thus one is limited in the accuracy one can obtain with a fixed damping layer.

When the damping layer is increased in length and moved further away, the results converge to the solution labelled "exact" in Figure 8. In Figure 9,we plot the surface elevation at $t = 10$ for various damping layers. Observe the convergence to the "exact" profile.

Our first application of the damping layers is to simulate the wave generation by an air-cushioned vehicle moving steadily over a water surface. Following previous workers[10], we apply a fixed surface pressure distribution on a steadily translating fluid. However, unlike previous work in which steady-state wave trains are calculated, we turn the pressure distribution on gradually so that the formation of the wave train can be studied. In particular we observe that rapid variations in the strength of the pressure distributions cause large and slowly decaying transients in the drag coefficients.

We choose[10] the surface pressure $p_0(x,t)$ to be

$$p_0 = \bar{p}(t) \quad |x| < \frac{L_2}{2}$$

$$p_0 = \frac{\bar{p}}{2}(t) \left\{1-\sin\left[\frac{\pi}{L_1}\left(x - \frac{L_2}{2}\right)\right]\right\}$$

$$\frac{L_2}{2} < |x| < \frac{L_2}{2} + L_1$$

$$p_0 = 0 \quad |x| > \frac{L_2}{2} + L_1$$

where $L = L_1 + L_2$ is a reference length for the pressure distribution and L_1/L_2 determines the steepness of the pressure distribution near its ends. For the results reported below we choose $L_1/L_2 = 1$. Here $\bar{p}(t)$ gives the strength of the pressure pulse; also $\bar{p}(t > T_p) = 0.016\ gL$. Finally, the Froude number, $F = u/(gL)^{1/2} = 0.461$.

The surface elevation is plotted for various times in Fig. 10 to show the development of the wave train. The damping layers were placed at $-4.5 < x < -2.5$ and $5. < x < 7.5$. The pressure distribution is increased steadily in time until it reaches its maximum value at a time $T_p = 8L/u$. The corresponding time variation of the wavedrag coefficient defined by

$$c_{WD} = \frac{\rho g}{2\bar{D}^2} \int p_0\, y_e\, dx \quad \text{is plotted in}$$

Figure 11a. Notice that the wavedrag coefficient attains a nearly constant value fairly quickly. However, when $T_p = 2L/u$, the wavedrag coefficient plotted in Fig. 11b, shows much stronger variation in time and the existence of large, long-lived transients.

Next we consider the waves generated by a submerged uniformly translating body. Previous workers[11] have discovered that when a body close to the surface is set impulsively into motion, the surface disturbance is strong. In fact, our calculations show that breaking waves form. Figure 12 shows the temporal change of the surface in a frame at rest with a cylinder of radius R that is moving horizontally with speed u. The center of the cylinder is at depth 3R beneath an initially flat surface. For accuracy, it was necessary to place the damping layers at $-15R < x < -10R$ and $10R < x < 15R$.

We have repeated the calculation for an ellipse with semi-minor axis R and semi-major axis 3R. A larger breaking wave develops as evident in Fig. 13. We expect this behaviour to be strongly dependent on Froude number (chosen in both cases as $F = u/(gR)^{1/2} = 0.8$). Further results, in particular the wave drag on the body, will be reported elsewhere. It should be emphasized that the computer code used to obtain the above results works with rather arbitrarily shaped bodies. Our formulation also allows us to include the self-consistent body motion along with the free-surface dynamics.

5. Generalizations and Other Applications

In Sec. 2, equations determining the motion of free surfaces of incompressible, inviscid irrotational flow were obtained as Fredholm integral equations of the second kind. The advantage of such a formulation is that the resulting equations may be solved iteratively by constructing successive terms of a Neumann series. The resulting scheme is globally convergent[12]. Moreover, improved first estimates for the solution at time t can be obtained by standard extrapolation techniques from values at previous time steps. In this way, the solutions are obtained using only a few (2-5) iterations per time step even for severely deformed geometries.

While the equations given in Sec. 2 are specifically for two-dimensional flow, there is a more general formulation, valid in three-dimensional flow. The potential evaluated at the field point $\vec{r}$, is given by

$$\phi(\vec{r}) = \sum_k \int \mu^{(Fk)}(\vec{r}') \frac{\partial}{\partial n'} g(\vec{r},\vec{r}')\, dr'$$

$$+ \sum_k \int \sigma^{(Bk)}(\vec{r}') g(\vec{r},\vec{r}')\, d\vec{r}' \qquad (15)$$

where $g(\vec{r},\vec{r}')$ is the free-space Green's function for Laplace's equation, $\frac{\partial g}{\partial n'}$ is the normal derivative on the surface, and the integration is over free surfaces for $\mu^{(Fk)}$ and over solid boundaries for $\sigma^{(Bk)}$. For two-

dimensional flow, $g = \frac{1}{2\pi}\log|r-r'|$; for three-dimensional flow, $g = 1/4\pi\,|r-r'|$; for axi-symmetric flow g can be expressed in terms of elliptic functions of the first kind.

Continuity of normal velocities at free surfaces is automatically satisfied by (15), but the requirement that the fluid has no normal velocity relative to solid boundaries leads to Fredholm integral equations of the second kind for $\mu^{(Bk)}$. The Neumann series for the solution to these equations, involving any of the Green's functions mentioned above, are globally convergent so the equations can be solved iteratively.

The dynamics of the flow gives equations for $\mu^{(Fk)}$. For incompressible, inviscid, irrotational, stratified layered flow there result Fredholm integral equations of the second kind for the Lagrangian time rate of $\mu^{(Fk)}$ [which are generalizations of (6)]. On the other hand, for porous media flow and at fluid-vacuum interfaces, the dynamics can be formulated as a Fredholm equation for $\mu^{(Fk)}$ itself. Other applications, like motion of a sea-bed, cavity flow, etc, are amenable to such modified formulations.

References

1. S. Bergman and M. Schiffer, Kernel Functions and Elliptic Differential Equations in Mathematical Physics (Academic, New York, 1953), p. 334.
2. G. R. Baker, D. I. Meiron, and S. A. Orszag, to be published.
3. G. R. Baker, D. I. Meiron, and S. A. Orszag, Phys. Fluids, 23, p. 1485, (1980).
4. M. A. Jaswon and G. T. Symme, Integral Equation Methods in Potential Theory and Elastostatics, (Academic, New York, 1973).
5. S. A. Orszag and M. Israeli, Approximation of Radiation Boundary Conditions, J. Comp. Phys. (1981) to appear.
6. M. S. Longuet-Higgins and E. D. Cokelet, Proc. R. Soc. London Ser. A. 304, 1, (1978).
7. J. D. Fenton and D. Mills, in Waves on Water of Variable Depth, Lecture Notes in Physics Vol. 64, p. 94 (1976).
8. D. H. Peregrine, E. D. Cokelet, and P. McIver in Proceedings of the 17th Conference on Coastal Engineering (to appear).
9. M. S. Longuet-Higgins, On the Overturning of Gravity Waves, Proc. R. Soc. London Ser. A (1981) (to appear).
10. C. von Kerczek and N. Salvesen, in Proceedings of the Second International Conference on Numerical Ship Hydrodynamics p. 292 (1977).
11. H. J. Haussling and R. M. Coleman, in Proceedings of the Second International Conference on Numerical Ship Hydrodynamics p.221 (1977).

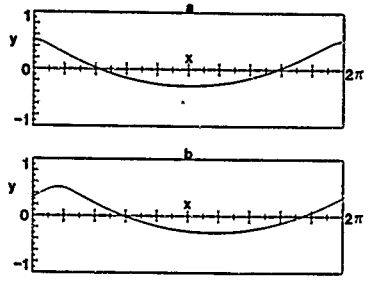


Figure 1. A plot of the Stokes wave profile (A=-1) at time t=0(a) and time t = 2 (b). The dots indicate the numerically computed position of the interface. The solid line is obtained from the nonlinear integral equations for the exact interfacial wave.

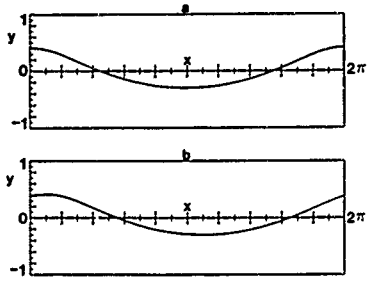


Figure 2. Same as Fig. 1 except A = -0.8182.

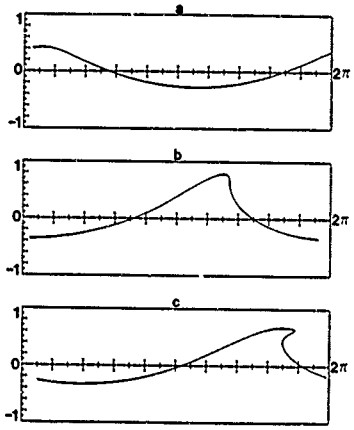


Figure 3. A plot at various times of the profile of a breaking wave on infinite depth. The height of the Stokes wave used as an initial condition if 80% of the maximum. The wave is forced by a pressure pulse moving in quadrature with the wave of the form $p(x,t) = p_0 \sin t \sin(x-ct)$ with $p_0 = 0.146$. The pressure pulse is turned off after $t = \pi$. The profile is shown at times (a) t =0.38, (b) t = 3.16, and (c) t = 4.22. Note that in (c) the wave has broken and a smooth jet has been ejected from the forward face.

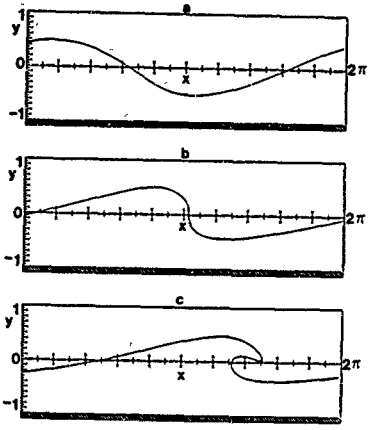


Figure 4. A plot at various times of the profile of a plunging breaker on finite depth. The initial condition corresponds to a sine wave with a large initial amplitude a = 0.5. The wave is plotted at times (a) t =0.46 (b) t = 1.84 and (c) t = 3.0. See text for discussion.

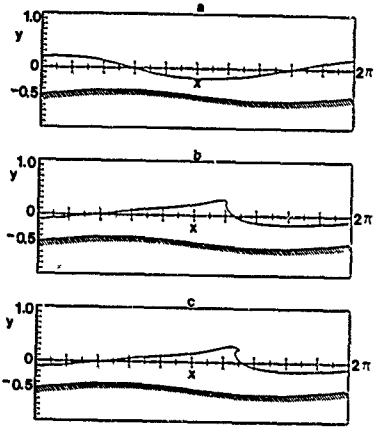


Figure 5. A plot at various times of the profile of a spilling breaker. The initial condition corresponds to a sine wave with initial amplitude a = 0.2. The bottom topography has the form $z_B(e) = e + i\,(-.5+.1\sin e)$. The wave is plotted at times (a) t =0.46, (b) t = 3.70, and (c) t = 4.0.

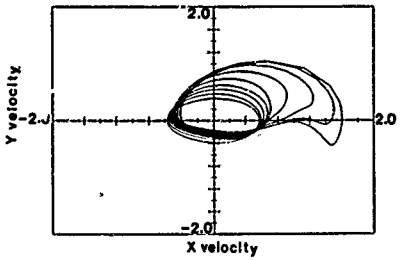


Figure 6. A phase portrait of the y-velocity versus x-velocity for the run shown in Fig. 4.

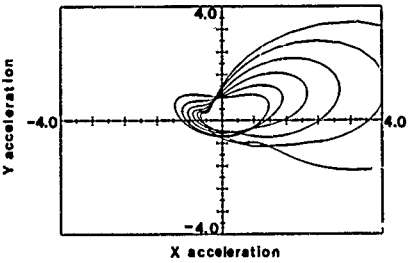


Figure 7. A phase portrait of the y-acceleration versus x-acceleration for the run shown in Fig. 4. The free fall point is located at (0.0, - 1.0).

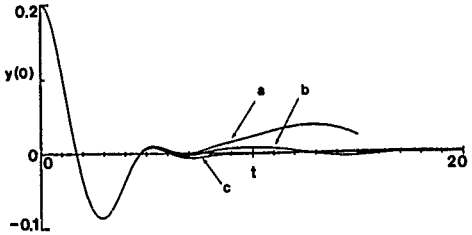


Figure 8. Surface elevation y(x=0) as a function of time for the test of the radiation conditions (see text):

a) no damping

b) $\nu(x) = 0.5(x-6)^2$, $6 < x < 10$

c) "exact" solution

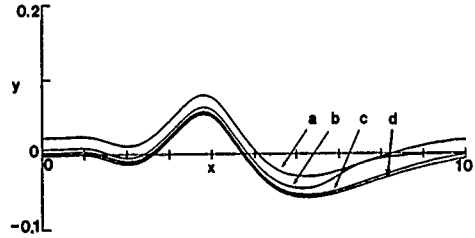


Figure 9. Surface elevation y(x) resulting from various applications of damping conditions:

a) no damping, computational domain ends at x = 10

b) $\nu(x) = 1/2(x-6)^2$, $6<x<10$

c) $\nu(x) = 1/8(x-12)^2$ $12<x<20$

d) $\nu(x) = 1/18(x-8)^2$ $8<x<30$

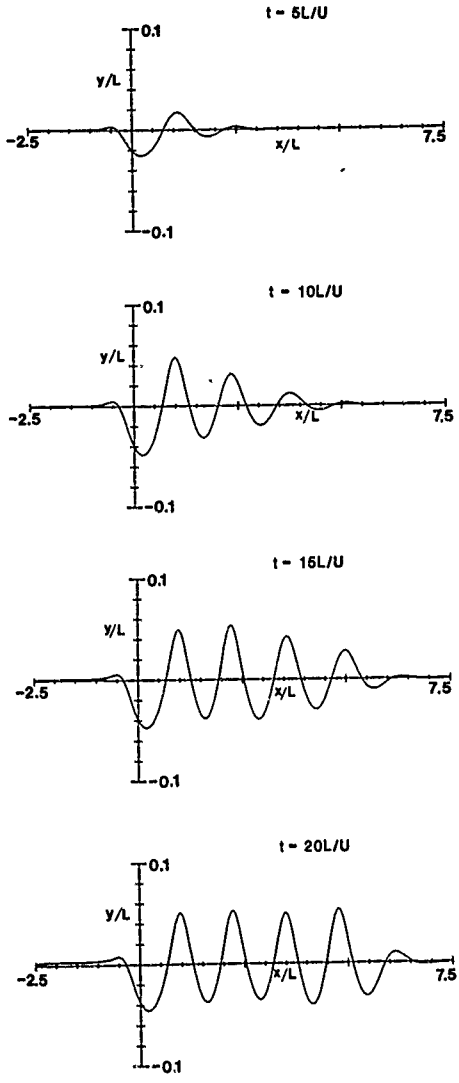
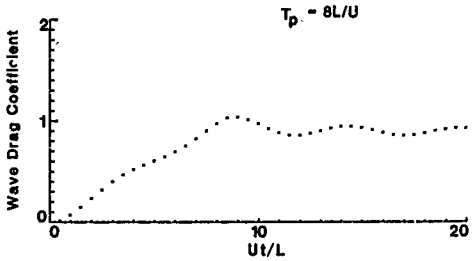


Figure 10. Free surface elevations resulting from application of time dependent surface pressure distribution. For more details see text. Free surface profile is shown at times (a) t = 5L/U, (b) t = 10L/U, (c) t = 15L/U, and (d) t = 20L/U.



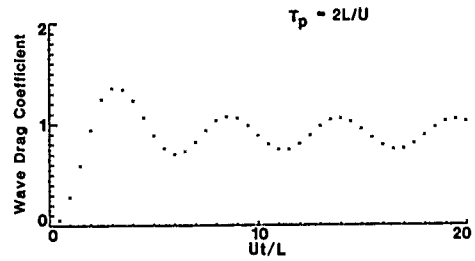


Figure 11. Coefficient of wave drag as a function of time for the flow past a surface pressure pulse (see Fig. 10 and text for more details). Drag coefficient is plotted for (a)T_p=8L/U and (b) T_p = 2L/U.

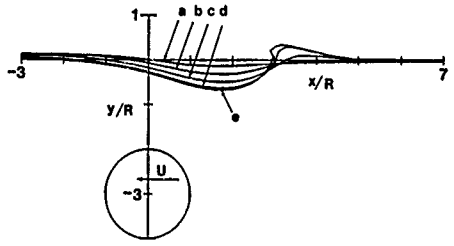


Figure 12. Free surface profiles above a submerged translating cylinder. Profiles are shown at times (a) Ut = 2R/4, (b) 4R/4, (c) 6R/4, (d) 8R/4, (e) 9.3R/4.

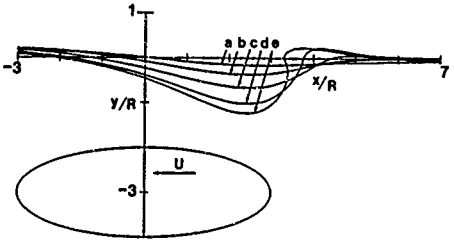


Figure 13. Free surface profiles above a submerged translating ellipse with eccentricity $\sqrt{8/3}$. Profiles are shown at times Ut= (a) 2R/4, (b) 4R/4, (c) 6R/4, (d) 8R/4, (e) 9R/4.

RECENT PROGRESS TOWARDS AN OPTIMAL COUPLING BETWEEN FINITE ELEMENTS AND SINGULARITY DISTRIBUTION PROCEDURES

D. Euvrard, A. Jami, M. Lenoir, D. Martin
École Nationale Supérieure de Techniques Avancées
Centre National de la Recherche Scientifique
Groupe Hydrodynamique Navale
Chemin de la Hunière, 91120 Palaiseau (France)

Abstract

This paper is a survey of linearized problems in ship hydrodynamics. Various approaches are presented which lead to problems set in a bounded domain. Moreover theoretical results are reported which give the essential support to understand the numerical discrepancies. By the way we prove that the Neumann-Kelvin problem for the velocity potential is always ill-posed in 2-D. We also prove the convergence for the localized finite element method ; this being approximately of order N^{-2} if N is the number of terms in the truncated series expansion of the solution. Finally we describe the coupling method between finite elements and an integral representation ; we place its functional framework which ensures convergence of the finite element approximation. Numerical results are given using the latter method which compare favourably with the others.

I. Introduction

The aim of this communication is to present some considerations on the problems in linearized ship hydrodynamics and on the numerical methods now available.

In the first part we take up the study of the so called *linearized sea-keeping* and *Neumann-Kelvin* problems. The former problem enters the scope of *diffraction problems* which have been studied for a long time by physicians and recently by mathematicians ; one can easily take advantage of this considerable theoretical and practical background. For the latter problem, the situation is quite different ; it seems that no similar problem can be found in the field of physics except in the study of baroclinic waves and this is the reason why its theoretical study is not developed.

In the second part, we bring out the inner principles of two of the main classes of methods currently in use to day :

- Localized Finite Elements
- Finite Elements and Integral Representation.

Finally, few numerical results are given using the last method which do not lay claim but to corroborate our subject.

Note that we consider the boundaries are regular enough to define their normal almost everywhere ; the normal vectors (and normal derivatives) are supposed external to the domains under consideration. Although the problems are generally set in 3-D, the figures are drawn in 2-D for the sake of simplicity.

II. The linearized sea-keeping problem

II.1. Formulation

This problem originates in the study of the potential flow around a rigid ship with zero mean speed which motion is generated by an incident wave with small amplitude ; it leads (see [1]) to the solution of seven boundary value problems of the same type (see fig. 1) :

$$\left.\begin{array}{l} \text{Find } \overset{\vee}{u} \in H^1_{loc}(\overset{\vee}{\Omega}), \text{such that} \\ \Delta \overset{\vee}{u} = 0 \text{ in the fluid domain } \overset{\vee}{\Omega}, \\ \dfrac{\partial \overset{\vee}{u}}{\partial n} = \nu \overset{\vee}{u} \text{ on the free surface } \overset{\vee}{FS},\ \nu > 0, \\ \dfrac{\partial \overset{\vee}{u}}{\partial n} = g \text{ given on the hull } \Gamma_0, \text{ and} \\ \lim\limits_{R \to \infty} \int\limits_{-\infty}^{0} \int\limits_{0}^{2\pi} R \left| \dfrac{\partial \overset{\vee}{u}}{\partial R} - i\nu \overset{\vee}{u} \right|^2 d\theta dz = 0, \\ \lim\limits_{z \to -\infty} \dfrac{\partial \overset{\vee}{u}}{\partial z} = 0, \end{array}\right\} (P_\nu)$$

where (R, θ, z) are the cylindrical coordinates.

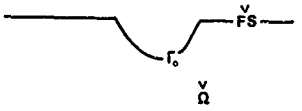


Fig.1 : The fluid domain $\overset{\vee}{\Omega}$, the hull Γ_0 and the free surface $\overset{\vee}{FS}$.

The problem $(\overset{\vee}{P}_\nu)$ is set in the case of an infinite depth. If there exists a bottom $(\overset{\vee}{B})$, horizontal at infinity with $z = -H$, the last condition in $(\overset{\vee}{P}_\nu)$ becomes $\frac{\partial \overset{\vee}{u}}{\partial n} = 0$ on $(\overset{\vee}{B})$, and the constant ν in the radiation condition must be replaced by the single positive root θ_0 of the equation $\text{th } H\theta_0 = \nu/\theta_0$. In that case we shall refer to problem $(\overset{\vee}{P}_{\nu,H})$ (see fig. 2).

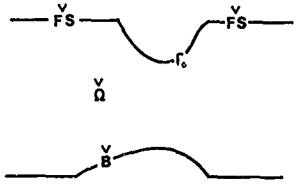


Fig.2 : The case of a bottom $(\overset{\vee}{B})$ of depth H at infinity.

A detailed analysis of these problems has been done ; recall that JOHN [2] studied $(\overset{\vee}{P}_\nu)$ but his results were only valid for a restricted class of hulls. We give in §3 of this chapter a glimpse of the complete solution of LENOIR, MARTIN [3] ; but let first show an instructive approach.

II.2. Solution with a radiation condition at finite distance

The main difficulty in solving $(\overset{\vee}{P}_\nu)$ or $(\overset{\vee}{P}_{\nu,H})$ is to deal with an unbounded domain. A rudimentary method consists in bounding the domain by a fictitious vertical surface Σ and, if necessary, a fictitious bottom B ; this approach has been followed by BAI [4] and OUSSET [5]. As shown on figure 3, the bounded domain is denoted Ω and the portion of free surface belonging to its boundary is denoted FS.

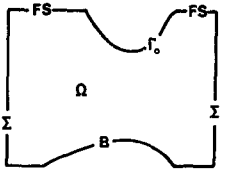


Fig.3 : The bounded domain Ω and the fictitious boundary Σ.

Therefore we have to solve the problem

$$\left.\begin{array}{l} \text{Find } u \in H^1(\Omega), \text{ such that} \\ \Delta u = 0 \text{ in } \Omega, \\ \frac{\partial u}{\partial n} = \nu u \text{ on FS}, \\ \frac{\partial u}{\partial n} = 0 \text{ on B}, \\ \frac{\partial u}{\partial n} = g \text{ on } \Gamma_0, \text{ and} \\ \frac{\partial u}{\partial n} = i\theta_0 u \text{ on } \Sigma. \end{array}\right\} (P_{\nu,H})$$

In the sequel we show that $(P_{\nu,H})$ is well-posed and in § IV.1 we shall give a terse presentation of its approximation with finite elements.

Note that as far as we know it has not been shown that the solution of $(P_{\nu,H})$ tends to the solution of $(\overset{\vee}{P}_{\nu,H})$ when the boundary Σ is removed towards infinity, nor that the solution of $(\overset{\vee}{P}_{\nu,H})$ tends to that of $(\overset{\vee}{P}_\nu)$ when the bottom B is let down ; nevertheless these assertions seem to be plausible.

Uniqueness. As $(P_{\nu,H})$ is linear, we just have to show that the null solution alone is possible when $g = 0$. Thus, let u be a solution of the homogeneous problem ; second Green's formula applied to u and $\bar{u}$ leads to

$$\int_\Omega |\text{grad } u|^2 d\omega - \nu \int_{FS} |u|^2 ds = i\nu \int_\Sigma |u|^2 ds \quad .$$

As the left-hand-side is real, u vanishes on Σ and also does $\frac{\partial u}{\partial n}$ by the boundary condition on Σ.

Now let $E_M(P)$ be the elementary solution of the Laplacian, it is well known that the function

$$f(M) = \int_{\partial\Omega} \{u(P)\frac{\partial E_M}{\partial n_P}(P) - \frac{\partial u}{\partial n_P}(P)E_M(P)\}ds_P$$

satisfies

$f(M) = 1_\Omega u(M)$ where 1_Ω is the characteristic function of the domain Ω, since u is harmonic in Ω. Moreover, we have

$$f(M) = \int_{\Gamma_0 \cup FS \cup B} \{u(P)\frac{\partial E_M}{\partial n_P}(P) - \frac{\partial u}{\partial n_P}(P)E_M(P)\}ds_P ,$$

from which we conclude that f is indefinitely derivable through Σ ; thus, by analytic continuation, f and consequently u vanish.

Existence. $(P_{\nu,H})$ is given a variational formulation which is equivalent to the functional equation

$$(I + K)u = F \text{ in } H^1(\Omega),$$

where I is the identity operator and where V $H^1(\Omega)$

$$\cdot\ (F|v)_{H^1(\Omega)} = \int_{\Gamma_0} g\bar{v}ds,$$

$$\cdot\ (Ku|v)_{H^1(\Omega)} = -\int_\Omega u\bar{v}d\omega - \nu\int_{FS} u\bar{v}ds - i\theta_0\int_\Sigma u\bar{v}ds,$$

and $(.|.)_{H^1(\Omega)}$ represents the scalar product in $H^1(\Omega)$.

The operator K is continuous from $H^{1/2}(\Omega)$ to $H^1(\Omega)$, therefore K is compact on $H^1(\Omega)$. From uniqueness, which holds true, we know that -1 is not an eigenvalue of K ; using then the Fredholm alternative, we conclude that $(I + K)u = F$ has one and only one solution.

Note that the proof given here does not take the dimension of the space into account ; therefore it is applicable in the 2-D and 3-D cases.

II.3. The problem set in an unbounded domain

We turn back to $(\overset{\vee}{P}_\nu)$ and we restrict this study to the 3-D case ; adjustments in 2-D and to the finite depth case are easily deduced.

Uniqueness. (F. JOHN [2])

Working as in §II.2. with $\overset{\vee}{u}$ a solution of homogeneous $(\overset{\vee}{P}_\nu)$ and Ω_R the domain bounded by Γ_0, C_R and the portion of free surface FS_R in-between, we have

$$\int_{\Omega_R} |\vec{grad}\ \overset{\vee}{u}|^2\, d\omega - \nu\int_{FS_R} |\overset{\vee}{u}|^2\, ds = \int_{C_R} \frac{\partial \overset{\vee}{u}}{\partial R}\,\overline{\overset{\vee}{u}}\, ds :$$

and then $\quad 0 = -2\nu \mathrm{Im}\{\int \frac{\partial \overset{\vee}{u}}{\partial R}\,\overline{\overset{\vee}{u}}\, ds\}$

$$= \int_{C_R} |\frac{\partial \overset{\vee}{u}}{\partial R}|^2\, ds + \nu^2\int_{C_R} |\overset{\vee}{u}|^2\, ds - \int_{C_R} R|\frac{\partial \overset{\vee}{u}}{\partial R} - i\nu u|^2\, d\theta dz.$$

The radiation condition leads to

(i) $A(R) = \int_{\Omega_R} |\vec{grad}\ \overset{\vee}{u}|^2\, d\omega - \nu\int_{FS_R} |\overset{\vee}{u}|^2 ds$ vanishes with $\frac{1}{R}$.

(ii) $\int_{C_R} |u|^2\, ds \to 0$ as $R \to \infty$. Put then

$$U(r,\theta) = \int_{-\infty}^{0} e^{\nu z}\, u(r,\theta,z)dz \ ;\ v_n(z) = \int_0^{2\pi} U(r,\theta)\cos(n\theta)d\theta$$

$v_n, v_n(z)$ satisfies a Bessel equation and decreases faster than 1/r at infinity ; thus v_n vanishes identically, and so does U .

Through an integration by parts, we get

$|u(r,\theta,0)| \le \frac{1}{2\nu}\int_{-\infty}^{0} |u_z(r,\theta,z)|^2\, dz$, and thus

$$B(R) = \nu|u|^2_{L^2(FS_R)} \le A(R),$$

with increasing B(R) and vanishing A(R), due to (i).

We then conclude that $u \equiv 0$, provided that each vertical line intersects the hull in at most one point. □

Existence. The proof consists in the application of the so-called principle of limiting absorption (see WILCOX [6]). We denote $(\overset{\vee}{P}_{\nu+ic})$ an intermediate problem defined from $(\overset{\vee}{P}_\nu)$ with $\nu + ic$, $c > 0$ instead of ν in the free surface condition and with an imposed decrease at infinity instead of the radiation condition. More precisely $(\overset{\vee}{P}_{\nu+ic})$ has the variational formulation :

$$\int_{\overset{\vee}{\Omega}} (\vec{grad}\ \overset{\vee}{u}_c|\vec{grad}\ \overline{\overset{\vee}{v}})d\omega - (\nu+ic)\int_{\overset{\vee}{FS}} \overset{\vee}{u}_c\,\overline{\overset{\vee}{v}}ds = \int_{\Gamma_0} g\bar{v}ds,$$

which is coercitive in the Hilbert space

$$V(\overset{\vee}{\Omega}) = \{u \in D'(\overset{\vee}{\Omega})\,|\,(1+r^2)^{1/2}\, u \in L^2(\overset{\vee}{\Omega}),$$
$$(\vec{grad}\ u) \in \{L^2(\Omega)\}^3 \text{ and } u_{|\overset{\vee}{FS}} \in L^2(\overset{\vee}{FS})\}$$

equipped with the graph norm.

Moreover one can find the unique Green function $G_{\nu+ic}(M,P)$ of $(\overset{\vee}{P}_{\nu+ic})$; at each fixed point M with negative height y_M, $G_{\nu+ic}(M,P)$ satisfies the free surface condition and the decrease condition at infinity. Then we have, $\forall M \in \overset{\vee}{\Omega}$, the integral representation formula

$$\overset{\vee}{u}_\varepsilon(M) = \int_{\Gamma_0} \{\overset{\vee}{u}_\varepsilon(P)\frac{\partial G_{\nu+i\varepsilon}}{\partial n_P}(M,P) - g(P)\, G_{\nu+i\varepsilon}(M,P)\}ds_P \,. \qquad (R_{\nu+i\varepsilon})$$

Indeed, the Green function $G_\nu(M,P)$ of $(\overset{\vee}{P}_\nu)$ is obtained as the limit of $G_{\nu+i\varepsilon}(M,P)$ as ε tends to zero with positive values (see GUEVEL [7]) ; therefore G_ν satisfies the free-surface condition and the radiation condition. From $(R_{\nu+i\varepsilon})$ and the well-known a priori estimates for elliptic operators,

(i) the application which relates $\varepsilon > 0$ to $\overset{\vee}{u}_\varepsilon \in H^1_{loc}(\overset{\vee}{\Omega})$ has a continuous extension up to $\varepsilon = 0$,

(ii) $\overset{\vee}{u}_0$ is a solution of $(\overset{\vee}{P}_\nu)$ and, $\forall M \in \overset{\vee}{\Omega}$,

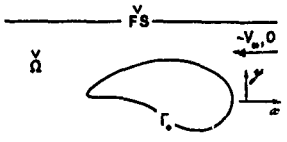
$$\overset{\vee}{u}_0(M) = \int_{\Gamma_0} \{\overset{\vee}{u}_0(P)\frac{\partial G_\nu}{\partial n_P}(M,P) - g(P)G_\nu(M,P)\}ds_P.$$

On account of the uniqueness for $(\overset{\vee}{P}_\nu)$ we put $\overset{\vee}{u}_0 = \overset{\vee}{u}$ and thus we get the existence.

III. The Neumann-Kelvin problem in 2-D

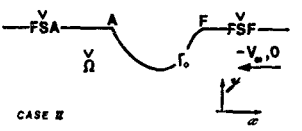
Let us say first the results in this chapter are incomplete ; *we mainly prove the Neumann-Kelvin problem for the velocity potential to be always ill-posed.* We also present a problem for the stream function amenable to a numerical solution.

The study concerns the velocity field past a fixed body which undergoes an incident uniform flow $(-V_\infty, 0)$ below a free surface. Two different situations may occur according as the body breaks through the free surface or not. Notations are shown on figures 4 and 5 for either case ; note that the points F and A indicate the "water line" fore and aft respectively in the case of a surface-piercing body.



CASE I

Fig.4 : The submerdged body - Case I



CASE II

Fig.5 : The surface-piercing body - Case II
$\overset{\vee}{FS} = \overset{\vee}{FSA} \cup \overset{\vee}{FSF}$

III.1. Statement of the problems

The problems for the velocity potential and the stream function are nonlinear in essence ; linearization can be considered only if the body is sunken enough or if it has a small draught (see FERNANDEZ [8]). We set the problems for the velocity potential $\overset{\vee}{\phi}$ and the stream function $\overset{\vee}{\psi}$ of the perturbation flow as they appear after the linearization of the free-surface condition.

Velocity potential. The lack of knowledge in the behavior at infinity of the solution leads us to the use of an artifice.

By Fourier transform, it can be shown that there exists one and only one Green's function $G^\phi_\nu(M,P)$ satisfying, for M fixed with a negative height and for the Froude number $\nu^{-1/2}$:

(i) $G^\phi_\nu(M,P)$ is an elementary solution of the Laplacian,

(ii) $\frac{\partial^2 G^\phi_\nu}{\partial x_P^2}(M,P) + \nu\frac{\partial G^\phi_\nu}{\partial y_P}(M,P) = 0, \forall P \in \overset{\vee}{FS}$,

(iii) $\vec{grad}_P\, G^\phi_\nu(M,P) \to 0$ as $x_P \to -\infty$.

Then we have

$$G^\phi_\nu(M,P) = \frac{1}{2\pi}\text{Log } MP.M'P - 2Y(x_P - x_M)Im\{e^{\nu Z}\} + \frac{1}{\pi}Re\{e^{\nu Z}\, E_1(\nu Z)\}$$

where $Z = y_P + y_M + i(x_P - x_M)$, M' is the image of M with respect to the linearized free surface, Y is the Heaviside function and E_1 the complex exponential integral (see [9]).

With the help of G^ϕ_ν for which only the condition (iii) has been imposed at infinity, we can now set a problem for ϕ ; we infer that $\overset{\vee}{\phi}$ is a solution of the Neumann-Kelvin problem if $\overset{\vee}{\phi} \in H^1_{loc}(\overset{\vee}{\Omega})$ and satisfies :

$$\Delta\overset{\vee}{\phi} = 0\ ,$$

$$\frac{\partial^2\overset{\vee}{\phi}}{\partial x^2} + \nu\frac{\partial\overset{\vee}{\phi}}{\partial y} = 0 \text{ on } F\overset{\vee}{S},$$

$$\frac{\partial\overset{\vee}{\phi}}{\partial n} = n_1 \text{ on } \Gamma_\phi, \qquad (\overset{\vee}{Q})$$

$n = (n_1, n_2)$ is the unit normal on Γ_ϕ,
and if $\overset{\vee}{M}$ is large enough

$$\overset{\vee}{\phi}(M) = \int_{\Gamma_\phi}\{\overset{\vee}{\phi}(P)\frac{\partial G_\nu^\phi}{\partial n_P}(M,P) - \frac{\partial\overset{\vee}{\phi}}{\partial n_P}(P)G_\nu^\phi(M,P)\}ds_P$$

$$+ \frac{\varepsilon}{\nu}\{\phi(P)\frac{\partial G_\nu^\phi}{\partial x_P}(M,P) - \frac{\partial\phi}{\partial x_P}(P)G_\nu^\phi(M,P)\}_{P=A}^{P=F}$$

with $\varepsilon = 0$ in case I and $\varepsilon = 1$ in case II.

Stream function. Here, the problems are different in each case ; recalling that case I refers to fig.4 and case II to fig.5, we denote $\overset{\vee}{\psi}_I$ and $\overset{\vee}{\psi}_{II}$ the corresponding stream functions.

Case I :

Find $\overset{\vee}{\psi}_I \in H^1_{loc}(\overset{\vee}{\Omega})$, such that

$$\Delta\overset{\vee}{\psi}_I = 0 \text{ in } \overset{\vee}{\Omega},$$

$$\frac{\partial\overset{\vee}{\psi}_I}{\partial n} = \nu\overset{\vee}{\psi}_I \text{ on } F\overset{\vee}{S},$$

$$\overset{\vee}{\psi}_I = C + y \text{ on } \Gamma_\phi, \text{ and}$$

$$\int_{-\infty}^{\infty}|\frac{\partial\overset{\vee}{\psi}_I}{\partial x}(x,y)|^2dy \text{ is bounded and vanishes when } x \to +\infty. \qquad (\overset{\vee}{R}_I^C)$$

Case II :

Find $\overset{\vee}{\psi}_{II} \in H^1_{loc}(\overset{\vee}{\Omega})$, such that

$$\Delta\overset{\vee}{\psi}_{II} = 0 \text{ in } \overset{\vee}{\Omega},$$

$$\frac{\partial\overset{\vee}{\psi}_{II}}{\partial n} = \nu\overset{\vee}{\psi}_{II} \text{ on } F\overset{\vee}{S}F,$$

$$\frac{\partial\overset{\vee}{\psi}_{II}}{\partial n} = \nu\overset{\vee}{\psi}_{II} + K \text{ on } F\overset{\vee}{S}A,$$

$$\overset{\vee}{\psi}_{II} = C + y \text{ on } \Gamma_\phi, \text{and}$$

$$\int_{-\infty}^{\infty}|\frac{\partial\overset{\vee}{\psi}_{II}}{\partial x}(x,y)|^2dy \text{ is bounded and vanishes as } x \to \infty. \qquad (\overset{\vee}{R}_{II}^{C,K})$$

Note that $(\overset{\vee}{R}_I^C)$ depends on an arbitrary constant which does not appear in $(\overset{\vee}{Q})$; a similar situation is known in aerodynamics. The value of C is related to the circulation of the velocity along Γ_ϕ. As $\overset{\vee}{\psi}$ in $(\overset{\vee}{Q})$ is supposed defined in $\overset{\vee}{\Omega}$ without cut, this circulation vanishes necessarily. In $(\overset{\vee}{R}_I^C)$ for $\overset{\vee}{\psi}$ this circulation cannot be evaluated but by an additional condition of regularity at the trailing edge if it exists ; this is the so-called Kutta-Joukovsky condition.

Case II is an awkward predicament ! the meanings of both arbitrary constants involved in $(\overset{\vee}{R}_{II}^{C,K})$ are not so evident. We interpret them on account of a study [8] of the nonlinear problem by matched asymptotic expansions valid if the draught-to-length ratio is small.

At point A, the stern, the phenomenon is similar to the trailing edge's for a wing section ; the asymptotic study suggests an adequate regularity of the velocity at A. Now if we refer to KONDRAT'EV [10], the solutions of $(\overset{\vee}{R}_\nu^{C,K})$ have, in the vicinity of A, an expansion on a basis of functions the first of which only generates an infinite velocity at A. Therefore we can infer reasonably, as for the K-J condition, the condition of continuous velocity at A is tantamount to a scalar equation.

At point F, the bow, the asymptotic expansion shows a jet which strength q is equal to the product of the draught by the velocity of the incident flow (in dimensionalized form). Note that the linearized free surface is a streamline far upstream and $\overset{\vee}{\psi}$ is almost zero along $F\overset{\vee}{S}F$ but near F ; we conclude that $C = q$.

III.2. Integral representation for the stream function

With the same notations as for G_ν^ϕ, the unique Green's function of $(\overset{\vee}{R}_I^C)$ satisfying the free surface condition and with vanishing first derivatives far downstream is given by

$$G_\nu^\psi(M,P) = \frac{1}{2\pi}\text{Log}\frac{MP}{M'P} + 2Y(x_P - x_M)Im\{e^{\nu Z}\}$$

$$- \frac{1}{\pi}Re\{e^{\nu Z}E_1(\nu Z)\}.$$

Then every solution $\overset{\vee}{\psi}_I^C$ of $(\overset{\vee}{R}_I^C)$ satisfies the integral representation formula

$$\overset{\vee}{\psi}_I^C(M) = \int_{\Gamma_\phi}\{\overset{\vee}{\psi}_I^C(P)\frac{\partial}{\partial n_P}G_\nu^\psi(M,P)$$

$$- \frac{\partial}{\partial n_P}\overset{\vee}{\psi}_I^C(P)\ G_\nu^\psi(M,P)\}ds_P. \qquad (1)$$

Moreover every solution $\overset{\nu}{\psi}{}^{C,K}_{II}$ of $(\overset{\nu}{R}{}^{C,K}_{II})$ can be written as

$$\overset{\nu}{\psi}{}^{C,K}_{II}(M) = \int_{\Gamma_0} \{\overset{\nu}{\psi}{}^{C,K}_{II}(P)\ \frac{\partial}{\partial n_P}\ G^{\Psi}_{\nu}(M,P) - \frac{\partial}{\partial n_P}\ \overset{\nu}{\psi}{}^{C,K}_{II}(P) G^{\Psi}_{\nu}(M,P)\} ds_P \qquad (2)$$

$$+ K\, L_1(M),$$

where

$$L_1(M) = \frac{1}{2\nu} - \frac{2}{\nu} y(x_A - x_M)[1 - e^{\nu y_M} \cos\nu(x_A - x_M)]$$

$$+ \frac{1}{\nu\pi}\, Im\{\mathrm{Log}\ \nu Z' + e^{\nu Z'} E_1(\nu Z')\}\ ;$$

$$Z' = y_M - i(x_A - x_M).$$

We can deduce that the study of $(\overset{\nu}{R}{}^{C,0}_{II})$ alone is needed ; indeed it is equivalent to say, for a given f on Γ_0, that

. $\overset{\nu}{\psi}$ is a solution of $(\overset{\nu}{R}{}^{C,0}_{II})$ with

. $\overset{\nu}{\psi}|_{\Gamma_0} = f - KL_1|_{\Gamma_0}$, or to say that

$u = \overset{\nu}{\psi} + KL_1$ satisfies $(\overset{\nu}{R}{}^{C,K}_{II})$ with $u|_{\Gamma_0} = f$.

III.3. Relation between velocity potential and stream function

From the theory of holomorphic functions we know that if $\overset{\nu}{\Omega}$ is simply connected (fig.5) to every $\overset{\nu}{\psi}$ harmonic it corresponds one and only one $\overset{\nu}{\phi}$ up to an additive constant such that $\overset{\nu}{\phi} + i\overset{\nu}{\psi}$ is holomorphic. This applies in the second case and if $\overset{\nu}{\psi}$ satisfies $(\overset{\nu}{R}{}^{C,K}_{II})$, the corresponding $\overset{\nu}{\phi}$ is a solution of $(\overset{\nu}{Q})$; moreover to two different pairs (C_1, K_1) and (C_2, K_2) there correspond two solutions $\overset{\nu}{\phi}_1$ and $\overset{\nu}{\phi}_2$ of the same problem $(\overset{\nu}{Q})$, the difference of which is not a constant !

In the first case, $\overset{\nu}{\Omega}$ is not simply connected and, to ensure that $\overset{\nu}{\phi}$ exists such that $\overset{\nu}{\phi} + i\overset{\nu}{\psi}$ is holomorphic, it is necessary and sufficient that the flux of $\overset{\nu}{\psi}$ through Γ_0, namely the circulation of velocity, vanishes. This condition assigns the value of the constant C such that a solution $\overset{\nu}{\psi}$ of $(\overset{\nu}{R}{}^{C}_{I})$ is associated to a solution $\overset{\nu}{\phi}$ of $(\overset{\nu}{Q})$.

III.4. Relation with diffraction problems

After the fashion of MEI, CHEN [11], we consider an auxiliary problem (D) ; let us call it a diffraction problem :

$$\left.\begin{array}{l} \text{Find } \xi_D \in H^1_{loc}(\overset{\nu}{\Omega}) \text{ such that} \\ \Delta\xi_D = 0 \text{ in } \overset{\nu}{\Omega}\ , \\ \dfrac{\partial \xi_D}{\partial n} - \nu\xi_D = 0 \text{ on } \overset{\nu}{FS}, \\ \xi_D|_{\Gamma_0} = -\xi_w|_{\Gamma_0}\ , \text{ where } \xi_w(M) = e^{\nu(y_M + ix_M)}, \\ \displaystyle\int_{-\infty}^{+\infty} \left|\frac{\partial \xi_D}{\partial x}(x,y) \mp i\nu\xi_D(x,y)\right|^2 dy \to 0 \text{ as } x \to \pm\infty \end{array}\right\} (D)$$

Such a problem differs by the Dirichlet condition on Γ_0 ; nevertheless it is easily shown that (D) is well-posed and that its solution satisfies

$$\xi_D(M) = \int_{\Gamma_0} \{\xi_D(P) \frac{\partial G_\nu}{\partial n_P}(M,P) - \frac{\partial \xi_D}{\partial n_P}(P) G_\nu(M,P)\} ds_P, \qquad (3)$$

where G_ν is the classical Green function for the 2D sea-keeping problem .

$$G_\nu(M,P) = \frac{1}{2\pi}\, \mathrm{Log}\, \frac{MP}{M'P} + \mathrm{sgn}(x_P - x_M)\, Im\{e^{\nu Z}\}$$

$$- \frac{1}{\pi}\, Re\, \{e^{\nu Z} E_1(\nu Z)\} - iRe\{e^{\nu Z}\}.$$

Subsequent to the essential relation

$$G_\nu(M,P) = G^{\Psi}_{\nu}(M,P) - i\overline{\xi}_w(P)\xi_w(M), \qquad (4)$$

and to (3), the total diffraction potential $\xi_T = \xi_w + \xi_D$ has the decomposition .

$\xi_T = \Xi^{\nu}_T \xi_w + \xi_{NK}$ where Ξ^{ν}_T is a complex constant and ξ_{NK} satisfies the conditions at infinity of $(\overset{\nu}{R}{}^{C}_{I})$ or $(\overset{\nu}{R}{}^{C,0}_{II})$.

III.5. Uniqueness for the stream function problem

Let us first suppose $\Xi^{\nu}_T = 0$, then $\xi_T = \xi_{NK}$ and as G^{Ψ}_{ν} is real, $Re\{\xi_T\}$ and $Im\{\xi_T\}$ both are solutions of homogeneous $(\overset{\nu}{R}{}^{0}_{I})$ or $(\overset{\nu}{R}{}^{0,0}_{II})$ However ξ_T cannot vanish identically(ξ_D and ξ_w would be opposite and ξ_w does not satisfy the radiation condition). Then we have found a non-vanis-

hing solution of homogeneous (R_I^0) or $(R_{II}^{0,0})$.

Conversely , if ζ is a solution of the homogeneous problem (R_I^0) or $(R_{II}^{0,0})$, using (4) in (1) or (2) we have $\zeta = Z\xi_\omega + \zeta_D$ where Z is a complex constant and ζ_D satisfies the radiation condition. Clearly then,
$\eta_0 = \zeta - Z\xi_T = \zeta_D - Z\xi_D$ vanishes as it is the unique solution of

$$\left.\begin{array}{l} \Delta\eta = 0 \text{ in } \overset{\vee}{\Omega}, \\ \eta_{|\Gamma_0} = 0, \\ \left(\frac{\partial\eta}{\partial n} - \nu\eta\right)_{|F_S^\vee} = 0, \\ \eta \text{ satisfies the radiation condition.} \end{array}\right\} (S)$$

Then we have $\zeta = Z\xi_T$ and $Z\,\Xi_T^\nu\xi_\omega = \zeta - Z\xi_{NK}$. Now, contrary of ζ and ξ_{NK}, the first derivatives of ξ_ω do not vanish far upstream ; it follows that $Z\,\Xi_T^\nu = 0$. Therefore we have shown that Z and of course ζ vanish *since* $\Xi_T^\nu \neq 0$; uniqueness for $(\overset{\vee}{R}_I^0)$ and $(\overset{\vee}{R}_{II}^{0,0})$ follows.

III.6. Existence for the stream function problem

Let η be a solution of (S) with the Dirichlet condition $\eta_{|\Gamma_0} = C + y_{|\Gamma_0}$; as usual now using (4), we have $\eta = H\xi_\omega + \eta_{NK}$. Therefore *if we suppose* $\Xi_T^\nu \neq 0$, it stands to reason that the function $\psi = Re\{\eta - \frac{H}{\Xi_T^\nu}\,\xi_T\} = Re\{\eta_{NK} - \frac{H}{\Xi_T^\nu}\,\xi_{NK}\}$ is a solution of $(\overset{\vee}{R}_I^C)$ or $(\overset{\vee}{R}_{II}^{C,0})$. Existence follows then for $(\overset{\vee}{R}_{II}^{C,K})$ $\forall(C,K)$ as we pointed out before.

III.7. Comments on the case of a surface-piercing body

If $\Xi_T^\nu \neq 0$ each problem $(\overset{\vee}{R}_{II}^{C,K})$ has a solution and then $(\overset{\vee}{R})$ has several solutions !

If, on the contrary $\Xi_T^\nu = 0$ then neither of the problems $(\overset{\vee}{R}_I^{C,K})$ has a solution nor $(\overset{\vee}{R})$; or one of the $(\overset{\vee}{R}_{II}^{C,K})$ has a solution which is not unique,and the same situation occurs for $(\overset{\vee}{R})$.

In conclusion for the case of a surface-piercing body, the problem $(\overset{\vee}{R})$ is always ill-posed.

On the other hand one can infer that the problem $(R_{II}^{q,K})$ with an additional condition of regularity at the stern is well-posed and its numerical solution could be tried.

IV. Some solutions with finite elements

IV.1. The radiation condition at finite distance

The problem $(P_{\nu,H})$(see II.2.) is set in the bounded domain shown on fig.3 ; its discretization by a finite element method does not show up any particular difficulty. Indeed, as we noticed before, the operator we face to approximate is composed of an automorphism and a compact operator on $H^1(\Omega)$; using then a theorem from AUBIN [12] it follows that the numerical solution will converge towards the exact solution as for a standard coercitive problem.

More precisely if the solution u of $(P_{\nu,H})$ belongs to $H^{k+1}(\Omega)$ and if we use finite elements of order k, the norm of the discrepancy $\|u-u_h\|_{H^1(\Omega)}$ between u and the approximate solution u_h, tends to zero as h^k where h is the mesh size. Note that missing coercitivity, it is not ensured that the approximate problem is well-posed but if h is small enough. Moreover we point out that the bilinear form associated with $(P_{\nu,H})$ in its variational formulation is symmetric but it is not self-adjoint.

IV.2. The localized finite element method

This method applies to $(\overset{\vee}{P}_{\nu,H})$ but it cannot be used in the case of an infinite depth. The description of the method we give refers to a paper by BAI, YEUNG [13] and the proofs are partly inspired with a paper by BARDOS and al.[14]. A first attempt in the mathematical analysis of the method can be found in ARANHA [15] and some of the ideas developed here have been noticed in MASMOUDI [16].

Let us restrict the description to the 2-D case. The unbounded domain $\overset{\vee}{\Omega}$ is divided in three parts Ω_a, Ω_1 and Ω_f which are separated by two vertical lines Σ_a and Σ_f ; in Ω_a and Ω_f the bottoms B_a and B_f are supposed horizontal $y = -H$.
Each normal is outer to the domain under consideration.

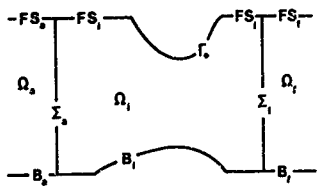


Fig.6 : The three domains in the localized finite element method.

Series expansions at infinity. The bilinear form

$$C(u,v) = \int_{\Sigma_a} \frac{du}{dy}\frac{dv}{dy}\,dy - \nu uv|_{FS\cap\Sigma_a} + \lambda_0 \int_{\Sigma_a} uv\,dy$$

and LIONS's lemma [17] lead to :

$\forall \varepsilon > 0, \exists\, C_\varepsilon > 0$ such that,

$$\|u\|^2_{H^{1/2}(\Sigma_a)} \le \varepsilon \|u\|^2_{H^1(\Sigma_a)} + C_\varepsilon \|u\|^2_{L^2(\Sigma_a)}.$$

Therefore if λ_0 is large enough, as we suppose now, C(u,v) is coercitive. Let f be given in $L^2(\Sigma_a)$ and $u = G_{\lambda_0} f$ be the unique solution of

$$C(u,v) = (f|v)_{L^2(\Sigma_a)}, \quad \forall v \in H^1(\Sigma_a).$$

The operator G_{λ_0} is continuous from $L^2(\Sigma_a)$ to $H^1(\Sigma_a)$ and then G_{λ_0} is compact on $L^2(\Sigma_a)$ and also on $H^1(\Sigma_a)$. Moreover G_{λ_0} is self-adjoint in $L^2(\Sigma_a)$; as a matter of fact let f and h be given in $H^1(\Sigma_a)$, we have

$$(f|G_{\lambda_0} h)_{L^2(\Sigma_a)} = C(G_{\lambda_0} f, G_{\lambda_0} h) = (G_{\lambda_0} f|h)_{L^2(\Sigma_a)}$$

and the symmetry proceeds on account of the density of $H^1(\Sigma_a)$ in $L^2(\Sigma_a)$.

From the spectral theory of self-adjoint operators in Hilbert spaces, we know

(i) G_{λ_0} has a numerable set of eigenvalues (μ_i) which accumulate at the origin,

(ii) the associated eigenfunctions f_i can be arranged to form a basis of $L^2(\Sigma_a)$; these functions are orthogonal

Moreover we have $G_{\lambda_0} f_i = \mu_i f_i$ or $\mu_i C(f_i,v) = (f_i|v)_{L^2(\Sigma_a)}$ $\forall v \in H^1(\Sigma_a)$ which means that f_i satisfies the Eigen-Value Problem

$$\left.\begin{aligned} &\frac{d^2 f_i}{dy^2} = \theta_i f_i, \text{with } \theta_i = \lambda_0 - \frac{1}{\mu_i}, \\ &\frac{df_i}{dy} = \nu f_i \text{ on } FS\cap\Sigma_a, \\ &\frac{df_i}{dy} = 0 \text{ on the bottom.} \end{aligned}\right\} \text{(EVP)}$$

The solutions of (EVP) are easily obtained and well known ; let us recall that

- θ_0 is the positive root of $th(H\theta_0) = \frac{\nu}{\theta_0}$ and $f_0 = ch\,\theta_0(y+H)$,
- $(\theta_i)_{i\ge 1}$ are the positive roots of $tgH\theta_i = -\frac{\nu}{\theta_i}$ and $f_i = \cos\theta_i(y+H)$.

If we point out that C(u,v) is a scalar product in $H^1(\Sigma_a)$ and G_{λ_0}, considered as an operator on $H^1(\Sigma_a)$, is self-adjoint with this scalar product, we can refine the results (i) and (ii). As a matter of fact the same lemma applies and the eigenfunctions form an orthogonal basis of $H^1(\Sigma_a)$ for the new scalar product C(u,v) , but, clearly these eigenfunctions are the very solutions f_i of (EVP) which then form a dense set in $H^{1/2}(\Sigma_a)$ and, from a density argument, in $H^{-1/2}(\Sigma_a)$.

Let us study now the operator $S_a : f \to \frac{\partial u_a}{\partial n}|_{\Sigma_a}$ where u_a is the solution of the following problem :

$$\left.\begin{aligned} &\Delta u_a = 0 \text{ in } \Omega_a, \\ &u_a|_{\Sigma_a} = f \text{ given in } H^{1/2}(\Sigma_a), \\ &\frac{\partial u_a}{\partial n} = \nu u_a \text{ on } FS_a, \\ &\frac{\partial u_a}{\partial n} = 0 \text{ on } B_a, \text{ and} \end{aligned}\right\} (D_a)$$

the radiation condition of $(P^{\nu}_{\nu,H})$. (see § II.1.)

Using the decomposition of f on the basis, we have $f = \lim_{N\to\infty} \sum_{i=0}^{N} C_i f_i$ where the limit is considered in the norm of $H^{1/2}(\Sigma_a)$; this leads to the solution of (D_a) with separate variables and to the relations

$$S_a f_\phi(y) = -i\,\theta_\phi f_\phi(y) \text{ and } S_a f_i(y) = \theta_i f_i(y)\ , i\geq 1$$

An explicit form of S_a follows which is written

$$S_a(\sum_0^\infty C_i f_i) = -i\,\theta_\phi C_\phi f_\phi + \sum_1^\infty \theta_i C_i f_i.$$

The same operation can of course be done in Ω_f ; therefore we define an operator S_f on $H^{1/2}(\Sigma_f)$ and, on account of the various changes in sign, we have

$$S_f(\sum_0^\infty C_i f_i) = -i\,\theta_\phi C_\phi f_\phi + \sum_1^\infty \theta_i C_i f_i.$$

The continuous problem

The variational formulation given by BAI [13] is equivalent to the following

Find $(u,\phi_a,\phi_f)\in V = H^1(\Omega_i)\times H^{1/2}(\Sigma_a)\times H^{1/2}(\Sigma_f)$, such that, $\forall (v,\psi_a,\psi_f) \in V$, we have

$$\left.\begin{aligned}
&\int_{\Omega_i} (\vec{\mathrm{grad}}\, u|\vec{\mathrm{grad}}\, v)d\omega - \nu\int_{FS_i} u\overline{v}dx + \int_{\Sigma_a} S_a\phi_a\overline{v}dy \\
&\quad + \int_{\Sigma_f} S_f\phi_f\overline{v}dy = \int_{\Gamma_0} g\overline{v}ds, \text{ and} \\
&-\frac{1}{2}\{\int_{\Sigma_a}(\phi_a S_a\overline{\psi}_a + \overline{\psi}_a S_a\phi_a)dy \\
&\quad + \int_{\Sigma_f}(\phi_f S_f\overline{\psi}_f + \overline{\psi}_f S_f\phi_f)dy\} \\
&\quad + \int_{\Sigma_a} uS_a\overline{\psi}_a dy + \int_{\Sigma_f} uS_f\overline{\psi}_f dy = 0.
\end{aligned}\right\} \quad \text{(LFE)}$$

Note that the second Green's formula applied in Ω_a and Ω_f shows that the last equation can be written as

$$\int_{\Sigma_a}(u-\phi_a)S_a\overline{\psi}_a dy = 0, \text{ and } \int_{\Sigma_f}(u-\phi_f)S_f\overline{\psi}_f dy = 0.$$

Therefore if $\overset{\vee}{u}$ is the solution of $(\overset{\vee}{P}_{\nu,H})$ $(\overset{\vee}{u}|_{\Omega_i}, \overset{\vee}{u}|_{\Sigma_a}, \overset{\vee}{u}|_{\Sigma_f})$ is a solution of (LFE) ; the problem of existence for (LFE) is thus in order.

On the other hand if (u,ϕ_a,ϕ_f) is a solution of (LFE), we have, using the first equation $\frac{\partial u}{\partial n}|_{\Sigma_a} = -S_a\phi_a$ and $\frac{\partial u}{\partial n}|_{\Sigma_f} = -S_f\phi_f$, and using the second equation, $u|_{\Sigma_a} = \phi_a$ and $u|_{\Sigma_f} = \phi_f$; hence u has an analytic continuation through Σ_a and Σ_f which satisfies $(\overset{\vee}{P}_{\nu,H})$, and from the uniqueness of the solution of $(\overset{\vee}{P}_{\nu,H})$ namely $\overset{\vee}{u}$, we get uniqueness for (LFE) and

$$u = \overset{\vee}{u}|_{\Omega_i}\ ,\ \phi_a = \overset{\vee}{u}|_{\Sigma_a}\ ,\ \phi_f = \overset{\vee}{u}|_{\Sigma_f}.$$

Projections. We denote Q_a^i the projection on (f_i) in the sense of $L^2(\Sigma_a)$ and P_a^N the projection on the space E_a^N generated by the N+1 first functions f_i in $L^2(\Sigma_a)$; we define similarly Q_f^i, P_f^N and E_f^N.

The discretization of (LFE) will be accomplished in two steps. We first give an approximation of S_a and S_f by finite sums instead of series ; this step is called semi-discretization. In the second step we use standard finite elements in Ω_i.

Semi-discretization. In the approximate space $V^N = H^1(\Omega_i) \times E_a^N \times E_f^N$ let us consider the problem

Find $(u^N, \phi_a^N, \phi_f^N) \in V^N$ such that $\forall (v, \psi_a^N, \psi_f^N) \in V^N$,

$$\left.\begin{aligned}
&\int_{\Omega_i} (\vec{\mathrm{grad}}\, u^N|\vec{\mathrm{grad}}\, v)d\omega - \nu\int_{FS_i} u^N\overline{v}dx + \int_{\Sigma_a} S_a\phi_a^N\overline{v}dy \\
&\quad + \int_{\Sigma_f} S_f\phi_f^N\overline{v}dy = \int_{\Gamma_0} g\overline{v}ds, \\
&-\frac{1}{2}\int_{\Sigma_a}(\phi_a^N S_a\overline{\psi}_a^N + \overline{\psi}_a^N S_a\phi_a^N)dy + \int_{\Sigma_a} u^N S_a\overline{\psi}_a^N dy = 0\ , \\
&\text{and} \\
&-\frac{1}{2}\int_{\Sigma_f}(\phi_f^N S_f\overline{\psi}_f^N + \overline{\psi}_f^N S_f\phi_f^N)dy + \int_{\Sigma_f} u^N S_f\overline{\psi}_f^N dy = 0.
\end{aligned}\right\} \quad \text{(LFE}^N\text{)}$$

Obviously, $S_a\psi_a^N$ generates E_a^N as ϕ_a^N does likewise ; therefore $\phi_a^N = P_a^N(u^N)$ and similarly $\phi_f^N = P_f^N(u^N)$. Thus, if $(u^N, \phi_a^N, \phi_f^N)$ satisfies (LFE^N), u^N is a solution of

Find $u^N \in H^1(\Omega_i)$ such that, $\forall v \in H^1(\Omega_i)$,

$$\left.\begin{aligned}&\int_{\Omega_i}(\vec{grad}\ u^N|\vec{grad}\ \overline{v})d\omega - \nu\int_{FS_i} u^N\overline{v}dx \\ &+ \int_{\Sigma_a} S_a P_a^N u^N \overline{v}dy + \int_{\Sigma_f} S_f P_f^N u^N \overline{v}dy = \int_{\Gamma_\phi} g\overline{v}ds\end{aligned}\right\} \text{(LFE'}^N\text{)}$$

In the same way we observe if (u, ϕ_a, ϕ_f) satisfies (LFE), u is a solution of

$$\left.\begin{aligned}&\text{Find } u \in H^1(\Omega_i) \text{ such that, } \forall v \in H^1(\Omega_i), \\ &\int_{\Omega_i}(\vec{grad}\ u|\vec{grad}\ \overline{v})d\omega - \nu\int_{FS_i} u\overline{v}dx + \int_{\Sigma_a} S_a u\overline{v}dy \\ &+ \int_{\Sigma_f} S_f u\overline{v}dy = \int_{\Gamma_\phi} g\overline{v}ds.\end{aligned}\right\} \text{(LFE')}$$

But indeed we can show that (LFE') is equivalent to (LFE) ; this is obtained by proving the uniqueness for (LFE'). Suppose u is a solution of homogeneous (LFE') and take $v = u$, then

$$Im\{\int_{\Sigma_a}\overline{u}S_a u dy + \int_{\Sigma_f}\overline{u}S_f u dy\} = 0 ;$$

the two terms being of opposite sign, let, say

$$Im\{\int_{\Sigma_a}\overline{u}S_a u dy\} \le 0 .$$

Using then problem (D_a) with $f = u_{|\Sigma_a}$ and the same analysis as for the proof of uniqueness for $(P_{\nu}^{\vee})$ we see that $\int_0^{\infty} |u_a(x,y)|^2 dy$ vanishes as $x \to -\infty$ and u_a vanishes in Ω_a ; then $u_{|\Sigma_a} = u_a|_{\Sigma_a} = 0$ and $\frac{\partial u}{\partial n}|_{\Sigma_a} = -S_a u_a = -\frac{\partial u_a}{\partial n}|_{\Sigma_a} = 0$, which proves with the same argument of analytic continuation as for uniqueness of $(P_{\nu,H})$ that u vanishes in Ω_i.

Henceforth we are interested in (LFE'^{N}) and (LFE') which are easier to handle from a theoretical point of view. However BAI's numerical approximation is done from the formulation (LFE^N) which avoids an explicit evaluation of the projections $P_a^N u^N$ and $P_f^N u^N$; anyway the solution of (LFE'^{N}) may not be more difficult.

Convergence of the semi-discretization. The variational formulation (LFE') is equivalent to the functional equation set in $H^1(\Omega_i)$:

$$(I + B + K)u = F \qquad (5)$$

where

. $(Ku|v)_{H^1(\Omega_i)} = -\int_{\Omega}\vec{uv}d\omega - \nu\int_{FS_i}\vec{uv}dx$, and

. $(Bu|v)_{H^1(\Omega_i)} = \int_{\Sigma_a} S_a u.\overline{v}dy + \int_{\Sigma_f} S_f u.\overline{v}dy$

As K is compact, if we prove B to be positive we shall get the same situation (coercitive + compact) as for the existence of $(P_{\nu,H})$ in §II.2.

Let show that $Re\{(Bu|u)_{H^1(\Omega_i)}\} \ge 0$. As u belongs to $H^1(\Omega_i)$, it has traces in $H^{1/2}$ and we have the series expansions :

$$u_{|\Sigma_a} = \sum_0^{\infty} c_a^i f_i \text{ and } u_{|\Sigma_f} = \sum_0^{\infty} c_f^i f_i .$$

Then, by orthogonality of the (f_i),

$$(Bu|u) = -i\theta_0(\|Q_a^0 u\|^2_{L^2(\Sigma_a)} + \|Q_f^0 u\|^2_{L^2(\Sigma_f)}$$

$$+ \sum_i^{\infty}\theta_i(\|Q_a^i u\|^2_{L^2(\Sigma_a)} + \|Q_f^i u\|^2_{L^2(\Sigma_f)})$$

which real part is positive since all the θ_i are positive.

In the same way, (LFE'^{N}) is equivalent to

$$(I + B^N + K)u^N = F \text{ in } H^1(\Omega_i), \qquad (6)$$

where

$$(B^N u|v)_{H^1(\Omega_i)} = \int_{\Sigma_a} S_a P_a^N u.\overline{v}dy + \int_{\Sigma_f} S_f P_f^N u.\overline{v}dy.$$

Following the previous argument, B^N is positive and $I + B^N$ is coercitive.

Using again the result of AUBIN [12] one can see that $(A + B^N + K)$ is an automorphism if N is large enough , in other words, (LFE'^{N}) is well-posed and

$$\|u-u^N\|_{H^1(\Omega_i)} \le C \sup_{w \in H^1(\Omega_i)} \frac{|((B-B^N)u|w)_{H^1(\Omega_i)}|}{\|w\|_{H^1(\Omega_i)}}$$

An estimate of the numerator in the right-hand-side is given as follows :

$$|((B-B^N)u|w)| \le K(\|S_a\|.\|u-P_a^N u\|_{H^{-1/2}(\Sigma_a)}$$

$$+ \|S_f\|.\|u-P_f^N u\|_{H^{-1/2}(\Sigma_f)})\|w\|_{H^1(\Omega_i)} .$$

Then, from the reading of BARDOS and al.[14] , the term $|u-P_a^N u|$ (or $|u-P_f^N u|$)is given an estimate since $u|_{\Sigma_a}$ belongs to $H^{1/2}(\Sigma_a)$ which holds true in view of the regularity of the solution of $(P^N_{\nu,H})$; we have

$$\|u-P_a^N u\|_{H^{-1/2}(\Sigma_a)} \le \frac{|u|_{H^{1/2}(\Sigma_a)}}{N^{2-\varepsilon}} , \forall \varepsilon > 0 .$$

Using the same result on the side Σ_f we conclude that the solution of the semi-discretized problem converges in $H^1(\Omega_i)$ towards the solution of the continuous problem almost as $\frac{1}{N^2}$.

More about the semi-discretized problem. In some cases one can prove that the semi-discretized problem is well posed for each value of N, and not only when N is large enough ; this is an interesting property of the localized finite element method.

Assume Γ_0 is such that two vertical lines σ_a and σ_f can be drawn from A and F respectively without intersecting Γ_0 (see figure 7), and denote ω_a the domain the vertical boundaries of which are σ_a and Σ_a, the bottom being flat inside ω_a. Similarly we define the domain ω_f, and we put $\Omega' = \Omega_i \setminus (\omega_a \cup \omega_f)$.

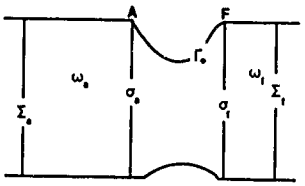


Fig.7 : A special case.

Our proof is based on the uniqueness of problem (LFE'^N), the existence being an obvious consequence. Just as for (LFE'), if u^N is a solution of homogeneous (LFE'^N), $Im(B^N u^N|u^N)_{H^1(\Omega_i)} = 0$, whence we infer

$$\|Q_a^0 u^N\|^2_{L^2(\Sigma_a)} + \|Q_f^0 u^N\|^2_{L^2(\Sigma_f)} = 0$$

Let us now consider the pure Neumann problem for the Laplacian operator in ω_a and ω_f ; the associated eigenfunctions involve separated variables and generate respectively $H^1(\omega_a)$ and $H^1(\omega_f)$. Indeed it is an easy matter to show that all functions in $H^1(\omega_a)$ and $H^1(\omega_f)$ can be written as

$\sum_{n=0}^{\infty} A_n^a(x)f_n(y)$, and $\sum_{n=0}^{\infty} A_n^f(x)f_n(y)$ respectively.

In other respects, by GREEN's formula applied to u^N and $\overline{\varepsilon}_0(x,y) = e^{i\theta_0 x}f_0(y)$ in ω_f, we have

$$\int_{\Sigma_f} \overline{\varepsilon}_0(\frac{\partial u^N}{\partial n} - i\theta_0 u^N)ds + \int_{\sigma_f} \overline{\varepsilon}_0(\frac{\partial u^n}{\partial n} + i\theta_0 u^N)ds = 0.$$

The first integral vanishes, for $\|Q_f^0 u^N\|_{L^2(\Sigma_f)}=0$ and, as $\frac{\partial u^N}{\partial n}|_{\Sigma_f} = S_f P_f^N u^N$, $\|Q_f^0 \frac{\partial u^N}{\partial n}\|_{L^2(\Sigma_f)} = 0$; thus $\frac{\partial u^N}{\partial n} + i\theta_0 u^N$ is orthogonal to f_0 in $L^2(\Sigma_f)$. Now on, replacing $u^N|_{\omega_f}$ by $\sum_{n=0}^{\infty} A_n^f(x)f_n(y)$, we are led to

$$-\frac{dA_0^f}{dx}(x) + i\theta_0 A_0^f(x) = 0 \text{ ; moreover}$$

$\|Q_f^0 u^N\|_{L^2(\Sigma_f)} = 0$ implies that $A_0^f|_{\Sigma_f} = 0$, and thus $A_0^f(x)$ vanishes.

Clearly then, $u^N|_{\omega_f} = \sum_{n=1}^{\infty} A_n^f(x)f_n(y)$, and similarly $u^N|_{\omega_a} = \sum_{n=1}^{\infty} A_n^a(x)f_n(y)$.

As B^N is positive, from the equality

$$\int_{\Omega_i} |\vec{grad}\, u^N|^2 d\omega - \nu\int_{FS_i} |u^N|^2 ds + (B^N u^N|u^N)_{H^1(\Omega_i)} = 0,$$

we deduce that

$$\int_{\Omega_i} |\vec{grad}\, u^N|^2 d\omega - \nu\int_{FS_i} |u^N|^2 ds \le 0. \text{ Finally, taking}$$

for $u^N|_{\omega_a}$ and $u^N|_{\omega_f}$ their series expansions,

we get $\int_{\Omega'} |\overrightarrow{grad}\, u^N|^2 d\omega + \int_{\omega_a \cup \omega_f} |\frac{\partial u^N}{\partial x}|^2 d\omega \leq 0$;

from which we infer u^N is constant over Ω', and thus vanishes as it is orthogonal to f_ϕ along Σ_f.

Convergence of the full discretization. If N is kept fixed, the problem (LFE^N) is equivalent to (LFE'^N) and to (6) ; a standard finite element discretization then applies for which error estimates are known. If h is the mesh size, u_h^N the solution of the full discretized problem and k the order of the finite elements, we have

$$\|u^N - u_h^N\|_{H^1(\Omega_1)} \leq Ch^k.$$

Finally the complete error estimate has the form

$$\|u - u_h^N\| \leq C_1 h^k + \frac{C_2}{N^{2-\epsilon}} ; \qquad (7)$$

a refinement of this result would exhibit the dependance of C_1 in terms of N.

IV.3. Coupling of finite elements and integral representation

This method has been introduced by LENOIR, JAMI [18] ; it takes advantage of finite elements for the near field and of integral equations for the radiation condition. In few words let us say that integral equations are solved with few unknowns and a weak order of convergence whereas localized finite elements allow a quicker convergence and need to discretize a relatively large domain.

We describe here our method on a sample, namely (P_v^V), but it applies as well to $(P_{v,H}^V)$ and more complex situations. Full theoretical and practical particulars are given by LENOIR [19] and JAMI, POLYZAKIS [20].

Problem set in a bounded domain. At once a fictitious and arbitrary boundary Γ_1 is drawn in $\overset{V}{\Omega}$ which surrounds Γ_0 and defines a bounded domain Ω.

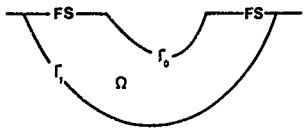


Fig.8 : The bounded domain Ω.

When u belongs to $H^1(\Omega)$ with Laplacian in $L^2(\Omega)$ we define the operator $D^\lambda u = \frac{\partial u}{\partial n}|_{\Gamma_1} + \lambda u|_{\Gamma_1}$ where λ is a complex constant. From the usual integral representation, if u is the solution of (P_v^V), $u^V|_\Omega$ satisfies

$$\left.\begin{array}{l} \text{Find } u^\lambda \text{ in } H^1(\Omega), \text{ such that} \\ \Delta u^\lambda = 0 \text{ in } \Omega, \\ \frac{\partial u^\lambda}{\partial n} - \omega^2 u^\lambda = 0 \text{ on FS}, \\ \frac{\partial u^\lambda}{\partial n} = g \text{ on } \Gamma_\phi, \text{ and} \\ D^\lambda u^\lambda(M) = \int_{\Gamma_0} \{u^\lambda(P) D_P^\lambda \frac{\partial G_\omega}{\partial n_P}(M,P) \\ \qquad - g(P) D_P^\lambda G_\omega(M,P)\} ds_P, \ \forall M \in \Gamma_1. \end{array}\right\} (P^\lambda)$$

If (P^λ) has a unique solution then necessarily $u^\lambda = u^V|_\Omega$ and to solve (P^λ) or (P_v^V) is equivalent ; the progress is notable for (P^λ) is set in a bounded domain.

Uniqueness. Here it is not necessary to involve an homogeneous problem. From u^λ, a solution of (P^λ), we define in $\overset{V}{\Omega}$

$$\overset{V}{u}_\lambda(N) = \int_{\Gamma_\phi} \{u^\lambda(P) \frac{\partial G_\omega}{\partial n_P}(N,P) - \frac{\partial u^\lambda}{\partial n_P}(P) G_\omega(N,P)\} ds_P \quad (8)$$

and we put, in Ω, $u'_\lambda = u^\lambda - \overset{V}{u}_\lambda|_\Omega$. On the other hand, u^λ being harmonic in Ω and satisfying, as G_ω, the free surface condition, it has the integral representation

$$u^\lambda(N) = \int_{\Gamma_\phi \cup \Gamma_1} \{u^\lambda(P) \frac{\partial G_\omega}{\partial n_P}(N,P) - \frac{\partial u^\lambda}{\partial n_P}(P) G_\omega(N,P)\} ds_P, \ \forall N \in \Omega .$$

Substracting both previous relations, we have

$$u'_\lambda(N) = \int_{\Gamma_1} \{u^\lambda(P) \frac{\partial G_\omega}{\partial n_P}(N,P) - \frac{\partial u^\lambda}{\partial n_P}(P) G_\omega(N,P)\} ds_P \quad (9)$$

which shows that u'_λ has an analytic continuation $\tilde{u}_\lambda$ inside the body.

Let denote $\widetilde{FS}$ the union of FS and its extension inside the hull and $\tilde{\Omega}$ the domain bounded by Γ_1 and $\widetilde{FS}$.

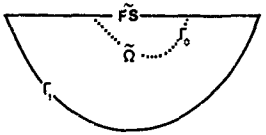


Fig.9 : The auxiliary bounded domain $\tilde{\Omega}$.

From (9), $\tilde{u}'_\lambda$ satisfies in $\tilde{\Omega}$ the problem

$$\left|\begin{array}{l} \text{Find } \tilde{u}'_\lambda \in H^1(\tilde{\Omega}), \text{such that} \\ \Delta\tilde{u}'_\lambda = 0 \quad \text{in } \tilde{\Omega}, \\ \dfrac{\partial\tilde{u}'_\lambda}{\partial n} - \nu\tilde{u}'_\lambda = 0 \quad \text{on } \widetilde{FS}, \text{ and} \\ D^\lambda\tilde{u}'_\lambda = 0 \quad \text{on } \Gamma_1. \end{array}\right.$$

This auxiliary problem is quite similar to $(P_{\nu,H})$; it is then well-posed since $Im\{\lambda\} \neq 0$, and $\tilde{u}'_\lambda = 0$. Therefore from formula (8) we obtain an extension of u^λ in $\overset{\vee}{\Omega}$ which satisfies $(\overset{\vee}{P}_\nu)$, the radiation condition being verified by G_ν. As a consequence of uniqueness for$(\overset{\vee}{P}_\nu)$, u^λ cannot be other than $\overset{\vee}{u}|_\Omega$.

Functional framework. We face to show that, once more we are in the scope of the sum of coercitive and compact operators. As a matter of fact, (P^λ) is given a variational formulation which solution is equivalent to

$$(A^\lambda + K^\lambda)u^\lambda = F \text{ in } H^1(\Omega),$$

where $\forall v \in H^1(\Omega)$,

$$\cdot\ (A^\lambda u|v)_{H^1(\Omega)} = \int_\Omega (\vec{grad}\ u|\vec{grad}\ v)d\omega + \lambda\int_{\Gamma_1} u\bar{v}ds,$$

$$\cdot\ (K^\lambda u|v)_{H^1(\Omega)} = -\int_{\Gamma_1} \bar{v}(M)\int_{\Gamma_\phi} u(P)D^\lambda\frac{\partial G_\nu}{\partial n_P}(M,P)ds_P ds_M$$
$$-\nu\int_{FS} u\bar{v}ds, \text{ and}$$

$$\cdot\ (F|v)_{H^1(\Omega)} = -\int_{\Gamma_1} \bar{v}(M)\int_{\Gamma_\phi} g(P)D^\lambda G_\nu(M,P)ds_P ds_M$$
$$+\int_{\Gamma_0} g\bar{v}ds\ .$$

As we choose λ such that $Im\{\lambda\} \neq 0$, the bilinear form associated with A^λ is coercitive in $H^1(\Omega)$. Moreover

$$|K^\lambda u|_{H^1(\Omega)} \leq \|u\|_{L^2(\Gamma)}\int_{\Gamma_1}\left|D^\lambda\frac{\partial G_\nu}{\partial n}(M,\cdot)\right|_{L^2(\Gamma_\phi)}ds_M$$
$$+ |u|_{L^2(\Gamma_0)}.$$

from which we can conclude that K^λ is a compact operator on $H^1(\Omega)$.

Now on, thanks to uniqueness we krow that -1 is not an eigenvalue of $(A^\lambda)^{-1}.K^\lambda$ and $A^\lambda+K^\lambda$ is an automorphism on $H^1(\Omega)$.

Discretization. A finite element approximation of (P^λ) in Ω does not raise any difficulty since as Γ_ϕ and Γ_1 have no common point, no singular kernel appears in the coupling condition ; thus, in the finite element approximation, every integral can be handled with numerical quadratures of general use.

Here again, convergence is proved which is only limited by the type of finite elements chosen and the regularity of the searched solution u^λ ; moreover, numerical tests have shown

(i) the approximate solution is independant of the value of λ, provided $Im\{\lambda\} \neq 0$,

(ii) the domain Ω can reduce to a portion of a ring overlayed by a single layer of elements.

V. Some numerical tests

Results are presented which are obtained by the last method described,for this method is now extensively used at the ENSTA. Indeed we have chosen the applications in 2-D and 3-D, which show the precision of the method but also the fact that irregular frequencies which occur with standard singularity distribution procedures are avoided.

V.1. Sea-keeping problem in 3-D

The results concern the heave motion of a semi-submerged sphere of unit radius ; using the symmetry properties of the problem, the domain Ω is reduced to one eighth of a shell. The discretization is made of four prismatic Lagrange-elements with eighteen nodes which represents fourty-five unknowns.

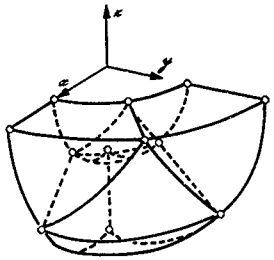


Fig.10 : A discretized eighth of a shell

If we take $\lambda = i$ for the solution of (P^{λ}), we get the results presented on fig.11 where the force coefficients are drawn versus the coefficient ν in non-dimensionalized form ; the precision of this result lies within 2 %.

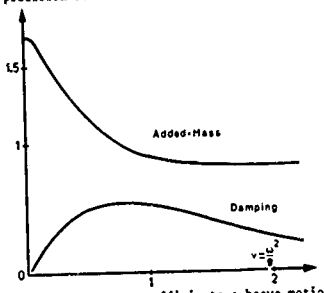


Fig.11 : Force coefficients ; heave motion of a semi-submerged sphere of unit radius.

If on the contrary taking $\lambda = 0$, we break the scope of the proof of uniqueness for (P^{λ}), irregular frequencies appear in the results (fig.12) ; these frequencies are the eigenvalues of the corresponding auxiliary problem.

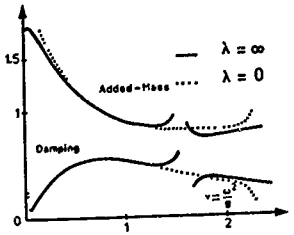


Fig.12 : Force coefficients ; irregular frequencies.

Note that the theoretical analysis has clearly specified the rules for a correct numerical procedure.

V.2. Wave-resistance in 2-D

If we restrict the study of $(\mathcal{P})$ to the case of a non-circulating flow around a submerged body, a numerical solution can be attempted.

For an immersed circular cylinder, the circular ring Ω has been "triangulated" with only sixteen elements with 8 nodes each. The wave resistance on figure 13 is given within a one per cent precision.

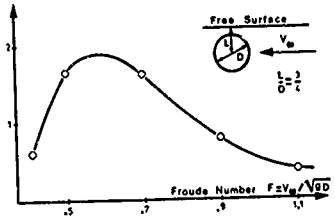


Fig.13: Wave resistance of a circular cylinder

At last, for a fixed Froude number and various mesh sizes, the wave resistance (ascribed to a known value) is plotted against the number of unknowns on the body ; this number governing the number of evaluations of the Green function needed as well in the last method described as in the singularity method. On fig.14, results by the latter method have been taken out from GUEVEL, CORDONNIER [21].

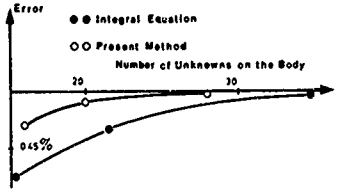


Fig.14 : Singularity method and coupling method with finite elements ; a sample for comparison.

VI. Concluding remarks

Linearized ship hydrodynamics have been a powerful factor for the development of numerical methods assigned to exterior linear problems involving various types of boundary conditions.

First of all is the singularity method which has already deserved many other fields of interest ; it leads to short procedures but results are obtained with a low order approximation.

With the coupling methods we have presented, better results are expected, especially for the wave resistance problem ; this going with an increasing complexity.

The localized finite element method has proved to be the most efficient in 2-D and when the depth is not too large. For an infinite depth or for the case of the 3-D Neumann-Kelvin problem (for which the eigenfunctions are difficult to evaluate), the coupling method between finite elements and integral representation do assert itself.

Aknowledgments

This work has been supported by the Direction des Recherches, Etudes et Techniques, Ministère de la Défense while the authors are assistant researchers at the Centre National de la Recherche Scientifique (M.L. and A.J.) and at the Institut National des Sciences Appliquées de Rennes (D.H.).

REFERENCES

[1] D. EUVRARD, A. JAMI, C. MORICE, Y. OUSSET : *"Calcul numérique des oscillations engendrées par la houle"*. I, J. Mécanique 16 (1977), 289-326.

[2] F. JOHN : *"On the motions of floating bodies"*, II, Comm. Pure Appl.Math.3 (1950), 45-101.

[3] M. LENOIR, D. MARTIN : *"An application of the principle of limiting absorption to the motions of floating bodies"*. J.Math. Anal.Appl. Vol.79, N°2 (1981), 370-383.

[4] K.J. BAI : *"A variational method in potential flows with a free-surface"* Ph.D.Thesis, University of California, Berkeley (1972).

[5] Y. OUSSET : *"Calcul numérique des efforts hydrodynamiques induits par la houle sur un navire"*, Thèse de 3ème cycle, Rennes (1975).

[6] C.H.WILCOX : *"Scattering theory for the d'Alembert equation in exterior domains"*. Lecture Notes in Mathematics, N°442, Springer Verlag, New-York, Berlin (1976).

[7] P. GUEVEL : *"Corps solide animé d'un mouvement quelconque dans un fluide illimité"*. Cours de l'E.N.S.M., Nantes (1976).

[8] G. FERNANDEZ : *"Non-linearity of the three-dimensional flow past a flat blunt ship"*. To appear in J. Fluid.Mech.

[9] M. ABRAMOWITZ, I.A. STEGUN : *"Handbook of Mathematical Functions"*, Dover Publications, New-York, 9th ed.(1970).

[10] V.A. KONDRAT'EV : *"Boundary Problems for Elliptic Equations in Domains with Conical or Angular Points"*. Transactions of the Moscow Mathematical Society, Vol. 16(1967).

[11] C.C.MEI, H.S. CHEN : *"A hybrid element method for steady linearized free surface flows"*. Int.J.Num.Meth.Eng.10(1976), 1153-1175.

[12] J.P. AUBIN : *"Approximation of Elliptic Boundary-Value Problems"*. Pure and Applied Mathematics, Vol XXVI, Wiley-Interscience (1972).

[13] K.J. BAI, R.W. YEUNG : *"Numerical solution to free-surface flow problems"*. Tenth Naval Hydrodynamics Symposium, Session VII, Cambridge, Massachusetts (1974).

[14] C. BARDOS, J. CEA, P.GRISVARD, LOZI : *"Calcul numérique de solutions singulières de problèmes aux limites"*. Colloque de Giens, Université d'Aix-Marseille (1978).

[15] J.A. ARANHA : *"Theoretical analysis of the hybrid element method"*, Ph.D.Thesis, Dep. of Civil Engineering, M.I.T. (1978).

[16] MASMOUDI : *"Résolution numérique de problèmes extérieurs"*. Thèse de doctorat de spécialité, Université de Nice (1979).

[17] J.L. LIONS : *"Problèmes aux limites elliptiques non-homogènes et applications."* Vol.1, Travaux et Recherches Mathématiques, Dunod (1968).

[18] M. LENOIR, A. JAMI : *"A variational formulation for exterior problems in linear hydrodynamics"*. Comp. Meth. Appl. Mech. Eng. 16(1978), 341-359.

[19] M. LENOIR : *"Error estimates for the coupling of finite elements and an integral representation, with application to the linearized sea-keeping problem"*. (to appear).

[20] A. JAMI, M. POLYZAKIS : *"A finite element solution of diffraction problems in unbounded domains"*. To appear in Comp. Meth. Appl. Mech. Eng.

[21] P. GUEVEL, J.P.V. CORDONNIER : *"Numerical solution of the Neumann-Kelvin problem by the method of singularities"*. Second International Conference on Ship Hydrodynamics, Berkeley, California (1977).

DISCUSSIONS
of the paper
by D. Euvrard, A. Jami, M. Lenoir, D. Martin

RECENT PROGRESS TOWARDS AN OPTIMAL COUPLING BETWEEN FINITE ELEMENTS AND SINGULARITY DISTRIBUTION PROCEDURES

Discussion
by P.A. Martin and F. Ursell

In section II.3 of their paper, the authors state the following lemma, concerning the behaviour at infinity of solutions of (P_ν) :

"If we have

(i) w is a harmonic function in $\overset{\nu}{\Omega}$ satisfying the free-surface condition, and

(ii) $$\int_{C_R} |w(R,\theta,z)|^2 R\,d\theta\,dz \to 0 \text{ as } R \to \infty$$

where C_R is the portion of a vertical cylinder with radius R belonging to $\overset{\nu}{\Omega}$, then necessarily w vanishes".

This lemma is false. (The analogous result in acoustics is known to be true, and is associated with the name of Rellich).

To disprove the lemma, we need a harmonic function which satisfies the free-surface condition and which decays as $o(R^{-1/2})$ as $R \to \infty$. It is well-known that the wavefree potentials

$$\frac{P^m_{m+2j}(\cos\phi)}{r^{m+2j+1}} + \frac{\nu}{2j}\,\frac{P^m_{m+2j-1}(\cos\phi)}{r^{m+2j}}\cos m\theta$$

(where $r\cos\phi = -z$ and $r\sin\phi = R$) have these properties, and therefore provide a counter-example to the lemma. Similar functions may be constructed in two dimensions, and when the water is of constant finite depth.

Authors' reply

We gratefully acknowledge to Professor Ursell to have pointed out this error, which make the proof of uniqueness in [3] , erroneous. As far as the authors know, there are only two proofs of the uniqueness of the sea-keeping problem which hold ; the first one is the well-known proof of F. John which is restricted to hulls entirely enclosed in the vertical cylinder built on their plane of flotation, the second is MAZ'JA's proof which apply to a certain type of submerged bodies, see :

MAZ'JA : Contribution to the stationary problem of the small oscillations of a fluid in presence of a submerged body. Proceedings of the S.L. Sobolev workshop (N° 2), Novosibirsk (1977), in Russian.

Progress are still to accomplish on that point, in particular, numerical tests suggest that the problem is always well-posed in the case of submerged bodies.

Discussion
by K. Eatock-Taylor

I should like to ask the authors about application of their coupled finite element-singularity distribution procedure. My question concerns wave diffraction and radiation analysis for some multi-body and shallow water problems. It is well known that difficulties can arise when certain discrete singularities are distributed over a body close to the seabed or over two bodies in close proximity. Since it appears that in the coupled procedure described in the paper singularities are still distributed over the surface of the body, I should like to ask the authors whether they have experienced any such difficulties. If such a problem does arise in direct application of their procedure, what is their method of overcoming it ?

Authors' reply

The difficulty Prof. Eatock Taylor points out proceeds from the fact that in the case of a multiply connected body, the diagonal coefficients (self-influence coefficients) of the matrix issued from the application of the singularity distribution method are not longer necessarily preponderant with respect to the coefficients of influence between any two connectivity components.

The method we propose is not liable to that kind of difficulty since the coupling coefficients that we compute produce from the influence of the physical boundaries on a fictitious boundary that encloses the whole of the multiply connected body.

Discussion
by G.E. Mearn

The coupling of the finite element and integral (or distribution) representations techniques are not only appropriate for solving the various rigid-body fluid structures interaction problem but also of course the hydroelastic/acoustic problems associated with a vibratory ship. Both Webster [1] and Mearn [2] have independently suggested that the hydroelastic problem be tackled by separating out the hydrodynamic effects through the deployment of "influence functions" rather than use the traditional Lewis of Lockwood Taylor coefficients

or iterate around a structural analysis-hydrodynamic analysis loop. This approach also overcomes any entanglement with the often misconceptualised "added mass" effect. However, the formulation leads to quite large algebraic systems especially when applied in 3 dimensional problems. Armand and Orsero [3] have coupled the structural finite element model of the ship and a finite element representation of the surrounding fluid. In some cases, Bettess [4] "infinite elements" are deployed to model the fluid domain. Have you employed your coupling technique to the analysis of a vibrating structure.

The removal of the irregular frequency problem by modifying the Green function is well quoted in the literature. Later in the conference Martin and Ursell tackle the problem using the "null field equation" approach. The results presented in Figures 11 and 12 are a consequence of utilising different operators in the problem P^{λ} could the authors explain what is happening when utilising these different operators and thus explain their resolution of the irregular frequency problem.

Finally, could the author be more specific regarding the appearance of reference 19.

[1] Webster, W.C. "Computations of the Hydrodynamic Forces Induced by General Vibration of Cylinders", J. Ship Research, vol. 23, n° 1 March 1979. Also available Institut für Schiffbau der Universitat Hamburg, Bericht NR 346, August 1976.

[2] Hearn, G.E. "Theoretical Treatment of Added Mass in Vibration Calculations", RINA Symposium in Propeller Induced Ship Vibration, London, Dec. 1979. Also available in part, BSRA NADV Progress Report n° 15, August 1976.

[3] Armand, J.L. and Orsero, P. "A Method for Evaluating the Hydrodynamic Added Mass in Ship Hull Vibrations", SNAME, 87th Annual Meeting, Nov. 1979, New York.

[4] Bettess, P. "Infinite Elements", Int. J. Num.Method in Engineering, Vol. 11, 1977.

Authors' reply

It is well know that the integral equation methods used for the solution of an exterior problem yield implicitly to an adjoint interior problem and that the so-called irregular frequencies are but the eigenvalues of that latter problem. If one replaces the usual GREEN Kernel with a suitable linear combination of itself and of its normal doublet, one is lead to a well-posed interior problem for all frequencies and thus gets rid of the irregular frequencies. The realization of the remark is some how difficult in singularity distribution method since one is then lead to compute finite parts of integrals.

As a matter of fact, it is quite easy to show that this type of remark holds for our coupling method ; but it is then much more easy to work it up as all the integrals represent long-distance coupling and thus imply only non-singular kernels.

More detailed explanations and a study of the convergence of the method can be found in H. Lenoir "Méthodes de couplage en hydrodynamique navale et application à la résistance de vagues bidimensionnelle (Coupling methods in ship hydrodynamics and application to the two-dimensional wave resistance problem)" Thesis, University of Paris VI (1982).

Let us finally say that we noticed the interest of the application of our method to the fluid-structure interaction problem, but we are now rather interested to its applications to the problems of acoustics.

NUMERICAL SOLVING OF TRANSIENT LINEAR HYDRODYNAMICS PROBLEMS BY COUPLING FINITE ELEMENTS AND INTEGRAL REPRESENTATION

A. Jami
École Nationale Supérieure de Techniques Avancées
Centre National de la Recherche Scientifique
Chemin de la Hunière, 91120 Palaiseau (France)

Abstract

The linearized problem of the potential flow past a submerged body in an arbitrary transient motion of small amplitude is studied in this paper.

Theoretical results are presented and the problem is solved numerically in the two-dimensional case by a finite element method.

The classical problem set in an unbounded domain is given an equivalent form in an arbitrary bounded domain using an integral representation formula as a complementing boundary condition. A variational formulation is worked out which is discretized by finite elements.

As we restrict our study to the case of a submerged body, the bounded domain can be chosen in such a way that it does not contain any portion of the free surface ; thus the free surface condition as well as the conditions at infinity, is taken into account by the Green function in the integral representation formula. In the case of a transient flow, this representation at time t involves an integral of convolution type over [0, t] which is equally split into time steps. Therefore the integrand is approximated in each interval and the linear system becomes similar to that of a steady flow ; the right member alone is modified at each time step and a factorization scheme can be used.

I. Introduction

In the field of naval hydrodynamics, some problems have not yet received a satisfactory numerical solution ; at least for them, a complete theoretical study must be carried on. On the other hand, due to modern developments in the field of functional analysis and the use of new generations of computers, extensions of known theoretical proofs and refinements of numerical algorithms are permitted.

The general philosophy of our work is to give a proof for the existence and uniqueness of the solution of a given problem. Then a problem is set in a bounded domain which is shown to be equivalent to the previous one and an adapted numerical algorithm of high precision and relative low cost is develcped. In our papers, numerical results are given for some simple test cases.

The purpose of this paper is to study the linearized problem for the potential flow produced by a submerged body undergoing an arbitrary transient motion of small amplitude. Numerical results are given for the transient forces acting on the body in two-dimensional cases only.

I.1. Statement of the problem.

We derive here the problem for the velocity potential in the small perturbation theory ; all the quantities are non-dimensionalized with respect to the length of the submerged body L, the density of the fluid ρ and the velocity of gravity waves $\sqrt{gL}$ where g is the gravity acceleration. Let (0 ; x, y, z) be a fixed reference frame with 0y upwards vertical. The fluid domain Ω is considered in its position at the time $t = 0$, due to small perturbation theory, Ω is bounded at any time $t > 0$ by the free surface Γ $y = 0$ and by the boundary S of the body in its initial position.

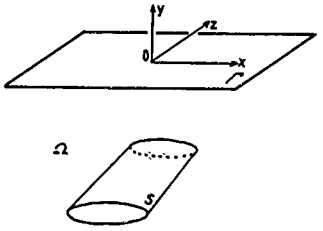


Fig. 1 : The domain Ω

At point M (x, y, z) in Ω and time t, the velocity potential $\Phi(M ; t)$ satisfies

$$\left.\begin{aligned} &\Delta\Phi = 0 \\ &\frac{\partial^2\Phi}{\partial t^2} + \frac{\partial\Phi}{\partial y} = 0 \text{ on } \Gamma \\ &\frac{\partial\Phi}{\partial n} = v\,(M ; t) \text{ on } S \end{aligned}\right\} \quad (P)$$

where

. the normal velocity v is known from the given motion of the body ; $\vec{n}$ is the unit normal to S external to the fluid domain Ω.

. the linearized free surface condition is obtained after elimination of the unknown free surface elevation from the kinematic condition and dynamic (constant pressure) condition.

At the initial time t = 0 the fluid is assumed to be at rest and the free surface to be unperturbated ; thus we have

$$\phi(M\ ;\ 0) = 0 \text{ and } \frac{\partial \phi}{\partial t}(M\ ;\ 0) = 0 \qquad (1)$$

for all M in the closure of Ω.

Moreover we suppose that for every time t > 0, the velocity field remains unperturbated far from the body ; more precisely we shall look for a solution ϕ of (P) which first derivatives are square integrable in Ω, that is

$$\int_{\Omega} \left| \vec{\text{grad}}\ \phi \right|^2 d\omega < \infty \qquad (2)$$

This condition will lead to the choice of a space of solutions of finite energy for ϕ.

Unsteady forces $\vec{F}(t)$ are expressed by using the linearized Bernoulli equation on the body ; as we suppose the body is totally immersed , we have

$$\vec{F}(t) = \int_S \frac{\partial \phi}{\partial t} \vec{n}\ ds \qquad (3)$$

I.2. Special cases

Two typical cases can already be discussed.

. If the normal velocity is constant in time ($\frac{\partial v}{\partial t} = 0$ for all t > 0) one expects a solution ϕ which would become stationary as time increases. In such a case, the resulting potential ϕ^S satisfies

$$\left.\begin{aligned} &\Delta \phi^S = 0 \\ &\frac{\partial \phi^S}{\partial y}\Big|_\Gamma = 0 \\ &\frac{\partial \phi^S}{\partial n}\Big|_S = v \end{aligned}\right\} \qquad (P^S)$$

where the free surface condition reduces to a symmetry condition as for a solid boundary. Therefore it is well known in aerodynamics from d'Alembert's paradox, that the corresponding flow contributes no net force.

. If the normal velocity is harmonic in time, one expects a solution ϕ which would become harmonic with the same frequency (but not the same phase). In such a case, the resulting potential ϕ_D can be interpreted as the solution of a diffraction or sea-keeping problem. Let us denote ω the reduced pulsation of the forced motion of the rigid body and for instance, let us take, for M on S

$$v(M\ ;\ t) = -\omega n_i \sin \omega t \qquad (4)$$

where n_i is the i-eth component of the normal at M on S . Therefore, taking the difference in phase into account, ϕ_D is written as

$$\phi_D = \phi_D^1 \cos \omega t + \phi_D^2 \sin \omega t$$

where the components $(\phi_D^j)_{j=1,2}$ do not deperd on time ; they satisfy

$$\left.\begin{aligned} &\Delta \phi_D^j = 0 \\ &\left(\frac{\partial \phi_D^j}{\partial y} - \omega^2 \phi_D^j\right)_\Gamma = 0 \\ &\frac{\partial \phi_D^j}{\partial n} = \begin{cases} -\omega n_i & \text{for } j = 1 \\ 0 & \text{for } j = 2 \end{cases} \end{aligned}\right\} \qquad (P_D^j)$$

together with radiation conditions that realize a coupling between problems (P_D^1) and (P_D^2) and make the latter non-homogeneous.

Note that if we introduce the complex valued potential

$$\tilde{\phi}_D = \phi_D^1 + \sqrt{-1}\ \phi_D^2 ,$$

it can be checked formally that $\tilde{\phi}_D$ is obtained by Fourier transform of ϕ in the D_t time variable: $\tilde{\phi}_D(\omega) = (\mathcal{F}_t\ \phi)(\omega)$.

The pair of coupled problems $(P_D^j)_{j=1,2}$ or the corresponding problem (P_D) for $\tilde{\phi}_D$ are well posed (see [1] and [2]) for Ω unbounded. Note that in the case where Ω is a bounded domain, (P_D) is ill posed for a numerable set of values of ω called eigenfrequencies of the internal problem ; this occurs as well if the boundary condition is of Dirichlet type. Each component of the resulting force is classically written in the form

$$F_D = A(\omega) \cos \omega t + B(\omega) \sin \omega t \qquad (5)$$

where $A(\omega)$ is called the added-mass coefficient and $B(\omega)$ the damping coefficient.

In the numerical applications of the transient problem (P) we shall refer to these two special cases.

I.3. Previous works.

Few numerical solutions of the transient problem have been given up to now. Let us note in [3] an application of the classical singularity distribution method , the authors established that the use of a single layer potential to represent the transient velocity potential leads to undesirable oscillations. The Fourier transform in time, from which the transient problem (P) is in correspondance with the diffraction problem (P_D) relates these oscillations to the well-known phenomenon of the irregular frequencies (see for example [4], [5]).

Concerning the theoretical study of our problem some results are yet known ; in the case of a bounded fluid domain (unsteady oscillations of a liquid in a tank) a fundamental work has been done in [6] and also in [7].

In the case of a finite depth of the fluid, a complete theoretical study is given in [8] to which we shall refer hereafter. More recently a quite modern study including the dynamics of the floating body has been given [9] and its numerical approximation has been developped in [10].

I.4. Outlines of the paper

We first give, in the sequel, the sketch for the proof of uniqueness and existence of a solution. The Green function is studied in the third chapter and an integral representation formula is given for this solution. In chapter four the method presented in [11] is summarized and the application to our problem is detailed. The fifth chapter is devoted to the finite element approximation and the numerical algorithm and in the last chapter we give some numerical results.

II. Theoretical results

In this chapter we restrict the study to the 3-D case for, in the 2-D case, the definitions of the functional spaces being different more technical results are needed.

The results we give are, for their first part, a direct application of the study of weighted Sobolev spaces in a half space (see [12], [13]). Let us define these functional spaces by their mechanical meanings ; we denote by $W^1_0(\Omega)$ the space of potentials of finite kinetic energy in Ω. Therefore

$$V(\Omega) = W^1_0(\Omega) \cap L^2(\Gamma)$$

is the Hilbert space of potentials of finite total energy in Ω equipped with the norm

$$\| u \| = \left(\int_\Omega |\vec{\text{grad}}\, u|^2 \, d\omega + \int_\Gamma |u|^2 \, d\gamma \right)^{1/2}$$

which is equivalent to the graph norm.

Let us now describe the three main features that give the basis of our proofs :

(i) Every function in $V(\Omega)$ is the limit of a set of functions infinitely derivable with compact support in $\bar{\Omega}$ (namely, $\mathcal{D}(\bar{\Omega})$ is dense in $V(\Omega)$).

(ii) Let be Γ_a the plane $(y = -a)$, $a > 0$ such that $\Gamma_a \cap S$ is empty, every function in $V(\Omega)$ has a trace in $L^2(\Gamma_a)$.

(iii) The bilinear form $a(u,v) = \int_\Omega (\vec{\text{grad}}\, u / \vec{\text{grad}}\, v)$ is coercive in $W^1_0(\Omega)$.

II.1. Uniqueness

It is sufficient to show that the homogeneous problem (P) has no other solution than the null function. This is easily obtained as for functions in $V(\Omega)$ with laplacian in L^2, the Green formula for ϕ and $\frac{\partial \phi}{\partial t}$ applies ; thus

$$E(t) = \int_\Omega |\vec{\text{grad}}\, \phi|^2 \, d\omega + \int_\Gamma \left| \frac{\partial \phi}{\partial t} \right|^2 d\gamma$$

is finite for $\phi \in V(\Omega)$ and has a null time derivative. Using then the homogeneous initial conditions, we have $E(t) = 0$ and $\phi(t)$ is constant almost everywhere in Ω ; thus $\phi|_\Gamma(t) = \phi|_\Gamma(0)$ and the constant is null.

II.2. Existence

Following [8] we can construct one solution of (P) in two steps. First we consider problems (P_0) and (P_1) which have a Dirichlet type boundary condition on Γ

$$\left.\begin{array}{l} \Delta\phi_0 = 0 \\ \dfrac{\partial \phi_0}{\partial n}\Big|_S = v \in L^2(S) \\ \phi_0|_\Gamma = 0 \end{array}\right\} (P_0) \qquad \left.\begin{array}{l} \Delta\phi_1 = 0 \\ \dfrac{\partial \phi_1}{\partial n}\Big|_S = 0 \\ \phi_1|_\Gamma = \phi \text{ given in } L^2(\Gamma) \end{array}\right\} (P_1)$$

Obviously, if ϕ is the trace of ϕ on Γ, $\phi_0 + \phi_1$ is a solution of (P). Therefore, from problem (P_1) we define the operator

$$K_1 : \phi \to \frac{\partial \phi_1}{\partial y}\Big|_\Gamma$$

By (iii) and the Lax-Milgram theorem, (P_0) and (P_1) which are of the same type have unique solutions respectively denoted by ϕ_0 and ϕ_1, in $W^1_0(\Omega)$; moreover they belong to $V(\Omega)$. Then by the Green identity, K_1 is shown to be a positive, self adjoint unbounded operator with domain $H^1(\Gamma)$ dense in $L^2(\Gamma)$ and K_1 does not depend on time.

In a second step, we consider the following equation of the type of the wave-equation on Γ.

$$\frac{\partial^2 \phi}{\partial t^2} + K_1 \phi = f \qquad (6)$$

with initial conditions $\phi(0) = 0$ and $\frac{\partial \phi}{\partial t}(0) = 0$.

From a classical result [14] we know that the solution of (6) can be written in the convolution form

$$\phi(t) = \int_0^t K_1^{1/2} \sin(t-\tau) K_1^{1/2} f(\tau) \, d\tau \qquad (7)$$

provided weak restrictions on the right-hand-side f(powers of an operator are defined in [15] for instance).

Hence, with $f = -\frac{\partial \phi_0}{\partial y}\Big|_\Gamma \in L^2(\Gamma)$, the chaining

$$v \xrightarrow{(P_0)} \phi_0 \xrightarrow{(6)} \phi \xrightarrow{(P_1)} \phi_1 \qquad (8)$$

gives the unique solution $\phi = \phi_0 + \phi_1$ of (P) in $V(\Omega)$.

III. The integral representation

Using a Green function for (P), that is an elementary source which satisfies the free surface condition, one gets an integral representation for the solution ϕ of (P) in $V(\Omega)$.

III.1. The Green function

Let us note $R^3_-=\{P(\xi,\eta,\zeta)/\eta<0\}$ the negative half space. The Green function of problem (P) is denoted $H_M(P\ ;\ t)$ and satisfies, for any $M(x,y,z)$ in R^3_- :

$$\Delta H_M(P\ ;\ t) = \delta_M(P)\delta(t)\ ;\ P \in R^3_-\ ,\ t \in R$$
$$\frac{\partial^2 H_M}{\partial t^2} + \frac{\partial H_M}{\partial \eta} = 0 \text{ for } \eta = 0 \qquad (9)$$

where $\delta_M(P)$ is the Dirac distribution in space at point M and
$\delta(t)$ is the Dirac distribution in time at the origin .

As for the study of (P), it is convenient to use the decomposition

$$H_M(P\ ;\ t) = \delta(t)\ G_M(P) + Y(t)\ F_M(P\ ;\ t) \qquad (10)$$

where $G_M(P)$ is the Green function of problem (P_δ) and $F_M(P\ ;\ t)$ is a regular function in $V(R^3_-)$ for every $t > 0$;
$Y(t)$ is the Heaviside function.

Let us note $E_M(P)$ the elementary solution for the laplacian in R^3 ($E_M(P) = -(4\pi|MP|)^{-1}$) and M' the image of M with respect to the free surface Γ ; we have

$$G_M(P) = E_M(P) - E_{M'}(P) \qquad (11)$$

and $F_M(P\ ;\ t)$ is the solution in $V(R^3_-)$ of the problem

$$\left.\begin{aligned} &\Delta F_M = 0 \\ &\frac{\partial^2 F_M}{\partial t^2} + \frac{\partial F_M}{\partial \eta} = 0 \\ &F_M\big|_{t=0} = 0 \\ &\frac{\partial F_M}{\partial t}\bigg|_{t=0} = 2\,\frac{\partial E_{M'}}{\partial \eta} \end{aligned}\right\} \text{ on } \eta = 0 \qquad (12)$$

This problem can be studied in a way similar to problem (P). Then F_M is evaluated by Fourier transform in the horizontal (ξ,τ) coordinates , returning to the physical plane, we have

$$F_M(P,t) = -\frac{1}{2\pi}\int_0^\infty \sqrt{s}\ e^{(y+\eta)s}\ J_0(sr)\sin(t\sqrt{s})ds \qquad (13)$$

where $r = \sqrt{(x-\xi)^2 + (z-\zeta)^2}$ and J_0 is the Bessel function of order zero. Note that this result was given a long time ago in [16].

A modified contour integration technique has been used to give another expression for F_M which is well suited for numerical evaluation :

$$F_M(P\ ;\ t) = -\frac{16}{\pi^2 t^3}\int_0^{\frac{\pi}{2}} \mathrm{Re}\left\{p^2\,\frac{d}{dp}[pL(p)]\right\}d\beta \qquad (14)$$

where

$$p = \frac{t^2}{4q}\ ;\ q = r + \sqrt{-1}(y+\eta)\cos\beta \qquad (15)$$

and

$$L(p) = \int_0^1 \exp\ (p(1-s^2))ds \qquad (16)$$

The asymptotic behavior of $F_M(P\ ;\ t)$ as $t \to \infty$ is easily deduced from the relation

$$L(p) \sim \frac{1}{2p} + \frac{1}{4p^2} + \ldots \text{ as } |p| \to \infty\ ; \qquad (17)$$

we have

$$F_M(P\ ;\ t) \sim \frac{2}{\pi t^3} \text{ as } t \to \infty \qquad (18)$$

III.2. Special cases

In view of justifying the results anticipated in I.2., we can give some particular results obtained when $t \to \infty$.

* By convolution in time of $H_M(P\ ;\ t)$ with the Heaviside function $Y(t)$, one gets the potential of a source of constant flow starting at $t = 0$:

$$K_M(P\ ;\ t) = Y(t)\ \{E_M(P + E_{M'}(P) + I_M(P\ ;\ t)\} \qquad (19)$$

where

$$I_M(P\ ;\ t) = \frac{2}{\pi^2}\int_0^{\frac{\pi}{2}} \mathrm{Re}\ \{\frac{1}{2q} - \frac{p}{q}\,L(p)\}d\beta \qquad (20)$$

Using then (17) we see that

$$I_M(P\ ;\ t) \sim -\frac{1}{\pi t^2} \text{ as } t \to \infty, \qquad (21)$$

and $K_M(P\ ;\ t)$ tends to be symmetrical with respect to the free surface. Therefore we can conclude :

The potential induced by a source of constant unit strength starting at $t = 0$ tends to be as time increases, a Green function for problem (P^δ).

* By convolution in time of $H_M(P\ ;\ t)$ with the function $Y(t)\cos\omega t$, it is a known result that the potential induced tends to be the Green function for the pair of coupled problems $(P^\delta_D)_{j=1,2}$.

* The same techniques hold true in the two-dimensional case. We have then

$$E_M(P) = \frac{1}{2\pi}\,\mathrm{Log}\ |MP| \qquad (22)$$

and

$$F_M(P\ ;\ t) = \frac{1}{\pi}\int_0^\infty e^{(y+\eta)s}\ \cos(s|x-\xi|)\sin(t\sqrt{s})\frac{ds}{\sqrt{s}} \qquad (23)$$
$$= \frac{4}{\pi t}\,\mathrm{Re}\ (pL(p))$$

where p is given by (15) with $q = |x-\xi| + \sqrt{-1}(y+\eta)$ and L(p) is given by (16).

Other expressions for $F_M(P\ ;\ t)$ can be found involving the complex exponential integral function or the error function. Some of these results are given in [17], in particular we have

$$L(p) = \sqrt{-1}\,\frac{w(\sqrt{p})}{\sqrt{p}} - \frac{\sqrt{\pi}}{2p}\,e^{-p} \qquad (24)$$

where w(z) is given in [18 p.297] and its numerical evaluation can be handled with popular techniques.

III.3. The Green theorem

The classical third Green formula can be applied to $Y(t)\ \phi\ (M\ ;\ t)$, ϕ solution of (P), and to the Green function $H_M(P\ ;\ \tau)$ defined above for real t and τ. Therefore, by convolution in time, one gets the formula

$$\phi(M\ ;\ t) = \int_S [\phi(P;t)\ \frac{\partial G_M}{\partial n_P}(P) - v(P;t) G_M(P)]\, ds_P + \int_0^t \int_S [\phi(P;t-\tau)\ \frac{\partial F_M}{\partial n_P}\ (P;\tau) - v(P;t-\tau)\ F_M(P;\tau)]\, ds_P d\tau \qquad (25)$$

Note that this formula is valid for all M in Ω and $t > 0$ and it does not involve any space integration on the free surface ; only the values of ϕ on S are involved in the right-hand-side. Let us also point out that the first integral over S is similar to that of a steady problem. As regards the second integral it contains all the "history" of the flow which influences the present time. It is obvious that the latter term represents the effect of the free surface deformations up to infinity for (25) can also be written

$$\phi(M\ ;\ t) = \int_S [\phi(P;t)\ \frac{\partial G_M}{\partial n_P}(P) - v(P;t) G_M(P)]\, ds_P + \int_\Gamma \phi(P;t)\ \frac{\partial G_M}{\partial n}(P)\, d\Gamma_P \quad ;$$

unfortunately, this instantaneous integral representation cannot be used in a numerical algorithm since the last integral extends up to infinity.

IV. Problem in a bounded domain

Reducing the unbounded domain to a bounded one leads to the introduction of an artificial boundary. When dealing with wave propagation problems, as (P_D), radiation conditions are known at infinity and they can be imposed at finite distance (see [5]). On the contrary, for transient flows, radiation conditions have no practical meaning.

Many authors, in or beyond the framework of naval hydrodynamics ([10], [19], [20]), have used approximate radiation conditions. These local boundary conditions lead to classical boundary value problem (at each time step) in a bounded domain ; these conditions are determined by a differential operator satisfied by the first terms of the asymptotic behavior of the searched solution. Nevertheless some reflected waves cannot be avoided even if the radiation boundary is fixed far from the obstacle ; moreover convergence of the resulting solution when the artificial boundary is shifted towards infinity has not been proved until now.

We shall not talk about the "localized finite element" methods discussed in [21].

Of course the use of an integral representation formula, as (25), takes the free surface condition as well as the behavior at infinity exactly into account. This property has made the singularity distribution method a practical tool for early numerical applications ; unfortunately, as everyone knows this method leads to an integral equation with a singular kernel which has not been solved but by low order approximations.

IV.1. The coupling method

Our original idea is to match the advantages of a modern numerical method, namely the finite element method, and those of the integral representation formula. This method presented in a first formulation in [22] has shown a real efficiency as regards the precision-to-cost ratio. It has been developed in [11] and a new formulation has been given in [23] and developed in [24]. Recent developments together with their theoretical support are presented in [25].

Subsequently we shall apply our coupling method in its first formulation to problem (P). We first define an arbitrary boundary Σ which encloses S without common points; as we restrict our study to the case of a submerged body, we can choose Σ close to S and without common points with Γ. As a consequence, the domain θ between S and Σ does not contain any portion of the free surface and, at each time t, the solution ϕ of (P) satisfies in θ : (for the sake of clarity, we use here the argument t).

$$\left.\begin{aligned} &\Delta\phi(t) = 0 \\ &\frac{\partial \phi}{\partial n}\Big|_S(t) = v(t) \\ &\phi|_\Sigma(t) = A\phi|_S(t) - Bv(t) \end{aligned}\right\} (Q)$$

$$+ \int_0^t [C(\tau)\phi|_S(t-\tau) - D(\tau)v(t-\tau)]\, d\tau$$

where the coupling condition for $\phi|_\Sigma$ with respect to $\phi|_S$ is a condensed form of equ. (25) for $M \in \Sigma$.

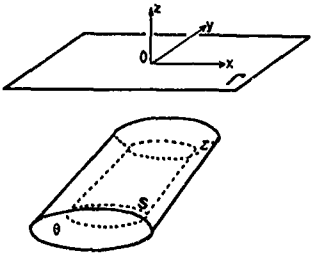


Fig. 2 : The bounded domain θ

Now the set of relations (Q) can be considered as a problem for $\phi \in H^1(\theta)$; the existence of a solution of this problem is obvious by its very construction. Uniqueness will not be proved here for a similar proof is given in the next paragraph.

IV.2. The time discretization

We face to solve (Q) by a time-marching scheme of constant steps Δt ; for this purpose, we define the indicial notation $t_n = n\Delta t$ and $\mu^n = \mu(t_n)$, where μ stands for any of the functions ϕ, v and the operators C and D involved in problem (Q). Now for the convolution integral, we approximate $\phi_{|S}$ and v by piecewise linear functions and the operators by piecewise constant functions ; this leads, for $n \geq 1$, to the formula

$$\int_0^{t_n} C(\tau)\,\phi_{|S}(t_n-\tau)\,d\tau = \frac{\Delta t}{2}\{C^{1/2}\,\phi^n_{|S} + \sum_{m=1}^{n-1} C^{m-1/2}[\phi^{n-m+1}_{|S} + \phi^{n-m}_{|S}] + C^{1/2}\,\phi^{n-1}_{|S} + C^{n-1/2}\phi^1_{|S}\} \qquad (26)$$

for the first term, and to an equivalent formula for the second term. Note that, in (26) we have taken the initial condition $\phi_{|S} = 0$ into account.

Therefore if it is inferred that at the n-ieth time step, all the values $\phi^m_{|S}$ for $m < n$ are known, ϕ^n will be a solution of

$$\left.\begin{aligned} &\Delta\phi^n = 0 \\ &\frac{\partial\phi^n}{\partial n}\Big|_S = v^n \\ &\phi^n_{|\Sigma} = (A+\frac{\Delta t}{2}C^{1/2})\,\phi^n_{|S} - (B+\frac{\Delta t}{2}D^{1/2})v^n \\ &\qquad + \frac{\Delta t}{2}\sum_{m=1}^{n} g^n_m \end{aligned}\right\} (Q_n)$$

with

$$g^n_m = C^{m-1/2}\{\epsilon_m\,\phi^{n-m+1}_{|S} + \epsilon'_m\,\phi^{n-m}_{|S}\} - D^{m-1/2}\{\epsilon_m\,v^{n-m+1} + \epsilon'_m\,v^{n-m}\} \qquad (27)$$

and

$$\epsilon_1 = 0\ ;\ \epsilon_m = 1\ ,\ 1 < m \leq n$$

$$\epsilon'_n = 0\ ;\ \epsilon'_m = 1\ ,\ 1 \leq m < n$$

IV.3. A variational formulation

Now the problem (Q_n) to be solved at each time step t_n is similar to those of the steady case. We refer to [11] for the derivation of the variational formulation. The coupling condition on Σ is equivalent to a boundary condition of Dirichlet type ; let f^n be the right-hand-side of this condition and assume $f^n \in H^{1/2}(\Sigma)$ and f^n is known. Thus we define an extension operator E from $H^{1/2}(\Sigma)$ to

$$H^1_{\phi,S}(\theta) = \{u \in H^1(\theta)/u_{|S} = 0\}\ ;$$

E is continuous and we can set a variational formulation for $\tilde\phi^n = \phi^n - Ef^n$ in

$$H^1_{\phi,\Sigma}(\theta) = \{u \in H^1(\theta)/u_{|\Sigma} = 0\}$$

For a given $v^n \in L^2(S)$; we have the problem

Find $\tilde\phi^n \in H^1_{\phi,\Sigma}(\theta)$ such that, $\forall\,\phi \in H^1_{\phi,\Sigma}(\theta)$

$$a(\tilde\phi^n,\phi) + a(E\{A + \frac{\Delta t}{2}C^{1/2}\}\tilde\phi^n_{|S},\phi) = \int_S v^n\,\phi\,ds + a(E\{B+\frac{\Delta t}{2}D^{1/2}\}v^n,\phi) + \frac{\Delta t}{2}\sum_{m=1}^{n} a(E\{g^n_m\},\phi) \qquad (Q^v_n)$$

where $a(\phi,\psi) = \int_\theta (\vec{\mathrm{grad}}\,\phi/\vec{\mathrm{grad}}\,\psi)\,d\omega$ and g^n_m given by (27).

Of course the extension E is not unique but the solution $\phi^n = \tilde\phi^n + Ef^n$ is irdependant of E ; thus a trivial extension will be used in the space discretization of (Q^v_n).

The uniqueness of the solution of (Q^v_n) is easily proved as in steady cases (see [21]), for (Q^v_n) is equivalent to

$$(J + K)\,\tilde\phi^n = F^n \text{ in } H^1_{\phi,\Sigma}(\theta), \qquad (28)$$

where

. J is a coercive operator on $H^1_{\phi,\Sigma}(\theta)$ associated with the bilinear form $a(\tilde\phi^n,\phi)$,

. K is a completely continuous operator on $H^1_{\phi,\Sigma}(\theta)$ associated with the bilinear form $a(E\{A+\frac{\Delta t}{2}C^{1/2}\}\,\tilde\phi^n_{|S},\phi)$,

. F^n is a function in $H^1_{\phi,\Sigma}(\theta)$ associated with the right-hand-side of (Q^v_n).

Therefore the Fredholm alternative gives the equivalence between existence (which holds true) and uniqueness of the solution of (28) provided -1 is not an eigenvalue of $J^{-1}K$. The proof of the last step, involves the study of a Dirichlet-type problem for the laplacian in the inner domain of boundary Σ ; this problem is always well-posed and the proof is settled.

V. A Finite Element Approximation

For a general introduction of the finite element method, we refer to [26] ; thus, for a terse presentation, we shall pass over a lot of preliminary hypothesis.

Concerning the convergence of the finite element approximation let us say that, from (28) and a result of AUBIN [27], it is proved in [25] that classical error-estimations for problems set in bounded domains are preserved.

V.1. Finite element discretization

We choose a regular triangulation $\mathcal{T}_h$ of diameter h with N nodes $(M_j)_{j=1,N}$ and we denote θ_h the approximate domain with boundaries ${}^hS_h$ and Σ_h ; V^n is the Hilbert space generated by a set of N continuous and piecewise polynomial functions $(\omega_i)_{i=1,N}$ with compact

support in $\overline{\Theta}_h$ and satisfying

- $\omega_i(M_j) = \delta_{ij}$; $i,j = 1,N$, δ_{ij} is the Kronecker's symbol
- $\overline{\Theta}_h = \bigcup_{i=1,N}$ (support of ω_i)

Therefore the approximate solution of problem (Q^V) reduces to the solution of a linear system of order $N-N_\Sigma$ where N_Σ is the number of nodes belonging to Σ ; similarly we denote by N_S the number of nodes belonging to S.

Let us first note that the approximate extension operator E_h is chosen as the simplest one in the finite element basis ; that is

$$(E_h\omega_j)(M) = 0 \text{ if } M_j \notin \Sigma_h \text{ or } M \notin \text{supp } \omega_j \ ;$$

then we define the "extension domain", by

$$\Sigma_h = \bigcup_{M_i \in \Sigma_h} (\text{support of } \omega_i)$$

Furthermore we denote

$$\begin{aligned}
&\cdot\ a_{ij} = a_h(\omega_j,\omega_i) \ ; \ M_i, M_j \in \overline{\Theta}_h \setminus \Sigma_h \\
&\cdot\ \Delta_{ij} = a_h(\omega_j,\omega_i) \ ; \ M_i \in \Sigma_h \setminus \Sigma_h, M_j \in \Sigma_h \qquad (29) \\
&\cdot\ \delta_{ij} = \int_{S_h} \omega_j\,\omega_i\,ds \ ; \ M_i, M_j \in S_h
\end{aligned}$$

$$\begin{aligned}
&\cdot\ \Gamma_{ij} = G_{M_i}(P_j) + \frac{\Delta t}{2} F_{M_i}(P_j;\tfrac{\Delta t}{2}) ; M_i \in \Sigma_h, P_j \in S_h \\
&\cdot\ D\Gamma_{ij} = \frac{\partial}{\partial n_{P_j}}\left(G_{M_i}(P_j) + \frac{\Delta t}{2} F_{M_i}(P_j;\tfrac{\Delta t}{2})\right); \ " \ " \\
&\cdot\ \Lambda^m_{ij} = \frac{\Delta t}{2} F_{M_i}(P_j \ ; \ t_m - \tfrac{\Delta t}{2}) \qquad ; \ " \ " \qquad (30) \\
&\cdot\ D\Lambda^m_{ij} = \frac{\Delta t}{2} \frac{\partial}{\partial n_{P_j}} F_{M_i}(P_j \ ; \ t_m - \tfrac{\Delta t}{2}) \qquad ; \ " \ "
\end{aligned}$$

Finally the linear system is written, using Einstein's convention as follows :

$$\begin{aligned}
\{[a_{ij} + \Delta_{ik}\, D\Gamma_{kl}\delta_{lj}]\,\varphi^n_j &= [\delta_{ij} + \Delta_{ik}\Gamma_{kl}\delta_{lj}]v^n_j \\
&+ \sum_{m=1}^{n} \Delta_{ik}\,[D\Lambda^m_{kl}\ \delta_{lj}(c\varphi_j^{n-m+1} + c'\varphi_j^{n-m}) \qquad (31) \\
&- \Lambda^m_{kl}\,\delta_{lj}(cv_j^{n-m+1} + c'v_j^{n-m})]\}_{i=1,N-N_\Sigma}
\end{aligned}$$

Let us point out some features about the numerical evaluation of the coefficients and the solution of this system.

. The coefficients defined in (29) are quite classical in a finite element method ; they are evaluated by numerical quadratures in each finite elements. The resulting matrices are sparse, symmetric and block-diagonal or made up of block-diagonal sub-matrices.

. The coefficients defined in (30) are combinations of values of the two terms of the Green function and their first derivatives ; the matrices (Γ_{ij}) and $(D\Gamma_{ij})$ are computed once before starting the time marching process when the matrices (Λ^m_{ij}) and $(D\Lambda^m_{ij})$ are computed and stored at the m-1eth time step. The latter matrices are full and non-symmetric ; therefore an effective subroutine has been worked out in order to perform, with a reduced time-consumption, their multiplication by the former matrices at further time steps and, by sommation to get the convolution term in the right-hand-side of (31).

. The matrice in the left-hand-side of (31) may be computed and factorized once before starting the time marching scheme as it does not depend of time ; this fact gives the method a good precision-to-cost ratio.

V.2. The numerical algorithm

We describe here the seven fundamental stages of a program for the solution of (31).

1. Give the coordinates of the nodes on S
2. Find the coordinates of the nodes on Σ
3. Define the finite elements (type, order..)
4. Describe the elements
   - . Compute in each element and collect the terms necessary to evaluate the coefficients (a_{ij}), (Δ_{ij}) and (δ_{ij})
   - . store the component of the normal at each node on S_h
5. Compute the coefficients (Γ_{ij}) and $(D\Gamma_{ij})$
6. Compute, factorize and store the matrix of the linear system (31)
7. Describe the time step n
   - . Compute and store (v^n_j), (Λ^n_{ij}) and $(D\Lambda^n_{ij})$
   - . Compute the right-hand-side of (31)
   - . Solve the linear system
   - . Compute the force-component and, if desired, the instantaneous free-surface elevation.

Note that the last step can be reproduced, from n = 1, as many times as necessary to describe the phenomenon.

External data

- . Coordinates of the nodes on S
- . Number and type of the elements
- . Order of the approximation and time step
- . Type of results

External functions

- . Boundary condition v
- . Green's function and its first derivatives in space.

That's it ! ... our program includes about three thousand FORTRAN instructions.

IV. Numerical results

As we said in the introduction we show few numerical results ; the convergence of the finite element method (i.e. with respect to the mesh size h) has yet been verified [11]. We mainly focus our attention on the stability of the results as time increases. In order to illustrate this stability, we have studied both problems discussed in the paragraphe I.2. and III.2. The results are given for the resulting force component with respect to time and for different values of the time step Δt.

For these two examples we have chosen a circular cylinder of unit diameter with center at $y = -1$; the bounded domain θ is then a circular annulus, its triangulation is made of 12 rectangular finite elements of order 2 (see fig. 3). The order of the system is 48.

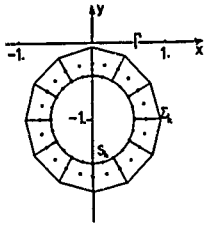


Fig.3 : The discretized domain and the nodes.

For the constant normal velocity, we have chosen

$$v(t) = -n_i \lambda(t) \ ;$$

obviously this transient problem has no physical meaning for the free surface condition is written in a fixed frame of reference. Nevertheless the velocity potential tends to the solution ϕ^S of (P^S). The first component of the force $F(t)$ alone is modified and tends, as previously stated, to zero as time increases. This is shown on figure 4 where the first time step is not significant because of the impulsive motion at this early stage.

For the time-harmonic slip condition we show the resulting first force component for a sway motion ; the normal velocity is then given by (4) with $i = 1$. On figure 5 and 6 results are shown for the frequencies $\omega = \pi$ and $\omega = 1$ respectively. Let us note that, here again, the first time step is not significant as the motion is impulsively started. The added mass $A(\omega)$ and damping $B(\omega)$ coefficients are given by the solution of (P_D) with the same kind of coupling method as presented here. From these results we point out the quite fast adjustement of the transient force in phase and amplitude to its limit.

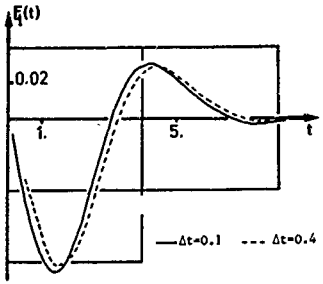
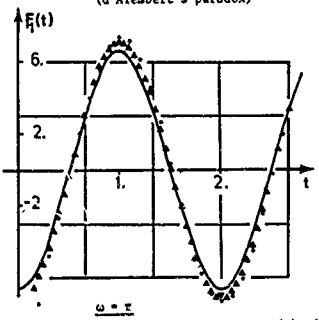
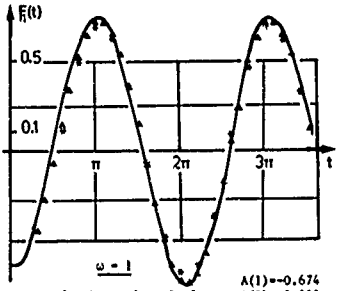


Fig 4 : Vanishing force coefficient (d'Alembert's paradox)



A(π)=-6.62
B(π)= 0.02

Fig.5 : ——— time harmonic solution
• • • Δt=0.1 ▲▲▲ Δt=0.05



A(1)=-0.674
B(1)= 0.305

———time harmonic solution
* * * Δt=π/5 ▲ ▲ ▲ Δt=π/10

Fig. 5 et 6 : Sway motion of a circular cylinder of unit diameter and center at y=-1.

VII. Comments

Other numerical results, in 3-D particularly, together with details of the theoretical study, will be published later on.

Concerning floating bodies, the method can be applied without any modification ; nevertheless, let us say that the free surface condition should be discretized, a portion of the free surface belonging to the boundary of the domain. There is of course no difficulty to obtain, as in [3] and [10], results for the half-cylinder, the solution being regular in the vicinity of the water-line in that case.

A direct development of this study is the fluid structure interaction in which the behavior of an elastic body in arbitrary motion should be taken into account.

At last, as for most results in linearized transient problems, we expect this work to be a first insight towards a decisive treatment of the non-linear problem.

Aknowledgements

This work has been supported by the Direction des Recherches, Etudes et Techniques, Ministère de la Défense while the author is assistant researcher of the Centre National de la Recherche Scientifique.

References

[1] F. JOHN : *On the motion of floating bodies* II, Comm. Pure and Applied Math., 3, p. 45-101 (1950).

[2] M. LENOIR, D. MARTIN : *An application of the principle of limiting absorption to the motion of floating bodies.* J. of Math. Analysis and Applications, vol. 79, N° 2, p. 370-383 (1981).

[3] H. ADACHI, S. OHMATSU : *On the influence of irregular frequencies in the integral equation solutions of the time-dependent free surface problems.* J. of the Society of Naval Architects of Japan, vol. 146, p. 119-128 (1979).

[4] W. FRANK : *Oscillation of cylinders in or below the free surface of deep fluids.* N.S.R.D.C. Report 2375 (Oct. 1967).

[5] D. EUVRARD, A. JAMI, C. MORICE, Y. OUSSET : *Calcul numérique des oscillations engendrées par la houle.* J. de mécanique, vol. 16, N°2, 3, p. 283-313, (1977).

[6] A. FRIEDMAN, M. SHINBROT : *The initial value problem for the linearized equations of water waves.* J. of Math. and Mechanics, vol. 17, n°2 (1967) and vol.18, n°12 (1969)

[7] J. BOUJOT : *Sur l'analyse des caractéristiques vibratoires d'un liquide contenu dans un réservoir.* J. de mécanique, vol.11 n° 4, p. 649-671 (1972).

[8] R.M. ÇARIPOV : *On the linear theory of gravity waves ; the theorem of existence and uniqueness.* Arch. of Rat. Mech. and Anal., vol. 24, p. 352-362 (1967).

[9] T. BEALE : *Eigenfunction expansion for an object floating in an open sea.* Comm. on Pure and Applied Math., vol. 30, p. 283-313 (1977).

[10] C. LICHT : *Etude theorique et numérique de l'évolution d'un système fluide-flotteur.* Thèse de D.I., Nantes (1980).

[11] M. LENOIR, A. JAMI : *A variational formulation for exterior problems in linear hydrodynamics.* Comp. Meth. in Applied Mech. and Engineering. Vol. 16, p. 341-359 (1978).

[12] B. HANOUZET : *Espaces de Sobolev avec poids ; application au problème de Dirichlet dans un demi-espace.* Rend. della Sem. Math. della Univ. Padova, vol. 46, p. 227-272 (1971).

[13] J.C. NEDELEC : *Approximation des équations intégrales en mécanique et en physique.* Cours de l'école d'été d'analyse numérique E.D.F. - I.R.I.A.-C.E.A. (1977)

[14] F. RIESZ, B. NAGY : *Functional Analysis,* New-York, Interscience Publishers, Inc. (1955)

[15] N. DUNFORD, J. SCHWARTZ : *Linear operators* New-York, Interscience Publishers, Inc.(1957)

[16] A. FINKELSTEIN : *The initial value problem for transient water waves.* Comm. on Pure and Applied Math. vol. 10, p. 511-522 (1957).

[17] N. DAOUD : *Potential flow near to a fine ship's bow.* Report N° 177, Dep. of Naval Arch. and Marine Eng. Univ. of Michigan (1975).

[18] M. ABRAMOVITZ, I. STEGUN : *Handbook of Mathematical Functions.* Dover Publications Inc., New-York (1970).

[19] L. HALPERN : *Etude de conditions aux limites absorbantes pour des schémas numériques relatifs à des équations hyperboliques linéaires.* Thèse de troisième cycle, Univ. Paris VI (Sept.1980).

[20] HAJDA, B. ENQUIST : *Absorbing boundary conditions for the numerical simulation of waves.* Math. of computation, vol.31, N° 139, p. 629-651. (1977).

[21] D. EUVRARD, A. JAMI, M. LENOIR, D. MARTIN *Recent progress towards an optimal coupling of finite elements and singularity distribution procedures in numerical ship hydrodynamics.* Third International Conference on Num. Ship. Hydrod. Paris (1981)

[22] A. JAMI, M. LENOIR : *Formulation variationnelle pour le couplage entre une méthode d'éléments finis et une représentation intégrale.* Comptes-rendus à l'Acad. des Sciences, Paris, vol. 285, A, (1978).

[23] A. JAMI : *Résolution numérique des problèmes de Helmholtz extérieurs par couplage entre éléments finis et représentation intégrale.* Comptes Rendus à l'Acad. des Sciences. Paris. Vol. 287, A, (1978).

[24] A. JAMI, M. POLYZAKIS : *A finite element solution of diffraction problems in unbounded domain.* Computer Methods in Applied Mech. and Eng. (to appear).

[25] M. LENOIR : *Error estimates for the coupling of finite elements and an integral representation, application to the linearized sea-keeping problem* (to appear).

[26] P. CIARLET : *The finite element method for elliptic problems, studies in Math. and its applications,* vol. 4, North Holland pub. comp. (1978).

[27] J.P. AUBIN : *Approximation of elliptic boundary-value problems.* Pure and Applied Math., vol. 26, Wiley Intersc. (1972).

TIME-DEPENDENT BEHAVIOUR OF FLOATING BODIES

Christian Licht
Institut Français du Pétrole
Direction Recherche Génie Maritime Pétrolier
1 et 4, avenue du Bois-Préau, 92500 Rueil Malmaison (France)

Abstract

Transient motions of floating bodies near equilibrium in an open sea have been treated by several methods. Here we propose a new efficient technique which results from an investigation of the theoretical linear problem using functional analysis.

This method (2D & 3D) uses, in fact, an implicit time discretisation of the equations, a truncation of the fluid domain with an absorbing boundary condition and finite elements in the truncated domain.

2D numerical results are discussed.

I. Introduction

It is only recently that the problem of the small transient motions of floating bodies has been solved by Beale (cf [2]) in a mathematically rigourous way. In view of the practical applications we complete his model by including external forces on the body, variable pressure on the sea surface and small motions on a part of the bottom of the sea (tsunamis).

If we consider the space $\mathcal{H}$ of the possible states u with finite energy of the system fluid-body, the problem can be expressed in the form of a linear evolution equation in $\mathcal{H}$ of the type $\frac{du}{dt} = Au + f(t)$, $u(0) = u^*$ where u^* and the function f of the time t are known.

This approach to the problem allows us to prove the convergence of our numerical method, an often disregarded view point in numerical naval hydrodynamics.

The numerical solution is available both in 2D and 3D. It is fast and easy to implement on a computer.

Finally we show and discuss results obtained with our 2D computer program.

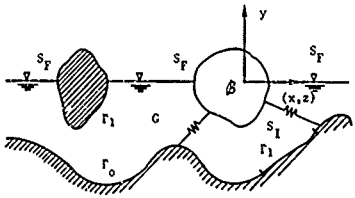
II. The theoretical problem

1. Formulation of the problem

We consider the linear problem connected with the small motions near equilibrium of a mechanical system comprising a floating body and the sea. The floating body $\mathcal{B}$ is rigid and partially or totally immersed in a heavy perfect and incompressible fluid. Effects of surface tension on the free surface are neglected. We assume the flow is irrotational.

O(x,y,z) is a right-handed coordinate system with Oy the upward vertical. G is the fluid domain at equilibrium. The boundary of G is

- S_I the immersed surface of $\mathcal{B}$ at equilibrium.
- S_F the still free surface
- Γ the bottom of the sea (eventually empty if we consider the case of infinite depth) and the middle positions of other bodies.



$\Gamma = \Gamma_o \cup \Gamma_1$

FIGURE 1

The mechanical state of the system can be described by four parameters ϕ, η, s, v :

- ϕ the potential of the flow
- η the elevation of the free surface
- s the parameters of position of $\mathcal{B}$
- v the parameters of velocity of $\mathcal{B}$

The following equations are classical (cf [6]):

$$\Delta\phi = 0 \qquad \text{in } G \tag{1}$$

$$\phi_t = -g\eta - \frac{p_o}{\rho} \qquad \text{on } S_F \tag{2}$$

ρ is the density of the fluid, g the gravitation acceleration and $p_o(x, z, t)$ is the atmospheric pressure.

$$\eta_t = \partial_n\phi \qquad \text{on } S_F \tag{3}$$

$$\partial_n\phi = v.p \qquad \text{on } S_I \tag{4}$$

p_i, $i = 1,3$, are the components of the normal $\vec{n}(M)$ pointing out of the fluid; p_i, $i = 4,6$, are the components of $\vec{OM} \wedge \vec{n}$ if ω is the inertial center of $\mathcal{B}$ in its equilibrium position.

$$Ev_t = -Ks - \int_{S_I} \phi_t p + F \tag{5}$$

ρE is the inertial matrix of $\mathcal{B}$, K is a symmetric matrix connected with hydrostatic and anchoring restoring force. ρF are other possible external force and moment applied to the body.

In order to include in this model a tsunami or the waves due to small motion of other bodies (for instance wave-maker), we split up Γ in two parts Γ_0 and Γ_1, and ϕ has to satisfy :

$$\partial_n\phi = 0 \qquad \text{on } \Gamma_0 \tag{6}$$

$$\partial_n\phi = \beta \qquad \text{on } \Gamma_1 \tag{7}$$

where β is a function of the time and of the position on Γ_1.

If p_o, F, b and the initial state u^o are given the problem (P) is to determine the state $u(t) = (\phi, \eta, s, v)$ at every instant.

2. Resolution of the problem (P)

Let us recall that the existence and the uniqueness of a generalized solution was obtained by Beale (cf [2]) when

i) the depth is finite

ii) K is definite - positive

iii) there are no excitations (i.e. $F \equiv 0$, $p_o \equiv 0$, $\beta \equiv 0$).

The mechanical energy of the system body-sea is proportional to :

$$\int_G |\nabla\phi|^2 + g\int_{S_F} \eta^2 + Ev.v + Ks.s \tag{8}$$

This expression defines the square of a Hilbert-norm on a space $\mathcal{H}$ of possible states with finite energy. The element $u = (\phi, \eta, s, v)$ satisfies in some sense (1), (4) and $\partial_n\phi = 0$ in Γ.

The homogenous problem connected with (1)-(7) can be expressed in the (weak) form of a linear evolution equation in $\mathcal{H}$ of the type :

$$\begin{cases} \dfrac{du}{dt} = Au \\ u(0) = u^* \end{cases} \tag{9}$$

A is a linear operator with domain $D(A)$ in $\mathcal{H}$. Its expression is constructed from the following notions.

If Ω is an open set of $\mathbb{R}^3$ we note by $L^2(\Omega)$ the space of mesurable functions for which the second power is integrable and by $H^1(\Omega)$ the Sobolev space of functions of $L^2(\Omega)$ for which all the first distributional derivatives are in $L^2(\Omega)$.

a) h_i, $i = 1,6$, is the unique solution in $H^1(G)$ of

$$\Delta h_i = 0 \qquad \text{in } G \tag{10}$$

$$h_i = 0 \qquad \text{on } S_F \tag{11}$$

$$\partial_n h_i = p_i \qquad \text{on } S_I \tag{12}$$

$$\partial_n h_i = 0 \qquad \text{on } \Gamma \tag{13}$$

b) H is the symmetric non-negative matrix :

$$H_{ij} = \int_{S_I} h_i p_j \tag{14}$$

c) B is the operator which associates to η ($\in L^2(S_F)$) the possible solution Ψ in $H^1(G)$ of the following problem :

$$\Delta\Psi = 0 \qquad G \qquad (15)$$

$$\Psi = \eta \qquad S_F \qquad (16)$$

$$\partial_n \Psi = 0 \qquad S_I \cup \Gamma \qquad (17)$$

Then, the components of Au in $\mathcal{H}$ are :

$$(Au)_4 = (E + H)^{-1} \left\{ - Ks + \int_{S_I} g\, Bn\, p \right\} \qquad (18)$$

$$(Au)_1 = - g\, Bn + (Au)_4 .h \qquad (19)$$

$$(Au)_2 = \partial_n \phi |_{S_F} \qquad (20)$$

$$(Au)_3 = v \qquad (21)$$

A is skew-adjoint, thus it is the infinitesimal generator of a continuous unitary group U(t) of operators on $\mathcal{H}$ and if $u_o \in D(A)$, (9) has a unique solution :

$$u(t) = U(t)\, u^o \qquad (22)$$

It is clear from this expression that the energy is conserved and that the evolution is time-reversible.

We can (cf [4]) adapt this method in order to take into account excitations of the system body-sea. We proceed to a decomposition of u into two parts :

$$u(t) = u_1(t) + (\phi_0(t),\ 0,0,0) \qquad (23)$$

ϕ_0 is, if $\beta \in L^2(\Gamma_1)$, the unique solution in $H^1(G)$ of :

$$\Delta\phi_0 = 0 \qquad G \qquad (24)$$

$$\partial_n \phi_0 + \phi_0 = 0 \qquad S_F \qquad (25)$$

$$\partial_n \phi_0 = 0 \qquad \Gamma_0 \cup S_I \qquad (26)$$

$$\partial_n \phi_0 = \beta \qquad \Gamma_1 \qquad (27)$$

The regularity of $t \to \phi_0(t) \in H^1(G)$ is that of $t \to \beta(t) \in L^2(\Gamma_1)$. So u_1 is an element of $\mathcal{H}$ and the equations to be satisfied by u_1 can be formulated in a weak form by :

$$\frac{du_1}{dt} = Au_1 + f_1(t) \qquad (28)$$

f_1 is the following element of $\mathcal{H}$:

$$f_1 = (- B\phi_{ot} - \frac{1}{\rho} BP_o + z.h, - \phi_o,\ 0,\ z)$$

$$z = (E+H)^{-1} \left\{ \int_{S_I} (B\phi_{ot} + \frac{1}{\rho} BP_o - \phi_{ot})P + F \right\} \qquad (29)$$

Using well known facts about the theory of semi-groups of linear operators, we can give sufficient conditions on u^1, β, P and F in order that (28) has a unique solution:

$$u_1(t) = U(t)u_1(o) + \int_o^t U(t-\tau) f_1(\tau) d\tau \qquad (30)$$

Consequently we can prove the existence and the uniqueness of a weak solution of problem (P).

At last we can (cf [4]) proceed to a study about regularity of this weak solution and give sufficient conditions in order that equations (1) - (7) are satisfied in a classical sense except in the vicinity of ∂S_F.

The previous method uses the fact that K is positive - definite, we can (cf [4]) disregard this and so obtain rigorously a necessary and sufficient condition of stability of an equilibrium position. This condition is the classical static condition.

If we replace $H^1(G)$ by the closure of the set of regular functions on $\bar{G}$ with the norme $\int_G |\nabla \Psi|^2 + \int_{S_F} \Psi^2$ we can obtain the same results if the depth of the fluid is infinite.

We also can consider the case where the anchoring restoring force and moment are a nonnecessary linear function Ψ of the displacement s. The problem is reduced to a non linear evolution equation in $\mathcal{H}$:

$$\frac{du}{dt} = Au + F(u) + f(t) \qquad (31)$$

For instance if Ψ is lipschitz-continuous in s (thus F is lipschitz continuous in u) we can conclude the existence and the uniqueness of a solution of (31) with the same conditions as previously.

Finally it is possible to include in ϕ an incident known potential with not necessarily finite energy.

III. Numerical analysis of the problem

1. Presentation of a method

With our formulation of the continuous problem, the numerical resolution reduces, then, to the approximation of an evolution equation in an Hilbert space. Because of the properties of A, it is well-known that the implicit time-discretisation scheme

$$\frac{u^{k+1}-u^k}{\Delta t} = A\,u^{k+1} + f^k \quad k=0,1,..m-1 \tag{32}$$

is uniformly convergent on the interval of study $[0,T]$. f^k is a suitable approximation of $f(k\Delta t)$, u^k is the approximation of $u(k\Delta t)$, Δt is the time step : $\Delta t = \frac{T}{m}$. It is very easy to obtain the state u^{k+1} from (32); we note $u^{k+1} = (\phi^{k+1}, \eta^{k+1}, s^{k+1}, v^{k+1})$, so we have :

a) Ψ is the solution in $H^1(G)$ of the elliptic problem

$$\left.\begin{aligned} &\Delta\Psi = 0 && \text{in } G\\ &\partial_n\Psi + \frac{1}{g(\Delta t)^2}\,\Psi = \\ &-\frac{1}{g\Delta t^2}\left(\phi^k - g\,\Delta t\,\eta^k - \Delta t\,\frac{P_0(k\Delta t)}{\rho}\right) && \text{on } S_F\\ &\partial_n\Psi = 0 && \text{in } S_I \cup \Gamma_0\\ &\partial_n\Psi = \delta\left((k+1)\,\Delta t\right) && \text{in } \Gamma_1 \end{aligned}\right\} \tag{33}$$

b) h'_i, i=1,6, is the solution in $H^1(G)$ of:

$$\left.\begin{aligned} &\Delta h'_i = 0 && \text{in } G\\ &\partial_n h'_i + \frac{1}{g(\Delta t)^2}\,h'_i = 0 && \text{on } S_F\\ &\partial_n h'_i = P_i && \text{on } S_I\\ &\partial_n h'_i = 0 && \text{on } \Gamma \end{aligned}\right\} \tag{34}$$

c) H' is the symmetric non-negative matrix

$$H'_{ij} = \int_{S_I} h'_i\,P_j \tag{35}$$

d)

$$\left[E + H' + (\Delta t)^2 K\right] v^{k+1} =$$

$$= Ev^k - \Delta t\,Ks^k + \Delta t\,F(k\Delta t) + \int_{S_I}(\phi^k - \Psi)P \tag{36}$$

e) $$\phi^{k+1} = \Psi + v^{k+1}.\,h' \tag{37}$$

f) $$s^{k+1} = s^k + \Delta t\,v^{k+1} \tag{38}$$

g)

$$\eta^{k+1} = -\frac{1}{g\Delta t}(\phi^{k+1} - \phi^k)\Big|_{S_F} - \frac{1}{\rho g}P_0\,(k\Delta t) \tag{39}$$

These formulae are nothing of course but an implicit discretisation of (1) - (7).

In practical terms the best we can do is to construct an approximation of the u^k. We build simultaneously a sequence of spaces F_q and operators A_q intented to approach $\mathcal{H}$ and A (cf [4]). This process takes into account the two difficulties in view of an immediate use of (33) - (39) : firstly truncation of the fluid-domain, secondly use of finite elements.

For a sufficiently large n, we note G(n), $S_F(n)$, $\Gamma_0(n)$ the troncature of G, S_F, Γ_0 by the vertical planes $|x| = n$, $|z| = n$. S(n) is the surface of truncation (i.e. $G \cap \{|x| = n \text{ or } |z| = n\}$).

We consider the problem (P_n) posed in G(n) with the same equations than the problem (P). At S(n) we impose to ϕ a supplementary condition in order that (P_n) is well-posed. We retain :

$$\left.\begin{aligned} &\text{i)} \quad \phi = 0 && S(n)\\ &\text{ii)} \quad \partial_n\phi = 0 && S(n)\\ &\text{iii)} \quad \phi_t + \nu\,\partial_n\phi = 0 \quad \nu>0 && S(n) \end{aligned}\right\} \tag{40}$$

All these conditions have obvious physical interpretations.

As in II.2, each of these problems can be expressed in the form of a linear evolution equation

$$\frac{du_n}{dt} = A_n u_n + f_n\,(t) \tag{41}$$

in a Hilbert Space $\mathcal{H}_n$. $\mathcal{H}_n$ is the space of the possible states with finite energy of a system "body-fluid in a bounded domain". Such an element $u_n = (\phi_n, \eta_n, s_n, v_n)$ verifies in a certain sense :

$\Delta\phi_n = 0$ in G(n), $\partial_n\phi_n = v_n \cdot p$ at S_I, $\partial_n\phi_n = 0$ on $\Gamma_0(n)$

and $\phi_n = 0$ on S(n) in the case i) or $\partial_n\phi_n = 0$ at S(n) in the case ii).

The operator A_n is again the infinitesimal generator of a semi-group and (41) has a unique solution for sufficiently regular data. In order to prove the convergence when $n \to \infty$, we use the theory of Trotter on approximation of semi-groups with variable spaces (cf [5]). Indeed because of the conditions used to define $\mathcal{H}$, the $\mathcal{H}_n$ cannot be subspaces of $\mathcal{H}$. The key step is to prove the convergence of the resolvant of A_n (i.e. $(I - \Delta t\, A_n)^{-1}$) in a certain topology. The formulae which give $(I - \Delta t\, A_n)^{-1} f_n$ are analogous to (33) - (39). The elliptic problems (33) and (34) are this time posed in G(n) with a condition at S(n). The convergence of the solutions of these problems results from an argument of continuous dependence as a function of the domain. Thus we can prove the convergence in energy of the solution of (P_n) with suitable initial data towards the solution of (P).

Next we proceed to the discretisation of $\mathcal{H}_n$ by use of finite elements in G(n) and build an operator A_n^h in $\mathcal{H}_n^h$. This technique works well because the definitions of $\mathcal{H}$ ($\mathcal{H}_n$) and A (A_n) can be expressed in variational form. In particular the convergence of the resolvants is a simple consequence of properties of the conforming finite elements method for solving elliptic problems. Finally by using implicit scheme in $\mathcal{H}_n^h$ we can define an effective numerical method whose convergence is thus proved when first $n \to \infty$ and next Δt and the spatial discretisation parameter h tend independently to 0. It is noticeable that in this step we can obtain an error estimation.

2. The algorithm

a) Preliminary calculus :

- approximation $(h'_j)_h$ by finite elements of ${}_nh'_j$ solution of :

$$\left.\begin{array}{ll} \Delta\, {}_nh'_j = 0 & G(n) \\ \partial_n\, {}_nh'_j + \dfrac{1}{g(\Delta t)^2}\, {}_nh'_j = 0 & S_F(n) \\ \partial_n\, {}_nh'_j = P_j & S_I \end{array}\right\} \quad (43)$$

$$\partial_n\, {}_nh'_j = 0 \qquad \Gamma(n)$$

$$\partial_n\, {}_nh'_j + \frac{1}{\nu\, \Delta t}\, {}_nh'_j = 0 \qquad S(n)$$

$$\nu \begin{cases} 0 & \text{Dirichlet condition (case i))} \\ > 0 & \text{absorption condition (case iii))} \\ \infty & \text{Neumann condition case ii))} \end{cases}$$

- factorisation of M

$$(H'_{ij})_h = \int_{S_I} (h'_i)_h\, P_j$$

$$M = E + H'_h + \Delta t^2\, K \qquad (43)$$

b) Initialisation

c) The m steps

$$u^k \to u^{k+1} \qquad k = 0,1 \ldots m-1$$

$$u^k = (\phi^k, \eta^k, s^k, v^k)$$

- approximation Ψ_h of Ψ solution of :

$$\left.\begin{array}{ll} \Delta\Psi = 0 & G(n) \\ \partial_n\Psi + \dfrac{1}{g\,\Delta t^2}\Psi = & \\ = \dfrac{1}{g\Delta t^2}(\phi^k - g\,\Delta t\,\eta^k - \dfrac{\Delta t}{\rho}\, p_0(k\,\Delta t)) & S_F(n) \\ \partial_n\Psi = 0 & S_I \cup \Gamma_0(n) \\ \partial_n\Psi = \beta((k+1)\,\Delta t) & \Gamma_1 \\ \partial_n\Psi + \dfrac{1}{\nu\,\Delta t}\Psi = \dfrac{1}{\nu\,\Delta t}\,\phi^k & S(n) \end{array}\right\} \quad (44)$$

- calculous of u^{k+1} :

$$\left.\begin{array}{l} v^{k+1} = M^{-1}\left\{Ev^k - \Delta t\, Ks^k + \Delta t\, F(k\Delta t) + \right. \\ \qquad \left. + \displaystyle\int_{S_I} (\phi^k - \Psi_h)\, \Gamma\right\} \\ \phi^{k+1} = \Psi_h + v^{k+1} \cdot (h')_h \\ s^{k+1} = s^k + \Delta t\, v^{k+1} \\ \eta^{k+1} = -\dfrac{1}{g\,\Delta t}(\phi^{k+1} - \phi^k)\Big|_{S_F(n)} - \dfrac{1}{\rho g} P_0(k\,\Delta t)\Big|_{S_F(n)} \end{array}\right\} \quad (45)$$

The computer implementation of this algorithm is easy. Our principal need is a finite element routine. At any step the symmetric matrix corresponding to (44) is the same, so once for all it is factorized by the Cholesky's method. Thus at each step the second member is calculated by combining informations stored only at the previous step. Therefore this method is fast and the required storage is essentially that of the "rigidity matrix".

3. Some remarks

The expression of $(I+\mu A)(I-\lambda A)^{-1} f$ ($f \in D(A)$; $\lambda, \mu > 0$) is also very simple (as obviously are the expressions for the approximating operators) so we can improve the time discretisation by use of a scheme of Crank-Nicholson.

It seems also possible to reduce the fluid-domain of calculus by using quasi localized finite element (cf [4]): i.e. finite elements in G(R) and harmonic functions in $G \setminus G(R)$ with vanishing normal derivatives on $\Gamma_0 \setminus \Gamma(R)$.

If anchoring is not linear we can determine u^{k+1} at each step by an iterative process.

IV. Numerical Results and Comments

The present method is available both in 2.D and 3.D. For convenience sake alone, we have written a 2D computer program.

Yet we have not obtained an error estimation as a function of the distance of truncation. If an interval $[0,T]$ of study is given, it is advisable to effect several runs until stability of the results is obtained (which is guaranteed by our proof of convergence). Now we show some heuristical considerations concerning the choice of the distance of truncation. We assume there are no excitations and that the depth is finite and equal to d. In the simple case of pure gravity waves (i.e. the body is absent) it is known (cf [6]) that a front of surface waves is outgoing pratically with a finite velocity $C = (gd)^{1/2}$. We have numerically verified this fact in the presence of a freely floating body by simulating the transient vertical motion of a cylinder with its rectangular section half-immersed at equilibrium. At t=0 the fluid is at rest and the body is kept without velocity from y_0 about static equilibrium. The figure 2 shows the evolution of the right part of the free surface. The Figure 3 shows the evolution of the free surface in some points M_i. In particular we can observe that $\frac{X_i^{-2}}{t_i} \simeq C$. So we can expect that a study on $[0,T]$ needs a troncation at a distance of CT of the support of the initial data.

In the cases of conservative approximation (ie Dirichlet or Neumann condition) energy stays in the truncated domain. After the instant when the front of surface waves reaches the surface of truncation, waves are reflected so we have not a good approximation of the transient motion in an unbounded domain for which energy goes to 0 generally (cf [2]). On the contrary in the case of dissipative approximation ($\phi_t + \nu\, \partial_n \phi = 0$ on $S(n)$), energy decays and the reflection of waves is reduced. Here remains to be found an optimal parameter ν. Figure 4 shows, step by step, the energy-norm of the discretised truncated system - the system and the initial state is the same as previously, the surface of truncation is 20m away from the center of the body. We note that it is when ν is close to C(≃ 7m/s in this example) that the dissipation is maximal. Moreover dissipation takes place after a time θ near of $\frac{20-2}{7}$ s. Figure 5 shows the vertical motion of the body. Previously we used truncations at farther distances and so we possess a good approximation for the first 8s of the motion in the open sea. We notice that at $\nu \simeq C$ gives the result. Before θ all the conditions give coherent results, after θ reflections are different. We have very often noticed that a good choice of ν ($\nu \simeq C$) allows us to divide by two or three the distance of truncation with regard to Dirichlet's or Neumann's approximations. In the same way we can extend in these proportions the time interval of validity of the approximation with a selected truncation. These results are not too surprising and it seems not too hard to justify them in the case of pure gravity waves.

Now we compare our results with those of [1] and [3]. In [3] a Fourier-Laplace transform with respect to time is used. [1] makes use of a transient Green's function and of integro-differential equations, moreover it contains experimental data. These two results deal with infinite depth. At the beginning, our study was undertaken with offshore-engineering in mind, resulting the primarly treatment of the case of finite depth; but the method is available with infinite depth: it suffices to use fictious deeper and deeper bottoms. Nevertheless our finite elements subroutine is conceived more for middle depths (d < 20a; a= caracteristic length of the body), beyond these the mesh should be too loose... Figure 6 shows the heave motion of a half immersed circular cylinder, we used d=10R. We observe a good agreement between numerical and experimental results.

Figures 7,8,9 show numerical results obtained by our computer program with various initial conditions. As in [1] we notice a low damping in the case of roll motion.

Finally we discuss the required computer-time. This time is subordinate to the number of nodes in the mesh and to the number of steps :

1) 130 nodes :
preparing the calculations ≃0,113s; one step ≃ 4.10^{-3}s.

2) 750 nodes :
preparing the calculations ≃0,867s; one step ≃ 0.033s. The computer is a CDC 7600 (C.I.S.I Rueil Malmaison).

It is important to recall that, as our program is a study tool, several extra calculations are done for the purpose of verifying some interesting facts (energy decay, propagation of waves, etc...).

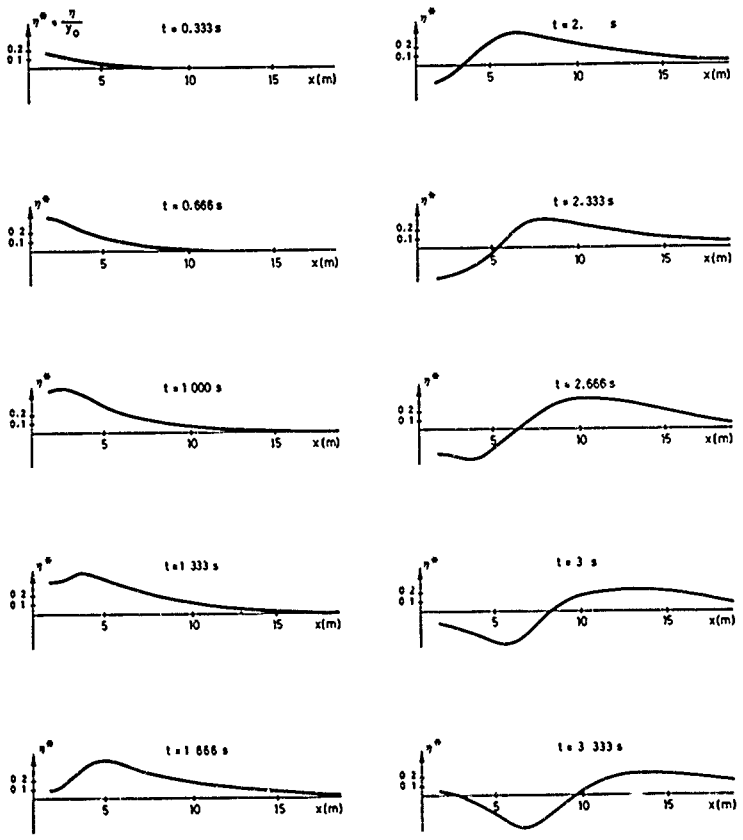


Figure 2 - FREE SURFACE PROFILE

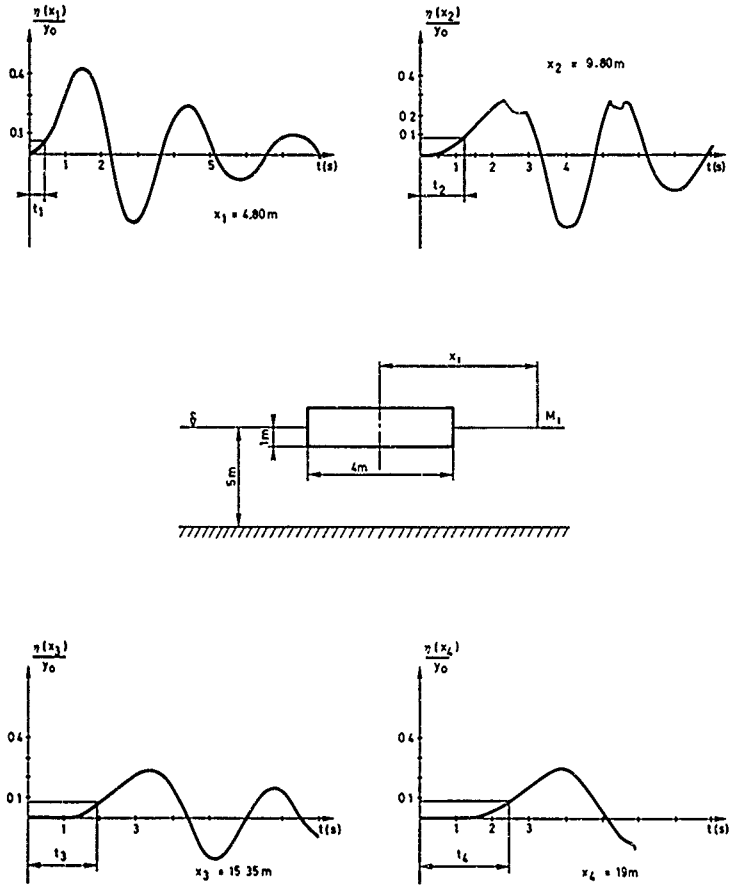


Figure 3 - FREE SURFACE ELEVATION IN SOME POINTS

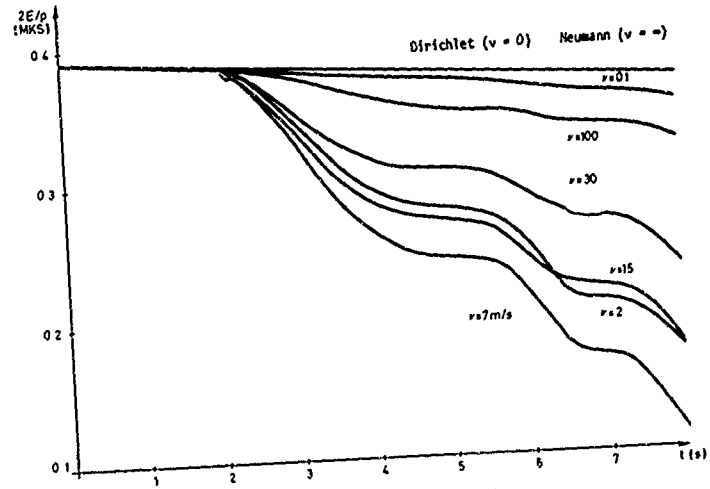


Figure 4 - ENERGY OF THE SYSTEM ($\phi_t + v\,\partial_n \phi$ = 0-20m away)

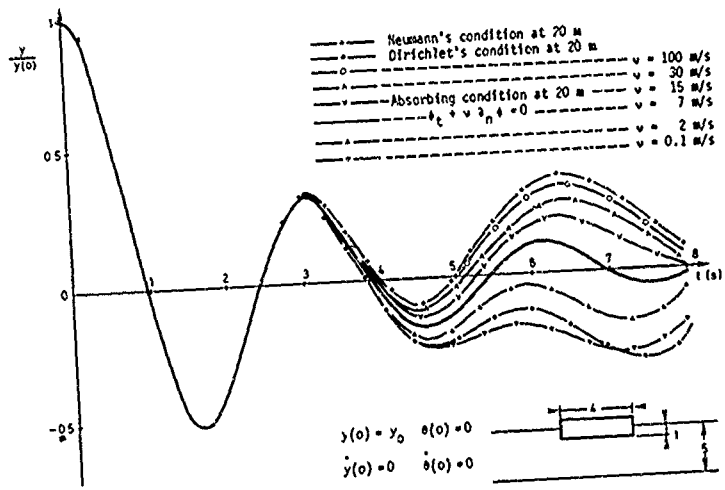


Figure 5 - BOUNDARY CONDITION INFLUENCE

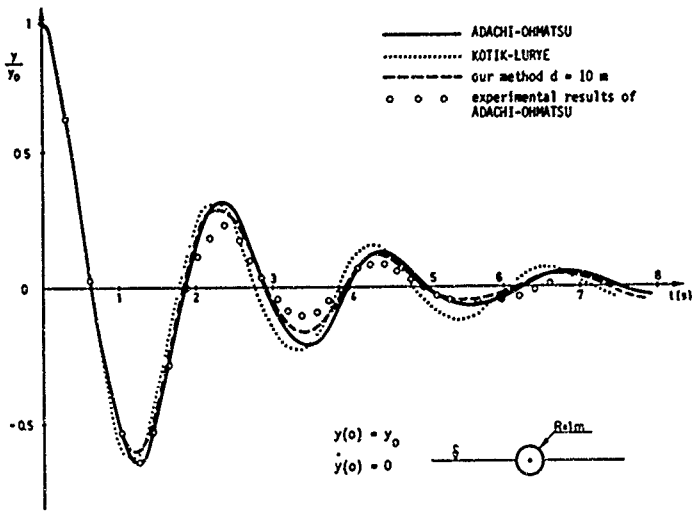


Figure 6 - HEAVE MOTION

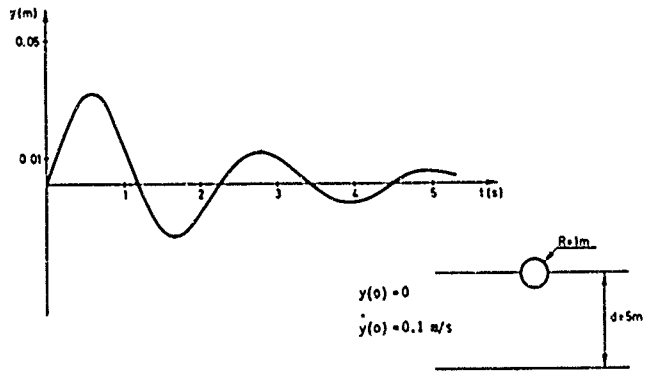
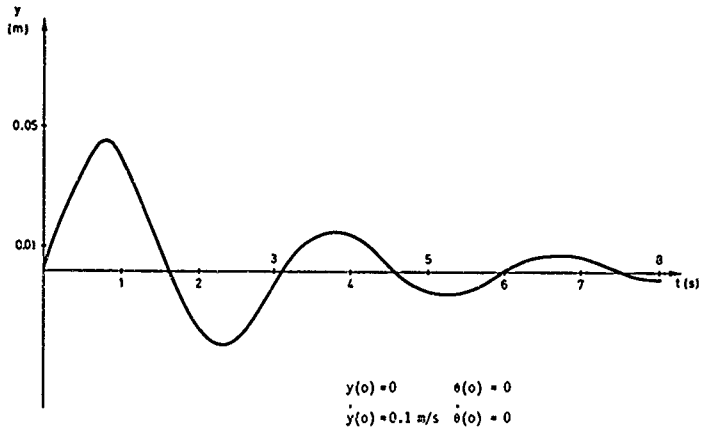


Figure 7 - HEAVE MOTION CIRCULAR CYLINDER



$y(o) = 0 \qquad \theta(o) = 0$

$\dot{y}(o) = 0.1$ m/s $\quad \dot{\theta}(o) = 0$

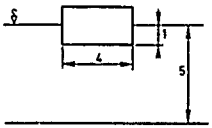
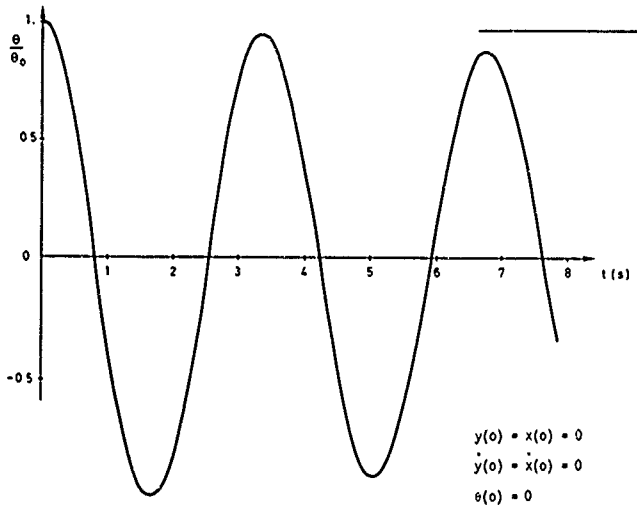


Figure 8 - HEAVE MOTION RECTANGULAR CYLINDER



$y(o) = x(o) = 0$

$\dot{y}(o) = \dot{x}(o) = 0$

$\theta(o) = 0$

$\dot{\theta}(o) = 0$

Figure 9 - ROLL MOTION RECTANGULAR CYLINDER

V. Conclusions

This paper shows the advantage in introducing functional analysis methods to naval hydrodynamics. The important questions of existence, unicity and regularity of the solutions can be solved quite easily. Moreover it permits the building of convergent numerical approximations.

Our method allows us to treat the most general linear problem connected with small transient motions of floating bodies. In particular we can consider a totally arbitrary shape of the fluid domain.

Implementation of this method is very easy. The computing times are reasonable and the use of an appropriate absorbing boundary condition allows to reduce the domain of computation and consequently the central-core memory space :

It should be interesting to develop even more efficient absorbing boundary conditions.

Aknowledgments

For this work the author benefitted from a research fellow ship with the Institut Français du Pétrole and he wishes to thank the Direction Recherche génie maritime pétrolier.

References

[1] Adachi-Ohmatsu : "On the time-dependent potential and its application to wave problem". 13th O.N.R. Symposium; 1980.

[2] Beale J.T. :"Eigenfunction expansion for object floating on an open sea". Communication on pure and applied math. vol XXX; 1977.

[3] Kotik-Lurye : "Heave oscillations of a floating cylinder or sphere". Schiffstechnik, Band 15 Heft 76; 1968.

[4] Licht . "Etude théorique et numérique de l'évolution d'un système fluide-flotteur". Thèse docteur-ingénieur, Nantes ;1980.

[5] Trotter : "Approximation of semi groups of operators". Pacific journal of mathematics; 1958.

[6] Wehausen-Laitone : "Surface waves". Handbuch der Physik, band IX; Springler Verlag; 1960.

DISCUSSION
of the paper
by C. Licht

TIME-DEPENDENT BEHAVIOUR OF FLOATING BODIES

Discussion
by F. Ursell

It may be interesting to add some remarks about the method used by Maskell and Ursell (1970) to determine the transient heaving motion of a half-immersed circular cylinder of radius a. It is well known that at any fixed real frequency $u(g/a)^{1/2}$ the resultant force exerted by the fluid on the cylinder is described by a complex-valued force coefficient $\Lambda(u)$ (equivalent to the virtual-mass and damping coefficients at that frequency). Then for an initial displacement the subsequent motion is described by the integral

$$h_2(\tau) = -\frac{1}{8} i \int_{-\infty}^{\infty} \frac{u(1 + \Lambda(u))e^{-iu\tau}du}{1 - \frac{1}{4}\pi u^2(1 + \Lambda(u))} , \qquad (A)$$

which is obtained by resolving the transient motion into its Fourier components. This involves $\Lambda(u)$ which must be obtained for every frequency by solving an integral equation or an infinite system of linear equations but note that we do not need to know the motion in the interior of the fluid.

The integrand in (A) is however oscillatory and tends to zero only slowly (like u^{-1}) when $u \to \infty$, and a direct evaluation of the integral is thus inconvenient. The path of integration was therefore deformed in the complex u-plane. Large damped harmonic contributions were found from 2 complex poles, and these could be found very accurately. The remaining contour integral could be made more rapidly convergent by using the known asymptotic properties of $\Lambda(u)$ when $u \to \infty$ in the complex plane and also involved the evaluation of $\Lambda(u)$ for complex frequencies.

Reference

S.J. Maskell and F. Ursell 1970, The transient motion of a floating body. J. Fluid Mech. 44, 303-313.

Author's reply

I thank Prof. Ursell for his comments. In the aforementioned paper it is shown that the heave motion $h_2(\tau)$ is the sum of a "polar component" (damped harmonic motion) and an (non oscillating) "integral component" $\hat{h}_2(\tau)$. The difference between h_2 and $\hat{h}_2$ is sensible at small and large τ, but for these last values h_2 is neglectible. So we can deduce a good approximation for h_2 from the study of the motion only during a small interval of time ; in this case our method gives a good result, by using a reasonable fluid-domain of calculus , for both the motion of the floating body and the fluid motion.

Session IV

TRANSIENT AND NONLINEAR SOLUTIONS TO BODY-WAVE AND WATER-WAVE PROBLEM

R. Whitehead
Session Chairman
Office of Naval Research
U.S.A.

TIME-DOMAIN METHOD FOR COMPUTING FORCES AND MOMENTS ACTING ON THREE-DIMENSIONAL SURFACE-PIERCING SHIP HULLS WITH FORWARD SPEED

Richard B Chapman
Science Applications, Inc.
La Jolla, California

Abstract

A time-domain simulation method for computing forces and moments acting on an arbitrary surface-piercing three-dimensional ship hull is presented. Arbitrary motions can be prescribed and are assumed to be sufficiently small so that the linearized method is valid. Forward speed effects are included under the assumption that the disturbance generated by forward motion is also small and interactions with the flow generated by the prescribed motions are of second order. The hull is represented by a set of quadrilateral surface panels in a body-fixed system, while the free surface is represented by its spectral coordinates in a space-fixed rectangular system. Small time steps are used to advance the flow. This time-domain computation can also be applied to compute linearized seakeeping responses in the frequency domain. For each degree of freedom, added mass and damping forces can be obtained from the time history of the force and moment resulting from a step function applied to the velocity. Wave-excited forces can be computed by a similar method. For a coarse representation of the hull and free surface, the computed heave added mass and damping for a semi-submerged sphere show good agreement with analytic results.

I. Introduction

This report describes a computational method designed to simulate arbitrary linearized motions of a surface-piercing three-dimensional ship hull in the time domain. The hull is specified by a set of quadralateral surface panels describing the hull portion directly beneath the static waterline. The numerical method calculates the forces and moments generated by arbitrary motions of the body and/or the action of an ambient wave field acting on the body under the assumption that the flow velocities can be linearized.

The method may be classified as a time-domain computation analogous to the frequency-domain methods developed by Chang (1) for three-dimensional ship hulls. The time-domain method is the more fundamentally numerical approach to this class of problems. The time-domain method does not use Green's functions representing solutions of the free-surface equations for singularities following prescribed conditions (i.e., moving with uniform speed and oscillating as in reference (1)). Thus the time domain method provides the flexibility of arbitrary motions. It can easily be generalized to include a time-dependent hull shape or other generalized features.

Limitations on computer times and storage do not, however, allow this "brute force" type method to serve as a practical tool in three dimensions at the present time. With continued improvements in computer technology, however, methods of this nature may, in the near future, be explored for practical applications. It is hoped that the techniques described here will provide a framework for later work of this nature.

A basic objective in the development of the computational method was to establish the method in as simple a form as possible. The resulting numerical technique described in following sections of this report, is a generalization of the two-dimensional method applied in reference [2], expanded to three dimensions with some improvements in the numerical method. Another objective was to examine the possible problem areas such as the free surface area interior to the hull and pressure computations. These areas are also discussed in this report. Direct application to linearized seakeeping computations is discussed. Finally a sample problem - heave oscillations of a semisubmerged sphere - is presented.

Problem Formulation

Consider a coordinate system (x, y, z, t) with z positive downward and z = 0 at the static waterline. Far from the origin the flow is at rest. This space-fixed coordinate system is the basis for describing the fluid flow in general and the free surface in particular. The velocity potential $\phi(\vec{x}, t)$ satisfies Laplaces equation throughout the fluid.

$$\nabla^2 \phi = 0 \qquad z > 0$$

The free surface elevation field $\eta(x, y, t)$ and its time derivative $\dot{\eta}(x, y, t)$ are defined over the entire plane z = 0. Their values at any time provide sufficient initial conditions to define the free surface problem. Exterior to the intersection of the hull surface the elevation field satisfies the dynamic and kinematic free surface conditions

$$\frac{\partial \phi}{\partial t} = -g\eta$$

and

$$\frac{\partial \phi}{\partial z} = -\frac{\partial \eta}{\partial t}$$

On the free surfaces interior to the hull any condition could be applied. In this case, however, we assume that the above linearized

equations apply over the entire $z = 0$ plane. An arbitrary surface-piercing hull is defined by the surface,

$$F(x, y, z, t) = 0 \qquad z > 0,$$

with the exciting normal velocity v_n induced by body motions or interactions with the ambient wave field prescribed on the surface of the hull,

$$v_n(\vec{x}, t) = \vec{v}^*(\vec{x}, t)\cdot\vec{n}, \ \vec{x} \in S_{hull} .$$

(In practice the normal acceleration is specified rather than the velocity.) The disturbance generated by the body motion is divided into two parts

$$\phi = \phi_{BD} + \phi_{FS}$$

where ϕ_{BD} represents the instantaneous effect of the body, while ϕ_{FS} represents the free surface disturbance generated by the body over all previous motions or interactions with the ambient wave field. In particular the boundary conditions at the free surface ($z = 0$) are

$$\phi_{BD} = 0 \qquad z = 0$$

$$\frac{\partial \phi_{FS}}{\partial t} = -g\eta \qquad z = 0$$

and on the body,

$$\frac{\partial}{\partial n}(\phi_{BD} + \phi_{FS}) = \vec{v}^*\cdot\vec{n} \qquad \vec{x} \in S_B$$

It is assumed that body component velocities are small, i.e.,

$$\vec{v}_{BD}(\vec{x}) = 0(\epsilon)$$

and

$$\vec{v}_{FS}(x) = 0(\epsilon) .$$

Any terms of order ϵ^2 are dropped. For example, this analysis applies to the problem of ship motion in a seaway at finite speed if it can be assumed that the flow field induced by forward motion alone and the flow field induced by the seaway acting on the ship are both small and do not interact. In this case of finite forward speed, the velocity at any point on the hull $\vec{x}$ is

$$\vec{v}^*(\vec{x}) = U\vec{e}_x + 0(\epsilon)$$

where U is the forward speed. The disturbance and resulting forces generated by forward speed alone are steady (for steady u) and are not addressed here (although this method could be easily applied). It is assumed that the velocity field generated by forward speed alone is of order ϵ.

Outline of Numerical Method

Starting from a condition of rest, the simulation is achieved by a series of small time increments. At each time step, three fundamental sets of variables - which essentially define the flow at the instant - are computed;

(a) The time rate of change of the strengths of the hull source panels in a hull-fixed system are computed from the hull acceleration boundary condition. This determines the time-derivative of the body-induced component of the flow, $\dot{\phi}_{BD}$ (as well as ϕ_{BD} through integration).

(b) The free surface elevation field $\eta(x,y)$ and its time derivative $\dot{\eta}(x,y)$ are computed by advancing the free surface by a small increment in time and adding the wave elevations generated by the hull source panels over that increment. This defines the free surface component of the flow, ϕ_{FS} and its time derivative in the space-fixed system.

(c) Pressures acting on the hull are computed separately for the free surface and body components: p_{FS}, p_{BD}. Both are computed at hull panel center points and added to yield total forces and moments.

Computation of Panel Source Strengths

The hull is represented numerically by a set of N_B quadralateral panels. Each panel is specified by the coordinates of the four corner points, a panel center point, and a normal vector. The fluid velocity at each center point in the normal direction may be written as

$$\vec{v}_{BD_i}\cdot\vec{n}_i + \vec{v}_{FS_i}\cdot\vec{n}_i = \vec{v}_i^*(t)\cdot\vec{n}_i$$

$$i = 1, 2, \ldots N_B$$

where $\vec{v}_i^*(t)$ is a prescribed forcing function depending on the motion of the hull and the ambient wave field. Since the free surface induced velocity $\vec{v}_{FS}$ is assumed to be available from the free surface representation, this equation fixes $\vec{v}_{BD_i}\cdot\vec{n}_i$ at the center point of each hull panel.

A simple source and its image is assumed to be distributed over each hull panel

$$G(x,y,z,x',y',z') = ((x-x')^2+(y-y')^2+(z-z')^2)^{-1/2} - ((x-x')^2+(y-y')^2+(z+z')^2)^{-1/2}$$

with

$$\phi_{BD}(x,y,z) = \sum_{i=1}^{N_B} \sigma_i \iint_{S_i'} G(x,y,z,x',y',z')\,dS',$$

where σ_i is the strength on the i^{th} source panel and S_i' represents the panel surface.

Consider a simple source of unit strength acting over a plane surfaces',

$$\phi(\vec{x}) = \iint dS' \frac{1}{|\vec{x}'-\vec{x}|}$$

Then it may be shown analytically that the velocity normal to the plane is identical to the solid angle occupied by the panel surface and the velocity tangential to the plane surface can be written as a line integral around the boundary of the panel. Numerical application of these results produces an array E_{ij} giving the normal velocity component at the center point of panel i induced by a uniform source distribution over panel j and its image,

$$\vec{v}_{BD_i} \cdot \vec{n}_i = \sum_{d=1}^{N_B} E_{ij}\,\sigma_j \qquad i = 1, \ldots N_B.$$

This provides a set of linearized equations which can be used to determine the source strengths σ_i. In practice, it was found that better estimates for body-induced pressures could be obtained by using the local acceleration rather than the velocity directly. The time derivative $\dot{\delta}_i$ relative to a hull fixed coordinate system[1] is computed at the beginning of each time step from

$$\sum_{d=1}^{N_B} E_{ij}\dot{\sigma}_j = \vec{a}_{BD}\cdot\vec{n}_i = a_i^*(t) - \vec{a}_{FS_i}\cdot\vec{n}_i - U\frac{\partial}{\partial x}\vec{v}_{FS_i}\cdot\vec{n}_i$$

where $\vec{a}_{FS_i}$ and $\vec{v}_{FS_i}$ are the free-surface induced acceleration and velocity (in space-fixed coordinates) at point i and $a_i^*(t)$ is the prescribed normal acceleration in hull-fixed coordinates. For example, if the body has surge acceleration $a_1(t)$, then $a_i^*(t) = a_1(t)\cdot n_{x_i}$. The source strengths at the center can be computed directly from the local velocities if desired. In practice it was found that they could be computed adequately by integrating their derivatives in time.

$$\sigma_i(t_n+\Delta t) \sim \sigma_i(t_n) + \Delta t\,\dot{\sigma}_i(t).$$

Representation of Wave Elevation Field

The representation of the wave elevation field and its time derivative by their spectral components allows the linearized free surface boundary conditions to be applied easily when adapting the free surface component of the flow. It also aids in computing free surface induced pressures and velocities on the hull. An arbitrary real continuous function $\eta(x,y)$ defined over the $z = 0$ plane can be written in the form

$$\eta(x,y) = \int_0^\infty dkx \int_{-\infty}^{\infty} dky\; A(kx,ky)e^{i(kx\cdot x + ky\cdot y)}$$

where A(kx,ky) is a complex function and the elevation $\eta(x,y)$ is taken to be the real part of the expression on the right hand side. Numerically $\eta(x,y)$ can be represented by

$$\eta(x,y) = \sum_{n=1}^{NKX}\Delta kx_n \sum_{m=1}^{NKY}\Delta ky_m \left[A_{nm}(t)e^{i(kx_n\cdot x + ky_m\cdot y)} + A^*_{nm}(t)e^{i(kx_n\cdot x - ky_m\cdot y)}\right]$$

Similarly if $\dot{\eta}(x,y)$ is defined as the time derivative of $\eta(x,y)$ due to free surface effects alone, that is the rate of change of $\eta(x,y)$ in the absence of the hull, it may be represented numerically by

$$\dot{\eta}(x,y) = \sum_{n=1}^{NKX}\Delta kx_n \sum_{m=1}^{MKY}\Delta ky_m \left[B_{nm}(t)\sigma_{nm}e^{i(kx_n\cdot x + ky_m\cdot y)} + B^*_{nm}(t)\sigma_{nm}e^{i(kx_n\cdot x - ky_m\cdot y)}\right]$$

where $\sigma_{nm} > 0$ is defined by

$$\sigma_{nm}^2 = g(kx_n^2 + ky_m^2)^{1/2}$$

Thus in the absence of the hull the time derivative of A_{nm} is given by

$$\frac{d}{dt}A_{nm}(t) = B_{nm}(t)\sigma_{nm}$$

and

$$\frac{d}{dt}A^*_{nm}(t) = B^*_{nm}(t)\sigma_{nm}$$

From the kinematic free surface condition for the free surface component alone,

$$\frac{\partial\eta}{\partial t} = -\frac{\partial\phi_{FS}}{\partial z}, \qquad z = 0$$

a special representation for the free surface potential may be derived

$$\phi_{FS}(x,y,z) = \sum_{n=1}\Delta kx_n \sum_{m=1}\Delta ky_m \left[B_{nm}(t)\sigma_{nm}k_{nm}^{-1}e^{i(kx_n\cdot x + ky_m\cdot y)} + B^*_{nm}(t)\sigma_{nm}k_{nm}^{-1}e^{i(kx_n\cdot x - ky_m\cdot y)}\right] e^{-k_{nm}\cdot z}$$

where

$$k_{nm}^2 = kx_n^2 + ky_m^2$$

now the dynamic free surface condition,

$$\frac{\partial\phi_{FS}}{\partial t} = -g\eta \qquad z = 0,$$

can be applied to yield the remaining equation to be used when updating the free surface in time,

$$\frac{d}{dt}B_{nm}(t) = -A_{nm}(t)\sigma_{nm}$$

$$\frac{d}{dt}B^*_{nm}(t) = -A^*_{nm}(t)\sigma_{nm}$$

The free surface induced pressure and normal component may be computed from A_{nm} and A^*_{nm} directly

$$P_{FS} = -\rho\frac{\partial\phi_{FS}}{\partial t} = \rho g \sum_{n=1}^{NKX}\Delta ky_n \sum_{m=1}^{NKY} ky_m e^{(ikx_n\cdot x - k_{nm}\cdot z)} \left[A_{nm}(t)e^{-iky_m\cdot y} + A^*_{nm}(t)e^{-iky_m\cdot y}\right]$$

and

$$\vec{a}_{FS}\cdot\vec{n} = -g\sum_{n=1}^{NKX}\Delta kx_n \sum_{m=1}^{NKY}\Delta ky_m e^{(ikx_n\cdot x - k_{nm}\cdot z)} \left[A_{nm}(t)\cdot e^{iky_m\cdot y}(ikx_n\cdot n_x + iky_m\cdot n_y - k_{nm}\cdot n_z) + A^*_{nm}(t)\cdot e^{-iky_m\cdot y}(ikx_n\cdot n_x - iky_m\cdot y - k_{nm}\cdot n_z)\right]$$

The distribution of values of kx_n and ky_m where A_{nm}, A^*_{nm} and B_{nm}, B^*_{nm} are specified is critical. For practical computing times, the

number of points should be kept to an absolute minimum. On the other hand, the free surface representation must be valid

(1) Over the hull surface throughout the flow in the immediate neighborhood of the hull surface and,

(2) Over the maximum anticipated time interval of the simulation.

The hull and the free surface flow is assumed to be located in the general neighborhood of the origin of the (x,y) plane. Suppose the free-surface component of the flow were periodic in space with periodic lengths $2\pi*Lx$ and $2\pi*Ly$ in the x and y directions respectively. Then the continuum of kx and ky are replaced by the discrete values

$$kx_n = n/L_x \qquad n = 1, 2, 3 \ldots$$

and

$$ky_m = m/L_y \qquad m = 1, 2, 3 \ldots$$

Similarly, if the free surface component of flow were periodic in time with a period of $2\pi T$, then

$$k = (kx^2+ky^2)^{1/2} = n^2/gt^2$$

These results are applied in obtaining a kx, ky distribution satisfying the following requirements. The free surface flow representation must be valid.

(1) Over a region extending L_x in the x direction and L_y in the y direction from the origin of the (x,y) plane,

(2) Over features with characteristic lengths of ℓ_x and ℓ_y or larger

(3) Over time intervals of length T or shorter

without significant influence from the discretization of kx and ky.

Condition (1) imposes maximum step sizes for kx_n and ky_m

$$kx_{n+1} - kx_n \le L_x^{-1}$$

$$ky_{m+1} - ky_m \le L_y^{-1} .$$

Condition (2) sets the minimum upper bounds for kx_n and ky_m

$$kx_{NKX} \ge \ell_x^{-1}$$

$$ky_{MKY} \ge \ell_y^{-1} .$$

Condition (3) cannot be applied directly for independent values of kx_n and ky_m. It can be adequately replaced by a pair of similar conditions,

$$\sqrt{kx_{n+1}} - \sqrt{kx_n} \le (T*\sqrt{g})^{-1}$$

and

$$\sqrt{ky_{m+1}} - \sqrt{ky_n} \le (T*\sqrt{g})^{-1}$$

These final conditions usually affect only the f · lowest values of kx and ky, depending on the values of the other parameters.

Advancement of the Free Surface in Time

With each time step, the free surface portion of the flow as represented by $A_{nm}(t)$, $A^*_{nm}(t)$ and $B_{nm}(t)$, $B^*_{nm}(t)$ (i.e., $\eta(x,y)$) must be advanced. The new values are those which would result if the hull were not present over the time interval (from t_n to $t_n+\Delta t$) added to estimates for the free surface flow generated by the body (i.e., by the source panels and their images) over the small time interval. The algorithms used to update the coefficients are

$$A_{nm}(t_n+\Delta t) = A_{nm}(t_n)\cos\sigma_{nm}\Delta t + B_{nm}(t_n)\sin\sigma_{nm}\Delta t + \Delta A^{BODY}_{nm}$$

$$B_{nm}(t_n+\Delta t) = B_{nm}(t_n)\cos\sigma_{nm}\Delta t - A_{nm}(t_n)\sin\sigma_{nm}\Delta t + \Delta B^{BODY}_{nm}$$

(with identical algorithms for updating A^*_{nm} and B^*_{nm}). Since the body-induced potential is defined as zero on the free surface,

$$\phi_{BD}(x,y,z) = 0, \qquad z = 0,$$

the influence of the body source panels and their images on B_{nm}, B^*_{nm} over this short time period are second order in Δt

$$\Delta B^{BODY}_{nm}, \ \Delta B^{BODY*}_{nm} = 0(\Delta t)^2$$

The free surface elevation induced by the body source panels and their images over a small time interval Δt may be computed by summing the contributions of each panel and its image. A panel with uniform density σ_i acting over a surface of area A_i is replaced by a single point source with strength

$$s_i(t) = A_i(\sigma_i(t_n) + (t-t_n)\dot{\sigma}(t_n))$$

located at the panel center point (x_i, y_i, z_i) as defined at the midpoint of the interval, $t = t_n + 1/2\ \Delta t$.

The vertical velocity at $z = 0$ induced by these source points and their images may be written as

$$\frac{\partial\phi_B(t)}{\partial z} = -\sum_{i=1}^{N_B} \frac{2z_i s_i(t)}{\left[(x-x_i)^2+(y-y_i)^2+z_i^2\right]^{3/2}} .$$

This can be expressed in integral form as

$$\Delta\eta_B(x,y) = \frac{2}{\pi}\int_{t_n}^{t_n+\Delta t} dt \sum_{i=1}^{N_B} s_i(t) \cdot \int_0^\infty dkx\, e^{ikx(x-x_i)} \int_{-\infty}^{\infty} dky \cos ky(y-y_i) \cdot e^{-(kx^2+ky^2)z_i}$$

Thus, to second order in Δt, ΔA_{nm}^{BODY} and ΔA_{nm}^{BODY*} can be written as

$$\Delta A_{nm}^{BODY} = 2\frac{\Delta t}{\pi}\sum_{i=1}^{N_B} s_i(t_n+\tfrac{1}{2}\Delta t) e^{-i(kx_n\cdot x_i + ky_m\cdot y_i)} \cdot e^{-k_{nm}z_i}$$

and

$$\Delta A_{nm}^{BODY*} = 2\frac{\Delta t}{\pi}\sum_{i=1}^{N_B} s_i(t_n+\tfrac{1}{2}\Delta t) e^{-i(kx_n\cdot x_i - ky_m\cdot y_i)} \cdot e^{-k_{nm}z_i}$$

Also in second order in Δt, the changes in B_{nm} induced by the body is

$$\Delta B_{nm}^{BODY} = -\frac{1}{2}\frac{\partial}{\partial t} A^{BODY}(t)\sigma_{nm}(\Delta t)^2$$

or

$$\Delta B_{nm}^{BODY} = -\frac{(\Delta t)^2}{\pi}\sum_{i=1}^{N_B} s_i(t_n) e^{-i(kx_n\cdot x_i + ky_m\cdot y_i)} \cdot e^{-k_{nm}z_i}\sigma_{nm}$$

with a similar expression for ΔB_{nm}^{BODY*}.

Computation of the Body-Induced Pressures

The total force acting on the hull surface is determined from the pressures computed at the center points of the hull panels. These pressures are assumed to act uniformly over the panel surface. From Bernoulli's equation, the pressure at a point fixed in space is

$$p = -\rho\frac{\partial\phi}{\partial t} + 0(\epsilon^2)$$

where the time derivative is in a space-fixed coordinate system and the velocity field relative to this space-fixed system is assumed to be of order ϵ. The pressure may be written as the sum of free-surface and body-induced components

$$p = p_{FS} + p_{BD}$$

where

$$p_{FS} = -\rho\frac{\partial\phi_{FS}}{\partial t}$$

and

$$p_{BD} = -\rho\frac{d\phi_{BD}}{dt} + \rho\vec{v}_s\cdot\vec{\nabla}\phi_{BD}$$

where $\vec{v}_s$ is the velocity of a point on the hull surface. If the body moves with translational velocity $\vec{v}_B$ and rotational velocity $\vec{\omega}_B$ then

$$\vec{v}_s = \vec{v}_B + \vec{\omega}_B \times \vec{x} .$$

The term $\frac{d\phi_{BD}}{dt}$ represents the time derivative of the potential at a point fixed on the hull (i.e. at a panel center). In most cases of interest

$$\vec{v}_s = U\vec{e}_x + 0(\epsilon)$$

where U is the forward speed and $\vec{e}_x$ is the unit vector in the x direction. Unless otherwise specified the body-induced pressure is assumed to be

$$p_{BD} = -\rho\frac{d\phi_{BD}}{dt} + \rho U\frac{\partial\phi_{BD}}{\partial x} .$$

The time derivative $\frac{d\phi_{BD_i}}{dt}$ at the center point of panel i can be calculated from the previously computed time derivative of the source strengths in a hull-fixed system,

$$\frac{d\phi_{BD_i}(t_n)}{dt} = \sum_{j=1}^{N_B} P_{ij}\dot{\sigma}_j(t_n)$$

where P_{ij} represents the potential at the center of panel i induced by a uniform source density of unit strength acting over panel j. Unfortunately, elements of the matrix P_{ij} giving the potential are not as easy to compute numerically as the matrix E_{ij} giving the velocity. At present integrals of the form

$$P_{ij} = \iint_{S_j} dS\left(\frac{1}{|\vec{x}_i-\vec{x}|} - \frac{1}{|\vec{x}_i-\vec{x}^I|}\right)$$

where $\vec{x}^I$ is the image of point $\vec{x}$ on surface S_j, are estimated by dividing the surface S_j into many small elements and integrating numerically with the integrand evaluated at the center of each subelement. This 'brute force' method can consume significant computing time if resonable accuracy is desired. These elements need be computed only once, however, if the hull does not change over the time period of simulation.

The forces and moments acting on the body in a hull-fixed coordinate system may be written in the form,

$$F_m = -\sum_{i=1}^{N_B} n_{mi}A_i p_i \qquad m = 1 \ldots 6$$

where F_m is a generalized force corresponding to the m^{th} degree of freedom, n_{mi} is the generalized normal, A_i is the panel area and p_i is the pressure on the i^{th} panel. From this form, the force F'_m resulting from the $d\phi_{BD}/dt$ term can be written as

$$F'_m = \rho\sum_{i=1}^{N_B} n_{mi}A_i\frac{d}{dt}\phi_{BD_i} = \rho\sum_{i=1}^{N_B} n_{mi}A_i\sum_{j=1}^{N_B} P_{ij}\dot{\sigma}_j = \rho\sum_{j=1}^{N_B} PP_{mj}\dot{\sigma}_j .$$

The $\underline{PP}_{mj}$ array of (6 x N_B) elements can be evaluated once at the beginning of the computation ($t = t_n$).

Similarly the methods used to calculate the E_{ij} matrix can also give elements of a matrix X_{ij} such that

$$\frac{\partial}{\partial x}\phi_{BD_i}(t_n) = \sum_{j=1}^{N_B} X_{ij}\sigma_j(t_n) .$$

The forces resulting from the second term of the equation for p_{BD} are

$$F''_m = -\rho U \sum_{j=1}^{N_B} n_{mi}A_i \sum_{j=1}^{N_B} X_{ij}\sigma_j(t_n)$$

$$= -\rho U \sum_{j=1}^{N_B} \underline{PX}_{mj}\,\sigma_j$$

where $\underline{PX}_{mj}$ is a (6 x N_B) matrix similar to $\underline{PP}_{mj}$.

Alternative Techniques

Certain subelements of the computation can be represented by alternative forms. The computational method described above was chosen from the following set of possibilities

(1) Either source or dipole panels can be used to represent the hull surface. If dipoles are used, then the normal velocity on the image panel is the negative of the velocity on the panel itself so that the net mass inflow into the region enclosed by the hull and its image is zero. The major numerical advantage of dipole panels is that the potential induced by a uniform dipole strength of unit magnitude is easily computed at any arbitrary point in space (it is simply the solid angle enclosed by the panel relative to that point). This allows one to compute the pressures induced by the time derivative of the body-induced potential much more easily numerically than if source panels were used. The primary disadvantage of dipole panels is that the free surface disturbance generated by them is discontinuous along points where the hull intersects the free surface. That is, there is a jump in elevation between the interior and exterior regions. This requires much finer resolution in the representation of the free-surface and, therefore, more points in k-space for the spectral distribution of the free-surface.

(2) Alternative conditions can be applied to the free surface interior to the hull. For example instead of using the linearized free-surface condition after the entire free surface, the surface elevation interior to the hull can be constrained to be uniformly zero by placing surface panels over this region. One possible advantage of "adding a lid" is that it suppresses standing waves which otherwise are excited in the hull interior. The major disadvantage of a "lid" is the extra computing time required. In theory these internal standing waves produce no net pressure on the (exterior) hull surface. That is the body-induced and free-surface induced components of pressures cancel at points exterior to the hull surface. In practice, they may not cancel unless the pressures are evaluated numerically in certain ways. It has been found that using the free surface induced acceleration, rather than velocity, in the hull normal boundary condition is very effective in removing any influence on the pressures from the standing waves generated internal to the hull.

(3) The spectral representation of the free surface can be used either as a rectangular or cylindrical representation in spectral space. That is $\eta(x, y)$, the elevation, can be represented either as

$$\eta(x,y) = \sum_{n=1}^{NKX} \Delta k_{x_n} \sum_{m=1}^{NKY} \Delta k_{y_m} e^{ik_{x_n}\cdot x} \cdot \left[A_{nm} e^{ik_{y_m}\cdot y} + A^*_{nm} e^{-ik_{y_m}\cdot y} \right]$$

or

$$\eta(x,y) = \sum_{n=1}^{NK} k_n \cdot \Delta k_n \sum_{m=1}^{NTH} \Delta\theta A_{nm} e^{ik_n(x\cos\theta_m + y\sin\theta_m)} .$$

$$(\theta_1 = -\tfrac{\pi}{2},\ \theta_{TH} = +\tfrac{\pi}{2})$$

Both methods have been programmed. They are very similar. The advantage of the rectangular system is that the length scales of the free surface are independent in the x and y directions. This is particularly useful for typical ship hulls where the hull length is much greater than the transverse dimensions of the ship and the flow is expected to change much more slowly in the x direction than in the y direction.

Application to Linearized Frequency-Domain Seakeeping Characteristics with Forward Speed

Consider a hull moving with forward speed U and oscillating about its mean position defined by the surface

$$F(x-Ut, y, z) = 0$$

The flow velocity perturbation induced by the forward motion alone is assumed to be small, i.e. $0(\epsilon)$. Harmonic perturbations about the mean flow field are also assumed to be of order ϵ. Interactions between the steady and harmonic portions of the flow field are assumed to be of higher order in ϵ.

Motions are described in a coordinate system (x^*, y^*, z^*) moving with the mean hull, i.e. with forward speed U. The coordinates of this moving system relative to that of the space-fixed (x, y, z) system are given by

$$x^* = x - Ut$$

$$y^* = y$$

$$z^* = z .$$

The velocities of the craft relative to a moving (x^*, y^*, z^*) ship-fixed system are written for the six degrees of freedom as

v_1 = surge velocity (+ forward)

v_2 = sway velocity (+ to starboard)

v_3 = heave velocity (+ downward)

v_4 = roll velocity (+ for right-hand rotations about x axis)

v_5 = pitch velocity (+ for right-hand rotations about y axis)

v_6 = yaw velocity (+ for right-hand rotations about z axis)

All velocities are assumed to be of order ε and harmonic in time with frequency ω. [Since these velocities are specified in a ship-fixed system, they are related to both velocities and angular displacements in a space-fixed system for finite forward speed. For example,

$$v_{3_{SHIP}}(t) = v_{3_{SPACE}}(t) - \theta_5(t)\cdot U$$

where U is the forward speed and θ_5 is the pitch angle.]

The normal velocity at a point $\vec{x}^*$ on the surface is given by harmonic velocities in a ship-fixed system with magnitude v_m and phase θ_m is

$$\vec{v}^*\cdot\vec{n} = \sum_{m=1}^{6} n_m(\vec{x}^*)\, v_m \cos(\omega t+\theta_m)$$

where $n_4(\vec{x}^*)$, $n_5(\vec{x}^*)$, and $n_6(\vec{x}^*)$ are generalized normals defined as

$$n_4(\vec{x}^*) = n_2(\vec{x}^*)\cdot x_3^* - n_3(\vec{x}^*)\cdot x_2^*$$

$$n_5(\vec{x}^*) = n_3(\vec{x}^*)\cdot x_1^* - n_1(\vec{x}^*)\cdot x_3^*$$

$$n_6(\vec{x}^*) = n_1(\vec{x}^*)\cdot x_2^* - n_2(\vec{x}^*)\cdot x_1^*$$

similarly the normal acceleration produced by the motion is

$$\vec{a}^*\cdot\vec{n} = -\sum_{m=1}^{6} n_m(\vec{x}^*)\, v_m \omega \sin(\omega t+\theta_m)$$

The problem is to compute the forces and moments induced by these harmonic motions for arbitrary ω from a set of time-domain solutions (one for each of the six degrees of freedom) for impulsive motions. Since the problem is linearized, a single degree of freedom can be considered without loss of generality. Consider, for example, the steady harmonic motion described by

$$\vec{v}^*\cdot\vec{n} = v_j n_j(\vec{x}^*)\cos\omega t$$

$$\vec{a}^*\cdot\vec{n} = -\omega\, v_j n_j(\vec{x}^*)\sin\omega t$$

Assume that the time-domain solution based on the computational method described above is available for the following problem in the limiting case as $\gamma\to 0$. The flow is at rest for $t<0$. Starting at time $t=0$ the flow is disturbed by motion in the j^{th} degree of freedom described by the body boundary condition,

$$\vec{v}^*\cdot\vec{n} = n_j(\vec{x}^*) \qquad 0 \le t$$

$$= 0 \qquad t < 0$$

i.e., $\vec{v}^*\cdot\vec{n} = n_j(\vec{x}^*)H(t)$

where H(t) is the unit step function and where x^* is any point on the hull surface. Define the resulting potential at a point x^* on the hull as

$$\tilde{\phi}_j(\vec{x}^*,t) \qquad t > 0$$

and the forces and moments relative to the (x^*,y^*,z^*) system in the six degrees of freedom as

$$\tilde{F}_{kj}(t) \qquad k = 1,2,3 \ldots 6 \qquad t > 0$$

The tilda symbol ~ indicates a time-domain solution obtained from the numerical simulation. The j subscript refers to the degree of freedom of the motion. The k subscript refers to the degree of freedom of the force or moment.

The forward speed U should be included in the time-domain computations. Although forward speed does not appear directly in the body boundary condition, it enters the computation in two ways. First the mean hull surface moves

$$F(x-Ut,y,z) = 0$$

with speed U so that over the time of the computation the space-fixed (x,y,z) and body fixed (x^*,y^*,z^*) coordinate are displaced with respect to each other. Secondly, the body-induced pressure contains a term proportional to forward speed

$$P_{BD} = -\rho\frac{d\phi_{BD}}{dt} + \rho U\frac{\partial\phi_{BD}}{\partial x}$$

It is assumed that the general form for the force and moment vector, $F_k(t)$ generated by a velocity of mode j and time history $v_j(t)$ in the ship fixed reference system,

$$\vec{v}^*\cdot\vec{n} = v_j(t)n_j(\vec{x}) \ ,$$

is

$$F_{kj}(t) = F_{kj(IMP)}\dot{v}(t) + \int_{-\infty}^{t} K_{kj}(t-\tau)v_j(\tau)\,d\tau$$

where the first term represents virtual mass effects and the second term contains the memory effects resulting from the free surface. If, for example, a step function is imposed in mode j,

$$\dot{v}_j = H(t)$$

then the solution is

$$\tilde{F}_{kj}(t) = \int_0^t K(\tau)d\tau \qquad t > 0$$

and $\tilde{F}_{kj(IMP)}$ is defined by

$$\tilde{F}_{kj(IMP)} = -\rho\iint_{S_B} dS_B\, \tilde{\phi}_j(\vec{x},0+)n_k(\vec{x})$$

From integration by parts for

$$\vec{v}^*\cdot\vec{n} = v_j n_j(\vec{x})\cos\omega t$$

the solution is

$$F_{kj}(t) = \omega\left[\tilde{F}_{kj(IMP)}\sin\omega t + \int_{0+}^{\infty}\tilde{F}_{kj}(\tau)\sin\omega(t-\tau)\right]$$

$$= \omega\sin\omega t\left[\tilde{F}_{kj(IMP)} + \int_{0+}^{\infty}\tilde{F}_{kj}(\tau)\cos\omega\tau\, d\tau\right]$$

$$- \omega\cos\omega t\int_{0+}^{\infty}\tilde{F}_{kj}(\tau)\sin\omega\tau\, d\tau$$

The first term in the expression for F_{kj} is in phase with the acceleration and may be thought of as a generalized added mass term. The second term, in phase with velocity, represents a damping. The hydrostatic effect, not included in these dynamic forces, would, of course, give a term proportional to displacement.

Wave excited forces for harmonic waves can be computed using similar techniques. Consider an ambient wave field defined by

$$\phi = \mathrm{Re}\left|A\, e^{ik(x\cos\theta+y\sin\theta)-kz-i\omega t}\right|$$

$$= \mathrm{Re}\left|A\, e^{ik(x^*\cos\theta+y^*\sin\theta-kz^*-i\omega_e t}\right|$$

where A is the complex asplitude and ω_e is the encounter frequency defined as

$$\omega_e = \omega - Uk\cos\theta.$$

The resulting ambient velocity and acceleration field can be written in the form

$$\vec{v}(\vec{x}^*,t) = \vec{v}_1(\vec{x}^*)\sin\omega_e t + \vec{v}_2(\vec{x}^*)\cos\omega_e t$$

and

$$\vec{a}(\vec{x}^*,t) = \omega_e\vec{v}_1(\vec{x}^*)\cos\omega_e t - \omega_e\vec{v}_2(\vec{x}^*)\sin\omega_e t$$

$$= a_1(t)\vec{v}_1(x^*) + a_2(t)\vec{v}_2(\vec{x}^*)$$

where

$$\vec{v}_1(x) = I_m\left|A\vec{V}\cdot e^{ik(x^*\cos\theta+y^*\sin\theta)-kz^*}\right|$$

$$\vec{v}_2(x) = \mathrm{Re}\left|A\vec{V}\cdot e^{ik(x^*\cos\theta+y^*\sin\theta)-kz^*}\right|$$

Now assume the time-domain method of solution is applied to the following pair of time step problems. In each case the hull and the surrounding fluid is at rest for t<0. After t=0; the body boundary conditions are

$$\vec{v}^*\cdot\vec{n} = \vec{v}_1(\vec{x}^*)\cdot\vec{n}(\vec{x}^*)a_1(t) \qquad t \geq 0$$

$$= \vec{v}_1(\vec{x}^*)n(\vec{x}^*)H(t), \text{ all } t$$

for the first case and

$$\vec{v}^*\cdot\vec{n} = \vec{v}_2(\vec{x}^*)\cdot\vec{n}(\vec{x}^*)a_2(t) \qquad t \geq 0$$

$$= \vec{v}_2(\vec{x}^*)\cdot\vec{n}(\vec{x})H(t), \text{ all } t.$$

and

$$a_1(t) = a_2(t) = H(t)$$

for the second case. The pair of time-domain forces and moments for each of the six degrees of freedom obtained by applying the time-domain computational solution to these two step problems for arbitrary $a_1(t)$ and $a_2(t)$

$$F_{k1}(t) = \tilde{F}_{k1(IMP)}a_1(t) + \int_0^t\tilde{F}_{k1}(\tau)a_1(t-\tau)d\tau$$

$$F_{k2}(t) = \tilde{F}_{k2(IMP)}a_2(t) + \int_0^t\tilde{F}_{k2}(\tau)a_2(t-\tau)d\tau$$

Where the pair of time-domain forces and moments for each of the six degrees of freedom obtained by applying the time-domain computational method to these two problems are written as

$$\tilde{F}_{k1}(t) \text{ and } \tilde{F}_{k2}(\tau),$$

respectively where the tilda ~ symbol indicates a time-domain solution, the subscript k refers to the degree of freedom of the force or moment, and the remaining subscript indicates which of the pair of body boundary conditions were employed.

The forces and moments generated by the harmonic velocity field

$$\vec{v}(\vec{x}^*,t) = \vec{v}_1(\vec{x}^*)\sin\omega_e t + \vec{v}_2(\vec{x}^*)\cos\omega_e t$$

may be expressed in terms of the time-domain solutions as

$$F_k = \omega_e\int_0^{\infty}\tilde{F}_{k1}(\tau)\cos\omega_e(t-\tau)d\tau$$

$$- \omega_e\int_0^{\infty}\tilde{F}_{k2}(\tau)\sin\omega_e(t-\tau)d\tau$$

$$F_k = \omega_e\cos\omega_e t\left[\tilde{F}_{k1(IMP)} + \int_{0+}^{\infty}\left|F_{k1}(\tau)\cos\omega_e\tau\right.\right.$$

$$\left.\left. + F_{k2}(\tau)\sin\omega_e\tau\right|d\tau\right]$$

$$- \omega_e\sin\omega_e t\left[\tilde{F}_{k2(IMP)} + \int_{0+}^{\infty}\left|\tilde{F}_{k2}(\tau)\cos\omega_e\tau\right.\right.$$

$$\left.\left. - \tilde{F}_{k1}(\tau)\sin\omega_e\tau\right|d\tau\right]$$

where

$$\tilde{F}_{k1(IMP)} = -\rho\gamma\iint_{S_B}ds\tilde{\phi}_1(\vec{x}^*,t_o)n_k(\vec{x}^*)$$

and

$$\tilde{F}_{k2(IMP)} = -\rho\gamma\iint_{S_B}ds\tilde{\phi}_2(\vec{x}^*,t_o)n_k(\vec{x}^*)$$

Heave Motion of a Floating Sphere

As a simple example of the method described above, the computer program capable of handling any three dimensional hull shape was applied to the case of heave motion for a semi-submerged sphere, i.e., a hemispherical hull. The computer program is completely general and makes no assumptions concerning either lateral or longitudinal symmetry of the body or the flow. For the case of zero forward speed, however, the symmetry of the hemispherical hull requires that only heave force result

from heave motion. The magnitudes of other forces calculated numerically should be one measure of the adequacy of the surface panels chosen to represent the body and the program itself.

In the test case 60 panels were used to represent the hemisphere with spacings specified by

$$\Delta\phi = 2\pi/12 \text{ and } \Delta\theta = \pi/5$$

where $0 \le \phi < 2\pi$ is the circumferential angle and $0 \le \theta \le \pi$ is the polar angle. The hull-fixed coordinates are specified at each of the four corners of each panel with coordinates given by

$$x^* = a \cos\phi \cos\theta$$

$$y^* = a \sin\phi \cos\theta$$

and $$z^* = a \sin\theta$$

with radius a set to unity in this test case.

If the hull is not flat over a panel, its finite size causes errors in the computation of the panel center and panel area. For simplicity the panel center is computed to be at the mean of the four corner points. For a convex hull such as the hemisphere these points fall slightly inside the physical hull rather than directly on it. More important is the error in the computed hull area. Again for simplicity, the pair of diagonals,

$$\vec{x}_{31} = \vec{x}_3 - \vec{x}_1$$

and

$$\vec{x}_{42} = \vec{x}_4 - \vec{x}_2$$

are used to estimate the panel area,

$$A = \frac{1}{2}|\vec{x}_{42} \times \vec{x}_{31}|$$

and unit normal,

$$\vec{n} = \vec{x}_{42} \times \vec{x}_{31} / |\vec{x}_{42} \times \vec{x}_{31}|$$

where x_1, x_2, x_3 and x_4 are the coordinates of the four corner points of the panel in the body-fixed system. Although it is immaterial whether any single panel normal points inward or outward, for simplicity all normals are assumed to be outward in the description of the method and in the sample problem. In the case of convex bodies the areas are underpredicted by an amount which depends on the panel size. Likewise, the areas are also underestimated for concave portions of the physical hull.

For the case of a hemispherical hull represented by sixty plane quadralateral panels the impulsive forces and moments resulting from an instantaneous change in the heave (z) velocity (+ downward) from zero at t=0- to unity at t=0+, was computed to be (for unit density, ρ=1):

$$\tilde{F}_{13(IMP)} = \text{surge force} = -0.00003$$

$$\tilde{F}_{23(IMP)} = \text{sway force} = .00656$$

$$\tilde{F}_{33(IMP)} = \text{heave force} = -1.00150$$

$$\tilde{F}_{45(IMP)} = \text{roll moment} = .00004$$

$$\tilde{F}_{53(IMP)} = \text{pitch moment} = -.00011$$

and $$\tilde{F}_{63(IMP)} = \text{yaw moment} = -.00012 .$$

From theory

$$\tilde{F}_{kj(IMP)} = 0 \qquad k \neq 3$$

and

$$\tilde{F}_{33(IMP)} = -\pi/3 = -1.04720 .$$

The computed terms are thus $\le O(10^{-3})$ for all forces and moments other than heave. The computed heave force is about 3 percent too low; a number which could be reduced with a finer hull resolution in the panels.

The time-domain numerical method was applied to the seaisubmerged sphere. Initially (t<0) the flow and the body was specified to be at rest. At time t=0, a step function was applied to the heave velocity. Forward speed was set at zero. Thus the hull velocity boundary condition is

$$(\vec{v}_{BD}(\vec{x}^*)+\vec{v}_{FS}(\vec{x}^*))\cdot\vec{n}(\vec{x}^*) = n_z(\vec{x}^*)H(t)$$

where $\vec{x}^*$ is any point on the hull surface and H(t) is the unit step function. For the initial impulse time step of infinitesmal duration starting at t=0, a velocity boundary condition was applied at each panel center as

$$\sum_{j=1}^{N_B} E_{ij}\sigma_j(t=0+) = \vec{v}_{BD_i}\cdot\vec{n}_i = n_{zi}$$

(since $\vec{v}_{FS_i}$ is zero at t=0+). The source strengths at t=0+, σ_i(t=0+) were then used to find the potentials on the panels and, therefore, the forces and moments acting on the body in all six degrees of freedom as a result of the initial impulsive step from zero to unity in heave velocity (the third mode). That is equivalent to

$$\tilde{F}_{kj(IMP)} \qquad k = 1,2, \ldots 6 .$$

In practice these impulsive forces are equivalent to the formula given earlier,

$$\tilde{F}_{kj(IMP)} = -\rho \iint_{S_B^*} dS_B \, \tilde{\phi}_j(\vec{x}^*,0+)n_k(\vec{x}^*)$$

For later time steps the time-domain force

$$\tilde{F}_{kj}(t) = \int_{0+}^{t} K_{kj}(\tau)d\tau, \qquad t > 0+$$

was computed using the method presented in this report with an acceleration body boundary condition of the form

$$\sum_{j=1}^{N_B} E_{ij}\dot{\sigma}_j(t) = a_i^*(t) - a_{ps}\cdot n_i - U\frac{\partial}{\partial x}\vec{v}_{xs} \qquad t > 0+$$

(with the forward speed U set to be zero)

since the prescribed normal acceleration a_i^* is identically zero for t>0+. The resulting values for $\dot{\sigma}_i(t)$, i.e., the time derivative

of the source strength density on each panel, gives the time rate of change of the body potential and, therefore, the body-induced pressure p_{BD_i} at each panel. By adding the free-surface induced pressures, the total pressure acting on each panel was determined. This produced the net computed force

$$\bar{F}_{k3}(t)$$

acting on the body for $t > 0+$.

For the numerical test case, the forces and moments of the class $\bar{F}_{k3}(t)$, $k \neq 3$ were all insignificant. Figure 1 shows $\bar{F}_{33}(t)$ computed under the following numerical conditions

L_x = maximum length scale in x = 2.5

ℓ_x = minimum length scale in x = 0.25

L_y = maximum length scale in y = 2.5

ℓ_y = minimum length scale in y = 0.25

T = maximum time scale = 8.0

g = acceleration of gravity = 1.0

ρ = fluid density = 1.0

a = radius of sphere = 1.0

Δt = time step size = 0.10

The first five of these conditions produce 17 wave lengths for the free surface representation in both the x and y directions or 17 x 17 modes. For the harmonic case

$$v_3(t) = \cos\omega t ,$$

the force acting in the z direction (+ downward) is given by

$$F_3(t) = -\omega\sin(\omega t)\left[\bar{F}_{33(IMP)} + \int_{0+}^{\infty} \bar{F}_{33}(\tau)\cos(\omega\tau)d\tau\right]$$

$$+\omega\cos(\omega t)\int_{0+}^{\infty} \bar{F}_{33}(\tau)\sin(\omega\tau)d\tau .$$

This formula can be evaluated numerically and compared with the classical results of Havelock [3].

Havelock expresses the z force induced by the heave oscillations

$$v_3 = \cos\omega t$$

as

$$Z = \frac{2}{3}\pi\rho a^3 k\sin\omega t - \frac{2}{3}\pi\rho a^3 2h\omega\cos\omega t$$

where a is the radius and ρ is the density (both are unity). The coefficients k (not a wave number) and 2h determine the added mass and hydrodynamic damping of the sphere in heave. These two coefficients are commonly expressed in terms of the nondimensional variable $\omega^2 a/g$.

These coefficients defined by Havelock are related to the values derived from the time-domain solution for a step function in the heave mode as

$$k(\omega^2 a/g) = -\frac{3}{2\pi}\left[\bar{F}_{33(IMP)} + \int_{0+}^{\infty} F_{33}(\tau)\cos(\omega\tau)d\tau\right]$$

and

$$2h(\omega^2 a/g) = -\frac{3}{2\pi}\int_{0+}^{\infty} \bar{F}_{33}(\tau)\sin(\omega\tau)d\tau$$

Figure 2 shows coefficients $k(\omega^2 a/g)$ and $2h(\omega^2 a/g)$ calculated in this manner using $\bar{F}_{33(IMP)} = -1.0015$ and $\bar{F}_{33}(\tau)$ as shown in Figure 1. The resulting curves, close to those predicted by Havelock using analytic methods, given in reference [3]. Tabular results for this problem were also given by Kim [4]. Table 1 below shows a comparison between Kim's results and the computed results for various values of $\omega^2 a/g$.

Acknowledgement

This work was sponsored by the Naval Sea Systems Command, General Hydromechanics Research Program, administered by David W. Taylor Naval Ship Research and Development Center, USA.

References

1. Chang, M. S., "Computations of Three-Dimensional Ship Motions with Forward Speed," Proceedings Second International Conference on Numerical Ship Hydrodynamics, September 1977, University of California Extension Publications, pp 124-135.

2. Chapman, R. B., "Large-Amplitude Transient Motion of Two-Dimensional Floating Bodies," Journal of Ship Research, Vol. 23, No. 1, March 1979, pp 20-31.

3. Havelock, T., "Waves Due to a Floating Sphere Making Heaving Oscillations," Proceedings Royal Society A, 231, 1955, pp 1-7.

4. Kim, W. D., "On the Harmonic Oscillations of a Rigid Body on a Free Surface," Journal of Fluid Mechanics, 1964.

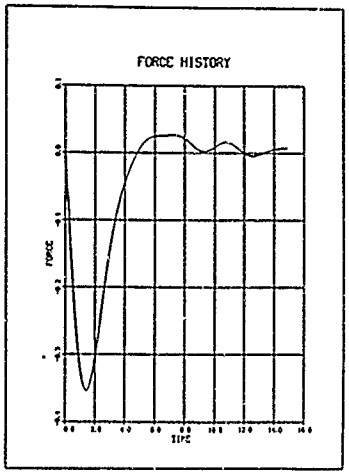


Figure 1 Time history of force history induced by a unit step in heave velocity starting at t=0 for a semisubmerged sphere

Table 1 Comparison of analytic and numerical results for added mass and damping coefficients of a semisubmerged sphere of radius a oscillating with frequency ω.

Added Mass Coefficients

$\omega^2 a/g$	$h(\omega^2 a/g)$ [Ref. [4]]	$h(\omega^2 a/g)$ [Computed]
0 50	0 60	0 58
1.00	0 43	0 43
1.50	0 39	0 39
2 00	0.38	0.39
2.50	0 40	0 39
3 00	0 41	0.38

Damping Coefficients

$\omega^2 a/g$	$2h(\omega^2 a/g)$ [Ref [4]]	$2h(\omega^2 a/g)$ [Computed]
0 50	0 34	0 33
1 00	0 25	0 25
1.50	0 17	0 17
2.00	0 11	0 12
2 50	0 07	0 10
3 00	0.06	0 06

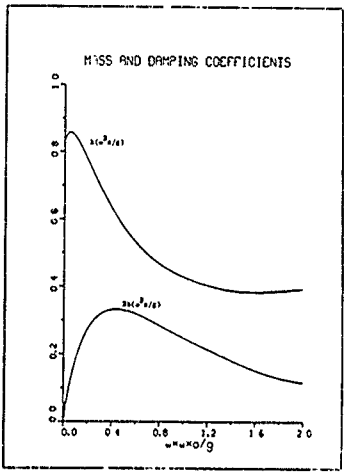


Figure 2 Added mass and damping coefficients from computation Corresponds to Figure 1 in Reference [3]

THREE-DIMENSIONAL TIME-DEPENDENT NONLINEAR SHIP MOTION SIMULATION USING THE INERTIAL MARKER PARTICLE TECHNIQUE*

George I. Bounanoff
Austin Research Associates, Inc.
1901 Rutland Drive, Austin, Texas 78758

Abstract

A nonlinear, three-dimensional, time-dependent ship motion simulation code is described which is formulated in terms of the primitive variables. The code solves Euler's equation for the flow field and the rigid body equations of motion for the ship to produce a time-marching solution. The code is capable of accepting arbitrary externally-applied forces on the ship such as mooring forces. Results are presented of a bank rejection simulation as well as results for the full-scale Esso Osaka maneuvering studies.

I. Introduction

The inertial marker particle technique was originally developed to allow simulation of ship motion in confined regions where the presence of bottoms and banks could significantly affect the flow. It was desired to have irregularly-shaped banks with essentially arbitrary shape. In addition, one wanted to add external time-dependent forces to the ship which would simulate such things as wind forces, propulsion forces, and mooring forces.

To meet these needs, we undertook development of a three-dimensional time-dependent technique which would solve Euler's equation on a fixed Cartesian grid. The ship's hull would constitute one boundary of the flow from which the hydrodynamic forces could be derived. The ship's motion would be calculated from the rigid body equations of motion taking account of the hydrodynamic forces, as well as all externally-applied forces. The flow field and the ship's velocity would be advanced in time in a forward time marching solution. The ship is free to move throughout the Cartesian grid.

The code was developed first as a two-dimensional code which has been reported on previously in Reference 1. This was used to calculate the mean second order drift force on a tanker moored in broadside waves.

A full nonlinear treatment of the free surface and ship motion has been included in both two and three-dimensional versions of the code.

II. Formulation

The basic formulation involves a finite difference solution to Euler's equation and the continuity equation shown in equations (1) and (2),

$$\frac{\partial \vec{V}}{\partial t} + (\vec{V}\cdot\vec{\nabla})\vec{V} = -\vec{\nabla}P + \vec{g} \tag{1}$$

where the pressure has been normalized with respect to density.

$$\nabla\cdot V = 0 \tag{2}$$

The continuity equation is enforced by iterating on the pressure. The free surface is defined by a surface height function $h(x,y,t)$ which satisfies the equation

$$\frac{\partial h}{\partial t} = V_z - V_x \frac{\partial h}{\partial x} - V_y \frac{\partial h}{\partial y} \tag{3}$$

The boundary condition on the free surface is

$$P = 0 \quad @ \quad Z = h \tag{4}$$

at the ship's hull, the kinematic condition on velocity is

$$V_{NF} = V_{NS} \tag{5}$$

*This work was sponsored by the Office of Maritime Technology of the U. S. Maritime Administration.

where

V_{NF} = fluid velocity normal to the ship's hull

V_{NF} = ship velocity in the direction normal to hull.

The tangential fluid velocities at the slip interface are given by the free slip condition. The pressure at the ship surface is found from equation (1) since all the velocities at the hull are defined and the pressure interior to the fluid is known.

The boundary conditions on rigid boundaries are very similar except that the normal fluid velocity is set to zero.

The normal fluid velocity on the free surface is determined from a cell divergence condition and the tangential velocities are derived from equation (1) using one-sided spatial derivatives in the vertical direction.

III. Numerical Implementation

The numerical implementation utilizes finite difference approximations referenced to a fixed Eulerian grid. Since the physical boundaries of the ship, banks and bottom do not in general coincide with cell boundaries, marker particles are used to define the actual location of boundaries within the mesh.

Each cell within the computational mesh is assigned a flag which controls the logic of the code. This flag field is time dependent and will change as the ship moves through the mesh.

The computation begins by reading in the various parameters associated with grid size, cell size, time steps, and ship parameters. The rigid boundaries are then defined by NE triangular plane segments which are defined by NG points.

The three coordinates for each of the NG points are read in so that

$$X(I),\ Y(I),\ Z(I) \qquad I=1,\ NG \tag{6}$$

are known. A set of connectivity relations are then read in to form the triangular segments as follows:

$$L1(I),\ L2(I),\ L3(I) \quad I=1,\ NE \tag{7}$$

Hence, the three points which define panel number 7 are:

$$X[L1(7)],\ Y[L1(7)],\ Z[L1(7)]$$

$$X[L2(7)],\ Y[L2(7)],\ Z[L2(7)] \tag{8}$$

$$X[L3(7)],\ Y[L3(7)],\ Z[L3(7)]$$

The points and connectivity relations are then read in to define the initial location of the ship. The next step is to associate these points with the Eulerian grid.

Each set of three points is used to form a plane segment analytically defined by

$$aX + bY + cZ = D \tag{9}$$

The intersection point of each plane segment with the lines corresponding to

$$x = i\Delta x = \text{constant}$$

$$y = j\Delta y = \text{constant}$$

$$z = k\Delta z = \text{constant}$$

are then calculated and stored. These intersection points are associated with the Eulerian cells and the flag field is set to indicate a boundary cell. There will be between 3 and 6 intersection points per cell. A best fit technique is used to define a plane segment lying totally within the specified cell. The area, normal direction and centerpoint of each small segment is associated with an Eulerian cell and stored for later use in satisfying boundary conditions at the hull's surface, as well as exterior boundaries.

Before one is able to advance the momentum equation and pressure field, the cell flagging must be completed. The flag for each cell consists of four significant figures, I_1, I_2, I_3, I_4. I_1 and I_2 digit have the meanings shown in Table 1.

TABLE 1

$I_1 = 0$	Empty Cell
$I_1 = 1$	Full Cell
$I_1 = 2$	Boundary Cell
$I_1 = 3$	Intersection Cell
$I_2 = 1$	Rigid Boundary
$I_2 = 2$	Moving Boundary
$I_2 = 3$	Free Surface
$I_2 = 4$	Inflow Boundary
$I_2 = 5$	Outflow Boundary

The I_2 digit has significance only for cells in which I_1 is equal to 2. The I_3 and I_4 digits are filled as follows. Each of the six faces of the cell under consideration are classified as open if fluid is free to flow through it and closed if the inverse is true. Each of the six faces is then assigned the value 1 if it is open and 0 if it is closed. A six-digit binary number is formed whose decimal equivalent is stored in I_3 I_4.

It is now possible to advance the momentum equation and pressure equations. The momentum equation is advanced by using centered finite differences for all spatial derivatives and an explicit forward difference for the time derivative.

The code expects a layer of "ghost cells" lying exterior to the fluid and adjacent to every boundary cell. The values of pressure and velocity in the ghost cell are such that the physical values shown in equations (4) and (5) result when one interpolates between the interior and exterior cell.

The pressure is advanced by the algorithm shown in equation (9).

$$p^{K+1} = p^K + \alpha \nabla \cdot v^K \tag{9a}$$

$$v^{K+1} = v^{n+1} - \beta \nabla p^{K+1} \tag{9b}$$

where

v^{n+1} is the velocity field resulting from the explicit time advance

$$v^{n+1} = v^n - (v^n \cdot \nabla)\, v^n - \gamma \nabla p^n - g \tag{10}$$

The equations in (9) are iterated until $p^{K+1} = p^K$ to within some specified limit at which time the continuity equation has been satisfied. By substituting (9b) into (10), we find

$$v^{K_{max}} = v^n - (v^n \cdot \nabla)\, v^n - (\gamma \nabla p^N + \beta \nabla p^{N+1}) \tag{11}$$

where K_{max} is the final iteration count. Thus a partial time centering of the pressure term is achieved.

At a rigid or reactive boundary cell, the pressure iteration is modified slightly from that shown in equation (9a) to that shown in equation (12),

$$p^{K+1} = p^K - \xi\, (V_{mp} - V_{mb}) \cdot n \tag{12}$$

where

ξ = constant

V_{mp} = the fluid velocity at the midpoint of the segment associated with the boundary cell.

V_{mb} = the boundary velocity.

n = unit normal to the ship's boundary.

In order to advance the rigid body forward in time, it is necessary to introduce a set of coordinates fixed in the body. The forces and moments are calculated in the fixed Cartesian frame, transformed to the body frame where the rigid body equations are advanced in time. The new velocity vector and angular velocity vector are transformed back to the Cartesian frame in order to provide boundary conditions for the hydrodynamic calculation. The transformation process is straightforward and details may be found in Reference 2.

The numerical stability of the code is dominated by the Courant condition since the momentum equations are advanced in an explicit manner. For three-dimensional explicit algorithms, the Courant condition is shown in Reference 3 to be

$$\frac{U_m\,t}{x} + \frac{V_m\,t}{y} + \frac{W_m\,t}{z} \leq 1 \qquad (13)$$

where

U_m = maximum fluid velocity in x direction.

V_m = maximum fluid velocity in y direction.

W_m = maximum fluid velocity in z direction.

In order to insure numerical stability, it is necessary to add a numerical viscosity which will overcome the effects of truncation errors. The amount of viscosity μ lies in the range

$$\frac{\Delta t}{2} \max\,(u^2, v^2, w^2) < \mu$$

$$\leq \frac{\Delta t}{2}\left(\frac{1}{\Delta x^2} + \frac{1}{\Delta y^2} + \frac{1}{\Delta z^2}\right) . \qquad (14)$$

IV. Bank Rejection Simulation

The geometry of the bank rejection simulation is shown in Figure 1.

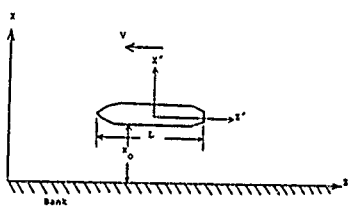


Figure 1. Geometry of Bank Rejection Simulation

The ship is positioned initially parallel to a bank located at X = 0. The channel depth was taken to be 1.5 times the draft. The particulars of the ship being simulated are shown in Table 2.

TABLE 2

Length between perpendiculars	1000 feet
Breadth	155 feet
Draft	65 feet
Height of C.G.	43.7 feet
Longitudinal Radius of Gyration	2500 feet
Transverse Radius of Gyration	56 feet

There were three sets of simulations run using this geometry. Two were captive tests in which the model was partially constrained and the third simulation had the model totally unconstrained. The unconstrained case utilized the model being propelled by a force applied at the approximate propeller location and directed along the axis of the ship. This effectively simulated a free-running model. One of the constrained cases allowed only surge motion, while the other simulation allowed only surge, heave, roll and pitch. In all the simulations, the ship was accelerated from rest to 6 knots during the initial 40 seconds of the simulation.

The simulation results consist of the three forces and three moments on the ship, the fluid velocity, pressure, and free-surface elevation. The forces and moments all exhibited a large overshoot associated with the transient start-up phenomenae, after which they settled down to an equilibrium value. The side force and side moment are normalized to yield a side force coefficient (C_X) and turning moment coefficient (C_N). The normalizing constants are respectively C_F and C_H shown below.

$$C_F = \tfrac{1}{2}\rho BDV^2$$

$$C_H = \tfrac{1}{2}\rho B^2DV^2 \qquad (15)$$

where

ρ = Water density

B = Ship's Beam

D = Ship's draft

V = Forward velocity.

Measured model results for this case are presented in Reference 4. Table 3 gives a comparison of measured versus computed results for two different ship-to-bank separation distances.

Table 3

Summary of Results

	Computed Values		Measured Values	
$\frac{x_0}{L}$	C_x	C_N	C_x	C_N
0.133	0.56	0.92	0.6	0.8
0.222	0.16	0.8	0.25	0.4

The flow fields which develop are shown in Figures 2 and 3, which show velocity vector plots at two water depths (depth 3 being closest to the bottom). In these figures, the asymmetry associated with the bank (located toward the bottom) is clearly evident. The entrainment in the wake region may also be readily seen.

V. Esso Osaka Simulation

During 1977, the U. S. Maritime Administration, in conjunction with the U. S. Coast Guard and the American Bureau of Shippers, undertook a set of full-scale maneuvering trials using the Esso Osaka in the Gulf of Mexico. The goal was to provide a data base of full-scale maneuvering studies in several water depths at several speeds.

The purpose of this simulation was to try to derive information concerning the distribution of side forces experienced by the tanker during turning maneuvers in intermediate water depths. In order to do this, the measured position, velocity and heading information obtained in the sea trials was used to force the simulation model to follow the same trajectory. The hydrodynamic forces on the ship were recorded from the simulation. These could then be compared to the centripital force and rudder force to gain some insight into the amount of added mass associated with the maneuver.

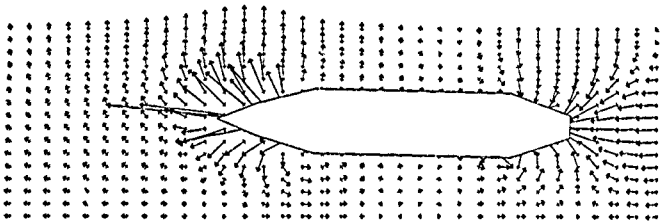


Figure 2. Velocity Vector Plot - Depth 9
Velocity Scale (FPS/INCH) 3.33

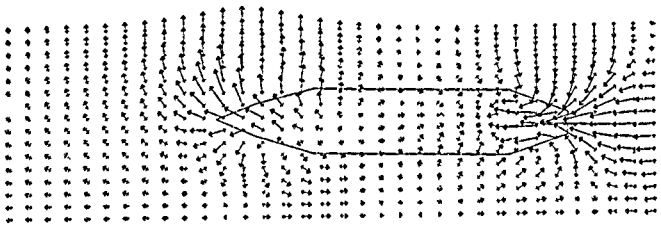


Figure 3. Velocity Vector Plot - Depth 3
Velocity Scale (FPS/INCH) 3.33

The scale of the simulation was large by any standard. It required 46,800 mesh points for the computational grid, which covered a region ½ mile by ½ mile by 100 feet deep. The one simulation reported here required about 150 hours of central processor time on a VAX 11/780 computer system. The simulation involved periodic rezoning of the grid, which allowed a subgrid containing the ship to be repositioned on the main grid as the hip moved through the mesh. Without this rezoning, the grid would have been four times as large.

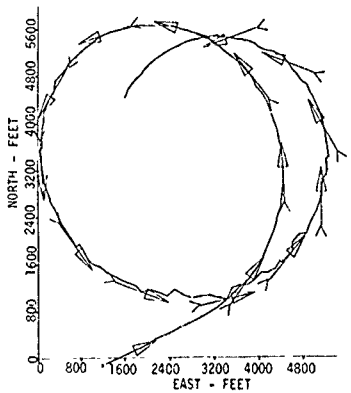


Figure 4. Run No. 4711

The results of the sea trial are described in Reference 5. We simulated Run 4711, which was a medium water depth turning circle maneuver, whose trajectory is shown in Figure 4. The duration of the maneuver was approximately one hour.

A theoretical rudder force was taken from empirical results presented in Reference 6. A centripital force was calculated according to equation (16)

$$F_S = MV^2/R \qquad (16)$$

where

M = Mass of ship.

V = Forward velocity of ship

R = Turning radius.

The primary result of this simulation is shown in Figure 5, which compares the computed hydrodynamic side force to the sum of the theoretical centripetal force and rudder force. The conclusion which may be drawn from the close agreement of the curves is that the added mass associated with the maneuver is small. This is borne out by an examination of the trajectory plot which shows that the ship stays nearly tangent to the turning circle during the course of the maneuver.

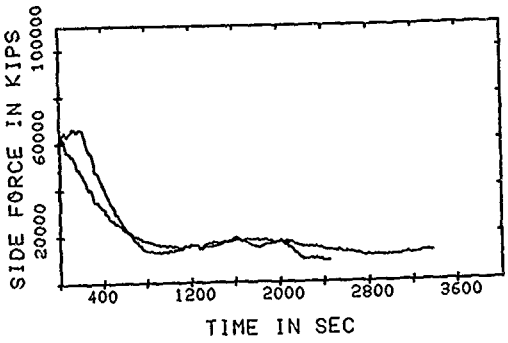


Figure 5. Run No. 4711

REFERENCES

1. G. I. Bourianoff and B. R. Penumalli, "Numerical Simulation of Ship Motion by Eulerian Hydrodynamic Techniques, The Proceedings of the Second International Conference on Numerical Ship Hydrodynamics, Berkeley, California, 1977.

2. G. I. Bourianoff and B. R. Penumalli, "Computational Prediction of Ship Motion in Confined Waters Using Inertial Marker Particles," Maritime Administration, Report No. MA-RD-940-77084A, November 1978.

3. Patrick J. Roache, Computational Fluid Dynamics, Hermosa Publishers, Albuquerque, NM, 1972.

4. I. W. Dand, "Hydrodynamic Aspects of Shallow Water Collisions," The Royal Institute of Naval Architects, Spring Meeting, 1976.

5. C. L. Crane, Jr., "Maneuvering Trials of the 278,000 DWT Esso Osaka in Shallow and Deep Water," U. S. Maritime Administration and U. S. Coast Guard, Report No. MA-RD-940-79018, January 1979.

6. E. Kerwin, Phillip Mandel and S. Dean Lewis, "Experimental Study of Flapped Rudders," Journal of Ship Research, December 1972.

DISCUSSIONS
of the paper
by G I Bounanoff

THREE-DIMENSIONAL TIME-DEPENDENT NONLINEAR SHIP MOTION SIMULATION USING THE INERTIAL MARKER PARTICLE TECHNIQUE

Discussion
by Choung M. Lee

I understand that when a ship is in turn there exist a significant magnitude of side force contributed by the so-called cross-flow drag. Your calculation is based on the inviscid fluid theory, and, yet, the agreement shown in Figure 5 is very good. What is your opinion on this point ?

I would also like to know if there is an appreciable merit of using your numerical method compared to the existing theoretical methods such as slender-body theory and singularity distribution method in calculating the bank-suction force.

Author's reply

The first question raised by Dr. Lee may be explained by noting that the bearing angle through the entire maneuver was very small, as may be observed in Figure 4. The information in Figure 4 is measured data and not a computational result. It is well known that the bearing angle is frequently small for turning circle maneuvers executed in shallow water. The water depth for the measurement was somewhat deeper than water where one would normally expect to encounter this type of behavior, but it was clearly in a transitional region

Discussion
by P. Thomsen

My comment is not directed to the lecture just listened to but to the general topic of this morning. I should like to take up the review lecture of Dr. Lugt this morning and point at the manoeuvring ship. Yesterday in Dr. Bourianoff's representation it experienced a suction force and a yawing moment when approaching and passing the underwater bank. The comparison computed/measured was good in force and poor in moment (0.8 calculated, 0.4 measured). No wonder. The rear ship representation of flow and lack of vortex replacement for the wake after the ship brought it about. In that respect I did not understand Dr. Bourianoff yesterday who in way of discussion seemed to argue to have covered the rear ship physics in all main features. It could have been possibly, using the after ship vortex model quoted in the review this morning. If I see it right following the Klein-Prandlt-Betz argumentation quoted in the review paper. The Euler equations as used by Bourianoff do suffice for the model of manoeuvring ship the wake of which being replaced by neck lace, bilge and propeller vortex filaments. I should be interested in Dr. Bourianoff's opinions on the total flow and its representation.

Author's reply

The calculation is, of course, inviscid. This fact will result in significant differences for the boundary layer separation point as well as the location and strength of vortex generation. I made no attempt in my code to generate vortices, although it is possible that such a routine could be added.

NONLINEAR SHIP MOTIONS

T. Vinje and P. Brevig
Norwegian Institute of Technology
and
Norwegian Hydrodynamic Laboratories
Trondheim, Norway

Abstract

A numerical method is presented for time simulation of the nonlinear motions of 2-D surface-piercing bodies of arbitrary shapes on finite water depths. The method is based on potential theory and periodicity in space is assumed. At each time-step Cauchy's integral theorem is applied to calculate the complex potential and its time derivative along the boundary. The solution is stepped forward in time by integrating the exact kinematic and dynamic free-surface boundary conditions as well as the equations of motion of the body.

The results are compared with results from linear theory for freely floating circular cylinders initially displaced from equilibrium, showing good agreement. The motion of the cylinder does not seem to be influenced to any great extent by nonlinear effects, even for extremely large initial displacements. The results also agree well with linear theory for a circular cylinder in forced heaving motion. However, large deviations occur between this method and Faltinsen's (ref. /6/) nonlinear method for larger amplitudes of forced heaving motions. Examples of nonlinear motions of ship-like bodies in beam seas are presented.

Introduction

Recent accidents with smaller fishing vessels and freighters have focused a certain interest on the problem of extreme ship motions, with a particular emphasis on the capsizing problem. There exist many modes of capsizing, and each of these modes seem to need a special theory to explain its development.

In this paper we will approach the problem of capsizing in beam seas, caused by extreme (often breaking) waves.

The numerical description of 2-D breaking waves has successfully been brought through by Longuet-Higgins and Cokelet /1/ and later by Vinje and Brevig /2/ (solving the problem in a slightly different way). Some confidence in the numerical model is gained by referring to McIver and Peregrine /3/ who have compared results from the different methods, and to Brevig et al. /4/ who have compared the numerically calculated wave form with experimental results furnished by the University of Edinburgh.

In reference /4/ the problem of calculating the forces on submerged, stationary cylinders under breaking waves has been treated, together with the more advanced problem of calculating the motion of submerged, freely floating (or moored) cylinders under breaking waves. This method has been further developed to deal with surface-piercing cylinders and this is what we will present in this paper.

Formulation of the problem

In the development of the present method we have been aiming at the problem of capsizing in extreme beam waves. This is a highly transient problem, and accordingly we are permitted to make one simplifying assumption, in addition to the assumption of potential flow (which is discussed by Nichols and Hirt /5/). This is: the boundary conditions at infinity are, as for the breaking wave, determined from periodicity in space. As long as this period in space, L, is long enough (or the actual time interval is short enough), the solution of the initial value problem will not be significantly affected. This in turn enables us to introduce a nonlinear incoming wave, which we otherwise would have had problems with introducing (see Faltinsen /6/). The transient nature of the problem also justifies treating it as an initial value problem, as long as the initial values are properly chosen.

The mixed Eulerian/Lagrangian description from reference /2/ is used, together with a modified Lagrangian

description on the body (following points fixed to the body surface). The fluid is assumed to be homogenous and incompressible and the flowfield irrotational. Together with the assumption of 2-D motion this means that the complex potential is applicable for describing the fluid flow:

$$\beta(z;t) = \phi(x,y;t) + i\psi(x,y;t) \qquad (1)$$

where $z = x + iy$.

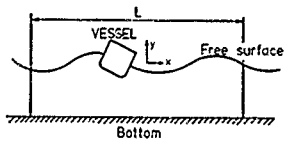


Figure 1 Definition sketch

The problem is, as indicated earlier, solved as an initial value problem with the position and velocity of the body as well as the elevation and velocity potential along the free surface given at $t = 0$. From these initial conditions the position and the potential of a fluid particle at the free surface are integrated in time from the kinematic boundary condition

$$\frac{Dz}{Dt} = u + iv = w^* \qquad (2)$$

and from the dynamic boundary condition

$$\frac{D\phi}{Dt} = \tfrac{1}{2}w\cdot w^* - gy - p_s/\rho \qquad (3)$$

where * denotes complex conjugation, $D(\ )/Dt$ the material derivative:

$$\frac{D(\ )}{Dt} = \frac{\partial(\ )}{\partial t} + \nabla\phi\cdot\nabla(\ ) \qquad (4)$$

and p_s is an arbitrary pressure distribution applied at the free surface.

Since $\beta = \phi + i\psi$ is analytic inside the fluid domain Cauchy's integral theorem is valid:

$$\int_C \frac{\phi + i\psi}{z - z_o}\,dz = 0 \qquad (5)$$

assuming C to be the closed contour consisting of the bottom, the submerged part of the body, the free surface and two vertical boundaries a distance L apart (see figure 1), and with z_o situated outside C, as shown on figure 2.

Assuming C to consist of C_ϕ and C_ψ, where ϕ is given on C_ϕ and ψ on C_ψ, and letting z_o approach C from the outside, the following two equations can be derived from equation 5:

$$\alpha\phi(x_o,y_o;t) + Re\{\int_C \frac{\phi + i\psi}{z - z_o}\,dz\} = 0 \qquad (6)$$

for z_o on C_ϕ and

$$\alpha\phi(x_o,y_o;t) + Re\{i\int_C \frac{\phi + i\psi}{z - z_o}\,dz\} = 0 \qquad (7)$$

for z_o on C_ψ. Here α is the angle between the two tangents of C at z_o. On a smooth curve $\alpha = \pi$. Equations 6 and 7 form a Fredholm's integral equation of the second kind, from which $\beta = \phi + i\psi$ can be found on C. Notice that both equations 5, 6 and 7 are valid when $\phi + i\psi$ is replaced by any analytic function, such as $\partial(\phi + i\psi)/\partial t$.

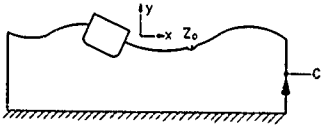


Figure 2 The contour C and the point z_o

On the free surface ϕ is given (according to equation 3) and hence this is part of C_ϕ. The bottom forms a streamline and accordingly is part of C_ψ. On the vertical boundaries both ϕ and ψ are unknown, but the application of periodicity furnishes us with the necessary additional conditions. On the vessel ψ is given from

$$\psi = -\tfrac{1}{2}\dot{\theta}\zeta\zeta^* - Im\{w_G\zeta^*\} \qquad (8)$$

where θ is the roll angle of the rigid body and w_G is the complex velocity, $w_G = \dot{z}_G$ of the reference point (center of gravity) G, fixed in the body. ζ is shown on figure 3.

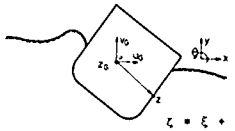


Figure 3

This obviously leads to the conclusion that the body surface is part of C_ψ

To step the solution forward in time we have to establish the dynamic equations of the vessel:

$$M_B \ddot{z}_G = -i \int_{C_B} p\,dz \qquad (9)$$

$$I_B \ddot{\theta} = -\mathrm{Re}\{ \int_{C_B} p\zeta\,dz \} \qquad (10)$$

where G is assumed to coincide with the center of gravity. M_B and I_B are the mass and the moment of inertia of the vessel, respectively, C_B is the wetted part of the body surface, and p is the pressure, calculated according to Bernoulli's equation:

$$-p/\rho = \frac{\partial\phi}{\partial t} + \tfrac{1}{2}w\cdot w^* + gy \qquad (11)$$

To evaluate p, $\partial\phi/\partial t$ has to be calculated. This is done according to equation 5, when $(\phi + i\psi)$ is replaced by $\partial(\phi + i\psi)/\partial t$. In this case we have

$$\frac{\partial\phi}{\partial t} = -\tfrac{1}{2}w\cdot w^* - gy - p_s/\rho \qquad (12)$$

on the free surface, $\partial\psi/\partial t$ constant on the bottom and $\partial\phi/\partial t$ and $\partial\psi/\partial t$ periodic on the vertical boundaries. On the body we have from equation 8:

$$\frac{\partial\phi}{\partial t} = n\dot{x}_G - \zeta\dot{y}_G - \tfrac{1}{2}\dot{\theta}|\zeta|^2$$

$$-\mathrm{Im}(w_G w) + \mathrm{Re}(\zeta(w_G^* - w)\dot{\theta}) \qquad (13)$$

where w is the complex fluid velocity at C_B, $w = u - iv$, and $\overline{\mathrm{Re}(z)}$ and $\mathrm{Im}(z)$ are the real and imaginary part of z, respectively. The development of this equation is found in appendix. The total solution, $\partial(\phi + i\psi)/\partial t$ now can be found on C in the following form:

$$\frac{\partial}{\partial t}(\phi + i\psi) = \phi_{1t}\ddot{x}_G + \phi_{2t}\ddot{y}_G + \phi_{3t}\ddot{\theta} + \phi_{4t} \qquad (14)$$

where ϕ_{jt} are uniquely determined from the boundary conditions. Introducing this into equations 9 and 10 yields:

$$(M_B + A_{xx})\ddot{x}_G + A_{xy}\ddot{y}_G + A_{x\theta}\ddot{\theta} = F_x$$

$$A_{yx}\ddot{x}_G + (M_B + A_{yy})\ddot{y}_G + A_{y\theta}\ddot{\theta} = F_y \qquad (15)$$

$$A_{\theta x}\ddot{x}_G + A_{\theta y}\ddot{y}_G + (I_B + A_{\theta\theta})\ddot{\theta} = F_\theta$$

where A_{pq} and F_p depend on the geometric form of C, while F_p also depends on $\dot{x}_G$, $\dot{y}_G$, $\dot{\theta}$ and the spacial distribution of the fluid velocity. The development of equations 14 and 15 is shown in appendix.

By eliminating $\ddot{x}_G$, $\ddot{y}_G$ and $\ddot{\theta}$ from equation 15, the equations of motion of the body are brought into the standard form:

$$\ddot{Y}_i = F_i(Y_j, \dot{Y}_j, t) \qquad (16)$$

Numerical solution

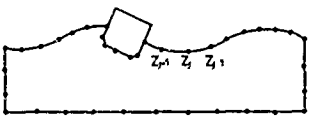


Figure 4 Elements along the boundary

To evaluate the integral of equation 5 we assume β (and $\partial\beta/\partial t$) to vary linearly between the nodal points on C (see figure 4).

The influence function of the variables at the nodal point z_j is therefore:

$$\lambda_j(z) = \frac{z - z_{j+1}}{z_j - z_{j+1}} \quad \text{for } z \text{ on C between } z_j \text{ and } z_{j+1}$$

$$\lambda_j(z) = \frac{z - z_{j-1}}{z_j - z_{j-1}} \quad \text{for } z \text{ on C between } z_{j-1} \text{ and } z_j \qquad (17)$$

and zero elsewhere on C.

Application of the collocation method then yields the following matrix equations:

$$\int_C \frac{\phi + i\psi}{z - z_k}\,dz = \sum_j \Gamma_{kj}\beta_j = 0 \qquad (18)$$

$$\int_C \frac{\partial\phi/\partial t + i\,\partial\psi/\partial t}{z - z_k}\,dz = \sum_j \Gamma_{kj}\frac{\partial\beta_j}{\partial t} = 0 \qquad (19)$$

where $\beta_j = \beta(z_j;t)$, $\partial\beta_j/\partial t = \partial\beta(z_j;t)/\partial t$ and

$$\Gamma_{kj} = \frac{z_k - z_{j-1}}{z_j - z_{j-1}}\ln\frac{z_j - z_k}{z_{j-1} - z_k} + \frac{z_k - z_{j+1}}{z_j - z_{j+1}}\ln\frac{z_{j+1} - z_k}{z_j - z_k}$$

with limiting values applied when k=j-1, j or j+1. If

$$\alpha = \frac{z_{j-1} - z_j}{z_j - z_k}$$

$$\alpha = \frac{z_{j+1} - z_j}{z_j - z_k}$$

are both small then we can use asympto-

tic expressions for the logarithms giving:

$$\Gamma = \frac{\delta - \epsilon}{2}\left[1 - \frac{\delta + \epsilon}{3}\right]$$

Introduction of this when appropriate reduces the cost of running the program by about 40%.

To do the time-stepping $w(z;t) = d\beta(z;t)/dz = u - iv$ has to be calculated along the boundary. In general $w(z_o;t)$ can be found from:

$$w(z_o;t) = \frac{1}{2\pi i}\oint_C \frac{\beta(z;t)}{(z-z_o)^2}\,dz \qquad (20)$$

(where z_o is inside the fluid domain). This expression turns out to be singular at the nodal points. This means that w on the boundary has to be calculated in a different way and a second order differentiation scheme is introduced.

To integrate equations 2, 3 and 16 in time Hamming's fourth-order predictor/corrector method is applied with a Runge-Kutta starting procedure. This method has shown to be remarkably stable and no numerical instability has been observed.

Numerical results

To gain a certain confidence in our numerical model we have compared our results to those given by Maskell and Ursell /8/ (the numerics kindly furnished by professor Ursell) for a circular cylinder, starting from rest with an initial displacement. Their solution is based on linear theory and on a semi-infinite fluid domain. To estimate the influence of our periodicity assumption we have modified the results of Maskell and Ursell by introducing a series of pulsating sources at a distance L apart and with source strengths given from the rate of change of the displaced volume of the cylinder (for details: see reference /7/). The surface elevation from these sources at the [illegible] of the cylinder is then introduced into the long-wave theory, yielding the broken line on figure 5. We have then run our program for a relative displacement $y(0)/R = 0.05$ and $R/L = 1/30$ (L as given on figure 1). The results seem to agree well with the modified linear theory.

Figure 6 shows our numerical results for $y(0)/R = 0.05$ and 0.9, with the intermediate values discarded. The results do not seem to be greatly affected by the nonlinearities, even for the extreme case, $y(0)/R = 0.9$. The largest deviation from the small amplitude solution occurs for the acceleration at $t = 0$, where it is about 40% larger in magnitude. However this value, $\ddot{y}(0)R/y(0)g = 0.901$, is in good agreement with the results of Kaplan and Silbert /13/, yielding the exact value: 0.910.

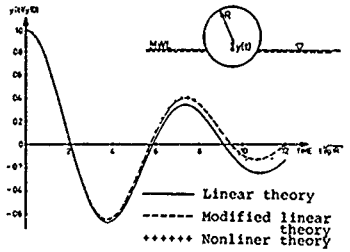


Figure 5 Motion of a freely floating circular cylinder with small initial displacement ($y(0)/R = 0.05$)

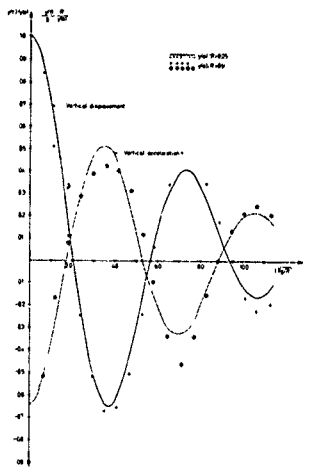


Figure 6 Motion of a freely floating circular cylinder with different initial displacements

In reference /6/ Faltinsen has given some results for forced harmonic heave motion of a circular cylinder starting from rest. With minor changes our pro-

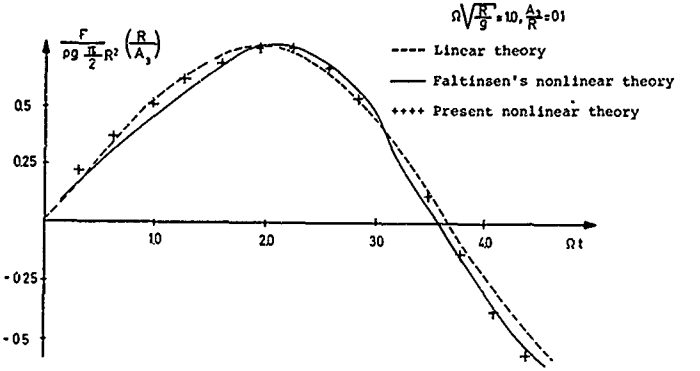


Figure 7 Hydrodynamic force on a half submerged circular cylinder in forced heave motion, $y(t) = A_3 \sin(\Omega t)$. The linear restoring force, $-2\rho g R y(t)$, is excluded. R is the radius of the cylinder

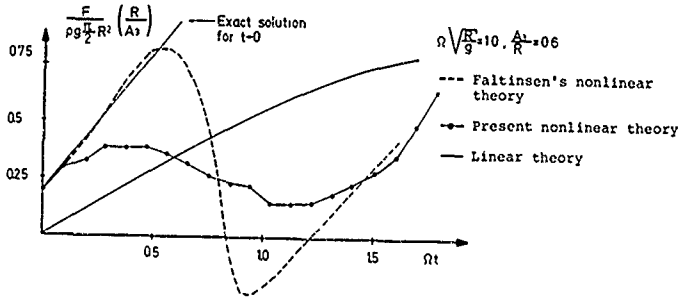


Figure 8 Hydrodynamic force on circular cylinder, $A_3/R = 0.6$

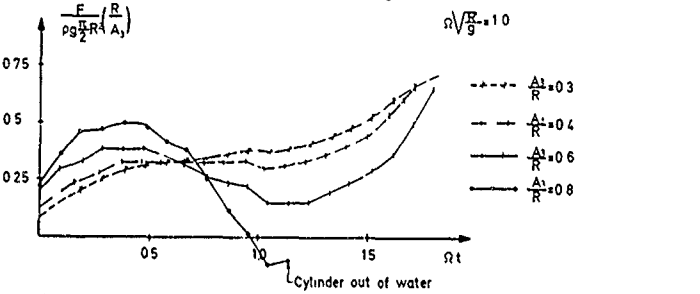


Figure 9 Hydrodynamic force on circular cylinder for different amplitudes of forced heave motions

gram was modified to deal with this problem, and comparisons of the results with the ones from reference /6/ are shown on figures 7 and 8.

Figure 7 clearly shows that both Faltinsen's and our results agree well with linear theory for smaller amplitudes of oscillation ($A_3/R = 0.05$).

When comparing the results for larger amplitudes ($A_3/R = 0.6$) rather large discrepancies occur , as shown on figure 7. The asymptotic expansion of the force for $t \to 0$, developed in reference /7/:

$$F = F_0 + F_1 t \qquad (21)$$

is drawn on figure 8. The two numerical solutions seem to agree well with it for small values of t, which does not indicate that any of them is in error. The plot on figure 8 of the linear solution does not give any clear indication either. Both solutions are that far away from this curve that no conclusion can be drawn.

What can cause the differences between the results given by the two methods? Faltinsen's thorough discussion of his b(t)-value and the results of figure 5 rule out that the matching between the "inner problem" and the "outer" can be the source for the discrepancies. Further more: the initial distribution of elements along the free surface and on the body is the same in both cases. The time-stepping procedure is not expected to give rise to large errors; both Faltinsen's (Runge-Kutta) and the present (Hamming's P/C) are expected to be stable and have rather small round-off errors. The differences between the methods appear in the way Laplace's equation is solved, the way the force is calculated and where the "marked particles" are situated on the elements. Without much detailed knowledge about Faltinsen's numerical results, it is hard to say which causes the difference. The solution of Laplace's equation is probably not the one. In this case the errors would expectedly had shown up for small amplitudes also. Though the calculation of the force is different, it is not expected to cause the trouble; a check by applying Faltinsen's method on our numerical solution did not give rise to differences of the actual order. What we then are left with is the way the particles on the free surface are situated and how their velocities are calculated. Especially the position of the particle closest to the body is of importance, both for estimation of the wetted surface (and hence the static force) and because of the possible singularity at the intersection point between the body and the free surface. (see discussion in ref. /7/). It is difficult to draw any conclusions from the fact that Faltinsen's "closest particle" is about half the distance away from the body compared with our "closest particle". To place the particle too close to a singularity (even if it is a weak one) can cause trouble when the numerical procedure is based on non-singular velocities. On the other hand: if the solution is non-singular at the intersection point, to put the particle closer to the body will give a better fit, and expectedly a better solution.

C.M. Lee /9/, Parissis /10/ and Potash/11/ have developed second order perturbation solutions for forced oscillations of a circular cylinder. These theories predict the amplitude of the second order force to be about 1/3 of that of the first order (for $\Omega\sqrt{R/g}=1.0$, $A_3/R = 0.6$). Faltinsen's linear calculations indicate that steady state is (approximately) reached at $\Omega t = 2.0$. These two statements indicate that the solution is expected to be within ± 50% of the linear solution from Ωt is, say 1.5, which is hardly the case for either of the two numerical solutions. The experiments of Tasai and Koterayama /12/ do not seem to give any additional information. We are, in other words, forced to conclude that we are unable to determine which of the two nonlinear methods is most in error.

Figure 9 shows our results for various amplitudes of forced motions. Notice that for $A_3/R = 0.8$ the cylinder leaves the water when Ωt is about 1.0.

Finally we have simulated the motions of a ship-like body in beam seas and tried to compare our results with those of model tests carried out at the Norwegian Hydrodynamic Laboratories. Because of the computer costs we tried to start the simulation in the middle of the run and had to estimate the initial conditions. Even though we had 8 wave recorders working in the experiments, the near field wave elevation was not available, and the same was the case with the velocity potential along the free surface. We therefore chose the arbitrary initial condition that the free surface elevation and the potential along it were given from the linear wave theory, with a phase estimated from the 8 wave records. The initial position and velocity of the body were taken from the model tests. On figure 10 the initial conditions are shown.

Some of our results are shown on figures 11 and 12. We have here followed the development in time for about one wave period. During this time the body has drifted against the wave, which seems rather strange. If we examine the sketches closer we observe unexpected

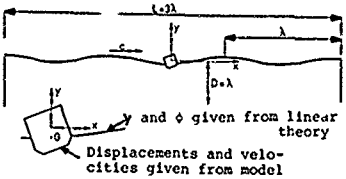


Figure 10 Initial conditions

Wave steepness	= 0.054
Wavelength/ beam of body	= 1.0
Wave period/natural roll period of body	= 1.05

irregularities on the free surface up to the time of the order t = T/2. Further more the vessel seem to oscillate in time at a period closer to the characteristic period in roll than to the wave period (this seems partly to be the case for the experiments too) and with a not completely developed steady list. All these observations indicate that the initial conditions are not properly chosen to fit into a steady state condition, and for sure not to match the experimental results.

On figure 12 we have plotted the calculated roll angle as a function of time together with the measured roll angle. In our opinion the agrement between the numerical and experimental results is fairly good considering the extreme roll angles we have simulated (as well as the uncertainties connected with the initial conditions).

More recently Dr. Greenhow has run the program for a breaking wave acting on the wave-power device, "Salter's Duck", and has found good agreement with measurements. His results will be published later.

Conclusion

A numerical time-stepping procedure has been presented, calculating the nonlinear motions of 2-D surface-piercing bodies in beam seas.

The motions of a freely floating circular cylinder initially displaced from equilibrium are calculated. For small initial displacement the results agree well with the linear theory of Maskell and Ursell. Even for initial displacements of 0.9 R there seem to be only minor nonlinear effects, except in the initial acceleration. The forces acting on a circular cylinder in forced heaving motion have also been calculated For small amplitudes of motions (A_3/R = 0.1) the results agree well with linear theory. For larger amplitudes of motions (A_3/R = 0.6) we have compared our results with those of Faltinsen finding large discrepancies in the vertical forces. We are not able to explain why these deviations occur.

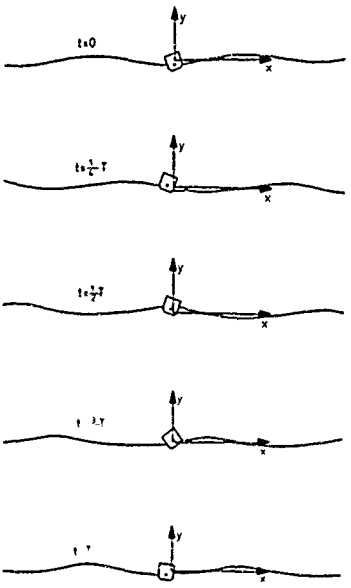


Figure 11 Motion of the body and the free surface as a function of time. T is the initial linear wave period

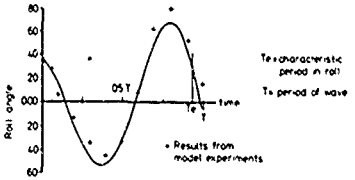


Figure 12 Roll motion, plotted versus experimental results

An example of the motions of a ship-like body in beam seas is presented. These results are compared with those of model tests, showing fairly good agreement. The discrepancies between the theoretical results and the model tests are expected to be due to the lack of proper data for the initial conditions used as input to the computer program.

Acknowledgement

A large amount of the programming used was developed under the research project: "Ships in Rough Seas", sponsored by The Royal Norwegian Council for Scientific and Industrial Research (NTNF), The Norwegian Fisheries Research Council (NFFR) and the Norwegian Maritime Directorate, and under the project: "Non-linear, 3D Hydrodynamic Theory", sponsored by NTNF.

The authors wish to thank Dr. Martin Greenhow for his valuable discussions and suggestions.

References

/1/ LONGUET-HIGGINS, M.S., and COKELET, E.D.:The deformation of steep surface waves on water, I. A numerical method of computation. Proc. Roy. Soc. London A, 350 1976

/2/ VINJE,T. and BREVIG,P.:Numerical simulation of breaking waves. 3rd Int.Conf. on Finite Elements in Water Resources, Univ. of Miss., Oxford, Miss., May 1980

/3/ McIVER,P., and PEREGRINE,D.H.:Comparison of Numerical and Analytical Results for Waves that are Starting to Break. International Conference on Hydrodynamics in Ocean Engineering, Trondheim, Norway, August 1981

/4/ BREVIG,P., GREENHOW,M. and VINJE,T.: Extreme Wave Forces on Submerged Cylinders, to appear

/5/ NICHOLS,B.D. and HIRT,C.W.:Non-linear Hydrodynamic Forces on Floating Bodies. Second International Conference on Numerical Ship Hydrodynamics, Univ. of California, Berkeley, USA, September 1977

/6/ FALTINSEN,O.M.:Numerical solutions of transient nonlinear free-surface motion outside or inside moving bodies. Second International Conference on Numerical Ship Hydrodynamics, Univ. of California, Berkeley, USA, September 1977

/7/ VINJE,T. and BREVIG,P.:Nonlinear two-dimensional ship motions. SIS-report, Norwegian Hydrodynamic Laboratories, 1980

/8/ MASKELL,S.J. and UPSELL,F.: The transient motion of a floating body J.Fluid.Mech., vol. 44, 1970

/9/ LEE,C.M.:The Second-order Theory of Heaving Cylinders in a Free Surface J.of Ship Research, December 1968

/10/ PARISSIS,G.:Second-order Potentials and Forces for Oscillating Cylinders on a Free Surface: Dissertation, MIT Report 66-10. 1966

/11/ POTASH,L.R.:Second-order Theory of Oscillating Cylinders. J. of Ship Research, December 1971

/12/ TASAI,F. and KOTERAYAMA,W.: On the Non-Linear Hydrodynamic Forces for Heaving Circular Cylinder on a Free Surface. Trans. of W.Japan Soc. of Naval Arch., No. 46, August 1973

/13/ KAPLAN,P. and SILBERT,M.N.: Impact Forces on Platform Horizontal Members in the Splash Zone, OTC-paper no. 2498, 1976

/14/ WHITTAKER,E.T.: A Treatise on the Analytical Dynamics of Particles and Rigid Bodies. 4th edition, Dover Publications, 1944

Appendix

Development of equations 13,14 and 15.

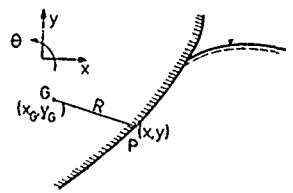


Figure A.1.

The value of ϕ along the wetted part of the body surface is given according to equation 8 as:

$$\phi = -\tfrac{1}{2}\dot{\theta}R^2 + u_G(y-y_G) - v_G(x-x_G) \qquad (A.1)$$

where R, (x_G,y_G) and (x,y) are given on figure A.1 and $\vec{v}_G = u_G\vec{i} + v_G\vec{j}$ is the velocity vector of the center of gravity G.

If we follow the point P, fixed to the body, the change in time of the

stream function becomes:

$$\frac{\delta\Phi_P}{dt} = (y-y_G)\frac{du_G}{dt} + u_G\frac{\delta}{dt}(y-y_G)$$

$$-(x-x_G)\frac{dv_G}{dt} - v_G\frac{\delta}{dt}(x-x_G)$$

$$-\tfrac{1}{2}R^2\frac{d\dot\theta}{dt} - \tfrac{1}{2}\dot\theta\frac{\delta R^2}{dt} \qquad (A.2)$$

where the operator δ/dt indicates the change in time when actually following the point .

According to Chasles theorem (see reference /14/) we have:

$$\frac{\delta}{dt}(x-x_G) = -\dot\theta(y-y_G)$$

$$\frac{\delta}{dt}(y-y_G) = \dot\theta(x-x_G) \qquad (A.3)$$

Substituting this, together with $\delta/dt\ R^2 = 0$, into equation A.2 yields:

$$\frac{\delta\Phi_P}{dt} = (y-y_G)\ddot x_G - (x-x_G)\ddot y_G - \tfrac{1}{2}\ddot\theta R^2$$

$$+\dot\theta(\dot x_G(x-x_G) + \dot y_G(y-y_G)) \qquad (A.4)$$

Equation A.4 is based purely on the determination of Ψ from equation 8, which only takes into account the rigid body motion. From "the fluid's point of view" $\delta\Psi_P/dt$ can be expressed as follows:

$$\frac{\delta\Psi_P}{dt} = \left(\frac{\partial\Psi}{\partial t}\right)_P - \vec v_P\cdot(\nabla\Psi)_P \qquad (A.5)$$

where $\vec v_P$ is the (rigid body) velocity of the point P:

$$\vec v_P = (\dot x_G - \dot\theta(y-y_G))\vec i + (\dot y_G + \dot\theta(x-x_G))\vec j \qquad (A.6)$$

and $(\nabla\Psi)_P$ is given in terms of the velocity, $\vec v = u\vec i + v\vec j$, of the fluid particle at the point P:

$$(\nabla\Psi)_P = -v\vec i + u\vec j \qquad (A.7)$$

yielding:

$$\vec v_P\cdot(\nabla\Psi)_P = -\dot x_G v + \dot y_G u + \dot\theta((x-x_G)u + (y-y_G)v) \qquad (A.8)$$

Combining equations A.2, A.5 and A.8 then finally gives:

$$\left(\frac{\partial\Phi}{\partial t}\right)_P = \frac{\delta\Phi_P}{dt} - \vec v_P\cdot(\nabla\Psi)_P = (y-y_G)\ddot x_G$$

$$-(x-x_G)\ddot y_G - \tfrac{1}{2}R^2\ddot\theta + \dot x_G v - \dot y_G u$$

$$+\dot\theta((\dot x_G - u)(x-x_G) + (\dot y_G - v)(y-y_G)) \qquad (A.9)$$

which is identical to equation 13.

Writing $(\partial\Phi/\partial t)_P$ in the following form:

$$\left(\frac{\partial\Phi}{\partial t}\right)_P = \frac{\partial\Phi_1}{\partial t}\ddot x_G + \frac{\partial\Phi_2}{\partial t}\ddot y_G + \frac{\partial\Phi_3}{\partial t}\ddot\theta + \frac{\partial\Phi_4}{\partial t} \qquad (A.10)$$

and

$$\frac{\partial\Phi}{\partial t} = -\tfrac{1}{2}w\cdot w^* - gy = \frac{\partial\Phi_4}{\partial t}$$

on the free surface we will find a unique solution on C, given as equation 14:

$$\left(\frac{\partial\Phi}{\partial t} + i\frac{\partial\Psi}{\partial t}\right) = \beta_{1t}\ddot x_G + \beta_{2t}\ddot y_G + \beta_{3t}\ddot\theta + \beta_{4t} \qquad (A.11)$$

where β_{jt} , $j = 1,2,3$ are found from the following problem:

$$\frac{\partial\Phi}{\partial t} = 0 \quad \text{on the free surface}$$

$$\frac{\partial\Psi}{\partial t} = \frac{\partial\Psi_j}{\partial t} \quad \text{on the body}$$

together with the homogenous boundary conditions on the bottom and on the vertical boundary lines. β_{4t} is then found from:

$$\frac{\partial\Phi}{\partial t} = \frac{\partial\Phi_4}{\partial t} \quad \text{on the free surface}$$

$$\frac{\partial\Psi}{\partial t} = \frac{\partial\Psi_4}{\partial t} \quad \text{on the body}$$

together with the same homogenous boundary conditions on the rest of C.

The solutions as such are found by replacing $(\Phi + i\Psi)$ by $(\partial\Phi/\partial t + i\,\partial\Psi/\partial t)$ in equation 5. This means that the matrix of the set of linear equations is unaltered (from the problem of finding $(\Phi + i\Psi)$), while the right hand side vector has to be reestablished for each problem.

The generalized forces:

$$f_j = -\int_{C_{WET}} p\,n_j\,d\,C \qquad (A.13)$$

acting on the body from the fluid now can be calculated as:

$$f_j = -\int_{C_{WET}} \rho\left(\frac{\partial\phi_1}{\partial t}\ddot{x}_G + \frac{\partial\phi_2}{\partial t}\ddot{y}_G + \frac{\partial\phi_3}{\partial t}\ddot{\theta}\right.$$

$$\left. + \frac{\partial\phi_4}{\partial t} + \tfrac{1}{2}w\cdot w^* + gy\right)n_j dC \quad (A.14)$$

where n_j is the generalized normal vector component. Now A_{pq}, of equation 15, is found as:

$$A_{pq} = \int_{C_{WET}} \rho \frac{\partial\phi_q}{\partial t} n_p dC \quad (A.15)$$

and F_p as:

$$F_p = -\int_{C_{WET}} \rho\left(\frac{\partial\phi_4}{\partial t} + \tfrac{1}{2}w\cdot w^* + gy\right)n_p dC \quad (A.16)$$

It is now easily seen that A_{pq} only depends on the geometric form of the contour C, while F_p depends on this geometric form plus $\ddot{x}_G$, $\ddot{y}_G$, $\ddot{\theta}$ and the spacial distribution of the fluid velocity.

DISCUSSIONS
of the paper
by Tor Vinje and Per Brevig

NONLINEAR SHIP MOTIONS

Discussion
by P. Thomsen

Mr. Brevig, you had left out the restoring moment in the equation of equilibrium. It seems to me that this is the *reason for certain discrepancies* versus experiment that you seemed to stress in your talk. It is the instantaneous position of the axis of rotation that the weight force in its lever for restoring moment refers to. That position, in turn, is obtained according to basic principles of mechanics by resulting instantaneous dynamic force and moment due to the pressure distribution along the contour as computed by your routine.

You could read, if you want, Grim "Roll motions of two-dimensional forms", HSVA report, about 1960. There this instantaneous axis and the full mechanics of the problem is done for rolling, non-capsizing bodies at free oscillations -as I remember now.

Authors' reply

I am afraid the question goes more on classical mechanics than on hydrodynamics and I will therefore try and answer very briefly. The problem is in principle stated in a way that we have a rigid body acted on by the forces from the fluid, which is the common way of formulation ship motion problems. What it then boils down to is : if it is permissible to use the center of gravity of the rigid body as a reference point for the motion of this body. The answer is undoubtedly yes, and I will only refer to : Landau & Lifshitz : Course of Theoretical Physics, Vol. 1, Mechanics, § 34 for a further discussion. Dr. Thomsen's suggestion that the instantaneous center of rotation should be used as the reference point has the advantage that only the rotation will become an unknown quantity directly connected to the motion of the body. On the other hand the equation of motion will, for this finite displacement problem, become a mess and in addition the position of the center of rotation has to be integrated in time. This method will be preferable for many problems in classical mechanics, but I doubt if it is sensible even to try to apply it to this problem.

Discussion
by Choung M. Lee

Linear roll-motion prediction based on potential-flow theory normally is significantly larger than the measured values at the resonant frequency. This discrepancy has been understood to be due to the absence of viscous damping in the calculation. The good agreement you have shown in Figure 12 seems to imply that an accurate pressure calculations at the instantaneous position of the body is sufficient to predict roll motion accurately, without introducing the viscous damping in the equations of motion. Do you have any comment on this point ?

Authors' reply

We will thank Dr. Lee for asking this question that points out that we have not stressed properly : the basis for the results of our figure 12. Namely, the initial conditions for the time history shown are picked from the experimental data. What is then compared are the experimental results and the numerical calculations based on the same initial condition (for t = 0 on the figure). Since the damping is small, the motions shown on the figure are dominated more by the initial conditions than by the integrated damping effect. One has to bear in mind that we originally were aiming at capsizing of smaller vessels, where everything happens that fast that the damping is not expected to play any important role (even though it is of great importance for the initial values chosen for the vessel motions in this case). I hope this answers Dr. Lee's question.

Discussion
by A. Papanikolaou

Illuminating the background of my following questions I would like first to refer to a paper presented by H. Nowacki and myself last fall in Tokyo [1] (13th ONR Symp. 1980) and some previous work of mine cited in [1] . In my opinion the known frequency-domain-techniques like ref. [9] - [11] in your paper and [1] (i.e. : regular perturbation expansions, frequency-domain transfer model assumption and solution of linear BVP by integral-equation methods)are till today much more successful in treating any nonlinear ship-motions related problems (2D case) than any of the known time domain techniques, Faltinsen's work (1977) included. I would appreciate the answers or comments of the authors to my following objections :

1.- Did you compare your results for other than the indicated section forms, e.g. for more difficult shapes like triangles, with frequency-

domain-techniques results ? Because our theoretical results in [1] are in very good agreement with experimental data by Tasai-Koterayama (1976) and Yamashita (1977) why did y not trust in a comparison with these well known results (forced-heaving-second order) ?

2.- Your aim in this paper was apart from the treatment of the initial behaviour of oscillating ships the computing of the periodic but nonlinear forces motions etc, when initial phenomena have gone to zero.With reference to your fig. 7, 8, 9 after how many time did you establish a periodic solution and at what period if at all ? In fig. 9 for $A_3/R = 0.8$ and $\Omega t \sim 1.1$ your cylinder is leaving the water. What is then the meaning of your definition for A_3 ?

3.- Did you include in your considerations drifting forces ? On page 6 (below) you mentioned that the body runs against the wave. Do you mean it is a negative horizontal drifting force present and now can be explained this in terms of potential theory by momentum considerations (Maruo (1960)) ?

Concluding I can not see any improvement in comparison to already existing solution procedures. But I concede that there are some good reasons to expect that a well working time domain technique can be very successful in studying for example capsizing problems or BVP with initial conditions.

Reference

[1] A. Papanikolaou, H. Nowacki, "Second-Order Theory of Oscillating Cylinders in a Regular Steep Wave", Proc. 13th Symp. Naval Hydrod., Tokyo, 1980

Authors' reply

The answer to Dr. Papanikolaou's first question is negative ; we have not compared our theory with results for forced heave motions of other bodies than circular, neither have we tried to reach the steady-state solution in our simulations. We would like to stress, however, that we had no intention of reaching the steady state solution, since this solution obviously would be influenced by our assumption about periodicity. Our only aim with the forced heave simulations has been to get a certain amount of confidence in our numerical scheme, we feel that this confidence to a certain extent is confirmed by the comparisons presented in this paper.

As stressed in the presentation, the parameter A3 is defined as the amplitude of the forced heave motion. In figure 9 we indicate that the cylinder leaves the water for A3 equals .8 cylinder radius. This might be due to numerical errors, since small errors in the surface profile near the intersection point easily could result in a "non surface-piercing" cylinder. On the other hand we can not see any reason (either physical or theoretical) that the cylinder can not leave the water at smaller heaving amplitudes than its radius.

Regarding Dr. Papanikolaou's third question, we would like to stress that our formulation of the problem is a fully non-linear one, and in addition is transient in time, which means that talking about drift-forces has no sense. We agree with Dr. Papanikolaou that second-order frequency-domain analysis are powerful tools for ship motion problems, but we doubt that such methods can be used to describe the capsizing problem.

A NUMERICAL SIMULATION OF LARGE AMPLITUDE SLOSHING

Thomas J. Bridges
Ocean Engineering Program
Texas A & M University
College Station, Texas 77843, U.S.A.

Abstract

The volume of fluid technique, in combination with the SOLA algorithm, has been modified to simulate two-dimensional liquid sloshing in a moving container. A literature review shows that previous numerical investigations have not taken into account the moving boundary conditions, at the tank walls, and large surface displacements. A moving coordinate system is used, reducing the tank to rest, and making the wall boundary conditions homogeneous. A new technique, known as the volume of fluid technique, is used to track the free surface. It is not restricted to gentle surface slopes or single valued surfaces. Baffles can be easily introduced when using this method and results of both baffled and unbaffled tanks are shown. The study shows that dynamic loads due to large amplitude tank excitation can be computed numerically.

1. Introduction

An analytic study of the liquid motion in an accelerating container is not new, nor is it a specialized phenomena. Liquid sloshing includes such practical problems as earthquake induced lake oscillations, harbor oscillations, tank trucks on highways, liquid fuel in spacecraft, and sloshing of liquid cargo in oceangoing vessels. Early analytic studies were crude until the 1950's when man's exploration into space required accurate knowledge of the effect of slosh induced loads on vehicle trajectory. Analytic studies became more sophisticated, but most of the propellant dynamics problems were concerned with the relatively low amplitude slosh encountered during flight [1]. The more complex problems were solved by experimental rather than analytical techniques.

In the 1960's, as larger and larger liquid natural gas (LNG) tankers were produced, it became obvious that slosh generated loads must be taken into account in tank and support structure design. Accounting for liquid impact loads in cargo tanks is not restricted to LNG carriers since similar problems have been experienced in other types of liquid transport ships such as bulk oil carriers. However, several factors make slosh loads more important with regard to LNG ship design. In addition, the need for continued evaporation to maintain low temperatures results in LNG tanks being partially full; a condition creating the highest impact loads from liquid sloshing. This is discussed in more detail in Ref. 6.

Although a number of simplified analytic techniques, some linear and some nonlinear, have appeared in the literature, very few numerical investigations have appeared. Feng [8] used a 3-D version of the Marker and Cell (MAC) method to study sloshing in a rectangular tank. He acknowledges the difficulty with this method and the results reported indicate the presence of an instability. Besides requiring extensive computer time and storage, extensive logic is necessary to maintain an adequate number of marker particles on the free surface [20]. Faltinsen [7] suggests a boundary integral technique for numerically simulating sloshing, which satisfies the nonlinear boundary condition at the free surface. The method is transient and includes an artificial "viscosity." However, a fixed coordinate system is used, limiting the amplitude of the tank motion, and the surface is represented by a single-valued function of the horizontal coordinate. A recent paper by Nakayama and Washizu [18] uses the finite element method to represent the fluid. A moving reference frame is employed, allowing large amplitude excitation, and the nonlinear free surface boundary conditions are addressed using an "incremental procedure." Since the finite element method is a Lagrangian technique, the method will encounter severe difficulty when large fluid distortions are encountered, limiting the method to "gentle" sloshing. Some additional numerical studies of sloshing have been discussed by Kerczek [15].

In this paper, a recently developed numerical method is modified to address the unique nature of the sloshing problem. The method allows large amplitude roll and pitch excitations, steep and multi-valued free surfaces and baffles can be easily introduced.

The method, which combines the SOLA algorithm with a versatile fluid surface tracking algroithm, has recently been developed at Los Alamos Scientific Laboratory by Hirt and Nichols [13]. An experimental version of this algorithm, known as the volume of fluid (VOF) technique, was first suggested in Ref. 20.

The originators have since refined the method and applied it to several problems including nuclear reactor vent clearing hydrodynamics [21]. This method allows steep and highly contorted free surfaces. Actual fluid regions are tracked, not surfaces, while the location of the fluid implies an implicit knowledge of the location of the interface. This new method is based on a function whose value is unity at any point occupied by fluid and zero elsewhere. The average value of this function, F, in a grid cell then represents the fractional volume of the cell occupied by fluid. Thus, a unit value of F indicates the cell is full of fluid, while a zero value indicates an empty cell. Cells with F values between zero and one must then contain an interface. Thus, only one variable per cell is stored, which is equivalent to the storage requirement for all other flow variables. In addition, the F distribution used in the VOF method has all the remaining properties desired of an interface tracking scheme. Surface locations, slopes and curvatures are easily computed for the setting of boundary conditions and the F distribution can be advanced in time by advection through the Eulerian grid. However, since F is a step function, it is necessary to use special advection algorithms. The encouraging results obtained by Nichols and Hirt [21] on reactor hydrodynamics and the inherent flexibility of this method suggest its use for numerical simulation of sloshing.

In an Eulerian frame of reference, the entire flow field is discretized into a computational mesh and the computation of the flow field variables proceeds as a function of time at fixed spatial points. This discrete Eulerian grid system does not readily accommodate the continuous motion of solid bodies.

In the case of liquid sloshing, the fluid-tank interface is travelling through a finite difference grid system and will not, in general, coincide with the computational cell boundary at the end of each time step. This solid boundary-computational cell nonalignment will require complicated logic for the setting of boundary conditions and will likely lower the order of accuracy.

For this reason, it may be convenient to choose a frame of reference relative to which the boundary is at rest. This is accomplished by a non-inertial coordinate transformation. The Eulerian grid is in essence "attached" to the tank containing the fluid. The effect of this attachment is the addition of relative acceleration terms in the equations of motion.

2. Mathematical Formulation

The fluids considered are homogeneous, viscous, Newtonian and almost incompressible. For simplification, the tank and fluid motion are assumed to be two dimensional in space. The domain will be an enclosed, rigid rectangular container partially filled with liquid. The physical laws governing the fluid motion include the conservation of mass and conservation of momentum.

For an incompressible fluid, the density would be constant and the fluid would be nondivergent. Since it may be desirable for the fluid to be slightly compressible, in some cases, this concept is included. A discussion and derivation of this concept and its introduction into incompressible hydrocodes can be found in a paper by Hirt and Nichols [12]. If we normalize the fluid mean density to one, the modified continuity equation becomes,

$$\frac{1}{c^2}\frac{\partial P}{\partial t} + \nabla\cdot\vec{U} = 0 \qquad (2.1)$$

where c is the adiabatic speed of sound in the fluid.

Conservation of momentum requires that the rate of change of linear momentum of the fluid be balanced by the sum of the forces acting on the fluid. Before writing this equation it is necessary to discuss the modification necessary when the equation is referred to a set of moving axes.

The acceleration of an element of fluid relative to the moving frame of reference may be different from the absolute acceleration in the Newtonian frame of reference, and the equations of motion must be modified accordingly. A rigorous derivation of the relationship between a moving frame and a fixed frame can be found in any thorough text on mechanics of particles [23]. Simply stated; if we assume the tank is rotating about a fixed point in Newtonian space, the absolute acceleration of a fluid element is

$$\vec{A} = \vec{a} + 2\vec{\Omega}\times\vec{U} + \dot{\vec{\Omega}}\times\vec{r} + \vec{\Omega}\times(\vec{\Omega}\times\vec{r}) \qquad (2.2)$$

where $\vec{r}$, $\vec{u}$, $\vec{a}$ are the position vector, velocity, and acceleration of the fluid element relative to the moving frame, and $\vec{\Omega}$ is the angular velocity. The equation of motion then becomes;

$$\vec{A} = \vec{F} \qquad (2.3)$$

where $\vec{F}$ includes the pressure, gravitational, and viscous forces per unit mass. The equation of motion of a fluid element in the moving frame is therefore identical in form with that in an absolute frame, provided we add the additional accelerations to the right hand side of the equation and refer to them as fictitious body forces.

The modified equation of motion then becomes:

$$\frac{\partial\vec{U}}{\partial t} + \vec{U}\cdot\nabla\vec{U} + \nabla P = \qquad (2.4)$$

$$-g\nabla h - 2\vec{\Omega}\times\vec{U} - \dot{\vec{\Omega}}\times\vec{r} - \vec{\Omega}\times(\vec{\Omega}\times\vec{r}) + \nu\nabla^2\vec{U}$$

where Vh is the rate of increase of elevation.

In this paper the tank is two dimensional, and it is forced to pitch about a fixed point as shown in Figure 2-1.

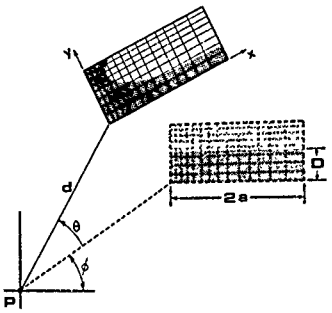


Figure 2-1. The Moving Coordinate System

The distance between the fixed point and the origin of the moving coordinate system is d and the equilibrium angle ϕ, is the angle between d and a horizontal line passing through the fixed point. x is chosen to correspond to the tank bottom and y is chosen to correspond to the left tank wall. In this frame θ, the angular displacement, is positive counterclockwise. Expanding the modified equation of motion yields the required equations for the two dimensional motion:

$$\frac{\partial u}{\partial t} + \vec{U}\cdot\nabla u + \frac{\partial P}{\partial x} = g\sin\theta + 2\dot{\theta}v \tag{2.5}$$

$$+ \ddot{\theta}(y + d\sin\phi) + \dot{\theta}^2(x + d\cos\phi) + \nu\nabla^2 u$$

$$\frac{\partial v}{\partial t} + \vec{U}\cdot\nabla v + \frac{\partial P}{\partial y} = g\cos\theta - 2\dot{\theta}u \tag{2.6}$$

$$- \ddot{\theta}(x + d\cos\phi) + \dot{\theta}^2(y + d\sin\phi) + \nu\nabla^2 v$$

$$\frac{1}{c^2}\frac{\partial P}{\partial t} + \frac{\partial u}{\partial x} + \frac{\partial v}{\partial y} = 0 \tag{2.7}$$

where g is the local acceleration of gravity.

When the apparent forces are added to the actual forces, the law of motion of an element relative to the moving frame is precisely the Newtonian Law; we say that the frame is reduced to rest by the introduction of these fictitious forces. The frame remains Eulerian and the boundary condition on the tank wall becomes homogeneous and simple to apply.

For the case of a viscous fluid, the boundary condition at a solid wall is that of no slip; i.e. both the normal and tangential components of the velocity must vanish on the surface. However, due to the finite grid size, an unnecessarily large boundary layer can be created using a numerical no-slip condition, therefore a free slip approximation is used on the tank walls.

At the free surface, the boundary conditions are based on the following principles; a) stress tangent to the surface must vanish, b) stress normal to the surface must exactly balance any externally applied normal stress such as atmospheric pressure. The mathematical statement of these principles is rather complex and must be simplified for numerical application. A derivation of the equations, in terms of the fluid momentum and viscosity, can be found in Alexander [2]. Due to the relatively high Reynolds number encountered in physical sloshing, the free surface boundary conditions used are inviscid boundary conditions.

3. Solution Technique

Liquid sloshing is essentially a free surface phenomena. When a moving container is completely filled with fluid, its motion is that of a rigid body. When a tank is partially filled, a free surface is present, and any rigid body acceleration of the tank will produce a subsequent "sloshing" of the fluid. In considering problems with a free surface, the use of the primitive variable system becomes recommended by history, since it has often been used successfully with these problems.

The marker and cell class of codes, originally developed in the early 1960's at the Los Alamos Laboratory, have been successfully used to treat problems involving complicated free surfaces. A new technique based on a MAC like algorithm, has been developed by Hirt and Nichols [13]. The method has been assigned the acronym; SOLA-VOF. The fluid equations of motion are satisfied using the well known SOLA algorithm which is discussed in Ref. 9. The location of the fluid in the mesh, and subsequently the interface, is tracked using the volume of fluid (VOF) technique.

As in most other fluid dynamics computing methods for transient problems, the SOLA-VOF technique works with a time cycle, or "movie-frame", point of view. This means that the calculation proceeds through a sequence of cycles, each advancing the entire fluid

configuration through a small, but finite, increment of time, δt. The results of each cycle act as initial conditions for the next one, and the calculation proceeds for as many cycles as the investigation requires.

At each time step the solution is based upon three major factors:

a) Explicit approximations of the velocity field from the momentum equations using old time level values for the advective, pressure, viscous and Coriolis terms and time centered values for the other apparent accelerations. Since the pressure is evaluated implicitly, its contribution to the new velocities is added in two parts. This can be easily explained using the x-momentum equation, with a constant mesh spacing, as an example:

$$U_{i,j}^{n+1} = U_{i,j}^{*} + \frac{\delta t}{\delta x}\left\{ P_{i,j}^{n+1} - P_{i+1,j}^{n+1} \right\} \quad (3.1)$$

where $U_{i,j}^{*}$ includes the viscous, advective and body force terms. The new pressures can be broken up into two parts

$$P_{i,j}^{n+1} = P_{i,j}^{n} + \delta P_{i,j} \quad (3.2)$$

Substituting this expression into (3.1) and combining $U_{i,j}^{*}$ with the old pressure gradient yields:

$$U_{i,j}^{n+1} = \widetilde{U}_{i,j} + \frac{\delta t}{\delta x}\left\{ \delta P_{i,j} - \delta P_{i+1,j} \right\} \quad (3.3)$$

The first contribution to the new velocities comes from the momentum equation and the second contribution is added after the new pressures are calculated.

b) In the second step the δp for each cell is calculated and added to the pressure obtained from the previous step. This value of δp is derived by substituting equation (3.3) into the continuity equation. Therefore, in this step, the continuity equation is satisfied, the new pressure field is calculated and the additional pressure contribution is added into the velocity field. An iteration is required since adjacent cells are coupled. After completion of this step, the new pressure and velocity field is known.

c) Using the new velocity field, the fluid, in the form of the volume of fluid function F, is advected with the local velocity to give the new fluid configuration.

Repetition of these steps will advance a solution through any desired time interval.

At each step, of course, suitable boundary conditions must be imposed at all mesh and free boundaries. Details of some of these steps are given in the following subsections.

Momentum Equation Approximations

A variable mesh is employed, which requires some modification to the finite difference approximations. The modified expressions can be derived using the SOLA [9] expressions as a basis. For the advection terms the $\vec{U}\cdot\nabla u$ form is suggested, since the divergence form appears to be inaccurate [13,22]. Ref. 9, 22 include a discussion of the finite difference forms used for the advection, viscous, and pressure terms. The addition of general body forces is new and is therefore mentioned here.

To express the ficticious body forces in finite difference form, one must consider their discretization in both space and time. Since they appear in the momentum equations, they should be centered at the cell walls. This is straightforward, except for the Coriolis terms. Since the grid is staggered, there is not a y-velocity at the cell right face or an x-velocity at the cell upper face. Therefore a weighted average of the four nearest velocities are used to evaluate the Coriolis terms.

In considering the time discretization, stability is of prime importance. The angular motion of the tank, being a prescribed function of time, remains bounded and therefore has no effect on the stability. However, the Coriolis terms, being a function of velocity, can be expected to influence the stability. Since they are linear, their stability properties can be addressed using a linear von-Neumann analysis. Reducing the momentum equations to simple "inertial flow" yields:

$$\frac{\partial u}{\partial t} - 2\dot{\theta}v = 0 \quad (3.4a)$$

$$\frac{\partial v}{\partial t} + 2\dot{\theta}u = 0 \quad (3.4b)$$

which can be written in the form:

$$\frac{\partial Z}{\partial t} + i2\dot{\theta}Z = 0 \quad (3.5a)$$

where

$$Z = u + iv \qquad i = \sqrt{-1} \quad (3.5b)$$

Using forward time differencing and evaluating the Coriolis term explicitly yields

$$Z^{n+1} = Z^{n} - i2\delta t\dot{\theta}Z^{n} \quad (3.6)$$

Substituting the Fourier component $\zeta^n = \zeta^n \exp(ik\delta x)$ and dividing through by the same yields:

$$\frac{\zeta^{n+1}}{\zeta^n} = 1 - i2\dot{\theta}\delta t \qquad (3.7)$$

Taking the magnitude yields the amplification factor:

$$|\Lambda| = \sqrt{1 + 4\dot{\theta}^2 \delta t^2} \qquad (3.8)$$

It is seen that the magnitude is larger than unity for $\dot{\theta} \neq 0$, implying that energy will be added at every time step. A similar analysis will show that an implicit form for the Coriolis term will yield an amplification factor always less than unity (damped), and consequently centering the Coriolis term at $n+\frac{1}{2}$ will yield an amplification factor of one.

At first glance this problem with the Coriolis term can be bewildering, but it has a fundamental explanation. Physically the Coriolis terms contribute no energy to the system. If a mechanical energy equation is formed from the momentum equations, the Coriolis terms drop out. Therefore, a finite difference energy equation formed from the finite difference momentum equation should exhibit the same property.

Further study and numerical experiments shows that the instability, resulting from an explicit form of the Coriolis terms, is small. A small amount of numerical or physical damping will negate the instability. Therefore, the Coriolis terms are evaluated at $t = n\delta t$, but the other prescribed body forces are evaluated at $n+\frac{1}{2}$.

Brief mention is made here of a higher order time splitting scheme suggested by MacCormack [17] which could allow time centering of the Coriolis terms. Hirt and Stein [10] have suggested a related method which can be easily introduced in the SOLA algorithm. In this method, the momentum equations are first advanced to $n+\frac{1}{2}$ using upstream differencing for the advection terms. Then using the values at $n+\frac{1}{2}$, the calculation is advanced to $n+1$ using downstream differencing for the advection terms. The result is a time centered scheme which is second order accurate in both time and space. This technique may have a wide application in explicit finite difference schemes where space centered advection is unstable. With the use of this method the Coriolis terms can be time centered. Calculations performed using this second order method do tend to be more accurate, but computation times are also increased.

Variable Mesh

The variable grid concept affords a method of analyzing particular sections of the problem in finer detail. Each cell is rectangular as it is in the fixed spacing model, but evaluation of the finite difference expressions is made more complex due to the unequal spacing. Although convenient, the variable grid spacing does introduce some subtleties. Hirt and Nichols [13] showed that the use of the divergence form of the advection terms resulted in a zeroth order finite difference approximation. Therefore the $\vec{U}\cdot\nabla\vec{U}$ form of the advection terms had to be used. The use of this form results in at least first order accurate approximations for all terms in the momentum equations when using a variable grid.

The approximation for the pressure gradient in the momentum equation, although first order accurate, is not centered at the cell wall when a variable spacing is used:

$$\frac{\partial P}{\partial x} \doteq \frac{P_{i+1,j} - P_{i,j}}{(\delta x_i + \delta x_{i+1})/2} \qquad (3.9)$$

When taking the divergence of the pressure gradient (by substitution into the mass equation), the divergence of the pressure gradient is not necessarily first order accurate. Since the solution for the pressure is similar to the solution of a Poisson equation, this could lead to errors in the pressure field if the mesh spacing varies too rapidly.

It does not follow, however, that variable meshes are necessarily less accurate because they do allow finer zoning in localized regions where flow variables are expected to vary most rapidly. Nevertheless, variable meshes must be used with care. It is best, for example, to allow for gradual variations in cell sizes to minimize the reduction in approximation order.

Boundary Conditions

In addition to free surface boundary conditions it is necessary to set conditions at all mesh boundaries and at surfaces of all internal obstacles. The fluid domain is bounded by the walls of a rigid enclosed tank. Due to the inconvenience of making the mesh fine enough at the walls to resolve the boundary layer, a free slip boundary condition is used at all four walls; the normal velocity is set at zero and the normal gradient of the tangential velocity is also set to zero.

In cells where a baffle is located, the velocity components on the faces of the cell are automatically set at zero. Because all velocity components within obstacle cells are set to zero, no-slip tangential velocity conditions at obstacle boundaries are only first order accurate. That is, tangential velocities are zero at locations shifted into the obstacles one-half of a cell width from the actual boundary location. This approximation is convenient and it also allows baffles to be constructed which are only one cell thick.

The inviscid free surface boundary

condition for normal stress is automatically satisfied by the implicit pressure calculation. This condition must be supplemented with the specifications of velocities immediately outside the surface, where these values are needed in the finite difference equations at points inside the surface. The specifications are identical to those used in many earlier MAC codes. If the surface cell has only one neighboring empty cell, the normal velocity is set to insure vanishing of the velocity divergence in the cell. When there are two or more empty cell neighbors, the individual contributions to the divergence are separately set to zero. Additionally, the normal gradient of tangential velocity, at the free surface is set to zero in order to prevent an unnecessary drag which would be induced on the fluid particle there.

The Volume of Fluid Function, F

The basis of the SOLA-VOF method is the fractional volume of fluid function for tracking free boundaries. A function F(x,y,t) is defined whose value is unity at any point occupied by fluid and zero elsewhere. Cells with F values between zero and one contain a free surface. In addition to defining which cells contain a boundary, the F function can also be used to define where the fluid is located in a boundary cell. The normal direction to the boundary lies in the direction in which the value of F changes most rapidly. When the normal direction and the value of F in a boundary cell are known, a line cutting the cell can be constructed that approximates the interface there.

The time dependence of F is governed by the Eulerian conservation equation:

$$\frac{\partial F}{\partial t} + \vec{U}\cdot\nabla F = 0 \qquad (3.10)$$

With the use of the incompressible continuity equation, this equation can be converted to divergence form:

$$\frac{\partial F}{\partial t} + \frac{\partial}{\partial x}(uF) + \frac{\partial}{\partial y}(vF) = 0 \qquad (3.11)$$

Even when the fluid is slightly compressible, this is still an acceptable approximation. This equation, in divergence form, is convenient for numerical approximation since changes in F in a cell reduce to fluxes of F across the cell faces. Since F is a step function, fluxes must be computed carefully to avoid smearing of the discontinuities. In the SOLA-VOF method, the donor-acceptor method is used. Generally, a pure acceptor method is unstable, but the donor-acceptor method uses some simple tests to determine more accurately the location of the fluid in a cell yielding a stable algorithm.

Each computational cell has four faces and the flux at each cell face is computed separately. Since a cell face joins two cells, one the donor and one the acceptor cell, they are updated together. The direction of the velocity at the interface indicates which cell is the donor and which is the acceptor.

A general but simple algorithm is used to flux the F function at each interface. If $V_x = U_{i,j}\delta t$, then:

$$\delta F = \mathrm{MIN}\left\{ F_D|V_x| + CF \;,\; F_D\delta x_D \right\} \qquad (3.12)$$

where

$$CF = \mathrm{MAX}\left\{ (1.-F_{AD})|V_x| - (1.-F_D)\delta x_D \;,\; 0.0 \right\} \qquad (3.13)$$

and

$$F_D = F_D^* - \frac{\delta F}{\delta x_D} \qquad (3.14a)$$

$$F_A = F_A^* + \frac{\delta F}{\delta x_A} \qquad (3.14b)$$

where the A subscript refers to the acceptor cell, D to the donor cell and AD is either acceptor or donor depending upon the local surface orientation. The F* value contains the old F plus any new flux contributions. For each cell there are four flux contributions as the mesh is swept row by row. The MIN feature presents fluxing of more fluid from the donor cell then it has to give, while the MAX feature accounts for an additional F flux CF, if the amount of void (1.0-F) to be fluxed exceeds the amount available. A similar expression is used for vertical flux through a horizontal cell face. Whether AD=A or AD=D is decided by the local surface orientation. AD=A when

a) Both cells are full cells.

b) The surface is advecting normal to itself.

c) The surface is advecting parallel to itself and the acceptor cell is empty.

d) The cell downstream of the donor cell

is empty and $F_D < F_A$.

AD=D when the surface is advecting nearly parallel to itself and condition (c) and (d) above are not met.

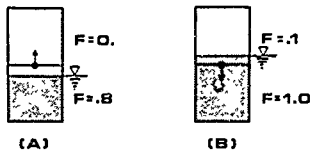


Figure 3-1. Examples of F Advection

Two simple examples, which frequently occur in sloshing, demonstrate why the MIN, MAX tests are necessary. Assuming the two cells shown are at the left tank wall and the fluid is gently sloshing up and down. For these cases the acceptor method is automatically used. Assuming a vertical Courant number of 0.3 we see that for case A, $CF = \delta F = 0.1\ \delta y_D$. Here the MAX function takes into account the void region which must be traversed before the fluid reaches the acceptor cell. In the second case (B), where the fluid is sloshing downward, we see that $CF = 0$ and $\delta F = 0.1 \delta y_D$. This shows how the MIN function prevents more fluid to be transported out of the donor cell than the cell contains.

After all the cells are swept and fluxes for each interface calculated, the resulting field of F corresponds to the time advanced location of the fluid interface.

4. Numerical Results

The liquid motion inside a rectangular tank has an infinite number of natural frequencies, but it is the lowest mode that is most likely to be excited by the motions of a ship. Most studies have therefore concentrated on investigating forced harmonic oscillation in the vicinity of the lowest natural frequency, where the natural frequency is defined as that predicted by linear theory

$$\omega_n^2 = \frac{g(2n+1)\pi}{2a} \tanh\left[(2n+1)\pi \frac{D}{2a}\right] \qquad (4.1)$$

where $n=0,1,2,\ldots$

where g is the gravitational acceleration, 2a the tank length and D the fill depth.

With the general moving coordinate system, virtually any tank excitation can be prescribed, such as a harmonic function, Fourier series, or a random time series. For the calculations presented in this paper, the excitation is that of forced sinusoidal rolling oscillation, where

$$\theta = \theta_0 \sin \omega t \quad \text{for} \quad t \geq 0 \qquad (4.2)$$

and the tank is rotating about the center of the tank bottom. The location of the point of rotation does have a profound effect on the fluid response and this is discussed in Reference 16. Although this simple excitation has been chosen, it should be noted that many complicated excitations could be input, including multicomponent excitations such as simultaneous heaving and pitching.

To ease study of the results generated, an extensive array of computer plotting has been used. Although this tends to make the program "sluggish", it does save user time. It has been found that a "snapshot" type plot showing the free surface, the velocity field, and the pressure distribution on the tank walls, at a particular time, is extremely valuable for display of the results. Time series of pressure and surface height are also plotted at prescribed locations. Hydrodynamic forces on the tank walls and baffles can also be easily determined from the pressure field.

A range of parameters which play an important role in liquid sloshing is chosen to demonstrate the versatility of the volume of fluid technique. A number of these cases have been compared with experimental results showing excellent agreement. The results also demonstrate how some phenomena, such as velocity kinematics, can easily be studied numerically but is difficult to observe in experiments. Baffles are easily introduced into the code by simply setting the velocities in obstacle cells to zero. Some simple baffle configurations are shown and a discussion of their advantages and disadvantages are given. Of course, many different baffle configurations can be tried in a numerical scheme, which might be easier than in an experiment.

Although the average time increment varied from case to case, the normalized δt, defined as δt divided by the forcing period, remained relatively constant at about $\delta t = .005$. Therefore about 200 time steps are required per forcing period. This appeared to be true regardless of discretization or how rigorous mass conservation was enforced. However, the amount of computer time per time step did vary from case to case. Computer times, on an AMDAHL 470/V6 at Texas A&M University, varied from about .15 seconds per time step to 3 seconds per time step depending on discretization and enforcement of mass conservation. Mass conservation (or volume conservation) becomes especially important in sloshing since any gain or loss in mass will result in a shift of the fluid

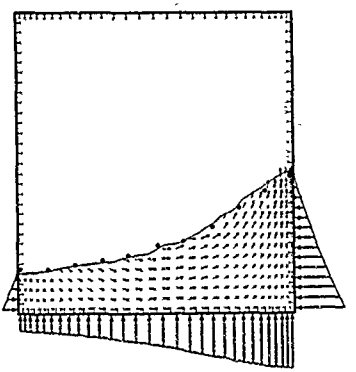


Figure 4-1. Shallow Water Sloshing in an Unbaffled Tank

$D/2a = .25$

$2a = 60$ ft

$\theta_o = 8°$

$\omega = .9942$ rad/sec

$t/\tau = .87$

$C_p = 2.73$

$C_v = 1.11$

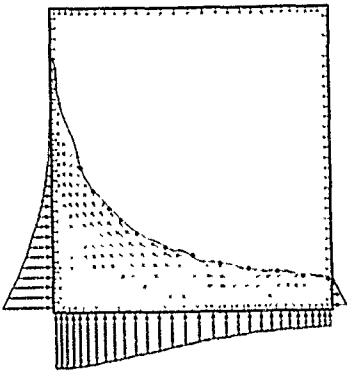


Figure 4-2. Shallow Water Sloshing in an Unbaffled Tank

$D/2a = .25$

$2a = 60$ ft

$\theta_o = 8°$

$\omega = .9942$

$t/\tau = 1.43$

$C_p = 2.38$

$C_v = 1.17$

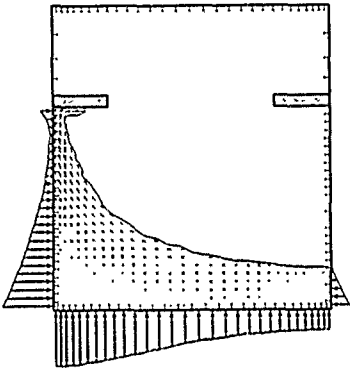


Figure 4-3. Shallow Water Sloshing in a Baffled Tank, Resulting in Mild Baffle Impact

$D/2a = .25$

$2a = 2$ ft

$\theta_o = 8°$

$\omega = 6.0737$ rad/sec

$t/\tau = 1.45$

$C_p = 2.50$

$C_v = 2.44$

natural frequency. However, fluid volume changes are tracked and printed out, and typically are less than one percent of the original volume.

In the calculations, a "cosmetic" kinematic viscosity of 1.1×10^{-5} ft^2/sec has been included. Generally, when using the first order SOLA method, the numerical diffusion like truncation error will dominate this value.

In the "snapshot" type plots shown, the box represents the tank and the tickmarks represent the cell edges and therefore the mesh configuration. The dots on some of the plots pertain to the experiment and are explained in a later subsection. The approximate location of the free surface lies at F = .5, simply requiring a contour fitting routine to plot. Each velocity vector originates at the center of a computational cell and is drawn with a direction and magnitude proportional to the average of the velocity components located at the cell sides. The pressure distribution plotted represents the pressure at the center of the cells adjacent to the walls. The maximum velocity is normalized by

$$C_V = \frac{V_{MAX}}{2a\omega\theta_0} \qquad (4.3)$$

and the maximum pressure is normalized by

$$C_P = \frac{P_{MAX}}{2a\gamma\theta_0} \qquad (4.4)$$

where 2a = the tank length, ω = forcing frequency, γ = fluid specific weight, and θ_0 = forcing amplitude. The dimensionless coefficients pertaining to each result are shown on each plot, and the rest of the velocities and pressures are scaled in relation to the maximums. The normalized time, defined as time divided by forcing period, and the amplitude of the tank angular displacement, θ_0, are also shown for each figure.

The following subsections describe in more detail various aspects of the results.

Unbaffled Tanks

In analytical techniques yielding closed form solutions, baffles cannot be readily accomodated, and methods employing a fixed coordinate system will encounter complicated boundary conditions at the fluid-baffle interface. Therefore, previous analytic investigations have been concerned primarily with sloshing in unbaffled tanks. Nevertheless, sloshing in unbaffled tanks is a very practical problem, since LNG cargo tanks can be considered unbaffled. Practically, the most dangerous fill depths occur when a tank is "almost full" or "almost empty".

Figures 4-1 and 4-2 show a shallow water non-baffled case, where D/2a = .25. The tank and fluid are initially at rest, and the tank begins oscillating harmonically at t = 0. The half amplitude is ±8°, and the forcing frequency is .9942 rad/sec, corresponding to 95% of the linear natural frequency. A mesh, consisting of 30 constant height cells in the vertical direction and 30 variable width cells in the horizontal direction was used. Finer spacing was used at the left and right walls to resolve the steep wave. Figure 4-1 shows the wave developing, and Figure 4-2 shows the well developed large amplitude wave. This non-linear type wave is very common in shallow water sloshing, and the VOF algorithm easily handles the resulting steep wave that is generated. The dots on the figures refer to the experiment and are explained later. Pertinent information is included in the figures.

Figure 4-3 is a similar case, with the exception of some arbitrarily located baffles. In this case, the baffles essentially lower the tank top rather than aid in restricting the fluid motion. This configuration could be effective when the tank is almost full, but is ineffective at this shallow depth. This figure displays the multi-valued surface capability of VOF and also the pseudo-tank-top interaction. Note the mild impact pressure at the left tank wall as the baffle is encountered.

Figure 4-4 shows an unbaffled deep water case where D/2a = .75. In this case, the tank begins oscillating at t = 0 with a half-amplitude of ±4°, and a forcing frequency of 1.2863 rad/sec, which corresponds to the linear natural frequency. The variable mesh is used here, with a course mesh near the tank bottom, where the fluid is relatively stagnant, and a finer mesh near the tank top. Almost immediately, the fluid encounters the tank top. Figure 4-5 shows the time trace of the pressure at the upper right corner cell. This is a gentle impact, where the duration is about one-tenth of the forcing period. Later, in time, this case does get rather violent and difficult to simulate. Nevertheless, it does demonstrate the ability of the algorithm to interact with the tank top, which is relatively common in "almost" full tanks, especially near resonance.

Fluid-Tank Top Interaction

When tanks are filled to higher fill depths, interaction with the tank top can occur. This interaction can be gentle, as evidenced by Figures 4-4 and 4-5, or it can be violent. In the latter case, pressure pulses are similar to those experienced in ship slamming, and the pressure variation is neither harmonic nor periodic because the magnitude and duration of the pressure peaks vary from cycle to cycle even though the tank is experiencing a harmonic excitation. When gentle interaction occurs, the technique seems to simulate the impact and subsequent retreating of the fluid quite well. However, when violent impact occurs, other factors come

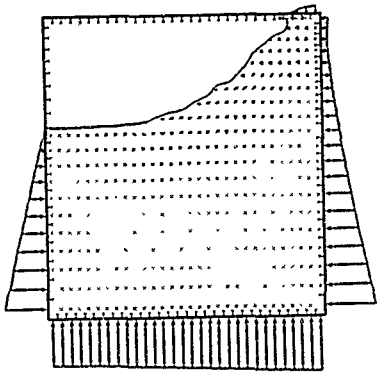


Figure 4-4. Deepwater Sloshing in an Unbaffled Tank, Resulting in Mild Tank-Top Impact

D/2a = .75

2a = 60 ft

θ_o = 4°

ω = 1.2863 rad/sec

t/τ = 1.43

C_p = 10.88

C_v = 5.37

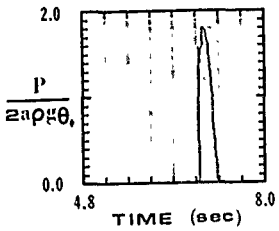


Figure 4-5. Gentle Impact Pressure

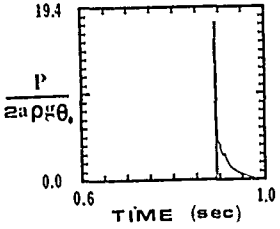


Figure 4-6. Violent Impact Pressure

Figure 4-7. Deepwater Sloshing in a Multi-Baffled Tank, Resulting in Violent Tank-Top Impact

D/2a = .75

2a = 2 ft

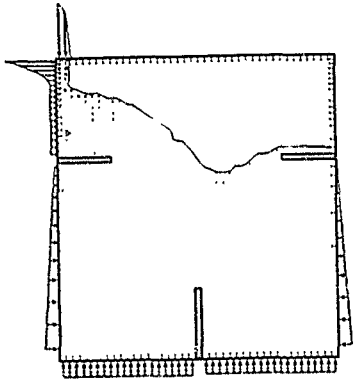
θ = 8°

ω = 7.[illegible].5 rad/sec

t/τ = 1.0

C_p = 17.[illegible]

C_v = 8.13



into play which make the simulation extremely difficult. Generally, after a violent impact the fluid splashes away from the tank top. Unless a very fine mesh is used, this splashing is subgrid scale, precluding application of the equations of motion. A special algorithm is likely to be necessary in order to correctly model this post impact phenomena. Also, impact of this type is statistical in nature. Pressure peaks vary from cycle to cycle requiring long term simulation and then careful statistical study. The trapping of air or gas during physical impact could also change the nature of the process. Although the violent impact problem is difficult, the initial impact can be studied.

Figure 4-7 is an example of a violent type impact. In this case the tank is filled to 75% of the tank height. The tank is forced to oscillate at a half amplitude of ±8° and a frequency of 7.0455 rad/sec corresponding to the linear unbaffled natural frequency. Two horizontal baffles are placed just below the still water level (SWL) and a vertical baffle is placed at the bottom. Again the variable mesh is used, allowing a fine grid to be used near the tank top and a coarse grid near the bottom. The plotted pressure distribution shows a large pressure ffeld that is developed at the tank top. Figure 4-6 shows the time trace of the pressure at this location. The spike duration is less than a millisecond and is typical of violent impact pressures witnessed in the experimental study [16]. One peculiar aspect of this case is that the baffle may be so restrictive that the upper portion of the fluid reacts as if the depth is shallow and may cause more damage than the same unbaffled case.

Although the problem of tank top interaction has been partially addressed in this paper, there are many factors which make this an extremely difficult problem. Hence numerical simulation of tank top interaction will require a great deal more study before reasonable conclusions can be drawn.

Baffles

Liquid sloshing inside a baffled tank exhibits many complex flow phenomena, and there are many baffle types and arrangements that may be considered. This study is limited to simple baffles that are rigid and fixed in location within the container. Baffles are generally used to minimize damage, and/or instabilities, which can occur from liquid motions. Some of the mechanisms by which baffles achieve this are:

a) Cause energy to be dissipated through eddy formation, turbulence, hydraulic jump formation, and wave breaking.

b) Shift the resonant frequency away from the unbaffled resonant frequency.

c) Restrict fluid motion. An extreme example would be placing a horizontal baffle at the still water level (SWL).

When baffles are introduced in a tank containing fluid, the resonant frequency will be shifted away from the unbaffled resonant frequency. Therefore when placing baffles in a tank, care must be exercised to avoid shifting the resonant frequency to a value near the forcing frequency. Generally, when baffles are submerged in the fluid, the resonant frequency is increased. This is desirable, since low frequencies are characteristic of ship oscillation. In some cases, the shift in resonance can have an adverse affect. As mentioned previously, in reference to Figure 4-7, the upper portion of the fluid volume may behave as if it were shallow water, possibly lowering the resonant frequency.

A partially filled tank (D/2a = .5) with a restrictive T-baffle is shown in Figure 4-8.

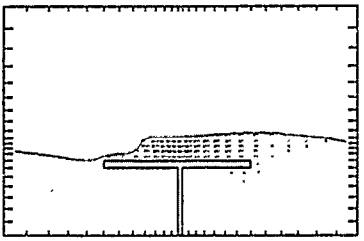


Figure 4.8. Effect of T-Baffle on Intermediate Depth Sloshing

The tank is forced to oscillate at an amplitude of ±8° and a forcing frequency which is 85% of the linear natural frequency. Here the lower fluid is so restricted, a shallow water effect is produced. This is manifested by the formation of a hydraulic jump type wave which is formed above the baffle and travels back and forth.

Figure 4-9 is of a shallow water case (D/2a = .5) where a simple vertical baffle is placed in the center. The tank is forced to oscillate at an amplitude of ±8° and a frequency corresponding to the linear natural frequency. Eddy formation is prominent, which aids in energy dissipation. Figure 4-10 shows a deep water case (D/2a = .75) where two simple horizontal "ring" baffles have been inserted. The tank is forced to oscillate at an amplitude of ±4° and a frequency close to the linear unbaffled natural frequency. Eddy formation is again evident, which contributes to energy dissipation.

Figure 4-12 shows how the introduction of two baffles increases eddy formation and subsequently energy dissipation. The tank is

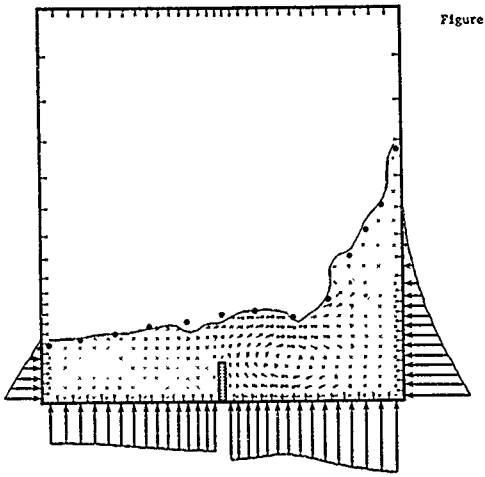


Figure 4-9. Effect of Single Vertical Baffle on Shallow Water Sloshing

D/2a = .25

2a = 60 ft

θ_o = 8°

ω = 1.0511 rad/sec

t/τ = 1.51

C_p = 1.99

C_v = 1.40

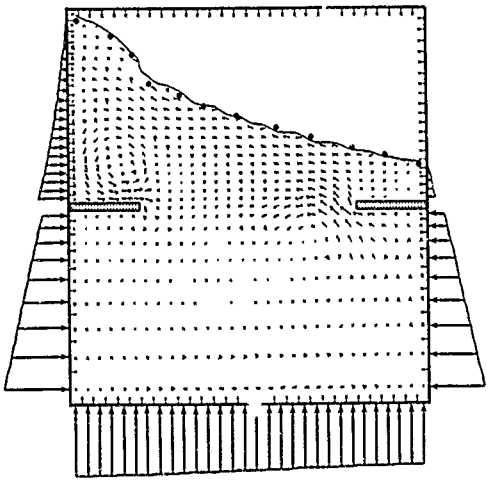


Figure 4-10. Effect of Horizontal baffles on Deepwater Sloshing

D/2a = .75

2a = 2.0 ft

θ_o = 4°

ω = 5.3165 rad/sec

t/τ = 1.35

C_p = 10.59

C_v = 2.20

oscillating at the linear unbaffled resonant frequency, but due to the resonance shift, and energy dissipation, the response is relatively gentle. The calculation reaches "almost" steady state after only four oscillation periods. The wave height at the left wall is shown in Figure 4-11. It is plotted by finding the height of the F = .5 value in a cell column. The result is that of a nonlinear wave, where the peak is much greater than the trough. The pressure at the left wall, just below the still water level is plotted in Figure 4-13. The double peaked pressure is typical of this type of large amplitude wave.

A baffle configuration can be found which restricts the motion for a prescribed fill depth and excitation. But, in the practical case, a tank would have to be designed with a particular set of baffles. This set of baffles would have to be effective for all fill depths and excitations to be encountered. When posed with this situation, the search for an effective baffle arrangement is difficult. Even if a theoretically effect arrangement is found, it must also use a reasonable amount of material and allow for internal cleaning and repair of the tank.

When studying liquid sloshing in a baffled tank, viscous effects could become important. Strong shear layers and eddies are formed in the tank, and viscosity could be playing an important role in dissipating the fluid energy.

Although the results presented here show relatively gentle sloshing in a baffled tank, observation of the experiment has shown that sloshing in a baffled tank can become quite violent, with the occurrence of turbulence, cavitation, and three-dimensional effects.

Experimental Comparison

At this point, it seems relevant to mention the validation of some of the results. There is an ongoing experimental study at Texas A&M University on sloshing in rectangular tanks. Some of the results have been reported in Reference 16. Movies were taken of some cases and snapshot photographs were made from particular sections of the film to compare with some of the numerical results. Although in transient calculations, it is difficult to compare exact times, the comparisons appear to be quite good.

Four figures include experimental comparison. On the figures, the experimental results are denoted by dots. Figures 4-1 and 4-2 show comparison for unbaffled results. Even for the very steep surface slope, shown in Figure 4-2, the comparison is very good. Figure 4-9 shows the comparison for a baffled case. Here a simple vertical baffle is inserted in the flow field. The excitation and fluid response are large amplitude and the agreement appears to be quite good. Figure 4-10 shows the comparison of a deep water case with baffles. Here the fluid is very close to the tank top and agreement with the experiment is again quite good.

The wave profile comparisons do suggest that the numerical scheme is accurate. However, before complete confidence can be assured other parameters, especially pressures, must be verified. Some pressure time histories are presently being compared, and appear to be in good agreement.

5. Conclusions

This study has demonstrated that the use of the moving coordinate system with the volume of fluid technique allows numerical treatment of liquid sloshing, in partially filled enclosed prismatic containers subjected to large amplitude excitation. Harmonic forcing functions were used in this study, but more complicated and multicomponent excitations could also be studied. Interaction of the fluid with the tank top is possible with this method and the inclusion of baffles in the flow field is straightforward.

The paper shows a variety of examples of sloshing in unbaffled and baffled enclosed tanks. Comparison of wave profiles with experimental results is excellent, but more detailed comparison is necessary, including comparison of impact pressures, to further verify the method.

This study could be extended to provide valuable information on the effect of various fill depths, excitations, and baffles. Another interesting extension of this work would be the effect of sloshing on ship dynamics. A model, similar to Dillirghams [5], could be used to couple the ship motions to the liquid movement. Similarly, a theoretical analysis of anti-rolling tanks could be performed.

6. Acknowledgements

The author wishes to thank Professor J. E. Flipse, his thesis advisor, for his guidance and the helpful comments on the material presented in this paper. The author also wishes to thank Professor T. C. Su for proposing the moving coordinate system and providing helpful discussions, and Professor Y. K. Lou for introducing the author to sloshing, providing the experimental results, and offering valuable discussion.

Fruitful discussion with C. W. Hirt of Flow Science, Inc. and B. D. Nichols of Los Alamos Scientific Laboratory were also helpful and are gratefully acknowledged.

This work has been partially supported by the University Research Programs of the Maritime Administration and the Department of Transportation.

7. References

1. Abramson, H.N., "The Dynamic Behavior of Liquids in Moving Containers With Application to Space Vehicle Technology," NASA-SP-106, 1966.

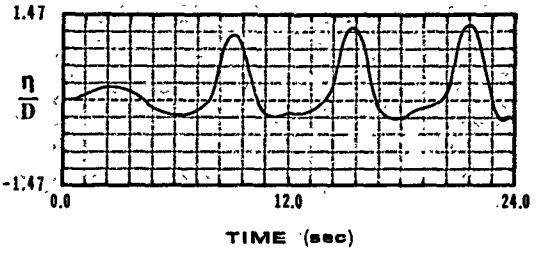


Figure 4-11. Surface Elevation at the Tank Left Wall

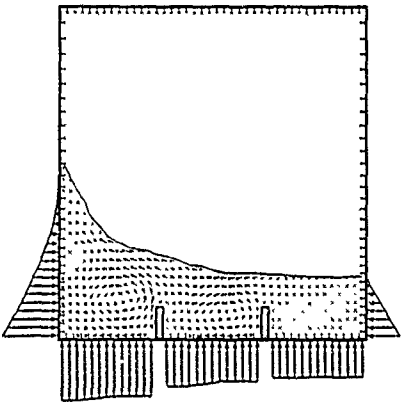


Figure 4-12. Effect of Two Vertical Baffles on Shallow Water Sloshing

$D/2a = .25$

$2a = 60$ ft

$\theta_o = 5°$

$\omega = 1.05$ rad/sec

$t/\tau = 1.51$

$C_p = 3.53$

$C_v = 1.44$

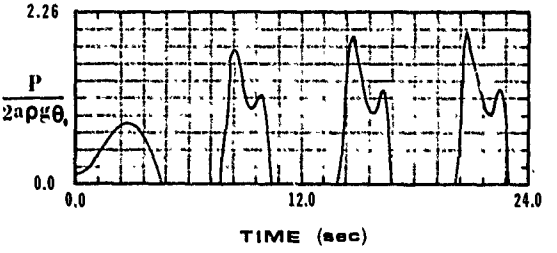


Figure 4-13. Pressure at Tank Left Wall Just Below SWL

2. Alexander, H., "Wave Forces by Numerical Simulation," Ph.D. Dissertation, Texas A&M University, College Station, Texas, 1979.

3. Brathu, H.C., Huther, M. and Planeix, J.M., "Computer Calculations of Liquid Motions in Tanks," Shipping World and Shipbuilder, Dec. 1972.

4. Bridges, T.J., "Numerical Simulation of Large Amplitude Liquid Sloshing in a Rigid Rectangular Tank," M.S. Thesis, Texas A&M University, College Station, Texas, in preparation.

5. Dillingham, J., "Motion Studies of a Vessel with Water on Deck," Marine Technology, SNAME, Vol. 18, No. 1, pp. 38-50, 1981.

6. Faltinsen, O.M., Olsen, H.A., Abramson, H.N., and Bass, R.L., "Liquid Slosh in LNG Carriers," Det Norske Veritas Publication No. 85, Sept. 1974.

7. Faltinsen, O.M., "A Numerical Nonlinear Method of Sloshing in Tanks With Two-Dimensional Flow," Journal of Ship Research, Vol. 22, No. 3, pp. 193-202, Sept. 1978.

8. Feng, G.C., "Dynamic Loads Due to Moving Liquid," AIAA Paper No. 73-409, 1973.

9. Hirt, C.W., Nichols, B.D., and Romero, N.C., "SOLA-A Numerical Solution Algorithm for Transient Fluid Flows," Los Alamos Scientific Laboratory Report LA-5852, April 1975; Addendum, LA-5852, Jan. 1976.

10. Hirt, C.W. and Stein, L.R., "A Simple Scheme for Second Order Accuracy in Marker-and-Cell Codes," Los Alamos Scientific Laboratory Unpublished Memo., 1976.

11. Hirt, C.W. and Nichols, B.D., "A Computational Method for Free Surface Hydrodynamics," American Society of Mechanical Engineers, Paper No. 80-C2/PVP-144, 1980.

12. Hirt, C.W. and Nichols, B.D., "Adding Limited Compressibility to Incompressible Hydrocodes," Journal of Computational Physics, Vol. 34, p. 390, 1980.

13. Hirt, C.W. and Nichols, B.D., "Volume of Fluid (VOF) Method for the Dynamics of Free Boundaries," Journal of Computational Physics, Vol. 39, No. 1, pp. 201-224, 1981.

14. Houghton, D., Kasahara, A., and Washington, W., "Long-Term Integration of the Barotropic Equations by the Lax-Wendroff Method," U.S. Monthly Weather Review, Vol. 94, No. 3, pp. 141-150, 1966.

15. vonKerczek, C.H., "Numerical Solution of Naval Free-Surface Hydrodynamics Problems," First International Conference on Numerical Ship Hydrodynamics, October 1975.

16. Lou, Y.K., Su, T.C., and Flipse, J.E., "A Non-Linear Analysis of Liquid Sloshing in Rigid Containers," Dept. of Commerce, Maritime Administration, Office of Maritime Technology, Report No. MA-RD-940-80092, Sept. 1980.

17. MacCormack, R.W., "Numerical Solution of the Interaction of a Shock Wave with a Laminar Boundary Layer," Proceedings of the Second International Conference on Numerical Methods in Fluid Dynamics, Lecture Notes in Physics, Vol. 8, Springer-Verlag, New York, 1971.

18. Nakayama, T. and Washizu, K., "Non-linear Analysis of Liquid Motion in a Container Subjected to Forced Pitching Oscillation," International Journal for Numerical Methods in Engineering, Vol. 15, p. 1207-1220, 1980.

19. Nichols, B.D., and Hirt, C.W., "Improved Free Surface Boundary Conditions for Numerical Incompressible-Flow Calculations," Journal of Computational Physics, Vol. 8, pp. 434-448, 1971.

20. Nichols, B.D., and Hirt, C.W., "Methods For Calculating Multi-Dimensional, Transient Free Surface Flows Past Bodies," Proc. of the First Inter. Conf. on Numerical Ship Hydrodynamics, Gaithersburg, MD, Oct. 1975.

21. Nichols, B.D. and Hirt, C.W., "Numerical Simulation of Boiling Water Reactor Vent-Clearing Hydrodynamics," Nuclear Science and Engineering, pp. 196-209, 1980.

22. Nichols, B.D., Hirt, C.W., and Hotchkiss, R.S., "SOLA-VOF: A Solution Algorithm for Transient Fluid Flow With Multiple Free Boundaries," Los Alamos Scientific Laboratory Report, LA-8355, August 1980.

23. Synge, J.L. and Griffith, B.A., Principles of Mechanics, pp. 138-145, 340-345, McGraw-Hill Book Co., New York, NY, 1942.

DISCUSSION
of the paper
by T.J. Bridges

A NUMERICAL SIMULATION OF LARGE AMPLITUDE SLOSHING.

Discussion
by G. Bourianoff

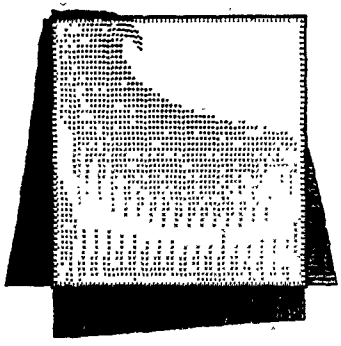
The boundary conditions on the tangential velocity at the free surface used in the code are

$$\frac{\partial V_T}{\partial N} = 0$$

where V_T is the tangential velocity component

N is the coordinate normal to the surface. This percludes the existence of linear gravity waves in the solution which have steep velocity gradients at the free surface.

I would like to know what wave solutions are permitted and how the lack of linear gravity waves affects the numerical solutions.



Author's reply

Although the natural frequency of a contained fluid is predicted fairly well with linear theory, the fluid response is not. In fact, a linear solution is produced only when the excitation frequency is far from resonance and the excitation amplitude is very small. If the fluid response is still "reasonable" the idea of using an extrapolated velocity field (Chan and Street, p. 79) is likely more accurate than the simple condition used here. However, the advantage of using the VOF technique is that it allows for a more general fluid response. In the case of large amplitude waves or contorted free surfaces, the idea of extrapolation becomes difficult, if not impossible, to implement, as evidenced by the example included below. The response in this case is no longer a travelling wave, and an extrapolated surface condition may not be more accurate. Therefore, the normal gradient of the tangential velocity is set to zero at the surface.

Ref. : R.K.C. Chan and R.L. Street, "A Computer Study of Finite Amplitude Water Waves", Journal of Computational Physics, Vol. 6, 1970, pp. 68-94.

THREE-DIMENSIONAL INSTABILITIES OF FINITE AMPLITUDE GRAVITY WAVES

J.W. McLean, Y.C. Ma, D.U. Martin
P.G. Saffman, and H.C. Yuen
TRW Defense and Space Systems Group
Redondo Beach, California 90278

ABSTRACT

Numerical computations based on the full water wave equations reveal that the instability of finite amplitude periodic gravity waves may be associated with resonances deduced from the linear dispersion relation. The lowest order resonance is responsible for the familiar sideband instability. Higher order resonances are shown to lead to predominantly three dimensional instabilities, and are the dominant instabilities for sufficiently steep waves. Comparison is made with existing theoretical results and some recent experiments.

INTRODUCTION

The subject of stability of deep-water gravity waves has been studied intensively in the past 15 years with significant progress. For more than a century after Stokes[1] published his solution for weakly nonlinear, steady, periodic, deep-water gravity waves (Stokes waves), the problem of stability had not received much attention. It therefore came as somewhat of a surprise when Sir James Lighthill[2], using Whitham's theory of slowly varying averaged Lagrangian, showed that a weakly nonlinear deep-water wave train is unstable to very long wavelength modulational perturbations. This result was confirmed experimentally by Benjamin & Feir[3], who also extended the results analytically to finite-wavelength perturbations. The theoretical treatment of this problem was also done apparently independently by Zakharov[4]. The now well-known Benjamin-Feir instability states that a uniform wave train with wavenumber k_o, and steepness $k_o a_o$, is unstable to perturbations with wavenumber lying in the range $(0, \sqrt{2}k_o a_o)$. The maximum instability occurs at a perturbation wavenumber $K = 2k_o a_o$, and grows with an exponential rate of $0.5\omega_o k_o a_o$, where $\omega_o = \sqrt{k_o}$ is the undisturbed frequency.

The above results are for two-dimensional (or unidirectional) disturbances on a weakly nonlinear wave train ($ka \to 0$). Extension of these results to finite amplitude wave trains, while still confined to two-dimensional disturbances, was done by Longuet-Higgins[5] by numerical calculations based on the unapproximated equations for perturbation wavenumbers equal to harmonics and low order rational multiples of k_o. On the other hand, extension to three-dimensional disturbances, while retaining the assumption that $ka \to 0$, was made Benney & Roskes[6], among others. An intermediate approach, valid for two- and three-dimensional perturbations on a wave train of small (but finite) amplitude was given by Crawford, Lake, Saffman and Yuen[7] using an integral equation due to Zakharov[8]. Their results compare well, in the two-dimensional case, to the results of Longuet-Higgins up to a wave steepness of about $ak = 0.3$, and removes some severe deficiencies in the stability results for three-dimensional disturbances obtained from weakly nonlinear assumptions.

Similar results have been obtained for finite depth periodic gravity waves by Benjamin[9], Whitham[10] and Zakharov & Kharitonov[11]. These studies showed that the wavetrain is unstable to two-dimensional perturbations, provided the depth is not too shallow. Extensions to three dimensional perturbations (Benney & Roskes[6]), indicates the wavetrain is unstable to three dimensional disturbances to arbitrarily shallow depths.

In this paper, we report on a numerical investigation of the stability of a finite amplitude periodic gravity wave to infinitesimal three dimensional perturbations based on the unapproximated equations. The instabilities are found to be associated with resonances deduced from the linear dispersion relation. The lowest order resonance is responsible for the well known sideband instability, and the present calculations confirm the perturbation analysis in the limit of small amplitude. The higher order resonances lead to additional instabilities which have not been obtained from perturbation analysis. These new instabilities are found to be predominantly three dimensional, and are the dominant instabilities for moderate to steep waves. Comparison is made with recent experimental observations by Su[12] on the evolution of periodic gravity waves.

GOVERNING EQUATION

We consider two dimensional steadily propigating surface gravity waves on an inviscid, irrotational, incompressible fluid. The effects of surface tension are neglected. In a frame of reference moving with the wave, the governing equations are:

$$\nabla^2\phi = 0 \qquad -h < z < \eta \tag{1}$$

$$\left.\begin{aligned} &\phi_t + \eta + \tfrac{1}{2}(\nabla\phi)^2 = \frac{B}{2} \\ &\eta_t + \nabla\phi\cdot\nabla\eta - \phi_z = 0 \end{aligned}\right\} \quad \text{on } z=\eta \tag{2}$$

where $\phi(x,y,z,t)$ is the velocity potential, $z=\eta(x,y,t)$ is the free surface, and B is the Bernoulli constant. For finite depth, the boundary condition on the horizontal bottom is $\phi_z=0$. For deep water ($h\to\infty$), the velocity is specified: $\phi \sim -Cx$ as $z\to-\infty$. Without loss of generality, we fix the gravitational acceleration to be one, and the steady wave has wavelength $\lambda=2\pi$. These equations admit steady solutions of the form:

$$\bar\eta(x) = \sum_{n=1}^{\infty} A_n \cos nx$$
$$\bar\phi(x,z) = -Cx + \sum_{n=1}^{\infty} B_n \sin nx \,\frac{\cosh n(z+h)}{\sinh nh} \tag{3}$$

Substitution of (3) into the boundary conditions (2) determines the coefficients $\{A_n,B_n\}$ and the phase speed C as functions of the wave steepness ak and depth kh.

We consider the stability of these two dimensional steady waves to an infinitesimal three dimensional disturbance. Let:

$$\eta = \bar\eta(x) + \eta'(x,y,t) \qquad \phi = \bar\phi(x,z) + \phi'(x,y,z,t)$$

where $\eta' \ll \bar\eta$ and $\phi' \ll \bar\phi$. Linearizing about the steady wave, the perturbations satisfy:

$$\nabla^2\phi' = 0 \qquad -h < z < \bar\eta \tag{4}$$

$$\left.\begin{aligned} &\phi'_t + \eta' + \bar\phi_x\phi'_x + \bar\phi_z\phi'_z \\ &\quad + (\bar\phi_x\bar\phi_{xz} + \bar\phi_z\bar\phi_{zz})\eta' = 0 \\ &\eta'_t + \bar\phi_x\eta'_x + \phi'_x\bar\eta_x - \phi'_z \\ &\quad + (\bar\phi_x\bar\eta_x - \bar\phi_{zz})\eta' = 0 \end{aligned}\right\} \quad \text{on } z=\bar\eta \tag{5}$$

The normal modes of these perturbations have the form:

$$\eta' = e^{-i\sigma t} e^{i(px+qy)} \sum_{j=-\infty}^{\infty} a_j e^{ijx}$$
$$\phi' = e^{-i\sigma t} e^{i(px+qy)} \tag{6}$$
$$\cdot \sum_{j=-\infty}^{\infty} b_j e^{ijx} \,\frac{\cosh[(p+j)^2+q^2]^{\frac{1}{2}}(z+h)}{\sinh[(p+j)^2+q^2]^{\frac{1}{2}}h}$$

where p and q are arbitrary real numbers. The physical disturbance corresponds to the real part of (6). Substitution of (6) into the equations (5) yields:

$$\sum[i(p+j)\bar\phi_x \cosh k_j(\bar\eta+h) + \bar\phi_z k_j \sinh k_j(\bar\eta+h)]$$
$$\cdot \frac{b_j e^{ijx}}{\sinh k_j h} + (1+\bar\phi_x\bar\phi_{xz}+\bar\phi_z\bar\phi_{zz})\sum a_j e^{ijx}$$
$$= i\sigma \sum b_j e^{ijx} \frac{\cosh k_j(\bar\eta+h)}{\sinh k_j h} \tag{7a}$$

$$\sum[i(p+j)\bar\eta_x \cosh k_j(\bar\eta+h) - k_j \sinh k_j(\bar\eta+h)]$$
$$\cdot \frac{b_j e^{ijx}}{\sinh k_j h} + \sum(\bar\phi_{xz}\bar\eta_x - \bar\phi_{zz} + i(p+j)\bar\phi_x)a_j e^{ijx}$$
$$= i\sigma \sum a_j e^{ijx} \tag{7b}$$

where $k_j=[(p+j)^2+q^2]^{\frac{1}{2}}$. These equations are to be satisfied for $0<x<2\pi$, and yield an eigenvalue problem for σ with $\{a_j\}$ and $\{b_j\}$ as the eigenfunctions. Instability corresponds to $\mathrm{Im}\sigma>0$.

For infinitesimal waves ($ka\to0$), the undisturbed state is the uniform flow:

$$\bar\eta = 0 \qquad \bar\phi = -Cx \qquad C=\sqrt{\tanh h} \tag{8}$$

The eigenvalues and eigenfunctions are:

$$\eta' = e^{-i\sigma_n t} e^{i[(p+m)x+qy]}$$
$$\sigma_n(p,q) = -C(p+m) \pm \sqrt{k\tanh kh} \tag{9}$$

where $k=|\underline{k}|=\sqrt{(p+m)^2+q^2}$. Recall that $k_1=m+p$ and $k_2=q$, so that (9) is just the linear dispersion relation in a frame of reference moving with speed C:

$$\sigma_n(p,q) = -Ck_1 \pm \omega(k) \tag{10}$$

where $\omega(k)=\sqrt{k\tanh(kh)}$.

We expect instability to occur when the eigenvalues associated with two distinct eigenvectors coalesce:

$$\sigma^{\pm}_{n_1}(p,q) = \sigma^{\pm}_{n_2}(p,q) \tag{11}$$

Direct calculations indicate two solutions:

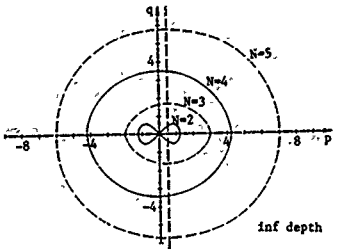
$$\left.\begin{aligned} \underline{k}_1 &= (m+p,q) \qquad \underline{k}_2 = (-m+p,q) \\ \sigma^+_m(p,q) &= \sigma^-_m(p,q) \end{aligned}\right\} \quad \text{Class I} \tag{12}$$

$$\left.\begin{aligned} \underline{k}_1 &= (m+p,q) \qquad \underline{k}_2 = (-m-1+p,q) \\ \sigma^+_m(p,q) &= \sigma^-_{-m-1}(p,q) \end{aligned}\right\} \quad \text{Class II} \tag{13}$$

The resonance conditions (12) and (13) may also be expressed as :

$$\underline{k}_1 = \underline{k}_2 + N\underline{k}_0$$
$$\omega_1 = -\omega_2 + N\omega_0 \tag{14}$$

where $\underline{k}_0=(1,0)$ and $\omega_i=\omega(k_i)$. Class I corresponds to N even, Class II is N odd. The N=2 curve is the figure "8" resonant curve of Phillips[13]. Other values of N give rise to additional curves (figure 1). Zakharov[8] stated that these resonances lead to instabilities of order $(ka)^N$, but only showed this for N=2. It appears that the higher order resonances have otherwise been overlooked.



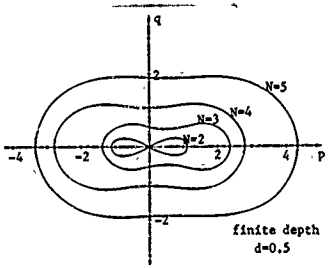


Figure 1. Resonance curves from the linear dispersion relation

NUMERICAL METHODS

The computations consist of two parts, calculation of the unperturbed wave $\bar{\eta}, \bar{\phi}$ and subsequent solution of the eigenvalue problem. To calculate the unperturbed wave, it proved convinient to solve for x and z as functions of the velocity potential ϕ and the stream function ψ. In these variables, the unperturbed flow can be expressed as:

$$x = \frac{\phi}{C} + \sum_{n=1}^{\infty} \frac{H_n}{n} \frac{\cosh n(\psi-\psi_0)/C}{\sinh(-n\psi_0/C)} \sin\frac{n\phi}{C} \tag{15}$$

$$z = \frac{\psi}{C} + \frac{H_0}{2} + \sum_{n=1}^{\infty} \frac{H_n}{n} \frac{\sinh n(\psi-\psi_0)/C}{\sinh(-n\psi_0/C)} \cos\frac{n\phi}{C}$$

The free surface is the streamline $\Psi=0$, and the bottom is $\Psi=\Psi_0$ (deep water corresponds to $\psi_0=-\infty$). The free surface boundary condition may be expressed as (Longuet-Higgins[14]):

$$\int_0^{2\pi C} e^{im\frac{\phi}{C}} \left[z(x_\phi + \lambda y_\phi) z_\phi \right]_{\psi=0} d\phi = 0 \qquad m=1,2,\cdots \tag{16}$$

$$\langle \eta \rangle = \frac{1}{2\pi} \int_0^{2\pi} \eta(x)\,dx = \frac{1}{2\pi} \int_0^{2\pi C} z(\phi,0)\, x_\phi(\phi,0)\, d\phi$$

$$= -\frac{1}{4\pi} \int_0^{2\pi C} \frac{d\phi}{x_\phi(\phi,\psi_0)} \tag{17}$$

where $\gamma_m = \coth(-m\psi_0/C)$. Substitution of (15) into (16) and (17) yields a set of algebraic equations for $\{H_n\}$:

$$2\frac{H_m}{m} + 2H_0 H_m \gamma_m + \sum_{n=1}^{m-1} \frac{H_n H_{m-n}}{n-m} (\gamma_n - \gamma_m) + \sum_{n=1}^{\infty} \frac{H_n H_{n+m}}{n} (\gamma_{n+m} + \gamma_n) + \sum_{n=1}^{m-1} \frac{H_n H_{m-n}}{n} (\gamma_{m-n} + \gamma_m) = 0 \qquad m=1,2,\cdots \tag{18}$$

$$\frac{1}{2}\left(H_0 + \sum_{n=1}^{\infty} \frac{H_n^2 \gamma_n}{n}\right) = -\frac{1}{4\pi} \int_0^{2\pi C} \frac{d\phi}{x_\phi(\phi,\psi_0)} \tag{19}$$

The mean depth is given by:

$$\langle \eta \rangle - z(\phi,\psi_0) = -\frac{\psi_0}{C} + \frac{1}{2} \sum_{n=1}^{\infty} \frac{H_n^2 \gamma_n}{n} \tag{20}$$

The wave is fixed by specifying the steepness ka (one half the crest-to-trough height), and the 'depth' of the fluid $d=-\psi_0/C$. The parameter d represents the depth of a uniform stream moving with velocity C which has the same mass flux as the steady wave. Differences between kh and d do not amount to more than a few percent. For a given ka and d, the nonlinear system (18) and (19) is truncated at L fourier modes and solved in double precision (14 digits) by Newtons method. The truncation L is increased until the last coefficient is less than 10^{-12} in magnitude. Using 50<L<350, the have calculated steady waves up to 90% of the steepest wave with this method. Integral properties such as the phase speed were checked against the results of Cokelet[15] and agree to the published accuracy (six figures).

Once the unperturbed wave has been calculated, we return to Cartesian coordinates to construct the eigenvalue problem. The perturbations (6) are truncated at M Fourier modes, and the unknown coefficients $\{a_j\}$, $\{b_j\}$ are chosen to satisfy (7) at 2M+1 points, spaced in equal arclength increments between adjacent crests of the unperturbed wave. The coefficients of (7) are computed from (15) using the fundamental relations:

$$(\phi_x, \phi_z, \psi_x, \psi_z) = \frac{(x_\phi, z_\phi, x_\psi, z_\psi)}{(x_\phi^2 + z_\phi^2)} \tag{21}$$

The resulting system of order 4M+2 is of the form:

$$(A - \sigma B)\underline{w} = 0, \tag{22}$$

where $\underline{w} = \{a_{-M}, \cdots a_{M}, b_{-M}, \cdots b_M\}$, and the matrices A and B are complex functions of p,q, and the unperturbed wave (which is a function of ka and d). The eigenvalues are obtained from a standard eigenvalue solver (QZ algorithm). The truncation M is increased until the relevant eigenvalues have converged. Computations were performed in double precision on a Prime 750 minicomputer.

RESULTS

To fix ideas, we first present the results for the deep water case. Results of the calculations are presented as stability plots in the p-q plane for specified values of ka, figure 2. The dashed lines delote the loci where the disturbances are neutrally stable. The growth

unperturbed wave		Class I instability				Class II instability			
ka	c^2	p	q	Reσ	Imσ	p	q	Reσ	Imσ
inf	$1+(ka)^2$	2ka	0	-ka	$(ka)^2/2$	0.5	q'	0	$0.59(ka)^3$
0.10	1.010050	0.18	0.00	-0.086	$4.09\cdot10^{-3}$	0.5	1.64	0.0	$6.00\cdot10^{-4}$
0.20	1.040814	0.32	0.00	-0.146	$1.33\cdot10^{-2}$	0.5	1.54	0.0	$5.23\cdot10^{-3}$
0.30	1.094149	0.47	0.00	-0.189	$2.26\cdot10^{-2}$	0.5	1.33	0.0	$2.15\cdot10^{-2}$
0.35	1.130018	0.60	0.00	-0.214	$2.27\cdot10^{-2}$	0.5	1.15	0.0	$4.13\cdot10^{-2}$
0.40	1.171211	----	----	stable	--------	0.5	0.79	0.0	$8.88\cdot10^{-2}$
0.41	1.179494	----	----	stable	--------	0.5	0.65	0.0	$1.1\cdot10^{-1}$
0.41	1.179494	----	----	stable	--------	0.5	0.00	0.0	$6.7\cdot10^{-2}$

Table 1. The maximum growth rate as a function of wave steepness. Infinite depth case. The first row gives results for ka<<1. $q'=\frac{3}{4}\sqrt{5}-3.2(ka)^2$

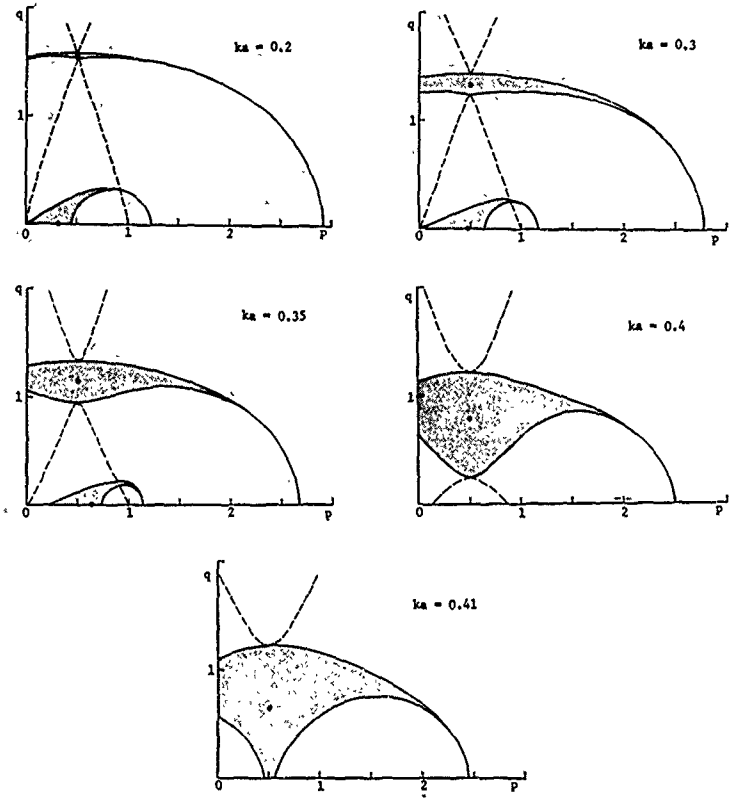


Figure 2. Stability diagram for N=2 and N=3, deep water. Shaded regions denote instability. The • denotes the point of maximum instability. Dashed curves denote neutral disturbances.

rates are given in Table 1. For q=0, p=O(ka), the Class I, m=1 instability has a growth rate $Im\sigma=O((ka)^2)$ for small ka, in agreement with the perturbation analysis of Benjamin & Feir. The instability near p=5/4 has a growth rate $O((ka)^4)$. For larger values of ka, the unstable region continues to grow until ka≃0.34, when the region detaches from the origin. Beyond this, the region shrinks as ka increases, finally dissappearing for ka≃0.39. Throughout this range of wave steepness, the maximum instability is attained for q=0, so this instability is predominantly two dimensional. Recall that the unstable eigenvector has dominant components at $k_x=(p+1)$ and $k_x=(p-1)$.

The Class II, m=1 instability is new. Near p=3, q=0, the growth rate is $O((ka)^3)$, while near p=1/2, $q=\frac{1}{2}\sqrt{3}$, the growth rate is $O((ka)^3)$. Thus, this instability is initially weaker than the Class I resonance. The corresponding eigenvector has dominant components at $k_x=p+1$ and $k_x=p-2$, so for p=1/2, the dominant wavenumber is ± 3/2. The maximum growth rate occurs at p=1/2, q≠0, so this instability is predominantly three dimensional. At ka≃0.31, the growth rate of this instability becomes larger than the growth rate of the Class I instability, and the most unstable disturbance switches from the two dimensional Benjamin-Feir type to this three dimensional perturbation. At ka≃0.405, the instability region touches the p axis yielding a two dimensional unstable disturbance, which was initially identified by Longuet-Higgins[5]. It should be noted however, that the strongest disturbance occurs for q≠0, and is three dimensional.

The point of maximum instability for the Class II resonance occurs with Reσ=0, thus the perturbation remains stationary (but increasing in amplitude) in a frame of reference moving with the unperturbed wave. In fact, Reσ=0 along the line p=1/2 in the unstable region, so at the stability boundary we have σ=0, and the perturbation is a neutral disturbance. This suggests the possibility that the unperturbed wave can bifurcate into a steady three dimensional wave pattern. Indeed, this neutral stability point touches the p axis at ka=0.405, in good agreement with the value found by Chen & Saffman[6] for two dimensional bifurcation of a Stokes wavetrain.

The trends exhibited by m=1 of Class I and II are reflected in the higher order interactions. For m=2, Class I, the maximum growth rate occurs for p=0, q≠0, and has a growth rate $Im\sigma=O((ka)^4)$ for small values of the wave steepness. For m=2, Class II, the point of maximum instability occurs at p=1/2, q≠0 and has an initial growth rate of $O((ka)^5)$. The maximum instability in these cases occurs with Reσ=0. For the range of wave heights considered here, 0<ka<0.41, the m=1 interactions produce the dominant instabilities. Comparison of the growth rates for the various instabilities is given in Figure 3.

For finite depth periodic gravity waves, it is well known that weakly nonlinear water waves are unstable or stable to two dimensional infintesimal perturbations if the depth kh is

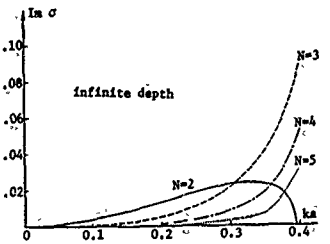


Figure 3. Maximum growth rates of deep water instabilities.

greater or less than 1.363 (Whitham[10]). For our numerical study, we have chosen three depths, one greater and two less than this value. The results are presented in Figures 4, 5, and 6 and Table 2. We first discuss the lowest order instability.

For d=2.0, the behavior of the lowest order instability (N=2) is very similar to the deep water case: for small ka, the steady wave is unstable to long wavelength perturbations which have a growth rate $O(ka)^2$. Note however that the dominant instability at this depth is three dimensional for small ka. For steeper waves, the long wavelength perturbations restabilize, and the most unstable wavenumber is two

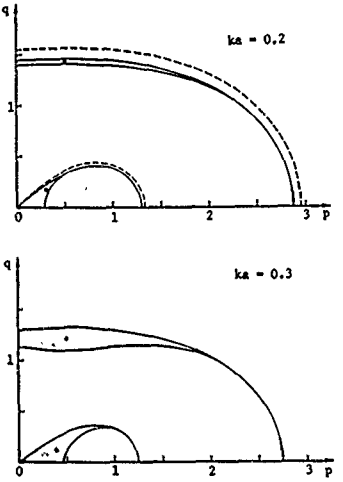


Figure 4a. Stability diagram for d=2.0. The dashed curve is the infinitesimal resonance.

d=2.0 Highest wave: ka=0.425

	unperturbed wave		Class I instability				Class II instability			
ka	C^2	<dep>	p	q	Reσ	Imσ	p	q	Reσ	Imσ
0.10	0.974883	2.005125	0.21	0.15	-0.0877	$3.19\cdot10^{-3}$	0.5	1.54	0.0	$7.24\cdot10^{-4}$
0.20	1.008101	2.019723	0.31	0.17	-0.1220	$1.13\cdot10^{-2}$	0.5	1.43	0.0	$6.34\cdot10^{-3}$
0.30	1.065604	2.041079	0.40	0.14	-0.1342	$2.39\cdot10^{-2}$	0.5	1.21	0.0	$2.65\cdot10^{-2}$
0.35	1.104017	2.052335	0.46	0.08	-0.1268	$3.31\cdot10^{-2}$	0.5	0.99	0.0	$5.23\cdot10^{-2}$
0.39	1.137932	2.059619	0.62	0.00	-0.1055	$4.60\cdot10^{-2}$	0.5	0.68	0.0	$1.01\cdot10^{-1}$

d=1.0 Highest wave: ka=0.325

	unperturbed wave		Class I instability				Class II instability			
ka	C^2	<dep>	p	q	Reσ	Imσ	p	q	Reσ	Imσ
0.10	0.781727	1.006339	0.28	0.19	-0.0618	$2.34\cdot10^{-3}$	0.5	0.99	0.0	$2.04\cdot10^{-3}$
0.20	0.839925	1.022771	0.42	0.24	-0.0964	$9.54\cdot10^{-3}$	0.5	0.90	0.0	$1.80\cdot10^{-2}$
0.29	0.919308	1.038987	0.55	0.19	-0.0888	$3.07\cdot10^{-2}$	0.5	0.62	0.0	$7.60\cdot10^{-2}$

d=0.5 Highest wave: ka=0.186

	unperturbed wave		Class I instability				Class II instability			
ka	C^2	<dep>	p	q	Reσ	Imσ	p	q	Reσ	Imσ
0.10	0.531461	0.508233	1.16	0.00	-0.2273	$4.44\cdot10^{-3}$	0.5	0.55	0.0	$8.77\cdot10^{-3}$
0.16	0.599622	0.515655	0.57	0.23	-0.0763	$1.45\cdot10^{-2}$	0.5	0.50	0.0	$3.76\cdot10^{-2}$

Table 2. Maximum growth rate as a function of wave steepness
Finite depth case. <dep> is the mean depth

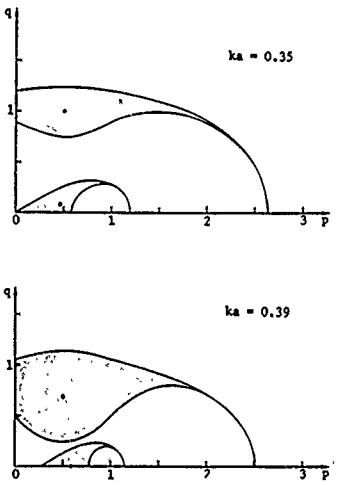


Figure 4b. Stability diagram for d=2.0

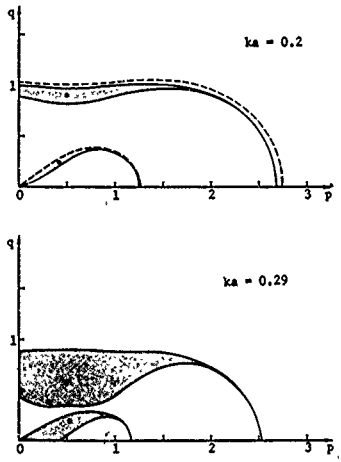


Figure 5. Stability diagram for d=1.0. The dashed curve is the infinitesimal resonance.

dimensional. For the range of amplitudes considered here, this lowest order instability did not completely restabilize as it does in deep water.

For d=1.0, the unperturbed wave is stable to long wavelength two dimensional perturbations for small amplitude, as predicted by Whitham. However, the wave is unstable to three dimensional perturbations. The growth rate of the unstable sidebands is $O(ka)^4$. For ka=0.29, two dimensional perturbations are found to be unstable, although they are dominated by three dimensional instabilities.

The shallowest case we have considered, d=0.5, is most unstable (at least for small ka) to a two dimensional perturbation with a length scale comparable to the length scale of the unperturbed wave, in contrast to the familiar two dimensional long wave perturbations which are the dominant instabilities in deep water. Two dimensional long wave perturbations are stable at this depth. For larger amplitudes, three dimensional instabilities again dominate.

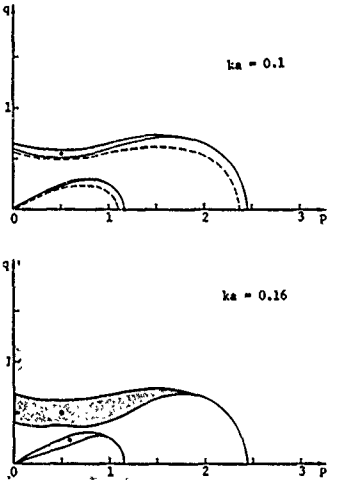


Figure 6. Stability diagram for d=0.5. The dashed curve is the infinitesimal resonance.

The next order resonance (N=3) is completely analogous to the deep water case: the maximum growth rate occurs for p=1/2, q≠0 and has $Im(\sigma)=O(ka)^3$, $Re(\sigma)=0$. Thus the dominant instability propagates with the unperturbed wave with twice the spatial period. The stability boundary at p=1/2 is a point of neutral stability ($\sigma=0$), and suggests a bifucation into a steady three dimensional wave pattern. While this third order resonance is initially weaker than the second order resonance, it becomes dominant for sufficiently steep waves, see Figure 7 and Table 2.

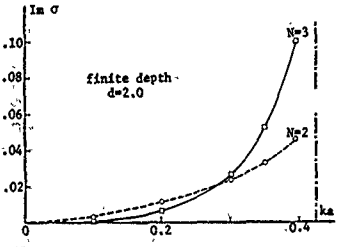


Figure 7. Maximum growth rates of finite depth instabilities, d=2.0. The dashed line on the right represents the highest wave.

COMPARISON WITH OBSERVATION

For deep water, the perturbation anaysis of Benjamin & Feir afforded an explanation of the observation that a gravity wave is unstable to two-dimensional perturbations. Improvements of the theory based on the nonlinear equations led to good agreement with experiment (Longuet-Higgins[5]). It is significant to note that the original experiments were for values of the wave steepness ka<0.17, a range in which the three dimensional instabilities are quite weak.

Recently, a series of spectacular experiments were performed by Su[12] in an outdoor basin and an indoor wave tank which exhibited distinct three-dimensional patterns on large amplitude gravity waves. Quoting Su's description: "(At about) $x = 24\lambda_0$, ...the wave train evolves quickly into a three-dimensional configuration. This stage of evolution has a distinct three-dimensionality that usually lasts about 10 wavelengths." This is illustrated by a photograph of the wave pattern (Figure 8). These patterns are observed for rather steep initial waves, with values of ka in the range 0.25 to 0.34. Su reported that 90% of his observations correspond to the case p = 0.5.

Before comparing Su's experimental observations to our results, we digress slightly to consider the existence of an apparently steady three-dimensional wave pattern which lasts for 10 wave periods.

Consider infinitesimal perturbations on a steady solution. A neutral stability point exists when both the real and imaginary parts of σ are zero in a frame of reference moving with the undisturbed solution. At this point, a new steady solution which is the superposition of the undisturbed solution and the infinitesimal disturbance exists. If this solution can be continued to finite perturbation amplitude, new steady solutions can be generated.

New steady two-dimensional steady solutions were obtained via this approach by Chen and Saffman[16] as bifurcations from the Stokes solutions, based on the unapproximated equations. These occur at large values of wave

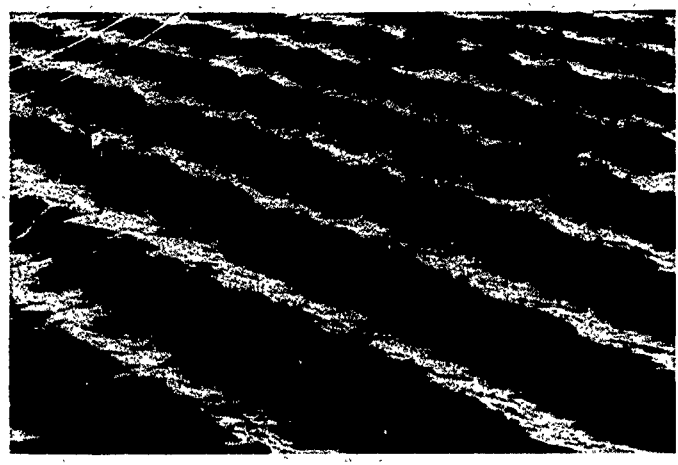


Figure 8. Three dimensional wave patterns. Photograph from Su.

steepness, and represent modulated steady wave trains. These results were extended to three-dimensions by Saffman and Yuen[17], who noticed that the critical wave steepness for bifurcation into three-dimensional solutions are typically much smaller, and therefore the analyses can be carried out using the Zakharov equation. Saffman and Yuen found two types of three-dimensional steady solutions, one symmetric and one antisymmetric.

The bifurcation theory, however, leaves an important question unanswered. For a given value of ka, the theory predicts bifurcation into wave forms with arbitrary values of p and q. What, then, is the selection rule which causes Su to observe a certain value of p and q for a given ka? Why is p = 0.5 preferred?

These questions find their answers in the present results. For ka$\geq$0.30 the most unstable perturbation is three dimensional and occurs with p=0.5, q$\neq$0. This instability has Reσ=0 and is the result of coalescence of two neutrally stable eigenvectors. The instability co-propigates with the undisturbed waves, and is indeed generic of the neutrally stable eigenvectors. The implies that this instability can trigger the bifurcation into a three-dimensional configuration. We further note that the e-folding time of the maximum instability of Type II for ka = 0.33 is about 25 wavelengths, which agrees very well with Su's observations. For the experimental value ka=0.33, Su measures the wavelength of the modulation to be λ_x=2.16m, λ_y=0.915m, yielding k_y/k_x=2.36. At this steepness, the present calculation predicts the most unstable disturbance will occur for p=0.5, q=1.23, yielding k_y/k_x=2.46. The wave profiles are compared in figure 9, where the amplitude of the eigenfunction (which is undetermined by the linearized equations) has been chosen for the best agreement with the experimental profile.

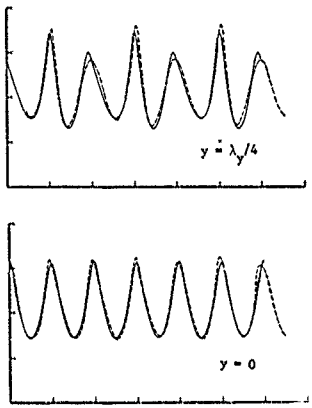


Figure 9. Comparison of experimental (dashed) and theoretical (solid) profiles. The vertical scale is exaggerated by a factor of 16.

These results have an important implication in oceanic applications: they predict that the existence of three-dimensional structures on ocean waves, which always have a lengthscale twice that of the dominant wavelength in the direction of propagation, and (for a wide range of ka) a lateral lengthscale of about one dominant wavelength. The structure is afixed to the dominant waves; and should be readily identifiable. For sufficiently large wave steepness, these three-dimensional features are strongly dominant. This is not to say that they are absent in small steepness, in fact, they are expected to co-exist with the two-dimensional Benjamin-Feir type instabilities.

REFERENCES

[1] G.G. Stokes, Trans. Camb. Phil. Soc. 8, 441 (1847)
[2] M.J. Lighthill, J. Inst. Math. Appl. 1, 269 (1965)
[3] T.B. Benjamin and J.E. Feir, J. Fluid Mech. 27, 417 (1967)
[4] V.E. Zakharov, J. Exper. Theor. Phys 51, 1107 (1966)
[5] M.S. Longuet-Higgins, Proc. Roy. Soc. London A360, 473 (1978)
[6] D.J. Benney and G. Roskes, Stud. Appl. Math. 48, 377 (1970)
[7] D.R. Crawford, B.M. Lake, P.G. Saffman, and H.C. Yuen, J. Fluid Mech 105, 177 (1981)
[8] V.E. Zakharov, J. Appl. Mech. Tech. Phys. 2, 190 (1968)
[9] T.B. Benjamin, Proc. Roy. Soc. London A299, 59 (1967)
[10] G.B. Whitham, J. Fluid Mech. 27, 399 (1967)
[11] V.E. Zakharov and V.G. Kharitonov, J. Appl. Mech. Tech. Phys. 11, 747 (1970)
[12] M.Y. Su, Submitted J. Fluid Mech. (1981)
[13] O.M. Phillips, J. Fluid Mech. 9, 193 (1960)
[14] M.S. Longuet-Higgins, J. Inst. Math. Appl. 22, 261 (1978)
[15] E.D. Cokelet, Phil. Trans. Roy. Soc. London A286, 184 (1977)
[16] B. Chen and P.G. Saffman, Stud. Appl. Math. 62, 1 (1980)
[17] P.G. Saffman and H.C. Yuen, J. Fluid Mech.101, 797 (1980)

DISCUSSION
of the paper
by J.W. McLean, Y.C. Ma, D.U. Martin, P.G. Saffman and H.C. Yuen

THREE-DIMENSIONAL INSTABILITIES OF FINITE AMPLITUDE GRAVITY WAVES

Discussion
by J.M. Vanden-Broeck

To compute the steady state solution before doing the perturbation analysis, you use a truncated Fourier expansion. Could you use instead an integral equation formulation to compute this steady state solution. If so, you could go to a higher steepness and much smaller depth.

Authors' reply

It would certainly be possible to use an integral equation to calculate steeper steady waves, but we are limited by resolution of the perturbations. For the steepest waves, an alternate formulation, possibly a local analysis about the wave crest, is required to obtain the stability properties.

Session V
VORTEX FLOWS AND LIFTING BODIES

S. Bindel
Session Chairman
Direction des Recherches,
Études et Techniques
France

NUMERICAL MODELLING OF VORTEX FLOWS IN SHIP HYDRODYNAMICS A REVIEW

Hans J. Lugt
David W. Taylor Naval Ship Research and Development Center
Bethesda, Maryland 20084

ABSTRACT

The increasing activity in the study of vortices in numerical ship hydrodynamics is closely linked with the rapid advances in computer technology and numerical analysis, largely influenced by successes in the sister field of aerodynamics. This review starts with a discussion of the distinct features of vortices around ships, their definitions and nomenclature. The numerical methods are treated by dividing the subject into techniques for inviscid flows, viscous motions, and turbulent vortices with special emphasis on ship-hydrodynamical problems.

1. BACKGROUND

Vortices are ordered structures of fluid motion, which nature prefers over chaos in many situations. Recent pictures from Voyagers 1 and 2 of the planet Jupiter confirm through the display of multiple vortex arrays the beauty of such order in the universe.

Vortices are omnipresent in flows about bodies of complex form, including marine structures like moving surface ships and submarines, and oil rigs in wind and ocean currents. Hence, their study does not start with the question of whether vortices are present but with the question of which vortices have a noticeable influence on the performance of naval vehicles and other structures.

Since the mathematical description of vortices is inherently a nonlinear problem (except for a few degenerate cases with similarity or symmetry properties), solutions of the basic equations of motion, which describe vortex flows, require the full exploitation of modern computers. The impact of the present rapid development of computer hardware and of the advances in numerical techniques on fluid dynamics was recently discussed in a review article devoted to aerodynamical problems by D. Chapman of the NASA Ames Research Center (1979). The increasing emphasis on vortices in aerodynamics is reflected in a summary by Peake and Tobak (1980), and a comprehensive survey on the general role of vortices in nature and technology was published in a book by the author (Lugt 1979a).

In recent years a number of good survey articles have appeared in the literature on basic vortex flows and their numerical computation (Fink and Soh 1974, Clements and Maull 1975, Lewellen 1976, Saffman and Baker 1979, Leonard 1980, and J.H.B. Smith 1980). Most of these surveys are restricted to inviscid fluid flows and are geared largely to problems in aerodynamics and meteorology and very little to problems in ship hydrodynamics. The question thus arises whether vortex problems in ship hydrodynamics are so different from those in aerodynamics that the flow models and numerical methods especially developed for aerodynamic problems cannot be applied to ship hydrodynamics at all (or only after modifications). Or one may ask whether vortices play only a minor role in ship hydrodynamics. The first question tacitly implies that aerodynamicists are more involved in numerical fluid dynamics than ship hydrodynamicists. The fact is that, due to industrial demands, the effort spent in funds and man power is an order of magnitude larger in numerical aerodynamics than in numerical ship hydrodynamics. It is, therefore, important to discuss briefly the major differences and similarities of the two fields.

The degree of relationship between aerodynamics and ship hydrodynamics may be considered to encompass three levels:

(1) Some ship problems have no counterparts in aerodynamics and, therefore, there is a real need for hydrodynamic research. Obviously, a ship operates relatively slowly in the free surface of an incompressible fluid, compared with an airplane or missile, which moves through air at sub- or supersonic speed. Both cases, however, have certain mathematical properties in common: the boundary conditions at the water surface and the shock wave in air are nonlinear, and the positions of these boundaries are not known a priori but must be determined as parts of the solutions. Typical vortex problems in ship hydrodynamics which do not occur in aerodynamics are those involving propeller-hull-rudder interactions, hydrofoils (Acosta 1973), the inception of cavitation (Morgan and Parkin 1979), and the rolling motion of a ship which generates bilge and stern vortices (Cox and Lloyd 1977).

(2) Many ship problems have elements which are shared with certain aerodynamic problems.

However, due to the special nature of these problems, approximations which are permissible in one field may not be realistic in the other (that is, there are differences in the physical models). This includes the fact that the importance of a problem may have different weights in the two fields. For instance, vortex breakdown can have a sizeable effect on the lift of a delta wing, depending on its location, while vortex breakdown behind the sail of a submarine may be insignificant for lift or propeller efficiency.

(3) Vortex problems in ship and aircraft applications of fluid dynamics may be the same, but the numerical method for a specific problem may have to be altered because geometry and parameter ranges differ (these are differences in numerical modelling). In this context it may be mentioned that, even for the same physical situation in the same engineering field, the numerical method may vary, depending on the question asked. For instance, the location of tip vortices can influence the lift of a downstream control surface. In this case, an inviscid-flow model may suffice. However, a viscous-flow model is needed to find the lowest pressure near the origin of the tip vortex of a marine propeller to determine the inception of cavitation.

This paper includes some sketches of typical vortex systems around the hulls of ships and around propellers to illustrate the occurrence of major vortices and their complexity. These figures may also serve to facilitate the discussion of the numerical methods applied to vortex flows and to clarify the nomenclature and definition of various types of vortices, since the literature is not consistent in these areas.

Probably the oldest comprehensive collection of drawings of vortices around surface ships and submarines can be found in Saunder's book on "Hydrodynamics in Ship Design" of 1955. The most important types of vortices in ship hydrodynamics are the tip, wake, necklace, and hub types. All are illustrated in Fig. 1a, which shows the main vortices about submarines. Notice that the tip vortices, which occur at the end of the sail ("fairwater"), sail planes, rudders, and stabilizers, correspond to the wing tip vortices of an aircraft. In these tip vortices the axial velocity component is relatively strong so that the vortex exhibits a swirling motion. If this velocity component is relatively small or nonexistent, as with the vortices at the leading and trailing edges of high-aspect ratio airfoils at large angles of attack, the vortex is labelled an "edge vortex" (Fig. 17 in Section 3.1). "Wake vortices" in the narrow sense (edge vortices are also wake vortices) develop in the rear of blunt bodies (Fig. 1b). They are shed when marine vehicles turn, and when the local angle of attack (drift angle) in general varies along the hull. At higher angles of attack "secondary vortices" can form in the wake. A "necklace vortex" is generated at the base of a cylinder or strut, attached to a larger solid surface. In Figs. 1a and 1c such vortices are drawn at the intersections of sail and hull, sail plane and sail, and rudder or stabilizer and hull. Necklace vortices are sometimes called "horseshoe vortices". This term, however, is usually reserved for the vortex system associated with wings in an inviscid flow (the "bound vortex" of the wing and the two tip vortices). In the necklace vortex of the hull-sail intersection the phenomenon of vortex breakdown can be observed (Granger 1974), as indicated in Fig. 1a.

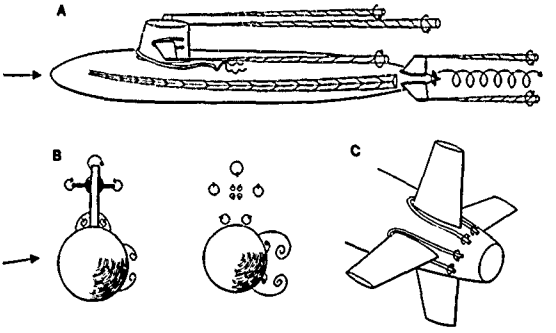


Figure 1 – (a) The major vortex configurations around a submarine at a small angle of attack in a slight turn. (b) Two cross-sections of the hull at the sail and behind. (c) Necklace vortices around the control surfaces at the stern.

Whenever a body rotates in a fluid, the axis of rotation, which is itself a vortex line, extends into the fluid in the form of vorticity lines. These lines are bent immediately in front of the rotating body and spread in spirals, but they remain bundled and straight in the rear of the body. They thus form the "hub vortex".

The hulls of surface ships can produce bilge, stern, and bow vortices, whose occurrence and strength depend on the geometry of the hull and the ship's movement. Bilge vortices form at sharp or high-curvature keels and are actually tip vortices (Fig. 2). Two types of bilge vortices have been identified: steady and unsteady. Steady-state vortices occur even when the ship is not rolling, swaying, or heaving. They are caused near the bow by the downward motion, in the rear by the upward flow (Tagori 1967). Unsteady bilge vortices are shed during rolling, swaying, and/or heaving with or without forward speed.

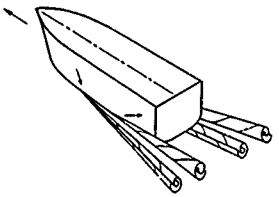


Figure 2 –
Steady bilge vortices of a surface ship. The two bow-bilge vortices rotate opposite to the two stern-bilge vortices (Lugt 1979a).

Stern vortices (Fig. 3) have a certain similarity to bilge vortices formed at the stern. They may be categorized as tip vortices too, although they are generated in the region where the convex surface of the hull becomes concave (Kux and Wieghardt 1980). According to Fig. 4 the generation of axial vorticity is caused in both cases by flow separation either at the keel or the bilge. Stern vortices have counterparts in aerodynamics, for instance on the fuselage of the conceptual "delta-wing Orbiter" space shuttle (Peake and Tobak 1980).

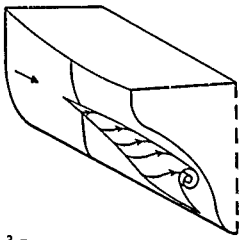


Figure 3 –
Stern vortex at the concave surface of the hull (after Hoekstra 1977).

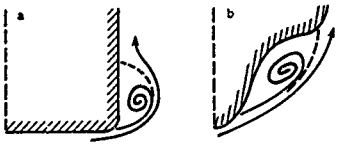


Figure 4 –
Difference between stern-bilge vortex at the bilge of a full ship (a) and stern vortex at the concave surface of the hull (b).

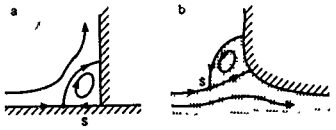


Figure 5 –
Necklace vortices sketched in the plane of symmetry, (a) around the strut on a solid surface, (b) bow vortex. S = stagnation point.

There is also a certain similarity between vortices at the bow of full ships (Dagan and Tulin 1972) and the necklace vortices around struts (Fig. 5). For bow vortices, of course, the bow wave determines the shape of the free surface whereas boundary-layer separation at a solid wall causes the necklace vortex. Notice the flow direction in these vortices. A particular kind of necklace vortex is formed at the stern of surface ships (Baba 1976) as shown in Fig. 6 for the flow behind a transom stern. Waves break behind the ship by generating vortex layers in the flow direction. For large Froude numbers the two layers shown in Fig. 6a extend far downstream; for smaller Froude numbers a breaking wave perpendicular to the

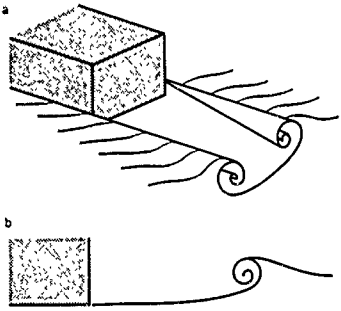


Figure 6 –
Vortex layers caused by wave breaking behind a transom stern; (a) perspective view for large Froude numbers, (b) side view for small Froude numbers.

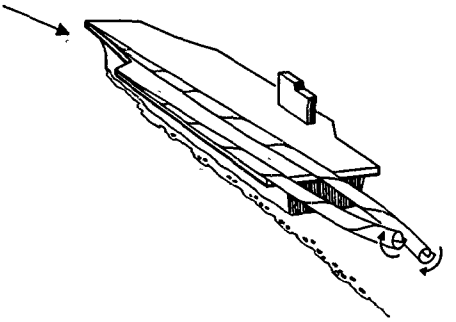


Figure 7 – Deck vortices on an aircraft carrier. Other major vortices like those around the island are omitted (for vortices around buildings see Hunt 1971).

flow also occurs (Fig. 6b), forming a necklace in a way opposite to those previously discussed.

Vortices above the water line are of naval interest as well as underwater vortices, but they are mentioned here only in passing. An example is furnished in Fig. 7 which shows the two tip vortices of the staggered flight deck of an aircraft carrier. Since these vortices rotate in the same direction, they also revolve about their common center and are a hazard for landing airplanes (Oh and Dean 1971). A similar problem exists behind large aircraft, where two or more tip vortices form on each side of the plane (Donaldson and Bilanin 1975). See also Fig. 15. On carrier flight decks with three protruding edges, three deck vortices of the same sign develop. The movements of three vortices have been studied by Aref (1979) and Leonard (1980).

Vortices shed from marine propellers are of special naval importance (Platzer and Souders 1979). Fig. 8a shows the hollow cavitation cores of four tip vortices from the blades and the cavitating hub vortex. The latter is not axisymmetric since it is fed by the four secondary flows between the blades (Fig. 8b). In many situations non-uniform

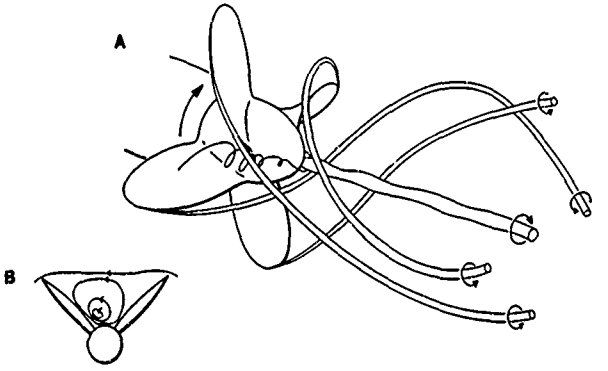


Figure 8 – Propeller vortices, which are visible through hollow-core cavitation. (a) Four tip vortices and hub vortex in perspective. Secondary flow between two blades is indicated only in one quarter. (b) Secondary flow circulation sketch in a reference frame fixed to the propeller.

inflow causes unsteadiness of the propeller flow, which results in noise and vibration of the blades (Brooks 1980). A review of cavitation in fluid machinery, including vortices, is given by Arndt (1981).

Vortex-generated noise was reviewed by Powell (1975). This subject leads to the study of vortices generated in the unstable shear flows of jets and boundary layers (Rockwell and Naudascher 1979).

Finally, the numerical treatment of vortex-induced vibration was recently reviewed by Sarpkaya (1979). Problems in this area are encountered when underwater vehicles are towed at the end of cables (Griffin et al. 1980).

Some vortex configurations may be described by inviscid-flow models, some by viscous-flow models, and some by a combination of the two by dividing the flow domain into suitable regions. Special attention must be given to turbulent vortices. The following review of numerical methods, illustrated by ship problems, is hence divided into three parts: Inviscid-flow models, viscous-flow models, and turbulent vortex models. This review, however, can present the various methods only in a general way because of the extent of the existing literature.

2. INVISCID-FLOW MODELS

According to Saffman and Baker (1979) a vortex in an inviscid fluid may be defined as a "finite volume of rotational fluid, bounded by irrotational fluid or solid walls". The vorticity vector, in contrast, is unambiguously defined as the curl of the velocity vector.

Potential flow around a cylinder with imbedded point vortices is the oldest mathematical model to simulate vortex flows near a body and goes back to Foppl in 1913. The early days of airfoil theories in the twenties and those of missile aerodynamics in the fifties (Nielsen 1960) were devoted to the study of one or several point vortices near a body. The advent of computers has made it possible to extend and refine those methods for many point vortices, and in the last two decades great progress has been made. This development was encouraged by the persistent difficulties of solving the Navier-Stokes equations for large Reynolds numbers. The extensive literature on point and line vortices includes the survey papers cited in the first chapter.

The neglect of viscosity in a flow model poses limitations which range from the fundamental physical question of how vorticity can be created to the numerical difficulties of instability and convergence. The creation of "frozen" vorticity in an inviscid fluid or of point vortices in a potential flow is already a questionable procedure, since according to Lagrange and Helmholtz vortices cannot form and cannot decay in an inviscid fluid (see Section 2.1). In particular, once vortices have been introduced into the fluid model artificially, they do not weaken when in contact with or close to a solid wall, and they do not dissipate and do not coalesce. Moreover, the lack of viscous damping causes instability problems. To overcome all these difficulties, the methods of discontinuity lines and point vortices must be encumbered with a number of ad-hoc assumptions. Thus, care must be taken in deciding if and when to use such inviscid-flow models.

On the other hand, inviscid-flow models are, in general, less expensive to evaluate numerically than viscous-flow techniques, and they have often proven to be in good agreement with experiments. Inviscid-flow solutions are also sometimes used as input for viscous-flow calculations (Chapter 3). This usefulness and the lack of better methods justify their extensive application to certain types of vortex problems. In the next sections, the strengths and weaknesses of these models are discussed.

2.1 Two-Dimensional Flows

The potential flow about a cylinder with two point vortices representing the wake of the body is quite unrealistic in two respects: (a) With certain positions and strengths of the two vortices, the drag can be negative (Vibrans 1962, Sarpkaya and Garrison 1963). (b) Viscous wake flows reveal that the center of the vortex is not a point of extremal vorticity as predicted by the point-vortex model. The reason for these deficiencies is that the sheet feeding vorticity from the body is ignored. A technique to overcome these difficulties was used a few years earlier than the above cited work by Brown, Michael, and Edwards, who introduced models to balance the force on the line between body and vortex. For a discussion of the relevant literature see J.H.B. Smith (1980).

It is tacitly assumed in inviscid-flow models that the layer feeding vorticity from the body in a viscous fluid degenerates into a spiral discontinuity sheet when the Reynolds number becomes infinite. This statement has never been proven mathematically, or at least such proofs as exist have not been universally accepted. In fact, the classical controversy is still alive between the claim of Hadamard (1903, 1926), who rejected the possibility of vorticity production in an inviscid fluid, and Klein (1910), who argued that Helmholtz's vorticity theorem must be interpreted in such a way that it includes vorticity production if the surface at which vorticity is generated shrinks to zero (as in the case of the potential vortex $v \sim 1/r$ at $r \to 0$). Subsequent discussions in the literature were either in support of Klein (Betz 1930, 1950) or against him (Ackeret 1935), all without compelling proofs.

Prandtl, although in general supporting Klein (see Prandtl 1922), nevertheless offered a solution to the problem in his ingenious, practical way by cutting the Gordian knot as follows: He argued that viscosity cannot be neglected. One therefore must look at the limiting process $Re \to \infty$ rather than analyzing the existence properties of the equations for inviscid fluids (which represent $Re = \infty$). If an inviscid-flow solution must be used as the

starting point, because at that time it was (and still is) difficult to construct solutions of the full Navier-Stokes equations, the discontinuity line must be introduced artificially. Prandtl did this for the roll-up of a discontinuity line by using a similarity argument and the Kutta-Joukowsky condition. It is significant that he called this artifice an "axiom", which is a clear indication of his opinion of the problem (Prandtl 1918). This approach was highly successful and has been followed to the present day by many scientists (see Pullin 1978). With regard to the limit as $Re \rightarrow \infty$, there seems to be a general consensus among experts that the roll-up sheet does, in fact, model the growth of a laminar vortex at high Reynolds numbers (in the subcritical range).

A related problem is the generation of lift of an airfoil in an inviscid fluid. The Lanchester-Prandtl theory, which introduces a "bound vortex" or circulation around the wing and the "Kutta-Joukowsky" condition at the trailing edge, is a hypothesis. It has never been proven mathematically that this hypothesis is the limit of a viscous fluid process as $Re \rightarrow \infty$ (Lagerstrom 1975). Still, the practical success of this hypothesis has been overwhelming, but in this case the inviscid-flow model seems to better represent the state of turbulent flow. Prandtl (1927) described the situation as "eigenartig" in German, which means "peculiar" (The English translation "unique characteristic" in the Roy. Aer. Soc. 31, 1927, 720, is incorrect).

An interesting complication enters the problem when inviscid fluids with free surface boundaries which can be penetrated are considered. Two thought-experiments of interest to ship hydrodynamics are depicted in Fig. 9, which shows the circulation generated when a simply-connected region (in which the motion is acyclic) becomes a multiply-connected one (in which the flow is cyclic).

In the following discussion the existence of singularities is assumed and postulated in the sense of Prandtl's "axiom". Unless proven otherwise in the future, the generation of such singularities in an inviscid fluid must be considered an artifice.

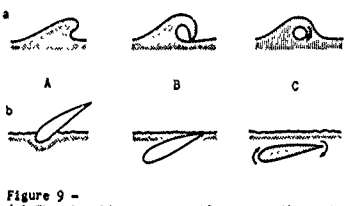


Figure 9 –
(a) The breaking-wave problem according to Prandtl (1949), (b) the water-entry problem. At situation A the flow domain is simply-connected, B is the transition state, and C is the flow situation with circulation around a border line in a doubly-connected region.

For numerical computations discontinuity lines and vorticity layers of nonzero width are often approximated in inviscid fluids by clouds, bands, and rows of point vortices or "blobs" of vortices (with nonzero core diameter) (Leonard 1980).

The discretization of discontinuity lines and bands introduces new difficulties. For simplicity, only rows of point vortices are discussed here. The replacement of a discontinuity line by a row of equally-spaced point vortices is a special case of discretization, which is merely the application of the trapezoidal rule (shown by Pullin 1978 for the circular discontinuity line). For unequal spacing, which occurs naturally when the paths of the individual vortices are computed, the method of discretization has frustrated workers in this field since Rosenhead's first attempt in 1931.

Before dwelling on these difficulties, the distinction must be made between a set of point vortices whose total number does not change over the time period considered (as in Rosenhead's problem of the roll-up of a periodically perturbed straight discontinuity line) and an assembly of vortices whose numbers increase with time by the admission of new point vortices (as in the roll-up behind a sharp wedge). In the first case the velocities of the point vortices define a Hamiltonian system with a constant Hamiltonian function. Birkhoff and Fisher (1959) have shown for this system that "the vorticity in the periodic array of point vortices cannot tend to become concentrated". In fact, this system is thermodynamically reversible, according to Poincaré.

The second case is complicated by the fact that vortices are created in a certain time interval. The introduction of such a nascent vortex between the body and the previously created vortex is quite a drastic procedure. The Hamiltonian still exists, but it is now a function of time. More fundamental, however, is the fact that the system is "open" in the thermodynamic sense. The author conjectures that the edge from which the discontinuity line (or the vortices) emanate is a source (and never a sink), which makes the birth of vortices an irreversible process in that open system. The importance of this conjecture lies in the fact that it preserves the essential feature of the Navier-Stokes equations to be dissipative (Prigonine 1980).

Numerically the introduction of a new vortex is a sensitive procedure and affects the accuracy of the pressure distribution on the body surface. The strength of the new vortex is determined by the Kutta-Joukowsky condition, which requires that the infinite velocity at the sharp edge of the body become finite through the presence of the new vortex. Additional assumptions must be made about where to place the new vortex.

The deficiency of vorticity gereration in an inviscid fluid becomes even more obvious when flow separation occurs on a blunt body without sharp edges. In this case both the

strength and the location of the origin of the vorticity sheet must be obtained from other sources, either from boundary-layer theory or from experimental data (Wardlaw 1973).

Rosenhead's results from 1931 indicate already nonconvergence of the point-vortex method, an observation which has been confirmed many times afterwards. A reason for this behavior was revealed by Fink and Soh (1974) in an important contribution, in which they showed that for unequal spacing a logarithmic error occurred. This error accumulates with time and leads to the above-mentioned irregularity. Fink and Soh remedied this deficiency by redistributing the row of vortices. They gave up trying to preserve the identity of the individual vortices and divided the discontinuity line into equal intervals after each time step. Vortices, whose strengths were computed from the known vorticity distribution along the discontinuity line, were placed in these intervals. The advantage of Fink and Soh's technique is displayed in Fig. 10, where the uncorrected and corrected results are compared for the abrupt start of a thin plate at an angle of attack of 45°. The severing of the rolled-up sheet from the developing one at the body does not happen automatically, and a new ad-hoc procedure must be built into the technique (Sarpkaya and Shoaff 1979b).

In this context another difficulty must be mentioned. A finite number of point vortices can only approximate the discontinuity spiral, which consists of infinitely many windings. Care must be taken with respect to the size of the intervals between two vortices and the distance of the windings (Pullin 1978). In addition, the finite number of point vortices can approximate only a certain number of windings and then a central vortex must be introduced to represent the rest of the spiral (Wedemeyer 1961). In reality, of course, the core of the vortex rotates like a solid body.

Baker (1980) found recently that an error still remains in the redistribution procedure because of curvature effects. Baker concludes, however, with the pessimistic remark that not only is Fink and Soh's technique unreliable but his own is also. At least he concedes that the redistribution process retards the growth of instabilities (Fig. 10).

On the basis of Fink and Soh's work and other improvements a number of fluid-flow problems have been investigated. Sarpkaya and Shoaff (1979a) studied the roll-up of vortex sheets from a vibrating circular cylinder in a parallel stream and could duplicate various physical phenomena known from experiments. For ship hydrodynamics proper, computer codes have been developed for vortex shedding from arbitrarily shaped cylinders. In one computer code use was made of exact conformal transformations to avoid errors of numerical mapping. This is particularly desirable for cylinders with fins as in Fig. 11, which is an example from a paper by Telste and Lugt (1980). Numerical conformal transformations were used by Mendenhall, Spangler, and Perkins (1979) for the Theodorsen transformation and by Shoaff and Franks in these Proceedings for arbitrarily shaped cylinders. Another numerical technique based on Fredholm integral equations was published by V.A. Golovkin and M.A. Golovkin (1979) on the subject of vortex shedding from arbitrarily shaped cylinders.

The rolling motion of a cylindrical body is of particular interest in ship hydrodynamics. Its inclusion in a computer program, however, requires the determination of coefficients of a Laurent series, which are difficult to obtain. A numerical method for computing these coefficients was presented by Telste and Lugt (1980).

What kind of physical problems can be solved with the two-dimensional point-vortex

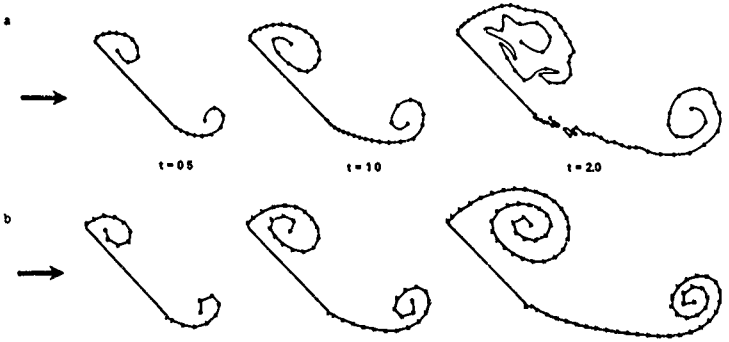


Figure 10 - Development of discontinuity lines after the abrupt start of a flat plate at an angle of attack of 45° to a constant speed U. The time is made dimensionless with U and the width of the plate. (a) Uncorrected results by Belotserkovskii and Nisht (1973). (b) Results corrected with Fink and Soh's method by Telste and Lugt (1980).

techniques? As a general rule, these methods give at least qualitative and often good quantitative results for technical problems if the flow is unsteady and the vortices are sufficiently far removed from solid surfaces. Otherwise, viscous effects must be considered. For instance, the leading edge vortex in Fig. 11a is in reality trapped between fin and body, and good results for times longer than that instant shown in Fig. 11a cannot be expected.

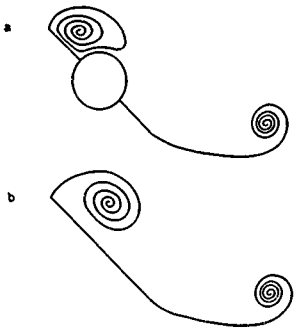


Figure 11 –
(a) Vortex sheets behind the two fins of a cylindrical body at a certain instant after the abrupt start of the body at an angle of attack of 45°. (b) Comparison with the flow past a flat plate (from Telste and Lugt 1980).

The application of point-vortex techniques to the investigation of hydrodynamic noise was studied by Grabowski and Telste (1978). They concluded that these techniques cannot adequately make acoustic predictions because the magnitude of the numerical noise far exceeds that of the real noise. It appears then that other work in acoustics based on point vortices (Davies et al. 1976 and Hardin and Mason 1977) should be carefully scrutinized.

Quite good agreement with experiments and observations has been achieved in the past when the time t in the (x,y)-plane of the unsteady flow is interpreted as the third spatial coordinate z in a steady three-dimensional flow according to the relationship t ≈ z/W, where W is the constant velocity component in the z-direction. This "unsteady cross-flow analogy", which is a kind of strip theory (see Marshall and Deffenbaugh 1974), is exact only for the u,v-velocity field with u and v the velocity components in the x and y directions, respectively. However, the vorticity field (being three-dimensional by nature) can only be approximated. This interesting behavior can be seen immediately from the Euler equations:

for unsteady two-dimensional flow:

$$\frac{\partial u}{\partial t} + u\frac{\partial u}{\partial x} + v\frac{\partial u}{\partial y} = -\frac{1}{\rho}\frac{\partial p}{\partial x},$$

for steady three-dimensional flow:

$$W\frac{\partial u}{\partial z} + u\frac{\partial u}{\partial x} + v\frac{\partial u}{\partial y} = -\frac{1}{\rho}\frac{\partial p}{\partial x},$$

with corresponding equations for the v-components. For the vorticity components of two-dimensional flow it is:

$$\omega_x = \omega_y = 0, \omega_z = \frac{\partial v}{\partial x} - \frac{\partial u}{\partial y},$$

But for three-dimensional flow it must be:

$$\omega_x = -\frac{\partial v}{\partial z} \sim \varepsilon, \omega_y = \frac{\partial u}{\partial z} \sim \varepsilon, \omega_z = \frac{\partial v}{\partial x} - \frac{\partial u}{\partial y}.$$

This can be accomplished only if

$$W \sim \frac{1}{\varepsilon} \text{ and } \frac{\partial}{\partial z} \sim \varepsilon.$$

Again the problem of the location of flow separation arises. While the sharp leading edge of a cylindrical body is a natural separation line, the location of this line and the strength of the vorticity shed are not known a priori on the smooth surface of a blunt body. Here too experiments or boundary-layer theory must give the missing information. Then, the computed results are usually in good agreement with experiments. The unsteady cross-flow analogy has been applied to rolled-up vortex sheets along cylinder-type bodies and to vortex wakes behind bodies.

The problem of providing information on the separation line as input data was solved by Angelucci (1971), who equated the separation point with the stagnation point of the cross flow. Wardlaw (1973) used experimental data, Marshall and Deffenbaugh (1974) and Nielsen and Mendenhall (1978) boundary-layer theory. These methods, originally developed for aerodynamical problems, can be applied directly to naval problems too, although the literature on these techniques in ship hydrodynamics is meager. Tatinclaux (1970a) investigated steady bilge vortices, representing them by several point vortices in only one cross-flow plane. He also computed the wake of a ship with a free surface by means of point vortices and additional simplifying assumptions (Tatinclaux 1970b). Beck (1971) solved the same problem with the assumption of a U-shaped vortex sheet. Himeno (1979) proposed the computation of the rolling motion of a ship including bilge vortices with a method tested for flows around an oscillating plate (see also the contributions of Ikeda and Himeno, and Kudo in these Proceedings). In addition, the technique of Shoaff and Franks in these Proceedings has been developed for vortex shedding from ship hulls.

Tip vortices, which have left the aircraft, have been studied by Steger and Kutler (1977), who solved the Euler equations with Lamb vortices as the initial condition.

Axisymmetric vortex sheets in an inviscid fluid are treated in a way similar to those in-plane two-dimensional flows. An example was furnished recently by Bernardinis, Graham, and Parker (1981) for the oscillatory flow around disks and through orifices. Here in axisymmetric flows, the situation becomes more complicated because of the possibility of vortex stretching and the appearance of self-induced velocity (see Sect. 2.2).

Finally, it may be mentioned that point-vortex methods can also be used to compute flow fields which are disturbed by the presence of solid bodies or free surfaces using methods similar to source panel methods. In this case, vortex distributions do not (or do not only) represent physical vortices but are mathematical devices. A combination of bound vortices and free (physical) vortices is the essence of airfoil theory. Examples of more recent work are the publications by Mokry (1978), Raj and Gray (1978), and Katz (1981). These "vortex-panel" methods can also be used to compute free water surfaces as demonstrated in these Proceedings by Baker, Meiron, and Orszag.

2.2 Three-dimensional Flows

Point vortices and vortex panels in plane or axisymmetric motions are special cases of vortex filaments and vortex sheets in three-dimensional flows (Brard 1972). The physical complexity due to vortex stretching and other three-dimensional interactions as well as the numerical difficulties involved are magnified considerably, and the use of large computers becomes mandatory.

The shortcomings of two-dimensional flow techniques due to the neglect of viscosity, discussed in Sect. 2.1, are compounded in three-dimensional flow.

Consider the velocity field induced by a vortex filament, as described by Biot-Savart's law. It may be sufficient here to invoke the "local induction approximation" of Arms (Hama 1961) which leads to

$$v = \frac{\Gamma}{4\pi R} \log\left[\frac{R}{\delta}\right] + 0 \quad (1)$$

where v is the induced velocity component perpendicular to the curvature plane, R the local radius of curvature, δ the core radius, and Γ the circulation. This equation reveals immediately the well-known fact that a curved filament of zero thickness causes an infinite value for v. Hence, curved vortex filaments must be replaced by vortex tubes of nonzero diameter, the size of the diameter being an arbitrary coefficient which must be determined with the aid of viscous fluid arguments.

Vortex sheets may be considered as composed of vortex filaments or vortex panels. In the past, various degrees of approximation and simplification were applied to model such vortex sheets. The oldest and simplest model is the "horseshoe" vortex which consists of three straight vortex lines representing the bound vortex of the wing and the two tip vortices. The horseshoe vortex is rigid in the sense that the tip vortices are straight lines of semi-infinite lengths. More refined structures, although still rigid, are the "lifting-line" and the "vortex-sheet" models, in which the individual elements are horseshoe vortices (Fig. 12b and c), either in a discrete or a continuous sense (Karamcheti 1966).

Two more recent methods of naval interest are the vortex-lattice and vortex-filament techniques (Fig. 12d and e). The vortex-lattice technique (NASA vortex-lattice Workshop 1976) divides the wing into circulation cells and the free vortex lines into segments. Boundary and Kutta-Joukowsky conditions determine the strengths of the circulation cells and the segments. The early work of the sixties (Kerwin 1961, Hedman 1966) was restricted to steady flow without tip vortices. An assessment of the accuracy of these methods was given by James (1972). Steady-flow techniques with tip vortices were developed by Belotserkovskii and Nisht (1976) and by Mook and Maddox (1974), Kandil (1974), and Kandil, Mook, and Nayfeh

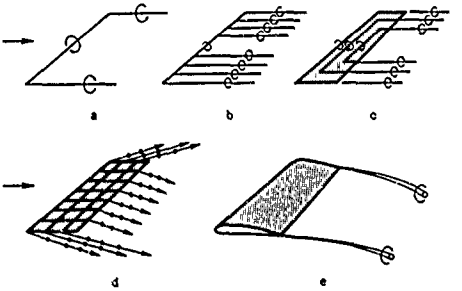


Figure 12 – Models of wing and tip vortices with increasing complexity. (a) Horseshoe vortex, (b) lifting line, (c) vortex sheet, (d) steady vortex lattice, and (e) vortex filament model.

(1976). Unsteady-flow techniques were published by Atta (1976) and Atta, Kandil, Mook, and Nayfeh (1976) for an unsteady free stream; and for the general movement of the body by Thrasher, Mook, Kandil, and Nayfeh (1977) and Thrasher, Mook, and Nayfeh (1978). The arrangement of the vortex lattice for unsteady flow is depicted in Fig. 13 and can be compared with the steady-flow case in Fig. 12d. The induced velocity field is at variance with that based on the equation at the beginning of Section 2.2. An example of steady flow with rolled-up vortex sheets is furnished in Fig. 14.

Parallel to the development of vortex-lattice methods was the development of doublet-lattice methods for lifting surfaces with and without tip vortices (Johnson et al. 1980, Koyama 1980). Difficulties of the vortex-lattice method, which are worth mentioning, are the doubtful application of the Kutta-Joukowsky condition to unsteady flow problems (Gostelow 1975) and the relatively long computer time necessary for complex flow problems. Vortex-lattice methods have been applied in ship hydrodynamics mainly to propeller and turbine problems as in the work of Kerwin (1981) and Yuasa et al. (1980) for steady and unsteady propeller forces and of Strickland, Webster, and Nguyen (1979) for the Darrieus turbine.

The most rigorous treatment of curved vortex sheets and filaments so far has been done by Leonard (1975, 1980) with the vortex-filament method Fig. 12e. This method takes into account the curvature effect expressed in the equation at the beginning of Section 2.2 and models the core of nonzero radius with a Gaussian vorticity distribution (Tung and Ting, 1967, Saffman, 1970). Thus, filament stretching and viscous diffusion can be incorporated

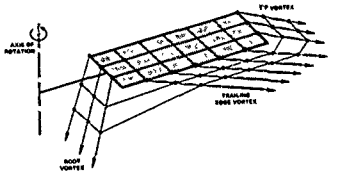


Figure 13 -
Vortex-lattice method for unsteady inviscid-fluid flow, illustrated with a helicopter blade. After each time step a row of elements is shed. The earliest segments, indicated by arrows, are semi-infinite vortex lines. For a marine propeller, the root vortex becomes the hub vortex.

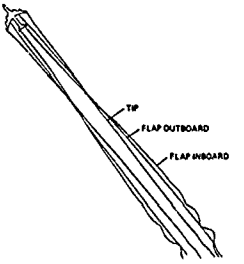


Figure 15 -
Computed vortex filaments in the wake of a Boeing 747 according to Leonard (1980). The beginning of instability of the flap-inboard vortex is clearly visible.

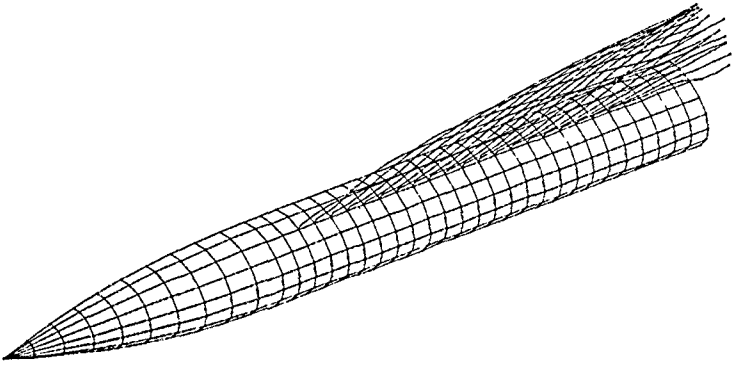


Figure 14 - Rolled-up vortex sheet on one side of a body, which consists of an ogive bow tangent to a cylindrical after-body at an angle of attack of 15°, computed with a vortex-lattice method (from F. Thrasher, DTNSRDC).

into the model. An example of the vortex-filament method is provided in Fig. 15. An improved method, which uses ideas to those similar expressed by Christiansen (1973) and Fink and Soh (1974) for point vortices, has been developed for three-dimensional filaments by Couët, Buneman, and Leonard (1980).

3. VISCOUS-FLOW MODELS

The exactness with which solutions of the Navier-Stokes equations can describe real fluid flows (at least Newtonian fluids like water and air) was first revealed about 1840 when the solution for the laminar flow in a circular pipe was compared with experiments. Since then the theory of the Navier-Stokes equations, which can describe the generation and decay of vortices, has been confirmed over and over again within the error limits of experimental measurements. Unfortunately, only a few closed-form solutions of the Navier-Stokes equations for vortices exist, and even most of these are not very practical because of their similarity or symmetry properties (Bellamy-Knights 1970). The difficulties in solving these equations in general are due to their nonlinearity.

The advent of modern computers has made it possible to obtain numerical solutions of the Navier-Stokes equations for moderate Reynolds numbers, that is roughly for $Re < 5000$ if the length scale is based on the diameter of cylindrical bodies. This advancement and the associated physical analyses have led to scrutinizing of a number of familiar fluid dynamical concepts. Two generations of fluid dynamicists have followed certain familiar concepts in their daily work on vortex flows: the Kutta-Joukowsky condition, the image vortex inside the body, the bound vortex, and the discontinuity line, all of which are off-springs of potential-flow theory. But in constructing solutions of the Navier-Stokes equations, the Kutta-Joukowsky condition has become superfluous, image vortices are no longer needed, the bound-vortex concept has lost its usefulness, and the Hadamard- Klein controversy (see Section 2.1) has become an academic question. Instead, the hypotheses and approximations of inviscid-flow models have been replaced by other difficulties, especially by the proper interpretation of numerical results and, above all, by the concern about the accuracy and validity of computer-generated data. Despite the criticism directed against numerical fluid dynamics, especially the sometimes justified condemnation of unsound and careless computer runs, the time for computer-based numerical analyses of viscous flows has arrived and their essential and growing role in fluid dynamics is indisputable. It must be acknowledged, however, that so far solutions of the Navier-Stokes equations are restricted to moderate Reynolds numbers in the laminar flow domain (with a few exceptions in simple turbulence modelling).

For viscous fluids the vortex definition of Chapter 2 is too restrictive. Unfortunately, a general definition of vortices in viscous fluids which includes rotating reference frames and stratification is very difficult. It may suffice here to indicate that any mass of fluid moving around a common axis constitutes a vortex. Mathematically, such motion can be described by closed or spiralling pathlines if a local reference frame exists in which the flow field becomes steady. Hence the definition requires a knowledge of the time history of the flow (Lugt, 1979b).

The study of vortices in a viscous fluid flow may be divided into three parts, depending on the severity of the truncation of the Navier-Stokes equations: (1) the classical boundary-layer approach, (2) the streamwise approximations of the Navier-Stokes equations, and (3) the full Navier-Stokes equations. Boundary-layer theory is merely mentioned here despite its importance in ship hydrodynamics. Boundary-layer calculations can roughly locate the separation line, which is needed for inviscid-flow models. In the following sections only the last two groups will be discussed.

3.1 Streamwise Approximations of the Navier-Stokes Equations

The integration of the Navier-Stokes equations can be simplified considerably if some knowledge of the flow field is available. This knowledge is particularly helpful if the direction of the main stream along the body is given, and the flow derivatives in this direction are much smaller than in the plane perpendicular to it. Such a situation exists for the tip vortices created at the edges of plates, wings, and blades.

One possible approach is the classical Oseen linearization, which has been applied to the tip-vortex problem by Davies and Breslin (1980). They also simplified the problem by assuming symmetry about an axis.

More involved and more realistic are two methods which approximate the Navier-Stokes equations in the streamwise direction. These methods "parabolize" the original equations of motion either completely or partly and thereby restrict the region of elliptic influence.

To illustrate the fully parabolic approximation, a simple Cartesian-coordinate formulation is chosen, with the flow mainly in the x-direction. The Navier-Stokes equations are then truncated to

$$u\frac{\partial u}{\partial x} + v\frac{\partial u}{\partial y} + w\frac{\partial u}{\partial z} = -\frac{1}{\rho}\frac{\partial p}{\partial x} + \nu\frac{\partial^2 u}{\partial y^2} + \nu\frac{\partial^2 u}{\partial z^2},$$

$$u\frac{\partial v}{\partial x} + v\frac{\partial v}{\partial y} + w\frac{\partial v}{\partial z} = -\frac{1}{\rho}\frac{\partial p}{\partial y} + \nu\frac{\partial^2 v}{\partial y^2} + \nu\frac{\partial^2 v}{\partial z^2},$$

$$u\frac{\partial w}{\partial x} + v\frac{\partial w}{\partial y} + w\frac{\partial w}{\partial z} = -\frac{1}{\rho}\frac{\partial p}{\partial z} + \nu\frac{\partial^2 w}{\partial y^2} + \nu\frac{\partial^2 w}{\partial z^2},$$

$$\frac{\partial u}{\partial x} + \frac{\partial v}{\partial y} + \frac{\partial w}{\partial z} = 0 .$$

Furthermore, a pressure decomposition is postulated as

$$p(x,y,z) = p_{inv}(x,y,z) + p_m(x) + p_c(y,z;x)$$

such that the static pressure $p(x,y,z)$ is the sum of a 3-D inviscid pressure $p_{inv}(x,y,z)$, a mean-pressure $p_m(x)$ and a cross-plane pressure $p_c(y,z;x)$ due to viscous effects.

This method has been employed by a number of researchers for low-speed flow and its several variants have appeared in the literature, e.g., Patankar and Spalding (1972), Briley (1974), Ghia, U., Ghia, K. and Studerus (1977), Ghia and Sokhey (1977) and by Ghia and Sathyanarayana (1979); Lin and Rubin (1973) as well as Lubard and Helliwell (1975) used an analogous aproach for high-speed flow. The numerical solution can be obtained very efficiently by a single marching in the forward streamwise direction. The method does not permit the consideration of streamwise flow separation but has a distinct advantage over 3-D boundary-layer theory as it can provide accurate treatment of cross-flow recirculation. Of relevance to ship hydrodynamics is the application of this method to the tip-vortex problem (Shamroth and Briley (1979)), whose solution took a few minutes on the CDC 7600 computer (Fig. 16a), and to curved three-dimensional geometries as they occur in propellers and turbines (Briley and McDonald 1979).

An approximate form of the Navier-Stokes equations that remains regular at points of streamwise flow separation is the one developed by Ghia et al. (1981) and reviewed by Rubin (1981). It belongs to the class of "semi-elliptic" formulations. The momentum transport equations are parabolized as in the fully parabolic model, but no particular decomposition is postulated for the pressure. In fact, the pressure is determined from a Poisson equation that serves to indirectly satisfy the mass-conservation equation as well as to partially retain ellipticity in the formulation. Application to flow through an asymmetrically constricted channel (Fig. 16b) shows that this model is completely capable of describing flows with streamwise flow separation, with definite computational advantages over the fully elliptic Navier-Stokes equations.

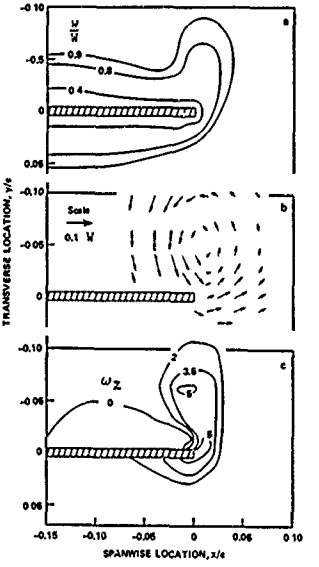


Figure 16a -
Tip vortex at the end of a flat-plate wing seen from the front parallel to the plate. Angle of attack = 6°, Reynolds number based on the chord = 10^6. (a) Streamwise velocity contours in the (x,y)-plane at z/c = 0.9, where c is the chord, (b) corresponding secondary flow, velocity vectors, and (c) equi-vorticity lines ω_z = const (from Shamroth and Briley 1979).

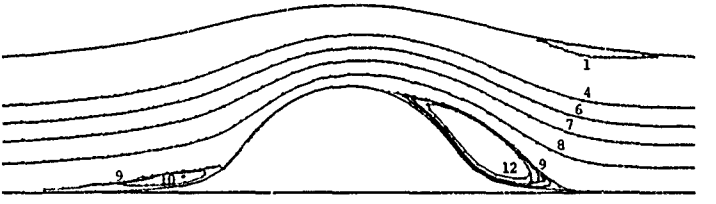


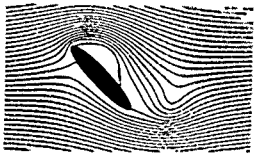
Figure 16b - Flow through an asymmetrically constricted two-dimensional channel. Streamlines from left to right for Re = 1000, based on the channel width at entrance. Notice the occurrence of three vortices at the channel walls (from U. Ghia et al. 1981).

3.2 Two-dimensional Solutions of the Navier-Stokes Equations

Since the pioneering work of Payne (1958) and Fromm (1963) on solving the time-dependent two-dimensional Navier-Stokes equations for an incompressible fluid, an increasing stream of publications has appeared with improved and sophisticated numerical techniques. Papers dealing with vortex shedding behind bodies are, in chronological order: Thoman and Szewczyk (1966) on circular cylinders; Lugt and Haussling (1971) on elliptic cylinders at high angles of attack (Fig. 17); Mehta and Lavan (1972) on airfoils; Jordan and Fromm (1972) on circular cylinders in a shear flow; Lugt and Ohring (1974) on rotating thin elliptic cylinders; Mehta (1977) and Wu, Sampath, and Sankar (1977) on oscillating airfoils (Fig. 18); Kinney (1977) on airfoils in unsteady flows; Hodge and Cooper (1977) on self-excited oscillation of stalled airfoils; Hankey, Hunter, and Harney (1979) on self-sustained oscillations on spike-tipped axisymmetric bodies in supersonic flows; and Ta Phuoc Loc (1980) on secondary vortices generated by an abruptly started circular cylinder.

The solution of flow problems of such increasing complexity was made possible by (a) the development of more sophisticated numerical techniques and (b) the availability of more powerful computers.

a



b



Figure 17 -
Laminar flow past an elliptic cylinder at a certain instant after the abrupt start for Re = 200, based on the width of the cylinder. (a) Streamlines (b) equi-vorticity lines (Lugt and Haussling 1971).

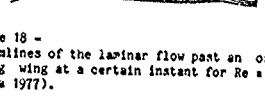


Figure 18 -
Streamlines of the laminar flow past an oscillating wing at a certain instant for Re = 5000 (Mehta 1977).

(a) The first breakthrough in the development of numerical methods after the period of overrelaxation techniques was the introduction in the sixties at Stanford University (Buneman 1969, Hockney 1970, Buzbee, Golub, and Nielson 1970) of Direct-Poisson solvers for plasma flows. These were applied in the early seventies to the Navier-Stokes equations, and capacitance matrix and embedding techniques were developed for irregular flow regions. Since the mid seventies five major advancements in solving the Navier-Stokes equations have been made: (1) The boundary-fitted coordinate method, which makes it possible to compute flows around arbitrarily shaped bodies with finite-difference techniques (Thompson, Thames, and Mastin 1974); (2) The adaptation of finite-element methods to viscous-flow problems (Chung 1978); (3) Higher-order techniques which include spline and spectral functions and Hermite polynomials (Orszag 1971, Hirsh 1975, Krause, Hirschel, and Kordulla, 1976, Rubin and Khosla 1976); (4) Adaptive grid techniques for controlling grid sizes automatically to improve efficiency of a method. These studies are going on for both finite-difference (NASA CP 2166, 1980) and finite-element methods (Babuška and Rheinboldt 1980). (5) Multi-grid method (Brandt 1977).

(b) Parallel to the development of more complex numerical techniques was the impressive advancement in computer hardware. The technology of semiconductor memory and parallel processing led to the present supercomputers, which include ILLIAC IV, STAR, CRAY 1S, CYBER 205, and BSP.

When numerical methods are applied to engineering problems, it is often unnecessary to solve the Navier-Stokes equations for the whole flow domain. Rather, the computation can be simplified by dividing the flow field into regions in which the vorticity is negligible and regions in which it is not. Wu (1976) presented a technique which confines the solution of the Navier-Stokes equations to areas of nonzero vorticity. The boundaries of these areas must be determined as part of the solution and may change in time. If the flow behavior is (at least roughly) predictable beforehand, the flow field can be divided into appropriate regions in advance. An example of naval interest is furnished in Fig. 19a for the axisymmetric flow past an underwater vehicle. Techniques and solutions based on this idea have been published by Schetz and Favin (1979). In this paper the propeller is included by using the actuator-disk model.

For studies of vortex flows in which (at least locally) the rotation axis is perpendicular to a solid wall, the flow field may be divided into three parts, a procedure which is a simplified version of Lewellen's partition of a tornado field (1976), Fig. 19b. Here, in region I similarity solutions of the type of Long (1958) predict the real flow behavior fairly well. In region II the flow has the characteristics of a boundary layer. Region III is the most difficult one, and here the full Navier-Stokes equations must be solved numerically. It may be mentioned that in this

region similarity solutions do exist but only up to a certain Reynolds number (Goldshtik's problem 1960). Solutions of these vortex flows are of particular interest in the study of cavitation.

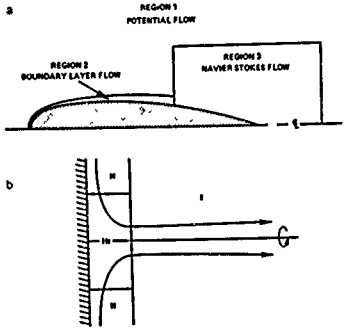


Figure 19 –
The division of flow regions (see text).

3.3 Three-dimensional Solutions of the Navier-Stokes Equations

The ultimate objective of any numerical analysis in fluid dynamics is the construction of solutions of the Navier-Stokes equations for time-dependent three-dimensional laminar or turbulent flows around bodies of arbitrary shape up to high Reynolds numbers. This goal is still a number of years away. Although the size and power of computers from the mid eighties on will make it possible to consider such flow problems (NASA CP-2032 Workshop), there is still a lack of physical insight into the fundamental nature of turbulence (see Chapter 4). Nevertheless, great progress has already been made in developing numerical techniques for three-dimensional flows. Most recent methods for two-dimensional motion, cited in Section 3.2, can be extended to three-dimensional flows.

Actual computations have been carried out most recently by Wray (1979), Daiguji, Shirahata, and Yamada (1979), Shang, Buning, Hankey, and Wirth (1980), Briley and McDonald (1980), and by Haase (1980). Wray computed the transition of an axisymmetric jet, which has an initial three-dimensional disturbance, to a turbulent state for Re = 20,000 and Mach number Ma = 0.5. The computer time on the ILLIAC IV was of the order of 7 hours (Fig. 20). Shang et al. used MacCormack's explicit scheme, vectorized for the CRAY-1 computer, to solve the transonic flow in a windtunnel diffusor. The other computations have potential applications in ship hydrodynamics: Daiguji et al. and Briley and McDonald studied the necklace-vortex problem, and Haase the flow past a prolate spheroid at nonzero angle of attack (Fig. 21). One aspect of Haase's difference scheme is the use of a "cell Reynolds number," which controls stability and convergence. This idea goes back to Il'in (1969) and Dawson and Marcus (1970).

The need for more advanced computer hardware to solve general three-dimensional flow problems is evident. Efforts in the USA to meet this requirement include the proposed "Numerical Aerodynamic Simulator" (NAS) with the following specifications (as of Spring 1981): speed- at least 1 billion arithmetic operations per sec; memory- at least 40 billion directly addressable words and at least 200 million block addressable words (information from NASA-Ames). Similar efforts are already underway, and further advanced in Japan for the National Aerospace Laboratory (equivalent to the NAS proposal in the USA) and at Hitachi (HAP-1) and Fujitsu.

Applications of viscous-flow methods to vortex problems in ship hydrodynamics are virtually nonexistent. Techniques for two-dimensional vortex flows can be applied to problems of cable-towing and ocean structures. Axisymmetric and three-dimensional flow techniques in combination with turbulence modelling (see following chapter) will find application in the study of bare hulls of fully submerged naval vehicles, in particular of the stern of such bodies (Intern. Towing Tank Conf. 1981).



Figure 20 – Decay of an axisymmetric jet into turbulence. Re = 20,000 and Ma = 0.5. Computer-generated equi-vorticity lines at a certain instant (Wray 1979).

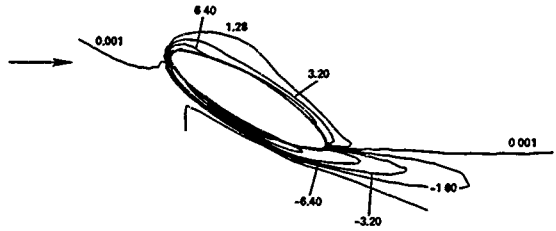


Figure 21 - Equi-vorticity lines in the plane of symmetry of a prolate spheroid 4:1 at an angle of attack of 30° for Re = 1000 based on the length of the body (from Haase 1980).

4. TURBULENT VORTICES

Almost 100 years have passed since Reynolds' basic experiments on turbulence. During these 100 years the problem of turbulence has remained probably the most challenging one in classical physics. Although it is far from solved, work on turbulence has received a new impetus in recent years by the recognition of the existence of coherent structures in the form of "large-scale eddies".

Turbulent motion may be thought of as a spectrum of "eddies" which, according to Tennekes and Lumley (1972), are vortices with a certain bandwidth of energy and which are statistical up to a certain size. Large eddies, which are coherent and identifiable, have an ordered structure and are non-statistical. Although such coherent structures were observed in the twenties by Nikuradse, their real significance has been recognized only in the last decade (Roshko 1976), and they are now the subject of experimental and numerical investigations. However, the hypothetical (or semi-empirical) nature of turbulence modelling remains in the subgrid range (Ferziger 1977). The confidence that solutions of the Navier-Stokes equations for laminar flows enjoy is here diminished by the necessity for closure assumptions because they are not universally valid for all flows and are thus tentative .

This review is certainly not the place to summarize the effort in numerical turbulence modelling, even if it were restricted to turbulent vortices. A few examples of special interest in ship hydrodynamics have been selected, and the remainder of this chapter is devoted to turbulence modelling based on standard Reynolds-stress averaging and on "large-scale eddies".

4.1 Methods Based on Reynolds-Stress Modelling

Although vortices are part of the general flow field, they often can be singled out and treated separately as in the example of vortex rings. When they change from the laminar to the turbulent state, their characteristics change too. Examples in addition to the vortex ring (Maxworthy 1974), are the turbulent line vortex (Hoffmann and Joubert 1963, Govindaraju and Saffman 1971, and M. Macagno and E. Macagno 1975) and the tip vortex with its swirling behavior (Donaldson and Bilanin 1975).

This change in flow behavior is usually ignored in inviscid-flow models. For instance, the roll-up of discontinuity sheets described in Chapter 2 is often tacitly assumed to represent a turbulent motion, although it is probably the limit of a laminar flow process when $Re \to \infty$ (Section 2.1). Nevertheless, this assumption may be acceptable as long as turbulence is modelled by a simple constant "eddy viscosity" which is merely a very large laminar viscosity coefficient.

For viscous-flow models it has long been recognized that a constant eddy viscosity is not realistic. "Closure" procedures, which become necessary when the Navier-Stokes equations are averaged, may be divided into two groups: (a) first-order procedures, in which the Navier-Stokes equations describe mean velocities and mean pressure (first-order quantities) and second-order quantities are modelled; (b) second-order procedures, in which first and second-order quantities are described by the equations of motion and third-order quantities are modelled (Rubesin 1977, Launder 1979, Mehta and Lomax 1981).

Recent applications of first-order procedures have been published by Raj and Iversen (1980) for tip vortices behind aircraft and by Shamroth and Gibeling (1980) on unsteady two-dimensional flows past airfoils at high angles of attack for $Re = 10^6$.

According to Donaldson (1972) it appears that at least second-order procedures are required to simulate turbulent vortices. Donaldson and his colleagues (Donaldson and Bilanin 1975, Bilanin, Teske, and Williamson 1977, Bilanin, Teske, and Hirsh 1978) have developed second-order techniques to compute tip vortices. Although these techniques are intended for studying tip vortices behind aircraft, they can be applied directly to tip vortices behind lifting surfaces of naval vehicles. Such techniques have also been applied to vortices near solid walls as in the study of tornadoes by Lewellen and Teske (1977).

More general than closure procedures for vortices are those which simulate shear flows and boundary layers with curvature and rotation. Prandtl (1929) noticed that curved streamlines of a turbulent motion have a stabilizing effect. A review of this effect and others was given by Bradshaw (1973). First-order closure techniques have been recently compared by Hah and Lakshminarayana (1980a) and applied to rotor blades (1980b). A recent second-order procedure has been presented by Gibson and Rodi (1981).

4.2 Large-eddy Simulation

What is the distinction between turbulent vortices and large eddies? Probably none conceptually. Turbulent vortices, such as turbulent tip vortices or vortex rings, may be considered as isolated entities in themselves, whereas large eddies like those in shear-flows are regarded as parts of an overall turbulent motion. Both, however, have in common that their substructures must be modelled as mentioned in Section 4.1. Large eddies must be filtered out from their less distinguished smaller companions. A general formulation of such a filtering scheme was given by Leonard (1974). Large scale eddies are computed directly, but small scale ones must be modelled. Direct turbulence calculations were done by Deardorff (1970), Schumann (1973), and Orszag and Pao (1974), among others. Work of this nature was recently reported by Ferziger (1977), Kim and Moin (1979), and Biringen and Reynolds (1981).

An interesting study of large-eddy simulation, which is based on an inviscid-vortex filament method by Leonard (1979), may be singled out here. The computer program calculates the growth of a turbulent spot triggered by a local disturbance in a laminar boundary layer. This idea has a strong similarity to the concept of the "horseshoe" structure in a boundary layer by Theodorsen (1955). It is remarkable how well this inviscid-flow model can simulate the essential features of the development of turbulent spots.

Finally, it may be pointed out that turbulent vortices can occur in a turbulent environment (so that they become large eddies according to the distinction made at the beginning of this section). This environment can be in the form of background turbulence or can consist of contact with a neighboring turbulent boundary layer. Bilanin, Teske, and Hirsh (1978) have computed the influence of background turbulence on tip vortices. Wind tunnel measurements were made by Mehta, Shabaka, and Bradshaw (1981) on longitudinal vortices imbedded in turbulent boundary layers. These studies are of particular interest in understanding the influence of vortices near the hull of naval vehicles.

5. CONCLUSIONS

The conclusions drawn from this review may be presented in two parts: an assessment of what can be done with presently available numerical techniques and computers, and what can be expected within the next decade.

5.1 Present State-Of-The-Art

In all fluid-flow areas covered in this review, methods and capabilities already exist to solve certain vortex problems. These capabilities are not yet fully exploited in ship hydrodynamics applications. A similar statement made by Brard (1972) almost a decade ago is confirmed by the very few papers on vortex flows in this conference. They are restricted to two-dimensional point-vortex methods.

As indicated in the abstract, however, activity in the study of vortices has increased, especially in the area of inviscid vortex flows. Here, techniques based on point vortices and vortex lattices are applied in the study and design of propeller blades and in the study of flow behavior around ship hulls with and without simple control surfaces. However, three-dimensional flow problems attacked with vortex-lattice methods require much computer time. In addition, they rely on available computer codes for three-dimensional potential flows and boundary layers with and without free surfaces. Full exploitation in ship design calls for more efficient techniques.

Tip vortices, which are generated at lifting surfaces, and their interference with downstream solid surfaces can be simulated with vortex filament methods, but they have not yet been exploited in ship hydrodynamics.

Techniques for viscous vortex flows are restricted at present essentially to two-dimensional vortex shedding from cylindrical bodies at moderate Reynolds numbers. Flows past cables and underwater structures, either fixed or oscillating, can be computed, although here too more economic methods are required to be practical. An analogous situation exists for axisymmetric flows.

For three-dimensional laminar flow problems, techniques for solving the parabolized Navier-Stokes equations are promising. Computer programs for solving the full Navier-Stokes equations are in their infancy.

The methods for laminar viscous flows can be extended by building in turbulence models. Such inclusion makes computer programs attractive for a wide area of technical problems.

It may be stressed at this point that the development and availability of computer programs is evolutionary in the sense that one does not have to wait to solve a problem until more efficient techniques and bigger computers are at hand. With their gradual availability more complex problems can be solved.

5.2 Future Outlook

In the next few years vortex lattice methods will become available for flows past fully submerged and surface ships with control surfaces. These methods require more accurate computer codes for potential flows and boundary

layers to obtain accurate data on the location of separation lines and rate of vortex shedding.

From the mid-eighties on, the computation of three-dimensional flows around fully submerged bodies, based on the Reynolds-averaged Navier-Stokes equations with suitable closure models for turbulence and with computers envisioned in the NAS-project, will be feasible. By that time the study of direct turbulence simulation (McCormack 1978) will make it possible to minimize the impact of closure models for the subgrid range. Still, the solution of complicated problems like three-dimensional flows around freely moving ships and hull-propeller-rudder interaction will have to wait.

Nevertheless, vortex simulation as part of numerical fluid dynamics will be revolutionized in the decade ahead.

Due to the wide areas covered, this review can give only a broad outline of the subject, and the more than 170 references quoted are in almost all cases only examples.

6. ACKNOWLEDGEMENTS

I owe thanks to a number of friends and colleagues for their criticism and recommendations. In particular, I want to thank Mrs. J. Schot, Dr. H.J. Haussling, and Mr. J. McCarthy of DTNSRDC for their help. I also enjoyed discussions with Dr. L. Schmid of the National Bureau of Standards, Prof. W. Melnik from the University of Maryland, and Prof. U. Ghia from the University of Cincinnati. Mrs. A. Phillips of DTNSRDC improved the readibility of the text considerably.

REFERENCES

Ackeret, J., ZAMM 15, 1935, 3.

Acosta, A.J., Ann. Rev. Fluid Mech. 5, 1973, 161.

Angelucci, S.B., Journ. Aircraft 8, 1971, 959.

Aref, H., Phys. Fluids 22, 1979, 393.

Arndt, R.E., Ann. Rev. Fluid Mech. 13, 1981, 56.

Atta, E.H., M.S. Thesis, Dept. Engineering Science and Mechanics, Virginia Polytechnic Inst. and State University, Blacksburg, Va. 1976.

Atta, E.H., Kandil, O.A., Mook, D.T., and Nayfeh, A.H., NASA SP-405, 1976, 407.

Baba, E., Seminar on Wave Resistance, Soc. Naval Architects of Japan. Feb. 1976, 75.

Babuška, I. and Rheinboldt, W., Comp. Methods in Nonlinear Mechanics. J.T. Oden, ed., North Holland Publ. Co. 1980, 67.

Baker, G.R., Journ. Fluid Mech. 100, 1980, 209.

Beck, R.F., Journ. Ship Res. 15, 1971, 196.

Bellamy-Knights, P.G., Journ. Fluid Mech. 41, 1970, 673.

Belotserkovskii, S.M. and Nisht, M.I., Fluid Dynamics 8, 1973, 772.

Belotserkovskii, S.M. and Nisht, M.I., Fluid Dynamics 1976, 583.

Bernardinis, B. de, Graham, J.M.R., and Parker, K.H., Journ. Fluid Mech. 102, 1981, 279.

Betz, A., ZAMM 10, 1930, 413.

Betz, A., Die Naturwissenschaften 37, 1950, 193.

Bilanin, A.J., Teske, M.E., and Hirsh, J.E., AIAA Journ. 16, 1978, 956.

Bilanin, A.J., Teske, M.E., and Williamson, G.G., AIAA Journ. 15, 1977, 250.

Biringen, S. and Reynolds, W.C., Journ. Fluid Mech. 103, 1981, 53.

Birkhoff, G. and Fisher, J., Rend. Circolo Mat. di Palermo, Serie II, Tomo VIII, 1959, 1.

Bradshaw, P., AGARDograph No. 169, 1973.

Brandt, A., Math. of Computation 31, 1977, 333.

Brard, R., Proc. Ninth Symp. Naval Hydrodynamics. ONR 1972, 1187.

Briley, W.R., Journ. Comp. Physics 14, 1974, 8.

Briley, W.R. and McDonald, H., AIAA paper 79-1453, 1979.

Briley, W.R. and McDonald, H., Seventh Intern. Conf. on Numerical Methods in Fluid Dynamics, June 1980.

Brooks, J.E., David Taylor NSRDC Rep. 80/056, April 1980.

Buneman, O., Stanford University Institute for Plasma Research, Rep. 294, 1969.

Buzbee, B.L., Golub, G.H., and Nielson, C.W., SIAM Journ. Num. Anal. 7, 1970, 627.

Chapman, D.R., AIAA Journ. 17, 1979, 1293.

Christiansen, J.P., Journ. Comp. Physics 13, 1973, 363.

Chung, T.J., Finite Element Analysis in Fluid Dynamics. McGraw-Hill 1978.

Clements, R.R. and Maull, D.J., Prog. Aerospace Sci. 16, 1975, 129.

Couët, B., Buneman, O., and Leonard, A., Journ. Comp. Physics 39, 1981, 305.

Cox, G.G. and Lloyd, A.R., SNAME Trans. 85, 1977, 51.

Dagan, G. and Tulin, M.P., Journ. Fluid Mech. 51, 1972, 529.

Daiguji, H., Shirahata, H., and Yamada, H., Bull. JSME 22, 1979, 925.

Davies, P.O.A.L. et al., Prog. in Astronautics and Aeronautics 43, 1976.

Davies, T.V. and Breslin, J.P., Stevens Inst. Tech. Rep. SIT-DL-80-9-2124, May 1980.

Dawson, C. and Marcus, M., Proc. 1970 Heat Transfer and Fluid Mechanics Inst., Stanford Univ. Press 1970, 323.

Deardorff, J.W., Journ. Fluid Mech. 41, 1970, 453.

Donaldson, C. DuP., AIAA Journ. 10, 1972, 4.

Donaldson, C. DuP. and Bilanin, A.J., AGARDograph No. 204, May 1975.

Ferziger, J.H., AIAA Journ. 15, 1977, 1261.

Fink, P.T. and Soh, W.K., Tenth Symp. Naval Hydrodynamics 1974, 463.

Föppl, L., Sitzungsberichte Kgl. Bayr. Akademie der Wiss., München 1913, 1.

Fromm, J.E., Los Alamos Rep. LA-2910, 1963.

Ghia, U., Ghia, K.N., Rubin, S.G., and Khosla, P.K., Comp. and Fluids 9, 1981, 123.

Ghia, U., Ghia, K.N., and Studerus, C.J., Intern. Journ. Comp. and Fluids 5, 1977, 205.

Ghia, U. and Sathyanarayana, K., Flow in Primary Non-rotating Passages in Turbomachines, ed. H.J. Herring, ASME Publ. 1979.

Ghia, K.N. and Sokhey, J.S., Journ. Fluids Eng. 99, 1977, 640.

Gibson, M.M. and Rodi, W., Journ. Fluid Mech. 103, 1981, 161.

Goldshtik, M.A., Prikladnaia Matematica Mekhanica 24, 1960, 913.

Golovkin, V.A. and Golovkin, M.A., Sixth Intern. Conf. Num. Methods in Fluid Dynamics. Lecture Notes in Physics, No.90, Springer-Verlag 1979, 253.

Gostelow, J.P., ASME 75-GT-94, 1975.

Govindaraju, S.P. and Saffman, P.G., Phys. Fluids 14, 1971, 2074.

Grabowski, W.J. and Telste, J.G., David Taylor NSRDC Rep. 78/050, June 1978.

Granger, R.A., Journ. Ship Res. 18, March 1974, 12.

Griffin, O.M. et al., Journ. Waterway Port Coastal and Ocean Div., Proc. ASCE 106, May 1980, 183.

Haase, W., Ph.D. Thesis, Tech. Univ. Berlin, Fachbereich 9, 1980.

Hadamard, J., Leçons sur la propagation des Ondes et les équations de l' Hydrodynamique. Paris, Hermann, 1903.

Hadamard, J., Proc. Second Intern. Congress Appl. Mech., Zürich 1926, 507.

Hah, C. and Lakshminarayana, B., AIAA Journ. 18, 1980a, 1196.

Hah, C. and Lakshminarayana, B., Trans. ASME Journ. Fluids Eng. 102, 1980b, 462.

Hama, F.R., Phys. Fluids 5, 1962, 1156.

Hankey, W., Hunter, L., and Harney, D., AFFDL-TM-79-23-FXM, Jan. 1979.

Hardin, J.C. and Mason, J.P., Third AIAA Aeroacoustics Conf., Palo Alto, California 1976.

Hardin, J.C. and Mason, J.P., AIAA Journ. 15, 1977, 632.

Hedman, S.G., FFA Rep. 105, Flygtekniska Forsoksanstalten, Stockholm 1966.

Himeno, Y., Univ. Michigan, Dept. Naval Arch. and Marine Eng., Rep. 220, July 1979.

Hirsh, R.S., Journ. Comp. Physics 19, 1975, 90.

Hockney, R.W., Methods in Comp. Phys. 9, 1970, 135.

Hodge, J.K. and Cooper, W.H., AFFDL-TM-77-94 FXM, Nov. 1977.

Hoekstra, M., Proc. Symp. Hydrodyn. Ship and Offshore, 1977.

Hoffmann, E.R. and Joubert, P.N., Journ. Fluid Mech. 16, 1963, 395.

Hunt, J.C.R., Phil. Trans. Roy. Soc. London A 269, 1971, 457.

Il'in, A.M., Math. Notes of the Academy of Sciences of the USSR 6, 1969, 596.

Intern. Towing Tank Conf., 16th, Leningrad, 1981.

James, R.M., Comp. Methods in Appl. Mech. and Eng. 1, 1972, 59.

Johnson, F.T., Tinoco, E.N., Lu, P., and Epton, M.A., AIAA Journ. 18, 1980, 367.

Jordan, S.K. and Fromm, J.E., Phys. Fluids 15, 1972, 972.

Kandil, O.A., Ph.D. Thesis, Dept. Eng. Mech., Virginia Polytechnic Institute and State University, Blacksburg, Va., 1974.

Kandil, O.A., Mook, D.T., and Nayfeh, A.H., Journ. Aircraft 13, 1976, 62.

Karamcheti, K., Principles of Ideal-Fluid Aerodynamics. Wiley 1966.

Katz, J., Journ. Fluid Mech. 102, 1981, 315.

Kerwin, J.E., Lectures, Dept. Naval Arch. and Marine Eng., MIT, June 1961.

Kerwin, J.E., Lectures, Dept. Naval Arch. and Marine Eng., MIT, April 1981.

Kim, J. and Moin, P., AGARD CP-271, 1979, 14.

Kinney, R.B., AGARD CP-227, 1977.

Klein, F., Zeitschrift Math. Physik 58, 1910, 259.

Koyama, K., 13th Symp. Naval Hydrodynamics, Tokyo, Oct. 1980.

Krause, E., Hirschel, E.H., and Koraulla, W., Comp. and Fluids 4, 1976, 77.

Kux, J. and Wieghardt, K., AFFDL-TR-80-3088, June 1980, 76.

Lagerstrom, P.A., SIAM Journ. Appl. Math. 28, 1975, 20.

Launder, B.E., AGARD CP-271, 1979, 13.

Leonard, A., Advances in Geophysics 18A, 1974, 237.

Leonard, A., Fourth Intern. Conf. Num. Methods in Fluid Dynamics. Lecture Notes in Physics. Springer 1975, 245.

Leonard, A., NASA TM 78579, May 1979.

Leonard, A. Journ. Comp. Physics 37, 1980, 289.

Lewellen, W.S., Symp. on Tornadoes. Lubbock, Texas, June 1976. Texas Tech. Univ., 107.

Lewellen, W.S. and Teske, M.E., Conf. on Severe Local Storms. Am. Meteor. Soc., Omaha, Nebraska, 1977, 291.

Lin, T.C. and Rubin, S.G., Journ. Fluid Mech. 59, 1973, 593.

Long, R.R., Journ. Fluid Mech. 11, 1961, 611.

Lubard, S.C. and Helliwell, W.S., AIAA Journ. 12, 1975, No. 7.

Lugt, H.J., Vortex Flow in Nature and Technology (in German). Braun-Verlag, Karlsruhe 1979a. English edition to be published by Wiley-Interscience in 1982.

Lugt, H.J., Recent Dev. in Theor. and Exp. Fluid Mechanics. Springer 1979b, 309.

Lugt, H.J. and Haussling, H.J., Lecture Notes in Physics 8, Springer 1971, 78.

Lugt, H.J. and Ohring, S., Lecture Notes in Physics 35, Springer 1974, 257.

Macagno, M. and Macagno, E., Phys. Fluids 18, 1975, 1595.

MacCormack, R.W., AGARD Lecture Series No. 94, 1978.

Marshall, F.J. and Deffenbaugh, F.D., NASA CR-2414, June 1974.

Maxworthy, T., Journ. Fluid Mech. 64, 1974, 227.

Mehta, R.D., Shabaka, I.M.M.A., Bradshaw, P., Symp. on Num. and Phys. Aspects of Aerodynamic Flows, Jan. 1981.

Mehta, U., AGARD CP-227, 1977.

Mehta, U. and Lavan, Z., AFOSR Tech. Rep. 73-0640, 1972.

Mehta, U. and Lomax, H., Symp. on Transonic Perspective, NASA-Ames, Feb. 1981.

Mendenhall, M.R., Spangler, S.B., and Perkins, S.C., AIAA paper 79-0026, 1979.

Mokry, M., National Res. Council Canada, NRC No. 17246, Aeron. Rep. LR-596, Nov. 1978.

Mook, D.T. and Maddox, S.A., Journ. Aircraft 11, 1974, 127.

Morgan, W.B. and Parkin, B.R., eds., Intern. Symp. on cavitation inception. ASME 1979.

NASA CP-2032, Feb. 1978.

NASA Workshop on Num. Grid Generation Techniques. Proc. NASA CP-2166, 1980.

NASA Vortex-Lattice Utilization Workshop, NASA SP-405, 1976.

Nielsen, J.N., Missile Aerodynamics. McGraw-Hill 1960.

Nielsen, J.N. and Mendenhall, M.R., Arch. Mech. 30, 1978, 531.

Oh, S.K. and Dean, J.S., David Taylor NSRDC, CND TN-32-71, July 1971.

Orszag, S.A., Studies in Appl. Math. L, 1971, 293.

Orszag, S.A. and Patterson, G.S., Phys. Rev. Letters 28, 1972, 76.

Patankar, S.V. and Spalding, D.B., Intern. Journ. Heat and Mass Transfer 15, 1972, 1787.

Payne, R.B., Journ. Fluid Mech. 4, 1958, 81.

Peake, D.J. and Tobak, M., AGARDograph No. 252, July 1980.

Platzer, G.P. and Souders, W.G., David Taylor NSRDC Rep. 79/051, Aug. 1979.

Powell, A., Noise-Con 75, National Bureau of Standards 1975, 33.

Prandtl, L., Nachr. Kgl. Gesellschaft der Wiss. Göttingen, Math.- phys. Klasse 1918, 451.

Prandtl, L., Über die Entstehung von Wirbeln (1922), see Ges. Abhandlungen, zweiter Teil. Springer 1961, 697.

Prandtl, L., Zeitschrift Flugtechnik und Motorluftschiffahrt 18, 1927, 489 (English transl. Journ. Roy. Aer. Soc. 31, 1927, 718.

Prandtl, L., NACA TM-625, 1929.

Prandtl, L., ZAMM 29, 1949, 8.

Prigogine, I., From being to becoming. Freeman and Co., San Francisco 1980.

Pullin, D.I., Journ. Fluid Mech. 88, 1978, 401.

Raj, P. and Gray, R.B., Journ. Aircraft 15, 1978, 698.

Raj, P. and Iversen, J.D., AIAA Journ. 18, 1980, 865.

Rockwell, D. and Naudascher, E., Ann. Rev. Fluid Mech. 11, 1979, 67.

Rosenhead, L., Proc. Roy. Soc. A134, 1931, 170.

Roshko, A., AIAA Journ. 14, 1976, 1349.

Rubesin, M.W., AGARD Lecture Series No.86, 1977, 3.

Rubin, S.G., Symp. Num. and Phys. Aspects of Aerodyn. Flows, Springer 1981.

Rubin, S.G. and Khosla, P.K., AIAA Journ. 14, 1976, 851.

Saffman, P.G., Studies Appl. Math. 44, 1970, 371.

Saffman, P.G. and Baker, G.R., Ann. Rev. Fluid Mech. 11, 1979, 95.

Sarpkaya, T., Journ. Appl. Mech. 46, 1979, 241.

Sarpkaya, T. and Garrison, C.J., Journ. Appl. Mech. 30, 1963, 16.

Sarpkaya, T. and Shoaff, R.L., AIAA Journ. 17, 1979a, 1193.

Sarpkaya, T. and Shoaff, R.L., Naval Postgraduate School, Monterey, California, Rep. NPS-69-SL 79011, Jan. 1979b.

Saunders, H.E., Hydrodynamics in Ship Design. Vol. III, SNAME 1965.

Schetz, J.A. and Favin, S., Journ. Hydronautics 13, 1979, 46.

Schumann, U., Journ. Comp. Phys. 18, 1975, 376.

Shamroth, S.J. and Briley, W.R., NASA CR 3184, Oct. 1979.

Shamroth, S.J. and Gibeling, H.J., AGARD Specialists Meeting on Boundary Layer Effects on Unsteady Airloads. Sept. 1980.

Shang, J.S., Buning, P.G., Hankey, W.L., and Wirth, M.C., AIAA Journ. 18, 1980, 1073.

Smith, J.H.B., Roy. Aircraft Establishment, TM Aero 1866, 1980.

Steger, J.L. and Kutler, P., AIAA Journ. 15, 1977, 581.

Strickland, J.H., Webster, B.T., and Nguyen, T., Trans. ASME, Journ. Fluids Eng. 101, 1979, 500.

Tagori, T., Proc. 11th Intern. Towing Tank Conf. Tokyo, 1967, 54.

Ta Phuoc Loc, Journ. Fluid Mech. 100, 1980, 111.

Tatinclaux, J.C., Schiffstechnik 17, 1970a, 37.

Tatinclaux, J.C., Journ. Ship Res. 14, 1970b, 84.

Telste, J.G. and Lugt, H.J., David Taylor NSRDC Rep. 80/124, Nov 1980.

Tennekes, H. and Lumley, J.L., A First Course in Turbulence. MIT Press 1972.

Theodorsen, Th., 50 Jahre Grenzschichtforschung, Vieweg 1955, 55.

Thoman, D.C. and Szewczyk, A.A., Univ. Notre Dame Dept. Mech. Eng. Tec. Rep. 66-14, 1966.

Thompson, J.F., Thames, F.C. and Mastin, C.W., Journ. Comp. Phys. 15, 1974, 299.

Thrasher, D.F., Mook, D.T., Kandil, O.A., and Nayfeh, A.H., AIAA paper 77-1157, 1977.

Thrasher, D.F., Mook, D.T., and Nayfeh, A.H., AIAA paper 78-1386, 1978.

Tung, C. and Ting, L., Phys. Fluids 10, 1967, 901.

Vibrans, G., Naval Weapons Lab. Rep. 1794, Nov. 1962.

Wardlaw, A.B., Naval Ordnance Lab. TR 73-209, Oct. 1973.

Wedemeyer, E., Ing.-Archiv 30, 1961, 187.

Wray, A., NASA-Ames 1979.

Wu, J.C., AIAA Journ. 14, 1976, 1042.

Wu, J.C., Sampath, S., and Sankar, N.L., AGARD CP-227, 1977.

Yanenko, N.N. et al., Lecture Notes in Physics 59, Springer 1976, 454.

Yusa, H., Ishii, N., Persson, B., Frydenlund,O., and Holden, K., 13th Symp. on Naval Hydrodynamics, Tokyo, Oct. 1980.

DISCUSSION
of the paper
by H.J. Lugt

NUMERICAL MODELLING OF VORTEX FLOWS IN SHIP HYDRODYNAMICS A REVIEW

Discussion
by D.I. Meiron

While it is true that no rigorous proofs have been offered as to the well-posedness of the classical roll-up problem, there exists a body of calculations which indeed refute this alleged well-posedness. Suspicions about the lack of well posedness were already voiced many years ago by G. Birkhoff in his studies of periodic Kelvin-Helmholtz instability. Recently, D.I. Moor has shown through an asymptotic analysis that after a finite time a curvature singularity (or, at any rate, a singularity in the second derivative of the interface) develops. At this time, the sheet is only slightly inclined about the roll-up point.

Baker, in his assessment of the method of Fink and Soh has not been overly pessimistic. The scheme does indeed give smooth results in problems where chaotic motion results in its absence. However, an analysis by Moor has shown that the redistribution process acts as a smoothing mechanism. Although certain experimental features are reproducible, examples have been offered recently in which unphysical phenomena result when the method is applied. On the other hand it has been shown that in a vortex simulation of the Rayleigh-Taylor instability of fluid into vaccuum, in which the Lagrangian motion of the vortex markers is followed, there appears to be no need to redistribute the vortex markers. The results remain smooth even for late times.

Author's reply

In my paper I have not addressed the question of whether the roll-up of an existing discontinuity line is a well-posed problem of not, although I briefly mentioned Birkhoff and Fisher's paper in which this question is raised. My concern is whether a discontinuity line can be generated at all in a potential flow ; and if it can be generated, what are the initial conditions . For instance, for a flow field due to an abruptly started wedge, governed by the Laplace equation, what are the initial conditions at $t = 0$, especially at the apex, where there is a singularity ? This question is still unanswered. The only attemps at an answer that I know of, is Prandtl's "initial" condition for $t = 0$, that is a self-similar spiral.

The development of numerical approximations of discontinuity lines adds another order of difficulties. The notion of "pessimism" appears justified. Fink and Soh contributed to the stabilization of a row of point vortices with their redistribution procedure. However, the point-vortex method is still plaged with ad-hoc assumptions. For instance, redistribution requires the introduction of a new artificial criterion to cut off a vortex during the shedding process (Sarpkaya and Shoaff). I believe that everybody who works with the engineering application of the point-vortex method will agree that it is a cumbersome art but not mathematical physics.

A DISCRETE VORTEX ANALYSIS OF FLOW ABOUT NONCIRCULAR CYLINDERS

R.L. Shoaff* and C.B. Franks**
David W. Taylor Naval Ship Research and Development Center
Bethesda, Maryland 20084

Abstract

This paper describes the application of the Discrete Vortex Method (DVM) to an impulsively started, uniform, two-dimensional, and separated flow about non-circular cylinders. Body shapes considered are typical of underwater vehicle cross sections and include those that can be transformed to the unit circle by both exact and approximate conformal transformations. The feeding mechanism for introducing circulation into the separated shear layers (represented by point vortices) uses a wake-boundary-layer interaction technique. Rediscretization is used to alleviate instabilities in the point vortex representation of the shear layers. The model also uses a method to account for the effect of viscosity and turbulence in the wake by circulation reduction. Considerations and problems associated with irregularly shaped non-circular cylinders are discussed, especially with respect to the difficulty caused by separation and reattachment of flow at points on the body upstream of the primary separation points. Calculations of the force coefficients are presented for each of the cross sections considered. The sensitivity of the results to the parameters of the analysis is also discussed.

I. Introduction

This paper describes the application and extension of the discrete vortex method (DVM) to the analysis of an impulsively started flow about bluff bodies of general cross section. The objectives are twofold. First, it is desired to extend the capabilities of the DVM to provide a tool by which designers can predict the cross-flow kinematics, drag and lift forces, and moment about cross-sectional shapes of interest to naval hydrodynamicists; and second, to develop a method by which researchers can perform numerical experiments to gain insight into the complex phenomena, not previously investigated, of flow separation about bluff bodies.

The challenge of numerically analyzing the complex phenomena associated with high Reynolds number flows about bluff bodies has encouraged researchers to exploit all viable methods of solution. Limitations of numerical techniques which attempt to solve the full Navier-Stokes equations have led to modeling in an attempt to gain further insight and predictive capability in the analysis of separated flows. Synonymous with modeling, however, is the introduction of assumptions and/or empiricisms based on experimental evidence and heuristic reasoning. Once modeling is resorted to, the assurances that come from demonstrating the convergence, stability, and consistency of the numerical solution of the equations are usually overshadowed by the limitations of the particular assumptions associated with the "model". This is especially true when the model uses a simulation of effects in addition to the solution of an approximate set of governing equations. Thus in order to gain confidence that the results represent the actual phenomenon being modeled, it is necessary to make comparisons with experimental evidence.

The DVM is an excellent example of a phenomenological model that makes extensive use of heuristic reasoning in its hybrid combination of boundary layer and potential flow theories. However, partly because of the inconsistencies that arise from attempting to model viscous effects by potential flow theory, and partly because of the lack of rigorous means to gain the assurances of an accurate analysis discussed above, the DVM has been pursued by a relatively small number of researchers. Although the challenges presented in the use of a potential flow representation of a viscous flow phenomenon are formidable, recent applications of the method have demonstrated a distinct and useful predictive capability. The reader is referred to Clements and Maull [1], Fink and Soh [2], or Clements [3] for extensive reviews of the applications of the DVM. Recent investigations of particular interest to this paper are Shoaff [4], Sarpkaya and Shoaff [5], and Telste and Lugt [6]. Great progress has been made in discrete vortex modeling; however, the fundamental problem remains

*Lieutenant Commander, U.S. Navy
**Aerospace Engineer

how to best account for the effects of viscosity and Reynolds number both on the body and in the wake.

The incompatibility of the potential flow representation of shed vorticity and the viscous phenomenon which generates that vorticity is most pronounced at the separation points. It is here that one must account for the generation of vorticity on the boundary of the body, its diffusion through the boundary layer, its separation, and its eventual representation by discrete vortices, all accomplished in a manner which maintains a mutual cause and effect relationship between the boundary layer and wake calculations. The fact that the separation points are mobile and sensitive to the changing vorticity distribution in the wake illustrates the difficulty of the problem. Furthermore, the arbitrariness of the cross sections considered in this study presents added difficulties in the application of boundary layer considerations in two areas. First, the cross sections being studied may have sharply rounded edges and/or changes in curvature on the upstream face of the body. These configurations generate multiple adverse pressure gradients ahead of the primary separation points and make boundary layer analysis difficult. These areas of adverse pressure gradient may also be sites of separation and reattachment. Second, cross-sectional shapes generated by exact conformal transformations may have sharp edges (mathematical singularities) which also complicate boundary layer considerations.

The effect of viscosity and Reynolds number on the shear layers in the wake is not well understood. Virtually all investigations of vortex strengths in the wake of bluff bodies have noted a deficit between the amount of vorticity shed at the separation points and that contained in the wake. This includes attempts at direct measurements by, among others, Schmidt and Tilman [7], and Bloor and Gerrard [8]. Similar results have been obtained by Schaefer and Eskinazi [9], Griffin [10], and Davies [11] by indirectly estimating vortex strengths based on their longitudinal and transverse spacing in the wake as computed from von Kármán's vortex street model. Estimates of 40 to 70 percent difference in vortex strengths in the wake compared to the amount of vorticity shed from the body have been reported. Although the measurement and estimation techniques are admittedly of limited accuracy, the qualitative results substantiate the observation that viscosity causes a diffusion of vorticity in the wake. Furthermore, the transition to turbulence in the shear layers moves upstream in the wake with increasing Reynolds number. According to Bloor [12], for a circular cylinder this begins at a Reynolds number of about 1000, and by Re=50000 the turbulence has reached the shoulder of the cylinder despite the fact that the boundary layer separating from the cylinder is laminar in this Reynolds number range. The occurrence of turbulence amplifies the effects of viscosity and results in an apparent reduction of vortex strengths. Thus any method that ignores the effect of viscosity and turbulence in the wake neglects an essential feature of the flow being modeled.

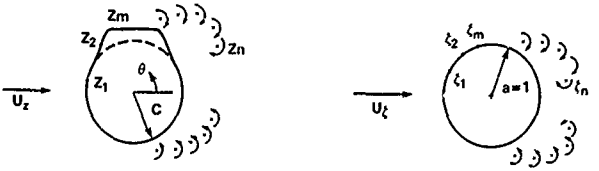
The remainder of this paper describes a comprehensive numerical model developed to investigate the characteristics of an impulsively started, two-dimensional, and uniform flow about non-circular cylinders. The development of the wake and the hydrodynamic forces are investigated from the start of motion to the quasi-steady state (i.e., multiple vortex sheddings). Extensive use is made of the DVM work previously reported by Sarpkaya and Shoaff [5] for the flow about circular cylinders. The extension of the DVM to investigate flow about arbitrary cross sections provides both naval hydrodynamicists and researchers with a useful tool to predict the flow characteristics about bodies of practical interest.

II. Theoretical and Phenomenological Basis of the DVM

The DVM is a potential flow representation of shear layers in which vorticity is confined to restricted subregions of the flow. It has been observed and experimentally verified by Fage and Johansen [13] that, at sufficiently high Reynolds numbers, the shear layers shed from a bluff body are thin and the vorticity is confined to restricted subregions of tightly spiralled vortex sheets. This fact alone suggests the division of the shear layer into small segments and the concentration of the vorticity of each segment into a point vortex. Once this discretization has been performed, the kinematics of the shear layer can be modeled by the motion of the point vortices. This fundamental application, namely the modeling of shear layer kinematics, is the essence of the DVM, the importance of which will become evident later. At this point suffice it to say that it is a basic premise of this paper that the potential flow equations can be used to represent only the kinematics of the wake and the velocity (and thus pressure) distribution on the body. Accounting for vorticity generation (or decay) in the hydrodynamic equations or using these equations directly to determine generation rates are clearly not feasible and give only the illusion of modeling the actual phenomenon.

Numerical Conformal Transformations

The use of the discrete vortex method to study the two-dimensional flow about



Physical Plane Computational Plane

Fig. 1 Transformation between physical and computational (circle) plane.

non-circular cylinders requires a conformal transformation which maps the points on and outside the body under consideration to the points on or outside a circle and vice versa, i.e.,

$$z = f(\zeta) \tag{1a}$$

$$\zeta = g(z) \tag{1b}$$

Figure 1 illustrates the transformation between the physical plane containing a non-circular cross section in a uniform flow of velocity U_z with point vortices in the wake and the corresponding flow about a circular cylinder in the computational (circle) plane. Note that the characteristic dimension in the physical plane is taken as the radius c of a circle inscribed in the cross section. The radius of the circle in the computational plane is unity and thus the uniform flow velocities U_z and U_ζ may be different.

Numerous exact conformal transformations exist which are of interest to naval hydrodynamicists, but most underwater vehicle cross sections of practical concern cannot be exactly transformed. The method utilized here to transform the cross sections with no exact conformal transformation is that of von Kerczek and Tuck [14], a truncated Laurent series expressed as

$$z = \sum_{j=1}^{J} B_j \zeta^{2-j} \tag{2a}$$

$$\zeta = \sum_{j=1}^{J} A_j z^{2-j} \tag{2b}$$

where the A_j's and B_j's are the coefficients of the series to be determined. Given the physical plane cross section shown in Fig. 1a, each of the z_m digitized points on the body can be mapped to the unit circle by

$$\zeta_m = \sum_{j=1}^{J} (\alpha_j + i\beta_j) z_m^{2-j} + R_m + iI_m \tag{3}$$

where R_m and I_m represent, respectively, the real and imaginary parts of the error associated with the truncation of the series to J terms, and the A_j coefficients are expressed in terms of their real and imaginary parts. Since the points in the computational plane are on the unit circle, the left side of Eq. (3) can be represented by $\zeta_m = \cos\theta_m + i \sin\theta_m$. The coefficients of the series can now be determined in a least-squared sense by defining a total error function

$$E_T = \sum_{m=1}^{M} (R_m^2 + I_m^2) \tag{4}$$

and minimizing this function with respect to α_j, β_j, and θ_m. This gives 2J+M unknowns in 2J linear plus M nonlinear simultaneous equations. The method of solution used is that of von Kerczek and Tuck [14] and is not discussed here. It is noted, however, that use of symmetry in the body being transformed can render the coefficients of the series as purely real or purely imaginary, thus simplifying and reducing the number of equations and unknowns. For the work reported here, the number of coefficients J is 13. Furthermore, all shapes have symmetry about one axis and thus the transformation is performed for a half-plane using 50 points to describe the shape. A computer program written by Dawson and Dean [15] was used to solve for the A_j and θ_m values.

Once the coefficients of the approximate g(z) transformation are known, the coefficients of the reverse transformation, f(ζ), can be found either by the expression

$$B_j = \frac{1}{2\pi I} \oint z^{j-1} \zeta dz$$

$$= \frac{1}{2\pi I} \oint z^{j-1} \zeta \frac{dz}{d\zeta} d\zeta \tag{5}$$

or by the same least-squared approach already used. In these calculations the A_j coefficients are determined first (along with the ζ_m's) and the B_j's are then determined using the same θ_m values,

thus reducing the solution of the reverse transformation to 2J linear equations in 2J unknowns. It should be noted that the use of Eq. (5) is algebraically cumbersome for values of J>2.

This method of determining an approximate conformal transformation is not without some restrictions and associated difficulties. For one, the type of bodies that can be successfully transformed is restricted to those having no excessively sharp edges, concave surfaces, or excessive deviation from a "circular" shape. As expected, the suitability of various cross sections to successful transformation is rather subjective. Also, the success of solving for the A_j and B_j values depends on the reasonableness of the body shape and a good first guess of the θ_m values. The second difficulty associated with the numerical transformation is that the finite number of terms in the series gives rise to fluctuating small errors in the velocity calculation along the surface of the body which, as is discussed in detail later, affect the boundary layer calculations.

Cross sections that have exact conformal transformations are also considered. Exact transformations offer the advantage of having no truncation error. However, this advantage must be weighed against the fact that most marine vehicle cross sections do not have an exact transformation; also, those cross sections with sharp corners pose additional problems in the calculation of the velocity distribution near these corners and thus restrict the use of boundary layer analyses. The form of the exact transformations used is presented later.

Potential Flow Model

Before proceeding, it is necessary to develop the hydrodynamic relationships which determine the kinematics and dynamics of the two-dimensional, uniform, incompressible, and inviscid flow about a non-circular cross section in the presence of point vortices. This development depends on the ability to conformally transform the kinematics of the flow in the computational or circle plane to that of the physical plane. Thus the transformations just discussed, either exact or approximate, are essential to this development.

The complex potential function w(z) governing the flow in the physical plane (see Fig. 1) is determined by the point vortex strengths Γ_n, their location in the physical plane z_n, the conformal transformation functions f(ζ) and g(z), and the circle-plane complex potential function w(ζ) for uniform flow past a circular cylinder of unit radius with point vortices located at corresponding $\zeta_n=g(z_n)$ positions, i.e.,

$$w(\zeta) = -U_\infty(\zeta+1/\zeta) + \frac{i}{2\pi}\sum_{n=1}^{N}\Gamma_n[\ell n(\zeta-\zeta_n) - \ell n(\zeta-1/\bar{\zeta}_n)] \qquad (6)$$

The sign convention is such that w'(ζ) gives the negative conjugate of the circle-plane velocity (note that the prime indicates differentiation with respect to the independent variable). Given Eq. (6), the velocity in the physical plane is given by

$$-u+iv = w'(z) = w'(\zeta)\frac{d\zeta}{dz} = w'(\zeta)g'(z) \qquad (7)$$

for non-vortex locations on or outside the body. To determine the velocity of the n-th point vortex, Routh's rule must be applied by subtracting the effect of Γ_n at z_n from the complex potential function and evaluating the derivative of w(z) at the vortex location, i.e.,

$$-u_n+iv_n = \lim_{z\to z_n}\left\{\frac{d}{dz}[w(z) - \frac{i\Gamma_n}{2\pi}\ell n(z-z_n)]\right\} \qquad (8)$$

To express Eq. (8) in terms of w(ζ),

$$w(z) - \frac{i\Gamma_n}{2\pi}\ell n(z-z_n) = w(\zeta) - \frac{i\Gamma_n}{2\pi}\ell n(\zeta-\zeta_n) \qquad (9)$$

or

$$w(z) = w(\zeta) - \frac{i\Gamma_n}{2\pi}\ell n\left(\frac{\zeta-\zeta_n}{z-z_n}\right) \qquad (10)$$

Substitution into Eq. (8) and evaluation of the limit gives

$$-u_n+iv_n = w'(\zeta_n)g'(z_n) + \frac{i\Gamma_n}{4\pi}\begin{cases}-g''(z_n)/g'(z_n)\\ \text{or}\\ f''(\zeta_n)/[f'(\zeta_n)]^2\end{cases} \qquad (11)$$

Substitution of Eq. (6) into Eq. (7) gives the velocity at non-vortex locations in the physical plane as

$$-u+iv = \left\{-U_\zeta(1-1/\zeta^2) + \frac{i}{2\pi}\sum_{n=1}^{N}\Gamma_n\left[\frac{1}{\zeta-\zeta_n} - \frac{1}{\zeta-1/\bar{\zeta}_n}\right]\right\}g'(z) \qquad (12)$$

It is advantageous to work with dimensionless parameters normalized with respect to the geometry and the uniform flow in the physical plane. Since the cross sections considered are of roughly circular shape, the characteristic length scale is chosen to be the radius c of a circle inscribed inside the cross section. The dimensionless form of the equations are obtained by the following change of variables:

$$\tilde{z} = z/c,\ \tilde{\zeta} = \zeta/c,\ \tilde{u}+i\tilde{v} = (u+iv)/U_z,$$

$$\tilde{\Gamma} = \Gamma/U_z c,\ \tilde{w}(\tilde{z}) = w(\tilde{z})/U_z c,$$

$$\tilde{w}(\tilde{\zeta}) = w(\tilde{\zeta})/U_z c,\ \tilde{t} = U_z t/c \qquad (13)$$

Note that U_z and U_ζ are related by the expression

$$U_z = U_\zeta \lim_{z\to\infty} g'(z) = A_1 U_\zeta \qquad (14)$$

Substitution of Eq. (13) into Eqs. (6), (11), and (12), letting $U_z = 1.0$, $c = 1.0$, and dropping the tildes for sake of simplicity, gives

$$w(\zeta) = -U_\zeta(\zeta+1/\zeta) + \frac{i}{2\pi}\sum_{n=1}^{N}\Gamma_n[\ell n(\zeta-\zeta_n) - \ell n(\zeta-1/\bar{\zeta}_n)] \qquad (15)$$

and

$$-u+iv = \left\{U_\zeta(1/\zeta^2-1) + \frac{i}{2\pi}\sum_{n=1}^{N}\Gamma_n\left(\frac{1}{\zeta-\zeta_n} - \frac{1}{\zeta-1/\bar{\zeta}_n}\right)\right\}g'(z) \qquad (16)$$

and

$$-u_n+iv_n = w'(\zeta_n)g'(\zeta_n) + \frac{i\Gamma_n}{4\pi}\begin{cases}-g''(z_n)/g'(z_n) \\ \text{or} \\ f''(\zeta_n)/[f'(\zeta_n)]^2\end{cases} \qquad (17)$$

where u, v, Γ, z, and ζ are now the normalized variables and w the normalized complex potential function. Hereafter, all measures of distance, time, velocity, and circulation are given in terms of these normalized variables unless otherwise stated.

The dynamics of the flow can be determined using the generalized form of Blasius' theorem (Milne-Thompson [16]). The forces and moment are expressed as

$$\overline{F_x+iF_y} = \frac{1}{2} i\rho \oint [w'(z)]^2 dz + i\rho \frac{\partial}{\partial t}\oint w dz$$

$$\hat{M}_z = \mathrm{Re}\left\{-\frac{1}{2}\rho \oint z[w'(z)]^2 dz + \rho \frac{\partial}{\partial t}\oint z w(z) dz\right\} \qquad (18)$$

where F_x and F_y represent, respectively, the drag and lift forces, and $\hat{M}_z$ the moment about the origin. Re refers to the real part of the expression in brackets. Although Eq. (18) can be expressed in terms of w(ζ) and the integration performed in the circle plane, the complexity of the transformation functions used in this study produces an algebraically intractable form. Therefore, the forces are computed by a numerical integration of the unsteady pressure distribution using Bernoulli's equation. For purposes of presenting the force and moment calculations in a normalized form, the following force and moment coefficients are defined:

$$C_D = \frac{F_x}{\rho U_z^2 c},\ C_L = \frac{F_y}{\rho U_z^2 c},\ M_z = \frac{\hat{M}_z}{\rho U_z^2 c} \qquad (19)$$

Vorticity Generation and Introduction

The DVM accounts for the generation and shedding of vorticity by the introduction of a vortex (referred to as a nascent vortex) at every separation point each time step of the analysis. The location of the separation points are either known (e.g., sharp edges) or determined by boundary layer considerations. There is no clear consensus between DVM investigators concerning how nascent vortex strengths should be determined. However, it is generally accepted that the nascent vortex strengths and their introduction positions should satisfy the Kutta condition at each separation point. The various methods used to determine nascent vortex strengths can be divided into three categories. First, the nascent vortex strengths are specified by boundary layer considerations which determine the flux of vorticity from the separating boundary layer into the outer flow; the nascent vortex introduction positions are then computed according

to the Kutta condition. The second approach selects the introduction positions and then determines the nascent vortex strengths necessary to satisfy the Kutta condition. The third method satisfies the Kutta condition and at the same time uses a force free condition on the connecting shear layer (represented by the nascent vortex) to relate the rate of change of circulation and the nascent vortex strength and velocity (see, for example, Fink and Soh [2]). The present study uses the first method.

The use of boundary layer considerations to calculate nascent vortex strengths requires the determination of the separation point locations and the flux of circulation in the separating shear layers. For smooth surfaces, where the location of the separation points are not obvious, a boundary layer separation calculation is performed using the velocity distribution on the body available through Eq. (16). Once the separation points have been determined, the rate of generation of vorticity is easily obtained by

$$\frac{d\Gamma}{dt} = \int_0^{\delta} \frac{\partial u}{\partial y}\, u\, dy \qquad (20)$$

where δ is the boundary layer thickness, u the velocity within the boundary layer, and y the distance along the outward normal. The contribution of $\partial v/\partial x$ is excluded from the vorticity expression in conformity with the approximations of the boundary layer theory. Integration of Eq. (20) to obtain the flux of circulation at a separation point gives

$$\frac{d\Gamma}{dt} = \frac{1}{2} U_s^2 \qquad (21)$$

where U_s is the tangential velocity at the predicted separation point. Ordinarily the circulation flux into the outer flow should be written as

$$\frac{d\Gamma}{dt} = \frac{1}{2} (U_1^2 - U_2^2) \qquad (22)$$

where U_1 and U_2 represent, respectively, the velocities at the outer and inner edges of the separating shear layer. However, extensive experiments with various bluff bodies by Fage and Johansen [13] have shown that U_2 is about 5 percent of U_1 and that the flux of circulation is accurately represented by $U_1^2/2$.

In numerical calculations $d\Gamma/dt$ is replaced by $\Delta\Gamma/\Delta t$ and the strength of the nascent vortex is calculated from

$$\Gamma_{nv} = \frac{1}{2} U_s^2 \Delta t \qquad (23)$$

Once the nascent vortex strengths are computed (one for each separation point), the vortices are introduced radially outward from the circle plane points which correspond to the locations of the physical plane separation. The nascent vortices are simultaneously introduced at distances which produce a stagnation point on the surface of the circle at each separation point.

The particular boundary layer analysis used depends on whether a laminar or turbulent separation criterion is desired. In some cases the high degree of curvature on the body makes the separation points obvious, in these cases a time consuming analysis is unnecessary and the flow is assumed to separate almost immediately after encountering an adverse velocity gradient. The amplitude and frequency of fluctuation of the separation point depends on the severity of the adverse pressure gradient and on the sensitivity of this gradient to the time dependent vorticity distribution in the wake. It should be noted that this combination of potential and viscous flow methods used in discrete vortex modeling cannot establish a one-to-one relationship between the Reynolds number and the flow characteristics. Thus it is the kind of separation criteria used that determines whether the flow is in the subcritical, critical, or turbulent Reynolds number regime.

In the application of boundary layer considerations, one must recognize the characteristics of the time-dependent location of the separation points on the surface of a body in an impulsively started flow and then choose an analysis method that will sufficiently account for those features. The characteristics of boundary layer separation for impulsively started flows are characterized by three regimes, which can be illustrated in the impulsively started flow about a circular cylinder. The flow does not separate immediately upon start because the boundary layer is just beginning to develop. Thus the first regime covers the time from the start of flow until the first occurrence of separation. The location of separation corresponds to the point of maximum adverse pressure gradient (rear stagnation point for circular cylinder) at a relative fluid displacement of (Schlichting [17])

$$t = \left[1 + \frac{4}{3\pi} \left|\frac{dU}{d\lambda}\right|_{max}\right]^{-1} \qquad (24)$$

where $\left|dU/d\lambda\right|_{max}$ is the maximum adverse velocity gradient. For the circular cylinder $\left|dU/d\lambda\right|_{max}=2.0$ (at the rear stagnation point) and thus t=0.351. The second regime begins as the separation point moves rapidly upstream from the point of first occurrence. During this

period there is no noticeable formation of separated shear layers in the wake and the velocity distribution about the body does not change appreciably. Thus the motion of the separation point is due primarily to the further development of the boundary layer. In the third regime, the motion of the separation point slows and the point eventually reaches the general location of its steady state value. This corresponds to the observation of distinct shear layer separation. In this final regime the motion of the separation point is dictated primarily by the changing velocity distribution on the body due to the accumulation of vorticity in the wake. The DVM is applicable only from the point at which distinct shear layer separation occurs. Although one might expect that a fully time dependent boundary layer analysis would be required, Sarpkaya and Shoaff [5] have demonstrated that unsteady and steady treatments of the boundary layer yield essentially identical motions of the separation point. This result was based on a comparison of Schuh's [18] unsteady analysis with Pohlhausen's (see Schlichting [17]) steady treatment for the starting flow about a circular cylinder. Sarpkaya and Shoaff chose the starting time of point vortex introductions as the time given by Eq. (24) plus the time required for the separation point to move from the point of maximum adverse pressure gradient to the point predicted by Pohlhausen's steady method for first separation. This second time delay is computed using Schuh's method. For symmetric cross sections this delay time establishes only the start time for the boundary layer calculations. However, this value takes on added significance for cross sections of irregular shape. In these cases the separation of flow may begin at more than one point and the start time of separation will vary from point to point, depending on the local severity of the adverse velocity gradient. For sharp edges, the flow separates at t=0.0.

The technique used to predict the instantaneous location of the separation points for the bodies considered in the present study is Pohlhausen's method for steady flow. As discussed later, however, highly irregularly shaped bodies may exhibit velocity distributions which are not suitable to analysis by Pohlhausen's method.

A problem not yet discussed is how to account for vorticity generation and introduction at sharp-edged separation points where the singular nature of the sharp edge makes the velocity distribution difficult to compute. Even if the velocity at the sharp edge can be calculated after the Kutta condition is satisfied (as in the case of the flat plate), the velocity distribution near the edge is difficult to obtain accurately. Also, unless the exact transformation function is easily expressed, the determination of the finite velocity at the sharp edge is algebraically intractable. Thus an application of boundary layer considerations similar to the method above has yet to be devised. However, in keeping with the premise that the nascent vortex strength should be determined independently of the choice of introduction position, the only method available is to base the vorticity generation rate on some representative velocity near the separation point. Two methods have been used. Sarpkaya [19] based the nascent vortex strengths on the velocity of the represented shear layer near the separation points. Clements [20] based the nascent vortex strength on the fluid velocity at a fixed point above the separation point; however, he gives no indication of the sensitivity of the results to the choice of the fixed position. The present study used a modification of the former method in which the nascent vortex strength at time t is computed from the velocity of the nascent vortex introduced in the previous time step; that is

$$\Gamma_{nv}(t+\Delta t) = \frac{1}{2}\left[u^2_{nv}(t) + v^2_{nv}(t)\right]\Delta t \quad (25)$$

For the first time step, the nascent vortices are introduced at fixed positions above the sharp-edged separation points. The location of each introduction position is arrived at iteratively to give a smooth transition between the first and subsequent time steps as judged by the continuity of the time variation of the flux of circulation dΓ/dt.

Pohlhausen's method has been used successfully to predict separation for the discrete vortex analysis of flow about circular cylinders [4,5]. However, difficulties can occur when this technique is applied to bodies that require numerical transformations. Most notable is the difficulty associated with the approximate nature of the transformation function which gives rise to an undulation of the velocity profile on the surface of the body. This is illustrated in Fig. 2, where the solid curve indicates the velocity distribution along the lower portion of the cross section shown in Fig. 1a. The undulation of this curve is caused by the inaccuracies associated with the numerical transformation and is not representative of the actual velocity distribution. As expected, the separation prediction technique is somewhat sensitive to these undulations. Accordingly, it is necessary to smooth the velocity profile before performing the boundary layer analysis. The method used for the particular shape illustrated was to least-square fit a polynomial to the velocity distribution. Since the body shape is

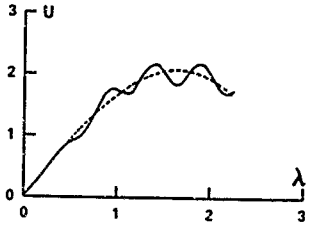


Fig. 2 Velocity profile before and after smoothing.

circular along the lower half, a polynomial of the form used by Hiemenz [21] to represent the velocity distribution about the forebody of a circular cylinder was used, that is

$$U(\lambda) = a_1\lambda + a_2\lambda^3 + a_3\lambda^5 \qquad (26)$$

where λ represents the arc length measured along the body surface from the forward stagnation point. The results of such a curve fit are shown by the dashed line in Fig. 2. Use of this curve fitting technique is restricted. Bodies of irregular shape may have multiple relative extremals in the velocity profile which correspond to changes in curvature on the body. Thus there may be one or more areas of adverse velocity gradient upstream of the point at which primary separation occurs. In some cases there may even be separation and reattachment upstream of the primary separation point. Attempting to remove the undulations in the velocity profile due to the approximate transformation function may also alter details which are representative of the actual flow. Therefore, this technique must be used with caution. Fortunately, for the cross sections considered here the location of the primary separation points is either amenable to boundary layer analysis or is obvious due to their shape and orientation to the flow. There are cases, however, which are clearly beyond present capabilities to handle. Such a case is illustrated in Fig. 3; the separation and reattachment in the areas near points A and A' clearly preclude the use of any available boundary layer prediction techniques in conjunction with the DVM to predict the location of the primary separation points B and B'.

Convection and Rediscretization of Shear Layers

The kinematics of the wake is accounted for by convecting each of the vortices according to its instantaneous velocity computed from Eq. (17), i.e.,

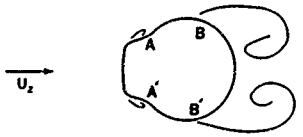


Fig. 3 Separation and reattachment followed by primary separation.

$$z_n(t+\Delta t) = z_n(t) + (u_n(t) + iv_n(t))\Delta t \qquad (27)$$

Although more complex integration methods could be used, Eq. (27) was found satisfactory when used with a sufficiently small time interval. One must bear in mind that nearly 90 percent of the computation time required in discrete vortex modeling is consumed in the computation of vortex velocities. The convection of the nascent vortices is treated as a special case in which their velocities are computed as the velocities at their introduction points prior to the actual placement of the vortices into the flow. The argument here is that the nascent vortices should be convected with velocities commensurate with the U_∞ values used to compute their strengths. Otherwise, the introduction of the nascent vortices alters the flow field in the vicinity of separation with the result that the vortices tend to linger, eventually leading to premature prediction of the separation points.

In order to avoid the logarithmic error in convecting the individual vortices, the discretization of the shear layers must be such that each vortex is located at the center of the segment it is to represent. This fact gave rise to the method of rediscretization or redistribution first proposed by Fink and Soh [2]. Discrete vortex analyses which allow the vortices to move in the form of clouds require special measures to eliminate the vortex-vortex proximity effects; indeed, the clouds result from a combination of the accumulation of logarithmic errors and the frequent necessity to coalesce vortices or use some modified velocity calculations when proximity problems occur. Not to be entirely critical, the use of vortex clouds can yield force coefficients nearly identical to those obtained with the use of rediscretized sheets.

The rediscretization method used in the present analysis is essentially that of Sarpkaya and Shoaff [5] which was used successfully to represent the shear layers emanating and shed from a circular cylinder. The technique is applied

to the vortex distribution in the computational (circle) plane since it is here that the logarithmic error term must be eliminated. The method computes the distribution of circulation along each shear layer, adjusts the vortex locations to ensure even spacing, and then determines a new strength for each vortex along the sheet according to the circulation distribution function. The reader is referred to reference [5] for details.

Vortex Shedding

Vortex shedding is understood as the mechanism whereby the feeding layer (i.e., that emanating from the separation point) is cut, allowing the shed vortex (spiralled sheet) to move downstream and be replaced by a newly developing vortex spiral. This process is illustrated by the sequence of flow pictures shown in Fig. 4. This process occurs alternately

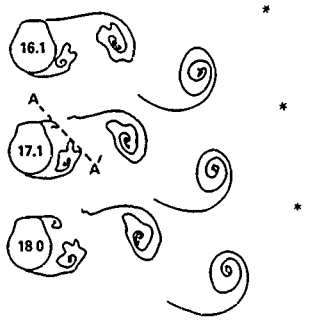


Fig. 4 Vortex shedding process.

from each side of the body in the familiar Kármán vortex shedding pattern. Inherent in the mechanics of making this cut are the questions of where, when and how to accomplish this process in a manner that will preserve the continuity of the flow field development, flux of circulation, motion of the separation point, etc. The method of Sarpkaya and Shoaff [5] uses an argument that is consistent with flow visualization results and heuristic reasoning. The method recognizes that the flux of vorticity at each separation point fluctuates periodically about a non-zero mean and that the occurrence of the minimum within each cycle corresponds to the time at which the connecting shear layer is being stretched by the downstream motion of the spiralled vortex about to be shed. The result of the simultaneous stretching and low introduction rate is to make the connecting shear layer most susceptible to cutting. Accordingly, Sarpkaya and Shoaff cut the sheet when the vorticity flux, $d\Gamma/dt$, was at its minimum value in each vortex shedding cycle. The actual cutting is accomplished by removing a single vortex (for one time step only) from the sheet at a distance of approximately 0.4 from the nascent vortex. This criterion was arrived at through numerous tests and was found to be satisfactory. Figure 4 also shows a coalescenced vortex from a previous cut (represented by the asterisk). This occurs as vortices enter the far wake and is done solely for the purpose of reducing the number of vortices in the flow field in order to reduce the computation time. The vortices in this sheet are coalesced into a single vortex located at the center of vorticity in the circle plane; the strength and position are computed as

$$\Gamma = \sum_{n=1}^{\hat{N}} \Gamma_n$$

$$\zeta = \frac{1}{\Gamma} \sum_{n=1}^{\hat{N}} \Gamma_n \zeta_n \qquad (28)$$

where $\hat{N}$ is the number of vortices in the detached sheet. Comparison with calculations in which detached shear layers were not coalesced showed an insignificant difference in the results, as was also observed by Sarpkaya and Shoaff.

Circulation Reduction

The experimental evidence and heuristic reasoning substantiating the need to account for the action of viscosity and turbulence in the wake have already been introduced. It should be added that the question of how much of the circulation remains in a vortex generated and shed from a body has been a topic of discussion since the time of Prandtl; he suggested that the net remaining circulation of a shed vortex (i.e., one downstream of the formation region) is about 60 percent of that generated. All applications of the DVM have recognized the importance of circulation reduction; however, none have realized reductions of greater than 15 percent without resorting to special techniques. The two circulation reducing mechanisms which are logically incorporated into the DVM are discussed first.

It has been noted by users of the DVM that circulation may be reduced by the removal of vortices that come too close to the surface of the body (and thus their image vortex inside the body). Accordingly, vortices which come closer than a predetermined distance of 0.04 from the surface of the body are annihilated. Experiments by Fage and Johansen [13] have shown that at most a 10 percent reduction is brought about by the

entrainment of fluid bearing circulation oppositely-signed from that of the flow downstream of the separation points. Use of this technique in the DVM shows similar results. Thus this mechanism alone, although necessary and realistic, accounts for only a small portion of the total circulation reduction.

The second mechanism for circulation reduction involves the interaction of oppositely-signed vortices in the wake. The technique is inherently part of the vortex shedding process already discussed. Again Fig. 4 shows that the end of the connecting shear layer cut in the shedding process tends to be drawn, or entrained, into the large, oppositely-signed vortex still attached to the body. Gerrard [22] proposed that the circulation of that portion of the shear layer drawn across the wake eventually becomes part of the attached sheet. A similar idea is employed in the present model by removing any vortices from the portion of the shear layer entrained into the region delineated by the line AA' in Fig. 4. The circulation of these vortices is distributed evenly among the nearby vortices of opposite sign across the wake. The location of the line AA' is chosen to be tangent to the outer spirals of the two connected shear layers. It should be emphasized that this circulation reduction mechanism is not sensitive to the precise location of the line AA'; the same is true for the selection of the 0.04 distance parameter discussed in the previous paragraph.

As noted earlier, the use of circulation reduction mechanisms such as those just described have failed to account for the observed reduction of circulation found by experiments. Furthermore, through inspired hindsight one can conclude that the poor comparison of DVM and experimental results for force coefficients, Strouhal number, separation point locations, etc. is largely due to the poor representation of vortex strengths in the wake. This observation led some researchers [23,24,25 and others] to impose a circulation reduction factor as large as 40 percent in the computation of nascent vortex strengths in order to bring the DVM results into closer agreement with experiments. This method, however, is not consistent with the measurements of shear layer vorticity distribution by Fage and Johansen [13] or observations that the amount of diffusion and dissipation of vortices varies with distance behind the body.

Recognizing the need to include a phenomenologically based circulation reduction mechanism, Sarpkaya and Shoaff [5] devised a heuristic model to reduce individual vortex strengths at each time step of the analysis by a factor (1-p); that is $\Gamma_n(t+\Delta t)=(1-p)\Gamma_n(t)$. The circulation reduction factor p depends on whether the vortex is within or downstream of the formation region in the wake of the body. The argument of Sarpkaya and Shoaff is that the diffusion of vorticity in a shear layer increase along the length of the shear layer, since the vortices nearest the core of the spiral are the oldest and hence most affected by circulation reduction. It is emphasized that this heuristic approach does not model viscous or turbulent diffusion directly but rather models the effect of diffusion which is an apparent reduction of vortex strengths. The parameter p used by Sarpkaya and Shoaff was as follows: p increases linearly from 0 to 0.01 for $t<9$; $p=0.01$ for $t>9$ in the region $0<x<10$; and p decreases from 0.01 to 0 at large distances. The particular form of p for $x>10$ had little or no effect on the results. Numerous variations in the choice of the p-factor in the analysis of flow about a circular cylinder were used by Sarpkaya and Shoaff and led to the following conclusions: i) the effect of using a circulation reduction factor was to bring the predicted values of force coefficients, base pressure coefficient, separation angles, Strouhal number, vortex spacing in the wake, motions of separation and stagnation points, and vortex strengths in the wake into closer agreement with experimentally observed values; ii) the best results were obtained when the p-factor was kept constant within the formation region ($0<x<10$); iii) the results of the model showed varying sensitivity to the magnitude of p, but none were so sensitive as to imply that the particular choice of p was unique; iv) it is possible to adjust the p-factor to bring the numerical predictions into conformity with experimental results; and finally, v) after adjusting the p-factor, the model could be applied to other flow conditions such as the vortex-shedding-induced oscillation of an elastically mounted circular cylinder [4] with good results, thus demonstrating the general applicability of the technique. In view of these conclusions, the same circulation reduction method used by Sarpkaya and Shoaff is applied to the present analysis.

III. Discussion of Results and Sensitivity Analysis

The principles of the DVM discussed here have been applied to study the impulsively started flow about two cross-sectional shapes. Only laminar flow separation (i.e. subcritical Reynolds number regime) is considered. Figures 5 and 6 show the time evolution of the wake for two cylinders, A and B, respectively. The number inside the body indicates the time elapsed from the impulsive start of flow. Drag and lift coefficients for both shapes are shown in Figs. 7 and 8. The particular details associated with each body are

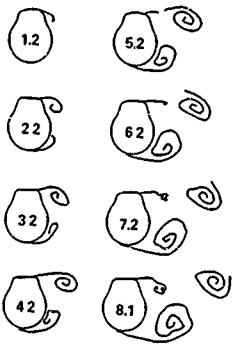


Fig. 5 Evolution of wake for cylinder A.

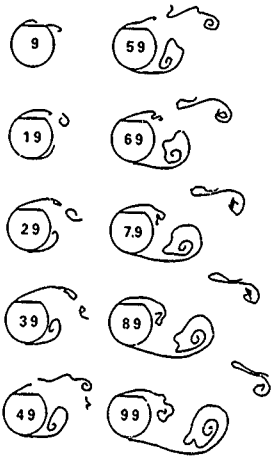


Fig. 6 Evolution of wake for cylinder B.

discussed separately, and a sensitivity analysis is presented at the conclusion of this section.

Cylinder A

Application of Pohlhausen's method to predict separation for this shape was successful only along the lower cylindrical portion. Where the deck joins the cylindrical body, the velocity distribution on the forebody has slight adverse

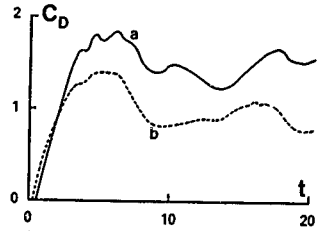


Fig. 7 Drag coefficient versus normalized time: a) cylinder A; b) cylinder B.

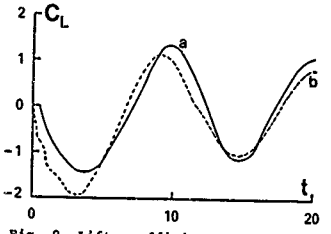


Fig. 8 Lift coefficient versus normalized time: a) cylinder A; b) cylinder B.

pressure gradients which cause Pohlhausen's method to yield an unrealistic prediction of the separation point. Application of Cebeci's [26] more accurate method (also for laminar separation) indicates that the flow does not separate until the rear shoulder; however, Cebeci's method is too time consuming to be used except for a few time steps. Therefore, the separation point was chosen at a location downstream of the point of maximum velocity near the rear shoulder where the velocity is 97 percent of the maximum. This criterion is not as arbitrary as one might expect. For instance, the location of the separation points for the circular cylinder studied by Sarpkaya and Shoaff [5] indicates that the ratio of the separation point velocity, U_s, to the maximum is very nearly 0.97. Furthermore, examination of Hiemenz's [21] experimentally determined velocity profile for a circular cylinder yields nearly the same result. A sensitivity study in which this ratio was varied from 0.95 to 1.0 indicated that the parameters of the analysis (force coefficients, etc.) change by only a few percent. It is concluded that the adverse velocity gradient is sufficiently steep that there is little difference in the location of the 100, 97, and 95 percent

velocity point.

Figure 9 shows the variation of the separation and forward stagnation points with time (angles θ_{sep} and θ_{stag} respectively). Angles are measured positive in the counter-clockwise direction (see Fig. 1) from the real axis. The terms "upper" and "lower" refer to the conditions at the upper and lower separation points on the body. The start times for vortex introduction at the upper and lower separation points are 0.35 and 1.0, respectively. Separation begins earlier at the rear edge of the deck because the adverse pressure gradient is stronger at that location. Figure 10 gives the flux of circulation, $d\Gamma/dt$, for each of the separation points used in the calculation of nascent vortex strengths. A comparison of the variation of each of these parameters to the development in the wake (Fig. 5) illustrates that the nascent vortex introduction method achieves the essential interdependence of the distribution of circulation in the wake and the location and flux of circulation introduction.

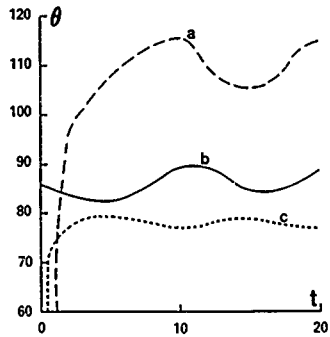


Fig. 9 Variation of forward stagnation angle and separation angles with normalized time for cylinder A: a) $-\theta_{sep}$ (lower); b) $\theta_{stag}-90$; c) θ_{sep} (upper).

Examination of the force coefficients indicates that the drag rises rapidly after the start of flow, reaches a maximum value of approximately 1.8 and then decreases to a mean value of about 1.4. The lift coefficient varies periodically with a period T=10.4. Defining a Strouhal number based on the characteristic diameter 2c as

$$St = \frac{2c}{U_\infty T} \qquad (29)$$

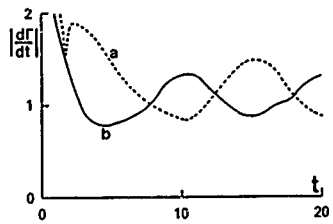


Fig. 10 Flux of circulation versus normalized time for cylinder A: a) lower; b) upper.

gives a value of St=0.19. The fluctuation of the drag for t>10 has a period half that of the lift. Somewhat surprisingly, the calculation of the moment yields a negligibly small value.

Cylinder B

The cross section for the D-cylinder has an exact conformal transformation given by Telste [27] as

$$\zeta = c_7 \frac{\left[c_8 \frac{z+c_2}{c_3 z+c_4}\right]^{\kappa} - c_5}{c_6\left[c_8 \frac{z+c_2}{c_3 z+c_4}\right]^{\kappa} - c_5} \qquad (30)$$

where

$$c_2 = e^{-i\beta}\ ,\quad c_3 = 1 - \frac{2\cos\beta}{i+e^{i\beta}}\ ,$$

$$c_4 = c_2 - i\,\frac{2\cos\beta}{i+e^{i\beta}}\ ,\quad c_5 = e^{-i\kappa\pi}\ ,$$

$$c_6 = e^{-i2\kappa\pi}\ ,\quad c_7 = \frac{i\kappa c_5 \sin\beta}{\sin\kappa\pi}\ ,$$

$$c_8 = e^{-i\alpha}\ ,\quad \kappa = \frac{1}{2-\alpha/\pi}$$

α and β are the angles indicated in Fig. 11 (β=0.9273 radians). Polhausen's

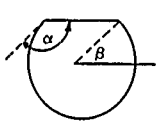


Fig. 11 Cylinder B.

method was used to determine the point of laminar separation on the lower cylindrical section. Use of an exact conformal

transformation obviates the need to smooth the velocity profile. Calculation of flux of circulation from the two sharp edges is based on the nascent vortex velocity introduced in the previous time step (see Eq. (25)). Examination of the circulation introduction rates in Fig. 12 indicates an interesting aspect of the flow about this body. At t=0 the

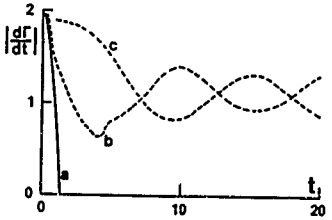


Fig. 12 Flux of circulation versus normalized time for cylinder B: a) upper rear edge; b) upper forward edge; c) lower separation point.

flow begins to separate from the two sharp edges. However, as the shear layer from the leading separation point approaches the rear edge (see Fig. 7), the flux of circulation rapidly drops to zero and remains negligibly small thereafter. For the calculation shown, the introduction of nascent vortices from the rear edge was discontinued when the flux became negligibly small. Without further vortex introduction the shear layer was essentially cut and the shed vortex was allowed to move downstream. Separation from the lower portion of the body began at t=1.0. The motions of the separation point and forward stagnation point are shown in Fig. 13. The flux of circulation for each separation point shown in Fig. 12 shows a definite dependence on the conditions in the wake.

Examination of the force coefficients in Figs. 7 and 8 indicates that the drag reaches a peak value of approximately 1.4 and then falls to its steady-state mean of about 0.8. The large flat area on the top of the cylinder gives rise to a large amplitude lift force with a Strouhal number St≅0.18. The moment for this body also is negligibly small.

Sensitivity Analysis

It is important to examine the sensitivity of the results to the circulation reduction factor and the time step increment, not only to establish the stability of the results, but to elucidate cause and effect relationships. The results already presented used a time step size Δt=0.125 and a circulation reduction factor p identical to that used by Sarpkaya and Shoaff [5] for the flow

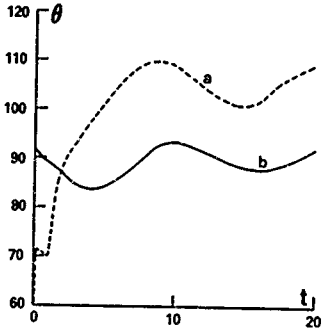


Fig. 13 Variation of separation angle and forward stagnation angle with normalized time: a) $-\theta_{sep}$ (lower); b) θ_{stag} -90.

about a circular cylinder.

The effect of reducing the p-factor is to increase C_D and C_L and to reduce St. The separation points move farther upstream and fluctuate with a larger amplitude. Reducing p to zero (keeping Δt=0.125) produced the following results for cylinder A: the drag attained a mean steady state value of 2.1 and fluctuated with an amplitude of about 0.2; the initial peak (overshoot) in the drag observed for p=0.01 was not present; the steady-state amplitude for the lift coefficient was 1.9; and the Strouhal number was St≅0.16. These results indicate that the circulation reduction causes the vortices in the wake to have reduced strengths and as a result the shedding frequency increases. Conversely, stronger vortex strengths decrease the shedding frequency. The combined effect of reduced vortex strengths and a reduced Strouhal number is to decrease both the amplitude and period of the fluctuations in lift, drag, separation and stagnation angles, etc. The mean value of the drag and the width of the wake also decrease.

Varying the size of the time step Δt from 0.1 to 0.2 produced little variation in the results. The drag coefficient remained essentially unchanged. Decreasing Δt did increase the amplitude of the lift slightly from approximately 1.2 for Δt=0.2 to approximately 1.4 for Δt=0.1. Attempts to reduce the time step further caused the shear layers emanating from the smooth separation points to be convected along the surface of the body and never to form a wake. This problem did not occur for the separation at sharp edges. It is concluded that, when the first and subsequent

nascent vortices are introduced too close to the surface of the body, they never attain a component of velocity normal to the surface sufficient to move the vortices into the wake. Thus there appears to be a lower limit to the time step size that can be used for body shapes that have separation at positions other than sharp edges. This limiting value varies with the degree of surface curvature near the separation point.

IV. Conclusions and Recommendations

Recent advances in discrete vortex modeling have been used in conjunction with numerical and exact conformal transformation functions to study the two-dimensional, separated flow about non-circular cylinders. The DVM approach utilizes shear layer rediscretization, boundary layer considerations for vorticity generation and introduction, and a circulation reduction method to account for the effects of viscosity and turbulence in the wake. The primary difficulty in applying the DVM to non-circular cross sections is related to the limitations of the separation prediction method to handle adverse velocity gradients upstream on the primary separation points. A method has been suggested which can overcome this difficulty in certain cases. It is recommended that an improved method be developed for predicting the location of primary separation about irregularly shaped bodies. It is also recommended that a separation prediction method for turbulent boundary layers be used to extend the applicability of the model to higher Reynolds numbers.

Acknowledgments

This work was jointly supported by the David W. Taylor Naval Ship Research and Development Center Independent Research Program, and the Mathematical Sciences and Hydromechanics Programs of the Naval Sea Systems Command. The authors are grateful to Drs. H. J. Lugt, H. J. Haussling, and Mr. J. G. Telste for their suggestions and assistance in performing this work.

References

1. Clements, R.R. and Maull, D.J., "The Representation of Sheets of Vorticity by Discrete Vortices," Prog. Aerospace Sci., v. 16, pp. 129-146, 1975.

2. Fink, P.T. and Soh, W.K., "Calculation of Vortex Sheets in Unsteady Flow and Applications in Ship Hydrodynamics," Tenth Symp. Naval Hydrodynamics, Cambridge, Mass., 1974.

3. Clements, R.R., "Flow Representation, Including Separated Regions, Using Discrete Vortices," AGARD Lecture Series on Computational Fluid Dynamics, No. 86, 1977.

4. Shoaff, R.L., "A Discrete Vortex Analysis of Flow About Stationary and Transversely Oscillating Circular Cylinders," Ph.D. Thesis, Naval Postgraduate School, Monterey, California, Dec. 1978.

5. Sarpkaya, T. and Shoaff, R.L., "Inviscid Model of Two-Dimensional Vortex Shedding," AIAA, v. 17, pp. 1193-1200, 1979.

6. Telste, J.G. and Lugt, H.J., "Vortex Shedding from Finned Cylinders," Report DTNSRDC-80/124, Nov. 1980.

7. Schmidt, D.V. and Tilmann, P.M., "On the Development of the Circulation in Water of Circular Cylinders," Acustica, v. 27, pp. 14-22, 1972.

8. Bloor, M.S. and Gerrard, J.H., "Measurements of Turbulent Vortices in a Cylinder Wake," Proc. Roy. Soc. A, v. 294, pp. 319-342, 1966.

9. Schaefer, J.W. and Eskinazi, S.W., "An Analysis of the Vortex Street Generated in a Viscous Fluid," J. Fluid Mech., v. 6, pp. 241-260, 1959.

10. Griffin, O.M., "Effects of Synchronized Cylinder Vibration on Vortex Formation and Mean Flow," Flow-Induced Structural Vibrations (ed. Eduard Naudascher), Springer-Verlag, Berlin, 1974.

11. Davies, M.E., "A Comparison of the Wake Structure of a Stationary and Oscillating Bluff Body, Using a Conditional Averaging Technique," J. Fluid Mech., v. 75, pp. 209-231, 1976.

12. Bloor, M.S., "The Transition to Turbulence in the Wake of a Circular Cylinder," J. Fluid Mech., v. 19, pp. 209-304, 1964.

13. Fage, A. and Johansen, F.C., "The Structure of Vortex Sheets," Aeronautical Research Council R and M 1143, 1927.

14. von Kerczek, C. and Tuck, E.O., "The Representation of Ship Hulls by Conformal Mapping Functions," J. Ship Research, pp. 284-298, Dec. 1969.

15. Dawson, C.W. and Dean, J.S., "CMAP: A Program to Conformally Map the Unit Circle onto a Simple Closed Curve," Computation, Mathematics, and Logistics Department, David W. Taylor Naval Ship R&D Center. Unpublished computer program, 1971.

16. Milne-Thomson, L.M., Theoretical Hydrodynamics, 5 ed., MacMillian, 1968.

17. Schlichting, H., Boundary Layer Theory, 6th ed., McGraw-Hill, 1968.

18. Schuh, H., "Unsteady Boundary Layers," Z.f. Flugwiss Heft. 5, pp. 123-131, 1953.

19. Sarpkaya, T., "An Inviscid Model of Two-Dimensional Vortex Shedding for Transient and Asymptotically Steady Separated Flow Over an Inclined Plate," J. Fluid Mech., v. 68, pp. 109-128, 1975.

20. Clements, R.R., An Inviscid Model of Two-Dimensional Vortex Shedding," J. Fluid Mech., v. 57, pp. 321-336, 1973.

21. Hiemenz, K., "Die Grenzschicht an Einem in der Gleichförmigen Flüssigheitsstrom Eingetauchten Geraden Kreiszylinder," Thesis, Göttingen, Dinglers Polytech J., v. 326, p. 32, 1911.

22. Gerrard, J.H., "The Measurement of the Formation Region of Vortices Behind Bluff Bodies," J. Fluid Mech., v. 1, pp. 401-413, 1966.

23. Gerrard, J.H., "Numerical Computation of the Magnitude and Frequency of the Lift on a Circular Cylinder," Philosophical Transaction of the Royal Society of London, v. 261, pp. 137-162, Jan. 1967.

24. Mendenhall, M.R., Spangler, S.B. and Perkins, S.C., "Vortex Shedding from Circular and Noncircular Bodies at High Angles of Attack," AIAA 17th Aerospace Sciences Meeting, New Orleans, LA, Paper No. 79-0026, Jan. 15-17, 1979.

25. Marshall, F.D. and Deffenbaugh, F.D., "Separated Flow Over Bodies of Revolution Using an Unsteady Discrete-Vorticity Cross Wake," NASA CR-2414, June 1974.

26. Cebeci, T., Chang, K.C. and Kaups, K., "A General Method for Calculating Three-Dimensional Laminar and Turbulent Boundary Layers on Ship Hulls," Douglas Aircraft Co., Report No. MDC J7998, Oct. 1978.

27. Telste, J.G., "A Conformal Transformation for a D-Cylinder," Computation, Mathematics, and Logistics Department, David W. Taylor Naval Ship R&D Center. Unpublished report, June 1979.

CALCULATION OF VORTEX-SHEDDING FLOW AROUND OSCILLATING CIRCULAR AND LEWIS-FORM CYLINDERS

Yoshiho Ikeda and Yoji Himeno
University of Osaka Prefecture
Sakai, Osaka

Abstract

Symmetric vortex-shedding flows around swaying circular and Lewis-form cylinders are calculated using a discrete vortex model.

The boundary layer on the body surface is replaced by a discrete vortex at the zero-shear point, where the location is obtained by Schlichting's oscillatory boundary layer theory and the strength is determined using the ordinary boundary layer assumption. The paths of the vortices downstream of the zero-shear point are determined by potential flow theory using a numerical time-step integration. The calculated flow fields are compared with the flow visualization results to show fairly good qualitative agreements. The pressure and the drag force shows an agreement with the experiment in the region of K-C number between 5 and 8, if the wake effect on the determination of the zero-shear point is empirically taken into account.

1. Introduction

For the prediction of the wave forces acting on ships and ocean structures, and for the estimation of their motions, it is important to develope a prediction method for the viscous forces of oscillating bluff bodies with a sufficient accuracy.

The experimental studies have been most common in this field, since the theoretical approach is difficult due to the existence of the flow separation. Keulegan and Carpenter [1] measured the viscous forces acting on a flat plate and circular cylinder submerged in the standing waves, and found that the viscous forces acting on the bluff bodies in an oscillating flow depend mainly on the relative displacement. The rolative displacement defined by them is usually called Keulegan-Carpenter number, namely K-C number. The K-C number is described as $U_{max} \cdot T/D$ (U_{max}; maximum speed, T; period, D; representative length), and becomes $2\pi y_a/D$ (y_a; amplitude of the motion) in the case of harmonically oscillating bodies with constant amplitude. Since then, many experimental studies [2,3,4] in this field have been carried out to confirm the fact. Nowadays, these experimental results for a circular cylinder and a flat plate are used on the practical estimations of the wave forces acting on pile [5] and the roll damping of the bilge keels of ships [6].

Recently, the experiments for the oscillating bluff bodies with various shapes other than a flat plate and a circular cylinder have been carried out by Bearman et al.[7] , Kudo et al. [8] and Tanaka et al.[9]. Tanaka et al.[9] found from their experiments that the drag coefficient of oscillating bluff bodies varies significantly with the slight change of the body shape at low K-C number region. The characteristics of the separation forces of oscillating bluff bodies are, therefore, much complicated.

The theoretical calculation is also one of powerful tools for clearifying the complicated charactaristics of the separated flow associated. Some theoretical works using discrete inviscid vortex model have recently been proposed, most of which treated the oscillating bodies with sharp edge like a flat plate set normal to the flow, or a rectangular cylinder [10,11,12]. There have been, however, a few theoretical works for the bodies with round corner like a circular cylinder or Lewis-form cylinder [13,14] mainly because of the difficulties in resonably determining the location of the vortex-shedding point and the vortex strength. Two ways to this problem can be considered; one is to apply the Kutta assumption or other method to determine the vortex strength at the empirically determined separation point, and another is to use a theoretical prediction formula from viscous-flow theory.

Sawaragi et al.[14] presented a calculation method for a circular cylinder in an oscillating flow using none of experimental informations They determined the location of the separation point using the oscillatory boundary layer theory of Schlichting [15] assuming the zero-shear point coincides with the separation point and the strength of shedding-vortex using ordinary boundary layer assumption in the same way as Sarpkaya [16]. They calculated the flow field, the pressure on the surface, the drag and the lift forces, though they treated only the first swing after the flow started.

Although the calculation method presented here is basically similar to that presented by Sawaragi et al.,soveral improvements are made, i.e., the determination of the separation point, the strength of the vortex and so on. The calculations are carried out in several swings in order to take the wake effect into account.

The application of the method to ship-like sections is important in the field of ship hydrodynamics. The present method for a circular cylinder is easily applicable to the ship-like sections since no empirical information is used. Using the Lewis transformation formula [17], several typical outcomes of the calculation for Lewis-form cylinders are also shown.

2. Calculation procedure

We consider here the case of a two-dimensional circular cylinder in a time-dependent flow instead of the cylinder oscillating in still water. The relative flow patterns with the fixed axis on the cylinder are the same for these two cases. The pressure on the cylinder surface and the force are, however, different due to the existence of the pressure gradient in the time-dependent main flow. Note that the coefficient of the hydrodynamic force proportional to the acceleration of the main-flow acting on a circular cylinder in a time-dependent flow is the twice of that for the oscillating one. We also assume that the flow field around the cylinder is symmetry.

The complex velocity potential w of the flow that there are a two-dimensional circular cylinder of radius R and a number N of vortices located at z_n with strength Γ_n in a time-dependent flow U, is given by

$$w = U(z + \frac{R^2}{z}) + \frac{i}{2\pi}\Big(\sum_{n=1}^{N}\Gamma_n \log(z-z_n) - \sum_{n=1}^{N}\Gamma_n \log(z-\frac{R^2}{z_n}) + \sum_{n=1}^{N}\Gamma_n \log z\Big) \qquad (1)$$

where Γ_n is assigned positive for clockwise circulation.

2.1. Path of vortex

The vortices move with their local velocities, so that the equation of motion of k-th vortex is given by

$$\frac{dx_k}{dt} - i\frac{dy_k}{dt} = u_k - iv_k = \frac{d(w-\frac{i}{2\pi}\Gamma_k \log(z-z_k))}{dz} \qquad (2)$$

where (x_k, y_k) denotes the location of the k-th vortex, and (u_k, v_k) the velocity components there.

As usually, the paths of the vortices are determined through equation (2) by a numerical time-step integration. The Euler formula is used in the present calculation in order to save the computation time.

2.2. Determination of shedding-vortex

In the oscillation problem of a sharp-edged bodies, the determination of the shedding point and strength of the shedding vortex is not so difficult, since we can find the shedding point easily and use Kutta assumption for determining the strength. The problem is, however, more difficult for bluff bodies with round corner like a circular cylinder and ship-like sections. Several researchers have used the empirically determined shedding-point and applied the Kutta assumption there.

Sawaragi et al.[14] applied the Schlichting's oscillatory boundary layer theory for predicting shedding-point and an ordinary boundary-layer assumption for the strength of shedding vortex. We also adopt here a similar method to Sawaragi et al. in order to easily apply the model to other body shapes as well as a circular cylinder without any experimental information.

By the Schlichting's oscillatory boundary layer theory, we can obtain the location of the zero-shear point where the velocity gradient du/dy at the cylinder surface becomes zero. It has been known from recent studies [18] that the zero-shear point does not coincide with the separation point where the vortex sheds from the surface into the outer potential flow in the oscillating case, and that the boundary layer assumption still holds at the zero-shear point. At the zero-shear point, the following expression is given by the Schlichting's theory,

$$-\frac{1}{\omega}\frac{dU_{ms}(\theta)}{dx} = -\frac{\sqrt{2}\sin(\omega t + \pi/4)}{\{(\sqrt{2}-1)\sin(2\omega t + \pi/4)-0.5\}} \qquad (3)$$

where $U_{ms}(\theta)$ denotes the amplitude of fluid velocity at the outer edge of the boundary layer at the zero-shear point, x the coordinate along the cylinder surface, the origin of which is located at the front stagnation point. Using equation(3) we can get the location of the zero-shear point for any arbitary cylinder. In the case of a circular cylinder, equation(3) takes the form,

$$\frac{K-C}{\pi}\cos\theta_s = -\frac{\sqrt{2}\sin(\omega t + \pi/4)}{2\{(\sqrt{2}-1)\sin(2\omega t + \pi/4)-0.5\}} \qquad (4)$$

where θ_s denotes the location angle of the zero-shear point from the rear stagnation point. The location of the zero-shear point at the moment of a certain time-phase ωt depends only on K-C number. The zero-shear point appears firstly at the rear stagnation point and then moves upstream. It reaches the mid beam of the circular cylinder ,where the velocity gradient $dU_{ms}(\theta)/dx$ is equal to zero, at the moment $\omega t = 3\pi/4$.

We can replace the boundary layer by a discrete vortex at the zero-shear point, and assume that the generated vortex keeps the strength constant since the wall shear stress is small downstream of the zero-shear point compared with that in upstream. The distance of the replaced vortex from the surface at the zero-shear point is assumed to be half of the boundary layer thickness. In the present calculation, the boundary layer thickness δ is assumed as $\delta = 4.61\sqrt{2\nu/\omega}$, which is determined as the velocity decrease in the boundary layer is 1% of the outer flow by the Stokes' solution for an oscillating flat plate [15].

The strength Γ of the vortex at the zero-shear point is a function of both time t and location s. Then Γ can be expressed as

$$d\Gamma = \frac{\partial\Gamma}{\partial t}dt + \frac{\partial\Gamma}{\partial s}ds \qquad (5)$$

Using the ordinary boundary layer assumption, equation(5) becomes to

$$\Delta\Gamma = -\frac{1}{2}(U(\theta_s))^2 \Delta t + U(\theta_s) R \Delta\theta \qquad (6)$$

where $U(\theta_s)$ denotes the velocity outside of the boundary layer at the zero-shear point and $\Delta\theta$ is the displacement of the location angle of the zero-shear point during the time increment Δt. If the zero-shear point does not move, as in the steady case, the second term vanishes.

Note that the pressure is impressed on the boundary layer by the outer flow at the zero-shear point since the boundary layer assumption still holds there and even downstream to the separation point. In other words, the pressure can be calculated by the potential flow theory excluding the vortices in the boundary layer.

2.3. Separation

In the present calculation, the vortex generated at the zero shear point moves downstream along the surface like a boundary layer as seen in the flow pattern at $\omega t=\pi/3$ shown in Figure 2. The separation takes place when the ratio of the vertical velocity to the horizontal one is of the order unity. The numerical value of the ratio for the separation criterion is assumed to be 0.3 in the present calculation. According to the recent studies on the unsteady separation [19], the ratio increases rapidly to the infinity near the separation point. Therefore, it can be safely said that the calculation results is not much affected by the slight change of the numerical value of the ratio.

2.4. Assumption of vortex diffusion

In the real fluid, the vortex gradually diffuses with time. Several authors took into account this effect on their inviscid vortex models [20]. In the present calculation, the circumferential velocity v_θ for the isolated viscous vortex described in the paper of J.W.Schaefer et al. [23] is also used.

$$v_\theta = \frac{\Gamma}{2\pi r} = \frac{\Gamma_0}{2\pi r}\{1 - \exp(-r^2/(4\nu(t-t_0)))\} \qquad (7)$$

The circumferential velocity v_θ shown in Figure 1 has a maximum at $r=r^*$, and the value r^* increases with time. In the inner region of r^*, the effect of viscosity is dominant. In the present calculation, the initial time t_0 in equation(7) is determined when it is created at the zero-shear point, with r^* equal to 0.5δ.

Using the present vortex model, we can avoid the infinite induced velocity in case when vortices get too close each other or to the surface. In the real fluid, a vortex close to the body surface loses its energy creating a boundary layer on the surface. In order to take into account this effect, we neglect the vortex within the distance r^* from the body surface.

2.5. Pressure

The pressure $p(\theta)$ on the cylinder surface can be obtained by the following pressure equation.

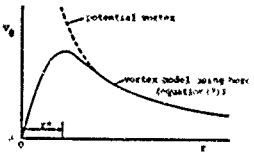


Fig.1 Peripheral velocity of isolated vortex model.

$$p(\theta) = -\rho\frac{\partial\phi}{\partial t} - \frac{1}{2}\rho U(\theta)^2\Big|_{at\ the\ surface} \qquad (8)$$

where ϕ is the velocity potential and $U(\theta)$ the velocity on the surface. The first term of equation(8) for a circular cylinder can be expressed as the form using equation(1),

$$-\rho\frac{\partial\phi}{\partial t} = -\rho\cdot real[z\frac{\partial U}{\partial t}R\cos\theta - \frac{i}{2\pi}\sum_{n=1}^{N}\Gamma_n\frac{u_n+iv_n}{z-z_n}$$

$$-\frac{i}{2\pi}\sum_{n=1}^{N}\Gamma_n\frac{R^2}{(z\bar{z}_n-R^2)\bar{z}_n}(u_n-iv_n)$$

$$+\frac{i}{2\pi}\sum_{n=1}^{N}\frac{\partial\Gamma_n}{\partial t}[\log(z-z_n)-\log(z-\frac{R^2}{\bar{z}_n})+\log z]] \qquad (9)$$

Since the vortex strength is assumed to be constant after the generation at the zero-shear point, the last term, which is proportional to $\partial\Gamma_n/\partial t$, is zero except at the moment of the generation. As mentioned above, the pressure is impressed on the boundary layer by the outer flow since the boundary layer assumption still holds at the zero-shear point. Then we may neglect the last term.

From a different viewpoint, it is possible to consider to take into account the term $\partial\Gamma_n/\partial t$ at the separation point where the vortex sheds into the outer potential flow. In the present calculation, the two methods for the pressure calculation are used, one excludes the last term of equation(9), and the other includes the term at the separation point.

2.6. Drag force

The lift force does not yield because we treat only the symmetrical flow in the present calculation. The drag force acting on the cylinder can be obtained by integrating the pressure over the surface. It can also be obtained more easily by using the time-dependent Blasius theorem or from the time-derivative of the total impulse [21].

$$F_D = \rho\sum_{n=1}^{N}\Gamma_n(v_n-v_{ni}) + \rho\sum_{n=1}^{N}\frac{\partial\Gamma_n}{\partial t}(y_n-y_{ni}) + 2\rho\pi R^2\frac{\partial U}{\partial t} \qquad (10)$$

where (x_n, y_n) denotes the location of the real vortex, (x_{ni}, y_{ni}) the location of the image vortex, (u_n, v_n) the velocity of the real vortex

at (x_n,y_n), and (u_{nI},v_{nI}) the velocity of the image vortex at (x_{nI},y_{nI}). The third term is derived from the potential flow theory without vortex, and is equal to $\rho\pi R^2(\partial U/\partial t)$ for a oscillating circular cylinder. The second term can be neglected with the same reason as the pressure mentioned above. Note that the drag obtained by integrating the pressure over the surface is slightly different from the one obtained by equation(10) since the induced vortex velocity is determined as equation(7) in the present calculation.

3. Calculation results

The calculation results of flow pattern around a circular cylinder in periodic flow at K-C number = 9 are shown in Figure 2. The circles in the figure denote the vortices with clockwise circulation, and the crosses those of opposite sign. The flow begins to move at $t=0$, with the velocity $U=U_m\sin(\omega t)$. According to the Schlichting's theory, the zero-shear point appears at the rear stagnation point at $\omega t=0.85$rad in this case, and then moves upstream. As seen from the flow pattern of $\omega t=\pi/3$ in Figure 2, the vortices form a line along the surface like a boundary layer, gradually roll up, and finally they form a lump of the separation region. Since the main flow velocity is small at the last stage of the first swing, the vortices gradually move toward upstream by the induced velocity of the image vortices. At $\omega t=5\pi/4$ after the reverse turn, the vortex lump created during the first swing moves downstream rapidly due to the main-flow in addition to the induced velocity of the image vortices and the real ones in the other side. At $\omega t=3\pi/2$, the vortex lump of the first swing lies far from the cylinder and the vortices with anticlockwise circulation create a new vortex lump behind the cylinder. At $\omega t=5\pi/2$ of the third swing, the first-swing vortex lump lies in the left of the cylinder about three times of the diameter, the second-swing vortex lump is in the right of the cylinder, and the new vortex lump created by the third swing is formed near the cylinder.

The strength of the vortices created in the second swing is greater than those created in the first swing as shown in Figure 3. This is caused by the wake effect of the vortices of the previous swing. The strength of the third-swing vortices is almost the same as those in the second swing.

Figure 4 shows the calculated pressure distributions on the cylinder surface for the same condition as the flow field calculations shown in Figure 2. The pressure coefficient C_p is defined as the amount of the pressure $p(\theta)$ obtained by equation(8) devided by $\rho U_m^2/2$. The black circles in the figure denote the pressure excluding the last term of equation(9) and the white circles denote that including the term $\partial\Gamma_n/\partial t$ at the separation point. The solid line shows the pressure distribution by the potential flow theory without vortex. Note that the pressure shown in Figure 4 is of the case for a

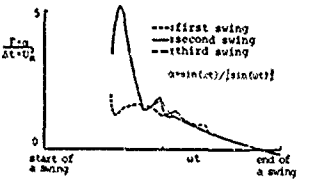


Fig.3 Strength of vortex generated at zero-shear point.

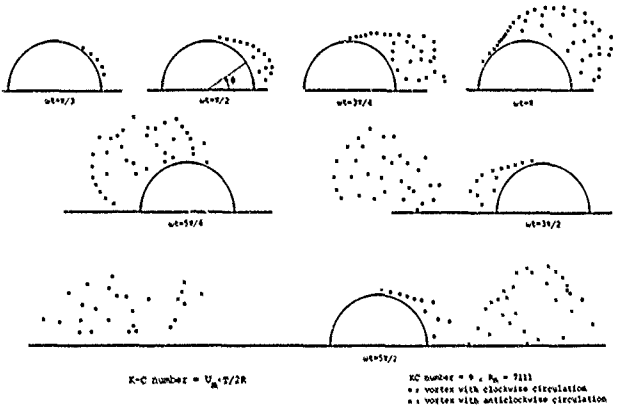


Fig.2 Calculated flow field around circular cylinder.

circular cylinder in a periodic flow, so that the pressure is different from that of an oscillating case by the amount $-\rho(dU/dt)R\cos(\theta)$. As seen from the result at $\omega t=\pi/2$, the pressure is nearly uniform over a large part of the rear of the cylinder like the case of steady flow. However, there is a slight negative peak near $\theta=30$ degree, and the peak becomes more recognizable at the moment of maximum flow velocity in the second and the third swing, $\omega t=3\pi/2$ and $\omega t=5\pi/2$. The pressure included the last term of equation(9) at the separation point has an abrupt discontinuity at the separation point as mentioned by several authors [14,21]. This discontinuity is due to the discrete vortex model. Sarpkaya [21] avoided the discrepancy by replacing the shear layers by a combination of ideal vortices and an infinite number of vortex sheets.

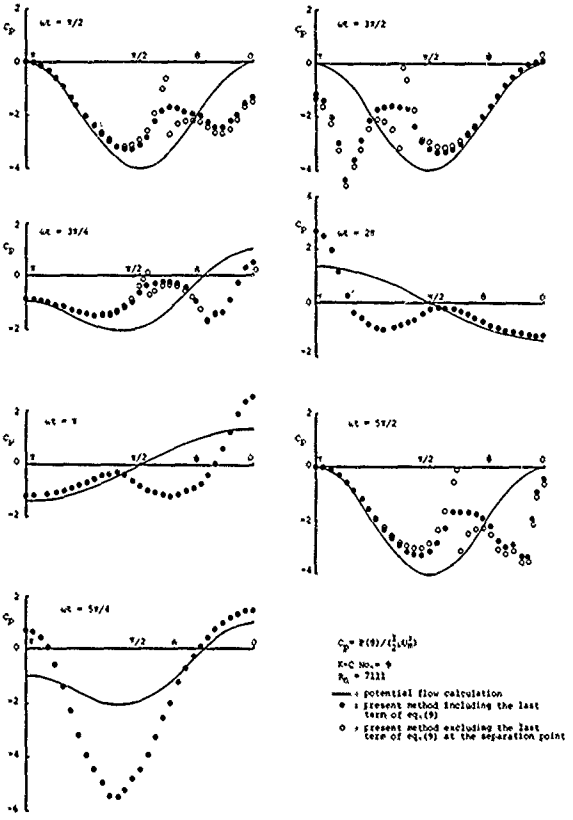


Fig.4 Calculated pressure distribution on circular cylinder in oscillating flow.

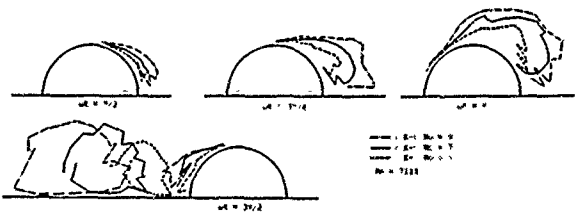


Fig.5 K-C number effect on calculated flow field around oscillating circular cylinder.

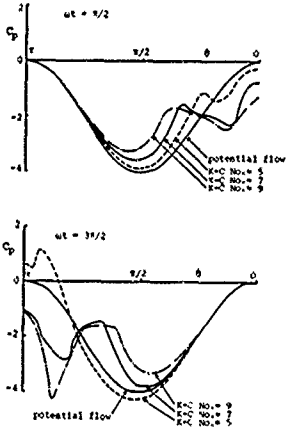


Fig.6 K-C number effect on surface pressure distribution for circular cylinder.

The flow field at different Keulegan-Carpenter number is shown in Figure 5. The scale of the vortex lump behind the circular cylinder is greater with the increase of K-C number, and the vortex lump created during the first swing separates far away with K-C number at ωt=3π/2. The pressure of the rear of the cylinder decreases with the increase of K-C number as seen from Figure 6.

Figure 7 shows the Reynolds number effect on the flow field. In the present calculation, the Reynolds number effect is caused by the difference of the initial location of the vortex at the zero-shear point and by the induced velocity decrement in the vortex core as described in chapter 2.3.. From Figure 7, it is found that the Reynolds number effect is not so large compared with the K-C number effect, and the tendency coincides with the experimental results.

An example of calculated drag forces is shown in Figure 8. The drag coefficient C_D and the inertia coefficient C_M can be obtained using following definitions with the calculated forces as in Figure 8.

$$C_D = -\frac{3}{4} \int_0^{2\pi} \frac{F_D \cos(\omega t)\, d(\omega t)}{\rho U_m^2 D} \qquad (11)$$

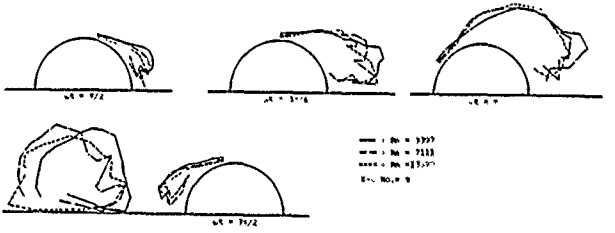


Fig.7 Reynolds number effect on calculated flow field around oscillating circular cylinder.

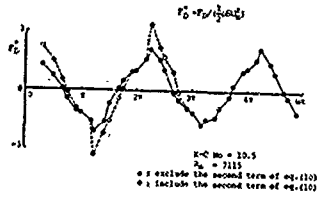


Fig.8 Calculated time history of drag force.

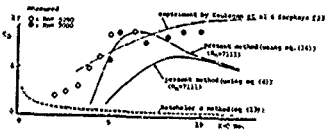


Fig.9 Drag coefficient of oscillating circular cylinder.

$$C_M = \frac{2}{\pi^3} \frac{U_m T}{D} \int_0^{2\pi} \frac{F_D \sin(\omega t)\, d(\omega t)}{\rho U_m^2 D} \qquad (12)$$

In the calculation of drag coefficient, the second term related with $\partial \Gamma_n / \partial t$ is neglected. The calculated drag coefficient is shown by a solid line in Figure 9. Though there is a similar tendency to the experiment, the calculated value is much lower than the experiment. The broken line in the figure represents the non-separation viscous drag force calculated by the Bachelor's method [22] which is described as follows,

$$C_D = 4\pi \left(\frac{\pi}{R_n \cdot K\text{-}C} \right)^{\frac{1}{2}} \qquad (13)$$

As seen from the figure, the non-separation drag force is much lower than the separation drag in the K-C number region above 4, and can be negligible at present discussion.

4. Improvement of the method

Although the calculated flow field is similar to the experimental ones, the calculated drag coefficient shown in Figure 9 has qualitative and quantitative disagreement with the experiments. For example, the calculated value seems to be have a maximum at lower K-C number region, and is lower than the experimental one in the whole range of K-C number.

On considering the reasons for these disagreements, it can be noted that two effects have not been taken into account in the present calculation. Firstly, the flow field is assumed to be symmetry, though the real flow is asymmetry at the K-C number above 8. For solving the former disagreement, it is necessary to calculate asymmetric vortex flow at the K-C number above 8. Secondly, no effect of the vortex wake of the former swing is taken into account on determination of the zero-shear point. As seen from Figure 2, there is a vortex lump created during the first swing near the cylinder on the early stage of the next swing to affect the location of the zero-shear point. It is, however, difficult to consider this effect exactly on the determination of the location of the zero-shear point.

Instead, we try to take into account the effect of the wake of the former swing in following simple method of the phase modification. The velocity measurement around an oscillating circular cylinder suggests that the wake effect due to the vortex lump created during the former swing can be considered as if the outer flow had the phase advance against the main sinusoidal flow. Figure 10 shows the results of the velocity measurements at the side top ($\theta = \pi/2$) of the oscillating circular cylinder. From this figure, the phase advance just outer edge of the boundary layer is about $\pi/8$ due to the wake effect. In Figure 11, the separation point obtained from the results of flow visualization for an oscillating circular cylinder are shown together with the zero-shear points by Schlichting's theory. It is a contradiction that the zero-shear point is located downstream of the separation point, because the zero-shear point occures earlier than the flow separation.

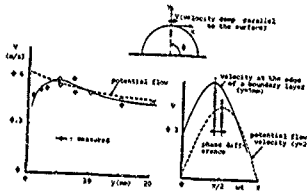


Fig.10 Experimental results of velocity distribution at the side top of an oscillating circular cylinder.

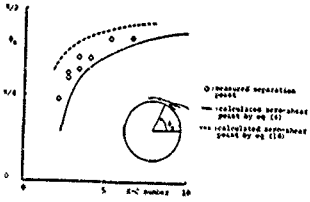


Fig.11 Location of separation point and zero-shear point.

On the basis of the experimental results shown in Figure 11, we assume that the phase advance of the outer flow is $\pi/8$. Then the equation for the zero-shear point takes the form,

$$-\frac{1}{\omega}\frac{dU_{\infty s}(\theta)}{dx} = -\frac{\sqrt{2}\sin(\omega t + 3\pi/8)}{(\sqrt{2}-1)\sin(2\omega t + \pi/2) - 0.5} \quad (14)$$

The zero-shear point obtained by equation(14) is also shown in Figure 11 by a broken line and located a little upstream of the measured separation point.

The calculation results of the drag coefficient using equation(14) on the determination of the zero-shear point shown in Figure 9 show better agreement with the experimental ones in the region of K-C number between 5 and 8. The calculation results tend to zero at nearly K-C=4, and the discrete vortex model may not be suitable in the low K-C number region under 4. In the region, the separated flow reattachs on the body surface to form a thin separation bubble as many flow visualization results show. If the separation bubble should be replaced by discrete vortices like the present method, the calculated surface pressure would rise because of the velocity reduction on the surface due to the vortex induced velocity and then the negative drag force would act on the body. It is one of the remaining problem how to theoretically obtain the drag force in such low K-C number region.

Figure 12 shows the comparison between the calculated and the measured Reynolds number effect on the drag force of a oscillating circular cylinder. The agreement is fairly good in the region of Reynolds number above 5000. At low Reynolds number under 5000, the experimental results are higher than the calculation. The disagreement may be resonable because the discrete invisid vortex model is meaningful at the high Reynolds number where the viscous effect is restricted in the thin region. In the present calculation, the initial location of the replaced vortex becomes too far from the surface in such a low Reynolds number.

The calculated inertia coefficient C_M shown in Figure 12 is also in good agreement with the experiment at K-C number under 7. The disagreement at K-C number above 8 may be caused by the difference of flow pattern between the calculation and the experiment as well as the case of drag coefficient.

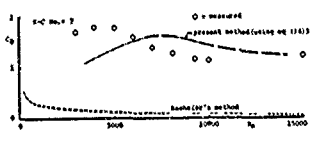


Fig.12 Reynolds number effect on drag coefficient for oscillating circular cylinder.

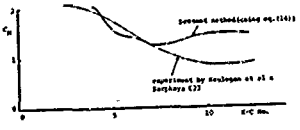


Fig.13 Inertia coefficient of circular cylinder in oscillating flow.

5. Application to Lewis-form cylinder

The present calculation model is easily applicable to ship-like sections using Lewis transformation. In this chapter, several examples of calculation of flow field around the oscillating Lewis-form cylinders are presented.

The mapping function of Lewis form can be represented as follows,

$$\frac{z}{M} = \zeta + \frac{a_1}{\zeta} + \frac{a_3}{\zeta^3} \quad (15)$$

$$z = x + iy$$
$$\zeta = \xi + i\eta$$

The coefficient a_1 and a_3 are the functions of the section shape, and M a magnification factor. This function transforms a unit circle in ζ-plane to the ship-like section in z-plane.
The equation of vortex motion at ζ-plane can be obtained from equation(1) and (15),

$$\frac{d\bar{\zeta}_k}{dt} - \frac{d\eta_k}{dt} = \frac{d(w - i\Gamma_k \log(\zeta - \zeta_k)/2\pi)}{d\zeta}\left|\frac{d\zeta}{dz}\right|^2 \quad (16)$$

where (ξ_k, η_k) denotes the coordinate of the k-th vortex in ζ-plane. We can get the instantaneous location of each vortex at the real plane using the mapping function of equation(15). In the same manner as the circular cylinder case, the location of the zero-shear point can be given by Schlichting's theory using the velocity distribution over the real section, and the strength of the vortex can be also be determined. For sake of simplicity, the vortex is here assumed to be a potential vortex, although a more sophisticated vortex has been used in the case of a circular cylinder.

Figure 14 is an example of the calculated flow field for a swaying bow-section (H_0(=half beam/draft)=0.33 and σ(=sectional area/beam x draft)=0.75) at K-C number 1.67. The zero-shear point for such a shape located at the side edge and hardly moves. In the first swing, the vortices form a large vortex lump behind the cylinder. At $\omega t = 3\pi/2$, the newly created vortex lump does not roll up round in good order like those in the first swing because the vortex lump created during the first swing is still located near the cylinder. As seen from the figure at $\omega t = 2\pi$, the vortices generated during the second swing are

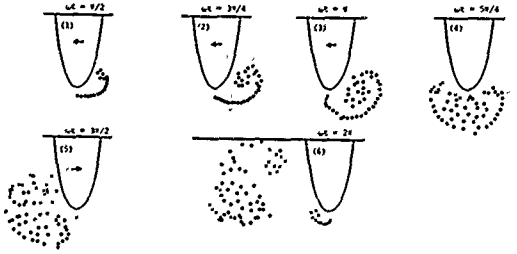


Fig.14 Calculated flow field around swaying bow-section cylinder(H_0=0.33, σ=0.75, K-C No.=1.67)

devided into two parts, and one of them moves downstream with the vortex lump created in the first swing due to its strong induced velocity.

The flow field for a swaying midship section at K-C number=2.1 is shown in Figure 15. For this section, there are two zero-shear points, and the downstream one appears firstly because the flow acceleration is greater there than that at the upstream one. At $\omega t=\pi/2$, the vortices are generated only at the downstream bilge. At $\omega t=3\pi/4$, the downstream vortices form a vortex lump, while the upstream vortices do not grow up. At $\omega t=5\pi/4$ after the reverse turn, the vortex lump moves towards downstream gradually. The vortex lump remains at the bottom even at $\omega t=3\pi/2$ and $7\pi/4$, affecting the new vortex generation and the growth. It is one of the problem how to take into account the damping of the strength of the vortex which remains near the body surface.

The flow field around the oscillating flat plate at K-C number=2 is shown in Figure 16. In the first swing, the vortices form a spiral vortex lump behind the plate, while in the second swing, the vortices do not form such a spiral lump in the same way as the case of the bow section shown in Figure 14.

The results of flow visualizations performed to check the calculations for Lewis-form cylinders are also shown in Figs. 17 thru 19. The cylinders are swaying in a small water tank by means of a forced oscillating mechanism. The oil particles with unit density in the tank are illuminated by a lamp through a slit. Particle tracks are taken by camera fixed to the cylinder with a relative long exposure of 1/15 sec..

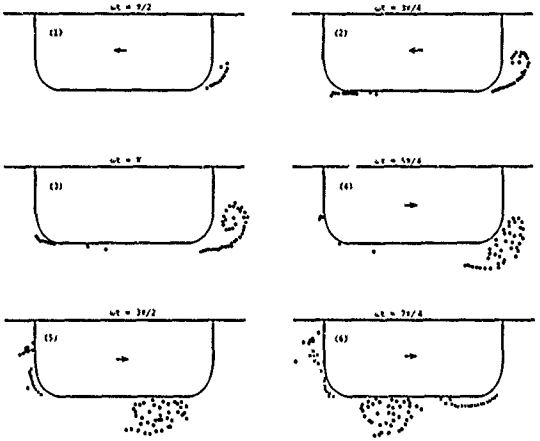


Fig.15 Calculated flow field around swaying midship-section cylinder(H_0=1.25, σ=0.97, K-C No.=2.1).

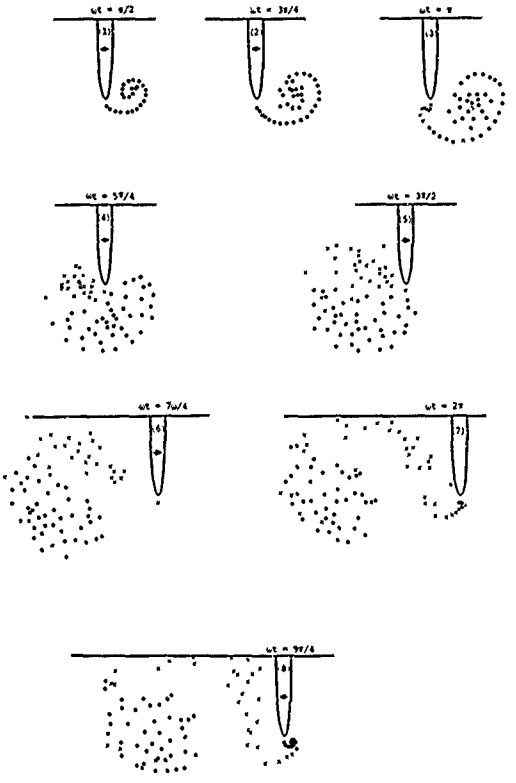


Fig.16 Calculated flow field around swaying flat plate(H_0=0.1, σ=0.85, K-C No.=2).

The ship-like section shown in Figure 17 is the SS 9 section of a container ship, and has the same H_0 and σ values as the Lewis-form cylinder shown in Figure 14. The cylinder shown in Figure 18 is also the midship section of the same ship corresponding to the Lewis-form cylinder shown in Figure 15. As seen from these figures, the vortices at the moment of maximum cylinder speed spread like a thin bubble on the cylinder surface. In the decreasing stage of the motion, the vortices roll up into a large-scale vortex lump. These experimental results agree qualitatively with the calculation results shown in Figures 14 and 15.

Figure 19 shows the results for a swaying flat

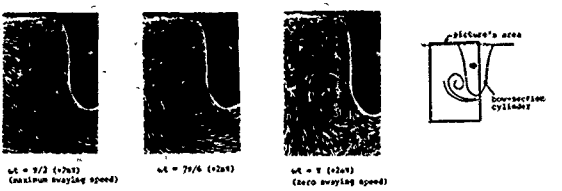


Fig.17 Flow visualization results around swaying bow-section cylinder(K-C number=1.67).

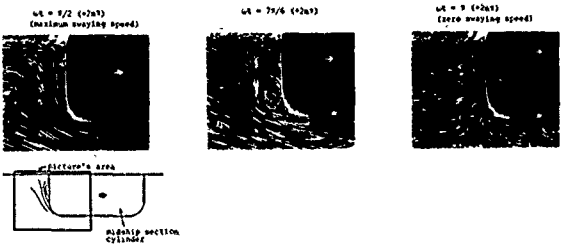


Fig.18 Flow visualization results around swaying midship-section cylinder(K-C number=2.1)

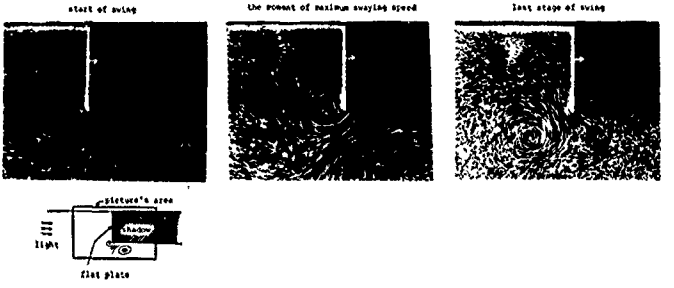


Fig.19 Flow visualization results around swaying flat plate(K-C number=0.62).

plate. A black shade in the right side of the photographs is a shadow of the plate because of using single slit lamp. The photographs show that the former vortex lump forms a vortex pair with the new vortex, and moves downstream gradually. The behavior of the vortices is similar to the calculated one shown in Figure 16.

6. Conclusions

In this paper, computation of the symmetrical vortex-shedding flows around swaying two-dimensional cylinders are made using a discrete vortex model. The results of the study can be summarized as the following items.

1) The calculated flow field by the present method is in fairly good qualitative agreement with the experiment.
2) The calculated forces acting on a circular cylinder show a similar tendency to the experiment though the values are lower than the experiment. When taking account the wake effect on the determination of the zero-shear point, the calculated forces are improved to show fairly good agreement with the experiment in the region of K-C number between 5 and 8.
3) It is necessary to treat asymmetric flow at K-C number above 8.
4) The vortices created during the previous swing significantly affect on the generation, the strength and the behavior of the new vortices.
5) The present method can easily be applicable to the ship-like sections using Lewis transform method, so that it would be useful for the prediction of the viscous effect on the ship motions and maneuvering.

The authors would like to thank Professor Norio Tanaka and Professor Toshio Hishida for their encouragements, and wish to thank Mr.Kenji Higashida and Mr.Yasuhiro Kashiwa, students of University of Osaka Prefecture, for their help on the numerical calculation and experiments. The computors FACOM M-200 and ACOS-600 at the computer center of Kyoto University and University of Osaka Prefecture were used for the numerical calculation.

References

1] G.H.Keulegan and L.H.Carpenter : Forces on Cylinders and Plates in an Oscillating Fluid, Journal of Research of the National Bureau of Standard, Vol.60, No.5, 1958
2] T.Sarpkaya : Periodic Flow About Bluff Bodies Part 1. Forces on Cylinders and Spheres in a sinusoidally Oscillating Fluid, Naval Postgraduate School Report, No.NPS-59, 1971
3] C.C.Shih and H.J.Buchanan : The drag on oscillating flat plates in liquids at low Reynolds number, Jour. of Fluid Mechanics, Vol.48 Part 2, 1971
4] A.Paapo and H.N.C.Breusers : The Influence of Pile Dimension on Forces Exerted by Waves, Proc. Tenth Conf. Coastal Engineering, Vol.2, ASCE, 1969
5] T.L.Shaw(Editor) : Mechanics of Wave-Induced Forces on Cylinders , Pitman Advanced Publishing Program, 1979
6] Y.Ikeda, Y.Himeno and N.Tanaka : Roll damping Force of Ship -Effects of Friction of Hull and Normal Force of Bilge Keels- , Jour. of the Kansai Society of Naval Architects,Japan, No.161 1979
7] P.W.Bearman, J.M.R.Graham and S.Singh : Forces on Cylinders in Harmonically Oscillating Flow, Mechanics of Wave-Induced Forces on Cylinders, Pitman Advanced Publishing, 1979
8] K.Kudo, A.Kinoshita and M.Nakato : Experimental Study on Hydrodynamic Forces Acting on the Oscillating Rectangular Cylinders, Jour. of the Kansai Society of Naval Archtects, Japan, No.177,1980
9] N.Tanaka, Y.Ikeda, Y.Himeno and Y.Fukutomi : Experimental Study on Hydrodynamic Viscous Force Acting on Oscillating Bluff Body, Jour. of the Kansai Society of Naval Architects, Japan, No.179,1980
10]K.Kudo : An Inviscid Model of Discrete-Vortex Shedding for Two-Dimensional Oscillating Flow Around a Flat Plate, Jour. of the Society of Naval Architects of Japan, No.145, 1979
11] J.M.R.Graham : The forces on sharp-edged cylinder in oscillatory flow at low Keulegan-Carpenter numbers, Jour. of Fluid Mechanics, Vol.97,Part 2, 1980
12] B.D.Bernardinis, J.M.R.Graham and K.H.Parker : Oscillatory flow around disks and through orifices, Jour. of Fluid Mechanics, Vol.102,1981
13] P.K.Stansby : An inviscid model of vortex shedding from a circular cylinder in steady and oscillatory far flows, Proc. Instn. Civil Engineering, Part 2, 1977
14] T.Sawaragi and T.Nakamura : Analytical study of wave force on a cylinder in oscillatory flow, Coastal Structures'79, 1979
15] H.Schlichting : Boundary Layer Theory, 6th edition, McGraw-Hill Book Co., 1968
16] T.Sarpkaya and C.J.Garrison : Vortex Formation and Resistance in Unsteady Flow, Transactions of the ASME, 1963
17] F.M.Lewis : The Inertia of the Water surrounding a Vibrating Ship, Transactions of SNAME, 1929
18] S.Shen : Unsteady Separation According to the Boundary-Layer Equation, Advances in Applied Mechanics, Vol.18
19] D.P.Telionis and D.TH.Tsahalis : Unsteady laminar separation over impulsively moved cylinders, Acta Astronautica, Vol.1, 1974
20] M.T.Landahl : Numerical Modeling of Blunt-Body Flows - Problems and Prospects , Aerodynamic Drag Mechanisms of Bluff Bodies and Road Vehicles, Plenum Publishing Co., 1978
21] T.Sarpkaya : An Analytical Study of Separated Flow About Circular Cylinders, Jour of Basic Engineering, Transactions of the ASME,1968
22] G.K.Batchelor : An Introduction to Fluid Dynamics, Cambridge University Press, 1970
23] J.W.Schaefer and S.Eskinazi : An analysis of the vortex street generated in a viscous fluid, Jour. of Fluid Mechanics, Vol.6, 1959

HYDRODYNAMIC FORCES OF THE OSCILLATING FLAT PLATE

Kimiaki Kudo
Hiroshima University
Hiroshima, Japan

Abstract

In order to investigate the nonlinear characteristics of the hydrodynamic forces acting on a flat plate normally oscillating to its plane, the behavior of the vortex sheet is simulated by a system of vortices. Especially, the part of the vortex sheet which would be continuously shed into the fluid is modelled as the development of the nascent point vortex. Since the fluid cannot support any forces physically, the model is assumed that both the forces and the moments must be totally counterbalanced. These dynamic conditions provide the equations of growth and motion of the nascent vortices. Supposing all the other vortices with constant circulations move along the flow, the problem is numerically solved step-by-step, together with the condition of the finite velocity at the separation point. As the time proceeds, however, the number of discrete vortices increases and the flow system becomes unstable. In order to prevent this difficulty, the vortices far off the flat plate is removed out of the system. The calculated normal force acting on the plate is examined in detail. Comparing the analysed hydrodynamic coefficients with those of experimental results, it is found that the present analysis is able to represent these nonlinear phenomena very well.

I. Introduction

Estimating the damping effect of the bilge keels against rolling, it is fundamental to investigate the hydrodynamic force on the flat plate normally oscillating to its plane. The force is caused by the vortices associated with the flow separation. This phenomenon, however, is so complicated that it has been investigated mainly by the experimental procedures [1,2].

The experimental results by Keulegan and Carpenter [1] show that both the added mass coefficient and the drag coefficient depend on the amplitude of the oscillation, but very little on the frequency, that is, on the Reynolds number in its higher range [2]. The latter fact implies that the fluid flow around the flat plate may be tractable with the potential flow theory because of the minor effect of the viscosity. On the other hand the former shows the nonlinear effect due to the vortex sheet shed into the fluid at the separation point.

The behavior of the vortex sheet is still so hard to treat directly that many theoretical approaches which approximate the vortex sheet with an array of inviscid discrete vortices have been proposed [3,4]. Such models have originally been utilized in investigating the mechanism of the Karman-vortex-street formation behind the circular cylinder in a uniform flow [5,6]. However, the separation points are not precedently assigned, and moreover, change with time as well.

In contrast with a circular cylinder, the body with the salient edges has the fixed separation points all the time, and it is unnecessary to make an assumption about these points. But even in this case it is still necessary to determine both the circulation and the position of the new vortex. This new vortex is called a nascent vortex and should be introduced near the separation point.

The most basic condition is the one which keeps the velocity finite at the edges. This will be referred to as a Kutta condition. In utilizing this Kutta condition, there have been various approaches which can be classified into two categories. In the first procedure, the position of the nascent vortex is for convenience fixed in advance, and the circulation is determined so as to meet the finite-velocity condition [4,7,8,9]. The other is an opposite procedure in which the circulation of the nascent vortex is at first assumed to be

$$\Delta\Gamma = \frac{1}{2} U_s^2 \, \Delta T \qquad (1)$$

and then the position has to be found so as to satisfy the Kutta condition. The U_s is a representative velocity which would correspond to the one at the outer edge of the boundary layer in the real fluid [10,11].

In either procedure, however, there is one disposable parameter which must be appropriately chosen so as to provide the satisfactory results compared with the experiments. This indefiniteness is due to the shortage of the conditions which could fix both the position and the circulation of the nascent vortex.

In this paper the inviscid discrete vortex

model is applied to the harmonically oscillating separation flow, and the nonlinear characteristics of the hydrodynamic forces acting on the flat plate is investigated, that is, the behavior of the vortex sheet is simulated by a system of discrete vortices. As for the nascent vortex, the process in which the vortex sheet is continuously shed into the fluid at the edge, is modelled as both shedding and growing of the point vortex. This model can eliminate the indefinite parameter.

As the time proceeds, the number of the discrete vortices is increasing and the old vortices stay around the flat plate. They are likely to make the system unstable. In order to prevent this difficulty from occurring, the vortex which is far away from the flat plate is removed from the system. This scheme seems to be reasonable in view of the eliminating process of the vorticity in the real fluid.

II. Growing Discrete-Vortex Model

In the potential flow theory the free shear layer can be modelled by a line of discontinuity of the velocities. The pressure, however, still remains to be continuous across the line since the fluid cannot support any internal forces. Therefore in the model which substitutes a system of discrete vortices for the free vortex sheet, each vortex must remain force-free. As a result of this dynamic condition, each vortex should have a certain circulation and they move with the velocity induced by the attached flow and the other vortices.

As a matter of course, the same principle should be applied to the nascent vortex. But this vortex is introduced to represent the imaginary piece of vortex sheet which would be continuously shed from the separation point into the fluid. In the growing discrete-vortex model, the nascent vortex is allowed to grow and move, to which another dynamic condition must be imposed.

Force-free model

When the vortex with a constant circulation is travelling along the flow, it does not feel any forces, but in the case of growing vortex it is not necessarily so. The flow field around the point vortex is represented by a logarithmic velocity potential,

$$f = \frac{\Gamma_\phi}{2\pi i} \log (z - z_\phi) \ . \qquad (2)$$

The growing vortex with circulation Γ_ϕ is at the point $z_\phi = x_\phi + iy_\phi$. Making a counterclockwise revolution around the vortex, the value of the velocity potential jumps by the circulation Γ_ϕ. Therefore, the jump of the pressure is,

$$[p] = \rho \dot{\Gamma}_\phi \ , \qquad (3)$$

where ρ is the density of the fluid and the dot over the Γ_ϕ means the time derivative. This pressure gap arises across the branch line connecting the nascent vortex to the separation point. This line is introduced to make the velocity potential single-valued over the plane. It is also referred to as a vortex-feeding sheet because the increment of the circulation of the growing vortex is supposed to be fed through it.

The free shear layer with some discontinuous velocities and a continuous pressure in a physical plane is now replaced by a vortex-feeding sheet with a continuous velocity and a discontinuous pressure in a mathematical model. The force brought about in the fluid must be totally counterbalanced with the lifting force exerted on the nascent vortex due to the relative motion against the surrounding fluid [12,13,14].

The force acting on the vortex-feeding sheet is

$$i\rho\dot{\Gamma}_\phi(z_\phi - z_s) \qquad (4)$$

where z_s is a coordinate of the separation point. On the other hand, the lifting force on the nascent vortex is

$$i\rho\Gamma_\phi(\dot{z}_\phi - \bar{\dot{w}}_\phi) \qquad (5)$$

where $\dot{z}_\phi$ is the complex velocity of the nascent vortex and $\bar{\dot{w}}_\phi$ means the local complex velocity induced at the point z_ϕ. Then the totally force-free condition gives the equations

$$\dot{z}_\phi + (z_\phi - z_s)\dot{\Gamma}_\phi/\Gamma_\phi = \bar{\dot{w}}_\phi \ . \qquad (6)$$

These equations show that the growth and the motion of the nascent vortex interact each other, and provide two relations between three derivatives $\dot{x}_\phi$, $\dot{y}_\phi$ and $\dot{\Gamma}_\phi$.

The Kutta condition provides one more relation between the circulation Γ_ϕ and the position z_ϕ. Thus the problem could be solved with the appropriate initial conditions, that is, the nascent vortex leaves the separation point at every beginning of shedding periods.

Improvement of the model

In the force-free model the new vortex is allowed to grow so that the model can meet in total the dynamic condition that the fluid does not support any forces. Nevertheless, there remain some moments in the fluid. The more elaborate model is now proposed by making allowance for the interaction between some of the nascent vortices so that the fluid supports neither forces nor moments. Although such a model would not be unique, it seems reasonable to partially improve the force-free model. The following are assumed,

(a) the nascent vortex Γ_ϕ grows and moves against the flow as before,

(b) the preceding nascent vortex Γ_1 at point z_1 is also allowed to grow, but it convects with the flow,

(c) the force-free and moment-free conditions

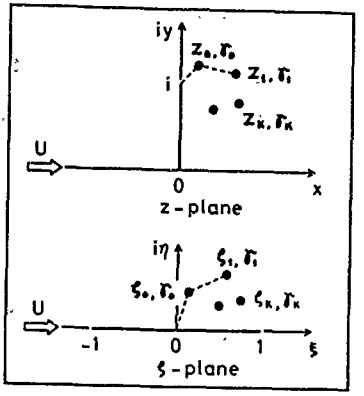


Figure 1. Flow in the physical z-plane and in the transformed ζ-plane with (n+1) pairs of discrete vortices.

are satisfied by the above two nascent vortices,

(d) all the other vortices are assumed to have constant circulations and travel along the flow.

There is no force acting on the preceding nascent vortex Γ_1, but the lifting force on the nascent vortex Γ_0 is given as the expression (5). The forces exerted on the vortex-feeding sheet are described as follows,

$$i\rho(\dot{\Gamma}_0 + \dot{\Gamma}_1)(z_0 - z_s) \quad \text{for } z_s \sim z_0 \tag{7}$$

$$i\rho\dot{\Gamma}_1(z_0 - z_1) \quad \text{for } z_0 \sim z_1 \tag{8}$$

Then the totally force-free condition becomes now,

$$\dot{z}_0 + (z_0 - z_s)\dot{\Gamma}_0/\Gamma_0 + (z_1 - z_s)\dot{\Gamma}_1/\Gamma_0 = \bar{W}_0 \tag{9}$$

In addition, the moments about the separation point z_s are counterbalanced if

$$2\mathrm{Re}[\Gamma_0(\bar{W}_0 - \bar{\dot{z}}_0)(\bar{z}_0 - \bar{z}_s)] = \dot{\Gamma}_0|z_0 - z_s|^2 + \dot{\Gamma}_1|z_1 - z_s|^2. \tag{10}$$

Although this improved model is more complicated than the force-free model, the former is expected to reduce the fluctuations caused by the discretization of the continuous process. In the following, this force-free and moment-free model is applied to the harmonically oscillating separation flow around the flat plate.

III. Oscillating Flow around Flat Plate

Formulation

The inviscid discrete-vortex model and the dynamic conditions for the development of the nascent vortices are applied to the harmonic flow around the the flat plate. It is assumed that the flow system is symmetrical and the separation points are fixed at the edges. The formulation of the flow model becomes simple in the ζ-plane which is conformally transformed from the physical z-plane as shown in Figure 1, where each plane neglects the lower half part, taking advantage of the symmetricity. The transformation between both planes is

$$z = (\zeta^2 - 1)^{1/2}. \tag{11}$$

Figure 1 also depicts 2 pairs of the nascent and preceding nascent growing vortices, and (n-1) pairs of vortices with each constant circulation.

All quantities are normalized as follows; coordinates by the semi-span b of the flat plate, velocities by the maximum otherwise uniform flow velocity U_{max}, and the circulation Γ_k by $2\pi bU_{max}$, defining

$$\gamma_k = \Gamma_k/2\pi bU_{max} \quad (k = 0,1,\ldots,n). \tag{12}$$

Suppose that the amplitude of motion is a and the frequency ω, then,

$$U_{max} = a\omega . \tag{13}$$

The time t is normalized as follows,

$$\tau = tU_{max}/a = \omega t. \tag{14}$$

Then the normalized uniform velocity is now described by

$$U = \sin\tau \quad (\tau > 0) . \tag{15}$$

The complex potential corresponding to Figure 1 is written as

$$f_n = U\zeta - i\sum_{k=0}^{n}\gamma_k \log(\zeta - \zeta_k)/(\zeta - \bar{\zeta}_k) . \tag{16}$$

The complex-conjugate velocity of the fluid at the k-th vortex is

$$W_k^{(n)} = \lim_{z\to z_k}\left(\frac{df_n}{dz} + \frac{i\gamma_k}{z - z_k}\right) = \frac{z_k}{\gamma_k}\left[U - i\sum_{\substack{j=0\\ j\neq k}}^{n}\gamma_j\left(\frac{1}{\zeta_k - \zeta_j} - \frac{1}{\zeta_k - \bar{\zeta}_j}\right) + i\gamma_k\left(\frac{1}{\zeta_k - \bar{\zeta}_k} - \frac{1}{2\zeta_k z_k}\right)\right] . \tag{17}$$

The Kutta condition at the edge $z_s = 1$,

which in ζ-plane is changed into the condition that the origin is a stagnation point, provides

$$\gamma_0 = -i U_n |\zeta_0|^2/(\zeta_0-\bar{\zeta}_0) \qquad (18)$$

where

$$U_n = U - i\sum_{k=1}^{n} \gamma_k(\zeta_k-\bar{\zeta}_k)/|\zeta_k|^2$$

$$U_0 = U \, . \qquad (19)$$

The force-free condition (9) and the moment-free condition (10) are normalized respectively

$$\dot{z}_0+(z_0-i)\dot{\gamma}_0/\gamma_0+(z_1-i)\dot{\gamma}_1/\gamma_0 = h\bar{W}_0^{(n)}, \qquad (20)$$

$$2\mathrm{Re}[\gamma_0(h\bar{W}_0^{(n)}-\dot{\bar{z}}_0)(\bar{z}_0+i)] = \dot{\gamma}_0|z_0-i|^2+\dot{\gamma}_1|z_1-i|^2$$

or making use of the equation (20), this can be rewritten as

$$\dot{\gamma}_1/\dot{\gamma}_0 = -|z_0-i|^2/\mathrm{Re}[(\bar{z}_1+i)(2z_0-z_1-i)]. \qquad (21)$$

Here the parameter h is the amplitude ratio,

$$h = a/b \qquad (22)$$

which is an important parameter in this problem, and is usually referred to as a K_c number,

$$K_c = \pi h \, . \qquad (23)$$

Since it is assured that all the other vortices except the nascent vortex move along the flow, the equations of motion are given by

$$\dot{z}_k = h\bar{W}_k^{(n)} \quad (k = 1,2,\ldots,n) \qquad (24)$$

The system of equations (18), (20), (21) and (24) is complete, governing the whole development of the flow. Now, these equations can be rewritten into more convenient forms, by means of the following relations derived from the equations (11), (18) and (19),

$$\dot{z}_k = \zeta_k\dot{\zeta}_k/z_k \qquad (25)$$

$$[1+\dot{\gamma}_1/\dot{\gamma}_0)|\zeta_0|^2\mathrm{Im}(\zeta_1)/|\zeta_1|^2\mathrm{Im}(\zeta_0)](\dot{\gamma}_0/\gamma_0)$$
$$= \dot{U}_n^*/U_n + 2\mathrm{Re}[\dot{\zeta}_0/\zeta_0] - \mathrm{Im}(\dot{\zeta}_0)/\mathrm{Im}(\zeta_0) \qquad (26)$$

where

$$\dot{U}_n^* = \dot{U} + 2\sum_{j=1}^{n} \gamma_j \mathrm{Im}[\dot{\zeta}_j/\zeta_j^2] \qquad (27)$$

Thus finally

$$A\dot{\zeta}_0 + B\bar{\zeta}_0 = C \qquad (28)$$

or

$$\dot{\zeta}_0 = (C\bar{A}-\bar{C}B)/(|A|^2-|B|^2) \qquad (29)$$

where

$$A = \zeta_0/z_0 - D\bar{\zeta}_0/\zeta_0(\zeta_0-\bar{\zeta}_0)$$

$$B = D\zeta_0/\bar{\zeta}_0(\zeta_0-\bar{\zeta}_0)$$

$$C = h\bar{W}_0^{(n)} - D\dot{U}_n^*/U_n$$

$$D = \frac{z_0-i+E(z_1-i)}{1+E|\zeta_0|^2\mathrm{Im}(\zeta_1)/|\zeta_1|^2\mathrm{Im}(\zeta_0)}$$

$$E = -|z_0-i|^2/\mathrm{Re}[(\bar{z}_1+i)(2z_0-z_1-i)] \, , \qquad (30)$$

and also

$$\dot{\zeta}_k = hz_k\bar{W}_k^{(n)}/\zeta_k \quad (k = 1,2,\ldots,n) \qquad (31)$$

Initial conditions

The system of equations (18), (21), (29) and (31) can be solved with the proper initial conditions. In this model the following are assumed in the numerical treatments,

(a) the new vortex begins to grow and move from the edge into the fluid at time $\tau = \tau_n$ when there are already shed n-pairs of vortices,

(b) the nascent vortex ceases developing at time $\tau = \tau_{n+1}$ after the prescribed period ΔT,

(c) and thereafter another similar system with one more vortex takes the place of it.

It can be readily seen that the equation of motion (28) becomes singular at each initial instant $\tau = \tau_n$. Accordingly, it is necessary to make clear the asymptotic behavior of the solution. At the instant $\tau = \tau_n$, there are n-pairs of vortices in the fluid, and the Kutta condition is satisfied by them, and the circulation of the new vortex is zero. Then,

$$U_n(\tau_n) = 0 \, . \qquad (32)$$

Therefore after a small amount of time $\Delta\tau$,

$$U_n(\tau) = U_n(\tau_n+\Delta\tau) - \dot{U}_n^*(\tau_n)\Delta\tau \, . \qquad (33)$$

As $\tau \to \tau_n$, the equation (21) is evaluated as

$$\dot{\gamma}_1/\dot{\gamma}_0 = |z_0-i|^2. \qquad (34)$$

In the equation (20), the third term is negligible because it is higher than the order of the second term. If we put

$$\zeta_0 = \rho_0(\Delta\tau)^m e^{i\theta}, \qquad (35)$$

then the equation (20) can be evaluated asymptotically

$$-\left(\frac{3m+1}{2}\right)i\rho_0^2 e^{2i\theta}(\Delta\tau)^{2m-1} = \sum_{j=1}^{n} Y_j(1/\zeta_j^2 - 1/\bar{\zeta}_j^2) - \frac{i\bar{U}_n(\tau_n)e^{i\theta}(\Delta\tau)^{1-m}}{\rho_0}\left(1 - \frac{1}{4\sin^2\theta} + \frac{fe^{i\theta}}{4\sin\theta}\right) \quad (36)$$

In case of $n = 0$

In this case, the first term of the right hand side of the equation (36) does not appear yet. Since the uniform velocity is given by (15)

$$U = \Delta\tau \ . \quad (37)$$

In order to make the equation (36) consistent, the following relations are necessary,

$$m = 2/3 \ , \quad \theta = \pi/4 \ , \quad \rho_0^2 = h/3\sqrt{2} \ . \quad (38)$$

In case of $n \geq 1$

In this case, the second term of the right hand side of the equation (36) becomes higher order than the first term. Neglecting that term, the following are obtained as before,

$$m = 1/2 \ , \quad \theta = \pi/2 \ , \quad \rho_0^2 = \frac{g}{5}h\sum_{j=1}^{n} Y_j \mathrm{Im}[1/\zeta_j^2] \ . \quad (39)$$

This result implies very important facts,

(a) the nascent vortex is shed into the fluid in the plane of the flat plate,

(b) and further the distance by which the nascent vortex appears after a short time, varies under the influence of the wake.

These facts have usually been assumed by the conventional discrete-vortex model. However, in the present work, these are the naturally derived results from the dynamic condition of the growing discrete-vortex model.

IV. Computational procedure

The equations of the growth and motion of the vortices has been consistently formulated in the preceding section as the simultaneous first order differential equations. These can successively be integrated by the numerical procedure. It has been assumed that the new vortex is introduced one after another at every time-interval ΔT. Here, two parameters, N_p and N_q, are defined as follows,

(a) in every half-period, N_q discrete-vortices are shed into the fluid, therefore,

$$\Delta T = \pi/N_q \ , \quad (40)$$

(b) the system is integrated N_p times before another vortex begins to grow, so that the minimum time-interval for the numerical integration is given by

$$\Delta\tau = \Delta T/N_p \ . \quad (41)$$

Thus, it can be expected that the greater the number N_q, the closer the discrete-vortex model, and also, the larger N_p would make the numerical integration more precise. But, these will need more calculation time. In this paper, $N_p = 5$ and $N_q = 20$ are used as a standard.

In solving the simultaneous differential equations for the growing nascent vortices, the Simple Runge Kutta method is applied. Suppose that the differential equation is given by

$$\dot{y} = f(t,y) \quad (42)$$

and the value at $t = t_n$

$$y_n = y(t_n) \ , \quad (43)$$

then the value at $t = t_{n+1} = t_n + \Delta t$ is estimated by

$$k_1 = f(t_n, y_n) \ , \quad k_2 = f(t_{n+1}, y_n + k_1\Delta t) \ , \quad y_{n+1} = y_n + (k_1 + k_2)\Delta t/2 \ . \quad (44)$$

On the other hand, a sirple trapezoidal rule is used for the other vortices.

As the time proceeds, the number of the discrete vortices increases, and it requires gradually more computation time to advance each step. In addition, the old vortices occasionally approaching near the flat plate are likely to make the system unstable. In order to prevent this undesirable situation from occurring, the vortex which is far away from the flat plate should be removed out of the flow system. This assumption seems to be reasonable in view of the eliminating process of the vortices in the real fluid.

In this paper, very primitive model is proposed, since there is no rational model for eliminating the vorticity. The idea of the elimination model is as follows,

(a) find the maximum distance over which the vortices sweep for the first half-period after the flow starts from rest,

(b) take a little larger distance than this, which is referred to as a delete-length,

(c) and finally when the vortex leave more than this delete-length off the plate, it is simply deleted out of the computation.

V. Hydrodynamic Forces

The normal force exerted on the flat plate at every instant can be evaluated by the generalized Blasius' theorem. Since the flow system is essentially assumed to be force-free, the normal force F is given by the time derivative of the total impulse. Thus,

$$F = dI/dt \tag{45}$$

where $$I = \rho\pi b^2 U + i\rho \sum_{k=0}^{n} \Gamma_k(\zeta_k - \overline{\zeta}_k) \ . \tag{46}$$

It is assumed in the model that all the variables are continuously developing, but that the nascent vortices are forced to stop growing at each conjunctive instant τ_n. Since the derivative of the impulse becomes discontinuous at that instant, the model allows the jump of the force. This is caused by the discretization of the continuous vortex sheet. Therefore, an average is made over the period ΔT, and this is assumed to be the normal force in this period.

The normal force coefficient is defined,

$$C_{nt} = (1/\Delta T)\int_{\tau_n}^{\tau_{n+1}} (F/\rho b U_{max}^2)\, d\tau$$

$$= (\pi/h\Delta T)[U - 4\sum_{k=0}^{n} Y_k \eta_k]_{\tau_n}^{\tau_{n+1}} \tag{47}$$

The first term of the right hand side is due to the attached flow and the second represents the influence of the shed vortices,

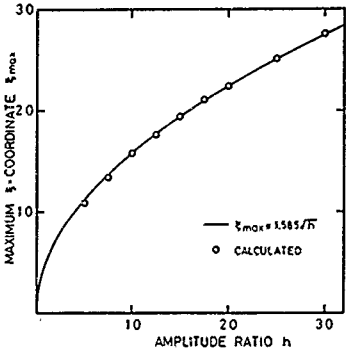


Figure 2. Maximum ξ-coordinate of the point vortices swept in the first half-period against amplitude ratio, (N_p=5, N_q=40).

$$C_n = -(4\pi/h\Delta T)[\sum_{k=0}^{n} Y_k \eta_k]_{\tau_n}^{\tau_{n+1}} \tag{48}$$

In order to compare the analysis with the results of experiments [1], the normal force is assumed as follows,

$$F = \rho\pi b^2 C_a(dU/dt) + \rho b C_d U|U| \ , \tag{49}$$

or in a nondimensional form,

$$C_{nt} = (\pi/h)C_a \dot{U} + C_d U|U| \ . \tag{50}$$

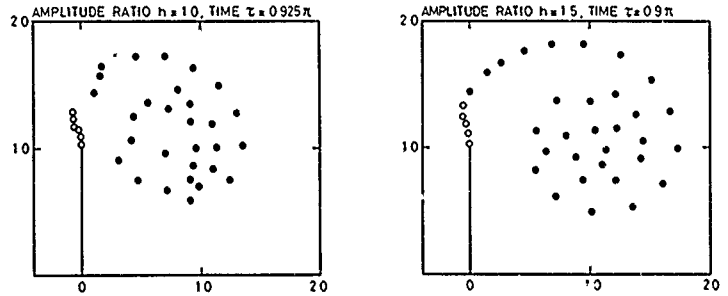


Figure 3. Flow fields when ξ max takes place, for amplitude-ratios h=1.0 and 1.5, (N_p=5, N_q=40), direction of rotation: ●, negative and ○, positive.

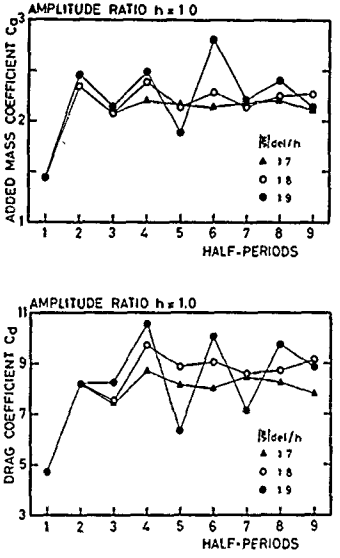


Figure 4. Variations of added mass and drag coefficients with every half-period in case of h=1.0, (Np=5, Nq=20), for various delete-lengths.

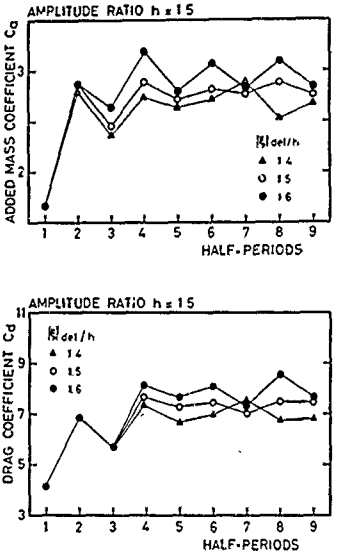


Figure 5. Variations of added mass and drag coefficients with every half-period in case of h=1.5, (Np=5, Nq=20), for various delete-lengths.

Both the added mass coefficient Ca and the drag coefficient Cd are evaluated at every half-period, as follows,

$$C_a = (h/\pi^2) \int_{n\pi}^{(n+1)\pi} C_{nt} \cos\tau \, d\tau \qquad (51)$$

$$C_d = (3/8) \int_{n\pi}^{(n+1)\pi} C_{nt} \sin\tau \, d\tau \qquad (52)$$

VI. Results and Discussions

Effect of delete-length

There is no rational rule determining the delete-length within the limit of the potential flow theory. It must be artificially introduced so as to make the flow system stable and also compare the calculated results well with the experiments, if possible.

This delete-length is introduced in the ζ-plane rather than in the z-plane, only for the sake of the convenience. Figure 2 shows the maximum ξ-coordinate, ξ_{max}, in the first half-period against the amplitude ratio h. In these calculations, N_p=5, N_q=40, that is, 40 vortices are shed in every half-period of motion. It can readily be seen that ξ_{max} is in proportion to $h^{1/2}$,

$$\xi_{max} = 1.585\sqrt{h} \, . \qquad (53)$$

The flows, when the ξ_{max} takes place for each amplitude ratio h = 1.0 and 1.5, are depicted in Figure 3. As the amplitude ratio becomes large, the instant at which the maximum occurs seems to advance.

The delete-length $|\xi|_{del}$ in ζ-plane should be taken a little larger than the ξ_{max}. In order to fix $|\xi|_{del}$ most reasonably, the hydrodynamic force coefficients obtained for the various delete-lengths are compared each other.

In Figure 4, the variations of the added mass coefficient Ca and the drag coefficient Cd with every half-period are shown in case of the amplitude ratio h = 1.0. When $|\xi|_{del}/h$ = 1.9, the calculated results show a little severe fluctuations. As it becomes less than 1.9, the calculations show the stable convergences. The same thing can be said for h = 1.5 as shown in Figure 5.

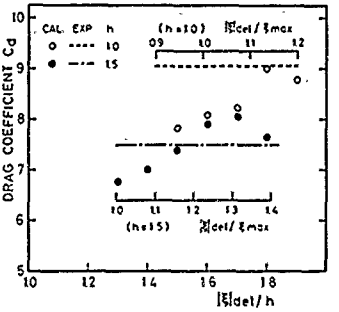


Figure 6. Drag coefficient versus delete-length ratio, for amplitude ratios h=1.0 and 1.5, (Np=5, Nq=20).

The variations of the coefficients seem to be in transient for the first three half-periods after which it may be said almost steady and the averages are made over six half-periods. The drag coefficients, obtained through the above-mentioned procedure, are plotted against the delete-length ratio $|E|_{del}/h$ in Figure 6. As the ratio increases, the drag coefficients become larger and after they reach the maximum, they finally decrease. Figure 6 also includes the experimental values which have been read in the diagrams of Keulegan and Carpenter's [1]. The ratio $|E|_{del}/h$, at which the calculated results almost agree with the experimental value, varies together with the amplitude ratio. On the other hand, the inner scales $|E|_{del}/E_{max}$ show that the delete-length should be taken about 10 ∿ 15 % larger than E_{max}. Thus, the delete-length ratio sould be chosen as follows,

$$|E|_{del}/h \propto 1.74/\sqrt{h} \sim 1.82/\sqrt{h} \ , \qquad (54)$$

Hydrodynamic force coefficients

The variations of the normal force coefficient Cn are drawn in Figure 7 for h = 1.0, where the ratio $|E|_{del}/h$ has been chosen as 1.8.

The similar calculations have been made for other amplitude ratios. The combinations of the parameters are shown together in Table 1. The delete-length ratios are settled within the range of the condition (54). The number Np and Nq are fixed to 5 and 20, respectively, in all these calculations. The calculated hydrodynamic coefficients are taken from the average over the several stable periods. These results are charted in Figures 8 and 9.

The dependence of the added mass coefficient upon the amplitude ratio is shown in Figure 8, and the drag coefficient in Figure 9. In these diagrams the experimental results [1] are also put together. Generally speaking, the present analytical results agree fairly well with the experimental ones. Also it explains the tendency that Ca increases but Cd decreases as the amplitude of oscillation increases.

The agreement of the added mass coefficients is rather poor except the range of the

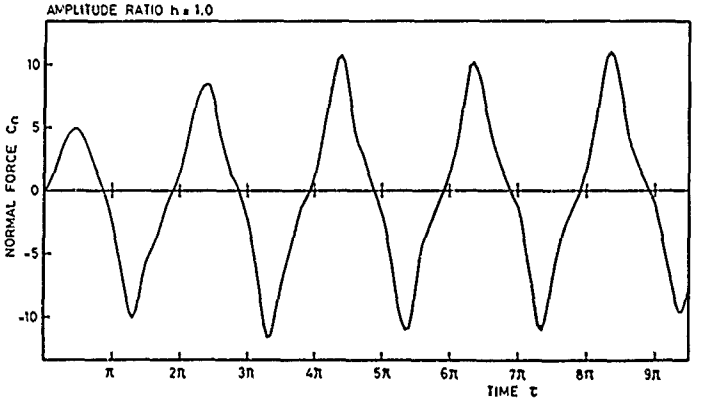


Figure 7. Variation of vortex force with time, (h=1.0, Np=5, Nq=20, |E|del/h=1.8)

Table 1 Combinations of parameters for calculation

h	|ζ|del/h	|ζ|del/ζmax	Np	Nq
0.5	2.45	1.09	5	20
1.0	1.8	1.14	5	20
1.5	1.5	1.16	5	20
2.0	1.3	1.16	5	20
2.5	1.1	1.10	5	20
3.0	1.0	1.09	5	20
3.5	0.95	1.12	5	20

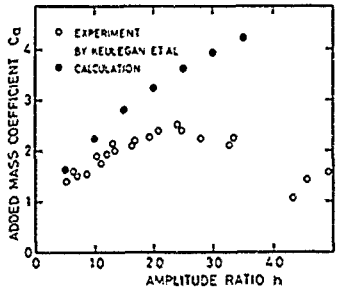


Figure 8. Added mass coefficient versus amplitude ratio.

smaller amplitude of motion. The analysis provides somewhat over-estimation. In addition, the calculated value is monotonously increasing

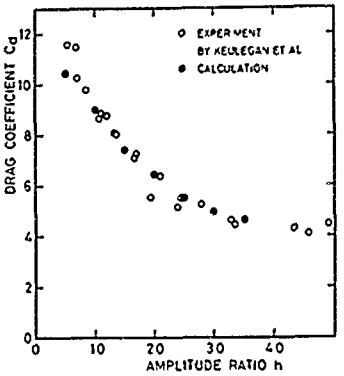


Figure 9. Drag coefficient versus amplitude ratio.

as the amplitude ratio increases, but in contrast the experiments show the irregular characteristics and the coefficient is rather decreasing for the higher amplitude of motion. This may be attributable to the asymmetric formation of eddies for the large amplitude ratio, which is, however, neglected in this paper.

The calculated drag coefficients coincide with the experimental values excellently. But,

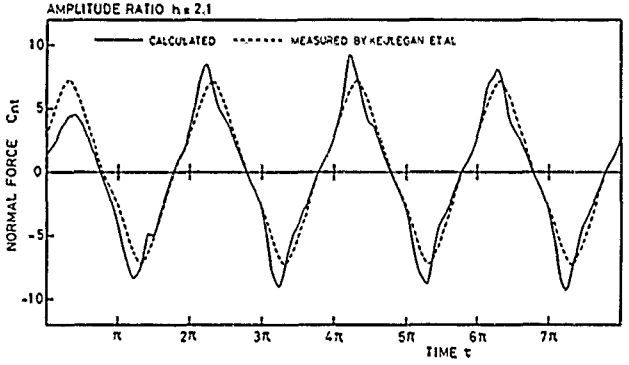


Figure 10. Variations of the total normal forces with time, for amplitude ratio h=2.1, calculated with N_p=5, N_q=30, and $|E|_{del}/h$=1.2.

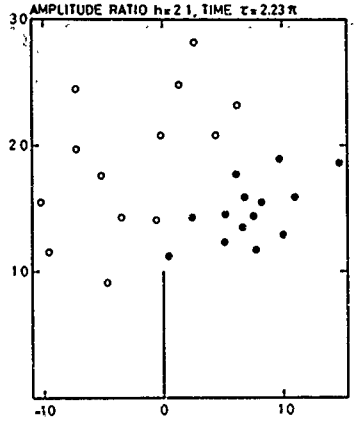


Figure 11. Flow around the flat plate at the instant when the normal force has its maximum, for h=2.1, corresponding to Figure 10.

in case of h = 0.5 the calculation gives somewhat lower values than the experimental. This seems to be caused by the artificial elimination of the vortices. When the amplitude ratio becomes small, the delete-region approaches the edge. Thus, the sudden disappearance of the vortex near the edge would infavorably affect the shedding of the nascent vortex. For the amplitude ratio h = 0.5, another calculation (N_P = 5, N_Q =10) without the elimination [13] gives Ca = 1.62, and Cd = 12.2 which is rather closer with the experiments. But this seems to need further investigations.

Variation of normal force with time

Both the added mass and drag coefficients are only the integrated characteristics of the normal forces. The direct comparison of the normal forces between the calculation and the experiment is depicted in Figure 10. The calculation is made for h = 2.1 with the parameters N_P = 5, N_Q =30 and $|E|d\sigma_1/h$ = 1.2. For comparison, the measured force which is taken from the graph (K_C = 6.6) of Keulegan and Carpenter [1] is also plotted.

The agreement between the calculated and experimental results is good except at the time when the amplitude attains its largest value. The calculation gives rather narrower peaks. The reason why this discrepancy arises may be explained as follows. Figure 11 shows the flow at the instant $\tau = 2.23\pi$ when the normal force takes its maximum. After the direction of the uniform flow has changed, the old vortices begin to approach the edge and induce there a large velocity by which the new vortices are forced to leave the separation point. As a result of this, the large normal forces are caused in the calculation.

VII. Conclusions

The discrete point vortex model is applied to the oscillating separation flow around the flat plate, and the characteristics of the normal forces acting upon it is investigated. In this respect two schemes have been developed, one of which is to fix the generation of the nascent point vortex, and the other is to delete the vortices travelling far off the flat plate.

The conditions that both the forces and the moments should be totally free in the fluid provide the characteristics of the growth and motion of the nascent vortices. The uncertain parameter of the conventional discrete-point-vortex model can be deleted in this mathematical model. Further, the nascent vortex is shed into the fluid along the flat plate, which is usually assumed, but is a natural result of the dynamic conditions in this model.

The proposed scheme for removing the vortices out of the fluid is very simple, nevertheless it is so useful in this oscillating flow problem that the stable calculation is made possible over a wide range of periods. By comparing the analysis of the hydrodynamic force with the experiment, it is found that the eliminating region should be a little larger than the wake made in the first half period of oscillation.

The normal force thus obtained is analysed into the added mass coefficient and the drag coefficient. The agreement of the hydrodynamic force coefficients between the analysis and the experiment is generally good. In case of the drag coefficient the agreement is excellent, but on the other hand the added mass coefficients agree only moderately. In either case, however, the nonlinear characteristics of the normal forces are explained very well in the range of the potential flow theory.

The comparison between the calculated and the experimental normal-forces has been made in the time history diagrams. The agreement is also good except the instant when the nascent vortices are forced to develop excessively. This seems to be caused by the remaining vortices with opposite circulations near the edge. The model with more elaborate scheme of the elimination of the vorticity may be expected to produce the closer result.

The author also expects developing this model to the problem of the asymmetric separation flows.

VIII. Acknowledgment

The author wishes to express his appreciation to Prof. H.Nakato and Prof. K. Mori of Hiroshima University for many valuable suggestions and discussions in preparing this paper.

The author would also like to thank Prof. S. Motora and Prof. M. Fujino of Tokyo University for the helpful advices they gave.

References

1. Keulegan, G.H. and Carpenter, L.H., "Forces on cylinders and plates in an oscillating fluid," J. R. of the National Bureau of Standards, Vol. 60, No. 5, 1958.

2. Shih, C. and Buchanan, H., "The drag on oscillating flat plates in liquids at low Reynolds numbers," J. Fluid Mech., vol.48, part 2, 1971.

3. Fink, P.T. and Soh, W.K., "Calculation of vortex sheets in unsteady flow and applications in ship hydrodynamics," Tenth Symp. Naval Hydrodynamics, Session V,1974.

4. Clements, R.R. and Maul, D.J., "The representation of sheets of vorticity by discrete vortices," Prog. Aerospace Sci., Vol. 16, No. 2, 1975.

5. Gerrard, J.H., "Numerical computation of the magnitude frequency of the lift on a circular cylinder," Philosophical Trans. Roy. Soc. London, Ser. A, Vol. 261, 1966.

6. Sarpkaya, T., "An Analytical Study of Separated Flow about Circular Cylinder," J. Basic Engng., 1968.

7. Soh, W.K. and Fink, P.T., "On potential flow modelling of action of ship's bilge keels," 4th Australasian Conference on Hydraulics and Fluid Mechanics, 1971.

8. Kuwahara, K., "Numerical Study of Flow past an Inclined Flat Plate by an Inviscid Model," J. Phys. Soc. Japan, Vol. 35, No. 5, 1973.

9. Belotserkovskii, S.M. and Nisht, M.I., "Two regimes of stalled flow around a plate," Sov. Phys. Dokl., Vol. 18, No. 12, 1973.

10. Clements, R.R., "An inviscid model of two-dimensional vortex shedding," J. Fluid Mech., vol. 57, part 2, 1973.

11. Sarpkaya, T., "An inviscid model of two-dimensional vortex shedding for transient and asymptotically steady separated flow over an inclined plate," J. Fluid Mech., vol. 68, part 1, 1975.

12. Bryson, A.E., "Symmetric Vortex Separation on Circular Cylinders and Cones," Trans. ASME, J. Appl. Mech., Vol. 26, Ser. E, No. 4, 1959.

13. Kudo, K., "An Inviscid Model of Discrete-Vortex Shedding for Two-Dimensional Oscillating Flow aro d a Flat Plate," J. Soc. Naval Arch. Japan, Vol. 145, 1979.

14. Graham, J.M.R., "The forces on sharp-edged cylinders in oscillating flow at low Keulegan-Carpenter numbers," J. Fluid Mech., vol. 97, part 1, 1980.

DISCUSSION
of the paper
by K. Kudo

HYDRODYNAMIC FORCES OF THE OSCILLATING FLAT PLATE

Discussion
by Shee-Mang Yen

I wish to make some comments on the evaluation of random error of the discrete vortex method.

(1) The vortex flow is statistical in nature, therefore, there are statistical features in the discrete vortex method.

(2) The statistical features lead to random errors which should be evaluated

(3) The random error depends on sampling. (The systematic error depends on modeling).

(4) I suggest that the sampling parameters (such as N_p and N_q used by Kudo in his paper) be varied to conduct numerical experiments and to control the random error so that it is less than the smallest "signal" to be detected.

(5) The random error (such as confidence limit) may be evaluated by obtaining solution for several samples (in flow representation, one may use color dots to represent the position of vortices. With one color for each sample, we can observe the statistical scatter).

(6) Samples referred to above are the sets of random numbers generated to obtain corresponding solutions (one for each sample).

Author's reply

The author is grateful to Prof. Shee-Mang Yen for his comments and the answers are as follows :

The discrete vortex model has necessarily the statistical features and includes the random errors due to both the discrete modeling of the vortex sheet and the step-by-step numerical integration. In a view-point of estimating the force on the body, however, the most significant factor is the rate of shedding of the vorticity near the body, which is caused by the integrated effects of the other vortices. The author expects that the random error included in each vortex may thus cancel each other out. He also believes that the parameters of the model should be chosen so as to reduce the numerical instability. The vortex flow in nature is clearly governed by the viscosity not only at the generation but also in the dissipation of the vorticity. The latter effect results in the flow stabilization. In suppressing the numerical random error, this effect should be taken into account, though this is not included in the potential flow regime.

MULTIGRID METHODS APPLIED TO A WATER-WAVE PROBLEM

Steve McCormick and J.W. Thomas
Department of Mathematics
Colorado State University
Fort Collins, Colorado 80523 U.S.A.

Abstract

The feasibility of applying multigrid methods to solve free boundary problems is investigated. The test problem considered is the two-dimensional, steady, irrotational flow of an inviscid liquid over a submerged vortex. Tests on this problem consist of first solving the problem using the trial free boundary method in conjunction with Gauss-Seidel relaxation, applying unigrid - a multigrid simulation scheme - to the inner loops, and applying grid continuation to reduce the number of outer loops necessary for a solution.

1. Introduction

The numerical solution of free-surface or free boundary problems is generally very difficult, although there are many methods that have been applied to such problems. One method that has been used somewhat successfully on free-surface problems is the trial free boundary method in conjunction with relaxation [7]. The method seems to work but is very slow, which all but eliminates its use for three-dimensional problems.

In recent years multigrid methods have attracted much attention for solving elliptic boundary value problems. Multigrid methods involve reduction of high frequency discrete Fourier components of the error on a given grid by relaxation and of the lower frequencies by relaxation sweeps performed on the residual error equation defined on coarser grids. When implemented to exploit full efficiency, this approach has the effect of reducing what otherwise would be many relaxation sweeps on the finest grid to an equivalent of six or seven.

The objective of this work is to investigate the feasibility of applying multigrid methods to solve free boundary problems. To accomplish this we have chosen as our model problem the equations of two-dimensional, steady, irrotational flow of an inviscid liquid over a submerged vortex. This problem was chosen because it is sufficiently complex to provide a suitable test and it is sufficiently easy to be able to securely evaluate our results. It is also helpful that the above described problem was previously solved by von Kerczek and Salvesen using a method based on relaxation [3].

The approach we shall use is to first solve the problem with a relaxation method. We shall then extend this approach to implement UNIGRID, which is a technique developed by McCormick and Ruge [5] that can be used as a quick and easy way to test the feasibility of multigrid application to a given problem. In a parallel effort, we shall implement a "mesh continuation" process which is simply a method for providing good initial guesses for the solution process on the finest grid. This process has the effect of reducing to one the number of "outer loop" iterations (i.e., the interplay between the stream function and height function describing the free surface). UNIGRID, which simulates multigrid, has the effect of reducing to a handful the number of "inner loop iterations" (i.e., the relaxations performed on the stream function). Together, they reduce the complexity of the overall solution process to a small amount of computational work which is directly proportional to the number of grid points.

2. Mathematical Formulation

Consider a vortex moving at constant velocity U from left to right at a fixed distance below the undisturbed free surface. The problem then is to determine the surface waves as well as the total flow field.

We use a coordinate system that moves along with the vortex. The origin of a two-coordinate system is placed in the undisturbed surface a fixed distance ahead of the vortex. (For numerical convenience we shall prescribe this distance at a later time.) The x-axis lies along the surface and the y-axis points upward. See Figure 1.

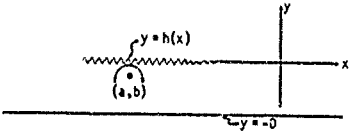


Figure 1

The flow is steady with respect to the moving coordinate system. We assume that the fluid is incompressible and inviscid and that the flow is irrotational. Formulating this problem in terms of the stream function ψ', we obtain the following problem which is the same as that considered in [3]:

$$(2.1)\quad \nabla^2\phi' = \phi'_{xx} + \phi'_{yy} = 0 \qquad \begin{cases} -\infty < x < \infty \\ -D < y < h(x) \end{cases}$$

$$(2.2)\quad \tfrac{1}{2}|\nabla\phi'|^2 + gy = \tfrac{1}{2}J^2 \qquad y = h(x),\ -\infty < x < \infty$$

$$(2.3)\quad \phi' = 0 \qquad y = h(x),\ -\infty < x < \infty$$

$$(2.4)\quad \psi' = UD \qquad y = -D,\ -\infty < x < \infty$$

$$(2.5)\quad \phi'_y \to -U \qquad \text{as } x \to \infty$$

$$(2.6)\quad \phi'_x \to 0 \qquad \text{as } x \to \infty$$

$$(2.7)\quad \phi'(x,y) = \phi'(x+\lambda,y) \qquad \text{as } x \to -\infty.$$

The above problem can be simplified by expressing ϕ' as $\psi + \Psi$ where Ψ is the stream function due to the vorticity, which we assume to be at point (a, b) and have strength τ. (Hence $\Psi = \frac{\tau}{4\pi}\log[(x-a)^2+(y-b)^2]$.) Problem (2.1) -(2.7) then becomes

$$(2.8)\quad \nabla^2\phi = 0 \qquad \begin{matrix} -\infty < x < \infty \\ -D < y < h(x) \end{matrix}$$

$$(2.9)\quad \tfrac{1}{2}|\nabla(\phi+\Psi)|^2 + gy = \tfrac{1}{2}U^2 \qquad \begin{cases} y = h(x) \\ -\infty < x < \infty \end{cases}$$

$$(2.10)\quad \phi(x,y) = -\Psi(x,y) \qquad y = h(x),\ -\infty < x < \infty$$

$$(2.11)\quad \phi(x,y) = UD - \Psi(x,y) \qquad y = -D,\ -\infty < x < \infty$$

$$(2.12)\quad \phi_y(x,y) \to -U - \Psi_y(x,y) \qquad \text{as } x \to \infty$$

$$(2.13)\quad \phi_x(x,y) \to -\Psi_x(x,y) \qquad \text{as } x \to \infty$$

$$(2.14)\quad \phi(x+\lambda,y) = \phi(x,y) + \frac{\tau}{4\pi}\{\log[(x-a)^2+(y-b)^2] - \log[(x+\lambda-a)^2+(y-b)^2]\} \qquad \text{as } x \to -\infty.$$

3. Numerical Formulation

To formulate the problem numerically, we first construct a uniform grid over the region of flow. We shall only consider the finite portion of this region as shown in Figure 2.

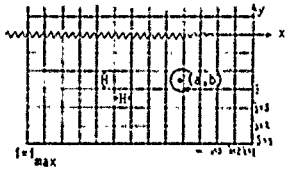


Figure 2

The grid points, denoted by (x_i, y_j) are numbered from the lower right-hand corner of the grid. We replace $h(x_i)$, $\phi(x_i,y_j)$ and $\phi(x_i,h(x_i))$ by the notation h_i, ϕ_{ij} and ϕ_{fs_i}, respectively.

Problem (2.8)-(2.14) must first be approximated on the finite region described in Figure 2. We use the same approximations as do von Kerczek and Salvesen in [3]. Hence, we apply boundary conditions (2.12) and (2.13) at $x = 0$ ($i = 1$) which take to be approximately $2\pi U^2/g$ upstream from the vortex. (Note that this determines the location of the origin.) We also substitute boundary condition (2.14) by an extrapolated value using the Lagrange three-point interpolation formula. This yields the numerical problem given below by equations (3.1)-(3.7). Equation (2.8) becomes

$$(3.1)\quad \phi^{n+1}_{ij} = \frac{\alpha\beta\gamma\delta}{(\gamma\delta+\alpha\beta)}\Big[\frac{\gamma\phi^{n+1}_{i,j-1} + \delta\phi^{n}_{i,j+1}}{(\gamma+\delta)\gamma\delta} + \frac{\delta\phi^{n+1}_{i-1,j} + \alpha\phi^{n}_{i+1,j}}{(\alpha+\beta)\alpha\beta}\Big] \quad \text{for } i=2,\ i_{max}-1 \quad j=2,\ j_{max}(i)-1$$

where α, β, γ and δ are as shown in Figure 3.

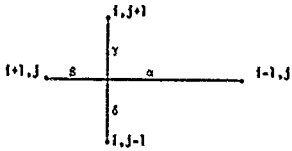


Figure 3

Note that when (i,j) has a regular star then $\alpha = \beta = \gamma = \delta = H$ and we obtain the usual Gauss-Seidel relaxation formula.

Boundary conditions (2.9)-(2.14) then become the following:

$$(3.2)\quad \tfrac{1}{2}|\nabla(\phi+\Psi)|^2 + gh_i = \tfrac{1}{2}U^2$$

where $\nabla(\phi+\Psi) = \left(\frac{1}{\cos\theta}\frac{\partial\phi}{\partial y}\right)_{1,h_1}$, θ is the angle between the vertical and the normal to the free surface, $\frac{1}{\cos\theta} = [1 + (\frac{dh}{dx})^2]^{1/2}$,

$(\frac{dh}{dx})_i = \frac{2}{3}(h_{i+1} - h_{i-1}) - \frac{1}{12}(h_{i+2} - h_{i-2})$,

$(\frac{\partial\phi}{\partial y})_{1,h_1} = \frac{\partial\psi}{\partial y}(x_i, h_i) + \frac{1}{H}[\Delta_0 + \frac{2p-1}{2}\Delta^2_0 + \frac{3p^2-6p+2}{6}\Delta^3_0]$

$\Delta_0 = \phi_{j_{max}} - \phi_{j_{max}-1}$, and $p = \gamma/H$ (γ as in Figure 3).

$$(3.3)\quad \phi_{fs_i} = -\Psi(x_i, h_i)$$

$$(3.4)\quad \phi_{i1} = UD - \Psi(x_i, -D)$$

$$(3.5)\quad \phi_{1j} = Uy_j - \Psi(0, y_j)$$

$$(3.6)\quad h_1 = h_2 = 0$$

$$(3.7)\quad \phi_{IMAX,j} = 3\phi_{IMAX-1,j} - 3\phi_{IMAX-2,j} + \phi_{IMAX-3,j}.$$

4. Multigrid (via Unigrid Simulation)

The so-called unigrid method is developed in [5] as a software simulation tool for

deciding on the feasibility of multigrid for a given application. Under general assumptions unigrid is theoretically equivalent to multigrid and therefore produces the the same results. However, although it is significantly more expensive in terms of numerical complexity, unigrid is vastly easier to implement than multigrid for a given application.

To describe unigrid for a specific case, suppose we write the stream function discretization (3.1) and (3.3)-(3.7) more generally as the problem

$$Av = f, \quad v \in R^n, \tag{4.1}$$

where A is an n x n real matrix and $f \in R^h$. We assume as in (3.1) and (3.3)-(3.7) that the problem stems from a two-dimensional discretization of a boundary value problem on region Ω with boundary $\partial\Omega$ and for convenience represent the components of v by the double subscripted $v_{i,j}$. By "i,j in Ω" we mean that i, j are subscripts specifying an interior grid point in Ω.

Many iterative methods for solving (3.1), (3.3)-(3.7) can be described as directional iterations in the following sense. With an approximation, ϕ, in R^n to v (such approximations will be represented by lower case), then a direction d in R^n is computed (the choice of direction d defines the method) and used to update ϕ in such a way that the new residual error is orthogonal to d. More precisely, let $r = Av - f$. Then an iteration with direction d is given by

$$\phi \leftarrow \phi - sd$$
$$s = \frac{\langle r, d\rangle}{\langle Ad, d\rangle}. \tag{4.2}$$

(Here we use the arrow to denote replacement in order to avoid the use of subscripts for iteration indices.) We write (4.2) in the compact form

$$\phi \leftarrow G_d(\phi).$$

One sweep of Gauss-Seidel applied to (4.1) can be written as several iterations of (4.2) covering all of the directions $d = e_{ij}$ in some sequence. Here, e_{ij} is the vector function of the interior grid points that is zero everywhere except at the i,j-th grid point. It is not difficult to see that these *spiked* directions do not reduce the error

$$E = \phi - v$$

very well. More precisely, the "oscillatory" error components are quickly reduced, but the "smoother" ones are not. The natural suggestion then is to also use smoother directions. To this end, suppose for simplicity that $n+2^m-1$ and define d^k_{ij} recursively by

$$d^m_{ij} = e_{ij}, \quad 1 \le i,j \le 2^m-1, \ i,j \text{ in } \Omega$$
$$d^k_{i,j} = \sum_{s,t=-1}^{1} 2^{-|t|-|s|} d^{k+1}_{2i+s,2j+t}, \tag{4.3}$$
$$1 \le i,j \le 2^k-1, \ 2^{m-k}(2^{m-k}j \text{ in } \Omega, \ 1 \le k \le m.$$

(These directions are actually intended for use with two-dimensional problems for which (4.1) is a discretization. Higher dimensional versions can be defined by combinations analogous to (4.3).) These directions are progressively smoother with decreasing k. Note that d^k_{ij} is the tent function centered at or near the midpoint of Ω.

With these directions, one cycle of unigrid on "level" m is now defined recursively in terms of parameters ν, μ by

Level 1 cycle: Perform one iteration via $\phi \leftarrow G_{d^1_{ij}}(\phi)$.

Level k cycle: Perform ν sweeps on directions d^k_{ij} where one sweep is to do $\phi \leftarrow G_{d^k_{ij}}(\phi)$ for all i,j in Ω in a specified order. Now perform μ cycles on level k - 1.

Conventional multigrid is a process of updating the fine grid approximation after many computations are performed on coarser levels m-1, m-2,...,1. It is easy to see [5] that multigrid is fully equivalent to unigrid if we define the fine-to-coarse grid transfer operator I^c_f in terms of the coarse-to-fine operator I^f_c as

$$I^c_f = I^f_c{}^T \tag{4.4}$$

and if the coarse grid operator, A_c, is defined in terms of the fine grid operator A_f as

$$A_c = I^c_f A_f I^f_c. \tag{4.5}$$

(For the finest level m, $A_f = A$.) For the way in which we have defined unigrid, I^f_c is linear interpolation although any reasonable interpolation process can be used with an analogous change in the definitions in (4.3). We call (4.4) and (4.5) the *variational conditions* because they are naturally satisfied by finite element-type discretizations and are advantageous designs for finite difference discretizations.

Unigrid is very easy to program. In fact, to modify an existing, possibly very complex software package (say one that solves a complex system of time dependent equations) that presently implements Gauss-Seidel (or SOR or some other relaxation scheme), one only has to modify the relaxation routine. Thus, design involves only computing the direction (which is equivalent but somewhat simpler than defining I^f_c); that is, the only real question is the choice of fine grid relaxation because interpolation is usually dictated by the discretization process that produced (3.1), (3.2)-(3.7). Implementing unigrid does not require defining any other grid transfer operators, scale factors, or coarse grid equations, and the design principles (4.4) and (4.5) are automatic. Moreover, unigrid does not impact the software data structure. If the directions are generated each time they are used, then no coarse grid information is stored. Finally, many algorithm

variations can be implemented and tested much more quickly and safely than with conventional multigrid. Once the design is completed, this multigrid "simulator" may be replaced by a careful implementation of conventional multigrid with the confidence that a good design was achieved and with the ability to use unigrid as a benchmark to ensure the correctness of the final product. (Unigrid is usually not suitable for production code because it is typically an order of magnitude more expensive than multigrid. Our intention here is to use it only in program development as a multigrid software simulator.)

So far in this section we have discussed the application of unigrid to the linear problem depicted in (4.1). In fact, unigrid (and, hence, multigrid) is well suited to the treatment of nonlinear problems of which the present application is an example. Specifically, the presence of the free boundary results in nonlinearity of (3.1)-(3.7) when the overall problem is considered. One obvious way to deal with this is in *the method of solution*, that is, by an iterative process that alternately improves the boundary and the stream function separately.

This is what is usually done in the solution of problems of this type. Note that the boundary adjustment phase of the algorithm has the potential of being much less expensive than the stream adjustment phase since it is essentially one-dimensional. The stream function adjustments are made by solving (3.1), (3.3)-(3.7) which we do by the linear version of unigrid described above.

A better approach to the free boundary problem is to apply a nonlinear version of multigrid directly to the complete problem. This would involve an FAS-type [1] version that would make most of the boundary adjustment on coarser grids, a further improvement in both computational complexity and robustness. Thus, the algorithm would be very inexpensive. One cycle would cost about the same as one cycle of multigrid applied to Laplaces equation in a fixed rectangle, and a full multigrid version (see the next section) of this approach would require only one cycle to produce an approximation below truncation error. Moreover, the algorithm would be more robust in the sense that convergence to the proper solution would be more assured and improper data and discretizations of (3.1)-(3.7) would be quickly discovered. Development of this approach is the next step in our research effort.

5. Mesh Continuation

The process of *mesh continuation* is similar to the *full multigrid* concept described in [1] and is essentially the same as the *mesh refinement* method treated in [4]. To describe it briefly, consider for the moment a sequence of nonlinear algebraic problems

$$F_k(U_k) = 0, \qquad (5.1)$$

$k = 1, 2, \ldots, m$, that are derived from the discretization of a two-dimensional differential operator problem on a (freely bounded) region Ω. Each F_k is defined in some (freely bounded) region of the Euclidean space R^2 and the number of unknowns, that is, elements of U_k is (free but) roughly proportional to h_k^{-2}, where h_k is the mesh spacing that is used to discretize Ω. We assume for simplicity and computational efficiency that $h_{k-1}=2h_k$ and that the solution of (5.1) is desired for $k=m$, the finest resolution.

(5.1) corresponds to our overall problem (3.1)-(3.7). Thus, we are solving (5.1) for $k=m$ by an iterative method that alternately adjusts the surface and the stream function. As with most nonlinear problems, it is critical to start with a good initial guess for U_m, not only for efficiency but to ensure that the iteration will even work. Because F_k (with fixed boundary) is used in the multigrid solution of the stream function phase of the algorithm, then (5.1) is available to us for use in a mesh continuation process for obtaining such a good guess for U_m.

Loosely speaking (see [4] for more detail), to start the iteration process on grid m, first solve the grid $m-1$ problem. The solution, U_{m-1}, to (5.1) with $k=m-1$ can then be interpolated via I_c^f to grid m to start the iteration there. Recursively, then, one first begins by solving (5.1) with $k=1$, using I_c^f to interpolate the result U_1 to start the iteration on (5.1) with $k=2$, and so on until grid m is reached and the iteration there has produced an acceptable approximation to U_m, the final desired result. This is the essence of mesh continuation, a simple but very effective process of using coarser problems ($k<m$) to provide good initial guesses for finer ones ($k+1$).

Note that grid 1 is probably so coarse that a very thorough but very inexpensive numerical investigation of this problem can be done to ensure that the proper solution is achieved. Since the solution U_k does not usually differ drastically from U_{k+1}, then this process represents a careful means for *tracking* the selected solution until the obtainable accuracy is met on grid m.

6. Results

The usual approach [3] for solving the free boundary value problem discretization (3.1)-(3.7) is to determine a grid on which the solution is desired and iterate alternately on the surface and the stream function. Because the problem is increasingly ill-conditioned with increasing numbers of grid points, this approach typically involves many inner loop iterations (e.g., relaxations on the stream function). Because this problem is often very nonlinear, this approach also typically involves many outer loop iterations (i.e., alternations between free surface and stream function adjustments).

Mesh continuation can be used to almost eliminate the effect of the nonlinearity so

that only one outer loop is usually needed to solve the fine grid problem. (The expense in solving the coarse grid problems does not total the work required on the finest grid.) Multigrid can be used to reduce the many inner loop iterations (the number increases dramatically with the number of fine grid points) down to an equivalent of less than ten. The combined process, which is called [1] full multigrid FAS, then has the effect of producing an approximate solution to (3.1)-(3.7) at a cost of less than ten relaxations on the finest grid! The accuracy in the result is to the level of accuracy obtainable on the finest grid.

Implementation of full multigrid FAS to our problem would be a serious undertaking. The main difficulties are in implementing the basic multigrid scheme that impacts the software structure of the application program and the FAS version that would apply to the free surface iterations as well as the stream function. However, testing the feasibility of multigrid can be done by using unigrid (to simulate the basic multigrid scheme) and mesh continuation (to simulate full multigrid). FAS can also be simulated by this approach, but the tests were not completed in time for publication. Nevertheless, the feasibility results described below demonstrate the dramatic improvement that multigrid can make in application to free surface (more generally, free boundary value) problems.

As a comparison problem (3.1)-(3.7) was solved using the trial free boundary method in conjunction with a Gauss-Seidel relaxation scheme. To make convergence both easier and cheaper we used a rough approximation of the linear wave solution as our initial guess. We used the solution found by von Kerczek and Salvesen [3] as our convergence criterion. In all test runs we used a stream velocity of 10 ft/sec, a depth of 10 ft, and a vortex strength of $\tau/2\pi = 1.15$.

The tests conducted using unigrid were aimed at showing that it is possible to drastically reduce the number of inner iterations that are necessary. The scheme used was to proceed exactly as we did in our straight Gauss-Seidel code. But after performing only a few relaxations on the fine grid we implement unigrid and then return to do a few final relaxations on the fine grid. The object of the initial fine grid relaxations is to take advantage of Gauss-Seidel when it works well. Returning to the fine grid after unigrid allowed us to compare the benefits of unigrid.

When we used H=1 and $i_{max} = 65$, 21 interior iterations of Gauss-Seidel were necessary to reduce the L^2 residual of ψ from 7.08136 to 0.00531. Using unigrid with three preliminary Gauss-Seidel iterations, unigrid (which when implemented as multigrid will be less work than one iteration on the fine mesh), and then three more Gauss-Seidel iterations reduced the L^2 residual of ψ from 7.08136 to 0.00281. That is, in less work than seven iterations unigrid was able to perform better than 21 Gauss-Seidel iterations.

With H=.5 and i_{max}=129, the results were similar. For example, unigrid plus six fine grid iterations reduced the L^2 residual from 1.03857 to 0.00340. The straight Gauss-Seidel iteration used 18 iterations to reduce the residual from 1.03857 to 0.00330. It should be noted that in the range of the fifteenth to the twentieth iteration Gauss-Seidel is slowing down rapidly. Unigrid, and hence multigrid, will continue at the same rate of convergence.

To test the benefits of grid continuation it is necessary to consider the complete solution of problem (3.1)-(3.7). Using the trial free boundary Gauss-Seidel method with i_{max}=129 and H=.5 six outer loop iterations were necessary to reduce the L^2 residuals of h and ψ to 0.00079 and 0.0042, respectively. This involved 293 inner iterations on ψ and 51 inner iterations on h. Using grid continuation with only two levels of grids (H=1 and i_{max}=65 and H=.5 and i_{max}=129) after one outer loop on the fine grid and only 44 inner iterations of ψ on the fine grid we have L^2 residuals of h and ψ 0.00022 and 0.00066, respectively. CPU time on Colorado State University's CYBER 172 was 142. seconds for the straight relaxation solution to 43. seconds for the grid continuation solution.

We then attempted to use three levels of grids: H=2, i_{max}=33; H=1, i_{max}=65; and H=.5, i_{max}=129. The results are again much better than straight Gauss-Seidel relaxation but not nearly as nice as we had hoped. After one outer loop on the fine grid which took 37 inner loop iterations the L^2 residuals of h and ψ were 0.0034 and 0.0032. Though more work must be done to explain this result we feel that the coarsest grid was too coarse for this problem.

7. Multigrid Potential and Future Work

Unigrid is significantly more expensive per operation than multigrid, but it has identical numerical properties. It is simply an easier but more expensive way to implement multigrid. The results of Section 6 clearly show that mesh-continuation-unigrid is very effective in solving our model problem. Full multigrid FAS would then be even more effective.

Multigrid has demonstrated (cf. [6]) its potential recently in a very large number of applications. For elliptic boundary value problems with irregular regions, multigrid has been shown to work with the efficiency that it exhibits in the model Poisson problems on rectangular domains. So at the veryleast, multigrid will no doubt be effective in solving the inner loop stream function problems that generalize our model. Moreover, mesh continuation will clearly be as effective in solving very general free surface problems unless the surface is so badly behaved that any coarser mesh cannot *begin* to resolve it. Even for time-dependent free surface problems where good initial guesses are provided from the previous time step, mesh continuation is advantageous if it is applied to the residual equations computed on the finest grid. In fact, multigrid

can usually be used to even greater computational savings for time dependent as opposed to static problems (cf. [4]).

The only open question of potential theoretical relates to the FAS multigrid scheme of treating the entire problem. Thus, the nonlinearity is reflected and treated on all grids in the coarse grid correction phase of multigrid. Hence, many of the changes now being done to the boundary would be relegated to changes in the coarse grid image of the fine grid boundary. There is no apparent reason why this will not lead to even greater efficiency in the solution process. Perhaps more importantly, it will open up the application to the full power of FAS (cf. [4]) for use of features such as truncation error estimation (to determine how accurate the approximation is to the *actual solution* of (2.8)-(2.14)), adaptive grid refinement (to increase accuracy in parts of Ω where it is necessary), small storage schemes (a sophisticated approach for solving a problem on a very fine grid without using internal or external storage), and time-dependent schemes (where great advantage is taken of the use of the previous time step computations in order to avoid find grid computations over many subsequent time steps). A fully implemented multigrid scheme applied to (2.8)-(2.14) and more general free surface problems will offer many features in addition to efficiency from which the numerical solution of these problems will benefit.

Some of the specific work to be pursued by the authors include: (i) studying the effect of a bad initial guess on the grid continuation scheme; (ii) studying alternative methods for moving the trial boundary, (iii) develop an FAS multigrid scheme for the entire problem (2.8)-(2.14); (iv) develop an adaptive grid refinement that is particularly sensitive to the boundary calculations; and (v) test multigrid techniques on a time dependent problem. (Specifically, we shall develop a multigrid scheme to solve the problem of potential flow about an accelerated circular cylinder (see [21].)

References

[1] A.Brandt, "Multilevel adaptive solutions to boundary value problems", Math.Comp., 31 (1977), 333-390.

[2] J.Haussling and P.M.Coleman, "Nonlinear Water Waves Generated by An Accelerating Circular Cylinder", J.Fluid Mechanics, vol.v., part 4 (1974).

[3] C.H.von Kerczek and N.Salvesen, "Numerical Solutions of Two-dimensional Nonlinear Wave Problems", ONR 10th Symposium on Naval Hydrodynamics, MIT, June, 1974.

[4] S.McCormick, "Mesh refinement methods for $Ax = \lambda Bx$", Math.Comp., 36 (1981), 485-498.

[5] S.McCormick and J.Ruge, "Unigrid for multigrid simulation", submitted.

[6] "Multigrid bibliography", Multigrid Newsletter 1 (April, 1981).

[7] Joanna Schot and Nils Salvesen, eds., Proc. of the First Int'l. Conf. on Numerical Ship Hydrodynamics, David W. Taylor Naval Ship Research and Development Center, Bethesda, MD (1975).

ADVANCED NUMERICAL METHODS HYDROFOIL SYSTEM DESIGN AND EXPERIMENTAL VERIFICATION

W. M. Feifel
Boeing Marine Systems
Seattle, Washington

Abstract

The forward foil system for the Boeing Jetfoil 929-115 hydrofoil ship has been designed applying advanced numerical methods. Compared to conventional designs the structurally and hydrodynamically optimized configuration achieved improved hydrodynamic performance combined with a significant increase in structural fatigue life and a 1,500-lb weight reduction. The hydrodynamic design utilized two- and three-dimensional potential-flow panel methods and an induced-drag optimization scheme. Generally, good agreement has been found between theoretical prediction and full- and model-scale observations in the fully wetted flow regime.

In sea state all foil systems at times encounter partially cavitated or ventilated flow conditions which eventually limit ship operation. The aft foil operating environment is severely affected by the wake shed from the canard foil. Present theory cannot address these phenomena and development of new methods is urgently needed.

Background

Boeing Jetfoil hydrofoil ships feature fully submerged foils with flaps actuated by an automatic stability and control system to provide a smooth ride at speeds up to 45 knots in sea state 4. Jetfoil model 929-100 has been in commercial service since 1975. Operational experience indicated the desire for a craft with higher payload capacity and a foil system structure designed for increased fatigue life. Advanced numerical methods were used to design this improved craft, which is designated Jetfoil model 929-115.

The significant hydrodynamic configuration changes between models 929-100 and 929-115 are shown in Figures 1 and 2. The model 929-100 forward foil has a rectangular planform and a conventional 7.5% thick foil section. A stab-sided pod forms the intersection between the foil and the strut. The model 929-115 forward foil uses a tapered planform with unique foil section shapes varying in thickness from 8.75 to 6.5%. These foil section shapes are optimized for best structural and hydrodynamic characteristics. The forward strut chord was lengthened from 45 to 50 in. The strut section thickness was increased from 12 to 13.5%, and the spanwise thickness distribution was changed for structural reasons. The section shape was especially designed for improved cavitation characteristics to delay the onset of ventilation under yawed conditions.

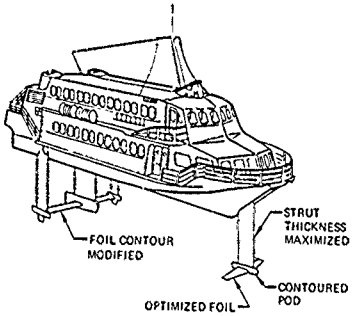


Figure 1. Model 929 115 Jetfoil Showing Principal Hydrodynamic Changes From Model 929-100

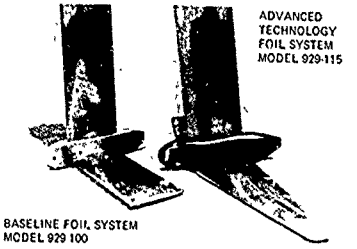


Figure 2. Forward Foil System

The model 929-115 dumbbell-shaped pod was contoured using three-dimensional methods to minimize perturbation of chordwise pressure distribution caused by mutual interference between foil system components. This allowed increased strut and foil thickness. The pod was placed so that the lower surface of the foil, which carries the highest tension loads, was left exposed for easy inspection.

Minimal structural changes were made to the aft foil system. Foil planform, strut shape, and pod shapes remained virtually unchanged. The basic foil shape was slightly modified from that of Jetfoil 929-100 by increasing the camber and changing the chordwise thickness distribution.

Numerical Methods Used

Numerical procedures were applied throughout the foil design and for the control of the foil manufacturing process. The hydrodynamic shapes were developed using two-dimensional and three-dimensional potential-flow programs. Three-dimensional potential-flow programs were used for the preliminary design studies and for validation of the final configuration. Most of the foil detail design was accomplished by two-dimensional modeling. The pod was designed using a combination of two- and three-dimensional potential-flow methods. All hydrodynamic computations were based on panel-type influence coefficient methods.

Of the three-dimensional methods only the one employed for most of the preliminary design studies shall be described in more detail because of its unique features. This computer code is referred to as the A372 program.

Boeing A372 Computer Program

The A372 computer program (ref. 1, 2) utilizes vortex lattices (Fig. 3) and source panels of constant strength to model three-dimensional configurations of arbitrary shape in potential flow. Ground effect or free-surface effect is simulated by the method of

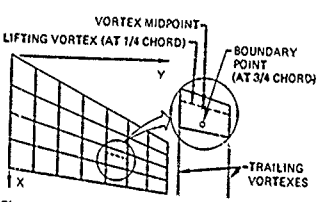


Figure 3. Division of Surface Into Panels and Location of Vortexes and Control Points in the A372 Computer Program

images. The program can be used in two modes. The analysis mode determines the flow properties for a fully defined configuration with only boundary conditions to be satisfied. In the optimizing or design mode portions of the configuration are not rigidly prescribed; instead, the program determines the orientation required for some of the panels to satisfy a set of force and/or moment constraint conditions while, at the same time, minimizing the induced drag. The induced drag is computed either by a near-field algorithm or by the usually more accurate far-field (Trefftz plane) formulation.

Whereas vortex lattice methods are widely applied for configuration analysis, their usefulness for configuration design and induced-drag minimization is not generally recognized. This is a unique feature of the A372 code. The problem can be stated as follows: Determine the configuration which yields minimum induced drag while meeting certain design requirements, such as prescribed lift, pitching moment, or rigidly defined geometry. In mathematics this amounts to finding the extremum of a function (the induced drag) subject to a set of constraints. Such a problem can be solved by the method of Lagrangian multipliers.

Induced-Drag Function. By applying Biot-Savart's law the forces $\vec{F}_j$ acting on each of the configuration bound vortexes are determined using either a near-field or far-field (Trefftz plane) formulation.

The force vector $\vec{F}_j$ comprises the panel drag components Dj and the lift vector $\vec{L}_j$, which by definition is oriented normal to the free-stream vector $\vec{u}_\infty$.

The induced drag of a whole configuration with n panels can be expressed as a quadratic function of all the panel vortex strengths γ in the form of the double sum:

$$D(\gamma_1 \ldots \gamma_n) = \sum_{j=1}^{n} \gamma_j \sum_{i=1}^{n} d_{ji}\, \gamma_i$$

The induced-drag influence coefficients d_{ji} contain only geometrical terms describing the drag force experienced by the panel j due to the panel i when their horseshoe vortexes are of unit strength. For a non-trivial minimum induced-drag solution, at least one constraint must be introduced.

Constraint Conditions. There are a large number of different constraint conditions, C, that can be imposed on a minimum induced-drag problem. In the present method, any meaningful combination of the following constraints may be specified:

1. Boundary conditions: The boundary condition for the panel j can be written in the generalized form

$$C(\gamma_1, \gamma_2 \ldots \gamma_n, \Delta\phi_j) = \sum_{i=1}^{n} \gamma_i f_{ji} - \Delta\phi_j a_j - \vec{N}_j \cdot \vec{u}_\infty = 0$$

where f_{ji} is the boundary-point influence coefficient indicating the velocity induced by a unit strength singularity γ_i parallel to the surface normal vector $\vec{N}_j$ on panel j; $\Delta\phi_j$ is the unknown rotation angle that may be required to reorient the panel j in order to satisfy the flow tangency at its boundary point in the design mode; a_j is the panel-reorientation influence coefficient that indicates the change in $\vec{N}_j \cdot \vec{u}_\infty$ when the panel j is rotated by $\Delta\phi = 1^\circ$ about the axis $\vec{R}_j$ as shown in Figure 4; and $\vec{u}_\infty$ is the free-stream velocity vector. The panel-reorientation influence coefficients are linearized with respect to the initial panel location. If the boundary condition has to be satisfied at the original position of the panel (analysis mode), then $\Delta\phi_j$ is zero.

2. Relationships between unknown singularities: The strength of certain vortexes or a relationship between groups of vortexes can be specified.

3. Relationships between the panel-reorientation parameters: The movements of panels or of groups of panels are controlled by the constraint equations that establish relationships between the unknowns $\Delta\phi$.

4. Force or moment relationships between groups of panels. Forces and moments due to individual panels or groups of panels are prescribed by equations of the following type:

$$C(Y_1,\ldots,Y_n) = \sum_{i=1}^{n} g_i h_j Y_i + g_{n+1} = 0$$

where the influence coefficient h_j indicates the force or moment of panel i for $Y_j=1$. The weights g_i can be assigned to describe the particular constraint relationship.

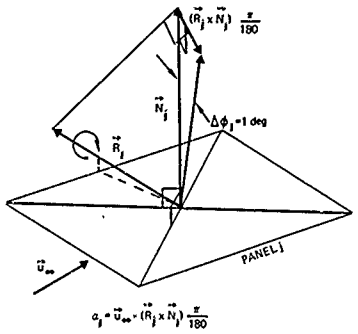


Figure 4. Panel Reorientation Influence Coefficient a_j Obtained by Tilting the Surface Normal $\vec{N}_j$ About the Axis $\vec{R}_j$

Minimum Drag Under Constraint Conditions. The induced-drag function D and the constraints C may be combined into a new quadratic function:

$$G(Y_1,\ldots Y_n,\Delta\phi_1,\ldots\Delta\phi_n,\lambda_1,\ldots\lambda_m) = D(Y_1,\ldots Y_n) + \sum_{i=1}^{m} \lambda_i C_i$$

where λ_i are the Lagrangian multipliers for m constraints imposed. A necessary requirement for the induced drag to be a minimum is that all the partial derivatives of G be zero. Differentiating the function G with respect to all its variables Y_i through λ_m yields a system of simultaneous linear equations for unknowns $Y, \Delta\phi$, and λ. Solution of this system of equations essentially completes the configuration analysis-optimization-design process, unless an iteration is required to update some of the slightly nonlinear influence coefficients of constraint equations or if the redesigned geometry deviates too much from the starting configuration.

For prudently selected boundary point locations the A372 code has been found to give reliable answers. Figure 5 shows the optimum circulation distribution on a wing with a 20% end plate as obtained by A372 with a single lifting line but using a different number of spanwise panels. The agreement with the exact solution of ref. 3 is excellent, except in the corner formed between the wing and the tip fin. There the vortex lattice solution obtained with 25 panels per half-wing deviates slightly from the exact solution. As shown in Figure 6, the induced-drag efficiency factors indicated by the vortex lattice method and by the exact solution are practically identical for this particular configuration, which is similar to the Jetfoil aft foil system.

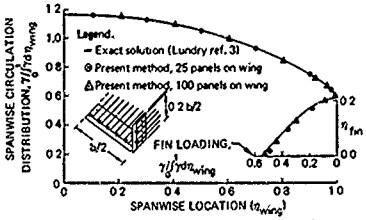


Figure 5. Optimum Load Distribution About a Wing With an End Plate

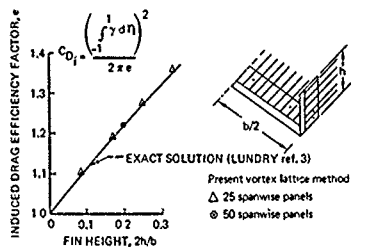


Figure 6. Induced Drag Efficiency Factor of End-Plated Wings With Optimum Load Distribution

Boeing A230 Computer Program

The Boeing A230 computer program is a general boundary-value problem solver that uses constant-strength doublet and source panels distributed on the configuration boundary surfaces and interiors. The panel singularity strengths are determined by solving of a set of linear equations satisfying boundary conditions that generally are specified at the panel centroids. Images are used for problems involving symmetry, ground effect, or free-surface effect. The A230 program is basically the outgrowth of the work reported in ref. 4 and includes a full complement of utility routines for geometry processing as well as computer graphics for display of input data and computational results. The output data available are:

1. Pressures and velocities at all boundary points.
2. Three-component forces and moments on each source-paneled surface, obtained from integrated surface pressures.
3. Velocities and pressures at any point in the flow field.
4. Streamlines, both on surfaces and in the field, traced either upstream or downstream.
5. Isobars on the surfaces.

Figure 7 shows the Jetfoil 929-100 foil system, including the water inlet paneled for A230 analysis (ref. 5). The paneling layout is a compromise between details that can be modeled and computing costs. About 2000 panels were used for this analysis.

Boeing A456 Computer Program

The A456 two-dimensional mixed-boundary-condi-

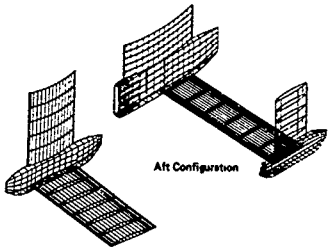


Figure 7. Potential-Flow Modeling of the Jetfoil Forward and Aft Configurations in the A230 Panel Method

tion airfoil design program is a subset of the three-dimensional PANAIR advanced panel method that is under development by The Boeing Company under NASA contract (ref. 6). PANAIR uses doublet and source panels with quadratically varying singularity strengths. Both analysis (Neumann) and design (Dirichlet) boundary conditions or combinations of the above (Poincare) can be treated by the program.

The design boundary conditions usually consist of tangential velocity components prescribed at a first guess for the configuration geometry. In addition, geometry closure conditions are imposed. The resultant potential-flow solution produces velocities normal to some of the panel surfaces. These normal velocities are used to update the panel locations. This process usually converges after a few cycles. A typical result obtained with A456 is shown in Figure 8, where part of the foil section upper surface was redesigned to yield a modified pressure distribution at the aft end, while retaining most of the original section shape.

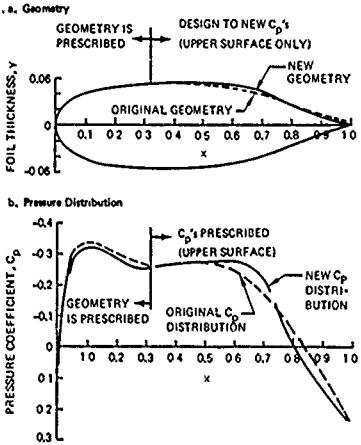


Figure 8. Modification of a Foil Section Using the A456 Poincare Boundary Condition Program

Boeing A304 Computer Program

Computer program A304 (ref. 7) calculates solutions for the potential flow about multiple two-dimensional bodies of arbitrary shape. It uses an influence-coefficient method, where the bodies are approximated by a polygon of straight panels carrying a linearly varying vortex and/or source distribution. Velocities, pressures, and forces acting on the configuration surfaces are calculated. Part of the program is a comprehensive geometry-manipulation subroutine. It can translate, rotate, scale, adjust camber and thickness, repanel, and smooth the surface of each configuration element, and generate the geometry for foils with a plane trailing edge flap of prescribed flap deflection angle. A structures program module computes the location of the principal axis, moments of inertia, and section modulus for a prescribed portion of a solid or a thin-wall foil section.

Foil System Analysis and Design

Extensive operational experience with Jetfoil 929-100 and the resulting calibration and validation of analytical methods guided the redesign of the foil system for Jetfoil 929-115. Jetfoils are designed to operate in sea state at approximately 43 knots. The objective of the new design was to accommodate the increase in ship weight and improve the structural characteristics of the foil system without degrading hydrodynamic performance. Emphasis in the hydrodynamic design of the new front foil was placed therefore on minimizing the induced drag and maximizing the cavitation-free angle of attack range at design speed and lift.

Induced-Drag Analysis

During cruise conditions approximately 30% of the Jetfoil drag is foil-system induced drag. Exact assessment of the induced drag is a difficult task due to the strong interference of the canard wake with the aft foil system. Especially critical is the location of the canard trailing vortexes relative to the aft foil system, which depends greatly on the amount of vortex rollup that takes place between the forward and aft foil system. Reliable prediction of vortex rollup is beyond present capabilities. Therefore, a potential-flow analysis was conducted with the canard wake located 0.3 ft and 4 ft, respectively, below the aft foil. The constraint conditions common to all cases analyzed are that the configuration lift coefficient C_L is 0.3 and that one-third of the ship's weight is carried by the canard.

The configuration spanwise load distributions yielding minimum induced drag were determined with the A372 computer program by Trefftz plane analysis. Two additional independent constraints were imposed: (1) The canard, aft foil, and struts are free to be warped for minimum induced drag. (2) The complete foil system is rigid and has no twist.

The nearer the canard wake is located to the aft foil the more the aft foil spanwise load distribution deviates from the load distribution of the isolated aft foil load. The outboard portions of the aft foil are highly loaded for the minimum induced-drag condition, as seen in Figure 9. In the case of a close-coupled forward foil wake, the trough in the aft foil load distribution is shaped such that if the canard load distribution is added, the combined load distribution approaches the minimum-induced-drag condition for the foil system, as it would be predicted by Munk's stagger

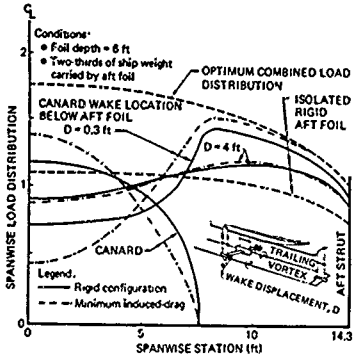


Figure 9. Spanwise Load Distributions for Jetfoil 929-100 Computed by A372

theorem (ref. 8). For minimum induced drag, the forward foil load distribution is more triangular shaped than the one for a rigid untwisted canard of rectangular planform, an indication that a tapered canard planform would be more advantageous. In Figure 10, configuration minimum induced drag is seen to initially increase when the canard wake is moved below the aft foil. This

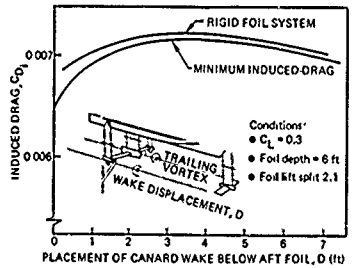


Figure 10 A372-Computed Dependance of Jetfoil 929-100 Induced Drag on Location of Canard Trailing-Vortex System Relative to Aft Foil

is due to the loss of the "flow-straightening effect" of the aft foil that recoups some of the kinetic energy contained in the vortex wake shed from the highly loaded canard wing. When the canard wake is even further lowered the induced drag decreases as both foils approach their individual optimum load conditions. This is also predicted by conventional biplane theory. The initial increase in induced drag is an indication that the canard span loading is too high and that the end-plated aft foil is a much more efficient lift producer.

This analysis led to the conclusion that the model 929-115 forward foil should be tapered and have increased span. Foil tapering is advantageous from structural considerations while a larger span tends to increase foil weight. Lengthy studies were performed to arrive at the Jetfoil 929-115 canard planform.

The proposed model 929-115 configuration was analyzed in the A372 program to determine its induced drag and to assess the aft foil characteristics. Figure 11 shows that a significant reduction in induced drag was predicted. Comparing the aft foil load distribution of the rigid foil system (Fig. 9) with that of model 929-115 (Fig. 12) indicated that only minor changes to the aft foil hydrodynamic characteristics should be expected and that aft foil performance would be satisfactory.

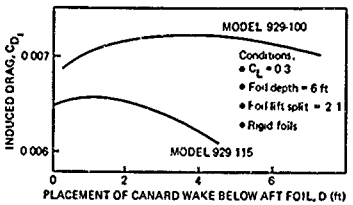


Figure 11. A372 Computed Dependence of Jetfoils 929-100 and 929-115 Induced Drag on Canard Wake Location

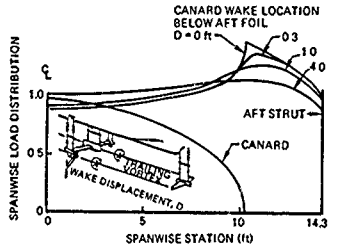


Figure 12. Spanwise Load Distribution for Jetfoil 929-115 Computed by A372 for Rigid Foil System at 6-ft Depth and 1:2 Lift Division Between Canard and Aft Foil

Delay of Cavitation Onset

Avoidance of cavitation was a prime concern in the shaping of hydrodynamic contours. At a speed of 45 kn and a foil depth of 6 ft in 59° F seawater, the calculated pressure coefficient for the onset of vaporous cavitation was -0.43. This value was used as the minimum allowable pressure coefficient for the foil design.

Canard Design. Structural analysis revealed the possibility of a 1500-lb weight reduction by using a thicker, built-up forward foil rather than the thin solid foil required by conventional hydrodynamic technology. For a built-up foil, a minimum section thickness ratio of 8.5% is necessary at the structurally critical spanwise station, Y = 41 inches. Detailed analysis had indicated that for this particular foil configuration the stress level is highest at station 41.

The canard spanwise variation of the section lift coefficient was obtained from three-dimensional potential-flow analysis. At spanwise station Y = 41, the section lift coefficient and the canard coefficient happen to be practically identical (Fig. 13). For this reason

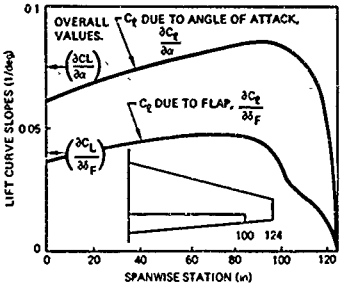


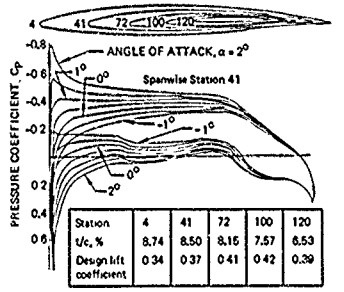
Figure 13. Variation of Jetfoil 929-115 Forward Foil Section Lift With Angle of Attack and Flap Deflection

the section at station 41 was used to initially characterize the behavior of the foil.

Parametric charts based on NACA 16-series (ref. 9) data and linearized airfoil theory guided the preliminary design of the new foil sections. For a speed of 45 kn and a section thickness of 8.5%, a lift coefficient of up to 0.35 was predicted before the onset of cavitation. This was judged sufficient for the ship's lift/speed operating envelope.

Using the A456 mixed-boundary-condition computer program, an 8.5% thick section was designed to provide a low-pressure level, limited by cavitation considerations, over a large portion of the foil upper surface, as indicated in Figure 14. The first 60% of the lower surface was shaped mainly for optimum structural characteristics. For additional lift, a region of high pressure was provided on the aft lower surface of the section. The resulting section shapes had the additional advantage of bringing the fatigue-critical lower surface in the flap hinge region (75% chord) closer to the structural neutral axis, thereby lowering the local stress level.

For an upper-surface minimum pressure coefficient of -0.43, a maximum cavitation-free lift coefficient of 0.37 was achieved. Under normal ship operation the lift coefficient is well below that maximum. The section was designed for a lift coefficient higher than normally experienced in cruise to provide a cavitation-free margin for increased ship weight or for accelerated flight conditions such as climbing waves or tight turns.



Station	4	41	72	100	120
t/c, %	8.74	8.50	8.15	7.57	6.53
Design lift coefficient	0.34	0.37	0.41	0.42	0.39

Figure 14 Forward Foil Section Shapes and Characteristic Chordwise Pressure Distribution

The next task was to adapt this new two-dimensional section to the requirements of a three-dimensional foil. Outboard of station 41, the section local lift coefficients are as much as 16% higher than the overall foil lift coefficient, while inboard section lift coefficients are lower, as shown in Figure 13. Section thickness can be increased as the lift coefficient is lowered. Fortunately, this trend coincides with structural requirements. Near the foil root, where the wing bending moment is the highest, the thickest section is required. Conversely, thinner sections may be used farther outboard, where local lift coefficients are higher and bending moments are lower. Figure 14 shows the thickness ratios and the design lift coefficients selected for the sections defining the canard. The camber of these sections varies with design lift coefficient. The three-dimensional A372 potential-flow program was employed for the initial camber-line design process. For this purpose, the canard was represented by a network of panels. A canard lift coefficient was prescribed and for each chordwise column of panels, a weighting function describing the chordwise load distribution was defined. The program calculated the panel orientation (slope) required to achieve this load distribution. Chordwise integration of the panel slopes yielded section camberline shape and angle of attack. An appropriate thickness distribution was applied to each of the section camberlines according to linearized airfoil theory. The resulting section shapes were then analyzed in two-dimensional potential-flow program A304. Where necessary, portions of the chordwise velocity distribution were changed and a modified section shape was determined using the mixed-boundary-condition program A456. Figure 14 shows the final foil-defining sections in their installed attitude, which includes the geometric twist necessary to obtain a hydrodynamically untwisted foil.

Pod Design. The canard and a newly developed 13.5% thick strut with the intersection formed by a slab-sided pod were analyzed with the A230 panel method, as reported in ref. 5. The results revealed unacceptably high velocities in the strut-pod-foil junction region. Using strip theory in conjunction with the two-dimensional A456 design program and A230 analysis the pod was recontoured to obtain a three-dimensional, dumbbell shape. Figure 15 shows the pressure distributions about critical regions of strut, foil, and pod before and after the redesign. The recontouring

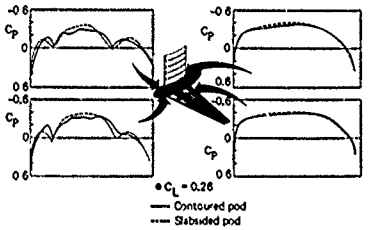


Figure 15. A230 Computed Pressure Increase in Strut Foil Junction Due to Three-Dimensional Pod Contouring

increased the cavitation-free operating speed range by about 2 kn, or conversely allowed a strut and foil root chord thickness increase of Δ t/c = 1%.

Sea State Analysis

The Jetfoil hydrofoil ship is designed to operate in sea state. Traversing a wave, the foil system experiences large angle-of-attack excursions due to the wave orbital motion. The automatic control system commands flap deflections to maintain constant dynamic lift. Neglecting the wave-induced horizontal velocity components the foil operates at a constant lift coefficient. Because of the high cost of three-dimensional computer analysis the two-dimensional potential-flow analysis program A304 was employed to explore foil off-design characteristics (at station spanwise 41) for various angles of attack and flap deflection angles. At constant lift, downward flap deflections cause a pressure peak at the upper-surface hinge line, while upward flap deflections cause a foil leading-edge pressure peak, as shown in Figure 16. Incipient cavitation is predicted to occur when the critical cavitation pressure level is reached anywhere on the section.

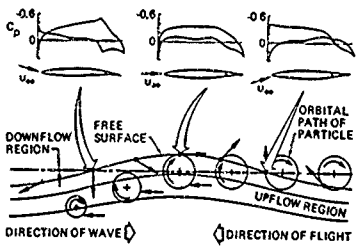


Figure 16 Potential-Flow Pressure Distribution About Section Station 41 During a Wave Traverse at Constant Lift

Experimental Verification

Jetfoil 929-115 ships have undergone extensive sea-trial evaluation since their introduction in 1978. In addition a model scale test has been conducted in 1979 in the Berlin Model Basin to assess the capability of laboratory experiments to simulate sea-trial experience. Comparisons between theoretical predictions and experimental data have been performed to establish the validity of current design techniques.

Sea-Trial Flow Observations

Engineering sea trials have been conducted with Jetfoil 929-115 in 1978. A summary of the results has been published in ref. 10.

Canard Foil. The forward foil was observed during steady-state operation over an angle of attack range of 5 deg. Except for a very small amount of cavitation due to the gap at the flap hinge region and the pod-foil intersection, the forward foil system was cavitation free in calm water up to speeds of 48 kn, as predicted by theory. Cavitation was observed in sea state 4 as expected. The observed progression of cavitation over the foil surface is in fair agreement with the isobar pattern generated by the A230 potential flow program, as can be seen by comparing Figures 17 and 18.

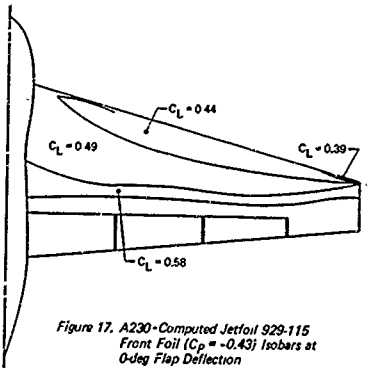


Figure 17. A230-Computed Jetfoil 929-115 Front Foil (C_p = -0.43) Isobars at 0-deg Flap Deflection



Figure 18. Forward Foil Cavitation Pattern for Jetfoil 929-115, Obtained in Sea Trials at 0.43 Cavitation Number

Cavitation pattern, ship pitch angle, flap-deflection angle, and ship speed are related as shown in Figure 19. The theoretically predicted incipient cavitation limit line approximately encloses the cavitation-free regime and was derived from two-dimensional potential-flow analysis of the section at canard spanwise station Y = 41. Flap deflections observed during operations of Jetfoil 929-115 in upper sea state 4 are also shown in Figure 19. These flap excursions, representing two standard deviations of the observed flap travel, are greater than the calculated cavitation-free flap-deflection limits of the sections. This results in leading-edge and hinge-line cavitation on the forward foil in sea state 4 for about 20% of the time.

Leading-edge cavitation extending over more than 40% foil chord was observed and caused no ship vibrations or measurable effects on performance. Leading-edge cavitation extending aft to the hinge line became unstable. This flow instability caused high-amplitude ship vibrations. At lower angles of attack, associated with positive flap deflections, cavitation appeared on the flaps, beginning near the flap hinge line. This cavitation was not accompanied by vibration but contributed to reduced flap effectiveness. These phenomena limit the operation of the ship in high sea state and cannot be treated with the analytical methods available.

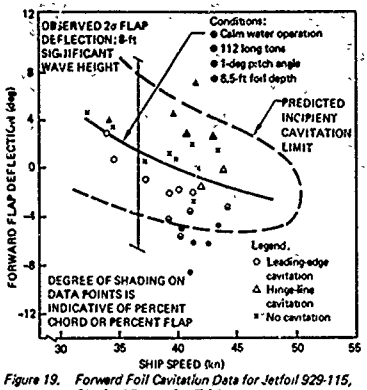


Figure 19. Forward Foil Cavitation Data for Jetfoil 929-115, Obtained During Sea Trials

Aft Foil. Foilborne observations of the aft foil system are more difficult because of the spray shed by the canard strut. The wake of the canard creates a highly nonuniform inflow field to the aft foil which causes the outboard third of the aft foil to be highly loaded and therefore cavitation prone. As predicted by theory, there was little difference between the cavitation characteristics of model 100 and model 115 aft foil systems.

Comparisons between sea-trial and theoretical results indicate the need for more advanced analysis techniques. The aft foil system of 929-100 was analyzed in the A230 program with the canard wake assumed to be located 1 ft below the aft foil. The predicted isobar contours indicate that cavitation is expected near the outboard pod root chord at cruise (Fig. 20). Actual observation of the aft foil at cruise shows the expected root chord cavitation (Fig. 21). But, cavitation is also experienced midspan due to the forward foil tip vortex upwash. This cavitation was not predicted. In Figure 21 the canard tip vortex core is seen passing over the top of the foil adjacent to the region of midspan cavitation.

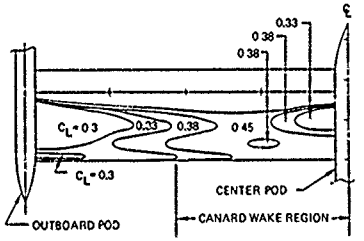


Figure 20. Jetfoil 929-100 Aft Foil Isobars for C_p = -0.43 Predicted by A230 Potential Flow Analysis



Figure 21. Jetfoil 929-100 Outboard Aft Foil at 0.43 Cavitation Number, Cavitation Pattern Obtained During Sea Trials

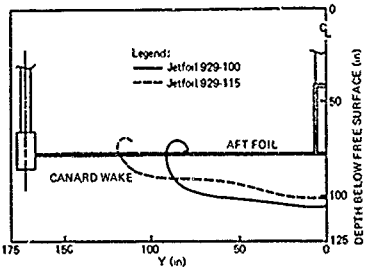


Figure 22. Rolled Up Canard Wake in the Vicinity of the Aft Foil (Reference 11)

A more detailed investigation of the front wake has been carried out on the computer algorithm of ref. 11. Free surface effects are not accounted for. In this program, the spanwise load distribution obtained from A230 was represented by 40 discrete vortexes distributed along the semispan according to a cosine spacing with maximum density at the tip. Calculated canard wake cross-sectional profiles in the vicinity of the aft foil are shown in Figure 22. The figure describes closely the observed wake rollup. This complex flow field, with the front wake providing a very close "coupling" between the front and aft configurations, cannot be properly simulated with the modeling techniques of the A230 computer system.

The interaction of the forward foil tip vortex and wake with the aft foil system poses a critical problem in the design and prediction of performance of the aft foil system. For this purpose, effects of canard-wake vortex rollup, vortex dissipation, and wake location, including the Froude-dependent depression of the free surface, need to be known. A detailed analysis of the aft foil pressure distribution in the vicinity of the forward foil wake must include a simulation of the Rankine-type movement of the fluid in the center of the tip vortex core shed by the canard.

Model Test

A one-sixth-scale model of the forward foil was tested in the Berlin Model Basin (VWS) depressurized free-surface circulating-water tank at full-scale Froude and cavitation numbers with Reynolds number greater than 1 million. The foil was evaluated from a fully wetted to fully cavitated flow condition. The experiment was especially formulated to obtain the nonlinear hydrodynamic characteristics induced by cavitation and ventilation that cannot be treated adequately by the analytical methods available. Six-component forces and moments and model surface pressures were measured over a range of simulated ship foilborne flow conditions from takeoff to cruise. Model pitch, yaw, flap deflection, and heave were systematically varied to define the foil system hydrodynamic characteristics. Details on the test procedures and typical test results have been published in ref. 12.

Agreement between predictions based on potential-flow theory and the test results is good in noncavitating flow, as is demonstrated in the following examples. Figure 23 shows the measured lift curve for the forward foil at 5.7 Froude number, 0.7 cavitation number, and a foil submergence of 2 chord (simulated ship speed of 35 kn). The lift curve slope is slightly overpredicted by

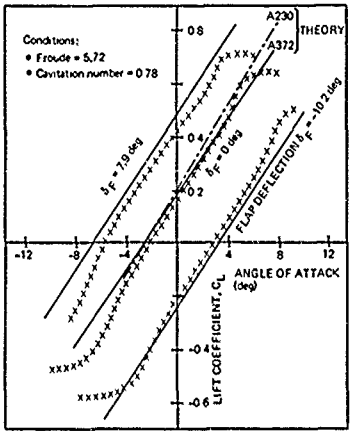


Figure 23 Predicted and Measured Lift for Jetfoil 929 115 1/6-Scale Canard Foil System at Two Chord Submergence.

the A230 program, which accounts for foil thickness. Analysis of the foil camber line only using the A372 vortex lattice method yields a lower lift-curve slope, which is in better agreement with the experiment. It is a fortuitus coincidence that the reduction in the slope of the foil lift curve due to the development of the boundary layer is of the same magnitude as the reduction in lift in potential-flow theory when thickness effects are neglected. Potential-flow theory expectedly overpredicts the change in lift due to flap deflection. The discrepancy is larger at the positive flap setting and has been identified to be due to cavitation at the flap upper-surface hinge line. The onset of leading-edge cavitation is marked by a rapid change in lift, which is a result of the change in effective foil camber due to the cavity. Present analytical methods do not model these cavitation phenomena.

A comparison between measured and predicted forward foil side-force characteristics at a simulated ship speed of 42 kn is shown in Figure 24. The

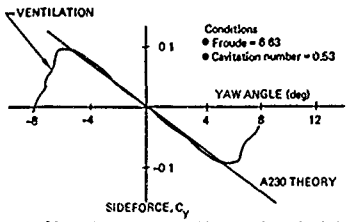


Figure 24. Predicted and Measured Sideforce for Jetfoil 929-115 1/6-Scale Canard Foil System at Two-Chord Submergence and 1.5-deg Angle of Attack

agreement is very good up to the point where force characteristics are abruptly changed by cavitation-induced strut ventilation. This unpredicted abrupt drop in side force can be critical to boat operation in sea state.

In sea-state operation, foil submergence varies as the foil traverses through waves. This was simulated in the model test by slowly lowering the model into the water. Figure 25 shows the resulting variation of lift at constant angle of attack. As the foil lower surface touches the water a small download is generated. Positive lift is generated as soon as the flow is fully wetted. Using the method of images, the foil camber

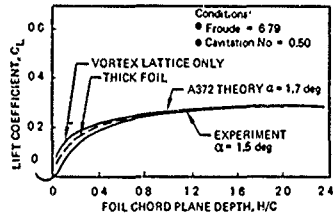


Figure 25 Predicted and Measured Free-Surface Effects for Jetfoil 929 115 1/6-Scale Canard System

line was analyzed in the A372 vortex lattice program. Up to a depth-to-chord ratio of 0.4, the experimental characteristics are in agreement with predictions. Close to the free surface the negative camber induced by the foil thickness becomes significant. The good agreement between theory and experiment is an indication that at the Froude number of interest, a simple singularity image system is adequate for most theoretical investigations of an isolated foil in the presence of a free surface.

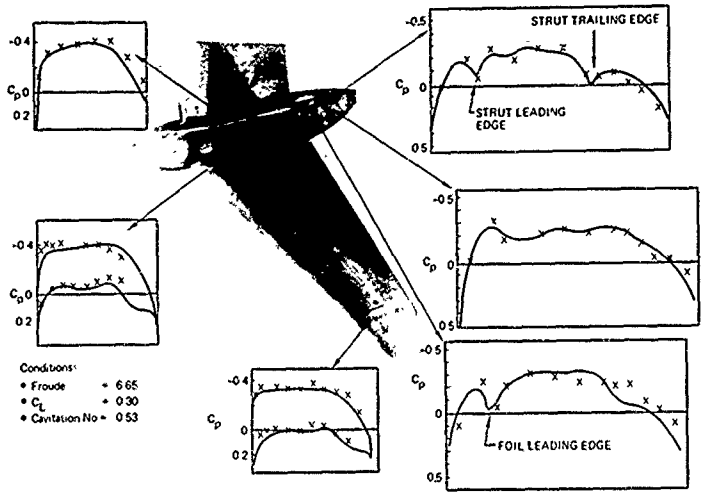


Figure 26. Predicted and Measured Pressure Distribution on Jetfoil 929-115 1/6-Scale Canard Foil System at Two-Chord Foil Depth

Figure 26 shows a comparison between measured pressures at a lift coefficient of 0.3 and A230 predictions. The foil is free of cavitation and the agreement is very good.

Conclusions

The forward foil system of a hydrofoil ship has been designed using mainly analytical methods. Good agreement between theoretical predictions, model experimental results, and sea trials indicates that advanced potential-flow methods provide an excellent tool for hydrofoil design. Cavitation inception is accurately predicted. For a fully submerged hydrofoil, free-surface effects seem to be in most cases adequately modeled in potential flow by a mirror-image system.

Development of methods to analyze partially cavitated foil systems is necessary for the prediction of the full operating envelope of hydrofoils in sea state.

The treatment of wings submerged in the wake of another wing located upstream is inadequate. Strut and foil ventilation eventually limit the sea-state capability of a foil system and at present cannot be treated reliably by theoretical methods.

References

1. Feifel, W. M., "Optimization and Design of Three-Dimensional Configurations of Arbitrary Shape by a Vortex Lattice Method," Vortex Lattice Utilization, NASA SP-405, May 1976.

2. Feifel, W. M., "3-Dimensional Potential Flow Analysis–Design–Optimization Program A372," Boeing Report D321-51510-1, January 1979.

3. Lundry, J. L., "A Numerical Solution for the Minimum Induced Drag, and the Corresponding Loading, of Nonplanar Wings," NASA CR-1218, issued by originator as Report DAC-66900, McDonnell Douglas Corp., Long Beach, Calif., 1968.

4. Rubbert, P. E., Saaris, G. R., Scholye, M. B., Standen, N. M., and Wallace, R. E., "A General Method for Determining the Aerodynamic Characteristics of Fan-in-Wing Configurations," USAAV Laboratories, Technical Report 67-61A, 1967.

5. Boctor, M., "Potential Flow Analysis of the Jetfoil Foil System," Boeing Report D320-1010-1, June 1977.

6. Johnson, F. T., "A General Panel Method for the Analysis and Design of Arbitrary Configurations in Incompressible Flows," NASA CR-3079, May 1980.

7. Feifel, W. M., "Two-Dimensional Flow Analysis and Jet Flap Simulation Program TEA304B," Boeing Document D6-43832TN, 1976.

8. Munk, M., "Isoperimetrische Aufgaben aus der Theorie des Fluges," Inaug. Dissertation, Göttingen, 1919.

9. Abbott, I. H., and Von Doenhoff, A. E., Theory Wing Sections–Including a Summary of Airfoil Data, Dover Publications, Inc., New York, 1959.

10. Noreen, A. E., Gill, P. R., and Feifel, W. M., "Foilborne Hydrodynamic Performance of Jetfoil," Journal of Hydronautics, 14 (2), (April 1980).

11. Lundry, J. L., "Development of Wake Turbulence Capability in 1975," Boeing Document D6-43796TN, September 1976.

12. Dixon, R. J., Schmiechen, M., Shrout, L. C., and Watanabe, R. K., "An Experimental Investigation of the Hydrodynamic Characteristics of a Partially Cavitating Hydrofoil," paper presented at the 19th American Towing Tank Conference, University of Michigan, Ann Arbor, Mich., July 1980.

DISCUSSIONS
of the paper
by W M. Feifel

ADVANCED NUMERICAL METHODS HYDROFOIL SYSTEM DESIGN AND EXPERIMENTAL VERIFICATION

Discussion
by Choung M. Lee

I understand that the Pan Air Method you have used in your work is a quite a versatile computer program for potential-flow problems. I would like to know if you have ever computed appendage drag of a small-aspect ratio control surface attached to a large body by using the Pan Air computer program.

Author's reply

I myself have not used Pan Air in this fashion ; but there is quite a large group of users and there is still considerable work being invested to complete the Pan Air System. Pan Air is a very complex program and is designed to handle both subsonic and supersonic cases. It was conceived to become a unified potential flow analysis and design method.

I am not sure if Pan Air would adequately treat the problem of a large body with small wings. I think even in Pan Air the amount of lift carried by the body is not clearly defined. The conventional Kutta condition cannot be applied at the aft end of a 3-dimensional body because of the predominance of viscous effects in this region. The viscous "liquid body" extending downstream of the physical body imposes a sort of Kutta condition. But for a potential flow analysis the exact location of the aft stagnation point must be prescribed, which is hard to do in such a case.

There are efforts underway to combine three dimensional boundary layer methods with Pan Air. But boundary layer approximations do not hold either in the vicinity of the rear stagnation point and one had to resort locally to a triple deck approximation or try to solve the Navier Stokes equations. In addition, if a body is at a higher angle of attack it sheds vortices from its upper surface. My personal opinion is that it will be quite a while before a solution method will be developed which is suited for engineering applications. Sure, by playing for three months on the computer a potential flow modeling scheme can be deviced to analyze a given case. But I find that it is always easier to find a numerical solution once experimental data have become available. It is much harder to produce a numerical solution, lock it away in a safe and then run the experiment just to find that the predictions were way off. But immediately once we have seen the real life flow pattern we know what we have done wrong and how we really should have modeled the problem. I don't want to put down the numerical approach. It is just that we are not quite smart enough to think of everything and nature is !

Discussion
by L.J. Doctors

In the presentation of the work, the speaker mentioned that the free-surface was modelled as a rigid flat surface. This statement is verified in the first paragraph of the Conclusions in the preprint, in which a "mirror-image" system is referred to.

This procedure represents the zero-Froude-number approximation given by $\partial\phi/\partial z = 0$ on $z = 0$. Would it not be better to use the infinite-Froude-number approximation given by $\partial^2\phi/\partial x^2 = 0$ on $z = 0$, since the Froude number based on the foil chord is indeed very large ?

It also seems to the discusser, that in either of the above two cases, the free-surface is not perfectly modelled. To what extent would this affect the comparisons between theory and experiment -particularly in regard to the observed cavitation patterns ?

Author's reply

I might have not clearly expressed myself when describing the free surface boundary condition used for the computations. When I referred to a "negative mirror image system" I meant a system where the images of sinks are sources. I referred to the image as "rigid" in the sense that the location of the image singularity is found as the mirror image with respect to an undistorted free surface. This indeed is the infinite Froude number approximation. In our experiments where we flew the foil system at a constant cavitation number and varied the chord Froude number between 4.5 and 6.5 we found very little change in the cavitation pattern. This indicates that the infinite Froude number approximation in this particular application probably is adequate.

Session VI
VORTEX FLOWS AND LIFTING BODIES

M Aucher
Session Chairman
Bassin d'Essais des Carènes
France

UNSTEADY 3-D LIFTING SURFACE THEORY WITH THE FREE-SURFACE EFFECT

by J. Leclerc and P. Salaün
Office National d'Études et de Recherches Aérospatiales
29, avenue de la Division-Leclerc, 92320 Châtillon (France)

Abstract

This theory concerns unsteady fluid/structure interactions with the gravity effect. Usual assumptions of the linear theories are made and the 3-D lifting surface method of the unsteady aerodynamics is used. Starting from the potential of the Havelock source, we are led to an integral equation, the kernel of which is expressed as a Fourier series with respect to the azimuthal angle. The coefficients of the Fourier expansion are simple integrals approximated by an asymptotic method for large indices. The integral equation is solved by the collocation technics. Problems such as flutter of subcavitating foil-systems or control dynamics in flight near the surface wave provide relevant applications of this theory.

I Introduction

Subcavitating foil systems are subject to the same kind of fluid/structure interaction instabilities as airfoils such as flutter or wrongly controlled flights near the surface wave. The study of these phenomena requires a 3-D unsteady lifting surface theory taking into account the free-surface effect. The purpose of this communication is to provide such a theory which, so far as we know, was not yet available. The usual assumptions of the linear theories are made and the lifting surface method of the unsteady aerodynamics is used here.

II. Problem formulation

Let (x,y,z) be an orthogonal coordinate system bound to the foil system with z-axis vertically upward, and x-axis horizontally backward (Fig. 1). Let V be the forward steady speed, c a reference half chord of the foil system, all coordinates are dimensionless and refered to c. Let :

$F = V/\sqrt{gc}$ (Froude number) ; $\tilde{\omega} = \omega c/V$ (reduced frequency), where ω is the angular frequency. Our purpose is to seek the distribution of the complex local lifting coefficient C_p corresponding to a given small transversal displacement $D(x,y,z)e^{i\tilde{\omega}t}$ along the normal to the lifting surface, the unit vector of which being $\vec{n}(x,y,z)$.

We assume the fluid incompressible and of infinite depth. The velocity field is irrotationnal. Thus, the perturbation velocity potential say $\phi(x,y,z;\omega)$ must verify :

$$\Delta\phi(x,y,z;\omega) = 0 \qquad , z<0 \qquad (1)$$

The boundary condition on the set E of all the submerged lifting surfaces, is :

$$\vec{n}.\mathrm{grad}\,\phi = V\left(\frac{\partial}{\partial x} + i\tilde{\omega}\right)D \quad , (x,y,z)\in E \qquad (2)$$

The linearized condition on the free surface is expressed by :

$$\left[\left(i\tilde{\omega}+\frac{\partial}{\partial x}\right)^2 + \frac{1}{F^2}\frac{\partial}{\partial z}\right]\phi = 0 \qquad , z=0 \qquad (3)$$

Let ω' be a complex number such as :

$$i\omega' = \alpha + i\omega \qquad \alpha > 0$$

When ω is changed in ω', we must have :

$$\mathrm{grad}\,\phi(x,y,z;\omega) \to 0 \ , \quad x^2+y^2+z^2 \to \infty \qquad (4)$$

$\phi(x,y,z;\omega)$ is the limit of $\phi(x,y,z;\omega')$ when $\alpha \to 0$.

By this way, we express the Sommerfeld condition and the attenuation at infinity. Moreover, we have to express the Kutta condition at the trailing edges of every lifting surfaces of the set (E).

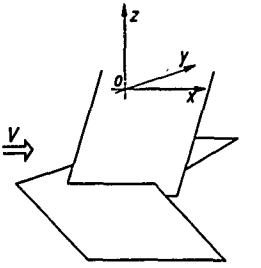


Figure 1. The free surface is the plane z = 0. The set of the lifting surfaces, in the figure, may represent, for instance a foil system.

III. Integral equation

We construct the solution ϕ by starting from the expression of the complex perturbation velocity potential $S(x,y,z,\xi,\eta,\zeta)e^{i\tilde{\omega}t}$ of the Havelock source (ξ,η,ζ) moving horizontally with the velocity V and pulsing with angular frequency ω. We write

$$x_0 = x-\xi = r_0\cos\lambda \ ; \ y_0 = y-\eta = r_0\sin\lambda \ ; \ z_0' = z+\zeta$$

When proceeding as in the unsteady aerodynamics [1], we find that C_p satisfies the following integral equation :

$$\iint_E \mathcal{N}(x_0,y_0,z,\zeta,\tau,F)C_p(\xi,\eta,\zeta)\,d\sigma = \left(\frac{\partial}{\partial x}+i\tilde{\omega}\right)\frac{D(x,y,z)}{c} \qquad (5)$$

where : $\tau = \omega V/g$ is assumed here to be greater than the critical value equal to 1/4

The kernel $\mathcal{N}$ can be written :

$$\mathcal{N} = \mathcal{N}_1 + N(x_0,y_0,z_0',\tau,F) \qquad (6)$$

$\mathcal{N}_0$ corresponds to the problem where the free surface condition is replaced by the nullity of the perturbation velocity potential and :

$$N=\frac{i}{4\pi^2 F^4}\left\{\int_0^{\pi} d\theta\left(\sin\ell\cos\beta\sin\theta,\cos\ell\cos\beta,-i\sin(\ell,\beta)\sin\theta\right)\cdot\right.$$
$$\left.\int_0^{\infty} du\,\frac{u^5 e^{\frac{u r_0}{F^2}}\exp\left(-i\frac{u r_0}{F^2}\cos(\theta,\lambda)\right)}{\left[(u\cos\theta+\tau)^2-u\right]\left[u\cos\theta+\tau\right]}\right\} \qquad (7)$$

where the omitted expression is the same except the change $\theta/-\theta$. $\ell = \ell(x, y, z)$ and $\beta = \beta(\xi, \eta, z)$ represents angles of E with the y-axis.

The path of integration in u-plane passes around every of the three poles u_j (j =-1, 0, 1), either in the upper or in the lower plane, according to the value of θ, when its affix is real, for the sake of the Sommerfeld convention.

By developping in a Fourier series the function $\exp\left[\frac{iu r_0}{F^2}\cos(\theta,\lambda)\right]$ with respect to λ, and integrating analytically with respect to θ, we find the expression :

$$N=-\frac{i}{2\pi F^4}\left[\cos\ell\cos\beta\sum_{m=0}^{\infty}\varepsilon_m G_{m,-}\cos m\lambda\cdot\right.$$
$$\left.-\sin\ell\sin\beta\sum_{m=0}^{\infty}\varepsilon_m G_{m,1}\cos m\lambda+i\sin(\ell,\beta)\sum_{m=0}^{\infty}\varepsilon_m G_{m,0}\sin m\lambda\right] \qquad (8)$$

where $\varepsilon_m = 1$ if $m = 0$, $\varepsilon_m = 2$ if $m > 1$, and

$$G_{m,k}=i^m\left[F_{m,k}-\frac{1}{2}F_{m-1,k}-\frac{1}{2}F_{m+1,k}\right],\quad k=-1,0,1$$

with :

$$F_{m,k}=\int_0^{\infty} du\,u\,e^{\frac{u r_0}{F^2}}J_m\left(\frac{u r_0}{F^2}\right)\left(\sqrt{\left(\frac{\tau}{u}+\frac{1}{\sqrt{u}}\right)^2-1}\right)^k\cdot \qquad (9)$$
$$\left[-\left(\frac{\tau}{u}+\frac{1}{\sqrt{u}}\right)+\sqrt{\left(\frac{\tau}{u}+\frac{1}{\sqrt{u}}\right)^2-1}\right]^m$$

For moderate values of m, the integrals $F_{m,k}$ are computed directly.

Let u'_j the positive root of $\left[\left(\frac{\tau}{u}+\frac{1}{\sqrt{u}}\right)^2-1\right]$; we observe that the integrand is real only for $0 < u < u'_j$. The numerical integration in this interval takes into account the algebraic singularities for u = 0 and $u = u'_j$. For $u > u'_j$, the integrand of $F_{m,k}$ becomes complex, but real and imaginary parts may be easily separated. The zeros of each part have two origins, ones from the factor at power m, the zeros of which being bounded, the other ones from $J_m\left(\frac{u r_0}{F^2}\right)$ which are unbounded. A partition into sub-intervals is made in the region of bounded zeros and an accelerated convergence algorithm is used beyond, with paying attention to the fact that $\frac{u r_0}{F^2}$ must be greater than 1 which is the affix ξ^* of the transition point of $J_m(m\xi^*)$, this for the sake of convergence.

Thanks to the factor $e^{\frac{u r_0}{F^2}}$, the extent of the integration may also often be limited. It can be shown that $G_{m,k}$ becomes decreasing for large values of m. Thus, the corresponding Fourier series is truncated as soon as :

$$\begin{cases}\dfrac{|G_{N_0,k}|}{\sup_{m<N_0}|G_{m,k}|} < \varepsilon & , k=-1,0,1\\ \text{where } \varepsilon \text{ is fixed arbitrary small, and}\\ |G_{m,k}| < |G_{N_0,k}| & \text{if } m > M_3\end{cases}$$

It is found that :

$$M_3 < 30 \quad \text{for} \quad \varepsilon = 1.10^{-3}, \quad \text{and}$$
$$\ell g\,\delta = \frac{z_0}{r_0} > 1$$

For smaller values of δ, a steepest descent method is used to get an asymptotic approximation of $G_{m,k}$ for $m > M_3$, which is already satisfactory for smaller values of m.

In this, we start from the first term of the uniform asymptotic expansion :

$$J_m(m\xi^*)\sim\left[\frac{4}{1-\xi^{*2}}\left(\frac{2}{3}\zeta\right)^{\frac{2}{3}}\right]^{\frac{1}{4}}m^{-\frac{1}{3}}Ai\left[\left(\frac{3}{2}m\zeta\right)^{\frac{2}{3}}\right]$$

where :

$$\zeta = \int_{\xi^*}^{1}\frac{\sqrt{1-\xi^2}}{\xi}d\xi$$

From this, it can be shown that except in the vicinities of the intervals :

$$-\infty < \xi^* < -1 \quad \text{and} \quad \xi^* > 1$$

we have :

$$J_m(m\xi^*)\sim\frac{1}{\sqrt{2\pi m}}\left[1-\xi^{*2}\right]^{-\frac{1}{4}}\exp m\int_1^{\xi^*}\frac{\sqrt{1-\xi^2}}{\xi}d\xi.$$

and that, out of a lens shaped domain D (Fig. 2) of the ξ plane, we have :

$$J_m(m\xi^*)\sim\frac{1}{\sqrt{2\pi m}}\left[\left[\sqrt{1-\xi^{*2}}\right]^{-\frac{1}{2}}\exp m\int_1^{\xi^*}\frac{\sqrt{1-\xi^2}}{\xi}d\xi\cdot\cdot\right.$$
$$\left.+\left[-\sqrt{1-\xi^{*2}}\right]^{-\frac{1}{2}}\exp -m\int_1^{\xi^*}\frac{\sqrt{1-\xi^2}}{\xi}d\xi\right]$$

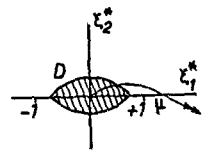


Figure 2

These two forms of J_m ($m\,\xi^*$) correspond to the first terms of the two Debye expansions of J_m ($m\,\xi^*$). It results that $F_{m,j,k}$, for large values of m, has the asymptotic form :

$$F_{m,j,k} \sim \int_0^\infty G_0(\xi^*; m,j,k)\, e^{m h_0(\xi^*; m,j,k)}\, d\xi^* \ldots + \int_\mu^\infty G_1(\xi^*; m,j,k)\, e^{m h_1(\xi^*; m,j,k)}\, d\xi^* \qquad (10)$$

where $G_0(\xi^*; m,j,k)$, $G_1(\xi^*; m,j,k)$, $h_0(\xi^*; m,j,k)$, $h_1(\xi^*; m,j,k)$ are slowly varying functions of m, and where the affix of μ may be taken anywhere at a finite distance from the origin and out of D (Fig 2).

The steepest descent method gives an asymptotic expansion for every integral of (10). In this, the path of integration of the first integral is replaced by the steepest descent line passing to a particular saddle-point of the graph of $|\exp m h_0(\xi^*; m,j,k)|$ in the ξ^*-plane.

For the second integral, μ is chosen at the intersection of this last line with the real axis, and the path of integration is also replaced by a steepest descent line of the function $|\exp m h_1(\xi^*; m,j,k)|$. This one does not pass to a saddle-point. It results that this integral is negligible provided that δ and λ are not simultaneously too small. In this latter case, the saddle-point to be considered tends to the point $\xi^* = 1$, the transition point of J_m ($m\,\xi^*$), in the vicinity of which, we have :

$$J_m(m\xi^*) \sim \left(\frac{2}{m}\right)^{\frac{1}{3}} Ai\left(-2^{\frac{1}{3}} m^{\frac{2}{3}} (\xi^* - 1)\right)$$

The approximation of $F_{m,j,k}$, in this case, turns to be asymptotically the same as in other cases, i.e. :

$$F_{m,j,k} \sim \int_0^\infty G_0(\xi^*; m,j,k)\, e^{m h_0(\xi^*; m,j,k)}\, d\xi^* \qquad (11)$$

which is therefore proper in all the cases.

The major contribution along the new path of integration which begins at the origin and passes to the saddle-point ξ^*_j (j = - 1, 0, 1) is just the vicinity of the saddle-point and we have :

$$F_{m,j,k} \sim \int_0^\infty G_0(\xi^*; m,j,k)\, e^{m h_0(\xi^*; m,j,k)}\, d\xi^* \qquad (12)$$

$$\sim G_0(\xi^*_j; m,j,k)\, e^{m h_0(\xi^*_j; m,j,k)} \sqrt{\frac{\pi}{-\frac{m}{2} h_0''(\xi^*_j; m,j,k)}}$$

where the affix ξ^*_j of the saddle-point is a complex solution of the equation :

$$-\xi^* \operatorname{tg}\delta + \sqrt{1-\xi^{*2}} + i\kappa' \frac{\tau\kappa' + \frac{2}{3}\sqrt{\xi^*}}{\sqrt{\xi^{*2} - \kappa'^2(\tau\kappa' + j\sqrt{\xi^*})^2}} = 0 \qquad (13)$$

with :

$$\kappa'^2 = \frac{g c r_0}{m V^2}$$

This equation is reducible to a cubic equation if j = 0.

For j = ± 1, the solution of (13) is real for $\delta = 0$ and can be obtained either by an iteration process or by successive interpolations for any value of $\tau > 1/4$, then it can be extended for $\delta > 0$ by the Newton's method.

In the vicinity of $\kappa' = \delta = 0$, that is to say when the two points M' and M, respectively integration and collocation point, are near the free surface, the solution ξ^*_j of (13), which is nearly equal to 1, can be developed in series of integer powers of κ' and of (tg δ), whence we get the expansion of the right-hand side of (12). Thus, it follow that the Fourier series :

$$\sum_{m=0}^{\infty} \varepsilon_m i^m F_{m,j,k}\, e^{\pm i m\lambda} \qquad (14)$$

is expansible in the form :

$$(-i)^k \frac{F^k}{r_0^k} \sum_{m=0}^{\infty} \varepsilon_m m\, e^{-i\frac{\tau r_0}{F^2} \pm i m\lambda} \left(1 + \ldots \right.$$

$$\left. \left[\frac{2}{4}\left(j\frac{\kappa'}{2} + i\operatorname{tg}\delta\right)\left(j\frac{\kappa'}{2} + 2i\operatorname{tg}\delta\right) - j^3\frac{\kappa'^3}{2}\right] + \ldots\right) \ldots$$

$$\exp\left(-m\operatorname{tg}\delta - \frac{i\delta}{F}\sqrt{r_0 m} + \frac{i}{6\sqrt{m}}\left(j\frac{\sqrt{r_0}}{2F} + i\sqrt{m}\operatorname{tg}\delta\right)^3 \frac{-j^3 r_0^{\frac{3}{2}}}{F^3\sqrt{m}} + \ldots\right) \qquad (15)$$

where the neglected terms are homogeneous in (κ', tg δ) of order greater than 2.

For j = ± 1, the series (15) are convergent according to the Abel rule because the partial sums

$$\sum_{m=M}^{M+p} m\, e^{-m\operatorname{tg}\delta - \frac{i\delta}{F}\sqrt{r_0 m}}$$

are bounded for any positive values of M and p.

The series j = 0, only, becomes singular as δ and λ are vanishing. When expanding every term of the series $\sum_{m=0}^{\infty} \varepsilon_m i^m F_{m,0,k}\, e^{\pm i m\lambda}$ only with respect to (tg δ) but for any value of

$$k = \tau\kappa'^2 = \frac{\omega c r_0}{m V^2}$$

one finds that singularity is the same as in the simpler series :

$$S = (-i)^k \frac{F^k}{r_0^k} \sum_{m=0}^{\infty} \varepsilon_m m \left(\sqrt{1+\kappa^2}\right)^{-k} \exp\left(-i\kappa\sqrt{1+\kappa^2}\operatorname{tg}\delta \pm i\lambda\right)$$

Since : $m = \tau r_0 / \kappa F^2$, when δ and λ are vanishing together, S has itself the same singularity as the integral

$$I = 2(-i)^k \frac{F^k}{r_0^k} \frac{\tau r_0}{F^2}\, e^{-i\frac{\tau r_0}{F^2}} \ldots \int_0^\infty \frac{1}{\kappa}\left(\sqrt{1+\kappa^2}\right)^{-k} e^{\frac{\tau r_0}{F^2}\left[-\frac{\sqrt{1+\kappa^2}}{\kappa}\operatorname{tg}\delta \pm i\frac{\lambda}{\kappa}\right]} d\left(\frac{\tau r_0}{\kappa F^2}\right)$$

$$= 2(-i)^k \tau^k e^{-i\frac{\tau r_0}{F^2}} \int_0^\infty \left(\frac{\sqrt{1+u^2}}{u}\right)^k u\, e^{\frac{\tau r_0}{F^2}\left[-\sqrt{1+u^2}\pm i\lambda u\right]} du$$

One finds that this integral I is asymptotically equal for any value of r_0 and k (k = -1, 0, 1), to :

$$I \sim (-i)^k \tau^k e^{-i\frac{\tau r_0}{F^2}} \left[\frac{tg^2\delta - \lambda^2 \pm 2i\lambda\, tg\,\delta}{tg^2\delta + \lambda^2} \cdot K_2\left(\frac{\tau r_0}{F^2}\sqrt{\lambda^2 + tg^2\delta}\right) + K_0\left(\frac{\tau r_0}{F^2}\sqrt{\lambda^2 + tg^2\delta}\right)\right] \quad (16)$$

If $\frac{\tau r_0}{F^2}\sqrt{\lambda^2 + tg^2\delta} \gg 1$, we can develop the two Bessel modified functions K_0 and K_2. We get finally :

$$\sum_{m\geq 0}^{\infty} \varepsilon_m i^m F_{m,\sigma,k}\, e^{\pm i m\lambda} \sim (-i)^k \frac{F^k}{r_0^k} e^{-i\frac{\tau r_0}{F^2}} \cdot \left[2\frac{tg^2\delta - \lambda^2 \pm 2i\lambda\, tg\,\delta}{(tg^2\delta + \lambda^2)^2} - \left(\frac{\tau r_0}{F^2}\right)^2 tg\left(\sqrt{\lambda^2 + tg^2\delta}\right) + \ldots\right] \quad (17)$$

This expression gives the singularity of the kernel N near the free surface, when $\lambda \to 0$.

In fact, to compute the series (14), the following partition is made :

$$\sum_{m\geq 0}^{\infty} \varepsilon_m i^m F_{m,j,k}\, e^{\pm i m\lambda} = \sum_{m=0}^{M_1} \ldots + \sum_{m=M_1+1}^{M_2} \ldots + \sum_{m=M_2+1}^{\infty} \varepsilon_m i^m F_{m,j,k}\, e^{\pm i m\lambda} \quad (18)$$

We have already indicated that $F_{m,j,k}$ is computed directly if $m < M_1$, and that in a range (M_1, M_2), where M_2 depends on the smallness of $\frac{\tau r_0}{F^2}\sqrt{\lambda^2 + tg^2\delta}$, $F_{m,j,k}$ is approximated by the expression (12).

As for the remaining sum of (18), $F_{m,j,k}$ is replaced by an asymptotic expression with gauge functions of $\sqrt{m}$, which leads to one of the two following forms for their contributions to N in (8),

$$\sum_{m\in M_2+1}^{\infty} m\, e^{-m\kappa} \cos(m\lambda + \beta - \ell) \quad (19)$$

if J = 0 and:

$$\sum_{m\in M_2+1}^{\infty} m\, e^{-m(\kappa \pm i\lambda)} \pm \frac{i}{F}\sqrt{m(r_0 \pm z_0)} \quad (20)$$

where : $th\,\alpha = tg\,\delta$, if $j = \pm 1$

The series (19) is well-known, and the second one is approximated with a good precision by means of the Euler MacLaurin sommation formula.

For a convenient computation of the second partial sum of (18), a polynomial interpolation with respect to the two variables tg δ and K_r is carried out with a special precision for small values of K (or great values of m), to approximate the solution ξ^* of the affix-equation (13).

Finally, after a factorization taking into account the singularity of N issued from (17), and the quasi-periodicity in r_0 expressed also by this last equation, the kernel N is interpolated by means of a polynomial of the three variables (z'_0, r_0, λ) in order to save time in the resolution of the integral equation (5).

A different way to calculate N, which has also been considered, consists in carrying out analytically one of the two integrations in the expressions of the Havelock source potential. Thus, we have to integrate functions containing themselves the exponential integral E_1.

An advantage of the present method is to avoid all the difficulties inherent to the non-uniformity of E_1, when its argument is complex. The two methods, the present one numerically, and the other analytically, indicate the existence of a wake rearwards M', at the free surface, out of which N is fading.

The larger is τ, the narrower is the wake-aperture, which explains why the free surface effects disappears for a given Froude number F, when τ becomes large. Moreover, the exponential decay of N with respect to z_0 ensures also a decreasing effect of the free surface with the depth of submergence.

Finally, to get the complete kernel $\mathcal{N}$, we have, according to (6), to add $\mathcal{N}_1$ to the expression of N. We do not insist on the numerical technique to compute $\mathcal{N}_1$ which is easily deduced from the kernel of the unsteady aerodynamics in incompressible medium, this latter being available in a large litterature, e.g. [1]. Although this expression of $\mathcal{N}_1$ is far from being simple, it remains very much simpler and, for instance, needs not any interpolation.

IV Solution of the integral equation

The integral equation (5) is of the first kind and has infinity of solutions. For the closure, we have to impose the true algebraic singularities of the solution c_0 at the two edges, that is to say, the leading and the trailing edge, which result from the Kutta condition. This is implicitly yielded by a proper mesh on E of integration points and of so many corresponding collocation points.

The kernel $\mathcal{N}$ has the same polar singularities as $\mathcal{N}_1$ which is not integrable in the Riemann's sense since, in the simple case of an horizontal wing, it is of the form :

$$\frac{1}{4\pi y_0^2}\left(1 + \frac{x_0}{\sqrt{x_0^2 + y_0^2}}\right) \quad (21)$$

The left hand side of (5) is therefore an Hadamard's distribution. It can be shown that the result of the integration with respect to η brings a new singularity of Cauchy type in x_0.

According to the remarks done by Multhopp [1] about the singularity in y_0, and to similar considerations about the Cauchy singularity in x_0, the integration of the Gaussian type taking into account the algebraic singularities of C_0 in the left-hand side of (5) can be extended in spite of the non integrable polar singularities in y_0 and in x_0. It is sufficient for this, that the collocation points belongs to a set of proper points corresponding to an equal number of integration points.

V Some numerical results

Let S_k (k = -1, 0, 1) be the three Fourier series appearing in the expression (8) of N. It can be seen that S_{-1} only occurs in N when both integration and collocation points concern the same horizontal planform ; S_1 only occurs when both integration and collocation points concern the same vertical planform , S_0 concerns the interaction between a horizontal and a vertical planform , for more general configurations, the three Fourier series occur simultaneously in N.

Figures 3, 4, 5 illustrate the oscillations of S_k (k = - 1, 0, 1) in function of r_0 for $\tau = 6.5$, $F = 1.5$, $z'_0 = -0.2$, $\lambda = 0$ for S_{-1} and S_1, $\lambda = 0.1$ for S_0 ; S_{-1} and S_1 are similar, and the wave length is nearly equal to that given in (17), which has the same singularities as S_{-1} and S_1 ; S_0 is slightly different.

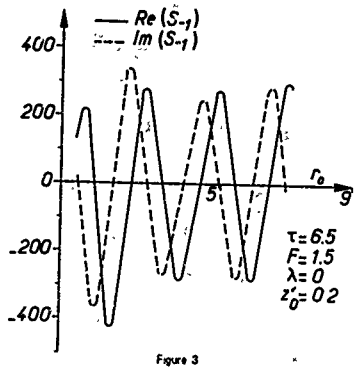


Figure 3

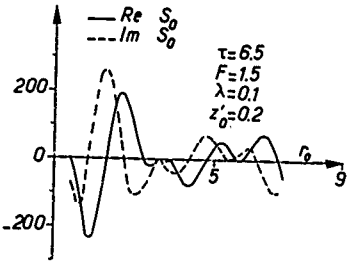


Figure 4

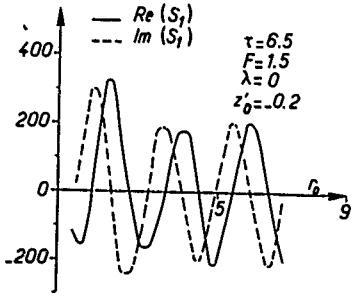


Figure 5

Figures 6, 7, 8 illustrate the simple dependence of S_k (k = - 1, 0, 1) upon z'_0 ; $|S_k|$ decreases fastly when $|z'_0|$ increases ; this means that the only part of a structure for which N occurs in the integral equation is the vicinity of the free surface.

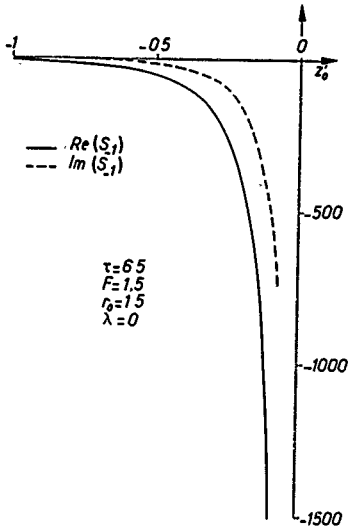


Figure 6

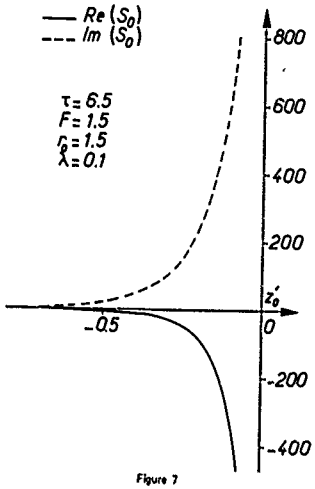


Figure 7

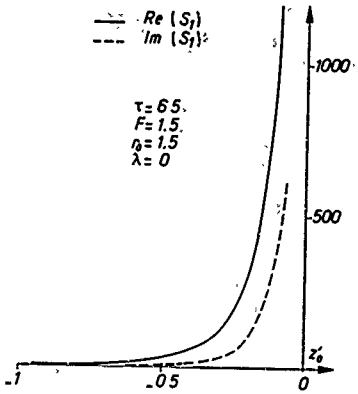


Figure 8

S_1 and S_{-1} being even functions of λ and S_0 odd function of λ, figures 9, 10, 11 illustrate the existence of a wake outside of which $|S_k|$ is negligible.

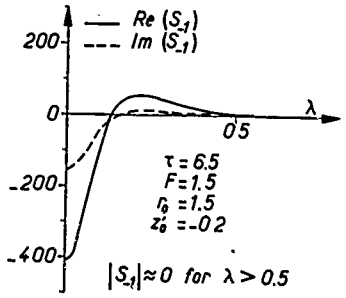


Figure 9

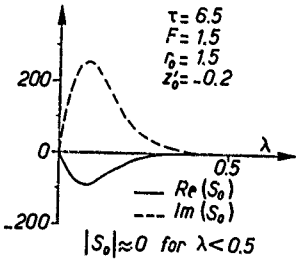


Figure 10

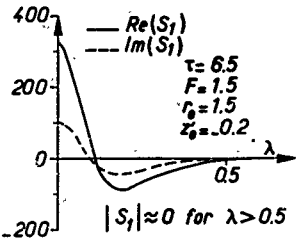


Figure 11

As it has been pointed out, $|S_k|$ decreases when τ increases, F being fixed, that is to say when the frequency increases, the velocity being fixed ; this is shown on figure 12.

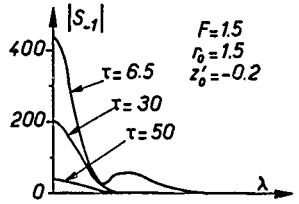


Figure 12

The linear system obtained by discretization of the integral equation is solved by the Gauss-Seidel method, which allows solution of high order systems.

For example, the pressure coefficient C_p has been computed for the vertical planform of figure 13, piercing the free surface where the effect is maximum.

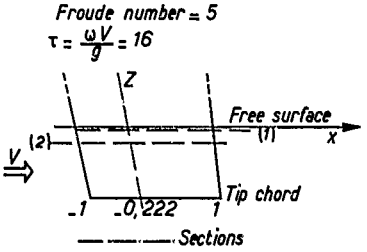


Figure 13

The mode shape is a pure translation at 5 Hertz, the velocity is 5 m/s ; τ is equal to 16 and the Froude number refered to half tip-chord, is equal to 5. 10 chordwise collocation points have proved to be necessary to yield a good result. The computing time for solving the integral equation is then 4.5 minutes on UNIVAC 1110

Figures 14, 15, 16 illustrate the real and imaginary part of C_p compared to the C_p obtained when the gravity effects are neglected, that is to say when the boundary condition on the free surface is the nullity of the perturbation potential.

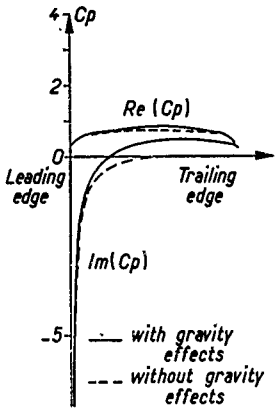


Figure 14 : Section 1

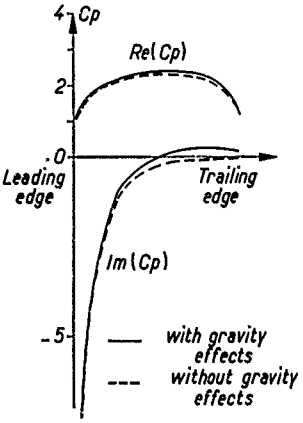


Figure 15 : Section 2

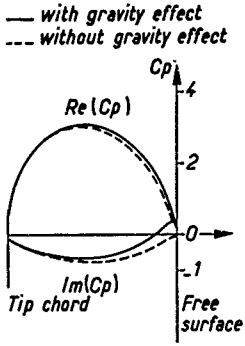


Figure 16

The depth of submergence is equal to the tip half choral ; figure 14 illustrates the variation of C_p along the chordwise section 1, situated at 3 8 % of the span ; the effect of gravity is greater on the imaginary part ; this effect decreases when the depth of the section increases, as is seen in figure 15, where the section 2 is at 22.2 % of the span.

The variation of the pressure coefficient C_p along a typical spanwise oblique section is shown in figure 16, emphasizing how much the gravity effect decreases with the depth.

The lack of time has prevented us to carry out analogous computations for other values of τ ; these computations are now in progress, and the gravity effects on C_p will likely turn out to be greater for values of τ less than 16.

Conclusion

It will now be possible to compute the hydrodynamic pressures and forces on more general submerged structures taking account of gravity effects. It is planned to study 3 D flutter of such structures, and control dynamics in flight near the surface wave.

References

[1] WILLIAMS, D E. - Three-dimensional subsonic theory. Manual of aeroelasticity - NATO-AGARD - Vol. 2, ch 3 - Edit. by W.P. Jones.

DISCUSSION
of the paper
by J. Leclerc and P. Salaün

UNSTEADY 3-D LIFTING SURFACE THEORY WITH THE FREE-SURFACE EFFECT

Discussion
by D. Euvrard

I was deeply impressed by the fullness of the mathematical and numerical work described in the present communication, and so my question is only related to a matter of physical parameters range : don't you believe that the first natural frequency of the foil-system (in the case of incompressible flow) is of such high mode that the free-surface effet has no significant importance ?

Authors' reply

According to our numerical experience, there is little doubt that the free surface-effect can be dropped in the prediction of foil-system flutters whose the range of reduced frequencies correspond to values of τ next, say, to 20. Only for very low mode-frequencies, the free surface-effect may come into play. For control dynamics in flight, much lower frequencies are encountered and the present theory is of interest".

BASE-VENTILATED FOILS

R. Beubeau
Bassin d'Essais des Carènes
Paris, France

Abstract

The author uses a prediction-correction method to determine the shape of a base-ventilated foil. As far as the naval architect is concerned for the preliminary design, the planform of the foil is given, as well as its maximum thickness and the repartition of the lift along the span. Also, the flight conditions of the hydrofoil being known, the depth of submergence, the Froude number (very large) and the ventilation number are thus imposed. In this restrictive context, the method is aimed at defining sections at angle of shock-free entry, the repartition of the lift coefficient along the chord being as smooth as possible in order to minimize the cavitation risks. The prediction method (inverse problem) is based on the asymptotic matching of the two dimensional Larock and Street theory (inner problem) and the tridimensional lifting line theory (outer problem). The correction method (direct problem) is based on the linear lifting surface theory. This problem is solved by the collocation theory. The integration of the velocity field is performed by use of the quasi-continuous Gauss method. A two dimensional regularization method developed by Lighthill , enables us to define the velocity at the leading edge. The resolution of these inverse and direct methods, using successive linear iterations, makes it possible to satisfy the predefined specifications.

I. Inverse Problem

A - Two-Dimensional Problem (1), (13)

I.A.1 - Larock and Street model, and recapitulation of the theory.

Larock and Street consider a ventilated foil in a two-dimensional flow only bounded by the free surface. Gravity is not taken into account.

The streamlines on the upper and lower surfaces extend downstream from the profile, and form a cavity along which the speed modulus (K being the ventilation number) is constant. At closing points C and D of the cavity, the streamlines roll around themselves.

Both streamlines then extend to infinity, forming a wake along which the velocity is constant and equal to U_∞.

On the free surface, the velocity modulus is constant and equal to U_∞ (which corresponds to the infinite Froude number condition).

The diagram in the physical plane Z (see figure 1a) can be represented in the potential plane F (see figure 1b), the transformation between F and Z being implicit.

Figure 1c shows this diagram in plane T, as defined by the following transformation :

$$f(Z) = t + TE \log \frac{TE + t}{TE} \quad (TE \text{ is a constant})$$

The velocity distribution $Q(\tau)$ is known all along the z-axis of plane T ; if we consider it to be known along the segment AB representing the profile, this corresponds to a Dirichlet problem with homogeneous boundary conditions.

In the general case of the inverse problem, only the distribution $Q(x)$ along the profile is known, and $Q(\tau)$ must be obtained by iteration, the iterative process being used until the solution on the physical plane corresponds to $Q(x)$.

In our case, a profile is sought for which the load distribution (i.e. the speed modulus, gravity being neglected) is constant, respectively on the major part of the upper and lower foil surfaces, which enables us to impose the velocity distribution along the segment AB of the plane T directly.

I.A.2 - Speed distribution $Q(\tau)$ along the τ-axis (see Figure 2).

$Q(\tau)$ is equal to U_∞ on segments $(-\infty, TC)$ and $(TD, +\infty)$ and to U_{cav} on segments (TC, TA) and (TB, TD).

Three elementary velocity distributions are defined such that $Q(\tau) = q_1(\tau) \cdot q_2(\tau) \cdot q_3(\tau)$

$$q_1(\tau) = U_\infty \qquad \text{if } -\infty < \tau < +\infty$$

$$\begin{cases} q_2(\tau) = \dfrac{U_{cav}}{U_\infty} = \dfrac{\sqrt{1+k}}{U_\infty} & \text{if } T_C < \tau < T_D \\ = 1 & \text{if } \tau < T_C \text{ or } \tau > T_D \end{cases}$$

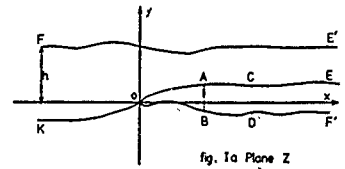


fig. Ia Plane Z
$z = x+iy$

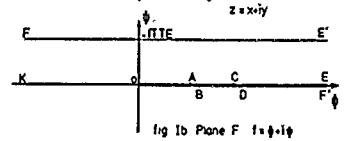


fig Ib Plane F $f = \phi + i\psi$

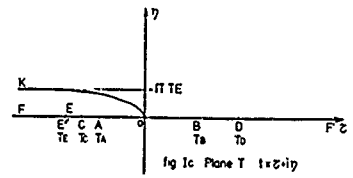


fig Ic Plane T $\tau = \zeta + i\eta$

fig.n°1

$$q_3(\tau) = q(\tau) \qquad \text{if } \tau_A < \tau < \tau_B$$

$$= 1 \qquad \text{if } \tau < \tau_A \text{ or } \tau > \tau_B$$

$q_3(\tau)$ previously defined is such that $q_3(A) = q_3(B) = 1$ and $q_3(0) = 0$ (stagnation point).

In order to make things easier we shall study $q(\tau) = \text{sign}(\tau) q_3(\tau)$, which is a continuous function between $-\infty$ et $+\infty$.

Study of $q(\tau)$ between τ_A and τ_B (fig. 2C)

- between τ_2 and τ_1 $q = q_{ex} < -1$

If $-Cp_e$ is the local upper surface load corresponding to a depression

$$q_{ex} = -\sqrt{\frac{1 - Cp_e}{1 + K}}$$

- between τ_3 and τ_4 $1 > q_{in} = q > 0$

Similarly, we have $q_{in} = \sqrt{\frac{1 - Cp_i}{1 + K}}$

- between (τ_A, τ_2) and (τ_4, τ_B) the matching is performed by using sine laws which allow a zero slope matching

$\tau_A < \tau < \tau_2$

$$q(\tau) = \frac{q_{ex}-1}{2} + \frac{q_{ex}+1}{2} \sin\left(\frac{\pi}{2} + \frac{2\tau - \tau_2 - \tau_A}{\tau_2 - \tau_A}\right)$$

$\tau_4 < \tau < \tau_B$

$$q(\tau) = \frac{q_{in}+1}{2} + \frac{q_{in}-1}{2} \sin\left(\frac{\pi}{2} + \frac{2\tau - \tau_4 - \tau_B}{\tau_4 - \tau_B}\right)$$

- between (τ_1, τ_3) matching is performed by using sine law :

$$q(\tau) = \frac{q_{in}-q_{ex}}{2} + \frac{q_{in}-q_{ex}}{2} \sin\left(\frac{\pi}{2} + (\alpha\tau^2 + \beta\tau + \gamma)\right)$$

where

$$\begin{cases} \gamma\,\tau_1^2 + \beta\tau_1 + \gamma = -1 \\ \gamma\,\tau_3^2 + \beta\tau_3 + \gamma = 1 \\ q(0) = \frac{q_{in}+q_{ex}}{2} + \frac{q_{in}-q_{ex}}{2} \sin\frac{\pi\gamma}{2} = 0 \\ q'(0) = \pi \frac{(q_{in}-q_{ex})}{4} \beta \cos\frac{\pi\gamma}{2} = d_1\, q_0 \\ q''(0) = \frac{\pi}{2}(q_{in}-q_{ex}) \left(\alpha\cos\frac{\pi\gamma}{2} - \frac{\pi}{4}\beta^2 \sin\frac{\pi\gamma}{2}\right) = d_2 q_0 \end{cases}$$

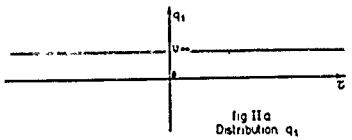


fig IIa
Distribution q_1

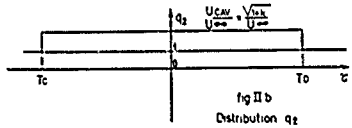


fig II b
Distribution q_2

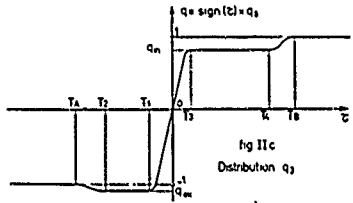


fig II c
Distribution q_3

fig n°2 Detail of the distribution of the velocity $Q = q_1 + q_2 + q_3$ our love ζ

These 5 equations determine τ_1, τ_3, α, β, γ and provide a zero slope matching (see figure 2); all these properties are of course conserved in the physical plane. We can thus impose directly the distribution $q(\tau)$ on the τ-axis of the plane T which leaves us with a simple Dirichle. oroblem to solve with homogeneous boundary conditions.

I.A.3 - Solution of the problem

In the half-plane $\eta > 0$, which is analytically completed, solving the problem consists in defining the complex function $\omega(t) = \log|Q(t)| - i\beta(t)$, the real part of which is known along the real axis.

The solution is given by

$$\omega(t) = \log U_\infty - i\beta_\infty - \frac{1}{\pi}\int_{TA}^{TB} \frac{\log|q(\tau)|}{t-\tau} d\tau - \frac{1}{\pi}\log\frac{\sqrt{1+K}}{U_\infty}\int_{TC}^{TD}\frac{d\tau}{t-\tau}$$

along the profile, $TA < \tau < TB$, $\eta = 0$ thus we have

$$\beta(\tau) = \beta_\infty - \frac{1}{\pi}\int_{TA}^{TB}\log\frac{|q(\tau')|}{\tau'-\tau}d\tau' - \frac{1}{\pi}\log\frac{\sqrt{1+K}}{U_\infty}\cdot\log\left|\frac{TD-\tau}{TC-\tau}\right|$$

The profile will then be constructed by means of the following equations :

$$dx = \frac{dx}{df}\frac{df}{dt}dt = \frac{\cos(\beta(\tau))}{q(\tau)}\frac{df}{dt}dt$$

$$dy = \frac{dy}{df}\frac{df}{dt}dt = \frac{\sin(\beta(\tau))}{q(\tau)}\frac{df}{dt}dt$$

If it is considered that $q < 0$ if $\tau < 0$, it is then necessary to define $\beta = \beta + \pi$ (modulo 2π) for $\tau < 0$.

Moreover, on $\tau = 0$, it is necessary to consider :

$\eta = 0$ $\quad \tau \to 0_+$ $\quad \beta \to \beta_0$

$\eta = 0$ $\quad \tau \to 0_-$ $\quad \beta \to \beta_0 + \pi$

$\eta = 0_+$ $\quad \tau = 0$ $\quad \beta \to \beta_0 + \frac{\pi}{2}$

Evaluation of β on the profile

The integral determining $\beta(t)$ presents a logarithmic singularity for $\tau = 0$, and a singularity for $\tau = t$. This is regularized by writing it in the following form

$$\beta(t) = \beta_\infty - \frac{1}{\pi}\int_{TA}^{TB}\frac{\log\left|\frac{q(\tau)}{\tau}\right| - \log\left|\frac{q(t)}{t}\right|}{t-\tau}d\tau - \frac{1}{\pi}\log\left|\frac{q(t)}{t}\right|\log\left|\frac{TB-t}{TA-t}\right| - \frac{1}{\pi}\int_{TA}^{TB}\frac{\log|\tau|}{t-\tau}d\tau - \frac{1}{\pi}\log\frac{\sqrt{1+K}}{U_\infty}\log\left|\frac{t-TD}{t-TC}\right|$$

The first integral will be evaluated numerically in the three matching regions: in the regions where $q(\tau)$ is constant (and also for the second integral of $\beta(t)$), we shall evaluate it analytically by means of the dilogarithm function.

The evaluation of $\beta'(o)$ and $\beta''(o)$ will be made by differentiating the expression of $\beta(t)$

We also need to evaluate β at TE (downstream infinity) and $\beta_1 = \lim(\beta - \beta_\infty)t$ if $\tau \to -\infty$.

I.A.4 - Study of the different iterations

Initialization

TA and TB, which are used to adjust the length of the upper and lower foil surfaces are defined as follows :

$$f(TA) = -L\, q_{ex}\, U_{cav} = TA + TE\log\left|\frac{TA-TE}{TE}\right|$$

$$f(TB) = L\, q_{in}\, U_{cav} = TB + TE\log\left|\frac{TB-TE}{TE}\right|$$

This is equivalent to writing that the curvilinear abscissa is equal to x, and that velocity distribution is constant over the segments (O - TA) and (O - TB).

T3 and T4 are arbitrarily adjusted, so that $f(T4) = T4_1 = f(TB)$ and $f(T2) = T2_1 = f(TA)$.

TE is used to adjust the depth of submergence of the profile ; as the flow-rate at upstream infinity between the free surface and the streamline arriving at the stagnation point, or between the free surface and the wake upper surface is $\Delta\phi = -\pi\, TE$.

Therefore, $-\frac{\pi\, TE}{U_\infty}$ corresponds to the section through which this flow takes place, i.e.

$$TE = -\frac{U_\infty H}{\pi}.$$

The initial value of the ratio $CEI = \frac{CPE}{CPI} = \frac{(1+K)\,q_{ex}^2 - 1}{(1+K)\,q_{in}^2 + 1}$ is arbitrarily chosen (generally $0.5 < CEI < 0.9$) and $CPI = \frac{2P}{1+T4_1+CEI(1+T2_1)}$.

The value of $d_1 q_0 = q'_0$ is related to the radius of curvature.

In fact, we know that for the osculatory parabole of the profile,

$$\frac{1}{RC} = \frac{dq}{ds}$$

with this approximation, we get :

$$\frac{1}{RC} = \frac{dq}{dt}\frac{dt}{df}\frac{df}{ds} = -q_0'^2\, TE(1+K)$$

i.e.

$$q'_0 = \sqrt{\frac{-1}{(1+K)RC\ TE}}$$

Calculation of TC and TD

TC and TD are determined so that $\beta(TE) = \beta_\infty$ and so that $\beta_1 = \lim(\beta - \beta_\infty)t = 0$ if $t \to -\infty$.

$\beta(TE)$ is therefore written in the form :

$$\beta(TE) = \beta_\infty + \text{CC} = \frac{1}{\pi}\log\frac{\sqrt{1+K}}{U_\infty}\log\left|\frac{TE-TD}{TE-TC}\right|$$

Moreover, if $t \to -\infty, \beta \sim \beta_\infty + \frac{\beta_1}{t}$ giving $\frac{dy}{dx} \sim \operatorname{tg}\beta_\infty + \frac{\beta_1}{x}$.

The streamline will therefore diverge if $\beta_1 \neq 0$.

Note

At this stage of the calculation, if the profile has no physical meaning, i.e. if TC is external to (TE, TA) or if TD < TB, it is necessary to decrease the value of K and to resume the complete calculation.

Determination of $d_2 q_o = q_o^*$ - Shock-free entry condition.

$$RC = \frac{ds}{d\beta} = \frac{ds}{df}\frac{df}{dt}\frac{dt}{d\beta} = \frac{f'}{q\,\beta},$$

and

$$\frac{dRC}{ds} = \frac{f'}{q\beta^*}\left(\frac{f''}{f'} - \frac{q'}{q^*} - \frac{\beta^*}{\beta^*}\right)$$

i.e.

$$\frac{\beta_o^*}{\beta_o^*} = \frac{q_o^*}{2q_o^*} - \frac{1}{TE} = \text{function } (q_o^*).$$

This iteration is perfectly linear, its slope being proportional to q_o^* and to TE.

Determination of the profile and the lift force

At this stage of the calculation we have all the required elements to define a profile, i.e. first to determine the distribution $\beta(t)$, and secondly to determine coordinates x(t), y(t) and total lift force.

Nevertheless, we obtain a profile which cannot be considered as satisfactory since there is no reason for it to have the chosen length (upper and lower foil surfaces), thickness and lift force.

If LE and LI are the effective upper and lower surface lengths obtained (in fact, very close to L), the values of TA and TB are modified as follows :

$$f(TA) = -\,q_{ox}\frac{L}{LE}\sqrt{1+K}$$

$$f(TB) = q_{in}\frac{L}{LI}\sqrt{1+K}$$

The thickness is adjusted linearly with respect to CEI, while modifying the lift force as little as possible.

The slope for this iteration is preset to - 1/lift, since the validity of this approximation has been established through practice.

For a lift force close enough to the sought line , we perform a linear iteration with respect to CPI (without altering CEI).

Definition of depth of submergence

At this stage, we have determined a profile which meets our conditions, but for which the depth of submergence (distance between the stagnation point and the free surface at rest) is not necessarily correct.

We shall calculate the deformation y_1 of the streamline running from upstream infinity to the stagnation point, by taking into account series expansions of y(z) and x(τ) when $\tau \to -\infty$.

Since $y_o = \frac{\pi TE}{U_\infty}$ is the distance between this streamline and the upstream infinity free surface, we may write $H = -y_o + y_1$.

Since y_1 is small and almost independent of H, we get

$$TE = -\frac{U_\infty}{\pi}(-y_1 + H)$$

B - Three-Dimensional Study -(2),(3),(4),(5),(6).

The present study deals with the flow past a base ventilated wing of high aspect ratio moving under the free surface (the Froude number being infinite).

I.B.1 - Construction of the solution

Definition of the Far-Field

The aspect ratio 1/ε is high, and the span is fixed. The flow (Prandtl lifting-line theory) tends to be that created by two vortex lines symmetrically located regarding the free surface.

$$\phi = x + \frac{1}{4\pi}\int_{-1}^{1}\frac{y\,y(z')\,dz'}{y^2+(z-z')^2}\left(1+\frac{x}{\sqrt{x^2+y^2+(z-z')^2}}\right)$$

$$+\frac{1}{4\pi}\int_{-1}^{1}\frac{(y-2h)y(z')dz'}{(y-2h)^2+(z-z')^2}\left(1+\frac{x}{\sqrt{x^2+(y-2h)^2+(z-z')^2}}\right)$$

Definition of the Near-Field

Considering this same wing, the chord length being fixed, the span tends to infinity as 1/ε.

In the "Near Field", the flow created will be calculated using inner X, Y and Z coordinates obtained from the previous ones by the relations :

$$X = \frac{x}{\varepsilon}$$

$$Y = \frac{y}{\varepsilon}$$

$$Z = z$$

In this zone, X, Y and Z are of order 1 or less. The potential $\Phi = \frac{1}{\varepsilon}\phi(x, y, z)$ must satisfy the Laplace equation

$$\frac{\partial^2\phi}{\partial x^2} + \frac{\partial^2\phi}{\partial y^2} + \frac{\partial^2\phi}{\partial z^2} = 0$$

i.e.

$$\frac{\partial^2\phi}{\partial X^2} + \frac{\partial^2\phi}{\partial Y^2} + \varepsilon^2\frac{\partial^2\phi}{\partial Z^2} = 0$$

At the first order, Φ is thus the solution to the two dimensional Laplace equation as studied in § I.A.

Asymptotic matching

The solution of the outer problem represents the flow in the upstream infinity region, while that of the inner problem represents the flow near the wing. In each of these regions, one solution will be valid, while the other will fail. Expressed in outer x, y, z coordinates, the outer solution will not be valid if x or y are of order ε, while in inner X, Y, Z coordinate, the inner solution will fail if X and Y are of order $1/\varepsilon$ (or if x and y are of the order of 1, X and Y being referenced to the outer coordinates).

Therefore, the problem will be to find a uniformly valid potential for which the limits within the outer and inner coordinates (and in the outer and inner domains) will be the same as those given by the solutions to the external and internal problems.

There exists a frontier domain in which the solutions should match, and be both valid according to their order of approximation.

In this region, both solutions must be equivalent, i.e. the limit of Φ_E if $x \to 0$ must be equal to the limit of Φ_I if $x \to -\infty$.

Limit of Φ_E if $X \to 0$

With the inner coordinates ($y(z) = \varepsilon\, \Gamma(Z)$), we obtain :

$$\frac{\partial \Phi_E(X,0,Z)}{\partial Y} \sim -\frac{\Gamma(Z)}{2\pi}\left(\frac{1}{X}+\frac{X}{4H^2+X^2}\right)$$

$$-\frac{1}{4\pi}\int_{-1}^{1}\frac{\partial \Gamma}{\partial Z'}\,\frac{dZ'}{Z-Z'}$$

$$-\frac{1}{4\pi}\int \frac{\partial \Gamma(Z')}{Z'}\,\frac{Z-Z'}{(Z-Z')^2+4H^2}\,dZ'$$

Note :

In the subsequent calculations, we shall consider the depth of submergence h as small (of order ε), but since the final expressions are coherent with the results obtained for infinite depth of submergence, these shall be used, whatever the value of $h = \varepsilon H$.

Limit of Φ_I if $X \to -\infty$.

The series expansion of Φ_I if $X \to -\infty$ is

$$\Phi_I \sim U_\infty \cos\beta_\infty (X + Y\,tg\beta + \beta_1\, tg^{-1}\frac{Y}{X}) + O(1)$$

where

$$\beta_1 = \lim_{t\to-\infty}\,(\beta-\beta_\infty\, t)$$

The equality of these two limits, which entails the existence of a domain in which both solutions are equally valid therefore imposes :

$$\begin{cases} U_\infty \cos\beta = 1 \\ tg\beta - \dfrac{\varepsilon}{4\pi}\left(\displaystyle\int_{-1}^{1}\frac{\partial\Gamma(Z')}{\partial Z'}\,\frac{dZ'}{Z-Z'}\right. \\ \qquad\qquad \left. \cdot\displaystyle\int_{-1}^{1}\frac{\partial\Gamma(Z')}{\partial Z'}\,\frac{(Z-Z')\,dZ'}{(Z-Z')^2+4H^2}\right) \\ \qquad = \alpha(Z) \\ \beta_1 = -\dfrac{\Gamma(Z)}{2\pi} \end{cases}$$

These three conditions must be applied to the calculation described in § A.

The common limit of Φ_E and Φ_I will be called Φ_ℓ

$$\Phi_\ell = X + Y\,tg\beta + \beta_1\, tg^{-1}\frac{Y}{X}$$

Giving :

$$\Phi = \Phi_E + \Phi_I - \Phi_\ell$$

I.B.2 - Evaluation of the depth of submergence

The depth of submergence H will be given by :

$$H = \int_0^{-\infty}\frac{\partial Y_I}{\partial X}\,dX + \int_0^{\infty}\frac{\partial Y_E}{\partial X}dX - \int_0^{-\infty}\frac{\partial Y_\ell}{\partial X}\,dX - \frac{\pi T\varepsilon}{U_\infty}$$

A very low value XNF is used, such that :

$$\int_0^{XNF}\frac{\partial Y_\ell}{\partial X}\,dX = \int_0^{XNF}\frac{\partial Y_E}{\partial X}\,dX$$

Using series expansion of $\frac{\partial Y_I}{\partial X_s}$ when $X_s \to -\infty$ we evaluate

$$I_R = \int_{-\infty}^{X_s}\left(\frac{\partial Y_I}{\partial X} - \frac{\partial Y_\ell}{\partial X}\right)dX$$

We get :

$$I_R \sim -\beta(T\varepsilon - tg\beta_\infty)\,\frac{(\log|X_s|+1)}{X_s} + \frac{\cos^2\beta_\infty}{X_s}\left(\beta_2 + \beta_1^2 tg^2\beta_\infty - \frac{\kappa_A}{\cos^2\beta_\infty}\right) + O\left(\frac{1}{X_s^2}\right)$$

where

$$\beta_1 = \lim_{t\to-\infty}(\beta-\beta_\infty)t$$

$$\beta_2 = \lim_{t\to-\infty}(\beta-\beta_\infty-\frac{\beta_1}{t})t^2$$

$$\kappa_A = \lim_{X\to-\infty}\left(\frac{1}{X} + \frac{1}{t\cos\beta_\infty}+(T\varepsilon - tg\,\beta_\infty)\frac{\log|X|}{X^2}\right)X^2)$$

Therefore, we obtain :

$$H = Y_I(X_s) - I_R - Y_\ell(XNF) - tg\beta(XS-XNF) - \beta_1\log\left|\frac{X_s}{XNF}\right| - \frac{\pi T\varepsilon}{U_\infty}$$

Numerically, $X_1(t)$ & $Y_1(t)$ will be calculated for values of t tending towards $-\infty$ until convergence is obtained.

In this manner, a new value of IE is obtained, which we will use to solve again the inner problem.

Note -

For paragraph A, we indicated that β_1 should be equal to zero, so as to be homogeneous with the three-dimensional study. In fact, this solution is not used in practice when solving the two-dimensional problem only, since it entails excessively high dissymetry for back and face cavity lengths. In general, authors impose $\phi_A = \phi_B$, which is very close to the three-dimensional result ($\beta_1 = -\frac{\Gamma}{2\pi}$ entails $\phi_A \sim \phi_B$).

II. The Direct Problem

The wing planform and the flight conditions being known, an attempt is made to determine the local and global characteristics of the ventilated wing.

A - Hypothesis

In a perfect fluid, the velocity potential of the three dimensional flow satisfies the Laplace equation and is determined by a surface integral (on the surface of the wing and its cavity) of Green functions representing the potential of elementary singularities.

Since, by hypothesis, the wing and its cavity are thin, linearized boundary conditions will be imposed on a portion of the horizontal plane. The singularities which we use to represent the flow will be distributed over this surface.

The cruising speed of a ship with lifting surfaces of this type being very high, the Froude number shall be considered as infinite.

Gravity and viscosity shall be neglected.

B - Boundary conditions

1.- On the wing

The velocity field must satisfy the wing slippage condition on the wing (a being outwardly normal to the wing). In linear theory this condition will be written respectively for the back and face of the wing

$$\begin{cases} \dfrac{\partial \phi}{\partial z}(x,y,0_+) = \dfrac{\partial \phi_0}{\partial z}(x,y,0) + \dfrac{\partial \phi_1}{\partial z}(x,y,0) = \dfrac{dy_{ex}}{dx} \\ \dfrac{\partial \phi}{\partial z}(x,y,0_-) = \dfrac{\partial \phi_0}{\partial z}(x,y,0) - \dfrac{\partial \phi_1}{\partial z}(x,y,0) = \dfrac{dy_{IN}}{dx} \end{cases} \quad (*)$$

(*) where y_{ex} (respect. y_{IN}) is the y-coordinate for the back (resp. face) of the wing.

or

$$\frac{\partial \phi_0}{\partial z} = \frac{1}{2}\left(\frac{dy_{ex}}{dx} + \frac{dy_{IN}}{dx}\right) \quad (1)$$

$$\frac{\partial \phi_1}{\partial z} = \frac{1}{2}\left(\frac{dy_{ex}}{dx} - \frac{dy_{IN}}{dx}\right) \quad (2)$$

2.- On the cavity.

We assume that the pressure is constant within the cavity. In linear theory, and on the plane surface representing the cavity, ϕ satisfies :

$$\frac{\partial \phi}{\partial x}(x, y, 0) = -\frac{K}{2} \quad (3)$$

(K ventilation number).

3.- Trailing edge.

The thickness of the wing-cavity assembly must not be discontinuous (at the first order) at the trailing edge of the wing. The derivative with respect to x of the thickness will be made continuous at the trailing edge.

4.- Cavity closing.

The cavity will be extended to down-stream infinity by a wake of constant thickness. The cavity closing line will be defined as the line on which the derivative with respect to x of the thickness cancels out. This modelization is the consequence of the singularities used in the schematization.

5.- Free surface.

Since the Froude number is infinite, the free-surface Poisson condition then degenerates to

$$\frac{\partial \phi}{\partial x}(x, y, H) = 0.$$

6.- Symmetry of the flow.

The wing and its cavity have a vertical plane of symmetry (parallel to the direction of the undisturbed flow). Only one half of the flow is modellized.

Note-

The condition n° 6 will be obtained automatically by associating to each singularity a singularity of the same strength, located symmetrically with respect to the plane of symmetry of the flow. For condition n° 5, the flow obtained with the above two singularities will be completed by two singularities located symmetrically with respect to the free surface and of equal strength (vortices) or opposite strength (sources).

C - Discretization of integrals representing the velocity field (9), (10)

1.- On the wing (see figure 4)

The wing is divided into elementary strips parallel to the direction of the undisturbed flow. The Jth strip is bounded by two straight lines, η_j and η_{j+1} such that :

$$\eta_j = env \cdot \sin\frac{(2j-2)\pi}{4n_s+2} < \eta < \eta_{j+1} = env \cdot \sin\left(\frac{2j\pi}{4n_s+2}\right)$$

(where $env = \frac{span}{2}$; n_s = number of strips).

Each of these strips is transformed into a rectangular strip of the same width and unit length by a linear change of abscissa $t = f(x)$.

We assume the strength of the different singularities used to be a function of t only for each of these strips. Thus, for each strip, the different Green functions will be first analytically integrated with respect to η, t being held constant. We then perform an integration with respect to t, using a quasi-continuous Gauss method ; results obtained for each strip will then be summed up.

2. On the cavity (see figure 4)

The cavity is divided into strips which are extensions of those defined on the wing. On these strips, trapezoidal boxes are defined, on which the strength of the singularities will be constant.

Since the shape of the cavity is one of the unknowns of the problem, the distribution of these boxes must extend down-stream from the previously determined closing line.

Integration on the cavity will be performed by double summation of the elementary integrals calculated analytically for each box, and for which the singularity strength is considered as constant.

3. Location of the test points (see figure 4).

The test points are points at which the boundary conditions defining the velocity potential must be satisfied.

On the wing, the x- and y- coordinates of the i^{th} test point located on the j^{th} strip, are given by :

$$x(i,\ j) = \frac{c(j)}{2}\left(1 - \cos\left(\frac{2i\pi}{2\ n_c+1}\right)\right) + x_A(j)$$

c(j) chord at y(j)-coordinate

$$y(j) = env \cdot \sin\frac{(2j-1)\pi}{4\ n_s+2}$$

$x_A(j)$ = x - coordinate of the leading edge at y(j)

n_c number of test points in each strip.

Using the Gauss method, this discretization will enable us to integrate the local forces calculated at the test points.

On the cavity, the test points will be located in the center of each box.

D - Singularities used (7), (8)

1.- Sources

$$\phi_S(x,\ y,z) = -\frac{1}{4\pi}\iint_S \frac{s(\xi,\eta)\ d\xi\ d\eta}{(x-\xi)^2+(y-\eta)^2+z^2}$$

The potential corresponds to a velocity field such that the surface of integration is a discontinuity surface for the w velocity, i.e.

$$\frac{\partial\phi_S}{\partial z}(x,\ y,\ 0_+) - \frac{\partial\phi_S}{\partial z}(x,\ y,\ 0_-) = s(x,\ y)$$

The boundary condition defined by equation 2 will be automatically satisfied by taking :

$$s(\xi,\eta) = \frac{1}{2}\left(\frac{dy_{ex}}{dx}(\xi,\eta) - \frac{dy_{IN}}{dx}(\xi,\eta)\right)$$

2. Vortices

$$\phi_t(x,y,z) = -\frac{1}{4\pi}\iint^{t(\xi,\eta)}\frac{\partial}{\partial z}\int_{-\infty}^{x}\frac{d\lambda\ d\eta\ d\xi}{\sqrt{(\lambda-\xi)^2+(y-\eta)^2+z^2}}$$

The potential is created by a distribution of bound horse shoe vortices on the horizontal surface S. This distribution is extended down-stream from the trailing edge by free vortices parallel to the direction of the undisturbed flow.

The surface of integration is a discontinuity surface for the velocity

$$u_t = \frac{\partial\phi_t}{\partial x}$$

$$\frac{\partial\phi_t}{\partial x}(x,y,0_+) - \frac{\partial\phi_t}{\partial x}(x,y,0_-) = t(x,y)$$

3. Pressure sources

$$\phi_{SP}(x,y,z) = -\frac{1}{4\pi}\iint_S SP(\xi,\eta)\int_{-\infty}^{x}\frac{d\lambda\ d\xi\ d\eta}{\sqrt{(\lambda-\xi)^2+(y-\eta)^2+z^2}}$$

The surface of integration is a discontinuity surface for the velocity $w = \frac{\partial\phi_{SP}}{\partial z}$ (x, y, 0). If we consider a box on which the distribution SP(ξ,η) is constant and equal to unity

$$\frac{\partial\phi_{SP}}{\partial z}(x,\ y,0_+) - \frac{\partial\phi_{SP}}{\partial z}(x,y,0_-) = 0 \qquad x < x_A$$

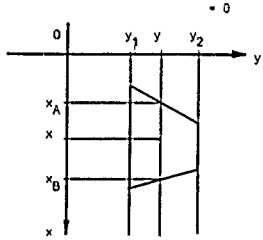
$$= x - x_A(y) \qquad x_A < x < x_B$$

$$= x_B(y) - x_A(y) \qquad x > x_B$$

with $y_1 < y < y_2$

and

$$= 0 \qquad y < y_1 \quad y > y_2$$



The fact that the discontinuity of the velocity w is zero at the leading edge of the elementary box, and therefore on the trailing edge of the wing, would entail a discontinuity in the derivative of the wing-cavity thickness at the trailing edge. To solve this, we extend continuously to downstream infinity the source distribution on the wing by a distribution of sources, the strength of which does not vary with x.

Distribution of such pressure sources also imposes the cavity closing diagram ; the cavity will be extended to down-stream infinity by a wake of the same width and of constant thickness. The closing line is defined as the line on which the derivative of the thickness cancels out. Downstream from this frontier, the pressure source boxes and the corresponding test points are eliminated.

The interest of such pressure source boxes is that they induce on themselves a maximum velocity $u = \frac{\partial \delta}{\partial x}$, which entails that the associated influence coefficient matrix will have a predominant main diagonal.

E - Resolution Method

The problem thus "discretized", using a conventional collocation method, leads to resolving the following linear equations :

- On the wing at test points C_i, i varying from 1 to $n_t = n_s + n_c$

$$\frac{1}{2}\left(\frac{dy_{ex}}{dz} - \frac{dy_{IN}}{dz}\right) - \alpha_i = \sum_{j=1}^{n_s} s_j A_{ij} + \sum_{j=1}^{n_t} t_j B_{ij} + \sum_{j=1}^{n_{SP}} SP_j C_{ij}$$

α_i is the angle of attack of the wing at : $x = x_i$.

It is possible to associate a different angle of attack to each elementary strip, and to reach by iteration the shock-free angle of attack for this strip.

- On the cavity, at test points C_i, i varying from 1 to n_{SP}

$$K - \sum_{j=1}^{n_s} s_j D_{ij} = \sum_{j=1}^{n_t} t_j E_{ij} + \sum_{s=1}^{n_{SP}} SP_j F_{ij}.$$

The Gauss-Seidel iterative method will be used to solve this system.

At each step of the iteration, the thickness of the cavity shall be calculated at each test point located on the cavity. On each of the elementary strips of the cavity, the derivative with respect to x of the thickness first increases and then decreases. The cavity being defined as the region where the derivative of the thickness is positive or equals zero, the boxes located downstream from this limit will be suppressed, together with the equations concerning the associated test points.

The method is well converging and the shape of the cavity stabilizes after a very small number of iterations.

As we know, at this step of the process, the strength of all singularities, we can then easily determine the velocity and therefore the pressure on the back and face of the wing.

Performing a double integration by Gauss's method, we determine the lift, non-viscous drag and global moment.

The velocity at the leading edge is not defined, as in any linearized problem ; but calculation of $\frac{\partial \delta}{\partial x}$ using the Gauss method enables us to evaluate the limit of $\frac{\partial \delta}{\partial x}(x,y,0)\sqrt{x-x_A(y)}$ if $x \to x_A(y)$, $x_A(y)$ being the abscissa of the leading edge at y-coordinate.

A two-dimensional velocity regularization method (Riegels or Lighthill method) will then be used to approximate the velocity at the leading edge. It can be expected that, as well as in the two-dimensional case, this method will be all the more valid as we approach the shock free angle of attack (11), (12).

III. Numerical Investigation and Conclusions

The figure defines the planform of a half-wing. The relative thickness of each section is 10 %.

The wing, submerged at a depth of 0.38 m, has a loading of 12 metric tons per sq.m; it is part of the lifting system of a hydrofoil craft moving at 72 knots. The spanwise distribution of the lift coefficient is given by :

$$Cp_o(y) = \frac{0.092\sqrt{0.647\ y_i}}{0.80 + 0.45\ y}$$

The ventilation coefficient is K = 0.035.

Resolution of the inverse problem leads us to define 8 sections for which the y-coordinates are defined by :

$$y_i = 0.80441 \sin\frac{(i-1)\pi}{15}.$$

The wing so defined is discretized as shown in figure 4. 84 test points are defined over the wing (7 along the span x 12 along the chord), and 140 are positioned in order to define the cavity (only the two first rows of boxes have been shown).

We then use the direct program to find the spanwise distribution of the lift coefficient Cp_i (y) and the value of the velocity at the leading edge.

A first set of linear iterations performed on the angle of attack of each of the 7 basic strips enables us to define a law $\alpha_i(y)$. The wing for which each strip is positioned at the shock free angle of attack by rotation $\alpha_i(y)$

has a spanwise distribution of the lift coefficient $Cp_2(y)$.

By using the program resolving the inverse problem, we define a new wing having a distribution of the lift coefficient :

$$Cp_3(y) = \frac{Cp_0^2(y)}{Cp_2(y)} .$$

As before, by determining a law $\alpha_3(y)$ by iteration, each elementary strip will be positioned at the shock-free angle of attack.

Figure 8 shows the spanwise distribution $\alpha_1(y)$ and $\alpha_2(y)$ of the shock-free angle of attack.

Distribution $Cp_1(y)$ of the lift coefficient will then be very similar to distribution $Cp_0(y)$.

Figure 6 shows the evolution of the spanwise distribution of the lift coefficient during the iterative process.

Figure 3 represents the wing with its 8 side view sections, while figure 5 represents section n° 3, y = 0.3272 in more details.

Figure 7 shows the chordwise distribution of the lift coefficient on the back and face of section y = 0.421188 of the wing.

Figure 9 shows the spanwise distribution $V_1(y)$ of the leading edge velocity obtained when we first use the direct program (before the iterative process). We can compare $V_1(y)$ with $V_2(y)$ obtained when the wing is defined by the purely bidimensional inverse method (without the three-dimensional correction). We can see the best adaptation of the wing. This also implies that the iterative process shall always converge and shall do so more rapidly.

To conclude, a convenient fitting between the direct and inverse theories can be observed. In particular, the inverse problem generates sections which are at an angle, close to the shock-free angle of attack, enabling rapid correction by iterations performed from the direct problem, and which do not call for recalculation of the influence coefficients.

Unfortunately, we have no experimental results to check out the adequacy of this method.

While remaining optimistic, we are fully conscious of the improvement which would be achieved by 1- our taking into account the Froude number, 2- a three-dimensional regularization method for the velocity at the leading edge and 3- a better schematization of the cavity.

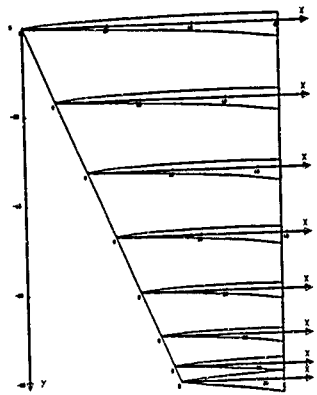


FIG 3 PLANFORM WITH SIDE VIEW OF 8 SECTIONS

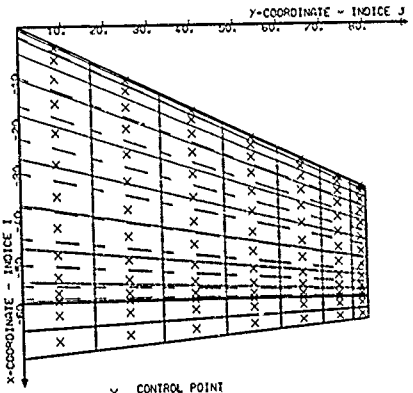


FIG 4 FOIL REPRESENTATION AND FRONT PART OF THE CAVITY

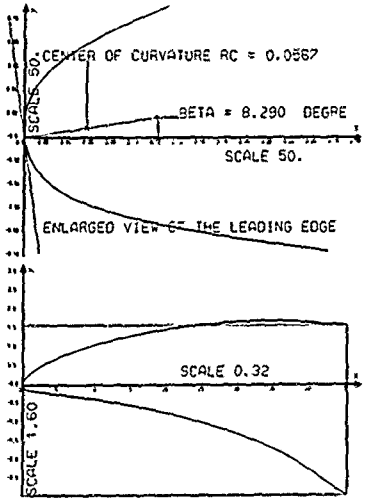


FIG 5 SECTION NO 3

CHORD L = 45.277
LEADING EDGE X = -14.723
H = 38.0
Z = 32.718

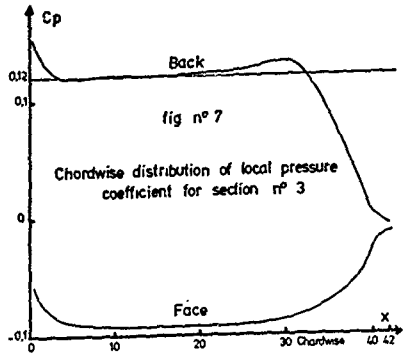


fig n° 7

Chordwise distribution of local pressure coefficient for section n° 3

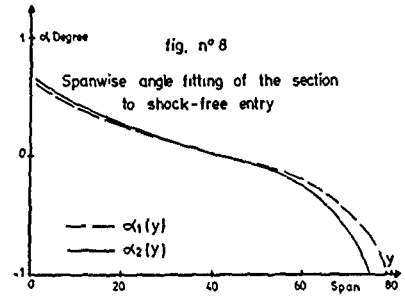


fig. n° 8

Spanwise angle fitting of the section to shock-free entry

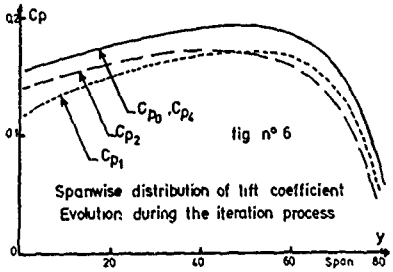


fig n° 6

Spanwise distribution of lift coefficient Evolution during the iteration process

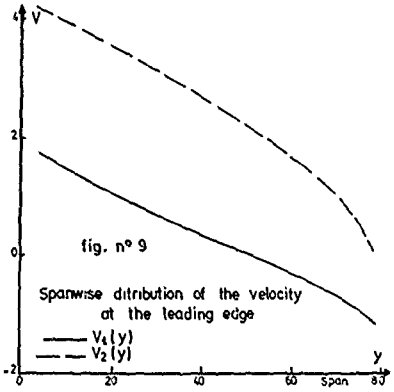


fig. n° 9

Spanwise ditribution of the velocity at the leading edge

References

(1) - B. LAROCK and R. STREET - Non Linear Solution For A Fully Cavitating Hydrofoil Beneath A Free Surface.
Journal of Ship Research, 11, 1967, p.131-140.

(2) - O. FURUYA - Three Dimensional Theory On Supercavitating Hydrofoils Near A Free Surface.
Journal of Fluid Mechanics,
Part 1, vol. 68, p.21-40,
Part 2, vol. 71, p. 337-359.

(3) - M. VAN DIKE - Perturbation Methods in Fluid Mechanics.
Academic Press 1964.

(4) - M. VAN DIKE - Lifting-Line Theory As A Singular Perturbation Problem.
Journal of Applied Mathematics and Mechanics, 28, 1964, p. 107-118.

(5) - A.J. ACOSTA and O. FURUYA - A Note On The Three Dimensional Supercavitating Hydrofoils.
Journal of Ship Research, vol. 19, n° 3, 1975, p. 164-165.

(6) - P. LEEMEY - Supercavitating Hydrofoil Of Finite Span.
UTAM Symposium, Leningrad, vol. 14, n° 5, 1975.

(7) - J. VERRON - Ecoulements Cavitants Autour d'Ailes d'Envergure Finie En Présence d'Une Surface Libre.
Journal de Mécanique, vol. 18, n° 4, 1979, p. 745-774.

(8) - J.F. UNRUH and R.L. BASS - A General Theory of Unsteady Loads on Cavitating Hydrofoils.
Final Report, Southwest Research Institute, December 1973

(9) - C.E. LAN - A Quasi Vortex Lattice Method For The Thin Wings Theory.
Journal of Aircraft, vol. 11, n° 9

(10) - H. VIVIAN and W. GHAZZI - Calcul Numérique d'Ecoulements Subsoniques Linéaires Autour d'Ailes.
La Recherche Aérospatiale, n° 5, 1974, p. 247-260.

(11) - M.J. LIGHTILL - A Technique For Rendering Approximate Solutions to Physical Problems Uniformly Valid.
Phil. Mag., vol. 40, n° 7, December 1979

(12) - R. BAUBEAU - Répartition des Vitesses Sur Un Profil par Une Méthode Uniformément Valable.

(13) - R. BAUBEAU - Définition de la géométrie des structures ventilées à la base.
La Houille Blanche, n° 5/6, 1977.

SUPERCAVITATING HYDROFOILS IN NONLINEAR THEORY*

C. Pellone and A. Rowe
Institut de Mécanique de Grenoble
B P. 53 X, 38041 Grenoble Cedex (France)

Abstract

A non-linear calculation method, based on a surface singularity distribution is used to determine the two- and three-dimensional flow of a perfect incompressible fluid around a supercavitating hydrofoil. The exact boundary conditions are satisfied on the foil and the cavity. The velocity potential is generated by a distribution of sources over the foil, tangential doublets over the cavity, normal doublets over the foil, the cavity and the wake and a distribution of linear sinks placed at the rear of the cavity. The numerical solution of the problem allows the non-linear calculation of the cavity geometry using an iterative procedure.

In two-dimensional flow, after calculation of a supercavitating hydrofoil with wetted upper side, the method is used to calculate the position of the point of cavity separation and to extend the calculation to the case of a foil geometry with unwetted upper side. The procedure also proved effective in treating the case of a hydrofoil followed by very short cavities. In three-dimensional flow, the case of a swept-back hydrofoil of non-zero thickness is presented.

I. Introduction

Two difficulties are encountered in calculating the hydrodynamic characteristics of a supercavitating structure :

a) the presence of a cavity followed by a two-phase and turbulent wake requires a certain degree of modelling in order to be able to deal with the problem within the framework of potential flow,

b) since it is a free boundary problem, it is particularly difficult to solve the non-linear direct problem.

* This study was sponsored by the French "Direction des Recherches, Etudes et Techniques" under contract No 78-490.

Many linear theory studies have been carried out using analytical methods in the case of two-dimensional flow, the aim of these studies being to validate the calculate schemes chosen to model the cavity, and to estimate the error due to linearisation [1] to [6] . The error due to linearisation is all the greater as the upper side of the hydrofoil becomes unwetted : in such a case, there is considerable flow deviation. When the foil has a rounded leading edge and the upper surface is wetted, flow deviation is less significant and the overall coefficients calculated are closer to reality, but the pressure distribution at the leading edge is singular. For these reasons, it seems necessary to develop a non-linear theory. However, the difficulties are such that, to date and to the author's knowledge, only the following two-dimensional flow problems have been resolved :

- the flat plate problem with or without consideration of gravity effect [7] and [8] ,
- the indeterminate problem related to a hydrofoil of undefined shape [9] ,
- the inverse problem related to a particular load law [10] ,
- the direct problem related to a hydrofoil with unwetted upper side and with lower side of arbitrary shape [11] .

It was therefore apparent that the resolution of the direct problem in non-linear theory concerning a supercavitating foil with wetted upper side and truncated rear had not been dealt with up till now.

In the framework of analytical methods, resolution of the three-dimensional problem can be considered by a perturbation method matching the lifting line solution according to PRANDLT's theory. If the solution is limited to the first order, the method is very simple to implement but, in this case, the three-dimensional character of the flow is extremely schematised. Such is the work carried out by R. BAUBEAU [10] and O. FURUYA [12] using a non-linear solution of the two-dimensional problem. Mention should also be made of the work of P. LEEHEY [13] who extended matching

to the second order, but on the basis of the linear two-dimensional solution.

In the framework of numerical methods, the problem of cavitating flow has already been dealt with in a number of studies. To the author's knowledge, all these studies were carried out on the basis of a linear theory : before the development of computers, T.S. LUU had already defined a rheo-electric simulation method [14] and [15] . The case of a hydrofoil with unwetted upper side followed by a cavity of finite length was dealt with by L.F. TSEN and M. GUILBAUD in 1970 [16] . VERRON [17] studied the case of a foil with wetted upper side, the cross-section of which was a symmetrical wedge. The method used by VERRON could be extended to the case of a foil with an arbitrary cross-section by making the solution regular at the leading edge by matching the solution obtained to a local regular three-dimensional solution, according to the technique proposed by J.P. DARROZES [18] . This solution would have the disadvantage of introducing errors at high angles of attack and, as a result, extension to the case of supercavitating hydrofoils with unwetted upper side could not be made without certain restrictions. Another possible approach to the non-linear problem would be to adapt the vortex lattice method used at the O.N.E.R.A. by C. REHBACH [19] . This approach creates difficulties since, when dealing with closed bodies of a certain thickness, the system matrix is singular. The means by which these difficulties may be overcome are not easy to justify.

The integral method presented in this study enables treatment of both two-dimensional and three-dimensional flow of a perfect incompressible fluid around a hydrofoil. In the case of potential flow around a supercavitating foil with wetted upper side, without lift effect, the potential is generated by a surface source distribution [20] , [21] , [22] . To introduce the lift effect, surface doublicity distribution is required [23] ; in this context, the non-linear problem of the thick foil can be treated by a surface source and doublicity distribution over the foil and a surface doublicity distribution over the wake [24] .

Treatment of the supercavitating foil is made possible by mathematical modelling of the cavity ; the main difficulties encountered are related, on the one hand, to the difference in nature of the boundary conditions which must be satisfied over the foil and the cavity, and on the other hand, to the unknown shape of the cavity. Since the geometric boundary of the cavity must consist of constant-pressure streamlines, the condition on this boundary is expressed by a tangential velocity condition. Assuming the cavity geometry to be known - as a first step - the solution to the problem is obtained by using a surface source distribution on the foil, a surface doublicity distribution (tangential doublets) over the cavity, and a surface doublicity distribution over the foil, the cavity and the wake (normal doublets), plus a linear sink distribution at the rear of the cavity, the total intensity of which is equal to the sum of the sources on the foil. Despite the fact that the solution to the boundary problem expressed is unique, there is not unicity in the distribution of singularities creating the same potential [24] ; consequently, the density of normal doublets over the wake, assumed to be non-deformable, and the cavity is characterised by a relation which is a function of the foil span ; this relation, combined with a linear relation as a function of the chord, allows the normal doublet density over the entire area of the foil to be defined. Calculation of the exact shape of the cavity requires an iterative procedure. As a result of the presence of sinks at the rear of the cavity, the cavity does not close completely ; consequently, the model chosen is a quasi-closed cavity model.

II. Two-dimensional study

The study presented considers the cavity pressure to be unknown ; as a result, the cavity length is imposed.

Consideration is given to the two-dimensional flow around the supercavitating foil (AB) (figure 1). The foil is placed below a free surface at a depth h.

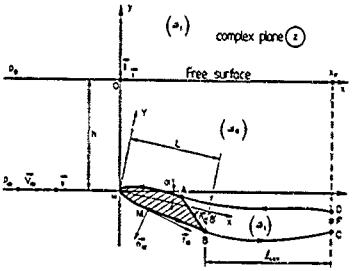


Fig.1

The hypotheses used are those of a perfect, incompressible, irrotational fluid in a semi-infinite field of flow. Since free surface deformations are small, the image method is used to consider the equivalent infinite field of flow. At any point M : $z = x + iy$, the potential Φ_M and the velocity $\vec{V}_M$ are written as follows :

$$\begin{cases} \Phi_M = |\vec{V}_\infty| x + \phi_M \\ \vec{V}_M = \vec{V}_\infty + \vec{v}_M \end{cases} \quad \text{with } \vec{v}_M = \overrightarrow{\text{grad}}_M \phi_M$$

$\vec{V}_\infty$ is the flow velocity at upstream infinity.

On the foil the NEUMANN condition gives :

$$\vec{v} \cdot \vec{n}_M = -\vec{V}_\infty \cdot \vec{n}_M \quad \text{for } M \in (AB) \qquad (1)$$

The constant pressure and NEUMANN conditions on the cavity (DAUBC) give :

$$\begin{cases} \text{For } M \in (DA \cup BC) \begin{cases} \vec{V}.\vec{t}_M = |\vec{V}_\infty| \epsilon_M \sqrt{1+K} - \vec{i}.\vec{t}_M) & (2) \\ \vec{V}.\vec{n}_M = -\vec{V}_\infty.\vec{n}_M & (3) \end{cases} \\ \text{With } \epsilon_M = \text{sign } (\vec{i}.\vec{t}_M) \end{cases}$$

where $K = \dfrac{p_\infty - p_{cav}}{\frac{1}{2}\rho \vec{V}_\infty^2}$ is the ventilation number.

p_∞ being the fluid pressure at upstream infinity at a submersion depth h,

p_{cav} being the pressure in the cavity.

For a given position of the foil, K is a function of cavity length ; since this length is imposed, K becomes an unknown parameter in the problem. In addition, in equations (2) and (3), the direction of the tangent vector $\vec{t}_M$ over the cavity is unknown. This leads to a choice of initial shape of the cavity (DAUBC) schematised in a simple manner.

Taking into consideration the discontinuities introduced by the singularities used, and using HADAMARD's notation [23] , the conditions (1) and (2) lead to the two following equations :

$$\text{Im}\left\{ \frac{1}{2\pi} \int_{(AB)} (\sigma_{M'} - i\gamma_{M'}) e^{i(\alpha_M - \alpha_{M'})} \frac{dz'}{z-z'} + \frac{1}{2\pi} \int_{(DA,BC)} \mu_{tM'} \frac{e^{i\alpha_M} dz'}{(z-z')^2} + \frac{Q_F}{2\pi} \frac{e^{i\alpha_M}}{z-z_F} + \tilde{\tilde{w}}(z) e^{i\alpha_M} \right\} + \frac{\sigma_M}{2} = -\vec{V}_\infty.\vec{n}_M \qquad \text{For } M \in (AB) \qquad (4)$$

$$\text{Re}\left\{ \frac{1}{2\pi} \int_{(AB)} (\sigma_{M'} - i\gamma_{M'}) e^{i(\alpha_M - \alpha_{M'})} \frac{dz'}{z-z'} + \frac{1}{2\pi} \int_{(DA,BC)} \mu_{tM'} \frac{e^{i\alpha_M} dz'}{(z-z')^2} + \frac{Q_F}{2\pi} \frac{e^{i\alpha_M}}{z-z_F} + \tilde{\tilde{w}}(z) e^{i\alpha_M} \right\} - \frac{2}{\pi} \frac{\mu_{tM}}{\Delta s_M} = |\vec{V}_\infty| \epsilon_M \sqrt{1+K} - \vec{i}.\vec{t}_M) \qquad \text{For } M \in (DA \cup BC) \qquad (5)$$

In these expressions :

$\mu_{tM'}$ is the tangential doublets distribution over the cavity,

$\sigma_{M'}$ is the source distribution over the foil,

$\gamma_{M'}$ is the vortex distribution over the foil,

Q_F is the strength of the sink placed at the rear of the cavity,

α_M is the oriented angle of the tangent unit vector $\vec{t}_M$ with the unit vector $\vec{i}$ of the axis $\vec{ox}$;

s_M designates the curvilinear abscissa of the point M on the oriented contour-line (DABC).

In addition, $\tilde{\tilde{w}}(z)$ represents the effect of symmetrical singularities with respect to $\vec{ox}$ at the point M (z).

Since fluid flow rate within the contour-line must be zero, we have :

$$Q_F = -\int_{(AB)} \sigma_{M'} \, ds_{M'}$$

The continuity conditions at points A and B at the boundary between foil and cavity are expressed by :

- the non lifting condition on the cavity

$$\gamma_M \to 0 \begin{cases} \text{when } M \to A \\ \text{and } M \to B \end{cases} \qquad (6)$$

- the zero normal velocity condition at these points

$$\begin{cases} (\vec{V}.\vec{n})_A = -\vec{V}_\infty.\vec{n}_A & (7) \\ (\vec{V}.\vec{n})_B = -\vec{V}_\infty.\vec{n}_B & (8) \end{cases}$$

The first calculation step consists in satisfying the equations (4), (5), (6), (7) and (8) by means of the initial shape of the cavity. From the solution to this problem, the shape of the cavity can be constructed so as to satisfy equation (3) and in the same manner, the procedure is continued until this condition (3) is satisfied exactly at all points over the cavity. The numerical convergence of this iterative procedure is guaranteed.

According to the classical method, the equations of the problem are discretised. The γ distributions are considered proportional to the size of the panels $\left[\gamma_n = \overline{\gamma}\Delta s_n\right]$ taking care to make the last two panels of the upper and lower sides of the trailing edge small, in order that the conditions (6) are automatically satisfied. The discretised equations (4), (5), (7) and (8) give a system of linear equations (N, N) :

$$\sum_{n=1}^{N} G_{mn} \, x_n = B_m \qquad (9)$$

x_n represents the singularities σ_n , μ_{tn} , or the singularity $\overline{\gamma}$, or the unknown parameter $\sqrt{1+K}$. The numbering of the equations and the unknown parameters corresponding to the best layout of the matrix [G] leads to the appearance of a zero on the main diagonal. For this reason, a GAUSS-SEIDEL type algorithm cannot be applied and a direct resolution method

of the HOUSEHOLDER type is adopted to calculate the solutions to the system (9). This method has the advantage of being stable and precise.

Thus, given the fact that the discrete values of the unknown parameters are known, the velocity at all the control points can be calculated. On this subject, it should be noted that the tangential doublets distribution introduces a normal velocity discontinuity proportional to $\frac{d\mu}{ds}$. At the m^{th} control point, $\frac{d\mu_m}{ds}$ is calculated by a finite difference scheme giving the result as a linear function of the values of μ_m. BERNOUILLI's equation gives the pressure coefficient as a function of the velocity, and the lift and drag coefficients are calculated by integrating this pressure coefficient on the foil.

Resolution of the problem by means of the initial shape of the cavity is step (o) of the iterative procedure. At step (1), the position of the panels forming the initial cavity is modified so that they are tangential to the velocity vector calculated at their control point, creating a new cavity geometry. From this new position of the cavity, the entire problem is recalculated. Further steps follow until convergence of the procedure. The calculation shows that when this procedure has converged, the cavity is not completely closed, and that the distance CD is about half the thickness of the foil AB : this result is due to the presence of the sink placed in F. If the streamlines around point F are drawn, it is found that there is a point downstream of F where the velocity is zero. The shape of the cavity could therefore have been extended as far as this point by continuity, but it seemed preferable to keep the half-thickness scheme which proves to be more practicable from the numerical standpoint. This remark justifies calling the model "quasi-closed". Indeed, such a model corresponds fairly well to the case of ventilated cavities.

After complete resolution of the problem, it is considered that the free surface must be a streamline ; to meet this condition, the free surface is deformed so that each constituent panel is parallel to the velocity vector calculated at its centre.

The above-mentioned theoretical study was implemented by a computer programme which comprised about one thousand Fortran instructions. The programme was run on a C.D.C. 6600 which is sufficiently powerful to process the overall matrix in the central memory, thereby saving time with respect to a procedure based on the use of data files. The arrangement of the panels on the foil is given by a cosine relation which ensures good geometrical representation of the leading edge and good numerical representation of the trailing edge. The geometry of the initial cavity is discretised according to a cosine relation which gives a fairly fine mesh of the geometry in the immediate vicinity of the foil and in the area around its closure point.

After step zero, for the following steps, the total calculation is not necessary ; this is because, among the mesh computation points of step (n), the only ones to have changed position are those belonging to the cavity ; consequently, at step (n+1), the velocity influences of the panels belonging to the foil at its control points do not have to be recalculated. This remark is valid for the matrix coefficients as well.

In all the cases dealt with, it was found that 5 steps were sufficient to obtain convergence of the method : the method convergence criterion is such that, for all the cavity control points, the NEUMANN condition is respected over the entire cavity with a relative precision of 10^{-3}.

The cases with the longest cavities require a total of 220 panels spread over both the foil and the cavity : the calculation time per step (resolution of the problem for a given cavity geometry) is about 40 seconds C.P.U. Resolution of the entire problem takes 200 seconds C.P.U.

III. Three-dimensional study

This problem is treated in an infinite field of flow in order to simplify the analysis. Compared to the two-dimensional problem, the three-dimensional problem has the following additional difficulties :

a) the length of the cavity is an a priori unknown function of foil span ;

b) the direction of the tangential velocity vector on the cavity surface is unknown.

The hypotheses concerning the fluid and the flow are the same as those made in Part II. The foil is placed in the reference system (oxy) so that the velocity at upstream infinity $\vec{V}_\infty$ is parallel to the axis $\vec{oy}$ (see figure 2).

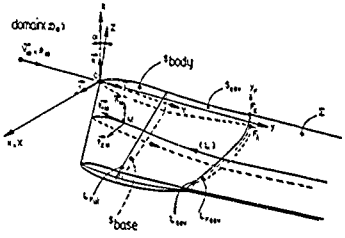


Fig.2

The foil, the cavity and the wake are symmetrical surfaces with respect to the plane (oyz). Since the flow has the same symmetry, only that part of the domain located on the positive side of the x-axis is considered. The various notations used are indicated on figure 2. An orthonormal reference system on the surface ($\vec{t}_{1M}$, $\vec{t}_{2M}$, $\vec{n}_M$) is defined so that the vector $\vec{t}_{1M}$ is orthogonal to the vector $\vec{i}$ of the axis $\vec{ox}$ and to the outward normal $\vec{n}_M$.

The boundary conditions are expressed by the following equations :

$$\vec{V}.\vec{n}_M = -\vec{V}_\infty.\vec{n}_M \quad \text{For } M\epsilon(S_{body}) \qquad (10)$$

$$\begin{cases} \text{For } M\epsilon(S_{cav}) \begin{cases} \vec{V}.\vec{t}_M = |\vec{V}_\infty|\epsilon_M\sqrt{1+K}-\vec{j}.\vec{t}_M) & (11) \\ \vec{V}.\vec{n}_M = -\vec{V}_\infty.\vec{n}_M & (12) \end{cases} \\ \text{With } \epsilon_M = \text{sign } (\vec{j}.\vec{t}_M) \end{cases}$$

The singularities are of the same nature as in the two dimensional problem. Equations (10) and (11) lead to the following integral equations :

$$\iint_{S_{body}} \sigma_p \vec{X}_\sigma.\vec{n}_M \, dS_p + H^o_\sigma \sigma_M + \iint_{S_{cav}} \mu_{tp} \vec{X}_t.\vec{n}_M dS_p$$
$$+ \iint_{S_{body}, S_{cav}, \Sigma} \mu_{np} \vec{X}_n.\vec{n}_M \, dS_p + H^o_{0n} \mu_{nM} +$$
$$\int_{L_{Fcav}} \lambda_p \vec{X}_\sigma.\vec{n}_M \, ds_p = -|\vec{V}_\infty|\vec{j}.\vec{n}_M \quad \text{For } M\epsilon(S_{body}) \qquad (13)$$

$$\iint_{S_{body}} \sigma_p \vec{X}_\sigma.\vec{t}_M \, dS_p + \iint_{S_{cav}} \mu_{tp} \vec{X}_t.\vec{t}_M dS_p + H^o_{0t} \mu_{tM}$$
$$+ \iint_{S_{body}, S_{cav}, \Sigma} \mu_{np} \vec{X}_n.\vec{t}_M \, dS_p - \frac{1}{2} \overrightarrow{\text{grad}}_M \mu_{nM}.\vec{t}_M$$
$$+ H^1_{0n} \mu_{nM} + \int_{L_{Fcav}} \lambda_p \vec{X}_\sigma.\vec{t}_M \, ds_p = |\vec{V}_\infty|\epsilon_M\sqrt{1+K} - \vec{j}.\vec{t}_M)$$
$$\text{For } M\epsilon(S_{cav}) \qquad (14)$$

where λ_p is a distribution of linear sinks placed on the curve L_{Fcav}. In the expressions (13) and (14), the vectors $\vec{X}$ correspond to the velocity influence of the corresponding singularities ; the sectioned integral $\iint$ is valid over the entire domain S except for an area So considered to be flat and small, the contour line of which encircles the influenced point M. The parameters H^o_σ or H^o_{0n} represent the normal velocity contribution due to the surface So supporting a source or a normal doublet distribution. Similarly, the parameters H^o_{0t} or H^1_{0n} represent the contribution of the tangential velocity due to the surface So supporting a tangential doublet or a normal doublet distribution respectively.

The condition of zero internal flow rate is expressed by the following relation :

$$\int_{L_{Fcav}} \lambda_p \, ds_p = \iint_{S_{body}} \sigma_p \, dS_p \qquad (15)$$

Given the non-unicity of singularity distribution, it is permissible to make a choice of the normal doublets distribution μ_n while at the same time respecting the distribution continuity at the trailing edge of the foil (curve L_{Fui}). Moreover, the distribution over the wake and the cavity is a function of the span only. For a section of the foil placed at a constant abscissa x , we can write :

$$\mu_{rP} = F(\bar{Y})\ \bar{\Pi}(x) \qquad (16)$$

In this expression, $\bar{Y} = \dfrac{Y_p - Y_o}{c(x_p)}$;

Y_p is the ordinate of point P, Y_o, the ordinate of the local leading edge, and C the local chord of the foil in the section considered.

F (Y) is an increasing function on the upper side and decreasing on the lower side, and is expressed as follows : $F(\bar{Y}) = \pm \frac{1}{2} \bar{Y}$

In a similar manner to the two-dimensional study, the zero normal velocity condition at the trailing edge of the foil must be guaranteed. For all the points of this curve, the following relation must hold true :

$$(\vec{V}.\vec{n})_M = -|\vec{V}_\infty|\vec{j}.\vec{n}_M \quad M\epsilon L_{Fui} \qquad (17)$$

For the points of the curve L_{Fui} belonging to the foil tip, no conditions are imposed since the velocity obtained at these points is the result of the problem. Moreover, considering the relation (16) in each strip limited by two sections of the foil parallel to the plane (oyz) and having abscissa x' and x" , unknowns of the same nature as in the two-dimensional problem are found. It can be seen that the problem raised in this manner leads to varying values of ventilation number K along the foil span. By making these values uniform, the length of the cavity as a function of foil span will be obtained.

The problem is discretised by dividing the foil, the cavity and the wake into strips k parallel to the plane (yoz) (figure 3).

The foil tip area is formed by curves passing through the end point A and spaced at equal intervals along the semi-circles defining the tip. From these curves, it is possible to define two strips as described above on which the normal doublets law is assumed to be linear with respect to the foil span. Discretisation of equation (16) leads to the choice of a constant value Γ_k for each strip k not belonging to the tip, the function F then being replaced by a cascade function. Assuming the ventilation number K to be constant in each strip k and equal to a value K(k), the discretised equations (13), (14), (15), (16) and (17) give a linear system of equations (N,N) :

$$\sum_{n=1}^{N} \bar{G}_{mn} \bar{x}_n = \bar{B}_m \qquad (18)$$

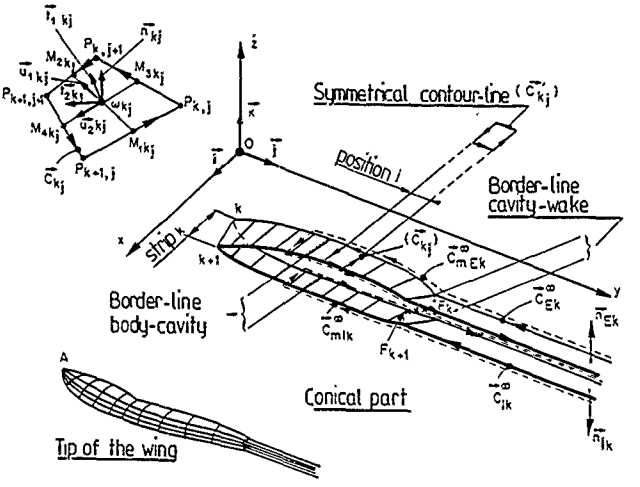


Fig. 3

$\bar{x}_n$ represents the singularities σ_n , $\frac{\mu_{in}}{l}$ or the Γ_k values, or the unknowns $\bar{X}_k = \sqrt{1+K(k)}$ The unknown parameters and the equations are numbered in such a manner as to obtain a line arrangement similar to that obtained in the two-dimensional study. By the manner in which the linear system (18) is established, the matrix $\bar{G}$ can be divided into sub-matrices G_{kl} ; the sub-matrix G_{kl} represents the influence of the unknowns concerning the strip l at the control points of the strip k . Consequently, the matrices G_{kk} have an identical structure to the matrix G of the system (9) in the two-dimensional study. The matrix $\bar{G}$ thus has zeros on its main diagonal, impossible to resolve by a GAUSS-SEIDEL type algorithm. Owing to the large size of the matrix $\bar{G}$, use of a direct method is also ruled out. Consequently, solutions to the system (18) are obtained using a block resolution method. The iterative algorithm used on the blocks is of the GAUSS-SEIDEL type, each block being treated by the HOUSEHOLDER method. In the case of the cavities studied, the matrix size may be as high as 1300. In these cases, convergence is obtained by a maximum of ten iterations and all the more rapidly as the cavity shape is realistic. In addition, this resolution method is very stable, since the block structure formed corresponds with the physical aspect of the problem.

The tangential doublets introduce a normal velocity discontinuity proportional to $(\overrightarrow{grad}_M \mu_{nM} \cdot \vec{i}_M)$. These two discontinuities are calculated using a three-dimensional finite difference scheme.

In formulating the problem, it is assumed that the geometrical shape of the cavity and the tangential direction of the velocity vector on the cavity are known. The cavity and the wake are initialised by a cylindrical surface, the generating lines of which are parallel to the velocity at infinity and rest on the trailing edge of the foil. The portion of this cylindrical surface bounded by the trailing edge of the foil and by an arbitrarily selected plane from the equation $y = y_E$, forms the initial shape of the cavity. The initial direction of the tangential velocity on this shape of cavity is taken to be parallel to the velocity $\bar{V}_\infty$.

Knowing the geometrical and vectorial characteristics of the cavity, it is possible to solve the problem. The first iterations enable the values of the ventilation numbers $K(k)$ to be made uniform by adjusting the length of the cavity l_{cav} according to the span of the foil through a logarithmic relation : given the results of iteration (n), iteration (n+1) gives the following for all the strips k :

$$l_{cav\ k+1}^{(n+1)} = \left\{(1-\omega) + \omega \frac{K_k^{(n)}}{K_1^{(n)}}\right\} l_{cav\ k+1}^{(n)} \quad (19)$$

By choosing a relaxation factor $\omega=2$, it was generally found that three iterations sufficed to obtain convergence. This gives the shape of the cavity in plan. The velocity field over the cavity shape obtained allows a preliminary value of the tangential velocity direction to be determined ; recommencing with this configuration, iterations are continued in order to obtain a more accurate shape of the cavity so that the equation (12) is satisfied over the entire cavity. In general, only one additional iteration was sufficient to make this adjustment with good accuracy. In certain calculation cases, it was found that, during the above-mentioned iterative procedure, the upper and lower sides of a given strip k could cut one another. In such cases, in the following iteration , care was taken to eliminate the portion of cavity downstream of the intersection.

The set of programmes required to solve the complete problem comprises about 2500 Fortran instructions. These programmes were run on a C.D.C. 6600 computer. The matrix of the linear system is large (about 1300). Determination of solutions by the GAUSS-SIEDEL iterative method in blocks allows a file recording of this matrix to be obtained line by line.

The calculation time for one iteration (resolution of the problem for a given cavity geometry) is about 6000 seconds C.P.U. (C.D.C. 6600).

IV. Results

IV.1. Two-dimensional applications

The two hydrofoils studied, designated 'foil 1' and 'foil 2', are shown on figure 4.

Foil 1 is a foil with truncated rear, the upper chord of which is equal to three-quarters of the lower chord ; foil 2 is a foil with upper and lower chords equal. Foil 1 was discretised into 46 panels and foil 2 into 48 panels. These two foils have already been the subject of numerous studies [5] , [25] , [26] , thereby enabling the validity of this calculation to be tested by comparison.

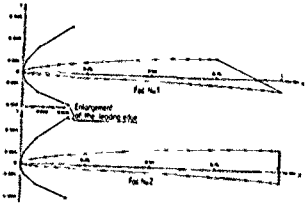


Fig 4 SHAPE AND MESH OF THE FOILS

IV.1.1. Supercavitating foil with wetted upper side

The results presented in this section and in section IV.1.2. concern foil 1. This foil is used for the successive study of the influence of cavity length, of ventilation number and of angle of attack on the various geometrical and hydrodynamic flow characteristics, and the problem of flow separation. The extension of the calculation to a supercavitating foil with unwetted upper side (problem of separation) is presented in section IV.1.2.

The foil is placed at a depth of $h = 1$ below a free surface with its angle of attack α equal to 0°. For a cavity length of 1 ($l_{ca} = 1$), the pressure coefficient distribution over the foil is represented (see figures 5 and 6).

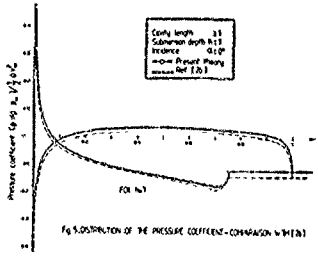


Fig 5 DISTRIBUTION OF THE PRESSURE COEFFICIENT - COMPARISON WITH [26]

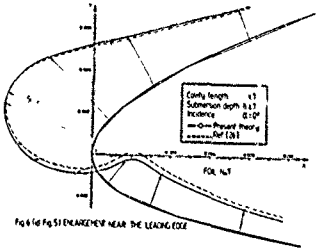


Fig 6 (of Fig 5) ENLARGEMENT NEAR THE LEADING EDGE

These figures show a comparison with the study [26] . The latter study was carried out using a linear theory. Comparison with the present results is possible because the ventilation number K remains small, the foil is thin and placed at a small angle of attack ($\alpha = 0°$). Figure 6 shows in particular the distribution of the pressure coefficient in the region of the leading edge and can be used as a basis for precise comparison between the two methods. Figure 5 shows that the deviation in the results obtained by the present method compared with those of [26] is fairly small ; for a given cavity length, the two methods give slightly different ventilation numbers : this difference is due mainly to the cavity closure models which are not equivalent. Figure 6 shows that at the leading edge of the foil, there is very good agreement between the two distributions. The distribution of [26] was obtained

from an asymptotic expansion matched with an exact local situation.

Two remarks can be made :

a) The method used in the present study gives a fairly precise description of the pressure coefficient at the leading edge of the foil, in spite of the discretisation effect ; this advantage is due to the fact that the integral calculation of the influence of a panel at a control point is analytical ;

b) these results enhance the value of the two methods, notably for the study [26] .

However, the method described here is more general since, as it enables the exact pressure coefficient to be obtained over the entire foil, it can be applied without difficulty to the case of a thick foil with angle of attack as well as the case of a foil followed by very short cavities. By comparison, the study [26] cannot deal with such cases. With the angle of attack of the foil always equal to 0°, the foil is placed at two immersion depths h = 1 and h = 2. Figure 7 represents the change in lift coefficient versus ventilation number K (C_z (K) relation)

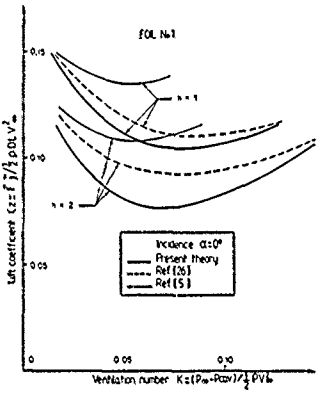


Fig 7, LIFT COEFFICIENT VERSUS THE VENTILATION NUMBER

For the two immersion depths studied, the results are compared with the studies [26] and [5]. Comparison of the curves with the study [5] shows that the deviation in results obtained increases with increase in the ventilation number. On the other hand, comparison of the curves with the study [26] shows that this deviation reaches a maximum for a finite ventilation number value ; in the extreme parts of these curves (where K tends towards zero or becomes very large), this deviation becomes smaller. It has been established that when K tends towards zero (infinite cavity length), all study methods possible must converge towards the same asymptotic value of the lift coefficient. This is explained by the fact that for long cavities, the influence of the cavity closure model on the foil becomes negligible and that, above the foil, the free surface slope becomes insensitive to changes in the model (to a ventilation number zero).

It is worth noting that the lift coefficients calculated in this study are less than the coefficients calculated using the methods [5] and [26].Here again, this result is in agreement with studies carried out previously, since the experimental results obtained up till now have shown that the models [5] and [26] gave overestimated theoretical results [27] . It is probable that the improvement inherent in the present model is due to the fact that, for a given cavity length, the calculated cavity pressure is closer to reality since the actual shape of this cavity is also more realistic.

The foil is placed at depth h = 1 ; with the ventilation number K fixed at a value of 0.0157, the effect of increasing incidence on the geometry of the free lines is represented on figure 8. It can be seen that the effect of angle of attack is to shorten the cavity and to swell the free surface above the foil ; this agrees with the results of previous known results.

IV.1.2. Supercavitating foil with unwetted upper side : flow separation at the leading edge

Foil 1 is placed at depth h = 1 with an angle of attack of 4°. The cavity length is at 2 (i.e., y_B = 3). In the study of the supercavitating foil with wetted upper side, the cavity forms at the upper side of the foil at point A with abscissa value X_A = 0.75. Thanks to the stability of the method, it is possible to extend this calculation to the case of a supercavitating foil with unwetted upper side to have a means of determining the position of the flow separation point at the leading edge of the foil; for this purpose, the position of point A is considered to be variable, moving over the foil towards the point ω of the leading edge ; for each of the points, the zero normal velocity condition is satisfied. The geometry is calculated for the following X_A values : 0.75, 0.5, 0.25, 4×10^{-2}, 10^{-2}, 5×10^{-3} and 3×10^{-4}.

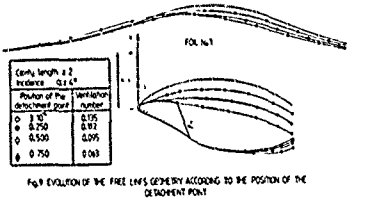
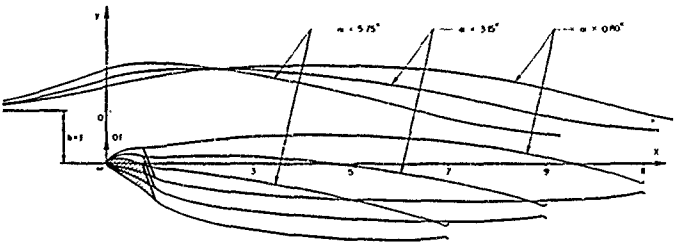


Fig 8 EVOLUTION OF THE FREE LINES GEOMETRY ACCORDING TO THE POSITION OF THE DETACHMENT POINT



FOIL N°1

Fig.8_INFLUENCE OF INCIDENCE ON THE FREE LINE GEOMETRY
CONSTANT VENTILATION NUMBER K=0.0157

Figure 9 shows the shape of the free-lines for four positions of the flow separation point. In the figures for the three cases corresponding to X_A values of 0.75, 0.5 and 0.25, the geometry of the upper side of the cavity has a point of inflexion in the vicinity of the separation point. This inflexion point results from the fact that in these cases, the minimum pressure is not the pressure prevailing in the cavity. On the other hand, for the position of point A corresponding to the X_A value of 3×10^{-4}, the geometry does not include any point of inflexion ; in this case, the pressure prevailing in the cavity is the minimum pressure. It should be noted that the shape of the lower part of the cavity is not very sensitive to the variation in position of the point of separation. In addition, the cavity becomes increasingly less well closed as the separation point approaches the leading edge of the foil : this is due to the quasi-closed cavity model.

From the different cases treated, it is possible to plot the variations in pressure coefficient as a function of X_A at the point of the foil placed immediately upstream of the separation point (control point of the panel AA_1), as well as the variation in ventilation number K. Figure 10 represents these curves with enlargements in the vicinity of the leading edge. The intersection of these two curves gives the separation points for which pressure coefficient continuity is respected. In the case in question, figure 10 shows that there are three possible positions of the separation point, only two of which correspond to stable equilibrium positions. Take, for example, the position of point A, corresponding to $X_A = 1.9 \times 10^{-3}$; consider a slight perturbation ΔX_A which shifts the point A to point A^+ if ΔX_A is positive, or to point A^- if ΔX_A is negative. The curves in figure 10 show that when ΔX_A is positive, there is a reduction in pressure coefficient on the panel AA_1 and an increase in relative pressure (-K) within the cavity. Consequently, at point A^+ : $(-K) > C_p$. Point A^+ is thus pushed back towards point A. Similar reasoning leads to the same result when

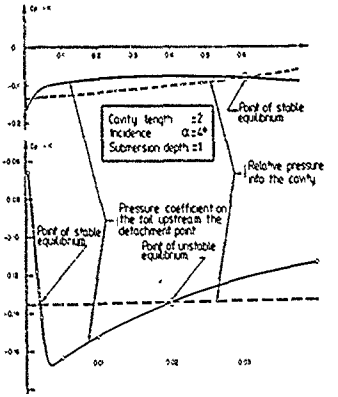


Fig.10_DETERMINATION OF THE POSITION OF THE DETACHMENT POINT (FOIL N°1)

ΔX_A is negative. This reasoning shows that the two separation points corresponding to $X_A = 1.9 \times 10^{-3}$ and $X_A = 0.6$ are the stable equilibrium positions. On the other hand, the separation point corresponding to $X_A = 0.02$ is an unstable equilibrium position.

Figure 11 shows the geometry of the free-lines at the stable separation point at the leading edge. The pressure coefficient distribution for this case is represented in figure 12. It is to be noted that despite the proximity of the separation point and the zero velocity point, an accurate description of the pressure coefficient can be obtained.

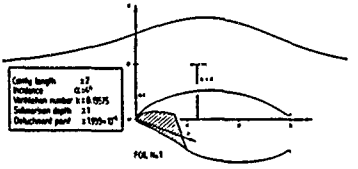


Fig 11. FREE LINES GEOMETRY CORRESPONDING TO THE STABLE DETACHMENT POINT NEAR THE LEADING EDGE

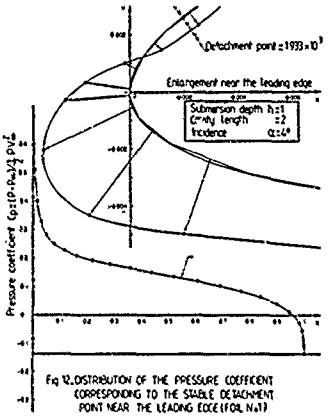


Fig 12. DISTRIBUTION OF THE PRESSURE COEFFICIENT CORRESPONDING TO THE STABLE DETACHMENT POINT NEAR THE LEADING EDGE (FOIL N°1)

IV.1.3. Supercavitating foil with wetted upper side : case of short cavities

The method can be used to extend the calculation to the case of a foil followed by a very short cavity. The results obtained in this respect relate to the foil 2. With the angle of attack maintained at zero, the foil is studied for the case of an infinite field of flow and with a submersion depth of h = 1. In the first case, three cavity lengths are dealt with (l_{cav} = 0.1, 1 and 3). For these three cases, the pressure coefficient distribution is represented by figure 13.

At the point on the upper side of the trailing edge, it is found that the pressure gradient changes sign when the cavity length changes from 0.1 to 1. It can therefore be assumed that there is a cavity length between 0.1 and 1 for which, at this point, the pressure gradient is zero.

For both cases, the variation in lift coefficient is plotted as a function of ventilation number (figure 14). It is found that for high values of K (K > 0.3), a reduction in ventilation number leads to a reduction in

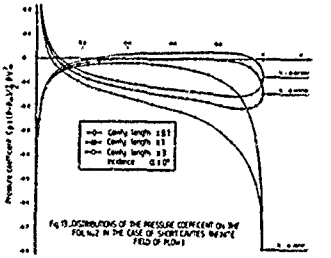


Fig 13. DISTRIBUTIONS OF THE PRESSURE COEFFICIENT ON THE FOIL N°2 IN THE CASE OF SHORT CAVITIES (INFINITE FIELD OF FLOW)

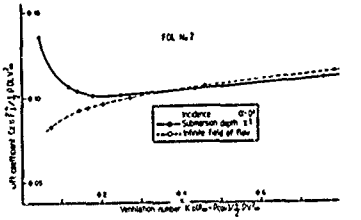


Fig 14. LIFT COEFFICIENT VERSUS THE VENTILATION NUMBER-CASE OF SHORT CAVITIES

lift coefficient for both cases considered. This shows that, in this zone, the behaviour of C_z is not related to the free surface. For ventilation numbers less than 0.2, the variations of these two curves are in opposite directions. In the case with free surface, when K tends towards zero (long cavities), the lift coefficient increases. As demonstrated in [5], this behaviour can be explained by an induced incidence effect resulting from the deformation of the cavity and the free surface. In the case of an infinite field of flow, when K tends towards zero, the lift coefficient decreases.

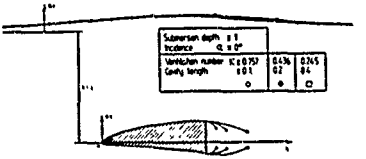


Fig 15. FREE LINES GEOMETRY IN THE CASE OF SHORT CAVITIES (FOIL N°2)

Figure 15 shows the geometry of the free-lines in three cases of a very short cavity (l_{cav} = 0.1, 0.2 and 0.4), with the foil placed at a depth h = 1. In this case, it is seen that free surface deformation is only very slightly affected by a variation in cavity length. Cavity closure is not found to be perfect. This does not raise any contradiction with experimentation

which shows that the cavity closure zone is not precise and that in this region the flow is very turbulent. In addition, the present method assumes stationary flow. Within the framework of the simplifications made, the quasi-closed cavity model seems valid.

IV.2. Three-dimensional application

The foil studied is a swept-back foil corresponding to 'foil 2' defined in section IV.1 above (figure 4). The plan shape of the foil is presented in figure 16 : the half span of the foil is given for XE = XA = XB = 9/8 ; the ordinates of points A and B are YA=3/4 and YB=5/4. The entire calculation was run for an incidence of $\alpha = 0°$; in this case, the cavity length in the median cross-section is taken to be 2 (i.e., $y_F = 3$).

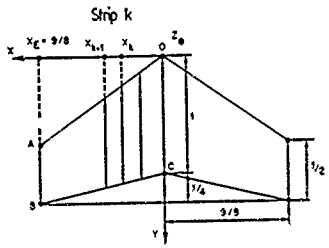


Fig.16

The part of the foil corresponding to the half plan shape OABC was divided into ten strips in geometric progression along the span axis $\overline{OX}$. In each strip, the foil part comprises $L_{body} = 48$ panels and the cavity part (upper side or lower side) comprises $N_{cav} = 24$ panels. Taking into account the two foil tip strips, there is a total of NF = 1152 panels to represent the surface of the foil and the cavity on the positive side of the X axis.

Figure 17 shows the plan geometrical shape of the initial cavity.

The first three iterations are made using the logarithmic correction law (19) and the resulting plan shape of the cavity is shown in figure 18. For each iteration (n), the values of the ventilation numbers $K_k^{(n)}$ for each strip k are given in the table below :

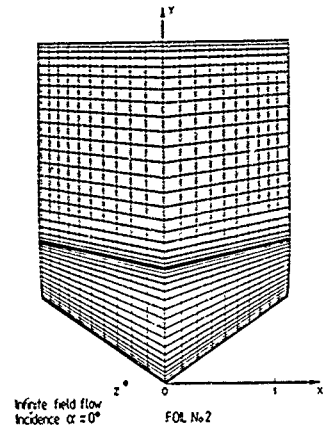


Fig.17 - INITIAL PLAN FORM OF THE UPPERSIDE - CONICAL WING

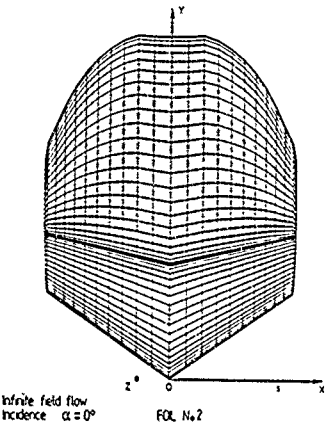


Fig.18 - THIRD PLAN FORM - CONICAL WING

Strip k	1	2	3	4	5	6	7	8	9	10
Iteration 1	0.0637	0.0638	0.0632	0.0622	0.0606	0.0586	0.0562	0.0532	0.0502	0.0490
Iteration 2	0.0634	0.0635	0.0633	0.0631	0.0630	0.0630	0.0630	0.0629	0.0625	0.0605
Iteration 3	0.0633	0.0634	0.0633	0.0632	0.0633	0.0633	0.0634	0.0633	0.0630	0.0611

This tsble shows that after three iterations, the values of $K_K^{(3)}$ are practically identical in all the strips. For the first eight strips, the deviation does not exceed one point on the last digit. For the last two strips, the deviation is slightly greater : this is due to the fact that, since these two strips are close to the tip, the flow component in the vector $\vec{v}_2$ direction is no longer negligible.

From the third plan shape obtained, the geometric shape of the cavity is obtained with greater precision (figure 19).

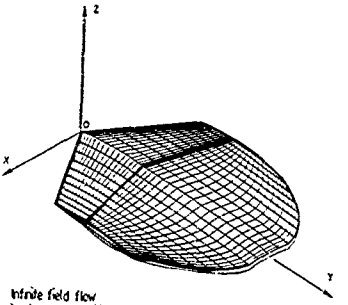


Fig.19-THIRD CAVITY SHAPE _CONICAL WING

It should be noted that in the cavity closure zone near the median plane, the cavity turns inwards. This result is in agreement with both experimental and theoretical results previously established with a linear theory [17] . Moreover, the portion of the cavity corresponding to the tip of the foil tends to swell to form what is generally called a "tip cavity". The formation of this tip cavity is due to the development of free tip vortices and to the fact that, at the rear of the tip, the zero normal velocity condition is not respected. Flow observation in a hydrodynamics tunnel shows that this condition is not always respected. These results, in agreement with the study [28] are also in agreement with the description of the behaviour of vortex lattices related to subcavitating foils [19].

The pressure coefficient distributions obtained are represented on figures [20] and [21].

Each of these figures shows the distribution over two strips, chosen close to the median section (strips k=1 and k=4) or near the tip (strips k=8 and k=10). In each strip, the shape of the pressure coefficient is similar to that obtained in two-dimensional flow conditions. The C_p distribution variations from one section to another show the three-dimensional effect of the aspect ratio.

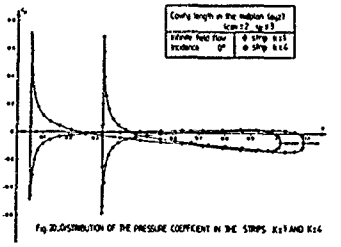


Fig.20-DISTRIBUTION OF THE PRESSURE COEFFICIENT IN THE STRIPS K=1 AND K=4

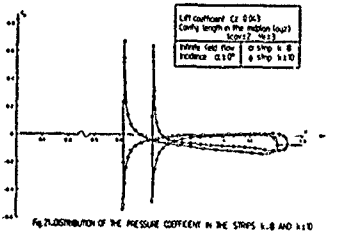


Fig.21-DISTRIBUTION OF THE PRESSURE COEFFICIENT IN THE STRIPS K.8 AND K:10

Figures 20 and 21 show that the overspeed zone is on the lower side and that cavitation on this side near the leading edge is possible. This pressure coefficient distribution shows that there is no zero velocity point ; this classical result is explained by the fact that transverse flow is predominant along the leading edge of the foil and this is accentuated by the sweep-back effect : the fluid flows along the leading edge towards the tip of the foil. The detailed analysis of the results obtained (see table below) shows that this effect is nevertheless very localised around the leading edge.

Strip k No.10 $\alpha = 0°$

$\vec{V}.\vec{t}_1$	$\vec{V}.\vec{t}_2$			$\vec{V}.\vec{t}_1$	$\vec{V}.\vec{t}_2$	
-0.60	0.35					
-0.26	0.50	upper side	lower side	0.74	0.56	
0.21	0.65			0.99	0.39	
0.58	0.62			1.20	0.08	→ maximum overspeed point
		(leading edge)				

Immediately after the leading edge, the velocity straightens out on the upper and lower sides. For these reasons, compared to a classical pseudo two-dimensional method, the proposed method would seem to be more efficient for forecasting the non-cavitation domain of a supercavitating hydrofoil with wetted upper side.

V. Conclusions

By the study described, a non-linear method of calculating supercavitating structures has been developed. Owing to the non-linearity conditions, an iterative procedure has to be used. The criteria used to guarantee convergence of the procedure prove to be effective. From this method, the true pressure coefficient at the leading edge can be obtained and this is essential for defining the non-cavitation domain. The non-linear calculation of the geometrical shape of the cavity is also possible : the quasi-closed model used is in agreement with the flow physics in the cavity closure area.

In two-dimensional flow, the case of the supercavitating foil with wetted upper side was treated ; with this method, the position of the point of formation of the cavity on the upper side can be determined and it is then possible to treat the case of a supercavitating foil with unwetted upper side. The numerical stability of the method enabled the calculation to be extended to the case of a foil followed by very short cavities. In the latter case, and assuming an infinite field of flow, the decrease in lift coefficient has been demonstrated, thereby validating the hypotheses put forward by A. ROWE in [27] . To the author's knowledge, these three problems have not previously been studied within the framework of a non-linear theory.

In three-dimensional flow, the convergence procedure proved to be effective. The flow configuration around the foil, especially in the vicinity of the leading edge is in good agreement with known studies on subcavitating foils. From the numerical standpoint, the matrix resolution difficulty was overcome by an iterative procedure using sub-matrices, which converges all the better as the geometrical shape of the cavity becomes realistic. The method involves fairly long computer calculation times but the wealth of information that it supplies concerning the hydrodynamic and geometrical flow characteristics may make it preferable to other methods requiring less computer time, but which do not give such a precise description.

A particularly interesting field of application is that of subcavitating structures operating with a partially extended cavity from the leading edge ; the size of the linear system decreases considerably and, as a result, numerical resolution is possible in very reasonable computation times.

Références

[1] CHEN, C.F. "Second order supercaviting hydrofoil theory". J. Fluid Mechanics 13, pp 321-332, June 1962.

[2] SONG, C.S. "A quasi linear theory for non separated and separated two-dimensional, incompressible irrotational flow about lifting bodies" St. Anthony Fall Hydraulic Laboratory, Technical paper No. 43, Series B, May 1963.

[3] TULIN, M.P. "Supercavitating flows, small perturbation theory" Hydraunautics Inc. Techn. Report 121-3, September 1963

[4] HSU, C.C. "Supercavitating lifting hydrofoils. Second order theory" Hydruanautics Inc. Techn. Report 121-6, March 1966.

[5] ROWE, A. ; MICHEL J.M. "Two-dimensional base-vented hydrofoils near a free surface : influence of the ventilation number". Journal of Fluids Engineering 97, pp 465-473, December 1975.

[6] MICHEL, J.M. "Wakes of developed cavities" J. of Ship Research, vol.21 No. 4, pp 225-238, 1977.

[7] WU, T.Y.T. "A wake model for free streamline flow theory. Part I : Fully and partially developed wake flows and cavity flows pas an oblique flat plate". J. Fluid Mech. 13 pp 161-181, June 1962.

[8] LAROCK, B.E. : STREET R.L. "A non-linear theory for a ful cavitating hydrofoil in a transverse gravity field" J. Fluid Mech. 29 pp 317-336, 1967.

[9] CELARD, B. "An approximate method for computing the pressure coefficients on the contour or two-dimensional base vented hydrofoils operating near a free surface". Rapport I.M.G. Contrat D.R.M.E. No. 71-237 Juin 1973.

[10] BALQUET, R.J.; BAUBEAU, R. "Définition de la géométrie des structures ventilées à la base" La Houille Blanche, 5/6, 1977, pp 459-469.

[11] FURUYA, O. "Nonlinear calculation of arbitrarily shaped supercavitating hydrofoils near a free surface" J. Fluid Mech. 68, 21-40.

[12] FURUYA, O. "Three-dimensional theory on supercavitating hydrofoils near a free surface". J. Fluid Mech. Vol. 71, part 2, pp 339-359, 1975.

[13] LEEHEY, P. "Supercavitating hydrofoils of finite span". Non-Steady Flow of Water at High Speeds, Proceeding of the I.U.T.A.M. Symposium in Leningrad, June 22-26, 1971, Nanka Publishing House, Moscow, 1973, p 279.

[14] LUU, T.S. "Hydrofoils supercavitants d'envergure finie. Simulation rhéoélectrique". Colloque international des techniques de calcul analogique et numérique en aéronautique. Liège, Septembre 1961.

[15] LUU, T.S. "Méthode de calcul et tracé des hydroptères supercavitants d'envergure finie" Bull. de l'A.T.M.A. Paris 1967.

[16] TSEN, L.F., GUILBAUD, M. "Méthode du potentiel d'accélération pour le calcul des ailes supercavitantes finies". Bull. de l'A.T.M.A. Paris 1970.

[17] VERRON J. "Ecoulements cavitants autour d'ailes d'envergure finie en présence d'une surface libre". Journal de Mécanique, Vol. 18. No. 4, 1979.

[18] DARROZES, J.S. "Comportement d'un écoulement subsonique au voisinage du bord d'attaque d'une aile mince " O.N.E.R.A. Note technique No. 1976-16.

[19] REHBACH, C. "Etude numérique de l'influence de la forme de l'extréaité d'une aile sur l'enroulement de la nappe tourbillonnaire". Recherche aérospatiale No. 1971-6 Novembre-Décembre.

[20] J.L. HESS, A.M.O. SMITH, "Calculation of non lifting potential flow about arbitrary three-dimensional bodies." Journal of Ship research, 8, No. 2, 22nd Sept. 1964.

[21] J.L. HESS, A.M.O. SMITH "Calculation of non-lifting potential flow about arbitrary bodies". Progress in Aeronautical Sciences. Vol. 8, Pergamon Press, 1967.

[22] J.L. HESS "The problem of three-dimensional lifting potential flow and its solution by means of surface singularity distribution". Theoretical Aerodynamics Section. Douglas Aircraft Company, 1970.

[23] T.S. LUU ; G. COULMY "Méthode des singularités à répartition discrétisée dans le domaine de l'hydro et de laérodynamique" L.I.M.S.I. 1975

[24] T.S. LUU ; G. COULMY, J. CORNIGLION "Calcul non linéaire de l'écoulement à potentiel autour d'une aile d'envergure finie de forme arbitraire". A.T.M.A. 1971.

[25] MICHEL, J.M. ; ROWE A. "Profils minces supercavitants à arrière tronqué. Définition et étude théorique de profils portants à nombre de ventilation nul, en présence d'une surface libre." La Houille Blanche No. 3, 1974.

[26] A. ROWE ; J.L. KUENY "Supercavitating hydrofoils with wetted upper sides" Journal de Mécanique, Vol. 19, No. 2, 1980.

[27] ROWE, A. "Thèse d'état : ailes supercavitantes à extrados mouillé en écoulement plan". U.S.M.G. et I.N.P.G. Grenoble 1978.

[28] ROWE A. "Evaluation study of a three-speed hydrofoil with wetted upper side" Journal of Ship Research, Vol. 23, March 1979, pp 55-65.

DISCUSSIONS
of the paper
by C. Pellone and A. Rowe

SUPERCAVITATING HYDROFOILS IN NONLINEAR THEORY

Discussion
by L.J. Doctors

The paper indicates that the "image" method is used to represent the influence of the free surface of the water. Could the authors please clarify the precise type of images and the corresponding physical situation being modelled ?

Authors' reply

The image method is used to treat the linearised free surface. The velocity perturbation introduced by the singularity distribution is orthogonal to the average plane of the free surface. It is considered that the free surface is deformed so that each constituent panel is parallel to the velocity vector calculated at its center.

Discussion
by K. Varsamov

Firt of all, let me thank you for your very interesting work. My question is concerning the two-dimensional flow aspect. Did you verify if the tangential derivative of the dipoles located on the free surface is equal to the velocity on that surface ?

Authors' reply

The tangential velocity is constant all over the cavity. At each step of the iterative procedure it is assumed constant on the shape of the cavity. At the first step, the Neumann condition is not satisfied on the cavity. The iterative procedure allows to construct the shape of the cavity so as to satisfy Neumann condition. In all the cases dealt with, it was found that 5 steps were sufficient to obtain convergence of the method.

FORCES ON RUDDERS BEHIND A MANEUVERING SHIP

Heinrich Söding
Institut für Schiffbau, Universität Hamburg

Abstract

To determine rudder forces in the presence of the ship's hull and the propeller slipstream, four highly simplified potential flow problems are investigated by means of integral equation methods:

1. Two-dimensional flow around a rudder with small angle of attack in a laterally discontinuous velocity distribution
2. Lifting line theory of the rudder near a rigid horizontal plane in a vertically inhomogeneous flow field
3. Three-dimensional flow around two plane plates (hull, rudder) in tandem arrangement
4. Slipstream contraction behind an actuator disc

The results of these investigations may be combined to determine transverse forces and steering moments of maneuvering ships. Comparison of those values with experimental data for two models shows that the rudder effectiveness is overpredicted by about 10 - 25 %.

Introduction

The purpose of this paper is the theoretical determination of the transverse forces and moments due to the ship's rudder during maneuvering motions. In this paper it is not yet tried to compute directly the complicated flow around the rudder in the hull's wake and the propeller slipstream. Instead, rudder forces are determined in several simplified conditions. Results found are combined in an intuitive manner and compared with model experiments. The fluid is assumed to be inviscid, incompressible and, if not mentioned otherwize, to extend without bounds in all directions. The flow is assumed to be stationary.

Lift of a foil in spanwize varying flow velocity

Fig.1 shows the problem and the coordinate system. A foil of given cord length c(z) is posed in a non-uniform flow velocity $u_o(z)$ which is, far off from the foil, anti-parallel to the x axis. The points one quarter of the cord length c behind the profile nose are presupposed to lie in a straight line coinciding with the z axis. The foil has a small angle of attack α so that the problem can be linearized with respect to α.

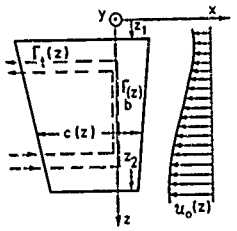


Fig.1 Foil in non-uniform flow velocity $u_o(z)$ (symbol definition)

According to the lifting line method, the flow is modelled by means of a bound vortex of circulation $\Gamma_b(z)$ in the z axis and by trailing vortices parallel to the x axis of circulation $\Gamma_t(z)$ per unit x length. The body boundary condition neglecting profile thickness is satisfied in the points 3/4 c behind the profile nose at y = 0.

The velocity v in y direction induced by the trailing vortices and by the bound vortex is

$$v(x,0,z) = \frac{1}{4\pi}\int_{z_1}^{z_2}\int_{-\infty}^{0} \frac{\Gamma_t(\zeta)(z-\zeta)\,d\xi\,d\zeta}{[(x-\xi)^2+(z-\zeta)^2]^{3/2}}$$

$$+\frac{1}{4\pi}\int_{z_1}^{z_2} \frac{\Gamma_b(\zeta)x\,d\zeta}{[x^2+(z-\zeta)^2]^{3/2}} \qquad (1)$$

The body boundary condition to be satisfied at $x = -c/2$ is

$$v(-\tfrac{c}{2}, z) = -\alpha\, u_o(z),\quad z_1 \le z \le z_2 \qquad (2)$$

The continuity of vortex lines implies

$$\Gamma_q(z) = \frac{d\Gamma_b(z)}{dz} \quad . \tag{3}$$

The integral over ξ in (1) can be solved analytically:

$$\int_{-\infty}^{0} \frac{d\xi}{[(x-\xi)^2+(z-\zeta)^2]^{3/2}} =$$

$$= \frac{1}{(z-\zeta)^2}\left(1-\frac{x}{\sqrt{x^2+(z-\zeta)^2}}\right) \tag{4}$$

Inserting (1), (3) and (4) into the boundary condition (2) yields the following integro-differential equation for $\Gamma_b(z)$:

$$\int_{z_1}^{z_2} \frac{d\Gamma_b(\zeta)/d\zeta}{z-\zeta}\left(1+\frac{c(z)/2}{\sqrt{\left(\frac{c(z)}{2}\right)^2+(z-\zeta)^2}}\right)d\zeta$$

$$+\int_{z_1}^{z_2} \frac{\Gamma_b(\zeta)\cdot\frac{c(z)}{2}\,d\zeta}{\left[\left(\frac{c(z)}{2}\right)^2+(z-\zeta)^2\right]^{3/2}} =$$

$$= -4\pi\alpha u_o(z) \quad , \qquad z_1 \le z \le z_2 \, . \tag{5}$$

To solve that equation, the interval $[z_1, z_2]$ is subdivided into J partitions of equal length

$$\Delta z = (z_2 - z_1)/J \quad . \tag{6}$$

If Γ_j is the bound circulation at the medium point z_j of partition j, equation (5) may be discretized to

$$\sum_{j=1}^{J+1} \frac{\Gamma_j - \Gamma_{j-1}}{z_m - \bar{z}_j}\left(1+\frac{c_m/2}{\sqrt{\left(\frac{c_m}{2}\right)^2+(z_m-\bar{z}_j)^2}}\right)$$

$$+\sum_{j=1}^{J} \frac{\Gamma_j\cdot\frac{c_m}{2}\cdot\Delta z}{\left[\left(\frac{c_m}{2}\right)^2+(z_m-z_j)^2\right]^{3/2}} =$$

$$= -4\pi\alpha u_{om} \tag{7}$$

for m = 1...J,

where $c_m = c(z_m)$, $u_{om} = u_o(z_m)$, $\Gamma_o = \Gamma_{J+1} = 0$,

$$\bar{z}_j = \tfrac{1}{2}(z_j + z_{j-1}). \tag{8}$$

The number J of partitions necessary to obtain a certain accuracy can be diminuished by assuming a parabolic distribution of bound circulation in the first and last partition instead of a linear one and modifying the system accordingly.

The linear system of equations (7) is solved for Γ_j. The lift L of the foil is, then, determined as

$$L = \varrho\,\Delta z \sum_{1}^{J} u_{oj}\Gamma_j \, . \tag{9}$$

For rectangular foil shape and constant flow velocity the known results are reproduced (fig. 2). In this case, the lift coefficient c_L may be approximated for arbitrary aspect ratio by

$$c_L = \frac{2\pi\alpha\Lambda(\Lambda+1)}{(\Lambda+2)^2} \quad . \tag{10}$$

Trapezoidal foils with a ratio of cord lengths of 2 : 1 yield essentially the same values if aspect ratio is defined, as usual, to be (span length)^2 over foil area.

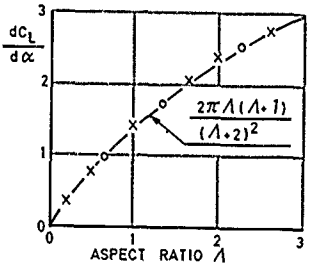


Fig.2 Lift coefficients per angle of attack of rectangular (x) and trapezoidal (o; cord ratio 1:2) foils in uniform flow velocity

For non-uniform flow velocity, no simple approximation formula of the lift was found. Fig.3 shows some examples of c_L/α. Here, c_L was defined as

$$c_L = \frac{L}{\int_{z_1}^{z_2} \frac{1}{2}\varrho u_o^2 c(z)\,dz} \quad . \tag{11}$$

The ship's hull and the water surface above the rudder impede the pressure drop at the upper edge of the rudder. In the flow model, this is approximated by assuming, additionally, a rigid plane wall at z = 0 of infinite extend. Correspondingly, the flow is now modeled by pairs of vortices symmetrical to this plane.

Instead of (5), we obtain the following integro-differential equation:

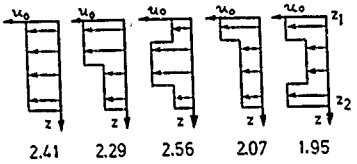
$$\int_{z_1}^{z_2} \frac{d\Gamma_0(\zeta)/d\zeta}{z-\zeta}\left(1+\frac{c(z)/2}{\sqrt{\left(\frac{c(z)}{2}\right)^2+(z-\zeta)^2}}\right)d\zeta$$

$$+\int_{z_1}^{z_2} \frac{d\Gamma_0(\zeta)/d\zeta}{z+\zeta}\left(1+\frac{c(z)/2}{\sqrt{\left(\frac{c(z)}{2}\right)^2+(z+\zeta)^2}}\right)d\zeta$$

$$+\int_{z_1}^{z_2} \frac{\Gamma_0(\zeta)\,c(z)/2\cdot d\zeta}{\left[\left(\frac{c(z)}{2}\right)^2+(z-\zeta)^2\right]^{3/2}}$$

$$+\int_{z_1}^{z_2} \frac{\Gamma_0(\zeta)\cdot c(z)/2\cdot d\zeta}{\left[\left(\frac{c(z)}{2}\right)^2+(z+\zeta)^2\right]^{3/2}}$$

$$=-4\pi\alpha u_0(z), \quad z_1 \le z \le z_2. \qquad (12)$$



2.41 2.29 2.56 2.07 1.95

Fig.3 Lift coefficients per angle of attack c_L/α for five different distributions of flow velocity $u_0(z)$ over span length for a rectangular foil of aspect ratio 2

The solution is obtained in the same way as that of equation (5). Fig.4 shows results for a rectangular foil in uniform flow. Λ_{eff} is the aspect ratio of a foil in unbounded fluid producing the same lift as that of a foil with aspect ratio Λ_{geom} under a rigid wall at z = 0.

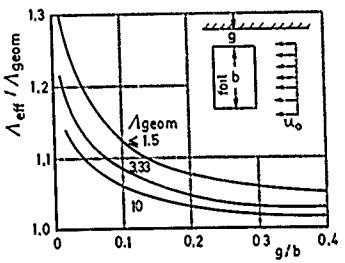


Fig.4 Increase of effective aspect ratio Λ_{eff} due to a rigid plane above the rudder

Lift of a foil in a flow field varying perpendicularly to the span direction

The finite lateral extend of the propeller slipstream influences the rudder lift. Therefore, the two-dimensional flow around a plane plate with small angle of attack α (linearization) in a symmetrical stepped flow velocity distribution is investigated (fig.5). The plate extends from x = -1/2 to x = 1/2. The flow is a potential flow with the exception of the unsteadiness (jet boundaries) near x = ± d. Values inside or outside the jet are marked by index i (interior) or e (exterior), resp.

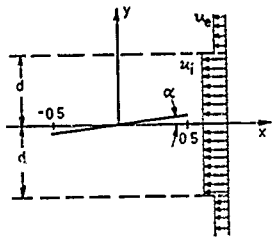


Fig.5 Plane plate in discontinuous velocity distribution (symbol definition)

The flow is described by two different potential functions Φ_i and Φ_e both satisfying the Laplace equation. Boundary conditions are:

Condition at the plate:

$$\Phi_{i_y} = \alpha u_i \quad \text{for } y = 0, \; -\tfrac{1}{2} \le x \le \tfrac{1}{2}. \qquad (13)$$

(Indices x and y indicate partial derivatives.)

Steady pressure at jet boundaries:

$$\Phi_{e_x}^2 - u_e^2 = \Phi_{i_x}^2 - u_i^2 \quad \text{for } y = \pm d \qquad (14)$$

Unique flow direction at jet boundaries:

$$\Phi_{e_y}/u_e = \Phi_{i_y}/u_i \quad \text{for } y = \pm d \qquad (15)$$

Kutta condition:

$$\lim_{x \to -\frac{1}{2}} \Gamma_i(x) = 0. \qquad (16)$$

Φ_i and Φ_e are modelled by means of vortex distributions Γ_i and Γ_e, resp., on the x axis between x = -1/2 and x = 1/2, and by source distributions Q_i and Q_e, resp., on both jet boundaries. Because of symmetry the source distributions on the two jet boundaries are of equal magnitude and opposite sign. The potentials are, therefore,

$$\phi_i = -u_i x + \int_{-\infty}^{\infty} \frac{Q_i(\xi)}{4\pi} \ln\frac{(x-\xi)^2+(y-d)^2}{(x-\xi)^2+(y+d)^2}\, d\xi$$

$$+ \int_{-1/2}^{1/2} \frac{\Gamma_i(\xi)}{2\pi} \arctan\frac{y}{x-\xi}\, d\xi \; ; \qquad (17)$$

ϕ_e correspondingly with index e instead of i.

Inserting these expressions into the boundary conditions (13) until (15) yields three integral equations for the four unknown functions Γ_i, Γ_e, Q_i and Q_e. Thus, once can specify one additional condition like, e.g., $\Gamma_e = 0$. However, the system of equations becomes simpler by postulating

$$u_e \Gamma_e(x) = u_i \Gamma_i(x), \qquad |x| \leq \tfrac{1}{2}, \qquad (18)$$

because the steady pressure boundary condition is then satisfied by the simple relation

$$u_e Q_e(x) = u_i Q_i(x), \qquad -\infty \leq x \leq \infty. \qquad (19)$$

(18) and (19) are used to eliminate Γ_e and Q_e. Then one obtains the following two coupled Fredholm integral equations of first and second kind:

$$\int_{-1/2}^{1/2} \frac{\Gamma_i(\xi)}{2\pi} \frac{d\xi}{x-\xi} - \int_{-\infty}^{\infty} \frac{Q_i}{4\pi} \frac{4d}{(x-\xi)^2+d^2}\, d\xi =$$

$$= \alpha u_i \; , \quad -\tfrac{1}{2} \leq x \leq \tfrac{1}{2} \; ; \qquad (20)$$

$$(u_i^2 - u_e^2)\left[\int_{-1/2}^{1/2} \frac{\Gamma_i(\xi)}{2\pi} \frac{x-\xi}{(x-\xi)^2+d^2}\, d\xi \right.$$

$$\left. + \int_{-\infty}^{\infty} \frac{Q_i(\xi)}{2\pi} \frac{-2d}{(x-\xi)^2+4d^2}\, d\xi \right]$$

$$+ (u_i^2 + u_e^2)\, \frac{Q_i(x)}{2} = 0, \quad -\infty \leq x \leq \infty \qquad (21)$$

($\int$ indicates the Cauchy principal value.)

To solve (20) and (21), the integration ranges (the infinite range is truncated appropriately) are subdivided into K and L, resp., partitions of equal length. Integrals are expressed by sums according to the rectangle rule. On the jet boundary, kernels are determined at the medium points x_ℓ in each partition, and equation (21) is satisfied at the same medium points now termed x_m. On the plane plate, however, integration kernels are determined at the points x_k 1/4 of the partition length behind its front end, and equation (20) is satisfied in the 3/4-points x_n of each partition. This arrangement proved to satisfy the Kutta condition as in the lifting line method and yielded consistent results. One obtains the following linear system of equations:

$$\sum_{k=1}^{K} \Gamma_k \frac{\Delta x_k}{x_n - x_k} - 2d \sum_{\ell=1}^{L} Q_\ell \frac{\Delta x_\ell}{(x_n - x_\ell)^2 + d^2} =$$

$$= 2\pi\alpha u_i \; , \qquad n = 1 \ldots K; \qquad (22)$$

$$\frac{1}{\pi} \frac{u_i^2 - u_e^2}{u_i^2 + u_e^2} \left[\sum_{k=1}^{K} \Gamma_k \frac{(x_m - x_k)\Delta x_k}{(x_m - x_k)^2 + d^2} \right.$$

$$\left. - 2d \sum_{\ell=1}^{L} Q_\ell \frac{\Delta x_\ell}{(x_m - x_\ell)^2 + 4d^2} \right]$$

$$+ Q_m = 0, \quad m = 1 \ldots L, \qquad (23)$$

with $\Delta x_k = 1/K$, Δx_ℓ = (Integration range substituted for $[-\infty, \infty]$)/L, $\Gamma_k = \Gamma_i(x_k)$, $Q_m = Q_i(x_m)$.

The unknowns Γ_k determined from these equations define the lift:

$$L = \varrho \Delta x_k u_i \sum_{1}^{K} \Gamma_k \qquad (24)$$

Fig.6 shows the lift coefficient over angle of attack depending on the parameters of the flow velocity distribution. For $u_i = u_e$, the well-known result $c_L/\alpha = 2\pi$ is obtained. Ratios of u_e/u_i greater than 1 correspond to conditions in twin-screw ships with a central rudder.

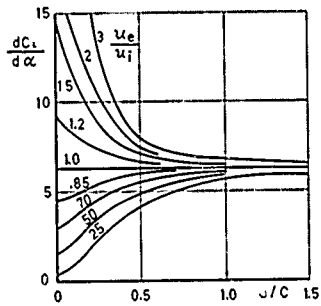


Fig.6 Lift coefficient over angle of attack of a foil with $\Lambda = \infty$ in a flow velocity distribution according to Fig.5

The results are approximated for $0 \leq d/c \leq 1$ and $0.25 \leq u_e/u_i \leq 1.5$ with errors ≤ 0.2 by the formula

$$\frac{c_L}{\alpha} = 2\pi \left(\frac{u_e}{u_i}\right)^f \qquad (25)$$

with

$$f = 2 \cdot \left(\frac{2}{2 + d/c}\right)^{\theta} \qquad (26)$$

Propeller slipstream contraction

The slipstream velocity u_s and the slipstream radius r_s far behind the propeller follow from simple momentum theory:

$$u_s = u_A\sqrt{1+c_T} \quad , \tag{30}$$

$$r_s = r_o\sqrt{\tfrac{1}{2}(1+u_A/u_s)} \quad , \tag{31}$$

where u_A = flow velocity well ahead of the propeller,

r_o = blade tip radius,

c_T = thrust loading coefficient.

Frequently, however, the rudder is not far enough behind the propeller to apply these asymptotic values. Therefore, the slipstream radius r(x) depending on the axial distance x from the front end of the propeller will be determined (fig.7). To avoid singularities not present in reality, the energy due to the propeller action is supplied steadily within a finite axial interval $[0, x_p]$. The propeller load is assumed to be constant over the disc area; there is no account of the finite number of propeller blades.

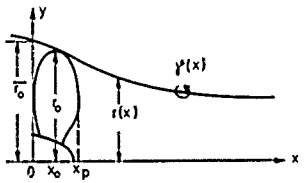


Fig.7 Propeller slipstream contraction (symbol definition)

The flow is modelled by means of a vortex tube of circumferential vortex lines of circulation $\gamma(x)$ per unit x length. The tube passes through the propeller blade tips. r(x) and $\gamma(x)$ have to satisfy the following two conditions:

i) The vortex tube extends in streamline direction:

$$\frac{v(x,r,0)}{u(x,r,0)} = \frac{dr}{dx} \tag{32}$$

The flow velocities u and v in x and y direction, resp., are unsteady at the vortex tube. Condition (32) holds for the values as well on the interior as on the exterior of the tube. In the following, the arithmetic means between both values are understood. They follow from the equations

$$u(x,r(x),0) = \frac{1}{4\pi}\int_0^\infty \gamma(\xi)\,(\xi) \cdot \int_0^{2\pi} \frac{(r(\xi)-r(x)\cos\varphi)\,d\varphi\,d\xi}{[(x-\xi)^2+r(x)^2+r(\xi)^2-2r(x)r(\xi)\cos\varphi]^{3/2}}$$

(33)

and

$$v(x,r(x),0) = \frac{1}{4\pi}\int_0^\infty \gamma(\xi)\,r(\xi)\,(x-\xi) \cdot \int_0^{2\pi} \frac{\cos\varphi\,d\varphi\,d\xi}{[(x-\xi)^2+r(x)^2+r(\xi)^2-2r(x)r(\xi)\cos\varphi]^{3/2}}$$

(34)

ii) The circulation satisfies the equation (Greenberg 1972)

$$\gamma(x) = \frac{1}{u(x,r(x),0)}\left(\frac{\Omega\Gamma}{2\pi} - \frac{\Gamma^2}{8\pi^2 r(x)^2}\right) \tag{35}$$

for $x > x_p$, where Ω is the propeller rotational velocity in radians per unit time, Γ is the hub vortex circulation. The derivation of the above equation requires to take account also of the hub vortex, the blade vortices and of the meridional vortices on the slipstream boundary. Because these vortices induce only circumferential velocities, they need not be regarde in (33) and (34). For $0 \leq x \leq x_p$ the values of $\gamma(x)$ according to (35) are multiplied by $[\sin(\pi x/2x_p)]^2$ to account for the gradual change of energy within the axial extent of the propeller.

r(x) and $\gamma(x)$ are determined for given values of Γ and Ω by means of an iteration scheme: Starting from $r(x) = r_o$ and $u = u_A$, $\gamma(x)$ is determined from (35), and improved values of u, v and dr/dx from (33), (34) and (32). r(x) is found from dr/dx by a numerical integration (predictor corrector method). With these functions the next iteration cycle could start. However, the iteration converges faster if, when determining γ, u, v and dr/dx for a certain x, the improved values obtained already for smaller x values are used together with extrapolations to greater x values of the changes in r and u during the current iteration loop.

Fig.8 shows slip stream boundaries for different thrust loading coefficients c_T which may be determined after completion of the iteration by inversion of formulae (30) and (31). It was found that for realistic Ω values the results do not depend noticeably on Ω.

Results may be approximated with errors less than 0.8 %, indeed much less for $x/r_o > 0.25$, by the formula

$$r(\xi) = r_o\,\frac{0.14(r_s/r_o)^3+(r_s/r_o)\xi^{16}}{0.14(r_s/r_o)^3+\xi^{16}} \tag{36}$$

with

$$\xi = \frac{x-x_o}{r_o} \tag{37}$$

$x-x_o$ is the distance measured from the mean x coordinate $x_p/2$ of the propeller. The mean axial slipstream velocity u follows from the continuity equation:

$$u(\xi)r(\xi)^2 = u_s r_s^2 \qquad (38)$$

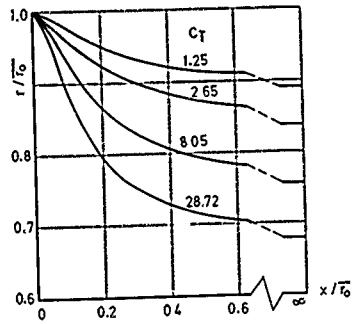


Fig.8 Slipstream boundaries depending on thrust loading coefficient c_T for a propeller with $x_p = 0.2 \cdot r_0$ (see Fig.7)

Lift of two foils in tandem arrangement

The problem is investigated in view of two applications: rudders with a fixed front part and a tail flap, and the influence of the ship's hull on transverse forces produced by the rudder. For simplification, both foils are assumed to be rectangular plane plates of equal span length 2T with or without a gap between them (fig.9). The forward and aft plates have different angles of attack α_H or α_R, resp., and are posed in a uniform flow velocity u_o. Especially for the last application, omitting the propeller and substituting the hull by a plane plate may be an oversimplification. Therefore, this model should be regarded as a first step only for determining the hull rudder interaction.

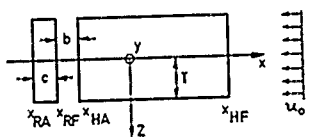


Fig.9 Two foils in tandem arrangement (symbol definition)

Because of the small aspect ratio of the ship's hull with its mirror image above the water surface, the lifting line method is inappropriate here. To simplify the lifting surface method, the spanwise distribution of bound circulation per unit x length of vortex lines parallel to the z axis is assumed to be elliptically:

$$\Gamma_b(x,z) = \Gamma(x) \cdot \sqrt{1-(z/T)^2} \qquad (39)$$

That is correct for very small aspect ratio foils. The problem is linearized with respect to the angles of attack. For very low aspect ratio foils, however, linearization is unreasonable. Therefore, in the application to the rudder hull interaction problem, the angle of attack α_H of the hull has to be zero to obtain reasonable results.

If Γ_t is the circulation of the trailing vortices parallel to the x axis per unit z length, there follows from vortex line continuity:

$$\frac{\partial \Gamma_t(x,z)}{\partial x} = -\frac{\partial \Gamma_b(x,z)}{\partial z} \qquad (40)$$

From (39) and (40) follows:

$$\Gamma_t(x,z) = \Gamma_{to}(x) \cdot \frac{z/T^2}{\sqrt{1-(z/T)^2}} \qquad (41)$$

$$\frac{d\Gamma_{to}}{dx} = \Gamma \,. \qquad (42)$$

Γ_t is zero at the front end of the forward foil. Therefore, (42) results in

$$\Gamma_{to}(x) = -\int_{x_{HF}}^{x} \Gamma(\xi)\,d\xi$$

with $\Gamma(x) = 0$ in the gap between the two foils $x_{RF} \leq x \leq x_{HA}$ and in the wake $x < x_{RA}$.

The boundary conditions on the plates are satisfied on the x axis only:

$$v(x,0,0) = u_o \cdot \alpha_R \text{ for } x_{RA} \leq x \leq x_{RF};$$

$$v(x,0,0) = u_o \cdot \alpha_H \text{ for } x_{HA} \leq x \leq x_{HF}.$$

Using (39) and (41), the transverse velocity v(x,0,0) induced by the vortex distribution is

$$v(x,0,0) = -\frac{1}{4\pi T}\int_{x_{RA}}^{x_{HF}}\int_{-T}^{T} \frac{\Gamma(\xi)\sqrt{T^2-\zeta^2}\,(x-\xi)}{[(x-\xi)^2+\zeta^2]^{3/2}}\,d\zeta\,d\xi$$

$$+\frac{1}{4\pi T}\int_{-\infty}^{x_{HF}}\int_{-T}^{T} \frac{\Gamma_{to}(\xi)\,\zeta^2\,d\zeta\,d\xi}{\sqrt{(T^2-\zeta^2)}[(x-\xi)^2+\zeta^2]^3} \qquad (46)$$

Integrals over the vertical coordinate ζ may be expressed by generalized elliptic integrals

$$B(k) = \int_0^{\pi/2} \frac{(\cos t)^2}{\sqrt{1-(k\cdot\sin t)^2}}\,dt \quad \text{and}$$

$$D(k) = \int_0^{\pi/2} \frac{(\sin t)^2}{\sqrt{1-(k\cdot\sin t)^2}}\,dt :$$

$$\int_0^T \frac{\sqrt{T^2-\zeta^2}}{[(x-\xi)^2+\zeta^2]^{3/2}}\,d\zeta = \frac{kT}{(x-\xi)^2}\cdot B(k) \quad , \quad (47)$$

$$\int_0^T \frac{\zeta^2\,d\zeta}{\sqrt{(T^2-\zeta^2)}[(x-\xi)^2+\zeta^2]^2} = \frac{k^3}{T}D(k) \quad , \quad (48)$$

where

$$k = \sqrt{\frac{T^2}{T^2+(x-\xi)^2}} \quad (49)$$

Thus, from (43) until (48) we obtain the following integral equation for Γ :

$$\int_{x_{RA}}^{x_{HF}} \Gamma(\xi)\cdot\frac{k\,B(k)}{x-\xi}\,d\xi$$
$$-\frac{1}{\pi^2}\int_{-\infty}^{x_{HF}} k^3 D(k) \int_{\xi}^{x_{HF}} \Gamma(\lambda)\,d\lambda\,d\xi$$
$$= 2\pi u_\infty \left\{ \begin{array}{l} \alpha_R \text{ for } x_{RA} \leq x \leq x_{RF} \\ \alpha_H \text{ for } x_{HA} \leq x \leq x_{HF} \end{array} \right\} \quad (50)$$

with further conditions

$\Gamma(x) = 0$ for $x_{RF} \leq x \leq x_{HA}$,

$\lim_{x\to x_{HA}} \Gamma(x) = \lim_{x\to x_{RA}} \Gamma(x) = 0$ (Kutta conditions)

The first integral in (50) constitutes the influence of the bound, the second that of the trailing vortices.

Equation (50) is solved by using equal length partitions within the properly truncated wake ($x \leq x_{RA}$), the aft foil ($x_{RA} \leq x \leq x_{RF}$) and the gap between the two foils ($x_{RF} \leq x \leq x_{HA}$). For applications with very small aspect ratio of the forward foil (ship's hull), unequal partitioning of the interval $x_{HA} \leq x \leq x_{HF}$ (forward foil) with much smaller partition lengths at both ends proved to be superior to equal length partitioning.

Integrals are transformed to sums according to the rectangle rule using kernels at the points 1/4 of the partition length behind the forward end of each partition. Equation (50) is satisfied in all partitions within the two foil intervals $x_{RA} \leq x \leq x_{RF}$ and $x_{HA} \leq x \leq x_{HF}$ at the 3/4 points of each interval to satisfy the Kutta conditions.

From the linear system of equations obtained, the circulation Γ is determined and used to compute the lift force L and its moment M:

$$L = \varrho u_\infty \int_{x_{RA}}^{x_{HF}} \Gamma(x)\,dx \quad , \quad (51)$$

$$M = \varrho u_\infty \int_{x_{RA}}^{x_{HF}} x\,\Gamma(x)\,dx \quad . \quad (52)$$

Results obtained with $\alpha_H = 0$ both with normal and extremely large gap lengths $x_{HA} - x_{RF}$ show that lift forces acting on the second foil (rudder) are decreased by the presence of the front foil (hull). However, additional lift forces are induced on the first foil. Taken together, the total lift is greater than without the front foil by a factor $1 + a_H$ (fig.10), and the center of pressure shifts forward by Δx_L (fig. 11). Both figures refer to large cord length of the front foil, i.e. to the rudder ship interaction problem. The results of figures 10 and 11 can be approximated by the formulae

$$a_H = \frac{1}{1+(4.3\,b/T+3\,c/T)^2} \quad (53)$$

$$\Delta x_L = \frac{0.3}{b/T+0.46} \quad (54)$$

with $c = x_{RF} - x_{RA}$, $b = x_{HA} - x_{RF}$.

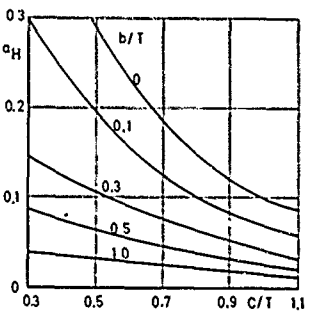


Fig.10 Relative increase a_H of total lift due to a long rectangular plane plate in free stream direction in front of a foil

Fig.12 shows results for the case without gap ($x_{RF} = x_{HA}$) applicable to a rudder with a fixed portion and a movable flap. R is the ratio between the total lift for $\alpha_H = 0$ to that for $\alpha_H = \alpha_R$, i.e. the lift of a flapped rudder with a front part in the flow direction to that of a rudder with equal total area consisting of one part only.

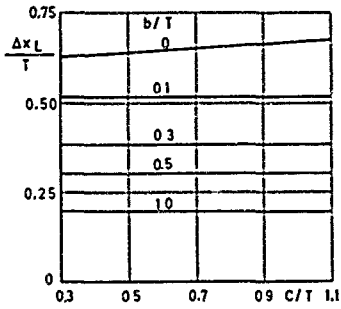


Fig.11 Forward shift Δx_L of center of total lift force due to a long rectangular plane plate in front of a foil

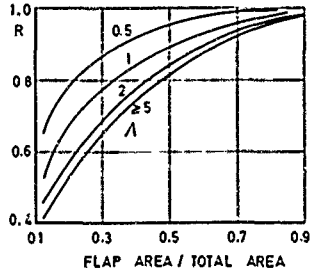


Fig.12 Ratio R between the lift of a flapped rudder with front part in flow direction to the lift of an all-movable rudder

The results can be approximated by

$$R = \frac{(1+a)\,\zeta}{1+a\,\zeta} \qquad (55)$$

with

$$a = 2.13\left(1 + \frac{0.35}{\Lambda}\right)^3 \qquad (56)$$

Λ aspect ratio including the fixed part,

ζ flap area/total area.

Experiments have shown that R decreases with increasing angle of attack of the flap.

Application

To estimate the forces and moments due to a rudder behind a ship, the following procedure is proposed tentatively: Determine

Effective propeller advance velocity u_A as usual for propeller design

Asymptotic values r_∞ and u_∞ of the slipstream by means of (30) and (31)

Slipstream radius r and velocity u_l at the mean cord length of the rudder from (36), (37) and (38)

Edge length $a = r\sqrt{\pi}$ of equivalent quadratic slipstream cross section

Lift reduction factor $\lambda = (u_l/u_A)^f$ with f according to (26), using $d = a/2$

L_l/α, where L_l is the share of rudder lift depending linearly on angle of attack α. Use the method of chapter I of this paper, taking into account the hull and the water surface above the rudder. Use $u_l\sqrt{\lambda}$ within the slipstream and u_A outside the slipstream as flow speeds well ahead of the rudder.

Mean rudder advance velocity

$$u_m = \sqrt{\left[A_{RS}\lambda u_l^2 + (A_R - A_{RS})u_A^2\right]/A_R} \qquad (57)$$

where A_{RS} is the rudder area within the propeller slipstream, A_R total rudder area, both including fixed parts.

Mean flow direction ε relative to the x axis at rudder position:

$$\varepsilon = \frac{u_A}{u_m}\,\mathrm{arc\,tg}\,\frac{v + x_A\dot{\psi}}{u} \qquad (58)$$

Here, u and v are longitudinal and transverse, resp., speed of the coordinate origin of the ship; $\dot{\psi}$ is the rate of rotation of the ship in radians per unit time. The formula disregards any influence of the hull upon the flow direction; however, no better information is available to the author.

Effective angle of attack α of the rudder:

$$\alpha = Rd - \varepsilon\,, \qquad (59)$$

where R = 1 for all-movable rudders; for flapped rudders determine R from (55) and (56).

Rudder lift including nonlinear effects:

$$L = \left(\frac{L_l}{\alpha} + \frac{1}{2}\rho u_m^2 A_R c_Q |\sin\alpha|\cos\alpha\right)\sin\alpha\,, \qquad (60)$$

where c_Q is a coefficient of which values between about 0.7 and 2 are given in various

papers. In the following examples, $c_Q = 1$ is used.

Rudder drag:

$$D = \frac{F_i^2}{\pi \Lambda} + \frac{1}{2} \rho u_m^2 A_R c_Q |\sin \alpha|^3 \qquad (61)$$

The first term is a lower bound of the induced rudder resistance. D is of minor importance only for $\delta \leq 30°$.

a_H and Δx_L from (53) and (54)

Longitudinal force (in centerline direction) due to the rudder:

$$X_R = -L \sin \varepsilon - D \cos \varepsilon \qquad (62)$$

Transverse force due to the rudder:

$$Y_R = (L \cos \varepsilon + D \sin \varepsilon)(1 + a_H) \qquad (63)$$

Moment around the vertical axis:

$$N_R = (L \cos \varepsilon + D \sin \varepsilon)(x_R + \Delta x_L)(1 + a_H) \qquad (64)$$

Comparison with model experiments

No experimental results are known to the author which permit to check single formulae

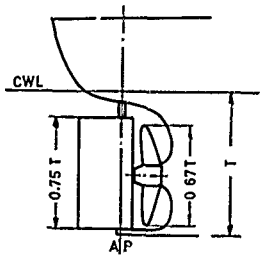


Fig.13 Rudder arrangement of the Series 60 Model

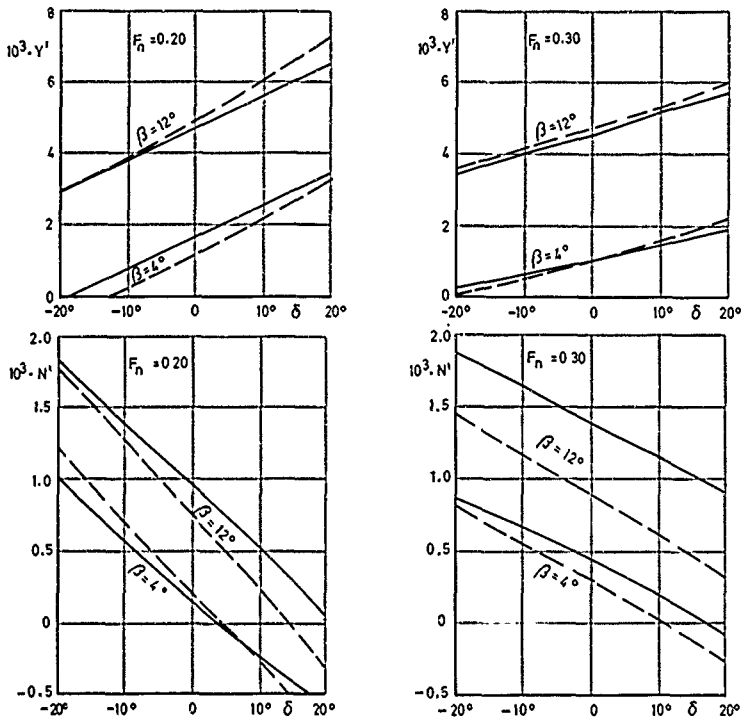


Fig.14 Non-dimensional transverse force Y' and moment N' of a Series 60 Model ($c_B = 0.60$) versus rudder angle δ for two different drift angles β and two Froude numbers F_n. Broken lines: computed as described; continuous lines: measured by Oltmann (1974)

derived in this paper. Therefore, the procedure described above was applied to a Series 60 Model (c_B = 0.60; rudder arrangement according to fig. 13) for which towing tests with working propeller, using different drift and rudder angles, were performed by Oltmann (1974). Experimental values of dimensionless transverse force Y' and moment around the vertical axis N' (fig.14) include also forces and moments due to the hull and the propeller. For comparison purposes, to the computed values Y_R and N_R additional terms were added giving the hull forces and moments due to slender body theory and some additional second-order terms similar to Ogawa and Kasai 1979. To compare the computed and measured rudder effectiveness only, the slopes of measured and computed curves over rudder angle should be considered.

For Froude number F_n = 0.2, these slopes are much greater than for F_n = 0.3, because for both Froude numbers the propeller revolutions were those corresponding to the self-propulsion point of the model with F_n = 0.30. The propeller loading was, therefore, much greater for F_n = 0.20. Results show that rudder effectiveness is overestimated by the calculation procedure by about 10 - 25 %.

In these experiments, the rudder was an all-movable fin fully immersed and with a relatively wide gap between its upper edge and the hull (fig.13). To test the procedure in another case, the mariner ship in the ITTC-recommended test condition, that is with a surface-piercing rudder (fig.15), was investigated also and compared with results published by Oltmann (1979), in this case without drift angle. The results (fig. 16) show the same overestimation of rudder effectiveness by about 15 %. For rudder angles exceeding 20°, greater deviations were found, presumably because of exceeding the stall angle of the rudder. This can be accounted for only by empirical corrections of the calculation procedure.

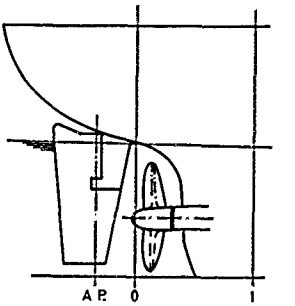
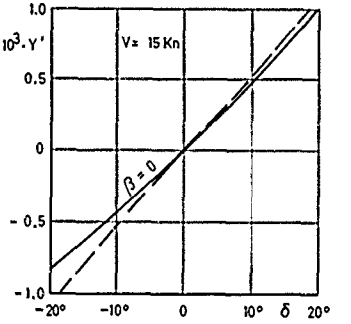


Fig.15 Rudder arrangement of the Mariner Model



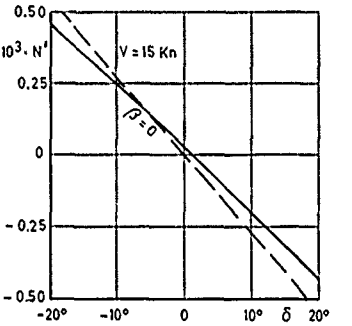


Fig.16 Non-dimensional transverse force Y' and moment N' of a Mariner Model versus rudder angle δ. Broken lines: computed as described; continuous lines: measured by Oltmann (1979)

References

Greenberg, M.D.: Nonlinear Actuator Disc Theory. Z. Flugwiss. 20 (1972), p. 90 - 98

Hess, F.: Lifting-Surface Theory Applied to Ship-Rudder Systems. International Shipb. Progress 1979, p. 299 - 305

Isay, W.H.: Vorlesungsmanuskript Inkompressible Strömungen, 1972 (unpublished)

Ogawa, A., and H. Kasai: On the Mathematical Model of Manoeuvring Motion of Ships. Intern. Shipb. Progress 1979, p. 306 - 319

Oltmann, P.: Schrägschleppversuche mit einem Schiffsmodell der Serie 60. Report of the Institut für Schiffbau No. 307 (1974)

Oltmann, P., and K. Wolff: Vergleichende Untersuchung über das Manövrierverhalten des Mariner-Standardschiffes. Report of the Institut für Schiffbau No. 385 (1979)

DISCUSSION
of the paper
by H. Söding

FORCES ON RUDDERS BEHIND A MANEUVERING SHIP

Discussion
by P. Thomsen

After the complimenting words of Prof. J. Breslin it is easier to me to state honestly that I feel like birthday today. A scheme was just published on the interaction of hull, propeller and rudder that well exceeds the so far reached status of the art. As a naval architect it is my opinion that the formulae and scheme are especially apt to be used in design on practical ships and practical requirements So far experimental results had to be taken and the characteristics in manoeuvring ability could be interpreted thereafter only. Now, by Söding's achievements an active way in open to first optimize those characteristics by computation and then to build the arrangement at predicted properties.

You spread the energy of propeller over the interval 0 to X_p. Could you please tell me the effects thereof upon the shape of the slip stream boundary shape or relevant consequences ?

Author's reply

My work is not as unique as it could seem from the friendly remarks of Prof. Thomsen : many others have published methods of predicting the maneuvering characteristics of a ship without performing experiments with a model the ship in question. These methods relied, however, to a great extent upon model or full-scale experiments with other ships. My intention is to better understand the outcome of such experiments by numerical calculations and thereby to improve the application of existing experimental results to new ship projects.

Schmidt and Sparenberg (On the edge singularity of an actuator disc with large constant normal loading. Journal of Ship Research, 21 (1977), p. 125) have shown that, instead of the smooth slipstream boundary on fig. 8, there occurs a singular, spiraling flow at the edge of the actuator disc with vanishing axial length X_p.

PROPELLER-INDUCED HULL PRESSURES AND FORCES

J P. Breslin
Davidson Laboratory
Stevens Institute of Technology
Hoboken, New Jersey

Introduction

A new procedure is described for estimating the vibratory pressures, sectional force densities and total forces and moments generated by a specified propeller on the hull. This development has been motivated by the need for *at least a comparative* evaluation of candidate propeller-stern configurations to permit a rational selection of that arrangement which would yield minimum excitation. Our minimum goal is set at achieving a comparative technique because the excitations arising from the various blade loadings attending each significant spatial harmonic of the wake) are directly dependent on these wake harmonics which are only approximately known from model measurements of the total nominal hull wake. In addition, large modulations in forces and pressures have been observed which are undoubtedly due to large scale temporal fluctuations in the wake for which neither current theory nor wake measurements account.

In spite of the acknowledged deficiences, it is still considered important to provide a means for comparative evaluation of hull vibratory forces and to compare on a continuing basis the predictions of these calculations with measurements made under controlled conditions.

The creation of an arbitrary hull in the presence of a specified propeller operating in her wake is effected by distributing normal dipoles on panels over the hull surface and its reflected image. It is demonstrated that the exterior Neumann problem can be converted to an interior Dirichlet problem in which the dipole densities are determined from an integral equation for which a numerical inversion procedure exists.

To ascertain a measure of the reflective effect of the hull, the ratios of the magnitudes of the pressures on the hull to those due to the propeller alone are examined. A flat surface above the propeller would yield a ratio of 2.0.

Correlations made with pressure measurements on a tanker model in Norway are presented herein, as well as with vertical vibratory "effective" force measurements made by the late Professor Emeritus F. M. Lewis.

The paper is concluded with observations pertaining to the numerical hydrodynamical aspects of the procedure. It is proposed that fairly extensive exercises be carried out for the case of a spheroidal ship form for which the surface pressures and forces generated by simple rotating and pulsating singularities can be independently calculated. This would provide a control or standard to ascertain the size and distribution of surface panels which are required to achieve a specified accuracy. It is also pointed out that there remains a need for additional experiments in which the wake can be controlled by the use of screens and pressures measured on a spheroidal afterbody, thus removing the uncertainty associated with the determination of effective ship model wake harmonics.

Analytical Representations

1. Velocity Potential of a Non-Cavitating Propeller in a Hull Wake

The form adopted at Davidson Laboratory for the velocity potential of a propeller in a spatially non-uniform, temporally invariant flow has been expounded in various publications and, hence, will be dealt with here only in broad outline to indicate the character of the mathematical representation employed.

The potential at any field point is composed of the contributions from blade thickness and blade loading, i.e., for a single blade (at first):

$$\phi = \phi_T + \phi_L \tag{1.1}$$

where

$$\phi_T = -\frac{2}{4\pi}\int_S \frac{Vt'}{R}\,dS \tag{1.2}$$

and, from integration of the linearized Euler equations:

$$\phi_L = -\frac{1}{\rho\bar{U}}\int_{-\infty}^{x} p_L(\xi,r,\theta,t-\frac{x-\xi}{\bar{U}})d\xi \tag{1.3}$$

where V is the resultant relative velocity at r = s

t' the gradient of the local blade semi-thickness (= $\partial t/\partial h$)

R the distance from any dummy point on the blade to any field point

h helical arc length along the blade section at any $r = s$

p_f the pressure change at any field point due to blade pressure loading

x, r, ϕ are cylindrical coordinates, x positive downstream of the origin at the center of the propeller on the axis of rotation. The angular coordinate ϕ is positive counterclockwise when viewing the propeller from downstream looking forward

For brevity, only the potential induced at field points due to pressure loading on the blade will be exhibited because it is indeed a many-faceted function, giving rise to many contributions via the mode of representation adopted.

The field pressure p_f generated by the distribution pressure jumps $\Delta p(s,h;\theta(t))$ over the blade surface S is given by

$$p_f(x,r,\phi;\theta(t)) = \frac{1}{4\pi} \int_S \Delta p \, \frac{\partial}{\partial n'} \frac{1}{R} \, dS \tag{1.4}$$

where n' is the normal at any dummy point and

$$R = [(x-x')^2 + r^2 + s^2 - 2rs\cos(\phi-\theta-\theta')]^{1/2} \tag{1.5}$$

(See Figure 1 for definition of geometrical quantities.)

Here, in principle, the singularities should be located on the blade helical surface which imposes the relationship

$$x' = \frac{P_f}{2\pi} \theta' \tag{1.6}$$

(The blade is taken to be without skew which could be incorporated by replacing θ by $\theta + \sigma$, σ being the skew angle.)

In the calculation reported herein, the singularities are located on the "fluid helix" adopted by Tsakonas as the reference surface, yielding the connection

$$x' = \frac{U}{\omega} \theta' = \theta'/a \tag{1.7}$$

To put into evidence the harmonic dependence of p_f on blade position angle, one may resort to one of several identities or Fourier series representations of $1/R$. The one adopted by Tsakonas is in a more accommodating form,

$$\frac{1}{R} = \frac{1}{\pi} \sum_{m=-\infty}^{\infty} \int_{-\infty}^{\infty} A_{|m|}(r,s,k) e^{ik(x-x')} \, dk \, e^{im(\phi-\theta-\theta')} \tag{1.8}$$

where

$$\begin{aligned} A_m &= I_{|m|}(|kr|) \, K_{|m|}(|ks|) \quad r < s \\ &= I_{|m|}(|ks|) \, K_{|m|}(|kr|) \quad r > s \end{aligned} \tag{1.9}$$

I_m and K_m being the modified Bessel functions of the second kind.

As the pressure jumps on the blades also vary cyclically with blade position angle, we can write

$$\Delta p(h,s,\theta) = \sum_{\lambda=-\infty}^{\infty} \Delta\hat{p}_\lambda(h,s) e^{i\lambda\theta} \tag{1.10}$$

and then the field pressures are expressed by

$$p_f = \frac{1}{4\pi^2} \sum_{\lambda=-\infty}^{\infty} \sum_{m=-\infty}^{\infty} \int_S \Delta\hat{p}_\lambda \frac{\partial}{\partial n'} \int_{-\infty}^{\infty} A_{|m|} e^{i(x-x')-m\theta')} \, dk \, dS \, e^{i(\lambda-m)\theta} \, e^{im\phi} \tag{1.11}$$

To obtain the totality of the contributions from n-equally spaced blades, simply replace θ by

$$\theta + \frac{2\pi\mu}{n}$$

to give the contribution from the μ^{th} blade and sum over μ from 0 to n-1. This sum, viz,

$$S_b = e^{i(\lambda-m)\theta} \sum_{\mu=0}^{n-1} e^{i(\lambda-m)\frac{2\pi\mu}{n}} \tag{1.12}$$

yields zero for $\lambda - m \neq qn$ and

$$\begin{aligned} S_b &= n \, e^{iqn\theta} \text{ for } \lambda - m = qn, \; q = 0,1,2,3 \\ &= n \, e^{-iqn\theta} \text{ for } \lambda - m = -qn \end{aligned} \tag{1.13}$$

where all the possible values of the m-series which can contribute are given by $m = \lambda - qn$ and $m = \lambda + qn$ coupled respectively with

$$ne^{iqn\theta} \text{ and } ne^{-iqn\theta}$$

Then, upon folding the λ-series, we find pairs of sums of complex conjugates, yielding for the qn-th harmonic of the pressure due to loading

$$(p_f)_{qn} = \frac{n}{2\pi^2} \sum_{\lambda=0}^{\infty} \int_S \frac{\partial}{\partial n'} G_{\lambda,n} \, dS \tag{1.14}$$

where

$$G_{\lambda,n} = \frac{\partial}{\partial n'} \int_{-\infty}^{\infty} R_e(F_\lambda e^{iqn\theta}) \, e^{ik(x-x')} dk \tag{1.14a}$$

and

$$F_\lambda = c_\lambda \Delta\hat{p} \; A_{|\lambda-qn|}(r,s,k) \, e^{-i(\lambda-qn)(\theta'-\phi)} + \Delta\hat{p}_{-\lambda} \, A_{\lambda+qn} e^{i(\lambda+qn)(\theta'-\phi)}$$

We see that the pressure at any point in the field is composed of contributions from all the blade loading pressures (paired values for each wake harmonic order λ) which are propagated by

amplitude functions

$$A_{|\lambda-qn|} \quad \text{and} \quad A_{|\lambda+qn|}.$$

For locations near the propeller, those associated with the mean loading on the blade, i.e., $\lambda = 0$, dominate, but, as they are propagated by

$$A_{qn}\, e^{-iqn\phi},$$

they rapidly become small with increasing distance from the propeller. As they oscillate rapidly with the spatial angle, i.e., as

$$\begin{matrix} sin \\ cos \end{matrix}(qn\phi),$$

these large near-field pressures do not contribute majorily to the "rigid" body force. In contrast, the contributions from the small loadings at blade frequency, i.e., $\Delta p_{qn}(\lambda=qn)$ involve

$$\Delta p_{qn}\, A_o + P_{-qn}\, A_{2qn} e^{-i2qn\phi}$$

in which the second term becomes negligible, but the first term, while small everywhere, decays so slowly with distance (and being independent of the angular coordinate ϕ) produces large contributions to the integrated "rigid" body force and is proportional to the fluctuating thrust on the shaft. In a similar manner, the next neighboring wake-associated blade loadings, $\lambda = qn-1$ and $\lambda = qn+1$, produce significantly large contributions.

Reverting to (1.3), the velocity potential is seen to require the integral of (1.14) in which x is to be replaced by ξ and time t by $t - (x-\xi)/U$ The time t is contained in (1.14) through $\theta = -\omega t$. The ξ-integrals can be effected to yield the following expression for the velocity potential

$$(\phi_t)_{qn} = -\frac{n}{4\pi\rho U} \sum_{0}^{\infty} \int_{S} \frac{\partial}{\partial n'} K_\lambda(x,r,\phi;x's,\theta';qn\theta)dS \tag{1.15}$$

where

$$K_\lambda = \int_{-\infty}^{\infty} [(\delta(\underline{k}-aqn) - \frac{ie^{i(k-aqn)x}}{k-aqn})\bar{\Gamma}_\lambda e^{iqnax} e^{iqn\theta}$$

$$+ (\delta(k+aqn) - \frac{ie^{i(k+aqn)x}}{k+aqn}) \tag{1.16}$$

$$\bar{\Gamma}_\lambda e^{-iqnax} e^{-iqn\theta}]e^{-ikx'}dk' \text{ , where}$$

$$\bar{\Gamma}_\lambda = \epsilon_\lambda \Delta\hat{p}_\lambda A(r,s,|k|_{|\lambda-qn|})e^{-i(\lambda-qn)(\theta'-\phi)}$$

$$+ \Delta\hat{p}_{-\lambda} A_{\lambda+qn} e^{i(\lambda+qn)(\theta'-\phi)}$$

$\bar{\Gamma}_\lambda$ = its complex

$\delta(v)$ is the Dirac-delta function, $a = \omega/u$

Further reduction of the integrals will not be exhibited here. Suffice it to note that the chordwise integral over the blade is effected by assuming two-dimensional mode shapes and the k-integrals involving the Dirac-δ functions are readily evaluated. The remaining k- and radial integrals over the blades are carried out by numerical quadratures. In effecting the k-integrals for increasing x, it is necessary to decrease the mesh size to retain accuracy. This aspect of the use of the Fourier transform representation of the amplitude functions in the expansion of 1/R gives rise to increased computer time.

Finally, the blade frequency part of the velocity potential arising from loading is reduced to

$$\phi_{1n}(x,r,\phi) = \sum_{\lambda=0}^{n+1} a_\lambda(x,r,\phi)\cos n\theta + \tag{1.17}$$

$$+ b_\lambda(x,r,\phi)\sin n\theta$$

where x,r,ϕ are specified by points on the hull and the summation is seen to be limited to those wake harmonic orders of significance, i.e., only up to one plus the number of blades. A similar but much simpler process, is applied to the potential arising from blade thickness which, because the thickness distribution is independent of blade position angle, is propagated only with amplitude functions

$$A_{qn} e^{iqn\phi}$$

and, hence, contributes only in the immediate vicinity of the propeller.

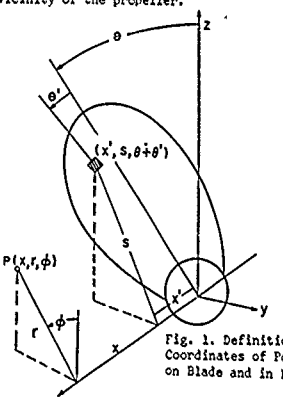


Fig. 1. Definition of Coordinates of Points on Blade and in Field

We see that the velocity potential $(\phi_t)_{qn}$ exhibits dependence on the space angular coordinate ϕ as

$$e^{i(\lambda-qn)\phi} \quad \text{and} \quad e^{-i(\lambda+qn)\phi}.$$

This means that the variation of the potential over panels extending to port and starboard of the centerplane can be rapid--dictating that the panel size must be small. As the $\cos(\lambda+qn)\phi$ first changes sign for $(\lambda+qn)\phi = \pi/2$ and as $\phi = -\tan^{-1} y/z$, we see that the value of y/z at which $\cos(\lambda+qn)\phi$ first vanishes is

$$\frac{|y_1|}{z_1} = + \tan\left(\frac{\pi}{2(q+qn)}\right)$$

and, for $\lambda = 4$ and $q = 1$, $n = 4$ in this case, $|y_1| = 0.20z$. As z_1 is of the order of $3/2r_o$ (r_o the propeller radius), then the buttock line on the hull at which $\cos 8\phi$ changes sign is $|y_1| = 0.30r_o$.

To secure an accurate variation of the potential, the panel width has to be small with respect to the interval in which the function changes sign. Providing two panels in $0 < |y_1| \leq 0.3r_o$ requires a panel width of $0.15r_o$. As one moves out and up, the frame of motion and the required panel width can be increased. We may note that, for $\lambda = 0$, $qn = 4$, The complete cycle of

$$\begin{matrix}\sin \\ \cos\end{matrix}\left(4 \tan^{-1}\left(\frac{y}{z}\right)\right)$$

is achieved only when $y = \pm \infty$.

Forward of the propeller, the potential falls or decays monotonically with x. At one diameter and beyond, it can be demonstrated that

$$(\phi_\ell)_{qn} \sim \frac{1}{x^{2|\lambda \pm qn| + 2}} ,$$

so that the contribution from the largest blade loading (i.e., for $\lambda = 0$) decays (at blade rate, $q = 1$) as $1/x^{10}$, whereas the contribution from the very small loading at blade frequency (i.e., $\lambda = n$, $q = 1$) is seen to decay as $1/x^2$. Thus, forward of the propeller, panel lengths of the order of $0.25r_o$ within one diameter are reasonable, and then can be lengthened for x beyond one diameter.

However, aft of the propeller the potential may be seen to be composed of similarly monotonically decaying parts *plus* non-decaying, harmonically-varying-with-x parts proportional to

$$e^{\pm iqnax} .$$

This may be seen by taking the contribution of the k-integrals in the equation yielded by the δ-functions. Limiting our attention to $q = 1$, $n = 4$, we see that the x-interval over which $\sin$ and $\cos 4ax$ pass through a complete cycle, is

$$\frac{x}{r_o} = \frac{\pi}{2ar_o} = \frac{\pi U}{2\omega r_o} = \frac{J}{2}$$

and, as ship-speed J (as used by Tsakonas) is 0.60

$$\frac{x}{r_o} = 0.30$$

To have at least 4 panels in these intervals, the panel lengths should not exceed $0.075\ r_o$. It is clear that this regular undulation of the potential produces a largely self-cancelling effect on the hull aft of the propeller, a residual remaining only because the hull changes sectionally with x. As in all finite element methods, a compromise must be struck between the requirements for accuracy and the computing capacity and expense.

In all of the foregoing, it has been tacitly assumed that the pressure jumps Δp_λ are known. These are found by inverting an integral equation requiring that the flows normal to the blade sections from each axial and tangential wake harmonic at order λ are annulled by the flow generated by each Δp_λ distribution on each blade in the presence of all other blades. This procedure has been discussed elsewhere[1] and, to conform to space limitations, will not be described herein. We may now turn to the generation of a ship hull in the presence of her propeller and the water surface.

2. Representation of the Hull

The foregoing development has indicated that a propeller in a wake generates cyclic disturbances at frequencies given by integer multiples of the number of blades and the shaft revolutions per unit time. As such frequencies are much larger than those which can give rise to surface waves on a flowing stream, the appropriate linearized boundary condition imposed by the presence of the water surface is that the total velocity potential be zero on the undisturbed locus of that surface. The flow about the hull alone (considered fixed in a uniform stream) will, indeed, exhibit surface distortions. From experience, we have noted negligible interaction between the propeller and the perturbed motion about the hull. The only influence of the hull-induced (Froude number dependent) flow included here is whatever influence is reflected in the measured hull wake, a necessary input to the propeller blade loading integral equation referred to above which determines the Δp_λ.

Taking axes fixed in the free surface waterplane above the propeller with positive z directed downward, positive x aft and positive y to port, the potential of the propeller in a streaming flow may be expressed in the form

$$\phi_p = \phi_p(x,y,h-z) - \bar{U}x \qquad (2.1)$$

where h is the depth of submergence of the propeller axis.

To meet the zero potential (high frequency) boundary condition on the plane $z = 0$, we add a "negative image" of the propeller and stream $-\bar{U}$ to achieve

$$\phi_p = \phi_p(x-y,h-z) - \phi_p(x,y,h+z) - \operatorname{sgn} \bar{U}x \qquad (2.2)$$

defining sgn z (= signum z) to be zero on $z \equiv 0$.

To insert a hull into the field of the propeller and its image, we have (at Davidson Laboratory) first employed surface distributions of sources plus their negative images over the wetted portion of the hull. The source (sink) densities are found by inverting an integral equation generated by the requirement that the normal velocity imposed by the propeller and

its negative image must be annulled at each hull element by the normal velocity induced in concert by these hull sources and their image sinks.

This procedure was found to require excessive computer effort since three components of the propeller-induced velocity must be dotted with the hull normal vector. We now employ the solution to the same *exterior* Neumann problem which is afforded by solving an *interior* Dirichlet problem which requires that the concerted *potential* of normal dipoles (evaluated on the interior side of the hull surface) annul the propeller potential at each and every hull element. Thus, the computing effort required to produce the input to the hull is reduced by *two-thirds*, i.e., only one function rather than three must be evaluated. A proof of this equivalent procedure is given in Appendix A.

The potential of the hull ϕ_h, as represented by normal dipoles and their negative counterparts to secure satisfaction of the free surface condition, may be expressed by

$$\phi_h(x,y,z,t) = -\frac{1}{4\pi}\int_{-a}^{f}\int_{0}^{\kappa(\xi)} \mu(\xi,\zeta,t)\, \vec{n}\cdot\vec{\nabla}\left(\frac{1}{R}-\frac{1}{R_1}\right) w' s' d\zeta d\xi \tag{2.3}$$

where a is the aft and f the forward extent of the waterplane; $\kappa(\xi)$ is the depth of the hull or keel along the centerplane and through the aperature; μ the unknown dipole density; n is the normal vector to the hull;

$$\vec{\nabla} = \vec{I}\frac{\partial}{\partial\xi} + \vec{J}\frac{\partial}{\partial\eta} + \vec{K}\frac{\partial}{\partial\zeta},$$

the vector differential operator; w,s, are arc lengths along any waterplane and along the ship sections, respectively, and $w' = dw/d\xi$, $s' = ds/d\zeta$;

$$\frac{1}{R} = \frac{1}{[(x-\xi)^2+(y-\eta)^2+(z-\zeta)^2]^{1/2}} \quad ; \qquad \frac{1}{R_1} = \frac{1}{[(x-\xi)^2+(y-\eta)^2+(z+\zeta)^2]^{1/2}} \tag{2.4}$$

It is clear from the structure of (2.3) and (2.4) that $\phi_h(x,y,0,t) \equiv 0$.

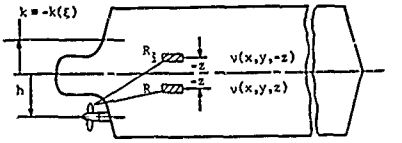
On the wetted hull, satisfaction of the condition that $\frac{\partial\phi_h}{\partial n}$ evaluated on the inner side of the surface ($\vec{n} = 0_-$) yields the Fredholm integral equation of the second kind:

$$\frac{\mu(x,z)}{2} - \frac{1}{4\pi}\int_{-a}^{f}\int_{0}^{\kappa} \mu(\xi,\zeta)\, \vec{n}\cdot\vec{\nabla}\left(\frac{1}{R}-\frac{1}{R_1}\right) w' s' d\zeta d\xi = -\left(\phi_p(x,h-z) - \phi_p(x,h+z)\right) \tag{2.5}$$

where $y = \pm b(x,z)$, b the half-breadth of the hull (positive to port) and $0 < z < \kappa(x)$.

Unfortunately, this integral equation is not of the same form for which an available inversion procedure has been developed by Hess and Smith[2]. Their process applies to the Fredholm equation with a kernel $\vec{n}\cdot\vec{\nabla}(R^{-1})$. However, it will now be shown that the problem posed by (2.5) can indeed be solved by exploiting a related problem involving the Hess-Smith kernel.

Consider the problem posed by generating a *double* hull in a boundless fluid in the presence of a *single* propeller as depicted schematically in Sketch 1 below.



Sketch 1. Schematic of double hull showing a dipole panel and its companion in upper reflection

We distribute dipoles normal to the hull surface of unknown densities $\nu(x,z)$. The integral equation for this problem is

$$\frac{\nu(x,z)}{2} - \frac{1}{4\pi}\int_{-a}^{f}\int_{-\kappa(\xi)}^{\kappa(\xi)} \nu(\xi,\zeta)\vec{n}\cdot\vec{\nabla}\left\{\frac{1}{[(x-\xi)^2+(y-\eta)^2+(z-\zeta)^2]^{1/2}}\right\} s' w' d\zeta d\xi = -\phi_p(x,y,h-z) \quad ; \quad y = \pm b(x,z) \quad ; \quad \eta = \pm b(\xi,\zeta) \tag{2.6}$$

$$-\kappa_{max} < z < \kappa_{max}$$

To secure a right-hand side which is identical to that in (2.5), replace z in (2.6) by -z and subtract the result from (2.6) to achieve

$$\frac{\nu(x,z)-\nu(x,-z)}{2} - \frac{1}{4\pi}\int_{-a}^{f}\int_{-\kappa(\xi)}^{\kappa(\xi)} \nu(\xi,\zeta)\,\vec{n}\cdot\vec{\nabla}\left(\frac{1}{R}-\frac{1}{R_1}\right) s' w' d\zeta d\xi = -\left[\phi_p(x,h-z) - \phi_p(x,h+z)\right] \tag{2.7}$$

where R and R_1 are defined in (2.4). We may now write the ζ-integral as

$$\int_{-\kappa(\xi)}^{0}(\quad)d\zeta + \int_{0}^{\kappa(\xi)}(\quad)d\zeta$$

and, in the first, replace ζ by $-\zeta$ and reverse the limits. As the ζ components of $\vec{n}$ and $\vec{\nabla}$ are odd functions of ζ, their scalar product is even in ζ as is also $s' = ds/d\zeta$. Then, as

$$\frac{1}{R(-\zeta)} = \frac{1}{R_1} \quad \text{and} \quad \frac{1}{R_1(-\zeta)} = \frac{1}{R(\zeta)} \quad ,$$

Eq. (2.7) can, by this manipulation, be recast to read:

$$\frac{\nu(x,z)-\nu(x,-z)}{2}=\frac{1}{4\pi}\int_{-a}^{f}\int_{0}^{\kappa(\xi)}(\nu(\xi,\zeta)-\nu(\xi,-\zeta))\,\vec{n}\cdot\vec{\nabla}$$

$$s'\ {}'d\zeta d\xi=-[\phi_p(x,h-z)-\phi_p(x,h+z)] \qquad (2.8)$$

Comparison of (2.8)and (2.5) shows that

$$\mu(x,z)=\nu(x,z)-\nu(x,-z) \qquad (2.9)$$

Thus, the dipole strength μ required for the solution of the flow problem posed by the wetted hull in the presence of the propeller and its high frequency image in the free surface can be obtained by solving the problem presented by the double hull in a boundless fluid in the presence of only the propeller by combining the dipole strengths ν in the manner defined by (2.9).

If a rigid, non-porous surface condition is imposed on the locus of the undisturbed water surface $-1/R_f$ is replaced by $1/R_f$ and the dipole strengths for this boundary condition are analogously

$$\nu_{rs}=\nu(x,z)+\nu(x,-z) \qquad (2.10)$$

This boundary condition may be expected to apply to water tunnel experiments in which the water surface between the model and tunnel boundary is covered by a wood "plate", provided that such a barrier is rigid.

Another remarkable aspect of the dipole procedure is that the dipole density is equal to the sum of the local value of the potential of the hull plus that due to the propeller as shown in Appendix A. Thus, for the double hull and single propeller, we have on the hull

$$\nu=-\{\phi_h^+(x,z)+\phi_p(x,h-z)\} \qquad (2.11)$$

The superscript + indicates the value on the exterior.

Then, as the pressure change is calculated from

$$\frac{p}{\rho}=-(\frac{\partial}{\partial t}+\frac{U\partial}{\partial x})(\phi_h^+ + \phi_p)=(\frac{\partial}{\partial t}+\frac{U\partial}{\partial x})\nu \qquad (2.12)$$

Then, the pressure at frequency order qn on the wetted hull in the presence of the water surface is the real part of

$$(p_{qn})_{hfs}=\{-iqn\omega(\hat{\nu}_{qn}(x,z)-\hat{\nu}_{qn}(x,-z)$$

$$+\ n_x U\rho\frac{\partial}{\partial w}(\hat{\nu}_{qn}(w,z)-\hat{\nu}_{qn}(w,-z)]e^{iqn\theta} \qquad (2.13)$$

n_x is the x-wise direction cosine, w the waterline variable. The corresponding expression when a rigid boundary so imposed on the water surface is the same except $-\hat{\nu}(x,-z)$ is replaced with $\hat{\nu}(x,-z)$. As ν_{qn} is only known numerically, the second term in the pressure requires numerical differentiation along the waterlines. Alternatively, the ν_{qn} can be inserted to the integral representing ϕ_h and the quadratures presented by $\partial\phi_h/\partial x$ on the hull evaluated by summing.

The contribution of the hull to the total pressure on that surface can be measured by the ratio of the total pressure to that which the propeller in the presence of the free surface would provide at the same point in the absence of the hull. As the pressure is dominated by the time derivative of the potential, the Surface Reflection Ratio can be defined by

$$S_r=\frac{|\phi_{pfs}+\phi_{hfs}|}{|\phi_{pfs}|} \qquad (2.14)$$

where ϕ_{pfs} and ϕ_{hfs} and the potentials of the propeller and the hull in the presence of the free surface.

Correlation of Theoretical and Experimental Hull Pressures

Dr. E. Huse[3] has provided extensive measurments of amplitudes and phases of blade frequency pressures at 34 locations on a 6.25m (20.4 ft.) model of a 250m (820 ft.) tanker fitted with a single Wageningen B-4 propeller operating without cavitation. Principal model, propeller and operating conditions are provided in Table I.

Table 1
Particular Dimensions and Operating Conditions of Norwegian Model 699 and Propeller

Length (LBP)	6.25m
Beam	1.05m
Draft	0.38m
Block Coefficient	0.80m
Speed, U	1.39m/s
Blades	4
Blade Area Ratio	0.55
Diameter	204.5mm
Pitch/Diameter	0.56
Revs/sec. N	11.33
Advance Ratio J = U/ND	0.600

The nominal wake data in the plane of the propeller has been resolved normal to the blade sections, i.e.,

$$\frac{v_n^{(\lambda)}}{U}=u_\lambda(r)\cos\theta_p(r)\cos\lambda\theta-v_\lambda(r)\sin\theta_p\sin\lambda\theta$$

$$\text{or}\quad =a_\lambda\cos\lambda\theta-b_\lambda\sin\lambda\theta$$

where

θ_{p_θ} is the local pitch angle of the blade

λ is the order of shaft frequency

u,v are the axial and tangential components in fraction of model speed.

The harmonic amplitudes u_λ and v_λ are calculated from the given total wake flow components by

$$u_\lambda=\frac{\epsilon_\lambda}{2\pi}\int_0^{2\pi}u(r,\theta)\cos\lambda\theta d\theta\ ;\quad \epsilon=1,\ \epsilon_\lambda=2,\ \lambda>0$$

$$v_\lambda = \frac{1}{\pi}\int_0^{2\pi} v(r,\theta)\sin\lambda\theta d\theta$$

Defining $a_\lambda = u_\lambda\cos\theta_p$ and $b_\lambda = v\sin\theta_p$, values of these coefficients determined at 8 radial locations (via interpolation of data at 8 radii) are exhibited in Table II.

and the null points at each panel. The propeller potential sum was computed at 268 points and taken to be zero at the remaining 212 distant panels. The H-S procedure then is employed to invert the surface integral equation defined by (2.6) for the dipole density μ, which would be obtained on the hull in the joint presence of the free surface and

Table II. Shaft-Order Harmonic Coefficients of Nominal Wake Velocity Normal to Blade Sections in Fraction of Model Speed (Positive Flow Aft, Negative Forward)

	$\lambda=0$		$\lambda=1$		$\lambda=2$		$\lambda=3$		$\lambda=4$		$\lambda=5$	
r/r_o	a_o	b_o	a_1	b_1	a_2	b_2	a_3	b_3	a_4	b_4	a_5	b_5
.25	.492	0	-.006	-.209	-.073	+.067	0	-.021	-.011	+.015	0	-.013
.35	.423	0	+.012	-.103	-.058	+.019	+.012	+.025	-.036	+.021	-.002	-.018
.45	.420	0	+.042	-.043	-.020	-.008	-.028	-.032	-.056	+.023	-.018	-.004
.55	.408	0	+.057	-.018	-.001	+.012	-.043	-.005	-.065	+.022	-.023	+.010
.65	.396	0	+.050	-.002	0	+.014	-.027	+.002	-.050	+.017	-.029	+.013
.75	.426	0	+.036	+.008	-.055	+.005	-.009	+.007	-.029	+.016	-.034	+.009
.85	.491	0	+.020	+.022	-.116	+.017	-.010	+.007	-.038	+.016	-.024	+.004
.95	.577	0	0	+.033	-.209	+.032	+.063	-.008	-.083	+.016	-.008	+.002

The propeller geometry, operating conditions and wake harmonics are employed as input to the Davidson Laboratory unsteady lifting surface program which yields the mean and unsteady (blade-angular dependent) pressure jump distributions on the blades at all shaft orders λ from 0 to one above the number of blades, i.e., $\lambda = 5$ in this case. Appropriate integrations and resolutions of these loadings yield the forces and moments acting on the shaft. These are displayed in Table III.

Table III. Calculated Mean and Unsteady Coefficients of Propeller Force and Moment Amplitudes in Wake of Norwegian Model 699

	Mean		Unsteady
Thrust	0.228	K_T	0.016
Torque	0.0244	K_Q	0.0014
Transverse Force	0.00145	K_{Fy}	0.0010
Mom. Abt. Trans. Axis	0.00140	K_{Qy}	0.0013
Vertical Force	-0.00174	K_{Fz}	0.0010
Mom. Abt. Vert. Axis	-0.00048	K_{Qz}	0.0016

It is noted that the Wageningen (Troost) chart value for $K_T = 0.173$ and $K_Q = 0.0178$. Thus, the calculated means are, disappointingly, 32 and 39 percent higher respectively than the chart values. This will be alluded to later.

The velocity potential associated with each wake harmonic and the thickness are added and applied to the double hull which was divided into 480 quadrilateral patches as shown for the wetted portion in its entirety in Figure 2 and in detail for the stern region in Figure 3. (See following page)

The coordinates of the corners of these panels (the smallest of which are somewhat larger than the criteria involved in the foregoing) are lifted off the drawing of the "wetted" portion. These coordinates, together with their reflected pairs on the "upper" portion of the double hull, are a basic input set to the Hess-Smith (H-S) program which computes the normals

the free surface potential of the propeller as specified by (2.9), is then calculated.

The pressure at each panel is calculated from (2.13). Evaluation showed that the convective pressure (i.e., that contribution proportional to U in (2.13)) is negligible. This can be seen by an order of magnitude analysis which shows that the convective pressure is of the order of $J/\pi = 0.05$. Hence, the modulus of the blade frequency pressure at any panel is

$$|\hat{p}_n| = \rho n\omega|\hat{\nu}_n(x,z) - \hat{\nu}(x,-z)|$$

The locations of the numbered pressure gages on Huse's model are shown on the scaled drawing in plan and side elevation in Fig. 5 . For each gage on the starboard side of the hull in the region of the skeg, there is a "companion" gage on the port side. Associated with each gage, as shown in Fig. 5, the ratio of the amplitudes of the calculated to the measured value is given. The numbers in parentheses are the reflection ratios, i.e., the modulus of the pressure generated by the propeller in the absence of all boundaries. (This denominator should be the modulus of the pressure generated by the propeller in the presence of the free surface (and in the absence of the hull). (However, this was not available at the time of writing.)

In Figs. 6 and 7, we provide graphical representations of computed and measured hull pressures at four sections through the hull.

Calculated and experimental magnitudes and phase angles are provided in Table IV. The phase angle is defined (following the unusual definition adopted by Huse) as the angle of the blade relative to the line in the vertical plane through the gage connecting the gage to the axis of the propeller, at which the pressure on the gage is a maximum negative or suction.

Discussion of the Correlation

It is clear from Figure 5 that the calcul-

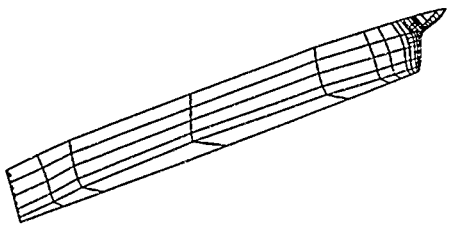


Fig. 2. Schematic of Dipole Panel Layout on Wetted Portion of Norwegian Model 699. Reflected Panels on Upper Portion of Double Hull

ated pressures are generally in excess of the measured pressures for regions forward of the propeller and are less than those measured on the transom aft of the propeller.

First of all, we cannot expect calculation of this sort to yield precise agreement with measurements which themselves are fraught with non-cyclic temporal amplitude modulation and the smallness of the pressure signatures.

As pointed out earlier, the wake harmonics deduced from the nominal wake are not what is sensed by the propeller which, as is known, produces an effective wake. This may be especially so in the case of this tanker which has a very high disc loading coefficient, $C_T = k/\pi K_T/J^2 = 4.9$. As noted previously, the calculated mean thrust is some 30 percent higher than the value given by the open-water K_T curve when interrogated at the mean advance J. Presumably, the application of a non-linear calculational procedure would have produced better agreement.

The larger-than-measured pressures forward and the less-than-measured aft of the propeller are expected to be due to constructive combination of blade thickness and hull potentials with the loading generated potentials forward and partially destructive (out-of-phase) combination of these aft. This has been seen in the free-space pressure field , yielding such larger blade frequency pressures forward than aft of the plane of the propeller. Thus, if the loading were decreased (to yield the correct thrust), the expectation is that the ratios of theoretical to measured pressure amplitudes would tend to unity both forward and aft. Only a recalculation can confirm this speculation.

Examination of the differences in phase angles in Table IV reveals that the theory does quite well with respect to phase. The average of the ratios

$$C_{p\ \text{theo.}}/C_{p\ \text{exp.}}$$

is 1.39 and, if results for gages P8 and P12 are excluded, this average is 1.16. Thus, for integrated effects, we may expect that the theory will give useful results well within the accuracy which should be expected of such calculations.

Integration of vertical force contributions from the panels in each of the sub-regions of the hull depicted in Fig. 4 produced the indicated percentages of the amplitude of the total vertical force. The regions forward of the propeller are seen to be most important.

The solid boundary reflection ratios similar to those defined by Eq. (2.14) are displayed for each gage location on Fig. 5 by the numbers in parentheses. Unfortunately, only the field pressures for the propeller in an unbounded fluid were available to use as a basis rather than those for a propeller in the presence of the free surface. The values found on the transom forward of the propeller are unbelievably large. Those elsewhere are generally less than the value of 2.0 used by many as an expedient.

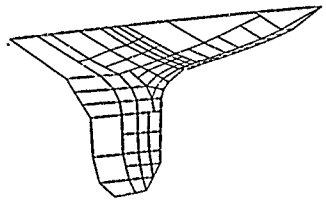


Fig. 3. Detail of Panel Layout in Stern of Norwegian Tanker Model 699. Reflected Arrangement on Upper Double Hull

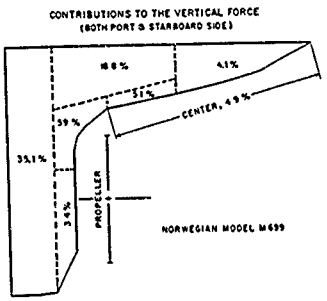


Fig. 4. Percentage Contributions of Indicated Regions to the Blade-Frequency Vertical Force

Correlation with Model Hull Force Experiment

The late Professor Emeritus F.M. Lewis[4] made many tests to determine what he termed the effective vertical and transverse forces due to propeller-generated hull and bearing forces. Here we give results for one of his hulls, a Series 60 ($C_B = 0.60$) V-form stern fitted with a 4-blade propeller. Heretofore, calculated results of the source-panel technique were reported[5] but, subsequently, errors were found. Here we present results obtained using the dipole procedure discussed in the foregoing. The double hull was divided into 276 and the resulting dipole densities, when multiplied by the panel areas and the vertical direction cosines were integrated to give the force contribution generated by each of the blade loadings arising from wake harmonics $\lambda = 0,1,2,3,4,5$ and the blade thickness. Results are summarized in Table V.

Table V. Contributions to Blade Frequency on Series 60 ($C_B = 0.60$) V-Stern from a Five-Bladed Propeller ($F_c/\rho n^2 d^4$)x10^{-2}

Wake Order λ	Magnitude of Coefficient	Phase Angle
0	0.244	23.3
1	0.078	21.6
2	0.142	29.1
3	0.047	32.7
4	0.252	46.8
5	0.013	30.4
Bl. Thick. Tot.	0.184	32.4
Surf. Force Vert.	0.771	32.0
Bearing Force Net	0.257	65.3
Vert. Force	0.624	36.4

The phase angle is defined as the angle of the blade measured counterclockwise (looking forward) when the force component is a positive (upward) maximum.

Here we note that the contributions to the hull force from the mean blade loading (zero wake harmonic), 0.00244, is more than matched by that from the miniscule 4th order blade loading, 0.00252, and the next significant contributor is that generated by blade thickness, 0.00184. The bearing force which was calculated from the DL Unsteady Propeller Force Program is partially opposed to the total surface force and the vector addition yields a force coefficient amplitude of 0.624×10^{-2}. The determination by F.M. Lewis of what he called an effective net vertical force on his propelled model resulted in a coefficient amplitude of 0.45×10^{-2}. Unfortunately, the measurement of Lewis cannot be directly compared to the theoretical value as will now be discussed.

Lewis excited a 10-foot model of this Series 60 variant which was constructed around a rigid truss to supposedly ensure that, when the model was excited by a known force, it would move as a rigid body. The known excitation was applied directly over the propeller location by an electro magnet at the blade rate excitation. Let this calibration distance from the center of gravity of the hull be x_c. He measured the response of the hull by a velocity pick-up gage at x_g units aft of the center of gravity. Using the equations of motion of a hull excited by a vertical force

$$\hat{F}_c e^{i\omega t}$$

at x_c, it is easy to show (because of the high frequency imposed) that the velocity observed at the gage should be

$$\hat{v}_g = \frac{\hat{F}_c}{\omega}\left[\frac{1}{M+M_a} + \frac{x_c x_g}{I+I_a}\right]$$

where M is the mass of the hull; M_a the added mass at essentially infinite frequency; I the mass moment of inertia and I_a the added mass moment of inertia. Thus, the analytic estimate of Lewis' calibration factor is

$$\frac{\hat{F}_c}{\hat{v}_g} = \frac{\omega}{\left[\frac{1}{M+M_a} + \frac{x_c x_g}{I+I_a}\right]} \quad ; \quad \frac{\text{Force}}{\text{Unit Velocity}}$$

Then the "effective" force reported by Lewis when the propeller produces a pressure distribution on the hull, and an attending moment, of course, is

$$\hat{Z} = \frac{\omega(\hat{v}_g)_D}{\left[\frac{1}{M+M_a} + \frac{x_c x_g}{I+I_a}\right]}$$

where $(\hat{v}_g)_D$ is the measured velocity output of the velocity pick up when the propeller is operating. Clearly, Lewis' effective force is parametrically dependent on the calibrating distance x_c. Had he used a location of his exciter forward of the propeller, i.e. closer to the center of applied propeller force, the denominator would be smaller and the effective force larger. Thus, it would appear that the theoretical force should be larger than Lewis' effective force and nothing more can be deduced.

Conclusions and Recommendations

It would, of course, be rash to draw firm conclusions on the basis of the foregoing experimental studies. It does appear that this method produces answers which are well within the order of magnitude of the data, warranting further applications to data secured in such a way as to insure accurate knowledge of all significant wake harmonics.

From a numerical hydrodynamic viewpoint, it is not meaningful to compare calculations with ship model data at the outset. Rather, exercises involving mathematical forms, such as slender spheroids, should be carried out with simple rotating and pulsating isolated singularities as exciting potentials. For such cases, analytical methods can be used to deduce local pressures and forces, providing a firm basis of comparison. In this way, optimum panel dimensions and the extent of panel coverage can be determined to yield specified accuracy requirements. It is hoped that an en-

Table IV. Calculated and Experimental Hull Pressure Coefficients and Phase Angles

Gage	Calc. C_p	Exp. C_p	Calc. Phase Angle	Exp. Phase Angle	$\frac{C_p \text{ calc.}}{C_p \text{ exp.}}$	Calc. Phase Minus Exp. Phase
C_1	.00568	.0048	235°	236°	1.18	-1°
C_2	.02229	.0156	261°	269°	1.43	-7°
P_1	.00105	.00076	244°	--	1.38	--
S_1	.00089	.00009	313°	--	0.99	--
P_2	.00032	.00006	237°	--	0.53	--
S_2	.00074	.0024	199°	--	0.31	--
P_3	.00501	.00420	228°	263°	1.19	-35°
S_3	.00468	.0062	237°	287°	0.76	-50°
P_4	.01453	.0113	240°	275°	1.28	-35°
S_4	.01186	.0101	256°	297°	1.17	-41°
P_5	.01752	.0100	248°	277°	1.75	-29°
S_5	.01334	.0084	270°	298°	1.59	-28°
P_7	.00306	.0022	226°	250°	1.39	-24°
S_7	.00154	.0028	261°	264°	0.55	-3°
P_8	.00231	.0010	199°	245°	2.30	-46°
S_8	.00046	.0014	340°	310°	0.33	+30°
P_9	.00272	--	172°	--	--	--
P_{10}	.01932	.0135	294°	298°	1.43	-4°
S_{10}	.01269	.0156	252°	268°	0.81	-16°
P_{11}	.01979	.0125	285°	291°	1.58	-6°
S_{11}	.01210	.0135	274°	273°	0.90	+1°
P_{12}	.00901	.0045	242°	273°	2.00	-31°
S_{12}	.00260	.0051	314°	322°	0.51	-8°
P_{13}	.01205	.0075	265°	282°	1.60	-17°
S_{13}	.00641	.0050	351°	282°	1.28	+69°
P_{14}	.01248	.0100	316°	306°	1.25	+10°
S_{14}	.01494	.0090	264°	278°	1.66	-14°
P_{15}	.01175	.0095	276°	273°	1.24	+3°
S_{15}	.01387	.0085	274°	283°	1.63	-9°
P_{16}	.00419	.0035	264°	288°	1.20	-24°
S_{16}	.00605	.0037	255°	256°	1.63	-1°

lightened contracts administrator can be found, who perceives the necessity of this basic study, and can find the funds for its execution. Beyond that, this frontal approach requires automation of input, and then the entire procedure will be attractive for routine use.

Acknowledgements

This work was carried out under the direction of Dr. S. Tsakonas, Research Professor of Ocean Engineering, with the assistance of Miss W. Jacobs, Senior Research Engineer, Davidson Laboratory. Without their abilities and dedicated efforts, this work could not have been accomplished. Miss J. Jones is thanked for her painstaking composition of the manuscript. We are indebted to Dr. E. Huse and colleagues at the Norwegian Hydrodynamic Laboratories for their painstaking assistance in supplying all pertinent data to make this correlation possible. The U.S. Maritime Administration is thanked for their support and for the encouragement afforded by Mr. Robert Falls, Program Manager, MARAD.

References

1. Tsakonas, S., Jacobs, W.R., and Ali, M.R.: "Propeller Blade Pressure Distribution Due to Loading and Thickness Effect" J. Ship Research, Vol. 23, No. 2, June 1979

2. Hess, J.L. and Smith, A.M.: "Calculation of Non-Lifting Potential Flow About Arbitrary Three-Dimensional Bodies" Douglas Aircraft Division, Report No. E.S. 40622, 15 March 1962

3. Huse, E.: "The Magnitude and Distribution of Propeller-Induced Vibratory Forces on a Single-Screw Ship Model" Norwegian Ship Model Experiment Tank Publication No. 100, December 1968

4. Lewis, F.M.. "Propeller Vibration Forces in Single-Screw Ships" Paper presented at the SNAME Annual Meeting, New York, Nov. 12-14, 1969

5. Tsakonas, S. and Valentine, D. "A Theoretical Procedure for Calculating Propeller-Induced Hull Forces" Davidson Laboratory Report SIT-DL-79-9-1979

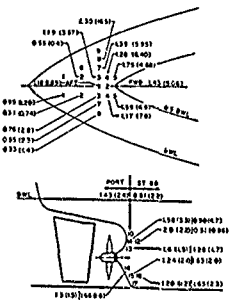


Fig. 5. Ratios of Theoretical to Measured Pressure Amplitudes at Indicated Gage Location and Values of the Reflection Ratio (in parentheses)

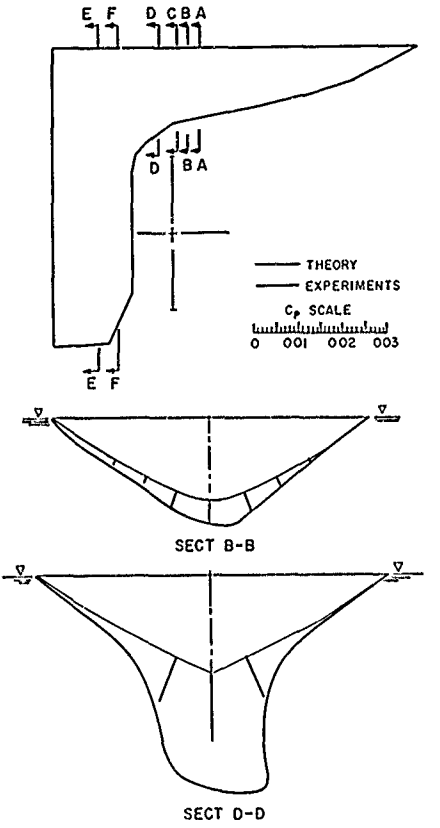


Fig. 6. Correlation of Measured and Calculated Pressures at Sections B-B and D-D.

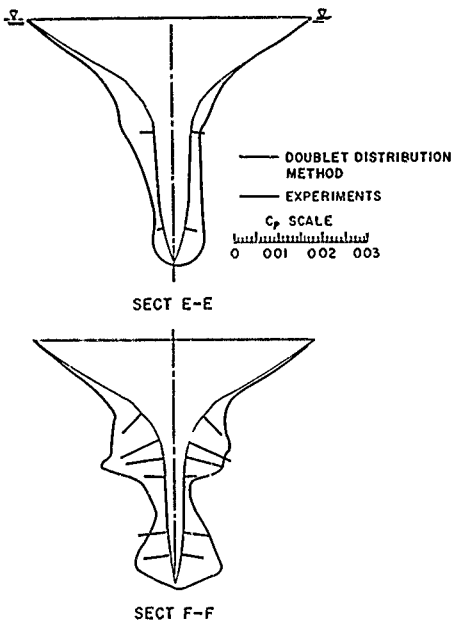


Fig. 7. Correlation of Measured and Calculated Pressures at Sections F-E and F-F.

Appendix A

Replacement of the Exterior Neumann Problem by an Interior Dirichlet Problem

The problem posed by the generation (or creation) of a double hull in the presence of a single propeller requires a hull potential ϕ_h which meets the *Neumann condition*

$$\frac{\partial \phi_h}{\partial n} = -\frac{\partial \phi}{\partial n} \quad ; \quad \text{on } S = S_h + S_i \tag{A-1}$$

where ϕ is the potential of the propeller, n is the outward normal from S, and S_h is the hull surface and S_i is the image or reflected hull; thus S is the double hull. The difficulty with solving the hull generation problem to meet (A-1) directly is that the right side of (A-1) is composed of three terms, i.e.,

$$\frac{\partial}{\partial n} = n_x \frac{\partial \phi}{\partial x} + n_y \frac{\partial \phi}{\partial y} + n_z \frac{\partial \phi}{\partial z}$$

and this calculation is highly consumptive of computer effort. Fortunately, the same Neumann condition can be met by solving the interior Dirichlet problem requiring within the interior of S that $\phi_h = -\phi$ (a single scalar function).

Let S denote a bounded, simple, smooth, closed surface. Let D_i denote the bounded interior domain of S, and let D_e indicate the unbounded exterior of S. Define $\underline{n}$ as the unit normal to S directed from D_i to D_e. Designate

$$R_s = [(x-\xi)^2 + (y-\eta)^2 + (z-\zeta)^2]^{1/2}$$
$$R = [(X-\xi)^2 + (Y-\eta)^2 + (Z-\zeta)^2]^{1/2} \tag{A-2}$$

where $Q(\xi,\eta,\zeta)$ and $P(x,y,z)$ are points on S and $T(X,Y,Z)$ is a point in either D_i or D_e. Let

$$\underline{\nabla} = \underline{i}\frac{\partial}{\partial \xi} + \underline{j}\frac{\partial}{\partial \eta} + \underline{k}\frac{\partial}{\partial \zeta}$$
$$\nabla = \underline{i}\frac{\partial}{\partial X} + \underline{j}\frac{\partial}{\partial Y} + \underline{k}\frac{\partial}{\partial Z} \tag{A-3}$$

in which $\underline{i},\underline{j},\underline{k}$ are unit vectors defining the orthogonal coordinate system.

Consider the surface integral of normal dipoles

$$\phi_h(T) = -\int_S v(Q)\, \underline{n}\cdot\underline{\nabla}\left(\frac{1}{R}\right) dS \tag{A-4}$$

which satisfies

$$\nabla\cdot\nabla\, \phi_h(T) = 0$$

for T in either D_i or D_e. The potential (A-4) is discontinuous at S (as shown, for example, in Kellogg "Foundations of Potential Theory", Reference 20). If

$$\phi_h^+(P) = \lim_{T\to P} \phi_h(T) \qquad T \text{ in } D_e \tag{A-5}$$

and

$$\phi_h^-(P) = \lim_{T\to P} \phi_h(T) \qquad T \text{ in } D_i \tag{A-6}$$

Then

$$\phi_h^+(P) = -2\pi v(P) - \int_S v(Q)\, \underline{n}\cdot\underline{\nabla}\left(\frac{1}{R_s}\right) dS \tag{A-7a}$$

$$\phi_h^-(P) = 2\pi v(P) - \int_S v(Q)\, \underline{n}\cdot\underline{\nabla}\left(\frac{1}{R_s}\right) dS \tag{A-7b}$$

where

$$v(P) = -\frac{1}{4\pi}\left(\phi_h^+(P) - \phi_h^-(P)\right) \tag{A-7c}$$

On the other hand, it is shown (Kellogg) that, if v(Q) is continuous of S and *if either of the limits*

$$\lim_{T\to P} \underline{n}\cdot\nabla\phi_h = \left(\frac{\partial \phi_h}{\partial n}\right)_e \qquad T \text{ in } D_e$$

or (A-8)

$$\lim_{T\to P} \underline{n}\cdot\nabla\phi_h = \left(\frac{\partial \phi_h}{\partial n}\right)_i \qquad T \text{ in } D_i$$

exists, then the other does and

$$\left(\frac{\partial \phi_h}{\partial n}\right)_e = \left(\frac{\partial \phi_h}{\partial n}\right)_i = \left(\frac{\partial \phi_h}{n}\right)_P \tag{A-9}$$

i.e., the normal derivative or velocity is continuous through the dipoled surface. Now suppose that

$$\phi_h(T) = -\int_S v(Q)\underline{n}\cdot\underline{\nabla}\left(\frac{1}{R}\right) dS \qquad T \text{ in } D_e \tag{A-10}$$

is to be such that

$$\left(\frac{\partial \phi_h}{\partial n}\right)_e = -\left(\frac{\partial \phi}{\partial n}\right) = \left(\frac{\partial \phi}{\partial n}\right)_i \tag{A-11}$$

where, in our case, ϕ is the potential of the propeller which is, of course, a regular harmonic function *in the domain containing the double hull surface S and its interior.*

In accordance with the above-cited properties of surface dipole distributions, this Neumann condition (A-11) can be satisfied if we demand that the dipole density v(Q) be such that

$$\phi_h(T) = -\phi(T) = -\int_S v(Q)\underline{n}\cdot\underline{\nabla}\left(\frac{1}{R}\right) dS \tag{A-12}$$

for all points T in D_i. This insures the satisfaction of

$$\left(\frac{\partial \phi_h}{\partial n}\right)_i = -\left(\frac{\partial \phi}{\partial n}\right)_i$$

and we see that the exterior Neumann problem is thus reduced to an interior Dirichlet problem for, as T → P (on interior (S), we see from (A-7b) that v must satisfy

$$-\phi(P) = 2\pi v(P) - \int_S v(Q)\underline{n}\cdot\underline{\nabla}\left(\frac{1}{R_s}\right) dS \tag{A-13}$$

a Fredholm integral equation of the second kind

of the form identical to that for which procedures are available for its numerical inversion.

Since $\phi_h^-(P) = -\phi(P)$, then, from the jump relation (A-7c), we obtain

$$v(P) = -\frac{1}{4\pi}(\phi_h^+(P) + \phi(P)) \qquad (A\text{-}14)$$

Hence, once v is found on the hull, the total pressure on the hull can be calculated from

$$\frac{p}{\rho} = -(\frac{\partial}{\partial t} + U\frac{\partial}{\partial x})(\phi_h^+ + \phi)$$

$$= 4\pi(\frac{\partial}{\partial t} + U\frac{\partial}{\partial x})\, v\,(w,s,t)$$

where w is arc length along a waterline and s is arc length along a section or frame line. If the half-breadths of the ship are expressed as $b = b(x,z)$, then the pressure at frequency ω_n can be deduced from

$$\frac{p_{\omega n}}{\rho} = 4\pi(-i\omega_n \hat{v}_{\omega n}(w,s) + n_x U(\frac{\partial \hat{v}}{\partial w'})_{\omega n} e^{i\omega n \theta}$$

where n_x is the x-component of the unit normal or the direction cosine (n,x). As $v_{\omega n}$, the complex amplitude is only known numerically, the evaluation of the second term requires numerical differentiation. Alternatively, $\hat{v}_{\omega n}$ can be inserted into (A-12) and the quadrature presented by $\partial\phi/\partial x$ on S evaluated by converting the integral to a sum.

DISCUSSIONS
of the paper
by J.P. Breslin

PROPELLER-INDUCED HULL PRESSURES AND FORCES

Discussion
by R. Lepeix

I should like to put three questions to Dr. Breslin :

1/- As shipbuilders we very much appreciate the efforts made to optimize the hull + propeller assembly from the point of view of vibration.

However, for the moment, we observe that, when estimating the pressures on the hull, the methods employing simple formulas of basically statistical origin (originating from real measurements at sea) are quite as exact as the present-day numeric methods of theoretical origin, I made this comparison a few months ago for a ship built in our shipyards, a 120 000 ton methane tanker.

My first question is therefore : Do you consider that in the future the computer programmes such as yours will provide more exact results than the semi-empirical formulas, notably in view of the accuracy of the wake measurements ?

2/- In your paper you only dealt with non-cavitating propellers. Now as a general rule, at least for merchant ships, it is only the cavitation on the propeller blades that can generate pressures really dangerous for the ship.

It would not appear, a priori, more difficult to take the cavitation into account in your computations. Naturally the accuracy might be lower. Is it for this reason that you have limited your paper to the case of non-cavitating propellers, and do you intend to extend it to the cavitating case ?

3/- I have always been extremely sceptical of the value 2 of the "solid boundary factor", which is theoretically false in the case of a ship. Moreover, in December 1974, I submitted a paper in this connection which you were good enough to comment on. This was at a symposium in Holland.

My question is : Do you consider that with the aids at your disposal it is possible to define more exact values of this reflection factor, an approach corresponding to that of Huse in his experiments on models at Trondheim ?

Author's reply

M. Lepeix has raised three good pragmatic questions to which I offer the following replies

1/- Surely empirical data are very useful and should be employed to secure guidance if they can be cast in forms which reflect the physics of the phenomenon. Indeed, the correlations of pressure levels with cracking of plates and objectionable levels of vibration as have been made by Holden et al (SNAME Annual Meeting, November 1980) are highly useful. However, I become skeptical of formulas elicited through regression analyses which do not evolve out of a rational theory. I believe that programs such as this, which include propeller and hull geometry and the functions which propagate each loading and thickness harmonic as dictated by the theory, can be used to secure (at a minimum) sound *comparative values* of excitation. Indeed, there is uncertainty in the wake harmonics which will remain with us until hull boundary layers and wakes can be computed at ship scale to a fine state. Near field pressures are dominated by the mean loading and blade thickness (for non-cavitating propellers). The mean loading is well predicted (since thrust is well estimated) and the blade thickness contribution is independent of the wake. However, the vibratory *forces on the* hull are dominantly dependent on the blade loadings arising from the (n-1), n and (n+1)th wake harmonics which are admittedly small and subject to variations with scale and vary with time. The best way to qualify computer-based procedures would be to apply them to full-scale cases where confidence in the measurements is high. Deviations could then be ascribed to a lack of precise knowledge of the wake. If such an effort were supported, we could have a far better basis for securing pragmatic results than from empirical formulae which do not reflect the functional forms provided by the mathematics employed in these rationally founded programs.

2/- M. Lepeix is surely correct in pointing out that pressures and forces generated by intermittently cavitating blades are much larger than those emanating from non-cavitating propellers. We did not include transient cavitation because we do not have a *procedure for it, nor* was it needed for the present correlation. The simultaneous presence of cavitation, loading and thickness requires solution of the mixed boundary-value problem via simultaneous integral equations. A program for transient cavitation on the blades has been recently evolved at MIT by Professor Kerwin. We have used the output of this program as input to our propeller-hull program and have secured good agreement with pressure measurements made on the hull of a Ro-Ro ship model in the

SSPA cavitation tunnel (when invoking the boundary condition appropriate to that imposed in the test facility on the locus of the water surface).

3/- I join M. Lepeix in his skepticism in regard to the utility of the reflection factor of 2 where the ship surface is highly curved or on skeg or fins across which pressure pumps are expected. It is a useful expendient in regard to estimating amplitude when the local surface above the propeller is relatively flat. I believe that the hull reaction pressures should be generally less than those applied by the propeller on curved counters (hence factors of less than 2) and may be greater on the skeg near the trailing edge. For curved surfaces there is no rational way of estimating the reflection factors, much less the phase of the net pressure, so I see no use of the concept for such geometries.

Discussion
by G.E. Hearn

The inclusion of the single propeller effect in generating the double hull model is a very nice peice of manipulation. However, the solution of the resulting integral equation must have adversely effected the calculations performed utilising the discretisations presented in Figures 2 and 3. The detailing around the aft end is to be commended in terms of geometric representation but it is rather inconsistent with the representation of the rest of the hull. Also the large aspect ratios of area near the free-surface in the stern section will I suspect, result in furter breakdown of the associated algebraic system with the main hull aft end interaction incorrectly modelled. The solid boundary reflection ratios are also likely to be adversely affected. However, in Dr. Breslin's own words "it would be rash to draw firm conclusions" without further calculation but 3D calculations performed at Newcastle suggest that the interplay of the modelling of the different parts of the hull significantly affect the detailed pressure distribution and associated dependent quantities.

Author's reply

Dr. Hearn commends the representation of the hull aft of the propeller but asserts that it is rather inconsistent with the discretisations elsewhere on the hull. It is pointed out on page 430 that, downstream of the propeller, the potential oscillates rapidly with longitudinal distance x requiring very fine subdivision, whereas forward of the propeller, the potential generated by mean loading drops off rapidly and monotonically with x. Transversely, there are oscillations which require fine mesh to each side of the center plane but, beyond about $0.3r_0$, the panel size can be increased. It is interesting to learn of the experience being gained at Newcastle. We have not been able to ascertain the optimum panel sizes and number, and to that end I call attention to the final remarks concerning the use of a spheroidal surface for which results can be independently secured and used as a solid basis for determining panel size and distribution. Surely Dr. Hearn's observations are most pertinent and are appreciated.

Session VII
FLOATING BODIES IN WAVES

P. Guével
Session Chairman
École Nationale Supérieure
de Mécanique
France

A LOCALIZED FINITE-ELEMENT METHOD FOR THREE-DIMENSIONAL SHIP MOTION PROBLEMS*

Kwang June Bai
David W. Taylor Naval Ship Research and Development Center
Bethesda, Maryland 20084

Abstract

An application of the localized finite-element method to a three-dimensional time-harmonic free surface flow in a canal is presented. Boundary conditions on both the free surface and the body are linearized and imposed on their equilibrium positions. By utilizing known set of eigenfunctions, the computation domain is reduced to a very small local domain where an eight-node linear three-dimensional element is used. Proper matching is also imposed between two sets of trial functions on the truncated boundary. To be solved are the problems concerning: (1) six degree-of-freedom radiation and diffraction in three dimensions, (2) two dimensional motion corresponding to the local flow at the midship cross-sectional plane, and (3) related eigenvalues. Specifically, two sets of results for two ship locations in a canal are presented. In both cases, the eigenvalues of the local cross-sectional plane are shown to play a significant role in the three-dimensional results. A remarkable similarity between exciting forces and moment and the damping coefficients corresponding to the modes of their motions are also observed in the results. The accuracy of the three-dimensional results presented here is also discussed by comparing two sets of eigenvalues computed by using two different sizes of finite elements.

I. Introduction

Steady-state time-harmonic motions of an inviscid, incompressible fluid with free surface in the presence of a body or bodies in it are described by a boundary-value problem governed by the Laplace equation with appropriate boundary conditions. In the past, problems of this type were generally solved by distributing sources (and/or dipoles) on the body boundary and using Green's theorem to obtain an integral equation for the strength of these boundary singularities; or, alternatively, by using sources and higher-order multipole expansions at an interior point within the body, the strengths of these singularities being determined so as to satisfy the body boundary condition. In all cases it is conventional to utilize the singularities which are solutions of the boundary-value problem stated above, except for the body boundary condition which is invoked separately to determine the singularity distribution.

*This work was supported by the Numerical Naval Hydrodynamics Program at the David W. Taylor Naval Ship R&D Center. This Program is jointly supported by NSRDC and the Office of Naval Research. Part of the present work was done while the author was a visiting professor at the Ecole Nationale Superieure de Techniques Avancees (ENSTA) in 1980, and partially supported by the Ministry of Defense, France.

For two- and three-dimensional motions in a fluid of infinite depth, or of finite but constant depth, the required singularities are well known, although of rather complicated analytical form, so that the approach described in the foregoing corresponds to solving a Fredholm integral equation over the body surface, with a rather complicated kernel function. An extensive list of literature on this subject can be found in Wehausen[1].

In this paper a numerically oriented as well as more versatile method is introduced as an alternative approach to the solution of the problem. This alternative approach is based on a variational principle which is utilized to determine the velocity potential throughout the fluid domain. The present work is a direct extension of the earlier work by Bai and Yeung[2] for a general three-dimensional body geometry in a canal. In this procedure, the known solution space in certain subdomains is made use of in order to reduce the 'computation box' to a size as small as possible. We call this drastically-reduced computation box the localized finite-element domain. The phrase "localized finite-element method" is used to denote the finite element method applied only in this localized subdomain. In this particular problem, i.e., in a free surface flow in a canal, the solution space is represented by the complete set of eigenfunctions in the subdomain. It is essential to make the domain of computation as small as possible because the practical success or failure of a numerical method, in general, mainly depends upon the size of the computation box. In the present procedure, the reduction of the original infinite fluid domain to a small localized subdomain is achieved by replacing the conventional radiation condition by the matching condition. This requires that the velocity potential and its normal derivative (i.e., normal velocity) represented by two sets of different trial functions, defined in the adjacent subdomains, be continuous along the fictitious interface juncture boundary surface. Then we approximate the potential in the localized finite-element domain by piecewise polynomial trial functions defined in each finite element. Thus, in effect, an integral equation over a body surface with a complicated kernel is replaced by a system of equations over a much larger fluid domain, but with a much simpler kernel.

Previous studies of the finite element method applied to time-harmonic ship motion problems have been made by Bai[3-6], Berkhoff[7], Smith[8], Chen and Mei[9], Seto and Yamamoto[10], Yue et al[11], Luvrard et al[12], and Chowdbury[13].

Additional numerical results of the related two-dimensional boundary-value and eigenvalue problems at the midship cross-sectional plane are also presented. Two different sizes of the finite elements in the midship cross-sectional plane are used in these additional computations. These results are used as reference in discussing the accuracy of the present three-dimensional results.

II Mathematical Formulation

Considered here is steady-state time-harmonic free-surface flow in the presence of a body floating or submerged in a canal with a rectangular uniform cross-section. However, a local variation of the bottom and side-wall geometry is present and a uniform rectangular cross-section of each side (not necessarily the same on both sides), can be similarly treated by the present method. The coordinate system is right-handed and rectangular. The y-axis is directed opposite to the force of gravity, and the xz-plane coincides with the undisturbed free surface. The bottom of the canal is in the $y = -H$ plane and the side walls are in the $z = \pm W/2$ planes. We neglect surface tension, and assume that the fluid is inviscid and incompressible and that the motion is irrotational. Furthermore, we assure that the motion of the body and, consequently, the generated wave, to be small in some sense, so that the boundary condition on the body and on the free surface can be linearized and satisfied at the mean equilibrium positions instead of at their instantaneous positions.

Let $\Phi(x, y, z, t)$ be the velocity potential describing the flow field. The continuity equation requires Φ to satisfy Laplace's equation. Let σ be the angular frequency of the time-harmonic solution. Then, introducing the usual time and spatial decomposition we have

$$\Phi(x, y, z, t) = Re\left[\phi^{(m)}(x, y, z)\, a^{(m)}(t)\right] \tag{1}$$

$$m = 1, \ldots, 7$$

where

$$\phi^{(m)} = \phi_1^{(m)} + i\phi_2^{(m)} \tag{2}$$

is the complex-valued spatial potential, and $a^{(m)}(t)$ is the complex time-harmonic motion amplitude of the body corresponding to the m-th mode, i.e.,

$$\begin{aligned} a_m(t) &= Re\left[a^{(m)}(t)\right] \\ &= Re\left[\left(a_1^{(m)} + ia_2^{(m)}\right)e^{-i\sigma t}\right] \end{aligned} \tag{3}$$

where $a_m(t)$ is the body motion amplitude. For $m = 7$, the diffraction problem corresponding to an incoming wave system of unit amplitude, one simply sets $a_1^{(7)} = 0$ and $a_2^{(7)} = 1/\sigma$ in Equation (3). The potential function $\phi(x, y, z)$ must satisfy

$$\left(\frac{\partial^2}{\partial x^2} + \frac{\partial^2}{\partial y^2} + \frac{\partial^2}{\partial z^2}\right)\phi(x, y, z) = 0 \tag{4}$$

in the fluid,

$$\phi_y - \nu\phi\big|_{S_F} = 0 \tag{5a}$$

$$\phi_n\big|_{S_O} = V_n = f(s) \tag{5b}$$

$$\phi_n\big|_{S_B} = 0 \tag{5c}$$

$$\phi_n\big|_{S_W} = 0 \tag{5d}$$

where $\nu = \sigma^2/g$

g — acceleration due to gravity

S_F — undisturbed free surface, $y = 0$, outside of the body

S_B — bottom surface

S_W — side walls

S_O — body surface below the mean free surface.

The normal velocity $f(s)$ depends upon the mode index m. For $m = 1, 2, \ldots, 6$, corresponding to the sway, heave, surge, roll, pitch, and yaw modes of motion, respectively, $f(s)$ is given by

$$f^{(i)}(s) = n_i \tag{6}$$

with

$$(n_1, n_2, n_3) = (n_x, n_y, n_z)$$

$$(n_4, n_5, n_6) = (\bar{r} - \bar{r}_c) \times \bar{n}$$

where $\bar{n}$ is the unit normal vector into the body with components (n_x, n_y, n_z), $\bar{r}_c$ is the vector from the origin to the center of rotation, and

$$\bar{r} = (x, y, z).$$

For $m = 7$,

$$f(s) = \frac{-\partial\phi_I}{\partial n} \tag{7}$$

where ϕ_I is the spatial potential associated with the incident wave system. The incident wave potential of unit amplitude incoming from $x = -\infty$ is given by

$$\phi_I(x, y, z) = -\frac{g}{\sigma}\frac{\cosh m_o(y + H)}{\cosh m_o H}\, e^{im_o x} \tag{8}$$

where m_o is wave number. Finally, to make the solution of this problem unique, we impose the radiation condition requiring that the generated waves must be outgoing.

III. Localized Finite Element Method

The fluid domain defined in the foregoing formulation is unbounded along the x-axis. For numerical computations, it is highly desirable that the computation box be made as small as possible. The goal of reducing the original infinite fluid domain to a manageable finite domain is achieved by making use of the known solution space in the truncated infinite subdomains which will be defined later. As a result, the computation domain is reduced to a very local subdomain, called a localized finite element domain, which may barely include any source of disturbance in the fluid. The present numerical method is called a localized finite element method because the finite element numerical computations are made only for a local domain. Throughout this section, the subscript m in the potential, defined in the Mathematical Formulation section is omitted with the understanding that ϕ will always depend upon m.

Let us draw two imaginary vertical planes J_1 and J_2 which separate the original fluid domain D into the three subdomains: D_o, D_1, D_2 as shown in Figure 1. We assure that D_o includes the ship (and/or any other sources of disturbance). The boundary surfaces ∂D_o, ∂D_1, and ∂D_2 are denoted, respectively, as

$$\begin{aligned} \partial D_o &= S_{Fo} + S_{Wo} + S_{Bo} + J_1 + J_2 + S_o \\ \partial D_i &= S_{Fi} + S_{Wi} + S_{Bi} + J_i + S_{Ri} \qquad i = 1,2 \end{aligned} \tag{9}$$

where S_{Fi}, S_{Bi}, and S_{Wi}, denote, respectively, the free surface, the bottom, and the canal side walls, in the subdomains D_i (for $i = 0, 1, 2$) and where S_{Ri} (for $i = 1, 2$) are the boundaries at infinity. The ship hull surface is denoted by S_o.

Let ϕ_o, ϕ_1, and ϕ_2 denote the velocity potentials defined in the subdomains D_o, D_1, and D_2, respectively. Then we have, from Equations (4) and (5),

$$\begin{aligned} \nabla^2\phi_o &= 0 && \text{in } D_o \\ \phi_{on} - \nu\phi_o &= 0 && \text{on } S_{Fo} \\ \phi_{on} &= f(s) && \text{on } S_o \\ \phi_{on} &= 0 && \text{on } S_{Bo} \cup S_{Wo} \end{aligned} \tag{10}$$

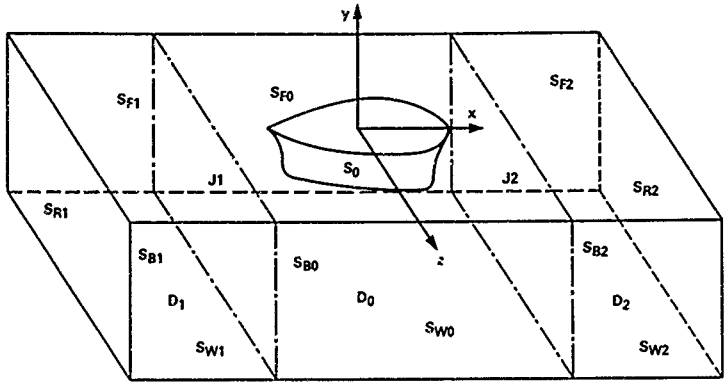


Figure 1 -- Boundary Configurations of the Three Subdivided Fluid Domains

and, for ϕ_i, $i = 1, 2$,

$$\begin{aligned} \nabla^2 \phi_i &= 0 && \text{in } D_i \\ \phi_{in} - \nu\phi_i &= 0 && \text{on } S_{Fi} \\ \phi_{in} &= 0 && \text{on } S_{Bi} \cup S_{Wi} \end{aligned} \tag{11}$$

It is understood in Equation (11) that a proper radiation condition is imposed at infinities for ϕ_1 and ϕ_2. In addition, we require

$$\left.\begin{aligned} \phi_o &= \phi_i \\ \phi_{on} + \phi_{in} &= 0 \end{aligned}\right\} \quad \text{on } J_i,\ i = 1, 2 \tag{12}$$

where the normal vector is taken outwards from the fluid subdomain defined for each potential, e g ,

$$\begin{aligned} \phi_{1n} &= \phi_{1x}, \quad \phi_{on} = -\phi_{ox} \quad \text{on } J_1 \\ \phi_{2n} &= -\phi_{2x}, \quad \phi_{on} = \phi_{ox} \quad \text{on } J_2 \end{aligned} \tag{13}$$

By the juncture conditions in Equations (12), the solutions of Equations (10) through (12) are unique and identical to the solution of the original formulation in the Mathematical Formulation section. (This can be shown by applying Green's theorem to the difference of the solution of the original equation, defined in the previous section, and the solutions ϕ_o, ϕ_1, and ϕ_2, defined in the three subdomains)

Let us assume that the general solutions of Equation (11) with appropriate radiation conditions, are known, i e , the complete set of eigenfunctions or Green's functions of the problems Then the first step toward the construction of the appropriate functional for our variational equation equivalent to the coupled partial differential equations defined in (10) through (12) is the choice of trial function space for each function ϕ_o, ϕ_1, and ϕ_2. If the bases of the trial functions for ϕ_1 and ϕ_2 are chosen from the solution space (the known general solutions), then we can obtain the following two functionals

$$K_1\{\phi_o,\phi_1,\phi_2\} = \iiint_{D_o} \tfrac{1}{2}(\nabla\phi_o)^2 dv - \frac{\nu}{2}\iint_{S_{Fo}} \phi_o^2 ds - \iint_{S_o} f(s)\phi_o ds + \iint_{J_1} (\phi_o - \tfrac{1}{2}\phi_1)\phi_{in} ds + \iint_{J_2} (\phi_o - \tfrac{1}{2}\phi_2)\phi_{2n} ds \tag{14}$$

and

$$K_2\{\phi_o,\phi_1,\phi_2\} = \iiint_{D_o} \tfrac{1}{2}(\nabla\phi_o)^2 dv - \frac{\nu}{2}\iint_{S_{Fo}} \phi_o^2 ds - \iint_{S_o} f(s)\phi_o ds + \iint_{J_1} [(\phi_1 - \phi_o)\phi_{on} + \tfrac{1}{2}\phi_1\phi_{1n}] ds + \iint_{J_2} [(\phi_2 - \phi_o)\phi_{on} + \tfrac{1}{2}\phi_2\phi_{2n}] ds \tag{15}$$

Setting the first variation of either functional to be zero, i e ,

$$\delta K_1\{\phi_o, \phi_1, \phi_2\} = 0 \tag{16a}$$

or

$$\delta K_2\{\phi_o, \phi_1, \phi_2\} = 0 \tag{16b}$$

is the same as solving Equations (10) through (12). It is easy to show this by taking the first variation and by using Green's theorem[2] The integral expressions of the functionals involve only the subdomain D_o which we call the "localized finite-element domain." If one takes the localized finite-element domain to be small, then the domain over which the integrals have to be computed will also be small On the other hand, one has to take many terms (eigenfunc-

tions) to represent the trial solutions ϕ_1 and ϕ_2 in the computation of the approximate solutions, and vice versa.

It is interesting that the stationary value of both functions are

$$K_1\{\phi_o, \phi_1, \phi_2\} = -\frac{1}{2}\iint_{S_o} f(s)\,\phi_o\,ds \tag{17a}$$

$$K_2\{\phi_o, \phi_1, \phi_2\} = -\frac{1}{2}\iint_{S_o} f(s)\,\phi_o\,ds \tag{17b}$$

if ϕ_o, ϕ_1, and ϕ_2 are the exact solutions. This stationary value is simply $(-1/2\varrho)$ times the added mass and $(-1/2\varrho\omega)$ times the damping coefficients.

Either functional, defined in (14) or (15), will give a variational equation mathematically equivalent to the original boundary-value problem at hand. The use of the functional given in (14) is slightly advantageous because the normal derivative of ϕ_o is not involved in the coupling integral terms. In the present computation, the functional given in Equation (14) is used. The equivalence of the differential equation to the variational problem is basic to the choice of the computational scheme. One significant difference between the functional method and the differential equation is the fact that the expressions for the associated functionals in (14) and (15) involve no second derivatives, owing to the integration by parts used to construct these functionals, i.e., Green's theorem is used here. It follows that the functionals will be well defined if only the first derivative of the function, rather than the second, is required to be bounded. Therefore, the class of admissible functions, in the problem to find the stationary point, is enlarged to a space bigger than that for the original differential equation. We now have the advantage, while searching for the stationary point of the functional, of being permitted to try functions outside the class of those originally admissible. In practice, this means that we can now try continuous functions whose first derivatives are only piecewise continuous. In other words, the first derivative can have finite discontinuities at the juncture boundary between adjacent elements. It is very easy to construct basis functions that satisfy the previous requirements.

In the localized finite element domain D_0, the basis for the trial function is chosen from a polynomial basis. Specifically, eight-node isoparametric, linear three-dimensional elements were used in the present numerical calculations. As mentioned earlier, the trial functions in D_1 and D_2 will be chosen from a subspace of the solution space which satisfies the Laplace equation with the free-surface condition, the side-wall condition, the bottom condition, and the radiation condition at infinity. The eigenfunctions or the Green functions of the above problem can represent the solution space. However, we will choose the eigen-function space in this paper for its simplicity.

The variational equation (16a) goes into operational form in the following way. Let q_{ij} ($i = 0, 1, 2$, and $j = 1, 2, \ldots M_i$) be the basis for the trial functions in each subdomain D_i ($i = 0, 1, 2$). Then the solution is assumed to be

$$\phi_i = \sum_{j=1}^{M_i} \varphi_{ij}\, q_{ij} \tag{18}$$

in D_i ($i = 0, 1, 2$), where φ_{ij} are coefficients to be determined. By substituting Equation (18) in the functional defined in Equation (14), the variational equation (16a) reduces to a set of linear algebraic equations. (In this procedure, only the coefficients are subject to variation.)

A complete set of eigenfunctions (the resonance frequencies are excluded) are given in Wehausen[14] as

$$\left\{e^{\mp \kappa_{no} x}\,\frac{\cosh m_o (y+H)}{\cosh m_o H}\cos\frac{n\pi}{W}\left(z-\frac{W}{2}\right),\right.$$
$$\left. e^{\pm K_{np} x}\cos m_p (y+H)\cos\frac{n\pi}{W}\left(z-\frac{W}{2}\right)\right\} \tag{19}$$

where W is the width of the tank and the upper and lower signs are to be taken in the subdomains D_1 and D_2, respectively, and where

$$K_{no} = \left[m_o^2 - \left(\frac{n\pi}{W}\right)^2\right]^{\left(\frac{1}{2}\right)}$$
$$K_{np} = \left[m_p^2 + \left(\frac{n\pi}{W}\right)^2\right]^{\left(\frac{1}{2}\right)} \tag{20}$$

and m_o and m_p ($p = 1, 2, \ldots$) are the real roots of

$$m_o \tanh m_o H = \nu$$
$$m_p \tan m_p H = -\nu \tag{21}$$

The exponent of the first term in Equation (19) becomes real when $n\pi/W > m_o$, resulting in a local disturbance, and if $n = 0$, it becomes purely a two-dimensional case. The case when $m_o = n\pi/W$ ($n = 1, 2, \ldots$), i.e., the case of resonance, is left out in the present study. Here we considered only the case of $m_o \neq n\pi/W$.

IV. Results and Discussions

After the potential $\phi^{(i)}$, defined in the Mathematical Formulation section, has been computed, the hydrodynamic coefficients can be computed by

$$\bar{\mu}_{ij} + \frac{1}{\omega}\bar{\lambda}_{ij} = \varrho\iint_{S_o} \phi^{(i)} n_j\,ds \tag{22}$$

where $\bar{\mu}_{ij}$ are the added masses for $i, j = 1, 2, 3$, moments of added mass for i (or j) $= 1, 2, 3$ and j (or i) $= 4, 5, 6$, and moments of inertia of added mass for $i, j = 4, 5, 6$, and where $\bar{\lambda}_{ij}$ ($i, j = 1, \ldots, 6$) are the damping coefficients. In presenting our results, the nondimensional hydrodynamic coefficients, μ_{ij} and λ_{ij} are defined by using the ship displacement V and the ship length L as follows:

$$\mu_{ij} = \bar{\mu}_{ij}/\varrho V, \qquad \lambda_{ij} = \bar{\lambda}_{ij}/\varrho\omega V \qquad i, j = 1, 2, 3$$

$$\mu_{ij} = \bar{\mu}_{ij}/\varrho VL, \qquad \lambda_{ij} = \bar{\lambda}_{ij}/\varrho\omega VL \quad \text{or} \quad \begin{matrix} i = 1, 2, 3, j = 4, 5, 6 \\ i = 4, 5, 6, j = 1, 2, 3 \end{matrix} \tag{23}$$

$$\mu_{ij} = \bar{\mu}_{ij}/\varrho VL^2, \qquad \lambda_{ij} = \bar{\lambda}_{ij}/\varrho\omega VL^2 \qquad i, j = 4, 5, 6$$

where $V = L\,B\,T$ is the ship displacement volume. The results of wave excitation forces and moments are also similarly nondimensionalized by using the unit amplitude

of the incoming wave, Y = 1, and the ship length L as

$$\left.\begin{aligned} F_i &= \bar{F}_i/\varrho g Y L^2 \\ M_i &= \bar{M}_i/\varrho g Y L^3 \end{aligned}\right\} \quad i = 1, 2, 3 \qquad (24)$$

where

$$\bar{F}_i = -i\omega\rho \iint_{S_o} (\phi^{(7)} + \phi_I)\, n_i\, ds$$

$$\bar{M}_i = -i\omega\rho \iint_{S_o} (\phi^{(7)} + \phi_I)\, n_{i+3}\, ds \qquad (25)$$

In the present computations, a rectangular barge which floats parallel to the tank walls, i e., the angle between the center plane of the barge and the xy-plane is zero, is treated for its simplicity in data preparation. However, any arbitrary angle and ship geometry can be handled by the present computer program. The midship section plane is assumed to coincide with the yz-plane for the present test model. The cross-section of the canal at the origin, i e., the yz-plane is given in Figure 2. We denote the distance between the ship center-plane and the xy-plane by s, as shown in Figure 2. The moment is computed with respect to the centroid of the ship's water-plane area, i e., $\bar{x}_c = (0, 0, s)$ in Equation (6). In presenting our numerical results, the nondimensional wave number, $\nu B = \omega^2 B/g$ is plotted along the abscissa.

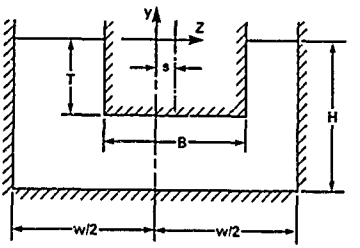


Figure 2 - Cross-Section at x=0

In the present computations, two locations of the body in a canal are computed; first, the ship is located at the center of the canal, i.e., s/B = 0, and second, the ship is at an off-center location in a canal. In both cases, the ship is parallel to the canal walls, as mentioned earlier. Specifically, the computations are made for W/B = H/T = W/H = B/T = 2 and L/T = 10 for both values of s/B = 0 and 0 125. Before we compute these two cases, we have done computations for a two-dimensional rectangular cylinder which is uniform between two walls, i e., the cylinder lies normal to the xy plane. These test results were compared with those computed by the results of our previous work in two-dimensional problems. The comparison was good.

Several sets of finite element subdivisions were initially tested in the present study. The total number of nodes tested are 180, 350, 507, 1404, and 1782 (the corresponding numbers of nodes on the ship boundary are, 44, 81, 81, 249, and 249, respectively). The indices n in the eigenfunction (Equation (19)) were taken between 6 and 10, and while the indices p were taken between 6 and 10 for n = 0, the values of p were reduced as n increased. The present computations were made for the range of non-dimensional wave numbers, $2\pi/m_o L$ = 0 52 through 2.72. This range was selected partly due to the limitation of numerical accuracy without taking very small finite elements, while the first mode of canal resonance, i.e., when $m_o W/\pi = 1$ (see the text following Equation (21)), is included. This first mode of the canal resonance, $m_o W/\pi = 1$, corresponds to $\nu B = 1.44066$ in the present ship-canal geometry.

Considering the wave number range to be tested and the computation time, we decided to use the 507-node model throughout the present computations. In subdividing the localized finite-element domain into a number of finite elements, we used four equal elements along the depth and four equal elements across the width of the canal. Five equal elements were used along both sides of the x-axis and five more elements were used further along both sides of the x-axis. The ship replaces the middle ten elements along the x-axis and the middle two elements along the z-axis and the two elements along the depth from the free surface. When the ship is at an off-center location in a canal, we simply stretch the elements on one side and shrink those on the other side mainly for the ease of data preparation, especially for the case when the off-center distance is not too great. Any complicated situation can be accommodated by the present method but only through more tedius data preparation.

For all cases treated here, the computations were made for 23 values of νB between 0 2 and 2 4 with a constant increment of 0.1 throughout the present computations. Then the 23 computed values of the hydrodynamic coefficients were plotted by a computer using a straight-line interpolation.

The computational results for the case when the ship is located at the center of a canal are presented in Figures 3 through 6 Figure 7 shows the hydrodynamic coefficients computed for the midship section, i e , the yz-plane as a purely two dimensional problem with no wave radiation present. The result for a two-dimensional model provides the resonance mode which plays a significant role in the local flow field in three-dimensional problem.

In Figure 3, the computed values of added mass and moment of inertia of added mass are shown. The surge added-mass coefficient, μ_{11}, shows an oscillatory behavior, being approximately zero at $\nu B = 0.9$ and reaching a local maximum at $\nu B = 1.4$. The heave added-mass coefficient μ_{22} is negative approximately between $\nu B = 0.20$ and 1.20. Both sway added-mass coefficients μ_{33} and roll moment of inertia of added mass μ_{44} change abruptly from positive peak values to negative peak values between $\nu B = 0.9$ and 1.0 A similar behavior is also observed in the yaw moment of inertia of added mass μ_{55} between $\nu B = 1.2$ and 1.3 The pitch moment of inertia of added mass μ_{66} is minimum around $\nu B = 1.3$.

In Figure 4, the six diagonal damping coefficients, λ_{ii} (i = 1, 6), are shown for s/B = 0 The value of λ_{11} decreases with increasing value of νB, and is approximately zero at νB = 1.2 and reaches a local maximum at 1 8. The values of λ_{22} decrease monotonically and also rapidly to zero at νB = 1. The values of λ_{33} and λ_{44} are zero between νB = 0 2 and 1.4, then sharply increase to local maxima at 2 0, and finally decrease. The value of λ_{55} shows a behavior similar to λ_{33} and λ_{44}, but becomes zero again at νB = 2 0 and increases again. The pitch damping coefficient λ_{66} decreases rather rapidly to zero between νB = 1.0 and 1.8. It is of interest to note that the values of λ_{33}, λ_{44}, and λ_{55} are zero for $\nu B \leq 1.4$. This is because the flow fields for the sway, roll, and yaw motions are purely due to local disturbances when $\nu B < \pi/2 \tanh \pi/2 = 1.4406$ (this value corresponds to the first mode over the canal resonance). (Note that the motions are asymmetric with respect to the xy-plane while the only admissible far field wave solution is pure two-dimensional)

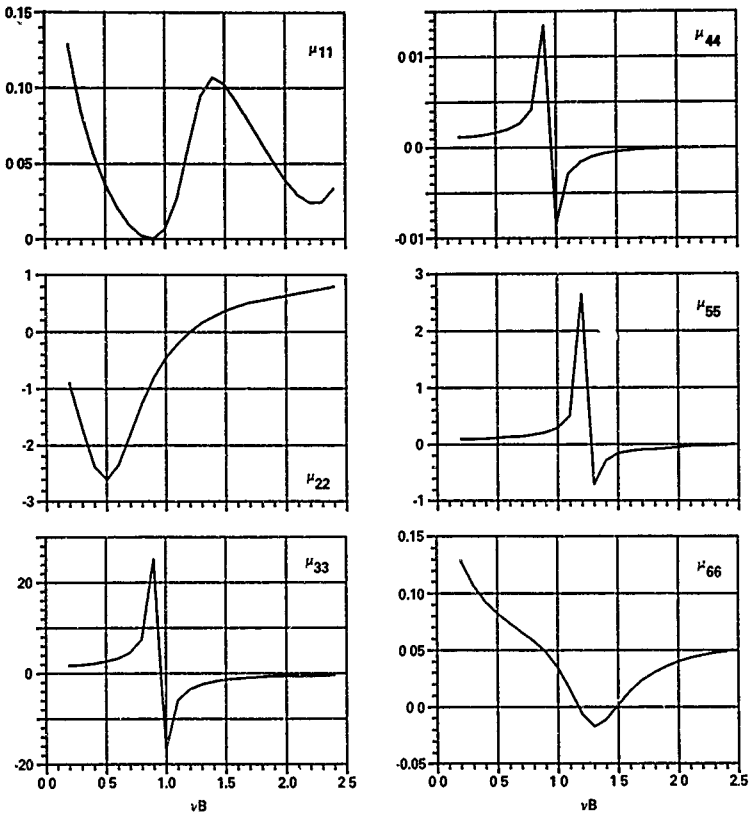


Figure 3 — Added Masses, and Moments of Inertia of Added Mass, μ_{ij} versus νB, for $s/B = 0$

Due to the symmetry of the body and the canal geometry with respect to the xy-plane and the yz plane, there are only four nonzero coupling hydrodynamic coefficients. These are shown in Figure 5. The pitch moment of surge added mass μ_{16} reaches a maximum at $\nu B = 1.1$ and then decreases. The roll-sway coupling term μ_{34} changes abruptly from a negative peak to a positive peak between $\nu B = 0.9$ and 1.0. The surge pitch coupling damping coefficient λ_{16} is a maximum at $\nu B = 1.4$ and slowly decreases to a positive constant. The sway-roll coupling damping coefficient λ_{34} is zero, as discussed earlier, between $\nu B = 0.2$ and 1.4, reaches a negative peak sharply, and then increases.

In Figure 6, the magnitudes of the wave excitation forces and moment are shown. The magnitude of the surge excitation force $|F_1|$ reaches a local minimum at $\nu B = 1.2$ and a local maximum at 1 6. The magnitude of the heave excitation force $|F_2|$ decreases monotonically from its value at $\nu B = 0$ 2 to zero at 1.2 and then reaches a local maximum at 1.8. it is of interest to note that the zero value of the heave excitation force would be at $\nu B = 1.0683$, which gives an incident wavelength equal to the ship length, if the Froude-Krylov approximation is made; this value is not too far from the computed result of $\nu B = 1.2$. The magnitude of the pitch excitation moment decreases from a local maximum of zero at $\nu B = 1.8$ and slowly increases to the next local maximum. The rest of the other excitation forces and moments, not shown here, are all zero, due to symmetry in the problem.

It should be noted in comparing the damping coefficients λ_{11}, λ_{22}, and λ_{66} in Figure 4, the excitation forces $|F_1|$ and $|F_2|$, and the moment $|M_3|$, in Figure 6, respectively. There exists a close similarity in the behavior of the

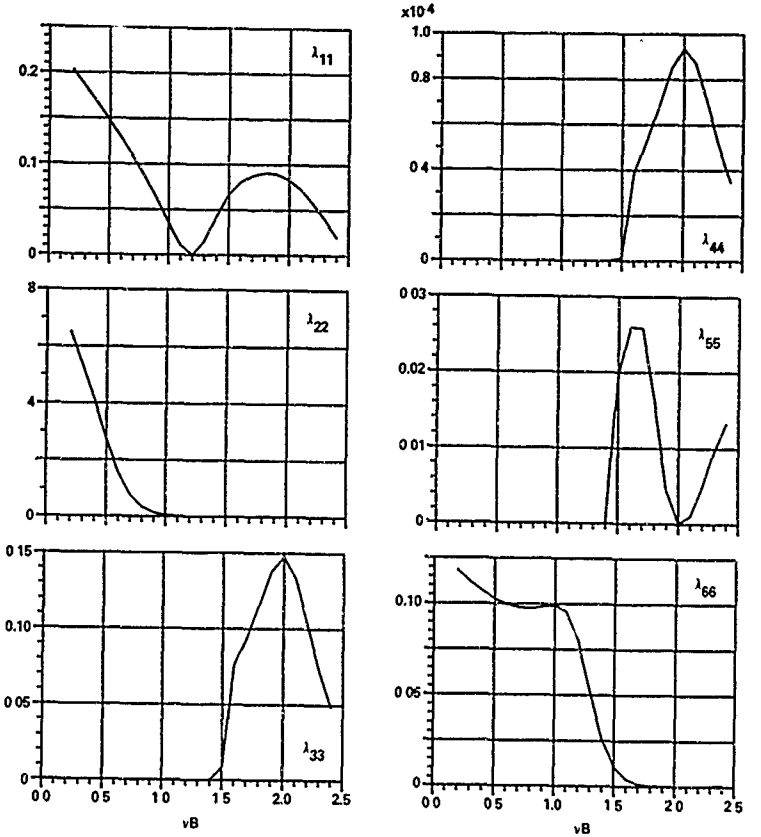


Figure 4 — Damping Coefficients, λ_{ij} versus vB, for $s/B = 0$

damping coefficients and that of wave excitations corresponding to each mode of motion in the range of the values $vB = 0.2$ through 1.44. This is not a coincidence because there exist, for $vB < 1.44$, only a purely two-dimensional radiating wave (see the text following Equation (21)). On the other hand, if the wavelength becomes short and if there exist many modes of the three-dimensional wave system, then this similarity may no longer hold.

In Figure 7, the hydrodynamic coefficients computed from a purely two-dimensional problem in the yz plane ($\tau = 0$) are presented as mentioned earlier. These computations are made because the added mass and moment of inertia of added-mass coefficients are mainly dependent upon the local flow field. Therefore, a two-dimensional result may be expected to provide some qualitative check because the ship is long compared with the length scale of the midship cross section in our problem at hand. In nondimensionalizing our two-dimensional hydrodynamic coefficients, we assume that the two-dimensional problem has a unit length so that the nondimensionalization of the hydrodynamic coefficients will be consistent with the definition given in Equations (23).

As expected, comparisons of μ_{33} and μ_{44} in Figure 3 and μ_{34} in Figure 5, with μ_{33}, μ_{44}, and μ_{34} in Figure 7, show remarkable similarities between them, except that the locations of the spikes in two- and three-dimensions are somewhat different. the spikes in the values of μ_{33}, μ_{44}, and μ_{34} occur at $vB = 0.784$ in two-dimensions and at vB

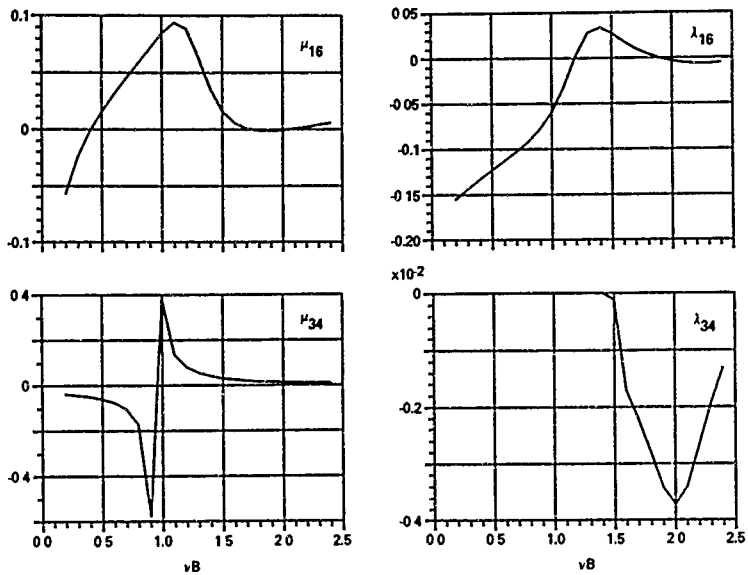


Figure 5 — Coupling Hydrodynamic Coefficients, μ_{ij} and λ_{ij} versus νB, for s/B = 0

= 0 9 through 1.0 in three-dimensions. Comparison of the heave added-mass coefficient μ_{22} in Figure 3 with that in Figure 7 also shows a similarity in their qualitative behavior when νB > 0 5. However, when νB < 0 5, the three-dimensionality effect seems to be more significant because the value of μ_{22} increases in three-dimensions, while it decreases more rapidly in two-dimensions, as νB decreases from 0 5 to 0 2.

A close examination of the local flow field at the mid ship cross-section corresponding to both positive and negative peaks, for example, in the sway added mass coef ficient μ_{33} in Figures 3 and 7, shows that the relative fluid motion under the ship is out of phase for the positive and in phase for the negative values of added mass. In order to have a close examination on the location of these spikes, in addition, we also treated an eigenvalue problem correspon ding to the foregoing two-dimensional boundary-value problem by a finite element method. When the finite element method is applied to the eigenvalue problem, the (original) eigenvalue problem defined in a partial differential equation reduces to a general matrix eigenvalue problem of a type $[A]\bar{X} = \lambda[C]\bar{X}$, where [A] and [C] are matrices and $\bar{X}$ is an eigenvector. In the present computations two sets of eigenvalue problems are solved. In the first set, [A] and [C] are identical to the matrices used in solving the boundary-value problem to obtain the results given in Figure 7. To obtain this set of matrices, 96 quadrilateral elements with a total of 345 nodes in the fluid and 18 nodes on the free surface are used. As a result, 18 eigen-values and eigenvectors are obtained in the first set In the second set, the submatrices are taken for [A] and [C] from the matrices constructed for our three-dimensional boundary value problem at hand by retaining the matrix elements corresponding to the nodes at the midship cross-sectional plane. In the second set, in which a coarse mesh subdivision (total of 25 nodes) is used, four eigenvalues and eigenvectors are obtained.

The lowest nonzero eigenvalue is νB = 0 78410 in the first set which has fine mesh subdivisions and νB = 0 82912 in the second coarse mesh subdivisions The higher modes of eigenvalues we computed are out of the range considered here However, the location of the spikes occurring in our three-dimensional results, for example μ_{33} in Figure 3, is between νB = 0.9 and 1.0 not at νB = 0.82912 If we had solved a three-dimensional eigenvalue problem corresponding to the three-dimensional boundary-value problem treated in the present paper, we could have obtained eigenvalues all of which have a nonzero imaginary part. However, the three-dimensional eigenvalue problem is not treated here. The eigenvalues of the two-dimensional problem treated here are a l real. From the comparisons among the two lowest eigenvalues, νB = 0 78410 and 0 82912, and the location of the spikes in the present three-dimensional numerical results (μ_{33}, μ_{44}, and μ_{34}, i e., νB is between 0 9 and 1.0), we can conclude that the difference in the locations of the spikes in μ_{33} in Figures 3 and 7 is caused partially by the inaccuracy in our three-dimensional computations (due to the use of not fine-enough mesh sub divisions) and partially by the nature of three-dimensionality.

It should be kept in mind that in the values of μ_{22} in Figure 7, if we had computed μ_{22} at νB = 0 7841, then we could have noticed a singular behavior like the spikes

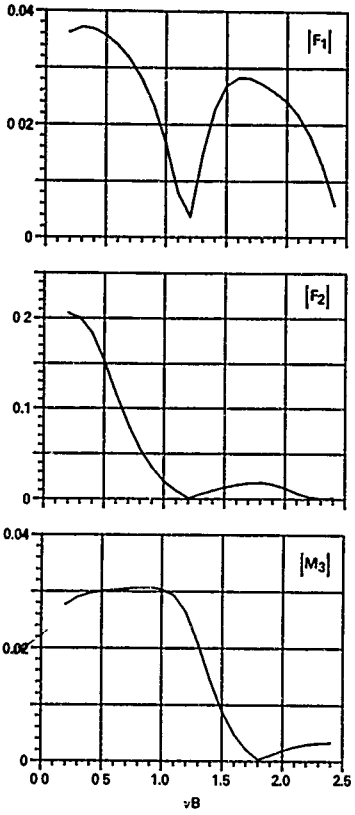


Figure 6 – Magnitudes of Excitation Forces and Moment versus νB

shown in the other curves, i.e., the resulting matrix equation for the eigenvalues being singular. It seems that the singular behavior of μ_{22} is much more localized than the other coefficients in Figure 7.

It is of interest to note that one can predict the lowest nonzero eigenvalue in the foregoing problem by a simple one-dimensional analysis as if treating a U-shaped pipe filled with water. This simple analysis gives the lowest eigenvalue, $\nu B = 2/3$, for the present case, which is not too bad. One can improve this value by introducing a few elementary potential functions, i.e., x, y, and $x^2 - y^2$, in a few finite elements, and performing simple integrations, as was done in Bai[6]. This improved approach gives the lowest eigenvalue, $\nu B = 0.75$. A more detailed finite element method applied to hydrodynamic eigenvalue problems will be reported in a separate paper in the near future.

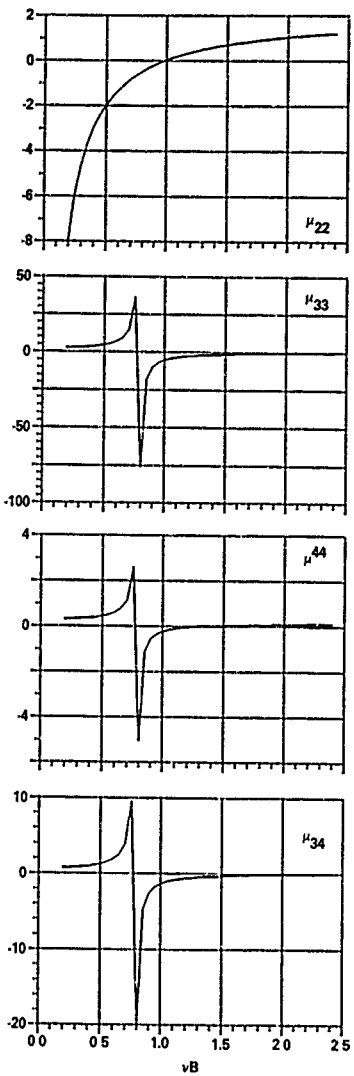


Figure 7 – Purely Two-Dimensional Added Masses and Moment of Added Mass versus νB (Due to the side walls, no wave radiation is present.)

We anticipated some singular behavior near νB = 1.44, which is the first mode of the canal resonance. So we made additional computations around this value (excluding this value as discussed earlier) by taking finer intervals in νB. Our computed results do not show any abnormality like spikes, contrary to our anticipation.

In Figures 8 through 10, the hydrodynamic coefficients, μ_{ij} and λ_{ij}, are shown for the case of an off-center location of a ship in a canal, s/B = 0.125. The excitation forces and moments for this case are shown in Figure 11. The general behavior of all results for an off-center case is similar to those previously shown, except that the appearance of more sudden spikes is observed. The values of μ_{11}, μ_{55}, and μ_{66} in Figure 8 show spikes at νB = 1.2 and 1.3. The values of μ_{22}, μ_{33}, and μ_{44} have spikes at νB = 0.9 and 1.0 in the same figure. Of interest is that the values of μ_{11}, μ_{22}, and μ_{66} in Figure 8 and μ_{15}, λ_{16}, and λ_{34} in Figure 10 show spikes which were not shown in the previous case (s/B = 0). This can be interpreted in the sense that the range of the influence of the local eigenvalues is larger in the case of s/B = 0.125 than in the case of s/B = 0.

Similar spikes are also observed in the damping coefficients in Figure 9. The damping coefficients λ_{33} and λ_{44} reach a maximum peak at νB = 1.0 and for λ_{55} at νB = 1.2. Some of the coupling hydrodynamic coefficients are shown in Figure 10. The magnitudes of wave excitation forces and moments are shown in Figure 11. The behavior of wave excitation forces and moments are very similar to the damping coefficients corresponding to motion which has already been discussed in the previous case of s/B = 0.

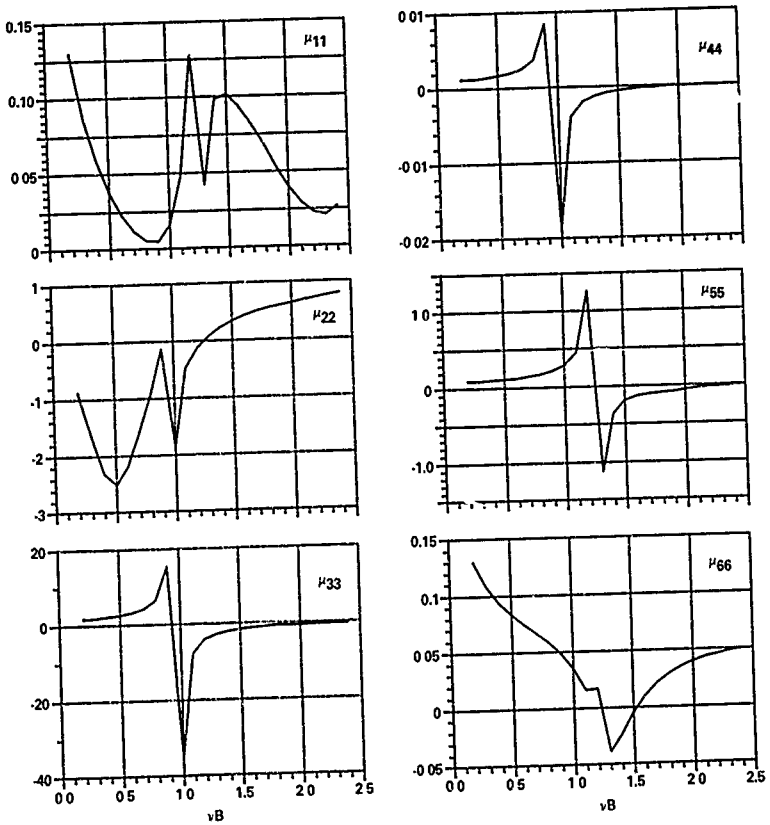


Figure 8 — Added Masses and Moments of Inertia of Added Mass, μ_{ij} versus νB, for s/B = 0.125 (Off-Center)

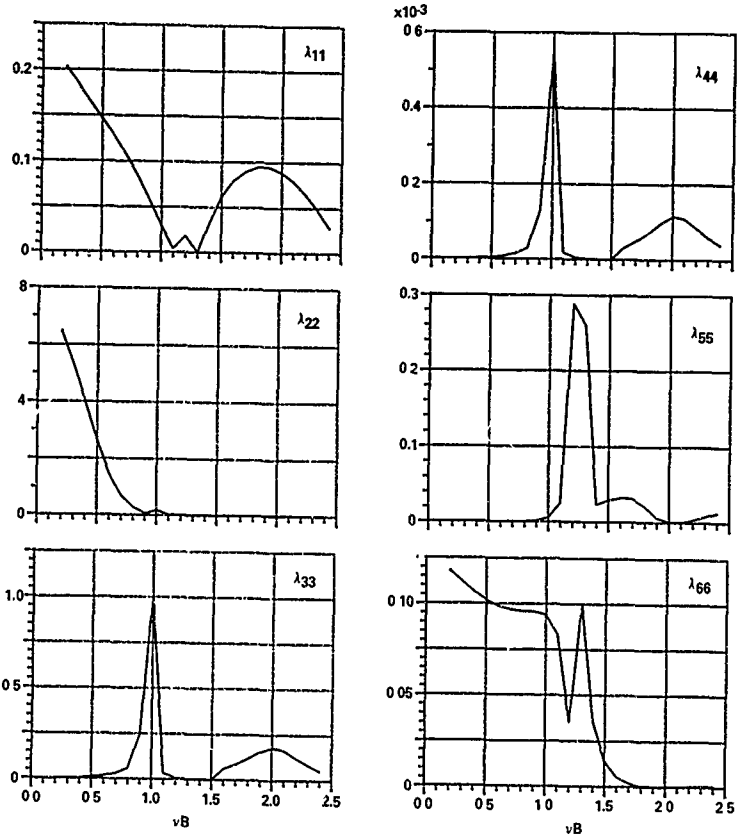


Figure 9 — Damping Coefficients, λ_{ij} versus νB, for s/B = 0.125

In Figure 12, the six hydrodynamic coefficients were computed by treating a purely two-dimensional restricted water problem (ship located at off-center) with no radiating wave present, as discussed earlier in connection with Figure 7. We computed two sets of eigenvalues as in the previous case: the smallest (nonzero) eigenvalue for this case is νB = 0.81140 computed with the fine mesh subdivisions, and is νB = 0.85796 computed with coarse mesh subdivisions which give submatrix corresponding nodes at the midship-section plane at x = 0 taken from the three-dimensional problem. When we compare these eigenvalues with those obtained earlier for s/B = 0, the smallest eigenvalue increases when a ship at the canal's center moves away from the center.

Most of the discussions given in the previous case of s/B = 0 hold for the present case of s/B = 0.125. From the results and discussions presented here, it seems necessary to make more refinements in future investigations. In the present investigation, we concentrated mainly on the application of the localized finite element method to solve a three-dimensional ship motion problem by taking a simple geometry with coarse mesh subdivisions. However, we tested two slightly different methods of solving the matrix equation. In the first method the final matrix which is complex banded and symmetric is solved by a Gaussian elimination. In the second method, we solve the real, banded symmetric submatrix equation first and then solve a rather small complex full-matrix equation. In the second

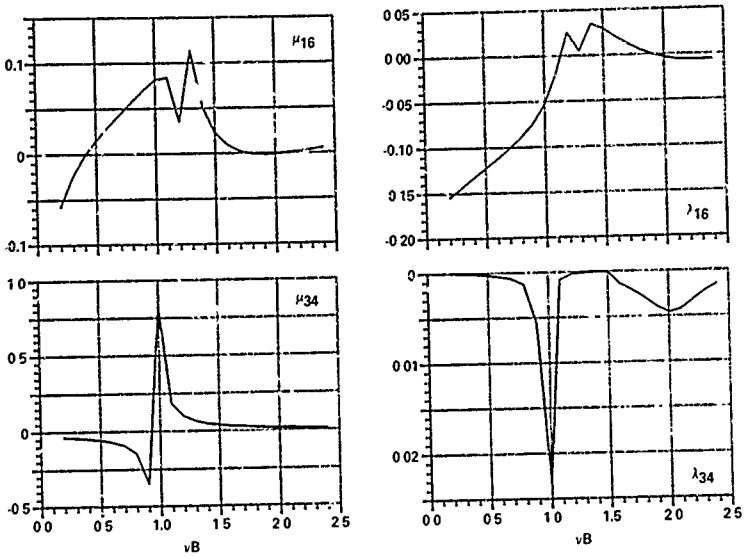


Figure 10 – Some of Coupling and Hydrodynamic Coefficients versus νB for s/B = 0.125

method, the main core memory space can be reduced by half roughly The Central Processor Unit Time in the CDC 6600 was approximately 40 seconds to compute six motions and one diffraction problem for one wave number by solving the complex matrix directly By the second method, approximately 20 percent of the total CPU time was saved In the present computer program, a considerable amount of time is used for the input-output operation due to out-of-core storage use

Acknowledgements

The author is grateful to Mr Fredd Thrasher for his help in obtaining computer plots in this paper The author is also grateful to Professor Daniel Euvrard, Drs A Jami, M Lenoir, and D Martin at ENSTA for many helpful discussions

References

1 Wehausen, J V and Laitone, E V , 1960, "Surface Waves," Handbuch der Physik, Vol IX, Springer Verlag, Berlin, pp 446-778

2 Bai, K J , and Yeung, R W , 1974, "Numerical Solutions to Free Surface Flow Problems," The Tenth Symposium on Naval Hydrodynamics, Office of Naval Research, held at MIT, Cambridge

3 Bai, K J , 1972, A Variational Method in Potential Flows with a Free Surface," Ph D dissertation, Dept of Naval Architecture, Univ of California, Berkeley

4 Bai, K J , 1975, "Diffraction of Oblique Waves by an Infinite Cylinder," J Fluid Mechanics, Vol 68, pp 513-535

5 Bai, K J , 1976, "The Added Mass and Damping Coefficients of and the Excitation Forces on Four Axisymmetric Ocean Platforms," David W Taylor Naval Ship R&D Center, Bethesda, SPD 670-01

6 Bai, K J , 1977, "The Added Mass of a Rectangular Cylinder in a Rectangular Canal," J Hydronautics, Vol 11, pp 29-32

7 Berkhoff, J C W , 1972, "Computation of Combined Refraction Diffraction," Proc 13th Coastal Engineering Conference, Vol 2, pp 471-490

8 Smith, D A , 1974, "Finite Element Analysis of the Forced Oscillation of Ship Hull Forms," M S Thesis, Naval Postgraduate School, Monterey

9 Chen, H S and Mei, C C , 1974, "Oscillations and Wave Forces in a Man-Made Harbor in the Open Sea," The Tenth Symposium on Naval Hydrodynamics, Office of Naval Research, held at MIT, Cambridge

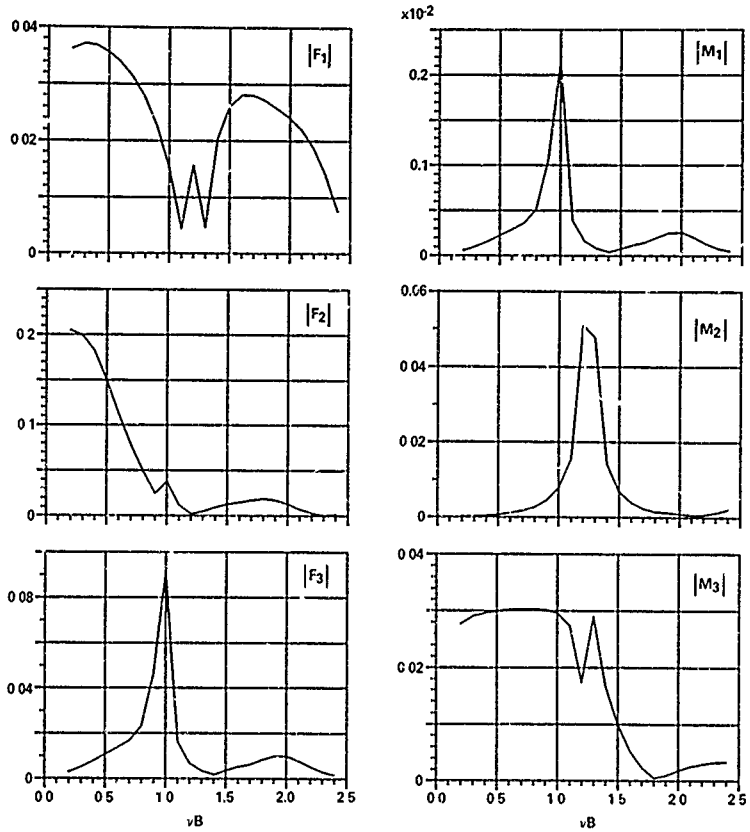


Figure 11 – Magnitudes of Wave Excitation Forces and Moments versus νB

10 Seto, H and Yamamoto, Y , 1975, "Finite Element Analysis of Surface Wave Problems by a Method of Superposition," The First International Conference on Numerical Ship Hydrodynamics, DTNSRDC, Bethesda, pp 49-70

11 Yue, D K P , Chen, H S , and Mei, C C , 1976, "Three-Dimensional Calculations of Wave Forces by a Hybrid Element Method," The Eleventh Symposium on Naval Hydrodynamics, Office of Naval Research, pp 325 332

12 Euvrard, D , Jami, A , Morice, C , and Ousset, Y , 1977, "Calcul Numerique des Oscillations d'un Navire Engendrees par la Houle," Part I & II, J Mecanique, Vol 16, No 2, pp 289 326, No 3, pp 327-394

13 Chowdbury, P C , 1972, "Fluid Finite Elements for Added Mass Calculations," Int Shipbuilding Progress, Vol 19, No 217, pp 302-309

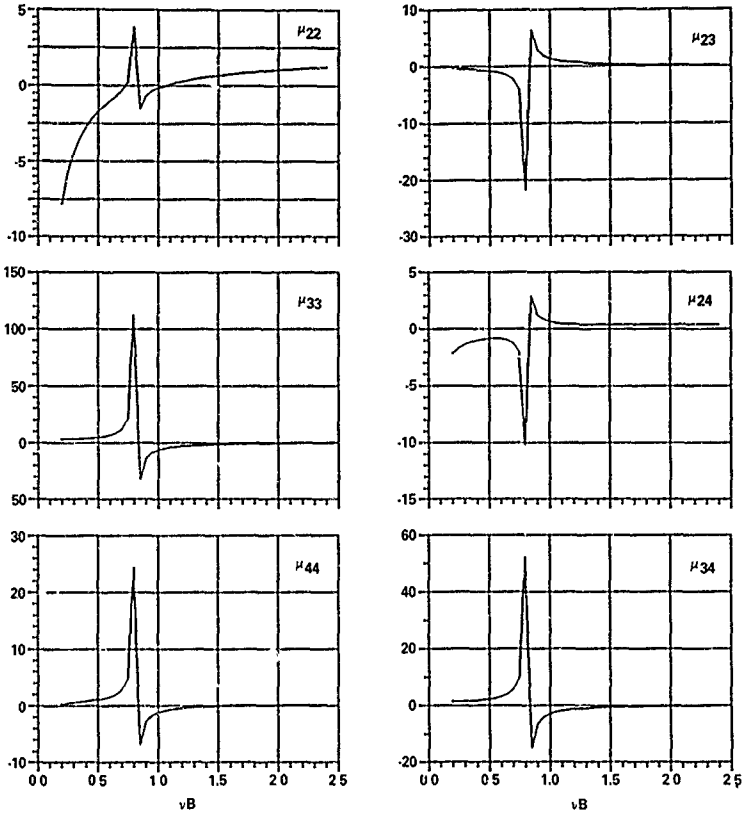


Figure 12 — Purely Two-Dimensional Added Masses and Moment of Added Mass versus νB for s/B = 0 125
(Due to the side walls, no wave radiation is present.)

DISCUSSION
of the paper
by K.J. Bai

A LOCALIZED FINITE-ELEMENT METHOD FOR THREE-DIMENSIONAL SHIP MOTION PROBLEMS

Discussion
by K. Eggers

It is with a certain nostalgy that I recall the decade of the 60th when maybe we had not so large computers, but much more liberal exchange of information.

I remember a certain DTMB Report 604 or so, where Motora reported on negative added mass for certain 2-D oscillatory motions, maybe in quite the same frequency interval as investigated by the author without any sidewise restriction. And, of course, under certain constellations we may achieve zero damping as well without existence of side walls (Motora or Nomoto, report of some manoeuvrability group session).

Author's reply

I would like to thank Professor K. Eggers for his interesting comments. I am well aware of the occurrence of negative added-mass and zero-damping coefficients for certain two-dimensional body geometries. However, the result shown in my paper is that the damping coefficients of sway and roll motions (i.e. λ_{33} and λ_{44} respectively) of any arbitrary three-dimensional ship geometry, symmetric with respect to the centerplane and located at the center of a tank, will be exactly zero when $\nu B < \pi/2 \tanh \pi/2 = 1.44$

COMPUTATION OF RELATIVE MOTION OF SHIPS TO WAVES

Choung M. Lee
David Taylor Naval Ship
R & D Center
Bethesda, Maryland, U.S.A.

Abstract

An analytical method is developed for predicting the vertical motion of a point on a ship relative to the motion of the free surface. The prediction method presented here takes into account the effect of the deformation of the incident waves on the relative motion. The causes of the deformation considered are the waves generated by diffraction and the waves generated by the motion of the ship. The method is based on the two-dimensional approximation of the flow around the cross sections of ships. The results reveal that the deformation of incident waves is so significant that it should be accounted for in the prediction of the relative motion of ships.

I. Introduction

The vertical motion of a point on a ship hull with respect to the undulating free surface is important information in the seakeeping investigation of ships. This motion is often called "Relative Motion." The relative motion has a direct effect on the inception of deck wetness, slamming of the ship bottom, and rudder and propeller emergence.

In general, the relative motion is computed under the assumption that the incident wave system is undisturbed. However, the incident waves can be significantly disturbed in the vicinity of a ship due to the diffraction by the ship surface and the waves generated by the motion of the ship. Hence, one can easily surmise that the cause of the poor correlation between the predicted and the measured [1,2,3] relative motion is the assumption of the undisturbed incident waves near a ship.

In this paper a method to account for the free-surface disturbance in the computation of relative motion is described. The method, as an initial attempt, is limited to a two-dimensional approximation within the context of strip theory. This approach is taken because firstly, the results can be readily incorporated into the existing computational schere of ship motion based on strip theory[4] and secondly, an evaluation of the two-dimensional approximation ought to be made before undertaking a more complex three-dimensional approach. The strip approach of obtaining the free-surface disturbances near a ship hull was encouraged by the success achieved by strip theory in the computation of the absolute motion of ships in waves.

The two-dimensional potentials are obtained by using the method of distribution of pulsating sources on the boundary of the cross section of the body. The source distribution is extended on the waterline inside the body to remove the irregular behaviors of the potentials at certain discrete frequencies. Various cross checkings of the numerical convergence are made to ensure the validity of the computed results.

The computed results of a pontoon having a uniform cross section identical to the midship of a mariner hull form are presented. The contribution from the various sources generating local waves near the pontoon are shown in the figures. The results indicate clearly that the free surface motion at the sides of a ship should be considered if a reliable prediction of the relative vertical motion is desired. The present study will be incorporated in a strip fashion into an existing ship-motion computer program, and the validity of the presently developed method will be investigated.

II. Analysis

The coordinate system to be used in the analysis is a right-handed Cartesian coordinate system which moves on the calm-water surface in the mean course of the ship with the ship speed. The origin is located directly above the center of gravity of the ship at its mean position, the x-axis is directed toward the bow; and the z-axis is directed vertically upward; see Figure 1.

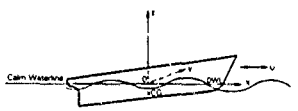


Figure 1 – Description of Coordinate System

We assume that the water is incompressible and its motion irrotational such that a velocity potential can be defined in the fluid region. We also assume that the water is infinitely deep and that no current exists.

If we denote the velocity potential which represents the disturbance of the fluid by $\Phi(x,y,z,t)$, then it can be decomposed in the following form for a ship moving with a constant velocity U in a regular plane wave system,

$$\Phi(x,y,z,t) = -Ux + \phi_s(x,y,z) + \mathrm{Re}[\phi_e(x,y,z)e^{j\omega_e t}] \quad (1)$$

Here, ω_e is the wave-encounter frequency, Re means the real part of what follows, ϕ_s is the steady potential, and ϕ_e is the oscillatory complex amplitude of the oscillatory potential which can be further decomposed into

$$\phi_e = \phi_I + \phi_D + \sum_{k=1}^{6} \phi_k \bar{\xi}_k \quad (2)$$

where ϕ_I is the incident-wave potential; ϕ_D the diffracted-wave potential; ϕ_k the forced-oscillation potential in the kth mode of motion; and $\bar{\xi}_k$ the complex amplitude of the displacement of the body due to oscillation in the kth mode. The incident-wave potential ϕ_I can be given explicitly by

$$\phi_I(x,y,z) = j\frac{g\zeta_A}{\omega} e^{-jk(x\cos\mu + y\sin\mu) + Kz} \quad (3)$$

where

- ω = wave frequency in radians per sec
- g = gravitational acceleration
- ζ_A = wave amplitude
- $K = \omega^2/g = 2\pi/\lambda$ = wave number for deep water
- λ = wave length
- μ = wave heading angle; $\mu = 0$ is following waves
- $j = \sqrt{-1}$

The free-surface elevation $\zeta(x,y,t)$ can be obtained from Bernoulli's equation in terms of the velocity potential by

$$\zeta(x,y,t) = -\frac{1}{g}\left(\frac{\partial}{\partial t} - U\frac{\partial}{\partial x}\right)\Phi(x,y,0,t) + O(\Phi^2)$$

$$= \frac{U}{g}\left[\phi_{sx}(x,y,0) + \phi_{ex}(x,y,0)e^{j\omega_e t}\right]^*$$

$$-j\frac{\omega_e}{g}\phi_e e^{j\omega_e t} = \zeta_s + \zeta_e e^{j\omega_e t} \quad (4)$$

where

$$\zeta_s(x,y) = \frac{U}{g}\phi_{sx}(x,y,0) \quad (4a)$$

$$\zeta_e(x,y) = \frac{1}{g}[U\phi_{ex}(x,y,0) - j\omega_e\phi_e] \quad (4b)$$

The vertical displacement of a point (x,y,z) on a ship, denoted by $\xi_v(\underline{x},t)$, is given by

$$\xi_v(\underline{x},t) = z + \xi_3(t) - x\xi_5(t) + y\xi_4(t) \quad (5)$$

where $\underline{x} = (x,y,z)$, and ξ_3, ξ_4 and ξ_5 are, respectively, the heave, roll and pitch displacement from the mean position of the body. The relative motion of a point with respect to the free surface motion at the same horizontal coordinates (x,y) is defined by

$$\xi_R(\underline{x},t) = \xi_v(\underline{x},t) - \zeta(x,y,t) \quad (6)$$

The vertical position of the point on the hull from the calm water surface at zero speed is not, of course, necessarily the same as that at a non-zero forward speed due to the sinkage and trim of the ship. In a strict sense, an inclusion of the sinkage and trim effect in the determination of the relative motion means that the second-order effects contributed by the terms such as $O(\phi_s\phi_e)$, $O(\phi_s^2)$, and $O(\phi_e^2)$ should also be included in the analysis. However, an investigation of the second-order effects will not be pursued in the present study. The analysis will be kept within the first order of the incident wave amplitude and of the slenderness parameter of the body.

Determination of Steady Free Surface

The free-surface deformation caused by a steady translation of a ship in calm water at constant speed U is obtained from the linearized Bernoulli's equation as

$$\zeta_s(x,y) = \frac{U}{g}\phi_{sx}(x,y,0) \quad (7)$$

The boundary-value problem for ϕ_s is as follows*

$$\phi_{sxx}(x,y,0) + \frac{g}{U^2}\phi_s = 0 \quad (8)$$

$$\phi_{sn}\Big|_{S_s} = \frac{\partial x}{\partial n}\Big|_{S_s} \quad (9)$$

where S_s denotes the hull surface below the calm-water surface, and $\underline{n} = (n_1,n_2,n_3)$ is the unit normal vector on S_s pointing into the body;

$$\phi_{sz}(x,y,-\infty) = 0 \quad (10)$$

and

$$\lim_{r\to\infty}\phi_s = \begin{cases} O(r^{-1/2}) & \text{for } x > 0 \\ o(1) & \text{for } x < 0 \end{cases} \quad (11)$$

where $r = \sqrt{x^2 + y^2}$

*When the spatial variables x, y, z and n (normal) are used as a subscript, it means a partial derivative with the respective variable. Also, when a complex function is multiplied by $e^{j\omega_e t}$, only the real part of the product should be realized.

To obtain the solution of the foregoing boundary-value problem, the thin-ship assumption will be used. If we represent the hull geometry by

$$y = \pm f(x,z), \tag{12}$$

then the unit normal vector on the ship hull surface pointing into the body can be determined by

$$\underline{n} = \frac{(f_x, \mp 1, f_z)}{\sqrt{1+f_x^2+f_z^2}}, \quad \text{on } y = \pm f \tag{13}$$

Substitution of Equation (13) into Equation (9) yields

$$f_x\phi_{sx}(x,\pm f,z) \mp \phi_{sy} + f_z\phi_{sz} = Uf_x \tag{14}$$

We assume that the ship in consideration is thin such that $f = O(\varepsilon)$ where ε is a small parameter representing the beam to length ratio of the ship. Then, from Equation (14), discarding the terms of $O(\varepsilon^2)$, we find that

$$\phi_{sy}(x,\pm 0,z) = \mp Uf_x \tag{15}$$

The solution of ϕ_s is well known from thin-ship theory (see, e.g., Wehausen and Laitone[5]) and is given by

$$\phi_s(x,y,z) = \frac{U}{2\pi}\iint_{S^{(\theta)}} \frac{f_\xi(\xi,\zeta)}{\sqrt{(x-\xi)^2+y^2+(z-\zeta)^2}}\, d\xi d\zeta$$

$$- \frac{U}{2\pi}\iint_{S^{(\theta)}} \hat{G}_\theta(x-\xi,y,z+\zeta) f_\xi(\xi,\zeta)\, d\xi d\zeta \tag{16}$$

where $S^{(\theta)}$ denotes the longitudinal center-plane of the ship, and

$$\hat{G}_\theta(x-\xi,y,z+\zeta) = \frac{1}{\sqrt{(x-\xi)^2+y^2+(z+\zeta)^2}}$$

$$+ \frac{4g}{\pi U^2}\int_0^{2\pi} d\theta \int_0^\infty ok\, e^{k(z+\zeta)}$$

$$\cdot \frac{\cos\{k(x-\xi)\cos\theta\}\cos(ky\sin\theta)}{k\cos^2\theta - g/U^2}$$

$$+ \frac{4g}{U^2}\int_0^{2\pi} d\theta \sec^2\theta\, e^{\frac{g}{U^2}(z+\zeta)\sec^2\theta} \sin\left\{\frac{g}{U^2}(x-\xi)\sec\theta\right\}$$

$$\cdot \cos\left(\frac{g}{U^2}\, y\sin\theta\sec^2\theta\right) \tag{17}$$

where $\int$ means the principal-value integral.

Thus, from Equations (7) and (16), we get

$$\zeta_s(x,y) = \frac{U}{g}\,\phi_{sx}(x,y,0)$$

$$= -\frac{U^2}{2\pi g}\iint_{S^{(\theta)}} \frac{(x-\xi)f_\xi(\xi,\zeta)}{[(x-\xi)^2+y^2+\zeta^2]^{3/2}}\, d\xi d\zeta$$

$$- \frac{U^2}{2\pi g}\iint_{S^{(\theta)}} \hat{G}_{\theta x}(x-\xi,y,z)\, f_\xi\, d\xi d\zeta \tag{18}$$

If we substitute the expression for $\hat{G}_{\theta x}(x-\xi,y,\zeta)$ from Equation (17) into Equation (18), we get

$$\zeta_s(x,y) = \frac{2}{\pi^2}\iint_{S^{(\theta)}} f_\xi(\xi,\zeta)d\xi d\zeta \int_0^{2\pi} d\theta\sec\theta$$

$$\cdot \int_0^\infty \frac{\sin\{k(x-\xi)\cos\theta\}}{k - \frac{g}{U^2}\sec^2\theta} \cos(ky\sin\theta) k e^{k\zeta} dk$$

$$- \frac{2g}{\pi U^2}\iint_{S^{(\theta)}} f_\xi\, d\xi d\zeta \int_0^{2\pi} d\theta \sec^3\theta\, e^{\frac{g}{U^2}\zeta\sec^2\theta}$$

$$\cdot \cos\left\{\frac{g}{U^2}(x-\xi)\sec\theta\right\} \cos\left(\frac{g}{U^2}\, y\sin^2\theta\sec^2\theta\right) \tag{19}$$

Within the first-order approximation, the wave profile along the side of the hull can be obtained by

$$\zeta_s(x,0) = \mathrm{Re}\left[-\frac{2I}{\pi^2}\iint_{S^{(\theta)}} f_\xi d\xi d\zeta \int_0^{2\pi} d\theta\sec\theta\right.$$

$$\cdot \int_0^\infty dk\, \frac{k e^{kZ'}}{k - k_\theta\sec^2\theta} - \frac{2g}{\pi U^2}\iint_{S^{(\theta)}} f_\xi d\xi d\zeta$$

$$\left. \cdot \int_0^{2\pi} d\theta \sec^3\theta\, e^{k_\theta \sec^2\theta Z'}\right] \tag{20}$$

where $k_\theta = \frac{g}{U^2}$, $Z' = \zeta + I(x-\xi)\cos\theta$, and $I = \sqrt{-1}$, or

$$\zeta_s(x,0) = \mathrm{Re}\left[-\frac{2I}{\pi^2}\iint_{S^{(\theta)}} f_\xi d\xi d\zeta\right.$$

$$\cdot \left\{\int_0^{2\pi} d\theta\sec\theta \int_0^\infty e^{kZ'} dk\right.$$

$$\left.\left. + k_\theta \int_0^{2\pi} \sec^3\theta d\theta \int_0^\infty \frac{e^{kZ'}}{k - k_\theta\sec^2\theta}\, dk\right\}\right.$$

$$- \frac{2g}{\pi U^2} \iint_{S(\Phi)} f_\xi d\xi d\zeta \int_0^{2\pi} d\theta \sec^3\theta \, e^{k_\Phi \sec^2\theta Z'} \Bigg] \qquad (21)$$

which amounts to the wave profile along the longitudinal centerplane.

Determination of Unsteady Free Surface

The free-surface deformation caused by the incident waves, diffracted waves, and motion-generated waves is obtained from Equations (4b) and (2). The unknown functions are ϕ_D, ϕ_k and $\bar{\zeta}_k$. In the following sections we describe procedures for obtaining these unknown quantities.

Diffraction Potential. From the kinematic boundary condition on the hull surface, we obtain from Equation (3)

$$\phi_{Dn}\Big|_{S_\Phi} = -\phi_{In}\Big|_{S_\Phi}$$

$$= K(jn_1\cos\mu + jn_2\sin\mu - n_3)\phi_I\Big|_{S_\Phi} \qquad (22)$$

If we assume that the ship is slender such that $n_1 \ll n_2$, n_3, then, discarding n_1 in Equation (22), we obtain

$$\phi_{Dn}\Big|_{S_\Phi} = K(jn_2\sin\mu - n_3)\phi_I$$

$$= j\omega\zeta_A(jn_2\sin\mu - n_3)$$

$$\cdot e^{-jK(x_\Phi\cos\mu + y_\Phi\sin\mu) + Kz_\Phi} \qquad (23)$$

where (x_Φ, y_Φ, z_Φ) indicates a point on the hull surface S_Φ.

From Equation (23) we can infer that

$$\phi_D(x,y,z) \approx \phi(y,z;x)e^{-jKx\cos\mu} \qquad (24)$$

where x affects ϕ as a parameter rather than an independent variable. By applying the Laplacian operator to the right-hand side of Equation (24), we obtain

$$\phi_{yy} + \phi_{zz} - K^2\cos^2\mu\phi = 0 \qquad (25)$$

An appropriate linearized free-surface condition for the velocity potential $\phi(y,z;x)$ is

$$\left(j\omega_e - U\frac{\partial}{\partial x}\right)^2 \phi(y,0;x)e^{-jKx\cos\mu}$$

$$+ g\phi_z \, e^{-jKx\cos\mu} = 0 \qquad (26)$$

or using the relation $\omega_e = \omega - KU\cos\mu$, we have

$$\phi_z(y,0;x) - K\phi = 0 \qquad (27)$$

The kinematic body-boundary condition for ϕ is

$$\phi_N\Big|_{C_\Phi(x)} = j\omega\zeta_A(jN_2\sin\mu - N_3)$$

$$\cdot e^{-jKy_\Phi\sin\mu + Kz_\Phi} \qquad (28)$$

where $\underline{N} = (N_2, N_3)$ is the two-dimensional unit vector on $\ell_\Phi(x)$ which is the immersed contour of a cross section at x. The far field condition as $|y| \to \infty$ is given as*

$$\phi \sim \begin{cases} e^{jK|y|\sin\mu} & \text{for } \mu \neq \pi \\ |y| & \text{for } \mu = \pi \end{cases} \qquad (29)$$

In fact, we find that the boundary-value problem for ϕ is confined in the y-z plane; hence, if we find an appropriate Green's function, G, which satisfies Equations (25), (27) and (29), we can obtain the solution in the form of

$$\phi(y,z;x) = \int_{C_\Phi(x)} Q(l)G(l;y,z)dl \qquad (30)$$

where the unknown function Q should be found from the remaining boundary condition (28). The appropriate Green's function was given by Ursell,[6] and the solution for ϕ was obtained by Choo[7] and Troesch.[8]

The approximation of ϕ_D by Equation (24), where the variable x is suppressed as a parameter, has led to the free surface condition (27) and the far-field condition (29). As one can readily observe, the forward-speed effect is nonexistent in the foregoing problem. The foregoing simplification can be criticized for the lack of consistency in the perturbation scheme. However, the analysis will be pursued on this basis with the assumption that the forward speed has no significant effect on the wave diffraction. Furthermore, under the assumption that the wave lengths of interest are greater than the order of ship beam, the Helmholz equation given by (25) will be replaced by the Laplace Equation, i.e.,

$$\phi_{yy} + \phi_{zz} = 0 \qquad (31)$$

which is exact for $\mu = \pi/2$, i.e., beam waves. A further digression from the original problem will be made with a heuristic argument, based on the success of strip theory, that the near-field solution derived with the radiation condition

$$\lim_{y \to \pm\infty} (\phi_y \mp jK\phi) = 0 \qquad (32)$$

is acceptable.*

*Although the diffraction potential is not explicitly solved in the usual ship motion theory based on the strip assumption, a similar radiation condition is invoked in applying the Haskind relation in the two dimensional sense.

Thus, the modified boundary-value problem now is reduced to an almost identical problem of forced oscillation of two-dimensional cylinders in a free surface in the combined modes of heave and sway. It should be noted that the diffraction potential is a function of the wave frequency ω. This is a noticeable difference from the strip solution used in the ship motion computation[4] in which the diffraction potential is treated as a function of wave-encounter frequency ω_e. In Appendix I, the process of solving the diffraction potential satisfying the two-dimensional Laplace Equation (31) with the boundary conditions (27), (28) and (32) is described. The description is given in a general form for any prescribed function replacing the right-hand side of Equation (28).

Motion and Radiation Potential. The motion of the ship is obtained by solving two sets of linearized coupled equations of motion, which, according to the coordinate system given in Figure 1, for k,ℓ = 1, 3, 5 and k,ℓ = 2, 4, 6, are

$$\sum_{\ell} (M_{k\ell} + A_{k\ell})\ddot{\xi}_\ell + B_{k\ell}\dot{\xi}_\ell + C_{k\ell}\xi_\ell = F_k^{(e)} \quad (33)$$

Here,

$$M_{k\ell} = \begin{cases} M(\text{mass of ship}) & \text{for } k=\ell \le 3 \\ I_{kk}(\text{mass moment of inertia}) & \text{for } k=\ell \ge 4 \\ 0 & \text{for } k\neq\ell \text{ except for } M_{24} = M_{42} = -z_g M \text{ where } z_g \text{ is the vertical coordinate of the center of gravity;} \end{cases}$$

$A_{k\ell}$ is the added mass coefficient in the kth mode due to the motion in the ℓth mode; $B_{k\ell}$ the corresponding damping coefficient; $C_{k\ell}$ the restoring coefficient; and $F_k^{(e)}$ the wave excited force or moment.

The coefficients in the equations of motion are obtained by slender-body strip theory.[4] The expressions are given as follows:

$$A_{k\ell} = \mathrm{Re}_j \left[-\frac{\rho}{\omega_e^2} \int_L dx \int_{C(x)} (\phi'_{kN}(y,z,x) - 2UN_3\delta_{k5} + 2UN_2\delta_{k6})\phi'_\ell \, d\ell \right] \quad (34)$$

$$B_{k\ell} = \mathrm{Im}_j \left[-\frac{\rho}{\omega_e} \int_L dx \int_{C(x)} (\phi'_{kN} - 2UN_3\delta_{k5} + 2UN_2\delta_{k6})\phi'_\ell \, d\ell \right] \quad (35)$$

for k,ℓ = 1, 2, . . . , 6.

where Re_j and Im_j are the real and imaginary parts, respectively, of a complex function, the imaginary part of which is preceded by $j = \sqrt{-1}$; $\int_L dx$ is the integral over the length in the positive x direction and $\int_{C(x)} d\ell$ the integral over the submerged contour of the cross section located at x; ϕ'_k is the two-dimensional approximation of ϕ_k; and $\delta_{k\ell}$ is the Kronecker delta.

The restoring coefficients $C_{k\ell}$ are given by $C_{33} = \rho g A_w$, $C_{23} = -\rho g M_w$, $C_{32} = \rho g M_w$, $C_{35} = C_{53} = \rho g M_w$, $C_{24} = \rho g \forall (I_{xx}/\forall - \overline{OB})$, and $C_{55} = \rho g \forall (I_{yy}/\forall - \overline{OB})$ where $\forall$ is the displaced volume, A_w the waterplane area, M_w the moment of the waterplane area about the y-axis, I_{xx} and I_{yy}, respectively, the mass moment of inertia about the x- and y-axis, and $\overline{OB}$ the vertical distance from the center of buoyancy to the calm waterline. The wave excited forces are given by

$$F_k^{(e)} = \rho \int_L dx \int_{C(x)} \left[-j\omega N_k + \frac{\omega}{\omega_e} \left\{ \phi'_k(y,z;x) + \frac{U}{j\omega_e}\phi'_2\delta_{k4} - \frac{U}{j\omega_e}\phi'_3\delta_{k5} \right\} \frac{\partial}{\partial N} \right] \phi_I \, d\ell \quad (36)$$

for k = 1, 2, . . . , 6, where $N_4 = yN_3 - zN_2$, $N_5 = -xN_3$ and $N_6 = xN_2$.

From the foregoing equations it is obvious that if the motion potentials $\phi'_k(y,z,x)$ are known, we can solve the equations of motion and find the six-degrees of freedom motion ξ_k. The first three of ξ_k are the linear displacements from the mean position of the ship in the x, y, and z directions, respectively, and the remaining three are the angular displacements about the x, y, and z axes, respectively. In numerical order of k these are called surge, sway, heave, roll, pitch and yaw motion. Utilizing the derivation shown in Appendix I, we can show that

$$\phi_0(x,y,z) = \phi_I + \phi_D(y,z;x) + \sum_{k=1}^{6} \phi'_k(y,z,x)\xi_k$$

$$= \phi_I + \phi_D + \phi'_1\xi_1 + \phi'_2\xi_2 + \phi'_3\xi_3 + \phi'_4\xi_4 - \left(x + \frac{iU}{\omega_e}\right)\phi'_3\xi_5 + \left(x + \frac{iU}{\omega_e}\right)\phi'_2\xi_6 \quad (37)$$

Substitution of Equation (37) into Equation (4b) yields

$$\zeta_0(x,y) = -\frac{i\omega}{g}(\phi_I(x,y,0) + \phi_D) + \frac{2U}{g}(\phi'_2\xi_4 - \phi'_3\xi_5) - \frac{j\omega_e}{g}[\phi'_1\xi_1 + \phi'_2(\xi_2 + x\xi_6) + \phi'_3(\xi_3 - x\xi_5)] \quad (38)$$

III. Numerical Checks

For the purpose of illustrating computations, a pontoon having uniform cross sections of the midship of a Mariner Class ship is chosen. The length of the pontoon is arbitrarily taken as five times the beam. The cross section is close to a rectangle except for the rounded bilges. The immersed dimension of the cross section is 23.06 m beam and 9.07 m draft. The offsets used to describe the section are given in Table 1 and the section view is given in Figure 2.

Table 1 — Offsets of Right Half of Midship Section of Mariner Class Ship

Y (m)	Z (m)
0.	-9 068
4 353	-9 068
8.705	-9 068
10 390	-8 458
10 958	-7 849
11 480	-6 629
11 534	-4 191
11 53	0.

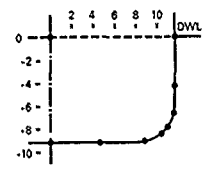


Figure 2 — Right Half Cross Section View of Midship of Mariner Class Ship

As described in Appendix I, the velocity potentials are obtained by using the method of source distribution on the immersed contour of the cross section of the body. As shown by Equation (I-7), an approximation is made by assuming a constant source strength on each line segment which makes up the contour. The line segments are made by connecting the adjacent two points on the contour by a straight line. The points chosen are as shown in Figure 2. It can be expected that numerical accuracy will increase as the number of points chosen on the contour increases; however, a compromise should be made to minimize computer costs. A total of eight boundary points are taken on the right half of the immersed contour of a cross section as shown by the black dots in Figure 2. The boundary points thus chosen provided the desired accuracy and yielded a satisfactory numerical convergence.

It is well known that the method of Green's function to solve for the velocity potential associated with an oscillating body in a free surface suffers from the existence of indefinite solutions at certain frequencies.[9] Descriptions of the existence of the indefinite solutions and their removal are given in Appendix II. To remove the indefinite solutions, the source distribution is extended on the line $z = 0$ inside the body, and a rigid wall condition, $\phi_z' = 0$, is imposed on that line, which will be referred to as "top deck" hereafter. According to Frank[10] the "irregular frequencies" for a rectangle of beam B and draft T are obtained by

$$K_m b = \omega_m^2 b/g = \frac{m\pi}{2} \coth(m\pi T/B), \quad m = 1, 2, 3, \ldots$$

where $b = \frac{B}{2}$. For the section considered here, $B/T = 2.54$, and therefore we get $K_1 b = 1.86$, and $K_2 b = 3.19$. In Figure 3, the singular behavior of the amplitude of the free surface motion due to beam regular waves at $y = 1.05b$ (the wave incident side) at the first irregular frequency is shown. The amplitude of the wave is normalized by the incident-wave amplitude, i.e., $|\zeta_0|/\zeta_A$ where ζ_0 is obtained by Equation (38). The solid line is obtained by taking two line segments on the top deck between $y = 0$ and $y = b$, and $y = 0$ and $y = -b$, and imposing the condition $\phi_z' = 0$. In Table 2, a comparison of the free-surface amplitudes is presented for various top-deck conditions. The values for the rigid-wall conditions imposed on up to six line segments on the top deck are given together with that obtained by imposing the $\phi' = 0$ condition on the two line segments on the top deck. Also shown are the values obtained by $\phi_z' = 4$ on the two line segments on the top deck at $Kb = 0.3$, 1.0 and 2.0. The latter values are shown to check Ohmatsu's statement[11] that any arbitrary values for ϕ_z' on the top deck, provided an appropriate symmetric or anti-symmetric condition is maintained, can be chosen to remove the irregular frequencies. It appears that the method holds in higher frequencies only in the present case. It looks obvious from Equation (II-6) that, unless $\phi_z' = 0$ or $\phi' = 0$ is imposed on the top deck, there is no guarantee that the trivial solution for ϕ' in the interior domain will be obtained. One would assume that more segments on the top deck should yield better results; however, the values obtained near $Kb = 1.0$ for 4 and 6 segments on the top deck show that the assumption is not necessarily true. Why more than two segments on the top deck show an irregular behavior in the vicinity of $Kb = 1.0$ is not yet clear. Based on this investigation, the two segments on the top deck, together with the other segments on the body contour, are chosen for the ensuing computations.

Table 2 — Free-Surface Amplitudes at y = 1.05b for Various Top-Deck Conditions

Kb	No Top	2 Seg	$\phi_z = 0$ 4	6	$\phi = 0$ 2 Seg.	$\phi_z = 4$ 2 Seg.
0 3	0 932	0 932	0 932	0 933	0 925	0 642
0 8	1 463	1 428	1.369	1.350	1 510	
0 9	1 528	1 470	1.381	1 366	1 508	
1 0	1.212	1 168	0 690	0.705	1 247	0 848
1.1	1.313	1 271	2 552	3 034	1.324	
1 2	1.945	1 877	2.367	2.427	1 838	
1 6	2.143	1 992	2 010	2 009	2 003	
1 65	2.156	1 985	1.989	1 986	1 996	
1 70	2 179	1 977	1 970	1 964	1 989	
1.75	2.228	1 970	1 953	1 944	1 982	
1 80	2.356	1 962	1 937	1 926	1 975	
1 85	3 386	1 955	1 922	1 909	1 968	
1 90	1 231	1 948	1 909	1 894	1 961	
1 95	1 734	1 941	1 897	1 880	1 954	
2 0	1 843	1 935	1 887	1 868	1.947	1 937
2 5	1 965	1 877	1 853	1 830	1 883	

Table 3 — Comparison of Wave Excited Forces Obtained by Eq (36) and Eq. (39)

	$\lvert F_2^{(e)}\rvert/A$		$\lvert F_3^{(e)}\rvert/A$		$\lvert F_4^{(e)}\rvert/A$	
Kb	(36)	(39)	(36)	(39)	(36)	(39)
0 1	0 1525	0 1536	0 8121	0 8175	0 0062	0 0062
0 5	0 5961	0 5989	0 5116	0 5161	0 0502	0 0500
0 9	0 5718	0 5761	0 3429	0 3449	0 0670	0 0668
1 4	0 4696	0 4776	0 2177	0 2101	0 0690	0 0692
2 0	0 3780	0 3903	0 1069	0 1104	0 0642	0 0654

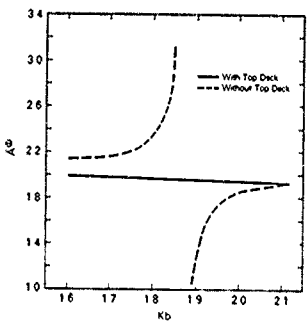


Figure 3 — Removal of Singular Behavior at Irregular Frequency

Several cross checks of the numerical results were made to ensure the accuracy of the computations. One was a correlation of the wave-excited forces computed by two independent methods; one by a direct computation using the expression given by Equation (36) and the other by an indirect method using the damping coefficients. The latter method is given by Newman[12] as

$$\left|F_k^{(e)}\right|/\zeta_A = (\rho g^2 B_{kk}/\omega)^{\frac{1}{2}} \qquad (39)$$

for two-dimensional bodies for $\mu = 90$ degrees. The comparison of the two independent results given in Table 3 shows a good agreement which gradually deteriorates up to about 3 percent difference at $Kb = 2$. In any case a 3 percent difference is well within the numerical errors resulting from the segmentation of the boundary contour of a cross section. The denominator A in Table 3 equals to $2\rho g b \zeta_A$ for $|F_2^{(e)}|$ and $|F_3^{(e)}|$ and $2\rho g b^2 \zeta_A$ for $|F_4^{(e)}|$.

The hydrodynamic coefficients resulting from the coupling between the sway and roll modes are A_{24}, A_{42}, B_{24}, and B_{42}. From Green's theorem we have

$$\iint_S (\phi_k \phi_{\ell n} - \phi_\ell \phi_{kn}) ds = 0 \qquad (40)$$

where S is the surface bounding the fluid domain which consists of the body surface S_ϕ, the free surface S_F, and a vertical cylinder surface S_R of a large radius R with a bottom closure S_B. Since $\phi_{kn} = \phi_{kz} = K\phi_k$ on S_F, $\phi_{kz} = 0$ on S_B, and $\phi_k = 0(1/\sqrt{R})$ on S_R, we can show that

$$\iint_{S_\phi} \phi_k \phi_{\ell n} ds = \iint_{S_\phi} \phi_\ell \phi_{kn} ds$$

which means that

$$A_{\ell k} = A_{k\ell} \quad \text{and} \quad B_{\ell k} = B_{k\ell}$$

from Equations (34) and (35). The values of these coefficients are shown in Table 4. Although the percent difference between the two values at the higher frequencies appears large, the error is within the bound which is associated with the number of segments chosen in the present case.

Table 4 — Comparison of Coupled Sway Roll ($\bar{A}_{24}$ and $\bar{B}_{24}$) and Roll Sway ($\bar{A}_{42}$ and $\bar{B}_{42}$) Coefficients

Kb	$\bar{A}_{24}$	$\bar{A}_{42}$	$\bar{B}_{24}$	$\bar{B}_{42}$
0 3	0 1272	0 1245	0 0334	0 0316
1 0	0 0603	0 0614	0 0965	0 0958
2 0	0 0059	0 0065	0 0667	0 0682

The expression for a pulsating source of unit strength below a free surface is given by Equation (I-5). The principal-value integral in this equation can be converted to an exponential integral in the form

$$\int_0^\infty \frac{e^{k(z+\zeta)}\cos k(y-\eta)}{\alpha - k} dk$$

$$= \mathrm{Re}\left\{-e^{-i\alpha S} E_1(-i\alpha S) \pm i\pi e^{-i\alpha S}\right\},$$

the plus sign for $y-\eta > 0$ and the minus sign for $y-\eta < 0$

where

$$S = (y-\eta) + i(z+\zeta)$$

$$E_1(S) = \int_S^\infty \frac{e^{-t}}{t} dt$$

$$= \gamma + \ln S + \sum_{n=1}^{\infty} \frac{(-1)^n S^n}{n\,n!}, \quad |\arg S| < \pi,$$

$\gamma = 0.57721566 \ldots$ = Euler's constant.

For the evaluation of $E_1(S)$, one can use the above equation; however, when $|S|$ is large, the infinite series makes the computation inefficient. Thus, one can use various rational and polynomial approximations for a large argument.[13] In this work the Laguerre quadrature method introduced by Todd[14] is used.

To obtain the free surface elevation $\zeta_\phi(x,y)$ the velocity potentials should be evaluated at $z = 0$, which in turn means that the Green's function given by Equation (I-5) should be evaluated at $z = 0$. Then, for the sources at the top deck, the principal-value integral becomes

$$\int_0^\infty \frac{\cos k(y-\eta) - i\sin k(y-\eta)}{\alpha - k} dk$$

$$= \cos\alpha X \, Ci(\alpha X) + \sin\alpha X \left[\frac{\pi}{2} + Si(\alpha X)\right]$$

$$- i\left[\sin\alpha X \, Ci(\alpha X) - \cos\alpha X \left\{\frac{\pi}{2} + Si(\alpha X)\right\}\right]$$

where $X = y-\eta$, and Si and Ci are the sine and cosine integrals, respectively, which are given by

$$Si(x) = \frac{\pi}{2} - \int_x^\infty \frac{\sin t}{t} dt = \sum_{n=0}^{\infty} \frac{(-1)^n x^{2n+1}}{(2n+1)(2n+1)!}$$

$$Ci(x) = -\int_x^\infty \frac{\cos t}{t} dt = \gamma + \ln x + \sum_{n=1}^{\infty} \frac{(-1)^n x^{2n}}{2n(2n)!}$$

Since these two functions approach zero in an oscillatory manner as $x \to \infty$, the series computation for large x is expected to require a large number of terms before converging to the desired accuracy (error less than 10^{-7}). The rational approximation of Hastings[15] (see, e.g., p. 233 of Reference 13) was employed to obtain the sine and cosine integrals, and the results were found to be identical to those of the Laguerre method of Todd.[14]

The amplitude of the radiating waves at $y = 100b$ generated by the sway and heave motion of unit amplitude are given in Table 5. The values given under the heading "Infinity" are obtained in terms of the damping, B_{ii}, by

$$\bar{A}^{(i)} = \frac{\omega}{g} (B_{ii}/\rho)^{\frac{1}{2}}, \quad i = 2, 3$$

which can be obtained from the principle of energy conservation and are exact at $y = \infty$. It appears that the radiating wave generated by sway motion yields better accuracy than that generated by heave motion.

Table 5 — Comparison of Radiating-Wave Amplitudes Due to Motion at y = 100b

Kb	$\bar{A}^{(2)}$		$\bar{A}^{(3)}$	
	Todd	∞	Todd	∞
0.3	0.269	0.267	0.363	0.361
1.0	1.111	1.100	0.613	0.625
2.0	1.599	1.570	0.350	0.430

IV. Results and Discussion

The sample computation is performed for the condition of zero speed, i.e., U = 0. Thus, there is no contribution from the steady translation to the free-surface elevation which is given by Equation (19).

To obtain the relative motion, the absolute vertical motion of the body should be known. In Figures 4 through 6, the motion amplitudes per unit incident-wave amplitude are shown versus the nondimensional frequencies $\omega^2 b/g = 2\pi b/\lambda$ for μ = 90, 135 and 180 degrees. Due to the symmetry of the body, there is no motion at $\mu = \pi$ (head waves) for sway and roll. To facilitate the understanding of the measure of the vertical displacement at the beam end which is contributed by roll, the roll amplitude is multiplied by the half beam b in Figure 6.

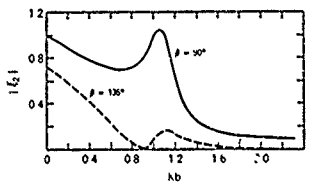


Figure 4 — Sway Amplitude at Zero Speed for Various Wave Headings

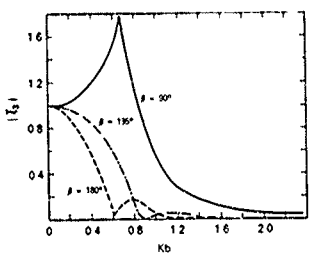


Figure 5 — Heave Amplitudes at Zero Speed for Various Wave Headings

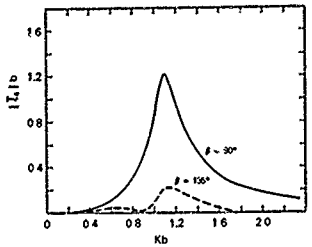


Figure 6 — Roll Amplitudes at Zero Speed for Various Wave Headings

Since the pontoon is symmetric fore and aft, the equations of motion given by Equation (33) (neglecting the surge motion and its coupling effects) can be reduced to the following form:

$$(M + A_{33})\ddot{\xi}_3 + B_{33}\dot{\xi}_3 + C_{33}\xi_3 = F_3^{(e)}$$

$$(M + A_{22})\ddot{\xi}_2 + B_{22}\dot{\xi}_2 + (A_{24} - Mz_0)\ddot{\xi}_4 + B_{24}\dot{\xi}_4 + C_{24}\xi_4 = F_2^{(e)} \qquad (41)$$

$$(A_{42} - Mz_0)\ddot{\xi}_2 + B_{42}\dot{\xi}_2 + (I_{44} + A_{44})\ddot{\xi}_4 + B_{44}\dot{\xi}_4 + C_{44}\xi_4 = F_4^{(e)}$$

The coefficients appearing in Equation (41) are obtained from Equations (34) and (35) In terms of the two-dimensional velocity potential $\phi'(y,z;x)$. The z-coordinate of the center of gravity, z_0, was approximated as that of the center of buoyancy. The radius of gyration for roll was assumed to be 0.6b such that $I_{yy} = M(0.6b)^2$.

It is well known that a prediction of roll motion based on linear damping obtained by a velocity potential at zero speed would yield an over-predicted peak roll at its resonant frequency. An iterative scheme to obtain a convergence of roll motion using the equivalent linear damping of the viscous damping could have been tried in order to suppress the peak roll; however, to avoid the ambiguity resulting from the approximation of the viscous damping, it was decided not to employ this scheme.

The strip method employed for the computation of motion does not take into account the end effects of the pontoon. Thus, the lengthwise integrals in evaluating the $A_{k\ell}$ and $B_{k\ell}$ become simple integrals such as

$$\int_{\ell} \alpha_{k\ell}\, dx = \alpha_{k\ell} L$$

or

$$\int_{\ell} \alpha_{k\ell} x^2\, dx = \alpha_{k\ell} L^3/12$$

where $\alpha_{k\ell}$ is the sectional quantity of $A_{k\ell}$ or $B_{k\ell}$. Similarly, for the wave excited forces $F_k(e)$, the contribution from the lengthwise integral becomes

$$\int_{-\frac{L}{2}}^{\frac{L}{2}} e^{jKx\cos\mu}\, dx = \frac{2 \sin\left(\frac{KL}{2}\cos\mu\right)}{K\cos\mu} \qquad (42a)$$

or

$$\int_{-\frac{L}{2}}^{\frac{L}{2}} x e^{jKx\cos\mu}\, dx = j\left[\frac{2 \sin\left(\frac{KL}{2}\cos\mu\right)}{K^2\cos^2\mu} - \frac{L\cos\left(\frac{KL}{2}\cos\mu\right)}{K\cos\mu}\right] \text{ for } \mu \neq \frac{\pi}{2} \qquad (42b)$$

$$= 0 \quad \text{for } \mu = \frac{\pi}{2}$$

For the arbitrary pontoon geometry chosen in the present sample calculation, the pitch and yaw motion for $\mu \neq \pi/2$ do not bear much significance because they are functions of the length of the body which is arbitrarily chosen in the present case. Thus, the results to be illustrated will be limited to beam waves, i.e., $\mu = \pi/2$, only. However, the motion amplitudes in Figures 4 to 6 for $\mu \neq \pi/2$ are presented to show that for a body which is symmetric fore and aft as well as port and starboard, beam waves could produce larger relative motion than the other wave headings. It is of interest to note in Figure 5 that the heave amplitude is less than the incident wave amplitude at all wave lengths for both $\mu = 135$ and 180 degrees. This fact seems to reflect the behavior of the function given by Equation (42b) which is the lengthwise contribution of the heave exciting force. One can readily see that the function $\sin x/x$ where $x = \cos\mu\, KL/2$ has the maximum value of unity at $x = 0$ and monotonically decreases as x increases. Thus, as either the absolute value of $\cos\mu$ or K increases, the wave excited heave force decreases. The sway motion contributes to the relative motion through its wavemaking which changes the free-surface elevation at the ship sides.

The local waves generated by the sway, heave, and roll motion are presented in Figure 7 as $\bar{A}_2$, $\bar{A}_3$, and $\bar{A}_4$, respectively, where the bar indicates that for heave and sway the amplitudes are divided by the respective motion amplitude, and for roll by $|\bar{\zeta}_4|b$. The beamwise location of these free-surface amplitudes is 1.05b from the origin. As can be observed in the figure the maximum local wave amplitudes occur at the same frequencies at which the respective motion amplitude becomes maximum. The trend of the curves shown in Figure 7 is found to be almost independent of the beamwise locations, although the magnitudes can change significantly. For the body chosen in the present case, the sway motion appears to be a better wavemaker than the heave motion per unit amplitude of the motion for higher frequencies, i.e., $Kb > 0.8$. However, when $\bar{A}_k$ is multiplied by the respective motion amplitude, one finds that the maximum local wave amplitude per unit incident-wave amplitude is produced by the heave motion.

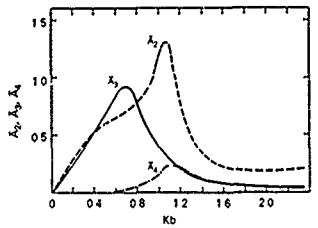


Figure 7 — Maximum Free-Surface Elevation at $y = \pm 1.05b$ Due to Motion in Sway ($\bar{A}_2$), Heave ($\bar{A}_3$) and Roll ($\bar{A}_4$)

Combination of these motion-generated waves will be a harmonically oscillating free surface. The amplitude of this free-surface oscillation at $y = \pm 1.05b$ is shown in Figure 8 as $\bar{A}_H$ which is a nondimensional quantity normalized by the incident wave amplitude. The free surface deformation due to the incident and diffracted waves should be added to the motion-generated free-surface disturbance to obtain the actual free-surface elevation at the sides of a ship. The diffracted waves are the reflected and the transmitted waves. At the incident side of the body, the free surface deformation is caused by the combination of the incident and reflected waves. The amplitude of the combined waves of incidence and reflection at the incident side at $y = 1.05b$ is indicated by $\bar{A}_H(I)$ in Figure 8. The transmitted wave amplitude at the lee side at $y = -1.05b$ is indicated by $\bar{A}_H(L)$. The bar sign indicates a nondimensionalization by the incident wave amplitude. As one can observe from Figure 8, the free surface oscillates near the body at the incident side with twice the amplitude of the incident wave for $Kb > 0.6$, i.e., the incident wave length less than about 10b. On the other hand, at the lee side the free surface fluctuates with less than about 40 percent of the incident wave amplitudes for $Kb > 0.6$.

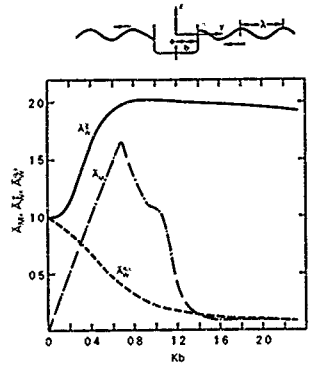


Figure 8 — Maximum Free-Surface Elevation at $y = \pm 1.05b$ Due to Motion ($\bar{A}_M$) and Diffraction ($\bar{A}_W^{(D)}$, $\bar{A}_W^{(I)}$) for Beam Waves

By the principle of the conservation of energy the following relation should hold

$$\left(\bar{A}_W^{(R)}\right)^2_{y=\infty} + \left(\bar{A}_W^{(T)}\right)^2_{y=+\infty} = 1$$

where $\bar{A}_W^{(R)}$ and $\bar{A}_W^{(T)}$ are, respectively, the amplitude ratios of the reflected and transmitted waves to the incident waves. A check was made at $|y| = 100b$ to confirm the foregoing relation. It was found that the relation holds true even at distances as short as 100b. However, when the distribution of the source is extended onto the waterline inside of the body, the square sum of the foregoing equation becomes slightly less than unity. This is construed as an indication that the added top deck may introduce a slightly greater numerical error than the case without the top deck. It is uncertain if $\bar{A}_W^{(I)}$ can be greater than 2 even at values of y as small as 1.05b. Although no firm proof is established, it appears that the values of $\bar{A}_W^{(I)}$ exceeding 2 are due to numerical errors resulting from the segment approximation.

The amplitudes of the free surface motion generated by the body motion and the incident and diffracted waves are shown in Figure 9 at the incident and the lee sides of the body. The prominent hump and hollow trend of the amplitude curves indicates the sensitivity of the free surface movement with respect to the incident wave frequency. The drastic change from the behavior of individual wave amplitudes shown in Figure 8 implies that the phase differences between the motion-generated waves and the diffracted waves can vary from 0 degree to ±180 degrees.

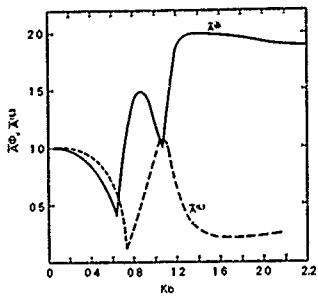


Figure 9 — Maximum Free-Surface Elevation at $y = \pm 1.05b$ Due to the Combined Effects of Motion and Diffraction for Beam Waves

To show the behavior of the amplitudes of the waves as a function of y, the motion-generated wave and the reflected wave at Kb = 0.8 are chosen and are presented in Figure 10. The values shown are those normalized by ζ_A. The solid curve is for the motion-generated wave, and the dotted one is for the reflected wave. A larger scale for y/b is taken near the hull to examine the behavior more closely. For Kb = 0.8 the wave length (λ) is 7.85b. One can observe at about $y = 12b \approx 1.5\lambda$ that the outgoing-wave amplitudes become identical to the far-field values. The local waves appear to be confined within one-beam distance from the hull. Generally, this trend is confirmed at other frequencies. However, when all the waves are superposed with their proper phases, the amplitude behavior becomes much more radical as shown by the chained curve in Figure 10. The sharpness of the curve is indicative of a possibility of breaking waves somewhere between y = 1.5b and 4.0b.

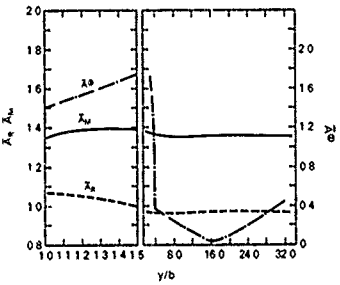


Figure 10 — Amplitude of Waves by Motion ($\bar{A}_M$) and Reflection ($\bar{A}_R$) at Kb = 0.8

The amplitudes of the absolute ($|\bar{\zeta}_V|$) and the relative ($|\bar{\zeta}_R|$) motion divided by the incident wave amplitude are shown in Figure 11 for y = 1.05b and in Figure 12 for y = -1.05b. The relative motion computed on the basis of no deformation of the incident wave is designated as "Old Rel." and the present calculation based on the deformation of the incident waves is designated as "New Rel.". A large difference between the old and new relative motion can be observed in Figure 11 at higher frequencies. The difference is almost a factor of two. This phenomenon is due to the fact that at higher frequencies the absolute vertical motion of the body diminishes while the reflection effect almost doubles the amplitude of the free surface motion on the side of the body. The old relative motion, however, assumes that there is no deformation of the incident wave; hence, the relative-motion amplitude becomes identical to the incident-wave amplitude. On the other hand, the new relative motion at the lee side diminishes at higher frequencies since both the absolute motion and transmitted wave amplitudes diminish, while the old relative motion amplitude becomes the same as the incident wave amplitude.

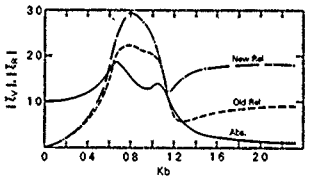


Figure 11 – Relative Motion and Absolute Motion at y = 1.05b for Beam Waves

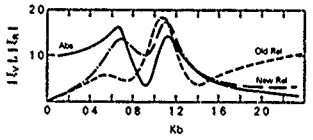


Figure 12 – Relative Motion and Absolute Motion at y = -1.05b for Beam Waves

V. Conclusion

From the present investigation it is found that neglecting the incident-wave deformation due to the body motion and diffraction could lead to a significant error in the prediction of the relative motion of ships. The computation should be extended to an actual ship at speed for various wave headings, and the results should be correlated with available model experimental results of relative motion.

VI. Acknowledgments

This study was sponsored by the Naval Sea Systems Command under the General Hydromechanics Program administered by the David Taylor Naval Ship R&D Center. Thanks are extended to Mr. V. J. Monacella and Dr. W. C. Lin for their kind support during the course of this work.

Appendix I

Determination of the Velocity Potentials $\phi_D^I(y,z)$ and $\phi_K^I(y,z)$

The boundary condition to be satisfied by the harmonic functions $\phi_D^I(y,z)$ and $\phi_K^I(y,z)$ are as follows:

$$\phi_z^I - \alpha\phi^I = 0 \quad \text{on } z = 0 \tag{I-1}$$

where $\alpha = \omega^2/g$ for ϕ_D^I and $\alpha = \omega_e^2/g$ for ϕ^I;

$$\phi_N^I\Big|_{C_0} = f \tag{I-2}$$

where C_0 is the contour below the calm water surface of a cross section of a ship and f, a complex function, is assumed to be known,

$$\lim_{y \to \pm\infty} (\phi_y^I \mp j\alpha\phi^I) = 0 \tag{I-3}$$

and

$$\phi_z^I = 0 \quad \text{as } z \to -\infty. \tag{I-4}$$

The Green's function $G(y,z;\eta,\zeta)$ which is in the form

$$G = \ell n\, r + H(y,z;\eta,\zeta)$$

where

$$r = [(y-\eta)^2 + (z-\zeta)^2]^{\frac{1}{2}}$$

and

$$\left(\frac{\partial^2}{\partial y^2} + \frac{\partial^2}{\partial z^2}\right) H = 0$$

in $z \leq 0$, is given in Wehausen and Laitone[5] as

$$G = \frac{1}{2\pi}\left[\ell n\, r - \ell n\, r' - 2\int_0^\infty \frac{e^{k(z+\zeta)}\cos k(y-\eta)}{k-\alpha}\, dk + j2\pi e^{\alpha(z+\zeta)}\cos\alpha(y-\eta)\right] \tag{I-5}$$

where $r' = [(y-\eta)^2 + (z+\zeta)^2]^{\frac{1}{2}}$. Using this Green's function, we can express ϕ^I by

$$\phi^I(y,z) = \int_{C_0} Q(l)G(l;y,z)\,dl \tag{I-6}$$

where Q is the unknown to be determined. Since G represents a pulsating source at a point below the calm water surface, Q can be regarded as an unknown source strength of complex value.

Following the procedure adopted by Frank,[10] we can show that

$$\phi'(y,z) \approx \sum_{i=1}^{N} Q_i \int_{C_i} G(1;y,z)\,dl \qquad (I\text{-}7)$$

where C_0 is divided into N even number of linear segments C_i, and Q_i is the constant source strength on the ith line segment C_i.

Let us assume that the prescribed function f can be divided into an even function, $f^{(e)}$, and an odd function, $f^{(o)}$, of y. The cross section in consideration here is assumed to be symmetric about the z-axis. Thus, we can also assume in general that ϕ' can be divided into an even part $\phi^{(e)}$ and an odd part $\phi^{(o)}$. Then, we can show that:

$$\phi^{(e)} \approx \sum_{i=1}^{M} Q_i^{(e)} \int_{C_i} G^{(e)}(1;y,z)\,dl \qquad (I\text{-}8)$$

$$\phi^{(o)} \approx \sum_{i=1}^{M} Q_i^{(o)} \int_{C_i} G^{(o)}\,dl \qquad (I\text{-}9)$$

where M = N/2 is the number of linear segments on the right-half of C_0, and

$$\left.\begin{matrix} G^{(e)} \\ G^{(o)} \end{matrix}\right\} = \frac{1}{2\pi}\left[\ln r \pm \ln r_1 - \ln r' \mp \ln r_1' \mp 2\int_0^{\infty} \frac{e^{k(z+\zeta)}\cos k(y\mp\eta)}{k-\alpha}\,dk \pm j2\pi e^{\alpha(z+\zeta)}\cos\alpha(y\mp\eta)\right] \qquad (I\text{-}10)$$

where the upper and lower signs correspond respectively to $G^{(e)}$ and $G^{(o)}$, and

$$r_1 = [(y+\eta)^2 + (z-\zeta)^2]^{\frac{1}{2}},$$

$$r_1' = [(y+\eta)^2 + (z+\zeta)^2]^{\frac{1}{2}}.$$

Now, if we take the normal derivative of $\phi^{(e)}$ and $\phi^{(o)}$ at the midpoints of C_i and designate them by $\phi_{iN}^{(e)}$ and $\phi_{iN}^{(o)}$, then due to the property of the surface distribution of source[10], we have

$$\phi_{iN}^{(e)} \equiv f_i^{(e)} = \frac{Q_i^{(e)}}{2} + \sum_{\substack{k=1 \\ k\neq i}}^{M} Q_k \int_{C_k} G_N^{(e)}(1;y_i,z_i)\,dl$$

$$\phi_{iN}^{(o)} \equiv f_i^{(o)} = \frac{Q_i^{(o)}}{2} + \sum_{\substack{k=1 \\ k\neq i}}^{M} Q_k \int_{C_k} G_N^{(o)}(1;y_i,z_i)\,dl \qquad (I\text{-}11)$$

These two equations can be expressed in algebraic form as

$$A^{(e)}Q^{(e)} = B^{(e)}$$

$$A^{(o)}Q^{(o)} = B^{(o)}$$

where $A^{(e)}$ and $A^{(o)}$ are M by M matrices, the elements of which are given by

$$A_{ik}^{(d)} = \int_{C_k} G_N^{(d)}(1;y_i,z_i)\,dl \text{ for (d) = (e) or (o)}$$

$Q^{(e)}$ and $Q^{(o)}$ are the column vectors, the elements of which are given by $Q_k^{(e)}$ and $Q_k^{(o)}$, respectively (however, if k=1, only half of the values should be taken), and $B^{(e)}$ and $B^{(o)}$ are the column vectors, the elements of which are given by $f_i^{(e)}$ and $f_i^{(o)}$, respectively.

Then, we can obtain the unknowns $Q^{(e)}$ and $Q^{(o)}$ by

$$Q^{(d)} = \left[A^{(d)}\right]^{-1} B^{(d)} \text{ for (d) = (e) or (o)}$$

and substitution of these into Equations (I-8) and (I-9) yields $\phi^{(e)}$ and $\phi^{(o)}$.

For the diffraction potential ϕ_D', we have

$$f \equiv f^{(e)} + f^{(o)} = -\frac{\partial}{\partial N}\left(\frac{jg\zeta_A}{\omega} e^{Kz - jKy\sin\mu}\right)\Bigg|_{C_0}$$

hence,

$$f^{(e)} = j\omega\zeta_A e^{Kz}[N_2 \sin\mu \sin(Ky\sin\mu) - N_3\cos(Ky\sin\mu)]$$

$$f^{(o)} = -\omega\zeta_A e^{Kz}[N_2 \sin\mu \cos(Ky\sin\mu) + N_3\sin(Ky\sin\mu)]$$

where (y,z) is a point on C_0 and N_2 and N_3 are respectively the y- and z-component of the unit vector on C_0 pointing into the body. For a symmetric body N_2 is an odd function of y and N_3 is an even function.

For the motion potential ϕ_k^i, we have the following boundary condition on C_0:

k	$f^{(e)}$	$f^{(o)}$
2	0	$j\omega_e N_2$
3	$j\omega_e N_3$	0
4	0	$j\omega_e N_4$

where $N_4 = yN_3 - zN_2$.

Appendix II

Irregular Frequencies

It is well known that the Green's function method[9] for the velocity potential function associated with an oscillating body in a free surface suffers from the existence of indefinite solutions at certain discrete frequencies. These frequencies are often referred to as "irregular frequencies." John[9] showed that they are equivalent to the eigenvalues of the boundary-value problem for the velocity potential defined in the internal fluid domain bounded by the body surface and the interior line $z = 0$. That is, if the velocity potential $\tilde{\phi}$ defined inside the body has nontrivial solutions for the boundary condition

$$\tilde{\phi}_z - \lambda\tilde{\phi} = 0 \quad \text{on } C_f (z = 0, -b < y < b)$$
$$\tilde{\phi} = 0 \quad \text{on } C_0 \tag{II-1}$$

for discrete values of λ, then $\omega_i = \sqrt{g\lambda_i}$ is the ith irregular frequency for $i = 1, 2, \ldots$

If the velocity potential ϕ defined in the fluid region R outside the body is expressed by

$$\phi(p) = \int_{C_0} Q(1)G(1;p)d1, \tag{II-2}$$

then

$$f(p_0) \equiv \phi_N(p)\Big|_{p\to p_0} = \pi Q(p_0) + \int_{C_0} Q(1)G_N(1;p_0)d1 \tag{II-3}$$

where $f(p_0)$ is prescribed. The Fredholm theorem states that Q has a unique solution if the associated homogeneous equation, i.e., $f = 0$ in Equation (II-3), has a trival solution only. From John's uniqueness proof[9] we know that if $\phi_N|_{C_0} = 0$, ϕ identically vanishes in R and on C_0. Since ϕ given by Equation (II-2) is continuous everywhere in $z \le 0$, it can be extended to the interior domain R'. If we let $\tilde{\phi}(p') = \int_{C_0} Q(1)G(1;P'\epsilon R')d1$, $\tilde{\phi}$ should have trivial solutions for the boundary condition (II-1) if ϕ is unique. But, the fact that for some λ_i, $\tilde{\phi}$ has nontrivial solutions implies that $\tilde{\phi}_N|_{C_0} \neq 0$; hence, $Q(1) = \tilde{\phi}_N(1) \neq 0$ on C_0 if $\lambda = \lambda_i$. The identity $Q(1) = \tilde{\phi}_N(1)$ can be easily proved. From Green's theorem we can show for any point p' in the interior domain R' bounded by C_0 and C_f that

$$\tilde{\phi}(p') = \int_{C_0} [\tilde{\phi}_N G(p') - \tilde{\phi} G_N]d1,$$
$$0 = \int_{C_0} [\phi_N G(p') - \phi G_N]d1, \tag{II-4}$$

hence, subtracting the two equations above, we get

$$\tilde{\phi}(p') = \int_{C_0} [(\tilde{\phi}_N - \phi_N)G(p') - (\tilde{\phi} - \phi)G_N]d1$$
$$= \int_{C_0} \tilde{\phi}_N G(p')d1 \tag{II-5}$$

since $\phi = \tilde{\phi} = \phi_N = 0$ on C_0, and from Equations (II-4) and (II-5) we find that $\tilde{\phi}_N(1) = Q(1)$. Since Q(1) cannot be identically zero on C_0, the associated homogeneous equation of (II-3) can have nontrivial solutions at $\lambda = \lambda_i$.

Frank[10] has shown that the added mass and damping coefficients of cylindrical bodies have discontinuities at certain discrete frequencies. Several investigators have shown either in published[11,17,18] or unpublished forms various methods for alleviating the irregular frequencies. The removal of the irregular frequencies is achieved in this work by imposing $\phi_z^i = 0$ or $\phi^i = 0$ on the interior waterline C_f. This imposed boundary condition on C_f then makes $\tilde{\phi} \equiv 0$ in R' since

$$\iint_{R'} |\nabla\tilde{\phi}|^2 \, ds = \int_{C_0+C_f} \tilde{\phi}\,\tilde{\phi}_N \, d1 = 0 \tag{II-6}$$

for $\tilde{\phi}|_{C_0} = 0$ and $\tilde{\phi}_N|_{C_f} = 0$ and, therefore, $|\nabla\tilde{\phi}| = 0$ in R' implies that $\tilde{\phi} \equiv 0$.

With this approach we can begin with a new definition of ϕ^i by

$$\phi^i(p) = \int_{C_0+C_f} Q(1)G(1;p)d1$$

and solve for Q from the Fredholm equation

$$f(p_0) = \phi_N^i(p_0) = \pi Q(p_0) + \int_{C_0+C_f} Q(1)G_N(1;p_0)d1$$

with

$$\phi_N'\Big|_{C_f} = \phi_z'\Big|_{C_f} = 0.$$

References

1. Gerzina, D.M. and E.L. Woo, "CVA 68 Relative Motion Investigation," DTNSRDC Report SPD-656-01, Dec. 1975.

2. Bales, N.K., et al., "Validity of a Strip Theory-Linear Superposition Approach to Predicting Probability of Deck Wetness for a Fishing Vessel," DTNSRDC Report SPD-643-01, Nov. 1975.

3. Cox, G.G. and D.M. Gerzina, "A Comparison of Predicted Experimental Seakeeping Characteristics for Ships with and without Large Bow Bulbs," DTNSRDC Report SPD-591-01, Nov. 1974.

4. Salvesen, N., et al., "Ship Motion and Sea Loads," SNAME Trans., Vol. 78, 1970.

5. Wehausen, J. and E.V. Laitone, "Surface Waves," Encyclopedia of Physics, Vol. 9, Springer-Verlag, 1960.

6. Ursell, F., "The Expansion of Water-Wave Potentials at Great Distances," Proc. Camb. Phil. Soc., Vol. 64, pp. 811-826, 1968.

7. Choo, K.Y., "Exciting Forces and Pressure Distribution on a Ship in Oblique Waves," Ph.D. Thesis at MIT, Ocean Eng. Dept., 1975.

8. Troesch, A.W., "The Diffraction Potential for a Slender Ship Moving Through Oblique Waves," Univ. of Mich., NAME Dept., Report No. 176, Feb. 1976.

9. John, F., "On the Motion of Floating Bodies: II. Simple Harmonic Motions," Commun. Pure Appl. Math., Vol. 13, pp. 45-101, 1950.

10. Frank, W., "Oscillation of Cylinders in or below the Free Surface of Deep Fluids," NSRDC Report 2375, 1967.

11. Ohmatsu, S., "On the Irregular Frequencies in the Theory of Oscillating Bodies in a Free Surface," Papers of Ship Res. Inst. (Japan) No. 48, 1975.

12. Newman, J.N., "The Exciting Forces on Fixed Bodies in Waves," J. Ship Res., Vol. 6, No. 3, 1962.

13. Abramowitz, M. and I.A. Stegun (Ed.), "Handbook of Mathematical Functions," National Bureau of Standards, Appl. Math. Ser. 55, 1964.

14. Todd, J., "Evaluation of the Exponential Integral for Large Complex Arguments," J. Research NBS 52, RP. 2508, pp. 313-317, 1954.

15. Hastings, C. Jr., "Approximations for Digital Computers," Princeton Univ. Press, Princeton, N.J., 1955.

16. Kellog, O.D., "Foundation of Potential Theory," Dover Publications, Inc., New York, 1953 (see p. 164).

17. Pien, P.C. and C.M. Lee, "Motion and Resistance of a Low-Waterplane Catamaran," The Ninth Symposium on Naval Hydrodynamics, Vol. 1, U.S. Government Printing Office, 1972.

18. Ogilvie, T.F. and Y.S. Shin, "Integral-Equation Solution for Time-Dependent Free-Surface Problems," J. of Soc. of Naval Arch. of Japan, Vol. 143, pp. 41-51, 1978.

THE INTERACTION OF AN INCIDENT WAVE FIELD WITH A FLOATING SLENDER BODY AT ZERO SPEED

P.D. Sclavounos
Department of Ocean Engineering
Massachusetts Institute of Technology
Cambridge, Massachusetts

Abstract

A linear slender-body theory is presented for the zero-speed motions of a ship in regular free-surface waves, valid for an arbitrary angle of incidence and all wavelengths of practical interest. The velocity potential of the "radiation" problem is obtained by the superposition of a particular solution, identical to that of the short-wavelength strip theory, and a homogeneous component that accounts for the longitudinal flow interactions. A similar representation is used for the "diffraction" problem where the particular solution is equal and opposite to the incident wave velocity potential.

Computations are presented for the vertical hydrodynamic force distribution and the heave and pitch added-mass and damping coefficients, exciting forces and motions for a Series 60 hull. Comparisons are made with strip theory, a three-dimensional theory and experiments.

1. Introduction

In the past twenty years slender-body theory techniques have found broad applications in ship hydrodynamics. The geometrical slenderness of the ship hull, however, is insufficient to justify an asymptotic theory. The length-scales introduced by the wavelength and/or the ship forward speed need also to be considered.

The wavelengths encountered in an ambient seaway are comparable to both the transverse and the longitudinal dimensions of conventional ships. It is therefore desirable that a theory for the motions of a ship advancing in waves would embrace all wavelengths encountered in practice. Newman (1978) developed the theoretical framework of such a slender-body theory where the ship slenderness is sufficient for the asymptotic analysis involved. The theory, hereafter referred to as "unified theory", was applied to the radiation problem by Newman and Sclavounos (1980) and was extended to the diffraction problem by Sclavounos (1981).

In the present paper the radiation and diffraction problems are combined to predict the zero-speed heave and pitch motions of a ship in waves. The theoretical derivation is presented in Section 2 including the radiation problem as derived by Newman (1978) for purposes of comparison with the diffraction problem. The short-wavelength approximations of the unified theory are derived in Section 3 where existing theories for the radiation and diffraction problems are recovered. An efficient numerical technique for the solution of two-dimensional free-surface problems is described in Section 4. A hybrid integral representation valid in a domain bounded by the body section, the free surface and a circular boundary lying in the fluid domain is matched to a multipole representation valid outside the matching circle. In Section 5 numerical computations are presented for the hydrodynamic force distribution and the motions for a Series 60 (C_B=0.7) hull and comparisons are made with existing theories and experimental data.

In what follows, a physical description of the method of solution is attempted. The ship is assumed to be slender, the fluid motion incompressible and irrotational and the ship motion amplitude small enough to validate the linear decomposition of the hydrodynamic disturbance in the radiation and the diffraction problems.

For the radiation problem, in an "inner" region close to the ship hull, the longitudinal flow gradients are small compared to the transverse ones. The field equation can therefore be reduced to the two-dimensional Laplace equation, supplemented by a two-dimensional body boundary condition and the zero-speed free-surface condition. For the diffraction problem the slenderness assumptions are invoked after the

longitudinal component of the incident wave is factored out. The two-dimensional modified Helmholtz equation turns out to be the relevant inner-field equation with a no flux body-boundary condition and the same free-surface condition as in the radiation problem.

In an "outer" region, located at radial distances greater or equal to the ship length, the flow gradients in all directions are of comparable magnitude. The three-dimensional Laplace equation is satisfied in the fluid domain for both problems, subject to the zero-speed free-surface condition and a condition of outgoing waves at infinity. The method of matched asymptotic expansions is used to enforce the compatibility of the inner and outer solutions in an intermediate "overlap" region.

The velocity potential of the inner radiation problem involves a particular solution identical to that of the short-wavelength strip theory and is supplemented by a homogeneous solution that represents standing waves at "infinity". The corresponding particular solution of the diffraction problem is equal and opposite to the incident wave potential with the longitudinal wave component factored out. The homogeneous part again satisfies standing waves at "infinity" and is regular for all headings.

The homogeneous solutions of both the radiation and the diffraction problems are multiplied by "interaction" coefficients, functions of the longitudinal coordinate, that are determined after the matching with the corresponding outer solutions. Two integral equations are solved, in that context, for the unknown three-dimensional source distributions along the ship axis that describe the outer solutions of both problems.

In the short-wavelength limit, the interaction coefficient of the radiation problem vanishes and the classical strip-theory solution is recovered (see Ogilvie and Tuck(1969)) At the same limit, the solutions of Choo (1975) and Troesh (1976) for the diffraction problem are recovered for oblique waves. The singularity that is present in these theories for head waves is due to a non-uniformity that is present when the short-wavelength approximation preceeds the transition from oblique to head incidence. For head waves the Maruo and Sasaki (1974) theory is recovered, apart from a minor analytical difference.

2. The Boundary Value Problem

We introduce a Cartesian coordinate system fixed in space with the free surface taken at z=0, the ship centerplane at y=0 and the positive axis pointing towards the bow. The ship is assumed to perform small oscillatory motions around its undisturbed floating position, all oscillatory quantities are expressed in complex form and the factor $e^{i\omega t}$ is understood hereafter. Only the symmetric heave and pitch motions are considered, since, to the same degree of accuracy, the longitudinal interactions are absent from the anti-symmetric modes for which strip theory is valid for all wavelengths. More details for the analysis that follows can be found in Newman (1978) and Sclavounos (1981).

For water of infinite depth the incident wave potential is given by

$$\varphi_I = \frac{igA}{\omega} \exp[\nu z - i\nu(x\cos\beta + y\sin\beta)], \quad (2.1)$$

where A is the wave amplitude, $\nu=\omega^2/g$ is the wavenumber and β the angle of incidence, with $\beta=180°$ for head incidence.

Let φ_j, j=3,5,7 be the complex velocity potentials associated with the unit amplitude heave and pitch motions and the symmetric diffraction problem respectively. Under the assumptions stated in the Introduction, the three-dimensional Laplace equation is satisfied in the fluid domain

$$\nabla^2\varphi_j = 0, \quad (2.2)$$

subject to the linear free-surface condition

$$\varphi_{jz} - \nu\varphi_j = 0 \qquad \text{on } z = 0, \quad (2.3)$$

and the body boundary condition applied at the mean position of the ship wetted surface $\bar{S}$

$$(\vec{n}\cdot\nabla)\varphi_j = \begin{cases} i\omega\, n_j \\ -(\vec{n}\cdot\nabla)\{\frac{ig}{\omega} e^{\nu z - i\nu x\cos\beta} \\ \qquad \cdot\cos(\nu y\sin\beta)\}, \; j=7 \end{cases} \quad \begin{matrix} \\ \\ , j=3,5 \end{matrix} , \quad (2.4)$$

where $\vec{n} = (n_1,n_2,n_3)$ is the unit normal vector pointing out of the fluid domain and $n_5 = -xn_3+zn_1$. The well-posedness of the previous boundary-value problems requires that the velocity potentials φ_j represent outgoing waves in the far field with the fluid velocity vanishing as $z\to-\infty$.

In the next two subsections the ship slenderness is invoked to approximate the flow equations in the outer and inner regions respectively.

2A. Outer Region

At radial distances comparable to or greater than the ship length, the flow is insensitive to the ship hull geometry details and the velocity potential can be approximated by a line distribution of three-dimensional sources along the ship centerline, given by

$$\varphi_j = e^{i\nu_o x}\,\psi_j(x,y,z)$$

$$= \int_L e^{i\nu_o \xi}\, q_j(\xi)\, G(x-\xi,y,z)\,d\xi, \qquad (2.5)$$

where ν_o is the characteristic wavenumber of the longitudinal distribution of the hull normal velocity ($\nu_o=0$ for the heave and pitch motions and $\nu_o = -\nu\cos\beta$ for the diffraction problem); $q_j(x)$ is the slowly varying part of the source strength distribution and $G(x-\xi,y,z)$ is the velocity potential due to a unit pulsating source located on the ship axis at $x=\xi$. In order to match the outer solution (2.5) to the corresponding expression of the inner problem we need to expand (2.5) for small νr, where $r = (y^2+z^2)^{\frac{1}{2}}$. It is convenient to take the Fourier transform of both sides of (2.5) to obtain,

$$\psi_j^*(y,z;k) = q_j^*(k)\; G^*(y,z;k-\nu_o), \qquad (2.6)$$

where

$$G^*(y,z;k) = \int_{-\infty}^{\infty} e^{ikx}\, G(x,y,z)\,dx$$

$$= -\frac{1}{2\pi}\int_0^{\infty} \frac{e^{z(u^2+k^2)^{\frac{1}{2}}}\cos uy}{(u^2+k^2)^{\frac{1}{2}}-\nu}\,du. \qquad (2.7)$$

For small νr, $\nu_o r$ and kr, G^* can be approximated in the form

$$G^*(y,z;k-\nu_o) = Pf\{G^*(y,z;-\nu_o)\}$$

$$-\frac{1}{2\pi}(1+\nu z)F^*(k-\nu_o) \qquad (2.8)$$

with an error factor $1+0(\nu^2r^2,\nu_o^2r^2,k^2r^2)$ and

$$F^*(k) = \ell n(|\nu_o|/|k|)+(1-\nu_o^2/\nu^2)^{-\frac{1}{2}}$$

$$\cdot\cosh^{-1}(|\nu/\nu_o|) - |1-k^2/\nu^2|^{-\frac{1}{2}}$$

$$\cdot\begin{bmatrix}\pi i+\cosh^{-1}(\nu/|k|)\\ -\pi+\cos^{-1}(\nu/|k|)\end{bmatrix}, \qquad (2.9)$$

where the upper or lower term in brackets is applicable according as $\nu/|k|\gtrless 1$ and $|\nu_o|\leq\nu$ for all cases of interest.

Expression (2.8) is a generalization of the corresponding approximation derived by Newman (1978, eq. 4.12) for the radiation problem. As $\nu_o\to 0$, the combination of the first two terms in (2.9) reduces to $\ell n(2\nu/|k|)$. Furthermore, $G^*(y,z;0) = R_{2D}(y,z)$ is the two-dimensional source potential that satisfies the Laplace equation, subject to the linear free-surface condition and a radiation condition of outgoing waves as $\nu|y|\to\infty$. Given that $\mathrm{Im}(R_{2D}) = \frac{1}{2}e^{\nu z}\cos(\nu y)$ and the fact that $e^{\nu z}\cos(\nu y) = (1+\nu z)[1+0(\nu^2r^2)]$ in the regime where (2.8) is valid, it follows that

$$G^*(y,z;k) = R_{2D}(y,z) - \frac{1}{2\pi}(1+\nu z)f^*(k), \qquad (2.10)$$

where

$$f^*(k) = \ell n(2\nu/|k|) + \pi i - |1-k^2/\nu^2|^{-\frac{1}{2}}\cdot\begin{bmatrix}\pi i+\cosh^{-1}(\nu/|k|)\\ -\pi+\cos^{-1}(\nu/|k|)\end{bmatrix}, \qquad (2.11)$$

which is identical to equation (4.12) of Newman (1978).

for the diffraction problem, $\nu_o = -\nu\cos\beta$, with $G^*(y,z;-\nu_o) = D_{2D}$ being the corresponding two-dimensional source potential that satisfies the Helmholtz equation $(\nabla_{2D}^2 - \nu_o^2)D_{2D} = 0$ and the same free-surface and radiation conditions as R_{2D}. It is essential to point out that $\mathrm{Im}(D_{2D}) = \frac{1}{2}\csc\beta e^{\nu z}\cos(\nu y\sin\beta)$ is singular for $|\cos\beta| = 1$ and, as opposed to the radiation problem, it is not present. Thus, the inner expansion of the outer solution for the diffraction problem is given by (2.6) and (2.8)-(2.9) and is regular for all headings.

In summary, the inner expansion of the outer solution transformed back in the physical x-space takes the form

$$\phi_j(x,y,z) = q_j(x)\begin{Bmatrix} R_{2D} \\ \mathrm{Re}(D_{2D}) \end{Bmatrix} - \frac{1}{2\pi}(1+\nu z)\,\mathcal{L}(q_j), \qquad (2.12)$$

where the linear operator $\mathcal{L}$ is obtained by taking the inverse Fourier transform of (2.6). It follows that

$$\mathcal{L}(q_j) = q_j(x)\left[\gamma + \begin{Bmatrix} \pi i \\ h(\beta) \end{Bmatrix}\right] + \int_L d\xi\, e^{-i\nu_o(x-\xi)}\left(\frac{1}{2}\mathrm{sgn}(x-\xi)\ln(2\nu|x-\xi|)\right. \cdot\left(\frac{d}{d\xi} + i\nu_o\right)q_j(\xi) - \frac{\pi\nu}{4}K[\nu(x-\xi)]q_j(\xi)\Big\}, \qquad (2.13)$$

where $\gamma = 0.57\ldots$ is the Euler constant,

$$h(\beta) = \csc\beta\cosh^{-1}(|\sec\beta|) - \ln(2|\sec\beta|) \qquad (2.14)$$

$$K(x) = Y_o(x) + 2i\,J_o(|x|) + H_o(|x|) \qquad (2.15)$$

with the upper or lower terms in brackets applying for the radiation (j=3,5 and $\nu_o=0$) and the diffraction (j=7 and $\nu_o = -\nu\cos\beta$) problems respectively.

2B. Inner Region

At transverse distances of the order of the ship beam, the relative order of the flow gradients in the longitudinal and transverse directions are dictated by the respective order of the geometry gradients. Assuming that both the y and z coordinates are of $O(\epsilon)$, a coordinate stretching suggests that

$$\frac{\partial}{\partial x} = O(1),\ \frac{\partial}{\partial y},\ \frac{\partial}{\partial z} = O(\epsilon^{-1}) \qquad (2.16)$$

when operating on ϕ_j defined in (2.5).

Applying (2.16) in (2.2)-(2.4) and using the definition of ϕ_j, we obtain the two-dimensional modified Helmholtz equation

$$\phi_{jyy} + \phi_{jzz} - \nu_o^2\phi_j = 0, \qquad (2.17)$$

subject to the free-surface condition

$$\phi_{jz} - \nu\phi_j = 0 \quad \text{on } z=0, \qquad (2.18)$$

and the body boundary condition

$$\frac{\partial}{\partial N}\phi_j = \begin{Bmatrix} i\omega N_j & , j=3,5 \\ -\frac{ig}{\omega}\frac{\partial}{\partial N}\{e^{\nu z}\cos(\nu y\sin\beta)\}, & j=7 \end{Bmatrix}, \qquad (2.19)$$

where to leading order in ϵ, $\vec{n} = (0, N_2, N_3)$, with $N_5 = -xN_3$.

The general solution of (2.17)-(2.19) can be obtained in the form

$$\phi_j = \phi_{jP} + C_j(x)\,\phi_{jH}, \qquad (2.20)$$

where ϕ_{jP} is a particular and ϕ_{jH} a homogeneous solution of (2.17)-(2.19) respectively. The "interaction" coefficient $C_j(x)$ is presently an arbitrary function of x that will be determined from the matching with the outer solution. No radiation condition needs to be satisfied in the inner region since the outer solution already represents outgoing waves at infinity.

Following Newman (1978), a particular solution of the radiation problem (j=3,5, $\nu_o=0$) is the short-wavelength strip theory potential ϕ_j that satisfies outgoing waves as $\nu|y|\to\infty$. The homogeneous solution can be physically regarded as the interaction of two incident symmetric waves with the ship section. The pure imaginary form of the body boundary condition suggests that $\phi_j + \bar{\phi}_j$ is a homogeneous solution, where the overbar stands for the complex conjugate of the quantity involved. Thus,

$$\varphi_j = \phi_j + C_j(x)(\phi_j + \bar{\phi}_j),\ j=3,5 \qquad (2.21)$$

with $\phi_6=-x\phi_3$. In the overlap region, at transverse distances large compared to the ship beam but still small compared to its length as $\epsilon\to 0$, ϕ_j can be expressed by their effective source strengths, in the form

$$\phi_j = \sigma_j R_{2D}(y,z), \tag{2.22}$$

where R_{2D} is the two-dimensional source potential that satisfies outgoing waves as $\nu|y|\to\infty$. We may thus approximate φ_j in the overlap region as follows,

$$\varphi_j = \{\sigma_j+C_j(x)(\sigma_j+\bar{\sigma}_j)\}R_{2D} - 2i\,C_j(x)\bar{\sigma}_j\,\mathrm{Im}(R_{2D}). \tag{2.23}$$

If we now set, $\mathrm{Im}(R_{2D})=\frac{1}{2}(1+\nu z)\{1+0(\nu^2r^2)\}$, the outer expansion of the inner solution becomes

$$\varphi_j = \{\sigma_j+C_j(x)(\sigma_j+\bar{\sigma}_j)\}R_{2D} - i\,C_j(x)\bar{\sigma}_j(1+\nu z). \tag{2.24}$$

Comparing (2.12) to (2.24) the matching conditions for the radiation problem are,

$$\sigma_j + C_j(x)(\sigma_j+\bar{\sigma}_j) = q_j \tag{2.25}$$

$$i\,C_j\,\bar{\sigma}_j = \frac{1}{2\pi}\mathcal{L}(q_j). \tag{2.26}$$

After eliminating C_j from (2.25)-(2.26), the outer source strength q_j is determined from the integral equation

$$q_j(x) - \frac{1}{2\pi i}(\sigma_j/\bar{\sigma}_j+1)\mathcal{L}(q_j) = \sigma_j(x) \quad j=3,5, \tag{2.27}$$

where $\mathcal{L}(q_j)$ is given by (2.13) with $\nu_o=0$.

A particular solution for the diffraction problem follows easily from the body boundary condition (2.19) and is equal and opposite to the symmetric part of the incident wave potential

$$\psi_{7P} = -\frac{ig}{\omega}e^{\nu z}\cos(\nu y\sin\beta). \tag{2.28}$$

The head sea limit of ψ_{7P} is the leading order solution in the short-wavelength theory of Faltinsen (1971).

The homogeneous solution again results from the interaction of two waves of unit amplitude and equal phase incident from opposite directions upon the ship section, and is obtained in the form

$$\psi_{7H} = \frac{ig}{\omega}e^{\nu z}\cos(\nu y\sin\beta)+\psi_D(y,z), \tag{2.29}$$

where ψ_D is constructed by using the two-dimensional source potential $\mathrm{Re}(D_{2D})$ that represents standing waves as $\nu|y|\to\infty$ and is regular for all headings. Thus,

$$\psi_7 = -\frac{ig}{\omega}e^{\nu z}\cos(\nu y\sin\beta)\{1-C_7(x)\} + C_7(x)\psi_D(y,z). \tag{2.30}$$

In the overlap region, ψ_7 can be approximated in the form

$$\phi_7 = -\frac{ig}{\omega}\{1-C_7(x)\}(1+\nu z) + C_7(x)\sigma_7(x)\,\mathrm{Re}(D_{2D}). \tag{2.31}$$

The matching requirements again follow easily from (2.12) and (2.31),

$$C_7\,\sigma_7 = q_7 \tag{2.32}$$

$$\frac{ig}{\omega}(1-C_7) = \frac{1}{2\pi}\mathcal{L}(q_7). \tag{2.33}$$

The elimination of C_7 from (2.32)-(2.33) results in the following integral equation for q_7,

$$q_7(x) - \frac{i\omega}{2\pi g}\sigma_7\,\mathcal{L}(q_7) = \sigma_7, \tag{2.34}$$

where $\mathcal{L}(q_7)$ is determined by (2.13) with $\nu_o=-\nu\cos\beta$.

The solution of equations (2.27) and (2.34) determines the outer source strength q_j, and the complete inner solutions follow in the form

$$\varphi_j = \phi_j + \frac{q_j-\sigma_j}{\sigma_j+\bar{\sigma}_j}(\phi_j+\bar{\phi}_j) \quad j=3,5 \tag{2.35}$$

for the radiation problem, and

$$\psi_7 = \frac{ig}{\omega}e^{\nu z}\cos(\nu y\sin\beta)(q_7/\sigma_7-1) + \psi_D q_7/\sigma_7 \tag{2.36}$$

for the diffraction problem.

3. Short-Wavelength Approximations

For wavelengths comparable to the ship transverse dimensions [$\nu L = O(\epsilon^{-1})$ as $\epsilon \to 0$], it is possible to approximate the linear operator $\mathcal{L}(q)$ defined in (2.13) using the techniques of asymptotic analysis. For the diffraction problem and $-1 \le \cos\beta \le 0$, it follows that

$$\mathcal{L}(q_7) = \tfrac{1}{2}(1-i)(\pi\nu)^{\frac{1}{2}} \int_x^{L/2} q_7(\xi) \frac{e^{-i\nu(\xi-x)(1+\cos\beta)}}{(\xi-x)^{\frac{1}{2}}} d\xi$$

$$-\pi i(\csc\beta - \tfrac{1}{2}|\sec\tfrac{\beta}{2}|) q_7(x) + O(\nu^{-\frac{1}{2}}). \quad (3.1)$$

The details of the derivation can be found in Sclavounos (1981). The corresponding approximation for the radiation problem follows from (2.13) and (3.1) with $\cos\beta = 0$, in the form

$$\mathcal{L}(q_j) = \tfrac{1}{2}(1-i)(\pi\nu)^{\frac{1}{2}} \int_x^{L/2} q_j(\xi) \frac{e^{-i\nu(\xi-x)}}{(\xi-x)^{\frac{1}{2}}} d\xi$$

$$+ \pi i \frac{\sqrt{2}}{2} q_j(x) + O(\nu^{-\frac{1}{2}}). \quad (3.2)$$

Proceeding with the radiation problem, the integral in (3.2) can be further approximated for large ν in the form

$$\int_x^{L/2} q_j(\xi) \frac{e^{-i\nu(\xi-x)}}{(\xi-x)^{\frac{1}{2}}} d\xi = -\left(\frac{\pi}{\nu}\right)^{\frac{1}{2}} e^{-\pi i/4} q_j(x). \quad (3.3)$$

The substitution of (3.3) in (3.2) cancels out the first two terms with the remaining part being of $O(\nu^{-\frac{1}{2}})$. Thus for short wavelengths

$$q_j(x) = \sigma_j(x) + O(\nu^{-\frac{1}{2}}), \quad (3.4)$$

and strip theory is recovered.

An approximation similar to (3.3) applied to (3.1) gives

$$\mathcal{L}(q_7) = -\pi i \csc\beta \; q_7(x) + O(\nu^{-\frac{1}{2}}). \quad (3.5)$$

The approximation (3.5) is singular for head waves due to a nonuniformity that is present in the asymptotic approximation of (3.1) when $1+\cos\beta = 0$. Substituting (3.5) in (2.34) we obtain an algebraic equation for $q_7(x)$ with a solution

$$q_7 = \sigma_7/(1 + \tfrac{\omega}{2g} \sigma_7 \csc\beta). \quad (3.6)$$

Substituting (2.33) and (2.32) in (2.30) and using (3.5), we may write the outer expansion of the inner solution in the form

$$\phi_7 = \tfrac{1}{2} i \csc\beta \; q_7(x)(1+\nu z) + q_7(x) \mathrm{Re}(D_{2D})$$

$$= q_7(x) \; D_{2D}, \quad (3.7)$$

where $1+\nu z = e^{\nu z} \cos(\nu y \sin\beta)[1+O(\nu^2 r^2)]$ in the overlap region. The two-dimensional source potential D_{2D} satifies outgoing waves as $\nu|y| \to \infty$ is singular for head waves and corresponds to the Green function used in the short-wavelength strip theory derived by Choo (1975) and Troesh (1976).

In the head-sea case ($\beta = 180°$), (3.1) reduces to (originally due to Faltinsen (1971))

$$\mathcal{L}(q_7) = \tfrac{1}{2}(1-i)(\pi\nu)^{\frac{1}{2}} \int_x^{L/2} \frac{q_7(\xi)}{(\xi-x)^{\frac{1}{2}}} d\xi, \quad (3.8)$$

and the Maruo and Sasaki (1974) theory is obtained apart from two analytical differences; the $\frac{1}{2}$ factor is missing in their theory and an additional $\pi i \, \sigma_7(x)/2$ term appears in their equation which corresponds to (3.8) that should not be present in a consistent short-wavelength approximation.

4. The Two-Dimensional Problem

In this section a numerical scheme for the solution of two-dimensional free-surface wave problems in water of infinite depth is described.

The application of spectral techniques to the solution of free-surface boundary-value problems is in general restricted to simple body profiles. Ursell (1949) obtained the solution of the heaving problem of a circular section in water of infinite depth by using a sequence of singularities located at the origin of the axes. The extention, however, of this method to more general body sections has not been yet formally established.

An efficient numerical technique to treat arbitrary body and bottom geometries has been developed by Yeung [Bai and Yeung (1974)]. In an inner region of changing topography, a hybrid integral equation is obtained by applying Green's theorem and using the fundamental logarithmic singularity as the relevant Green function. This representation is then matched to an eigenfunction expansion in an outer region of constant depth. Liapis and Faltinsen (1980) extended this method to the case where the Helmholtz equation is satisfied in the fluid domain. A comprehensive survey of existing techniques for the solution of two-dimensional free-surface wave problems is given by Wehausen (1974).

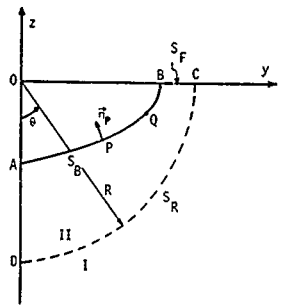


Figure 1.

The present approach is a coupling of a multipole expansion and a hybrid integral representation, valid respectively in the domains I and II of Figure 1, separated by a matching circle S_R. The water depth is assumed infinite and the body section symmetric with respect to the y=0 axis. The Helmholtz equation is in general satisfied in the fluid domain

$$\nabla^2\phi - \ell^2\phi = 0, \tag{4.1}$$

subject to the free-surface condition

$$\phi_z - \nu\phi = 0 \qquad \text{on } z=0, \tag{4.2}$$

to a general body-boundary condition

$$(\vec{n}_P\cdot\nabla)\phi = V(P) \qquad \text{on } S_B\ , \tag{4.3}$$

and to a condition of standing or outgoing waves as $\nu|y|\to\infty$. For all cases of interest $0\le\ell\le\nu$.

Assuming a symmetric flow with respect to the y=0 axis, we may write the velocity potential in region I in the form [Ursell (1949, 1968)]

$$\phi^I = a_o\, W_o(r,\theta) + \sum_{m=1}^{\infty} a_m\, W_m(r,\theta), \tag{4.4}$$

where a_o is the effective source strength, W_o is the relevant wave source potential due to a unit source located at the origin, and $W_m(r,\theta)$ are wave-free multipoles. For $\ell=\nu|\cos\beta|>0$, $W_o=\mathrm{Re}(D_{2D})$ with D_{2D} defined in Section 2, and

$$W_m(r,\theta) = K_{2m-2}(\ell r)\cos(2m-2)\theta + K_{2m}(\ell r)\cos 2m\theta + 2|\sec\beta|K_{2m-1}(\ell r)\cos(2m-1)\theta \tag{4.5}$$

where $K_n(x)$ is the modified Bessel function of order n defined in Abramowitz and Stegun (1964). For $\ell=0$, $W_m=R_{2D}$ with R_{2D} defined in Section 2, and

$$W_m(r,\theta) = \frac{\cos 2m\theta}{r^{2m}} + \frac{\nu}{2m-1}\,\frac{\cos(2m-1)\theta}{r^{2m-1}} \tag{4.6}$$

Applying Green's theorem in region II (ABCDA), using the symmetry of the flow and the free surface condition (4.2), we obtain

$$-\frac{1}{2}\phi^{II}(Q) + \int_{S_B\cup S_R} ds(P)\phi^{II}(P)(\vec{n}_P\cdot\nabla_P)F(P,Q) + \int_{S_F} ds(P)\phi^{II}(P)[(\vec{n}_P\cdot\nabla_P)-\nu]F(P,Q) - \int_{S_R} ds(P)F(P,Q)(n_P\cdot\nabla_P)\phi^{II}(P) = \int_{S_B} ds(P)\,F(P,Q)\,V(P), \tag{4.7}$$

where $\vec{n}_P$ is the unit normal vector pointing out of domain II and

$$F(P,Q) = G(P,Q^+) + G(P,Q^-), \tag{4.8}$$

with $Q^+ = Q$ lying on $S_B\cup S_F\cup S_R$ and Q^- being the symmetric of Q with respect to the y=0 axis; G(P,Q) is the velocity potential at P due to a fundamental unit source located at Q, given by

$$G(P,Q) = \begin{cases} \frac{1}{2\pi}\ell\sigma(r_{PQ}) & ,\ \ell=0 \\ -\frac{1}{2}K_o(\ell r_{PQ}) & ,\ \ell>0 \end{cases}, \tag{4.9}$$

where $K_o(x)$ is the modified Bessel function of zeroth order.

A grid is selected along the contours S_B, S_F and S_R with the velocity potential ϕ^I assumed constant along the segments joining two consecutive grid points. Let N_B, N_F and N_R be the number of segments along S_B, S_F and S_R respectively. Taking the segment lengths to be of equal length along the matching circle and keeping N_R-1 terms in the series (4.4), the velocity potential ϕ^I and its r-derivative ϕ^I_r at the segment midpoints can be written in a matrix form

$$\vec{\phi}^I = A\,\vec{a} \tag{4.10}$$

$$\vec{\phi}^I_r = B\,\vec{a}, \tag{4.11}$$

where the column vectors $\vec{\phi}^I$, $\vec{a}$ and the matrixes A and B are defined as follows

$$\vec{\phi}^I = \{\phi^I(R,\theta_1),\ldots,\phi^I(R,\theta_{N_R})\}^T \tag{4.12}$$

$$\vec{a} = \{a_0,\ldots,a_{N_R-1}\}^T \tag{4.13}$$

and

$$A = A_{ij} = W_{j-1}(R,\theta_i), B = \frac{\partial A}{\partial r}\Big|_{r=R}$$

$$i,j = 1,\ldots,N_R, \tag{4.14}$$

where (R,θ_i), $i=1,\ldots,N_R$ are the polar coordinates of the segment midpoints along the discretized circle S_R, with θ_i decreasing to zero as i increases.

If we left-multiply both sides of equation (4.10) by BA^{-1}, we obtain a relation between the velocity potential ϕ^I and the normal velocity ϕ^I_r, in the form

$$\phi^I_r = B\,A^{-1}\,\vec{\phi}^I. \tag{4.15}$$

We next proceed to the discretization of equation (4.7). The velocity potential at the midpoint of the i-th segment is denoted by ϕ^{II}_i, where the indexing starts from the point A of Fig. 1. It follows that

$$\sum_{j=1}^{N_T}(C_{ij}-\tfrac{1}{2}\delta_{ij})\phi^{II}_j - \sum_{j=N_F+1}^{N_T} S_{ij}\,\phi^{II}_j = \sum_{j=1}^{N_B} S_{ij}\,V_j, \tag{4.16}$$

where $N_T = N_B+N_F+N_R$, V_i is the body boundary normal velocity, δ_{ij} the Kronecker delta and

$$C_{ij} = \begin{bmatrix} D_{ij} & j=1,\ldots,N_B \text{ and } j=N_F+1,\ldots,N_T \\ D_{ij}-S_{ij} & j=N_B+1,\ldots,N_F \end{bmatrix} \tag{4.17}$$

with $i=1,\ldots,N_T$. The influence matrixes S_{ij}, D_{ij} $i,j = 1,\ldots,N_T$ are defined as follows

$$S_{ij} = \int_{S_j} ds(P)F(P,Q_i) \tag{4.18}$$

$$D_{ij} = \int_{S_j} ds(P)\,(\vec{n}_P\cdot\vec{V}_F)F(P,Q_i), \tag{4.19}$$

where $F(P,Q)$ is defined in (4.8)-(4.9), the point Q_i is located at the midpoint of the i-th segment and the integrations in (4.18)-(4.19) are performed over the j-th segment S_j.

The matching conditions of continuous pressure and normal velocity across the matching circle S_R can be expressed in the form

$$\phi^I(R,\theta_i) = \phi^{II}_{i+N} \tag{4.20}$$

$$\phi^I_r(R,\theta_i) = \phi^{II}_{r,i+N}, \tag{4.21}$$

where $i=1,\ldots,N_R$ and $N=N_B+N_F$. Using (4.20)-(4.21) and (4.15) in the second sum of (4.16), we end up with a matrix equation for ϕ^{II}_j, $j=1,\ldots,N_T$

$$\{C-\tfrac{1}{2}\,I-E\}\vec{\phi}^{II} = S\,\vec{V}, \tag{4.22}$$

where,

$$\vec{\phi}^{II} = \{\phi^{II}_i\}^T \qquad i=1,\ldots,N_T \tag{4.23}$$

$$\hat{V} = \{V_i,\underbrace{0,\ldots,0}_{N_F+N_R}\}^T \quad i=1,\ldots,N_B \tag{4.24}$$

$$\left.\begin{aligned} I_{ij} &= \delta_{ij} \\ S &= S_{ij} \end{aligned}\right\} \qquad i,j=1,\ldots,N_T \tag{4.25}$$

$$E=E_{ij}=\begin{bmatrix} 0 & & \\ \sum_{k=N+1}^{N_T} S_{ik} & \sum_{m=1}^{N_R} B_{k-N,m}\, A^{-1}_{m,j-N}, & \\ & j=1,\ldots,N & \\ & j=N+1,\ldots,N_T & \end{bmatrix} \qquad (4.26)$$

with $i=1,\ldots,N_T$ and $A=A_{ij}$, $B=B_{ij}$, $i,j=1,\ldots,N_T$ defined in (4.14).

The velocity potential ϕ along the contours S_B, S_F and S_R is determined from the solution of the system of equations (4.22). The effective source strength a_Q in (4.4) is obtained by left-multiplying (4.10) by A^{-1}.

The present scheme is free from irregular frequencies. Furthermore, only one evaluation of the wave-source potential W_Q is necessary. This reduces substantially the total computation time required, in comparison to the alternative approach of a wave-source distribution on the body boundary, especially when $\ell>0$.

The described technique has been applied for $\ell=\nu|\cos\beta|>0$ in the context of the diffraction problem. Selecting, the matching circle radius R 10% greater than the body-section maximum radius and 15, 10 and 15 segments on S_B, S_F and S_R respectively, proved to be sufficient for $0 < \frac{\nu B}{2} \leq \pi$, where B is the beam of the body section. The same estimates are expected to hold in the special case of $\ell=0$. For this paper, the two-dimensional solutions of the radiation problem are obtained by using a computer program due to Yeung (1975), based on his hybrid integral equation technique.

5. Hydrodynamic Forces and Motions

The quantities of interest for the evaluation of the ship motions are the hydrodynamic pressure force and moment acting on the ship in the radiation and the diffraction problems. For a ship undergoing a steady-state small amplitude oscillatory heave and pitch motion in an otherwise calm free surface, the resulting complex force amplitude can be written in the form

$$H_i = \sum_{j=3,5} \eta_j\, t_{ij}, \quad i=3,5, \qquad (5.1)$$

where η_j is the complex amplitude of the ship's displacement and

$$t_{ij} = \omega^2 a_{ij} - i\omega\, b_{ij} - c_{ij}\ . \qquad (5.2)$$

The coefficients a_{ij}, b_{ij}, c_{ij} are real and correspond respectively to the force components in phase with the acceleration, velocity and static displacement of the ship. The added-mass (a_{ij}) and damping (b_{ij}) coefficients can be derived from the inner velocity potential (2.21) of the radiation problem by integrating the linearized pressure obtained from Bernoulli's equation over the ship wetted surface. It follows that

$$\omega^2 a_{ij} - i\omega b_{ij} = -i\omega\rho \iint n_i \phi_j\, ds$$

$$-i\omega\rho \iint n_i C_j(x)(\phi_j+\bar{\phi}_j)\, ds, \qquad (5.3)$$

where all the quantities are defined in Section 2B.

The first integral in (5.3) corresponds to the strip-theory contribution. The second integral is the correction due to the three-dimensional interaction effects introduced by the unified theory. As $\nu\to\infty$, it follows from (2.25) and (3.4) that $C_j(x)\to 0$ and the strip-theory is recovered.

Proceeding to the diffraction problem, the resulting complex amplitude of the wave exciting force is simply

$$F_i = A\, X_i, \qquad i=3,5, \qquad (5.4)$$

where A is the amplitude of the incident wave. Using the incident-wave potential (2.1) with A=1 and the diffraction potential φ_7, the unit-amplitude exciting force X_i can be expressed in the form

$$X_i = -i\omega\rho \iint (\varphi_I + \varphi_7)\, n_i\, ds. \qquad (5.5)$$

An alternative expression can be obtained by using the Haskind relations. Combining the body-boundary condition (2.4) for the radiation problem and applying Green's theorem in (5.5), we obtain

$$X_i = -\rho \iint (i\omega n_i \varphi_I - \varphi_i \frac{\partial \varphi_I}{\partial n})\, ds, \qquad (5.6)$$

where φ_i is the radiation potential due to the i-th mode of oscillation. With the velocity potentials φ_7 and φ_i assumed known, no assumptions are involved

regarding the wavelength or the body geometry in (5.5) and (5.6). The advantage however in using (5.6) is that the solution of the diffraction problem is not needed for the evaluation of the exciting force and moment of a body in waves.

For a slender ship, the inner diffraction velocity potential defined in (2.5) and (2.36) is used together with (2.1) to give

$$X_i = -i\omega\rho\iint e^{-i\nu x\cos\beta} C_7(x)\, \psi_{7H} n_i ds \quad (5.7)$$

where C_7 and ψ_{7H} are defined in Section 2B. The corresponding expression for (5.6) is obtained by substituting the unified-theory radiation potential (2.21) in (5.6). If follows that

$$X_i = -\rho\iint (i\omega n_i \varphi_I - \phi_i \frac{\partial \varphi_I}{\partial n})ds$$

$$+ \rho\iint C_i(x)(\phi_i + \bar{\phi}_i) \frac{\partial \varphi_I}{\partial n} ds . \quad (5.8)$$

As $\nu \to \infty$, the interaction coefficient $C_i(x) \to 0$ and expression (5.8) reduces to the exciting force obtained in the strip theory of Salvesen, Tuck and Faltinsen (1970). The short-wavelength limit of (5.7), however, does not lead to the same result since the slender-body approximations involved in (5.7) and (5.8) are different.

The relative error involved in the inner diffraction problem is a factor $1+0(\epsilon^2\nu\cos\beta)$. The corresponding error factor for the radiation problem is $1+0(\epsilon^2)$ for all wavelengths. It is thus expected that, unlike the radiation velocity potential and the exciting force (5.8), the accuracy of the diffraction potential ψ_{7H} and the corresponding exciting force (5.7) decreases with decreasing wavelength. This is supported by the comparison of the exciting force and moment predicted by (5.7) and (5.8) with an exact three-dimensional theory.

The equations of motion follow by equating the inertia forces to the sum of the pressure forces and the ship weight. Combining (5.1) and (5.4) and taking the origin of the coordinates on the ship centerline and above the center of gravity, the equations of the heave and pitch motions follow in the form

$$\sum_{j=3,5} n_j c_{ij} + A X_i = -\omega^2 \sum_{j=3,5} M_{ij} n_j , \quad (5.9)$$

where $M_{33}=\rho\nabla$ is the ship mass, M_{55} is the ship moment of inertia with respect to the y-axis and $M_{35}=M_{53}=0$ due to the special choice of the coordinate system. Substituting (5.2) in (5.9) and rearranging terms we get

$$\sum_{j=3,5} n_j\{-\omega^2(M_{ij}+a_{ij})+i\omega b_{ij}+C_{ij}\}$$

$$= AX_i , \qquad i=3,5. \quad (5.10)$$

This is a system of linear equations that can be easily solved for the complex amplitudes n_j, $j=3,5$.

Numerical computations of the hydrodynamic forces and motions were performed for a Series 60 hull ($C_B=0.7$, parent form). The Salvesen, et al. (1970) strip-theory results are also shown together with an exact three-dimensional numerical solution by Inglis (1980) and experimental data, where available.

The results for the radiation problem are shown in Figures 2 and 3, and are compared to experimental data of Gerritsma (1966). The agreement between the unified theory and experiments is very good both for the hydrodynamic force distribution (Figure 2) and the added-mass and damping coefficients (Figure 3 adapted from Newman and Sclavounos (1980)), and indicates a notable improvement over strip theory. The deviation of a_{55} from the experiments that occurs at low frequencies is supported by the excellent agreement between the unified theory and the exact three-dimensional solution of Inglis (1980) for all frequencies.

The slowly varying sectional hydrodynamic force distribution for the diffraction problem is given by

$$F_3'(x) = -i\omega\rho A C_7(x) \int_C \psi_{7H} n_3 dl. \quad (5.11)$$

The corresponding expression for the Salvesen et al. (1970) strip theory is obtained from (5.8) with $C_i(x)=0$, in the form

$$F_3'(x) = -\frac{i\rho g A}{\omega} \int_C (i\omega N_3 - \phi_3 \frac{\partial}{\partial N}) \cdot$$

$$e^{\nu z}\cos(\nu y\sin\beta) dl , \quad (5.12)$$

where all the quantities in (5.11) and (5.12) are defined in Section 2B. The results for F_3' and the amplitudes of the exciting force and moment shown in Figures 4 and 5 respectively, indicate that the strip-theory predictions are in general higher than those of the

unified theory.

The two expressions of the exciting force and moment (5.7) and (5.8), derived respectively by pressure integration and using the Haskind relations, compare well with each other, being in closer agreement for smaller values of $\nu|\cos\beta|$. For head waves, both agree well with the experimental data of Vugts (1971) and the three-dimensional solution, with a relatively more favorable agreement of (5.8) with the theory of Inglis (1980).

Finally, the motions of the ship free to heave and pitch are presented in Figure 6, where comparisons are made with three different sets of experimental data due to Nakamura (1966), Shintani (1966) and Yamanouchi and Ando (1966). For the model tested, the center of gravity is taken at the origin of the coordinates and the longitudinal radius of gyration is taken equal to 1/4 of the ship's length L.

All theories agree well in general with the experiments, except for short waves at $\beta=180°$. The conclusions drawn for the exciting forces and moments predicted by (5.7) and (5.8) remain unchanged for the respective ship motion amplitude predictions, since the added-mass and damping coefficients are the same in the two versions.

Before comparing the motion amplitudes predicted by strip theory and the rest of the theories, it is interesting to make the following observations; for the radiation problem, strip theory underpredicts a_{33} and a_{55}, and overpredicts b_{33} and b_{55} for moderate to low frequencies, being in good agreement for high frequencies. Both these effects contribute to an overprediction of the modulus of the transfer function of the left-handside of equation (5.10). The effects of the cross-coupling coefficients are taken into account in the computations but are relatively unimportant and are neglected in the present discussion.

For the diffraction problem, strip theory again overpredicts the exciting force and moment amplitude and since the motion amplitudes are the ratios of the quantities discussed, strip theory is in general in good agreement with the rest of the theories. The theoretical predictions of the phases agree well in general, with the exception of the heave phase at $\beta=135°$ and a departure of the three-dimensional theory for the pitch phase at $\beta=180°$.

In conclusion, the unified theory is in excellent agreement with the exact three-dimensional theory, and both agree very well with the experimental data. The strip theory predicts well the motion amplitudes and phases but is in less satisfactory agreement with the other theories and experiments for the hydrodynamic coefficients and the exciting forces.

The integral equations (2.27) and (2.34) are solved by iteration and the solution obtained in this manner has been checked against an independent matrix inversion solution. The computation time required for this task is minimal, leaving the solution of the two-dimensional problems as the main computational effort involved in the unified theory.

Ackowledgements

The author wishes to thank Professor J. N. Newman for his guidance during the course of this work. It is also a pleasure to acknowledge the fruitfull interaction with Professor O. M. Faltinsen during his stay at M.I.T., and the financial support provided by the Office of Naval Research, National Science Foundation, and the Naval Sea System Command's General Hydromechanics Research Program administered by the David W. Taylor Ship Research and Development Center.

References

1. Abramowitz, M., and Stegun, I. (1964). "Handbook of Mathematical Functions." U.S. Gov. Print. Off., Washington, D.C.

2. Bai, K. J., and Yeung, R. W. (1974). Numerical solutions to free-surface flow problems. *Proc. Symp Nav. Hydrodyn., 10th* ACR-204, pp. 609-647. Off. Nav. Res., Washington, D.C.

3. Choo, K. Y. (1975). Exciting forces and pressure distribution on a ship in oblique waves. Ph.D. Thesis, Massachusetts Institute of Technology, Cambridge, MA.

4. Faltinsen, O. (1971). Wave forces on a restrained ship in head-sea waves. Ph.D., Thesis, University of Michigan, Ann Arbor.

5. Gerritsma, J. (1966). Distribution of Hydrodynamic forces along the length of a ship model in waves. Rep. No. 144. Shipbuild ng Lab., Delft University of Technology, Delft.

6. Inglis, R. B. (1980). A three-dimensional analysis of the motion of a rigid ship in waves. Ph.D. Thesis, Department of Mechanical Engineering, University College, London.

7. Liapis, N., and Faltinsen, O. M. (1980). Diffraction of waves around a ship. *J. Ship Res.* 24(3), 147-155.

8. Maruo, H., and Sasaki, N. (1974). On the wave pressure acting on the surface of an elongated body fixed

in head seas. *J. Soc. Nav. Archit. Jpn.* 136, 34-42.

9. Nakamura, S. (1966). Experiments on a Series 60, C_B=0.6 and 0.7 ship models in regular head waves. Contribution to the 11th I.T.T.C. 1966.

10. Newman, J. N. (1978). The theory of ship motions. *Adv. Appl. Mech.* 18, 221-283.

11. Newman, J. N., and Sclavounos, P. (1980). The unified theory of ship motions. *Proc. Symp. Nav. Hydrodyn., 13th*, Tokyo 1980.

12. Ogilvie, T. F., and Tuck, E. O. (1969). A rational strip theory for ship motions. Part 1. Rep. No. 013. Dep. Nav. Archit. Mar. Eng., University of Michigan, Ann Arbor.

13. Salvesen, N., Tuck, E. C., and Faltinsen, O. (1970). Ship motions and sea loads. *Soc. Nav. Archit. Mar. Eng. Trans.* 78, 250-287.

14. Sclavounos, P. D. (1981). On the diffraction of free surface waves by a slender ship. Ph.D. Thesis, Department of Ocean Engineering, Massachusetts Institute of Technology, Cambridge, Massachusetts.

15. Shintani, A. (1966). Comparison of computer program results and experiments for ship behavior in regular head seas. Contribution to the 11th I.T.T.C. 1966.

16. Troesch, A. W. (1976). The diffraction potential for a slender ship moving through oblique waves. Ph.D., Thesis, University of Michigan, Ann Arbor.

17. Ursell, F. (1949). On the heaving motion of a circular cylinder on the surface of a fluid. *Q. J. Mech. Appl. Math.* 2, 218-231.

18. Ursell, F. (1968). The expansion of water-wave potentials at great distances. *Proc. Cambridge Philos. Soc.* 64, 811-826.

19. Vugts, J. H. (1971). The hydrodynamic forces and ship motions in oblique waves. Neth. Res. Center, TNO Report 150S.

20. Yamanouchi, Y., and Ando S. (1966). Experiments on a Series 60, C_B=0.7 ship model in oblique regular waves. Contribution to the 11th I.T.T.C. 1966.

21. Yeung, R. W. (1975). A hybrid integral-equation method for time-harmonic free-surface flow. *Proc. Int. Conf. Numer. Ship Hydrodyn., 1st*, pp. 518-607, Gaithersburg, Maryland.

22. Wehausen, J. V. (1974). Methods for boundary-value problems in free-surface flows. The Third Annual David W. Taylor Lectures.

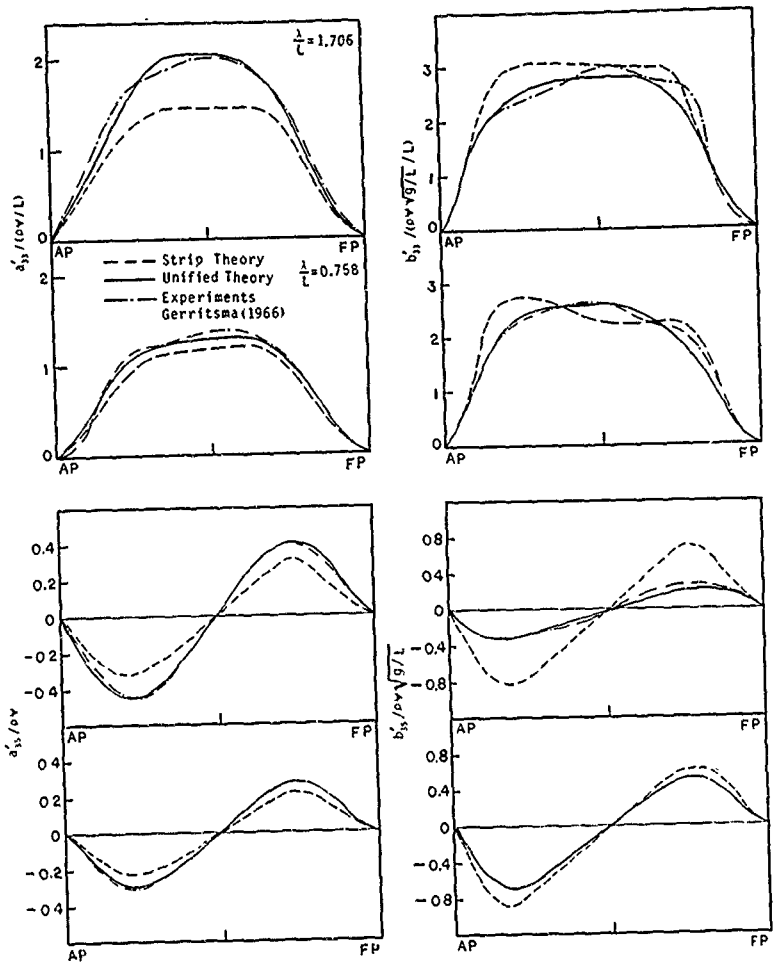


Figure 2 - Longitudinal distribution of the added-mass and damping sectional hydrodynamic force for a Series 60 hull (C_B=0.7) at λ/L= 1.706, 0.758 and U=0.

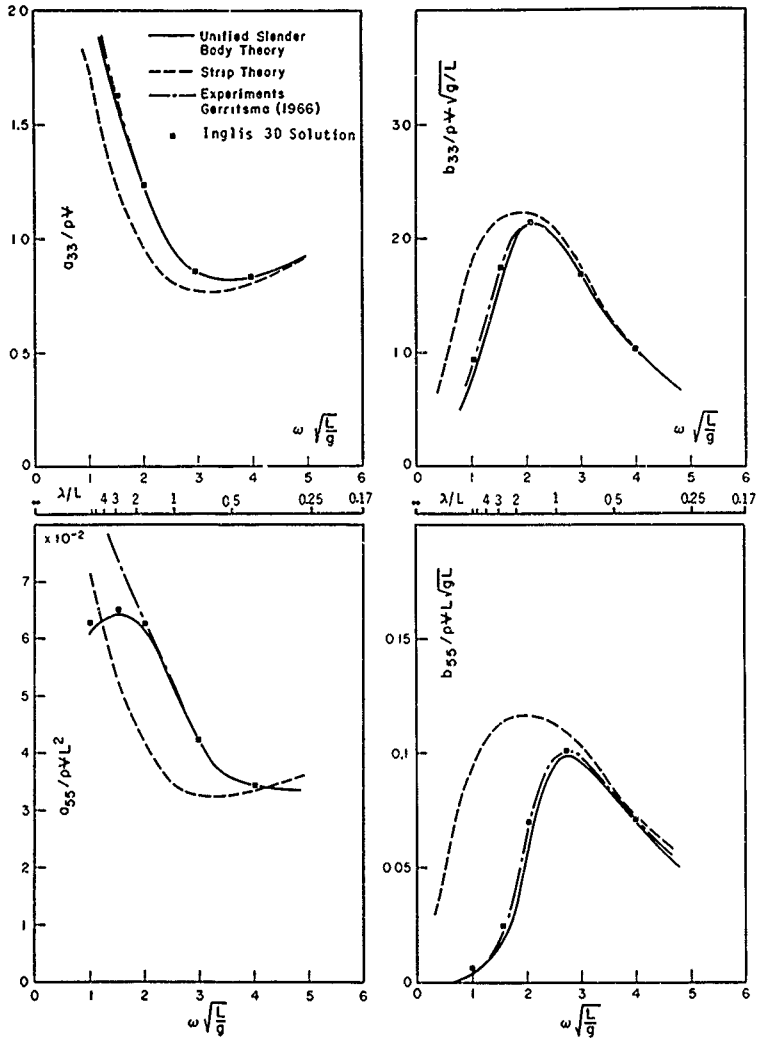


Figure 3 - Heave and pitch added-mass and damping coefficients for a Series 60 hull (C_B=0.7) at U=0 (Adapted from Newman and Sclavounos(1980))

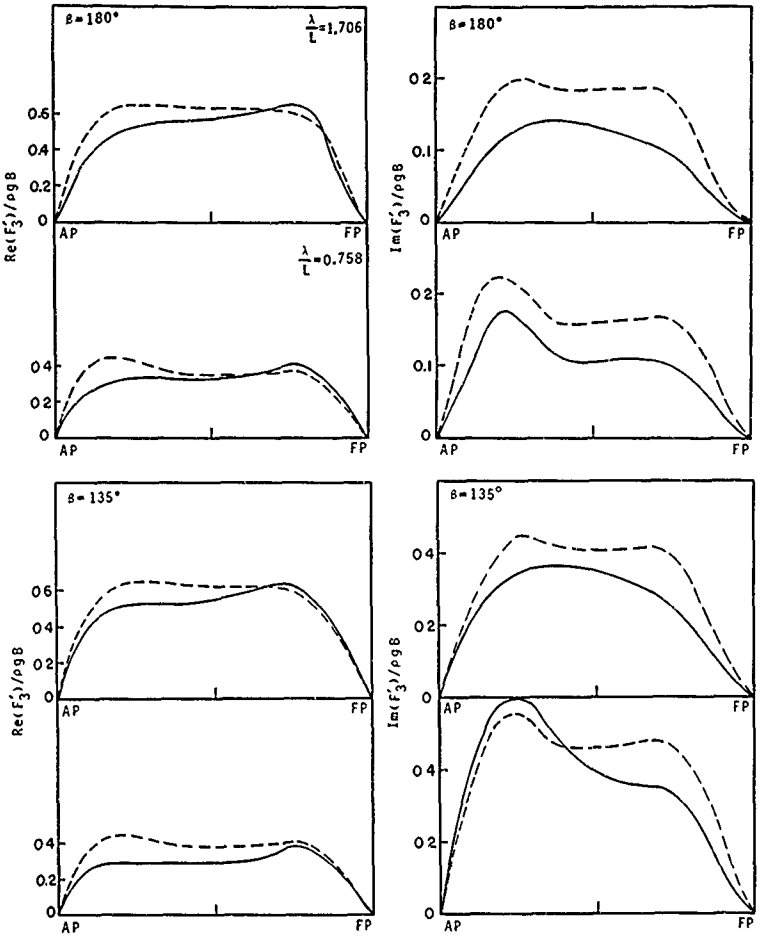


Figure 4 - Longitudinal distribution of the real and imaginary part of the sectional exciting force (with the exp(iw xcosβ) component factored out) for a Series 60 hull (C_B=0.7) fixed in head (β=180°) and bow (β=135°) waves at λ/L= 1.706, 0.758 and U=0.

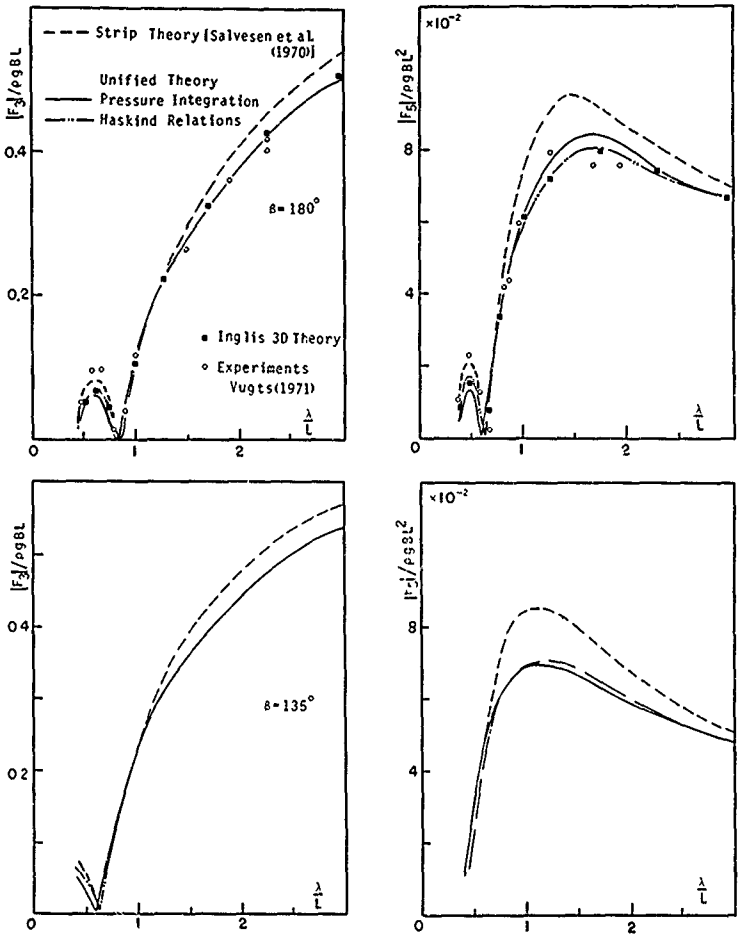


Figure 5 - Heave and pitch exciting force and moment amplitude for a Series 60 hull (C_B=0.7) fixed in head (β=180°) and bow (β=135°) waves at U=0.

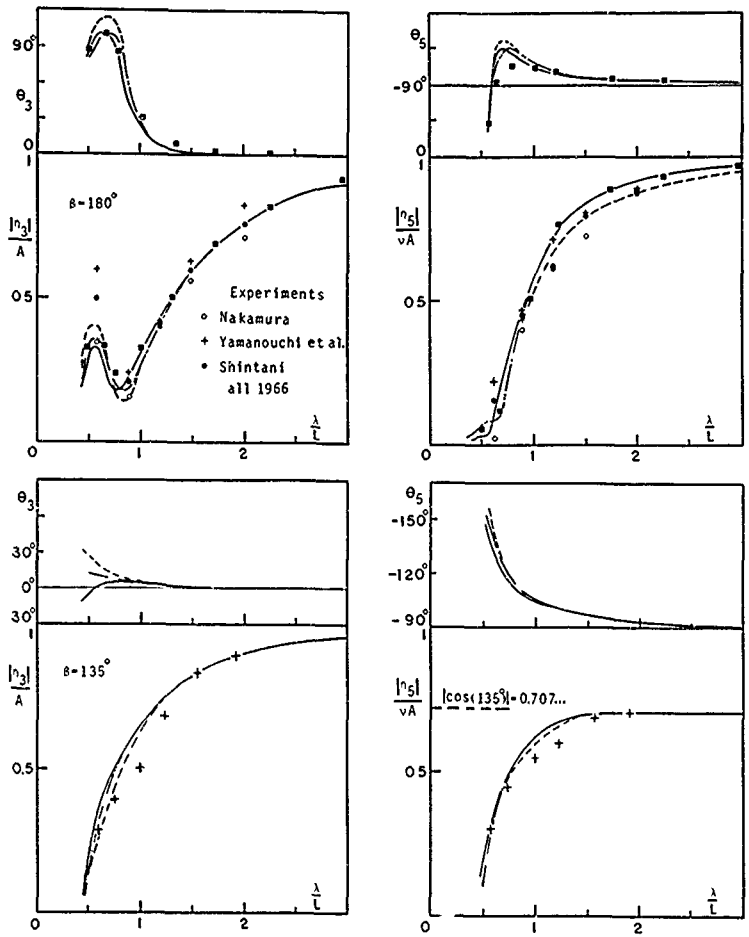


Figure 6 - Heave and pitch motion amplitude and phase of a Series 60 model (C_B=0.7) in head (β=180°) and bow (β=135°) waves at U=0.

DISCUSSION
of the paper
by P D Sclavounos

THE INTERACTION OF AN INCIDENT WAVE FIELD WITH A FLOATING SLENDER BODY AT ZERO SPEED

Discussion
by J. Geer

The inner expansion you use (by chopping the ϕ_{xx} term) is valid over most of the region near the body, but not near the ends of the body (i.e. near the bow and stern). In these regions a separate inner expansion is needed or some kind of uniform expansion should be employed. However, your results look very good and certainly agree well with experiments. Can we conclude from this that "end effects" are simply not important in the types of problems you are considering here ?

Author's reply

The author wishes to thank Prof. Geer for his interesting comments on a sensitive aspect of slender-body theory.

In response to the concluding statement of Prof. Geer, I would like to point out that "end effects" are indeed unimportant in the prediction of the linear hydrodynamic forces on a ship interacting with waves at zero speed. This is mainly due to the fact that the main contribution to the integrated forces results from the pressure integration along the ship middle body. This is especially true for the modes with sectional force distributions of the same sign in the fore and after part of the body and for conventional ship forms with small beam at the ends. Moreover in the zero-speed problem the free-surface condition is exactly satisfied in the near field. This, combined with the good agreement with experiments of the unified theory predictions, in a way validates the sensitivity of the solution-accuracy on the use of the exact free-surface condition.

RADIATION FORCES ON SHIPS WITH FORWARD SPEED

Ronald W. Yeung and Sea-Heon Kim
Massachusetts Institute of Technology
Cambridge, Massachusetts

Abstract

This paper presents a new formulation, based on an integral-equation technique, for solving the radiation forces due to a moving ship. This approach does not require the complex three-dimensional solution of the original problem. By taking a fixed frame of reference and by letting the ship pierce through a sequence of control planes, the forward-speed effects on the free-surface condition can be included in a quasi-three-dimensional manner. The field equation is still two-dimensional, after exploiting the slenderness assumption, but the hydrodynamic problem is unsteady. An integral relation describing the flow on the control plane is obtained by applying Green's theorem to the time-derivative of the potential and to a Green function, satisfying the linearized unsteady free-surface condition and the proper initial conditions. The numerical results are given for the half-immersed spheroid and the destroyer hull. The present method provides an improvement over the strip theory predictions at low and moderate frequencies.

I. Introduction

Oceangoing ships are designed to operate in a wave environment which is quite irregular in nature. However, prediction of ship motions and the dynamic sea loads is such a complex problem that the early research in ship hydrodynamics was devoted primarily to operations in calm water. Since the well-known paper of St. Denis and Pierson (1953) on the application of the principle of superposition to the ship-motion problem, there has been much development in both experimental and theoretical efforts for the ship-motion problem in regular waves, which, by linear superposition, is ultimately applicable to an irregular seaway. With the assumption of small unsteady motions of the ship and of the surrounding fluid, the ship motion problem can be decomposed linearly into two problems: the radiation problem and the diffraction problem. Thus, we can consider separately the radiation problem where the ship undergoes prescribed oscillatory motions in otherwise calm water, and the diffraction problem, where incident waves act upon the ship in its steady-state equilibrium position. The present paper is concerned only with the former problem, and is restricted to the solution of the radiation problem for forced heave and pitch motions of the ship which is moving steadily with constant forward velocity U.

The strip theory for heave and pitch motions in head waves of Korvin-Kroukovsky and Jacobs (1957) was the first motion theory utilizing the two-dimensional results as an approximation for the three-dimensional ship-motion problem. They solved two-dimensional boundary-value problems for each cross-section of the ship. The two-dimensional solutions were then adjusted to include certain three-dimensional forward speed effects based on intuitive, physical arguments. Even though their theory was derived mainly from "physical intuition" rather than a rational mathematics, there is no doubt that this original strip theory deserves its recognition as one of the most significant contributions in the field of seakeeping. This original strip theory gives generally satisfactory agreement with experiments, for the heave and pitch motions of the ship in head waves. But the cross-coupling coefficients in the theory of Korvin-Kroukovsky and Jacobs did not satisfy the symmetry relations proved by Timman and Newman (1962), and that has raised a major objection to this theory. This original strip theory has since been modified and extended by many authors. For example, a modified strip theory, which includes the forward-speed effects on the cross-coupling terms, was used for the evaluation of head-sea motions by Gerritsma and Beukelman (1967). Their calculation yields good agreement with experiments (Gerritsma and Beukelman, 1964, 1967, and Smith, 1967). Salvesen et al. (1970) provided yet another formulation with the forward-speed effects through the hull boundary condition; the hull boundary condition is represented in terms of the oscillatory motion of the ship within a steady flow field generated by its steady-state forward motion. But the free-surface condition in their formulation turned out to be independent of the ship's forward speed.

It should be mentioned that Ogilvie and Tuck (1969) derived a completely new strip theory for head seas by using slender-body theory. By consistently retaining the higher-order terms of relative magnitude $\epsilon^{1/2}$ in their perturbation analysis, ϵ being the slenderness parameter, Ogilvie and Tuck obtained the

additional contributions to the cross-coupling coefficients. These additional contributions, represented by some integral terms over the free-surface, are essentially due to the forward-speed effects on the free-surface condition. Faltinsen (1974) noted that better agreement with experiments was achieved by using the Ogilvie-Tuck cross-coupling coefficients. But Ogilvie and Tuck did not get certain terms proportional to the speed squared in the pitch added-mass and damping coefficients which are present in the coefficients of Salvesen et al. These terms were discarded as higher-order effects in the particular perturbation scheme of Ogilvie and Tuck. Another new theory, which embraces the ordinary slender-body theory and strip theory applicable respectively in the low and high-frequency limit, has been developed recently by Newman (1978). In this so-called unified theory, the flow field is divided into two regions; an inner region close to the hull and an outer region far apart from the hull. The flow in the near field is two-dimensional, satisfying the two-dimensional Laplace equation, and the linearized time-harmonic free-surface condition, together with the hull boundary condition. The fully three-dimensional flow in the outer region satisfies the three-dimensional Laplace equation, subject to the complete linearized free-surface condition and the radiation condition at infinity. The complete solution is obtained by matching outer and inner solutions in a suitably defined overlap region. The unified theory was applied to the motion of the floating spheroid for the special case of zero forward-velocity (Mays, 1978), and to the forced heave and pitch motions of the ship in head seas (Newman and Sclavounos, 1980). The computational results are in quite satisfactory agreement with experiments. However, it is worthwhile to point out that the free-surface condition in the inner problem does not include any forward-speed effects, while the hull boundary condition does.

The conventional strip theory is deficient, since the forward-speed effects are taken into account only through the hull boundary condition, while the free-surface condition in such procedure is customarily taken as time harmonic with no forward-speed dependence. However, one will not expect the time harmonic free-surface condition in two dimension to remain physically valid if the characteristic time associated with the ship speed is comparable to the period of oscillation. Chang (1977) has developed the numerical technique for calculating the linearized three-dimensional ship motion problem. In a fully three-dimensional theory of Chang, the effect of forward speed on the free-surface condition was taken into account by modifying the fundamental singularity. The results show satisfactory agreement with the experiments and also give an improvement over the strip theory predictions. A complementary two-dimensional approach, which includes the forward-speed effects on the free-surface condition, was initiated by Chapman (1975,1977). The flow at each cross-section of the ship was analyzed in a quasi-two-dimensional manner along the characteristic lines defined in his formulation, with interactions propagated downstream by the free-surface condition.

In the present formulation, it is assumed that the ratio of speed of ship to the wave celerity is greater than 1/4, $\nu = \omega U/g > 1/4$; there is no wave radiation ahead of the ship and the interactions due to the motion of the adjacent cross-sections propagate downstream only (Wehausen and Laitone, 1960). By letting the ship pierce through a sequence of control planes defined in a fixed frame of reference and by solving the initial boundary-value problem on a control plane, the forward-speed effects on the free-surface condition can be included, in a quasi-three-dimensional manner, in this approach. The field equation on the control plane reduces to the two-dimensional one, after exploiting the slenderness assumption, but the hydrodynamic problem i unsteady even for time-harmonic pitching and heaving motions. Since no outer matching is used in this formulation, the exact three-dimensionality cannot be reproduced. The resulting mathematical problem is similar to Chapman's, even though the approach is different. A numerical procedure based on integral-equation method has been developed for solving such unsteady problems and applied to the calculation of three-dimensional added-mass and damping.

II. Mathematical Formulation

We consider two right-handed Cartesian coordinate systems, with $\vec{x}_o = (x_o, y_o, z_o)$ fixed in space, and $\vec{x} = (x,y,z)$ moving in steady translation with the mean forward velocity U of the ship. Let $z_o = 0$ be the plane of undisturbed free surface with the x_o-axis positive in the direction of the ship's forward motion, and z_o-axis pointing upwards. The steady-moving coordinate system is defined by the transformation (Figure 1),

$$\vec{x} = (x_o - Ut + L/2,\ y_o,\ z_o) \ . \tag{1}$$

In the context of irrotational flow, it is not difficult to show that the linearized problem for the velocity potential $\phi(x_o, y_o, z_o, t)$ is defined by

$$\nabla^2\phi(x_o,y_o,z_o,t) = 0, \text{ in the fluid domain;} \tag{2}$$

$$\left.\frac{\partial\phi}{\partial n}\right|_S = \vec{\alpha}\cdot\vec{n} \ , \tag{3}$$

$$\phi_{tt}(x_o,y_o,0,t) + g\phi_{z_o} = 0 \ , \tag{4}$$

where S is the *instantaneous* submerged portion of the ship's surface, $\vec{\alpha}$ the local velocity of the ship's wetted surface, and $\vec{n}$ an outward normal to the fluid. Another alternative to

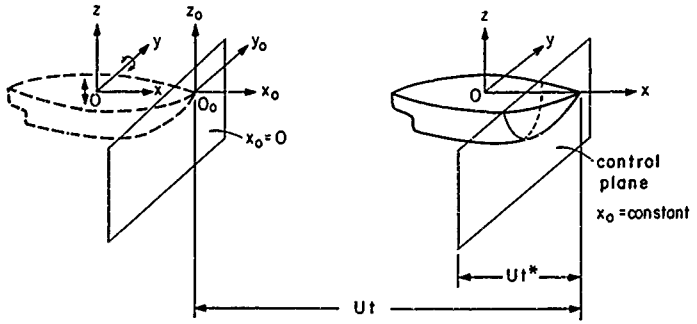


Figure 1. The Reference Frame

(3) was given by Timman and Newman (1962), which replaced the instantaneous position S of the ship's wetted surface by its steady-state mean $\bar{S}$. A consistent derivation then yields.

$$\frac{\partial \phi}{\partial n}\bigg|_{\bar{S}} = [\dot{\vec{\alpha}} + \nabla\times(\vec{\alpha}\times\vec{w})]\cdot\vec{n} \ , \tag{5}$$

where $\vec{w} = UV(\bar{\phi}-x)$ is the velocity vector of the steady flow relative to the moving frame of reference, with $\bar{\phi}$ being the disturbance potential of the steady flow, and $\vec{\alpha}$ is the local oscillatory displacement of the ship's wetted surface. Since $\vec{\alpha}$ is a small oscillatory quantity, this vector displacement can be expressed as

$$\vec{\alpha} = \vec{\xi} + \vec{\Omega}\times\vec{x} \ , \tag{6}$$

where $\vec{\xi}$ and $\vec{\Omega}$ denote the unsteady translation and rotation of the ship relative to the origin $\vec{x} = 0$. Now we introduce two small parameters ε and δ, where ε represents the slenderness ratio of the ship hull (beam B or draft T to length ratio), and δ the ship oscillation-amplitude to the transverse dimensions ratio, both assumed to be small, i.e. $\varepsilon,\delta << 1$. Thus, the unsteady velocity potential ϕ can be decomposed linearly into separate components due to each of six rigid-body motions $\vec{\xi}$ and $\vec{\Omega}$. In this paper, we restrict our attention to the case of pitch and heave motions only, both, as stated earlier, assumed small. Hence, we write

$$\phi = \phi_3 + \phi_5 \ , \tag{7}$$

where ϕ_3 and ϕ_5 are the velocity potentials due to the heave and pitch motion respectively.

In the inner region where $(y,z) = O(\varepsilon)$ and $x = O(1)$, the velocity potential is, to the leading order, the solution of the following boundary-value problem in space-fixed coordinates.

$$\nabla^2_{2D}\phi_j(y_0,z_0,t;x_0) = 0 \ , \ -\infty < y_0 < \infty, \ z_0 \le 0; \tag{8}$$

$$\frac{\partial \phi_j}{\partial N}\bigg|_{\bar{S}(t)} = \dot{\xi}_j(t)n_j + U\xi_j(t)m_j \ , \tag{9}$$

$$\phi_{jtt}(y_0,0,t;x_0) + g\phi_{jz_0} = 0, \text{ for } j = 3,5, \tag{10}$$

where $\bar{S}(t)$ is the time-averaged ship's wetted surface profile at x_0=constant, $\vec{N}$ the two-dimensional unit vector normal to $\bar{S}(t)$, and the geometrical quantities n_j and m_j (j=3,5) become, to the leading order;

$$n_5 = -xn_3 + O(\varepsilon) \ , \tag{11}$$

$$m_3 = -n_2\bar{\phi}_{yz} - n_3\bar{\phi}_{zz} + O(\varepsilon) \ , \tag{12}$$

$$m_5 = -xm_3 + n_3 + O(\varepsilon) \ , \tag{13}$$

The heave and pitch motions of the ship are denoted by

$$\xi_3(t) = R_e(\xi_3^o e^{i\omega t}) \ , \tag{14}$$

$$\xi_5(t) = R_e(\xi_5^o e^{i\omega t}) \ , \quad i = \sqrt{-1} \tag{15}$$

where ξ_3^o and ξ_5^o are the complex heave and pitch amplitudes of the ship, respectively, and ω is the angular frequency.

Consider solving the inner problem on a control plane x_o=constant, where different x_o will correspond to different planes. If t^*=0 corresponds to the time when the ship pierces the plane x_o=0, and if x_o=constant characterizes the control plane in front of the bow at t=0 (Figure 1), then

$$x_o = (x + Ut - L/2, y, z) = (U(t-t^*), y, z) \tag{16a}$$

$$t^* = (x - L/2)/U \tag{16b}$$

where t^* evidently represents the relative time on the control plane since it was first pierced by the bow. The boundary conditions (9), expressed in terms of space-fixed coordinate system in plane x_o and relative time t^*, are therefore:

$$\frac{\partial \phi_3}{\partial N}(y_o, z_o, t^*; x_o)\Big|_{\bar{S}(t^*)} = \xi_3^o i\omega e^{i\omega x_o/U}\,[e^{i\omega t^*} n_3] + U\xi_3^o e^{i\omega x_o/U}[e^{i\omega t^*} m_3] \tag{17a}$$

$$\frac{\partial \phi_5}{\partial N}(y_o, z_o, t^*; x_o)\Big|_{\bar{S}(t^*)} = \xi_5^o i\omega e^{i\omega x_o/U}[-x e^{i\omega t^*} n_3] + U\xi_5^o e^{i\omega x_o/U}[e^{i\omega t^*} n_3] + U\xi_5^o e^{i\omega x_o/U}[-x e^{i\omega t^*} m_3] \tag{17b}$$

where $\bar{S}(t^*)$ is the intersection of $\bar{S}$ with the control plane. Let $\psi_j(t^*)$ and $\hat{\psi}_j(t^*)$ be the transient solutions of the initial boundary-value problem which satisfies the two-dimensional Laplace equation (8), subject to the unsteady free-surface condition (10) and the following hull boundary conditions on $\bar{S}(t^*)$

$$\psi_{3N}(t^*) = e^{i\omega t^*} n_3 \ , \tag{18a}$$

$$\psi_{5N}(t^*) = -x e^{i\omega t^*} n_3 \ , \tag{18b}$$

$$\hat{\psi}_{3N}(t^*) = e^{i\omega t^*} m_3 \ , \tag{18c}$$

$$\hat{\psi}_{5N}(t^*) = -x e^{i\omega t^*} m_3 \ . \tag{18d}$$

Since it was assumed that there was no radiation ahead of the ship, the initial condition for ψ_j and $\hat{\psi}_j$ as well as the associated free-surface elevation become identically zero. In terms of ψ_j and $\hat{\psi}_j$, the solution of the inner problem can now be expressed as:

$$\phi_3(y_o, z_o, t^*; x_o) = \xi_3^o i\omega e^{i\omega x_o/U} \psi_3(t^*) + U\xi_3^o e^{i\omega x_o/U} \hat{\psi}_3(t^*) , \tag{19a}$$

$$\phi_5(y_o, z_o, t^*; x_o) = \xi_5^o i\omega e^{i\omega x_o/U} \psi_5(t^*) + U\xi_5^o e^{i\omega x_o/U} \psi_3(t^*) + U\xi_5^o e^{i\omega x_o/U} \hat{\psi}_5(t^*) \tag{19b}$$

The principle task is therefore reduced to solving for the complex velocity potentials ψ_j and $\hat{\psi}_j$ (j=3,5), which have identical conditions, except for the hull boundary condition. Note that the effect of the control plane variable x_o is automatically absorbed in the $\exp(i\omega x_o/U)$ factor in (19), which reflects that each control plane has identical time histories of the hull shape $\bar{S}(t^*)$ and their solutions are related simply by a phase factor. From the practical viewpoint, this means that one "sweep" of the solution in relative time will generate the potential on the entire hull for all t.

III. Integral Equation for ψ_j and $\hat{\psi}_j$

Let us consider the initial boundary-value problem defined by

$$\nabla_{2D}^2 \phi(y_o, z_o, t^*; x_o) = 0, \quad -\infty < y_o < \infty, \ z_o \le 0; \tag{20}$$

$$\frac{\partial \phi}{\partial N}\Big|_{\bar{S}(t^*)} = f(t^*) \ , \tag{21}$$

$$\phi_{t^*t^*}(y_o, 0, t^*; x_o) + g\phi_{z_o} = 0 \ , \tag{22}$$

$$\phi(y_o, z_o, 0; x_o) = \phi_{t^*}(y_o, z_o, 0; x_o) = 0 \ , \tag{23}$$

where $\bar{S}(t^*)$ is the steady-state time-averaged boundary contour of the ship's wetted surface at x_o=constant, and $\bar{N}$ denotes the two-dimensional unit vector normal to $\bar{S}(t^*)$ in the y_o-z_o plane (see Figure 2). The linearized free-surface elevation $Y(y_o, t^*; x_o)$ is related to ϕ by:

$$Y(y_o, t^*; x_o) = -1/g\ \phi_{t^*}(y_o, 0, t^*; x_o) \ . \tag{24}$$

An integral equation for ϕ can be derived using Volterra's method. To accomplish this, it is necessary to introduce an unsteady Green function G of the form·

$$G(P,Q,t^*-\tau) = \log r/r_1 + H(P,Q,t^*-\tau) \quad , \quad (25)$$

where r is the distance between the field point $P = (y_0,z_0)$ and the source point $Q = (\eta,\zeta)$, r_1 the distance between the field point and the image of the source point $\bar{Q} = (\eta,-\zeta)$, and τ is a dummy time variable representing the instant G brought into existence. The function H is to be harmonic in the fluid domain and to be so constructed that

$$G_{\tau\tau}(P;\eta,0;t^*-\tau) + gG_\zeta = 0 \qquad (26)$$

$$G(P;\eta,0;0) = G_\tau(P;\eta,0;0) = 0 \qquad (27)$$

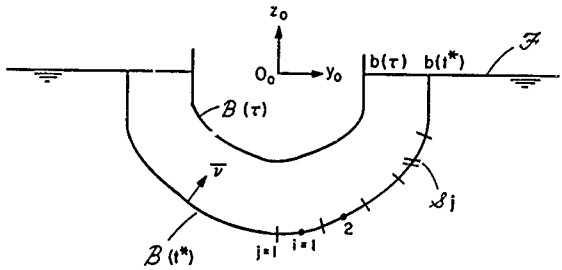


Figure 2. The Inner Problem near the Ship Hull

If we apply Green's second identity to $\phi_\tau(P,\tau)$ and G, and integrate the resulting expression from $\tau=0$ to $\tau=t^*$, then for $P \notin S(t^*)$,

$$2\pi[\phi(P,t^*)-\phi(P,0)] = \int_0^{t^*} d\tau \int_{S(t^*)} ds(Q)[\phi_\tau(Q,\tau)\times$$

$$G_\nu(P,Q;t^*-\tau)-\phi_{\nu\tau}G\,] + \int_0^{t^*} d\tau \int_{F(t^*)} d\eta \times$$

$$[\phi_\tau(\eta,0,\tau)G_\zeta - \phi_{\tau\zeta}G]_{\zeta=0} \qquad (28)$$

where $\partial/\partial\nu = \vec{N}\cdot(\partial/\partial\eta, \partial/\partial\zeta)$, and F is the undisturbed free surface. By (22), (24), and (26), the bracketed quantity evaluated at $\zeta=0$ can be written as

$$[\phi_\tau G_\zeta - \phi_{\tau\zeta}G]_{\zeta=0} = -\frac{\partial}{\partial\tau}[1/g\ \phi_\tau G_\tau + \phi_\zeta G]_{\zeta=0}$$

$$= \frac{\partial}{\partial\tau}[YG_\tau - Y_\tau G]$$

which vanishes at the upper limit, $\tau=t^*$, because of (27). To avoid solving an integro-differential equation, we integrate the body terms by parts once. Hence

$$2\pi\phi(P,t^*) = 2\pi\phi(P,0) - \int_{S(t^*)} [\phi(Q,0)\frac{\partial}{\partial\nu} - \phi_\nu]\times$$

$$G(P,Q,t^*)ds - \int_{F(t^*)} [Y(\eta,0)G_\tau(P;\eta,0;t^*)$$

$$- Y_\tau G]d\eta + \int_{S(t^*)} [\phi(Q,t^*)\frac{\partial}{\partial\nu} - \phi_\nu]G(P,Q,0)ds$$

$$- \int_0^{t^*} d\tau \int_{S(t^*)} [\phi(Q,\tau)\frac{\partial}{\partial\nu} - \phi_\nu]H_\tau ds \qquad (29)$$

Also from Green's theorem

$$\int_0^{t^*} d\tau \int_{S(t^*)} [\phi(Q,\tau)\frac{\partial}{\partial\nu} - \phi_\nu]H_\tau ds$$

$$= \int_0^{t^*} d\tau \int_{S(\tau)} [\phi(Q,\tau)\frac{\partial}{\partial\nu} - \phi_\nu]H_\tau ds +$$

$$\{\int_{-b(t^*)}^{-b(0)} + \int_{b(0)}^{b(t^*)} d\eta[YH_\tau - \phi H_\zeta]_{\zeta=0}\} + \int_0^{t^*} d\tau \frac{db}{d\tau} \times$$

$$[\phi(b,0,\tau)[H_\zeta(P;-b,0;t^*-\tau) + H_\tau(P;b,0;t^*-\tau)]$$

$$- Y(b,\tau)[H_\tau(P;-b,0;t^*-\tau)+H_\tau(P;b,0;t^*-\tau)]] \qquad (30)$$

where the symmetry of the profile is used;

$\phi(-b,0,\tau) = \phi(b,0,\tau)$ and $Y(-b,0,\tau) = Y(b,0,\tau)$.

The equation (29) is almost in the same form as one obtained by Yeung (1981) in his problem

related to the transient motion of a two-dimensional cylinder.

We shall now explain the physical nature of the various inhomogeneous terms in (29). Let

$$L[\phi] = 2\pi\phi(P,t^*) - \int_{S(t^*)} \phi(Q,t^*)G_\nu(P,Q,0)ds$$

$$- \int_0^{t^*} d\tau \int_{S(\tau)} \phi(Q,\tau)H_{\tau\nu}(P,Q,t^*-\tau)ds -$$

$$\left\{ \int_{-b(t^*)}^{-b(0)} + \int_{b(0)}^{b(t^*)} d\eta[YH_\tau - \phi H_\zeta]_{\zeta=0} \right\} - \int_0^{t^*} d\tau \frac{db}{d\tau} \times$$

$$\{\phi(b,0,\tau)[H_\zeta(P;-b,0;t^*-\tau) + H_\zeta(P;b,0;t^*-\tau)]$$

$$- Y(b,\tau)[H_\tau(P;-b,0;t^*-\tau) + H_\tau(P;b,0;t^*-\tau)]\}$$

(31)

The potential on the control plane at relative time t^* can be decomposed into a sum of three separate effects as follows:

$$L[\phi_B] = -\int_{S(t^*)} \phi_\nu(Q,t^*)G(P,Q,0)ds$$

$$+\int_0^{t^*} d\tau \int_{S(\tau)} \phi_\nu(Q,\tau;x_0)H_\tau(P,Q,t^*-\tau)ds \quad (32a)$$

$$L[\phi_{F_1}] = \int_{F(t^*)} Y(\eta,0,0)H_\tau(P;\eta,0;t^*)d\eta \quad (32b)$$

$$L[\phi_{F_2}] = \int_{F(t^*)} Y_\tau H(P;\eta,0;t^*)d\eta + 2\pi\phi(P,0)$$

$$- \int_{S(t^*)} [\phi(Q,0)\frac{\partial}{\partial\nu} - \phi_\nu] G(P,Q,t^*)ds$$

$$= - \int_{F(t^*)} \phi(\eta,0,0)H_{\tau\tau}(P;\eta,0;t^*)d\eta \quad (32c)$$

The component ϕ_B is evidently the fluid motion in the control plane, x_0=constant, generated by the body boundary condition for $t^* \geq 0^+$, assuming no previous disturbances existed in the fluid. In other words, the first term of this component represents the fluid motion generated by the instantaneous hull boundary condition at t^*, while the second term represents the *memory* effects on the control plane generated by the hull boundary conditions at different times $\tau(0^+ \leq \tau \leq t^*)$, during the passage of the ship's wetted surface profile through the control plane. ϕ_{F_1} describes the fluid motion in the presence of the ship due to an *initial* free-surface elevation on the control plane and its subsequent evolution. ϕ_{F_2} describes the corresponding fluid motion due to an initial velocity on the free surface. The simplification on the right-hand side of (32c) is obtained by using Green's theorem and recognizing that $\phi(P,0)$ corresponds to a potential field induced by $Y_\tau(\eta,0)$ on ζ=0. Thus, the combination of ϕ_{F_1} and ϕ_{F_2} represents essentially the 'diffraction' potential due to the presence of the ship which moves with constant forward velocity U, during the evolution of a Cauchy-Poisson wave system.

For the problem at hand, we have assumed that the fluid is initially at rest and that there is no radiation ahead of the ship; $\kappa = \omega U/g > 1/4$, there exist no disturbances upstream except an exponentially decaying one (Wehausen and Laitone, 1960). Thus, it is only necessary to solve for ϕ_B, whose subscript will be omitted henceforth. An integral equation for ϕ on $S(t^*)$ can be readily obtained by letting P approach $S(t^*)$. The net effect is that the factor 2π in (31) is now replaced by π. If we define

$$\hat{L}[\phi] = \pi\phi(P,t^*) - \int_{S(t^*)} \phi(Q,t^*)G_\nu(P,Q,0)ds$$

$$- \int_0^{t^*} d\tau \int_{S(\tau)} \phi(Q,\tau)H_{\tau\nu}(P,Q,t^*-\tau)ds -$$

$$\left\{ \int_{-b(t^*)}^{-b(0)} + \int_{b(0)}^{b(t^*)} d\eta[YH_\tau - \phi H_\zeta]_{\zeta=0} \right\} - \int_0^{t^*} d\tau \frac{db}{d\tau} \times$$

$$\{\phi(b,0,\tau)[H_\zeta(P;-b,0;t^*-\tau) + H_\zeta(P;b,0;t^*-\tau)]$$

$$- Y(b,\tau)[H_\tau(P;-b,0;t^*-\tau) + H_\tau(P;b,0;t^*-\tau)]\}$$

(33)

then the integral equation for ϕ on $S(t^*)$ is

$$\hat{L}[\phi] = -\int_{S(t^*)} f(t^*)G(P,Q,0)ds$$

$$-\int_0^{t^*} d\tau \int_{S(\tau)} f(\tau)H_\tau(P,Q,t^*-\tau)ds \quad (34)$$

Equation (34) must be solved for $t^*(0^+ \leq t^* \leq t_e^*)$, where t_e^* corresponds to the relative time at which the stern of the ship passes through the control plane.

The unsteady Green function is available from Finkelstein (1957). If we introduce the complex variables $Z = y + iz$ and $Z' = \eta + i\zeta$, with $i = \sqrt{-1}$, we can write

$$G(P,Q,t^*) = Re[\log(Z-Z') - \log(Z-\bar{Z}')$$

$$-2\int_0^\infty \frac{dk}{k}(1-\cos\sqrt{gk}\,t^*)e^{-ik(Z-\bar{Z}')}] \quad (35)$$

where the overhead bar denotes the complex conjugate and the *Re* stands for the real part of the expression. From (35) it is evident that

$$G(P,Q,0) = \log r/r_1 \tag{36}$$

which represents the flow in an infinite fluid about a two-dimensional cylinder described by the profile of the ship on the plane x_0=constant, and its image above the free surface. This is compatible with the first condition in (34). The "memory" kernels H_τ and H_ζ are given by the expression:

$$H_\tau(P,Q,t^*-\tau) = Re\{2\int_0^\infty \frac{dk}{k}\sin\sqrt{gk}(t^*-\tau)e^{-ik(Z-\bar{Z}')}\} \tag{37}$$

$$H_\zeta(P,Q,t^*-\tau) = -Im\{2\int_0^\infty \frac{dk}{k^2}[1-\cos\sqrt{gk}(t^*-\tau)]\times e^{-ik(Z-\bar{Z}')}\} \tag{38}$$

where *Im* stands for the imaginary part of the expression.

IV. Numerical Solution of the Unsteady Inner Problem

The numerical solution of the integral equation (34) is sought at discrete instances of relative time t_k^*, k=0, 1,2,..., with $t_0^* = 0^+$. To facilitate the evaluation of the boundary integrals, we employ a polygonal representation of $S(t^*)$ by defining a set of grid points $(\eta_j^{(k)}, \zeta_j^{(k)})$, j = 1,2,..., N + 1, which are joined successively by straight-line segment designated here as $S_j^{(k)}$, j = 1,2,..., N (Figure 2). Let $\phi_i^{(k)}$ and $f_i^{(k)}$ be the "spatial-average" of the potential and the local normal velocity of the ship profile on $S_i^{(k)}$ at t_k^*. Using the notation introduced, we can now write (34) as

$$\pi\phi_i^{(k)} - \sum_{j=1}^{N}\phi_j^{(k)}\alpha_{ij} + \sum_{j=1}^{N} f_j^{(k)}\beta_{ij} = A_i^{(k)}, \qquad i = 1,2\ldots, N \tag{39}$$

where all memory terms have been transposed to the right-hand side of (39). The coefficients α_{ij} and β_{ij} are integrals associated with the terms $G_\nu(P,Q,0;x_0)$ and $G(P,Q,0;x_0)$ along $S_j^{(k)}$ respectively. Their treatment is well known (see, e.g. Frank, 1967). By definition, the memory integral $A_i^{(k)}$, as observed at the i-th control point $P_i^{(k)}$, where (34) is satisfied, is given by the expression

$$A_i^{(k)} = \int_0^{t_k^*} d\tau\{\sum_{j=1}^{N}\int_{S_j(\tau)}[\phi(Q,\tau;x_0)\frac{\partial}{\partial\nu} - f(Q,\tau;x_0)]\times H_\tau(P_i,Q,t_k^*-\tau;x_0)ds(Q) + \int_0^{t_k^*} d\tau \frac{db}{d\tau}\times\{[\phi H_\zeta - \gamma H_\tau]_{\eta=-b} + [\phi H_\zeta - \gamma H_\tau]_{\eta=b}\} \tag{40}$$

It was found that H_τ and H_ζ could oscillate very rapidly, particularly when P_i is close to the free surface and $t_k^*-\tau$ is large, while both ϕ and f may be relatively slow-varying function of time (Yeung, 1981). Generally speaking, the term associated with the infinite-frequency kernel is more important than $A_i^{(k)}$ when $P_i^{(k)}$ is near the bottom of the ship profile, and the opposite is true when $P_i^{(k)}$ is near the free surface. This is congruent to the fact that the bottom of the ship experiences less wave motion than the sides.

If the time step is chosen so that ϕ and f do not change rapidly within the time step, it is possible to integrate out the oscillatory parts in the integrand as follows:

$$A_i^{(k)} = \sum_{m=1}^{k}\sum_{j=1}^{N}[\bar{\phi}_j^{(m)}\gamma_{ij}^{(m)} - \bar{f}_j^{(m)}\lambda_{ij}^{(m)}] + \sum_{m=1}^{k}\overline{\frac{db}{d\tau}}^{(m)}[\bar{\phi}_o^{(m)}\gamma_{io}^{(m)} - \bar{\gamma}_o^{(m)}\lambda_{io}^{(m)}] \tag{41}$$

where

$$\begin{matrix}\gamma_{ij}^{(m)}\\ \lambda_{ij}^{(m)}\end{matrix} = \int_{t_{m-1}^*}^{t_m^*} d\tau \int_{S_j(\tau)} ds(Q) \begin{matrix}H_{t\nu}(P_i,Q,t_k^*-\tau;x_o)\\ H_\tau(P_i,Q,t_k^*-\tau;x_o)\end{matrix} \tag{42a}$$

$$\begin{matrix}\gamma_{io}^{(m)}\\ \lambda_{io}^{(m)}\end{matrix} = \int_{t_{m-1}^*}^{t_m^*} d\tau \begin{matrix}H_\zeta(P_i;-b,0;t_k^*-\tau;x_o)+H_\zeta(P_i;b,0;t_k^*-\tau;x_o)\\ H_\tau(P_i;-b,0;t_k^*-\tau;x_o)+H_\tau(P_i;b,0;t_k^*-\tau;x_o)\end{matrix} \tag{42b}$$

where $\bar{\phi}_o^{(m)}$ and $\bar{\gamma}_o^{(m)}$ are the "time-averaged" velocity potential and the free-surface elevation at the intersection of the ship profile with the undisturbed free-surface. A convenient choice of the time-averaged values is simply $[\phi^{(m-1)} + \phi^{(m)}]/2$, $[f^{(m-1)} + f^{(m)}]/2$, and $[\gamma^{(m-1)} + \gamma^{(m)}]/2$. This approximation implies an implicit dependence of $A_i^{(k)}$ on the unknown values of $\phi^{(k)}$ and the known values of $f^{(k)}$ at t_k^*; a dependence which, strictly speaking, is absent in (40) since $H_\tau(P_i,Q,0;x_0) = 0$. In practice, it was found that the effects due to these implicit terms are negligible. Therefore, we now formally have

$$\pi\phi_i^{(k)} - \sum_{j=1}^{N}\phi_j^{(k)}(\alpha_{ij} - \gamma_{ij}^{(k)}/2) + \sum_{j=1}^{N} f_j^{(k)}(\beta_{ij} - \lambda_{ij}^{(k)}/2) - \phi_o^{(k)}\overline{\frac{db}{d\tau}}^{(k)}[\gamma_{io}^{(k)}/2 + \lambda_{io}^{(k)}/g\Delta t_k] = \sum_{m=1}^{k-1}\sum_{j=1}^{N}[\bar{\phi}_j^{(m)}\gamma_{ij}^{(m)} - \bar{f}_j^{(m)}\lambda_{ij}^{(m)}]$$

$$+ 1/2 \sum_{j=1}^{N} [\phi_j^{(k-1)} Y_{ij}^{(k)} - f_j^{(k)} \lambda_{ij}^{(k)}]$$

$$+ \sum_{n=1}^{k-1} \frac{\overline{db}^{(n)}}{dt} [\bar{\phi}_o^{(n)} Y_{io}^{(n)} - \bar{Y}_o^{(n)} \lambda_{io}^{(n)}]$$

$$+ \phi_o^{(k-1)} \frac{\overline{db}^{(k)}}{dt} [Y_{io}^{(k)}/2 - \lambda_{io}^{(k)}/g\delta t_k] \qquad (43)$$

where all known quantities are transposed to the right-hand side. As expected, the major computation efforts are in the evaluation of the kernels, Y_{ij}, λ_{ij}, Y_{io}, and λ_{io}, and an efficient scheme based on the use of complex error function integrals was used. More details can be found in Yeung (1981).

The evaluation of f_j associated with m_3 is not a trivial problem because m_3 is defined in terms of double-derivatives of the steady-state perturbation potential $\bar{\phi}$ through (12). Since the proper way to evaluate m_3 exactly is not available at this time (this is the classical non-linear steady-state wave-resistance problem), the contributions due to m_3 were not included in the present calculation.

V. Hydrodynamic Force and Moment

We consider the unsteady hydrodynamic pressure forces acting on the ship hull, with the usual assumption that the oscillatory motions of the ship and the fluid are small. If one makes use of the inner potential (19) and the unsteady Bernoulli equation, the following expression for the linearized hydrodynamic pressure $p(y,z,t;x)$ can be obtained (Newman, 1978):

$$p(y,z,t;x) = -\rho(\phi_t + \vec{W} \cdot \nabla\phi + 1/2\, \vec{a} \cdot \nabla W^2)_{\bar{s}} \qquad (44)$$

The last term in (44) gives an additional buoyancy force to the hydrostatic restoring force, which is due to the unsteady motion of the ship within the steady pressure field. Since we are now interested in the linearized unsteady pressure forces associated with the added-mass and damping, we will use (44) without the last term. Following the conventional definition of added-mass and damping coefficients, we can write the hydrodynamic pressure force and moment in a form:

$$F_i(t) = \iint_S p n_i ds = -\rho \iint_S (\phi_{jt} + \vec{W} \cdot \nabla\phi_j) n_i ds$$

$$= -\sum_j (a_{ij} + b_{ij}/i\omega)\, \ddot{\xi}_j(t), \quad \begin{matrix} i = 3,5 \\ j = 3,5 \end{matrix} \qquad (45)$$

where all moments are taken about midship. The quantities a_{ij} and b_{ij} are the added-mass and damping coefficients, corresponding to the force (moment) in the i-th direction due to j-th mode of motion. By using a theorem due to Tuck (Ogilvie and Tuck, 1969), equation (45) can be transformed to

$$F_i(t) = -\sum_j \rho \Big[\iint_{\bar{S}} (\phi_{jt} n_i - U\phi_j m_i) ds$$

$$- U \oint_C \phi_j (\vec{\tau} \cdot \vec{W})\, n_i dl \Big] \qquad (46)$$

Here the line integral along the waterline, where $\vec{\tau}$ is the unit vector tangent to the ship hull at the waterline, can be ignored by assuming that the angle between the waterline and x-axis is small. Thus

$$a_{ij} + b_{ij}/i\omega = \rho/\ddot{\xi}_j(t) \iint_{\bar{S}} (\phi_{jt} n_i - U\phi_j m_i) ds \qquad (47)$$

Now we shall "map" the inner potentials (19) in the x_o-t^* plane to those in the x-t plane:

$$\phi_3(y,z,t;x) = \xi_3^o i\omega e^{i\omega(t-t^*)} \psi_3(t^*) + U\xi_3^o \times$$

$$e^{i\omega(t-t^*)} \dot{\psi}_3(t^*) \qquad (48a)$$

$$\phi_5(y,z,t;x) = \xi_5^o i\omega e^{i\omega(t-t^*)} \psi_5(t^*) + U\xi_5^o \times$$

$$e^{i\omega(t-t^*)} \psi_3(t^*) + U\xi_5^o e^{i\omega(t-t^*)} \dot{\psi}_5(t^*) \qquad (48b)$$

where t^* is given in terms of U and x by (16b). The "mapping" of the potential in the x_o-t^* plane to the x-t plane is described schematically in Figure 3. From (47) and (48), the following expression for added-mass and damping coefficients can be derived after some calculations:

$$a_{33} + b_{33}/i\omega = z_{33}^{(n)} - (U/i\omega)[z_{33}^{(m)} - \hat{z}_{33}^{(n)}]$$

$$- (U/i\omega)^2 \hat{z}_{33}^{(m)}, \qquad (49a)$$

$$a_{53} + b_{53}/i\omega = z_{53}^{(n)} - (U/i\omega)\, z_{33}^{(n)}$$

$$- (U/i\omega)[z_{53}^{(m)} - \hat{z}_{53}^{(n)}]$$

$$- (U/i\omega)^2 [z_{33}^{(n)} + \hat{z}_{53}^{(m)}], \qquad (49b)$$

$$a_{35} + b_{35}/i\omega = z_{35}^{(n)} + (U/i\omega)\, z_{33}^{(n)}$$

$$- (U/i\omega)[z_{35}^{(m)} - \hat{z}_{35}^{(n)}]$$

$$- (U/i\omega)^2 [z_{33}^{(m)} + \hat{z}_{35}^{(m)}], \qquad (49c)$$

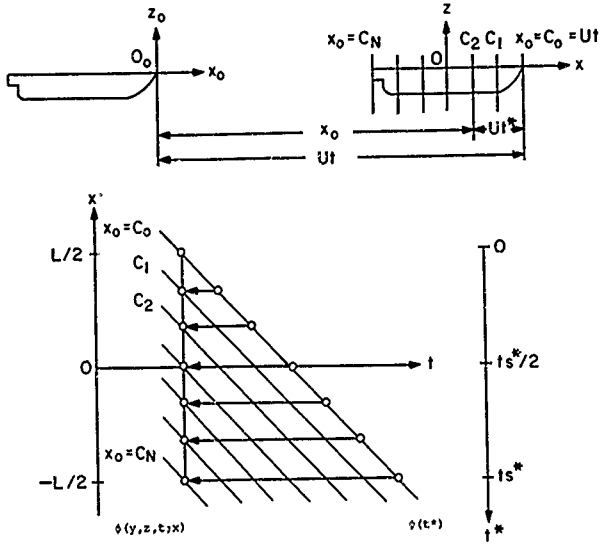


Figure 3. Mapping of the Potential from $x_o t^*$ plane to x-t plane

$$a_{55} + b_{55}/i\omega = z_{55}^{(n)} - (U/i\omega)[z_{25}^{(n)} - z_{53}^{(n)}]$$
$$- (U/i\omega)^2 z_{33}^{(n)} - (U/i\omega)[z_{55}^{(m)} - \hat{z}_{55}^{(n)}]$$
$$- (U/i\omega)^2[z_{53}^{(m)} + \hat{z}_{35}^{(n)} + \hat{z}_{55}^{(m)}] , \qquad (49d)$$

where

$$z_{ij}^{(n)} = F_i\left[\int_{B(t^*)} \phi_j(s,t^*) n_3 ds\right] \qquad \begin{matrix} i=3,5 \\ j=3,5 \end{matrix} \quad (50)$$

$$\hat{z}_{ij}^{(n)} = F_i\left[\int_{B(t^*)} \hat{\phi}_j(s,t^*) n_3 ds\right] \qquad \begin{matrix} i=3,5 \\ j=3,5 \end{matrix} \quad (51)$$

$$z_{ij}^{(m)} = F_i\left[\int_{B(t^*)} \phi_j(s,t^*) m_3 ds\right] \qquad \begin{matrix} i=3,5 \\ j=3,5 \end{matrix} \quad (52)$$

$$\hat{z}_{ij}^{(m)} = F_i\left[\int_{B(t^*)} \hat{\phi}_j(s,t^*) m_3 ds\right] \qquad \begin{matrix} i=3,5 \\ j=3,5 \end{matrix} \quad (53)$$

with F_i representing the integration along the hull (or the 'finite-time' transform with respect to t^*):

$$\begin{matrix} F_3 \\ F_5 \end{matrix}[f(t^*)] = \rho \int_{-L/2}^{L/2} \begin{pmatrix} 1 \\ -x \end{pmatrix} e^{-i\omega t^*} f(t^*) dx$$
$$= \rho U \int_0^{t_s^*} \begin{pmatrix} 1 \\ Ut^* - L/2 \end{pmatrix} e^{-i\omega t^*} f(t^*) dt^* , \qquad (54)$$

where the relative time t_s^* is evidently L/U. One should note that the end term contributions were not included in (49) with the assumption

that the ship has pointed ends. Here, equations (51)-(53) are terms representing interactions between the steady-state forward motion with the oscillatory motions.

At this point, it is of interest to compare the results presented here with some traditional theories for heave and pitch motions in head waves. In the intuitive approach, gradients of the steady-state forward-motion velocity field are neglected with the result that the only nonzero element of n_j (j=3,5) is $n_5 = n_3$, leading to $\hat{\phi}_3(t^*) = \hat{\phi}_5(t^*) = 0$.

$$a_{33} + b_{33}/i\omega = z_{33}^{(n)} , \tag{55a}$$

$$a_{53} + b_{53}/i\omega = z_{53}^{(n)} - (U/i\omega) z_{33}^{(n)} , \tag{55b}$$

$$a_{35} + b_{35}/i\omega = z_{35}^{(n)} + (U/i\omega) z_{33}^{(n)} , \tag{55c}$$

$$a_{55} + b_{55}/i\omega = z_{55}^{(n)} - (U/i\omega)[z_{35}^{(n)} - z_{53}^{(n)}] - (U/i\omega)^2 z_{33}^{(n)} . \tag{55d}$$

These equations are 'structurally' very similar to the strip theory results for heave and pitch motions derived by Salvesen et al. (1970). But our coefficients $z_{jj}^{(n)}$ in (55) are the quasi-three-dimensional ones which could implicitly involve the forward-speed effects via the free-surface condition (4) or (10), while those of traditional strip theories are their corresponding two-dimensional values without forward-speed effects. As mentioned in the Introduction, somewhat different results are obtained in the systematic perturbation analysis of Ogilvie and Tuck (1969), where some integral terms over the free-surface are added to the cross-coupling coefficients while the term proportional to $(U/\omega)^2$ in the moment is discarded as a higher order effect. The added-mass and damping coefficients in (55) are compared with the other strip theory results in Table 1.

We emphasize, in the Mathematical Formulation, to obtain the complex coefficients $z_{jj}^{(k)}$, k = 1,4, amounts to solving the two-dimensional unsteady boundary-value-problem only once with four different boundary conditions on the right-hand side of (43), followed by relatively trivial calculations of the integrals (50)-(54).

VI. Results and Discussion

The method of solution described in the present paper has been applied to calculate motion coefficients for a floating spheroid of beam-length ratio 1/6 and the Friesland class frigate hull (block coefficient 0.554), where experimental data are available (Loe and Paulling, 1966, and Smith, 1966). In each case we show the experiments, the strip theory predictions of Salvesen et al. (1970), and the computations based on the present formulation but neglecting the contribution from the potential $\hat{\phi}_3$.

The results for a floating spheroid are shown in Figure 4, for a Froude number of 0.264. In comparison with the experiments, the agreement between experiments and the present theory is generally favorable, with the noticeable exception of the damping coefficient b_{33} whose predictions by the strip theory and the present theory have been shown to be considerably higher than the experimental values. Even though the discrepancy between experiments and both theories precludes a definite judgement of the degree of improvement of the present theory relative to strip theory, the experiments generally support the present prediction at low and moderate frequencies.

Our subsequent computations are performed for the Friesland class frigate hull. The results in Figure 5 and Figure 6 are for Froude numbers of 0.15 and 0.35, respectively. It is seen from Figure 5 that, in comparison to the measurements, the present results agree very well with the experimental results except the cross-coupling coefficients b_{53}, a_{35}, and b_{35}, and give better agreement for the remaining coefficients than those from strip theory. Note that, even though the present calculation for the cross-coupling coefficients b_{35}, a_{35}, and b_{35} considerably underpredicts the experimental values, it resembles fairly well the trend of experimental results as functions of frequencies. Similar behavior can be noticed for the higher Froude number. In this case, unlike the lower Froude number case, the cross-coupling coefficient b_{53} has an excellent correlation with the experimental values.

These comparisons between the predicted and measured added mass and damping coefficients can be summarized as follows. In general, the diagonal coefficients a_{33}, b_{33}, a_{55}, and b_{55} together with the cross-coupling coefficient a_{53}, predicted by the present method and by strip theory, are shown to agree well with experimental data. But the present method, including the forward-speed effect on free surface condition, can be shown to provide a noticeable improvement over the strip theory in those coefficients. Due to large discrepancies between experiments and theoretical predictions, it is difficult to judge the degree of improvement of the present calculations relative to the strip theory predictions for the remaining cross-coupling coefficients b_{53}, a_{35}, and b_{35}. It is, however, shown that the present method resembles fairly well the experimental trend.

As mentioned earlier, the contributions due to the steady perturbation potential ϕ were not included in the present calculation. To improve the computation, it may be necessary to include these additional speed-dependent terms. Another possible explanation for these discrepancies is that the present method cannot reproduce the exact three-dimensionality, since no outer matching is used.

Table 1 Added-mass and damping coefficients

Coefficients	Salvesen, Tuck, and Faltinsen (1970) and Others	Ogilvie and Tuck (1969)	Present Formulation
$a_{33}+ b_{33}/i\omega$	$a_{33}^{(o)}+ b_{33}^{(o)}/i\omega$	$a_{33}^{(o)}+ b_{33}^{(o)}/i\omega$	$z_{33}^{(n)}$
$a_{53}+ b_{53}/i\omega$	$[a_{53}^{(o)}+ b_{53}^{(o)}/i\omega]$ $-(U/i\omega)[a_{33}^{(o)}+ b_{33}^{(o)}/i\omega]$	$[a_{53}^{(o)}+ b_{53}^{(o)}/i\omega]$ $-(U/i\omega)[a_{33}^{(o)}+ b_{33}^{(o)}/i\omega]$ $+(2i\rho\omega U/g)\int_F ds\ \phi^2$	$z_{53}^{(n)}- (U/i\omega)\ z_{33}^{(n)}$
$a_{35}+ b_{35}/i\omega$	$[a_{35}^{(o)}+ b_{35}^{(o)}/i\omega]$ $+(U/i\omega)[a_{33}^{(o)}+ b_{33}^{(o)}/i\omega]$	$[a_{35}^{(o)}+ b_{35}^{(o)}/i\omega]$ $+(U/i\omega)[a_{33}^{(o)}+ b_{33}^{(o)}/i\omega]$ $-(2i\rho\omega U/g)\int_F ds\ \phi^2$	$z_{35}^{(n)}+ (U/i\omega)\ z_{33}^{(n)}$
$a_{55}+ b_{55}/i\omega$	$[a_{55}^{(o)}+ b_{55}^{(o)}/i\omega]$ $-(U/i\omega)^2[a_{33}^{(o)}+ b_{33}^{(o)}/i\omega]$	$[a_{55}^{(o)}+ b_{55}^{(o)}/i\omega]$	$z_{55}^{(n)}- (U/i\omega)^2\ z_{33}^{(n)}$ $-(U/i\omega)[z_{35}^{(n)}- z_{53}^{(n)}]$

VII. Conclusions

In this paper, a new formulation, based on an integral-equation technique, for solving the radiation problem due to a moving ship, is presented. By taking a fixed frame of reference and by letting the ship pierce through a sequence of control planes, the forward-speed effect on the free-surface condition can be easily included without solving the complex three-dimensional problem, while it cannot be easily included in strip theory. Comparisons with experimental results indicate that this approach produces more satisfactory results than does strip theory for the hydrodynamic coefficients with forward speed.

Acknowledgement

We would like to thank Dr. P. Sclavounos of M.I.T. for valuable discussions during the course of this work.

Acknowledgement for support of this research is made to the Office of Naval Research under Task NR-62-611, and to the Naval Sea Systems Command General Hydromechanics Research Program administered by David W. Taylor Naval Ship Research and Development Center under Contract N00014-78-C-0110.

References

Chang, M.-S., "Computations of Three-Dimensional Ship Motions with Forward Speed", 2nd Int. Conf. on Numer. Ship Hydrodyn., Univ. California, Berkeley, pp. 124-135, 1977.

Chapman, R.B., "Numerical Solution for Hydrodynamic Forces on a Surface-Piercing Plate Oscillating in Yaw and Sway", 1st Int. Conf. on Numer. Ship Hydrodyn., Gaithersburg, Maryland, pp. 333-350, 1975.

Chapman, R.B., "Survey of Numerical Solutions for Free-Surface Problems", 2nd Int. Conf. on Numer. Ship Hydrodyn., Univ. California, Berkeley, pp. 5-16, 1977.

Faltinsen, O., "A Numerical Evaluation of the Ogilvie-Tuck Formulas for Added Mass and Damping Coefficients", J. Ship Res., Vol. 18, pp. 221-283, 1974.

Frank, W., "Oscillation of Cylinders in or below the Free Surface of Deep Fluids", NSRDC Rept. No. 2375, 1967.

Gerritsma, J., and Beukelman, W., "The Distribution of the Hydrodynamic Forces on a Heaving and Pitching Ship Model in Still Water", 5th Symp. Nav. Hydrodyn., 1964.

Gerritsma, J., and Beukelman, W., "Analysis of the Modified Strip Theory for the Calculation of Ship Motions and Bending Moments", International Shipbuilding Progress, Vol. 14, No. 156, pp. 319-337, 1967.

Korvin-Kroukovsky, B.V., and Jacobs, W.R., "Pitching and Heaving Motions of a Ship in Regular Waves", Trans. SNAME, Vol. 65, pp. 590-632, 1957.

Lee, C.M., and Paulling, J.R., "Measurements of Pressures on a Heaving Prolate Spheroid", Univ. California, Berkeley, Rept. No. NA-66-4, 1966.

Mays, J.H., "Wave Radiation and Diffraction by a Floating Slender Body", Ph.D Thesis, Massachusetts Institute of Technology, 1978.

Newman, J.N., "The Theory of Ship Motions", Adv. Appl. Mech., Vol. 18, pp. 221-283, 1978.

Newman, J.N., and Sclavounos, P., "The Unified Theory of Ship Motions", 13th Symp. Nav. Hydrodyn., 1980.

Ogilvie, T.F., and Tuck, E.O., "A Rational Strip Theory for Ship Motions", Part 1, Dept. Nav. Arch. Mar. Eng., Univ. Michigan, Rept. No. 13, 1969.

Salvesen, N., Tuck, E.O., and Faltinsen, O., "Ship Motions and Sea Loads", Trans. SNAME, Vol. 78, pp. 250-287, 1970.

Smith, W.E., "Equation of Motion Coefficients for a Pitching and Heaving Destroyer Model", Delft Shipbuilding Lab. Rept. No. 154, 1966.

St. Denis, M., and Pierson, W.J., "On the Motion of Ships in Confused Seas", Trans. SNAME, Vol. 61, pp. 280-354, 1953.

Tasai, F., and Newman, J.N., "The Coupled Damping Coefficients of Symmetric Ships", J. Ship Res., Vol. 5, No. 4, pp. 34-55, 1962.

Wehausen, J.V., and Laitone, E.V., "Surface Waves", Handbuch der Physik, Vol. 13, pp. 446-778, 1960.

Yeung, R.W., "The Transient Heaving Motion of Floating Cylinders", J. Engng. Math., 1981.

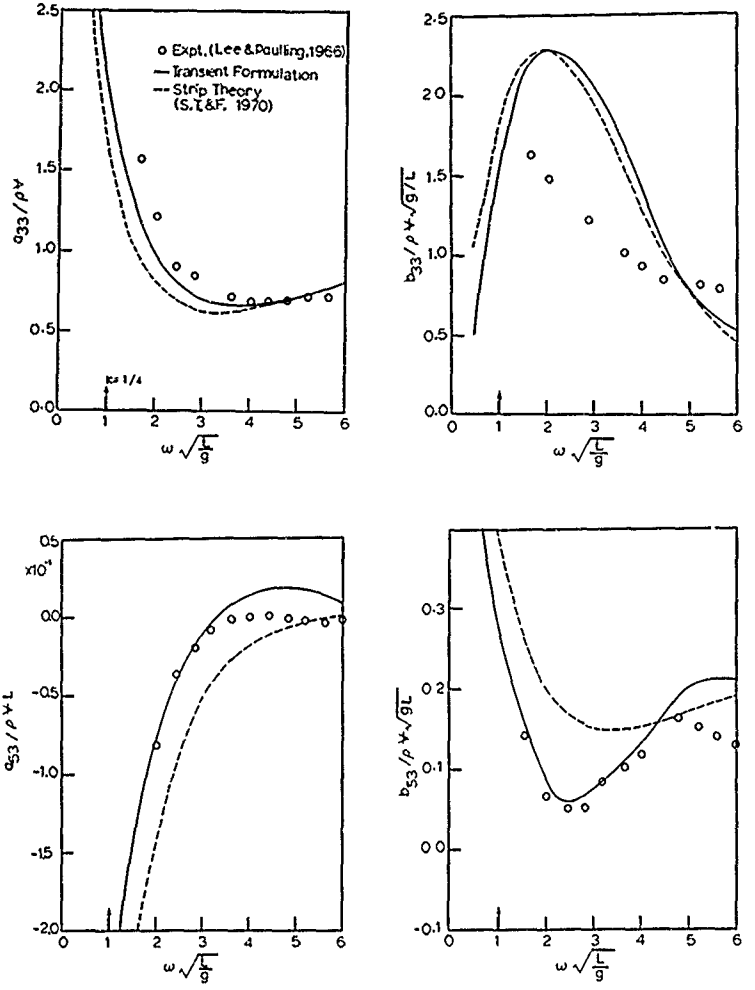


Figure 4. Added-mass and damping coefficients of a prolate spheroid (B/L = 1/6) at Fr = 0.246

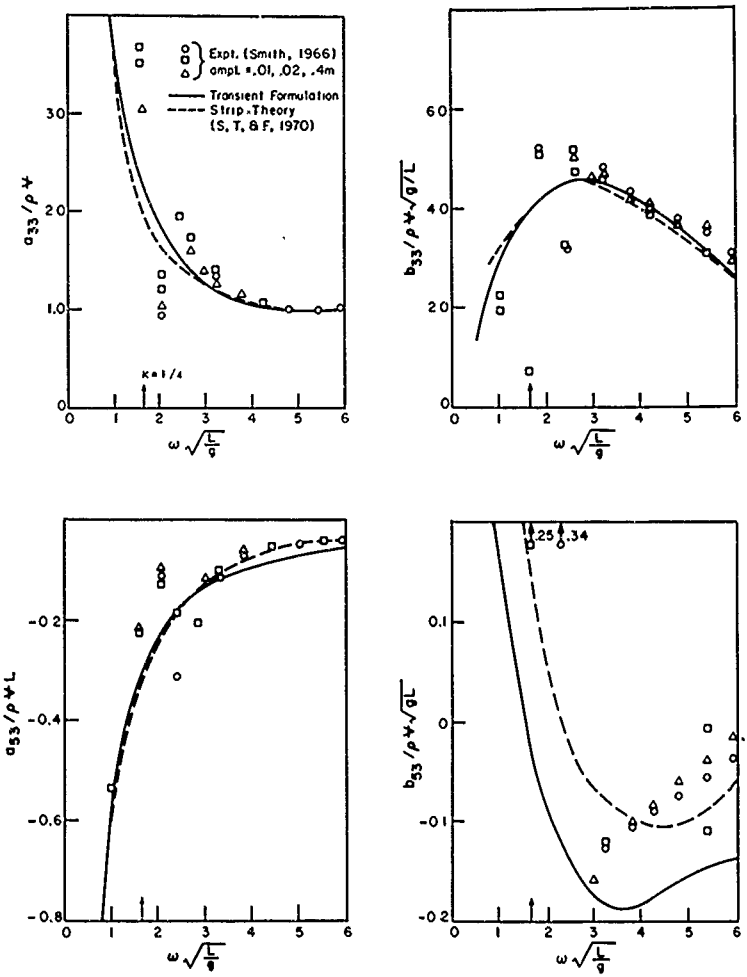


Figure 5. Added-mass and damping coefficients of a frigate hull (C_B = 0.55) at Fr = 0.15

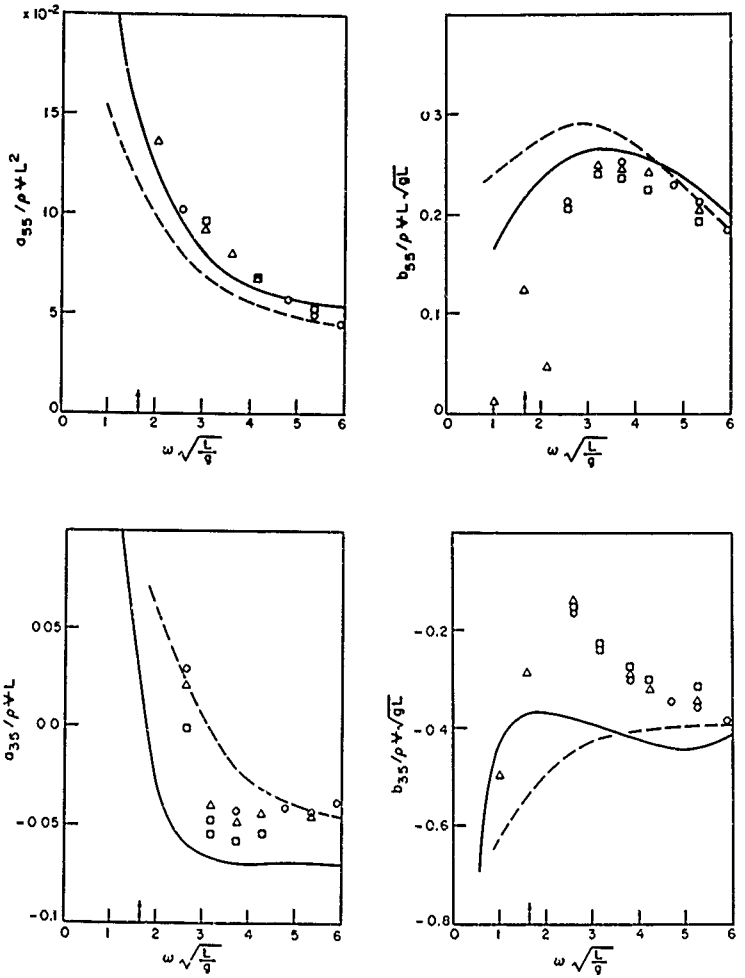


Figure 5. continued

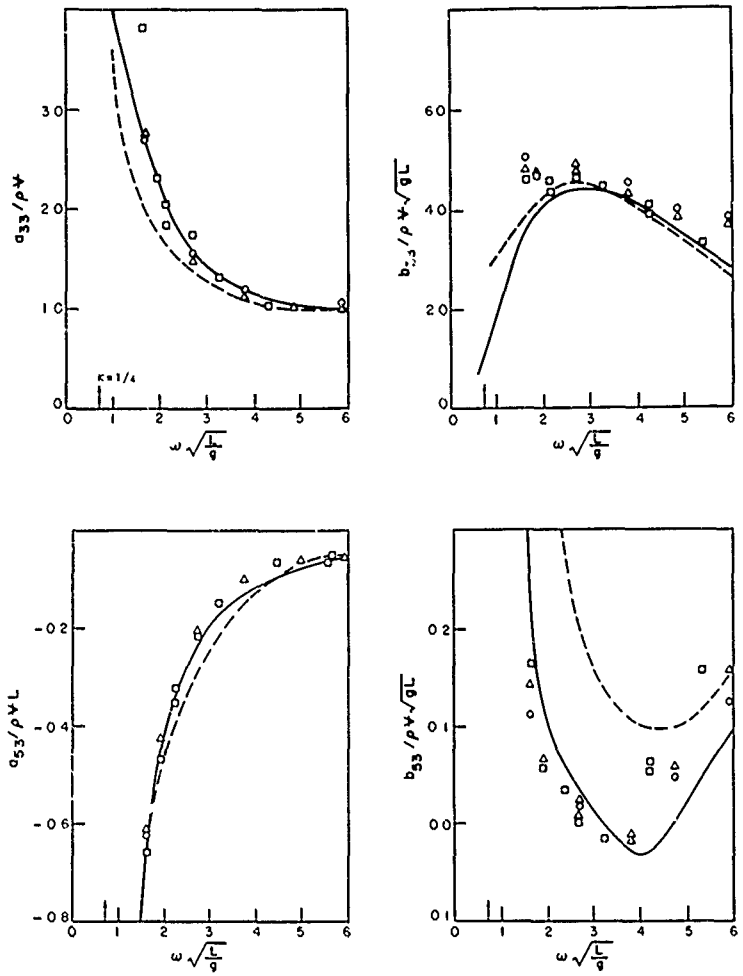


Figure 6. Added-mass and damping coefficients of a frigate hull (C_B = 0.55) at Fr = 0.35

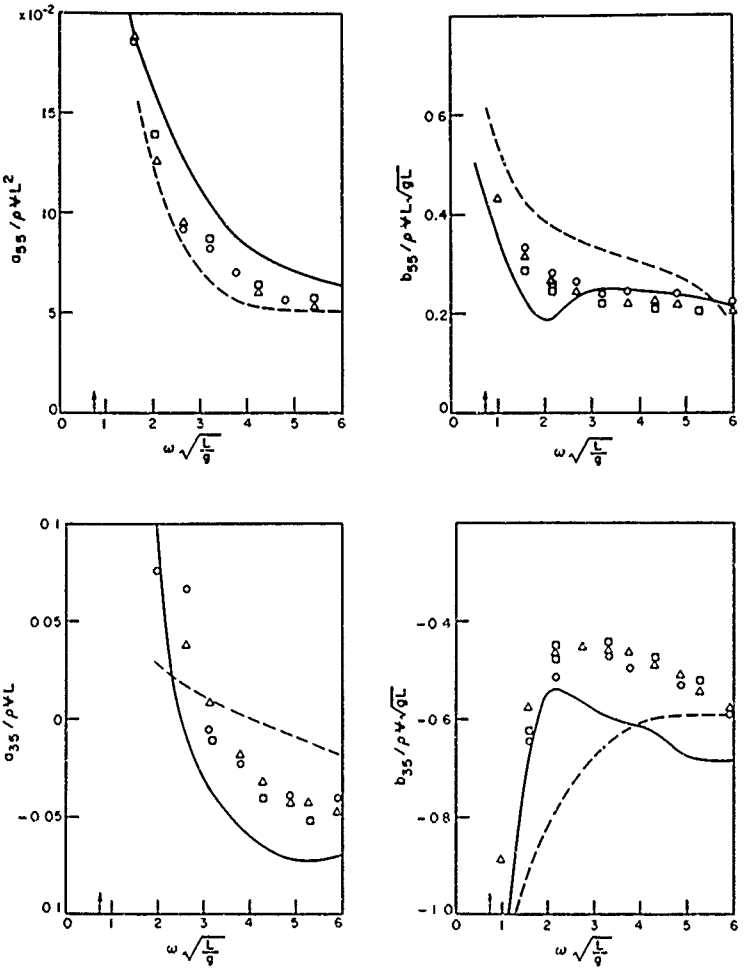


Figure 6. continued

FORCES AND MOMENTS IN THE RIGID CONNECTIONS BETWEEN A BARGE AND ITS TUG WITH FORWARD SPEED IN WAVE

J. Bougis
Laboratoire d'Hydrodynamique Navale
École Nationale Supérieure de Mécanique
1, rue de la Noë, 44072 Nantes Cedex (France)
and
P. Vallier
Ateliers et Chantiers de Bretagne - Alsthom Atlantique
Boulevard de la Prairie-au-Duc, Cedex n° 2, 44040 Nantes Cedex (France)

Abstract

We propose in this paper a 3D method to compute forces and moments in the rigid connections between the two parts of an ocean going tug-barge system.

As the relative movements of the tug and its barge are small as compared to the motions in the waves,this physically complex problem is reduced to the determination of the potential of the flow around the immersed part of the two bodies together.Boundary conditions are linearized and calculated at the mean boundary position of each hull.

The total velocity potential is obtained by summing incident,diffraction and radiation velocity potentials.Each simple problem is resolved by a 3D integral method using a distribution of sources on the bodies.

When the motions in wave of the tug and barge are fixed,we can calculate the forces and moments on the tug (or the barge)and introduce connections forces and moments as unknowns.The very classic equation which binds these forces and relativedisplacements owing to stiffness matrix gives us the elements of movements between the two bodies.

The last step consists in calculating first the displacement and then the forces on each connection.

We have compared our numerical results to experimental results of a tug-barge system,obtained in David W.Taylor Naval Ship Research and Development Center.

I.General problems raised by tug-barges

The use of barges and tug-boats is not a new idea.However,the innovation was to place the tug at the aft.Part of the barge and to more or less connect it to the barge.Such idea enables to obtain an improved efficiency of the tug-barge assembly with respect to the other traditional towing solution using ropes or cables.The two main advantages to be obtained by the tug-barge system are a decrease of the resistance in operation,a better running stability and manoeuvrability.The two advantages have direct financial incidents on exploitation : energy costs reduced, barge rotation speed increased.

The differences between the various tug-barge systems depend on the mechanical particulars of the connection between the components of the assembly :

- the flexible system where the tug keeps all or part of its free motions with respect to the barge.
- the rigid system where the tug is embedded in a slot,the shape of which is adapted to the aft part of the barge.

The two systems present the same advantages and disadvantages as regards the agitation of the water in which the assembly is working :

- calm water (rivers,small lakes),simple pushing
- "sheltered" water (lakes,coastal waters) : flexible system where certain motions (lateral) are blocked. (soft lines)
- agitated waters (oceans,seas,wide lakes)integrated system.

The main problems met with are in connection with :

- manoeuvring problems (for example :disengagement of a tug "soft lines" to pass in simple towing)
- problems of structures : stresses due to swell on the connection system and on the structures of the barge and the tug.

The solution to this latter problem constitutes the object of present studies carried out at ACB.

In this paper we deal in particular with the rigid connection systems,in which the tug-barge assembly forms a conical system with respect to the forces due to swell.

The connection technique we wish to modelize is that patented by ACB.

This technique uses,for the connections between the tug and the barge,an assembly of hydraulically inflated rubber cushions connected to accumulators,enabling to absorb the pressure and contact surface variations during working operations.

The movements regarding this type of connection are of about a few millimetres.

Furthermore, the cushions have four advantages :

- a very easy fitting of the tug in the barge notch, as they can be deflated (resulting in the reduction of the manufacturing allowances)
- a quick setting (simple inflation and adjustment by hydraulic circuits)
- a possibility of adjustment of pressure, therefore of the forces and surface contacts.
- a possibility or damping or regulation by hydraulic accumulators.

Thanks to the aforesaid,it becomes easy to obtain sea trial results,as the only thing to do is to record the pressures in each cushion.

The cushions have a parallelepipedic shape (1000x1000x120cm)and a rigid tug-barge connection is comprised of about thirty cushions plus on longitudinal link (for example under the form or an articulated bar which will be prestressed by pressurization of the cushions).

The object of our study is therefore to calculate,in particular,the efforts applied on each cushion when the assembly in running in swell. So, it was suitable to use a hydrodynamical theory taking into account the running speed of the assembly in swell.

Besides, the dimensions of the barges used (low L/B ratio) as well the necessity to calculate the hydrodynamic efforts on the tug located at the aft part of the assembly forming one and only ship,bind us to use a three-dimensional hydrodynamic model (the end effects not being represented in the strip theory in spite of certain attemps of corrections)

Therefore, we present hereunder a calculation program,DYNAPLOUS 81,developed by the ENSM,using a traditional method to solve the problem of diffraction-radiation with running speed.

The program does not calculate the resistance to operation which will be taken into account only under the form of a constant torque applied by the tug propelling system on the connection.

II. General assumptions regarding the model and limits

The assumptions concern the mechanic and the hydrodynamic.

The mechanical basis of the DYNAPLOUS 81 program is that of the linear theory.The tug-barge assembly is regarded as a rigid package. The combined movements are very important with respect to the relative displacements.

The rigidity matrix of the connection is therefore assumed as practically infinite in a first step. This permits to solve the hydrodynamical problem for a single body.

The therefore try to find out the effects due to a sinusoidal swell,said of low amplitude, single float.

The program calculates the forced reply of the same frequence as that of excitation. The movements are also assumed of low amplitude and what we only do is to set up the conditions at the limits on the frame said as "medium" which is the frame corresponding to the ship at rest (hydrostatic equilibrium).We therefore obtain the linear equations of the movements.

Thereby,it is useless to try to find something else than a linear representation of the connection.

By the way,we shall note the importance of the assumption of linearity on the hydrostatic matrix.

Each bearing point (or cushion) of the connection, assumed as punctual, is modelized by a linearized displacement stiffness matrix given in a local frame.

No damping term relating to the connection is taken into account. This point could make the object of further studies.

In the rigid connections, the relative tug-barge displacements being very weak due to its design, the problems relative to the friction on the bearing may be disregarded.

We therefore see that the assumptions made on the connection do not restrict the use of the program to only the calculations of the forces on hydraulic cushions. It is even possible to thus take into account the local stiffness of the structure but which also need to be linearized.

III. Hydrodynamic problem

III.1. Notations and hypotheses

Let S be the surface of the hull (tug and barge together) and $\vec{n}$ its external normal vector.

SL is the free surface, C is the waterline and D is the whole fluid domain.

(0,x,y,z) is a moving system of axis binded to the mean position of the two bodies which translates with the uniform velocity $U.\vec{i}$ in a fixed frame. Oscillations are defined by the velocity $\vec{V}(t)$ and the angular velocity vector $\vec{\Omega}(t)$.

Incident wave is characterized by its incidence β, its pulsation ω and its amplitude a.

We shall assume the following hypotesises

(i) The fluid is almost perfect*, isovolume and its flow is irrotationnal ;
(ii)The incident wave has a small degree of steepness ;
(iii)The motions of the two bodies are small around their mean position.

---

* The general equation of the almost perfect fluid is $\frac{1}{\rho}\,\mathrm{grad}\,p = \vec{f} - \vec{\gamma} - 2\,\vec{\Omega} \wedge \vec{v}$ where ϵ is a very small positive time constant.

III.2. Boundary problem

These hypothesises imply the existence of a velocity potential function $\phi(M;t)$ in D. In the moving frame, the absolute potential is the solution of the following boundary problem (to collate 4)

$$\Delta\phi(M;t)=0 \quad \forall M \in D \tag{1}$$

$$\frac{\partial^2}{\partial t^2}\phi(M;t) - 2U\frac{\partial^2}{\partial t\partial x}\phi(M;t) + U^2\frac{\partial^2}{\partial x^2}\phi(M;t)$$

$$+ 2c\frac{\partial}{\partial t}\phi(M;t) - 2Uc\frac{\partial}{\partial x}\phi(M;t) + g\frac{\partial}{\partial z}\phi(M;t) = 0$$

$$\forall M \in SL \tag{2}$$

$$\lim_{z\to-\infty}\phi(M;t) = 0 \quad \forall M \in D \tag{3}$$

$$\frac{\partial}{\partial n}\phi(M;t) = \left[\vec{U} + \vec{V}(t) + \vec{\Omega}(t)\wedge\vec{OM}\right].\vec{n} \quad \forall M \in D \tag{4}$$

$$\lim_{|\vec{OM}|\to\infty}\left[\phi(M;t) - \phi_I(M;t)\right] = 0 \quad \forall M \in D \tag{5}$$

$$\phi_I(M;t) = -\frac{ag}{\sigma}e^{k_0 z}\cos\left[k_0(x\cos\beta + y\sin\beta) - \sigma t\right]$$

$$\forall M \in D \tag{6}$$

$$\omega = \sigma - Uk_0\cos\beta \quad \text{with } k_0 = \frac{\sigma^2}{g} \tag{7}$$

Let $\phi_P(M;t)$ be the velocity potential function defined by

$$\phi_P(M;t) = \phi(M;t) - \phi_I(M;t) \tag{8}$$

$\phi_P(M;t)$ must satisfy equations (1),(2),(3) and (5), and the equation (9) can be substitued to (4)

$$\frac{\partial}{\partial n}\phi_P(M;t) = \vec{U}.\vec{n} - \frac{\partial}{\partial n}\phi_I(M;t) + \left[\vec{V}(t)+\vec{\Omega}(t)\wedge\vec{OM}\right].\vec{n}$$

The different parts of the right-hand side characterize respectively :
(i) Neumann Kelvin problem, the solution $\phi_H(M;t)$ of which is not dependent on the time in the relative frame. Tus induces constant loads on the hull, the mean position of which is changed but this problem can be traited separately.
(ii) Diffraction problem, the solution of which is $\phi_D(M;t)$, $\phi_I(M;t)$ and $\phi_D(M;t)$ excite the ships with a sinusoïdale load of encounter pulsation ω. Thus, the bodies perform sinusoïdal oscillations of pulsation around their mean position.
(iii) Radiation problem in the six modes. Solutions $\phi_{Rj}(M;t)$ of these are linear functions of twelve constants (six amplitudes and six phases) We can solve the radiation problems for only six movements without phases, and we can deduce from same the results for a phase of $\pi/2$.

Therefore, we now only have to solve seven simple boundary problems : one for the diffraction and six for the radiation (one in each mode).

III.3. Determination of the motions

After having computed $\phi_D(M;t)$ and $\phi_{Rj}(M;t)$ $j \in [1,6]$ we can compute the pressure on the hull with lagrange linearized formula. Thus we obtain hydrodynamic coefficients and forces.

The Newton equation gives us a linear system of twelve equations whereas the motions of the two bodies together are the twelve unknowns.

III.4. Integral equation for the distribution of sources

The application of the third Green formula and the introduction of the Green function $G(M,M';t)$, give us an integral formulation of the potential function.

If we consider the particular case where the potential is continued and the normal velocity $\frac{\partial}{\partial n}\phi(M,t)$ only is discontinued on the boundary, thus we obtain the following expressions.

$$-\frac{1}{4\pi}\iint_S\left[\sigma^*(M')G^*(M,M') - \sigma^{**}(M')G^{**}(M,M')\right]dS(M')$$

$$-\frac{U^2}{4\pi g}\int_C\left[\sigma^*(M')G^*(M,M') - \sigma^{**}(M')G^{**}(M,M')\right](\vec{n}'.\vec{I}_x)dy' = \phi^*(M)$$

$$-\frac{1}{4\pi}\iint_S\left[\sigma^{**}(M')G^*(M,M') + \sigma^*(M')G^{**}(M,M')\right]dS(M')$$

$$-\frac{U^2}{4\pi g}\int_C\left[\sigma^{**}(M')G^*(M,M') + \sigma^*(M')G^{**}(M,M')\right](\vec{n}'.\vec{I}_x)dy' = \phi^{**}(M)$$

formulae in which $\sigma(M;t)$ is the discontinuity of the normal velocity with

$$\sigma(M;t) = \sigma^*(M)\cos\omega t + \sigma^{**}(M)\sin\omega t \tag{12}$$

$$\phi(M;t) = \phi^*(M)\cos\omega t + \phi^{**}(M)\sin\omega t \tag{13}$$

$$G(M,M';t) = G^*(M,M')\cos\omega t + G^{**}(M,M')\sin\omega t \tag{14}$$

Writing the normal velocity in each point of the hull, we obtain an integral equation where the unknown is the discontinuity $\sigma(M;t)$

Thus the superficial distribution of singularities, kinematically equivalent to the hull, is $\sigma(M,t)$. This distribution of sources satisfies the following integral equations.

$$-\frac{1}{4\pi}\iint_S\left[\sigma^*(M')\frac{\partial}{\partial n}G^*(M,M') - \sigma^{**}(M')\frac{\partial}{\partial n}G^{**}(M,M')\right]dS(M')$$

$$-\frac{U^2}{4\pi g}\int_C\left[\sigma^*(M')\frac{\partial}{\partial n}G^*(M,M') - \sigma^{**}(M')\frac{\partial}{\partial n}G^{**}(M,M')\right](\vec{n}'.\vec{I}_x)dy'$$

$$+\frac{1}{2}\sigma^*(M) = \frac{\partial}{\partial n}\phi^*(M) \tag{15}$$

$$-\frac{1}{4\pi}\iint_S\left[\sigma^{**}(M')\frac{\partial}{\partial n}G^*(M,M') + \sigma^*(M')\frac{\partial}{\partial n}G^{**}(M,M')\right]dS(M')$$

$$-\frac{U^2}{4\pi g}\int_C\left[\sigma^{**}(M')\frac{\partial}{\partial n}G^*(M,M') + \sigma^*(M')\frac{\partial}{\partial n}G^{**}(M,M')\right](\vec{n}'.\vec{I}_x)dy'$$

$$+\frac{1}{2}\sigma^{**}(M) = \frac{\partial}{\partial n}\phi^{**}(M) \tag{16}$$

The right-hand sides of these equations are given by the following formulae

$$\frac{\partial}{\partial n}\phi_D^*(M) = -\frac{\partial}{\partial n}\phi_I^*(M); \quad \frac{\partial}{\partial n}\phi_D^{**}(M) = -\frac{\partial}{\partial n}\phi_I^{**}(M) \quad (17)$$

$$\frac{\partial}{\partial n}\phi_{Rj}^*(M) = \vec{V}_{Ej}^*.\vec{n} \quad ; \quad \frac{\partial}{\partial n}\phi_{Rj}^{**}(M) = \vec{V}_{Ej}^{**}.\vec{n} \quad (18)$$

The integral equations will now be solved with a method of discretization. Let the hull be discretized with N panels. We shall assume that on each panel the density of singularity is constant. Thus we have a linear system of 2N equations with 2N unknowns (N σ^* and N σ^{**}).

III.5.Green function

The Green function of the diffraction-radiation whit forward speed is given by the following integral expression (to collate 4 and 13)

$$G(M,M';t) = \left\{\frac{1}{|\overrightarrow{MM'}|} - \frac{1}{|\overrightarrow{MM'_1}|}\right\}\cos\omega t \quad (19)$$

$$-\lim_{\varepsilon\to 0^+}\frac{1}{\pi i}\,\mathrm{Re}\left\{e^{i\omega t}\int_{-\pi/2}^{\pi/2}\frac{d\theta}{\cos\theta}\int_0^\infty \frac{e^{K(Z+Z'+i\Omega)}\,K\,dK}{(\omega-FK\cos\theta)^2-K+2i\varepsilon(\omega-FK\cos\theta)}\right\}$$

$$-\lim_{\varepsilon\to 0^+}\frac{1}{\pi i}\,\mathrm{Re}\left\{e^{-i\omega t}\int_{-\pi/2}^{\pi/2}\frac{d\theta}{\cos\theta}\int_0^\infty \frac{e^{K(Z+Z'+i\Omega)}\,K\,dK}{(\omega+FK\cos\theta)^2-K+2i\varepsilon(\omega+FK\cos\theta)}\right\}$$

expression in which

$$X = \frac{x}{l} \quad ; \quad Y = \frac{y}{l} \quad ; \quad Z = \frac{z}{l}$$

$$\hat{\omega} = \omega\sqrt{\frac{l}{g}} \quad ; \quad \hat{\varepsilon} = \varepsilon\sqrt{\frac{l}{g}} \quad ; \quad F = \frac{U}{\sqrt{gl}}$$

and $\Omega = (X-X')\cos\theta + (Y-Y')\sin\theta$

N' is the point symmetrical to M' in relation to the free surface.

This Green function satisfy the equations (1) (except in M'), (2), (3) and (5)

IV.EQUATIONS OF THE MECHANICS

IV.1.Combined movements

The movements of the tug and barge assembly are very wide with respect to the relative displacements. The regidity matrix of the connection is assumed as infinite for the resolution of the equations of the movement. Therefore

$$n_{\text{ }} = n_B = E \ll n_T, n_B \quad (20)$$

n_T = Tub displacement vector

n_B = Barge displacement vector

E = Relative displacement vector

The equation of the mechanics at 6 degrees of freedom is written for the assembly. All the torques are reduced to a same point O (Whatever a priori) :

$$\left[M+MA\right]_{T+B}\ddot{\vec{n}} + TA_{T+B}\dot{\vec{n}} + TH_{T+B}\vec{n} = \left[F_I+F_D\right]_{T+B}$$

The matricial system represents 12 equations with 12 unknown quantities (6 amplitudes and 6 phases)

$n = n_1,\ldots n_6$ Vector of the combined movements

$n_i = n_i^* \cos\omega t + n_i^{**}\sin\omega t$

The n_i^* and n_i^{**} are the unknown quantities

M inert mass matrix
MA added water mass matrix
TA Damping terms matrix
TH Hydrostatic matrix

F_i column vector of the Froude-Krilov excitation forces

F_D column vector of the diffraction excitation forces

The résolution of the equations (21) enable to fix vector n after having solved the hydrodynamical problems.

IV.2.Calculation of the connection efforts torque

Need only be to fix the connection torque between the barge and its tug, write down the equation of the mechanics for one of the two floats.

For the tug, we thus have :

$$\left[M+MA\right]_T\ddot{\vec{n}} + TA_T\dot{\vec{n}} + TH_T\vec{n} = \left[F_I+F_D\right]_T + F_{B+T} \quad (22)$$

F_{B+T} . Torque of the connection efforts exerted by the barge on the tug.

The equation (22) permits to calculate F_{B+T} as we know the displacement vector n

IV.3.Calculation of the relative movements

By virtue of relation (20) we now have a simple problem of decomposition of a torque on a elastic bearing system.

$$F_{B+T} = -K_{eq}\,E \quad (23)$$

K_{eq} : Equivalent stiffness matrix of the flexible connection of the assembly reduced to point O.

The connection is modelized by punctual flexible bearings points each one of the n bearings, an (Fig. 1) is defined by :

- $\vec{OA}_n$: position vector in the general frame
- k_n : Local displacement stiffness matrix
- P_n : Matrix of passage from the local frame of the bearing to the general frame.

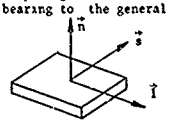


Figure 1 : Bearing (cushion)

$$K_n = \begin{bmatrix} k_{xx} & k_{xy} & k_{xz} \\ k_{yx} & k_{yy} & k_{yz} \\ k_{zx} & k_{zy} & k_{zz} \end{bmatrix} \qquad P_n = \begin{bmatrix} l_x & s_x & n_x \\ l_y & s_y & n_y \\ l_z & s_z & n_z \end{bmatrix}$$

From these data it is possible to calculate the stiffness matrix equivalent to point O :

$$K'_{eq} = \begin{bmatrix} \sum_n K_n & \sum_n K_n B_n^T \\ \sum_n B_n K_n & \sum_n B_n K_n B_n^T \end{bmatrix}$$

with $K_n = P_n \lambda_n P_n^{-1}$

and B_n : Vectorial product matrix of $\vec{OA}_n$ such as : $\vec{OA}_n \wedge \vec{E}_n = B_n \vec{E}_n$

It is therefore possible to calculate $\vec{E}$, relative displacement vector, with equation (23).

IV.4. Calculations of the efforts on each bearing

Knowing the relative displacement $\vec{E}$ in the general frame, it is possible to calculate the displacements on each bearing, and then the local efforts.

We have : $\vec{d}_n = P_n^{-1} \vec{E}_n$

$\vec{d}_n$: local displacement vector on bearing n

$\vec{F}_n$: local force vector on bearing n

Vectors $\vec{F}_n$ and $\vec{d}_n$ have three components as we simulate only punctual bearings.

V. RESULTS AND COMPARISON WITH MODEL TESTS

V.1. Choice of the tests

Our comparison between calculations and basin tests is based on the report intented for Maritime Administration, U.S. Department of Commerce. "Experimental research relative to improving the hydrodynamic performance of ocean going tub/barge systems".

This report is composed of four chapters and we mainly used Part B "Seaworthiness experiments" by Grant A. Rossignol.

In this report, experiments have been carried out on two pushed barge concepts
- first concept : rigidly connection
- second concept : articuled connection

In this paper we are only dealing with the first concept.

The tug and barge together shape a 60.000 T ship with a block coefficient of $C_B = 0.75$. The main characteristics of the pusher, of the barge and of the tug-barge system are sumed up in table 1.

In the model tests the tug and the barge was joined together at three points (N° 1,2 and 3 in Fig. 2). The centerline block gage arrangement

Particular	Symbol	Tug	Barge	T/B
Length P.P	LPP (m)	56,4	-	232
Length waterline	LWL (m)	53	204	235,9
Beam max.	B (m)	23,5	32	32
Draft mean	T (m)	10,67	10,67	10,67
Displacement	Δ (Tf)	5892	55068	60960

Figure 2 shows the tug-barge system.

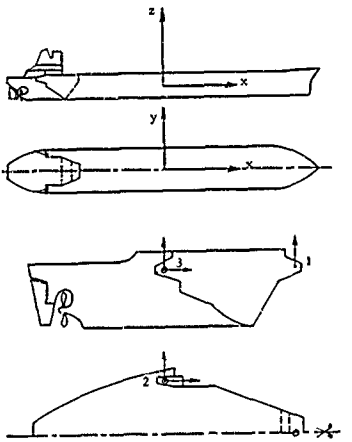


Figure 2

(N° 1) provides only vertical restraint. The other connections points are port (N°2) and starbvard (N°3) pins which provide total translatory restraint.

The locations of the three connection points and the accelerations measurement point are given in table 2.

The deatiled informations about model, connection, instrumentation are given in the mentionned report of the David W. Taylor Naval Ship Research and Development Center.

The measured variables necessary to our comparisons are :
- Heave of the overall concept LCG ; Z (fig 3)
- Pitch of the overall concept ; (fig 4)
- Roll of the overall concept ; (fig 5)
- Vertical acceleration of the tug pilot house; ZPH

- longitudinal acceleration of the tug pilot house ; XPH
- Vertical force between the tug and barge at the centerline (N°1) ; FVCL
- Vertical force between the tug and barge at the starboard pin (N°3) : FZS
- Vertical force between the tug and barge at the port pin (N°2) ; FZP
- Longitudinal force between the tug and barge at the starboard pin (N°3) ; FXS
- longitudinal force between the tug and barge at the port pin (N°2) ; FXP
- Transverse force between the tug and barge at the starboard pin (N°3) ; FYS
- Transverse force between the tug and barge at the port pin (N°2) ; FYP

From this measurements, the following results was computed by NSRDC :
- total vertical pin force between the tug and barge : FVPN : FZS + FZP (Fig. 9)
- total longitudinal pin force between the tug and barge : FLPN : FXS + FXP (Fig. 10)
- total transverse pin force between the tug and barge : FTPN : FYS + FYP (Fig. 11)
- Axial moment about the longitudinal axis between the tug and the barge (Roll moment) : ML = d/2 x (FZS - FZP) (Fig. 12)
- Axial moment about the vertical axis between the tug and barge (Yaw moment) : MV = d/2 (FXS - FXP) (Fig. 13)

Where d is the transverse distance between pin locations (d = 22,42 m)

	Connection points			Acceleration
	1 (m)	2 (m)	3 (m)	tug pilot house
X to A.P.	54.2	26.6	26.6	46.4
X to C.L.	0.	+ 11.2	- 11.2	0.
Z to B.L.	16.05	12.6	12.6	25.

The comparisons of the previous results and the computer program DYNAPLOUS 81 are only based on the regular wave experiments.

The tug barge system has been tested for a forward speed of 16 knots (the Froude number is equal to 0.171) at headings of 0, 45, 90, 180 and 225 degrees.

In the computer program the immersed part of the pusher has been discretized with 18 panels on the half hull, and the immersed part of the barge has been discretized with 44 panels on the half hull. The part of the two hulls between the bodies has not been taken into account to compute the hydrodynamic coefficients.
The hydrostatic particulars were calculated for the tug and barge separately and together equally for the wetted part of the tug.
The three connection joints of the tug/barge are modelised by elastic bearing strings in the same directions as those of the block gage arrangements (i.e chapter4). The stiffness characteristics are not important as the whole connection is isostatic. The program has run at the ACB computer center on a UNIVAC 1100/10.

V.2. Motions of the two bodies together

We present here only three movements (heave pitch and roll) because the experimental results was given only for these modes. Nevertheless the computer program gives the results for all the six modes in the same theoretical conditions.

The results of the movements are nondimensional. The amplitude of the heave response is divided by the wave amplitude a, and the amplitudes of the pitch and roll responses are divided by the product of the amplitude and the wave number k_o.

Figure 3 shows the tug-barge heave transfer function at various headings. This results gives the proof of a good agreement between the experiments and our numerical method for all the angles of incidence. Perhaps the difference between the results when β is equal to 225° and little λ/L_B, comes from natural frequency response which is always more stiff for the numerical results than for the experimental results.

Figure 4 shows the tug-barge pitch transfer function at various headings. This results show a fairly good accuracy in our results with experimental mesurements except to the angle of incidence β equal to 45°. The same remark, than the aforesaid, can be made here because the difference is localized around the natural frequency.

Figure 5 shows the tug-barge roll transfer function at various headings. Naturally, the difference between the motions calculated and mesured is sensible for two reasons. Firsthy the non - linear effects are not negligeable in this case, because the hemichrone roll appears for λ' equal to $(3/2)^2 \lambda$ (where λ is the wave-length of the natural frequency). Secondly the viscous effect are very important for this mode ; the computer program can take into account damping coefficient arising from the logarithmic decrement calculated from model tests result. Nevertheless we have not use this possibility for the present calculations.

V.3. Accelerations of the tug pilot house

We present in this chapter the vertical acceleration and the longitudinal acceleration of the tug pilot house.

The results of the accelerations are nondimensional. The amplitude of these accelerations are divided by the produit of the amplitude of the wave and the square of the encounter angular frequency.

Figure 6 shows the tug pilot house vertical acceleration transfer functions at various headings. This results proves a good correlation between the experiments and the numerical method except for the angle β equal to 45° that is a consequence of the results of the pitch motion and the same natural frequency remarks mentioned above is valid.

Figure 7 shows the tug pilot house longitudinal acceleration transfer function at various headings. This results do not permit to conclude

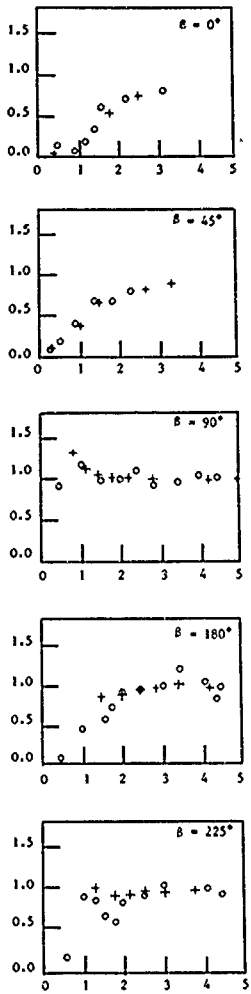


Figure 3 - Nondimensional Tug/Barge Heave Transfer Function versus Wavelength/Barge Length for the Tug/Barge at Various Headings.
o experimental results
+ numerical results

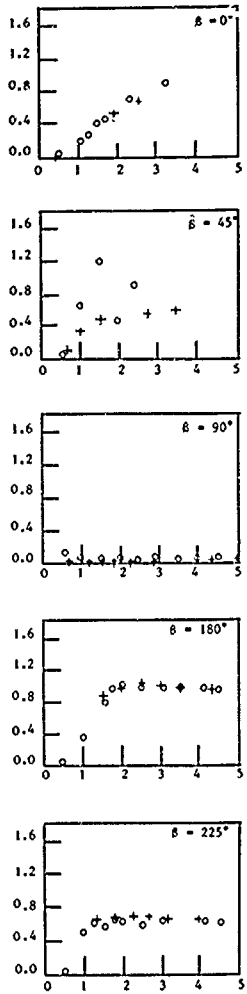


Figure 4 - Nondimensional Tug/Barge Pitch Transfer Function versus Wavelength/Barge Length for the Tug/Barge at various Headings
o experimental results
+ numerical results

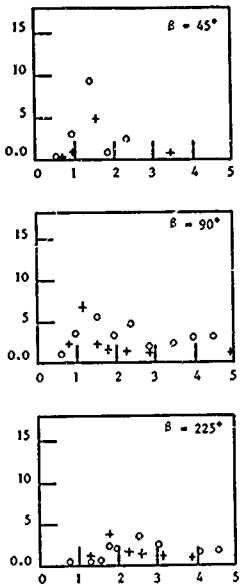


Figure 5 - Nondimensional Tug/Barge Roll transfer Function versus Wavelength/Barge Length for the Tug/Barge at Various Headings.

o experimental results
+ numerical results

because the values are very small and the precision of the plots is not fairly good.

V.4. Forces between the tug and barge

We present here the forces between the tug and barge for all the modes except the transversal moment.

The results of the forces and moments are nondimensional. The amplitude of the forces are multiplied by the barge lenght and divided by the product of the weight of the barge and the wave amplitude. The amplitude of the moments are divided by the product of the weight of the barge and the amplitude of wave.

Figure 8 shows the vertical centerline force transfer function at various headings. The comparison between the numerical results and the experimental results shows a fairly good relationship for this forces.

Figure 9 shows the vertical pin face transfer function at various headings. These results give the proof of a very good agreement between the experiments and calculations.

Figure 10 shows the longitudinal pin force transfer function at various headings. At first sight, the results seem to be very bad. Nevertheless the experimental tests for this component are very difficult because the longitudinal force is in the same direction as that of the forward speed and the problems of speed stability and added wave resistance are very important in this case as the model is self propelled.

Figure 11 shows the transverse pin force transfer function at various headings the comparison between the experiments and calculations is very good except for the natural frequency of rool at 90° of heading. In quartering sea, the difference between the test and the numerical points is probabily due to the steering control. In fact it is impossible to take into account, in the computer program, the directional instability of a real ship running in following seas.

Figure 12 shows longitudinal axial moment transfer function at various headings. Comparaison between experiments and calculations is very good for 90° and 225° of heading. A great difference appears for a angle of incidence of 45° in the range of λ/L_B around 1, as the for the previous results at same heading.

Figure 13 shows vertical axial moment transfer function at various headings. This results do not permit to conclude because the values are very small and the precision of the plots is not fairly good.

VI - ANALYSIS OF THE RESULTS

The previous comparisons between experimental and numerical results show a good relationship. The sensible differences occur for longitudinal pin force transfer function (fig. 10) and for the various peak responses throughout the experimental results.

We present hereunder some comments to explain these differences :
The real tug is fit into the barge afterbody with a 6 inch gap full scale. But the forebody shapes of the tug model are made to wedge tightly into the notch of the barge model (see. afore mentionned report phase II ; part A page 2)

This remark is very important for two reasons :
- firstly we must take the correct part of the hydrostatic force on the tug model.
We have made different calculations with the hydrostatics of the entire tug or only the after body wetted surface of the tug.
We have taken into account the problem of the hydrostatic couplings between two joint bodies
Some differences may occur because we do not know the exact configuration of seakeeping tests.

- Secondly in full scale the laws of the pressure variations in the clearance between tug and barge are very difficult to modelise but perhaps these effects are of second order in the

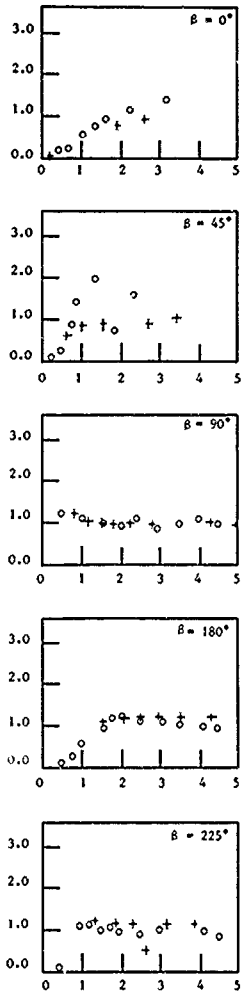


Figure 6 - Nondimensional Tug Pilot House Vertical acceleration Transfer Function versus wavelength/Barge Length for the Tug/Barge at Various Headings.
o experimental results
+ numerical results

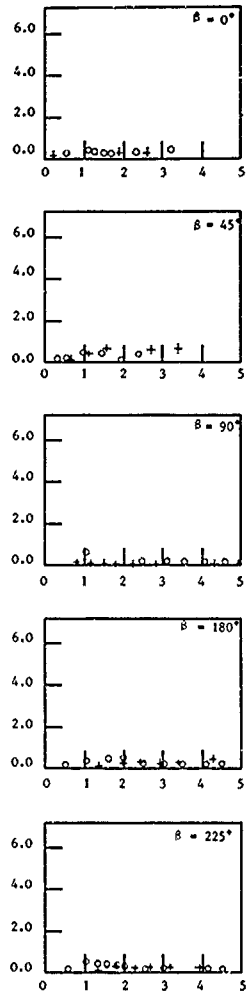


Figure 7 - Nondimensional Tug Pilot House longitudinal Acceleration Transfer function versus Wavelength/barge Length for the Tug/Barge at Various Headings.
o experimental results
+ numerical results

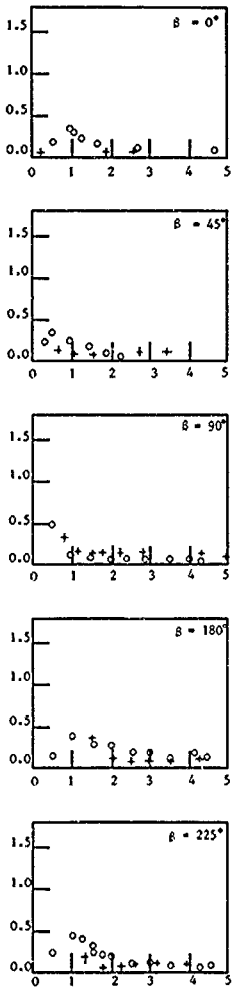


Figure 8 - Nondimensional Vertical Centerline Force Transfer Function Versus Wavelength/Barge Length for the Tug/barge at Various Headings.

o experimental results
+ numerical results

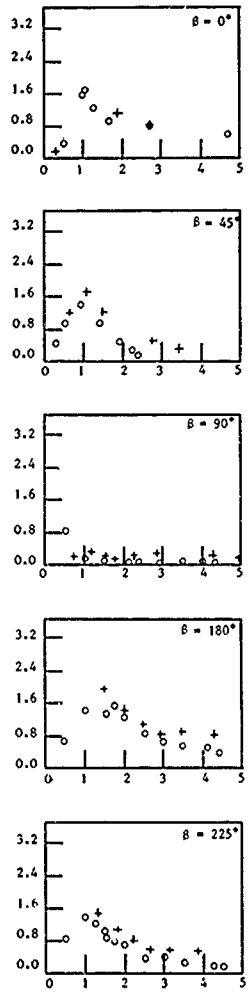


Figure 9 - Nondimensional Vertical Pin force Transfer Function versus Wavelength/ Barge Length for the Tug/Barge at Various Headings.

o experimental results
+ numerical results

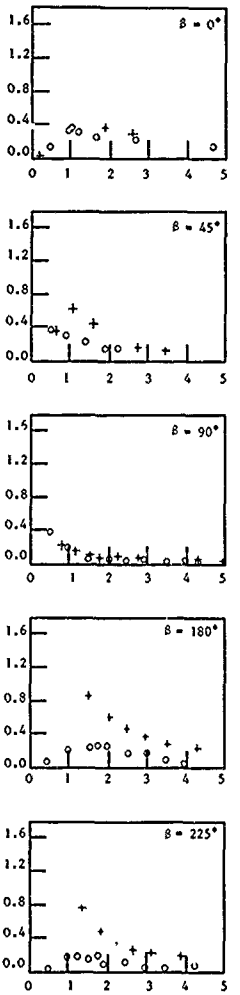


Figure 10 - Nondimensional Longitudinal Pin Force Transfer Function versus Wavelength/Barge Length for the Tug/Barge at Various Headings

o experimental results
+ numerical results

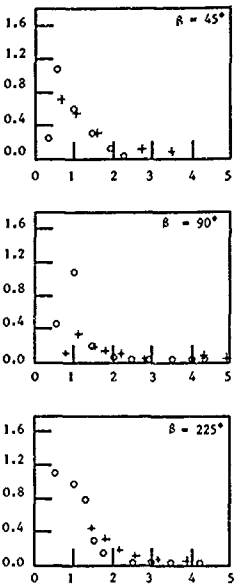


Figure 11 - Nondimensional Transverse Pin Force Transfer Function versus Wavelength/ Barge Length for the Tug/Barge at Various Headings

o experimental results
+ numerical results

calculation fo the forces.

An important difference between model tests and calculations are the different non-linearity effects. These are evident for the hydrostatic in particular for those on the tug only because its aft location.
The non-linear damping effects (for example due to viscosity) are not corrected in the program. This explains the difference in peak responses on roll.

The model was self-propelled and steered. This introcudes important differences between the conditions of the tests and calculations.

- firstly we have not taken in account the whole resistance at the forward speed. That could be made with a constant torque simulating the propulsation forces.

- Secondly we do not calculate the added resistance of ship with forward speed in waves. Studies about this 3 D problem have alreasy starded at E.N.S.M.

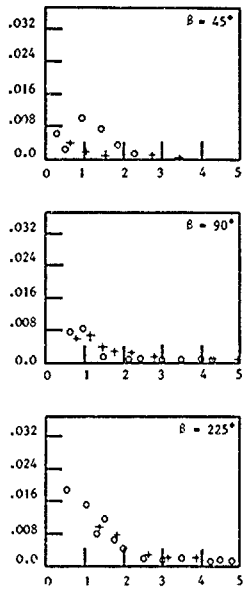


Figure 12 - Nondimensional Longitudinal Axial (Roll) Moment Transfer Function versus Wavelength/Barge Length for the Tug/Barge at Various Headings

o experimental results
+ numerical results

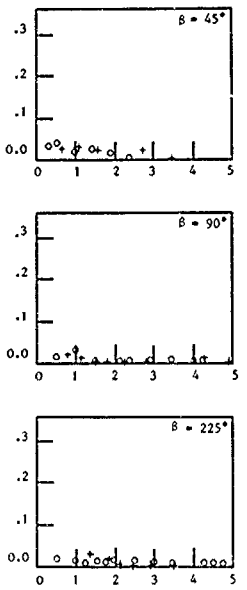


Figure 13 - Nondimensional Vertical Axial (Yaw) Moment Transfer Function versus Wavelength/Barge Length for the Tug Barge at Various Headings.

o experimental results
+ numerical results

- Thirdly the variation in immersion (or emmersion ?) of the propeller introduce distorsion effects on the measured forces.

- Fourthly the directionnal course stability in self-steered tests present serious difficulties particularly in following seas (the same problem is known in full scale).
These instabilities involve supplementary forces in roll and yaw.

All these reasons explains certain differences between measurements and calculations specially for the longitudinal pin force (see Fig. 10)

An indirect effect of the non-linearities are perhaps the hemichrone roll which appear in certain figures. In particular to our mind the peak responses at 45 degrees of heading forpitch (Fig.4), roll (Fig.5), tug pilot house vertical acceleration (Fig.6), vertical transversal forces and in the moments (Fig.8, 9, 10,11,12,13) are due to this previously mentionned effect.

This phenomenon due to the change in metacentric height with time is increased by the lack of bilge keels on the model which involve a small roll damping. In addition a coupling between heaving and rolling exist (See. Fig.3 ; secondary peaks for 0,45 and 90 degrees), this accentuate the variation in metacentric height and thus the hemichrone roll.

In connection with this phenomenon due to non-linearly roll responses, two other effects contribute probably to the differences between experiments and calculations at 45° , of heading

- firstly the induced non-linearity in pitch (the peak response in Fig.4 is very high)

- secondly the maximum excitation forces occur for $\lambda / LWL \approx 1$ or $\lambda / LB \approx 1,14$ and are in the same frequency game than the hemichrone roll.

In spite of these remarks on the whole the agreement between theory and experiment is correct.

VII. POSSIBLE EXTENSION OF THE METHOD

The connection hydraulic cushions have in fact non linear stiffness characteristics.

In this program the approximation is made by linearizing these characteristics around a médium point of operation.

We envisage to solve the mechanical part thanks to the ised simulation program. In this case we shall be in a position to follow-up the evolution in course of time of the forces on the bearings whatever their ty of stiffness characteristics.

The equations of the mechanics as non linear should be written down again.

Like wise, the non linear hydrostatic characteristics that we already possess, have to be integrated with this program.

The resolution of the hydrodynamic problem will, unfortunately remain linear till new theoretical developments are obtained.

An other more simple extension is the modelization of flexible bearings at 6 degrees of freedom.

So, this results in a local stiffnees matrix of 6 x 6, and not any more of 3 x 3.

In this case, the bearings are not any longer punctual and it could forthermore be possible to envisage to take the local frictions into account.

VIII. ANTICIPATED EXTENSIONS

A second program is envisaged to solve the problem of the tug-barge for which certain relative movements in relation to the barge have been released.

In this case, equation (20) is not any more true and we must solve both the hydrodynamic problem and the coupled equations of the twin body mechanics.

The n body hydrodynamic with forward running speed is already solved at E.N.S.M.

The n body mechanics on elastic bearing is written, remaining in the assumption of linearity. This should permit to solve the problem of calculation of the efforts in the case of an assembly of several barges articulated together.

Besides, in the same assumptions, we could solve the problem of traditional towing with one or several floats.

The problems of the non linear dynamic characteristics of the connections should not be underestimated.

In a first step, it will be possible to have recourse to simulation models such as indicated in 7.

In this paper we have not shown any comparison of calculations/basin tests in random waves. This will be done later on.

Finally, thanks to the technology of the ACB Hydraulic cushions, it will be possible ot make calculation/sea trials comparisons providing that we have, at the same time as the measurements of the efforts, a correct evaluation of the meteoceanic conditions.

IX. CONCLUSION

The present comparisons between experimental results and numerical results shows that the computer program DYNAPLOUS 81 permits to forgeast, with a good accuracy, the first order motions of a floating body, the accelerations at any point and the forces between two parts of this body.

The qualities of the numerical results given by the computer program are well adapted to study the forces in each connections point between the two parts of a rigid ocean-going tug barge system.

The results of mesurement on real tug-barge system may give us the possibility to make new comparisons without scale effects or problems binded with basin tests.

The computer program is now adapted for an industrial use and must allow any development of hydrodynamic studies concerning all the system of rigid floating bodies at sea.

ACKNOWLEDGMENTS

This work was supported by tug-barge development program at A.C.B./Alsthom-Atlantique and research studies at Laboratoire d'Hydrodynamique Navale of E.N.S.M.

The authors wish to express their deep appreciation to the authors of the experimental reports on tug barge issued from David W. Taylor Naval Ship Research and Development Center and prepared for Maritime Administration.

The authors also thank Mr Hervé Digabel for his assistance in informatic and the technicians who have helped us for the realization of this article.

REFERENCES

1 BAI, K.J. & YEUNG, R.W. /1974/
"Numerical Solutions to Free-Surface Flows problems"
10 th symposium on Naval Hydrodynamics.
Cambridge Massachussets.

2 BOUGIS, J. /1978/
"Application de la méthode des tranches à la détermination des forces et moments de dérive sur houle d'un navire au point fixe"
Rapport de recherche. Nantes.

3 BOUGIS, J. & CLEMENT, A. /1979/
"Action de la houle sur un flotteur élancé à Froude zéro en profondeur finie"
Bulletin de l'ATMA. Paris.

4 BOUGIS, J. /1980/
"Etude de la diffraction radiation dans le cas d'un flotteur indéformable animé d'une vitesse moyenne constante et sollicité par une houle sinusoïdale de faible amplitude"
Thèse de Docteur-Ingénieur, Nantes, juillet 1980.

5 BRARD, R. /1948/
"Introduction à l'étude théorique du tangage en marche"
Pulletin de l'ATMA. Paris

6 BRARD, R. /1972/
"The representation of a Given Ship Form by Singularity Distribution when the Boundary Condition on the Free Surface is linearized"
Journal of Ship Research, vol. 16, n° 1.

7 CHANG, M.S. & PIEN, P.C. /1975/
"Hydrodynamics Forces on a Body Moving Beneath a Free Surface"
Conference on Computational Ship Hydrodynamics Berkeley.

8 CHANG, M.S. & PIEN, P.C. /1976/
"Velocity Potentials of Submerged Bodies near a Free Surface - Application to Wave - Excited Forces and Motions"
11th Symposium on Naval Hydrodynamics. London.

9 CHANG, M.S. /1977/
"Computations of three-dimensional Ship Motions with Forward Speed"
2nd Conference on Computation Ship Hydrodynamics. Berkeley.

10 DELHOMMEAU, G. /1976/
"Contribution à l'étude théorique et à la résolution numérique du problème de la résistance de vagues"
Thèse de Docteur-Ingénieur. Nantes.

11 EUVRARD, D., JAMI, A., MORICE, C. & OUSSET, Y. /1977/
"Calcul numérique des oscillations d'un navire engendrées par la houle"
Journal de Mécanique, vol. 16, n° 2 et 3.
Paris.

12 GUEVEL, P. /1979/
"Hydrodynamique Navale"
Cours de la Section Spéciale d'Hydrodynamique Navale Avancées. Nantes.

13 GUEVEL, P., BOUGIS, J.
"Ship-motions with forward speed in infinite depth
under publication

14 GUEVEL, P., VAUSSY, P. & KOBUS, J.M. /1974/
"The Distribution of Singularities Kinematically Equivalent to a Moving Hull in the Presence of a Free Surface"
International Ship building progress, vol. 21, n° 243.

15 GUEVEL, P. & DELHOMMEAU G. /1977/
"Méthodes de calcul de la résistance de vagues"
Rapport I.R.C.N. Nantes.

16 GUEVEL, P., DAUBISSE, J.C. & DELHOMMEAU, G. /1978/
"Oscillations des corps flottants soumis à l'action de la houle"
Bulletin de l'ATMA. Paris.

17 GUEVEL, P., BOUGIS, J. & HONG, D.C. /1979/
"Formulation du problème des oscillations des corps flottants animés d'une vitesse de route moyenne constante et sollicité par la houle"
Quatrième Congrès Français de Mécanique. Nancy.

18 HAVELOCK, T.H. /1958/
"The Effect of Speed of Advance upon the Damping of the Heave and Pitch"
Transactions of the Royal Institution of Naval Architects. Vol. 100.

19 HESS, J.L. /1970/
"The Problem of Three-dimensional Lifting Potential Flow and its solution by means of Surface Singularity Distribution"
Theorical Aerodynamics Section, Douglas Aircraft Company.

20 KOBUS J.M. /1976/
"Application de la méthode des singularités au problème des flotteurs cylindriques soumis à des oscillations harmoniques forcées de faible amplitude"
Thèse de Docteur Ingénieur. Nantes.

21 LEBRETON, J.C. & MARGNAC, A. /1968/
"Calcul des mouvements d'un navire ou d'une plateforme amarrés dans la houle"
La Houille Blanche, n° 5.

22 WEHAUSEN, J.V. & LAITONE, E.V. /1960/
"Surface Waves"
Handbuch der Physik, vol. 9, Springer Verlag Berlin.

23 WEHAUSEN, J.V. /1971/
"The Motion of Floating Bodies"
Annual Review of Fluid Mechanics

24 ROSSIGNOL G.A. /1974/
Experimental research relative to improving the hydrodynamic performance of ocean-going tug/barge systems.
Report n° PB 263 537 Naval Ship Research and Development Center.

DISCUSSION
of the paper
by J. Bougis and P. Vallier

FORCES AND MOMENTS IN THE RIGID CONNECTIONS BETWEEN A BARGE AND ITS TUG WITH FORWARD SPEED IN WAVE

Discussion
by Choung M. Lee

I would like to know how you have evaluated the line contour integral shown in Eq. (16). I understand that it is not an easy task to carry out.

Authors' reply

It is very difficult to evaluate the line contour integral because it is not a convergent integral ! Nevertheless, for the problem of diffraction-radiation with forward speed, the surface integral on the hull is also not a convergent integral. Only the sum of the two integrals is finite.

If we calculate separately the two different terms, we must compute the infinite minus the infinite. This method gives poor result. If we use Professor Guevel's Method developed to study Neumann-Kelvin problem, we can obtain good result. This method consists of analytically integrating by the Stokes theorem with regard to the space coordinates. The surface integral is transformed into a contour integral on each panel. We have therefore two contour integrals on the segments which are located between the last panel and the free surface. The sum of the two parts is transformed analytically to give us only a finite term which is easy to compute. It is because this analytical analysis has been done that we can calculate the line contour integral.

POTENTIAL OF A MOVING PULSATING SOURCE

J F. Demenche
Bassin d'Essais des Carènes
Paris, France

The purpose of this study is the determination of the Green function corresponding to a source moving with a constant forward velocity U and having a strength which is a harmonic function of time (pulsation ω). In this study, we assume the fluid to be perfect and the free surface boundary condition to be linearized. The bottom of the fluid is a horizontal plane at finite or infinite depth.

The frame of reference and the notation used are defined below. The vertical axis Oz is positive upward ; z = 0 corresponds to the undisturbed free surface. The axis Ox is in the direction of the velocity of the source. z' is the vertical coordinate of the source. In this moving frame of reference having its origin on the free surface, on the same vertical line as the source, the field point is identified by its rectangular coordinates x, y, z or its cylindrical coordinates r, θ, z.

The Green function $\Phi(r, \theta, z, z', t)$ is sought as the real part of $\phi(r, \theta, z, z') e^{i\omega t}$. ϕ is a complex function, solution to the following boundary value problem.

$\Delta\phi = 0$ throughout the fluid domain except at the point (0, 0, z') where ϕ is not defined and in the vicinity of which

$$\phi \sim \frac{1}{\sqrt{r^2 + (z-z')^2}}$$

$\frac{\partial \phi}{\partial z} = 0$ at $z = -h$ (h is the depth ; it may become infinite).

$g \frac{\partial \phi}{\partial z} + (U \frac{\partial}{\partial x} + i\omega)^2 \phi = 0$ at $z = 0$ (free surface)

In fact, in order to deal with a function which is regular throughout the fluid domain, we write $\phi = S + \varphi$ where S is a function behaving like $1/\sqrt{r^2 + (z - z')^2}$ in the vicinity of the source and being harmonic everywhere else. φ will then be the solution to the following boundary-value problem.

1-a/ $\Delta\varphi = 0$ throughout the fluid domain

1-b/ $\frac{\partial \varphi}{\partial z} = 0$ on the bottom ($z = -h$)

1-c/ $g \frac{\partial \varphi}{\partial z} + (U \frac{\partial}{\partial x} + i\omega)^2 \varphi = -g \frac{\partial S}{\partial z} - (U \frac{\partial}{\partial x} + i\omega)^2 S$

on the free surface ($z = 0$).

To find the solution to this problem we shall make use of a transform which we describe below.

The $\overline{\mathcal{G}}$ Transform

Definition

Let us consider a function defined univocally in the plane $f(r,\theta)$. From this function, let us compute the double sequence $\gamma_{n,k}$ of functions of one variable by

$$\gamma_{n,1}(u) = \frac{1}{\pi}\int_0^\infty \int_0^{2\pi} f(r,\theta)\cos n\theta d\theta \, J_n(ur)\, rdr$$

n from 0 to ∞

$$\gamma_{n,2}(u) = \frac{1}{\pi}\int_0^\infty \int_0^{2\pi} f(r,\theta) \sin n\theta d\theta \, J_n(ur) rdr$$

n from 1 to ∞

The studied function is completely characterized by defining either the function of two variables $f(r,\theta)$ or the double sequence of functions of one variable $\gamma_{n,1}(u)$, $\gamma_{n,2}(u)$. As it can be seen using the properties of the Fourier series and the Hankel transforms, we can go from the second representation to the first one by the formula

$$f(r,\theta) = \int_0^\infty \left[\gamma_{0,1}(u) \frac{J_0(ur)}{2} + \overline{\sum_{n=1}^{\infty}} \gamma_{n,1}(u) J_n(ur)\cos n\theta + \right.$$

$$\left. + \overline{\sum_{n=1}^{\infty}} \gamma_{n,2}(u) J_n(ur) \sin n\theta \right] du$$

Properties of the $\overline{\mathcal{G}}$ transform

Let $\overline{\mathcal{G}}$ be the transform from the first representation ($f(r,\theta)$) to the second one (sequence of $\gamma_{n,k}$), we give here some of its properties which we shall use later on.

The $\overline{\mathcal{G}}$ transform is linear and homogeneous

$\overline{\mathcal{G}}$ being a one to one transform $f(r,\theta)$ leads to $\gamma_{n,k}(u) \equiv 0$ for all n, k and vice-versa.

If the $\mathcal{C}$ transform of a function f is the sequence $\hat{f}_{n,k}$ then the $\mathcal{C}$ transform of

- its laplacian is the sequence $-u^2 \hat{f}_{n,k}$

- $\partial f/\partial x$ is the sequence having

as zeroth-order term $u\hat{f}_{1,k}$

as nth-order term $\frac{u}{2}(\hat{f}_{n+1,k}-\hat{f}_{n-1,k})$ for $n \geq 1$

- $\partial f/\partial y$ is the sequence having

as zeroth-order term $\frac{1}{2}(k+1)\, u\, \hat{f}_{1,2}$

as nth-order term $\frac{1}{2}(-u)^{k-1}(\hat{f}_{n+1,3-k} + \hat{f}_{n-1,3-k})$

If the function f depends on a parameter λ, the $\mathcal{C}$ transform of $\frac{\partial f}{\partial x}$ is the sequence $\frac{\partial}{\partial x}\hat{f}_{n,k}$.

The $\mathcal{C}$ transform of even functions of y(or θ) will have the terms $\hat{f}_{n,2}(u)$ identical to zero. As we are going to deal with such functions (due to physical symmetry), we shall drop from now the second index and write $\hat{f}_n(u)$ for $\hat{f}_{n,1}(u)$.

The Green function in the case of infinite depth

The $\mathcal{C}$ transform of the boundary value problem

Let us go back to the problem defined by equations 1. In the case of infinite depth, let us take $S = 1/\sqrt{r^2 + (z-z')^2}$.

Let $\varphi(r, \theta, z, z')$ be the solution to this problem and $\hat{\varphi}_n(u, z, z')$ the sequence obtained by performing a $\mathcal{C}$ transform on this solution.

1.a/ becomes

$$\frac{\partial^2 \hat{\varphi}_n}{\partial z^2} - u^2 \hat{\varphi}_n = 0 \quad \text{for all } n$$

and 1.b/ becomes

$$\frac{\partial \hat{\varphi}_n}{\partial z} = 0 \quad \text{for } z = -\infty$$

$\hat{\varphi}_n$ is thus of the form $K(u, z')e^{uz}$. Considering the symmetry between z and z', we can write

2/ $\qquad \varphi_n(u, z, z') = A_n(u)\, e^{u(z+z')}$

We are left with the problem of determining the sequence of functions of one variable $A_n(u)$ by imposing the boundary condition (1-c) on the bottom to be satisfied. The $\mathcal{C}$ transform of $1/\sqrt{r^2+(z-z')^2}$ being a sequence having all its terms equal to zero, except the zeroth-order term which is $\frac{2}{u} e^{-u(z-z')}$, the $\mathcal{C}$ transform of the boundary condition on the bottom is a sequence for which

the zeroth order term is

$$e^{uz'}\left[\frac{u^2u^2}{2}(A_2 - A_0) + 2iu\omega UA_1 + (gu - \omega^2)A_0\right] =$$

$$e^{uz'}\left[u^2u + 2\frac{\omega^2}{U} + 2g\right]$$

the first-order term is

$$e^{uz'}\left[\frac{u^2u^2}{4}(A_3 - 3A_1) + iu\omega U(A_2 - A_0) + (gu - \omega^2)A_1\right] =$$

$$2\, i\, U\omega\, e^{uz'}$$

the second-order term is

$$e^{uz'}\left[\frac{u^2u^2}{4}(A_4 - 2A_2 + A_0) + iu\omega U(A_3 - A_1) + (gu - \omega^2)A_2\right] =$$

$$-\frac{1}{2}U^2\, u\, e^{uz'}$$

the nth-order term, for $n > 2$, is :

$$e^{uz'}\left[\frac{u^2u^2}{4}(A_{n+2} - 2A_n + A_{n-2}) + iu\omega U(A_{n+1} - A_{n-1}) + (gu - \omega^2) A_n\right] = 0$$

writing $\alpha = \frac{\omega}{Uu}$ and $\beta = \frac{1}{U}\sqrt{\frac{g}{u}}$,

these equations become :

3-a/ $\quad A_2 - A_0 + 4i\alpha A_1 + 2(\beta^2 - \alpha^2)A_0 = 2(1 + 2\alpha^2 + 2\beta^2)/u$

3-b/ $\quad A_3 - 3A_1 + 4i\alpha(A_2 - A_0) + 4(\beta^2 - \alpha^2)A_1 = 8i\alpha/u$

3-c/ $\quad A_4 - 2A_2 + A_0 + 4i\alpha(A_3 - A_1) + 4(\beta^2 - \alpha^2)A_2 = -2/u$

3-d/ $\quad A_{n+2} - 2A_n + A_{n-2} + 4i\alpha(A_{n+1} - A_{n-1}) + 4(\beta^2 - \alpha^2)A_n = 0$

Solution to the transformed problem

Equation 3-d shows that we have to deal, from A_1 on, with the classical problem of determining the terms of a Fibonacci sequence. We know that these terms are of the form

$$A_n = \lambda_1 Z_1^n + \lambda_2 Z_2^n + \lambda_1' Z_1'^n + \lambda_2' Z_2'^n$$

where λ_1, λ_1', λ_2 and λ_2' are arbitrary and Z_1, Z_1', Z_2 and Z_2' are the roots of the characteristic equation[2].

$$Z^4 + 4i\alpha(Z^3 - Z) + (4\beta^2 - 4\alpha^2 - 2)Z^2 + 1 = 0$$

which can be decomposed into

$$Z_1^2 + 2i(\alpha + \beta)Z_1 - 1 = 0$$

$$Z_2^2 + 2i(\alpha - \beta)Z_2 - 1 = 0$$

From this we get the roots :

$$Z_1 = \begin{cases} \sqrt{1-(\alpha+\beta)^2} - i(\alpha+\beta) & \text{if } \alpha+\beta < 1 \\ i\left[\sqrt{(\alpha+\beta)^2-1} - (\alpha+\beta)\right] & \text{if } \alpha+\beta > 1 \end{cases}$$

$$Z_1' = \begin{cases} -\sqrt{1-(\alpha+\beta)^2} - i(\alpha+\beta) & \text{if } \alpha+\beta < 1 \\ -i\left[\sqrt{(\alpha+\beta)^2-1} + \alpha+\beta\right] & \text{if } \alpha+\beta > 1 \end{cases}$$

$$Z_2 = \begin{cases} \sqrt{1-(\alpha-\beta)^2} - i(\alpha-\beta) & \text{if } |\alpha-\beta| < 1 \\ i\left[\sqrt{(\alpha-\beta)^2-1} - (\alpha-\beta)\right] & \text{if } \alpha-\beta > 1 \\ -i\left[\sqrt{(\alpha-\beta)^2-1} + (\alpha-\beta)\right] & \text{if } \alpha-\beta < -1 \end{cases}$$

$$Z_2' = \begin{cases} -\sqrt{1-(\alpha-\beta)^2} - i(\alpha-\beta) & \text{if } |\alpha-\beta|<1 \\ -1\left[\sqrt{(\alpha-\beta)^2-1} + \alpha-\beta\right] & \text{if } \alpha-\beta>1 \\ 1\left[\sqrt{(\alpha-\beta)^2-1} - (\alpha-\beta)\right] & \text{if } \alpha-\beta<-1 \end{cases}$$

The moduli of Z_1 and Z_2 are less than or equal to 1, whereas the moduli of Z_1' and Z_2' are greater than or equal to 1.

In the case where the roots have their moduli equal to 1, we can introduce a positive, evanescent, fictitious viscosity in the free surface boundary condition in order to take into account the irreversibility of the problem of the source motion, and show that $|Z_1|$ and $|Z_2|$ tend to 1⁻ whereas $|Z_1'|$ and $|Z_2'|$ tend to 1⁺(*). Under these conditions, in order for A_n to go to a finite limit when $n \to \infty$, it must be of the form

$$A_n = \lambda_1 Z_1^n + \lambda_2 Z_2^n \quad \text{for } n \geq 1.$$

Substituting A_n into 3-c and taking into account the characteristic equation, give :

$$A_0 = (\lambda_1 + \lambda_2) - \frac{2}{U}.$$

Equations 3-a and 3-b where the A_n's are replaced by their expressions, give a system of two linear equations for λ_1 and λ_2, for which the solution is given by :

$$\lambda_1 = 4i\frac{\beta}{U}\frac{Z_1}{Z_1^2+1} \qquad \lambda_2 = -4i\frac{\beta}{U}\frac{Z_2}{Z_2^2+1}$$

Expression for the Green function

Knowing the expressions for the A_n's, we get the $\hat{\varphi}_n$'s by using equation 2. ϕ is obtained by performing an inverse $\mathfrak{C}$ transform.

The Green function sought is given by :

$$\phi = 1/\sqrt{r^2+(z-z')^2} - \int_0^\infty e^{u(z+z')} J_0(ur)\,du + \ldots$$

$$+ \int_0^\infty \left[\frac{\lambda_1+\lambda_2}{2} J_0(ur) + \sum_{n=1}^{\infty} (\lambda_1 Z_1^n + \lambda_2 Z_2^n)\cos n\theta\, J_n(ur) \right] e^{u(z+z')}\,du$$

i.e.

$$\phi = 1/\sqrt{r^2+(z-z')^2} - 1/\sqrt{r^2+(z+z')^2} + \ldots$$

$$+ \frac{4i\sqrt{\pi}}{U} \int_0^\infty \left[\left(\frac{Z_1}{Z_1^2+1} - \frac{Z_2}{Z_2^2+1}\right) \frac{J_0(ur)}{2} \right.$$

$$\left. + \sum_{n=1}^{\infty} \left(\frac{Z_1^{n+1}}{Z_1^2+1} - \frac{Z_2^{n+1}}{Z_2^2+1}\right) J_n(ur)\cos n\theta \right] e^{u(z+z')} \frac{du}{\sqrt{u}}$$

where Z_1 and Z_2 are explicit functions of u through α and β. The second term can be seen to be the potential of a sink symmetrical from the studied source.

(*) See fig. 1

The Green function in the case of finite depth

The $\mathfrak{C}$ transform of the boundary-value problem

In the case of finite depth, we impose S to be the function $\frac{1}{\sqrt{r^2+(z-z')^2}} + \frac{1}{\sqrt{r^2+(z+z'+2h)^2}}$, that is to say, we add to the ordinary source, its symmetrical with respect to the bottom. Under these conditions, $\mathfrak{C}$ transforms

1-a/ into

$$\frac{\partial^2 \hat{\varphi}_n}{\partial z^2} - u^2 \hat{\varphi}_n = 0 \text{ for all } n.$$

and 1-b/ into

$$\frac{\partial \hat{\varphi}_n}{\partial z} = 0 \text{ for } z = -h.$$

$\hat{\varphi}_n(u, z, z')$ is thus of the form $K(u, z')\,\mathrm{ch}\,u(z+h)$. Considering the symmetry between z and z' we can write :

$$\hat{\varphi}_n(u, z, z') = A_n(u)\,\frac{\mathrm{ch}\,u(z+h)\,\mathrm{ch}\,u(z'+h)}{\mathrm{ch}^2 uh}$$

Notice that the $\mathfrak{C}$ transform of S is a sequence reduced to it's zeroth-order term : $\frac{2}{u}\left[e^{-u(z-z')} + e^{-u(z+z'+2h)}\right]$. The $\mathfrak{C}$ transform of the free surface boundary condition is obtained as in the case of infinite depth and, writing

$$\alpha = \frac{\omega}{U\sqrt{u}} \quad \text{and} \quad \beta = \frac{1}{U}\sqrt{\frac{g}{u}}\,\mathrm{th}\,uh$$

we get the set of equations

$$4\text{-a/ } A_2 - A_0 + 4i\,A_1 + 2(\beta^2-\alpha^2)A_0 + \frac{4}{U}(1+2\alpha^2+2\beta/\mathrm{th}uh)e^{-uh}\mathrm{ch}\,uh$$

$$4\text{-b/ } A_3 - 3A_1 + 4i\alpha(A_2-A_0) + 4(\beta^2-\alpha^2)A_1 + 16\frac{i\alpha}{U}e^{-uh}\mathrm{ch}\,uh$$

$$4\text{-c/ } A_4 - 2A_2 + A_0 + 4i\alpha(A_3-A_1) + 4(\beta^2-\alpha^2)A_2 = -\frac{4}{U}e^{-uh}\mathrm{ch}\,uh$$

$$4\text{-d/ } A_{n+1} - 2A_n + A_{n-2} + 4i\alpha(A_{n+1}-A_{n-1}) + 4(\beta^2-\alpha^2)A_n = 0$$

These equations are identical to the equations 3, apart from the right-hand side, and the recurrence formula is the same, whence :

$$A_n = \lambda_1 Z_1^n + \lambda_2 Z_2^n \quad \text{for } n \geq 1,$$

with the same expression for Z_1 and Z_2 as functions of α and β, as in the case of infinite depth.

Equation 4-c enables us to calculate A_0 :

$$A_0 = \lambda_1 + \lambda_2 - 4e^{-uh}\mathrm{ch}\,uh/u$$

The linear system obtained after substituting A_n into equations 4-a and 4-b enables us to evaluate λ_1 and λ_2.

$$\lambda_1 = 4i\frac{\beta}{u\,\mathrm{th}uh}\frac{Z_1}{Z_1^2+1} \qquad \lambda_2 = -4i\frac{\beta}{u\,\mathrm{th}uh}\frac{Z_2}{Z_2^2+1}$$

From which we obtain the Green function :

$$\Phi(r,\theta,z,z') = \frac{1}{\sqrt{r^2+(z-z')^2}} + \frac{1}{\sqrt{r^2+(z+z'+2h)^2}} \ldots$$

$$\ldots -2\int_0^\infty e^{-uh}\,\frac{ch\,u(z+h)ch\,u(z'+h)}{ch\,uh}\,J_0(ur)du \ldots$$

$$\ldots \frac{2i\sqrt{g}}{U}\int_0^\infty \frac{ch\,u(z+h)ch\,u(z'+h)}{ch^2uh\sqrt{gth\,uh}}\left(\frac{Z_1}{Z_1^2+1} - \frac{\bar{Z}_2}{\bar{Z}_2^2+1}\right)J_0(ur)du \ldots$$

$$\ldots + \frac{4i\sqrt{g}}{U}\int_0^\infty \frac{ch\,u(z+h)ch\,u(z'+h)}{ch^2uh\sqrt{gth\,uh}} \left[\sum_{n=1}^{\infty}\left(\frac{Z_1^{n+1}}{Z_1^{n+1}+1} - \frac{\bar{Z}_2^{n+1}}{\bar{Z}_2^{n+1}+1}\right)\cos n\theta J_n(ur)\right]du$$

The integrands are once again explicit functions of the integration variable u. It can be noted that the limit for infinite h of this expression is the expression previously obtained for infinite depth.

Discussion

Roots Z_1 and Z_2 of the characteristic equation

In order to know the behaviour of the integrand which can be seen in the expression for the Green function, it is necessary to inspect the values of Z_1 and Z_2 when u varies from zero to infinity. It can be easily established that the points representing Z_1 and Z_2 in the Argan-Cauchy plane are located on the unit circle and its vertical diameter.

Thick lines on figures 1 show the trajectory of the roots Z_1 and Z_2 (fig. 1.a with regard to Z_1, fig. 1.b, 1.c and 1.d with regard to Z_2 in different cases).

Z_1 moves monotically first along the OA segment then along the AB arc. B is reached for infinite u.

Z_2 moves along the OA segment then along a trajectory ABH located on the positive real part half circle with a possible complement on the vertical diameter. Then Z_2 moves, in the

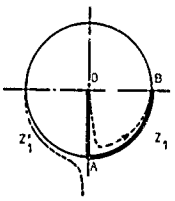


Figure 1.a
Locus of the roots Z_1 and Z'_1

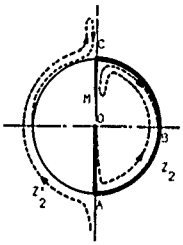


Figure 1.b
Subcritical regime

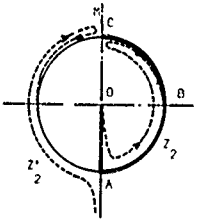


Figure 1.c
Critical regime

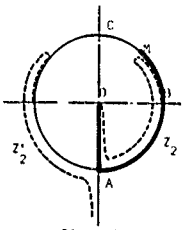


Figure 1.d
Hypercritical regime

LOCUS OF THE ROOTS Z_2 AND Z'_2

opposite direction along the MB trajectory, reaching B for infinite u. Three cases can be distinguished : subcritical, critical and hypercritical whether M is located on OC, strictly on C or on BC i.e. whether the equation $Z_2=1$ (or $\alpha - \beta + 1 = 0$) has two roots, a double root or no roots at all.

Dashed lines on the figures 1 show the trajectory of all the roots of the characteristic equation when σ small, but strictly positive, numerical viscosity is introduced. This makes clear the behaviour of Z_n on its backward trajectory MB and shows that the roots Z_1' and Z_2' have a modulus greater than 1.

When the depth is infinite, it can easily be shown that the critical case corresponds to a Strouhal number $\frac{\omega l}{c}$ equal to 1/4. When the depth is finite, there is no explicit equation relating the critical values of U, ω and h. However, denoting by U_c, ω_c and h these values, and by v_c the double root, we can write :

5-a/ $$\mathcal{F}_c = \frac{U_c}{\sqrt{gh}} = \frac{1}{2}\,\frac{th\nu + \nu(1-th^2\nu)}{\sqrt{\nu th\,\nu}}$$

5-b/ $$\tilde{\omega}_c = \omega_c\sqrt{\frac{h}{g}} = \frac{\nu}{2}\,\frac{th\nu - \nu(1-th^2\nu)}{\sqrt{\nu th\,\nu}}$$

where $\nu = v_c\, h$

It should be noted that, if the depth is finite, the regime is always hypercritical when the Froude number based on the depth is greater than one.

Behaviour of the integrand

Performing a limited series expansion of Z_1 and Z_2 for small u shows that Z_1 and Z_2 are both equivalent to $-\frac{1}{2}\frac{U^2}{\omega}u$. Thus the integrand is finite or zero when $u = 0$.

When u becomes infinite, the integrand behaves like $e^{u(z-z')}u^{-3/2}$ whether or not the depth is finite. This expression decreases fast enough to ensure the convergence of the integral despite the infinite limit of integration, whatever z and z' may be.

The integrand becomes infinite when Z_1 or Z_2 becomes equal to ± 1. Let us note that :

$Z_1 = 1$ has no root.

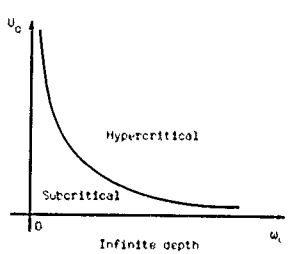
$Z_1 = -1$ and $Z_2 = -1$ have one simple root.

$Z_2 = 1$ has no roots in the hypercritical regime

has two simple roots in the subcritical regime

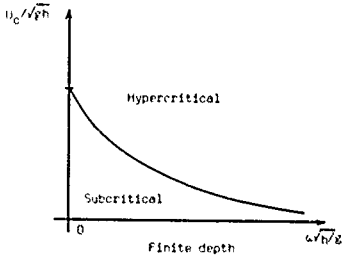
has one double root in the critical regime.

Consequently, except in the critical regime which we shall deal with below, the singularities behave like $1/\sqrt{u - u_0}$ and the integral is convergent.



Infinite depth

Figure 2.a



Finite depth

Figure 2.b

DOMAINS CORRESPONDING TO THE DIFFERENT REGIMES

Critical regime

In the vicinity of the double root u_c of the equation $Z_n = i$, the integrand behaves like $1/\sqrt{(u-u_c)^3}$. This singularity cannot be regarded as a pole, in which case the integral could have been computed as a Cauchy principal value. As a matter of fact we had to select for the square root a branch that makes the integrand behave like $1/|u-u_c|$. In the critical regime, the integral is not defined, neither is the Green function. When approaching the critical regime, they both tend to infinity.

However, the real Green function Φ is the real part of $\delta e^{i\omega t}$. If we denote by $R(x,y,z,z',\omega,U,h)$ the residue of the integrand for the critical value of u, and τ the argument of this residue, the real part of $Re^{i\omega t}$ is zero for values of t such that $\tau + \omega t = \frac{\pi}{2} + k\pi$. For these values of t the Green function is finite in the vicinity of the critical line. This function tends towards a different limit depending on the regime (subcritical or hypercritical) from which the critical point is approached. The jump value of the potential Φ when crossing the critical line for suitable values of t is the real part of $i\pi\ Re^{i\omega t}$, that is $\pi|R|$.

For infinite depth

$$R = \frac{2ig}{U_c^2} e^{g(z+z')/(4U_c^2)} \left[J_0\left(\frac{gr}{4U_c^2}\right) + 2\sum_{n=1}^{\infty} J_n\left(\frac{gr}{4U_c^2}\right)\cos n\theta \right]$$

$$= \frac{2ig}{U_c^2} e^{g(z+z'+ix)/(4U_c^2)}$$

The locus of the points at which the potential tends to a limit when approaching the critical regime is a set of straight lines of equation $\frac{gx}{4U_c^2} + \omega_c t = \pi/2 + k\pi$

i.e. $$x = U_c t + \frac{4U_c^2}{g}(\pi/2 + k\pi)$$

These lines are orthogonal to the direction of the source speed and move backwards in the moving frame of reference with a velocity U_c. Consequently they are motionless in the fixed frame of reference. The value of the jump is :

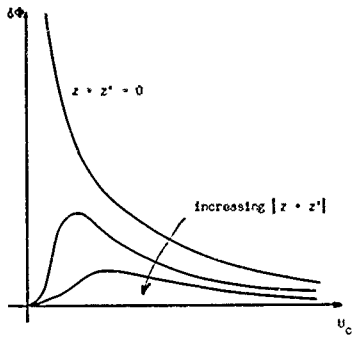
$$\delta\Phi = \frac{2\pi g}{U_c^2} e^{g(z+z')/(4U_c^2)}$$

In the case of finite depth, neither the location of the points of finite potential nor the value of the jump can be given explicitly in terms of the physical parameters (U_c, ω_c and h) alone. The parameter u_c (or $\nu = \frac{\omega_c^2}{g}h$) cannot be eliminated. Once again the potential stays finite on straight lines orthogonal to the direction of the source speed. These lines move backwards in the moving frame of reference with a speed :

$$\frac{\omega_c}{U_c} = \frac{1}{2}\sqrt{\frac{g}{h}}\,\frac{th\nu - \nu(1-th^2\nu)}{\sqrt{\nu th\,\nu}} = U_c - \frac{\nu(1-th^2\nu)}{\sqrt{\nu th\,\nu}}$$

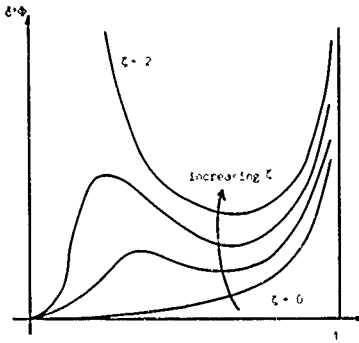
In the fixed frame of reference, these lines move in the same direction as the source with a speed :

$$(1 - th^2\nu)\sqrt{\frac{\nu}{th\nu}}$$



Infinite depth

Figure 3.a



Finite depth

Figure 3.b

JUMP OF THE GREEN FUNCTION

The jump value of the potential is given by :

$$h\,\delta\Phi = \frac{\operatorname{ch}\nu(1+z/h)\operatorname{ch}\nu(1+z'/h)}{\operatorname{ch}^2\nu}\,\frac{\pi}{\sqrt{\mathcal{F}_c H(\mathcal{F}_c^2-1+2\nu^2\mathcal{F}_c H^3)}}$$

where

$$\nu = \nu_c\, h$$

$$\mathcal{F}_c = U_c/\sqrt{gh}$$

$$H = \sqrt{\operatorname{th}\nu\,\nu}$$

The figure 3.a shows, in the case of infinite depth, the value of the jump, as a function of the speed U_c and the quantity $\xi = r+z'$.

The figure 3.b represents the function of $\mathcal{F}_c = \frac{U_c}{\sqrt{gh}}$ and ξ defined by :

$$\delta'\Phi = \frac{1}{2}\,\frac{\operatorname{ch}\nu\xi}{\operatorname{ch}^2\nu}\,\frac{\pi}{\sqrt{\mathcal{F}_c H}\,\sqrt{\mathcal{F}_c^2-1+2\nu^2\,\mathcal{F}_c H^3}}$$

In the case of finite depth, the value of the jump of the potential is :

$$\delta\Phi = \delta'\Phi\,(2+(z+z')/h) + \delta'\Phi\,(\,|z-z'|/h).$$

The value of the jump can be obtained by using twice the figure 3.b.

The consideration of the limit of the potential and its jump in the critical case may appear as an academic matter since the linearization of the free surface condition is no more valid when approaching such a regime. However it has practical applications. There is no set of values of the parameters U, ω, x, y, z, z' and h for which the value of the Green function is known and thus no possibility of checking the correctness and the accuracy of a computer program designed to provide the value of this Green function. However the comparison of the value of the jump given by the aforementioned expression with the value given by the program allows a checking of this program.

Derivatives of the Green function

Calculation of the derivatives

As we know the terms of the $\tilde{G}$ transform of the Green function, it is easy to calculate the terms corresponding to its derivatives. For z or z' derivatives, we simply proceed to the derivation of each term. For x and y derivatives we use the relations given in the section entitled "properties of the $\tilde{G}$ transform". The use of these relations must be repeated if we deal with derivatives of order greater than 1. If the order of the derivative with respect to y is odd, the sequence will have no $\tilde{\varphi}_{n,1}$ terms but only $\tilde{\varphi}_{n,2}$ terms. Having obtained the sequence we are looking for, we can go back to the usual representation by using the inverse $\tilde{G}$ transform.

In that way, the potential of different multipoles and the velocity generated by them can be obtained.

Pressure generated by a source

As an example, compute the pressure generated by a pulsating moving source in the case of infinite depth.

The pressure is given by the Bernoulli equation :

$$p = -\rho\,\frac{\partial}{\partial t} = \rho\,\Re\left\{(U\,\frac{\partial}{\partial x} + i\omega)\varphi.e^{i\omega t}\right\}$$

If we set apart the terms $\frac{1}{\sqrt{r^2+(z+z')^2}}$ - $\frac{1}{\sqrt{r^2+(z+z')^2}}$, in the (r,θ) representation, the $\tilde{G}$ transform of the remainder is a sequence of terms

$$\tilde{\varphi}_{n,1} = (\lambda_1 Z_1^n + \lambda_2 Z_2^n)e^{\nu(z+z')}$$

The $\tilde{G}$ transform of the pressure is a sequence which has

a zeroth-order term $\tilde{p}_0 = \rho(U\nu\tilde{\varphi}_1 + i\omega\tilde{\varphi}_0)$

and nth-order terms $\tilde{p}_n = \rho\,\frac{U\nu}{2}\,(\tilde{\varphi}_{n+1} - \tilde{\varphi}_{n-1}) + i\omega\tilde{\varphi}_n$

that is for the zeroth-order term

$$\rho e^{\nu(z+z')}\left[U\nu(\lambda_1 Z_1 + \lambda_2 Z_2) + i\omega(\lambda_1 + \lambda_2)\right]$$

$$= -\frac{4\rho g}{U}\,e^{\nu(z+z')}\,\frac{1}{\nu}\,\left(\frac{Z_1}{Z_1^2+1} + \frac{Z_2}{Z_2^2+1}\right)$$

and for the nthorder term (n > 1)

$$\rho e^{\nu(z+z')}\left[\frac{U\nu}{2}\,(\lambda_1(Z_1^{n+1}-Z_1^{n-1}) + \lambda_2(Z_2^{n+1}-Z_2^{n-1})) + i\omega(\lambda_1 Z_1^n + \lambda_2 Z_2^n)\right]$$

$$= -\frac{4\rho g}{U}\,e^{\nu(z+z')}\,\frac{1}{\nu}\,\left(\frac{Z_1^{n+1}}{Z_1^2+1} + \frac{Z_2^{n+1}}{Z_2^2+1}\right)$$

Using an inverse $\tilde{G}$ transform we get :

$$p = \rho(U\,\frac{\partial}{\partial x} + i\omega)\left(\frac{1}{\sqrt{r^2+(z-z')^2}} - \frac{1}{\sqrt{r^2+(z+z')^2}}\right) + \ldots$$

$$\ldots + \frac{2\rho g}{U}\int_0^\infty \left(\frac{Z_1}{Z_1^2+1} + \frac{Z_2}{Z_2^2+1}\right)e^{\nu(z+z')}J_0(\nu r)\,d\nu + \ldots$$

$$\ldots + \frac{4\rho g}{U}\sum_{n=1}^{\infty}\cos n\theta\int_0^\infty \left(\frac{Z_1^{n+1}}{Z_1^2+1} + \frac{Z_2^{n+1}}{Z_2^2+1}\right)e^{\nu(z+z')}J_n(\nu r)\,d\nu$$

Session VIII
WATER WAVES AND FLOATING BODIES

R.D. Cooper
Session Chairman
Flow Research
U.S.A.

ON THE NULL-FIELD EQUATIONS FOR WATER-WAVE RADIATION PROBLEMS

P.A. Martin and F. Ursell
Department of Mathematics, University of Manchester,
Manchester, M13 9PL, England

Abstract

Consider a rigid body which is performing simple-harmonic oscillations in the free surface of deep water under gravity. Under certain geometrical conditions on ∂D, the wetted surface of the body, it is known that the linear boundary-value problem $\mathcal{P}$ for the corresponding velocity potential ϕ is uniquely solvable at all frequencies. The usual method for solving $\mathcal{P}$ is to derive a Fredholm integral equation of the second kind over ∂D. It is also well-known that the usual boundary integral equations are uniquely solvable, except at an infinite discrete set of frequencies (the irregular frequencies). In this paper, we shall describe an alternative method for solving $\mathcal{P}$, called the 'null-field' method; this method was originally devised by Waterman for acoustic and electromagnetic scattering problems. We derive an infinite system of moment-like equations (the 'null-field' equations), which are to be solved for the boundary values of ϕ. These equations are uniquely solvable at all frequencies - the unphysical irregular frequencies do not occur. For the special case of a half-immersed circular cylinder, we find a simple connection between the null-field method and the method of multipoles. We discuss the numerical solution of the null-field equations and present some results for the heaving, half-immersed, elliptic cylinder. Finally, we sketch how the null-field method can be extended to three-dimensional problems and to problems where the water is of constant finite depth.

1. Introduction

Consider a rigid body which is floating in the free surface of a fluid. We suppose that the fluid is incompressible and inviscid, and assume that the effects of surface tension are negligible. We denote the fluid domain by D, the free surface by F and the wetted surface of the body by ∂D, which we assume has

Properties J (John, 1950). Let ∂D^* denote the union of the surface ∂D and its mirror image in the plane of the free surface. We shall say that ∂D has properties J if ∂D^* is a convex, twice-differentiable surface. (In particular, ∂D must intersect the free surface perpendicularly.)

Let us assume, for simplicity, that the fluid is of infinite depth and that the body is a horizontal cylinder of infinte length. We take Cartesian coordinates (x, y, z) with the z-axis parallel to the generators of the cylinder and the y-axis vertical (y increasing with depth), such that F occupies a region of the plane $y = 0$.

Suppose that the cylinder performs simple-harmonic oscillations of small amplitude and radian frequency ω. The motion is assumed to be independent of z and so, for irrotational motion, we can formulate the following well-known, linear, two-dimensional boundary-value problem for a velocity potential $\mathrm{Re}\{(\phi(x, y) \exp(-i\omega t))\}$:

Boundary-value problem $\mathcal{P}$

Determine a function $\phi(P)$ satisfying Laplace's equation,

$$\left(\frac{\partial^2}{\partial x^2} + \frac{\partial^2}{\partial y^2}\right) \phi(P) = 0 \quad \text{in } D,$$

the free-surface condition

$$K\phi + \frac{\partial \phi}{\partial y} = 0 \quad \text{on } F \qquad (1.1)$$

and the boundary condition

$$\frac{\partial \phi(p)}{\partial n_p} = V(p) \quad \text{on } \partial D, \qquad (1.2)$$

where $K = \omega^2/g$, g is the acceleration due to gravity, and the function $V(p)$ is prescribed on ∂D (see Figure 1). In addition, there is the radiation condition that waves travel outwards to infinity, and the condition that the fluid motion vanishes as $y \to \infty$.

The notation is as follows: capital letters P, Q denote points of D; small letters p, q denote points of ∂D; the origin O is assumed to lie in F_-, the portion of the x-axis which is inside the cylinder; D_- denotes the interior of the body, i.e. the region with boundary $\partial D \cup F_-$; P_-, Q_- denote points of D_-; r_p is the length OP; $\partial/\partial n_p$ denotes normal differentiation at the point p, in the direction from ∂D into D.

The following theorem on the solvability of $\mathcal{P}$ has been proved by John (1950):

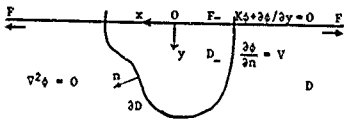


Figure 1. The floating cylinder.

Theorem 1. Suppose that ∂D has properties J and that V(q) is continuous on ∂D. Then, there exists a unique solution of the boundary-value problem $\mathcal{P}$, for all real values of K.

We shall henceforth assume that the conditions of Theorem 1 are always satisfied.

The usual approach for solving the boundary-value problem $\mathcal{P}$ is to derive an integral equation of the second kind, over the boundary ∂D. One way of doing this is to assume that φ(P) can be represented as a distribution of sources over ∂D; the source strength is then found to be the solution of a Fredholm integral equation of the second kind. Alternatively, an integral equation of the second kind can be derived directly from Green's theorem. It is well known that both of these methods (which will be described in section 2) lead to boundary integral equations of the second kind which are singular at a certain infinite discrete set of frequencies, corresponding to the eigenvalues of a related interior problem. This phenomenon is clearly a consequence of the method of solution, for we have already remarked that the original boundary-value problem $\mathcal{P}$ is known to have a unique solution at all frequencies, provided that ∂D has properties J and V(q) is continuous (Theorem 1).

A different approach to the related problems in acoustics has been employed by Waterman (1969). His method is based on solving the Helmholtz formula in the interior of the body and leads to an infinite system of equations, rather than a single (integral) equation. Martin (1980) has studied these equations (called the 'null-field equations of acoustics'), and proved that they always have a unique solution, i.e. difficulties at interior eigenvalues do not occur with this method.

In this paper, we shall derive the corresponding equations for water-wave radiation problems. After a review of integral-equation methods in section 2, we derive the null-field equations for water waves in section 3. In section 4, we consider the special case of an oscillating half-immersed circular cylinder. For this geometry, we show that the null-field equations may be obtained by suitably modifying Ursell's method of multipoles. In section 5, we discuss the numerical solution of the null-field equations. We propose a simple numerical scheme which we use, in section 6, to solve the equations corresponding to a heaving, half-immersed, elliptic cylinder. We obtain good agreement with other published results (for the virtual-mass coefficient). Finally, we briefly describe how the null-field method may be extended to solve problems in three dimensions and problems where the fluid is of constant finite depth.

2. Boundary Integral Equations

Let $G_0(P, Q)$ be the potential at P due to a simple wave-source at Q, i.e. (Thorne, 1953)

$$G_0(P, Q) \equiv G_0(x, y; \xi, \eta) = \tag{2.1}$$
$$= \tfrac{1}{2}\log\frac{(x-\xi)^2+(y-\eta)^2}{(x-\xi)^2+(y+\eta)^2} - 2\int_0^\infty e^{-k(y+\eta)}\cos k(x-\xi)\frac{dk}{k-K},$$

where, in order to satisfy the radiation condition, the path of integration passes below the pole of the integrand at $k = K$. $G_0(P, Q)$ also satisfies Laplace's equation in D (except at $P = Q$, where it has a logarithmic singularity) and the free-surface condition (1.1).

If we apply Green's theorem in D, to φ(P) and $G_0(P, Q)$, we obtain the following three equations, depending on the location of P:

$$2\pi\phi(P) = \int_{\partial D}\{G_0(P,q)\frac{\partial}{\partial n_q}\phi(q) - \phi(q)\frac{\partial}{\partial n_q}G_0(P,q)\}ds_q, \tag{2.2}$$

$$\pi\phi(p) = \int_{\partial D}\{G_0(p,q)\frac{\partial}{\partial n_q}\phi(q) - \phi(q)\frac{\partial}{\partial n_q}G_0(p,q)\}ds_q, \tag{2.3}$$

$$0 = \int_{\partial D}\{G_0(P_-,q)\frac{\partial}{\partial n_q}\phi(q) - \phi(q)\frac{\partial}{\partial n_q}G_0(P_-,q)\}ds_q. \tag{2.4}$$

(Here, the radiation condition on φ and G_0 ensures that there is no contribution from infinity.) These equations are called the Helmholtz formulae in acoustics (see, e.g. Baker and Copson, 1950); we shall use the same terminology here.

If we use the boundary condition (1.2) in (2.3), we obtain

$$\pi\phi(p) + \int_{\partial D}\phi(q)\frac{\partial}{\partial n_q}G_0(p,q)ds_q = \int_{\partial D}G_0(p,q)V(q)ds_q, \tag{2.5}$$

which is a Fredholm integral equation of the second kind for the unknown boundary values of φ. This integral equation (Green's integral equation) possesses a unique solution unless the corresponding homogeneous integral equation,

$$\pi\phi(p) + \int_{\partial D}\phi(q)\frac{\partial}{\partial n_q}G_0(p,q)ds_q = 0, \tag{2.6}$$

has a non-trivial solution. It was shown by John (1950) that (2.6) does have non-trivial solutions whenever K coincides with an eigenvalue of the 'interior wave-Dirichlet problem', where the Dirichlet condition φ = 0 is satisfied on ∂D and the free-surface condition (1.1) is satisfied on F_-. At such values of K (called irregular by John), Green's integral equation (2.5) does not have a unique solution for general V(p).

A different approach for solving $\hat{P}$ is to represent $\phi(P)$ by a distribution of simple wave-sources over ∂D,

$$\phi(P) = \int_{\partial D} \mu(q) G_0(P,q) ds_q. \qquad (2.7)$$

On applying the boundary condition (1.2), we find that the unknown source strength $\mu(q)$ satisfies

$$\pm\mu(p) + \int_{\partial D} \mu(q) \frac{\partial}{\partial n_p} G_0(p,q) ds_q = V(p). \qquad (2.8)$$

This integral equation (the source integral equation) is of the same form as (2.5), except that the kernel of (2.8) is the transpose of the kernel appearing in (2.5). (Here, we have used the symmetry of (2.1).) Hence, (2.8) has the same irregular values as (2.5).

When K is not an irregular value, we can construct the solution of $\hat{P}$ by substituting the unique solution of (2.8) into (2.7). For the representation (2.7) satisfies Laplace's equation in D, the radiation condition and the free-surface condition (for any continuous $\mu(q)$), whilst it automatically satisfies the boundary condition (1.2) on ∂D if $\mu(q)$ satisfies (2.8). The situation is not so straight-forward with Green's integral equation (2.5). Nevertheless, if we substitute the unique solution of (2.5) into (2.2), and then use the boundary condition (1.2), we can define a function $U(P)$, say, by

$$U(P) = \frac{1}{2\pi} \int_{\partial D} \{G_0(P,q) V(q) - \phi(q) \frac{\partial}{\partial n_q} G_0(P,q)\} ds_q$$

which does solve $\hat{P}$. (A proof is given by Martin (1981); it is necessary to show that U satisfies the boundary condition on ∂D.)

When K is an irregular value, the integral equations (2.5) and (2.8) are not uniquely solvable for general $V(p)$ (actually, (2.5) has more than one solution whilst (2.8) has none). This difficulty was first overcome by John (1950). He was able to prove that $\hat{P}$ is uniquely solvable at the irregular values by giving a rather complicated argument involving the non-trivial solutions of the homogeneous form of equation (2.8). Another way of overcoming the difficulty at the irregular values is to use a different fundamental solution in place of the simple wave-source $G_0(P,Q)$, see, e.g., Ursell (1953, 1981) and Sayer (1980).

Numerical solutions of the integral equations (2.5) and (2.8) have been obtained by many authors, for various ∂D and $V(q)$. It is known that the discretised versions of these integral equations become ill-conditioned within a narrow band of frequencies around each irregular frequency. Although several computational devices have been used to alleviate this difficulty, it is not pertinent to describe them all here; for a recent review, see Mei (1978); for a comparison between several methods, see Bérresen (1980).

Let us now examine (2.4), the third of the Helmholtz formulae. This is an integral relation which asserts that the potential induced in D_- by the sources on ∂D is exactly cancelled by the potential induced by the dipoles on ∂D. In other words, although the continuation of the actual potential in D (i.e. the solution of the boundary-value problem $\hat{P}$), across ∂D, does not vanish in D_- (otherwise, it would vanish everywhere), the potential generated by the source and dipole distributions over ∂D (which are used to represent the actual potential in D) does vanish throughout D_-. Waterman (1969) calls this the 'extended boundary condition', and (2.4) the 'extended integral equation'. According to Mei (1978, p.402), (2.4) has not been used for water-wave calculations. In acoustics, however, Waterman (1969) has replaced the interior integral relation (2.4) by an infinite system of equations, called the null-field equations. More recently, Martin (1981) has obtained the corresponding equations for water-wave problems. These will be derived in the next section.

3. The Null-Field Equations for Water Waves

Recently, Ursell (1981) has shown that the simple wave-source (2.1) has a bilinear expansion, i.e.

$$G_0(P,Q) = \sum_{m=0}^{\infty} \sum_{\sigma=1}^{2} \alpha_m^{\sigma}(P) \phi_m^{\sigma}(Q). \qquad (3.1)$$

for $r_Q > r_P$, where the harmonic functions α_m^{σ} and ϕ_m^{σ} are defined in an appendix below; α_m^{σ} are regular and satisfy the free-surface condition (1.1), whilst ϕ_m^{σ} satisfy the free-surface and radiations conditions, and are singular at O (ϕ_m^{σ} are usually known as 'multipole' potentials: ϕ_0^1 and ϕ_0^2 correspond to a source and a horizontal dipole, at O, respectively, whilst ϕ_m^{σ}, for $m > 0$, are wave-free potentials).

Let C_- be the inscribed circle to ∂D^*, which is centred on O. Similarly, let C_+ be the escribed circle to ∂D^*. Let D_N be the semi-circular region which is bounded by F_- and the lower half of C_- (see Figure 2). When P_- lies inside D_N (where $r_P < r_Q$), we may substitute the bilinear expansion (3.1) into the third of the Helmholtz formulae, (2.4), to give

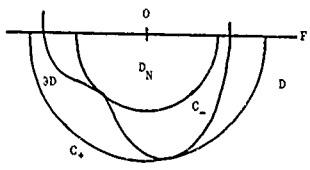


Figure 2. The inscribed and escribed semi-circles.

$$\sum_{m=0}^{\infty}\sum_{\sigma=1}^{2} a_m^{\sigma}(P_-)\int_{\partial D}\{\phi(q)\frac{\partial}{\partial n_q}\phi_m^{\sigma}(q) - V(q)\phi_m^{\sigma}(q)\}ds_q = 0, \tag{3.2}$$

where we have used the boundary condition (1.2). (3.2) holds for all P_- in D_N. Since the functions $\phi_m^{\sigma}(P_-)$ are regular solutions of Laplace's equation in D_N, it follows that each term in (3.2) must vanish, and so we obtain the following set of equations:

$$\int_{\partial D}\{\phi(q)\frac{\partial}{\partial n_q}\phi_m^{\sigma}(q) - V(q)\phi_m^{\sigma}(q)\}ds_q = 0, \qquad (N.F)$$

$\sigma = 1, 2$ and $m = 0, 1, \ldots$. We call these the null-field equations for water waves. Equations of this type were first obtained by Waterman (1965), for electromagnetic scattering problems. Since then, the null-field method (also called the 'T-matrix' method) has been used to solve many such problems, as well as problems in acoustics and elastodynamics; for a collection of papers on these topics, see the conference proceedings edited by Varadan and Varadan (1980). However, the null-field equations for water waves appear to be new.

Having obtained the null-field equations, we would like to know whether they are solvable. The following theorem has been proved by Martin (1981):

Theorem 2. Suppose that ∂D has properties J and that $V(q)$ is continuous on ∂D. Then, the null-field equations for water waves, (N.F), possess a unique solution for all values of K.

The proof of this theorem involves showing that ϕ satisfies (N.F) if and only if ϕ satisfies a Fredholm integral equation of the second kind, which is itself known to possess a unique solution. Such an integral equation has been obtained by Ursell (1981). He replaced G_0 by a different fundamental solution, G_1, defined by

$$G_1(P,Q) = G_0(P,Q) + \sum_{m=0}^{N}\sum_{\sigma=1}^{2} a_m^{\sigma}\phi_m^{\sigma}(P)\phi_m^{\sigma}(Q), \tag{3.3}$$

where a_m^{σ} are constants. Applying Green's theorem in D, to $\phi(P)$ and $G_1(P,Q)$ (as in section 2), then gives

$$\pi\phi(p) + \int_{\partial D}\phi(q)\frac{\partial}{\partial n_q}G_1(p,q)ds_q = \int_{\partial D}G_1(p,q)V(q)ds_q. \tag{3.4}$$

This is another Fredholm integral equation of the second kind for $\phi(q)$. Ursell (1981) has proved

Theorem 3. Let ∂D have properties J and let the constants a_m^{σ} in (3.3) be chosen such that $\mathrm{Im}(a_m^{\sigma}) > 0$ for $\sigma = 1, 2$ and $m = 0, 1, \ldots N$. Then, the integral equation (3.4) is uniquely solvable at any given value of K, provided that N is sufficiently large.

We now know that the null-field equations are uniquely solvable, but what is the solution of the original boundary-value problem? It can be shown that if $\phi(q)$ satisfies the null-field equations (or, equivalently, the integral equation (3.4)), then the solution of P is given by

$$\phi(P) = \frac{1}{2\pi}\int_{\partial D}\{G_1(P,q)V(q) - \phi(q)\frac{\partial}{\partial n_q}G_1(P,q)\}ds_q. \tag{3.5}$$

Suppose, now, that P lies outside C_+ (see Figure 2). Then, we can again use the bilinear expansion of G_0, (3.1), in (3.5) (together with (N.F) and (3.3)) to obtain

$$\phi(P) = \sum_{m=0}^{\infty}\sum_{\sigma=1}^{2} c_m^{\sigma}\phi_m^{\sigma}(P), \tag{3.6}$$

where the coefficients c_m^{σ} are given by

$$c_m^{\sigma} = \frac{1}{2\pi}\int_{\partial D}\{\alpha_m^{\sigma}(q)V(q) - \phi(q)\frac{\partial}{\partial n_q}\alpha_m^{\sigma}(q)\}ds_q,$$

$$\sigma = 1, 2; \; m = 0, 1, \ldots .$$

(3.6) implies that, exterior to C_+, $\phi(P)$ has an expansion in terms of a set of functions $\{\phi_m^{\sigma}\}$, each of which satisfies Laplace's equation in D, the free-surface condition and the radiation condition. Expansions of this type were first used by Ursell (1949) to solve the problem of the heaving, half-immersed circular cylinder (see section 4). Later (1950), he proved that the set $\{\phi_m^{\sigma}\}$ is complete. Therefore, we can assume that (3.6) holds exterior to C_+ and then proceed to give an alternative derivation of the null-field equations: Apply Green's theorem to $\phi(P)$ and $\phi_m^{\sigma}(P)$ in the region bounded by ∂D, F and S, where S is a large semi-circle, of radius r, enclosing ∂D and centred on O. There is no contribution from integrating over F, since ϕ and ϕ_m^{σ} both satisfy (1.1). We can show that the contribution from integrating over S vanishes as $r \to \infty$, by using (3.6), and then using asymptotic properties of ϕ_m^{σ} to prove that

$$\lim_{r\to\infty}\int_{-\frac{1}{2}\pi}^{\frac{1}{2}\pi}\{\phi_m^{\sigma}(r,\theta)\frac{\partial}{\partial r}\phi_n^{\nu}(r,\theta) - \phi_n^{\nu}(r,\theta)\frac{\partial}{\partial r}\phi_m^{\sigma}(r,\theta)\}r\,d\theta = 0. \tag{3.7}$$

(Here, we have assigned plane polar coordinates (r, θ), $-\frac{1}{2}\pi \le \theta \le \frac{1}{2}\pi$, to points on S.) If we now choose appropriate values for m and σ, we obtain the complete set of null-field equations, (N.F).

Thus, we see that the null-field equations do not depend, essentially, on the bilinear expansion of the wave-source, (3.1), or on the interior integral relation (2.4), but on the expansion of potentials which satisfy the free-surface and radiation conditions, as (3.6).

4. The Half-Immersed Circular Cylinder

Consider the special case of a half-immersed circular cylinder, with wetted surface C, floating in the free surface of deep water. We define circular polar coordinates (r,θ) such that points on C have coordinates (a,θ), with $-\frac{1}{2}\pi \le \theta \le \frac{1}{2}\pi$. The symmetric boundary-value problem $\mathcal{P}$ corresponding to vertical oscillations of the cylinder was first solved by Ursell (1949a). We shall now briefly describe his method (the 'method of multipoles').

For the particular geometry considered here, C_* coincides with C. Thus, we can represent ϕ as an infinite series of multipole potentials, throughout the entire fluid domain D, i.e. we can write

$$\phi(r,\theta) = \sum_{n=0}^{\infty} c_n \phi_n^1(r,\theta) \text{ for } r \ge a, \ -\tfrac{1}{2}\pi \le \theta \le \tfrac{1}{2}\pi, \quad (4.1)$$

where ϕ_0^1 is the potential due to a simple wave-source at 0 and ϕ_n^1, $n > 0$, are symmetric wave-free potentials; see the appendix.

(4.1) satisfies Laplace's equation in D, the free-surface condition (1.1) and the radiation condition. (4.1) also satisfies the boundary condition (1.2) on C if the coefficients c_n can be chosen such that

$$V(a,\theta) = U_0 \cos\theta = \sum_{n=0}^{\infty} c_n \left\langle \frac{\partial}{\partial r}\phi_n^1(r,\theta) \right\rangle, \quad 0 \le \theta \le \tfrac{1}{2}\pi, \quad (4.2)$$

where U_0 is a constant and angular brackets indicate that r is to be put equal to a.

To find the unknown coefficients c_n, Ursell suggested two methods. In one of these, he multiplied (4.2) by the complete set $\{\cos 2m\theta\}$, $m = 0,1,\ldots$, and integrated over C to give

$$\int_0^{\frac{1}{2}\pi} V(a,\theta)\cos 2m\theta \, a\,d\theta = \sum_{n=0}^{\infty} c_n \int_0^{\frac{1}{2}\pi} \left\langle a\frac{\partial}{\partial r}\phi_n^1(r,\theta) \right\rangle \cos 2m\theta \, d\theta, \ m = 0,1,\ldots .$$

This is an infinite system of linear algebraic equations for c_n; approximate values for c_n may be obtained by numerically solving a truncated system of equations.

Instead of multiplying (4.2) by $\{\cos 2m\theta\}$, let us multiply by the complete set $\{\phi_m^1(a,\theta)\}$, $m = 0,1,\ldots$, and integrate over C. We obtain

$$\int_0^{\frac{1}{2}\pi} V(a,\theta)\phi_m^1(a,\theta)\,a\,d\theta = \sum_{n=0}^{\infty} c_n \int_0^{\frac{1}{2}\pi} \left\langle a\frac{\partial}{\partial r}\phi_n^1(r,\theta) \right\rangle \phi_m^1(a,\theta)\,d\theta. \quad (4.3)$$

We now apply Green's theorem to ϕ_n^1 and ϕ_m^1 in the region bounded by C, F and S_∞, where S_∞ is a large semi-circle of radius r_∞. There is no contribution from integrating over F and the contribution from integrating over S_∞ also vanishes as $r_\infty \to \infty$, by (3.7). Hence, (4.3) becomes

$$\int_0^{\frac{1}{2}\pi} V(a,\theta)\phi_m^1(a,\theta)\,a\,d\theta = \sum_{n=0}^{\infty} c_n \int_0^{\frac{1}{2}\pi} \left\langle a\frac{\partial}{\partial r}\phi_m^1(r,\theta) \right\rangle \phi_n^1(a,\theta)\,d\theta = \int_0^{\frac{1}{2}\pi} \phi(a,\theta)\left\langle a\frac{\partial}{\partial r}\phi_m^1(r,\theta) \right\rangle d\theta, \quad (4.4)$$

$m = 0,1,\ldots$, by (4.1). We see that (4.4) are precisely the null-field equations for the symmetric oscillations of a half-immersed circular cylinder. This may be compared with the corresponding exterior problem of acoustics: for an oscillating circular cylinder, the null-field equations simply yield the Fourier components of the well-known exact solution; for all other geometries, the null-field equations of acoustics must be solved numerically. For water-wave problems, the null-field equations must always be solved numerically; this will be discussed in the next section.

5. Numerical Solution of the null-field equations

The null-field equations may be written as

$$\int_{\partial D} \phi(q)\frac{\partial}{\partial n_q}\phi_m^\sigma(q)\,ds_q = V_m^\sigma, \ \sigma = 1,2; \ m = 0,1,\ldots \quad (5.1)$$

where $\phi(q)$ is to be determined and the known constants V_m^σ are given by

$$V_m^\sigma = \int_{\partial D} V(q)\phi_m^\sigma(q)\,ds_q.$$

Before considering how to solve (5.1), we remark that the null-field equations are not integral equations; they form an infinite set of moment-like equations.

Let $\{\psi_n(q)\}$ be a set of functions which is complete over ∂D. Write

$$\phi(q) = \sum_{n=0}^{\infty} a_n \psi_n(q) \quad (5.2)$$

where the coefficients a_n are to be determined. Substituting (5.2) into (5.1) gives

$$\sum_{n=0}^{\infty} K_{mn} a_n = V_m, \quad m = 0,1,\ldots, \quad (5.3)$$

where

$$K_{mn} = \int_{\partial D} \psi_n(q)\frac{\partial}{\partial n_q}\phi_m(q)\,ds_q \quad (5.4)$$

and we have suppressed the dependence on σ. Clearly, the best choice for $\{\psi_n\}$ would be $\{\gamma_n\}$, where

$$\int_{\partial D} \gamma_n(q)\frac{\partial}{\partial n_q}\phi_m(q)\,ds_q = \delta_{mn}, \ m,n = 0,1,\ldots \quad (5.5)$$

(δ_{mn} is the Kronecker delta), for then (5.3) yields $a_m = V_m$ and (5.2) becomes

$$\phi(q) = \sum_{n=0}^{\infty} V_n \psi_n(q).$$

However, we do not know a priori which functions $\{\psi_n\}$ satisfy the orthogonality relation, (5.5), for a given boundary ∂D; for each value of n, the determination of ψ_n is equivalent to solving the null-field equations (with V_m replaced by δ_{mn}). Computationally, it is not worth while to determine $\{\psi_n\}$ (see Bates and Wall (1977, p.57) for some considerations of this point, in acoustics). However, it may be possible to choose $\{\psi_n\}$ so that (5.5) is nearly satisfied, i.e. so that the infinite system of equations (5.3) is diagonally-dominant. Assuming that such a choice can be made, we truncate the infinite system and obtain

$$\sum_{n=0}^{N} K_{mn} a_n = V_m, \qquad m = 0,1,\ldots,N. \tag{5.6}$$

This is a system of N+1 simultaneous, linear, algebraic equations for the N+1 coefficients a_n, $n = 0,1,\ldots,N$. Note that we have now made two approximations: we have only used the first N+1 of the null-field equations and we have only used N+1 of the complete set $\{\psi_n\}$ to represent ϕ on ∂D.

To obtain a practical numerical method, we must now choose the set of functions $\{\psi_n\}$. Simple choices, such as trigonometric functions or orthogonal polynomials, will often be satisfactory, but sometimes, other choices (perhaps functions which depend on K) will be more appropriate. Also, from computational experience gained by solving the analogous exterior problem of acoustics, we expect that the system (5.6) will be ill-conditioned for elongated bodies. Several methods for alleviating this difficulty have been devised (see, e.g., Wall, 1980), but, even in acoustics, no satisfactory algorithm exists for choosing $\{\psi_n\}$. Nevertheless, if we have made a reasonable choice for $\{\psi_n\}$, we can solve (5.6) and obtain a good approximation to $\phi(q)$; in the next section, we shall describe the use of this procedure to solve a particular problem $\mathcal{P}$.

6. The Half-Immersed Elliptic Cylinder

We consider the vertical oscillations of a half-immersed elliptic cylinder. The corresponding boundary-value problem $\mathcal{P}$ has been treated by several authors. For example, Porter (1960) (cf. Ursell, 1949b) has used conformal mapping and the method of multipoles, whilst Kim (1965) has solved the source integral equation (2.8).

Let an arbitrary point $q \equiv (x, y)$ on the wetted surface of the cylinder have coordinates

$$x = a\sin\eta, \quad y = b\cos\eta, \quad -\tfrac{1}{2}\pi \le \eta \le \tfrac{1}{2}\pi,$$

where $2a$ and b are the beam and draught, respectively, of the cylinder. In circular polar coordinates (r,θ), we have

$$x = r\sin\theta, \quad y = r\cos\theta, \quad -\tfrac{1}{2}\pi \le \theta \le \tfrac{1}{2}\pi,$$

where

$$r = b(\cos^2\eta + H^2\sin^2\eta)^{\frac{1}{2}}, \quad \tan\theta = H\tan\eta$$

and $H = a/b$. Since the motion is symmetric about $\theta = 0$ ($\eta = 0$), we only require the even ($\sigma = 1$) null-field equations, and only need to integrate over half of ∂D. Moreover, we have $V(q)ds_q = U_0 a\cos\eta\, d\eta$, where the cylinder is oscillating with vertical velocity $\mathrm{Re}\{U_0 e^{-i\omega t}\}$. Thus, the null-field equations become

$$\int_0^{\frac{1}{2}\pi} \phi(\eta)\{b\frac{\partial}{\partial n}\phi_m^1(q)\}(\sin^2\eta + H^2\cos^2\eta)^{\frac{1}{2}}d\eta = U_0 a V_m, \qquad m = 0,1,\ldots \tag{6.1}$$

where the constants V_m are given by

$$V_m = \int_0^{\frac{1}{2}\pi} \phi_m^1(r,\theta)\cos\eta\, d\eta. \tag{6.2}$$

The source potential, ϕ_0^1, may be evaluated using the expansion given by Yu and Ursell (1961), namely

$$\phi_0^1(r,\theta) = -\{(\log Kr - i\pi + \gamma)\cos(Kr\sin\theta) + \theta\sin(Kr\sin\theta)\}\exp(-Kr\cos\theta) + \sum_{m=1}^{\infty} \frac{(-Kr)^m}{m!}\{\frac{1}{1} + \frac{1}{2} + \ldots + \frac{1}{m}\}\cos m\theta,$$

where $\gamma = 0.5772\ldots$ is Euler's constant. The wave-free potentials, ϕ_m^1, are real and are given by

$$\phi_m^1(r,\theta) = \frac{\cos 2m\theta}{r^{2m}} + \frac{K}{(2m-1)}\frac{\cos(2m-1)\theta}{r^{2m-1}}, \qquad m = 1,2,\ldots .$$

The normal derivative of ϕ_m^1, $m = 0,1,\ldots$, may be evaluated using

$$\frac{\partial}{\partial n}\phi(r,\theta) = \cos(\alpha-\theta)\frac{\partial\phi}{\partial r} + \sin(\alpha-\theta)\frac{1}{r}\frac{\partial\phi}{\partial\theta},$$

where $H\tan\alpha = \tan\eta$.

To solve the null-field equations, we use the method outlined in section 5: write

$$\phi(\eta) = U_0 a \sum_{n=0}^{N} a_n \psi_n(\eta)$$

and substitute into the first N+1 of (6.1). We obtain the system (5.11), with V_m given by (6.2) and K_{mn} given by

$$K_{mn} = \int_0^{\frac{1}{2}\pi} \psi_n(\eta)\{b\frac{\partial}{\partial n}\phi_m^1(r,\theta)\}(\sin^2\eta + H^2\cos^2\eta)^{\frac{1}{2}}d\eta.$$

V_m and K_{mn} may be evaluated numerically using any suitable quadrature formula (the

integrands are non-singular). In our numerical work, we tried $\phi_n(\eta) = \cos 2n\eta$ and $\phi_n(\eta) = T_{2n}(2\eta/\pi)$ ($T_n(x)$ is a Chebyshev polynomial: $T_n(\cos\theta) = \cos n\theta$); although other choices could have been made, we found the Chebyshev polynomials to be quite satisfactory for our problem.

In Table 1, we give values of the virtual-mass coefficient for various values of Ka and H, where

$$\text{virtual-mass coefficient} = -\frac{4}{\pi}\int_0^{\frac{1}{2}\pi} \mathrm{Re}\{\frac{\phi(\eta)}{U_0 a}\}\cos\eta\, d\eta.$$

(Here, the virtual mass has been normalised by the mass of the fluid displaced by a half-immersed circular cylinder of radius a.) All the results shown were obtained using Chebyshev polynomials and $N \leq 7$. Comparing our numerical values with the graphical results of Porter (1960, Fig.13) and Kim (1965, Fig.15), we see that the agreement is good (Kim's results must be multiplied by $2/\pi$). We believe that these are correct to 4 significant figures.

As expected our simple numerical scheme for solving the null-field equations does not converge for very thin ellipses ($H < 0.4$ and $H > 3$, approximately), even though the complete set of equations is guaranteed to have a unique solution. It is hoped that this difficulty can be overcome by using a more sophisticated numerical technique; see, e.g., Varadan and Varadan (1980), where various techniques for solving the null-field equations of acoustics are described. However, when the equations are not too ill-conditioned, our simple scheme is very efficient; the machine-time required is rather less than that required by integral-equation methods. In addition, the null-field method does not exhibit irregular frequencies; this is important, computationally, because the location of these frequencies in the spectrum is unknown a priori for an arbitrary curve $\mathcal{B}$. Thus, the null-field method may be computationally attractive, especially for problems which are fully three-dimensional (see section 7).

H	Wavenumber, Ka			
	0.5	1.0	1.5	2.0
0.6	0.54584	0.64426	0.74904	0.81580
0.7	0.56600	0.62149	0.71830	0.78765
0.8	0.59115	0.60915	0.69457	0.76333
0.9	0.61795	0.60440	0.67711	0.74303
1.0	0.64463	0.60498	0.66493	0.72658
1.1	0.67029	0.60917	0.65702	0.71362
1.2	0.69453	0.61575	0.65248	0.70371
1.3	0.71718	0.62384	0.65056	0.69637
1.4	0.73824	0.63282	0.65063	0.69119
1.5	0.75777	0.64227	0.65219	0.68778
1.6	0.77586	0.65190	0.65486	0.68580
1.7	0.79262	0.66152	0.65834	0.68499
1.8	0.80816	0.67098	0.66239	0.68509
1.9	0.82257	0.68020	0.66683	0.68593
2.0	0.83598	0.68912	0.67153	0.68734

Table 1. Virtual-mass coefficient for heaving elliptic cylinder, for various Ka and H, where H = a/b = half-beam/draught.

7. Conclusion

The best known method for treating water-wave radiation problems is to solve an integral equation of the second kind over the (mean) wetted surface. However, it is also well-known that the usual boundary integral equations are not uniquely solvable at the irregular values of K. In this paper, we have described an alternative method, which is to solve the infinite system of null-field equations. These equations (which appear to be new in the context of water-wave problems) always have a unique solution - the unphysical irregular values do not occur. Moreover, this solution may be used to solve the original boundary-value problem $\mathcal{P}$.

For simplicity, we have only presented the null-field equations for two-dimensional motions in deep water. However, the method may be extended to three-dimensional motions and to water of constant finite depth. For the two-dimensional, finite-depth case, we simply replace ϕ_m^σ by the corresponding multipole potentials; see Thorne (1953) or Ursell (1981). The three-dimensional case is similar and is treated by Martin (1981); the corresponding multipole potentials were also obtained by Thorne (1953), and the bilinear expansion of the point wave-source, corresponding to (3.1), has been given by Martin (1981). In each case, it can be shown that the infinite set of null-field equations has precisely one solution, for all values of K.

In section 5, we examined several aspects of the numerical solution of the null-field equations. We described a simple exact method for reducing the null-field equations to an infinite system of linear algebraic equations. Truncating this system leads to a practical method for solving the null-field equations. In section 6, we described a successful application of this method to the two-dimensional problem $\mathcal{P}$ corresponding to the vertical oscillations of a half-immersed, elliptic cylinder.

It is clear that much work remains to be done on the development of more sophisticated techniques for solving the null-field equations. Nevertheless, the null-field method does provide an alternative approach which, it is hoped, will be as computationally useful as it is already known to be in other branches of mathematical physics.

Appendix

The following theorem has been proved by Ursell (1981):

Theorem. When $r_P < r_Q$, the two-dimensional source potential, defined by (2.1) can be expanded as

$$G_0(P,Q) = \sum_{m=0}^{\infty}\sum_{\sigma=1}^{2} a_m^\sigma(P)\phi_m^\sigma(Q),$$

where

$$\phi_0^1(P) = \int_0^\infty e^{-ky}\cos kx \frac{dk}{k-K}, \quad \phi_0^2(P) = -\frac{\partial}{\partial x}\phi_0^1(P),$$

$$\phi_m^1(P) = \frac{\cos 2m\theta}{r^{2m}} + \frac{K}{2m-1}\frac{\cos(2m-1)\theta}{r^{2m-1}},$$

$$\phi_m^2(P) = \frac{\sin(2m+1)\theta}{r^{2m+1}} + \frac{K}{2m}\frac{\sin 2m\theta}{r^{2m}},$$

$$a_0^1(P) = -2e^{-Ky}\cos Kx, \quad a_0^2(P) = \frac{-2}{K}e^{-Ky}\sin Kx,$$

$$a_m^1(P) = \frac{-2(2m-1)!}{K^{2m}} \sum_{q=2m}^{\infty} \frac{(-Kr)^q}{q!}\cos q\theta,$$

$$a_m^2(P) = \frac{2(2m)!}{K^{2m+1}} \sum_{q=2m+1}^{\infty} \frac{(-Kr)^q}{q!}\sin q\theta,$$

$m = 1,2,\ldots,$ and the point $P \equiv (x, y)$ has circular polar coordinates given by $x = r\sin\theta$, $y = r\cos\theta$ (with $r = r_p$).

References

Baker, B.B. and Copson, E.T. 1950 The mathematical theory of Huygens' principle, 2nd ed. Oxford University Press.

Bates, R.H.T. and Wall, D.J.N. 1977 Null field approach to scalar diffraction, I. General method. Phil. Trans. Roy. Soc. A287, 45-78.

Børresen, R. 1980 On the irregular frequency problem in the theory of ship motions. Det norske Veritas Rep. No. 80-0674.

John, F. 1950 On the motion of floating bodies II. Comm. Pure Appl. Math. 3, 45-101.

Kim, W.D. 1965 On the harmonic oscillations of a rigid body on a free surface. J. Fluid Mech. 21, 427-451.

Martin, P.A. 1980 On the null-field equations for the exterior problems of acoustics. Quart. J. Mech. Appl. Math. 33, 385-396.

Martin, P.A. 1981 On the null-field equations for water-wave radiation problems. J. Fluid Mech. To appear.

Mei, C.C. 1978 Numerical methods in water-wave diffraction and radiation. Ann. Rev. Fluid Mech. 10, 393-416.

Porter, W.R. 1960 Pressure distributions, added-mass, and damping coefficients for cylinders oscillating in a free surface. Dissertation, Univ. California, Berkeley.

Sayer, P. 1980 An integral-equation method for determining the fluid motion due to a cylinder heaving on water of finite depth. Proc. Roy. Soc. A372, 93-110.

Thorne, R.C. 1953 Multipole expansions in the theory of surface waves. Proc. Cambridge Phil. Soc. 49, 707-716.

Ursell, F. 1949a On the heaving motion of a circular cylinder on the surface of a fluid. Quart. J. Mech. Appl. Math. 2, 218-231.

Ursell, F. 1949b On the rolling motion of cylinders in the surface of a fluid. Quart. J. Mech. Appl. Math. 3, 335-353.

Ursell, F. 1950 Surface waves on deep water in the presence of a submerged circular cylinder. II. Proc. Camrbidge Phil. Soc. 46, 153-158.

Ursell, F. 1953 Short surface waves due to an oscillating immersed body. Proc. Roy. Soc. A 220, 90-103.

Ursell, F. 1981 Irregular frequencies and the motion of floating bodies. J. Fluid Mech. 105, 143-156.

Varadan, V.K. and Varadan, V.V. (ed.) 1980 Acoustic, electromagnetic and elastic wave scattering - Focus on the T-matrix approach. Pergamon Press, New York.

Wall, D.J.N. 1980 Methods of overcoming numerical instabilities associated with the T-matrix method. pp.269-286 of Varadan and Varadan (1980).

Waterman, P.C. 1965 Matrix formulation of electromagnetic scattering. Proc IEEE 53, 805-812.

Waterman, P.C. 1969 New formulation of acoustic scattering. J. Acoust. Soc. Am. 45, 1417-1429.

Yu, Y.S. and Ursell, F. 1961 Surface waves generated by an oscillating circular cylinder on shallow water: theory and experiment. J. Fluid Mech. 11, 529-551.

SOME RESULTS ON APPROXIMATION BY EXPONENTIAL SERIES APPLIED TO HYDRODYNAMIC PROBLEMS

Jean-Claude Daubisse
École Nationale Supérieure de Mécanique
1, rue de la Noë, 44072 Nantes Cedex (France)

Abstract

For solving an extensive number of problems, it seems important to be able to approximate a function known by points or analytically, by a sum of exponential functions. In this paper, several algorithms are described, enabling such a smoothing to be performed. Besides, a number of applications to naval hydrodynamics are also introduced.

1. Introduction

In every fields, in which the use of Fourier Transform is very important, sophisticated approximation methods seem to be of the utmost interest.

This is especially the case for naval hydrodynamics, at least as far as the boundary value problems approached by the perfect fluid theory are concerned : wave resistance of a ship with a constant sailing speed in calm water, behaviour of off-shore structures or ships subjected to wave effects, transient phenomena etc...

The selection of the n basic functions $g_i(x)$ enabling the approximation $\sum_{i=1}^{n} a_i g_i(x)$ of the f(x) function, the Fourier transform of which have to be calculated, is governed by the following requirements :

- The approximation has to be satisfactory in the [0,X] interval, with X sufficiently large so that the difference between the approximating function and the function itself does not have any numerical effect on the rest of the computation procedure.

- The $g_i(x)$ basic functions has to appear under a sufficiently simple form so that their own Fourier Transform can be calculated analytically.

Such conditions naturally call for smoothing methods of using multipoles or exponentials.

Multipoles have already been used for wave calculation of a fully submerged body [1], in this paper, several algorithms using exponential functions are developed.

More generally, functions defined on an interval [a,b] either analytically or by points can be replaced by exponential series in order to be able to perform further calculations analytically.

2. Principle of the method

The principle of the method is based on Lanczos and Prony [2] studies, taken-up by Fröberg [3].

e.g a f function defined in (n+1) equi-spaced points (x_r, y_r) r=0,...,n.

Approximation is endeavoured by exponential series of $\sum_{i=1}^{n} a_i e^{\lambda_i x}$ form, where a_i and λ_i are complex unknowns.

Let us assume $x_r = x_o + rh$, $C_i = a_i e^{\lambda_i x_o}$ and $V_i = e^{\lambda_i h}$ (2.1)

Assuming that the approximating function shall pass through the base points, we thus obtain the following ((n+1) n) system :

$$\left\{\begin{array}{l} C_1 + C_2 + \ldots\ldots\ldots + C_n = y_o \\ C_1V_1 + C_2V_2 + \ldots\ldots + C_nV_n = y_1 \\ \qquad\qquad\qquad\qquad\qquad\qquad\qquad\qquad \text{system } (n\ n) \\ C_1V_1^{n-1} + C_2V_2^{n-1} + \ldots + C_nV_n^{n-1} = y_{n-1} \end{array}\right. \quad (2.2)$$

$$\left\{\begin{array}{l} C_1V_1^{n} + C_2V_2^{n} + \ldots + C_nV_n^{n} = y_n \\ \qquad\qquad\qquad\qquad\qquad\qquad\qquad\qquad \text{system } ((n+1)\ n) \\ C_1V_1^{n} + C_2V_2^{n} + \ldots\ldots + C_nV_n^{n} = y_n \end{array}\right. \quad (2.3)$$

e.g the n degree polynome the roots of which are the V_i :

$$P_n(V) = \prod_{i=1}^{n} (V - V_i) = \sum_{k=0}^{n} s_k V^{n-k} \quad (2.4)$$

with $s_o = 1$

Only considering the (n+1) first lines of the (2.3) system, and multiplying each line by the appropriate s_i coefficient (s_{n-k} for the k^{th} line at the first stage), we obtain, after summing up, and account taken of the fact that $P_n(V_i) = 0$

$$y_{n-1}s_1 + y_{n-2}s_2 + \ldots\ldots + y_o s_n = -y_n$$

By one-line shift each time, and by repeating the above operation until n, the following (n-m+1) =m system is obtained :

$$\begin{cases} y_{m-1}\,s_1 + y_{m-2}\,s_2 + \cdots + y_0\,s_m = -y_m \\ y_m\,s_1 + y_{m-1}\,s_2 + \cdots + y_1\,s_m = -y_{m+1} \\ \cdots\cdots\cdots\cdots\cdots\cdots\cdots \\ y_{n-1}\,s_1 + y_{n-2}\,s_2 + \cdots + y_{n-m}\,s_m = -y_n \end{cases} \qquad (2.5)$$

If n > 2m-1, the system is overdetermined and can be solved by a least square method, thus enabling the s_i to be obtained.

The V_i are the root of (2.4), so the λ_i can be determined by

$$\lambda_i = \frac{\text{Log } V_i}{h}$$

Fröberg suggests calculating the C_i from regular sub-matrixes issued from (2.3), by suppressing (m-n) lines arbitrarily (e.g the (2.2) matrix).

Hence $a_i = C_i\, e^{-\lambda_i x_0}$

Algorithm 1

A direct application of the above method leads, for obtaining the C_i, to the resolution of a regular system (2.2).

This is an artifice which favours the points involved in the retained relationships, to the detriment of the neglected points.

This has been evidenced in the tests that we have performed.

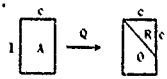
Algorithm 2 - General case - Complex λ_i

Generally, it is desirable to obtain an homogeneous approximation over the full definition interval. Therefore, we have been led to solve the complete over-determined system(2.3)by a least square method, using unitary transformation of the Householder type.

For solving (2.5) and (2.3), we have therefore adopted the same type of algorithm, the main stages for the real case are recalled in the following (for example [4]).

We have to solve $A\underline{x} = \underline{b}$ (A(l C) avec l > C) minimizing $\| A\underline{x} - \underline{b} \|^2$.

For doing so, A is transformed in upper "triangular" matrix by applying an orthogonal operator Q.



The Q matrixes are the products of elementary orthogonal and symmetrical matrixes of the following form

$$H = I - 2\,\underline{u}\,\underline{u}^T$$

$\underline{u} \in R^l \qquad H \in R^{l\times l}$ and such as

$H\,\underline{a} = \alpha \underline{e_1}$ with $\underline{a} \in R^l$

$\underline{e_1} = (1.0,\ldots 0) \in R^l \qquad \alpha \in R$

Thus $\text{Min} \| A\underline{x} - \underline{b} \|^2 = \text{Min} \| QA\underline{x} - Q\underline{b} \|^2$

$$= \left\| \begin{bmatrix} R \\ 0 \end{bmatrix} \underline{x} - \begin{bmatrix} \underline{\tilde{b}}_1 \\ \underline{\tilde{b}}_2 \end{bmatrix} \right\|^2 = \| R\underline{x} - \underline{\tilde{b}}_1 \|^2 + \| \underline{\tilde{b}}_2 \|^2$$

with $\underline{\tilde{b}} = Q\,\underline{b}$

The $\hat{x}$ optimum solution is obtained by solving $R\underline{x} = \underline{\tilde{b}}_1$ and the minimizing error

$$E = \| \underline{\tilde{b}}_2 \|^2 \qquad (2.6)$$

We shall see in the following that this error may have a certain importance on the "optimum" selection of the m number of exponentials.

Both programs have been developed separately the complex case being sensibly different from the real case.

This second algorithm has been tested in various configurations :

Example 1.

e.g $x \to f(x) \quad e^{-0.5x} + 2e^{-x} + 3e^{-2x} + 4e^{-3x}$

$x \in [0,10]$

e.g. ϵ_{max} the maximum absolute error at the base and at certain interpolation points.

We are giving below a summary table of the results of the (a_i, λ_i) couples in function of the number m of selected exponentials.

Number of reference points 21

m	λ_i calculated	a_i calculated	ϵ_{max}
3	- 3,82.. - 1,35.. - 0,55..	5,49 3,06 1,44	1.10^{-3}
4	- 3. - 2. - 1. - 0.5	4. 3. 2. 1.	2.10^{-15}
5	- 3. - 0.5 - 2. - 1. - 2.8 + 6.2 i	4. 1. 3. 2. 0.2 10^{-13} + 0.i	2.10^{-15}

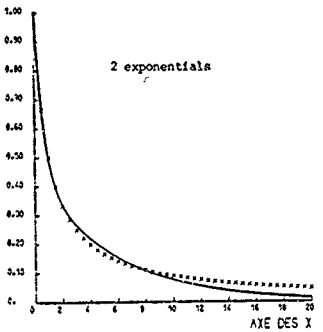
This example is purely academic, but the results of this table show that the algorithm

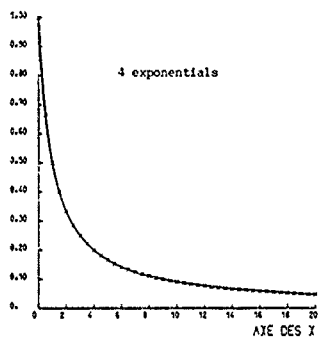
enables the accurate determination of the number and values of the (a_i, λ_i) couples of a function constituted by a sum of exponentials.

Besides, we can note that with $m = 3$, the approximation is rather poor, and that for $m > 4$ the a_i coefficients corresponding to the additional λ_i are practically nil.

Example 2. Decreasing monotonic function

e.g. $x \to f(x) = \frac{1}{1+x}$ $\quad x \in [0,20]$





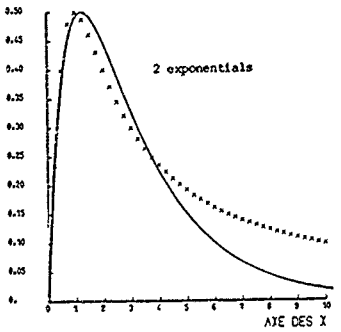
Only a few problems are involved by such functions.

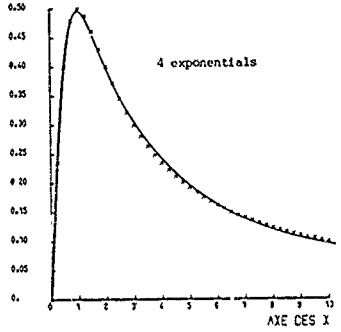
The approximation is good with a few number of exponentials.

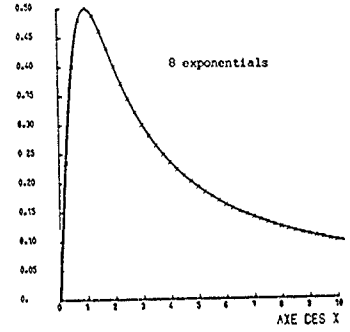
With $m = 4$; $h = 0.5 \to \varepsilon_{max} = 3.10^{-4}$

Example 3. Non oscillating function with extremum.

$x \to f(x) = \frac{x}{x^2+1}$ $\quad x \in [0,10]$ $\quad n = 40$







The tests carried out on this type of functions give rise to the following general remarks :

i) for such functions, it does not seem necessary to take many reference points especially, a step $h \geq 0.25$ is generally sufficient.

ii) There is a minimum number m of exponentials to be reached for obtaining a correct approximation ; below the result is poor, and above, the additional (a_i, λ_i) couples are used for improving the results. This is a phenomenon which has been evidenced in most tests that we have carried out.

iii) The accuracy at the interpolation points within the first discretisation intervals is often less good than in any other point of the definition interval.

To overcome this drawback, it is necessary to increase m or, better, take the necessary arrangements so that the phenomenen be rejected beyond the approximation validity limits. For doing so, the reference points are increased by a few additional points determined either analytically, or by an extrapolation method, the abscissae of which are lower than the lower limit of the initial interval.

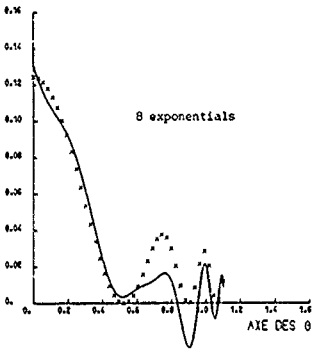
iv) Empirically, the "optimal" number of exponentials is comprised between n/5 and n/3, where n is the reference point.

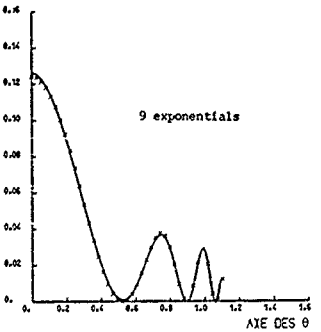
Example 4. Oscillating functions

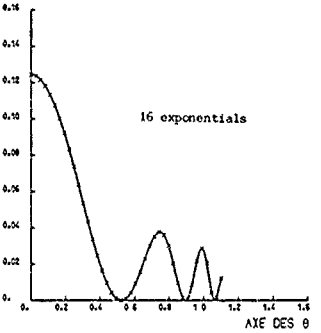
$$F(\theta) = (\cos 3\theta + J_2\left(\frac{2}{\cos^2\theta}\right) * \cos\theta)^2$$

(J_2, 2nd category Bessel's function).

$\theta \in [0, 1.1]$ $\quad n = 40$







The remarks are quite the same as for the preceding example. However, if the number of significant oscillations is relatively high, the number of reference points must be large enough for ensuring a good definition of the function to be approximated. As corollary, the number m of exponentials (generally complex) must be higher so that the approximating function be in phase with the oscillations of the initial function.

Algorithms 3 and 4. Real(a_i, λ_i)

In general, the λ_i are complex, expecially if m is large. The trigonometric functions connected with the imaginary part may, for certain types of functions, introduce interference oscillations and thus impair the accuracy, and especially within the first discretisation intervals.

Furthermore, in certain cases, for simplifying the future calculation processes, the approximation by real exponential functions becomes essential.

Calculation of the λ_i is performed as described in the foregoing, but only the real parts are kept. The approximation function is then of the $\Sigma a_i e^{\lambda_i x}$ type, with λ_i fixed $\in R$.

Then it is sufficient to calculate the new a_i coefficients.

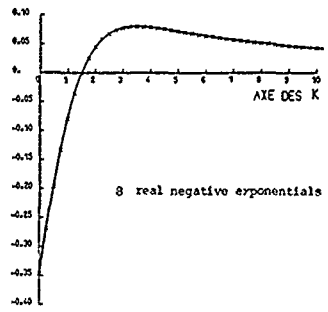
For doing so, two procedures have been used

i) A least square method (L_2 norm). The following has to be minimized :

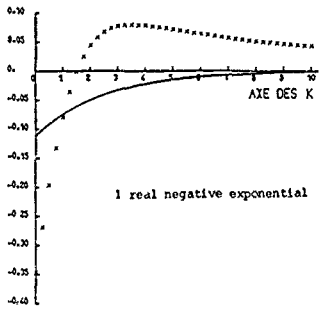
$$S = \sum_{i=0}^{n} \left(y_i - \sum_{j=1}^{m} a_j e^{\lambda_j x_i}\right)^2$$

$\frac{\partial S}{\partial a_j} = 0 \quad j = 1,\ldots m$ leads to a m rank symmetrical system.

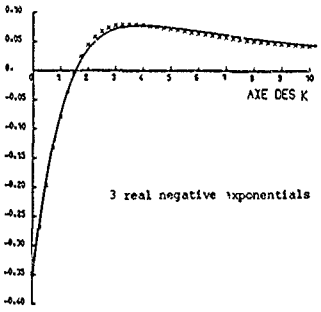
Example 5 : Function (3.17) with $K_0 = 0.8$
$K \in [0,10]$ $n=40$



8 real negative exponentials



1 real negative exponential



3 real negative exponentials

This N° 3 algorithm shall be used for classes of decreasing monotonic functions, or functions with a reduced number of extremes.

In such case, with the same number of expocntials, the obtained results are generally equivalent, or slightly better than the previous results.

ii) Use of a L_∞ or L_1 norm

e.g. $g(a,x) = \sum_{i=1}^{m} a_i e^{\lambda_i x}$ with $a \in E^m$

and λ_i fixed $\in R$

This may lead to minimizing

$$\|g(a,x) - y\|_1 = \sum_{j=1}^{n} |g(a,x_j) - y_j| \quad \text{Norm } L_1$$

or

$$\|g(a,x) - y\|_\infty = \max_j |g(a,x_j) - y_j| \quad \text{Norm } L_\infty$$

Both above minimizations can be reduced to a linear programming problem (refer to [5]) which has been solved by Simplex type methods.

The approximations thus obtained are comparable to the preceding approximations.

However, an interesting feature of this type of algorithms is that certain constraints can be added, especially on the a_i coefficients, or on the first and second derivatives of the approximating function (refer to [6]).

To conclude .

- Whatever the selected algorithm, for monotonic functions featuring a single extremum only, very fine discretisation proves to be useless.

- In the case of oscillating functions, the definition shall be better, and in corollary, the number m of exponentials shall be larger.

- The tests carried out led to the selection of $m \in [n/5, n/3]$, n = number of reference points.

We also noted that the error in solving over-determined systems $\|\underline{e}_2\|^2$ (2.6) reaches its minimum within that interval.

If n >> m, i.e. if the number of lines of the system is much greater than the number of columns, the resolution may be poor.

At the other end, we have the condition $m \leq (n+1)/2$ so that the resolution be possible.

Finally, at fixed n, an automatic selection of m can be performed by testing, for example, the average quadratic error obtained at the reference points and at certain number of interpolation points.

3. Some direct applications to hydrodynamic problems

Numerical calculation of the integral exponential functions

Whatever the method used for solving a free surface problem, functions of the following type have to be calculated many and many times :

$$G(\zeta) = e^{\zeta} E_1(\zeta) \tag{3.1}$$

$$E_1(\zeta) = \int_{\zeta}^{\infty} \frac{e^{-t}}{t}\, dt \qquad -\pi < \mathrm{Arg}\ \zeta < \pi \tag{3.2}$$

designating the exponential integral of first order.

Therefore, it is essential to use very performing approximation formulae ; amongst these, the most extensively used is the Hess and Smith formula [7]

$$\left.\begin{aligned} G(\zeta) &= \frac{M+N}{D} + \varepsilon(\zeta) \qquad \begin{cases} 0 < |\zeta| < \infty \\ |\varepsilon(\zeta)| \leq 7.10^{-6} \end{cases} \\ M &= -(1+m_1\zeta + m_2\zeta^2 + m_3\zeta^3 + m_4\zeta^4)\log\zeta\ , \\ &\qquad -\pi < \mathrm{Arg}\ \zeta < \pi \\ N &= -\gamma(n_0+n_1\zeta + n_2\zeta^2 + n_3\zeta^3 + n_4\zeta^4 + n_5\zeta^5) \\ &\quad + d_1\zeta + d_2\zeta^2 + d_3\zeta^3 + d_4\zeta^4 + d_5\zeta^5 + d_6\zeta^6 \end{aligned}\right\} \tag{3.3}$$

γ designating the Euler constant.

m_i, n_i, d_i being given numerical coefficients.

We shall also mention the work of D. Martin [8] who has performed an exhaustive study enabling the selection of the best approximation formulae to be used depending on the position occupied by the point of affix ζ.

Approximation formulae obtained by a smoothing method using a series of exponentials are proposed in the following.

First, let us consider the case where $R_e(\zeta) \geq 0$, we can write

$$G(\zeta) = \int_0^{\infty} \frac{e^{-\zeta t}}{t+1}\, dt \tag{3.4}$$

and hence, by approximating the $1/(t+1)$ function for $t \geq 0$, by a series $\sum_{i=1}^{m} a_i e^{\lambda_i t}$:

$$G(\zeta) = \sum_{i=1}^{m} \frac{a_i}{\zeta - \lambda_i} \tag{3.5}$$

In the case where $R_e(\zeta) < 0$, the following distinction shall be made :

$$\left.\begin{aligned} G(\zeta) &= \int_0^{\infty} \frac{e^{i\zeta t}}{t+1}\, dt \quad \text{if } \Pi_m \zeta > 0 \\ G(\zeta) &= \int_0^{\infty} \frac{e^{-i\zeta t}}{t-1}\, dt \quad \text{if } \Pi_m \zeta < 0 \end{aligned}\right\} \tag{3.6}$$

Now, by approximating the $1/(t+i)$ function, for $t > 0$, by $\sum_{i=1}^{m} b_i e^{\mu_i t}$, we obtain :

$$\left.\begin{aligned} G(\zeta) &= -\sum_{j=1}^{m} \frac{b_j}{\mu_j + i\zeta} \\ G(\zeta) &= -\sum_{j=1}^{m} \frac{\bar{b}_j}{\bar{\mu}_j - i\zeta} \end{aligned}\right\} \tag{3.7}$$

We have performed numerical tests for validating the formulae (3.5) and (3.7). As far as (3.5) is concerned, we have obtained a precision of 1.10^{-6}, by approximating $1/(t+1)$ by a sum of 8 exponentials. On the contrary, 12 exponentials have been necessary when using the formula (3.7).

In both cases as compared to formula (3.3), time saving is substantial.

Construction of the Green function associated with a distribution of Kelvin singularities Bidimensional problem

Within a plane (xoy) of a bi-dimensional flow, a distribution of the Rankine singularities located in the half plane $y < 0$ is considered ; this generates a potential function $\phi(x,y\,;t)$ to which it is proposed to associate a $\varphi(x,y\,;t)$ harmonic function, regular in the half plane $y < 0$, and which shall be determined in such a way that the $\phi_0 = \phi + \varphi$ potential satisfies a free surface condition in any point of the $y = 0$ axis.

Such calculations require, the expression of the inverse Fourier transform of the function $\phi(x,o\,;t)$.

$$\text{e.g. } \hat{\phi}(k,t) \qquad \int_{-\infty}^{+\infty} \phi(x,t)\, e^{ikx}\, dk \tag{3.8}$$

The $\phi(x,t)$ function may still be considered as the superposition of the elementary potentials generated by a series of multipoles :

$$\phi(x,t) \qquad R_e \sum \frac{a_n(t)}{(x - z_0(t))^n}$$

Also, as an example, we will perform the calculation of the Fourier transform corresponding to one of these elementary potentials ; to illustrate the smoothing method in the most adverse case, we have selected, amongst these potentials, that which vanishes the less rapidly at infinity, i.e. : (refer to example 3)

$$\phi_1(x) = \frac{x}{x^2+1} \qquad (3.9)$$

When performing smoothing by a sum of 16 exponentials, on the [0, 15] interval, the approximation of its Fourier transform is obtained,

$$\text{i.e. : } \hat{\phi}_1^*(k) = \sum_{j=1}^{16} a_j \frac{2ik}{\lambda_j^2 + k^2}$$

The table below enables the $\hat{\phi}_1^*(k)$ values thus obtained to be compared with those given by the exact formula :

$$\hat{\phi}_1^*(k) = i\pi e^{-k}$$

k	Approached value	Exact value
0.1	2.838 143	2.842 631
0.2	2.572 292	2.572 119
0.3	2.327 331	2.327 349
0.4	2.105 874	2.105 873
0.5	1.905 473	1.905 473
1.	1.155 727	1.155 727
2.	0.425 168	0.425 168
5.	0.021 168	0.021 168
10.	0.000 142	0.000 142

Resolution of the tridimensional diffraction radiation problem in finite water depth : [9]

Let us first remind the expression of the potential generated at any M(x,y,z) by a Kelvin pulsating source Q $Q' \cos \omega t$, centered on the M'(x',y',z') point within the $-h < z < 0$ domain e.g. :

$$\phi(M,t) = -\frac{Q}{4\pi}\frac{1}{h}\cos\omega t \left(\frac{1}{MM'} + \frac{1}{MM'_0}\right) - \frac{Q}{4\pi}\frac{1}{h} R_e\, e^{i\omega t} \times \int_{-\pi}^{\pi} d\theta \int_0^{\infty} \frac{(K+K_0)\, e^{-K}\, ch\,K(Z+1)\, ch\,K(Z'+1)}{K\,sh\,K - K_0\, ch\,K + i(0)}\, e^{i K\Omega}\, dK \qquad (3.11)$$

with

$$X = \frac{x}{h}\ ,\ Y = \frac{y}{h}\ ,\ Z = \frac{z}{h}\ ;\ X' = \frac{x'}{h}\ ,\ \ldots$$

$$\Omega = (X-X')\cos\theta + (Y-Y')\sin\theta$$

$$K_0 = \frac{\omega^2 h}{g}$$

M'_0 being the symmetric of M' in regard to the bottom.

The integral kernel relating to the variable k used in (3.11) can be written under the following form

$$\frac{(K+K_0)\, e^{-K}\, ch\,K(Z+1)\, ch\,K(Z'+1)\, e^{i K\Omega}}{K\,sh\,K - K_0\, ch\,K + i(0)} =$$

$$F(K)\, e^{-2K}\, ch\,K(Z+1)\, ch\,K(Z'+1)\, e^{iK\Omega} \qquad (3.13)$$

setting :

$$F(K) = \frac{(K+K_0)\, e^{K}}{K\,sh\,K - K_0\, ch\,K + i(0)} \qquad (3.14)$$

the term $K\,sh\,K - K_0\,ch\,K$ is cancelled out on the integration interval for a single value of K, $K = M_0$, M_0 being the positive root of the implicite equation :

$$M_0\, th M_0 = K_0 \qquad (3.15)$$

The principal part of F(K) for K close to M_0 is :

$$F_0(K) = \frac{A_0}{K - (M_0 - i(0))}\ ,\ A_0 = \frac{M_0^2 + K_0^2}{M_0^2 - K_0^2 + K_0}$$

Then, we shall set :

$$F(K) = F_1(K) + \frac{A_0}{K - (M_0 - i(0))} + 2 \qquad (3.16)$$

in order to indroduce $F_1(K)$

$$F_1(K) = \frac{(K+K_0)\, e^{K}}{K\,sh\,K - K_0\,ch\,K} - \frac{A_0}{K - M_0} - 2 \qquad (3.17)$$

which does not possess any pole on the integration interval, and vanishing as $1/k$, for $k \to \infty$

With these notations, the integral related to the k variable takes the following form :

$$I = \int_0^{\infty} \left\{ F_1(K) + \frac{A_0}{K - (M_0 - i(0))} + 2 \right\} \times e^{-2Y}\, ch\,K(Z+1)\, ch\,K(Z'+1)\, e^{iK\Omega}\, dK \qquad (3.18)$$

e.g. replacing the product $ch\,K(Z+1)\,ch\,K(Z'+1)$ by a sum of exponentials

$$I = \frac{1}{4}\int_0^{\infty} \left\{ F_1(K) + \frac{A_0}{K - (M_0 - i(0))} + 2 \right\} \times \left(e^{\zeta_1 K} + e^{\zeta_2 K} + e^{\zeta_3 K} + e^{\zeta_4 K}\right) dK \qquad (3.19)$$

with

$$\zeta_1 = Z+Z' + i\Omega \qquad \zeta_2 = -Z+Z' - 2 + i\Omega$$
$$\zeta_3 = Z-Z' - 2 + i\Omega \qquad \zeta_4 = -(Z+Z'+4 - i\Omega) \qquad (3.20)$$

The contribution of the second term appearing between brackets in (3.19) can be expressed without difficulties from the conventional exponential integral ; the contributions of the third term is immediate.

Finally, for calculating the integral

$$I_1 = \frac{1}{4}\int_0^{\infty} F_1(K)\,(e^{\zeta_1 K} + e^{\zeta_2 K} + e^{\zeta_3 K} + e^{\zeta_4 K})\,d\lambda \quad (3.21)$$

we have approximated $F_1(K)$, for $K > 0$, by $\sum_{i=1}^{m} a_i\, e^{\lambda_i \lambda}$. We thus have :

$$I_1 = -\frac{1}{4}\sum_{i=1}^{m} a_i \left(\frac{1}{\zeta_1+\lambda_i} + \frac{1}{\zeta_2+\lambda_i} + \frac{1}{\zeta_3+\lambda_i} + \frac{1}{\zeta_4+\lambda_i}\right)$$

For easier performance of further calculations we choosed the smoothing method that yields to a sum of negative real exponentials. In fact, where λ_i is real negative, the integrals related to the θ (3.11) are explained analytically, as well as the surface integrals which have still to be calculated to obtain the influence coefficient, when using a singularity method.

This method has been tested for calculating the influence coefficients of the diffraction-radiation problem in finite water-depth.

Case 1. Influence coefficients related to the integral (3.21) have been computed. An analytical quadrature on the plane element is followed by a numerical integration over θ, $F_1(k)$ being approximation by complex exponentials.

Case 2. The same calculations are performed but the quadrature over θ is analytical, $F_1(k)$ being smoothed by real negative exponentials.

In this last case, the computing time is divided by a approximate factor of 25 while the global calculation of influence coefficients is five times faster.

4. Conclusion

Each proposed algorithm has been tested in several applications. If the number of exponentials is defined in a suitable way, the obtained approximation is good.

This smoothing technique seems quite promising, especially for naval hydrodynamic applications. Until now, this technique has been used mainly as an alternative tool to other methods for solved problems (diffraction-radiation with or without forward velocity, evolution problems), as we were mainly concerned by the reduction of C.P.U. costs.

Second order terms which appear in the free surface condition for perfect fluid will be taken into account with help of this method in a near future.

Acknowledgement

We wish to gratefully acknowledge Professor Guével who pointed out this study to us and suggested the aforementionned examples.
We also thank Doctor Delhommeau for his efficient help especially during numerical tests.

References

1 Guével P. , Daubisse J.C. , Cordonnier J.P. , Delhommeau G. /1979/
Calcul de la résistance de vagues des navires par une méthode de singularités.
A.T.M.A. Paris

2 Lanczos C. /1961/
Applied analysis.
Prentice Hall

3 Frŏberg C.E. /1969/
Introduction to numerical analysis.
Addison-Wesley

4 Steward G.W. /1973/
Introduction to matrix computation.
Academic Press

5 Barrodale I. /1967/
Approximation in the L_1 and L_∞ norms by linear programming.
Ph.D. th. U. of Liverpool
Liverpool, England

6 Lafata P. , Rosen J.B. /1970/
An interactive display for approximation by linear programming.
Communication of the A.C.M.
Vol 13/Number 11 , November 1970

7 Hess J.L. , Smith A.M.O. /1967/
Progress in aeronautical sciences.
Vol 8 , 1967

8 Martin D. /1980/
Thèse de Doctorat 3ème cycle.
Rennes 1980

9 Guével P. , Daubisse J.C. , Delhommeau G.
Le problème de diffraction-radiation sans vitesse d'avance en profondeur limitée.
Communication Congrès A.U.M.
Marseille Septembre 1981

SOLUTION OF TWO-DIMENSIONAL SLAMMING BY MEANS OF FINITE PRESSURE ELEMENTS

Lawrence J. Doctors
University of New South Wales
Kensington, New South Wales 2033, Australia

Abstract

A method has been developed to solve the unsteady fluid motion caused by the entry of a solid two-dimensional body into the water. The body can have an arbitrary profile and would therefore typically represent the slamming of the bow of various advanced marine vehicles currently being designed. The solution procedure requires replacing the downward and forward motion of the body by the equivalent time-varying pressure distribution. This pressure is then decomposed into elements. The pressure elements are assembled in both time and space, with an additional array of elements added at the end of each increment of time. The magnitudes of the pressures at each time step are found by applying the kinematic condition, which states that the water surface is deformed to match the shape of the body. The extent of the wetted surface of the body at each instant of the time represents part of the solution and this is achieved by an examination (within the computer program) of the behavior of the water surface near the body. Results of the computer program show that the method yields pressure distributions which satisfy the principles of similarity for simple wedge impacts and are consistent with previous analytic results. Further test cases illustrate the effects of asymmetric bow motion and ambient waves on the free surface.

1. Introduction

One of the most critical aspects of the operation of high-speed marine vehicles is that of bow slamming. Both the frequency and intensity of the impact increase with the forward speed of the vehicle. Hence the problems of slamming associated with advanced vehicles - such as the air-cushion vehicle (ACV), surface-effect ship (SES), and the small-waterplane twin-hulled ship (SWATH) - are considerably worse than those of conventional ships.

Generally speaking, the designer is concerned with the craft structure: both the locally induced loads (due to impact pressures) and the overall loads (such as induced bending moments) are important. Furthermore, severe motions may result, and the increased drag usually results in a reduced speed.

The theoretical approach to slamming has always been based on the slender-body assumption. The local beam of the craft is considered to be small, so that each transverse section of the boat is assumed to move purely in the vertical plane, and independently of the other sections. Hence, the analysis is reduced to one examining only the downward vertical motion of a two-dimensional shape. Wagner[1*] was one of the first to propose this method.

The theory was frequently directed at determining the hydrodynamic forces on seaplane floats. Drop tests have also been carried out on models. In these experiments, the forward and downward components of the velocity were monitored during the impact, but an attempt at keeping them constant was also made.

Later, many attempts were made to correlate slender-body theory with experiments on planing boats - usually those with prismatic sections. One of the problems highlighted was the difficulty of obtaining consistent experimental results - particularly for the impact pressure itself. Considerable scatter in the data was evident. Savitsky[2] was one of those researchers who obtained good correlation between the semi-empirical theory and experiment.

A particularly interesting feature of slamming is the possibility of trapping air under the ship. This results in a greatly reduced level of the peak pressure registered on the hull, and is one of the causes of the above-mentioned scatter in the data. A theoretical approach to determining the influence of the trapped air was given by Whitman and Panciono[3]. High-speed photographs have revealed that the air is trapped only if the deadrise angle of the section is less than about three degrees, and this then causes a considerable reduction in the maximum pressure recorded during the slam.

It should be pointed out that in all of the theories developed to date, the influence of gravity is strictly ignored. This assumption is valid if the impact velocity is sufficiently high, and it leads to a quasi-steady situation for the flow around the ship section. One feature of the flow that has received attention is the development of the spray-root region at each extremity of the ever-increasing wetted surface.

In this region, the pressure varies approxi-

* The references are listed at the end.

mately with the inverse of the square root of the distance from the spray line. A more careful non-linear, but gravity-free, analysis of this aspect was carried out by Pierson and Leshnover[4] using a conformal-mapping procedure. A similar approach was used by Hughes[5] to compute the entire flow around a plunging symmetric wedge. Again, gravity was ignored, so that the quasi-steady analysis yields a similarity solution for the flow behavior.

Non-slender surfaces have also been considered, by Huang and Sibul[6], for example. Such work is applicable to the impacting of the bow of an SES or an ACV, and also to parts of the cross structure of a SWATH.

Present Work

It appears to the author that the only way to correctly model the hydrodynamic behavior of a slamming bow is to utilize a numerical technique which develops the flow from a set of initial conditions. For example, Haussling and Van Eseltine[7] studied the planing motion of a boat starting from rest - a problem similar to the present one. They solved the Laplace equation throughout the field, subject to the free-surface conditions, at each step in time. One of the chief difficulties is the determination of the wetted length of the body. This was solved by examining the behavior of the free surface near the attachment and the detachment points. Using between 30 and 40 points along the body, they obtained the right form of the pressure distribution, and the correct steady-state condition was approached. However, the predicted wetted length was found to be slightly too large compared with the steady-state linear theory. Other unsteady free-surface problems were examined by Hirt, Nichols and Romero[8].

It is the intention here to utilize the finite-element concept previously developed by the writor[9]. In that work, the steadily planing surface was represented by the equivalent pressure distribution, which itself was replaced by a series of overlapping triangular pressure elements. The method combined the known disturbances from each unit element in order to satisfy the kinematic condition at a discrete number of points along the surface. As few as ten elements were needed to predict convergent results for the lift, center of pressure, and other quantities, which were in agreement with the results obtained by a more analytic procedure given by Squire[10].

The pressure-element method was later applied by Doctors[11] to the modelling of the hydroelastic behavior of flexible planing seals used for the containment of the air cushion at the bow and stern of an SES. In that work, it was necessary to develop the formulas for the influence coefficients for the flexural behavior of the seal, as well as for the wave system generated.

Finally, in a third paper, Doctors[12] extended the procedure to three dimensions. Here, the three-dimensional pressure element took the form of a pyramid whose rectangular base represents its contribution to the wetted surface of the planing craft, and whose height indicates the local pressure. The elements overlap by 50 percent in each direction, yielding a continuous pressure distribution. Comparisons were made with the experimental results of Savitsky[2]. It was shown that the correct performance of the boat with respect to length-to-beam ratio, deadrise angle, and Froude number could be predicted.

For the subject of the present work, the two-dimensional elements[9,11] will be modified to include the unsteady effects so that the true influence of the free surface will be accounted for - in contrast to the infinite-Froude-number approximation made by others.

2. The Unsteady Pressure Element

Solution for a Pressure Pulse

We first consider a unit pressure pulse given by

$$p(x,t) = \delta(x)\,\delta(t) \ , \qquad (1)$$

acting on the free surface of the water. Here x is the horizontal coordinate and t is the time. The disturbance for the pressure element will later be obtained by integrating the disturbance from this pulse. The solution for this elementary pulse can be obtained if one assumes inviscid and incompressible potential-flow theory with linearized free-surface conditions.

Hence, the potential ϕ, whose gradient is the local velocity, satisfies the Laplace equation

$$\phi_{xx} + \phi_{zz} = 0 \ , \qquad (2)$$

where z is the vertical coordinate measured upward from the undisturbed surface. In addition, ϕ must satisfy the kinematic free-surface condition

$$\phi_z - \zeta_t = 0 \quad \text{on} \quad z = 0 \ , \qquad (3)$$

where ζ is the local free-surface elevation. The second free-surface requirement is the dynamic condition, which is obtained from the Bernoulli equation:

$$\phi_t + g\zeta + p/\rho = 0 \quad \text{on} \quad z = 0 \ , \qquad (4)$$

in which g is the acceleration of gravity and ρ is the density of the water. Equations (3) and (4) may be combined by eliminating ζ to yield

$$\phi_{tt} + g\phi_z = -p_t/\rho \quad \text{on} \quad z = 0 \ . \qquad (5)$$

Finally, the condition of no flow at great depth is imposed:

$$\phi_z = 0 \quad \text{as} \quad z \to -\infty \ . \qquad (6)$$

The reader is referred to Stoker[13] (p. 149) for a fuller derivation of these equations. The solution to the equations may be found by applying the Fourier transform with respect to space and the Laplace transform with respect to time, as detailed by Stoker. The final result only, (p. 159) will be quoted here:

$$\zeta(x,t) = -\frac{1}{\pi\rho\sqrt{g}} \int_0^\infty \sqrt{k}\,\sin(\sqrt{gk}\,t)\cos(kx)\,dk \ . \qquad (7)$$

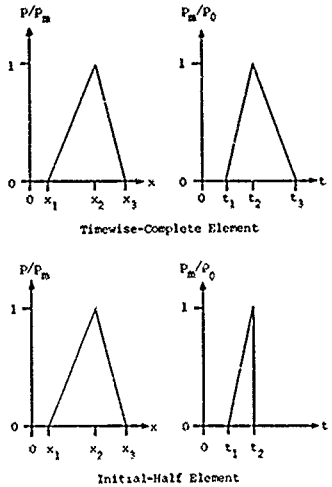


Figure 1: The Basic Pressure Element

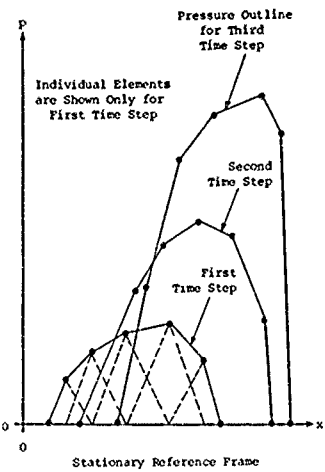


Figure 2. Typical Assembly of Elements

It may be noted that this integral is divergent, and therefore must first be employed to construct a finite pressure element before it can be applied to a problem.

The Four Wave Functions

Figure 1 shows the two basic elements used as building blocks for the pressure distribution generated by the impact of the two-dimensional bow on the water surface. Both the *complete* and the *half* element are triangular with respect to the space coordinate, and overlap as shown in Figure 2 in order to produce a continuous distribution in the x direction. The elements are asymmetric in general, and this allows concentrating them where the pressure varies more rapidly.

Figure 2 shows individual rows of elements at the end of each time step. The rows are placed together temporally in a similar fashion. Hence the total disturbance of the surface at any time instant may be obtained by adding the individual influences from all the elements. At each time step, one additional row of elements is added.

It should be noted that a *half* element is needed for the last row of elements at each time step. Its use is dictated by the fact that there is no influence from that part of the element which extends into the future.

In order to integrate Equation (7) over space and time, we need the cosine- and sine-Fresnel integrals defined by Abramowitz and Stegun[14] (p. 300) as follows:

$$\begin{matrix} C \\ S \end{matrix}(z) = \int_0^z \begin{matrix} \cos \\ \sin \end{matrix}(\tfrac{\pi}{2} t^2)\, dt \,. \qquad (8)$$

The usual auxiliary functions for the Fresnel integrals have been replaced here by slightly modified ones:

$$f^*(z) = \sin(\tfrac{\pi}{2} z^2)\, C(z) - \cos(\tfrac{\pi}{2} z^2)\, S(z)$$

and (9)

$$g^*(z) = -\cos(\tfrac{\pi}{2} z^2)\, C(z) - \sin(\tfrac{\pi}{2} z^2)\, S(z) \,.$$

The integrals of these two functions are defined as

$$I_f(z) = \int f^*(z)\, dz$$

and (10)

$$I_g(z) = \int g^*(x)\, dz = -\tfrac{1}{2}\left[C^2(z) + S^2(z) \right] .$$

Finally, four special wave functions, F_1, F_2, F_3 and F_4, may also be defined as follows:

$$F_1(z) = -2 I_g$$

$$= C^2(z) + S^2(z) \ , \qquad (11)$$

$$F_2(z) = \int F_1(z)\, dz$$

$$= z F_1(z) - \frac{2}{\pi} \zeta^*(z) \ , \qquad (12)$$

$$F_3(z) = \int z^{-3} F_1(z)\, dz$$

$$= -\frac{1}{2z^2} F_1(z) + \frac{1}{z} g^*(z) + \ln(z) - \pi I_f \qquad (13)$$

and

$$F_4(z) = \int z^{-4} F_2(z)\, dz$$

$$= \frac{1}{3}\left[F_3(z) - \frac{1}{2z^2} F_1(z) + \frac{1}{\pi z^3} f^*(z)\right] \ , \qquad (14)$$

and also

$$z^3 F_4(z) = \int z^2 F_3(z)\, dz \ . \qquad (15)$$

These equations may be derived by integrating by parts, or they may be proven by simply differentiating the final result in each case.

The four wave functions, given by Equations (11) through (14) are plotted in Figure 3. The logarithmic behavior of F_3 and F_4 near the origin is evident.

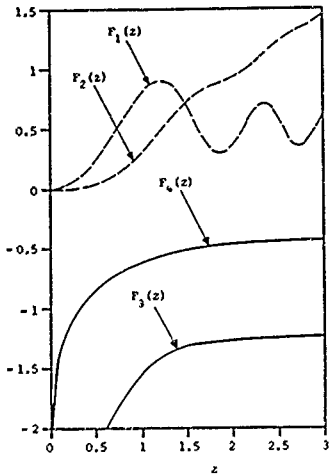


Figure 3: The Four Wave Functions

Integration of the Pressure Pulse

We are now in a position to develop the formula for the behavior of a pressure element from that of a pulse. We note that the spatial variation of pressure within an element, in Figure 1, is given by

$$p = p_m\left[1 + (x - x_2)/\Delta x_1\right] \text{ for } x < x_2$$

and (16)

$$p = p_m\left[1 - (x - x_2)/\Delta x_3\right] \text{ for } x > x_2 \ ,$$

where $p_m(t)$ is the instantaneous peak pressure at each moment of time. The element is spatially defined by the points x_1 , x_2 and x_3 . These give the two increments

$$\Delta x_1 = x_2 - x_1$$

and (17)

$$\Delta x_3 = x_3 - x_2 \ .$$

Equation (16) is now used together with Equation (7), with the source point of the latter shifted from $x = 0$ to ξ , and from $t = 0$ to τ:

$$\zeta = -\frac{p_m}{\pi\rho\sqrt{g}} \int_{x_1}^{x_3} \left\{ \begin{matrix} 1 + (\xi - x_2)/\Delta x_1 \\ 1 - (\xi - x_2)/\Delta x_3 \end{matrix} \right\} \int_0^{\infty} \sqrt{k}\, \sin\left[\sqrt{gk}\ (t-\tau)\right] \times$$

$$\times \cos\left[k(x - \xi)\right]\, dk\, d\xi \ .$$

The upper expression in the stacked factor is used when $\zeta < x_2$ and the lower one when $\zeta > x_2$. The equation is next integrated by parts with respect to the cosine factor. After some simplification and a change of variable given by $k = z^2$, one obtains

$$\zeta = -\frac{2p_m}{\pi\rho\sqrt{g}} \int_{x_1}^{x_3} \left\{ \begin{matrix} 1/\Delta x_1 \\ -1/\Delta x_3 \end{matrix} \right\} d\xi \int_0^{\infty} \sin\left[\sqrt{g}(t - \tau)z\right] \times$$

$$\times \sin\left[(x - \xi)z^2\right]\, dz \ .$$

The integration with respect to z can now be effected using formula 3.691/4 of Gradshteyn and Ryzhik[15]:

$$\zeta = \frac{2p_m}{\rho} \int_{x_1}^{x_3} \left\{ \begin{matrix} 1/\Delta x_1 \\ -1/\Delta x_3 \end{matrix} \right\} \mathrm{sgn}(x - \xi)\, \frac{1}{\sqrt{2\pi g|x - \xi|}} \times$$

$$\times g^*\left(\sqrt{\frac{g(t - \tau)^2}{2\pi|x - \xi|}}\right) d\xi \ . \qquad (18)$$

At this stage it is convenient to introduce the temporal integration. The instantaneous peak pressure for a *complete* element in Figure 1 may be expressed as

$$p_m = p_0\left[1 + (t - t_2)/\Delta t_1\right] \quad \text{for} \quad t < t_2$$

and (19)

$$p_m = p_0[1 - (t - t_2)/\Delta t_3] \quad \text{for} \quad t > t_2 ,$$

where p_0 is the nominal element pressure, and the temporal limits of the triangle are t_1, t_2 and t_3. The two time increments in Equation (19) are

$$\Delta t_1 = t_2 - t_1$$

and (20)

$$\Delta t_3 = t_3 - t_2 .$$

We may now integrate Equation (18) again using the pressure given by Equation (19):

$$\zeta = \frac{2p_0}{\rho} \int_{x_1}^{x_3} \begin{pmatrix} 1/\Delta x_1 \\ -1/\Delta x_3 \end{pmatrix} \operatorname{sgn}(x - \xi) \frac{1}{\sqrt{2\pi g|x - \xi|}} d\xi \times$$

$$\times \int_{t_1}^{t_3} \begin{pmatrix} 1 + (\tau - t_2)/\Delta t_1 \\ 1 - (\tau - t_2)/\Delta t_3 \end{pmatrix} g^*(|z|)\, dt , \quad (21)$$

in which $$z = \sqrt{\frac{g(t - \tau)^2}{2\pi|x - \xi|}} . \quad (22)$$

Equation (21) is integrated (with respect to ξ) by parts, with respect to the g^* function, using Equations (10) and (11), producing

$$\frac{\rho g \zeta}{p_0} = -\int_{x_1}^{x_3} \begin{pmatrix} 1/\Delta x_1 \\ -1/\Delta x_3 \end{pmatrix} \operatorname{sgn}(x - \xi)\, d\xi \times$$

$$\times \int_{t_1}^{t_3} \begin{pmatrix} 1/\Delta t_1 \\ -1/\Delta t_3 \end{pmatrix} F_1(z)\, dt . \quad (23)$$

The members of the stacked terms represent the partial slopes of the sides of the pyramid pressure element. Thus it is seen that the F_1 function is fundamental to water-wave problems, and, indeed, represents the disturbance created by a unit pressure band which is semi-infinite in extent and which is instantaneously applied to the water surface, and maintained.

We now complete the space integration using the change of variable implied by Equation (22). The latter gives

$$\operatorname{sgn}(x - \xi)\, d\xi = \frac{g(t - \tau)^2}{\pi z^3} dz \quad \text{for constant} \quad \tau ,$$

and hence

$$\frac{\rho g \zeta}{p_0} = -\frac{g}{\pi} \int_{t_1}^{t_3} \begin{pmatrix} 1/\Delta t_1 \\ -1/\Delta t_3 \end{pmatrix} (t - \tau)^2\, d$$

cont.

$$\times \int_{z_{\tau,1}}^{z_{\tau,3}} \begin{pmatrix} 1/\Delta x_1 \\ -1/\Delta x_3 \end{pmatrix} \frac{F_1(z)}{z^3} dz ,$$

in which the limits of the second integration, namely $z_{\tau,1}$ and $z_{\tau,3}$, are given by Equation (22), with x_1 and x_3 substituted for ξ, respectively.

Equation (13) is now invoked. Appropriate substitution of the limits leads to the penultimate stage in this calculation:

$$\frac{\rho g \zeta}{p_0} = -\frac{g}{\pi} \int_{t_1}^{t_3} \begin{pmatrix} 1/\Delta t_1 \\ -1/\Delta t_3 \end{pmatrix} (t - \tau)^2 \times$$

$$\times \left[-\frac{F_3^{\tau,1}}{\Delta x_1} + \frac{F_3^{\tau,2}}{\Delta x_2} - \frac{F_3^{\tau,3}}{\Delta x_3} \right] dt . \quad (24)$$

In this equation, the following pseudo-increment has been used:

$$\frac{1}{\Delta x_2} = \frac{1}{\Delta x_1} + \frac{1}{\Delta x_3} , \quad (25)$$

while the superscripts on the F_3 functions indicate the relevant limits.

Finally, the time integration of Equation (24) is carried out using the same substitution as before, which now gives

$$dt = -\sqrt{\frac{2\pi|x - x_i|}{g}}\, dz \quad \text{for constant} \quad x_i .$$

The three terms in Equation (24) can be separately integrated using the definition of Equation (15). After some algebra, the following final result is obtained:

$$\frac{\rho g \zeta}{p_0} = \frac{1}{\pi}\left[-\frac{g(t - t_1)^3}{\Delta t_1}\left(-\frac{F_4^{11}}{\Delta x_1} + \frac{F_4^{12}}{\Delta x_2} - \frac{F_4^{13}}{\Delta x_3} \right) + \right.$$

$$+ \frac{g(t - t_2)^3}{\Delta t_2}\left(-\frac{F_4^{21}}{\Delta x_1} + \frac{F_4^{22}}{\Delta x_2} - \frac{F_4^{23}}{\Delta x_3} \right) -$$

$$\left. - \frac{g(t - t_3)^3}{\Delta t_3}\left(-\frac{F_4^{31}}{\Delta x_1} + \frac{F_4^{32}}{\Delta x_2} - \frac{F_4^{33}}{\Delta x_3} \right) \right] , \quad (26)$$

where

$$\frac{1}{\Delta t_2} = \frac{1}{\Delta t_1} + \frac{1}{\Delta t_3} . \quad (27)$$

The superscripts on the F_4 functions indicate that the argument is to be evaluated at that point in time and space. It may be seen from Equation (26) that the elemental disturbance essentially consists of contributions from each of the nine "corners" of the element in time and space.

The Initial-Half Element

It has been pointed out that the source time of the last row of elements in Figure 2 corres-

ponds with the field time. For this case, the part of the wave pattern generated by the second half of the element is not required. The easiest way to achieve the desired result is to take the limit of Equation (26) as $\Delta t_3 \to 0$, and to substitute $t = t_2$.

This process is equivalent to performing a time differentiation, and requires the last two lines of Equation (26). Use is made of Equation (15). After some algebra, we obtain

$$\frac{\rho g \zeta}{P_0} = -\frac{g(t_2 - t_1)^3}{\pi \Delta t_1}\left(-\frac{P_4^{11}}{\Delta x_1} + \frac{P_4^{12}}{\Delta x_2} - \frac{P_4^{13}}{\Delta x_3}\right) \quad (28)$$

Interestingly, Equation (28) represents just the first line of Equation (26).

3. Numerical Investigations with Pressure Element

Background

The purpose of this section is to examine different pressure variations with respect to time, which can be used to test the disturbance function for a pressure element given by Equations (26) and (28). The different timewise behaviors considered are shown in Figure 4.

These pressure variations can all be constructed by superposing the basic pressure elements in the time domain. In fact, this representation can be made exact for three out of the four cases in Figure 4. In the third case, the sinusoidal waveform can be represented closely by the use of a sufficient number of elements per cycle.

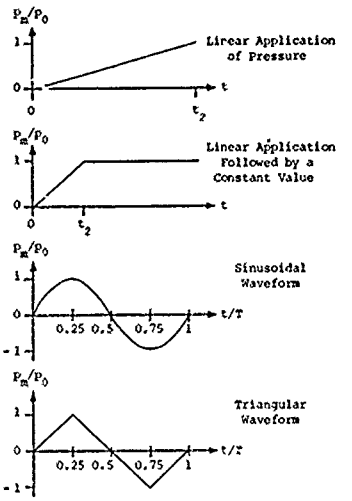


Figure 4: Sample Pressure Variations

Behavior of a Single Element

We first examine the case of a single spatially symmetric ($\Delta x_1 = \Delta x_3$) and temporally symmetric ($\Delta t_1 = \Delta t_3$) element in Figure 5a. For all the curves in this diagram, the time is equal to or greater than the last time point of the element ($t \geq t_3$, where $t_3 = 2\Delta t$ in this example). Hence Equation (26) applies to all the cases plotted.

As the element is symmetric, the free-surface is symmetric, so that only $x > 0$ has been considered. Early in the history, at the first time instant shown ($t\sqrt{g/\Delta x} = 2$), the water moves down under the element ($|x| < \Delta x$) due to the action of the pressure. Just outside this region, the water moves upward in order to satisfy the equation of continuity. The disturbance is then seen to travel outwards. It moves at a constant acceleration. This can be verified in Equation (22), which shows that for a constant phase of the argument z, $x \propto t^2$.

Figure 5b depicts the wave profile generated at the end of the initial-half element. The temporal pressure variation is thus a ramp function - the first case shown in Figure 4. The curves in Figure 5b were generated using Equation (28). Different rates of application of the pressure are considered, as indicated by the value of t_2 attached to the curves.

As one would expect, for a sufficiently gradual application of the pressure ($t_2\sqrt{g/\Delta x} = 8$), an almost quasi-steady situation occurs, and the wave elevation is seen to be the result of purely hydrostatic considerations: at $x = 0$, $\zeta = -p_0/\rho g$ and at $x = \Delta x$, $\zeta = 0$. This statement is less true further away from the element because the waves take a finite time to be propagated away.

Linear Application of Pressure Followed by a Constant Value

We now consider the temporal pressure variation depicted in the second part of Figure 4. Two sets of results are shown in Figure 6, in which the elements are overlapped in the time domain.

One would expect the hydrostatic situation to pertain after a sufficient length of time, and this is found to be the case in Figure 6a, where a spatially symmetric ($\Delta x_1 = \Delta x_3$) element is again used. For large values of the time, the dimensionless depression under the element varies from unity down to zero at its edge. Further away, the approach to the steady state is somewhat slower.

In Figure 6b, a spatially *asymmetric* element is considered. Indeed, Δx_1 is made extremely large, and Δx_3 very small. In this case, the triangular element has degenerated into a semi-infinite pressure band acting to the left of $x < 0$. The resulting surface profiles are seen to be antisymmetric about the origin, as dictated by the need to conserve the fluid volume. The steady-state is seen to be achieved immediately

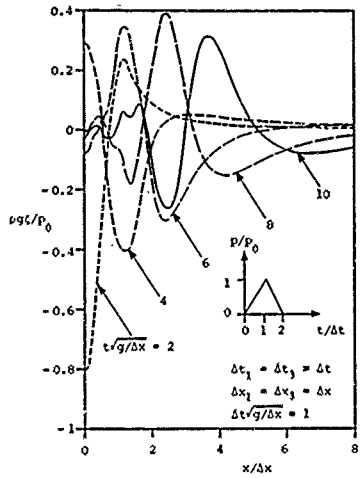


Figure 5: Behavior of a Single Element
(a) Timewise-Complete Element

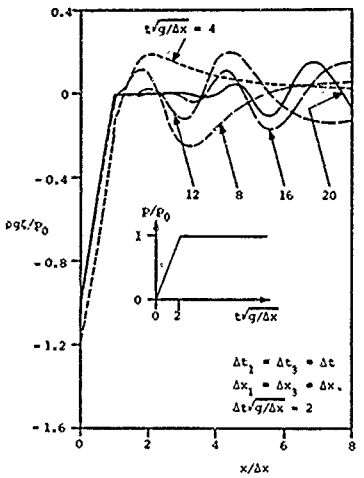


Figure 6: Pressure is Applied Linearly and Then Kept Constant. (a) Triangular Element

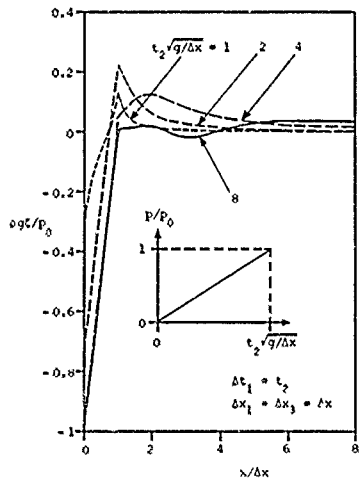


Figure 5: Behavior of a Single Element
(b) Initial-Half Element

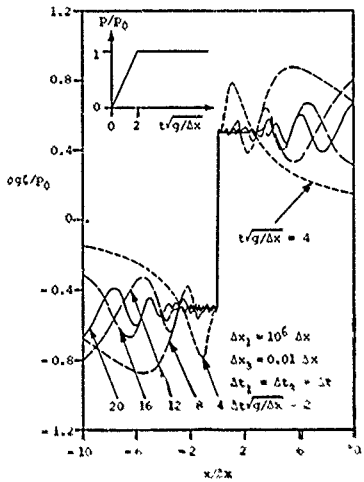


Figure 6: Pressure is Applied Linearly and Then Kept Constant. (b) Semi-Infinite Element

in the region near the origin. Further away, the time required for the wave profile to settle to the dimensionless value of $\pm$ 0.5 is longer.

Another interesting feature of the curves is the high-frequency (short-wavelength) oscillations near the origin. It is well known that the unsteady disturbance consists of a spectrum of waves (see Equation (7)), and that the short-wavelength ones travel the slowest, and are therefore left behind the other wavelets.

Sinusoidal Waveform

We now consider that the pressure varies harmonically with the time, as shown in the third part of Figure 4. Hence the peak pressure of the element is given by

$$p_m = p_0 \sin(\sigma t) \ , \qquad (29)$$

where the circular frequency σ is related to the period T by means of the equation

$$\sigma = 2\pi/T \ . \qquad (30)$$

The analytic solution to this problem may be found by solving the set of Equations (2) through (6). Equation (4) is modified by adding the term $\mu\phi$ to the left-hand side. Here μ is the so-called artificial viscosity which is assumed to be positive but vanishingly small. The steady-state solution is developed by taking the pressure to be the imaginary part of

$$p(x,t) = \hat{p}(x)\, e^{i\sigma t} \ , \qquad (31)$$

and assuming a periodic solution for the potential given by

$$\phi(x,z,t) = \hat{\phi}(x,z)\, e^{i\sigma t} \ . \qquad (32)$$

One may next use the Fourier-transform method which, after some algebra, gives

$$\zeta = -\frac{\sigma^2 e^{i\sigma t}}{\pi\rho g^2} \int_0^\infty \frac{\exp(ikx)}{k - \sigma^2/g + i\mu\sigma}\, dk = \frac{p}{\rho g} \ . \qquad (33)$$

The location of the pole in the integral is seen to be given by

$$k = \frac{\sigma^2}{g} - i\mu\sigma \ , \qquad (34)$$

indicating that the k integral should be deformed above the pole if $\sigma > 0$, and below the pole if $\sigma < 0$. We can extract the desired imaginary part of Equation (33) by evaluating one half of the difference of two solutions in which σ is positive, and negative, respectively.

After some further work, the following result is obtained:

$$\zeta = \frac{k}{\rho g}\left[\cos(\sigma t - k|x|) - \frac{1}{\pi}\,\bar{g}(|kx|)\,\sin(\sigma t)\right] - p/\rho g \ , \qquad (35)$$

where

$$k = \sigma^2/g \ , \qquad (36)$$

and $\bar{g}$ is one of the two auxiliary functions for the cosine and sine integrals which are defined by Abramowitz and Stegun (p. 232) as

$$\begin{matrix}\bar{g} \\ \bar{f}\end{matrix}(z) = \int_0^\infty \frac{\cos}{\sin}(t)\, \frac{dt}{z+t} \ . \qquad (37)$$

The last step in the calculation is to integrate the solution in Equation (35), which is for a pressure given by Equation (31), in order to obtain the result for a triangular element. This process requires the following two formulas:

$$\int \bar{g}(|z|)\, dz = \mathrm{sgn}(z)\,\left[\frac{\pi}{2} - \bar{f}(|z|)\right]$$

and (38)

$$\int \mathrm{sgn}(z)\, \bar{f}(|z|)\, dz = \bar{g}(|z|) + \ln(|z|) = gl(|z|) \ .$$

The result after some algebra is

$$\frac{\rho g\zeta}{p_0} =$$

$$= \frac{1}{k}\Big\{ -\frac{1}{\Delta x_1}\left[\cos(\sigma t - k|x-x_1|) - \frac{1}{\pi} gl(k|x-x_1|)\,\sin(\sigma t)\right] +$$

$$+ \frac{1}{\Delta x_2}\left[\cos(\sigma t - k|x-x_2|) - \frac{1}{\pi} gl(k|x-x_2|)\,\sin(\sigma t)\right] -$$

$$- \frac{1}{\Delta x_3}\left[\cos(\sigma t - k|x-x_3|) - \frac{1}{\pi} gl(k|x-x_3|)\,\sin(\sigma t)\right]\Big\} . \qquad (39)$$

It may be noted that, for a symmetric element ($\Delta x_1 = \Delta x_3 = \Delta x$) centered at the origin ($x_2 = 0$), the limit at a great distance is

$$\frac{\rho g\zeta}{p_0} = \frac{4}{k\Delta x}\,\sin^2\left(\tfrac{1}{2}k\Delta x\right)\cos(\sigma t - k|x|) \ , \qquad (40)$$

showing that no free wave is generated when

$$\tfrac{1}{2}k\Delta x = n\pi \quad \text{for} \quad n = 1, 2, 3 \ldots \qquad (41)$$

Figure 7 illustrates some numerical experiments with a harmonic waveform generated by combining elementary pressure triangles. By using 16 elements per cycle, a very good approximation to a sinusoid may be achieved.

Figure 7a corresponds to a spatially symmetric element with a dimensionless period given by $T\sqrt{g/\Delta x} = 6$. The wave profile is shown after a time of 2, 4, 6 and 8 cycles have elapsed. The development of the steady-state profile is clearly seen, with the part further away taking longer to be established.

Figure 7b shows the *discrepancy* in the results of Figure 7a from the steady-state analytic result of Equation (39). The discrepancy is defined as the actual wave elevation minus the steady-state value. After 8 cycles, the steady-state profile is developed over a dimensionless distance of about 10.

A situation in which no steady-state wave will occur is displayed in Figure 7c. In this

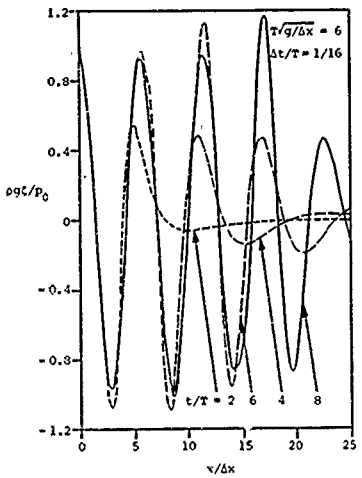


Figure 7: Sinusoidal Waveform
(a) Wave-Generating Frequency

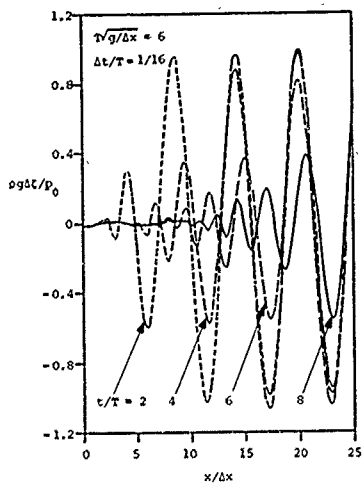


Figure 7: Sinusoidal Waveform
(b) Discrepancy at Wave-Generating Frequency

case, after an elapsed time of 8 cycles, the profile has reached the steady-state zero value over a dimensionless distance of about 1.5 .

Test cases were also computed for the triangular waveform shown in Figure 4. Similar results to those for the sinusoidal one were obtained, but are omitted here for the sake of brevity.

Travelling Pressure Element

The last test we consider is depicted in Figure 8. In the four cases shown, the pressure is increased uniformly at first, up to a dimensionless time given by $t\sqrt{g/\Delta x} = 5$, and then maintained constant. The element is also "accelerated" uniformly up to the desired speed by the same time, and then kept running at a constant speed.

It should be emphasized here that a pure travelling and time-varying element was not developed. However, the continuous travelling behavior can be approximated by positioning each additional element (which is stationary) at a new position at each time step.

Figures 8a and 8b show the profiles developed when the Froude number based on the element length of $2\Delta x$ is 0.5 . Figure 8a relates to the case in which a rather coarse time step of $\Delta t\sqrt{g/\Delta x} = 1.5$ is used, while an obviously superior value of 0.375 is used in Figure 8b.

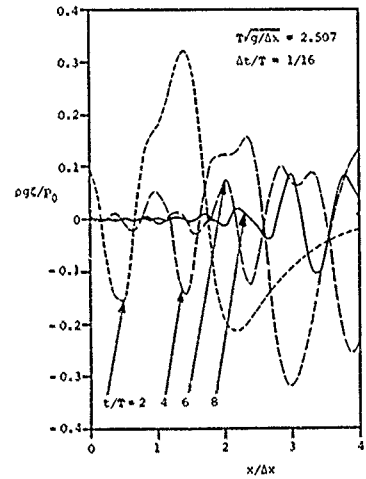


Figure 7: Sinusoidal Waveform
(c) Nonwave-Generating Frequency

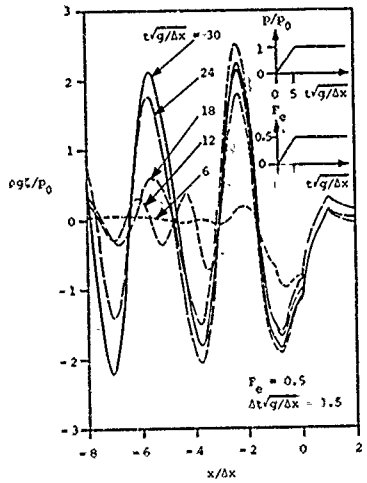


Figure 8: Constant Forward Velocity
(a) High Speed with $\Delta t\sqrt{g/\Delta x} = 1.5$

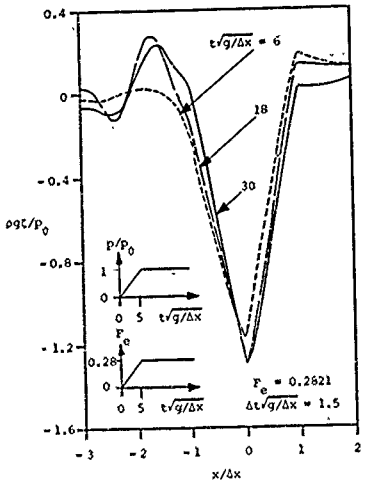


Figure 8: Constant Forward Velocity
(c) Low Speed with $\Delta t\sqrt{g/\Delta x} = 1.5$

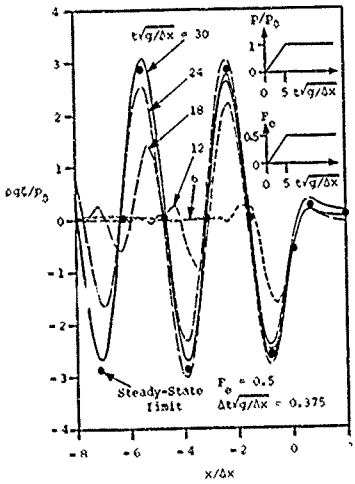


Figure 8: Constant Forward Velocity
(b) High Speed with $\Delta t\sqrt{g/\Delta x} = 0.375$

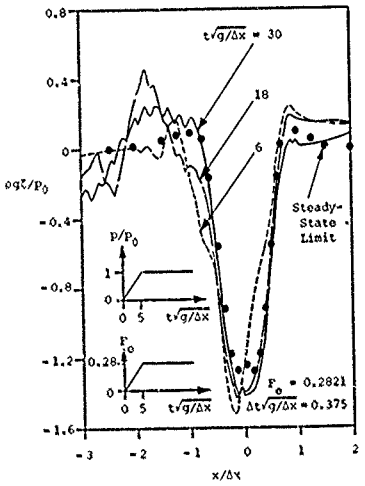


Figure 8: Constant Forward Velocity
(d) Low Speed with $\Delta t\sqrt{g/\Delta x} = 0.375$

If we concentrate on Figure 8b, it is possible to see the development of additional wave crests as the time increases. Also shown on the diagram are a series of points indicating the steady-state limit. The solution for this last case was given by Doctors[12] as

$$\frac{\rho g \zeta}{p_0} = \frac{k_0}{k_0}\left[\frac{1}{\Delta x_1}\left\{\frac{1}{\pi}\mathrm{gl}(|\lambda_1|) + H(-\lambda_1)[2\sin(\lambda_1) - \lambda_1]\right\} + \right.$$

$$+\frac{1}{\Delta x_2}\left\{\frac{1}{\pi}\mathrm{gl}(|\lambda_2|) + H(-\lambda_2)[2\sin(\lambda_2) - \lambda_2]\right\} -$$

$$\left.-\frac{1}{\Delta x_3}\left\{\frac{1}{\pi}\mathrm{gl}(|\lambda_3|) + H(-\lambda_3)[2\sin(\lambda_3) - \lambda_3]\right\}\right], \tag{42}$$

where H is the Heaviside step function, k_0 is the fundamental wave number given by

$$k_0 = g/c^2 \tag{43}$$

and

$$\lambda_{1,2,3} = k_0(x - x_{1,2,3}) \ . \tag{44}$$

After an elapsed time of $t\sqrt{g/\Delta x} = 30$, one can see that the steady-state wave profile has almost been developed over the range covered by Figure 8b.

The downstream limit ($x \to -\infty$) of Equation (42) is easily found to be

$$\frac{\rho g \zeta}{p_0} = \frac{8}{k_0 \Delta x}\sin^2\left(\tfrac{1}{2}k_0\Delta x\right)\sin(k_0 x) \ , \tag{45}$$

from which it can be seen that there should be no trailing wave when

$$\tfrac{1}{2}k_0\Delta x = n\pi \quad \text{for} \quad n = 1, 2, 3 \ldots \tag{46}$$

A case with no steady-state downstream wave is considered in Figures 8c and 8d, with the same two time steps used in Figures 8a and 8b. The convergence to the steady limit is perhaps not quite as rapid at this lower Froude number. Nevertheless, it is possible to see the development of the peculiar kink in the free-surface profile at $x = 0$ (the center of the element), which is verified by the steady-state result of Equation (42).

4. Assembly of the Elements

Problem Definition

Figure 9 shows the bow in two positions. In the first case, the bow has just made contact with the water. We shall assume that the surface is initially deformed by the presence of a simple travelling wave as follows:

$$z_w = h_w \cos[k_w(x + s(t) - x_{w0}) - \sigma_w t) \ . \tag{47}$$

where h_w is the wave amplitude, k_w is the wave number and x_{w0} is the origin of the wave. The horizontal distance travelled by the bow $s(t)$ also enters the equation because the reference frame is moving with the craft. The wave number is related to the wave length λ_w by the equation

$$k_w = 2\pi/\lambda_w \ , \tag{48}$$

and the angular frequency of the wave is given by

$$\sigma_w = \sqrt{gk_w} \ . \tag{49}$$

The bow has an initial height h_0 given by Equation (47), with $t = 0$, $x = 0$ and $s = 0$:

$$h_0 = h_w \cos(k_w x_{w0}) \ . \tag{50}$$

After the initial point of contact, the height of the bow h (positive upward) may be an arbitrary function of time.

The horizontal motion of the bow $s(t)$ and its pitch angle $\alpha(t)$ (positive upward) are also given functions of time. Finally, the bow itself is assumed to be flat ($z = 0$) behind the knuckle ($x < 0$), and to have a prescribed shape $z(x)$ ahead of the knuckle ($x > 0$).

The Kinematic Condition

Because the bow is replaced by the equivalent pressure distribution (see Figures 2 and 10), the geometric requirement that the water must be deformed in order to match the bow profile may be expressed by adding the influences of all the pressure elements. In the following equation, i and i' are the field-point position and time indices, and j and j' are the corresponding source-point indices:

$$\sum_{j=2}^{n_x}\sum_{j'=2}^{i'} p_{jj'}\hat{\zeta}_{ii'jj'} = \rho g(h_{i'} + \alpha_{i'}x_i + z_i - z_w) \ , \tag{51}$$

in which it is assumed that n_x elements are in use at each time step. The shorthand notation used in Equation (51) is defined as follows:

$$p_{jj'} = p(x_j, t_{j'}) \tag{52}$$

and

$$\hat{\zeta}_{ii'jj'} = \rho g\zeta/p_0 \ . \tag{53}$$

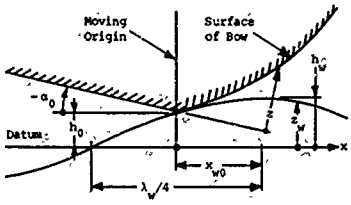
Either side of Equation (53) represents the disturbance (that is, the free-surface elevation) at the field point $(x_i, t_{i'})$ due to a pressure element of unit magnitude at the source point $(x_j, t_{j'})$.

The Method of Solution

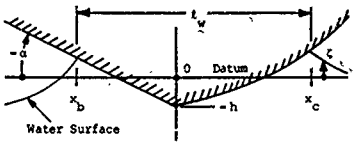
The solution proceeds by marching through the time. In order to apply Equation (51), one must know the wetted length. The movements in the attachment and detachment points x_c and x_b are computed from a consideration of the relative slope of the bow to the water surface at the previous time step, as well as the downward movement of the bow during that interval:

$$\Delta x_c = -\mu_h \Delta h \Big/ \left[\frac{\partial z}{\partial x} + \alpha - \frac{\partial z_w}{\partial x}\right]_{x=x_c} \ , \tag{54}$$

where Δh is the movement of the bow during

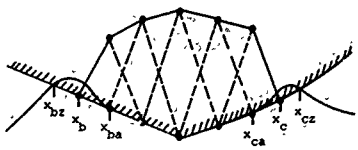


Configuration at Point of Contact

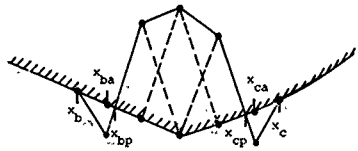


Configuration During the Slam

Figure 9: Problem Definition



Interference of Water Surface with Body



Occurrence of Negative Pressure

Figure 10: The Attachment and Detachment Points

time increment (negative downward), and ν_h is a factor usually chosen to be $\pi/2$, which takes into account the rise of the water during the impacting process. Of course, at the start of the slam the wetted length is zero, that is, $x_b = x_c = 0$. A formula similar to Equation (54) is used to evaluate the correction Δx_b.

For the first time step, there is only one row of pressure elements ($i' = 2$ in Equation (51) because $i' = 1$ corresponds to the time at the point of impact), and these may be found from a solution of the set of simultaneous linear equations.

For later time steps, the pressures at the *earlier* steps are known, and their contributions to the disturbance can be determined. Thus, at each time step, an extra row of pressure elements is added to the system, as shown in Figure 2.

The extrapolations for the wetted length in Equation (54) are corrected if, for example, the resulting water surface intersects the bow as shown in the upper part of Figure 10. Such an occurrence implies that the wetted length is to be increased, and the correction

$$\Delta x_c' = \nu_z (x_{cz} - x_{ca}) \qquad (55)$$

is *added* to that in Equation (54) at the next time step. Here x_{cz} is the point of intersection of the water with the bow near the attachment point, x_{ca} is the outermost point where the kinematic condition is applied and ν_z is a damping factor, usually taken to be unity. A similar correction may apply at the detachment point x_b.

Should the wetted-length estimate be too large, this would be indicated by the appearance of a negative pressure, as shown in the lower part of Figure 10. In such a case, the adjustment

$$\Delta x_c'' = \nu_p (x_{cp} - x_c) \qquad (56)$$

is made to Equation (54) at the next time step. Here x_{cp} defines the point at which the pressure becomes negative. Again, a similar equation to this one is used should there be a region of negative pressure near the detachment point x_b.

Finally, the wetted length is given by

$$\ell_w = x_c - x_b . \qquad (57)$$

The Forces

The forces can be computed at each instant by summing the effects of each element. First, the contribution to the lift from one element is

$$\Delta L_i = \frac{1}{2}\rho_i (x_{i+1} - x_{i-1}) . \qquad (58)$$

The total lift, drag and center of pressure can then be found from the three formulas:

$$L = \sum_{i=2}^{n_x} \Delta L_i \ , \qquad (59)$$

$$D = \sum_{i=2}^{n_x} \Delta L_i \left(\alpha + \left[\frac{\partial z}{\partial x}\right]_{x=x_i}\right) \ , \qquad (60)$$

and

$$\bar{x} = \frac{1}{3L} \sum_{i=2}^{n_x} \Delta L_i \ (x_{i-1} + x_i + x_{i+1}) \ . \qquad (61)$$

The last quantity of interest is the surface shape around the bow, which is obtained from summing the disturbances from all the pressure elements in both space and time:

$$\zeta = z_w + \frac{1}{\rho g} \sum_{j=2}^{n_x} \sum_{j'=2}^{j} P_{jj'} \hat{\zeta}_{jj'} \ . \qquad (62)$$

5. Numerical Experiments

Symmetric Wedge Plunging at a Constant Velocity

For the first test case, we examine the standard problem of a wedge entering a previously undisturbed water surface, as shown in the small sub-diagram of Figure 11.

In this diagram, as in the rest of the figures, the results have been made dimensionless with respect to ρ, g and ℓ, the latter being a nominal horizontal length. In addition, items such as the free-surface elevation ζ, and the lift L are further divided by α_0, the wedge angle. This second process is required because of the linearized nature of the mathematical problem.

Four cases are shown in Figure 11a, all depicting the shape of the water surface at a dimensionless time $t\sqrt{g/\ell} = 0.2$, for a case when the wedge possesses a uniform downward velocity. That is, $V/\alpha_0\sqrt{g\ell} = 1$, where $V = -\dot{h}$, the plunge velocity. The calculation made use of a uniform time step of $\Delta t\sqrt{g/\ell} = 0.1$, so that the curves correspond to the state after one time step. Now the curve with $n_u = 1$ was obtained using the method described in the previous section. The procedure was found to be unstable, and the first attempt to cure it consisted of dividing each time step into n_u sub-time steps. In this way, it was anticipated that one could approximate an element which varied *continuously in length* between time steps. (The length of an element is non-varying.) The curves indeed show that using 8 such sub-time steps essentially models a continuously varying pressure element.

We turn now to the pressure distributions in Figure 11b, which highlight the unstable nature of the numerical process. It is remarkable that such different pressure distributions can both satisfy the kinematic condition given by Equation (51) and produce almost identical wave profiles in Figure 11a.

The predicted lift given by Equation (59) is next plotted as a series of symbols in Figure 11c. Using the previously mentioned numbers of sub-time steps ($n_u = 1$, 2, 4 and 8), one obtains essentially the same lift at the end of the first time step, when $t\sqrt{g/\ell} = 0.2$. At the end of the second time step ($t\sqrt{g/\ell} = 0.4$), there is a considerable scatter. At later time steps, the situation has deteriorated so badly that a *negative* lift is even predicted when $n_u = 4$. This was caused by the pressures at an earlier time having too large an effect later on. As a consequence, the later pressures had to be over-corrected. No results are shown for $n_u = 1$, 2 and 8 for these later times, as the program automatically stopped on encountering pressure distributions which would yield multiple values of x_{bp} and x_{cp} (see Figure 10).

It is instructive to compare these results with those of Pierson[16]. His Equation (22) may be quoted as

$$p/\rho = \sqrt{a^2 - x^2}\ \dot{V} + V^2/\lambda\sqrt{1 - x^2/a^2} - V^2/2(a^2/x^2 - 1) + V^2/2 \ , \qquad (63)$$

where $a = \ell_w/2$, the half-wetted length. The expansion parameter λ in Equation (63) may be used to obtain the wetted length by means of the relationship:

$$\lambda = V/\frac{da}{dt} = \frac{2}{\pi} \tan\alpha_0 \ . \qquad (64)$$

We shall now substitute this result in Equation (63), and take the linearized limit as α_0 approaches zero. This gives

$$p = \frac{\pi\rho V^2}{2\alpha_0} \frac{1}{\sqrt{1 - x^2/a^2}} \ , \qquad (65)$$

in which

$$a = \frac{\pi V}{2\alpha_0} t \ . \qquad (66)$$

Equation (65) shows that only the instant speed is important when gravity is neglected in the linearized theory. Equation (66) implies that the wetted length is $\pi/2$ greater than the value obtained from hydrostatic considerations alone. The lift may be obtained by integrating Equation (65) over the wetted length, that is, from $-a$ to a. The result obtained is

$$\frac{L}{\alpha_0 \rho g \ell^2} = \frac{\pi^3}{4} \left(\frac{V}{\alpha_0\sqrt{g\ell}}\right)^3 t\sqrt{g/\ell} \ . \qquad (67)$$

This curve has been plotted as a continuous line in Figure 11c. It should be pointed out that the linear relationship of this last equation appears as a curve in the graph because the ordinate is plotted on an inverse-hyperbolic-sine scale - a scale which is linear for small arguments and logarithmic for large ones. This curve does show that if an impact speed of

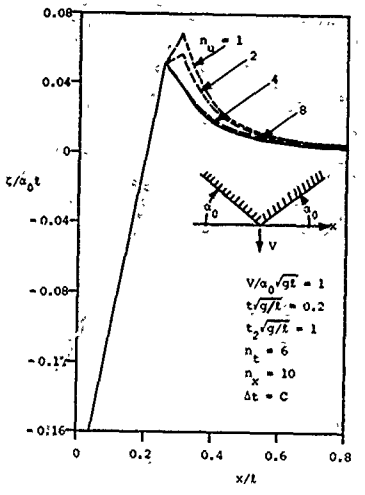


Figure 11: Symmetric Wedge Plunging at a Constant Velocity. (a) Free-Surface Profiles

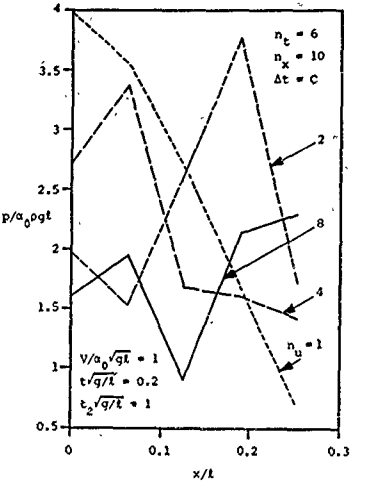


Figure 11: Symmetric Wedge Plunging at a Constant Velocity. (b) Pressure Distributions

$V/a_0\sqrt{gt} = 1$ can be considered high enough for gravity to be neglected, then the numerical technique does start off correctly before beginning to oscillate.

Symmetric Wedge Plunging with a Constant Acceleration

Experiments with a wedge impinging on the water surface with a constant downward *acceleration* of unity are displayed in Figure 12. This example shows much greater numerical stability than the previous one for a constant velocity.

The free-surface profiles in Figure 12a behave in a manner to be expected from a linear theory. There is, of course, no spray jet at the edge of the wetted surface. The shapes are further seen to be approximately similar. Only in the infinite-velocity case (no gravity) could the hydrodynamics be solved on a similarity basis.

Figure 12b illustrates the development of the pressure distributions. One can see a pressure peak developing near the ideal spray line, and ultimately with a fine enough mesh (a sufficiently large value of n_x), the square-root singularity contained in Equation (65) would be reproduced. The figure also shows the tendency of the pressure to misbehave near the center. A region of negative pressure is seen there when $t\sqrt{g/t} = 0.4$.

The wetted length is plotted as a series of symbols in Figure 12c. The different symbols

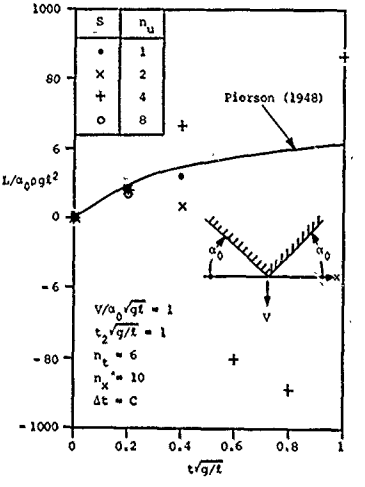


Figure 11: Symmetric Wedge Plunging at a Constant Velocity. (c) The Lift Force

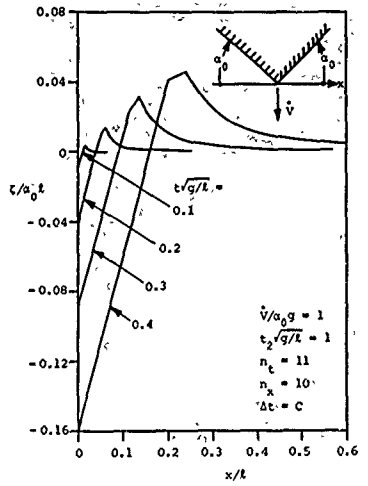


Figure 12: Symmetric Wedge Plunging at a Constant Acceleration. (a) Free-Surface Profiles

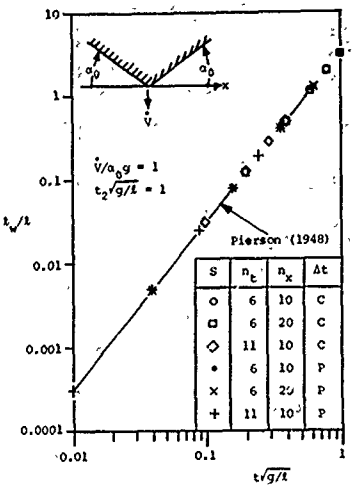


Figure 12: Symmetric Wedge Plunging at a Constant Acceleration. (c) The Wetted Length

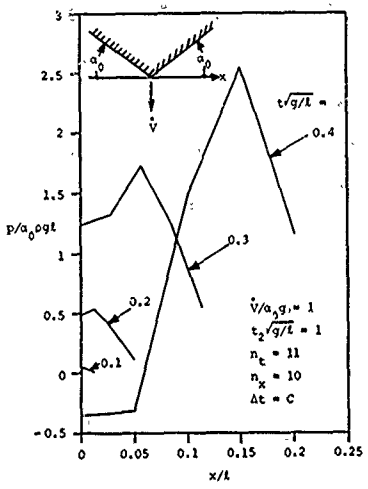


Figure 12: Symmetric Wedge Plunging at a Constant Acceleration. (b) Pressure Distributions

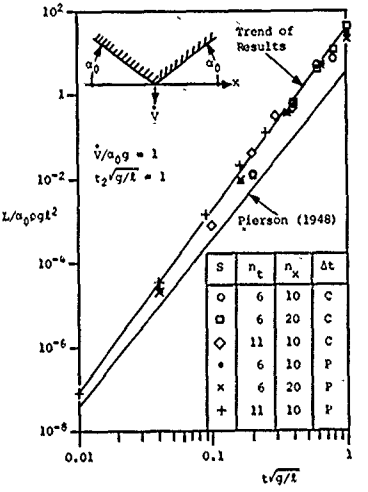


Figure 12: Symmetric Wedge Plunging at a Constant Acceleration. (d) The Lift Force

correspond to various numerical experiments in which both constant time steps (indicated with a "C"), and time steps proportional to the time (indicated with a "P"), were used. Two different mesh sizes, related to the value of n_x, were also tested. These results collapse onto the line developed by Pierson, equivalent to Equation (64)

Finally, the lift is plotted in Figure 12d, where again the validity of the numerical procedure is supported by the way the results of the various experiments collapse onto a single line. In this example of constant downward acceleration, the linearized gravity-free result of Pierson, analogous to Equation (67) is

$$\frac{L}{a_0 \rho g t^2} = \frac{\pi^3}{8}\left(\frac{\dot{V}}{a_0 g}\right)^3 (t\sqrt{g/l})^4 \quad . \qquad (68)$$

Without attempting to interpret the comparison too literally, it is possible to see that the *relative* effect of the gravity is more important at large values of the time. In fact, it is clear that initially the impact must obey the laws of similarity. Only when the wetted length becomes appreciable, do the gravitational effects come into play.

The Entry of a Bow into a Wave

As a last example, we consider the impact of a bow into a wave. The initial configuration is shown in the sub-diagrams of Figure 13, where it should be noted that the wave is travelling to the left. The bow motion consists of a downward acceleration $\dot{V}$, and an angular rotation $\omega = -\dot{\alpha}$.

Figure 13a displays the development of the fluid motion after the initial impact. One can see the rise in water around the bow. It is interesting to note that the "hole" made by the bow is not purely wedge shaped. This indicates that the wetted length is generally too small - particularly near the attachment point x_c. At each time step, the formulation given by Equation (55) is insufficient to increase the length properly. A larger value of the parameter μ_x would cure this problem.

Figure 13b shows the pressure distibution at various points in time. The asymmetry in this problem is revealed by the generally higher pressures on the forward face of the bow - leading to a positive value of the drag.

The wetted length is plotted in Figure 13c, in which the test results from various computer runs collapse onto a single slightly curved line when plotted on the double-logarithmic scale.

Figure 13d shows that the lift tends to drop off in logarithmic terms as the slam progresses.

The drag (positive to the left) is shown in Figure 13e, and the center of pressure of the lift in Figure 13f. The scatter of the numerical results is somewhat greater in these two diagrams. The center of pressure is slightly ahead of the bow knuckle, indicating that the effect of the water on the forward side is greater than that on the underside.

6. Concluding Remarks

Present Work

The results of this paper fall into two groups. The first group concerns the disturbance generated by a single pressure element undergoing various types of time-varying motion, and may be seen in Figures 5 through 8.

These trial cases were developed to test the formulation of the pressure-element behavior - particularly in regard to the final result in Equations (26) and (28).

The second group of results refer to the bow-slamming problem itself, and they can be seen in Figures 11, 12 and 13. There is a note of disappointment because of the instability difficulties referred to in the previous section.

Additional attempts to eliminate the numerical oscillations were made. One of them was to make an adjustment to the locations of the row of pressure elements at the last sub-time step. This correction was based on the fact that the elements in the latest row are in fact only *half* elements. Since those elements are half-triangular with respect to time (see the lower part of Figure 1), their effective centers of effort should be displaced to positions obtained by back-tracking one-third of a sub-time step. This modification, however, produced no appreciable improvement in the stability.

One other major change to the computer program incorporated smoothing of the pressure distribution at each time step, in an attempt to prevent the occurrence of negative pressures near the center. This idea was also unsuccessful.

The last modification was to allow the use of an uneven mesh in the spatial direction. However, concentrating elements near the ends of the wetted length only exacerbated the problem.

On the other hand, it was encouraging to see the consistency of the results using differing numbers of elements (the value of n_x in Equation (51)), different time steps, and different *types* of time step (both constant and proportional).

Furthermore, the numerical results correlated well with previously obtained gravity-free analytic results - thus confirming the validity of the basic numerical method outlined here.

Future Work

Further effort should be expended on removing the temporal instability displayed in some of the figures of this paper.

One approach with a good chance of success is to satisfy the kinematic equation by matching the vertical *velocity* of the bow and water at the field points, rather than by matching the vertical *positions* in Equation (51).

This idea involves developing the response $d\zeta/dt$ from a pressure element. The result is obtained by differentiating Equations (26) and

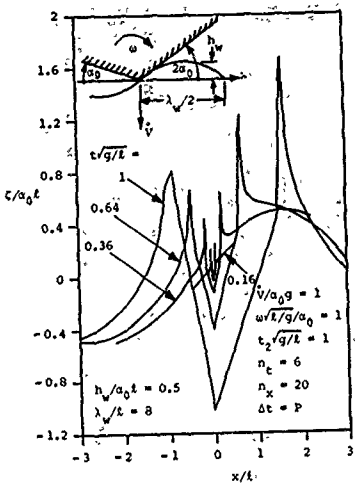


Figure 13: Entry of a Bow into a Wave
(a) Free-Surface Profiles

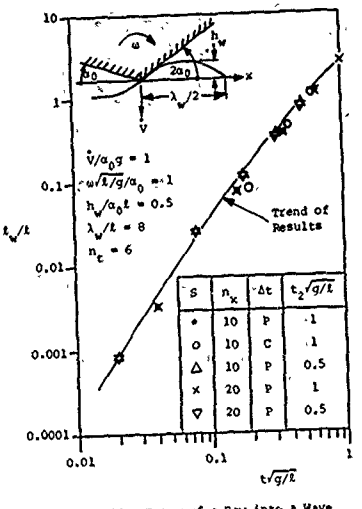


Figure 13: Entry of a Bow into a Wave
(c) The Wetted Length

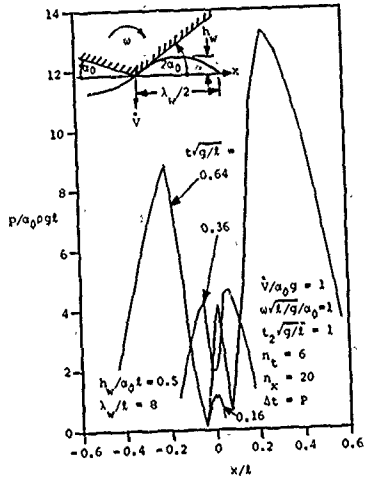


Figure 13: Entry of a Bow into a Wave
(b) Pressure Distributions

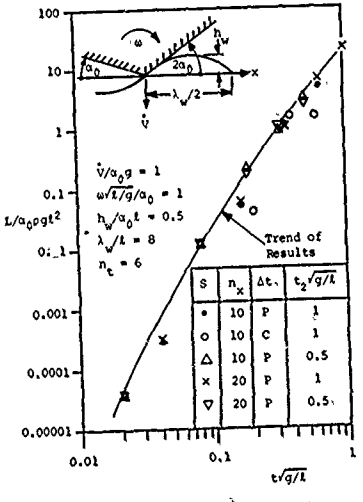


Figure 13: Entry of a Bow into a Wave
(d) The Lift Force

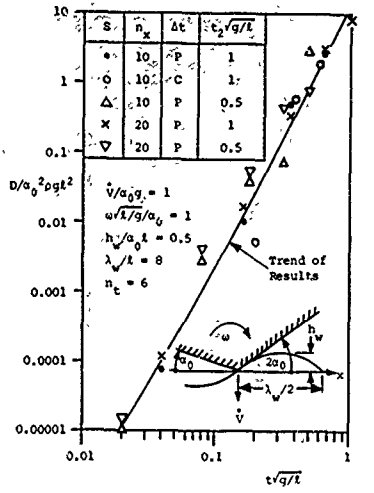


Figure 13: Entry of a Bow into a Wave
(e) The Drag Force

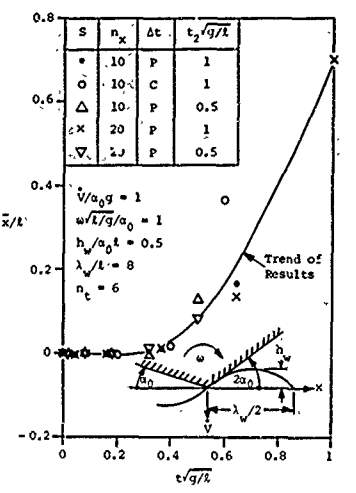


Figure 13: Entry of a Bow into a Wave
(f) The Center of Pressure

(28) with respect to time.

One then needs to differentiate Equation (51) in a similar manner. The resulting computer program would require only minor modifications in order to accept this fundamental alteration to the numerical procedure.

7. Acknowledgements

Part of the work reported here was performed by the writer when located in the Aviation and Surface Effects Department (ASED) of the David W. Taylor Naval Ship Research and Development Center (DTNSRDC) from December 1976 to February 1978. The work was conducted for the Stevens Institute of Technology (SIT), New Jersey, under contract to the Naval Sea Systems Command (PMS-304), and administered by the Office of Naval Research (ONR) through contract N00014-77-C0121, Task NR062-567, DTNSRDC Project 1630-050. The author would like to express his appreciation to Mr S. Davis (PMS-304), Mr A. G. Ford (ASED, DTNSRDC), Mr R. D. Cooper (ONR), and to Prof. J. P. Breslin (SIT), for arranging his assignment to DTNSRDC.

8. References

1. Wagner, H.: "Planing of Watercraft", National Advisory Committee for Aeronautics (NACA), Technical Memorandum 1139, 41 pp (1948). (Translation of "Uber das Gleiten von Wasserfahrzeugen", *Jahrbuch der Schiffbautechnik*, Vol. 34, pp 205-227 (1933).)

2. Savitsky, D.: "Hydrodynamic Design of Planing Hulls", *Marine Technology*, Vol. 1, No. 1, pp 71-95 (1964)

3. Whitman, A.M. and Pancione, M.C.: "A Similitude Relation for Flat-Plate Hydrodynamic Impact", *J. Ship Research*, Vol. 17, No. 1, pp 38-42 (1973)

4. Pierson, J.D. and Leshnover, S.: "An Analysis of the Fluid Flow in the Spray Root and Wake Regions of Flat Planing Surfaces", Experimental Towing Tank, Stevens Institute of Technology, Report 335, 65+ii pp (1948)

5. Hughes, O.F.: "solution of the Wedge Entry Problem by Numerical Conformal Mapping", *J. Fluid Mechanics*, Vol. 56, Part 1, pp 173-192 (1972)

6. Huang, R.T. and Sibul, O.J.: "Slamming Pressures on a Barge Model", *Society of Naval Architects and Marine Engineers*, Panel HS-2 (Slamming), Full Structure Committee, Technical and Research Report R-12, 29+iii pp (1971)

7. Haussling, H.J. and Van Eseltine, R.T.: "Numerical Solution of Planing-Body Problems", David W. Taylor Naval Ship Research and Development Center, Report 76-0118, 23+v pp (1976)

8. Hirt, C.W., Nichols, B.D. and Romero, N.C.:

"SOLA - A Numerical Solution Algorithm for Transient Fluid Flows", University of California, Los Alamos Scientific Laboratory, Report LA-5852, 50 pp (1975)

9. Doctors, L.J.: "Representation of Planing Surfaces by Finite Pressure Elements", *Proc. Fifth Australasian Conference on Hydraulics and Fluid Mechanics*, University of Canterbury, Christchurch, New Zealand, 9-13 December 1974, Vol. 2, pp 480-488 (1974)

10. Squire, H.B.: "The Motion of a Simple Wedge along the Water Surface", *Proc. Royal Society of London*, Series A, Vol. 243, pp 48-64 (1957)

11. Doctors, L.J.: "Theory of Compliant Planing Surfaces", *Proc. Second International Conference on Numerical Ship Hydrodynamics*, Berkeley, Ca., 19-21 September 1977, Sponsored by the David W. Taylor Naval Ship Research and Development Center, the University of California and the Office of Naval Research, Washington, D.C., pp 185-197 (1977)

12. Doctors, L.J.: "Representation of Three-Dimensional Planing Surfaces by Finite Elements", *Proc. First International Conference on Numerical Ship Hydrodynamics*, Gaithersburg, Md., 20-22 October 1975, Sponsored by the David W. Taylor Naval Ship Research and Development Center and the Office of Naval Research, Washington, D.C., pp 517-537 (1975)

13. Stoker, J.J.: *Water Waves*, Pure and Applied Mathematics, Vol. 4, Edited by R. Courant and others, Interscience Publishers, Inc., New York, 567+xv+viii pp (1957)

14. Abramowitz, M. and Stegun, I.A.: *Handbook of Mathematical Functions*, Applied Mathematical Series - 55, National Bureau of Standards, U.S. Government Printing Office, Washington, D.C., 1046+xiv pp (1965)

15. Gradshteyn, I.S. and Ryzhik, I.M.: *Tables of Integrals, Series, and Products*, Fourth Edition, Academic Press, New York, 1086+xlv pp (1965)

16. Pierson, J.D.: "On the Pressure Distribution for a Wedge Penetrating a Fluid Surface", Experimental Towing Tank, Stevens Institute of Technology, Report 336, 37+ii pp (1948)

INITIAL ASYMPTOTICS IN PROBLEM OF BLUNT BODY ENTRANCE INTO LIQUID

V.V. Pukhnachov and A.A. Korobkin
Lavrentjev Institute of Hydrodynamics
630090 Novosibirsk, U S S.R.

Abstract. Some problems conserning of the initial period of interaction between solid body and ideal incompressible liquid are investigated. In the moment t=0 the body touchs liquid free surface. Typical examples of this situation are following: the symmetrical entrance of parabolic contour into liquid filling a half - plane and the impact of liquid drop on a solid plane. In this paper the method for calculating of the similar motion initial asymptotics is suggested. This method consists in construction of outer and inner expansions (relatively to the contact line) for Euler equations which are written in Lagrange coordinates. Here the role of a small parameter plays the small t. The offering method admits generalization on non-symmetrical and three-dimensional motions and allows to take into account the presence of gravity and surface tension also.

Introduction. This paper deals with the problem of unsteady liquid motion occupying the volume changing in time, with its boundary consisting of a free surface, a solid wall and a contact line between them. The velocity range is assumed such that the Reynolds number is $R \gg 1$, and the Mach number $M < 1$. It allows the liquid to be considered ideal and incompressible. Besides, in most cases under consideration external mass forces and surface tensions will be ignored.

Firstly the problem of the blunt body entrance into liquid (a plane case) was considered by H. Wagner in 1932[1]. The method for calculating the resistance force developed by Wagner is based on the assumption that the velocity distribution on a free surface at each instant of time is identical to that immediately after the impact of a floating plate whose width is to be determined. Using this assumption it is possible to determine the free surface configuration at any instant of time. In 1953 C. Schmieden applied this method for calculating of the rotation body entrance [2].

The problem of the body entrance into liquid has the following peculiarities:

1. The flow region is not pre-determined.
2. It is necessary to find not only the flow region, but also the contact line.
3. It is possible that at the interface between a free surface and solid body there can appear some singularities of the solution.

The new approach to solving such type problems is based on introducing Lagrange coordinates in which the flow region has already been fixed [3]. This approach is applicable for describing a wide class of problems about the interaction between a solid body and a

free surface, in particular, the problem of the drop impact onto a plane. The problems under consideration in an exact statement are very complicated. Below the method of extracting a main asymptotics term of an initial motion stage will be suggested.

Let Ω be flow region in Lagrange Cartesian coordinates ξ, η, ζ, which is predetermined. In Lagrange variables unknown functions are the coordinates x, y, z of a liquid particle which, at $t=0$, takes the position ξ, η, ζ.

The Euler equations written down in Lagrange coordinates take the form[3]

$$M^* \vec{x}_{tt} + \gamma^{-1} \nabla_\xi p = 0, \quad \det M = 1 \text{ in } \Omega. \tag{0.1}$$

The boundary conditions are in the form

$$p\,|_{\Gamma_t} = 0, \quad (\vec{x}_t - \vec{v}) \cdot \vec{n}\,|_{\Sigma_t} = 0 \tag{0.2}$$

and the initial conditions are as follows:

$$\vec{x}\,|_{t=0} = \vec{\xi}, \quad \vec{x}_t\,|_{t=0} = 0 \tag{0.3}$$

Here $M = \partial(\vec{x})/\partial(\vec{\xi})$ is the Jacoby matrix, M^* is the matrix conjugated with M, p the pressure, γ the density, $\vec{n}$ the normal to Σ_t. A free boundary and solid impermeable surface whose position in Euler coordinates is known, are denoted by Γ_t and Σ_t, respectively. It is worthy to note that although the flow region Ω is fixed, the dividing of its boundary into components Γ_t and Σ_t is to be determined, together with the solution of the problem (0.1)-(0.3).

As any information about the solution of the problem (0.1)-(0.3) in an exact statement is not available. Let us analyze its approximate formulation based on linearization of this problem in the vicinity of an initial state of rest. It can be expected that the study of a linear model gives the idea about the asymptotics of the liquid motion, if $t \to 0$.

Let us determine the particle displacement from the formula $\vec{X} = \vec{x} - \vec{\xi}$, where $X = (X, Y, Z)$. Let us linearize the equation (0.1) holding the terms of zero and first order smallness with respect to displacements. We obtain

$$\vec{X}_{tt} + \gamma^{-1} \nabla_\xi p = 0, \quad \operatorname{div}_\xi \vec{X} = 0.$$

This suggests that for the linearized problem it is possible to introduce the displacement potential $\Phi = \Phi(\xi, \eta, \zeta)$, so that $\vec{X} = \nabla_\xi \Phi$. Due to equation of continuity, Φ will be the function harmonic in Ω. It follows from the linearized equation of impulse that there exist the connection between the pressure and displacement potential:

$$p = -\gamma \Phi_{tt}. \tag{0.5}$$

With taking into account (0.5), the condition on a free surface, after a double integration over t and with the use of initial conditions, is written down in the form $\Phi\,|_{\Gamma_t} = 0$. The slip condition dependent on a solid wall configuration, is to be linearized in each case separately.

1. A plane problem. This problem deals with the case of a plane unsteady motion of an ideal incompressible liquid filling a half-plane $y' < 0$ at the instant of time $t'=0$ and initially resting (here and below dimensional variables are primed). The line $y'=0$ at an initial instant of time is a free boundary. It is assumed that a surface tension and external mass forces are absent.

Let K and V be positive constants. At fixed t' the equation

$$y' = \frac{1}{2} K x'^2 - Vt' \tag{1.1}$$

defines a parabola on the plane x', y', which will be identified with a solid undeformable contour.

When $t'=0$, this contour is tangent to a free surface at point $x'=0$. The relation (1.1) prescribes the contour motion along axis y' with constant velocity V. It is required to find the motion of liquid assuming that a part

of its boundary, not being a part of a solid contour, rests free. The above-mentioned assumption means that on the plane of Lagrange coordinates ξ', η' the region occupied by liquid is known. This is a half - plane $\eta' < 0$.

Let the radius of curvature $1/K$ of parabola (1.1) at point $x'=0$ and $1/KV$ be assumed as the length scale and time scale respectively, now turn to dimensionless variables (here dimensionless variables aren't primed). In Lagrange variables the unknown functions are dimensionless coordinated x,y of the liquid particle which takes a position ξ, η if $t=0$. Now it is appropriate to turn to the displacements $X(\xi,\eta,t)$, $Y(\xi,\eta,t)$ of liquid particles defined by the equalities $X=x-\xi$, $Y=y-\eta$. The functions X, Y satisfy the following equations [3]:

$$X_\xi + Y_\eta + X_\xi Y_\eta - X_\eta Y_\xi = 0, \quad (1.2)$$

$$X_{\eta t} - Y_{\xi t} + X_\xi X_{\eta t} + Y_\xi Y_{\eta t} - X_\eta X_{\xi t} - Y_\eta Y_{\xi t} = 0. \quad (1.3)$$

The first of them is the equation of continuity, and the second expresses the condition of the absence of eddies (it should be noted that the motion is generated from the state of rest and external forces are absent). It is required to find the solution of the system (1.2), (1.3) in the domain $\eta < 0$, $0 < t < T$ at the initial conditions

$$X=Y=0, \; X_t=Y_t=0 \text{ when } t=0 \quad (1.4)$$

and the boundary conditions which will be formulated below.

A physical statement of the problem possesses a symmetry that makes it possible to find its solutions where X and Y are uneven and even functions of the coordinate ξ respectively. It is assumed that for any t from the interval $[0,T]$ the line $\eta = 0$ bounding liquid consists of the three components:
$\xi < -a(t)$, $|\xi| \le a(t)$, $\xi > a(t)$,
where $a(t)$ is to be determined. The sections $|\xi| > a(t)$ of this line are free boundaries on which we assume that

$$X_{tt} + X_\xi X_{tt} + Y_\xi Y_{tt} = 0 \quad (1.5)$$
$$\text{when } \eta = 0, \; |\xi| > a(t).$$

The above condition is the sequence of the impulse equation having a Lagrange form and constant pressure equation on the free surface [3]. Now, let us assume that the image of section $|\xi| \le a(t)$, $\eta = 0$, when mapping to the plane of Euler coordinates x,y, coincides with the part of a rigid contour wetted at the instant of time t. On this section the condition of flowing round is prescribed, and, according to (1.1), in terms of displacements, has the form

$$Y - \frac{1}{2}(\xi + X)^2 + t = 0$$

$$\text{when } \eta=0, \; |\xi| \le a(t). \quad (1.6)$$

Besides the equalities (1.4)-(1.6), the functions X,Y must satisfy the inequality

$$\eta + Y - \frac{1}{2}(\xi + X)^2 + t \le 0 \quad (1.7)$$

when $\eta \le 0$ and for any ξ. The inequality (1.7) means that moving liquid particles can't work into the "forbidden" region bounded by moving impermeable contour and determined on plane x,y by the inequality $y - x^2/2 + t > 0$.

2. Linear approximation. It follows from the statement of the problem (1.2)-(1.7) that $a=0$, $X=Y=0$ when $t=0$. Let us linearize the above-mentioned relations holding only the zero- and first-order terms with respect to the required functions. When linearizing (1.6), it is worthy to note that when $|\xi| \le a(t)$, ξX is a quadratically small term. As a result the following problem is obtained: it is necessary to find the functions $X(\xi,\eta,t)$, $Y(\xi,\eta,t)$ and

$a(t)$ so that in the region $\eta < 0$, $t > 0$ the following equations are satisfied:

$$X_\xi + Y_\eta = 0, \quad X_\eta t - Y_\xi t = 0, \qquad (2.1)$$

when $t=0$, the initial conditions

$$X = Y = 0, \quad X_t = Y_t = 0, \quad a = 0, \qquad (2.2)$$

when $\eta = 0$, $|\xi| > a(t)$, the boundary condition

$$X_{tt} = 0; \qquad (2.3)$$

when $\eta = 0$, $|\xi| < a(t)$, the boundary condition

$$Y = \frac{1}{2}\xi^2 - t, \qquad (2.4)$$

as well as when $t \geq 0$, $\eta \leq 0$ and for any ξ the additional condition

$$Y \leq \frac{1}{2}\xi^2 - t - \eta - \xi X \qquad (2.5)$$

are satisfied.

The relation (2.1)-(2.4) can be simplified. Integrating the second equation of (2.1) over t and using the condition (2.2), we come to the Cauchy-Riemann system for functions X, Y in variables ξ, η. It is assumed that the function $a(t)$ monotonously increases (this assumption will be valid aposteriori). Then it follows from (2.5), after integrating over t, with allowance for (2.2), that $X=0$ when $\eta = 0$, $|\xi| > a(t)$.

After the substitution of variables in the obtained equalities

$$\xi = a\lambda, \quad \eta = a\mu, \quad X = a^2 v, \quad Y = a^2 u, \qquad (2.6)$$

we come to the following problem: in a half-plane $\mu < 0$ it is necessary to find the solution of Cauchy-Riemann system

$$u_\lambda - v_\mu = 0, \quad u_\mu + v_\lambda = 0 \qquad (2.7)$$

under the conditions

$$u = \frac{1}{2}\lambda^2 - q(t) \text{ when } \mu = 0, \ |\lambda| \leq 1 \qquad (2.8)$$

$$v = 0 \text{ when } \mu = 0, \ |\lambda| > 1 \qquad (2.9)$$

where $q = a^{-2} \cdot t$. In new variables the condition (2.5) takes the form

$$u \leq \frac{1}{2}\lambda^2 - q - a^{-1}\mu + a\lambda v$$

when $\mu \leq 0$. (2.10)

Evidently, the description of an initial stage of motion in a linear approximation reduces to solving the two-dimensional problem, i.e. the variable t enters into the relations (2.7)-(2.10) as a parameter. Designate $\zeta = \lambda + i\mu$; by virtue of (2.7) the function $w(\zeta) = u + iv$ will be an analytical function of ζ-variable in the region $\operatorname{Im}\zeta < 0$. Restrict ourselves with solving the problem (2.7)-(2.9), where the function $w(\zeta)$ has a finite limit when $\zeta \to \infty$ and integrable singularities at point $\zeta = \pm 1$. Accoding to the Keldysh-Sedov theorem [4], the general solution of the problem (2.7)-(2.9) in the above-stated class has the form

$$w = \frac{1}{4}(\zeta - \sqrt{\zeta^2 - 1})^2 + \frac{A_0 + A_1\zeta}{\sqrt{\zeta^2 - 1}} + \frac{1}{4} - q. \qquad (2.11)$$

Here A_0, A_1 are the real constants, function $\sqrt{\zeta^2 - 1}$ has positive values when $\zeta > 1$ are real.

The constructed solution of (2.1)-(2.9) contains two arbitrary constants and an arbitrary function of t. An additional one-side inequality (2.10) can't eliminate this arbitrarity. Now let's put one more condition to the solution, namely, the condition of finiteness of the kinetic energy of the liquid motion. The motion energy divided by $\gamma V^2 K^{-2}$, where γ is the liquid density, is expressed by the integral

$$k(t) = \frac{1}{2}\int\int_{\eta<0} (X_t^2 + Y_t^2)\, d\xi\, d\eta.$$

It follows from (2.6), (2.11) that this integral converges if and only if $A_0 = A_1 = 0$, and $da/dt = 2$. From here and from the condition $a(0) = 0$ it follows that $q = 1/4$,

$$w = \frac{1}{4}(\zeta - \sqrt{\zeta^2 - 1})^2, \qquad (2.12)$$

$$a = 2\sqrt{t} \quad . \tag{2.13}$$

Now, let us show that for sufficiently small $t > 0$ the obtained solution satisfies the inequality (2.10) with $q = 1/4$. According to (2.12), $v \geq 0$ when $\lambda \geq 0$, the function v is uneven in λ, and consequently, $\lambda v \geq 0$. Thus, the validity of (2.10) can be established after having proved that

$$u \leq \frac{1}{2}\lambda^2 - \frac{1}{4} - \frac{\mu}{2\sqrt{t}} \quad . \tag{2.14}$$

Let us replace the variable $\zeta + \sqrt{\zeta^2 - 1} = z = r(\cos\varphi + i\cos\varphi)$. In plane z the domain $\mu \leq 0$ corresponds to $r \geq 1$, $-\pi \leq \varphi \leq 0$. With allowance for (2.12), the inequality (2.14) is transformed as follows:

$$r^2 - \frac{1}{r^2} - \frac{4r}{\sqrt{t}} \sin\varphi - \left(r + \frac{1}{r}\right)^2 \sin^2\varphi \geq$$
$$\geq 0 \quad .$$

It is evident that the latter holds true when $r \geq 1$, $-\pi \leq \varphi \leq 0$, $0 \leq t \leq 1$. This means that the inequality (2.10) also takes place at least for $t \in [0,1]$.

In conclusion let us calculate in a linear approximation the free boundary position in plane x, y and the resistance force acting to a body. The free surface equation is easy to obtain from (2.6), (2.12), (2.13):

$$y = 4t^2 / \left(x + \sqrt{x^2 - 4t}\right)^2,$$
$$|x| \geq 2\sqrt{t} \quad . \tag{2.15}$$

The free surface height, $y = t$, is maximum at the contact points $x = \pm 2\sqrt{t}$ with the solid body, and the tangential to the free surface at the above points is directled vertically.

To calculate the resistance force, let us use the impulse equation (0.4), Neglecting non-complicated calculations based on the impulse equation and the relation (2.6),(2.12),(2.13), we obtain the expression for dimensionless pressure p in the wetted part of the contour:

$$p(\xi, 0, t) = \frac{2}{\sqrt{4t - \xi^2}} \quad ,$$

$$|\xi| < 2\sqrt{t} \quad . \tag{2.16}$$

Substituting it into the formula for the resistance force in the linear approximation

$$F(t) = \int_{-2\sqrt{t}}^{2\sqrt{t}} p(\xi, 0, t)\, d\xi \quad ,$$

we obtain that $F = 2\pi$.

3. Some remarks. It becomes evident from the above considerations that the problem under investigation is rather trivial. Nevertheless, its solution has some peculiarities typical for more complicated problems of a similar type, such as a three-dimensional analog of this problem, the problem of a drop falling onto a solid plane, the problem of blunt body entrance into a heavy liquid in their linear statements.

If gravity and capillarity are absent, when linearizing at rest we come to stationary problems with time as a parameter. These problems have efficient solutions in a plane and axisymmetrical cases. Particularly, using the method described it is appropriate to consider the problem of entering into water symmetric smooth contour moving with a variable velocity. In this case the condition (2.4) is changed by

$$Y = l(\xi) - s(t) \quad \text{when} \quad \eta = 0, \ |\xi| \leq a(t).$$

Here l and s are the smooth function of their arguments, $l(0) = s(0) = 0$, $l(x) > 0$ and $s(x) > 0$ when $x > 0$, and the function l is even. It is proposed that $l(x) = bx^{2m} + O(x^{2m+2})$, $s(t) = At^{n+1} + O(t^{n+2})$, where b, A are the positive constants, n is non-negative, and $m \geq 1$ is an integer. In so doing the main term of the flow asymptotics is self-similar and takes the form $X = a^{2m} v(\lambda, \mu)$, $Y = a^{2m} u(\lambda, \mu)$. The functions u, v

of variables $\lambda = a^{-1}\xi$, $\mu = a^{-1}\eta$ are found solving the boundary value problem (2.7)-(2.9) where the condition (2.9) is replaces by

$$u = b\lambda^{2m} - q$$

when $\mu = 0$, $|\lambda| < 1$.

The condition (2.10) is transformed in a similar manner. The constant

$$q = 2^{-2m}(2m)!\,(m!)^{-2}b$$

is defined uniquely by the requirement of the fluid energy finiteness. The problem solution is written down in quadratures. The function a(t) has the form $a = ct^{\beta}$, where $\beta = (n+1)/2m$, $c = (q/A)^{1/2m}$.

The method described admits generalizations over plane non-symmetric flows. A non-symmetry may be conditioned by the profile configuration or by the fact that it enters liquid at an arbitrary angle. Here, instead of a function a(t), we have to defined two functions prescribing the contact point coordinates $\xi_k = a_k(t)$, $\eta = 0$, $k = 1,2$.

Taking into account the gravity force and surface tension in a linearized statement leads to replacing the condition (2.3) by

$$Y_{tt} + Fr^{-1}Y_{\xi} - We^{-1}Y_{\xi\xi\xi} = 0 \qquad (3.1)$$

when $\eta = 0$, $|\xi| > a(t)$

Here $Fr = V^2K/g$ is Froude number, $We = \gamma V^2/K\sigma$ - Weber number the gravity force acceleration, g the surface tension coefficient. To (3.1) the following relation is added:

$$Y_{\xi} = \operatorname{tg}\theta$$

when $\eta = 0$, $|\xi| = a(t)$,

where θ is the given boundary angle. A formal solution of the problem (2.1)-(2.5) with the changes condition (2.3) is as follows:

$$a = t^{1/2}\sum_{k=0}^{\infty} c_k t^{k/2},$$
$$Y = a^2\sum_{k=0}^{\infty} t^{k/2} v_k(\lambda,\mu), \qquad (3.2)$$

$$Y = a^2\sum_{k=0}^{\infty} t^{k/2} u_k(\lambda,\mu),$$

where the constants c_k and functions u_k, v_k are found from the solution of a recurrent sequence of the boundary problems such as (2.1)-(2.5). The functions u_k, v_k if $k = 1,2\ldots$ turn out to be determined non-uniquely and possess some singularities at the contact points $|\xi| = a(t)$, $\eta = 0$. Thus, series (3.2) are to be interpreted as an "external expansion" of this problem solution with respect to the contact points. In a small vicinity of these points the nonlinear terms of initial relations (1.2)-(1.6) are of great importance. Below this problem will be considered in more detail. But here it should be noted that on constructing the external expansion the gravity effect is observed from the third term of the series (3.2) and the capillarity effect - from the forth one.

Substantiation of a linear approximation in the problem under consideration is rather complicated (a rough picture of it is given in [3]). The first stage of constructing the solution is a formal asymptotic expansion satisfying (1.2)-(1.7) accurate to $O(t^{\alpha})$ uniformly in ξ and η if $t \to 0$ where α is any pre-scribed positive number. It is worthy to note that the solution of the linearized problem (2.1)-(2.5) satisfies the above-mentioned relations throughout with an accuracy of $O(\sqrt{t})$ except narrow zones in the vicinity of the contact points $\eta = 0$, $\xi = \pm 2\sqrt{t}$ which size is of the order of $t^{3/2}$ when $t \to 0$. Within them the linear approximation is invalid, and it is necessary to construct an "internal" expansion describing a fine structure of flow in the vicinity of the contact points.

4. Internal expansion. Let us consider a small vicinity of the contact point $\xi = a(t), \eta = 0$, gathered up to one point when $t \to 0$. The vicinity of the second contact point $\xi = -a(t)$, $\eta = 0$ is analyzed in a similar manner. Let us determine "internal variables" α, β and some unknown functions P, Q from the formulas

$$\xi = 2\sqrt{t} + t^k \alpha, \quad \eta = t^k \beta,$$
$$X = t^m Q(\alpha, \beta, t), \qquad (4.1)$$
$$Y = t + t^m P(\alpha, \beta, t),$$

where k and m are the positive numbers and $k > 1/2$.

It should be noted that usually the method of matching of asymptotic expansions [5] is applied for solving problems containing a small parameter. In our case t plays the role of it.

Substitute (4.1) into (1.2)-(1.6) and hold main terms when $t \to 0$. The condition of the non - trivial solution of the problem with respect to P and Q leads to the requirement that $k=m$. In this case P and Q satisfy the relations

$$P_{\alpha\alpha} - Q_{\alpha\beta} + P_\beta P_{\alpha\alpha} - P_\alpha P_{\alpha\beta} + Q_\beta Q_{\alpha\alpha} - Q_\alpha Q_{\alpha\beta} = 0,$$
$$P_\beta + Q_\alpha + P_\beta P_\alpha - P_\alpha Q_\beta \quad \text{when } \beta < 0, \qquad (4.2)$$

$$P_\alpha^2 + Q_\alpha^2 + 2Q_\alpha = 0 \text{ when } \alpha > 0, \beta = 0, \qquad (4.3)$$

$$P = 0 \quad \text{when } \alpha < 0, \beta = 0, \qquad (4.4)$$

where t appears as a parameter. According to the asymptotic expansion matching principle [5] it follows from (2.12), (2.13), (4.1) that

$$t^{m-k/2-3/4}(\alpha + i\beta)^{-1/2}(P + iQ) \to -2$$
$$\text{when } t \to 0$$

$((\alpha + i\beta)^{1/2} > 0$ when $\alpha > 0)$. From here $m = k/2 + 3/4$, and $m = k = 3/2$. Now the above - mentioned condition gives the external limit of the internal expansion:

$$(\alpha + i\beta)^{-1/2}(P + iQ) \to -2$$
$$\text{when } \alpha + i\beta \to \infty \qquad (4.5)$$

The one - side inequality (1.7) written down in internal variables takes the form

$$P + \beta \le 0 \quad \text{when } \beta \le 0 \qquad (4.6)$$

Considering that the region, in which the internal expansion is constructed, vanishes in limit when $t \to 0$, the initial conditions (1.4) don't lead to additional restrictions for P and Q.

The relations (4.2)-(4.6) form a non- linear boundary - value problem with a restriction in plane (α, β). The main difficulty in study of this problem is connected with the fact that the quasilinear system (4.2) is of compound type, namely, in any solution of P and Q of this system there exist two families of complex characteristics and a real family $\beta = \text{const}$. In future it is proposed to study this problem numerically. In this paper the authors restrict themselves with analyzing the approximate model of the problem (4.2)-(4.6) based on linearisation of (4.2). In this case a non - linear condition on a free boundary remains constant.

The approximation described corresponds to the substitution of the Cauchy--Riemann system with a simultaneous conservation of the condition (1.5) in a rigorous form for (1.2)-(1.4). Firstly such a model was used by V.I. Nalimov in study of Cauchy-Poisson problem [6]. The problem (4.2)-(4.5) in Nalimov's model is written in the form

$$\sigma_\alpha - \tau_\beta = 0, \quad \sigma_\beta + \tau_\alpha = 0 \text{ when } \beta < 0$$
$$\sigma^2 + \tau^2 + 2\tau = 0 \quad \text{when } \alpha > 0, \beta = 0$$

$$\sigma = 0 \quad \text{when} \quad \alpha < 0, \beta = 0$$

$$\sigma + i\tau \to -\omega^{-1/2} \quad \text{when} \quad \omega \to \infty \qquad (4.7)$$

Here $\sigma = P_\alpha$, $\tau = Q_\alpha$, $\omega = \alpha + i\beta$. When deriving these relations the second, linearized equation (4.2) and the condition (4.4) were differentiated with respect to α. The condition (4.7) expresses the matching condition in terms of new unknown functions σ and τ.

The obtained problem can be exactly solved by the godograph method. In the godograph plane $\sigma + i\tau = \chi$ the half - circle $\sigma^2 + \tau^2 + 2\tau < 0$, $\sigma < 0$ is the definition domain of the unknown analytical functin $\omega(\chi)$. The boundary conditions for ω are following: $\mathrm{Im}\,\omega = 0$ on the half - - circle boundary, $\chi^2\omega \to 1$ when $\chi \to 0$. It is easy to check that the function

$$\omega = -\frac{1}{4}\left(1 + \frac{2i}{\chi}\right)^2 \qquad (4.8)$$

satisfies the necessary conditions. Using symmetry principle and Luiville theorem [4] it is established that the solution (4.8) is unique in the class of functions having the second - -order pole at the point $\chi = 0$.

Resolving the relation (4.8) with respect to χ and integrating the equality $d(P + iQ)/d\omega = \chi(\omega)$ with the condition (4.5) we obtain:

$$P + iQ = -2\sqrt{\omega} - i\ln\left(1 + 2i\sqrt{\omega}\right) \qquad (4.9)$$

($\ln 1 = 0$). Due to (4.9), we have $P \le 0$ when $\beta = 0$ for any α. From here the validity of (4.6) resusts.

In conclusion it is worthy to note that the obtained solution has two important qualitative properties. Firstly, as is seen from (4.9), the free boundary $\alpha > 0$, $\beta = 0$ comes to the contact point at a zero angle. (Note that in the external expansion the tangent to the free boundary at a contact point was vertical (see 2.15). Second, pressure on the wetted part of the contour is limited, and at the contact point $\alpha = \beta = 0$ turns to zero. The above - mentioned statements result from the expression for pressure in internal variabler. To obtain it, it is appropriate to use the impulse equation (0.1) in projection to the axis ξ ($\gamma = 1$)

$$(1 + X_\xi)X_{tt} + Y_\xi Y_{tt} + p_\xi = 0,$$

and turn to internal variables. Assuming $p = t^{-1}\Pi(\alpha, \beta, t)$ and using (4.1) in the main order we have $(1+Q_\alpha)Q_{\alpha\alpha} + P_\alpha P_{\alpha\alpha} + \Pi_\alpha = 0$ when $t \to 0$. From here and the condition $\Pi \to 0$ when $\alpha \to \infty$, $\beta = 0$, we obtain $\Pi = -Q_\alpha - (P^2 + Q_\alpha^2)/2$. On the wetted part of the contour we have $\Pi(\alpha, 0) \approx 4|\alpha|^{1/2}(1 + 2|\alpha|^{1/2})^{-2}$, $\alpha < 0$. In external variables this corresponds to the equality

$$p(\xi, 0, t) = \frac{4\sqrt{2t^{1/2} - \xi}}{t^{1/4}(t^{3/4} + 2\sqrt{2t^{1/2} - \xi})^2} \qquad (4.10)$$

when $\xi < 2t^{1/2}$, $2t^{1/2} - \xi = O(t^{3/2})$, $t \to 0$ if $\alpha = t^{-3/2}(\xi - 2t^{1/2}) \to \infty$ and $\alpha t \to 0$ when $t \to 0$, the main pressure terms determined from the formulas (2.16) and (4.10) coincide: $p = t^{-1}|\alpha|^{-1/2}[1 + o(1)]$. Along with the abovementioned at the contact point $\xi = 2\sqrt{t}$, $\eta = 0$ the formula (2.10) gives an infinite pressure value, as, $p(2\sqrt{t}, 0, t) = 0$ according to (4.10). After all, it should be noted that at fixed t "the internal pressure" on the contour $p(\xi, 0, t)$ achieves its maximum at point $\xi = 2t^{1/2} - t^{3/2}/2$ equal to $1/2t$.

5. Elliptic paraboloid entrance. In the previous section the plane motions were considered. Even the simplest three-dimensional of this class, i.e. an initial stage of the elliptic paraboloid entrance into a weightless liquid, leads to a non-trivial problem with an unknown boundary for a harmonic function in a half-space. Distinct to Section 1, where it was necessary to find the function of one variable a(t) only, here the curve $\Gamma(t)$ on the plane $\zeta = 0$ must be found. Its image in Euler coordinates is the interface between a free-surface and a solid body.

So, let us consider the unsteady motion of an ideal liquid filling in the half-space $z' < 0$ and initially being at rest, when $t' = 0$. The equation

$$z' = b\left(\frac{x'^2}{a^2} + \frac{y'^2}{b^2}\right) - Vt' \qquad (5.1)$$

determines the elliptic paraboloid ($b > a$) moving along the axis z' with velocity $-V$ and at an initial moment tangent to a free surface at an origin.

In Lagrange coordinates ξ', η', ζ' the half-space $\zeta' < 0$ is the region occupied by liquid. To determine the motion asymptotics when $t' \to 0$, the scheme suggested in Section 2 is used. After having linearized the relations (0.1), (0.2), we come to the boundary-value problem for the displacement potential $\Phi(\xi, \eta, \zeta, t)$:

$$\Delta\Phi = 0 \quad \text{when} \quad \zeta < 0$$
$$\Phi = 0 \quad \text{when} \quad \zeta = 0, \ (\xi, \eta) \in R^2 \setminus D \qquad (5.2)$$
$$\Phi_\zeta = (1 - \varepsilon^2)^{-1}\xi^2 + \eta^2 - t \quad \text{when} \quad \zeta = 0, (\xi, \eta) \in D$$

The equation (5.2) are written down in dimensionless variables

$$\vec{\xi} = b^{-1}\vec{\xi}', \quad t = b^{-1}Vt, \quad \Phi = b^{-2}\Phi'.$$

The ellipse eccentricity formed on intersection of the surface (5.1) with planes $z' = \text{const}$ is designated by $\varepsilon = (1 - a^2/b^2)^{1/2}$. The domain $D(t)$ in plane $\zeta = 0$ is a pre-image of the wetted part of the paraboloid in Lagrange coordinates. The boundary D is designated by l.

The problem (5.2) admits a self-similar solution, where $\Phi(\xi, \eta, \zeta, t) = t^{3/2}\bar{\Phi}(\xi/\sqrt{t}, \eta/\sqrt{t}, \zeta/\sqrt{t})$ and l is determined by the equation $F(\xi/\sqrt{t}, \eta/\sqrt{t}) = 0$. Now the curve l is to be found in the class of ellipses with a great half-axis $\sigma t^{1/2}$ and eccentricity e,

$$(1 - e^2)^{-1}\xi^2 + \eta^2 = \sigma^2 t .$$

Let us determine self-similar variables u, v, w and a new unknown function Φ_0 from formulas

$$u = \xi/\sigma\sqrt{t}, \ v = \eta/\sigma\sqrt{t}, \ w = \zeta/\sigma\sqrt{t},$$
$$\Phi = \sigma t^{3/2}\Phi_0(u, v, w), \qquad (5.3)$$

In plane $w = 0$ the domain

$$D_0 = \{u, v, w: \ (1-e^2)^{-1}u^2 + v^2 < 1, \ w = 0\}$$

corresponds to D.

Let us continue the function Φ_0 to an upper half-space in an uneven manner. Now the free boundary condition is satisfied automatically. For the function $\psi = \partial\Phi_0/\partial w$ the Dirichlet problem outside the elliptic disk D_0 is obtained with an additional condition $\psi = 0$ at infinity. This problem solution can be written down in an explicit form, with the help of ellipsoidal coordinates ρ, μ, ν connected with Cartesian relations [7]

$$e^2(1-e^2)u = (\rho^2 - e^2)(\mu^2 - e^2)(e^2 - \nu^2),$$
$$e^2 v^2 = \rho^2 \mu^2 \nu^2 ,$$
$$(1-e^2)w = (\rho^2 - 1)(1 - \mu^2)(1 - \nu^2),$$

thereby $0 < \nu < e < \mu < 1 < \rho$.

It follows from the infinity condition for ϕ that σ and e^2 are interconnected

$$\sigma^2 = \frac{3(1-\varepsilon^2)}{2-\varepsilon^2-e^2}$$

The expression for ϕ takes the form

$$\phi = \frac{9}{2e(2-e^2-\varepsilon^2)\sqrt{e^4-e^2+1}}\left(\frac{\alpha_2\varepsilon^2-e^2}{1-\alpha_1}\times\right.$$

$$\times(\mu^2-\alpha_1)(\nu^2-\alpha_1)\frac{S_7(\rho)}{S_7(1)} -$$

$$\left. - \frac{\alpha_1 e^2}{1-\alpha_2}(\mu^2-\alpha_2)(\nu^2-\alpha_2)\frac{S_8(\rho)}{S_8(1)}\right), \qquad (5.4)$$

where $\alpha_1=[1+e^2+(1-e^2+e^4)^{1/2}]/3$,
$\alpha_2=[1+e^2-(1-e^2+e^4)^{1/2}]/3$,
and $S_7(\rho)$, $S_8(\rho)$ are the Lame functions [7],

$$S_7(\rho)=5(\rho^2-\alpha_1)\int_\rho^\infty \frac{d\rho}{(\rho^2-\alpha_1)^2\sqrt{(\rho^2-e^2)(\rho^2-1)}}$$

$$S_8(\rho)=5(\rho^2-\alpha_2)\int_\rho^\infty \frac{d\rho}{(\rho^2-\alpha_2)^2\sqrt{(\rho^2-e^2)(\rho^2-1)}}$$

Coming back to variables u , v , w in (5.4) and integrating the result over w , we obtain the function Φ_0 through which, due to (5.5) the unknown potential $\Phi(\xi, \eta, \zeta, t)$ is expressed. Pressure p is determined from (0.5). In this case, as in a plane one, pressure has an integrable singularity at the interface between the free surface and the solid body.

However, in contrast to a plane case, the problem (5.2) has a non-unique solution, i.e. eccentricity e of ellipse 1 is arbitrarily selected. It is supposed that the above - mentioned non - uniqueness can be eliminated when matching the obtained solution with the internal expansion in the vicinity of the contact point (see Section 4). It should be noted that in an axisymmetrical case, $\varepsilon = 0$, the solution of (5.2) is unique and in agreement with the method suggested in [2].

6. Drop impact onto a plane.

The above - considered method for studying the initial motion stage is applicable to a wide class of plane and axisymmetrical problems of interaction of liquid masses with solid surfaces. As an example, let us consider the axisymmetrical problem of a spherical drop fall onto a solid plane.

The drop radius a and $a/2V$ (V -the impact velocity) are taken as a length scale and time scale, respectively and turn to dimensionless variables. As unknown function of a linearized problem (see (5.2)) the displacement potential is taken, $\Phi = \Phi(r,\theta,t)$, where radius r and angle θ are the spherical Lagrange coordinates connected with the centres of drop masses. This coordinate system is not inertial, however, the mass center velocity change turns out to have the order $O(t^{3/2})$ when $t \to 0$. To calculate the main asymptotics term it is expedient to assume it constant. Now it is suitable to introduce the new function $u(r, \theta, t)$ such that

$$u(r,\theta,t)=2\Phi(r,\theta,t)-(1-2t)rP_1(\cos\theta)-$$

$$-(t-1)r^2P_2(\cos\theta)/2,$$

where $P_n(\kappa)$ are Legendre polinomials. The boundary - value problem written down for $u(r, \theta, t)$ takes the form

$$\Delta u = 0 \quad \text{when} \quad r < 1,$$

$$u=(2t-1)P_1(\cos\theta)+(1-t)P_2(\cos\theta)/2$$

$$\text{when} \quad r = 1, \quad \theta_0 < \theta \le \pi \qquad (6.1)$$

$u_r = 0$ when $r = 1$, $0 \le \theta < \theta_0(t)$

where $\theta = \theta_0(t)$ is the pre-image of the interface between the free drop surface and the solid surface $\theta_0(t)$ and $u(r, \theta, t)$ are the unknown functions. The distinctive feature of the problem under consideration as opposed to all previous problems is that it doesn't admit a self-similar solution.

The solution of (6.1) is as follows

$$u = \sum_{n=0}^{\infty} A_n(t) r^n P_n(\cos\theta). \qquad (6.2)$$

Accoding to [8], the problem (6.1) may be reduced to regular integral Fredholm equation for a supplementary function $\varphi(x, t)$:

$$\varphi(x,t) + \frac{1}{\pi}\int_{\theta_0(t)}^{\pi} K(x,y)\,\varphi(y,t)\,dy =$$

$$= \frac{1}{\pi}\left(2A_0(t) - \frac{t-1}{2}\right)\sin\frac{x}{2} + \frac{2}{\pi}(1-2t)\times \qquad (6.3)$$

$$\times \sin\frac{3x}{2} + \frac{1}{\pi}(t-1)\sin\frac{5x}{2},$$

whose kernel has the form

$$K(x,y) = \sum_{n=1}^{\infty} \frac{1}{n}\sin\left(n+\frac{1}{2}\right)x \sin\left(n+\frac{1}{2}\right)y.$$

Having found $\varphi(x,t)$ at the given $A_0(t)$, it is possible to calculate the coefficients in the representation (6.2) by the formulas

$$A_n(t) = \frac{2n+1}{2n}\int_{\theta_0(t)}^{\pi} \varphi(y,t) \times$$

$$\times \sin\left(n+\frac{1}{2}\right)y\,dy$$

and then to find $A_0(t)$ from the equation

$$\int_{\theta_0(t)}^{\pi} \varphi(y,t)\sin\frac{y}{2}\,dy = 0$$

It is evident that $\theta_0 \to 0$ when $t \to 0$. If in (6.3) it is assumed that $\theta_0 = 0$ it has an exact solution. This makes it possible to find the solution asymptotics for (6.3) at small θ_0:

$$\varphi(x,t) = \frac{4}{3\pi}(2t-1)\sin\frac{3x}{2} + \frac{4}{5\pi}(1-t)\times$$

$$\times \sin\frac{5x}{2} + O(\theta_0^4) \text{ when } t \to 0 \qquad (6.4)$$

The radial displacement of the liquid particle which is placed on the drop surface when $t=0$, is expressed by the formula

$$\Phi_r(1, \theta, t) = \frac{1}{2}\frac{\varphi(\theta_0(t), t)}{\sqrt{2(\cos\theta_0 - \cos\theta)}} +$$

$$+ \frac{1}{2}\int_{\theta_0(t)}^{\pi} \frac{\varphi_y(y, t)\,dy}{\sqrt{2(\cos y - \cos\theta)}} +$$

$$+ \left(\frac{1}{2} - t\right)P_1(\cos\theta) - \frac{1}{2}(t-1)P_2(\cos\theta),$$

where $\theta > \theta_0(t)$. From here it is evident that only under the condition

$$\varphi(\theta_0(t), t) = 0 \qquad (6.5)$$

the liquid particles couldn't penetrate through the solid surface $r\cos\theta = t - 1$. A posteriori it is checked that the condition (6.5) is also sufficient for a fulfilment of the one - side displacement inequality. Using (6.4) and (6.5), it is possible to obtain

$$\theta_0(t) = \sqrt{\frac{2t}{2}} + O(t^{3/2}) \text{ when } t \to 0$$

Following from the representation (6.2) and formula (0.5), we calculate the pressure in the contact area. In dimensional variables we have

$$p = \frac{3\gamma V^2}{\pi \sqrt{2(\cos\theta - \cos\theta_0)}} + O(1),$$

when $t \to 0$, $0 \le \theta < \theta_0(t)$ and $r=1$. Integrating the expression for the contact area pressure, we find the impact force dependence F on time when $t \to 0$:

$$F = 6\gamma (3a^3 Vt)^{1/2} + O(t)$$

7. Conclusive commentaries.

A quantitative information on the collision process of liquid massed and solid surfaces can be obtained only from numerical calculations.

However, the calculation accuracy is essentially discreased at the moments, when the flow topology is changes, the pressure field singularities or infinite accelarations of liquid particles are induced, etc. The analytical methods of distinguishing such type singularities were suggested above.

In most analytical and numerical investigations of the phenomena under consideration [9-12] the model of an ideal compressible fluid is used. The work [13] dealt with the numerical calculation of the problem of the drop impact onto a plane in the assumption of fluid incompressibility is an exception to this rule. The effects of gravity and surface tension aren't taken into account. As results from the works cited the compressibility effect tells within a rather small time interval as long as the shock front doesn't go outside the contact area. As the experiments show [14], the integral characteristics of the blunt body entrance into liquid are weakly affected by Mach number within the range $0 \le M \le 0.75$.

In conclusion it should be noted that there can exist another approach to investigation of the linearized submergence problem based on reducing it to a variational inequality [15]. The problem of an simple solvability of the inequality is non-trivial due to the flow region unboundedness and non-coercitivity entering into the inequality of bi - linear form. In the case of bounded flow region (e.g., for a drop falling onto a plane) a variational statement gives the theorem of existence and uniqueness of a solution, as well as method for its numerical construction.

References

1. Wagner H. Uber Stoss und Gleitvorgänge an der Oberfläche von Flüssigkeiten. 1932, Band 12, Heft 4, ZAMM, s.193-215.
2. Schmieden C. Der Aufschlag von Rotationskörpern auf eine Wasseroberfläche. 1953, Band 33, Heft 4, ZAMM, s.147-151.
3. Nalimov, V.L., Pukhnachov, V.V. Unsteady motions of free-boundary ideal liquid. Novosibirsk, 1975.
4. Lavrentjev, M.A., Shabat, B.V. Methods for functions theory of complex variable. Moscow, "Nauka", 1965.
5. F.D.Cole. Perturbation Methods in Applied Mathematics. Blaisdell Publ. Company. London, 1968.
6. Nalimov, V.I. New model of Cauchy-Poisson problem. "Dinamika sploshnoi sredy", Novosibirsk, 1972, 12 p.86-123.
7. H.Bateman, A.Erdelyi. Higher Transcendental Functions. Vol.3, Mc Graw-Hill Book Company. New York, 1955.
8. Ufland, Ja.S. Method of paired equations in problems of mathematical physics. Leningrad, 1977.

9. Heymann F.J. High-Speed impact between a liquid drop and a solid surface. J.of Applied physics, v.40, N13, p.5113-5122.
10. Skalak R., Feit D. Impact on the surface of a compressible fluid. Trans.ASME. J.Engng Industry,1966, Ser. B 88, No2.
11. Gorshkov A.G., Grigoljuk E.I.Problem of impact of elastic rotationary shells onto incompressible fluid. In: "Kolebania uprugih konstruktsii S Zhidkostju", Novosibirsk, 1973, p.16-27.
12. Gonor,A.L., Jakovlev, V.Ja. On some results of the theory of drop impact onto a solid body. In: "Struinye i otryvnye techeniia" Institute of Mechanics, Moscow State University, 1979, p.70-75.
13. Petrenko,V.E. On calculation methods for viscous incompressible liquid flow with great deformations. In: "Kolebaniia uprugih konstruktsii s zhidkostju", Novosibirsk, 1973, p.145-152.
14. Heroshin, V.A., Romanenko,N.I., Serebryakov,I.V. Jakimov,Ji.A. Hydrodynamical forces at an impact of blunt bodies onto surface of compressible liquid. Izv.Acad. Nauk SSSR, Ser.MZG, N6,1980,p.44-51.
15. Duvant G., Lions J.-L. Les inéquations en mécanique et en physique. Dunod, Paris, 1972.

DISCUSSION
of the paper
by V.V. Pukhnachov and A.A. Korobkin

INITIAL ASYMPTOTICS IN PROBLEM OF BLUNT BODY ENTRANCE INTO LIQUID

Discussion
by J.C.W. Rogers

I submit this discussion following the paper of V.V. Pukhnachov and A.A. Korobkin, as it describes results for the initial asymptotics in the case when at the moment of impact, the rigid body surface and the water surface have in common a surface Σ (as would be the case, for example, if the rigid body had a flat bottom and fell onto a flat surface). In such a case the appropriate hydrodynamic flow in a nonclassical (energy-dissipating) flow which satisfies generalized Euler equations. The energy which has been lost is assumed to have been dissipated by turbulence. For example, suppose the water is initially quiescent, Σ is flat, and the rigid body of mass M initially has a speed V and is moving in the direction of the inner normal to the water surface at Σ. We can define an added mass M_a as the density of the water times the integral over Σ of θ, where the Laplancian of θ is 0 inside the water, θ is 0 on the water surface except for Σ, and the derivative of θ in the direction of the outer normal to the water surface is 1 on Σ. The decrease in the total energy of the rigid body and water upon impact is

$$\frac{1}{2} V^2 \frac{M_a M^2}{(M_a+M)^2}$$

In actuality, collisions of rigid bodies with water surfaces in which, at the moment of initial impact, the rigid body and water have a common surface Σ of positive (nonzero) measure will occur with probability 0. However, there may occur cases such that this "almost" happens, for which a cavity is formed between the water and rigid body and subsequently collapses, all in a short time interval. The hydrodynamic flows describing such cases are also nonclassical and satisfy the generalized Euler equations. The energy lost to turbulence in these situations may be expected to be given approximately by the expression above.

Authors' reply

The decrease in total energy of the body and water upon impact is a very difficult problem, and it seems to be doubtful this expression is satisfactory for quantity of dissipating energy. The energy is dissipated because of viscosity and turbulence. A part of the energy is spent on shock wave in water. Therefore, expression for dissipating energy must contain characteristics of this phenomena.

Moreover, in our opinion, distribution of pressure on blunt body bottom is more important characteristics for practice than amount of dissipating energy.

A air layer may be formed between a solid body bottom and free surface of liquid when the body falls onto free surface [1, 2]. This lead to an essential change of entry process characteristics. Theoretical papers are concerned mainly with falling solid flat plates onto the free surface of an ideal incompressible liquid. The process may be divided into two parts. In the first stage a air flow is formed when the flat plate approaches to the free surface. This air flow deforms the free surface before the plate touches liquid. Formed cavity is closed in the moment when the plate edges reach the deformed free surface. In the second stage air in the cavity is compressed and the cavity is submerged with body into liquid. Thus the body transferces energy to water through the air layer. A size of hydrodynamic pressure on the body bottom depends on characteristics of the air layer.

However, this air layer is important only for the flat body bottom and only in definite scope of body velocities [3].

1 Verhagen, J.H.G., The impact of a flat plate on a water surface. Int. Ship. Res., 1967, 11, n° 4, 211-223.

2 Fujita, Y., On the impulsive pressure of a circular plate falling upon a water surface J. Soc.-Nav. Archit. Japan, 1954, 94, 105-110.

3 Laumbach, D., Impact shock on a blunt-nosed missile striking water with its axis, normal to the water surface. Dallas, Sept., 1964, SC-TM-64-987.

LIST OF PARTICIPANTS

AANESLAND, VIDAR, Norwegian Institute of Technology, Trondheim, Norway
AUCHER, MAX, Bassin d Essais des Carènes, Paris, France
BABA, EIICHI, Mitsubishi Heavy Industries, Nagasaki, Japan
BAI, KWANG JUNE, David W. Taylor Naval Ship Research and Development Center, Bethesda, U S A.
BAKER, GREGORY R., Massachusetts Institute of Technology, Cambridge, U S.A.
BAUBEAU, ROBERT, Bassin d'Essais des Carènes, Paris, France
BERHAULT, CHRISTIAN, Institut Français du Pétrole, Rueil-Malmaison, France
BERTRAND, JEAN-PAUL, Bassin d'Essais des Carènes, Paris, France
BINDEL, SERGE, Direction des Recherches, Études et Techniques, Paris, France
BORLETEAU, JEAN-PAUL, S.A Franlab Informatique, Rueil-Malmaison, France
BOUGIS, JEAN, École Nationale Supérieure de Mécanique, Nantes, France
BOURIANOFF, GEORGE I., Austin Research Associates, Austin, U S.A.
BOVIS, ALAIN, Bassin d'Essais des Carènes, Paris, France
BRATU, CHRISTIAN, Institut Français du Pétrole, Paris, France
BRESLIN, J P., Stevens Institute of Technology, Hoboken, U S A.
BREVIG, PER, Norwegian Institute of Technology, Trondheim, Norway
BRIDGES, THOMAS J , Texas A. & M. University, College Station, U S.A.
CHABROLIN, BRUNO, C.T.I C M , Puteaux, France
CHUITON, ANDRÉ, Bassin d'Essais des Carènes, Paris, France
CLEMENT, ALAIN, E.N.S T.A., Paris, France
COLEMAN, RODERICK M , David W. Taylor Naval Ship Research and Development Center, Bethesda, U S A.
COOPER, RALPH D., Flow Research Company, Silver Spring, U S.A.
CRANCE, COME, Bassin d'Essais des Carènes, Paris, France
DAGAN, GEDEON, Tel Aviv University, Tel Aviv, Israel
DARCHE, MICHEL. Société ECA, Meudon-Bellevue, France
DAUBE, O , Laboratoire d'Informatique pour la Mécanique et les Sciences, Orsay, France
DAUBERT, ODILE, Laboratoire National d'Hydraulique, E.D F , Chatou, France
DAUBISSE, JEAN-CLAUDE, École Nationale Supérieure de Mécanique, Nantes, France
DAVID, GEORGES, Bassin d'Essais des Carènes, Paris, France
DELHOMMEAU, GÉRARD, École Nationale Supérieure de Mécanique, Nantes, France
DEMANCHE, JEAN-FRANÇOIS, Bassin d'Essais des Carènes, Paris, France
DENNIS, STANLEY C.R., University of Western Ontario, London, Canada
DERN, JEAN-CLAUDE, Bassin d'Essais des Carènes, Paris, France
DOCTORS, L.J , University of New South Wales, Kensington, Australia
DUC, JEAN-MICHEL, Direction des Recherches, Études et Techniques, Paris, France
DULIEU, ANNIE, Laboratoire d'Informatique pour la Mécanique et les Sciences, Orsay, France
DUPRIEZ, FRANCIS, Institut de Mécanique des Fluides, Lille, France
EGGERS, KLAUS, Institut für Schiffbau der Universität Hamburg, Hamburg, West Germany
ERUYZLU, NUMAN E., Canadian Coast Guard, Ottawa, Canada
EUVRARD, DANIEL, École Nationale Supérieure de Techniques Avancées, Palaiseau, France
FEIFEL, W.M., Boeing Marine Systems, Seattle, U S.A.
FERNANDEZ, GILLES, Bassin d'Essais des Carènes, Paris, France
FEUILLET, JACQUES, Électricité de France, Chatou, France
FRANCESCUTTO, ALBERTO, Istituto di Architettura Navale, Rome, Italy
FRANKS, CHARLES B., David W. Taylor Naval Ship Research and Development Center, Bethesda, U S.A.

GAROT, CATHERINE, C.I.S.I., Gif-sur-Yvette, France
GEER, JAMES, S.U.N.Y., Binghamton, U.S.A.
GHIA, K.H., University of Cincinnati, Cincinnati, U.S.A.
GHIA, URMILA, University of Cincinnati, Cincinnati, U.S.A.
GIOVACHINI, JEAN-LUC, Institut de Recherche des Transports, Arcueil, France
GLEISSNER, GENE H., David W. Taylor Naval Ship Research and Development Center, Bethesda, U.S.A.
GOMEZ, PEDRO, Sener, Sistemas Marinos S.A., Madrid, Spain
GRASES, JORGE, Sener, Tecnica Industrial Y Naval, S.A., Las Arenas, Spain
GUÉVEL, PIERRE, École Nationale Supérieure de Mécanique, Nantes, France
GUTTMAN, C., École Nationale Supérieure de Techniques Avancées, Paris, France
HALL, D.R., University of Illinois, Urbana, U.S.A.
HAUSSLING, HENRY J., David W. Taylor Naval Ship Research and Development Center, Bethesda, U.S.A.
HEARN, GRANT E., University of Newcastle-upon-Tyne, Newcastle-Upon-Tyne, Great Britain
HERNANDEZ, PIERRE, Bassin d'Essais des Carènes, Paris, France
HIMENO, YOJI, University of Osaka, Osaka, Japan
HOLLOCOU, YANN, Service Technique des Phares et Balises, Paris, France
HSIUNG, CHI-CHAO, Memorial University of Newfoundland, St Johns, Canada
HUYSMANS, R.H.M., Netherlands Ship Model Basin, Wageningen, The Netherlands
IKEDA, YOSHIHO, University of Osaka Prefecture, Osaka, Japan
INNIS, GEORGES, Science Applications, Inc., La Jolla, U.S.A.
JACOBSEN, BENT KOFEO, Danish Ship Research Laboratory, Lyngby, Denmark
JAMI, A., École Nationale Supérieure de Techniques Avancées, Palaiseau, France
JAUNET, J.P., Bureau Véritas, Paris, France
JONAS, WOLFGANG, Technical University of Berlin, Berlin, West Germany
JOUAILLEC, FRANÇOIS, Direction des Recherches, Études et Techniques, Paris, France
KAJITANI, HISASHI, University of Tokyo, Tokyo, Japan
KANSCHINE, ANDRÉ, Service Technique des Phares et Balises, Paris, France
KARPPINEN, TUOMO, Espoo, Finland
KELLER, J.B., Stanford University, Stanford, U.S.A.
KIM, SEA HEON, Massachusetts Institute of Technology, Cambridge, U.S.A.
KORVING, CORNELIS, Delft University of Technology, Delft, The Netherlands
KOSTILAINEN, VALTER, Helsinki University of Technology, Helsinki, Finland
KUDO, K., Hiroshima University, Hiroshima, Japan
LAHALLE, DOMINIQUE, École Nationale Supérieure des Techniques Avancées, Palaiseau, France
LAMBERTI, BERTRAND, Bassin d'Essais des Carènes, Paris, France
LASSABLIÈRE, JACQUES, Det Norske Veritas, Hovik, Norway
LAURENT, ALAIN, Office National d'Études et de Recherches Aérospatiales, Châtillon sur-Bagneux, France
LE BONNIEC, BERNARD, Bassin d'Essais des Carènes, Paris, France
LEDUCQ, DANIEL, Bertin et Cie, Plaisir, France
LEE, CHOUNG M., David W. Taylor Naval Ship Research and Development Center, Bethesda, U.S.A.
LE GOFF, JEAN-PIERRE, Direction des Recherches, Études et Techniques, Paris, France
LE GUET, PIERRE-LOÏC, Bassin d'Essais des Carènes, Paris, France
LENOIR, M., École Nationale Supérieure de Techniques Avancées, Palaiseau, France
LEPEIX, ROGER, Chantiers de l'Atlantique, Saint-Nazaire, France
LE ROY, JACQUES, Bassin d'Essais des Carènes, Paris, France
LIAPIS, NICOLAS, Norwegian Hydrodynamic Laboratories, Trondheim, Norway
LICHT, CHRISTIAN, Institut Français du Pétrole, Paris, France
LOESER, DOUGLAS, Science Applications, Inc., La Jolla, U.S.A.
LUGT, HANS J., David W. Taylor Naval Ship Research and Development Center, Bethesda, U.S.A.
MA, Y.C., TRW Defense and Space Systems Group, Redondo Beach, U.S.A.
MANRY, DANIEL, Groupe d'Études Sous-marines de l'Atlantique, Paris, France
MARCOUYGUX, SYLVAIN, Bassin d'Essais des Carènes, Paris, France
MARTIN, D.U., TRW Defense and Space Systems Group, Redondo, U.S.A.
MARTIN, PAUL ANDREW, University of Manchester, Manchester, Great Britain
MATHISEN, JAN, Det Norske Veritas, Hovik, Norway
McCARTHY, JUSTIN, David W. Taylor Naval Ship Research and Development Center, Bethesda, U.S.A.
McCORMICK, STEVE, Colorado State University, Fort Collins, U.S.A.
McGREGOR, ROBERT CHARLES, Glasgow University, Glasgow, Great Britain
McLEAN, J.W., TRW Defense and Space Systems Group, Redondo Beach, U.S.A.
MEIRON, D.I., Massachusetts Institute of Technology, Cambridge, U.S.A.
MIYATA, HIDEAKI, University of Tokyo, Tokyo, Japan
MOHAN, MARTIN, Technical University of Berlin, Berlin, West Germany
MORAN, D.D., U.S. Naval Academy, Annapolis, U.S.A.
MULLER, JEAN, Chantiers Navals de La Ciotat, La Ciotat, France

MURTHY, T., C M L. Publications, Southempton, Great Britain
NABERGOJ, RADOSLAV, Istituto di Architettura Navale, Roma, Italy
NIELSEN, JACK N., Nielsen Engineering and Research, Inc., Mountain View, U.S.A.
ODABASI, AHMET YUCEL, British Ship Research Association, London, Great Britain
OHMATSU, SHIGEO, Ship Research Institute, Tokyo, Japan
OMNES, YVES, Bassin d'Essais des Carènes, Paris, France.
OOMEN, JOE, Netherlands Ship Model Basin, Wageningen, The Netherlands
ORSZAG, S.A., Massachusetts Institute of Technology, Cambridge, U S.A.
OSORIO, ALFONSO, Las Arenas, Spain
PAPANIKOLAOU, APOSTOLOS, Technical University of Berlin, Berlin, West Germany
PAQUET, JEAN-BERNARD, Institut de Mécanique des Fluides, Lille, France
PAROT, JEAN-MARC, Metravib, Ecully, France
PELLONE, C., Institut de Mécanique de Grenoble, Grenoble, France
PETTERSEN, BJONAR, Skipsmodelltanken, Trondheim, Norway
PIAZZOLI, GÉRARD, Office National d'Études et de Recherches Aérospatiales, Châtillon-sur-Bagneux, France
PUKHNACHOV, VLADISLAV V., Lavrentjev Institute of Hydrodynamics, Novosibirsk, U S S R.
RAVEN, HOYTE, Netherlands Ship Model Basin, Wageningen, The Netherlands
ROGERS, JOËL, Johns Hopkins University, Laurel, U S A.
ROWE, A., Institut de Mécanique de Grenoble, Grenoble, France
SAFFMAN, P G., TRW Defense and Space Systems Group, Redondo Beach, U S.A.
SAKAGUCHI, Y., Bridgestone Tir C°, Ltd, Dusseldorf, West Germany
SALAÜN, P., Office National d'Études et de Recherches Aérospatiales, Châtillon-sur Bagneux, France
SANDBERG, WILLIAM, Naval Sea Systems Command, Washington, U S.A.
SANDER, CALISAL, University of British Columbia, Vancouver, Canada
SAYER, PHILIP, University of Strathclyde, Glasgow, Great Britain
SCHMIECHEN, MICHAEL, Berlin Model Basin, Berlin, West Germany
SCHMIED, LOYS, Service Technique des Phares et Balises, Paris, France
SCHMITT, JACQUES, Institut Français du Pétrole, Rueil-Malmaison, France
SCHOT, JOANNA W., David W. Taylor Naval Ship Research and Development Center, Bethesda, U S.A.
SCLAVOUNOS, PAUL, Massachusetts Institute of Technology, Cambridge, U S.A.
SHIN, C.T., University of Cincinnati, Cincinnati, U S.A.
SHOAFF, RAY L., David W. Taylor Naval Ship Research and Development Center, Bethesda, U S.A.
SÖDING, HENRICH, Institut für Schiffbau, Hamburg, West Germany
STEWART, STEPHEN E., Southwest Research Institute, San Antonio, U S.A.
SULMONT, PATRICE, École Nationale Supérieure de Mécanique, Nantes, France
SUZUKI, A., University of Tokyo, Tokyo, Japan
SUZUKI, K, National Defense Academy, Yokosuka, Japan
TAYLOR, EATOCH, University College London Mechanical, London, Great Britain
TAYLOR, THOMAS D, Johns Hopkins University, Laurel, U S A.
TENNANT, JEFFREY S., Florida Atlantic University, Boca Raton, U S.A.
THOMAS, J.W., Colorado State University, Fort Collins, U S A.
THOMSEN, PETER, Hamburg, West Germany
TINKER, SIMON JONATHAN, Admiralty Marine Technology Establishment, Haslar, Gosport, Great Britain
URAM, EARL M., Earl M. Uram Associates, Delray Beach, U S A.
VADA, TORGEIR, University of Oslo, Oslo, Norway
VALLIER, P, Ateliers et Chantiers de Bretagne, Nantes, France
VANDEN-BROECK, J.-MARC, Stanford University, Stanford, U.S.A.
VAN ESELTINE, RICHARD T., David W. Taylor Naval Ship Research and Development Center, Bethesda, U S A.
VARSAMOV, KIRIL, Bulgarian Ship Hydrodynamics Centre, Varna, Bulgaria
VASSORT, CHARLES, Bassin d'Essais des Carènes, Paris, France
VELLUET, MARCEL, Direction des Recherches, Études et Techniques, Paris, France
VIGNAT, PHILIPPE, Neyrtec, Alsthom-Atlantique, Grenoble, France
VINJE, TOR, University of Trondheim, Trondheim, Norway
WEHAUSEN, JOHN, University of California, Berkeley, U S.A.
WEISS, JEAN-PIERRE, S N.A.C.R P., La Rochelle-Pallice, France
WHITEHEAD, ROBERT, Office of Naval Research, Arlington, U.S.A.
YEN, SHEE-MANG, University of Illinois, Urbana, U.S.A.
YEUNG, R.W, Massachusetts Institute of Technology, Cambridge, U S.A.
YIM, BOHYUN, David W. Taylor Naval Ship Research and Development Center, Bethesda, U.S.A.
YUEN, H C., TRW Defense and Space Systems Group, Redondo Beach, U S.A.
ZLATEV, PETER, Bulgarian Ship Hydrodynamics Centre, Varna, Bulgaria

INDEX TO AUTHORS AND DISCUSSERS

Names of discussers and the corresponding numbers of pages are in italic type

Baba, E. 9
Bai, K.J. 449
Baker, G R. 179
Baubeau, R. 387
Bougis, J. 517
Bourianoff, G I. 249, *284*
Breslin, J.P. 427
Brevig, P. 257
Bridges, T.J. 269

Chapman, R B. 237
Coleman, R.M.

Daube, O. 73
Daubisse, J.C. 551
Demanche, J.F. 533
Doctors, L.J. *376, 413,* 559
Dulieu, A. 73

Eatock-Taylor, R. 209
Eggers, K. 109, 463
Euvrard, J. 151, 193, *386*

Feifel, W.M. 365
Fernandez, G. 94
Franks, C.B. 319

Geer, J. 498
Ghia, K.N. 133
Ghia, U. 133

Hall, D R. 163
Haussling, H J. 111, 121
Hearn, G.E. *94,* 209, *445*
Himeno, Y. 335

Ikeda, Y. 335

Jami, A. 193, 211

Kajitani, H. 37
Keller, J.B. 97
Kim, S.H. 499
Korobkin, A.A. 579
Kudo, K. 347

Leclerc, J. 379
Lee, C M. *53, 256, 267, 376,* 465, *531*
Lenoir, M. *94,* 193
Lepeix, R. 444
Licht, C. 221
Lugt, H.J. 297

Ma, Y.C. 285
Martin, D. 193
Martin, D.U. 285
Martin, P.A. *209,* 543
McCormick, S 359
McLean, J.W. 285
Melron, D1: 179, *317*
Miyata, H. 37, *71, 131*
Mori, K. 53

Oomen, A. 27
Orszag, S.A. 179

Papanikolaou, A. 267
Pellone, C. 399
Pukhnachov, V.V. 579

Raven, H.C. 53
Rogers, J.C.W. 592
Rowe, A. 399

Saffman, P.G. 285
Salaün, P. 379
Sclavounos, P.D. *109,* 481
Shin, C.T. 133
Shoaff, R L. 319
Söding, H. 415
Suzuki, A. 37
Suzuki, K. 83

Thomas, J.W. 359
Thomsen, P. 256, 267, 425

Ursell, F. 209, 233, 543

Vallier, P. 517
Vanden-Broeck, J.C. 97, *294*
Van Eseltine, R.T. 121, *177*
Varsamov, K. 413
Vinje, T. 257

Wehausen, J.V. 147

Yen, S.M. *119, 131, 163, 358*
Yeung, R.W. 499
Yim, B. 55
Yuen, H.C. 285